ICAROB 2017

PROCEEDINGS OF THE 2017 INTERNATIONAL CONFERENCE ON ARTIFICIAL LIFE AND ROBOTICS

January 19-22, 2017
Seagaia Convention Center, Miyazaki, JAPAN
International Meeting Series

Editor-in-Chief
Masanori Sugisaka
Editors: Yingmin Jia, Takao Ito, Ju-Jang Lee
ISBN 978-4-9908350-2-6

Proceedings of The 2017 International Conference on

ARTIFICIAL LIFE AND ROBOTICS

(ICAROB2017)

January 19-22, 2017
Seagaia Convention Center, Miyazaki, JAPAN
International Meeting Series

Editor-in-Chief
Masanori Sugisaka
Editors: Yingmin Jia, Takao Ito, Ju-Jang Lee
ISBN 978-4-9908350-2-6

Contents

SPONSERED

AROB (ALife Robotics Corporation Ltd.)

ORGANIZED BY

International Steering Committee of International Conference on Artificial Life and Robotics (ICAROB)

TECHNICAL Co-SPONSORED BY

IEEE Fukuoka Section (Japan)

IEEE Robotics and Automation Society (USA)

CO-ORGANIZED BY

University of Miyazaki, Japan

Chinese Association for Artificial Intelligence (CAAI, P. R. China)

SUPPORTRD BY

Miyazaki Prefectural Government

ADVISORY COMMITTEE CHAIR

Moshe Kam (New Jersy Institute of Technology, Former IEEE President, USA)

ADVISORY COMMITTEE

Adam Grzech (Wroclaw University of Technology, Poland)
Bruce Eisenstein (Drexel University, Former IEEE President, USA)
Fumio Harashima (Former The University of Tokyo, Japan)
Guang-Ren Duan (Harbin Institute of Technology, P.R.China)
Hidenori Kimura (JST, Japan)
Jeffrey Johnson (The Open University, UK)
Jerzy Świątek (Wroclaw University of Technology, Poland)
Joshua M. Epstein (The Johns Hopkins University, USA)
Kai-Tai Song (National Chiao Tung University, Taiwan)
Kazuhiko Terashima (Toyohashi University of Technology, Japan)
Kazuo Kyuma (Mitsubishi Electric Corporation, Japan)
Masayoshi Tomizuka (University of California Berkeley, USA)
Moshe Kam (New Jersey Institute of Technology, Former IEEE President, USA)
Paul Kalata (Drexel University, USA)
Paul Oh (Drexel University, USA)
Robert Fischl (Drexel University, USA)
Steen Rasmussen (University of Southern Denmark, Denmark)
Toshio Fukuda (Meijyo University, Japan)
ZengqiSun (Tsighua University, P.R. China)

GENERAL CHAIR

Masanori Sugisaka (Alife Robotics Corporation Ltd., Japan)
(Visiting Professor, Open University, UK)

CO-GENERAL CHAIRS

Yingmin Jia (Beihang Univesty, P. R. China)
Takao Ito (Hiroshima University, Japan)
Ju-Jang Lee (KAIST, Korea)

VICE GENERAL CHAIR

Changshui. Zhang (Tinghua University, P. R. China)
Henrik. H. Lund (Technical University of Denmark, Denmark)
John. L. Casti (International Institute for Applied Systems Analysis, Austria)
Jangmyung Lee (Pusan National University, Korea)
Luigi Pagliarini (Technical University of Denmark, Denmark)
(Academy of Fine Arts of Macerata, Italy)
Mohd Rizon bin Mohamed Juhari (National Culture Arts and Heritage Academy, Malaysia)
Yongguang Zhang (Academia Sinica, P. R. China)

PROGRAM CHAIRMAN

Makoto Sakamoto (University of Miyazaki, Japan)

CO-PROGRAM CHAIR

Marion Oswald (The Vienna University of Technology, Austria)

INTERNATIONAL ORGANIZING COMMITTEE

Akira Fukuda (Kyushu University, Japan)
Eiji Hayashi (Kyushu Institute of Technology, Japan)
Evgeni Magid (Kazan Federal University, Russia)
Hazry Desa (University of Malaysia, Perlis, Malaysia)
Hidehiko Yamamoto (Gifu University, Japan)
Hideyuki Suzuki (The University of Tokyo, Japan)
Hiroki Tamura (The University of Miyazaki, Japan)
Hiroshi Kage ((Mitsubishi Electric Corporation, Japan)
Hiroshi Matsuno (Yamaguchi University, Japan)
Jiwu Wang (Beijing Jiaotong University, P. R. China)

Jovana Jovic (CNRS-AIST JRL, Japan, France)
Katsunori Shimohara (Doshisha University, Japan)
Kenichi Tanaka (Meii University, Japan)
Kenji Hashimoto (Waseda University, Japan)
Kevin Voges (Canterbury University, New Zealand)
Kohei Ohtsu (Tokyo University of Marine Science and Technology, Japan)
Kuo-Hsien Hsia (Far East University, Taiwan)
Kuo-Lan Su (National Yunlin University of Science and Technology, Taiwan)
Kyungho Park (Director for Micro-System Programs, RDECOM, ITC-PAC, U.S. ARMY, Japan and USA)
Masao Kubo (National Defense Academy of Japan, Japan)
Masanao Obayashi (Yamaguchi University, Japan)
Mehta Rajiv (New Jersey Institute of Technology, USA)
Peter Sapaty (Ukrainian Academy of Science, Ukraine)
Qu Yanbin (Harbin Institute of Technology, P. R. China)
Takashi Kohno (LIMMS/CNRS-IIS, Institute of Industrial Science, The University of Tokyo, Japan)
Takashi Ogata (Iwate Prefectural Univerity)
Teruhisa Hochin (Kyoto Prefectural University, Japan)
Tetsuro Hattori (Kagawa University, Japan)
Thi Thi Zin (University of Miyazaki, Japan)
Thomas S. Ray (University of Oklahoma, USA)
Toru Yamamoto (Hiroshima University, Japan)
Victor Berdonosov (Komsomolsk-on-Amur State University of Technology, Russia)
Yasunari Yoshitomi (Kyoto Prefectural University, Japan)
Yo Horikawa (Kagawa University, Japan)
Yoshifumi Morita (Nagoya Institute of Technology, Japan)
Yoshiro Imai (Kagawa University, Japan)
Yuichi Tanji (Kagawa University, Japan)

INTERNATIONAL PROGRAM COMMITTEE

Akira Nakamura (AIST, Japan)
Ali Selamat (University of Technology of Malaysia (UTM), Malaysia)
Arsit Boonyaprapasorn (Chulachomkloa Royal Military Academy, Thailand)
Bin Fu (Shanghai Jiaotong University, P. R. China)
Dongmei Ai (University of Science and Technology Beijing, P. R. China)
Endra Joelianto (Bandung Institute of Technology, Indonesia)
Fengzhi Dai (Tianjin University of Science & Technology, P. R. China)
Haruna Matsushita (Kagawa University)
Hidetsugu Suto (Muroran Institute of Technology, Japan)
Hiroyuki Iizuka (Osaka University, Japan)
Huailin Zhao (Shanghai Institute of Technology, P. R. China)
Hussein Abbass (University of New South Wales and ADFA, Australia)
Istvan Harmati (Budapest Institute of Technology and Economics, Hungary)

Ivan Tanev (Doshisha University, Japan)
Jiandong Zhao (Beijing Jiaotong University, P. R. China)
Jinglu Hu (Waseda University, Japan)
Joono Cheong (Korea University, Korea)
Kathryn Elizabeth Merrick (University of New South Wales and ADFA, Australia)
Kunikazu Kobayashi (Aichi Prefectural University, Japan)
Manabu Yamada (Nagoya Institute of Technology, Japan)
Masahide Ito (Aichi Prefectural University, Japan)
Malachy Eaton (University of Limerick, Ireland)
Masayoshi Kano (Chukyou University, Japan)
Masayoshi Tabuse (Kyoto Prefectural University, Japan
Masaomi Hatakeyama (University of Zurich, Switzerland)
Norrima Mokhtar (University of Malaya, Malaysia)
Noritaka Sato(Nagoya Institute of Technology, Japan)
Palakorn Tantrakool (King Mongkut's Institute of Technology Thonburi, Thailand)
Satoshi Ikeda (The University of Miyazaki, Japan)
Sanjay S. Joshi (College of Engineering, University of California, USA)
Seong-Ik Han (Pusan National University, Korea)
Shingo Mabu (Yamaguchi University, Japan)
Shyi-Ming Chen (National Taichung University of Education, Taiwan)
Takashi Kuremoto (Yamaguchi University, Japan)
Takayoshi Yamada (Gifu University, Japan)
Taishiro Kishimoto (Keio University, Japan)
Tao Zhang (Tsinghua University, P. R. China)
Takashi Iwamoto (Mitsubishi Electric Corporation, Advanced Technology R&D Center, Japan)
Tetsuro Katayama (The University of Miyazaki, Japan)
Thunyaseth Sethaput (Thammasat University, Thailand)
Toshinori Nawata (Kumamoto National College of Technology, Japan)
Tsunehiro Yoshinaga (Tokuyama National College of Technology, Japan)
Weicun Zhang (University of Science and Technology Beijing, P. R. China)
Yuanyuan Shang (Capital Normal University, P. R. China)
Yueyue Fan (University of California-Davis, USA)
Young Im Cho (The University of Suwon, Korea)

LOCAL ARRANGEMENT COMMITTEE

Makoto Sakamoto (University of Miyazaki,
Japan) Masanori Sugisaka (ALife Robotics Corporation Ltd., Japan)
(Visiting Professor, Open University, UK)
Satoshi Ikeda (University of Miyazaki, Japan)
Takao Ito (Hiroshima University, Japan)
Tetsuro Katayama (University of Miyazaki, Japan)

HISTORY

The International Conference on Artificial Life and Robotics (ICAROB) resulted from the AROB-symposium (International Symposium on Artificial Life and Robotics) whose first edition was held in 1996 and the eighteenth and last edition in 2013. The AROB symposium was annually organized by Oita University, Nippon Bunri University (NBU), and ALife Robotics Corporation Ltd., under the sponsorship of the Science and Technology Policy Bureau, the Ministry of Education, Science, Sports, and Culture (Monbusho), presently, the Ministry of Education, Culture, Sports, Science, and Technology (Monkasho), Japanese Government, Japan Society for the Promotion of Science (JSPS), the Commemorative Organization for the Japan World Exposition ('70), Air Force Office of Scientific Research, Asian Office of Aerospace Research and Development (AFOSR/AOARD), USA. I would like to express my sincere thanks to not only Monkasho (annually fund support from 1996 to 2013) but also JSPS, the Commemorative Organization for the Japan World Exposition ('70), and various other Japanese companies for their repeated support. The old symposium (this symposium has been held every year at B-Con Plaza, Beppu, Oita, Japan except in Oita, Japan (AROB 5th ’00) and in Tokyo, Japan (AROB 6th ’01).) was organized by the International Organizing Committee of AROB and was co-operated by the Santa Fe Institute (USA), RSJ, IEEJ, ICASE (Now ICROS) (Korea), CAAI (P. R. China), ISCIE, IEICE, IEEE (Japan Council), JARA, and SICE. The old AROB-symposium expanded much by absorbing much new knowledge and technologies into it. This history and character of the former AROB symposiums are passed on the current ICAROB conference and to this journal, International Journal of Robotics, Networking and Artificial Life (JRNAL). From now on, ALife Robotics Corporation Ltd. is in charge of management of both the conference and the journal. The future of the ICAROB is brilliant from a point of view of yielding new technologies to human society in the 21st century. This conference invites you all.

AIMS AND SCOPE

The objective of this conference is the development of new technologies for artificial life and robotics which have been recently born in Japan and are expected to be applied in various fields. This conference presents original technical papers and authoritative state-of-the-art reviews on the development of new technologies concerning robotics, networking and artificial life and, especially computer-based simulation and hardware for the twenty-first century. This conference covers a broad multidisciplinary field, including areas such as:

Artificial intelligence & complexity
Artificial living
Artificial mind research
Artificial nervous systems for robots
Artificial sciences
Bipedal robot
Brain science and computing
Chaos
Cognitive science

Computational Molecular biology
Computer graphics
Data mining
Disasters robotics
DNA computing
Empirical research on network and MOT
Environment navigation and localization
Evolutionary computations
Facial expression analysis, music recommendation and augmented reality
Foundation of computation and its application
Fuzzy control
Genetic algorithms
Human-welfare robotics
Image processing
Insect-like aero vehicles
Intelligence in biological systems
Intelligent control
Management of technology
Medical surgical robot
Micro-machines
Multi-agent systems
Nano-biology
Nano-robotics
Networking
Neural circuits
Neuro-computer
Neuromorphic Systems
Neuroscience
Pattern recognition
Quantum computing
Reinforcement learning system & genetic programing
Robotics
Software development support method
System cybernetics
Unmanned underwater vehicles
Unmanned Aerial Systems Technologies
Unmanned Aerial Systems designing, controls and navigation
Unmanned Aero vehicles
Virtual reality
Visualization
Hardware-oriented submissions are particularly welcome. This conference will discuss new results in the field of artificial life and robotics

COPYRIGHTS

Accepted papers will be published in the proceeding of The 2017 International Conference on Artificial Life and Robotics (ICAROB 2017) by ALife Robotics Corp. Ltd. Copyright belongs to ALife Robotics Corp. Ltd. Some of high quality papers in the proceeding will be requested to re-submit their papers for the consideration of publication in an international journal ROBOTICS, NETWORKING AND ARTIFICIAL LIFE under agreement of both Editor-in- Chief Dr. Masanori Sugisaka and 3 reviewers. All correspondence related to the conference should be addressed to ICAROB Office.

ICAROB Office

ALife Robotics Corporation Ltd.
3661-8 Oaza Shimohanda, Oita 870-1112, JAPAN
TEL/FAX：+81-97-597-7760
E-MAIL：
icarob@alife-robotics.co.jp
Home Page：http://alife-robotics.co.jp/

MESSAGES

Masanori Sugisaka
General Char

(Professors, Open University (UK), University of Malaysia-Peris (Malaysia) and President of Alife Robotics Co., Ltd. (Japan))

Masanori Sugisaka

Masanori Sugisaka

General Chair of ICAROB

It is my great honor to invite you all to The 2017 International Conference on Artificial Life and Robotics (ICAROB 2017).
This Conference is changed as the old symposium from the first (1996) to the Eighteenth (2013) annually which were organized by Oita University, Nippon Bunri University(NBU), and ALife Robotics Corporation Ltd. under the sponsorship of the Science and Technology Policy Bureau, the Ministry of Education, Science, Sports, and Culture (Monbusho), presently, the Ministry of Education, Culture, Sports, Science, and Technology (Monkasho), Japanese Government, Japan Society for the Promotion of Science (JSPS), The Commemorative Organization for the Japan World Exposition ('70), Air Force Office of Scientific Research, Asian Office of Aerospace Research and Development (AFOSR/AOARD), USA. I would like to express my sincere thanks to not only Monkasho (annually fund support from 1996 to 2013) but also JSPS, the Commemorative Organization for the Japan World Exposition ('70) , Japanese companies for their repeated support.
The old symposium was organized by International Organizing Committee of AROB and was co-operated by the Santa Fe Institute (USA), RSJ, IEEJ, ICASE (Now ICROS) (Korea), CAAI (P. R. China), ISCIE, IEICE, IEEE (Japan Council), JARA, and SICE. The old AROB symposium was growing up by absorbing many new knowledge and technologies into it.
This history and character was inherited also from ICAROB 2014(The 2014 International Conference on Artificial Life and Robotics, included a series of ICAROB proceedings in **SCOPUS** and **CPCI** now. From now on, ALife Robotics Corporation Ltd. is in charge of management. This year we have The 2017 International Conference on Artificial Life and Robotics (ICAROB2017) (22nd AROB Anniversary). The future of The ICAROB is brilliant from a point of view of yielding new technologies to human society in 21st century.
I hope that fruitful discussions and exchange of ideas between researchers during Conference (ICAROB2017) will yield new merged technologies for happiness of human beings and, hence, will facilitate the establishment of an international joint research institute on Artificial Life and Robotics in future.

Yingmin Jia
Co-General Chair
(Professor, Beihang University, R .P. China)

Yingmin Jia

Co-General Chair of ICAROB

It is my great pleasure to invite you to The 2017 International Conference on Artificial Life and Robotics (ICAROB 2017), in Miyazaki, Japan from Jan. 19th to 22nd, 2017.

ICAROB develops from the AROB that was created in 1996 by Prof. Masanori Sugisaka and will celebrate her birthday of 22nd years old in 2017. Doubtless, new mission and big challenges in the field of artificial life and robotics will promote ICAROB to start a new stage and attract wide interests among scientist, researchers, and engineers around the world.

For a successful meeting, many people have contributed their great efforts to ICAROB. Here, I would like to express my special thanks to all authors and speakers, and the meeting organizing team for their excellent works.

Looking forward to meeting you at ICAROB in Miyazaki and wishing you enjoy your stay in Japan.

Takao Ito
Co-General Chair
(Professor Hiroshima University, Japan)

Takao Ito

Co General Chair of ICAROB

It is my great honor to invite you all to The 2017 International Conference on Artificial Life and Robotics (ICAROB 2017). This Conference is changed as the old symposium from the first (1996) to the Eighteenth. I am pleased to welcome you to The 2017 International Conference on Artificial Life and Robotics in the wonderful city of Miyazaki City, Miyazaki Prefecture, Japan. The ICAROB has its long history. The former organization of the ICAROB was developed under the strong leadership of the President, famous Professor Masanori Sugisaka, the father of AROB. We gathered many researchers, faculty members, graduate students from all over the world, and published many high-quality proceedings and journals every year.
Over the years, dramatic improvements have been made in the field of artificial life and its applications. The ICAROB has becoming the unifying the exchange of scientific information on the study of man-made systems that exhibit the behavioral characteristic of natural living systems including software, hardware and/or wetware. Our conference shapes the development of artificial life, extending our empirical research beyond the territory circumscribed by life-as-we-know-it and into the domain of life-as-it-could–be. It will provide us a good place to present our new research results, excellent ideas, and valuable information about artificial intelligence, complex systems theories, robotics, management of technology, etc.
The conference site is Seagaia Convention Center, one of the most famous resort hotels in Japan. You can find many fantastic scenic spots and splendid historical places in Miyazaki city. Enjoy your stay and take your time to visit the city of Miyazaki.
I am looking forward to meeting you in Miyazaki during the ICAROB 2017 and to sharing a most pleasant, interesting and fruitful conference.

Ju-Jang Lee
Co-General Chair
(Professor, KAIST)

Ju-Jang Lee

Co-General Chair of ICAROB

The First International Conference on Artificial Life and Robotics (ICAROB) was held in Oita City, Oita, Japan from Jan. 11th to 13th, 2014. This year's Conference will be held amidst the high expectation of the increasingly important role of the new interdisciplinary paradigm of science and engineering represented by the field of artificial life and robotics that continuously attracts wide interests among scientist, researchers, and engineers around the globe.

Distinguished researchers and technologists from around the world are looking forward to attending and meeting at ICAROB. ICAROB is becoming the annual excellent forum that represents a unique opportunity for the academic and industrial communities to meet and assess the latest developments in this fast growing artificial life and robotics field. ICAROB enables them to address new challenges, share solutions, discuss research directions for the future, exchange views and ideas, view the results of applied research, present and discuss the latest development of new technologies and relevant applications.

In addition, ICAROB offers the opportunity of hearing the opinions of well-known leading experts in the field through the keynote sessions, provides the bases for regional and international collaborative research, and enables to foresee the future evolution of new scientific paradigms and theories contributed by the field of artificial life and robotics and associated research area. The twenty-first century will become the century of artificial life and intelligent machines in support of humankind and ICAROB is contributing through wide technical topics of interest that support this direction.

It is a great honor for me as a Co-General Chair of the 4th ICAROB 2017 to welcome everyone to this important event. Also, I would like to extend my special thanks to all authors and speakers for contributing their research works, the participants, and the organizing team of the 4th ICAROB.

I'm looking forward to meeting you at the 4th ICAROB in Miyazaki City, Miyazaki Prefecture and wishing you all the best.

GENERAL SESSION TOPICS

GS1 Artificial Neural Network & Bio-Signal Controlled Robotics (3)	GS2 Automated Guided Vehicles I (6)
GS3 Automated Guided Vehicles II (3)	GS4 Biological Systems (4)
GS5 Filtering & Control Systems (2)	GS6 Human-Welfare Robotic System & Medical Application (5)
GS7 Micro-Machines & Robotics I (6)	GS8 Micro-Machines & Robotics II (3)
GS9 Neuromorphic Robotic Systems (5)	GS10 Reinforcement & Evolutionary Computations (3)
GS11 Others (12)	

ORGANIZED SESSION TOPICS

OS1 Informational Narratology and Automated Content Generation (5)	OS2 Intelligence Control Systems and Applications I (6)
OS3 Intelligence Control Systems and Applications II (6)	OS4 Human-In-The-Loop (HITL) Systems (4)
OS5 Human Interface and Content Security (5)	OS6 Software Development Support Method (6)
OS7 Advances in Marine Robotics and Applications (6)	OS8 Multiagent systems and Reality Mining (4)
OS9 Theory and Implementation of Neuromorphic Systems (5)	OS10 Biological Signal Sensing Technology, Device and Its Applications (5)
OS11 Robot Control and Localization (4)	OS12 Machine Learning and Its Applications (4)
OS13 Intelligent Control (6)	OS14 Advanced Control (5)
OS15 Recognition and Control (8)	OS16 Image Recognition and Chaotic Systems (8)
OS17 Natural Computing and Biology (4)	OS18 Advanced Management and Technology (4)
OS19 Kansei Engineering and Applications (4)	OS20 Image Processing and Computer Graphics (6)
OS21 Computer Science and Information Processing (5)	OS22 Robotic Technology for Competition (4)

1/19(Thu.) 17:30-19:30	Welcome Party (Conference Site: Gibraltar)
1/19(Thu.) - 1/22(Sun.)	ICAROB Secretariat
1/22(Sun.) 16:45-17:15	Farewell Party (Conference Site: Gibraltar)

TIME TABLE (1/20)

1/20(Fri.)	Fountain Room (A1) 2nd F	Orchard Room (A2) 2nd F, N	Orchard Room (A3) 2nd F, S
8:40-	Registration		
9:00-10:15	OS14 Advanced Control (5)	GS6 Human-Welfare Robotic System & Medical Application (5)	OS15 Recognition and Control (8) & OS16 Image Recognition and Chaotic Systems (8)
10:15-10:30	Coffee break		
10:30-11:00	Opening Ceremony (Fountain Room (A1) 2nd F)		
11:10-12:10	Chair: Takao Ito Invited session IS-2, IS-4 (Fountain Room (A1) 2nd F) Henrik Hautop Lund		
12:10-13:10	Lunch		
13:10-13:50	Chair: Jangmyung Lee Invited session IS-1 (Fountain Room (A1) 2nd F) Luigi Pagliarini		
13:50-14:10	Invited session IS-3 (Fountain Room (A1) 2nd F) Ismael Baira Ojeda		
14:10-14:30	Coffee break		
14:30-16:00	OS3 Intelligence Control Systems and Applications (II) (6)	OS5 Human Interface and Content Security (5)	GS7 Micro-Machines & Robotics I (6)
16:00-16:20	Coffee break		
16:20-17:50	OS2 Intelligence Control Systems and Applications (I) (6)	OS9 Theory and Implementation of Neuromorphic Systems (5)	OS7 Advances in Marine Robotics and Applications (6)

TIME TEBLE (1/21)

1/21(Sat.)	Fountain Room (A1) 2nd F	Orchard Room (A2) 2nd F, N	Orchard Room (A3) 2nd F, S
8:40-	Registration		
9:00-11:00	OS6 Software Development Support Method (6)	GS2 Automated Guided Vehicles I (6)	OS4 Human-In-The-Loop (HITL) Systems (4) & OS11 Robot Control and Localization (4)
11:00-11:15	Coffee break		
11:15-12:00	GS5 Filtering & Control Systems (2)	GS8 Micro-Machines & Robotics II (3)	GS1 Artificial Neural Network and Bio-Signal Controlled Robotics (3)
12:00-13:00	Lunch		
13:00-14:00	Chair: Yingmin Jia Plenary Speech PS1(Fountain Room (A1) 2nd F) Kazuo Ishii		
14:00-14:20	Coffee break		
14:20-15:50	OS20 Image Processing and Computer Graphics (6)	OS13 Intelligent Control (6)	OS8 Multiagent systems and Reality Mining (4)
15:50-16:10	Coffee break		
16:10-17:25	GS9 Neuromorphic Robotic Systems (5)	OS22 Robotic Technology for Competition (4)	GS4 Biological Systems (4)
18:00-20:00	Banquet: Tenzui (4th F)		

TIME TABLE (1/22)

1/22(Sun.)	Fountain Room (A1) 2nd F	Orchard Room (A2) 2nd F, N	Orchard Room (A3) 2nd F, S
8:50-	Registration		
9:10-10:25	OS10 Biological Signal Sensing Technology, Device and Its Applications (5)	OS19 Kansei Engineering and Applications (4)	OS1 Informational Narratology and Automated Content Generation (5)
10:25-10:40	Coffee break		
10:40-11:40	Chair: Makoto Sakamoto Plenary Speech PS2 (Fountain Room (A1) 2nd F) Tomoyuki Nishita		
11:40-13:00	Lunch		
13:00-13:50	Chair: Takao Ito Invited session IS-5 (Fountain Room (A1) 2nd F) Peter Sapaty		
13:50-14:10	Coffee break		
14:10-15:10	OS18 Advanced Management and Technology (4)	OS17 Natural Computing and Biology (4)	OS12 Machine Learning and Its Applications (4)
15:10-15:30	Coffee break		
15:30-16:45	GS10 Reinforcement & Evolutionary Computations (3)	GS3 Automated Guided Vehicles II (3)	OS21 Computer Science and Information Processing (5)
Farewell Party (16:45-17:15)			

The 2017 International Conference on ARTIFICIAL LIFE AND ROBOTICS (ICAROB2017)

January 19 (Thursday)

17:30-19:30 Welcome Party (Conference Site: Gibraltar 2nd F)

January 20 (Friday)

10:30-11:00

Opening Ceremony (Fountain Room (A1) 2nd F)

Chair: Marion Oswald (The Vienna University of Technology, Austria)

Welcome Addresses

1. General Chairman of ICAROB	Masanori Sugisaka (ALife Robotics Corporation Ltd. Japan)
2. Co-General Chairman of ICAROB	Yingmin Jia (Beihang University, China)
3. Co-General Chairman of ICAROB	TaKao Ito (Hiroshima University, Japan)
4. Vice General Chair of ICAROB	Henrik Hautop Lund (Technical University of Denmark, Denmark)
5. Vice General Chair of ICAROB	Jangmyung Lee (Pusan National University, South Korea)

January 21 (Saturday)

Banquet: Tenzui (4th F)

18:00-20:00

Chair: T. Ito (Hiroshima University, Japan)

Welcome Addresses

Prof. Yingmin Jia (Beihang University, P.R. China.)

Prof. Jang-Myung Lee (Pusan National University, South Korea)

Prof. Marion Oswald (The Vienna University of Technology, Austria)

Prof. Saori Iwanaga (Japan Coast Guard Academy, Japan)

TECHNICAL PAPER INDEX

January 20 (Friday)

08:40-Registration

Fountain Room (A1) 2nd F
9:00-10:15 OS14 Advanced Control (5)
Chair: Yingmin Jia (Beihang University, P.R. China)
Co-Chair: Weicun Zhang (University of Sciences and Technology Beijing, P.R. China)

OS14-1 *Targeting Chaos System via Minimum Principle Control*
Yunzhong Song, Ziyi Fu, Fuzhong Wang (Henan Polytechnic University, P.R.China,)

OS 14-2 *Three-dimensional Leader-Follower Formation Flocking of Multi-Agent System*
Yongnan Jia, Weicun Zhang (University of Sciences and Technology Beijing, China)

OS14-3 *Leader-follower Formation Control of Mobile Robots with Sliding Mode*
Wenhao Zheng and Yingmin Jia (Beihang University, P.R.China)

OS14-4 H_∞ *Containment Control for Nonlinear Multi-agent Systems with Parameter Uncertainties and Communication Delays*
Ping Wang[1], Yingmin Jia[2] ([1] North China Electric Power University, [2]Beihang University, P.R.China)

OS14-5 *Stochastic Resonance in an Array of Dynamical Saturating Nonlinearity with Second-Order*
Yumei Ma, Lin Zhao, Zhenkuan Pan and Jinpeng Yu*(Qingdao University , P.R.China)

10:30-11:00 Opening Ceremony
Chair: Marion Oswald (The Vienna University of Technology, Austria)

11:10-12:10
Invited session IS-2, IS-4
Chair: Takao Ito (Hiroshima University, Japan)

IS-2 *Playware ABC: Engineering Play for Everybody*
Henrik Hautop Lund (Technical University of Denmark, Denmark)

IS-4 *Playware ABC2: a Disruptive Technology for Global Development*
Henrik Hautop Lund (Technical University of Denmark, Denmark)

13:10-13:50

Invited session IS-1

Chair: Jang-Myung Lee (Pusan National University, South Korea)

IS-1 *The future of Robotics Technology*.
Luigi Pagliarini [1,2], Henrik Hautop Lund [1] ([1] Technical University of Denmark, Denmark, [2] Academy of Fine Arts of Macerata, Italy)

13:50-14:10

Invited session IS-3

Chair: Jang-Myung Lee (Pusan National University, South Korea)

IS-3 *A combination of Machine Learning and Cerebellar models for the Motor Control and Learning of a Modular Robot*
Ismael Baira Ojeda, Silvia Tolu, Moisés Pachecho, David Johan Christensen and Henrik Hautop Lund (Technical University of Denmark, Denmark)

14:30-16:00 OS3 Intelligence Control Systems and Applications II (6)

Chair: Chian C. Ho (National Yunlin University of Science & Technology, Taiwan)

Co-Chair: Chia-Nan Ko (Nan Kai University of Technology, Taiwan)

OS3-1 *Image Compression Using Hybrid Evolution Based Takagi-Sugeno Fuzzy Neural Network*
[1]Chia-Nan Ko and [2]Ching-I Lee ([1,2] Nan Kai University of Technology, Taiwan)

OS3-2 *MQPSO Algorithm Based Fuzzy PID Control for a Pendubot System*
[1]Li-Chun Lai, [2]Yu-Yi Fu, and [3]Chia-Nan Ko ([1]National Pingtung University, [2,3]Nan Kai University of Technology, Taiwan)

OS3-3 *A Sensorless Ultra-High Speed Motor Driver*
Chung-Wen Hung, Yan-Ting Yu, Bo-Kai Huang, Wei-Lung Mao (National Yunlin University of Science and Technology, Taiwan)

OS3-4 *Android-Based Patrol Robot Featuring Automatic Vehicle Patrolling and Automatic Plate Recognition*
Chian C. Ho, Shih-Jui Yang, Jian-Yuan Chen, Chang-Yun Chiang, and Hsin-Fu Chen (National Yunlin University of Science and Technology, Taiwan)

OS3-5 *Adaptive CMAC Filter for Chaotic Time Series Prediction*
Wei-Lung Mao, Suprapto, Chung-Wen Hung (National Yunlin University of Science and Technology, Taiwan)

OS3-6 *Surface Defect Detection for Anodized Aluminum Tube Based on Automatic Optical Inspection*
Hsien-Huang P. Wu and Hsuan-Min Sun
(National Yunlin University of Science and Technology, Taiwan)

16:20-17:50

OS2 Intelligence Control Systems and Applications I (6)

Chair: Kuo-Hsien Hsia (Far East University, Taiwan)

Co-Chair: Kuo-Lan Su (National Yunlin University of Science & Technology, Taiwan)

OS2-1 *Develop Low Cost IoT Module with Multi-Agent Method*
Jr-Hung Guo, Kuo-Hsien Hsia, Kuo-Lan Su
(National Yunlin University of Science and Technology, Taiwan)

OS2-2 *Based on Short Motion Paths and Artificial Intelligence Method for Chinese Chess Game*
Chien-Ming Hung, Jr-Hung Guo, Kuo-Lan Su
(National Yunlin University of Science and Technology, Taiwan)

OS2-3 *Design and Implementation of the SCARA Robot Arm*
Jian-Fu Weng, Bo-Yi Li, Kuo-Lan Su
(National Yunlin University of Science and Technology, Taiwan)

OS2-4 *Transmission Power Control for Wireless Sensor Network*
Kuo-Hsien Hsia[1], Chung-Wen Hung[2], Hsuan T. Chang, Yuan-Hao Lai[2]
([1]Far East University, Taiwan, [2]National Yunlin University of Science and Technology, Taiwan)

OS2-5 *Mechanism of Autonomous Mowing Robot for Long Grass*
Kuo-Hsien Hsia[1], Yao-Shing Huang[2], Kuo-Lan Su[2] and Jr-Hung Guo[2]
([1]Far East University, Taiwan, [2]National Yunlin University of Science and Technology, Taiwan)

OS2-6 *Design of Optimal Position Controller for Three-Phase Brushless DC Motor Applying Adaptive Sliding Mode Control*
Tai-Huan Tsai, Mei-Yung Chen (National Taiwan Normal University, Taiwan)

Orchard Room (A2) 2nd F, N

9:00-10:15 GS6 Human-Welfare Robotic System & Medical Application (5)

Chair:

GS6-1 *Virtual surgery system with realistic visual effects and haptic interaction*
Vlada Kugurakova, Murad Khafizov, Ruslan Akhmetsharipov, Alexei Lushnikov, Diana Galimova, Vitaly Abramov (Kazan Federal University, Russia),
Omar Correa Madrigal (University of Informatic Sciences, Cuba)

GS6-2 *A Human Reaching Movement Model for Myoelectric Prosthesis Control*
Go Nakamura[*1, 5], Taro Shibanoki[*2], Yuichiro Honda[*1], Futoshi Mizobe[*3], Akito Masuda[*4], Takaaki Chin[*1], Toshio Tsuji[*5], [*1](Robot Rehabilitation Center in The Hyogo institute of Assistive Technology, Japan), [*2](Ibaraki University, Japan), [*3](Hyogo Rehabilitation Center, Japan) [*4](Kinki Gishi Corporation, Japan), [*5](Hiroshima University, Japan)

GS6-3 *Re-creation of a membrane puncture's sense of an object constituted of liquid and an outer membrane by a haptic device and a deformation simulation of the virtual objects*
Takahiro Okada, Eiji Hayashi (Kyusyu Institute of Technology, Japan)

GS6-4 *Exercise classification using CNN with image frames produced from time-series motion data*
Hajime Itoh, Naohiko Hanajima, (Muroran Institute of Technology, Japan), Yohei Muraoka, Makoto Ohata, (Steel Memorial Muroran Hospital, Japan), Masato Mizukami, Yoshinori Fujihira, (Muroran Institute of Technology, Japan)

GS6-5 *Proposal and Evaluation of the Gait Classification Method using Arm Acceleration Data and Decision Tree*
Kodai Kitagawa, Yu Taguchi, Nobuyuki Toya
(National Institute of Technology, Kushiro Collage, Japan)

14:30-16:00 OS5 Human Interface and Content Security (5)
Chair: Yasunari Yoshitomi (Kyoto Prefectural University, Japan)
Co-Chair: Masayoshi Tabuse (Kyoto Prefectural University, Japan)

OS5-1 *A Method for Secure Communication Using a Discrete Wavelet Transform for Audio Data and Improvement of Speaker Authentication*
Kouhei Nishimura, Yasunari Yoshitomi, Taro Asada, and Masayoshi Tabuse
(Kyoto Prefectural University, Japan)

OS5-2 *A Recipe Decision Support System Using Knowledge Information and Agent*
Keita Saito, Taro Asada, Yasunari Yoshitomi, Ryota Kato, and Masayoshi Tabuse
(Kyoto Prefectural University, Japan)

OS5-3 *A System for Analyzing Facial Expression and Verbal Response of a Person While Answering Interview Questions on Video*
Taro Asada, Yasunari Yoshitomi, and Masayoshi Tabuse (Kyoto Prefectural University, Japan)

OS5-4 *Real-Time System for Horizontal Asymmetry Analysis on Facial Expression and Its Visualization*
Ryoichi Shimada, Taro Asada, Yasunari Yoshitomi, and Masayoshi Tabuse
(Kyoto Prefectural University, Japan)

OS5-5 *Development of Mouse System for Physically Disabled Person by Face Movement Using Kinect*
Junpei Miyachi, Masayoshi Tabuse (Kyoto Prefectural University, Japan)

16:20-17:35 OS9 Theory and Implementation of Neuromorphic Systems (5)
Chair: Takashi Kohno (The University of Tokyo, Japan)
Co-Chair: Takuya Nanami (The University of Tokyo, Japan)

OS9-1 *Implementation of Multi-FPGA Communication using Pulse-Coupled Phase Oscillators*
Dinda Pramanta, Takashi Morie, Hakaru Tamukoh (Kyushu Institute of Technology, Japan)

OS9-2 *Multi-Valued Quantization Convolutional Neural Networks toward Hardware Implementation*
Yoshiya Aratani, Yoeng Jye Yeoh, Daisuke Shuto, Takashi Morie, Hakaru Tamukoh
(Kyushu Institute of Technology, Japan)

OS9-3 *An Improved Parameter Value Optimization Technique for the Reflectionless Transmission-Line Model of the Cochlea*
Takemori Orima and Yoshihiko Horio (Tohoku University, Japan)

OS9-4 *A parameter optimization method for Digital Spiking Silicon Neuron model*
Takuya Nanami and Takashi Kohno (The University of Tokyo, Japan)

OS9-5 *A Multistage Heuristic Tuning Algorithm for an Analog Silicon Neuron Circuit*
Ethan Green and Takashi Kohno (The University of Tokyo, Japan)

Orchard Room (A3) 2nd F, S

9:00-10:15 OS15 Recognition and Control (8)
Chair: Fengzhi Dai (Tianjin University of Science and Technology, China)
Co-Chair: Hongtao Zhang (Tianjin University of Science and Technology, China)

OS15-1 *Integral Design of Intelligent Home Equipment*
Yuxing Ouyang [1], Fengzhi Dai [1*], Yiqiao Qin [1], Ce Bian [1], Bo Liu [2], Hongwei Jiao [3] ([1] Tianjin University of Science & Technology, [2] Inner Mongolia University, [3] Tianjin Technology School of Printing and Decoration, China)

OS15-2 *Research on Underwater Robot Recognition*
Binhu Song[1], Fengzhi Dai[1]*, Qijia Kang[1], Haifang Man[1], Hongtao Zhang[1], Long Li[2], Hongwei Jiao[3] ([1] Tianjin University of Science and Technology, [2] Tianjin Electric Locomotive Co., Ltd, [3] Tianjin Technology School of Printing & Decoration, China)

OS15-3 *Design of Intellectual Vehicles with Path Memorizing Function*
Yiqiao Qin [1], Fengzhi Dai [1*], Yuxing Ouyang [1], Baochang Wei [1], Simini Chen [2], Hongwei Jiao [3]
([1] Tianjin University of Science & Technology, [2] Palace Museum, [3] Tianjin Technology School of Printing & Decoration, China)

OS15-4 *Action Recognition based on Binocular Vision*
Yiwei Ru [1,2,*], Hongyue Du [1], Shuxiao Li [2], Hongxing Chang [2] ([1] Harbin University of Science and Technology, China, [2] Institute of Automation Chinese Academy of Sciences, China)

OS15-5 *Analysis and Control of a Novel 4D Chaotic System*
Hong Niu (Tianjin University of Science and Technology, China)

OS15-6 *Analysis of a three-dimensional chaotic system and its FPGA implementation*
Hefei Li [*], Xianghui Hu (Tianjin University of Science and Technology, China)

OS15-7 *Image Encryption Based on Fractional-order Chaotic Model of PMSM*
Wei Xue [*], Mei Zhang, Shilong Liu, Xue Li (Tianjin University of Science and Technology, China)

OS15-8 *The Application of a Novel Fractional Hyper-chaotic in Image Encryption*
Wei Xue [*], Shilong Liu, Mei Zhang, Xue Li (Tianjin University of Science and Technology, China)

OS16 Image Recognition and Chaotic Systems (8)

Chair: Huailin Zhao (Shanghai Institute of Technology, China)
Co-Chair: Shunzhou Wang (Shanghai Institute of Technology, China)

OS16-1 *A Method of Detecting Abnormal Crowd Behavior Events Applied in Patrol Robot*
Huailin Zhao, Shunzhou Wang, Shifang Xu, Yani Zhang (Shanghai Institute of Technology, China), Masanori Sugisaka (ALife Robotics Corp. Ltd, Japan)

OS16-2 *Design of the Multi-Car Collaboration System*
Huailin Zhao, Yangguang Guo (Shanghai Institute of Technology, China)
Masanori Sugisaka (ALife Robotics Corp. Ltd, Japan)

OS16-3 *Research on an Algorithm of the Character Recognition with Self-learning the Recognition Errors*
Huailin Zhao, Yawei Hou, Shifang Xu, Congdao Han (Shanghai Institute of Technology, China), Masanori Sugisaka (ALife Robotics Corp. Ltd, Japan)

OS16-4 *An Improved Method of the Power System Short Term Load Forecasting Based on the Neural Network*
Shunzhou Wang, Huailin Zhao, Yani Zhang, Peng Bai (Shanghai Institute of Technology, China)

OS16-5 *Improvement on LEACH Agreement of Mine Wireless Communication Network*
Liu Yun-xiang and Zhang Wei (Shanghai Institute of Technology, China)

OS16-6 *A New Four-Wing Chaotic System Generated by Sign Function*
Hongyan Jia, Shanfeng Wang, Yongjun Wu (Tianjin University of Science and Technology, China)

OS16-7 *A Three-Dimensional Chaotic System Generating Single-wing or Two-Wing Chaotic Attractors*
Hongyan Jia, Yongjun Wu, Shanfeng Wang (Tianjin University of Science and Technology, China)

OS16-8 *Circuit implementation of a new fractional-order hyperchaotic system*
Xuyang Wu, Hongyan Jia, Ning Bai, Weibo Jia
(Tianjin University of Science and Technology, China)

14:30-16:00 GS7 Micro-Machine & Robotics I (6)

Chair:

GS7-1 *Estimation and Categorization of Errors in Error Recovery Using Task Stratification and Error Classification*
Akira Nakamura[*1], Kazuyuki Nagata[*1], Kensuke Harada[*2] and Natsuki Yamanobe[*1]
([*1] National Institute of Advanced Industrial Science and Technology (AIST),
[*2] Osaka University, Japan)

GS7-2 *The Suitable Timing of Visual Sensing in Error Recovery Using Task Stratification and Error Classification*
Akira Nakamura[*1], Kazuyuki Nagata[*1], Kensuke Harada[*2] and Natsuki Yamanobe[*1]
([*1] National Institute of Advanced Industrial Science and Technology (AIST),
[*2] Osaka University, Japan)

GS7-3 *Hexapod Type MEMS Microrobot Equipped with an Artificial Neural Networks IC*
Kazuki Sugita, Taisuke Tanaka, Yuya Nakata, Minami Takato, Ken Saito, Fumio Uchikoba
(Nihon University, Japan)

GS7-4 *Heat Distribution of Current Output Type Artificial Neural Networks IC for the MEMS Microrobot*
Taisuke Tanaka, Yuya Nakata, Kazuki Sugita, Minami Takato, Ken Saito, Fumio Uchikoba
(Nihon University, Japan)

GS7-5 *AGV with Mind and its production simulations for autonomous decentralized FMSs*
Masato Chikamatsu, Hidehiko Yamamoto, Takayoshi Yamada (Gifu University, Japan)

GS7-6 *UNARM System to Decide Units Locations of Cell-type Assembly Machines with Robots Arms*
Hirotaka Moribe, Hidehiko Yamamoto and Takayoshi Yamada (Gifu University, Japan)

16:20-17:50 OS7 Advances in Marine Robotics and Applications (6)
Chair: Kazuo Ishii (Kyushu Institute of Technology, Japan)
Co-Chair: Keisuke Watanabe (Tokai University, Japan)

OS7-1 *Development of a Hydraulic Underwater Manipulator for Deep-Sea Survey AUV*
Kazuo Ishii, Amir Ali Forough Nassiraei, Ivan Godler, Takashi Sonoda, Tharindu Weerakoon
(Kyushu Institute of Technology, Japan)

OS7-2 *Experiments of floatable UAV drone for wave dissipating block inspection(I)*
Keisuke Watanabe, Kazuho Mitsumura, Koshi Utsunomiya, Shiyun Takasaki
(Tokai University, Japan)

OS7-3 *Experiments of floatable UAV drone for wave dissipating block inspection(II)*
Keisuke Watanabe, Kazuho Mitsumura, Koshi Utsunomiya, Shiyun Takasaki
(Tokai University, Japan)

OS7-4 *Development of self-diagnostic system of an autonomous underwater vehicle Tuna-Sand 2*
Naoya Fujii, Yuya Nishida, Kazuo Ishii (Kyushu Institute of Technology, Japan)

OS7-5 *Development of Underwater Wireless Power Supply System Using resonant energy transfer*
Kazuo Ishii, Hidaka Shota, Keisuke Watanabe
(Kyushu Institute of Technology, Tokai University, Japan)

OS7-6 *Development of End-effector for Sampling-AUV "TUNA-SAND2"*
Kazuo Ishii, Takashi Sonoda, Atsushi Nishjima, Keisuke Watanabe
(Kyushu Institute of Technology, Tokai University, Japan)

January 21 (Saturday)

08:40-Registration

Fountain Room (A1) 2nd F

9:00-10:30 OS6 Software Development Support Method (6)

Chair: Tetsuro Katayama (University of Miyazaki, Japan)

Co-Chair: Tomohiko Takagi (Kagawa University, Japan

OS6-1 *Development of a Tool for Extended Place/transition Net-Based Mutation Testing*
Tomohiko Takagi[1], Shogo Morimoto[1], Tetsuro Katayama[2]
([1]Kagawa University, [2]University of Miyazaki, Japan)

OS6-2 *Improvement of Decision Table Automatic Generation Tool VDTable for let in Statement*
Yinuo Huang*, Tetsuro Katayama* Yoshihiro Kita†, Hisaaki Yamaba*, and Naonobu Okazaki*
(*University of Miyazaki, Japan, †Tokyo University of Technology, Japan)

OS6-3 *Prototype of Test Cases Automatic Generation Tool BWDM Based on Boundary Value Analysis with VDM++*
Hiroki Tachiyama*, Tetsuro Katayama* Yoshihiro Kita†, Hisaaki Yamaba*, and Naonobu Okazaki*
(*University of Miyazaki, Japan,†Tokyo University of Technology, Japan)

OS6-4 *Prototype of Refactoring Support Tool MCC Focusing on the Naming of Variables*
Satoshi Tanoue*, Tetsuro Katayama* Yoshihiro Kita†, Hisaaki Yamaba*, and Naonobu Okazaki*
(*University of Miyazaki, Japan,†Tokyo University of Technology, Japan)

OS6-5 *Improvement of Transitions and Flow Visualization TFVIS for Exception Handling.*
Takuya Sato*, Tetsuro Katayama*, Yoshihiro Kita†, Hisaaki Yamaba*, and Naonobu Okazaki*
(*University of Miyazaki, Japan,†Tokyo University of Technology, Japan)

OS6-6 *Automatically Business Decision Making System for Software Development by using CMMI*
Hnin Thandar Tun†, Tetsuro Katayama*, Kunihito Yamamori*, and Khine Khine Oo†
(*University of Miyazaki, Japan, †University of Computer Studies, Myanmar)

11:15-11:45 GS5 Filtering & Control Systems (2)

Chair:

GS5-1 *An Application of Collaborative Filtering in Student Grade Prediction*
Chaloemphon Sirikayon and Panita Thusaranon (Dhurakij Pundit University, Thailand)

GS5-2 *An improved detection method for railway fasteners*
Jiwu Wang[1], Yan Long[1], Masanori Sugisaka [2] (Beijing Jiaotong University, China[1], Alife Robotics Corporation Ltd, Japan and Open University, United Kingdom[2])

13:00-14:00

Plenary Speech PS1

Chair: Yingmin Jia (Beihang University, P.R. China)

PS1 *A New Tool to Access Deep-Sea Floor "Sampling-AUV"*

Kazuo Ishii, Takashi Sonoda, Yuya Nishida, Shinsuke Yasukawa and Tamaki Ura (Kyushu Institute of Technology, Japan)

14:20-15:50 OS20: Image Processing and Computer Graphics (6)
Chair: Thi Thi Zin (University of Miyazaki, Japan)
Co-Chair: Masayuki Mukunoki (University of Miyazaki, Japan)

OS20-1 *An effective method for detecting snatch thieves in video surveillance*
Hiroaki Tsushita[1], Thi Thi Zin[2] ([1, 2] University of Miyazaki, Japan)

OS20-2 *Color and Shape based Method for Detecting and Classifying Card Images*
Cho Nilar Phyo[1], Thi Thi Zin[2], Hiroshi Kamada[3], Takashi Toriu[4] ([1, 2] University of Miyazaki, Japan, [3] Kanazawa Institute of Technology, Japan [4] Osaka City University, Japan)

OS20-3 *Automatic Assessing Body Condition Score from Digital Images by Active Shape Model and Multiple Regression Technique*
Nay Chi Lynn, Thi Thi Zin, Ikuo Kobayashi (University of Miyazaki, Japan)

OS20-4 *General Image Categorization Using Collaborative Mean Attraction*
Hiroki Ogihara, Masayuki Mukunoki (University of Miyazaki, Japan)

OS20-5 *Consideration on the Photo-Realistic Rendering of Fruits by 3DCG*
Haruka Tsuboi[1], Makoto Sakamoto[1], Sho Yamada[1], Kensuke Ando[1], Chongyang Sun[1], Makoto Nagatomo[1], Koshiro Mitsuhashi[2], Yukari Kodama[2] ([1]University of Miyazaki, Japan, [2]Miyazaki Multimedia Academy, Japan)

OS20-6 *Consideration for the Possibility to the Tourism by the AR Technology*
Masamichi Hori[1], Makoto Sakamoto[1], Koshiro Mitsuhashi[2], Yukari Kodama[2], Takeshi Tanaka[1], Mihoko Fukushima[1], Chikashi Deguchi[1], Masahiro Yokomichi[1], Masayuki Mukunoki[1], Kunihito Yamamori[1], Atsushi Iiboshi[3] ([1]University of Miyazaki, Japan, [2]Miyazaki Multimedia Academy, Japan, [3]Takachiho Muratabi Co., Ltd., Japan)

16:10-17:25 GS9 Neuromorphic Robotic Systems (5)
Chair:

GS9-1 *Development of Cloud Actions for Seamless Robot Using Backpropagation Neural Network*
Wisanu Jitviriya[1], Jiraphan Inthiam[2] and Eiji Hayashi[3] ([1]King Mongkut’s University of Technology North Bangkok, Thailand, [2,3]Kyushu Institute of Technology, Japan)

GS9-2 *Mathematical modelling of human fear and disgust emotional reactions based on skin surface electric potential changes*
Gaisina Kristina and Gaisin Ruslan (Kazan Federal University, Russia)

GS9-3 *Neuromorphic Robot Dream: A Spike Based Reasoning System*
Alexander Toschev, Max Talanov (Kazan Federal University, Russia),
Alexander Tchitchigin (Innopolis University and Kazan Federal University, Russia),
Salvatore Distefano (Kazan Federal University, Russia)

GS9-4 *Development of Behavioral Robot using Imitated Multiplex Neurotransmitters System*
Saji Keita[1], Wisanu Jitviriya[2] and Eiji Hayashi[3] ([1,3] Kyushu Institute of Technology, Japan)
([2] King Mongkut's University of Technology North Bangkok, Thailand)

GS9-5 *Nonlinear Estimation Strategies Applied on an RRR Robotic Manipulator*
Jacob Goodman[1], Jinho Kim[1], Andrew S. Lee[1], S. Andrew Gadsden[1,2]
([1]University of Maryland, USA) ([2]University of Guelph, Canada)

Orchard Room (A2) 2nd F, N

9:00-10:30 GS2 Automated Guided Vehicles I (6)

Chair:

GS2-1 *Adaptive Negotiation-rules Acquisition Methods in Decentralized AGV Transportation Systems by Reinforcement Learning with a State Space Filter*
Masato Nagayoshi, Simon Elderton (Niigata College of Nursing)
Kazutoshi Sakakibara (Toyama Prefectural Univ.), Hisashi Tamaki (Kobe Univ.)

GS2-2 *Modeling and Control of a Quadrotor Vehicle Subject to Disturbance Load*
Jun Wang, Song Xin*, Yuxi Zhang (Beihang University, P. R. China)

GS2-3 *A multithreaded algorithm of UAV visual localization based on a 3D model of environment: implementation with CUDA technology and CNN filtering of minor importance objects*
Alexander Buyval, Mikhail Gavrilenkov (Bryansk State Technical University, Russia)
Evgeni Magid (Kazan Federal University, Russia)

GS2-4 *Modelling a crawler-type UGV for urban search and rescue in Gazebo environment*
Maxim Sokolov, Aidar Gabdullin, Roman Lavrenov, Ilya Afanasyev (Innopolis University, Russia), Leysan Sabirova, Evgeni Magid (Kazan Federal University, Russia)

GS2-5 *Development of Autonomous Robot for Laborsaving of the Forestry - Positioning of the Robot using IMU, GPS, and Encoder -*
Sho Yamana, and Eiji Hayashi (Kyushu Institute of Technology, JAPAN)

GS2-6 *Development of Autonomous Robot for Laborsaving of the Forestry - Detection of young plants by RGB and Depth Sensor -*
Nobuo Miyakawa and Eiji Hayashi (Kyushu Institute of Technology, Japan)

11:15-12:00 GS8 Micro-Machine & Robotics II (3)
Chair:

GS8-1 *Development of arm trajectory planning of Seamless Robot*
Teedanai Pramanpol, Eiji Hayashi (Kyushu Institute of Technology, Japan)

GS8-2 *Localization Method of Autonomous Moving Robot for Forest Industry*
Ayumu Tominaga, Eiji Hayashi (Kyushu Institute of Technology, Japan), Tsutomu Sasao (Meiji University, Japan)

GS8-3 *Dynamic Modeling and Motion Control of an RRR Robotic Manipulator*
Jinho Kim[1], Kevin Chang[1], Brian Schwarz[1], Andrew S. Lee[1], S. Andrew Gadsden[1,2]
([1]University of Maryland, USA), ([2]University of Guelph, Canada)

14:20-15:50 OS13: Intelligent Control (6)
Chair: Yingmin Jia (Beihang University (BUAA), P.R.China)
Co-Chair: Fuzhong Wang (Henan Polytechnic University, P.R.China)

OS13-1 *Modeling and Simulation for a Quadrotor Vehicle with Adaptive Wing*
Qunpo Liu ,Fuzhong Wang, Hongqi Wang, Jikai Si (Henan Polytechnic University, P.R.China)
Hanajima Naohiko (Muroran Institute of Technology, Japan)

OS13-2 *Fuzzy self-tuning PID control algorithm for belt conveyor driven by multi-motor*
Caixia Gao, Fuzhong Wang, Ziyi Fu (Henan Polytechnic University, P.R. China)

OS13-3 *Continuous Non-singular Fast Terminal Sliding Mode Control for an Active Gravity Field Simulator*
Jiao Jia, Yingmin Jia and Shihao Sun(Beihang University (BUAA), P.R.China)

OS13-4 *Weighted Multiple Model Adaptive Control for a Category of Systems with Colored Noise*
Yuzhen Zhang, Qing Li and Weicun Zhang
(University of Science and Technology Beijing, P. R. China)

OS13-5 *Neutral Networks-Based Adaptive Fixed-Time Consensus Tracking Control for Uncertain Multiple AUVs*
Lin Zhao[1,*], Yingmin Jia[2] and Jinpeng Yu[1]
([1]Qingdao University, P.R.China; [2] Beihang University (BUAA), P.R. China)

OS13-6 *Conducted electromagnetic interference prediction of the Buck Converter via Neural Networks*
Sumin Han, Fuzhong Wang (Henan Polytechnic University, P.R. China)

16:10-17:10 OS22 Robotic Technology for Competition (4)
Chair: Kazuo Ishii (Kyushu Institute of Technology, Japan)
Co-Chair: Keisuke Watanabe (Tokai University, Japan)

OS22-1 *Development of a Tomato Harvesting Robot*
Bingh Li, Shinsuke Yasukawa, Takashi Sonoda, Kazuo Ishii
(Kyushu Institute of Technology, Japan)

OS22-2 *Development of SOM algorithm for Relationship between Roles and Individual's Role in Rugby.*
2nd Reports: University Rugby teams analysis using Physical and Psychological data
Yasunori Takemura (Nishi Nippon Institute of Technology, Japan)

OS22-3 *Ball Dribbling Control for RoboCup Soccer Robot*
Shota Chikushi, Kenji Kimura, Kazuo Ishii
(Nippon-Bunri University, Kyushu Institute of Technology, Japan)

OS22-4 *Strategy Analysis of RoboCup Soccer Teams Using Self-Organizing Map*
Moeko Tominaga, Yasunori Takemura, Kazuo Ishii
(Kyushu Institute of Technology, NishiNippon Institute of Technology, Japan)

Orchard Room (A3) 2nd F, S
9:00-11:00 OS4 Human-In-The-Loop (HITL) Systems (4)
Chair: Toru Yamamoto (Hiroshima University, Japan)

OS4-1 *Feature Extraction for Digging Operation of Excavator*
Kazushige Koiwai*, Toru Yamamoto (Hiroshima University, Japan)
Takao Nanjo, Yoichiro Yamazaki, Yoshiaki Fujimoto (KOBELCO Construction Machinery CO., LTD. , Japan)

OS4-2 *Design of a Data-Oriented Kansei Feedback System*
Takuya Kinoshita and Toru Yamamoto (Hiroshima University, Japan)

OS4-3 Parameter Estimation of Skill Evaluation Model
Kazuo Kawada, Toru Yamamoto (Hiroshima University, Japan)

OS4-4 *Human Skill Quantification for Excavator Operation using Random Forest*
Hiromu Imaji, Kazushige Koiwai*, Toru Yamamoto (Hiroshima University, Japan)
Koji Ueda, Yoichiro Yamazaki, Yoshiaki Fujimoto (KOBELCO Construction Machinery CO., LTD. , Japan)

OS11 Robot Control and Localization (4)
Chair: Jang-Myung Lee (Pusan National University, South Korea)
Co-Chair: Min-Cheol Lee (Pusan National University, South Korea)

OS11-1 *Marker Recognition System for Localization of the Rover on the Lunar Space*
Na-Hyun Lee, Jang-Myung Lee (Pusan National University, South Korea)

OS11-2 *Dynamic Model and Finite-Time SMC and Backstepping Control of a Mabile Manipulator System*
Seongik Han, Hyunuk Ha, and Jangmyung Lee (Pusan National University, Korea)

OS11-3 *Bilateral Control of Hydraulic Servo System for 1DOF Master Slave Manipulator*
Jie Wang, Karam Dad and Min Cheol Lee (Pusan National University, Korea)

OS11-4 *Advanced impedance control of haptic joystick for effective mobile robot handling*
Gyung-I Choi, Jang-Myung Lee (Pusan National University, South Korea)

11:15-12:00 GS1 Artificial Neural Network and Bio-Signal Controlled Robotics (3)
Chair:

GS1-1 *Obstacle Avoidance Method for Electric Wheelchairs Based on a Multi-Layered Non-Contact Impedance Model*
Haruna Kokubo, Taro Shibanoki (Ibaraki University, Japan), Takaaki Chin (Hyogo Rehabilitation Center, Japan), and Toshio Tsuji (Hiroshima University, Japan)

GS1-2 *A Voice Signal-Based Manipulation Method for the Bio-Remote Environment Control System Based on Candidate Word Discriminations*
Taro Shibanoki (Ibaraki University, Japan), Go Nakamura, Takaki Chin (Hyogo Rehabilitation Center, Japan), and Toshio Tsuji (Hiroshima University)

GS1-3 *Experiments on classification of electroencephalography (EEG) signals in imagination of direction using Stacked Autoencoder*
Kenta Tomonaga, Takuya Hayakawa, Jun Kobayashi (Kyushu Institute of Technology, Japan)

14:20-15:20 OS8 Multiagent systems and Reality Mining (4)
Chair: Masao Kubo (National Defense Academy, Japan)
Co-Chair: Saori Iwanaga (Japan Coast Guard Academy, Japan)

OS8-1 *Influence of Partner Selection on Functional Differentiation:*
Emergence of Diversity by Isolated Interaction and Preference Change
Saori Iwanaga (Japan Coast Guard Academy, Japan),
Akira Namatame (National Defense Academy, Japan)

OS8-2 *Beacon-based tourist information system to identify visiting trends of tourists*
Akihiro Yamaguchi[1], Masashi Hashimoto[1], Kiyohiro Urata[1], Yu Tanigawa[1], Tetsuya Nagaie[1], Toshitaka Maki[1], Toshihiko Wakahara[1], Akihisa Kodate[2], Toru Kobayashi[3] and Noboru Sonehara[4] ([1] Fukuoka Institute of Technology, Japan) ([2] Tsuda College, Japan) ([3] Nagasaki University, Japan) ([4] National Institute of Informatics, Japan)

OS8-3 *Analysis of Survey on Employment Trends*
Masao Kubo, Hiroshi Sato (National Defense Academy, Japan),
Akihiro Yamaguchi (Fukuoka Institute of Technology, Japan),
Yuji Aruka (Chuo University, Japan)

OS8-4 *Direction switch behavior to enclose a target*
Masao Kubo, Nhuhai Phung, Hiroshi Sato (National Defense Academy, Japan),

16:10-17:10 GS4 Biological Systems (4)

Chair:

GS4-1 *Force and Motion Analysis of larval zebrafish (Danio rerio) using a body dynamics model*
Naohisa Mukaidani[1], Zu Soh[1], Shinichi Higashijima[2], Toshio Tsuji[1] ([1]Hiroshima University, Japan, [2]National Institutes of Natural Sciences, Okazaki Institute for Integrative Bioscience, National Institute for Physiological Sciences, Japan)

GS4-2 *Behavior Analysis on Boolean and ODE models for Extension of Genetic Toggle Switch from Bi-Stable to Tri-stable.*
Masashi Kubota, Manabu Sugii, Hiroshi Matsuno (Yamaguchi University, Japan)

GS4-3 *Boolean modeling of mammalian cell cycle and cancer pathways*
Hideaki Tanaka, Hiroshi Matsuno, Adrien Fauré(Yamaguchi University, Japan)

GS4-4 *An Estimation Method for Environmental Friction Based on Body Dynamic Model of Caenorhabditis elegans*
Zu Soh (Hiroshima University, Japan), Michiyo Suzuki (National Institutes for Quantum and Radiological Science and Technology, Japan), Toshio Tsuji (Hiroshima University, Japan)

January 22 (Sunday)

08:50-Registration

Fountain Room (A1) 2nd F

9:10-10:25 OS10 Biological Signal Sensing Technology, Device and Its Applications (5)

Chair: Hiroki Tamura (University of Miyazaki, Japan)

Co-Chair: Koichi Tanno (University of Miyazaki, Japan)

OS10-1 *Mouse Cursor-like Control System in Consideration of the DC-EOG Signals using EOG-sEMG Human Interface*
Mingmin Yan, Yu Cheng, Keiko Sakurai, Hiroki Tamura, Koichi Tanno
(University of Miyazaki, Japan)

OS10-2 *A Study on Eyes Tracking Method using Analysis of Electrooculogram Signals*
Keiko Sakurai, Mingmin Yan, Hiroki Tamura, Koichi Tanno (University of Miyazaki, Japan)

OS10-3 *Development of Diagnosis Evaluation System of Facial Nerve Paralysis Using sEMG*
Shogo Okazaki, Misaki Syoichizono, Hiroki Tamura, Takahiro Nakashima, Eiji Kato,
Tetsuya Tono (University of Miyazaki)

OS10-4 *High CMRR and Wideband Current Feedback Instrumentation Amplifier Using Current Conveyors*
Shota Mago, Hiroki Tamura, Koichi Tanno (University of Miyazaki, Japan)

OS10-5 *Voltage Rectifier Circuit with Voltage Doubler Using New Active Diode*
Masayuki Uchihara, Hiroki Tamura, Kochi Tanno (University of Miyazaki, Japan)

10:40-11:40 Plenary Speech PS2

Chair: Makoto Sakamoto (University of Miyazaki, Japan)

PS2 *Realistic Visualization of Complex Systems such as Natural Phenomena based on Particle Behaver*
Tomoyuki Nishita (Hiroshima Shudo University/UEI research)

13:00-13:50 Invited Session IS-5

Chair: Takao Ito (Hiroshima University, Japan)

IS-5 *Towards Unified Human-Robotic Societies*

Peter Sapaty (Academy of Sciences, Ukraine), Masanori Sugisaka (ALife Robotics, Japan)

Takao Ito (Hiroshima University, Japan)

14:10-15:10 OS18 Advanced Management and Technology (4)
Chair: Kensuke Ogata (University of Nagasaki, Japan)
Co-Chair: Takao Ito (Hiroshima University, Japan)

OS18-1 *Development of English Text for the engineers to preserve the environment of North-East Asia*
Yuji Minami, Kenji Fukuchi, Shinya Tagawa (National Institute of Technology, Ube, Japan)

OS18-2 *Measuring Fragility and its Implications in Networked Systems*
Tsutomu Ito*, Katsuhiko Takahashi, Katsumi Morikawa, Takao Ito (Hiroshima University, Japan), Rajiv Mehta (New Jersey Institute of Technology, USA), Seigo Matsuno (Ube National College of Technology, Japan), Makoto Sakamoto (University of Miyazaki, Japan)

OS18-3 *A Formation of Standard Setter to Transplant Global Standards into Domestic Institution*
Kensuke Ogata (University of Nagasaki, Japan)

OS18-4 *A Comparison Study on the Vertical Integration and Horizontal Specialization of Chinese ICT Companies*
Yunju Chen (Shiga University, Japan), Yousin Park (Prefectural University of Hiroshima, Japan)
Iori Nakaoka (National Institute of Technology, Ube College, Japan)

15:30-16:15 GS10 Reinforcement & Evolutionary Computations (3)
Chair:

GS10-1 *The Optimized Function Selection Using Wolf Algorithm for Classification*
Duangjai Jitkongchuen, Worapat Paireekreng (Dhurakij Pundit University, Thailand)

GS10-2 *Tell Agent Where to Go: Human Coaching for Accelerating Reinforcement Learning*
Nakarin Suppakun[1], Suriya Natsupakpong[2], and Thavida Maneewarn[3]
(Mongkut's University of Technology Thonburi, Thailand)

GS10-3 *Fall Risk Reduction for Elderly Using Mobile Robots Based on the Deep Reinforcement Learning*
Takaaki Namba (Nagoya University, Japan)

Orchard Room (A2) 2nd F, N
9:10-10:10 OS19 Kansei Engineering and Applications (4)
Chair: Tetsuo Hattori (Kagawa University)
Co-Chair: Hiromich Kawano (NTT AT)

OS19-1 *Histogram Matching Based on Gaussian Distribution Using Regression Analysis Variance Estimation*
Yusuke Kawakami (DynaxT Co., Ltd., Japan), Tetsuo Hattori, Yoshiro Imai, Kazuaki Ando, Yo Horikawa (Kagawa University, Japan)
R. P. C. Janaka Rajapakse (Tainan National University of the Arts, Taiwan)

OS19-2 *Histogram Matching Based on Gaussian Distribution Using Variance Estimation -- Comparison between Curvature Computation and Regression Analysis –*
Yusuke Kawakami (DynaxT Co., Ltd., Japan), Tetsuo Hattori, Yoshiro Imai, Kazuaki Ando, Yo Horikawa (Kagawa University, Japan)
R. P. C. Janaka Rajapakse (Tainan National University of the Arts, Taiwan)

OS19-3 *An Extended Optimal Stopping Method for Structural Change Point Detection Problem*
Yoshihide Koyama, Tetsuo Hattori, Yoshiro Imai, Yo Horikawa, Hiromichi Kawano*, Yusuke Kawakami** (Kagawa University, Kagawa, Japan, *NTT advanced technology Company Ltd, Japan, ** DynaxT Co., Ltd., Japan)

OS19-4 *A Study of Sentimental Value Analysis for Tweeting Message*
Shunsuke Doi*, Shinya Hara*, Yoshiro Imai*, Yusuke Kawakami** and Tetsuo Hattori*
(* Kagawa University, Japan, **DynaxT Co., Ltd., Japan)

14:10-15:10 OS17 Natural Computing and Biology (4)
Chair: Marion Oswald (The Vienna University of Technology, Austria)
Co-Chair: Yasuhiro Suzuki (Graduate School of Information Science, Nagoya University, Japan)

OS17-1 *Molecular Artificial Intelligence by using DNA reactions*
Yasuhiro Suzuki, Rie Taniguchi (Nagoya University, Japan)

OS17-2 *Neural Networks by using Self-Reinforcement Reactions*
Yasuhiro Suzuki (Nagoya University, Japan)

OS17-3 *Artificial Chemistry by Sound Waves*
Yasuhiro Suzuki (Nagoya University, Japan)

OS17-4 *Variants of spiking neural P systems with energy control*
Rudolf Freund, Marion Oswald (TU Wien, Vienna, Austria)

15:30-16:15 GS3 Automated Guided Vehicles II (3)
Chair:

GS3-1 *Motion Improvement of Four-Wheeled Omnidirectional Mobile Robots for Indoor Terrain*
Amornphun Phunopas[1] and, Shinichi Inoue[2] ([1]King Mongkut's University of Technology North Bangkok, Thailand, [2]Kyushu Institute of Technology, Japan)

GS3-2 *An Improved Algorithm for Obstacle Avoidance by Follow the gap method combined Potential Field*
Chakhrit La-orworrakhun, Suriya Natsupakpong (King Mongkut's University Technology Thonburi, Thailand)

GS3-3 *Study on the target positioning for an Omni-directional 3 DOF mobile manipulator based on machine vision*
Jiwu Wang, Yao Du, Wensheng Xu (Beijing Jiaotong University, China)
Masanori Sugisaka (ALife Robotics Corporation Ltd., Japan and Open University, United Kingdom)

Orchard Room (A3) 2nd F, S
9:10-10:25 OS1 Informational Narratology and Automated Content Generation (5)
Chair: Takashi Ogata (Iwate Prefectural University, Japan)
Co-Chair: Yoji Kawamura (Kindai University, Japan)

OS1-1 *Informational Narratology and Automated Content Generation*
Takashi Ogata (Iwate Prefectural University, Japan), Yoji Kawamura (Kindai University, Japan)
Akihito Kanai (Hosei University, Japan)

OS1-2 *Analyzing Multiple Narrative Structures of Kabuki based on the Frameworks of Narrative Generation Systems*
Takashi Ogata (Iwate Prefectural University, Japan)

OS1-3 *Rhetoric of Commercial Film and the Response of Viewers*
Yoji Kawamura (Kindai University, Japan)

OS1-4 *Comparison Between Variational Autoencoder and Encodder-Decoder Models for Short Conversation*
Shin Asakawa (Tokyo Women's Christian University, Japan)
Takashi Ogata (Iwate Prefectural University, Japan)

OS1-5 *Changing and Transforming a Story for a Framework of an Automatic Narrative Generation Game*
Jumpei Ono and Takashi Ogata (Iwate Prefectural University, Japan)

14:10-15:10 OS12 Machine Learning and Its Applications (4)
Chair: Kunikazu Kobayashi (Aichi Prefectural University, Japan)
Co-Chair: Shingo Mabu (Yamaguchi University, Japan)

OS12-1 *A Rule-Based Classification System Enhanced by Multi-Objective Genetic Algorithm*
Kenzoh Azakami, Shingo Mabu, Masanao Obayashi, Takashi Kuremoto
(Yamaguchi University, Japan)

OS12-2 *A Method of Feature Extraction for EEG Signals Recognition using by ROC curve*
Takashi Kuremoto, Yuki Baba, Masanao Obayashi, Shingo Mabu
(Yamaguchi University, Japan)
Kunikazu Kobayashi (Aichi Prefectural University, Japan)

OS12-3 *Forecasting Real Time Series Data using Deep Belief Net and Reinforcement Learning*
Takaomi Hirata, Takashi Kuremoto, Masanao Obayashi, Shingo Mabu
(Yamaguchi University, Japan), Kunikazu Kobayashi (Aichi Prefectural University, Japan)

OS12-4 *Improvement of Robot's Self-localization by Using Observer View Positional Information*
Yo Aizawa, Takuo Suzuki, and Kunikazu Kobayashi (Aichi Prefectural University, Japan)

15:30-16:45 OS21 Computer Science and Information Processing (5)
Chair: Makoto Sakamoto (University of Miyazaki, Japan)
Co-Chair: Yu-an Zhang (Qinghai University, China)

OS21-1 *Consideration on the Recognizability of Three-Dimensional Patterns*
Chongyang Sun[1], Makoto Sakamoto[2], Makoto Nagatomo[3], Yu-an Zhang[2], Shinnosuke Yano[1], Satoshi Ikeda[2], Takao Ito[4], Tsutomu Ito[4], Yasuo Uchida[5], Tsunehiro Yoshinaga[6], ([1, 2, 3] University of Miyazaki, Japan), ([4] Hiroshima University, Japan), ([5] Ube National College of Technology, Japan), ([6] Tokuyama college of Technology, Japan)

OS21-2 *Some Properties of Four-Dimensional Homogeneous Systolic Pyramid Automata*
Makoto Nagatomo[1], Makoto Sakamoto[2], Yu-an Zhang[2], Chongyang Sun[3], Shinnosuke Yano[3], Satoshi Ikeda[2], Takao Ito[4], Tsutomu Ito[4], Yasuo Uchida[5], Tsunehiro Yoshinaga[6] ([1, 2, 3] University of Miyazaki, Japan) ([4] Hiroshima University, Japan) ([5]Ube National College of Technology, Japan) ([6] Tokuyama college of Technology, Japan)

OS21-3 *Reduction of the search space to find perfect play of 6×6 board Othello*
Yuki Takeshita[1], Makoto Sakamoto[1], Takao Ito[2], Tsutomu Ito[2], Satoshi Ikeda[1]
([1]University of Miyazaki, [2]Hiroshima University, Japan)

OS21-4 *A comparative study on the delisting ratings of firms from the UN Global Compact in the international management environment*
Kanako Negishi (National Institute of Technology, Ube college, Japan)

OS21-5 *Application of ViSC to the Natural Grazing in Qinghai Tibet Plateau*
Cheng-shui Niu[1], Bing-fen Li[1], Yu-an Zhang[1], Makoto Sakamoto[2] ([1]Qinghai University, P.R. China, [2]University of Miyazaki, Japan)

Farewell Party

GS11 Others (12)

GS11-1 *Clinical Evaluation of UR-System-PARKO for Recovery of Motor Function of Severe Plegic Hand after Stroke*
Hirofumi Tanabe (Shonan University of Medical Sciences, Japan)
Yoshifumi Morita (Nagoya Institute of Technology, Japan)

GS11-2 *A Piston Finger Device for Restoring the Motor Function of Chronic Plegic Fingers: Analysis of the Piston Finger Technique*
Mengsu Wang (Nagoya Institute of Technology: Nitech, Japan)
Hirofumi Tanabe (Shonan University of Medical Sciences, Japan)
Kenji Ooka (Nitech, Japan), Yoshifumi Morita (Nitech, Japan)

GS11-3 *Verifying the Sleep-Inducing Effect of a Mother's Rocking Motion in Adults*
Hiroaki Shibagaki, Keishi Ashida, Yoshifumi Morita (Nagoya Institute of Technology, Japan), Ryojun Ikeura (Mie University, Japan) and Kiyoko Yokoyama (Nagoya City University, Japan)

GS11-4 *Design of Automated Real-Time BCI Application Using EEG Signals*
Chong Yeh Sai, Norrima Mokhtar, Hamzah Arof, Masahiro Iwahashi
(University of Malaya, Malaysia / Nagaoka University of Technology, Japan)

GS11-5 *A Hybrid Simulated Kalman Filter - Gravitational Search Algorithm (SKF-GSA)*
Badaruddin Muhammad, Zuwairie Ibrahim, Mohd Falfazli Mat Jusof (Universiti Malaysia Pahang, Malaysia), Nor Hidayati Abdul Aziz, Nor Azlina Ab. Aziz (Multimedia University, Malaysia), Norrima Mokhtar (University of Malaya, Malaysia)

GS11-6 *Simulated Kalman Filter with Randomized Q and R Parameters*
Nor Hidayati Abdul Aziz, Nor Azlina Ab. Aziz (Multimedia University, Malaysia)
Zuwairie Ibrahim, Saifudin Razali, Mohd Falfazli Mat Jusof (Universiti Malaysia Pahang, Malaysia), Khairul Hamimah Abas, Mohd Saberi Mohamad (Universiti Teknologi Malaysia, Malaysia), Norrima Mokhtar (University of Malaya, Malaysia)

GS11-7 *Real Detection of 3D Human Hand Orientation Based Morphology*
Abadal-Salam T. Hussain, Hazry D., Waleed A. Oraibi, M.S Jawad, Zuradzman M. Razlan, A. Wesam Al-Mufti, S. Faiz Ahmed, Taha A. Taha, Khairunizam WAN, Shahriman A.B
(Universiti Malaysia Perlis, Malaysia)

GS11-8 *Multilevel Non-Inverting Inverter Based Smart Green Charger System*
Abadal-Salam T. Hussain, Waleed A. Oraibi, Hazry D, Zuradzman M. Razlan, S. Faiz Ahmed, Taha A. Taha, Khairunizam WAN & Shahriman AB (Universiti Malaysia Perlis, Malaysia)

GS11-9 *Design A New Model of Unmanned Aerial Vehicle Quadrotor Using The Variation in The Length of The Arm*
Yasameen Kamil, D. Hazry, Khairunizam Wan, Zuradzman M. Razlan, Shahriman AB
(Universiti Malaysia Perlis, Malaysia)

GS11-10 *Development of Automatic Take Off and Smooth Landing Control System for Quadrotor UAV*
Syed. F. Ahmed (Universiti Kuala Lumpur, British Malaysian Institute, Malaysia, Universiti Malaysia Perlis, Malaysia), D. Hazry (Universiti Malaysia Perlis, Malaysia), Kushsairy Kadir (University Kuala Lumpur, British Malaysian Institute, Malaysia), Abadal Salam T. Hussain, Zuradzman M. Razlan, Shahriman AB (Universiti Malaysia Perlis, Malaysia)

GS11-11 *Auto Pilot Ship Heading Angle Control Using Adaptive Control Algorithm*
Abadal-Salam T. Hussain, Hazry D., S. Faiz Ahmed, Wail A. A. Alward, Zuradzman M. Razlan & Taha A. Taha (Universiti Malaysia Perlis, Malaysia)

GS11-12 *Classification of Hippocampal Region using Extreme Learning Machine*
Muhammad Hafiz Md Zaini, Mohd Ibrahim Shapiai (Universiti Teknologi Malaysia)
Ahmad Rithauddin Mohamed (Hospital Kuala Lumpur)
Norrima Mokhtar (University of Malaya), Zuwairie Ibrahim (Universiti Malaysia Pahang)

PS abstracts

PS1 A New Tool to Access Deep-Sea Floor "Sampling-AUV"

Kazuo Ishii, Takashi Sonoda, Yuya Nishida, Shinsuke Yasukawa and Tamaki Ura (Kyushu Institute of Technology, Japan)

Underwater robot is one of the important research tools to explore deep-sea. Especially, Autonomous Underwater Vehicles (AUVs) attract attentions as new tools because they are un-tethered and suitable for wide area observation. As the next generation AUV, we have been developing a Sampling-AUV that can dive into deep-sea and bring back marine creatures using a mounted manipulator. In the mission, the AUV transmits the deep-sea floor images to the support ship using acoustic communication, and the operator selects the marine creatures to sample and bring back them. In this talk, we introduce the new AUV, the underwater manipulator and image processing techniques for sampling.

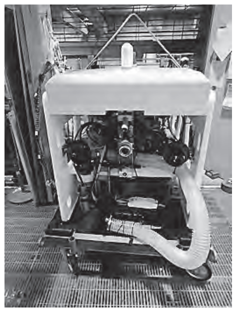

PS2 Realistic Visualization of Complex Systems such as Natural Phenomena based on Particle Behaver

Tomoyuki Nishita (Hiroshima Shudo University/UEI research)

Computer graphics (CG) is very useful tool for visualization of scientific simulation, computer aided design, arts, education, and games. Researches on complex systems and AI (acritical intelligence) including artificial life also become popular recently. Complex systems is a field of science studying how parts of a system give rise to the collective behaviors of the system, and how the system interacts with its environment. Examples are Earth's global climate, organisms, social organization, a living cell, and ultimately the entire universe. In complex systems, neural network, cellar automation, fractal, chaos dynamics, and GA are useful techniques. These are also used in CG. The purpose of CG is reality with interactive speed. In recent years, point primitives have received growing attention in CG. The particle system refers to CG technique to simulate certain fuzzy phenomena. My talk also includes pioneers of CG, my research history, and CG application related to AI.

IS abstracts

IS-1 The future of Robotics Technology.

Luigi Pagliarini[1,2], Henrik Hautop Lund[1]
([1] Technical University of Denmark, Denmark, [2]Academy of Fine Arts of Macerata, Italy)

In the last decade the robotics industry has created millions of additional jobs led by consumer electronics and the electric vehicle industry, and by 2020, robotics will be a $100 billion worth industry, as big as the tourism industry.. For example, the rehabilitation robot market has grown 10 times between 2010 and 2016, thanks to advancements in rehab/therapy robots, active prostheses, exoskeletons, and wearable robotics. In short, the very next decade robotics will become vital components in a number of applications and robots paired with AI will be able to perform complex actions that are capable of learning from humans, driving the intelligent automation phenomenon. Therefore, in this paper we try to depict the direction and the fields of application of such important sector of future markets, and scientific research.

IS-2 Playware ABC: Engineering Play for Everybody

Henrik Hautop Lund (Technical University of Denmark, Denmark)

This paper describes the Playware ABC concept, and how it allows anybody, anywhere, anytime to be building bodies and brains, which facilitates users to construct, combine and create. The Playware ABC concept focuses engineering and IT system development on creating solutions that are usable by all kinds of users and contexts. The result becomes solutions, often based on modular technologies that are highly flexible and adaptable to different contexts, users, and applications.

IS-3 A combination of Machine Learning and Cerebellar models for the Motor Control and Learning of a Modular Robot

Ismael Baira Ojeda, Silvia Tolu, Moisés Pachecho, David Johan Christensen, Henrik Hautop Lund
(Technical University of Denmark, Denmark)

We scaled up a bio-inspired control architecture for the motor control and motor learning of a real modular robot. In our approach, the Locally Weighted Projection Regression algorithm (LWPR) and a cerebellar microcircuit coexist, forming a Unit Learning Machine. The LWPR optimizes the input space and learns the internal model of a single robot module to command the robot to follow a desired trajectory with its end-effector. The cerebellar microcircuit refines the LWPR output delivering corrective commands. We contrasted distinct cerebellar circuits including analytical models and spiking models implemented on the SpiNNaker platform, showing promising performance and robustness results.

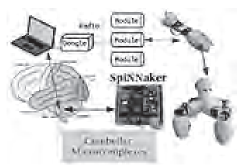

IS-4 Playware ABC 2: as a Disruptive Technology for Global Development

Henrik Hautop Lund (Technical University of Denmark, Denmark)

This paper describes the Playware ABC concept, and how it allows anybody, anywhere, anytime to be building bodies and brains, which facilitates users to construct, combine and create. The Playware ABC concept focuses engineering and IT system development on creating solutions that are usable by all kinds of users and contexts in our globalized society. The result becomes solutions that are highly flexible and adaptable to different contexts, users, and applications. The paper gives examples of how playware becomes a disruptive technology for global development, for instance in the health sector.

IS-5 Towards Unified Human-Robotic Societies

Peter Sapaty (Academy of Sciences, Ukraine), Masanori Sugisaka (ALife Robotics, Japan)
Takao Ito (Hiroshima University, Japan)

Large numbers of robotic facilities are accumulated worldwide, but existing robots still remain specialized devices rather than intelligent collaborators for humans. To efficiently integrate massive robotics into human societies, more general and universal approaches are needed. The presentation will reveal higher-level, semantic, model supported by Spatial Grasp Language (SGL) in which top operations and decisions in distributed spaces are expressed in extremely compact form, with traditional system management shifted to automatic SGL interpretation. Communicating SGL interpreters associated with humans and robots allow us to organize goal driven teams up to entire societies operating under unified control. Presentation will exhibit numerous scenarios in SGL from most critical applications.

OS abstracts

OS1 Informational Narratology and Automated Content Generation (5)

OS1-1 Informational Narratology and Automated Content Generation

Takashi Ogata (Iwate Prefectural University, Japan) Yoji Kawamura (Kindai University, Japan)
Akihito Kanai (Hosei University, Japan)

Authors have been proposing a new concept called “informational narratology” or “information narratology”. In this concept, we integrate narratological studies including various literary theories into information technologies, such as AI and cognitive science to mainly design and develop systems that automatically generate, create or produce digital narrative contents including a variety of existing or future genres. Under this idea’s framework, the three authors respectively design and develop narrative generation systems (Ogata), advertising image processing systems (Kawamura), and narrative film processing systems (Kanai). In this paper, we propose the concept or idea of informational narratology and introduce the above three researches as concert approaches to the informational narratology.

OS1-2 Analyzing Multiple Narrative Structures of *Kabuki* based on the Frameworks of Narrative Generation Systems

Takashi Ogata (Iwate Prefectural University, Japan)

Although *kabuki* is a genre of, so to speak, traditional performing arts, it has many characteristics, as a contemporary genre including various elements such as narrative, drama, dance, music, and so on, that can contribute to the design and development of digital narrative generation studies. Previously, we have surveyed and analyzed *kabuki*’s narrative structures, the generation or production and reception or consumption process from the viewpoint of the multiple narrative structures model. In the multiple narrative structures model of *kabuki*, we mean that the entire structure of *kabuki* is constructed through multiple usages of relating information. For example, the element of a “person” in *kabuki* is divided into a “character” in a narrative work, the existence of an actor with a historical flow and a name as the actor, and a real human with a true name. And this multiplicity, for instance, give a kind of multiple and deep characteristic to a person. Based on this previous studies, in this presentation, we show a method that bridges this *kabuki* analysis to system design through our two narrative generation systems: “Integrated Narrative Generation System (INGS)” and “Geino Information System (GIS)”.

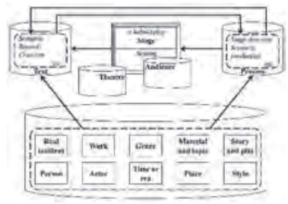

OS1-3 Rhetoric of Commercial Film and the Response of Viewers

Yoji Kawamura (Kindai University, Japan)

In this paper, firstly the way of thinking of commercial film techniques and rhetoric is shown. Next, based on the various investigations, the relationships between rhetoric of commercial film and the response of viewers are summarized. Then, by using the summarized relationship as a rule, the expression know-how of commercial film is extracted, and how to make information system is considered. By introducing a framework called "overall rhetorical type" as a combination of commercial film techniques and using the fact that there is a correlation between the overall rhetorical type and the viewer's response (favorable factor, acceptance image), it is possible to build an information system to promote the interest and purchase willingness of the viewers.

OS1-4 Comparison Between Variational Autoencoder and Encodder-Decoder Models for Short Conversation

Shin Asakawa (Tokyo Women's Christian University, Japan)
Takashi Ogata (Iwate Prefectural University, Japan)

Conversational modeling is an important task in language understanding and generation. Recent models in this area have improved their performances based on recurrent neural network model (RNN). RNN models can generate sentenses and conversation. It is not always restricted to any specified handcrafted rules. The variational autoencoder and encoder-decoder models might be considered as a promissing model among them. They were able to extract knowledge from the training dataset. Samples from the prior over these sentence representations produced diverse and well-formed sentences through simple deterministic decoding. We tried to compare them with several different data set and to reveal underlying mechanism between them. By examining paths through latent space, we are able to generate coherent novel sentences that interpolate between known sentences. Our preliminary results suggest that optimizing the wrong objective function might play a role producing some kinds of convsersation.

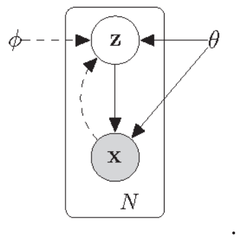

OS1-5 Changing and Transforming a Story for a Framework of an Automatic Narrative Generation Game

Jumpei Ono and Takashi Ogata (Iwate Prefectural University, Japan)

Authors has proposed an idea of a game system including an automatic story generation function based on tabletop-top role playing game (TRPG). In this idea, stories are generated or transformed through the communication between a "game manager (GM)" who controls story generation and "Players (PLs)" who change and transform the content of a story proposed by a GM. This paper focuses on the mechanism for changing and transforming a proposed story by a GM. In particular, this mechanism has various techniques from macro level techniques related to the entire structures of a story to micro level techniques related to the partial structures of a story. For instance, when a GM is a real human, these techniques in PLs who are computer agents can produce changed and transformed stories which the GM has not imagined originally.

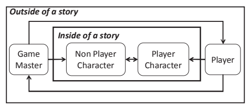

OS2 Intelligence Control Systems and Applications I (6)

OS2-1 Develop Low Cost IoT Module with Multi-Agent Method

Jr-Hung Guo, Kuo-Hsien Hsia, Kuo-Lan Su
(National Yunlin University of Science and Technology, Taiwan)

IOT (Internet of Thing) is a very hot topic recently, many of the important issues in the field of research. But to the conventional apparatus or systems and network connections, sometimes we need complex modifications or expensive costs. Therefore, this paper using the MCS-51 series single-chip integration of analog, digital signal input, and ETHERNET, WIFI and other communication interface, to develop general-purpose IoT modules. This module can be used to replace existing equipment or devices, or combination use with the original device. We also use the module in a Multi-Agent Method, we can ensure that the module in signal capture or communication failure can be replaced or assisted by other modules.

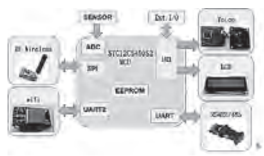

OS2-2 Based on Short Motion Paths and Artificial Intelligence Method for Chinese Chess Game

Chien-Ming Hung, Jr-Hung Guo, Kuo-Lan Su
(National Yunlin University of Science and Technology, Taiwan)

The article develops the decision rules to win each set of the Chinese chess game using evaluation algorithm and artificial intelligence method, and uses the mobile robot to be instead of the chess, and presents the movement scenarios using the shortest motion paths for mobile robots. User can play the Chinese chess game according to the game rules with the supervised computer. The supervised computer decides the optimal motion path to win the set using artificial intelligence method, and controls mobile robots according to the programmed motion paths of the chesses moving on the platform via wireless RF interface. We use enhanced A* searching algorithm to solve the shortest path problem of the assigned chess, and solve the collision problems of the motion paths for two mobile robots moving on the platform simultaneously. We implement a famous set to be called "wild horses run in farm" using the proposed method. First we use simulation method to display the motion paths of the assigned chesses for the player and the supervised computer. Then the supervised computer implements the simulation results on the chessboard platform using mobile robots. Mobile robots move on the chessboard platform according to the programmed motion paths and is guided to move on the centre line of the corridor, and avoid the obstacles (chesses), and detect the cross point of the platform using three reflective IR modules.

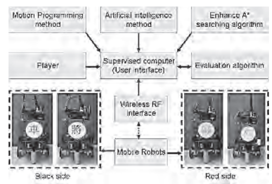

OS2-3 Design and Implementation of the SCARA Robot Arm

Jian-Fu Weng, Bo-Yi Li, Kuo-Lan Su (National Yunlin University of Science and Technology, Taiwan)

The article designs a four-joint robot arm using PLC-based control system. The control system is all in one device to be produced by the DELTA Company, and contain four axis controllers and drivers. The robot arm contains four AC servomotors, four driver devices and a vision system. The PLC-based controller also programs motion commands of the gripper to finish the assigned tasks using Ladder Diagram (LG), Function Block Diagram (FBD), Sequential Function Chart (SFC), Instruction List (LL) and Structure Test (ST). Each driver has been tuned the parameters of the PID controller for the robot arm. The human machine interface (HMI) is a touch panel to be used for the robot arm. Users can control the motion path of any joint on the user interface. In the experimental results, users can program English or Chinese words or plot assigned graphs on the human machine interface. The SCARA robot arm catches the pencil, and put down to touch the assigned position repeat on the platform, and identifies the precious of the robot arm, and catches various objects to put down the assigned positions.

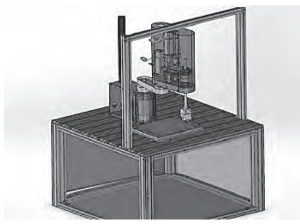

OS2-4 Transmission Power Control for Wireless Sensor Network

Kuo-Hsien Hsia[1], Chung-Wen Hung[2], Hsuan T. Chang, and Yuan-Hao Lai[2]
([1]Far East University, Taiwan) ([2]National Yunlin University of Science and Technology, Taiwan)

Wireless sensor networks can be widely applied for a security system or a smart home system. Since some of the wireless remote sensor nodes may be powered by energy storage devices such as batteries, it is a very important issue to transmit signals at lower power with the consideration of the communication effectiveness. In this paper, we will provide a fuzzy controller with two inputs and one output for received signal strength indicator (RSSI) and link quality indicator (LQI) to adjust transmission power suitably in order to maintaining a certain communication level with a reduced energy consumption. And we will divide the sampling period of a sensor node into four intervals so that the sensor node radio device does not in receiving or transmission status all the time. Hence the sensor node can adjust transmission power automatically and reduce sensor node power consumption. Experimental results show that the battery life can be extended to about 10 times for the designed sensor node comparing to a normal node.

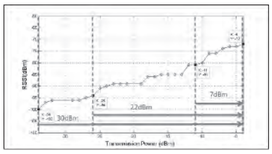

OS2-5 Mechanism of Autonomous Mowing Robot for Long Grass

Kuo-Hsien Hsia[1], Yao-Shing Huang[2], Kuo-Lan Su[2] and Jr-Hung Guo[2]
([1]Far East University, Taiwan)
([2]National Yunlin University of Science and Technology, Taiwan)

A land full of grass can be easily seen all over the world. For example, a golf course, a large playground, garden and waste plowed farmland and wild wasteland, all of above are full of grass. Almost all mowing work are operated by manpower, especially the long grass section. There have been some autonomous mowing robots for short grass up to now. However, there is almost no commodity for long grass mowing in the market. The main possible consideration may be the issue of safety. It is highly possible that a sharp mower blade may cause harm under the condition that the mower is not operated directly by a skilled person. In this paper, we will focus on the mechanism design for an autonomous mowing robot that can cut long grass safely. We will also outline the safety requirements for an autonomous mowing robot for long grass.

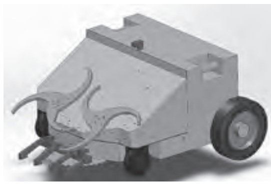

OS2-6 Design of Optimal Position Controller for Three-Phase Brushless DC Motor Applying Adaptive Sliding Mode Control

Tai-Huan Tsai, Mei-Yung Chen
(National Taiwan Normal University, Taiwan)

In this paper, we design an adaptive sliding mode controller which is applied on optimal position tracking of three-phase brushless DC motor. Consider the uncertainties and external disturbances of a three-phase brushless DC motor, we choose the sliding mode control (SMC) to be major one. Usually we can't figure out the motor's uncertainty, so we propose an adaptive control to tune the motor's uncertainty, that would be able to handle the unknown uncertainties and disturbances. Then we proof the stability of system by Lyapunov function, and the simulation results show excellent performance of this controller.

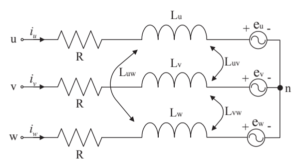

OS3 Intelligence Control Systems and Applications II (6)

OS3-1 Image Compression Using Hybrid Evolution Based Takagi-Sugeno Fuzzy Neural Network

[1]Chia-Nan Ko and [2]Ching-I Lee
([1,2] Nan Kai University of Technology)

This article proposes a model of hybrid evolution-based Takagi-Sugeno fuzzy neural networks (TSFNNs). The model is to research and analyze how to improve the efficiency of image compression. In the proposed model, the hybrid evolution method integrates the advantages of improved quantum-behaved particle swarm optimization, adaptive annealing learning, and mutation operation to train Takagi-Sugeno fuzzy neural networks. The proposed hybrid evolution-based quantum-behaved particle swarm optimization Takagi-Sugeno fuzzy neural networks (HEQPSO-TSFNNs) can improve the coding result around boundaries to enhance the coding efficiency of the lossless compression of images.

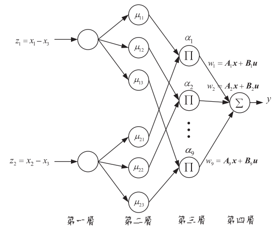

OS3-2 MQPSO Algorithm Based Fuzzy PID Control for a Pendubot System

[1]Li-Chun Lai, [2]Yu-Yi Fu, and [3]Chia-Nan Ko
([1] National Pingtung University, Taiwan)
([2,3] Nan Kai University of Technology, Taiwan)

In this study, a modified quantum-behaved particle swarm optimization (MQPSO) approach is proposed to design an optimal fuzzy PID controller for asymptotical stabilization of a pendubot system. In the fuzzy PID controller, parameters are determined by using MQPSO algorithm. The MQPSO method and other PSO methods are then applied to design an optimal fuzzy PID controller in a pendubot system. Comparing the simulation results, the feasibility of the MQPSO are verified.

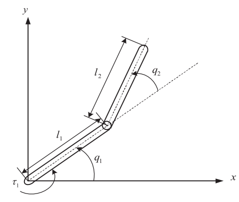

OS3-3 A Sensorless Ultra-High Speed Motor Driver

Chung-Wen Hung, Yan-Ting Yu, Bo-Kai Huang and Wei-Lung Mao
(National Yunlin University of Science and Technology, Taiwan)

An ultra-high speed motor is important in machine tools. A speed sensor-less ultra-high speed motor driver is proposed in this paper. Due to cost, only few drivers build up a closed-loop control, which could improve driver's performance. Therefore, a sensor-less speed estimation for ultra-high speed motors is developed. The design and implementation of the driver and feedback circuits are detailed in this paper. And experimental results show that the proposed system is workable.

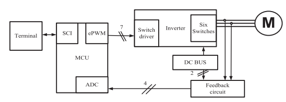

OS3-4 Android-Based Patrol Robot Featuring Automatic Vehicle Patrolling and Automatic Plate Recognition

Chian C. Ho, Shih-Jui Yang, Jian-Yuan Chen, Chang-Yun Chiang, and Hsin-Fu Chen
(National Yunlin University of Science and Technology, Taiwan)

This work develops an Android-based patrol robot featuring Automatic Vehicle Patrolling (AVP) and Automatic Plate Recognition (APR). The AVP feature integrates 3 novel methods, wheel-wheelcover-based AdaBoost wheel detection, contour-wheel-oriented vehicle approaching, and Ad-Hoc-based remote motion control. The APR feature integrates 4 novel methods, Wiener-deconvolution vertical edge enhancement, AdaBoost plus vertical-edge plate detection, vertical-edge horizontal-projection histogram-segmentation stain removal, and customized optical character recognition. Implementation results show the vehicle detection rate and plate recognition rate of the Android-based patrol robot are over 96% and over 94%, respectively, under various scene conditions. On the other hand, the average execution time of AVP and APR of the Android-based patrol robot takes at most 8 second per round and at most 0.8 second per frame, respectively.

OS3-5 Adaptive CMAC Filter for Chaotic Time Series Prediction

Wei-Lung Mao, Suprapto, and Chung-Wen Hung
(National Yunlin University of Science and Technology, Taiwan)

Chaotic signal is a natural phenomenon exhibiting in every condition of dynamical system. Chaotic signals are almost unpredictable, noise-like, uncertain and irregular behavior, yet they are very useful in numerous applications of signal processing. Due to their behaviors, the quest of a good method to model and analyze of the chaotic signal is very crucial. This paper present a novel strategy to analyze chaotic signal using the cerebellar model articulation controller (CMAC) network combined with evolutionary algorithms (EAs) such as biogeography-based optimization (BBO), genetic algorithm (GA) and particle swarm optimization (PSO). Mackey-glass chaotic signal time series is tested and demonstrated by the conventional and the proposed algorithms. They are compared with each other to determine the optimal filtering and prediction. The result demonstrated that the CMAC combined with EAs could filter, predict and estimate chaotic signal time series well rather than the conventional methods. The best result of the algorithms tested for chaotic signal time series is the CMAC combined with BBO algorithm.

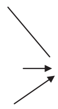

OS3-6 Surface Defect Detection for Anodized Aluminum Tube Based on Automatic Optical Inspection

Hsien-Huang P. Wu and Hsuan-Min Sun (National Yunlin University of Science and Technology, Taiwan)

This paper proposed using the automated optical inspection (AOI) technology to develop a system which can automatically detect and classify defects for the shock absorber tube (SAT) made with steel. It is a high economic product which requires high-quality even under mass production. Nevertheless, the current manual quality-inspection is not only error-prone but also very manpower demanding. Due to the strong reflective property of the surface, as well as its various sizes and subtle flaws, it is very difficult to take good quality image for automatic inspection. However, based on the surface properties and shape of the SAT, lighting and proper structure combined with line scan camera have been designed to acquire image with good quality. Methods were proposed to detect various kinds of defects, and experimental results show that all the defects can be detected in real time. We believe the proposed system can greatly increase the efficiency and accuracy of defect detection and decrease the cost of manual labor.

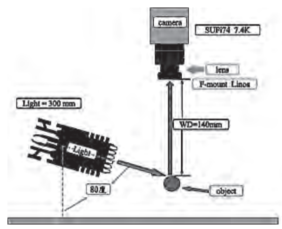

OS4 Human-In-The-Loop (HITL) Systems (4)

OS4-1 Feature Extraction for Digging Operation of Excavator

Kazushige Koiwai, Toru Yamamoto (Hiroshima University, Japan), Takao Nanjo, Yoichiro Yamazaki, Yoshiaki Fujimoto (KOBELCO Construction Machinery CO., LTD. , Japan)

Japanese Ministry of Land, Infrastructure, Transport and Tourism pushes a policy of “i-construction”. The technologies of Information and Communication Technology (ICT), Internet of Things (IoT), Big Data, and AI are applied to some construction equipments based on the policy. As the result, manpower-saving are achieved. However, the manpower is still required continuously in the construction field because skilled operators are needed for complicated conditions. Those skilled operators who have the unique technique are reduced in these days. In this study, the skill difference of digging operations between the skilled operator and the novice operator are evaluated based on the view of the control engineering. The database driven human skill based PID controller is applied to the skill evaluation for the digging operation. In considering a human to be a controller, the skill can be evaluated numerically. Moreover, it would be possible to apply the skill improvement for the operation.

OS4-2 Design of a Data-Oriented Kansei Feedback System

Takuya Kinoshita, Toru Yamamoto (Hiroshima University, Japan)

In the development of the aging society, it is important for patients with hemiplegia to introduce the adaptive welfare equipment. However, it is difficult to support them by using general welfare equipment because there are a lot of individual disabilities. Therefore, an adaptive welfare equipment is needed in near future. However, it is very difficult to determine the suitable reference signal for each person. In this study, the design of a data-oriented cascade control system based on Kansei is proposed. In the proposed control system, there are two controllers which are a data-driven controller and a fixed controller. In particular, a data-driven controller is for a human and it can calculate the suitable reference signal of a welfare equipment based on Kansei. The effectiveness of the proposed scheme is verified by simulation results.

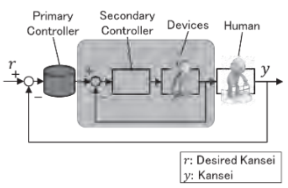

OS4-3 Parameter Estimation of Skill Evaluation Model

Kazuo Kawada, Toru Yamamoto (Hiroshima University, Japan)

In this study, the aim is to construct "teacher-student model" for optimal skill acquisition. To support the optimal skill acquisition, modeling and estimation of individual learning process are very important. The first-order system with dead time (system gain K, time constant T, and dead time L) is introduced as individual learning process model based the control engineering approach. These system parameters included in the learning process model are estimated by using a real-coded genetic algorithm (GA). In order to evaluate the effectiveness of the proposed scheme, it is employed for the classification task of fastener components.

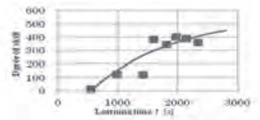

OS4-4 Human Skill Quantification for Excavator Operation using Random Forest

Hiromu Imaji, Kazushige Koiwai, Toru Yamamoto (Hiroshima University, Japan)
Koji Ueda, Yoichiro Yamazaki, Yoshiaki Fujimoto (KOBELCO Construction Machinery CO., LTD. , Japan)

In the construction field, the improvement of the work efficiency is one of important problems. However, the work efficiency using construction equipments is depend on their operation skills. Thus, in order to increase the work efficiency, operation skill is required to be quantitatively evaluated. In this study, the Random Forest (RF), one of machine learning method, is adopted as the quantitatively evaluation for the operation skill of construction equipment. Evaluated target is the operation on excavation to load onto a truck for a hydraulic excavator. The RF learns to classify some states by the pilot of expert's operation. States are defined as 'excavate', 'lift', 'dump', 'return' and 'rest'. The RF with the learning result of expert is applied to other operator's operation. It is revealed that the rate of 'rest' is related to their skill.

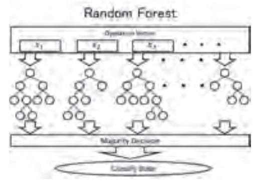

OS5 Human Interface and Content Security (5)

OS5-1 A Method for Secure Communication Using a Discrete Wavelet Transform for Audio Data and Improvement of Speaker Authentication

Kouhei Nishimura, Yasunari Yoshitomi, Taro Asada, Masayoshi Tabuse (Kyoto Prefectural University, Japan)

We developed a secure communication method using a discrete wavelet transform. Two users must both have a copy of the same piece of music to be able to communicate with each other. The music and the sender's message are encoded using the scaling coefficients obtained from a discrete wavelet transformation. The message receiver can produce the audio data similar to the sending user's speech using an inverse discrete wavelet transform, together with information on the difference between these two codes. For improving the speaker authentication accuracy, the quantization level for the scaling coefficients is increased. Furthermore, the amount of data sent to the message receiver is remarkably reduced exploiting the characteristic of those data.

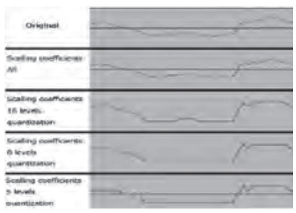

OS5-2 A Recipe Decision Support System Using Knowledge Information and Agent

Keita Saito, Taro Asada, Yasunari Yoshitomi, Ryota Kato, Masayoshi Tabuse
(Kyoto Prefectural University, Japan)

We have developed a system for recipe recommendation using collaborative filtering and impression words. As a human interface, we have adopted an agent named as MMDAgent. In the proposed system, the first recommendation process using collaborative filtering is terminated when no users in the reference list have the same preference of recommended recipe as that of a new user. Then, the second recommendation process finds the most similar recipe, by exploiting the scores for impression words, to those successfully recommended among recipes not recommended up to the moment. The recommendation accuracy of the proposed system was much better than that of random recommendation. As a final step, one recipe is selected from all successfully recommended recipes for the user by using the reputation for them in a database and interaction between the user and the agent.

OS5-3 A System for Analyzing Facial Expression and Verbal Response of a Person While Answering Interview Questions on Video

Taro Asada, Yasunari Yoshitomi, and Masayoshi Tabuse
(Kyoto Prefectural University, Japan)

We have developed a system for analyzing facial expressions of a person while answering interview questions on video. A video captured an answerer at an interview is analyzed using image processing software (OpenCV) and the previously proposed feature parameter (facial expression intensity), which is measured for an eye-part area in addition to the mouth-part area focused in our reported research. Moreover, the time to utterance of the answerer just after an interview question is measured for analyzing the mental state of the answerer. In our previously reported system for analyzing facial expression of a person during conversation with another person, facial expression intensity could be affected by (1) a conversation topic, (2) a partner and (3)the facial expression of the partner. In this study, all of (1), (2) and (3) are fixed by using an interview video. The experimental result shows the usefulness of the proposed system.

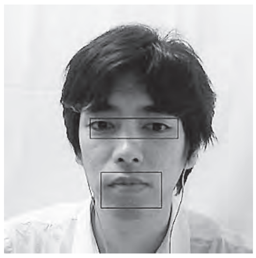

OS5-4 Real-Time System for Horizontal Asymmetry Analysis on Facial Expression and Its Visualization

Ryoichi Shimada, Taro Asada, Yasunari Yoshitomi, and Masayoshi Tabuse
(Kyoto Prefectural University, Japan)

We have been developing a real-time system for horizontal asymmetry analysis on facial expression and its visualization. The image signal input from web camera is analyzed by our real-time system using image processing software (OpenCV) and the feature parameter (facial expression intensity), which is separately measured for the left and right half regions in the mouth-part area. Our real-time system draws the graph expressing the facial expression intensity change using OpenCV. The experimental result suggests the usability of this system for a test where a real-time reaction of the facial expressions is one of important factors.

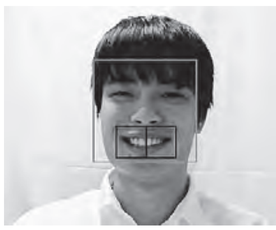

OS5-5 Development of Mouse System for Physically Disabled Person by Face Movement Using Kinect

Junpei Miyachi, Masayoshi Tabuse (Kyoto Prefectural University, Japan)

It is necessary to support of computer operation for a physically disabled person. One of the possible physical movements of the physically disabled person is facial movement. Recognition of facial movement of a person makes it possible to operate a computer. Furthermore without the adjustment for a user and adjustment for the distance from a user, it is possible to reduce the burden on a user. We developed a system to resolve these problems. In our system, Kinect is used to obtain the face direction and extract feature points of the face. Changing the face direction, we can move a mouse cursor. Recognizing an open mouth or closed eye, we can carry out an operation of mouse click. In this paper, we evaluated the effect on operability due to the face direction and recognition rate due to distance.

OS6 Software Development Support Method (6)

OS6-1 Development of a Tool for Extended Place/transition Net-Based Mutation Testing

Tomohiko Takagi[1], Shogo Morimoto[1], Tetsuro Katayama[2]
([1]Kagawa University, [2]University of Miyazaki, Japan)

This paper shows a tool for EPNBMT (Extended Place/transition Net-Based Mutation Testing) to evaluate and improve the quality of test cases for concurrent software. The tool consists of the following four functions: (1) an original EPN can be created to define the expected behavior of concurrent software under test, (2) mutant EPNs including intended failures can be created by applying mutation operators to the original EPN, (3) arbitrary test cases to be evaluated can be converted to execution paths on the original EPN, and (4) each mutant EPN can be executed by the converted test cases in order to calculate a mutation score. If the mutation score is not good, the test cases are improved based on mutant EPNs whose failures have not been detected.

OS6-2 Improvement of Decision Table Automatic Generation Tool VDTable for let in Statement

Yinuo Huang*, Tetsuro Katayama* Yoshihiro Kita†, Hisaaki Yamaba*, Naonobu Okazaki*
(*University of Miyazaki, Japan, †Tokyo University of Technology, Japan)

Formal methods, in software development, is one of the means to describe the specification strictly. On the other hand, the decision table is one of the testing techniques to exhaustively represent the logical combination included in software. The VDTable can automatically generate the decision table, from the specification written in specification description language VDM++ (VDM++ specification). But, the VDTable, since many VDM++ syntax is not corresponded, its usefulness is limited. To improve the usefulness, this paper expands VDTable. Specifically, VDTable is improved to be able to correspond to the statement "let in", which is one of the VDM++ syntax, that the existing VDTable does not support.

OS6-3 Prototype of Test Cases Automatic Generation Tool BWDM Based on Boundary Value Analysis with VDM++

Hiroki Tachiyama*, Tetsuro Katayama* Yoshihiro Kita†, Hisaaki Yamaba*, Naonobu Okazaki*
(*University of Miyazaki, Japan, † Tokyo University of Technology, Japan)

As a method to eliminate the ambiguity and to write strictly specification, VDM++ (one of the Formal Methods) is proposed. However, it takes the time and effort of testers to design test cases and to carry out software testing, from specification written in VDM++.Therefore, to optimize testing process, we developed BWDM; the tool of automatic generation of test cases from VDM++ specification. BWDM analyzes boundary value of if-expressions and argument types in definition of functions. And, it generates test case automatically from a result of the analysis. This tool aims to optimize software testing process by both of automatically generation and designing test cases based on a boundary value analysis, which can detect statements that bugs seem to be included in.

OS6-4 Prototype of Refactoring Support Tool MCC Focusing on the Naming of Variables

Satoshi Tanoue*, Tetsuro Katayama* Yoshihiro Kita†, Hisaaki Yamaba*, Naonobu Okazaki*
(*University of Miyazaki, Japan,†Tokyo University of Technology, Japan)

This research has implemented a prototype of refactoring support tool MCC(Make Clean Coder) which focuses on the naming of variables. This prototype helps to describe a clean code by static analysis for the source code written in C language. And, it can help to reduce factors that prevent programmers understanding the source code when they modify it by pointing out improper variable names. We applied some source codes written in C language to the prototype, and confirmed that it works properly. By using this prototype, because it can reduce reduction of time to understand the source code, programmers can shorten the coding time, lower the possibility of embedded bugs, and decrease in the time required to add functions.

OS6-5 Improvement of Transitions and Flow Visualization TFVIS for Exception Handling.

Takuya Sato*, Tetsuro Katayama*, Yoshihiro Kita†, Hisaaki Yamaba*, Naonobu Okazaki*
(*University of Miyazaki, Japan,†Tokyo University of Technology, Japan)

In software development, it takes much time in debugging process. To find bugs in a program effectively, it's important to understand the dynamic behavior of the program. But it's difficult since the dynamic behavior of the program is generally invisible. So we developed TFVIS(transitions and flow visualization), which can visualize the dynamic behavior of Java programs. It provides visualization of data transitions in each method and flow of the whole program. But it's not useful because it visualizes only some control structures and expressions. We aim at the improvement of the usefulness by corresponding an unsupported structure. This paper focuses on Exception-handling, which is one of the feature of Java program, and especially corresponds to Try-Catch syntax.

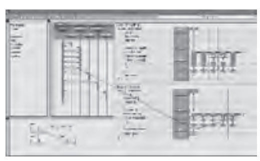

OS6-6 Automatically Business Decision Making System for Software Developmentby using CMMI

Hnin Thandar Tun†, Tetsuro Katayama*, Kunihito Yamamori*, Khine Khine Oo†
(*University of Miyazaki, Japan, †University of Computer Studies, Myanmar)

In the current software development, business decision making system is important process to support the suggestive business goals automatically in a specified area or project. In this paper, we proposed the CMMI model that is used to define the business goals for monitoring and control measurements applied by GQM approach. This paper suggests the key processes of CMMI which is necessarily for support on business effective process improvement, needs design implementation, and needs techniques and tools for achieving the future targets of goals systematically. For this illustration purpose, we need to define the business data which will be defined goals by senior level management to come out business goals aligned with resources functionality.

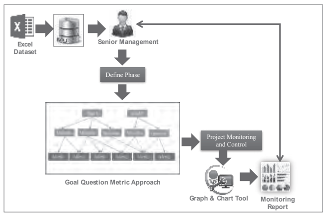

OS7: Advances in Marine Robotics and Applications (6)

OS7-1 Development of a Hydraulic Underwater Manipulator for Deep-Sea Survey AUV

Kazuo Ishii, Amir Ali Forough Nassiraei, Ivan Godler, Takashi Sonoda, Tharindu Weerakoon
(Kyushu Institute of Technology, Japan)

We are developing a group of AUVs whose mission is to capture underwater creatures or acquire in-situ biological samples in the deep sea. The AUV under developing has a hydraulic manipulator to capture the target creature, and sends underwater images that provide biologists (operators) with information to determine which creatures should be targeted and captured during the operation. In this paper, the concept and design of hydraulic actuator for 5-axis manipulator, and the mechanics of manipulator is proposed, and the experimental results of manipulator control at 10 and 20 M Pa pressure are shown.

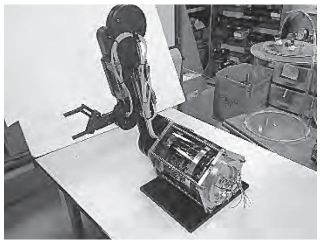

OS7-2 Experiments of floatable UAV drone for wave dissipating block inspection(I)

Watanabe, Kazuho Mitsumura, Koshi Utsunomiya, Shiyun Takasaki (Tokai University, Japan)

Determination of underwater coordinates is important in such activities like underwater vehicle operation, installation of underwater structure and so on. The determination methods are using LBL, SSBL or an inertia navigation sensor, which are all very expensive. In his paper, a floating LBL concept is presented. The LBL system consists of at least three floating buoys each of which has a GPS, a pair of ultrasound transmitter and receiver, wireless communication device and a microcomputer board which controls the total procedure. We will introduce and explain about each module of the buoy system, ultrasound transmitter/receiver measuring distance experimental results as the first step of this research

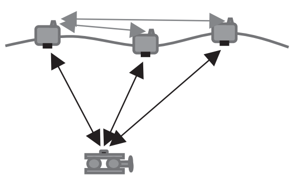

OS7-3 Experiments of floatable UAV drone for wave dissipating block inspection(II)

Keisuke Watanabe, Kazuho Mitsumura, Koshi Utsunomiya, Shiyun Takasaki (Tokai University, Japan)

UAV drones are an effective low cost photographing apparatus for ocean environment monitoring. Taking images is essential for these environment monitoring such as coastal line monitoring where beach erosion is severe, inspection of offshore structures like wind power stations or coral reef observation etc. In this presentation, we present our modification experience of making a drone watertight and floatable. Then we present several experiments on taking pictures considering ocean monitoring in the sea near our campus. The waterproof experiment is done from our school's pier. In this experiment, we repeated to start flying the drone from the sea surface and fall it down into the water several times. We can see the shoreline very clearly from more than 200m high as a macro image and also we can inspect the blocks looking around its stacks as well as approaching near the sea surface where waves break and wave splash washes the drone.

OS7-4 Development of self-diagnostic system of an autonomous underwater vehicle Tuna-Sand 2

Naoya Fujii, Yuya Nishida, Kazuo Ishii (Kyushu Institute of Technology, Japan)

For autonomous underwater vehicle (AUV), high autonomy is required in order to accomplish mission such as inspection, observation, manipulation under extreme environments, deep-ocean. One of necessary function for AUV is the self-diagnosis system to detect the abnormality can be said to be an important feature . In this paper, we propose a self-diagnostic system using the dynamical model of Sampling-AUV "TUNA-SAND2", where the fault device detection is carried out using the model, and evaluated through tank tests.

OS7-5 Development of Underwater Wireless Power Supply System Using resonant energy transfer

Kazuo Ishii, Hidaka Shota, [1]Keisuke Watanabe
(Kyushu Institute of Technology, [1]Tokai University, Japan)

Autonomous Underwater Vehicles (AUV) is one of the key technologies for deep ocean research. However, AUV cannot work for long time due to the limitation of battery capacity. To solve this problem, a noncontact wireless power supply is required for AUV to conduct observations for long period. In this study, we developed a resonant energy transfer system, which is mounted into a small AUV "DaryaBird" and the simulations and evaluation tests are carried out in the test tank.

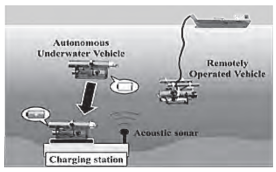

OS7-6 Development of End-effector for Sampling-AUV "TUNA-SAND2"

Kazuo Ishii, Takashi Sonoda Atsushi Nishjima, [1]Keisuke Watanabe
(Kyushu Institute of Technology, [1]Tokai University, Japan)

AUV requires high autonomy to accomplish various deep-ocean observation missions, and the next AUV is expected to have sampling function of marine benthos, that is, the end-effector to catch and bring back marine creatures. However, sampling is not easy task for AUV as the shape, size, motion of targets differs. One of the effective end-effectors is the slurp-gun type device to absorb the target with water. In this research, we had developed a sampling device for deep-ocean observation and sampling AUV, Sampling-AUV TUNA-SAND2 in order to inspection of marine ecosystem.

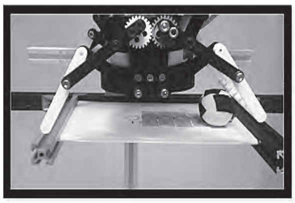

OS8 Multiagent systems and Reality Mining (4)

OS8-1 Influence of Partner Selection on Functional Differentiation: Emergence of Diversity by Isolated Interaction and Preference Change

Saori Iwanaga (Japan Coast Guard Academy, Japan), Akira Namatame (National Defense Academy, Japan)

Functional differentiation is important in nature. For example, in an ant colony, there are ants which work and does not work. I focused on how the heterogeneity emerged. I modeled that each agent can self- reinforce own preference in homogeneous population. There, the behavior reinforce the property and the property reinforce the behavior of an agent. Then, I found that interaction with steady agents enforce the properties. But, interaction with steady partners doesn't lead optimal collective behavior. We found that the partner change is good method for optimal collective behavior for both each agent and population.

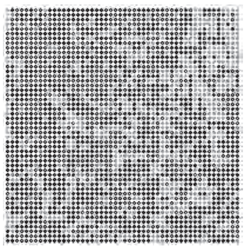

OS8-2 Beacon-based tourist information system to identify visiting trends of tourists

Akihiro Yamaguchi[1], Masashi Hashimoto[1], Kiyohiro Urata[1], Yu Tanigawa[1], Tetsuya Nagaie[1], Toshitaka Maki[1], Toshihiko Wakahara[1], Akihisa Kodate[2], Toru Kobayashi[3], Noboru Sonehara[4]
([1]Fukuoka Institute of Technology, Japan) ([2] Tsuda College, Japan) ([3] Nagasaki University, Japan)
([4] National Institute of Informatics, Japan)

In this study, we propose a system that provides tourist information and obtains trends of visiting tourists using beacons and cloud service. As part of our research, we are working on the promotion of local area tourism in cooperation with a local community. A low energy Bluetooth device is used as a beacon to transmit a universally unique identifier. In addition, beacons are placed at sightseeing spots and tourist facilities. Our proposed system comprises two application programs; one is a client-side application program that provides area-specific tourist information corresponding to the detected beacon. The other is a server-side application to record time and location information of the detected beacons. In this paper, we describe the scheme of our system, and present the results of experiments conducted using the prototype system in the local tourist area. In addition, we discuss an open platform for information collection services using beacons.

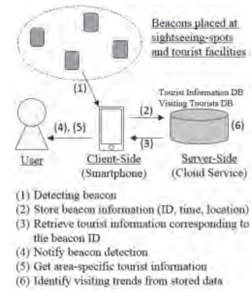

OS8-3 Analysis of Survey on Employment Trends

Masao Kubo (National Defense Academy, Japan), Hiroshi Sato (National Defense Academy, Japan), Akihiro Yamaguchi (Fukuoka Institute of Technology, Japan), Yuji Aruka (Chuo University, Japan)

Employment is a major important issue of economics and it has been difficult for the public to collect authentic information about employment because this is a sort of information should be kept secret on the both side, employer and employee. Therefore we try to reveal a trend of recent employment of Japan from Survey on Employment Trends of Japan which is a report published from Health, Labor and Welfare Ministry. This questionnaire data is mainly categorized by industrial sectors so we need extra works to know the relations and correlations over sectors. In this paper, we show results of traditional machine learning methods to this issue.

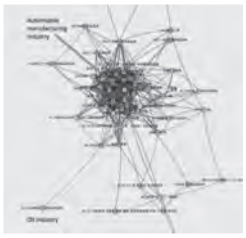

OS8-4 Direction switch behavior to enclose a target

Masao Kubo, Nhuhai Phung, Hiroshi Sato (National Defense Academy, Japan),

This paper discusses a target enclosing behavior when a part of the orbit is blocked. Usually, an orbit to enclose a target supposes to be clear. However, this situation often takes place in realistic environment. For this issue we propose an online adaptive method to enclose a target. The group of robots communicate their direction until they resolve their difficulties.

OS9 Theory and Implementation of Neuromorphic Systems (5)

OS9-1 Implementation of Multi-FPGA Communication using Pulse-Coupled Phase Oscillators

Dinda Pramanta, Takashi Morie, Hakaru Tamukoh (Kyushu Institute of Technology, Japan)

This paper proposes an implementation of multi-Field Programmable Gate Array (FPGA) communication using pulse-coupled phase oscillators. First, serial communication between two boards of FPGAs architecture are developed. First Input First Outputs (FIFOs) are used as an interface of data buffer. Second, we construct a network over two FPGAs for evaluation as shown in Fig. 1. By using a multi-FPGA as a hardware processor through the Gigabit Transceiver (GTX) clock domain, pulse-coupled phase oscillators of Winfree's model are utilized as a spike generator and we expect the ideal of model circuit will synchronize. We employ two Virtex6-Ml605 FPGA boards to construct a mult-FPGA and implement four oscillators on a hardware level. Experimental results show that each board (two oscillators) obtains the required number of resources of 16 % IOB, 434.972 MHz maximum frequency, and first spike synchronizing over two FPGAs takes 12.47 μsec with data bit speed stream 3.2 Gbps.

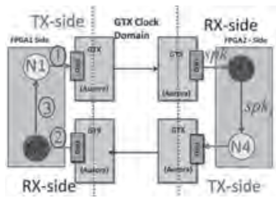

Fig.1 Communication over two FPGA boards using pulse-coupled phase oscillators

OS9-2 Multi-Valued Quantization Convolutional Neural Networks toward Hardware Implementation

Yoshiya Aratani, Yoeng Jye Yeoh, Daisuke Shuto, Takashi Morie, Hakaru Tamukoh
(Kyushu Institute of Technology, Japan)

This paper proposes a Multi-Valued Quantization (MVQ) of connecting weight for efficient hardware implementation of Convolutional Neural Network (CNN). The proposed method multiplies an input value by a multi-valued quantization weight during the forward and backward propagations, while retaining precision of the stored weights for the update process. In the both propagation processes, multipliers can be replaced with adders and shifters by setting appropriate quantized weights. We train two- to six-valued quantization CNNs with MNIST and CIFAR-10 dataset to compare the performance of them with a 32-bit floating point CNN. In the four-valued quantization, random noise is added to the quantized weight to improve the performance of generalization ability. In addition, the robustness of MVQ CNN to noise is evaluated. Experimental results show that the MVQ CNNs achieve better learning accuracy than the floating point CNN and the four-valued CNN is highly robust to the noise.

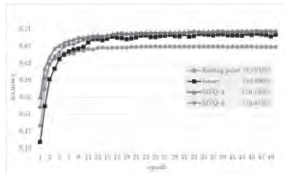

Fig.1 Comparison among floating point, BinaryConnect, MVQ-4 and -6.

OS9-3 An Improved Parameter Value Optimization Technique for the Reflectionless Transmission-Line Model of the Cochlea

Takemori Orima, Yoshihiko Horio (Tohoku University, Japan)

The reflectionless transmission-line model of the cochlea can reproduce physiological cochlear properties by adjusting its parameter values. We have employed an optimization technique to obtain good parameter values that give a desired cochlear property. However, we found that, in some case, it is difficult to find the sub-optimal parameter values because of complex dependencies between parameters. In this paper, we explicitly formulate the cochlear properties in the reflectionless transmission-line model to understand the dependencies. Furthermore, based on the results, we propose an improved optimization technique for determining the parameter values.

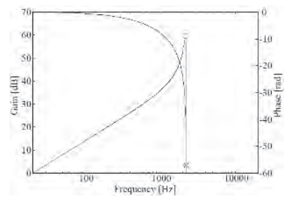

OS9-4 A parameter optimization method for Digital Spiking Silicon Neuron model

Takuya Nanami, Takashi Kohno (The University of Tokyo, Japan)

DSSN model is a qualitative neuronal model designed for efficient implementation in a digital arithmetic circuit. In our previous studies, we extended this model to support a wide variety of neuronal classes. Parameters of the DSSN model were hand-fitted to reproduce neuronal activity precisely. In this work, we studied automatic parameter fitting procedure for the DSSN model. We optimized parameters of the model by a GPU-based implementation of the differential evolution algorithm in order to reproduce waveforms of the ionic-conductance models and reduce necessary circuit resources for the implementation.

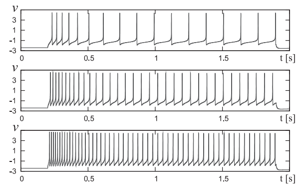

OS9-5 A Multistage Heuristic Tuning Algorithm for an Analog Silicon Neuron Circuit

Ethan Green and Takashi Kohno (The University of Tokyo, Japan)

Analog silicon neurons, electronic circuits that mimic the electrophysiological characteristics of neuronal cells, may in the future be used as fundamental building blocks of neuromorphic technologies like brain-mimetic computers. This research looks at an ultra-low power subthreshold-operated silicon neuron circuit designed with qualitative neuronal modeling. One technical challenge to future implementation of such circuits is parameter tuning—a problem stemming from temperature sensitivity of subthreshold-operated MOSFETs and the uniqueness of individual circuits in a neuronal network due to transistor variation. This research proposes a fully automated parameter tuning algorithm that combines two heuristic approaches to search for appropriate circuit parameters over a range of temperatures. The algorithm only requires the user to input the benchmark circuit characteristics and can tune the circuit to behave as a Class I or Class II neuron.

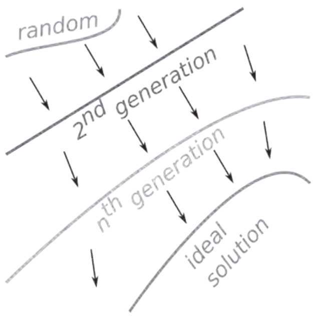

OS10 Biological Signal Sensing Technology, Device and Its Applications (5)

OS10-1 Mouse Cursor-like Control System in Consideration of the DC-EOG Signals using EOG-sEMG Human Interface

Mingmin Yan, Yu Cheng, Keiko Sakurai, Hiroki Tamura, Koichi Tanno
(University of Miyazaki, Japan)

Patients who suffered with the limb disorders cannot take care of themselves by communication barrier. However, it is possible to improve the communication abilities of the patients by using biological signal such as ocular potential and muscle potential which is caused by moving eyes or facial muscle. Therefore, we have developed the human interface using the electrooculogram (EOG) and the facial surface electromyogram (sEMG) signals which can control PC. However, this system could not control the mouse cursor in accordance with the direction and magnitude of the movement of eyes to control PC smoothly and intuitively. Thus, we proposed a new mouse cursor-like control system in consideration of the DC elements of EOG signals using the EOG-sEMG human interface. Our proposed method has both drift and blink countermeasures which had better performance in mouse cursor control, and all subjects could control the mouse cursor for both moving and clicking flexibility.

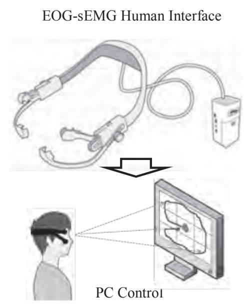

OS10-2 A Study on Eyes Tracking Method using Analysis of Electrooculogram Signals

Keiko Sakurai, Mingmin Yan, Hiroki Tamura, Koichi Tanno (University of Miyazaki, Japan)

Gaze estimation has been an active research in the past years and it is an important technique for transmitting the intention for seriously physically handicapped person who cannot move their body. In this paper, we proposed eye tracking method using electrooculogram signals which is widely applied in medical field. The proposed method has the merit to have low burden of the patient, but there is the problem not to be so high in resolution. Therefore, we carried out the experiments by electrooculogram method to make a study the calculation method of the electrooculogram element with strong correlation for the change of the eyeball movements. Specifically, we examined by comparing next values; alternating current signals, direct current (DC) signals, integral value of DC signals and DC difference values. From these experimental results, we show the possibility of eyes tracking method using the analysis of electrooculogram signals.

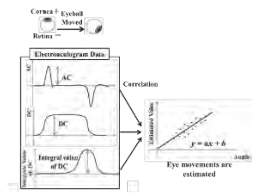

OS10-3 Development of Diagnosis Evaluation System of Facial Nerve Paralysis Using sEMG

Shogo Okazaki, Misaki Syoichizono Hiroki Tamura, Takahiro Nakashima, Eiji Kato, Tetsuya Tono (University of Miyazaki, Japan)

In Japan, diagnostic of facial nerve paralysis is mainly used the electroneuronography (ENoG) method. However, this method has the possibility that there is variability of the diagnosis results by doctors. Therefore, it is necessary the quantitative diagnostic methodology. Previous our research showed the certain correlation between diagnosis results of ENoG and surface-electromyogram (sEMG) data. In this paper, we developed the diagnosis evaluation system of facial nerve paralysis using sEMG by software. We compared with our developed software and manual by experimental person. From simulation results, our developed software showed the correlation coefficient (R^2) between ENoG is 0.68. In our future works, we evaluate our system by the opinion of otolaryngologist.

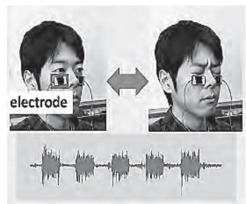

OS10-4 High CMRR and Wideband Current Feedback Instrumentation Amplifier Using Current Conveyors

Shota Mago, Hiroki Tamura, Koichi Tanno (University of Miyazaki, Japan)

This paper presents a high CMRR and wideband current feedback Instrumentation Amplifier (IA). The proposed IA architecture consist of Fully Balanced Differential Difference Amplifier (FBDDA) and Differential Difference Amplifier (DDA) based on 2nd generation current conveyor (CCII) with a buffer. The proposed IA was evaluated by using HSPICE simulation with 1P 3M 0.6-um CMOS process. From the simulation results, the proposed IA exhibits average CMRR was 109.3 dB higher than the conventional one. Furthermore, since the current feedback based on CCII is adopted, the proposed IA can get higher closed-loop gain over a larger bandwidth than corresponding voltage feedback.

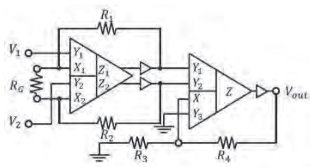

OS10-5 Voltage Rectifier Circuit with Voltage Doubler Using New Active Diode

Masayuki Uchihara, Hiroki Tamura, Kochi Tanno (University of Miyazaki, Japan)

In this paper, voltage rectifier circuit with voltage doubler using new Active Diode (AD) is proposed for battery less biological signal measurement system using smartphone. Firstly, we propose the new AD which consists of AD core circuit and Bulk Regulation Transistor (BRT). The advantage of proposed AD is insensitive to the threshold voltage of MOSFETs and very useful for low power and low voltage operation. Next, the voltage rectifier circuit with voltage doubler using the proposed ADs is presented. Thanks to the good performance of the proposed AD, the designed rectifier could operate as theory by only the sin waves from the earphone terminal of smartphone. The proposed circuits were fabricated actually using 1-P 2-M 0.6-um CMOS process. The detailed simulation and measurement results are reported in this paper.

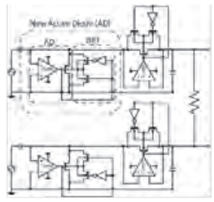

The voltage rectifier circuit with voltage doubler using the proposed ADs

OS11: Robot Control and Localization (4)

OS11-1 Marker Recognition System for Localization of the Rover on the Lunar Space

Na-Hyun Lee, Jang-Myung Lee (Pusan National University, South Korea)

This paper proposes a marker realization system for rover localization in lunar environment. CPU used in the space environment is not as sensitive to changes of the surrounding environment differently from normal CPU, but it has a lower performance. So it is necessary to use an algorithm reduced amount of computation. In order to reduce the amount of computation, we propose a marker-based algorithm. It has a smaller quantity of computation than map-based localization algorithm commonly used in the space environment. For constructing this algorithm, we performed a marker detection test, and then extracted the center point coordinate of the marker.

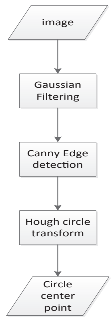

OS11-2 Dynamic Model and Finite-Time SMC and Backstepping Control of a Mabile-Manipulator System

Seongik Han, Hyunuk Ha, and Jangmyung Lee (Pusan National University, Korea)

A mobile manipulator was designed by combining three-wheeled mobile robot equipped with the DC motor and three-links manipulator equipped with dynamixel motor. The kinematic relation and dynamic model were built via nonholonomic constraint and Euler-Lagrange equation. For the decoupled model of this system, adaptive finite-time controllers sliding mode controller (SMC) and backstepping controller were designed respectively to obtain fast tracking response. Simulation and experimental results show the efficacy of the proposed control scheme.

OS11-3 Bilateral Control of Hydraulic Servo System for 1DOF Master Slave Manipulator

Jie Wang, Karam Dad and Min Cheol Lee (Pusan National University ,Korea)

In this research reaction force estimation method based on Sliding mode control with sliding perturbation observer (SMCSPO) of a bilateral control in hydraulic servo system for one degree of freedom (DOF) master-slave manipulators is proposed. 1DOF hydraulic servo system used in dismantling nuclear power plant. The reaction force at the end effector of slaver is estimated by sliding perturbation observer (SPO) without using any sensor. This research verifies through experiment that slaver can follow the trajectory of the master device using the proposed bilateral control strategy and reaction force estimation method.

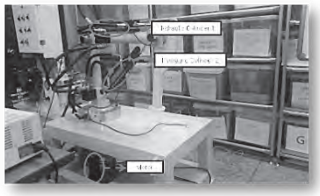

OS11-4 Advanced impedance control of haptic joystick for effective mobile robot handling

Gyung-I Choi, Jang-Myung Lee (Pusan National University, South Korea)

This paper proposes optimized structure of 6 D.O.F. haptic joystick and tele-operated mobile robot system based on haptic interfaces. Kinematic analysis of specially designed 6 D.O.F. haptic joystick derives the coordinate of end effect. The designed haptic joystick transfers operator's moving command to mobile platform with force controlled coordinate information. Attached ultra-sonic sensors detect nearby obstacles including walls and retransfer the distance between mobile platform and obstacles to the haptic joystick. Attained real-time displacement information controls DC motors between links supporting the handle for effective user handling. Practical simulations and real experiments verified proposed impedance control and its tele-operation system of intelligent haptic joystick.

OS12 Machine Learning and Its Applications (4)

OS12-1 A Rule-Based Classification System Enhanced by Multi-Objective Genetic Algorithm

Kenzoh Azakami, Shingo Mabu, Masanao Obayashi, Takashi Kuremoto (Yamaguchi University, Japan)

Recent years, information is diversified, and the enormous amount of data is left unorganized. Data mining is a technique of extracting rules from big data. In this paper, we aim to realize a classification system using a rule extraction method named genetic network programming (GNP). However, there are some problems to be considered, that is, a large number of rules are extracted, so it is difficult to judge important rules; and even in simple classification problems, e.g., two-class problems, a variety of patterns potentially exist in each class. To select important rules and make rule clusters corresponding to the potential patterns, a rule clustering algorithm using multi-objective genetic algorithm (MOGA) is proposed to enhance our conventional classification system.

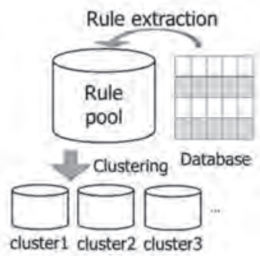

Rule clustering

OS12-2 A Method of Feature Extraction for EEG Signals Recognition using by ROC curve

Takashi Kuremoto, Yuki Baba, Masanao Obayashi, Shingo Mabu (Yamaguchi University, Japan)
Kunikazu Kobayashi (Aichi Prefectural University, Japan)

The feature extraction for EEG signal Recognition plays an important role for all kinds of classifiers. However, it is difficult to recognize the activities and mental tasks in the brain using EEG signals because the difference between individuals and the change of mental states. In this study, we propose a method of extract EEG signals using by FFT and receiver operating characteristic (ROC) curve. At first, the raw EEG data are processed by discrete Fourier transform (DFT). After that, data of frequency-spectrum of different mental tasks were compared by the value of area under the curve (AUC), and the data with higher AUC (near 1.0) were chosen as feature vectors. Experiment results using benchmark data of EEG signals showed the effectiveness of the proposed feature extraction method in the cases of self-organizing map (SOM), support vector machine (SVM) , and multi-layer perceptron (MLP).

Table 1 Mental tasks in a benchmark database.

Mental Task	Contents
Baseline	Relaxing as much as possible
Multiplication	Calculating multiplication mentally.
Letter-composing	Considering the contents of the letter
Rotation	Imagining rotation of a 3-D object
Counting	Imagining writing a number in order

OS12-3 Forecasting Real Time Series Data using Deep Belief Net and Reinforcement Learning

Takaomi Hirata, Takashi Kuremoto, Masanao Obayashi, Shingo Mabu (Yamaguchi University, Japan);
Kunikazu Kobayashi (Aichi Prefectural University, Japan)

Artificial neural networks (ANNs) typified by deep learning (DL) is one of the artificial intelligence technology which is attracting the most attention of researchers recently. However, the learning algorithm used in DL is usually with the famous error-back propagation (BP) method. BP is a very powerful parameter optimization method, however, it also learns the unpredictable noises of the data. In this paper, we adopt a reinforcement learning (RL) algorithm "Stochastic Gradient Ascent (SGA)" into a Deep Belief Nets (DBN) with multiple restricted Boltzmann machines (RBM). Prediction experiments used a benchmark of time series forecasting competition and realistic data verified the effectiveness of the proposed DL method.

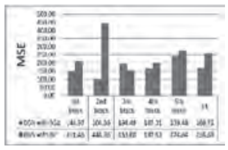

Comparison of prediction mean squared errors between different learning methods

OS12-4 Improvement of Robot's Self-localization by Using Observer View Positional Information

Yo Aizawa, Takuo Suzuki, and Kunikazu Kobayashi (Aichi Prefectural University, Japan)

This study aimed to improve the precision of the robot's self-position estimation in the standard platform league of RoboCup, i.e. a robotic soccer competition. For the precision improvement of the self-position estimation, we suggest a new technique that uses a camera out of the field for assistance. Robots in the field use the unscented particle filter that estimates their position from landmark. When a robot which is equipped with the filter cannot recognize landmarks exactly, particles spread and the estimation precision of the self-position decreases. Therefore, the overlooking camera out of the field observes each robot's position. When particles spread, the camera out of the field estimates the foot of a robot, and then the robot sprinkles particles on the neighborhood again. In this way, even if a robot cannot recognize landmarks exactly, assists of camera out of the field revise the position of particles and improve the precision.

Resampled position of particles

OS13: Intelligent Control (6)

OS13-1 Modeling and Simulation for a Quadrotor Vehicle with Adaptive Wing

Qunpo Liu , Fuzhong Wang, Hongqi Wang, Jikai Si (Henan Polytechnic University, P.R.China)
Hanajima Naohiko (Muroran Institute of Technology, Japan)

This study intends to address the questions of low effective and high cost in the process of artificial sorting and packing of fruit. In this paper, a kind of automatic packaging and plastic foam net packing robot based on neural network plastic foam netting is presented. The round fruit can be filtered and classified by neural network controller based on fruit's size, skin roughness and color which are based on machine vision. And the expansion degree of plastic foam nets is adjusted adaptively according to fruit size. The system was simulated by V-REP simulation software. The simulation results showed that the system could complete the classification and packing with plastic foam mesh of round fruit.

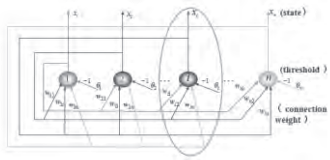

OS13-2 Fuzzy self-tuning PID control algorithm for belt conveyor driven by multi-motor

Caixia Gao, Fuzhong Wang, Ziyi Fu (Henan Polytechnic University, P.R. China)

Aiming at the problems of low efficiency when long distance and high-inclination belt conveyor driven by multi-motor is in light or idle run as well as electrical power unbalance. Control strategy for belt conveyor driven by four-motor via fuzzy self-tuning PID control algorithm was proposed. The Speed setting algorithm of belt conveyor and fuzzy self-tuning PID algorithm for speed control and power balance control are introduced. The application shows that, according to the coal flow changes of the belt conveyor in real-time, the speed can be automatically adjusted through this algorithm, making the power of the four motors convergence ,whose speed control error and the power control error both lower than 2.6%.

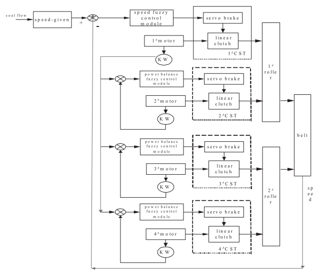

OS13-3 Continuous Non-singular Fast Terminal Sliding Mode Control for an Active Gravity Field Simulator

Jiao Jia, Yingmin Jia and Shihao Sun(Beihang University (BUAA), P.R.China)

In this study, a non-singular fast terminal sliding mode (FTSM) controller is designed for an active gravity field simulator (AGFS). Some sufficient conditions are established to guarantee the stability by using the Lyapunov theory. It is shown that the proposed controller can eliminate the chattering effect without losing the robustness property. Simulation results show that faster and high-precision tracking performance can be obtained compared with the conventional continuous sliding mode control method.

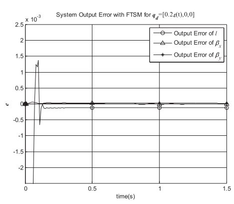

OS13-4 Weighted Multiple Model Adaptive Control for a Category of Systems with Colored Noise

Yuzhen Zhang, Qing Li and Weicun Zhang (University of Science and Technology Beijing, P. R. China)

The multiple model adaptive control (MMAC) of discrete-time stochastic system with colored noise is considered in this paper. Model set consists of a finite number of fixed and one adaptive identification models. After that, based on the output errors of the models, a simple weighting algorithm is adopted with convergence guaranteed. The proofs of global stability and the convergence of the overall system are presented. Besides, the influence of initial value selection of adaptive model on system performance is described. Finally, computer simulation results are shown to verify the theoretical results.

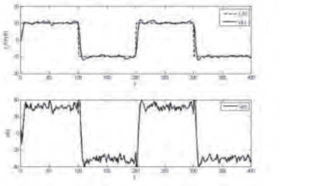

OS13-5 Neutral Networks-Based Adaptive Fixed-Time Consensus Tracking Control for Uncertain Multiple AUVs

Lin Zhao[1], Yingmin Jia[2] and Jinpeng Yu[1]
([1]Qingdao University, P.R.China; [2]BeihangUniversity (BUAA), P.R. China)

This paper is concerned with the fixed-time consensus tracking problem for multi-AUV (autonomous underwater vehicle) systems with uncertain parameters and external disturbances. Firstly, a fixed-time terminal sliding mode is proposed, which can avoid the singularity problem. Then, a continuous distributed consensus tracking control law is designed based on Neutral Networks approximation technique, which can guarantee the consensus tracking errors converge to the desired regions in fixed time. A simulation example is given to show the effectiveness of proposed methods.

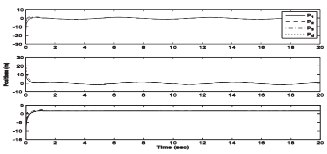

OS13-6 Conducted electromagnetic interference prediction of the Buck Converter via Neural Networks

Sumin Han, Fuzhong Wang (Henan Polytechnic University, P.R. China)

This paper proposes an approach to predict conducted electromagnetic interference (EMI) on the power supply side in the buck converter. The experimental scheme is designed to collect the input and output target samples, whose correlativity is analyzed to verify their correlation degree. The paper establishes a three-layer network including one hidden layer, whose activation function is of the hyperbolic tangent type to ensure the rapidity of convergence .The conducted EMI predicting model is established by sample training, the differential mode(DM) and common mode (CM) interference prediction waveforms is obtained and analyzed . The results demonstrate that the forecasted and measured waveform is in decent consistency of time domain and power spectrum.

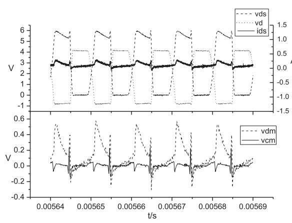

OS14 Advanced Control (5)

OS14-1 Targeting Chaos System via Minimum Principle Control

Yunzhong Song, Ziyi Fu, Fuzhong Wang (Henan Polytechnic University, P, .R.China,)

Chaos targeting via Minimum Principle Control (MPC) was suggested here, where like the already existing results, the targeting via MPC can stabilize all the non-stable equilibrium when the extra added control was introduced in the first or the second equation of the chaos system, however, unlike the already existing results, when the extra added control was introduced in the third equation of the chaos system, the non-stable equilibrium can not be stabilized at all with the already existing methods, to be unique, the MPC can still be effective when the added extra control was introduced in the third equation, albeit with the cost of switching control direction for a duration.

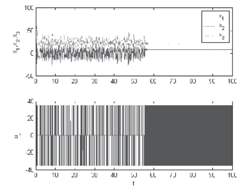

OS14-2 Three-dimensional Leader-Follower Formation Flocking of Multi-Agent System

Yongnan Jia, Weicun Zhang (University of Sciences and Technology, Beijing, China)

This paper aims to investigate the three-dimensional formation flocking problem of multi-agent system with leader-follower structure. We consider each agent as an extended unicycle. Based on the nearest neighbor interaction rules, a kind of distributed control algorithm is proposed with the combination of consensus algorithm and attractive/repulsive functions. The proposed algorithm enables all unmanned aerial vehicles asymptotically converge to fly with the same velocity and approach the expected formation with their neighbors, provided that the initial interaction network of the system is leader-follower connected. Numerical simulations are carried on the multi-agent system with large-scale to validate the functionality of the proposed algorithm.

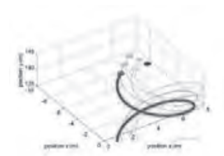

OS14-3 Leader-follower Formation Control of Mobile Robots with Sliding Mode

Wenhao Zheng and Yingmin Jia (Beihang University, P.R.China)

This paper considers the formation control of nonholonomic mobile robots. The formation problem is converted to the tracking error model based on the leader-follower structure. A sliding mode controller, which is proved to be globally finite time stable by Lyapunov stability theory, is presented in this study. In addition, a continuous reaching law is designed to reduce the chattering which caused by the computation time delays and limitations of control. The results of simulation and experiment verifies the feasibility and effectiveness of the control strategy.

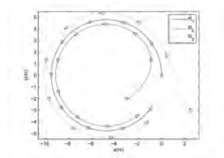

OS14-4 H_∞ Containment Control for Nonlinear Multi-agent Systems with Parameter Uncertainties and Communication Delays

Ping Wang[1], Yingmin Jia[2] ([1] North China Electric Power University, [2]Beihang University, P.R.China)

This paper considers robust containment control problem for uncertain multi-agent systems with inherent nonlinear dynamics. A distributed protocol is proposed using local delayed state information, and then the original problem is converted into an H_∞ control problem by defining an appropriate controlled output function. Based on robust H_∞ control theory, sufficient conditions in terms of linear matrix inequalities (LMIs) are derived to ensure the prescribed H_∞ containment. A numerical example is provided to demonstrate the effectiveness of our theoretical results.

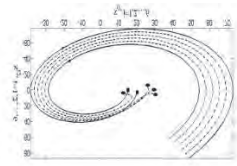

OS14-5 Stochastic Resonance in an Array of Dynamical Saturating Nonlinearity with Second-Order

Yumei Ma, Lin Zhao, Zhenkuan Pan and Jinpeng Yu (Qingdao University P.R.China)

We study the Stochastic Resonance (SR) in parallel array of dynamical saturating nonlinearities with second-order via the measure of output signal-to-noise ratio (SNR). Firstly, the numerical results demonstrate that the output SNR can be enhanced by parallel array of dynamical saturating nonlinearities with second-order by tuning the internal noise and the self-coupling coefficient. Then, the SR effects of the dynamical nonlinearity with second-order are superior to the dynamical nonlinearity with first-order.

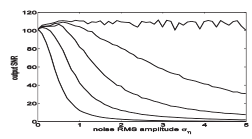

OS15 Recognition and Control (8)

OS15-1 Integral Design of Intelligent Home Equipment

Yuxing Ouyang [1], Fengzhi Dai [1*], Yiqiao Qin [1], Ce Bian [1], Bo Liu [2], Hongwei Jiao [3]
([1] Tianjin University of Science & Technology, [2] Inner Mongolia University,
[3] Tianjin Technology School of Printing and Decoration, China)

The set of equipment is designed to all household equipment network monitoring and control. Using WIFI module for wireless networking purpose is to upload information of all connected smart home devices to the server through the network, and it can be remotely controlled by the external network and monitoring of household equipment information. For simple household equipment, the control is directly taken to the built-in MCU's WIFI module, and for the complex household equipment, it is through the external MCU and WIFI module for communication control. Take the Airkiss distribution mode to connect the WIFI master module to the network, and the other WIFI module devices to adopt the ad hoc network mode for wireless networking.

OS15-2 Research on Underwater Robot Recognition

Binhu Song[1], Fengzhi Dai[1]*, Qijia Kang[1], Haifang Man[1], Hongtao Zhang[1], Long Li[2], Hongwei Jiao[3] ([1] Tianjin University of Science and Technology, [2] Tianjin Electric Locomotive Co., Ltd, [3] Tianjin Technology School of Printing & Decoration, China)

Due to the characteristics of the underwater robot, the computer vision technology for pedestrian detection and object detection is not adapt better to a variety of underwater robots. The recognition algorithm must be more robust and extensive that can adapt to the changing environment. Support vector machine (SVM) method is a kind of good classification algorithm that is used in many aspects. Its kernel function analysis is very advanced. After the optimization, the kernel function can be adapted to a large number of underwater robot images that are difficult to be recognized by other methods.

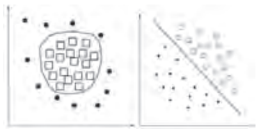

OS15-3 Design of Intellectual Vehicles with Path Memorizing Function

Yiqiao Qin [1], Fengzhi Dai [1*], Yuxing Ouyang [1], Baochang Wei [1], Simini Chen [2], Hongwei Jiao [3] ([1] Tianjin University of Science & Technology, [2] Palace Museum, [3] Tianjin Technology School of Printing & Decoration, China)

In this paper, after analyzed the deficiencies of current intelligent transportation vehicles, the design of a new transport vehicle system that has the function of path memorization (a new algorithm to recognize the position and path of the vehicle) is proposed. It neither relies on external positioning methods such as GPS, wifi, etc, nor on the electromagnetic or photoelectric rails. This algorithm sets the starting point as the coordinate origin to recognize the position and the path, and compares its current position with the ideal path, enabling the vehicle to travel on an established path. On the basis of this algorithm, we design a kind of intelligent transportation system by NXP ARM-M4 K60 Singlechip. This system is not affected by the ground condition, so there is no need for any ground signs. Still, it can transport goods in factories scattered with water and iron scrap, and on open-air dirt roads or rainy outdoor environments.

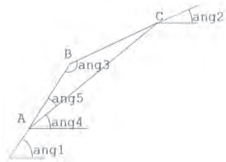

OS15-4 Action Recognition based on Binocular Vision

Yiwei Ru [1,2,*], Hongyue Du [1], Shuxiao Li [2], Hongxing Chang [2] ([1] Harbin University of Science & Technology, [2] Chinese Academy of Sciences, China)

Aimed at the problem that the recognition accuracy of the monocular camera is low, a binocular vision recognition algorithm based on CNN (convolutional neural network) is proposed. Firstly, the left and right views obtained by the binocular camera are matched to obtain the depth map of the human body under the camera coordinate system (O-XYZ). Then the depth information is projected onto the three planes of O-XY, O-YZ and O-ZX respectively in the camera coordinate system to overcome the problem that the human body motion detection is prone to error in the absence of the overhead view and the side view of the monocular camera. In order to reflect the motion of the timing information, the projection images of three directions were used to construct MHI (motion history image), and then the three MHIs were constructed as the three channels of the image to construct a new image. Using CNN to train the classifier. Experimental results show that the binocular recognition algorithm is 12% more accurate than the monocular recognition algorithm, which meets the requirements of practical application .

OS15-5 Analysis and Control of a Novel 4D Chaotic System

Hong Niu (Tianjin University of Science and Technology, China)

In this paper, a novel four-dimensional(4D) autonomous chaotic system is presented. For chaos control of the 4D system, a linear feedback controller only with one variable is designed via matching the variable coefficients of the Lyapunov function, so that the system is no longer chaotic or periodic but globally asymptotically converges to the equilibrium point at the origin. The numerical simulation results are given to illustrate the feasibility and effectiveness of the method.

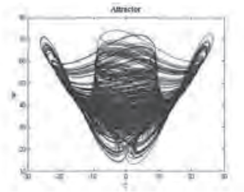

OS15-6 Analysis of a three-dimensional chaotic system and its FPGA implementation

Hefei Li, Xianghui Hu
(Tianjin University of Science and Technology, China)

In this paper, a three-dimensional chaotic system is implemented based on the Field Programmable Gate Array (FPGA). The 3-D chaotic system has a very complex chaotic characteristic with its real four-wing chaotic attractor. By means of numerical simulation, phase orbits, bifurcation diagram and Lyapunov exponents are given and analyzed to observe dynamic characteristics of the three-dimensional chaotic system. Numerical simulation and the results of implementation in FPGA show that this chaotic system really has many obvious characteristics of chaos.

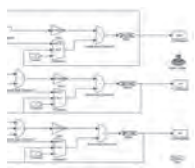

OS15-7 Image Encryption Based on Fractional-order Chaotic Model of PMSM

Wei Xue*, Mei Zhang, Shilong Liu, Xue Li
(Tianjin University of Science and Technology, China)

The permanent magnet synchronous motor (PMSM) is a nonlinear system with multi-variable and significant coupling. When PMSM works in certain conditions, the chaotic behavior will occur. In this paper, a application of image encryption based on fractional-order PMSM chaotic model is investigated. By the mean of drawing histogram, adjacent pixels correlation, key sensitivity of the ciphertext were analyzed. The results show that the image encryption based on fractional-order chaotic model of PMSM have a large key space and high security.

OS15-8 The Application of a Novel Fractional Hyper-chaotic in Image Encryption

Wei Xue *, Shilong Liu, Mei Zhang, Xue Li.
(Tianjin University of Science and Technology, China)

In this paper, a novel fractional-order hyper-chaotic system is proposed, and its dynamic characteristics are analyzed by drawing the phase trajectory and Lyapunov exponent spectrum. The simulation results show that the fractional-order chaotic system has hyper-chaotic characteristic. Then, image encryption implementation based on the fractional-order hyper-chaotic system is investigated, a three-color separation of color pictures and scrambling the image pixel location, the histogram, key space, pixel distribution, correlation coefficient and key sensitivity of ciphertext are tested and analyzed. The results show that the algorithm has good security and practicability.

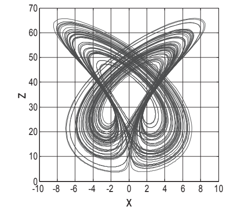

OS16 Image Recognition and Chaotic Systems (8)

OS16-1 A Method of Detecting Abnormal Crowd Behavior Events Applied in Patrol Robot

Huailin Zhao, Shunzhou Wang, Shifang Xu,Yani Zhang ,
(Shanghai Institute of Technology, China) Masanori Sugisaka (ALife Robotics Corp.Ltd.)

When the ground or air patrol robot monitors a certain area, one of the important intelligent functions is to estimate the crowd density of the monitored area. This paper analyzes the typical crowd density estimation algorithm, and proposes a convolution neural network model for crowd density estimation. Combining the crowd density estimation and the crowd speed calculated by the optical flow algorithm, we can predict and detect abnormal behavior events of the crowd. The method can not only estimate the population density of the specified area, but also analyze and detect the abnormal behavior events of the crowd. This application provides an important technical support for enhancing the patrol robot monitoring effect.

The flowchart of the whole algorithm

OS16-2 Design of the Multi-Car Collaboration System

Huailin Zhao,Yangguang Guo (Shanghai Institute of Technology, China)
Masanori Sugisaka (ALife Robotics Corp.Ltd., Japan)

With the development of the computer and electronical technology, it is an irresistable trend to make the multiple intelligent agents cooperate with each other to complete a specific complex task. Due to the high cost of real vehicles, most of the researches are based on simulation softwares. In our project, a few real small smart cars are used, and the design of multi-car cooperation system is completed. A system platform of the small smart cars is established, which can simulate the behaver such as positioning, formation and so on. In the experiment field, a global camera is used to achieve global synchronical positioning. The simulation results show that the multiple smart cars can get collaborating.

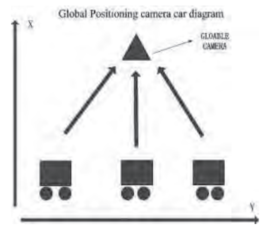

OS16-3 Research on an Algorithm of the Character Recognition with Self-learning the Recognition Errors

Huailin Zhao, Yawei Hou, Shifang Xu, Congdao Han (Shanghai Institute of Technology, China)
Masanori Sugisaka (ALife Robotics Corp.Ltd., Japan)

With the development of science and technology, the character recognition technology has been widely applied in people's daily life. The related researchers are studying on it in order to achieve the technology with higher recognition rate. In this paper, a new recognition algorithm is proposed based on self-learning the recognition errors. The method is able to identify whether the learning result is correct or not and then recognize the correctness of the learning result by itself, correct the recognition result of the error and simultaneously memorize it. When the same kind of error is recognized again, it is automatically corrected. This article has carried on the simulation verification on the Matlab platform to prove the effectiveness of this method. The simulation results show that the method can improve the character recognition rate.

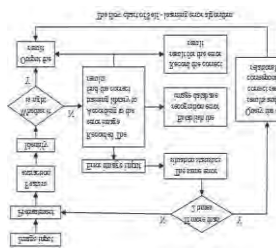

OS16-4 An Improved Method of the Power System Short Term Load Forecasting Based on the Neural Network

Shunzhou Wang, Huailin Zhao, Yani Zhang, Peng Bai
(Shanghai Institute of Technology, China)

Load forecasting is an important content of planning and operating power system. It is the prerequisite to ensure the reliable power supply and economic operation. In this paper, an improved method of short-term load forecasting for load data of two different regions is proposed. Firstly, multiple linear regression and quadratic regression are used to analyze the regression relationship between weather factors and load, and then the greatest impact on load of weather factors are selected. The Elman neural network is used to predict unknown one-week load data taking into account without whether factors situation and whether factors situation. In the predicting situation of considering whether factors, the multi-weather factors are integrated with the temperature and humidity index , which are used as the neural network input training samples. The prediction result is good.

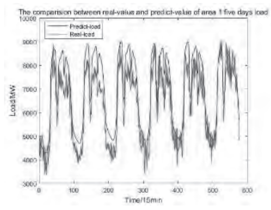

OS16-5 Improvement on LEACH Agreement of Mine Wireless Communication Network

Liu Yun-xiang and Zhang Wei (Shanghai Institute of Technology, China)

According to the features of mine communication with wireless sensor network, a routing algorithm called LEACH-KPPE based on K-means++ was proposed. The clustering was optimized. According to the energy and distance factors, the selection of cluster head node was optimized. The problem of uneven distribution of cluster head node, network stability and energy inequality on the LEACH algorithm was improved effectively. The simulation results show that the LEACH-KPPE algorithm could better improve the energy consumption of the whole network, improve the utilization of energy and effectively prolong network life cycle.

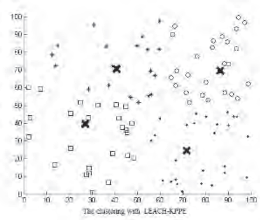

OS16-6 A New Four-Wing Chaotic System Generated by Sign Function

Hongyan Jia, Shanfeng Wang,Yongjun Wu
(Tianjin University of Science and Technology, China)

In the paper, a new chaotic system is obtained by adding a Sign Function to a three-dimensional chaotic system. Its some basic characteristics including the equilibrium point, phase trajectory, bifurcation diagram, Lyapunov exponent and so on, are subsequently calculated. Moreover, the dynamic characteristics of the new chaotic system is also analyzed with the variation of the system parameters. In the end, the paper design an analog circuit to implement the chaotic system, the results from the circuit are consistent with those from the numerical analysis, and thus the chaotic characteristics of the new system is verified physically. The new chaotic system can provide a new model for engineering applications.

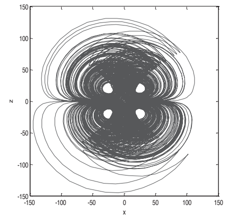

OS16-7 A Three-Dimensional Chaotic System Generating Single-wing or Two-Wing Chaotic Attractors

Hongyan Jia, Yongjun Wu, Shanfeng Wang.
(Tianjin University of Science and Technology, China)

In this paper, a three-dimensional chaotic system is proposed based on a simple 3-D autonomous system by adding a linear piecewise function. It is very interesting is that the new three-dimensional chaotic system can generate single-wing or two-wing chaotic attractors with variation of parameter. Several basic characteristics of the system, such as bifurcation diagram, phase orbits, and Lyapunov exponents are given to investigate different chaotic motions for the new system. The new system is found to be chaotic in a wide parameter range, and to show many complex dynamical behaviors. That is, the results obviously show the system is chaotic and its dynamics are very complex.

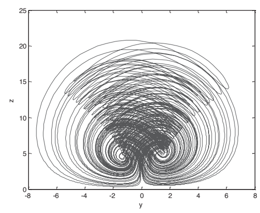

OS16-8 Circuit implementation of a new fractional-order hyperchaotic system

Xuyang Wu, Hongyan Jia, Ning Bai, Weibo Jia
(Tianjin University of Science and Technology, China)

In the paper, some basic dynamic properties of a new fractional-order hyper-chaotic system are firstly investigated, such as the equilibrium point, phase trajectory, bifurcation diagram, Lyapunov exponent, and so on. Then the paper design an analog circuit to implement the fractional-order hyper-chaotic system, the results from the circuit are consistent with those from the numerical analysis, and thus the hyper-chaotic characteristics of the new fractional-order system is verified physically. It is very important to implement fractional-order hyper-chaotic system with more complicated dynamics for theoretical research and practical application. The new hyper-chaotic system can provide a new model for engineering applications.

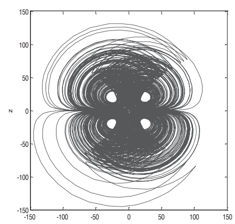

OS17 Natural Computing and Biology (4)

OS17-1 Molecular Artificial Intelligence by using DNA reactions

Yasuhiro Suzuki, Rie Taniguchi (Nagoya University, Japan)

We have developed molecular Artificial Intelligence system by using DNA molecules, where "intelligence" means that the reaction system can "select" DNA molecules to sustain their reactions. We have bio-chemically implemented the reaction system by using the DNA strand-displacement reaction and have obtained several mutated DNA sequences that can sustain the reactions and we have investigated behaviors of reactions when there are several mutated DNA sequences.

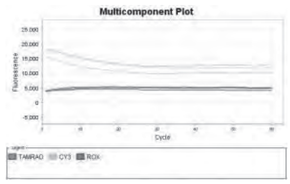

OS17-2 Neural Networks by using Self-Reinforcement Reactions

Yasuhiro Suzuki (Nagoya University, Japan)

We consider a chemical reaction network model in which selections of reaction are stochastic and depend on past history. In this chemical reaction network, we found the emergence of Auto-Catalytic Sets (ACS) and complex dynamics in which ACS are repeatedly created and destroyed; we have called this reaction system as the Self-Reinforcement Reactions, SRR. We developed a neural-networks system by using SRR and confirm the neural network of SRR can solve a linear classification problem.

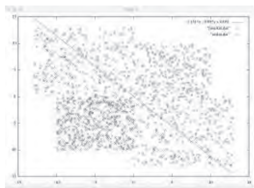

OS17-3 Artificial Chemistry by Sound Waves

Yasuhiro Suzuki (Nagoya University, Japan)

We have proposed an Artificial Chemistry based on a rewriting system on multisets and developed various models such as computational protocells in Artificial Life. However, such an Artificial Chemistries are implemented in silico and cannot interact with its environment out of the silico (e.g. a computer system). Hence we have transformed and Artificial Chemistry, Abstract Rewiring System on Multisets, ARMS into sound waves interactions systems; where every abstract chemical is a sound waves and artificial chemical reaction is interaction with sound waves. By using this system, the artificial chemical reactions inside silico is able to interact with its environment through sound waves.

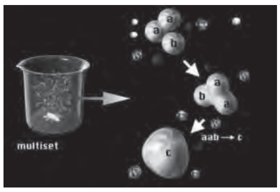

OS17-4 Variants of spiking neural P systems with energy control

Rudolf Freund, Marion Oswald (TU Wien, Vienna, Austria)

We consider several variants of spiking neural P systems (SNPSs), theoretical frameworks for brain modeling. Whereas the original variant only allows for one kind of spikes, in this paper special emphasis is laid on SNPSs with different colors or SNPSs with anti-spikes. Moreover, instead of choosing the rules in the neurons based on the current contents being in a regular set, we (also) consider the way of choosing the rule to be applied in each neuron consuming the maximal energy. This choice can be accomplished by assigning energy values to each rule or by assigning (different) energy directly to the colored spikes.

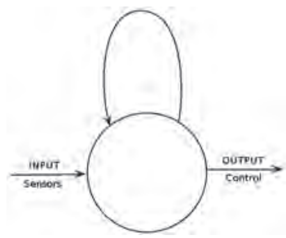

OS18 Advanced Management and Technology (4)

OS18-1 Development of English Text for the engineers to preserve the environment of North-East Asia

Yuji Minami, Kenji Fukuchi, Shinya Tagawa (National Institute of Technology, Ube, Japan)

Our research began in 2007 as a part of the activities of ‘Good Practice’ for Education of Engineers in cooperation with the UMICNEA, that is, “Union of Machinery Industrial Cities in North-East Asia”. Through our study, we found it necessary to acquire the knowledge of ‘Fish Breeding Forest’ when developing and preserving the area of North-East Asia, where the river Amur plays an important role for sustaining the environment of this region. We made the research of the origin of the river Amur, named ‘the river Onon’, located in the area of ‘Strictly Protected Area’ in Mongolia by the agreement of Mongolia, Russia, and China in 2005. We plan to make it clear that future engineers should find a good way of cooperation through English as a communication tool for the purpose of playing an active part together.

都市(City)	緯度(Latitude)	経度(Longitude)
nikol.ru	53° 8'32.60"N	140° 43'53.30"E
kmscity.ru	50° 34'1.33"N	137° 0'1.88"E
khabarovskadm.ru	48° 30'9.83"N	135° 3'58.54"E
admblag.ru	50° 16'21.99"N	127° 32'25.45"E
heihe.gov.cn	50° 14'42.46"N	127° 31'41.88"E
Beiji	53° 28'49.94"N	122° 21'32.89"E
Shilka	51° 50'55.43"N	116° 1'58.17"E
Chindant	50° 34'31.71"N	115° 24'27.24"E
Ulacha	50° 24'12.99"N	113° 16'2.22"E
Onon	48° 37'7.01"N	110° 36'18.30"E
ulaanbaatar.mn	47° 55'11.44"N	106° 55'11.81"E

OS18-2 Measuring Fragility and its Implications in Networked Systems

Tsutomu Ito*, Katsuhiko Takahashi, Katsumi Morikawa, Takao Ito (Hiroshima University, Japan), Rajiv Mehta (New Jersey Institute of Technology, USA), Seigo Matsuno (Ube National College of Technology, Japan), Makoto Sakamoto (University of Miyazaki, Japan)

A survey the literature reveals that a plethora of network analytic facets, such as degree, eigenvalue, density, block, cluster, have been developed and employed to further our understanding of network structures. To extend our understanding of network systems, additional dimensions need to be identified that shed light on the dynamic processes among individual member nodes within network structures. Specific to the context of networked systems, this paper proposes a new concept of fragility. Specifically, it develops and empirically tests a mathematical model of fragility from the standpoint of how ties among network members significantly influence corporate performance. Using data drawn from two well-known network organizations, Mazda and Toyota, this research attempts to calculate the relationship between degree and fragility, thus confirming the validity of the new concept. Furthermore, the relationship between fragility and corporate performance is also assessed. This paper makes a contribution to extant thought by: 1) Defining fragility, 2) Discussing the nature of the relationship between fragility and corporate performance, and 3) Empirically testing the dimensional differences among fragility and corporate performance, thus enabling a contrast between Mazda and Toyota. Based on the findings, the managerial implications are discussed, the study limitations are identified and directions for further research are suggested.

OS18-3 A Formation of Standard Setter to Transplant Global Standards into Domestic Institution

Kensuke Ogata (University of Nagasaki, Japan)

Japanese accounting standard setter, the ASBJ, developed lots of domestic accounting regulations to converge with the global standards in the period of 2005-2008, which substantially differs from the period of 2001-2004. A general organizations theory states that organizations make a change in their strategy and structure aimed at changing their performance. Based on this theory, we analyzed the change in organizational structure of the ASBJ using social network analysis. According to our result, the ASBJ formed a network in which accounting professions played a central role. The reason could be that the ASBJ made use of knowledge and wisdoms on the global standards Japanese big accounting firms has through their global networks.

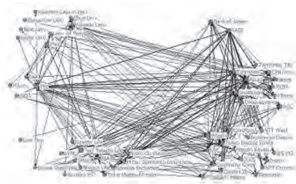

OS18-4 A Comparison Study on the Vertical Integration and Horizontal Specialization of Chinese ICT Companies

Yunju Chen (Shiga University, Japan), Yousin Park (Prefectural University of Hiroshima, Japan)
Iori Nakaoka (National Institute of Technology, Ube College, Japan)

The debate between vertical integration vs. horizontal specialization appears to be reinvigorated. The decision of vertical integration or horizontal specialization affects a firm's profit and competitive advantage, especially in the ICT industry which is difficult to create added value due to the commoditization of digital products. The ongoing commoditization of smartphone brings the arising of Chinese ICT companies but these companies adopt different operation systems to create their own competitive advantages. In this paper, we focus on top-shared Chinese companies in global smartphone industry, Huawei and Xiaomi, to examine how they design their operation systems in R&D and gain competitive advantages, also to compare their systems with each other. The patent information of these two companies is used to visualize their technical orientations and operation systems in R&D by text mining

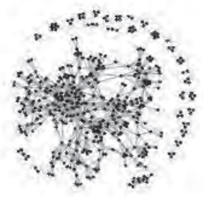

The patent (inventors) network of Xiaomi

OS19 Kansei Engineering and Applications (4)

OS19-1 Histogram Matching Based on Gaussian Distribution Using Regression Analysis Variance Estimation

Yusuke Kawakami (DynaxT Co., Ltd., Japan)
Tetsuo Hattori, Yoshiro Imai, Kazuaki Ando, Yo Horikawa (Kagawa University, Japan)
R. P. C. Janaka Rajapakse (Tainan National University of the Arts, Taiwan)

This paper describes an improved method for variance estimation which is used in Histogram Matching based on Gaussian Distribution (HMGD). In the previous papers, based on curvature computation, we have described that how to estimate the variance of reference histogram, which is used in HMGD processing. However, we have considered that the histogram of original image is not always ideal shape. And the variance estimation method based on curvature computation might not have high reliability. In this paper, we propose improvement variance estimation method using regression analysis. As for the method, first, we detect the histogram peak of original image by using curvature computation; next, we perform regression analysis using approximation formula of curvature. Then, we illustrate processing results through some experimentation.

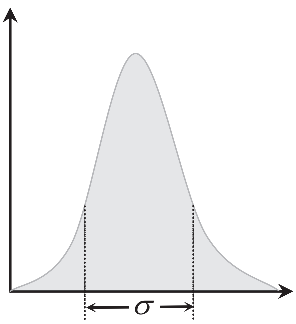

OS19-2 Histogram Matching Based on Gaussian Distribution Using Variance Estimation -- Comparison between Curvature Computation and Regression Analysis –

Yusuke Kawakami (DynaxT Co., Ltd., Japan)
Tetsuo Hattori, Yoshiro Imai, Kazuaki Ando, Yo Horikawa (Kagawa University, Japan)
R. P. C. Janaka Rajapakse (Tainan National University of the Arts, Taiwan)

This paper describes variance estimation method comparing between regression analysis and curvature computation which is used in Histogram Matching based on Gaussian Distribution (HMGD). In the previous paper, we have described and illustrated that the variance estimation method have been considered of value for HMGD processing results. Though we have considered that histogram of original image is not always ideal. So, in this paper we propose improvement variance estimation method using regression analysis. First of all, we describe the principle of variance estimation methods using curvature computation, and regression analysis. Then, through some HMGD processing experiment, we compare between curvature computation results and regression analysis.

OS19-3 An Extended Optimal Stopping Method for Structural Change Point Detection Problem

Yoshihide Koyama, Tetsuo Hattori, Yoshiro Imai, Yo Horikawa (Kagawa University, Japan)
Hiromichi Kawano (NTT advanced technology Company Ltd,, Japan)
Yusuke Kawakami (DynaxT Co., Ltd., Japan)

Previously, we have proposed and formulated the SCPD (Structural Change Point Detection) problem in time series data as an Optimal Stopping one using the concept of DP (Dynamic Programming). And also we have shown the solution theorem in the form of inequality. In this paper, based on the relation between the solution of Optimal Stopping and SPRT (Sequential Probability Ratio Test), we present the extended Optimal Stopping Method in order to obtain more practical one, considering a loss cost and an action cost involved by failure prediction.

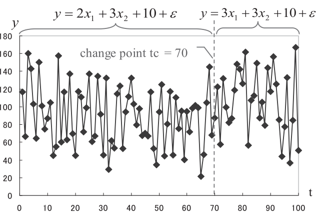

OS19-4 A Study of Sentimental Value Analysis for Tweeting Message

Shunsuke Doi, Shinya Hara, Yoshiro Imai, Tetsuo Hattor (Kagawa University, Japan)
Yusuke Kawakami (DynaxT Co., Ltd., Japan)

This paper focuses on Twitter used by students of universities, and analyzes tweeting data (messages) by students from Twitter, and calculates sentimental values from the according data. It also investigates existence of some relations between calculated sentimental values and practical thought of students. Moreover, this paper discusses whether the above procedure and analysis can visualize conventionally hidden relationship between contents of tweeting messages and characteristic behavior of students in categorized universities.

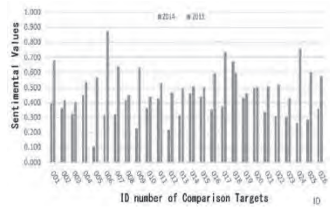

OS20: Image Processing and Computer Graphics (6)

OS20-1 An effective method for detecting snatch thieves in video surveillance

Hiroaki Tsushita, Thi Thi Zin (University of Miyazaki, Japan)

Nowadays, a tremendous amount of accidents and terrorisms has been occurred all over the world no exception Japan. Thus, detection of suspicious activities in public areas such as railway stations, shopping malls and many other areas using video surveillance becomes important. However, very little has been achieved regarding real-time event recognition of two person interactions such as snatch theft events. Moreover the way of snatch theft has been increasing like using a motorcycle and so on. In this paper, we propose an effective method for detecting the snatch theft event between two persons. Specifically, the proposed method consists of several steps: pedestrian tracking, feature computation and snatch theft detection. For feature computation, shape and motion features are used. To confirm the validity of proposed method some experimental results in a various situations are shown by using some collected video sequences.

OS20-2 Color and Shape based Method for Detecting and Classifying Card Images

Cho Nilar Phyo, Thi Thi Zin (University of Miyazaki, Japan) Hiroshi Kamada (Kanazawa Institute of Technology, Japan) Takashi Toriu (Osaka City University, Japan)

In this paper we propose an effective method for detecting and classifying card images by using color and shape features. Generally, color card images have been widely used for teaching and learning programing languages in interactive classrooms lessons. For this purpose, we first extract the area of card color by squeezing from the entire image by using the color information. Then we remove the regions of low possibility with the aids of shape features particularly aspect ratios. Moreover, by taking the classroom size and the distance from the camera, we classify the image according to the sizes. Thus our method can extract even quite small cards in the classroom activities. In order to confirm the proposed method, we conduct a sequence of experiments by taking our own video sequences. Our experimental results show that the proposed method is very promising compared to some existing methods.

OS20-3 Automatic Assessing Body Condition Score from Digital Images by Active Shape Model and Multiple Regression Technique

Nay Chi Lynn, Thi Thi Zin, Ikuo Kobayashi (University of Miyazaki, Japan)

Body Condition Scoring is a magnificent indicator for determining nutritional status, energy reserves, fatness or thinness of cows. The purpose of this study is to assess body condition scores (BCS) of dairy cattle by exploiting digital images of back view of cows. To determine back shape of the cows and its tail head area, anatomical landmark points labelling is performed. Next, active shape model is used to extract the angle features from these cow's tail head contours. In this study, we choose the hook and tail head depression angle from the cow's tail head area. Those angle features with their respective BCS are used to estimate body condition scores by employing multiple regression analysis. Using threshold value on the residuals between the actual BCS and predicted BCS is determined to confirm the proposed method. Moreover, the experimental results show that the proposed system is promising compared to some existing methods.

OS20-4 General Image Categorization Using Collaborative Mean Attraction

Hiroki Ogihara, Masayuki Mukunoki (University of Miyazaki, Japan)

In this paper, we apply Collaborative Mean Attraction (CMA) method, which has been developed for person re-identification problem with multi-camera, to general image categorization problem. CMA is a generic identification method, so once training images are given, CMA can identify test images into a class of the training images. It means that CMA can be used for image categorization. Experimental results using the caltech101 dataset reveal that CMA shows better categorization accuracy than standard SVM method, particularly in the case when the size of training data is relatively small. We also apply CMA to caltech256 dataset, which is more difficult to categorize than caltech101. Even for caltech256, CMA shows better results than other methods, especially for small training data. Furthermore, we discuss the parameter settings for CMA through several experiments.

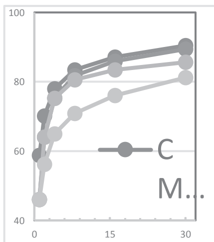

OS20-5 Consideration on the Photo-Realistic Rendering of Fruits by 3DCG

Haruka Tsuboi, Makoto Sakamoto, Sho Yamada, Kensuke Ando, Chongyang Sun,
Makoto Nagatomo (University of Miyazaki, Japan)
Koshiro Mitsuhashi, Yukari Kodama (Miyazaki Multimedia Academy, Japan)

Three-dimensional computer graphics (3DCG) is the technique of creating an image having a stereoscopic effect by converting an object in the virtual three-dimensional space into two-dimensional information. It is also possible to produce an image that cannot be distinguished from the real thing by using the 3DCG. 3DCG is expected for the application to visual representations very much. However, it is difficult to express the "freshness" of fresh food by 3DCG.Therefore, expressiveness of 3DCG is considered to be improved by overcoming this weakness. In this paper, we consider the photo-realistic rendering of fruits by 3DCG. The algorithm is implemented by using the Visual C++ 2010 and C on a personal computer. Through this trial, we hope to improve the representation in photo-realistic rendering by 3DCG.

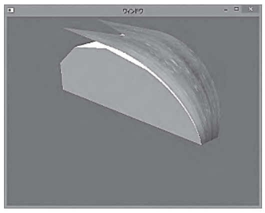

OS20-6 Consideration for the Possibility to the Tourism by the AR Technology

Masamichi Hori, Makoto Sakamoto, Takeshi Tanaka, Mihoko Fukushima, Chikashi Deguchi,
Masahiro Yokomichi, Masayuki Mukunoki, Kunihito Yamamori (University of Miyazaki, Japan)
Yukari Kodama, Koshiro Mitsuhashi (Miyazaki Multimedia Academy, Japan)
Atsushi Iiboshi, Takachiho (Muratabi Co., Ltd., Japan)

The promotion of the tourism nation became the important problem of our country, and we expect increase of the number of the foreign tourists visiting Japan. Therefore, we have to make sightseeing spots of our country more attractive them, so we must contribute plain guidance information to the foreigners who cannot understand Japanese, guidance markers, and so on. On the other hand, AR (augmented reality) is becoming the boom recently, but this is information technology to let the reality world compose the virtual world. In this paper, when we use the AR technology for tourism and sightseeing, we inspect what kind of possibilities we have through some experiments.

OS21 Computer Science and Information Processing (5)

OS21-1 Consideration on the Recognizability of Three-Dimensional Patterns

Chongyang Sun, Makoto Sakamoto, Makoto Nagatomo, Yu-an Zhang, Shinnosuke Yano, Satoshi Ikeda (University of Miyazaki, Japan) Takao Ito, Tsutomu Ito (Hiroshima University, Japan) Yasuo Uchida (Ube National College of Technology, Japan) Tsunehiro Yoshinaga (Tokuyama college of Technology, Japan)

Due to the advances in computer vision, robotics, and so forth, it has become increasingly apparent that the study of three-dimensional pattern processing should be very important. Thus, the study of three-dimensional automata as the computational model of three-dimensional information processing has been significant. During the past about thirty years, automata on a three-dimensional tape have been obtained. On the other hand, it is well-known that whether or not the pattern on a two- or three-dimensional rectangular tape is connected can be decided by a deterministic one-marker finite automata. As far as we know, however, it is unknown whether a similar result holds for recognition of the connectedness of patterns on three-dimensional arbitrarily shaped tape. In this paper, we consider whether or not the pattern on a three-dimensional arbitrarily shaped tape is connected can be decided by a deterministic multi-marker finite automaton.

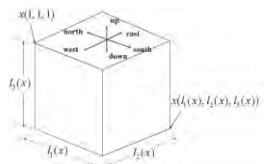

OS21-2 Some Properties of Four-Dimensional Homogeneous Systolic Pyramid Automata

Makoto Nagatomo, Makoto Sakamoto, Yu-an Zhang, Chongyang Sun, Shinnosuke Yano, Satoshi Ikeda (University of Miyazaki, Japan) Takao Ito, Tsutomu Ito (Hiroshima University, Japan) Yasuo Uchida (Ube National College of Technology, Japan) Tsunehiro Yoshinaga (Tokuyama college of Technology, Japan)

The question of whether processing four-dimensional digital patterns is much more difficult than three-dimensional ones is of great interest from the theoretical and practical standpoints. Thus, the study of four-dimensional automata as a computational model of four-dimensional pattern processing has been meaningful. Cellular automata were investigated not only in the viewpoint of formal language theory, but also in the viewpoint of pattern recognition. Cellular automata can be classified into some types. A systolic pyramid automaton is also one parallel model of various cellular automata. In this paper, we propose a homogeneous systolic pyramid automaton with four-dimensional layers (4-*HSPA*), and investigate some properties of real-time 4-*HSPA*.

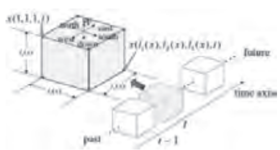

OS21-3 Reduction of the search space to find perfect play of 6×6 board Othello

Yuki Takeshita[1], Makoto Sakamoto[1], Takao Ito[2], Tsutomu Ito[2], Satoshi Ikeda[1]
([1]University of Miyazaki, [2]Hiroshima University, Japan)

In 1993, mathematician Feinstein found out perfect play on 6×6 board of Othello gives 16-20 loss for the first player by using computer. He reported on the Web that it took two weeks to search forty billion positions in order to obtain the result. In our previous papers, we confirmed the perfect play he found is correct. And we also found another perfect play different from the one he found to search 884 billion positions. In order to search efficiently, we attempted to reduce the search space to find some perfect play. In this paper, we introduce some techniques to solve 6×6 Othello by searching about fifteen billion positions.

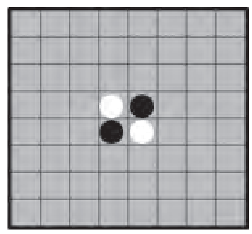

OS21-4 A comparative study on the delisting ratings of firms from the UN Global Compact in the international management environment

Kanako Negishi (National Institute of Technology, Ube college, Japan)

This paper explores the international management environment for Japanese manufacturing firms' sustainability strategies. In particular, it clarifies firms' positioning and characteristics in the environment. Firms have adopted voluntary standards for environmental protection provided by NGOs and international institutions like the GRI and United Nations. Although there are various standards without legal binding, there is a recent trend toward integration to achieve comparability for firms' international management of sustainability. It then bound firms' management as a de facto standard. This paper discovers Japanese firms' unique characteristics related to the environment though the comparison.

Comparison of the average delisting ratings from the UN Global Compact

Country	Firm type	Ratio
Japan	Company	0.00%
	SME	77.59%
Spain	Company	41.10%
	SME	48.17%
USA	Company	34.86%
	SME	63.43%
China	Company	58.66%
	SME	57.38%

OS21-5 Application of ViSC to the Natural Grazing in Qinghai Tibet Plateau

Cheng-shui Niu[1], Bing-fen Li[1], Yu-an Zhang[1], Makoto Sakamoto[2]
([1]Qinghai University, P.R. China, [2]University of Miyazaki, Japan)

"Sanjiangyuan Region" is a complex ecosystem with typical characteristics of alpine grassland, which the livestock production mainly relies on the yak grazing. In recent years, artificial destruction were due to grassland degradation, the reduction of herdsmen income and on-going deterioration of the ecological environment. It is necessary to establish a grazing mode which ecological animal husbandry and grassland sustainable development. In this study applying the ViSC that combined with optimization theory, we establish sustainable grazing system in alpine grassland yak, which provides a theoretical basis for scientific grazing.

OS22 Robotic Technology for Competition (4)

OS22-1 Development of a Tomato Harvesting Robot

Bingh Li, Shinsuke Yasukawa, Takashi Sonoda, Kazuo Ishii (Kyushu Institute of Technology, Japan)

Most of commercialized robots are for industry, and the robots for agriculture, forestry and fisheries are under developing and not commercialized yet. The reasons for the difficulty are caused by cost-efficiency of the robotization, safety ensuring of the works using robots, outdoor operations, and knowledge transfer problem from farmers to computer so on. Tomato is one of important fruit vegetables and most tomatoes are produced in the greenhouses, or large-scale farms, where the high temperature and humidity, and long harvest age force the farmers heavy works. With an aim to promote the automation of tomato harvesting, we have organized the tomato harvesting robot competition and developed a tomato harvesting robot. In this paper, we propose the system of tomato harvesting robot.

OS22-2 Development of SOM algorithm for Relationship between Roles and Individual's Role in Rugby 2nd Reports: University Rugby teams analysis using Physical and Psychological data

Yasunori Takemura (NishiNippon Institute of Technology, Japan)

Victory or defeat in team sports depends on each player's technique, physical strength, and psychological condition. It follows that team performance depends on the player's adaptation to (suitability for) a certain role (position in the team) and the relationships between different roles. We assume that team performance is related to physical and psychological features. Many researchers have proposed that physical features determine a player's suitability for a position. Psychological features have also been researched as factors of position adaptation. However, each feature has been investigated independently. The present research aims to develop a clustering method that considers both physical and psychological features in judging an individual's role and adaptation in the game. This paper reports the concept of the algorithm and result of analysis using both physical data and psychological data[O1].

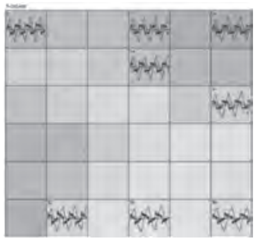

OS22-3 Ball Dribbling Control for RoboCup Soccer Robot

Shota Chikushi, Kenji Kimura, Kazuo Ishii (Nippon-Bunri University, Kyushu Institute of Technology, Japan)

RoboCup is a platform designed to promote the research fields such as Artificial Intelligent (AI) and robotics. We also organize a RoboCup team "Hibikino-Musashi", and working on co-operated behavior control system using multiple autonomous mobile vehicles. In this paper, motion analysis and control of a ball operated by two active wheels mounted on upper side of the ball is discussed. Based on the analysis and simulation, a ball dribbling mechanism is developed. The kinetics of ball and two-active wheels is derived and evaluated using the developed ball dribbling mechanism.

OS22-4 Strategy Analysis of RoboCup Soccer Teams Using Self-Organizing Map

Moeko Tominaga, Yasunori Takemura, Kazuo Ishii
(Kyushu Institute of Technology, NishiNippon Institute of Technology, Japan)

In the soccer games, the player's behavior changes depending on the game situation such as wining or losing, score gap, remaining time. The players act more offensive when their team is losing, or more defensive when their team is winning with minimum score difference. Currently most of robot teams keep the same strategy during the game so that the result of game depends on the ability of each player like speed of robot, quality of localization, obstacle avoidance and ball handling. Next issue for the robot intelligence is collaborated team behavior and strategy. In this paper, the team strategy is analyzed based on parameters such as the positions of robots, the number of robots in play, scores, time and actions of robots using Self-Organizing Map.

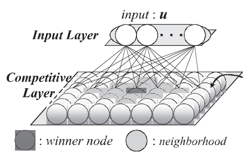

GS abstracts

GS1 Artificial Neural Network & Bio-Signal Controlled Robotics (3)

GS1-1 Obstacle Avoidance Method for Electric Wheelchairs Based on a Multi-Layered Non-Contact Impedance Model

Haruna Kokubo, Taro Shibanoki (Ibaraki University, Japan),
Takaaki Chin (Hyogo Rehabilitation Center, Japan), and Toshio Tsuji (Hiroshima University, Japan)

This paper proposes an obstacle avoidance method based on a multi-layered non-contact impedance model for the biosignal-controlled electric wheelchair. The proposed system can calculate a virtual repulsive force before the collision by multi-layered impedance fields, which have different impedance parameters, covered around the robot. In this way, this system regulates desired path to avoid obstacles in a variety of situations such as a natural evasion and an emergency avoidance. In the simulation and practical experiments, the mobile robot moved to a desired position, and some obstacles were appeared on their moving paths. The results showed that the robot passed through obstacles smoothly, and could stop emergently to avoid the obstacle in front of the robot owing to virtual forces calculated by the proposed model

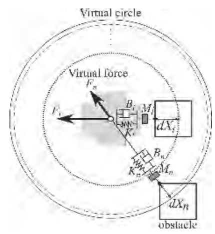

GS1-2 A Voice Signal-Based Manipulation Method for the Bio-Remote Environment Control System Based on Candidate Word Discriminations

Taro Shibanoki (Ibaraki University, Japan), Go Nakamura, Takaki Chin
(Hyogo Rehabilitation Center, Japan), and Toshio Tsuji (Hiroshima University)

This paper proposes a voice signal-based manipulation method for the Bio-Remote environment control system. The proposed system learns relationships between multiple candidate words' phonemes extracted by a large-vocabulary speaker-independent model and control commands for domestic appliances based on a self-learning look-up table (self-learning LUT). This allows the user to control various devices even if false recognition results are extracted because of slurred speech. The efficacy of the proposed system was demonstrated through speech recognition for slurred words and domestic appliance control experiments conducted with healthy male participants. The results showed that the method could be used to accurately discriminate seven slurred words (average discrimination rate: 93.9 ± 2.2 [%]), and that the subject was able to voluntarily control domestic appliances as intended.

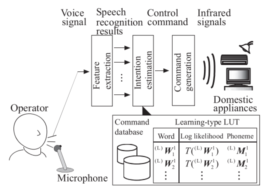

GS1-3 Experiments on classification of electroencephalography (EEG) signals in imagination of direction using Stacked Autoencoder

Kenta Tomonaga, Takuya Hayakawa, Jun Kobayashi (Kyushu Institute of Technology, Japan)

This study presents experimental results of classification methods for brain activity in the imagination of direction. We used a wireless portable electroencephalography (EEG) headset to collect EEG data from subjects in experiments, during which the subjects imagined arrows indicating one of the four direction: up, down, right, left. The classification methods estimated the direction that the subjects imagined on the basis of their brain wave signals measured by an electrode on the portable EEG headset. The classification methods implemented in our previous studies consisted of a band-pass filter, fast Fourier transformation, principal component analysis (PCA), and neural network. The PCA works for feature extraction and selection. In this study, we have implemented Stacked Autoencoder (SAE) for EEG signal classification. The SAE carries out not only feature extraction but also classification in the form of multi-layered neural network. Experimental results showed that the SAE outperformed the previous classifier with PCA.

GS2 Automated Guided Vehicles I (6)

GS2-1 Adaptive Negotiation-rules Acquisition Methods in Decentralized AGV Transportation Systems by Reinforcement Learning with a State Space Filter

Masato Nagayoshi, Simon Elderton (Niigata College of Nursing),
Kazutoshi Sakakibara (Toyama Prefectural Univ.), Hisashi Tamaki (Kobe Univ.)

In this paper, we introduce an autonomous decentralized method for multiple Automated Guided Vehicles (AGVs). Transportation route plans of AGVs are expected to minimize the transportation time without collisions between the AGVs in the systems. In our proposed system, each AGV as an agent computes its transportation route by referring to the static path information. route. Once potential collisions are detected, one of the two agents chosen by a negotiation rule modifies its route plan. The rules are improved by reinforcement learning with a state space filter. Then, the performance is confirmed with regard to the adaptive negotiation rules.

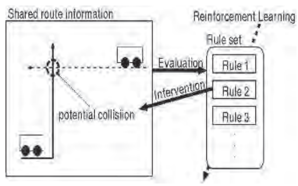

GS2-2 Modeling and Control of a Quadrotor Vehicle Subject to Disturbance Load

Jun Wang, Song Xin, Yuxi Zhang (Beihang University, P. R. China)

In this paper, a dynamic model of quadrotor, an unmanned aerial vehicle (UAV), is derived for theoretic and practical evaluation. Four transfer functions in different channels are converted from the state equations. To study the behavior of quadrotor subject to the external disturbance load, a fuzzy logic controller (FLC) is designed to compare with the PID (proportional-integral-derivative) control method. Subsequently, Liapounov function is applied for stability analysis. Finally, simulation results are presented to illustrate the performance between FLC and PID. Considering model error, the evaluation simulations are divided into two parts, which describe the ability for rejecting external disturbance, setpoint tracking and disturbance rejection respectively. The simulation scheme demonstrates the FLC method outperforms the PID control scheme.

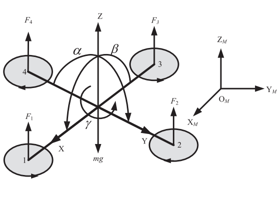

GS2-3 A multithreaded algorithm of UAV visual localization based on a 3D model of environment: implementation with CUDA technology and CNN filtering of minor importance objects

Alexander Buyval, Mikhail Gavrilenkov (Bryansk State Technical University, Russia)
Evgeni Magid (Kazan Federal University, Russia)

Visual based navigation plays an important role in localization and path planning, especially in GPS-denied environments. This paper presents a visual based localization algorithm for a UAV within an indoor environment. The algorithm uses multithreaded computing CUDA technology and CNN-preprocessing filtering, which is responsible for filtering out minor importance objects. We assume that while an initial 3D model of environment is available, the scene may undergo minor dynamical changes, e.g., new objects may appear in the scene as the time passes. The localization is performed in two steps. Initially, a neural filtering module detects new objects in the scene and filters them out. Next, the filtered data is passed to a multithreaded edge-computing module, which compares it with the initial 3D model. The algorithm is simulated in ROS/Gazebo environment with two different approaches – one uses CPU only and the other uses CPU and GPU - and their performance is compared.

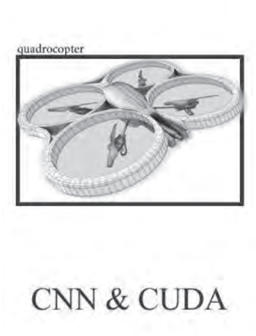

GS2-4 Modelling a crawler-type UGV for urban search and rescue in Gazebo environment

Maxim Sokolov, Aidar Gabdullin, Roman Lavrenov, Ilya Afanasyev (Innopolis University, Russia)
Leysan Sabirova, Evgeni Magid (Kazan Federal University, Russia)

A long-standing goal of robotics is to substitute humans in unreachable or dangerous environments. One of the most dangerous and human unfriendly environments is urban search and rescue (USAR) domain, where a rescue robot is used for victims search and environment monitoring purposes. To deal with USAR tasks we have selected a novel Russian crawler robot “Engineer”, and this paper presents our first successful steps toward modelling the robot in ROS/Gazebo environment. We convert the provided by “Engineer” developers CAD models into workable ROS-based 3D simulation and incorporate physical parameters of the mechanisms into the model. Robot motion and relative interplay of its visible mechanical parts is visualized in RViz software. The proposed model is integrated into a ready-to-use ROS navigation stack and the model’s behavior is thoroughly investigated while navigating through static obstacles populated scene in Gazebo environment.

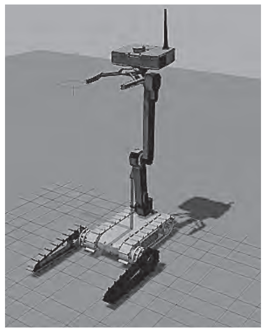

GS2-5 Development of Autonomous Robot for Laborsaving of the Forestry - Positioning of the Robot using IMU, GPS, and Encoder -

Sho Yamana, and Eiji Hayashi (Kyushu Institute of Technology, JAPAN)

This paper presents about the positioning of the autonomous robot using IMU, GPS, and encoder devices. Using acceleration and orientation from IMU sensor that is used to calculate the position of the robot. To locate the position, need to know the distance when the robot moved. Distance is calculated by integrating of velocity and also the velocity is considered by integrating of acceleration. Results showed distance measured using only IMU. It shows the difficulty of locating using only IMU. Therefore, GPS and encoder devices need to be combined into the system for position measurements.

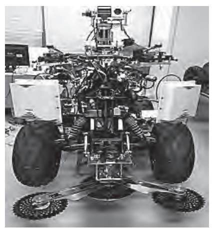

GS2-6 Development of Autonomous Robot for Laborsaving of the Forestry - Detection of young plants by RGB and Depth Sensor -

Nobuo Miyakawa, Eiji Hayashi
(Kyushu Institute of Technology, Japan)

Nowadays In Japan, the forest industry have problem about safety and labor shorting. This research is about development of the autonomous moving robot in the forest focused on solving the problem. As the first phase of automation of forest industry, autonomous movement control system must be developed. Because, the environment surrounding the robot changes every moment in forest. For example, the tree and weed in forest is growing every day. So this dynamic environment has to be considered for the robot to continue moving in the forest. Therefore we aim at the development of autonomous system that movement in the forest in this study. This paper proposes to detect plants of autonomous robot system in the forest.

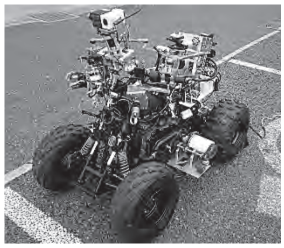

GS3 Automated Guided Vehicles II (3)

GS3-1 Motion Improvement of Four-Wheeled Omnidirectional Mobile Robots for Indoor Terrain

Amornphun Phunopas (King Mongkut's University of Technology, Thailand)
Shinichi Inoue (Kyushu Institute of Technology, Japan)

The four-wheeled omnidirectional platform is great to use for an indoor mobile robot. It can increasingly move and change heading direction. However, The robot is easy to slip when it is moving. As well as, one or more wheels are sometimes not touching the ground. Therefore the robot may miss the planned path, or in the worst case, the robot possibly gets stuck due to unrecognized circumstances. This paper approaches to solving the problems by computational simulation in locomotion. Mathematical models simulate the robot movement. The robot struggles to go to the target with randomly simulated slip and inactive wheel circumstances. The robot can estimate the positions using the Kalman filter and readjust itself to the planned path. Consequently, this paper demonstrates the motion improvement and compare the results of decreasing error.

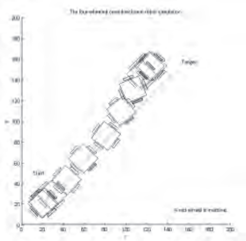

GS3-2 An Improved Algorithm for Obstacle Avoidance by Follow the gap method combined Potential Field

Chakhrit La-orworrakhun, Suriya Natsupakpong (Institute of Field Robotics, King Mongkut's University Technology Thonburi, Thailand)

This paper proposes a novel obstacle avoidance algorithm for boat survey. The proposed algorithm, "Follow the Gap Plus", for boat navigation is presented by combining the "Follow the Gap" method and adapting the "Potential Field" method with an attractive field of obstacles. Then the simulation environment for testing system and algorithm are generated in various situations and similar real-world environment. The results show that the survey boat simulation with proposed algorithm can go to the desired destination with better performance than "Follow the Gap" method in the environment with obstacles about 4.47 percentage of total distance, about 7.63 percentage of total time used, and about 54.33 percentage of average change of direction.

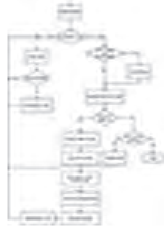

GS3-3 Study on the target positioning for an Omni-directional 3 DOF mobile manipulator based on machine vision

Jiwu Wang, Yao Du, Wensheng Xu (Beijing Jiaotong University, China)
Masanori Sugisaka (ALife Robotics Corporation Ltd, Japan)

The omni-directional mobile robot with multi DOF, because the operation posture and operation accuracy of the manipulator can be better controlled in a narrow or crowded workplace compared with the general manipulator, is getting more interested in practical applications. The present problem is to improve its flexibility for operating multiple different targets. Target recognition with image processing is an effective solution. Based on the image processing, the position and posture of the target can be determined. Then the signal will be sent to the arm control system. In this paper, the illumination conditions, distortion, etc. are studied in the target recognition. The target position with image processing, is verified with real coordinates. The experiments show target recognition with image processing can effectively improve the flexibility of our robot

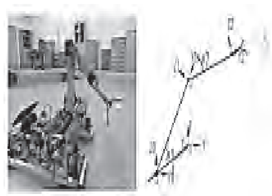

GS4 Biological Systems (4)

GS4-1 Force and Motion Analysis of larval zebrafish (*Danio rerio*) using a body dynamics model

Naohisa Mukaidani, Zu Soh, Toshio Tsuji ([1]Hiroshima University, Japan)
Shinichi Higashijima (National Institutes of Natural Sciences, Japan.)

Larval zebrafish are often employed as a vertebrate model to study the phenomena during the stages of development. This study proposes a method of body dynamics analysis for larval zebrafish incorporating a viscoelastic body model and a fluidic environment model to support the study of development mechanisms in motion generation. An algorithm for estimation of the external drag forces acting on larval zebrafish enabled calculation of thrust forces resulting from body motion. The results showed that the estimated fluid drag coefficients enabled the body dynamics model to approximate the paths of actual larvae with a high accuracy level of 0.76 ± 0.74 [%] of the total length. Based on the analysis results, we found that the fins generate dominant forces at the initiation of swimming, but have little role during swimming.

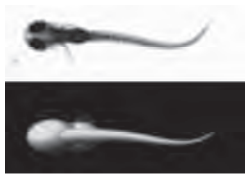

GS4-2 Behavior Analysis on Boolean and ODE models for Extension of Genetic Toggle Switch from Bi-Stable to Tri-stable.

Masashi Kubota, Manabu Sugii, Hiroshi Matsuno (Yamaguchi University, Japan)

The artificial genetic circuit (AGC) is a gene network in which its expression timing, period and function are designed by computational and biological technique. The AGCs for the functions of electronic circuits like a toggle switch and an oscillation circuit were realized in E.coli by Gardner and Elowitz in 2000, respectively. We visualized and verified the structure and behavior of Boolean network (BN) and ordinary differential equation (ODE) models for 2-variable genetic toggle switch in the phase plane by using GINsim and Scilab. ODE has been the most widely used formalism for biological processes, but BN model allows us to easily understand mathematical expression of biological processes. Then, we extended the models for 3-variable genetic toggle switch from the 2-variable ones, and we demonstrate a mathematical formalization by showing correspondence between state transitions of BN and trajectory paths of ODEs in the phase space.

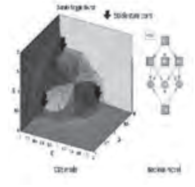

GS4-3 Boolean modeling of mammalian cell cycle and cancer pathways

Hideaki Tanaka, Hiroshi Matsuno, Adrien Fauré (Yamaguchi University, Japan)

The cell division cycle is controlled by a complex molecular network: a recent model of the cell cycle and cancer pathways includes close to a hundred genes [Fumiã and Martins, 2013]. To cope with such complexity, different approaches have been used by modelers. Recently, Deritei et al [2016] have emphasized modularity as a key organizational principle. Their model however, includes only 22 components. This raises the question how the approach would fare on larger models such as the one published by Fumiã and Martins. To explore that question we first convert these two models to a common modeling framework [Naldi et al., 2009]. Preliminary results show that there is only limited overlap between the two models, with shared variables being controlled by different regulators. This suggests that at this stage module definition may still depend on the modeler and thus may not yet reflect actual biological organization.

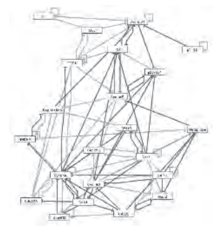

GS4-4 An Estimation Method for Environmental Friction Based on Body Dynamic Model of *Caenorhabditis elegans*

Zu Soh (Hiroshima University, Japan), Michiyo Suzuki (National Institutes for Quantum and Radiological Science and Technology, Japan), Toshio Tsuji (Hiroshima University, Japan)

Caenorhabditis elegans is a small worm which is approximately 1.3 mm in length. For the reason of technological limits, it has been difficult to measure the friction between the body and environments. The present study proposes an estimation method for frictional force using locomotion information obtained from video analysis of actual worms. The results indicate that the body model driven by the estimated frictional force can trace the locomotion of the worm within 4% of the body length. The proposed method may be able to be applied to analyze the relationship between friction and gait control.

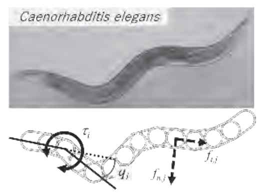

GS5 Filtering & Control Systems (2)

GS5-1 An Application of Collaborative Filtering in Student Grade Prediction

Chaloemphon Sirikayon and Panita Thusaranon (Dhurakij Pundit University, Thailand)

This research proposed the process of student performance prediction by using the collaborative filtering (CF) technique. The benefit of this research includes assist instructor to identify student performance, personalized advising, and student degree planning. The CF technique composes of similarity calculation and prediction. In our experiments, different techniques are compared to calculate students' similarity. We also found that a prior course clustering with heuristic knowledge can be used to enhance predictability. The data used for this study obtained from Dhurakij Pundit University with enrollments of 200 undergraduate students between 2012 and 2016 from the Faculty of Information Technology. The performance of each student has been predicted since semester 2, 2014 by using existing grades available at that time. The A-F letter grades were converted to the 4–0 scale, which is actually discrete. In additional, we also conducted the experiment by using actual score from each courses.

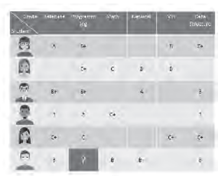

GS5-2 An improved detection method for railway fasteners

Jiwu Wang, Yan Long (Beijing Jiaotong University, China)
Sugisaka Masanori (ALife Robotics Corporation Ltd, Japan)

Aiming at the disadvantages of low efficiency and poor stability of the existing methods of fastener detection, this paper proposes a method of fastener detection based on template matching. Firstly, the image is processed by noise reduction, this method does not need to be based on histogram can match template directly. We choose a standard fastener image as template, read template firstly, then slide the image blocks on the input image to match the template and the input image. Experimental results show that this method can effectively detect the flaw, deformation and obstacles of railway fastener occlusion. This method has a fast matching speed and a good robustness, it’s detection accuracy is up to 96%

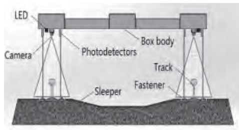

GS6 Human-Welfare Robotic System & Medical Application (5)

GS6-1 Virtual surgery system with realistic visual effects and haptic interaction.

Vlada Kugurakova, Murad Khafizov, Ruslan Akhmetsharipov, Alexei Lushnikov, Diana Galimova, Vitaly Abramov (Kazan Federal University, Russia)
Omar Correa Madrigal (University of Informatic Sciences, Cuba)

Currently, educational processes in medical surgery field involve not only theoretical in-class studies that are immediately followed by practical lessons in mortuaries and hospitals, but also involve simulations of various levels of reality. This paper describes our current progress in Virtual Surgery System development, which is targeted to support educational processes in medical surgery. With this system, all surgery operations are performed using a virtual reality headset and haptic manipulators with force feedback. The main feature of our approach is applying a voxel data structure of a human body that provides an opportunity to simulate realistic behavior of the body. Thus, cutting, sewing, and welding of human tissues processes become realistic. Together with a realistically simulated virtual surgery scene, these will significantly speed up educational processes.

GS6-2 A Human Reaching Movement Model for Myoelectric Prosthesis Control

Go Nakamura[*1, 5], Taro Shibanoki[*2], Yuichiro Honda[*1], Futoshi Mizobe[*3], Akito Masuda[*4], Takaaki Chin[*1], Toshio Tsuji[*5]
[*1](Robot Rehabilitation Center in The Hyogo institute of Assistive Technology, Japan)
[*2](Ibaraki University, Japan) [*3](Hyogo Rehabilitation Center, Japan)
[*4](Kinki Gishi Corporation, Japan) [*5](Hiroshima University, Japan)

This paper proposes a human reaching movement model for myoelectric prosthesis control. The main purpose of the proposed model is to generate desired trajectories provided in a reaching training system for myoelectric prosthesis control. First, an experiment was performed to observe reaching movements with a healthy subject and a myoelectric prosthesis user (upper limb amputee). Then, we found several distinctive features shown in reaching movements for the myoelectric prosthesis user, and constructed a model considering the observed characteristics by using a logistic function. The proposed model can generate three different types of hand trajectory such as straight line paths, circular arc paths and S-shaped paths with bell-shaped speed profile by adjusting only a few parameters. It was indicated that the proposed model could generate both hand trajectories of the healthy subject and the myoelectric prosthesis user from the comparison results between observed and simulated trajectories.

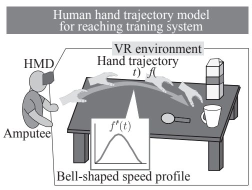

GS6-3 Re-creation of a membrane puncture's sense of an object constituted of liquid and an outer membrane by a haptic device and a deformation simulation of the virtual objects

Takahiro Okada, Eiji Hayashi (Kyusyu Institute of Technology, Japan)

Technologies that can accurately perform minute work are now being sought for medical treatment and bio-technology field. Such minute work is improved by using micromanipulators, but their operation is difficult because the operator has no sense of force. The operator relies only on sight through a microscope. As a result, a person skilled in the use of this technology is needed for all minute work. For the efficiency of minute work, we used a haptic device and amplified the force feedback from a minute sample. The purpose of this research is to develop a combined sense system that uses both force feedback and visual feedback on a deformation simulation. Especially, I focused a way to recreate a membrane puncture's sense of salmon rows assumed a cell.

GS6-4 Exercise classification using CNN with image frames produced from time-series motion data

Hajime Itoh, Naohiko Hanajima (Muroran Institute of Technology, Japan)
Yohei Muraoka, Makoto Ohata (Steel Memorial Muroran Hospital, Japan)
Masato Mizukami, Yoshinori Fujihira (Muroran Institute of Technology, Japan)

To enhance the strength of the elderly is important for the care prevention. Exercise support systems for the elderly have been developed and some were equipped with a motion sensor. Normally it provides three-dimensional time-series data of over 20 joints. It is important to integrate such large data and evaluate the motion of the users. In this study, we propose to apply Convolutional Neural Network (CNN) methodology to the motion evaluation. The deep learning has a success in integrating big data, for example, image classification. Our main idea is to convert the motion data of one exercise interval into one gray scale image by taking joint types for the row direction and time for the column direction and by changing the data into the gray scale value. From simulation results, the CNN was possible to classify the images into specified motions. It can potentially be used for exercises classification.

GS6-5 Proposal and Evaluation of the Gait Classification Method using Arm Acceleration Data and Decision Tree

Kodai Kitagawa, Yu Taguchi, Nobuyuki Toya
(National Institute of Technology, Kushiro Collage, Japan)

We have been developed a system to classify gait patterns based on stride length and foot clearance by acceleration sensors of Smartphone as simple sensors for fall prevention. This system places a Smartphone around an arm as a convenient location. In this paper, we propose gait classification method using arm acceleration data and decision tree. Also, we evaluate whether decision tree using three-axis accelerations as feature quantities can classify three gait patterns. (Three gait patterns are "Normal", "High step" and "Long step".) The result showed that this method can classify three gait patterns of some subjects. Besides, it was found that x-direction accelerations and composite accelerations were important feature quantities for gait classification by decision tree.

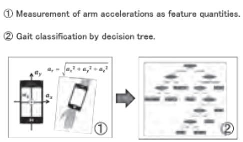

GS7 Micro-Machines & Robotics I (6)

GS7-1 Estimation and Categorization of Errors in Error Recovery Using Task Stratification and Error Classification

Akira Nakamura[*1], Kazuyuki Nagata[*1], Kensuke Harada[*2] and Natsuki Yamanobe[*1]
([*1] National Institute of Advanced Industrial Science and Technology (AIST), [*2] Osaka University, Japan)

In manipulation tasks of plant maintenance and industrial production, error recovery is an important research theme for robots. However, systematical methods of error recovery have not been appeared yet. We have proposed error recovery using the concepts of both task stratification and error classification. In the error recovery, the judgment of the error is carried out on a process of the practice of the system. In our method, classification of errors that occurred is carried out based on an estimated cause. Specifically, errors are classified into several categories such as sensing errors, modeling errors, planning errors and execution errors. When an error is classified correctly, a possibility that the most suitable recovery is performed becomes high. In this paper, a procedure of the categorization of the error that we have considered is described..

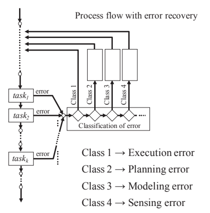

GS7-2 The Suitable Timing of Visual Sensing in Error Recovery Using Task Stratification and Error Classification

Akira Nakamura[*1], Kazuyuki Nagata[*1], Kensuke Harada[*2] and Natsuki Yamanobe[*1]
([*1] National Institute of Advanced Industrial Science and Technology (AIST), [*2] Osaka University, Japan)

In manipulation tasks of industrial production and housework, the techniques of error recovery become important since robots need to perform complicated tasks. We have proposed error recovery using the concepts of task stratification and error classification. In the error recovery, the judgment of the error is performed in processes of the practice of the system. Ideally, it is desirable for the judgment of the error to be carried out in many timings. However, in that case, many sensors are needed and it leads to disturb a workflow. Therefore it becomes important to be judged by the most suitable timing in a little number of times. In this paper, an efficient timing of visual sensing in an error recovery is described.

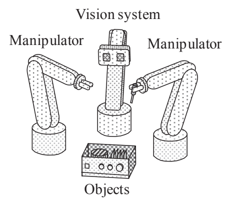

GS7-3 Hexapod Type MEMS Microrobot Equipped with an Artificial Neural Networks IC

Kazuki Sugita, Taisuke Tanaka, Yuya Nakata, Minami Takato, Ken Saito, Fumio Uchikoba
(Nihon University, Japan)

This paper proposes the hexapod type microrobot controlled by the artificial neural networks. The silicon based structural component of microrobot is produced by micro electro mechanical systems (MEMS). The rotary actuator is constructed from the artificial muscle wire of shape memory alloy (SMA) material. The actuator generates the locomotion of the microrobot by supplying the electrical current to artificial muscle wires. The microrobot was controlled by using artificial neural networks IC. The IC includes cell body models, inhibitory synaptic models and current mirror circuits. In addition, the artificial neural networks IC outputs the electric current whose pulse waveform. We installed the lead wires in the microrobot's interior. When the driving circuit is equipped on the MEMS microrobot, the internal placements of the lead wires reduced the wiring length, and achieved excellent weight balance and structurally stable performance of the MEMS microrobot.

GS7-4 Heat Distribution of Current Output Type Artificial Neural Networks IC for the MEMS Microrobot

Taisuke Tanaka, Yuya Nakata, Kazuki Sugita, Minami Takato, Ken Saito, Humio Uchikoba
(Nihon University, Japan)

Heat distribution of the artificial neural networks IC developed to driving circuit of microrobot were described in this paper. We previously constructed the microrobot imitating the insects with micro electro mechanical systems (MEMS) technology. The rotary actuator of MEMS microrobot is composed of shape memory alloy (SMA) based artificial muscle wires. The rotary motion is generated by passing an electric current through artificial muscle wires. We constructed artificial neural networks on IC chip as a driving circuit for the MEMS microrobot. The current mirror circuits also constructed, for the actuator is electric current driven type. The design rule of the IC was 4 metal 2 poly CMOS 0.35μm. We measured the heat distribution in the two types ICs having different stage number of the current mirror circuits by thermography. In addition, we examined heat generation mechanisms.

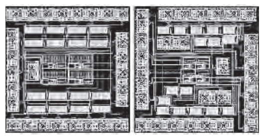

GS7-5 AGV with Mind and its production simulations for autonomous decentralized FMSs

Masato Chikamatsu, Hidehiko Yamamoto, Takayoshi Yamada (Gifu University, Japan)

The autonomous decentralized FMS does not have a management mechanism to integrate the entire system and each agent like Automated Guided Vehicles (AGVs) autonomously determine the acts by recognizing other agents. This study controls AGVs moving by using a mind model in order to avoid AGVs' interference in an autonomous decentralized FMS. The mind model can avoid the AGVs' interference by repeating the two types of mind changes, the arrogant mind and modest mind. AGV with the arrogant mind takes the action to approach forcibly at the destination. AGV with the modest mind takes the action to make way for other AGVs. By applying the mind to several FMSs, the production simulations were carried out. As a result, AGVs can avoid the path interference flexibly even if the shape of the production floor is changed and it is ascertained that the mind model is able to control the AGV actions of autonomous decentralized FMSs.

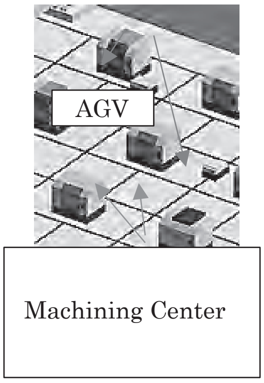

GS7-6 UNARM System to Decide Units Locations of Cell-type Assembly Machines with Robots Arms

Hirotaka Moribe, Hidehiko Yamamoto and Takayoshi Yamada (Gifu University, Japan)

This study develops the system called Units-layout Nomination for Assembly with Robot Mechanism (UNARM).UNARM assists a production engineers when they design an assembly machine with a both arms robot. To design the assembly machine, the engineers must decide the locations of parts and assembly jig (we call them as units) which become the objects assembled in the assembly machine. By using UNARM, every unit location can be automatically decided. To develop UNARM, we adopt Reinforcement Learning as a key technology. UNARM's characteristics are not only to decide the units locations but also to incorporate the both arms waiting time concept so that the both arms collisions do not occur. We applied UNARM to the assembly machine for the inline motor of an electric vehicle. The machine has 8 units in total. After carrying out UNARM simulations, the assembly time was decreased and the usefulness of UNARM was ascertained.

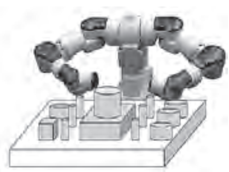

GS8 Micro-Machines & Robotics II (3)

GS8-1 Development of arm trajectory planning of Seamless Robot

Teedanai Pramanpol, Eiji Hayashi (Kyushu Institute of Technology, Japan)

This paper presents arm trajectory planning of Seamless Robot. The Seamless Robot is a Human Support Robot (HSR) which is the ongoing developed project at Hayashi Laboratory, this robot is consist of three main parts base, body and arms, this paper will focus on controlling arm movement. Each arm has been designed with four degrees of freedom with a limitation of each joint is set to values close to a human arm. In order to solve for each joint angle the Levenberg Marquardt method is used for solving the inverse kinematic problem for calculating point to create a trajectory planning of robot`s arms. The result of trajectory planning has been proven in simulation and compare with the experimental result from the robot.

GS8-2 Localization Method of Autonomous Moving Robot for Forest Industry

Ayumu Tominaga, Eiji Hayashi (Kyushu Institute of Technology, Japan), Tsutomu Sasao (Meiji University., Japan)

In the past, the working time of labor was spent too much for the forest management and maintenance. Particularly, survey of a forest and elimination of weed plants place a huge burden on the workers. We would like to propose an autonomous moving robot, which has the weeding mechanism. The robot can achieve the large labor-saving of forest industry. In this study, we are developing an autonomous moving robot for labor-saving of forest industry. Traditional forest management and maintenance consumes excessive labor time. Particularly, the survey and weeding in the forest place large labor burden on the workers. Therefore, the robot which has the weeding mechanism can achieve to reduce the workload. We installed a depth sensor into an all-terrain vehicle. The trajectory path of the robot is determined from the obtained depth information. In addition, we are using the Monte Carlo Localization for localize of the robot in the forest. Experimental results that show the feasibility of an autonomous moving in the real environment.

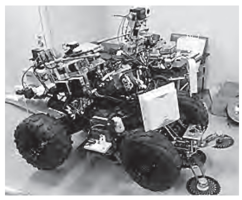

GS8-3 Dynamic Modeling and Motion Control of an RRR Robotic Manipulator

Jinho Kim[1], Kevin Chang[1], Brian Schwarz[1], Andrew S. Lee[1], S. Andrew Gadsden[1,2]
([1]University of Maryland, USA) ([2]University of Guelph, Canada)

This paper presents the dynamic modeling and motion control of a three-link robotic manipulator, also known as the RRR robot. The Kinect motion capture system by Microsoft is used in conjunction with the manipulator. Kinect is used to capture the motion of a user's arm and tracks certain angles made by parts of the arm. We consider a pinhole camera model to generate reference angles as per the Kinect model in our simulations. These desired angles are fed into the controller and are used by the RRR robot in an effort to copy the movement of the user. A proportional-integral-divider (PID) controller is developed and applied to the manipulator for improved trajectory tracking. The RRR robot manipulator is dynamically modeled and the results of the proposed control strategy demonstrate good trajectory following.

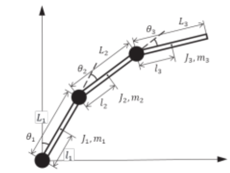

Fig 1. Configuration of the RRR robotic manipulator.

GS9 Neuromorphic Robotic Systems (5)

GS9-1 Development of Cloud Actions for Seamless Robot Using Backpropagation Neural Network

Wisanu Jitviriya (King Mongkut's University of Technology, Thailand)
Jiraphan Inthiam, Eiji Hayashi (Kyushu Institute of Technology, Japan)

This paper presents the cloud actions for a five DOF Seamless robotic arm using the inverse kinematics solution based on artificial neural network (ANN). Levenberg-Marquardt method is used in training algorithm. The desired position and orientation of the end effector is defined as the input pattern of neural network. In addition, we propose the cloud actions which are the movement patterns of the robotic arm. The cloud actions platform is created in order to perform the basic behaviors of the Seamless robot such as "Catch", "Approach", "Interest", "Look around", "Alert" and "Avoid" actions. Experimental results show the suitable structure of artificial neural network used for solving the inverse kinematics equation, and the testing points in the robot's workspace were verified with the robotic arm.

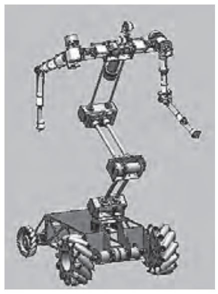

GS9-2 Mathematical modelling of human fear and disgust emotional reactions based on skin surface electric potential changes

Gaisina Kristina, Gaisin Ruslan (Kazan Federal University, Russia)

An appropriate numerical representation of neurotransmitters' level allows applying numerical methods for a study of psycho-emotional human reaction to various external stimuli, which could be further integrated into artificial life and robotic systems to reproduce human emotions and reactions. This paper deals with skin surface electric potential data registration of a human while the human is watching specially selected videos that are supposed to activate basic emotions of fear and disgust. We describe the selected video materials and data logging process and present human emotional reactions model, which was implemented with numerical methods. We demonstrate experimental results for fear and disgust psycho-emotional states that were obtained from 100 respondents. We believe that our findings might be applied for conditional measuring of neurotransmitters' levels.

GS9-3 Neuromorphic Robot Dream: A Spike Based Reasoning System

Alexander Toschev, Max Talanov, Salvatore Distefano (Kazan Federal University, Russia)
Alexander Tchitchigin (Innopolis University & Kazan Federal University, Russia)

Re-implementation of bio plausible processes in a real-time robotic system is one of challenging problems. We propose a novel approach for an integration of biologically plausible simulation of a mammalian brain with a real-time/semi-real-time autonomous robotic system using metaphor of "wake" and "dream" phases of a mammalian life. During the "wake" phase the robotic system makes its decisions applying a light-weight rule-based system and stores inbound sensory information in a form of pseudo-neuronal activities. During the "dream" phase the "sleeping brain" plays-back the stored pseudo-neural activities over a simulated spiking neural network and later via the "reverse translation" translates the updated neuronal structures in the form of light-weight rules of the robotic system. We call the proposed architecture the "Robot dream"

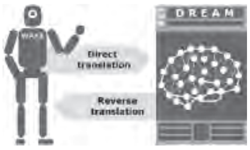

GS9-4 Development of Behavioral Robot using Imitated Multiplex Neurotransmitters System

Saji Keita[1], Wisanu Jitviriya[2] and Eiji Hayashi[1]
([1]Kyushu Institute of Technology, Japan)
([2]King Mongkut's University of Technology, Thailand)

This paper presents the design of robot's behavior by using the Imitated Multiplex Neurotransmitter system. The major neurotransmitter that consists of Dopamine, Noradrenaline and Serotonin, which called monoamine neurotransmitter and it is related to motivation for behavior and feeling. The proposed system is based on Wundt's three-dimensional theory of feeling. So, Dopamine is applied as a comfort dimension, Noradrenaline is defined as a tense dimension, Serotonin is considered as an energetic dimension. In our robot, three neurotransmitters are generated in each of different factors and the motivation is calculated. Next, the robot's motivation and some external information are classified into behavior and emotion by Self-Organizing Map learning. Finally, robot's behavior and emotion are decided by Markov's stochastic model.

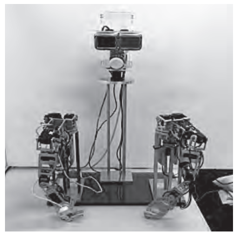

GS9-5 Nonlinear Estimation Strategies Applied on an RRR Robotic Manipulator

Jacob Goodman[1], Jinho Kim[1], Andrew S. Lee[1], S. Andrew Gadsden[1,2]
([1]University of Maryland, USA) ([2]University of Guelph, Canada)

Nonlinear estimation strategies are important for accurate and reliable control of robotic manipulators. This paper studies and compares two strategies known as the extended Kalman filter (EKF) and the smooth variable structure filter (SVSF). An overview of the two strategies, including their advantages and disadvantages, are provided. The algorithms and pseudocode are also included. The EKF and SVSF are applied to a dynamically modelled three-link (RRR) robotic manipulator. The results of the paper demonstrate that the EKF provides good state estimates, however lacks robustness to modeling uncertainties and disturbances. The SVSF provides sub-optimal estimates, yet is very robust to uncertainties and disturbances. Suggestions for future estimation and robotics research is also provided.

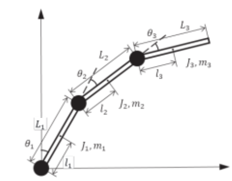

Fig 2. Configuration of the RRR robotic manipulator.

GS10 Reinforcement & Evolutionary Computations (3)

GS10-1 The Optimized Function Selection Using Wolf Algorithm for Classification

Duangjai Jitkongchuen, Worapat Paireekreng (Dhurakij Pundit University, Thailand)

Several classification techniques have been widely explored during the past decade. One of the novel approaches is Nature Based Algorithm. The focus of Nature Based Algorithm mostly is related to selection the optimized functions for self-learning. However, Some Nature Based Algorithms are suitable for general situation, some may be suitable for customized situation. This research proposes the Featured-Wolf (F-Wolf) algorithm to optimize the function selection problem in classification. The proposed algorithm applies the movement of a wolf and characteristics of wolves' leaders which can be more than one leader in a pack. Therefore, the pack can have more than one dominant leader which can help to select the most optimized functions to selection the most relevant features in the dataset. The experiment shows the comparison among other popular Nature Based Algorithms such as Ant Colony Optimization. The preliminary results show that F-Wolf performs comparable results in terms of F-measure.

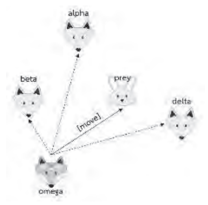

GS10-2 Tell Agent Where to Go: Human Coaching for Accelerating Reinforcement Learning

Nakarin Suppakun, Suriya Natsupakpon, Thavida Maneewarn
(King Mongkut's University of Technology Thonburi, Thailand)

In this work, we proposed a method to accelerate learning by allowing a human to coach a robot behavior by inserting an intermediate goal at the early phase of the reinforcement learning. By using an intermediate goal, the different pair of policy and reward function was temporarily used to select an action that most likely to drive the robot toward the intermediate location, while the global reward function is still used for updating the state-action value. Q learning algorithm was used to test with the proposed method on three learning tasks: ball following, obstacle avoidance, and mountain car. The proposed technique resulted in less number of accumulated failed episodes than the traditional RL

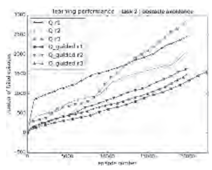

GS10-3 Fall Risk Reduction for Elderly Using Mobile Robots Based on the Deep Reinforcement Learning

Takaaki Namba (Nagoya University, Japan)

Slip-induced fall is one of the main factors causing serious fracture among the elderly. This paper proposes a deep learning based fall risk reduction measurement by the mobile assistant robot for the elderly. First, we collect preparatory data regarding past incidents and accidents data as input data to analyze fall risks and to learn examples of risk reduction measurement. Second, we use a deep convolutional neural network to analyze fall risks of elderly. Third, we apply a deep reinforcement learning to control mobile robots and reduce slip-induced fall risks of elderly. Moreover, we evaluate the effect of risk reduction. The results suggest that the applicability of our method to other cases of the fall and other cases of accidents.

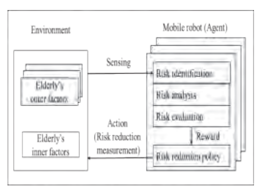

Fig. 1 Deep reinforcement learning for fall risk reduction of elderly.

GS11 Others (12)

GS11-1 Clinical Evaluation of UR-System-PARKO for Recovery of Motor Function of Severe Plegic Hand after Stroke

Hirofumi Tanabe (Shonan University of Medical Sciences, Japan)
Yoshifumi Morita (Nagoya Institute of Technology, Japan)

The first author has developed TANABE therapy for severe hemiplegic stroke patients. In the therapy, he performed repeated facilitation training using his hands on patients to help them recover their motor function and achieved a good treatment outcome. In this paper we developed a training system (UR-System-PARKO) on the basis of TANABE therapy. The clinical test of the therapeutic effect of the UR-System-PARKO was performed in severe plegic hand. As a result, the active ranges of motion of finger extension were improved, and Electromyogram ignition increased after the training. Moreover, the Modified Ashworth Scale scores of finger extension were increased. These results show the effectiveness of the training by the UR-System-PARKO for recovery of motor function for finger extension of the severe plegic hand.

GS11-2 A Piston Finger Device for Restoring the Motor Function of Chronic Plegic Fingers: Analysis of the Piston Finger Technique

Mengsu Wang (Nagoya Institute of Technology: Nitech, Japan), Hirofumi Tanabe (Shonan University of Medical Sciences, Japan), Kenji Ooka (Nitech, Japan), Yoshifumi Morita (Nitech, Japan)

The second author has developed Piston Finger Technique (PFT) for restoring motor function of chronic plegic fingers and has achieved a good treatment outcome, namely reduction of spasticity and improvement of muscle shortening. In this paper, before developing a piston finger device (PFD) simulating the PFT, we analyzed the PFT by the second author by using a motion capture system. The patent's finger motion of a chronic plegic index finger was investigated when the patient received two types of treatment based on the PFT. As a result, the ranges of motion of the proximal interphalangeal joint and the metacarpophalangeal joint of the index finger as well as the vibration width and frequency during treatment were revealed. These results will be useful for developing a PFD in the near future.

GS11-3 Verifying the Sleep-Inducing Effect of a Mother's Rocking Motion in Adults

Hiroaki Shibagaki, Keishi Ashida, Yoshifumi Morita (Nagoya Institute of Technology, Japan), Ryojun Ikeura (Mie University, Japan) and Kiyoko Yokoyama (Nagoya City University, Japan)

In our previous study, from subjective experimental results, we have found that, of the ten types of rocking motions examined, the linear motion component of a mother's rocking motion was the most effective rocking motion for inducing sleep in adults. This motion was referred to as the candidate rocking motion. In this study, we confirmed that the candidate rocking motion was effective for inducing sleep by using electroencephalogram analysis in comparison with the case without rocking motion. Moreover, we also compared the candidate rocking motion and aromatherapy. As a result, in the case of aromatherapy the effectiveness for inducing sleep varied between individuals. In the case of the candidate rocking motion individual variation in the effectiveness was small. We concluded that the candidate rocking motion was effective.

GS11-4 Design of Automated Real-Time BCI Application Using EEG Signals

Chong Yeh Sai, Norrima Mokhtar, Hamzah Arof, Masahiro Iwahashi
(University of Malaya, Malaysia / Nagaoka University of Technology, Japan)

This study proposed a design of real time BCI application using EEG recording, pre-processing, feature extraction and classification of EEG signals. Recorded EEG signals are highly contaminated by noises and artifacts that originate from outside of cerebral origin. In this study, pre-processing of EEG signals using wavelet multiresolution analysis and independent component analysis is applied to automatically remove the noises and artifacts. Consequently, features of interest are extracted as descriptive properties of the EEG signals. Finally, classification algorithms using artificial neural network is used to distinguish the state of EEG signals for real time BCI application.

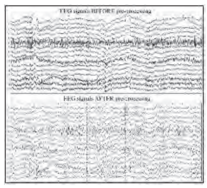

GS11-5 A Hybrid Simulated Kalman Filter - Gravitational Search Algorithm (SKF-GSA)

Badaruddin Muhammad, Zuwairie Ibrahim, Mohd Falfazli Mat Jusof (Universiti Malaysia Pahang, Malaysia)
Nor Hidayati Abdul Aziz, Nor Azlina Ab. Aziz (Multimedia University, Malaysia)
Norrima Mokhtar (University of Malaya, Malaysia)

In this paper, simulated Kalman filter (SKF) and gravitational search algorithm (GSA) are hybridized in such a way that GSA is employed as prediction operator in SKF. The performance is compared using CEC2014 benchmark dataset. The proposed hybrid SKF-GSA shown to perform better than individual SKF and GSA algorithm.

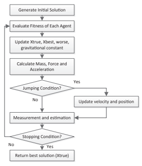

GS11-6 Simulated Kalman Filter with Randomized Q and R Parameters

Nor Hidayati Abdul Aziz, Nor Azlina Ab. Aziz (Multimedia University, Malaysia)
Zuwairie Ibrahim, Saifudin Razali, Mohd Falfazli Mat Jusof (Universiti Malaysia Pahang, Malaysia)
Khairul Hamimah Abas, Mohd Saberi Mohamad (Universiti Teknologi Malaysia, Malaysia)
Norrima Mokhtar (University of Malaya, Malaysia)

Inspired by Kalman filtering, simulated Kalman filter (SKF) has been introduced as a new population-based optimization algorithm. The SKF is not a parameter-less algorithm. Three parameter values should be assigned to P, Q, and R, which denotes error covariance, process noise, and measurement noise, respectively. While analysis of P has been studied, this paper emphasizes on Q and R parameters. Instead of using constant values for Q and R, random values are used in this study. Experimental result shows that the use of randomized Q and R values did not degrade the performance of SKF and hence, one step closer to the realization of a parameter-less SKF.

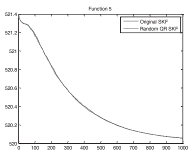

GS11-7 Real Detection of 3D Human Hand Orientation Based Morphology

Abadal-Salam T. Hussain, Hazry D., Waleed A. Oraibi, M.S Jawad, Zuradzman M. Razlan, A. Wesam Al-Mufti, S. Faiz Ahmed, Taha A. Taha, Khairunizam WAN, Shahriman A.B
(Universiti Malaysia Perlis, Malaysia)

This paper describes a new methodology to track a human hand movements in 3D space and estimate its orientation and position in real time. The objective of this algorithm development is to ultimately using it in robotic spherical wrist system application. This method involves image processing and morphology techniques in conjunction with various mathematical formulae to calculate the hand position and orientation. The advantage of this technique is that, there is no need for continuous camera calibration which is required in other conventional methods in similar applications. The result of proposed method shows correctly identifying a large number of hand movements and its orientations. The proposed method could therefore be used with different types of tele operated robotic manipulators or in other human-computer interaction applications. This method is more robust and less computationally expensive, unlike other approaches that use costly leaning functions. The high performance is achieved during experiments testing because of its accurate hand movement identification and the low computational load.

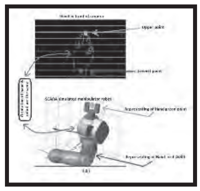

GS11-8 Multilevel Non-Inverting Inverter Based Smart Green Charger System

Abadal-Salam T. Hussain, Waleed A. Oraibi, Hazry D, Zuradzman M. Razlan, S. Faiz Ahmed, Taha A. Taha, Khairunizam WAN & Shahriman AB (Universiti Malaysia Perlis, Malaysia)

This paper discusses about the development of low cost efficient battery charging system using PIC Microcontroller. The demand of efficient battery charging system are going increase day by day, because of its usage in various applications such as it use in Hybrid electric cars, PV solar electric generation system, other energy storage systems and many more. In this paper an efficient and cost effective battery charging system is presented that use buck-boost converter topology. First, the software (PIC Programming) simulation is performed using Micro C software and then hardware is developed and tested to check the performance of the developed battery charger system. The efficiency of circuit is 85.66% and it can be use in any battery charging application

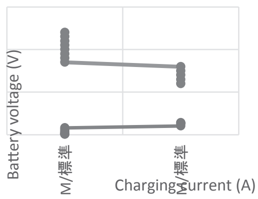

GS11-9 Design A New Model of Unmanned Aerial Vehicle Quadrotor Using The Variation in The Length of The Arm

Yasameen Kamil, D. Hazry, Khairunizam Wan, Zuradzman M. Razlan, Shahriman AB
(Universiti Malaysia Perlis, Malaysia)

The direction of technological advancement toward autonomous aerial vehicle is increased. As a consequence of this evolution, the quad rotor used to accomplish a complex task in several fields. This paper presents the dynamic model of this miniature aerial vehicle in altitude and new dynamic model for yaw attitude movement, based on varying the arm length of quadrotor instead of varying the speed of motors to obtain a rotation around z-axis. This achieved by fixed a stepper motor in the arm of quadrotor to increase or decrease the length of the arm according to controller command for yawing movement. The controller command achieved by design PID controller with specific parameters to maintain the stability of the quadrotor in the flight path. The equipped energy to the motors during flight and maneuvering is reduced by selecting the motors' speed. The MATLAB software code used to evaluate and presents the comparison between the proposed and conventional quadrotor dynamic model. Simulation results show the robustness performance of the proposed model due to the movement around the z-axis with high system stability.

GS11-10 Development of Automatic Take Off and Smooth Landing Control System for Quadrotor UAV

Syed. F. Ahmed (Universiti Kuala Lumpur, British Malaysian Institute, Malaysia
Universiti Malaysia Perlis, Malaysia)
D. Hazry (Universiti Malaysia Perlis, Malaysia)
Kushsairy Kadir (University Kuala Lumpur, British Malaysian Institute, Malaysia)
Abadal Salam T. Hussain, Zuradzman M. Razlan, Shahriman AB
(Universiti Malaysia Perlis, Malaysia)

This paper covers the development of automatic takeoff and smooth landing control system for UAV Quadrotor. This paper includes development, simulation, mathematical modeling and experimental results of flight test. In the developed UAV model has a system to stabilize the quadrotor. Altitude stabilization in quadrotor make the quadrotor can perform take off and smooth landing perfectly and can avoid crash during landing which was proved during experiment. Yaw, pitch, and roll in quadrotor body is detected by gyro sensor when flying is balanced by gyro sensor. Gyro sensor act as input that detect stabilization problem and input data will be sent to microcontroller to make new output for quadrotor.

GS11-11 Auto Pilot Ship Heading Angle Control Using Adaptive Control Algorithm

Abadal-Salam T. Hussain Hazry D., S. Faiz Ahmed, Wail A. A. Alward, Zuradzman M. Razlan & Taha A. Taha (Universiti Malaysia Perlis, Malaysia)

In this paper discussed about development of an auto pilot system for ships using adaptive filter. Adaptive filter in the application of auto pilots for ships is presented for controlling the ship such that it follows its predetermined trajectory. Due to random environmental effects such as wind speed or direction and sea current, the path of the ship may alter. The objective of this research is to investigate that whether proposed system will adapts to the random changes and maintain the desired ship trajectory. The proposed auto pilot system is developed using Least Mean Square algorithm (LMS) adaptive filter. The performances of the system are analyzed based on accuracy and computational times. MATLAB Simulink model tool is used for execute the simulations of the auto pilot system for ships.

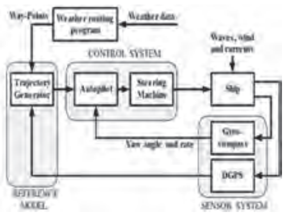

GS11-12 Classification of Hippocampal Region using Extreme Learning Machine

Muhammad Hafiz Md Zaini, Mohd Ibrahim Shapiai (Universiti Teknologi Malaysia)
Ahmad Rithauddin Mohamed (Hospital Kuala Lumpur)
Norrima Mokhtar (University of Malaya)
Zuwairie Ibrahim (Universiti Malaysia Pahang)

Important brain parts like hippocampal usually being manually segmented by doctors. But with the introduction of hybrid between machine learning along with neuroimaging technique, it has proved to shows some promising results regarding on segmenting subcortical structures. However, it is known that Extreme Learning Machine (ELM) is to be superior machine learning technique. This study will investigate on the usage of ELM to segment hippocampal by using various hidden nodes configuration. This study also will address on the usage of full image and region of interest (ROI) using ELM. Bag of features is used as a feature extractor where it will segment the hippocampal of the MRI in order to get its visual words. ELM will used it to learn its feature. Results shows that with suitable hidden nodes, it could achieve up to 100% performance on both cases for full image and ROI in hippocampal segmentation.

AUTHORS INDEX

Notation of session name

PS: Plenary Session IS: Invited Session, OS: Organized Session, GS: General Session,

Note: 33/90 = (page no. in Technical Paper Index) / (page no. in Abstracts)


Seagaia Convention Center

シーガイアコンベンションセンター　2F「ファウンテン」
【ICAROB2017 様　学会会場】
スクール形式 96名＋コーヒーブレイク用90cm丸テーブル4卓

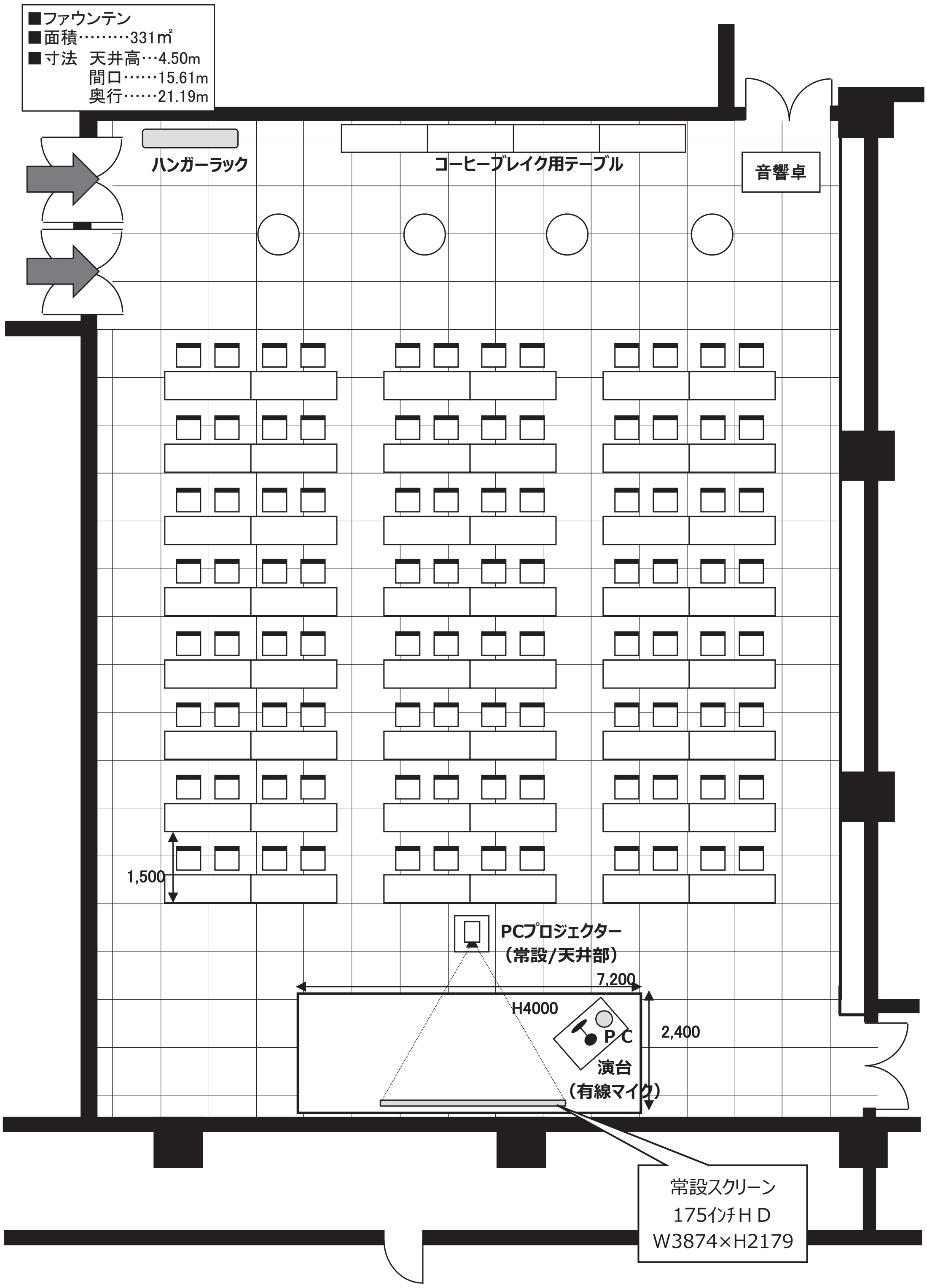

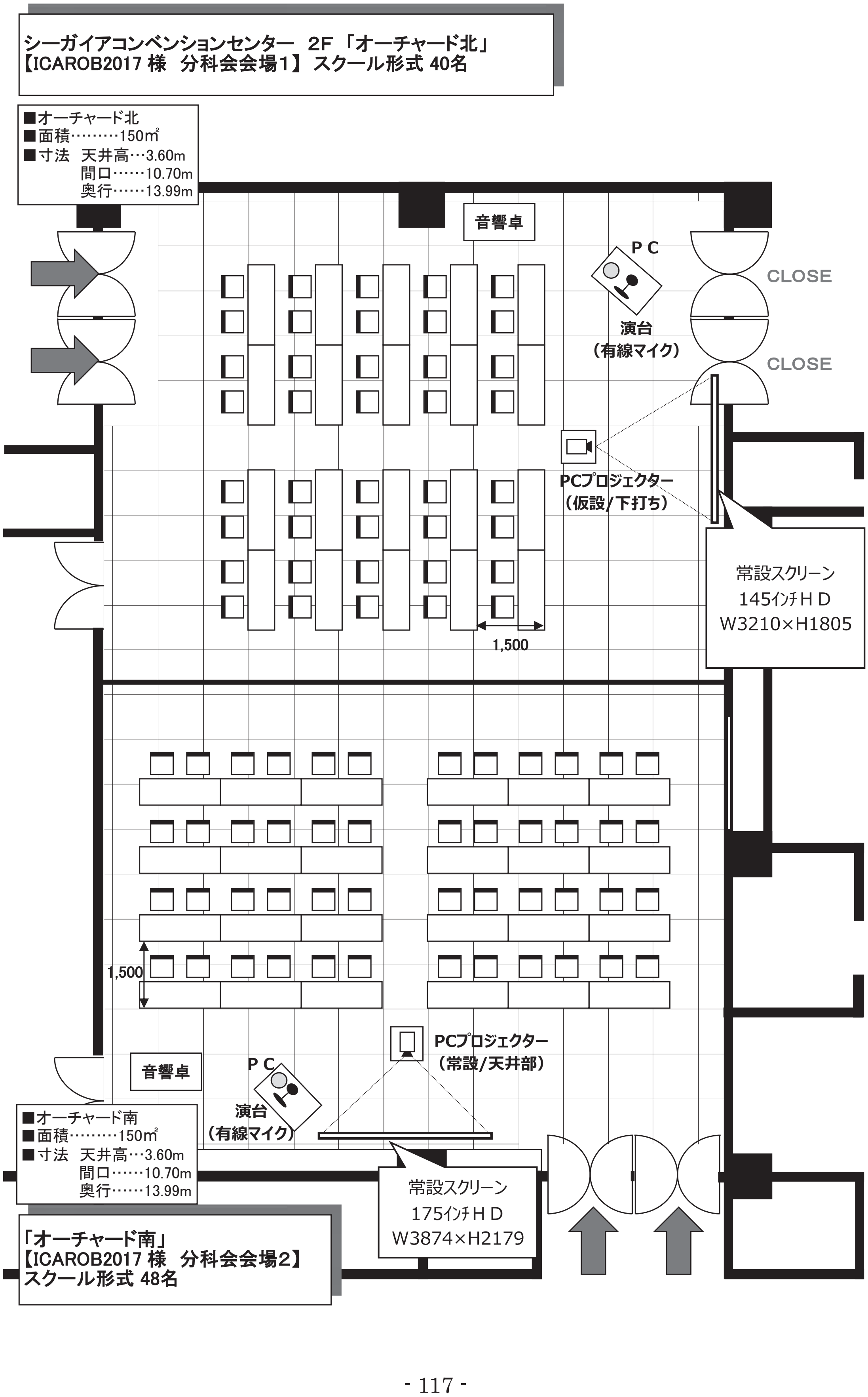
シーガイアコンベンションセンター 2F 「オーチャード北」
【ICAROB2017 様 分科会会場1】 スクール形式 40名
■オーチャード北
■面積………150㎡
■寸法 天井高…3.60m
間口……10.70m
奥行……13.99m
音響卓
ＰＣ
CLOSE
演台
（有線マイク）
CLOSE
PCプロジェクター
（仮設/下打ち）
常設スクリーン
145ｲﾝﾁＨＤ
W3210×H1805
1,500
1,500
PCプロジェクター
（常設/天井部）
音響卓
ＰＣ
演台
（有線マイク）
■オーチャード南
■面積………150㎡
■寸法 天井高…3.60m
間口……10.70m
奥行……13.99m
常設スクリーン
175ｲﾝﾁＨＤ
W3874×H2179
「オーチャード南」
【ICAROB2017 様 分科会会場2】
スクール形式 48名

シーガイアコンベンションセンター　2F 「プライベートレストラン」
【ICAROB2017 様　事務局】 椅子12席

■プライベートレストラン
■面積………59㎡
■寸法　天井高…3.30m
　　　　間口……5.60m
　　　　奥行……10.00m

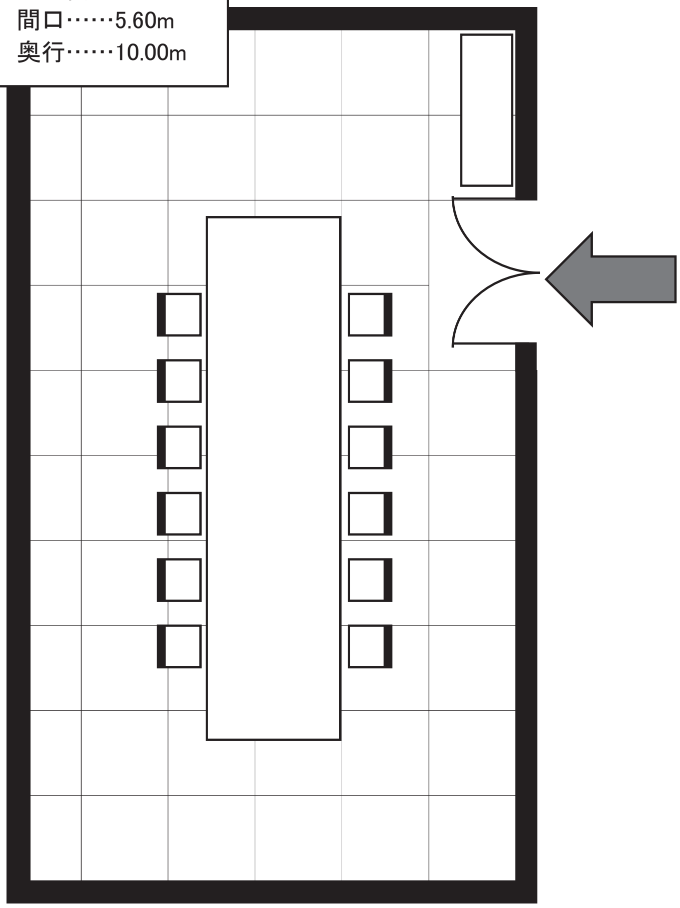

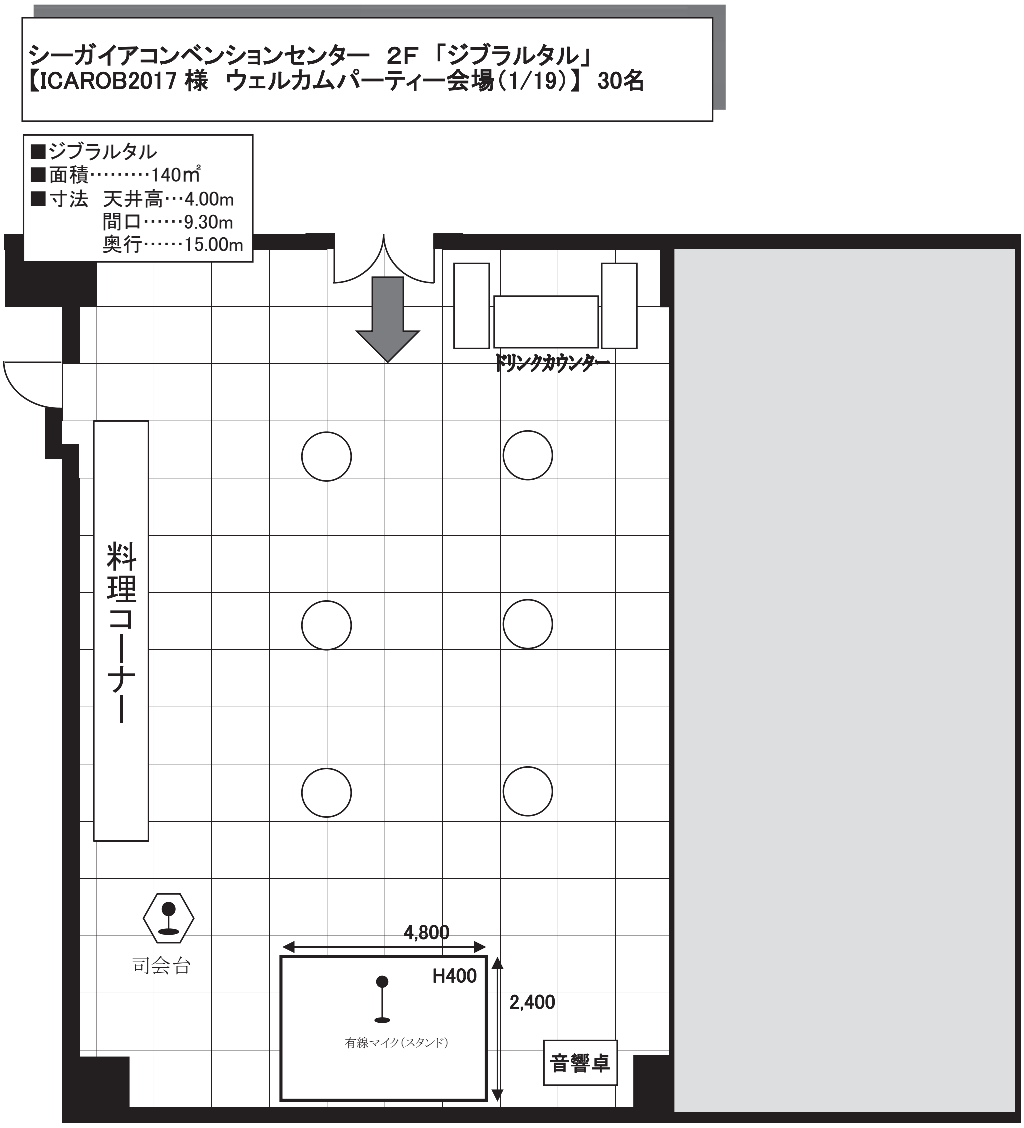
シーガイアコンベンションセンター 2F 「ジブラルタル」
【ICAROB2017 様 ウェルカムパーティー会場（1/19）】 30名
■ジブラルタル
■面積………140㎡
■寸法 天井高…4.00m
間口……9.30m
奥行……15.00m
ドリンクカウンター
料理コーナー
司会台
4,800
H400
2,400
有線マイク（スタンド）
音響卓

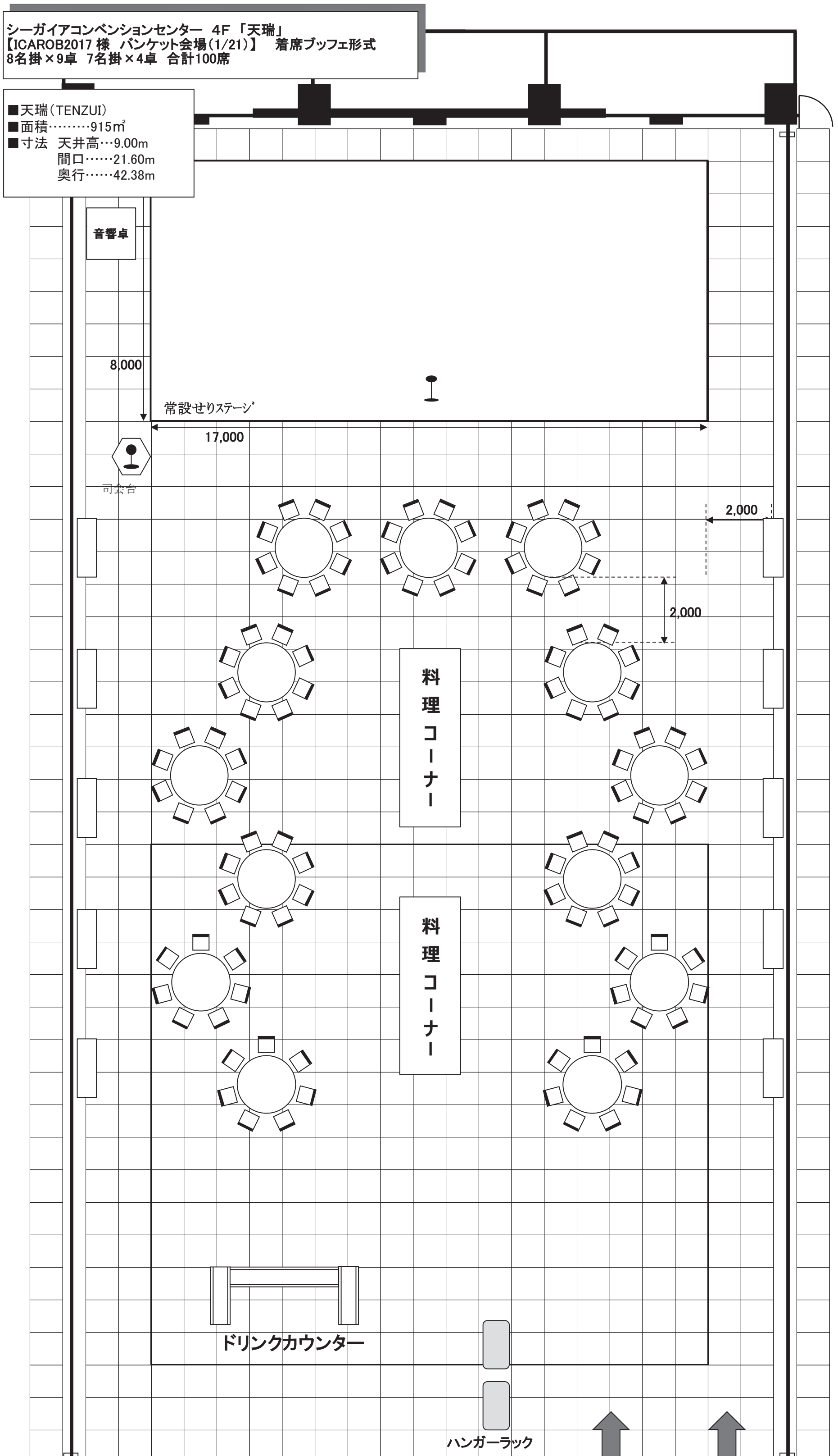
シーガイアコンベンションセンター 4F「天瑞」
【ICAROB2017 様 バンケット会場(1/21)】 着席ブッフェ形式
8名掛×9卓 7名掛×4卓 合計100席
■天瑞(TENZUI)
■面積………915㎡
■寸法 天井高…9.00m
間口……21.60m
奥行……42.38m
音響卓
8,000
常設せりステージ
17,000
司会台
2,000
2,000
料理コーナー
料理コーナー
ドリンクカウンター
ハンガーラック
CLOSE
CLOSE
CLOSE
CLOSE

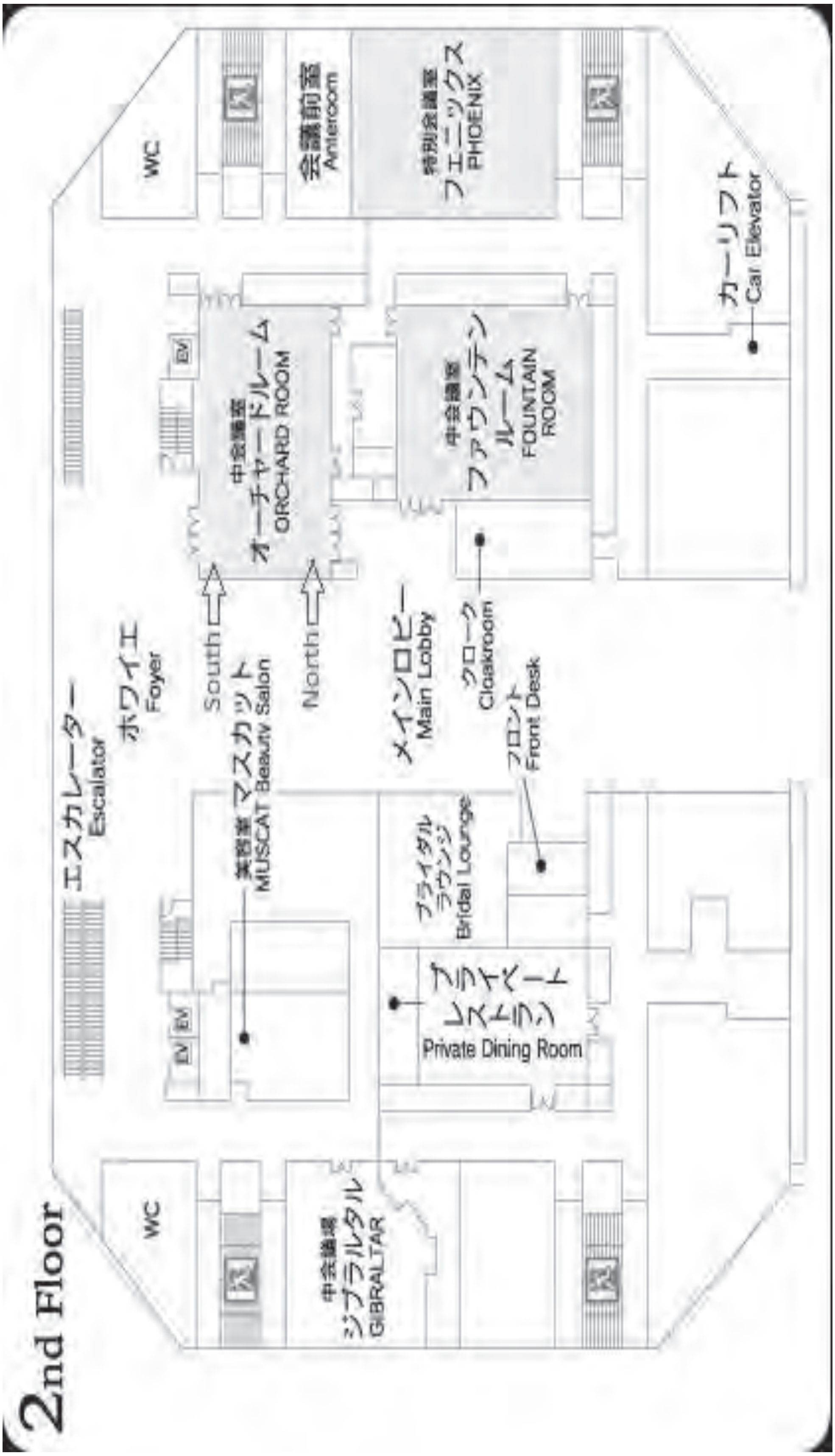
2nd Floor
WC
会議前室
Anteroom
特別会議室
フェニックス
PHOENIX
カーリフト
Car Elevator
EV
中会議室
オーチャードルーム
ORCHARD ROOM
中会議室
ファウンテン
ルーム
FOUNTAIN
ROOM
エスカレーター
Escalator
ホワイエ
Foyer
South
North
メインロビー
Main Lobby
クローク
Cloakroom
フロント
Front Desk
美容室 マスカット
MUSCAT Beauty Salon
ブライダル
ラウンジ
Bridal Lounge
プライベート
レストラン
Private Dining Room
EV
EV
WC
中会議室
ジブラルタル
GIBRALTAR

Targeting Chaos System via Minimum Principle Control

Yunzhong Song, Ziyi Fu, Fuzhong Wang
College of Electrical Engineering and Automation, Henan Polytechnic University, 2001 Century Avenue, Jiaozuo, 454003, P.R.China
E-mail: songhpu@126.com, fuzy@hpu.edu.cn, wangfzh@hpu.edu.cn
www.hpu.edu.cn

Abstract

Chaos targeting via Minimum Principle Control (MPC) was suggested here, to be unique, the targeting via MPC can not only stabilize all the non-stable equilibrium when the control was introduced in the first or the second equation of the chaos system, but also does the extra added control was introduced in the third equation, with the cost of switching control direction for a duration.

Keywords: chaos system, Minimum Principle Control (MPC), Hamiltonian function, switching control

1. Introduction

An additive, scalar, and inequality constrained control method has been introduced to the well known chaotic system Lorenz system by Yu-Chu Tian, Mose O Tade, David Levy which appeared in Physics Letters A296(2002)87-90, please referring to Ref. 1. The resulting control law is bang-bang one and can stabilize the unstable equilibrium, two cases such that control action added at the first and second equations of the Lorenz system are reported. And Professor Song, together with the other others, has addressed the tough obstacle that when the control action was added in the third equation, whereas the Tian's method was out of control, please referring to Reference 2. Since then, seldom results of constrained control to chaos system were reported and extended. In this paper, we will extend the suggested strategy to another chaos system, i.e the Chen chaos system, please referring to Reference 3, besides the control action being added in the first or the second equation, we will consider the case, where control action added on the third equation of the Chen chaos system. Thanks to the uniqueness of the nonlinear system, different systems may express different behavior, so do the Chen chaos system; and even further, the switching surface resulted from the Hamiltonian function and the Minimum Principle Control (MPC) will also be distinct from each other, without saying the parameters selection of the controller. And the most striking point is with the completion of Chen chaos system control via MPC strategy, the belief in Lorenz family chaos system control can come into mature naturally, and more importantly, the wait to go style of chaos system control is re-recognized to be the first candidate when the other strategies fail.

The rest of the paper is as follows. First, at the second part, we will give some preliminaries about Chen chaos system and MPC with constraints; and then the main results will be introduced in the third part; the conclusion and some prospects will be provided in the end.

2. Preliminaries

2.1. *Glimpse of chen chaos system*

For Chen chaos system

$$\begin{aligned}\dot{x}_1 &= f_1(x_1, x_2, x_3) = a(x_2 - x_1),\\ \dot{x}_2 &= f_2(x_1, x_2, x_3) = (c-a)x_1 - x_1x_3 + cx_2,\\ \dot{x}_3 &= f_3(x_1, x_2, x_3) = x_1x_2 - bx_3.\end{aligned} \tag{1}$$

when the parameters and their values are deployed as $a = 35, b = 3, c = 28$, the Chen chaos system will demonstrate chaotic behavior and in that case has three different equilibriums, and all of them are not stable.

$$\begin{aligned}x_e^{(1)} &= [0,0,0]^T,\\ x_e^{(2,3)} &= [\pm\sqrt{(2c-a)b}, \pm\sqrt{(2c-a)b}, 2c-a]\\ &= [\pm 7.9373, \pm 7.9373, 21].\end{aligned} \tag{2}$$

2.2. *Glimpse of constrained control via MPC*

Consider continuous and nonlinear chaotic system

$$\dot{x} = f(x), x(t_0) = x_0, 0 = \dot{x}_e = f(x_e), \tag{3}$$

where $x \in R^n, f \in R^n, t_0$ is the initial time constant. And x_e demonstrates the equilibrium of the system, the introduction of control action aims to drive the unstable equilibrium into stable states. Assumed we introduce one constrained scalar control action to system (3), the system under control will turn into

$$\dot{x} = f(x) + Bu, x(t_0) = x_0, |u| \le M, M > 0, \tag{4}$$

The column vector B only has one non-zero cell among its n cells, i.e. $b_k = 1, k \in \{1, 2, \cdots, n\}$, and M is constant, which clamps the amplitude of the control action. The constrained control problem is find the control action, which meets the constraint defined in Eq. (3) to drive the chaos system of (1) from the arbitrary initial state $x(t_0)$ to the desired non-stable equilibrium $x(T) = x_e$. And T is the free terminal time. The further requirement of chaos system control is that when the chaos system is driven to the desired non-stable equilibrium, system state was required to stick to that states forever.

Assume the Hamiltonian function of system (4) as

$$H(x, u, \lambda, t) = \lambda^T [f(x) + Bu] \tag{5}$$

where $\lambda \in R^n$ is the unknown adjoint variable, which can be defined by the following equation

$$\dot{\lambda} = -\frac{\partial H}{\partial x} = -\lambda^T \frac{\partial f}{\partial x} \tag{6}$$

In order to identify the optimal control action u, it is necessary for us to come to the helps MPC, then

$$H(x^*, u^*, \lambda^*, t) \le H(x^*, u^* + \delta u, \lambda^*, t) \tag{7}$$

To arbitrary δu, constraint defined by (7) can stand. And δ is deployed to represent variation, and the superscript "∗" is assigned to represent the optimal value. To Hamiltonian function (5), under constraint of (7), it is easy for us to get

$$(\lambda^*)^T Bu^* \le (\lambda^*)^T Bu \tag{8}$$

And the optimal control action comes naturally

$$u^* = -M\,\mathrm{sgn}[(\lambda^*)^T B] \tag{9}$$

where sgn demonstrates the sign function mathematically. And in this case, the optimal control is bang-bang format, and the corresponding switching curve is defined as

$$(\lambda^*)^T B = 0 \tag{10}$$

To linear time invariant system (4), Hamiltonian function (5) will keep constant in locus of (10). And we only consider the free terminal time constant case here, then

$$0 = H(x, u, \lambda, t) = \lambda^T [f(x) + Bu] \tag{11}$$

Results and Analysis

Control here aims at stabilizing $x_e^{(2)}$ or $x_e^{(3)}$ via added outside action u for Equation (4). Here, M is assigned as 35, and $x_0 = [0.1, 0, 0]^T$, in case of completeness, control action added in the first sub-equation f_1, through the second sub-equation f_2 and across the third sub-equation f_3 are covered.

3.1. *Control action added in the first sub-equation*

First of all, the control action added in the first sub-equation is touched upon. And in this case $B = [1, 0, 0]^T$, from Equ. (10), we have $\lambda_1 = 0, \dot{\lambda}_1 = 0$. If we assumed $[\lambda_2, \lambda_3]^T$ has non-zero solution, then from (6), we can have

$$\lambda_2 \frac{\partial f_2}{\partial x_1} + \lambda_3 \frac{\partial f_3}{\partial x_1} = 0 \tag{12}$$

Connected with (11) and (4), we can have

$$\lambda_2 f_2 + \lambda_3 f_3 = 0 \tag{13}$$

It is easy to find that the following stands if (12) and (13) are joined verified.

$$S(x) = f_2 \frac{\partial f_3}{\partial x_1} - f_3 \frac{\partial f_2}{\partial x_1} = cx_2^2 - bx_3^2 + (c-a)bx_3 = 0 \quad (14)$$

Obviously, $x_e^{(2)}$ and $x_e^{(3)}$ meets the constraints of Eq. (14), so the two feasible control law can be listed as $u_+ = -M\,\mathrm{sgn}[S(x)], u_- = M\,\mathrm{sgn}[S(x)]$; where u_+, u_- are assigned to $x_e^{(3)}, x_e^{(2)}$, separately. The result of u_- is illustrated in Figure 1.

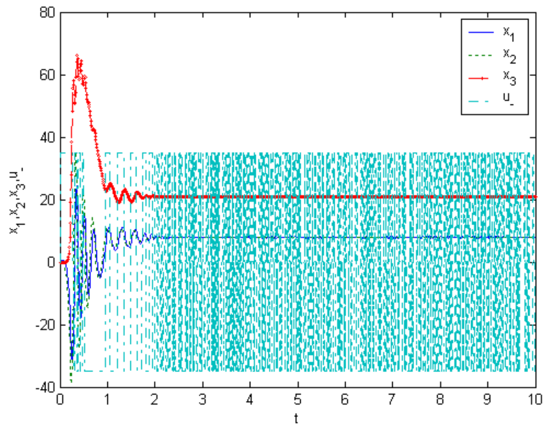

Fig.1. System states and control action transient curves with u- added in the first equation.

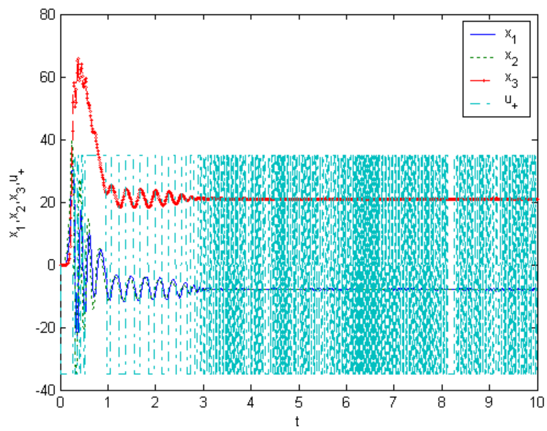

Fig.2. System states and control action transient curves with u+ added in the first equation.

And for initial state x_0, after duration of the transient process, state will be driven to and stabilized on $x_e^{(2)}$, and control action switches between -35 and +35, and further more, because the satisfaction of $x_e^{(2)}$ with the switching curve, the switching frequency will become much more often when state comes to the $x_e^{(2)}$ nearby. Similarly, the result of u_+ is illustrated in Figure 2.

In case of the space limitation, we omit the comments to Figure (2).

3.2. *Control action added in the second sub-equation*

And in this case, the switching curve is transformed into

$$S(x) = f_1 \frac{\partial f_3}{\partial x_2} - f_3 \frac{\partial f_1}{\partial x_2} = -ax_1^2 + abx_3 \quad (15)$$

Similarly, the results of u_-, u_+ can be successfully demonstrated for their capability in stabilizing the unstable equilibriums. In case of space limitation, the illustration of the resulted curves is omitted here.

3.3. *Control action added in the third sub-equation*

And in this case, the switching curve is transformed into

$$S(x) = f_1 \frac{\partial f_2}{\partial x_3} - f_2 \frac{\partial f_1}{\partial x_3} = ax_1x_2 - ax_1^2 \quad (16)$$

To be curious, u_- can not stabilize $x_e^{(2)}$, however, u_+ can still hold its capability in stabilizing $x_e^{(3)}$, the results about u_- is illustrated in figure (3), and the result of u_+ is also omitted here.

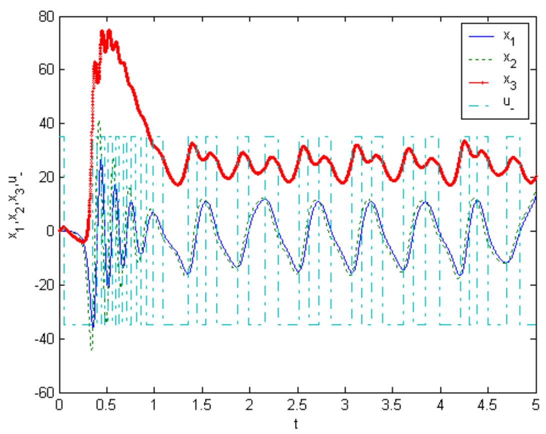

Fig.3. System states and control action transient curves with u- added in the third equation

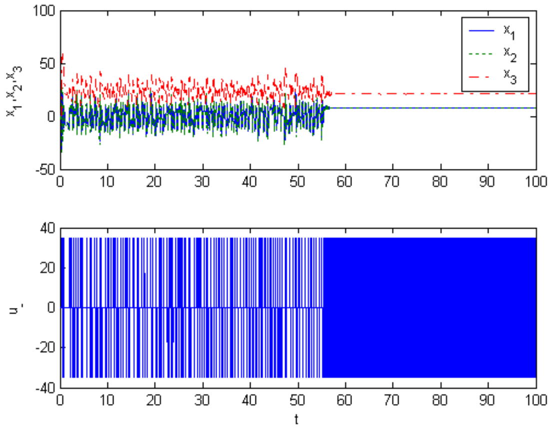

Fig.4. System states and control action transient curves with improved u- added in the third equation

In order to stabilize $x_e^{(2)}$, inspired by the initial sensitive peculiarity of chaos system, the sub-control action $u\_$ is segmented further into

$$u_- = \begin{cases} u_+; |x_1 - \mathrm{c}| \le \sigma \\ 0; |x_1 - \mathrm{c}| > \sigma. \end{cases} \quad (17)$$

where x_1 is the first sub-state variable of chaos system, while c and σ are constants, and c and be chosen as $x_{e1}^{(2)}$ itself, σ can be viewed as the threshold value, here we assumed as 2, and after this kind of reform, the result of $u\_$ is illustrated as figure (4)

And by this wait to go style, the sub-equation based control can fully functions for all the non-stable equilibrium.

3. Conclusion

In this paper, inspired by the initial value sensitive peculiarity of the chaos system, in helps of the MPC, the wait to go style sub-control action is extra introduced to make it possible to realize the full scale stabilization of the non-stable equilibrium of Chen chaos system, and the suggested strategy deserves its further exploration in the future.

Acknowledgements

This work is partially supported by NSFC Grant (61340041 and 61374079) and the Project-sponsored by SRF for ROCS, SEM to Yunzhong Song.

References

1. Y. Tian, M. Tade and D.Levy, Constrained control of chaos, *Physics Letters A*, **296** (2002) 87-90.
2. Y. Song, G. Zhao and D. Qi, Some Comments on constrained control of chaos, *Physics Letters A*, **359** (2006) 624-626.
3. G. Chen and T.Ueta, Yet another chaotic attractor, *Int. J. of Bifurcation and Chaos*, **9** (1999) 1465-1466.

Three-Dimensional Leader-Follower Formation Flocking of Multi-Agent System

Yongnan Jia, Weicun Zhang
School of Automation and Electrical Engineeringt, University of Sciences and Technology Beijing
30 Xueyuan Road, Haidian District, Beijing, 100083, China
E-mail: ynjia@pku.edu.cn, weicunzhang@263.net
www.ustb.edu.cn

Abstract

This paper aims to investigate the three-dimensional formation flocking of multi-agent system with leader-follower structure. Based on the nearest neighbor interaction rules, a kind of distributed control algorithm is proposed, which enables all the agents asymptotically converge to fly with the same velocity and approach the expected formation with their neighbors, provided that the initial interaction network of the system is leader-follower connected. Numerical simulations are carried on the multi-agent system to validate the functionality of the proposed algorithm.

Keywords: Formation control, flocking cooperation, leader-follower structure, multi-agent system.

1. Introduction

Formation control of multi-agent system has received more and more attention from the scholars all over the world, due to its widespread applications on military and civilian areas. Except for these traditional methods, such as leader-follower [1]-[2], behavior-based [3]-[4], virtual structure [5]-[7], new algorithms are investigated to give some new results on formation control problem [8]-[9]. In this paper, we try to apply the flocking strategy to solve the formation control problem of multi-agent system in this paper.

Flocking is such a collective phenomenon that can be widely observed from the social animals in nature, and it is also a kind of typical distributed behavior worth to be investigated in further [10]-[13]. For example, the wild gooses fly as a herringbone three-dimensional formation when they migrate from one place to another. Therein, the leading wild goose plays an important role. We introduce leader-follower structure to the multi-agent system for the purpose of simulating the formation behavior of the wild gooses. Thus, in this paper, we aim to investigate the three-dimensional leader-follower formation flocking problem of multi-agent system.

We consider the multi-agent system consists of one leader and several followers. Each agent is modeled as an extended second-order unicycle with limited interaction capability. Graph theory is used to depict the interaction network of the multi-agent system. A distributed algorithm is proposed with the combination of consensus algorithm and artificial potential field method. The numerical simulation based on MATLAB further validates the functionality of the proposed algorithm for a heterogenous multi-agent system with one leader and nine followers.

The rest of this paper is organized as follows. The model of each agent is given and the formation flocking problem is formulated in section II. Section III presents a distributed control algorithm to solve the formation flocking problem. In section IV, the simulation results are shown by six agents. Finally, the conclusions are drawn in section V.

2. Model and Problem Statement

Firstly, we model each agent by the following kinematic equation

$$\begin{aligned} &\dot{x}_i(t) = \upsilon_i(t)\cos\phi_i(t)\cos\theta_i(t) - \omega_i(t)l_i\cos\phi_i(t)\sin\theta_i(t) \\ &\dot{y}_i(t) = \upsilon_i(t)\sin\phi_i(t) \\ &\dot{z}_i(t) = \upsilon_i(t)\cos\phi_i(t)\sin\theta_i(t) + \omega_i(t)l_i\cos\phi_i(t)\cos\theta_i(t) \\ &\dot{\theta}_i(t) = \omega_i(t) \\ &\dot{\upsilon}_i(t) = a_i(t) \\ &\dot{\omega}_i(t) = b_i(t)/l_i \\ &\dot{\phi}_i(t) = c_i(t) \end{aligned} \tag{1}$$

where $p_i(t) = [x_i(t), y_i(t), z_i(t)]^T \in \mathbb{R}^3$ is the position vector of the agent i at time t, $\theta_i \in [0, 2\pi)$ is the yaw angle of the agent i at time t, $\phi_i \in (-\frac{\pi}{2}, \frac{\pi}{2})$ is the pitch angle of the agent i at time t, $q_i(t) = [\upsilon_i(t), \omega_i l_i(t)]^T = [\upsilon_i(t), \vartheta_i(t)]^T$ is the velocity vector of the agent i at time t, $\upsilon_i \in \mathbb{R}$ is the thrusting speed of the agent i at time t, $\omega_i(t) \in \mathbb{R}$ is the rotational speed of the agent i at time t, l_i is the distance between the geometrical center C_i and the mass center M_i of the agent i, $\vartheta_i(t) = \omega_i(t)l_i \in \mathbb{R}$ is the tangential speed of the agent i at time t, $a_i(t) \in \mathbb{R}$ is the thrusting acceleration of the agent i at time t, $b_i(t) \in \mathbb{R}$ is the rotational acceleration of the agent i at time t, and $c_i(t) \in \mathbb{R}$ is the pitching acceleration of the agent i at time t, l_i is a positive constant, $i = 1, \cdots, N$.

With $p_i(t) = [x_i(t), y_i(t), z_i(t)]^T$ and $q_i(t) = [\upsilon_i(t), \omega_i l_i(t)]^T$, some equations in (1) can be merged as the following matrix form

$$\begin{aligned} &\dot{p}_i(t) = H_i^T(t) q_i(t) \\ &\dot{q}_i(t) = u_i(t) \end{aligned} \tag{2}$$

where

$$\begin{aligned} H_i(t) &= [\vec{t_i}, \vec{n_i}]^T \\ &= \begin{bmatrix} \cos\phi_i(t)\cos\theta_i(t) & \sin\phi_i(t) & \cos\phi_i(t)\sin\theta_i(t) \\ -\cos\phi_i(t)\sin\theta_i(t) & 0 & \cos\phi_i(t)\cos\theta_i(t) \end{bmatrix} \end{aligned} \tag{3}$$

and $u_i(t) = [a_i(t), b_i(t)]^T$. Besides, $uu_i(t) = [a_i(t), b_i(t), c_i(t)]^T$ is taken as the control input of the agent i.

The multi-agent system under consideration consists of one leader and $N-1$ followers. Let leader set be $\mathrm{L} = \{1\}$ and follower set be $\mathrm{F} = \{2, ..., N\}$. If an agent is dominated by external control input, we call it a leader; otherwise, we call it a follower. Let $N_i(t)$ denote the neighbor set of the follower $i \in \mathrm{F}$ at time t, and the initial neighbor set of the follower i is defined as

$$N_i(0) = \{j \mid \| p_i(0) - p_j(0) \| < D, j = 1, \cdots, N, j \neq i\} \tag{4}$$

where $D > 0$ is a constant satisfying $D > 2\mathrm{R}$, and $\|\bullet\|$ is the Euclidean norm. We suppose that for a follower, interconnection with the leader is unidirectional, that is to say, the information of the leader may be obtained by the follower if the follower has a leader neighbor. Meanwhile, we suppose that the interconnection between any two followers is bidirectional.

The interaction network $G(t)$ is a dynamic directed graph consisting of a vertex set $\nu = \{1, \cdots, N\}$ indexed by agents and a time-varying edge set $\varepsilon(t) = \{(i,j) \mid (i,j) \in \mathrm{F} \times \nu, j \in N_i(t)\}$. Therein, the followers' interaction network $\hat{G}(t)$ with vertex set F and edge set $\hat{\varepsilon}(t) = \{(i,j) \mid (i,j) \in \mathrm{F} \times \mathrm{F}, j \in N_i(t)\}$ is an undirected graph. In order to clarify the neighbor relationship, we introduce the adjacency matrix $A_N(t)$ of the graph $G(t)$ and the Laplacian matrix $L_{N-1}(t)$ of the graph $\hat{G}(t)$. $A_N(t) = [w_{ij}(t)]_{N \times N}$ is defined as

$$w_{ij}(t) = \begin{cases} 1, & i = 1, j = 1 \\ 1, & i \in \mathrm{F}, j \in N_i(t) \\ 0, & otherwise \end{cases} \tag{5}$$

and $L_{N-1}(t) = [l_{ij}(t)]_{(N-1)\times(N-1)}$ is given by

$$l_{ij}(t) = \begin{cases} -w_{ij}(t), & i \neq j \\ \sum_{k=2,k\neq i}^{N} w_{ik}(t), & i = j. \end{cases} \tag{6}$$

As $\hat{G}(t)$ is an undirected graph, the Laplacian matrix $L_{N-1}(t)$ is symmetric and positive semi-definite.

Given that $G(0)$ is a leader-follower connected graph.

$G(t)$ is a fixed graph in each nonempty, bounded, and contiguous time-interval $[t_r, t_{r+1})$, where $r = 0, 1, \cdots$.

3. Control Algorithm Design

For the external input of the leader is zero, that is,

$$uu_1(t) = \begin{bmatrix} a_1(t) \\ b_1(t) \\ c_1(t) \end{bmatrix} = \mathbf{0}, \tag{7}$$

provided that the leader does a curve motion with a constant thrusting speed υ_1, a constant rotational speed ω_1 ($\omega_1 \neq 0$), and a constant pitch angle ϕ_1 ($\phi_1 \neq 0$). Note that $q_1 = [\upsilon_1, l_1\omega_1]$ is a constant vector. Here, **0** denotes the zero vector.

Unless specified otherwise, all variables in this paper are time-variant. Thus, in the following sections, we may use p_i instead of $p_i(t)$ for example. Let $\hat{\upsilon}_i = \upsilon_i - w_{i1}\upsilon_1$, $\hat{\theta}_i = \theta_i - w_{i1}\theta_1$, $\hat{\omega}_i = \omega_i - w_{i1}\omega_1$, $\hat{\phi}_i = \phi_i - w_{i1}\phi_1$, and $\hat{q}_i = q_i - w_{i1}q_1$, $i = 1, \cdots, N$. Coupled with (2), we have

$$\dot{\hat{p}} = \dot{p}_i - \dot{p}_i^* = H_i^T q_i - w_{i1} H_i^T q_1 = H_i^T \hat{q}_i \tag{8}$$

Given a desired geometric pattern χ that has N vertices $p_i^d = [x_i^d, y_i^d]^T$, $i = 1, \dots, N$. Then, the control protocol for follower i ($i = 2, \dots, N$) is designed by

$$\begin{aligned} a_i &= -\sum_{j \in N_i(t)} (\dot{\hat{p}}_i^T - \dot{\hat{p}}_j^T)\vec{t}_i - \sum_{j \in N_i(t)} \nabla_{\tilde{p}_{ij}} V(\| \tilde{p}_{ij} \|)^T \vec{t}_i \\ b_i &= -l_i \sum_{j \in N_i(t)} (\hat{\theta}_i - \hat{\theta}_j) - \sum_{j \in N_i(t)} (\dot{\hat{p}}_i^T - \dot{\hat{p}}_j^T)\vec{n}_i \\ &\quad - \sum_{j \in N_i(t)} \nabla_{\tilde{p}_{ij}} V(\| \tilde{p}_{ij} \|)^T \vec{n}_i \\ c_i &= -\sum_{j \in N_i(t)} (\hat{\phi}_i(t) - \hat{\phi}_j(t)). \end{aligned} \tag{9}$$

where $\hat{p}_{ij} = \hat{p}_i - \hat{p}_j$, $\tilde{p}_{ij} = \frac{\| \hat{p}_{ij}(t) \|}{\| p_{ij}^d \|}$, $\vec{t}_i = [\cos\phi_i \cos\theta_i, \sin\phi_i, \cos\phi_i \sin\theta_i]^T$, and $\vec{n}_i = [-\cos\phi_i \sin\theta_i, 0, \cos\phi_i \cos\theta_i]^T$. $\vec{t}_i$ and $\vec{n}_i$ are two unit vectors orthogonal to each other, and $\nabla_{\hat{p}_{ij}} V(\| \hat{p}_{ij} \|)$ is the gradient of an artificial potential function $V(\| \hat{p}_{ij} \|)$.

Definition 1 (Potential Function): Potential $V(\| \hat{p}_{ij} \|)$ is a differentiable, nonnegative, radially unbounded function of the distance $\| \hat{p}_{ij} \|$ between agent i and j, such that

(1) $V(\| \hat{p}_{ij} \|) \to \infty$ as $\| \hat{p}_{ij} \| \to 2R^*$ ($R < R^* < D$);

(2) $V(\| \hat{p}_{ij} \|) \to \infty$ as $\| \hat{p}_{ij} \| \to 2D$;

(3) $V(\| \hat{p}_{ij} \|)$ attains its unique minimum when $\| \hat{p}_{ij} \|$ equals to a desired value between $2R^*$ and $2D$.

Besides, the total potential of the system is

$$V = \sum_{i \in \mathrm{F}} \sum_{j \in N_i} V(\| \hat{p}_{ij} \|) + \sum_{j \in N_l} V(\| \hat{p}_{1j} \|) \tag{10}$$

where $N_l = \{ i \mid w_{i1} = 1, i \in \mathrm{F} \}$ denotes the set of followers who have one leader neighbor. The potential function $V(\| p_{ij}(t) \|)$ reaches its minimal value at the point of $\| p_{ij}(t) \| = 1$.

So far, we are able to state our main result on the leader-follower formation flocking problem. LaSalle-Krasovskii invariance principle and graph theory are used to prove that the agents (1) applying the control protocol (9) will be asymptotically stable.

Consider a system of N agents with kinematics (1). The leader and followers are respectively steered by control protocols (7) and (9). Suppose that the initial interaction topology $G(0)$ of the system is a leader-follower connected graph. Then the following statements hold:

- No collision happens between neighbors for two authors: D. Ruan, T. Li.
- The connectivity of the interaction topology is preserved at all times.
- The thrusting speed, the rotational speed, the yaw angle, and the pitch angle of each follower asymptotically become the same as those of the leader.
- The system approaches a desired geometric configuration χ that minimizes the total potential.

4. Simulation Results

The initial interaction network of the leader-follower multi-agent system is a leader-follower connected graph. The initial attitudes of six agents are generate randomly. The simulation results are shown in Fig. 1.

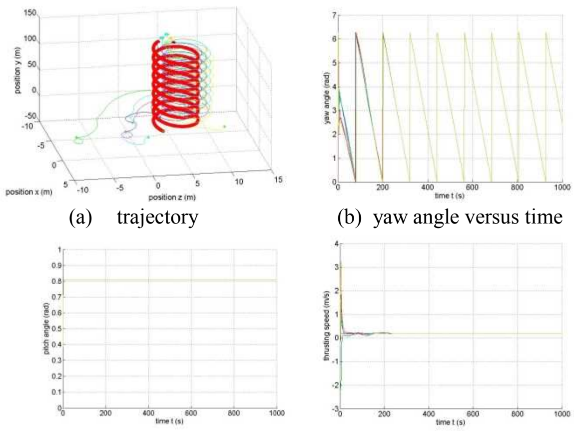

(a) trajectory (b) yaw angle versus time

(c) pitch angle versus time (d)thrusting speed versus time

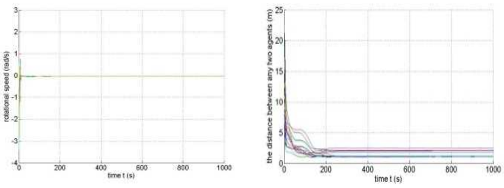

(e) rotational speed versus time (f) distances between any two agents versus time

Fig. 1 Numerical simulation results for leader-follower formation flocking cooperation of six agents.

5. Conclusion

We have investigated the three-dimensional formation flocking coordination problem of multi-agent system consisting of one leader and several followers. Each agent is modeled as an extended second-order unicycle with limited communication capability. According to LaSalle-Krasovskii invariance principle and the graph theory, the followers asymptotically track the leader's velocity and form a table geometrical configuration with their neighbors. The numerical simulations are carried on six agents to further validate the functionality of the proposed algorithm for multi-agent system.

Acknowledgements

The authors would like to thank the support from National Natural Science Foundation of
China (No. 61603362) and Long Wang of Peking University for his helpful discussions and valuable assistance.

References

1. G. L. Mariottini and F. Morbidi and D. Prattichizzo and N. Vander Valk and N. Michael and G. Pappas and K. Daniilidis, Vision-Based Localization for Leader-Follower Formation Control, *IEEE Transactions on Robotics*. 25(2009) 1431-1438.
2. A. Loria and J. Dasdemir and N. Alvarez Jarquin, Leader-Follower Formation and Tracking Control of Mobile Robots Along Straight Paths, *IEEE Transactions on Control Systems Technology*. 24(2016)727-732.
3. T. Balch and R. C. Arkin, *Behavior-based formation control for multirobot teams*(1998).
4. S. Monteiro and E. Bicho, A dynamical systems approach to behavior-based formation control, in *Proceedings of IEEE International Conference on Robotics and Automation*. 3(2002)2606-2611.
5. W. Ren and R. W. Beard, Formation feedback control for multiple spacecraft via virtual structures, *IEEE Proceedings of Control Theory and Applications*. 151(2004)357-368.
6. C. B. Low, A dynamic virtual structure formation control for fixed-wing UAVs, in *9th IEEE International Conference on Control and Automation*. (2011) 627-632.
7. L. Chen and M. Baoli, A nonlinear formation control of wheeled mobile robots with virtual structure approach, in *34th Chinese Control Conference*. (2015)1080-1085.
8. M. Defoort and T. Floquet and A. Kokosy and W. Perruquetti, Sliding-Mode Formation Control for Cooperative Autonomous Mobile Robots, *IEEE Transactions on Industrial Electronics*. 55(2008)3944-3953.
9. H. Xiao and Z. Li and C. L. Philip Chen, Formation Control of Leader-Follower Mobile Robots' Systems Using Model Predictive Control Based on Neural-Dynamic Optimization, *IEEE Transactions on Industrial Electronics.* 63(2016)5752-5762.
10. C. W. Reynolds, Flocks, herds, and schools: a distributed behavioral model, *Comput. Graph.*. 21(1987)25-34.
11. R. Olfati-Saber, Flocking for multi-agent dynamic systems: algorithms and theory, *IEEE Trans. Autom. Control*. 51(2006)401-420.
12. F. Cuker and S. Smale, Emergent behavior in flocks, *IEEE Trans. Autom. Control*. 52(2007)852-862.
13. E. Ferrante and A. E. Turgut and C. Huepe and A. Stranieri and C. Pinciroli and M. Dorigo, Self-organized flocking with a mobile robot swarm: a novel motion control method, *Adaptive Behavior*. 20(2012)460–477.

Leader-follower Formation Control of Mobile Robots with Sliding Mode

Wenhao Zheng, **Yingmin Jia**
The Seventh Research Division and the Center for Information and Control,
School of Automation Science and Electrical Engineering,
Beihang University (BUAA), 37 Xueyuan Road, Haidian District,
Beijing 100191, China
E-mail: zhengwenhao@163.com, ymjia@buaa.edu.cn
www.buaa.edu.cn

Abstract

This paper considers the formation control of nonholonomic mobile robots. The formation problem is converted to the error model based on the leader-follower structure. A sliding mode controller, which is proved to be globally finite-time stable by Lyapunov stability theory, is presented in this study. In addition, a continuous reaching law is designed to reduce the chattering which caused by the computation time delays and limitations of control. Simulation results verify the feasibility and effectiveness of the control strategy.

Keywords: nonholonomic mobile robot, leader-follower, formation control, sliding mode, continuous reaching law.

1. Introduction

Formation control of differential-drive mobile robots have been widely researched in recent years. The mobile robots are supposed to maintain the desired geometric configuration in lots of different situations including personnel rescue, logistics transportation, military affairs and environmental exploration. Various formation control strategies have been proposed, such as feedback linearization[1], backstepping[2], sliding-mode control[3] and sorts of intelligent control method. In Ref.3, the kinematic model and the dynamic model were both considered, then a sliding mode controller was proposed to deal with model uncertainties and disturbances, furthermore, the voltage inputs of driving motors were taken as control inputs, which are more realistic than the velocity. Basic controller based on backstepping method was presented in Ref.4, a bioinspired neurodynamics based approach was further developed to solve the impractical velocity jumps problem. In Ref.5, a controller with time-varying parameters which were designed to limited control inputs, was presented by Lyapunov theory, and geometric analysis contributed to the designment of optimal feedback functions which made the controller more effective.

This paper mainly focuses on the formation control of nonholonomic mobile robots with sliding mode. The formation problem is proposed with leader-follower setup, which is used to deduce the error model. Then, a simple sliding mode surface is chose to design control law. And a continuous reaching law is presented to reduce the chattering. Moreover, the formation error model is proved to be globally finite-time stable. Comparing with existing results, this paper primarily contributes to the novel solution of the formation control with sliding mode.

The structure of the rest paper is organized as follows. The section 2 introduces leader-follower system and the formation error model. In the section 3, the sliding mode controller is designed with a continuous reaching law. Simulation results are presented to show the validity of the control law in the section 4. In the end, the section 5 summarizes the whole paper and draws the conclusion.

2. Problem Statement

2.1. *Kinematic model of nonholonomic mobile robot*

In this paper, the differential-drive mobile robot is considered as the research object, which is subject to nonholonomic constraint (1).

As shown in figure 1, let v_L and v_R be the velocities of the left and right driving wheel. The control inputs are usually taken as the linear speed v and the rotational angular velocity ω . The relation between control inputs and driving wheels can be expressed as (2).

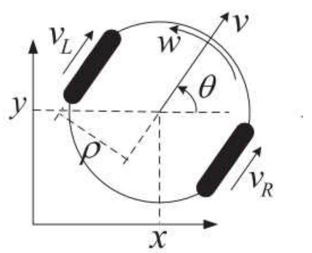

Fig. 1. The configuration of a two-wheeled mobile robot.

In practical systems, control inputs of mobile robots are bounded.

$$\dot{y}\cos\theta - \dot{x}\sin\theta = 0 \tag{1}$$

$$v = (v_L + v_R)/2,\ \omega = (v_R - v_L)/2\rho \tag{2}$$

$$\dot{x}=v\cos\theta,\quad \dot{y} = v\sin\dot{\theta},\quad \dot{\theta} = \omega \tag{3}$$

where (x, y) are the robot position and θ is the robot orientation. Moreover, the kinematic of the mobile robot can be expressed as equation (3).

2.2. *Leader-follower system*

In the figure 2, leader-follower formation structure is presented in Cartesian coordinates. The nonholonomic mobile robot R_l is treated as the leader. The center of the leader $C_l(x_l, y_l, \theta_l)$ describes the position and the orientation of the leader in the world frame. And (v_l, ω_l) are control inputs. The follower is the robot R_f . The center of the robot $C_f(x_f, y_f, \theta_f)$ and inputs (v_f, ω_f) have the analogous definitions like the leader. Assume that the distance between the point $O_f(x_{of}, y_{of}, \theta_f)$ and C_l is d . The relation can be presented as (4)

$$\begin{aligned} x_{of} &= x_f + d\cos\theta_f \\ y_{of} &= y_f + d\sin\theta_f \end{aligned} \tag{4}$$

Differentiating the above equations leads to

$$\begin{aligned} \dot{x}_{of} &= v_f\cos\theta_f - d\omega_f\sin\theta_f \\ \dot{y}_{of} &= v_f\sin\theta_f + d\omega_f\cos\theta_f \end{aligned} \tag{5}$$

The desired geometric shape can be denoted by

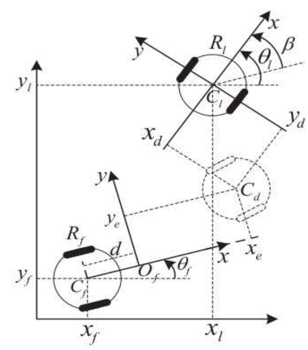

Fig. 2. Leader-follower formation structure

coordinate representation. The expected position of the follower should be expressed as (x_d, y_d) in the coordinate system of the leader. And the real position $C_d(x_c, y_c)$ in world frame can be deduced as equation (6).

$$\begin{pmatrix} x_c \\ y_c \end{pmatrix} = \begin{pmatrix} x_l \\ y_l \end{pmatrix} + \begin{pmatrix} \cos\theta_l & -\sin\theta_l \\ \sin\theta_l & \cos\theta_l \end{pmatrix}\begin{pmatrix} x_d \\ y_d \end{pmatrix} \tag{6}$$

(x_d, y_d) are considered as constants, and differentiating both side of (6) will refer to

$$\begin{pmatrix} \dot{x}_c \\ \dot{y}_c \end{pmatrix} = \begin{pmatrix} \cos\theta_l & -\sin\theta_l \\ \sin\theta_l & \cos\theta_l \end{pmatrix}\begin{pmatrix} v_l - y_d\omega_l \\ x_d\omega_l \end{pmatrix} \tag{7}$$

We can define the formation errors as the Eq. (8).

$$\begin{pmatrix} x_e \\ y_e \end{pmatrix} = \begin{pmatrix} \cos\theta_f & \sin\theta_f \\ -\sin\theta_f & \cos\theta_f \end{pmatrix}\begin{pmatrix} x_c - x_{of} \\ y_c - y_{of} \end{pmatrix} \tag{8}$$

Moreover, the angular difference between the leader and the follower is remarked as (9).

$$\beta = \theta_l - \theta_f,\quad \dot{\beta} = \omega_l - \omega_f \tag{9}$$

Combining the equations from (4) to (7) and differentiating both sides of (8), formation error model can be expressed as

$$\begin{aligned}\dot{x}_e &= -v_f + \omega_f y_e + (v_l - y_d\omega_l)\cos\beta - x_d\omega_l \sin\beta \\ \dot{y}_e &= -(d + x_e)\omega_f + (v_l - y_d\omega_l)\sin\beta + x_d\omega_l \cos\beta\end{aligned} \tag{10}$$

The destination of control law design is to find the appropriate control inputs (v_f, ω_f) to meet the desired outcome:

$$\lim_{t\to 0} x_e \to 0,\ \lim_{t\to 0} y_e \to 0,\ |\beta| < \sigma(\sigma > 0) \tag{11}$$

3. Sliding-Mode Controller Design

3.1. *Sliding surface design*

The most significant process of sliding mode control is to choose the suitable sliding surface. Here, we design the sliding surface which ensures that the formation error will converge to zero when the system trajectory lies on the sliding surface (12).

$$s = \begin{bmatrix} s_1 \\ s_2 \end{bmatrix} = \begin{bmatrix} x_e \cos\beta + y_e \sin\beta \\ -x_e \sin\beta + y_e \cos\beta \end{bmatrix} \tag{12}$$

Let $V = 0.5 s^T s$, thus we can deduce $V = 0.5(s_1^2 + s_2^2)$ $= 0.5(x_e^2 + y_e^2)$ from equation (12), which indicates that if $s_1 \to 0,\ s_2 \to 0$, the $x_e \to 0,\ y_e \to 0$ will hold. Hence, when the sliding surface converges to zero, the geometric shapes of the robot formation will be established.

Differentiating the formula (12) will conclude (13)

$$\begin{aligned}\dot{s}_1 &= -v_f \cos\beta - d\omega_f \sin\beta + v_l - y_d\omega_l + s_2\omega_l \\ \dot{s}_2 &= v_f \sin\beta - d\omega_f \cos\beta + x_d\omega_l - s_1\omega_l\end{aligned} \tag{13}$$

Furthermore, the formation controller can be simply written as:

$$\begin{aligned}v_f &= (v_l - y_d\omega_l)\cos\beta - x_d\omega_l \sin\beta + y_e\omega_l - \dot{s}_1\cos\beta + \dot{s}_2 \sin\beta \\ \omega_f &= [(v_l - y_d\omega_l)\sin\beta + x_d\omega_l\cos\beta - x_e\omega_l - \dot{s}_1 \sin\beta - \dot{s}_2\cos\beta]/d\end{aligned} \tag{14}$$

3.2. *Controller design with the reaching law*

In this paper, a continuous reaching law is adopted to make each state reaching the sliding surface. Comparing with the switching function of general reaching law, a saturation function is taken in order to reduce the chattering which caused by the computation time delays and limitations of control. The reaching law is as follow:

$$\dot{s} = -\varepsilon s - k f(s) \tag{15}$$

Here, $f(s)$ is given as (16) and $\mathrm{sgn}(s)$ is a sign function. Besides, $\varepsilon = (\varepsilon_1, \varepsilon_2)^T$, $k = (k_1, k_2)^T$, $\alpha = (\alpha_1, \alpha_2)^T$, $\varphi > 0$ and $\varepsilon_1,\ \varepsilon_2,\ k_1,\ k_2 > 0,\ 0 < \alpha_1, \alpha_2 < 1$.

$$f_i(s) = \begin{cases} |s_i|^{\alpha_i}\,\mathrm{sgn}(s_i) & if\ |s_i| \le \varphi \\ s_i\varphi / |s_i| & if\ |s_i| > \varphi \end{cases} \tag{16}$$

Thus, we can get the sliding mode controller (17) from equation (12), (14) and (15).

$$\begin{aligned}v_f &= (v_l - y_d\omega_l)\cos\beta - x_d\omega_l\sin\beta + y_e\omega_l + \\ &\quad (\varepsilon_1 s_1 + k_1 f_1(x))\cos\beta - (\varepsilon_2 s_2 + k_2 f_2(x))\sin\beta \\ \omega_f &= \frac{1}{d}[(v_l - y_d\omega_l)\sin\beta + x_d\omega_l\cos\beta - x_e\omega_l + \\ &\quad (\varepsilon_1 s_1 + k_1 f_1(x))\sin\beta + (\varepsilon_2 s_2 + k_2 f_2(x))\cos\beta]\end{aligned} \tag{17}$$

Theorem 1. *Consider the formation error system (10). Using the control law (17), the sliding surface (12) will converge to zero in finite time* T_r, *and* $x_e \to 0,\ y_e \to 0$ *as* $t = T_r$.

Proof. Choose the Lyapunov function as $V_i = s_i^2/2$ $(i = 1,2)$. It is easy to refer to

$$\dot{V}_i = s_i\dot{s}_i = -\varepsilon_i s_i^2 - k_i f_i(s_i)s_i \tag{18}$$

Case1: if $|s_i| < \varphi$, the equation (18) will be converted to $\dot{V}_i = -2\varepsilon_i V_i - 2^{(1+\alpha_i)/2} k_i V_i^{(1+\alpha_i)/2}$. Define $V = V_i(0)$ at $t = 0$. By solving differential equation, we can deduce formula

$$V_i^{\frac{1-\alpha_i}{2}} = -2^{\frac{\alpha_i - 1}{2}}\frac{k}{\varepsilon} + (2^{\frac{\alpha_i - 1}{2}}\frac{k}{\varepsilon} + V_i^{\frac{1-\alpha_i}{2}}(0))e^{-(1-\alpha_i)\varepsilon t} \tag{19}$$

Let $V_i = 0$; the reaching time can be expressed as

$$T_{ri} = \frac{1}{(1-\alpha_i)\varepsilon}\ln\left(\frac{2^{\frac{\alpha_i-1}{2}}\frac{k}{\varepsilon} + V_i^{\frac{1-\alpha_i}{2}}(0)}{2^{\frac{\alpha_i-1}{2}}k}\right) \tag{20}$$

Therefore, $s_i (i = 1,2)$ will converge to zero at $t = T_r =$ $\max(T_{ri})$ $(i = 1,2)$ and $x_e \to 0,\ y_e \to 0$ as $t = T_r$.

Case 2: if $|s_i| < \varphi$, the equation (18) can be presented as the formula (21).

$$\dot{V}_i = -2\varepsilon_i s_i^2 - k_i |s_i| \varphi^{\alpha_i} < 0 \tag{21}$$

Consequently, there must be a $T_{r\varphi}$ which makes $s_i \to \varphi$. Thus, formation error model will be globally finite time stable. □

Theorem 2. *Consider the equation (9) with the control law (17). β will be bounded, if the velocity of the leader $0 < v_l < const$, $|\beta_0| < \pi$ at $t = 0$ and the boundedness of the angular velocity ω_l hold.*

Proof. Combining the formula (9) with the control law, we can obtain the equation (22).

$$\begin{aligned}&\dot{\beta} = -(v_l \sin\beta)/d + \phi(t)\\&\phi(t) = \omega_l - \frac{1}{d}[-y_d\omega_l \sin\beta + x_d\omega_l \cos\beta - x_e\omega_l + \\&(\varepsilon_1 s_1 + k_1 f_1(s_1))\cos\beta + (\varepsilon_2 s_2 + k_2 f_2(s_2)^{\alpha_2})\sin\beta]\end{aligned} \quad (22)$$

The nominal system can be given as $\dot{\beta} = -(v_l \sin\beta)/d$ at $\phi = 0$. Select the Lyapunov function as $V_\beta = 1 - \cos\beta$. So we can get $\dot{V}_\beta = -(v_l \sin^2\beta)/d \le 0$ and V_β is non-increasing. $|\beta_0| < \pi$ at $t = 0$, there must exist a positive constant δ which meets $\beta_0 \in [-\pi+\delta, \pi-\delta]$. Then, $V_\beta \in [0, 2-\delta)$, $\beta(t) \in [-\pi+\delta, \pi-\delta]$ and $\dot{V}_\beta \le -(v_l/d)\delta V_\beta$. Besides, $V_\beta = 2\sin^2(\beta/2)$, it is easy to obtain $2\beta^2/\pi^2 < V_\beta < \beta^2/2$ at $\beta \in (-\pi, \pi)$. Thus, the nominal system is exponentially stable using the Lyapunov method. Obviously, $\omega_l, x_e, s_1, s_2, \sin\beta$ and $\cos\beta$ are bounded, which can be used to deduce the conclusion that $\phi(t)$ is bounded. Therefore, in the system (21), β is bounded by using the stability theory of perturbed systems. □

4. Simulation Results

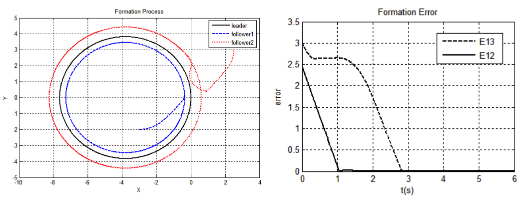

Fig. 4. Formation process and formation errors.

Three robots are expected to keep a triangle formation and the expected formation shapes are designed as $x_{d1} = x_{d2} = -1m$, $y_{d1} = 0.5m$, $y_{d3} = -0.5m$. The movement of the leader robot is set as the circular motion with $v_l = 1m/s$, $\omega_l = \pi/12rad/s$, and the initial poses of three robots are (0, 0, π/2), (−3, −2, 0) and (2.5, −3, −π/2). Moreover, Controller (16) is used with $\varepsilon_1 = \varepsilon_2 = 5$, $k_1 = k_2 = 7$, $\alpha_1 = \alpha_2 = 1/3$, $\varphi = 5$, $d_2 = d_3 = 0.25m$. The control inputs are limited as $v_f \le 3m/s, \omega_f \le \pi/2rad/s$. The formation error is denoted as $E = \sqrt{x_e^2 + y_e^2}$, . The simulation results are presented in Fig.3 and Fig.4.

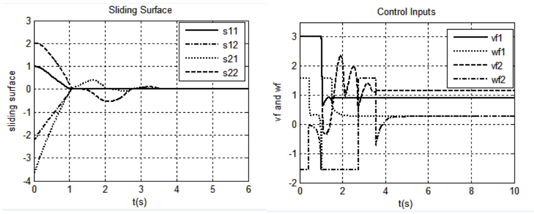

Fig. 4. The sliding surface and inputs of followers.

5. Conclusion

In this paper, the formation control problem of the nonholonomic mobile robot has been solved. A controller with sliding mode is proposed using a continuous reaching law. The simulation results show that the control law can guarantee great formation performance and the specified geometrical shapes of multi-mobile robots will be achieved in finite time.

Acknowledgements

This work was supported by the NSFC (61327807, 61520106010, 61521091, 61134005) and the National Basic Research Program of China (973 Program: 2012CB821200, 2012CB821201)

References

1. J. P. Desai, J. P. Ostrowski, and V. Kumar, "Modeling and control of formations of nonholonomic mobile robots," *IEEE Trans. Robot. Autom,* vol. 17, no. 6, pp. 905–908, Dec. 2001.
2. X. Li, J. Xiao, and Z. Cai, "Backstepping based multiple mobile robots formation control," in *Proc. Conf. Intell. Robots Syst.*, 2005, pp. 887–892.
3. Park, Bong Seok, B. P. Jin, and Y. H. Choi. "Robust formation control of electrically driven nonholonomic mobile robots via sliding mode technique." *International Journal of Control, Automation and Systems* 9.5(2011): 888-894.
4. Peng, Zhaoxia, et al. "Leader–follower formation control of nonholonomic mobile robots based on a bioinspired neurodynamic based approach." *Robotics & Autonomous Systems* 61.9(2013):988-996.
5. Chen, X., and Y. Jia. "Input-constrained formation control of differential-drive mobile robots: geometric analysis and optimization." *IET Control Theory & Applications* 8.7 (2014):522-533.

H_∞ Containment Control for Nonlinear Multi-agent Systems with Parameter Uncertainties and Communication Delays

Ping Wang
The Department of Mathematics and Physics, North China Electric Power University, 619 Yonghua North Street Baoding, 100073, China

Yingmin Jia
The Seventh Research Division and the Center for Information and Control, School of Automation Science and Electrical Engineering, Beihang University (BUAA), 37 Xueyuan Road, Haidian District Beijing, 100191, China
E-mail: wangpinglh2014@126.com; ymjia@buaa.edu.cn
www.ncepu.edu.cn

Abstract

This paper considers robust containment control problem for uncertain multi-agent systems with inherent nonlinear dynamics. A distributed protocol is proposed using local delayed state information, and then the original problem is converted into an H_∞ control problem by defining an appropriate controlled output function. Based on robust H_∞ theory, sufficient conditions in terms of linear matrix inequalities (LMIs) are derived to ensure the H_∞ containment. A numerical example is provided to demonstrate the effectiveness of our theoretical results.

Keywords: multi-agent systems, containment control, robust H_∞ control, inherent nonlinear dynamics.

1. Introduction

Containment control of multi-agent systems has received considerable attention due to its potential applications, such as earth monitoring, stellar observation for satellite formation[1], removing hazardous materials for autonomous robots[2], and so on. Containment control problem arises in the presence of multiple leaders, where its objective is to drive the followers into the convex hull spanned by the leaders.

In engineering practice, multi-agent systems are often subject to parameter uncertainties and external disturbances, which might degrade the system performance and even cause the network system to diverge or oscillate. For such cases, H_∞ containment control problems for second-order and uncertain multi-agent systems with inherent nonlinear dynamics were considered in Refs. 3 and 4, respectively. Whereas, the effects of communication delays on H_∞ containment control are not considered in the existing works.

Motivated by the above analysis, we employ H_∞ control approach to investigate the containment control problem of nonlinear multi-agent systems with parameter uncertainties and communication delays. Based on the local delayed state information, a distributed protocol is proposed, and then the original problem is reformulated as an H_∞ control problem by defining an appropriate controlled output function. Sufficient conditions in terms of LMIs are derived to ensure the containment performance with a desired H_∞ disturbance attenuation level. Moreover, the proposed protocol can be determined by solving only two LMIs with the same dimensions as a single agent.

2. Preliminaries and Problem Formulation

2.1. *Preliminaries*

Directed graphs[5] are used to model the interaction topologies among agents. Suppose that a multi-agent system consists of M followers and $N-M$ leaders. An agent is called a leader if the agent has no neighbor, and a follower if the agent has at least one neighbor. Due to the fact that the leaders have no neighbor, the Laplacian matrix L associated with graph G can be partitioned as

$$L = \begin{bmatrix} L_1 & L_2 \\ 0_{(N-M)\times M} & 0_{(N-M)\times(N-M)} \end{bmatrix} \quad (1)$$

where $L_1 \in R^{M\times M}$ and $L_2 \in R^{M\times(N-M)}$.

Assumption 1. *Suppose that for each follower, there exists at least one leader that has a directed path to that follower. Moreover, the interaction topology among the M followers is undirected.*

Lemma 1.[6] *Under Assumption* 1, L_1 *is positive definite,* $-L_1^{-1}L_2$ *is nonnegative, and the sum of the entries in each row equals* 1.

2.2. *Problem formulation*

Consider the multi-agent system consisting of M followers and $N-M$ leaders. We use $F \triangleq \{1,\cdots,M\}$ and $R \triangleq \{M+1,\cdots,N\}$ to denote the follower set and the leader set, respectively. Each follower with nonlinear dynamics is represented as

$$\dot{x}_i(t) = Ax_i(t) + B_1u_i(t) + B_2\omega_i(t) + B_3 f(t, x_i(t)), \quad i \in F \quad (2)$$

where $x_i(t) \in R^m, u_i(t) \in R^{m_1}$ are the state and the control input (or protocol), respectively, $\omega_i(t) \in R^{m_2}$ is the external disturbance that belongs to $L_2[0,\infty)$, and $f: R\times R^m \to R^m$ is the inherent nonlinear dynamics of the ith follower.

The leaders of the concerned multi-agent system are described by

$$\dot{x}_i(t) = Ax_i(t) + B_3 f(t, x_i(t)), \; i \in R \quad (3)$$

where $x_i(t) \in R^m$ is the state of the leader i.

Assumption 2. *Given* $\eta_1,\cdots,\eta_{N-M}$ *with* $\sum_{i=1}^{N-M}\eta_i = 1$ *and* $\eta_i \ge 0, i = 1,\cdots,N-M$. *There exists a nonnegative constant* ρ *such that nonlinear function* $f(t,x(t))$ *satisfies*

$$\| f(t,x(t)) - \sum_{i=1}^{N-M}\eta_i f(t,y_i(t)) \| \le \rho \| x(t) - \sum_{i=1}^{N-M}\eta_i y_i(t) \| \quad (4)$$

$\forall x, y_i \in R^m, i = 1,2,\cdots N-M, \forall t \ge 0.$

When system matrices A, B_1, B_2, B_3 are uncertain, they are assumed to be of the following form

$$\begin{aligned} A &= A_0 + \Delta A(t), & B_1 &= B_{10} + \Delta B_1(t), \\ B_2 &= B_{20} + \Delta B_2(t), & B_3 &= B_{30} + \Delta B_3(t) \end{aligned} \quad (5)$$

where $A_0, B_{10}, B_{20}, B_{30}$ are known real constant matrices, $\Delta A(t), \Delta B_1(t), \Delta B_2(t), \Delta B_3(t)$ are unknown real norm-bounded matrix functions satisfying

$$\left[\Delta A(t), \Delta B_1(t), \Delta B_2(t), \Delta B_3(t)\right] = E\Sigma(t)\left[F_1, F_2, F_3, F_4\right] \quad (6)$$

with E, F_1, F_2, F_3 and F_4 being known constant matrices, and $\Sigma(t)$ being an unknown real time-varying matrix that satisfies $\Sigma^T(t)\Sigma(t) \le I$. It is also assumed that (A_0, B_{10}) is stabilized.

Define a controlled output function $z(t) = \left[z_1^T(t), z_2^T(t), \cdots, z_M^T(t)\right]^T$ with

$$z_i(t) = x_i(t) - y_i(t), \quad i \in F, y_i(t) \in \Omega(t) \quad (7)$$

to quantitatively analyze the effect of external disturbances on the containment control problem, where, $\Omega(t) = \{\sum_{i=M+1}^{N}\alpha_i x_i \mid \alpha_i \in R, \alpha_i \ge 0, \sum_{i=M+1}^{N}\alpha_i = 1\}$. Obviously, if $\lim_{t\to\infty} z(t) = 0$, the containment control problem of the multi-agent system (2)-(3) can be solved. Thus, the attenuating ability of multi-agent system against external disturbances can be quantitatively measured by

$$\| T_{z\omega}(s) \|_\infty = \sup_{0 \ne \omega(t) \in L_2[0,\infty)} \frac{\| z(t) \|_2}{\| \omega(t) \|_2} \quad (8)$$

where $\omega(t) = \left[\omega_1^T(t), \cdots, \omega_M^T(t)\right]^T$, $\| z(t) \|_2^2 = \int_0^\infty z^T(t)z(t)dt$, $\| \omega(t) \|_2^2 = \int_0^\infty \omega^T(t)\omega(t)dt$, $T_{z\omega}(s)$ represents the closed-loop transfer function matrix from the external disturbance $\omega(t)$ to the controlled output $z(t)$.

3. Main Results

3.1. *Protocol design and problem reformulation*

A distributed protocol is proposed using local delayed state information.

$$u_i(t) = K \sum_{j \in F \cup R} a_{ij}[x_j(t-\tau(t)) - x_i(t-\tau(t))], \; i \in F \quad (9)$$

where K is a feedback gain matrix to be determined later, $\tau(t)$ is the time-varying communication delay which satisfies $0 \le \tau(t) \le h, \forall t \ge 0$.

Denote

$$x_f(t) = [x_1^T(t), \cdots, x_M^T(t)]^T, x_l(t) = [x_{M+1}^T(t), \cdots, x_N^T(t)]^T,$$

$$F(t, x_f(t)) = [f^T(t, x_1(t)), \cdots, f^T(t, x_M(t))]^T,$$

$$F(t, x_l(t)) = [f^T(t, x_{M+1}(t)), \cdots, f^T(t, x_N(t))]^T.$$

Let $\bar{x}(t) = x_f(t) - (-L_1^{-1}L_2 \otimes I_m)x_l(t)$, the closed-loop system (2) and (3) under protocol (9) can be written as

$$\begin{aligned}\dot{\bar{x}}(t) &= (I_M \otimes A)\bar{x}(t) - (L_1 \otimes B_1 K)\bar{x}(t-\tau(t)) \\ &\quad +(I_M \otimes B_2)\omega(t) + (I_M \otimes B_3)\bar{F}(t)\end{aligned}$$

where $\bar{F}(t) = F(t, x_f(t)) + (L_1^{-1}L_2 \otimes I_m)F(t, x_l(t))$.

By Lemma 1, $-(L_1^{-1}L_2 \otimes I_m)x_l(t)$ is in the convex hull spanned by the leaders. In this paper, the controlled output function $z(t)$ is defined as

$$z(t) = \bar{x}(t). \tag{10}$$

Until now, the containment control problem can be reformulated as the following H_∞ control problem

$$\begin{aligned}\dot{\bar{x}}(t) &= (I_M \otimes A)\bar{x}(t) - (L_1 \otimes B_1 K)\bar{x}(t-\tau(t)) \\ &\quad +(I_M \otimes B_2)\omega(t) + (I_M \otimes B_3)\bar{F}(t) \\ z(t) &= \bar{x}(t).\end{aligned} \tag{11}$$

Therefore, if the system (11) is asymptotically stable with $\| T_{z\omega}(s) \|_\infty < \gamma$ satisfied, then H_∞ containment control for the multi-agent system (2)-(3) can be solved.

3.2. *Conditions for H_∞ containment performance*

Lemma 2. *Suppose that Assumptions* 1 *and* 2 *hold. System* (11) *is asymptotically stable with* $\| T_{z\omega}(s) \|_\infty < \gamma$ *satisfied, if there exist positive definite matrices* $P, R \in R^{m\times m}$ *such that the inequality*

$$\begin{bmatrix} \Psi_{11}^i & \Psi_{12}^i & PB_2 & PB_3 & I_m & \Psi_{16}^i \\ * & -R & 0_{m\times m_2} & 0_m & 0_m & \Psi_{26}^i \\ * & * & -\gamma^2 I_{m_2} & 0_{m_2\times m} & 0_{m_2\times m} & hB_2^T R \\ * & * & * & -I_m & 0_m & hB_3^T R \\ * & * & * & * & -\dfrac{I_m}{\rho^2+1} & 0_m \\ * & * & * & * & * & -R \end{bmatrix} < 0 \tag{12}$$

$$\Psi_{11}^i = PA + A^T P - \lambda_i (PB_1 K + K^T B_1^T P),$$

$$\Psi_{12}^i = \lambda_i PB_1 K, \Psi_{16}^i = h(A^T - \lambda_i K^T B_1^T)R,$$

$$\Psi_{26}^i = h\lambda_i K^T B_1^T R$$

is simultaneously satisfied for all $i \in F$, where λ_i is the ith eigenvalue of the matrix L_1.

Theorem 1. *Suppose that Assumptions* 1 *and* 2 *hold. Protocol* (9) *solves the containment control problem with* $\| T_{z\omega}(s) \|_\infty < \gamma$ *satisfied, if there exist a positive definite matrix* $X \in R^{m\times m}$, *a matrix* $W \in R^{m_1\times m}$ *and positive scalars c and* η *such that the following LMI*

$$\begin{bmatrix} \Phi_{11}^i & \Phi_{12}^i & B_{20} & B_{30} & X & \Phi_{16}^i & \eta E & \Phi_{18}^i \\ * & -cX & 0_{m\times m_2} & 0_m & 0_m & \Phi_{26}^i & 0_m & \lambda_i W^T F_2^T \\ * & * & -\gamma^2 I_{m_2} & 0_{m_2\times m} & 0_{m_2\times m} & hcB_{20}^T & 0_{m_2\times m} & F_3^T \\ * & * & * & -I_m & 0_m & hcB_{30}^T & 0_m & F_4^T \\ * & * & * & * & -\dfrac{I_m}{\rho^2+1} & 0_m & 0_m & 0_m \\ * & * & * & * & * & -cX & \eta hcE & 0_m \\ * & * & * & * & * & * & -\eta I_m & 0_m \\ * & * & * & * & * & * & * & -\eta I_m \end{bmatrix} < 0,$$

$$\begin{aligned}&\Phi_{11}^i = A_0 X + XA_0^T - \lambda_i (B_{10}W + W^T B_{10}^T), \\ &\Phi_{12}^i = \lambda_i B_{10}W, \Phi_{16}^i = hc(XA_0^T - \lambda_i W^T B_{10}^T), \\ &\Phi_{18}^i = X^T F_1^T - \lambda_i W^T F_2^T, \Phi_{26}^i = hc\lambda_i W^T B_{10}^T\end{aligned} \tag{13}$$

is simultaneously satisfied for $i = 1$ *and* M. *Moreover, when the above two LMIs are feasible, the feedback matrix of the protocol* (9) *is designed as* $K = WX^{-1}$.

Proof. Denote

$$\bar{F} = [E^T P^T, 0_m, 0_{m\times m_2}, 0_m, 0_m, hcE^T P^T]^T,$$

$$\bar{H} = [F_1 - \lambda_i F_2 K, \lambda_i F_2 K, F_3, F_4, 0_m, 0_m], i \in F.$$

$$\tilde{\Psi}^i = \begin{bmatrix} \tilde{\Psi}_{11}^i & \tilde{\Psi}_{12}^i & PB_{20} & PB_{30} & I_m & \tilde{\Psi}_{16}^i \\ * & -R & 0_{m\times m_2} & 0_m & 0_m & \tilde{\Psi}_{26}^i \\ * & * & -\gamma^2 I_{m_2} & 0_{m_2\times m} & 0_{m_2\times m} & hB_{20}^T R \\ * & * & * & -I_m & 0_m & hB_{30}^T R \\ * & * & * & * & -\dfrac{I_m}{\rho^2+1} & 0_m \\ * & * & * & * & * & -R \end{bmatrix}$$

$$\tilde{\Psi}_{11}^i = PA_0 + A_0^T P - \lambda_i (PB_{10}K + K^T B_{10}^T P),$$

$$\tilde{\Psi}_{12}^i = \lambda_i PB_{10}K, \tilde{\Psi}_{16}^i = h(A_0^T - \lambda_i K^T B_{10}^T)R,$$

$$\tilde{\Psi}_{26}^i = h\lambda_i K^T B_{10}^T R.$$

Substituting (5) and (6) into (12) results in the following inequality

$$\tilde{\Psi}^i + \bar{F}\Sigma(t)\bar{H}_i + \bar{H}_i^T \Sigma^T(t)\bar{F}^T < 0. \tag{14}$$

Due to the fact that $\Sigma^T(t)\Sigma(t) \le I$, inequality (14) holds if and only if there exists a scalar $\eta > 0$ such that

$$\tilde{\Psi}^i + \eta\bar{F}\bar{F}^T + \eta^{-1}\bar{H}_i^T \bar{H}_i < 0. \tag{15}$$

By Schur Complement, inequality (15) can be transformed to a matrix inequality. Let $R = cP, c > 0$. Pre- and post-multiplying the above inequality with

$\Gamma = diag\{P^{-1}, P^{-1}, I_{m_2}, I_m, I_m, P^{-1}, I_m, I_m\}$ and Γ^T, respectively, and then denoting $X = P^{-1}, KP^{-1} = W$, we can obtain an equivalent inequality (13), which is an LMI with respect to variable W and X. Due to the fact that $0 < \lambda_1 \le \lambda_2 \le \cdots \le \lambda_M$, in view of its convex property, when LMI (13) holds for λ_1 and λ_M simultaneously, it holds for all λ_i, $i \in F$. By Lemma 2, the containment control problem can be solved with $\| T_{z\omega}(s) \|_\infty < \gamma$ satisfied. □

4. Simulation

Consider a network consisting of four followers and two leaders, whose dynamics are described by (2) and (3) respectively, with

$$A_0 = \begin{bmatrix} 0 & -1 \\ 2 & 1 \end{bmatrix}, B_{10} = \begin{bmatrix} 1 & 0 \\ 0 & 2 \end{bmatrix}, B_{20} = \begin{bmatrix} 0 \\ 1 \end{bmatrix}, B_{30} = \begin{bmatrix} 0 & 0 \\ 0 & 1 \end{bmatrix},$$

$$E = \begin{bmatrix} 0 & 0 \\ 0.2 & 0.2 \end{bmatrix}, \Sigma(t) = \begin{bmatrix} \sin(t) & 0 \\ 0 & 1-e^{-t} \end{bmatrix}, F_1 = \begin{bmatrix} 0.1 & 0 \\ 0 & 0.1 \end{bmatrix},$$

$$F_2 = \begin{bmatrix} 0.2 & 0 \\ 0 & 0.2 \end{bmatrix}, F_3 = \begin{bmatrix} 0.3 \\ 0.3 \end{bmatrix}, F_2 = \begin{bmatrix} 0.4 & 0 \\ 0 & 0.4 \end{bmatrix},$$

$$x_i(t) = \begin{bmatrix} x_{i1}(t) \\ x_{i2}(t) \end{bmatrix}, f(t, x_i(t)) = \begin{bmatrix} 0.5\sin(t)x_{i1}(t) \\ 0.5\cos(t)x_{i2}(t) \end{bmatrix}.$$

The external disturbance is supposed to be $\omega(t) = [\psi(t), 1.5\psi(t), 2\psi(t), -\psi(t)]^T$, where $\psi(t)$ is the band-limited white noise with noise power 0.5, whose action time interval is [0, 2].

Fig.1. shows the communication graph with 0-1 weights, where nodes 5 and 6 are two leaders and the others are followers. The smallest and largest eigenvalues of the matrix L_1 are $\lambda_1 = 0.3820$ and $\lambda_4 = 3.6180$, respectively.

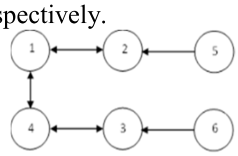

Fig.1. The communication graph

Take $\rho = 0.5, c = 30$, and $\gamma = 1$. Solving LMI (13) related to λ_1 and λ_4, we obtain the maximal allowable delay $h \le 0.042$. Here we take the communication delay in networks as $\tau(t) = 0.04\sin^2(t)$.

When there are no external disturbances, the initial states of the followers are chosen randomly from the box $[10,30] \times [-5,5]$, and the leaders' initial states are given as $x_5(0) = [15,-1]^T$ and $x_6(0) = [20,1]^T$, respectively. Fig.2. give the state trajectories of the network and the energy relationship between $z(t)$ and $\omega(t)$, respectively. Clearly, the containment control problem is indeed solved with $\| T_{z\omega} \| < 1$ satisfied.

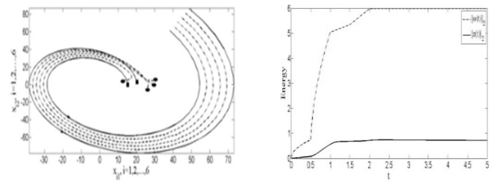

Fig.2. Left: trajectories of the network. Right: trajectories of $z(t)$ and $\omega(t)$.

5. Conclusions

In this paper, we have employed H_∞ control approach to solve the containment control problem for nonlinear multi-agent systems with parameter uncertainties and communication delays. Sufficient conditions in terms of LMIs have been derived to ensure the H_∞ containment performance. Moreover, the proposed protocol has been designed by solving only two LMIs with the same dimensions as a single agent.

Acknowledgements

This work was supported by the National Basic Research Program of China (973 Program: 2012CB821200, 2012CB821201), the NSFC (61134005, 61521091, 61327807) and the Fundamental Research Funds for the Central Universities 2016MS129.

References

1. D.V. Dimarogonas, P. Tsiotras and K.J. Kyriakopoulos, Leader-follower cooperative attitude control of multiple rigid bodies, *Syst. Control Lett.*, 58(6) (2009) 429–435.
2. G. Notarstefano, M. Egerstedt and M. Haque, Containment in leader-follower networks with switching communication topologies, *Automatica*, 47(5) (2011) 1035–1040.
3. P. Wang and Y. Jia, Robust H_∞ containment control for second-order multi-agent systems with nonlinear dynamics in directed networks, *Neurocomputing*, 153 (2015) 235–241.
4. P. Wang and Y. Jia, Robust H_∞ containment control for uncertain multi-agent systems with inherent nonlinear dynamics, *Int. J. Syst. Sci.*, 47(5) (2016) 1073–1083.
5. C. Godsil and G. Royle, *Algebraic Graph Theory*, (Springer-Verlag, New York, 2001).
6. W. Ren and Y. Cao, *Distributed Coordination of Multi-agent Networks: Emergent Problems, Models and Issues*, (Springer-Verlag, London, 2011).

Stochastic Resonance in an Array of Dynamical Saturating Nonlinearity with Second-Order

Yumei Ma
College of Computer Science & Technology, Qingdao University, 308 Ningxia Road, Shinan District Qingdao, 266071, China

Lin Zhao
College of Automation and Electrical Engineering, Qingdao University, 308 Ningxia Road, Shinan District Qingdao, 266071, China

Zhenkuan Pan
College of Computer Science & Technology, Qingdao University, 308 Ningxia Road, Shinan District Qingdao, 266071,China

Jinpeng Yu
College of Automation and Electrical Engineering, Qingdao University, 308 Ningxia Road, Shinan District Qingdao, 266071, China
E-mail: mayumei_qdu@163.com; zhaolin1585@163.com;zkpan@qdu.edu.cn; yjp1109@hotmail.com
www.qdu.edu.cn

Abstract

The transmission of weak noisy signal byparallel array of dynamical saturating nonlinearities with second-order is studied. Firstly, the numerical results demonstrate that the output SNR can be enhanced by parallel array of dynamical saturating nonlinearities with second-order by tuning the internal noise. Secondly, the SR effects can be optimized by the self-coupling coefficient of the dynamical nonlinearity.Then, the SR effects when the non-Gaussian noise acts as the external noise are superior to that with external Gaussian noise.

Keywords: stochastic resonance, dynamical nonlinearity, second-order, signal-to-noise ratio

1. Introduction

Stochastic resonance (SR) establishes a phenomenon where the additive noise can enhance the performance of some certain nonlinear systems [1-18]. Benziinitially observed the SR effect in climate modelseveral decades ago [1]. Then, the existence of SR is proved with experiments by McNamara [2].Later, some new types of SR models are applied in many research fields. When Collins designed the neuron network model, summing nonlinear units intoa parallel array, the system performance can be enhanced by adjustingthe coupling strength andthearray noise intensity [3]. Subsequently,various SReffects as types of array SR are investigated, for instance, the Supra threshold SR [4].The positive role of the array noise has been found in some complex networks, e.g. stochastic pooling networks [5], scale-free networks [6] and small-world networks [7].Recently, the SR in some physical system focuses on the noisy bi stable system, such as the bi stable fractrional-order system, asymmetric bi stable system and fractional harmonic oscillator and so on [8-10]. The SR effects can be measured by signal-to-noise ratio, the fisher information [11], etc.

In this paper,the SR effect in parallel array of dynamical saturating nonlinearities with second-orderis firstly studied.It is demonstrated that, the SR effect occurs in arrays of dynamical saturating nonlinearities with second-order as increasing the array size and the array noise intensity. And diverse forms of the output SNR appear which against the array noise intensity and the array scale.When the Gaussian noise acts as the external noise, the self-coupling coefficient has a greater impact on the output SNR. While the self-coupling coefficient takes smaller value, the SR effect is obviously visible. With larger value of the self-coupling coefficient, the bell-shape behavior of the outputis not clearly.As the array size $N \to \infty$, the output of the nonlinear systemswith the external Laplacian noise precedes that with the external Gaussian noise.

2. Theoretical Model

We considera weak periodic sinusoid signal $s(\mathrm{t})$ added to a white noise $\theta(\mathrm{t})$, which is independent of $s(\mathrm{t})$ with a probability density function (PDF) f_θ and variance $\sigma_\theta^2 = E_\theta[\mathrm{x}^2] = \int_{-\infty}^{\infty} x^2 f_\theta(\mathrm{x})\,\mathrm{dx}$. The maximal amplitude of $s(\mathrm{t})$ is A ($|s(\mathrm{t})| \le A$) and the period is T. Next, the input mixture $\gamma(\mathrm{t}) = s(\mathrm{t}) + \theta(\mathrm{t})$ is applied to each identical subsystem of an uncoupled parallel array. $\alpha_i(\mathrm{t})$ plays a role of array noise, independent of $\gamma(\mathrm{t})$, with the same PDF and variance σ_α^2.Then the output of a subsystem as

$$\mathrm{y}_i(\mathrm{t}) = k[\gamma(\mathrm{t}) + \alpha_i(\mathrm{t})] \tag{1}$$

Then the system output $Z(\mathrm{t})$ is written as

$$Z(\mathrm{t}) = \frac{1}{N}\sum_{i=1}^{N} y_i(\mathrm{t}) \tag{2}$$

The output SNR can be a measure of the system performance, which is defined as the power contained in the outputspectral line at fundamental frequency $1/T$ divided by the power contained in the

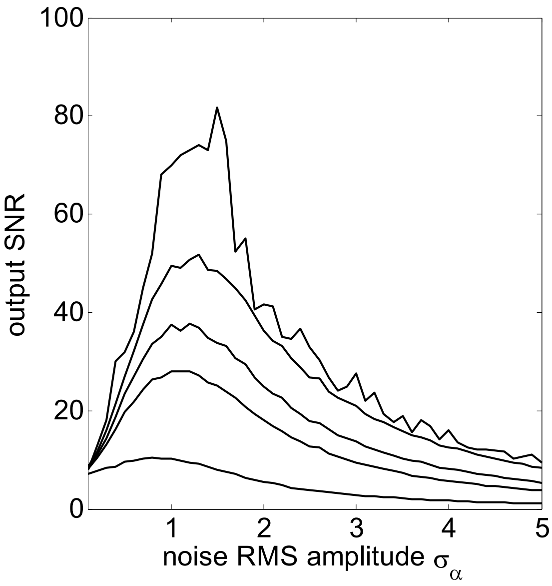

Fig. 1. Output SNR as a function of the RMS amplitude σ_α of the array noise $\alpha_i(\mathrm{t})$.

noisebackground in a small frequency bin ΔB around $1/T$, that is

$$R_{out} = \frac{|\langle E[\mathrm{Z(t)}]\exp(-i2\pi t/T)\rangle|^2}{\langle \mathrm{var}[\mathrm{Z(t)}]\rangle H(1/T_s)\Delta B} \tag{3}$$

Similarly,the input SNR is given by

$$R_{in} = \frac{|\langle s(\mathrm{t})\exp(-i2\pi t/T)\rangle|^2}{\sigma_\theta^2 \Delta t \Delta B} \tag{4}$$

When a sinusoidal signal buried in white noise as the input signal, the input SNR is written as

$$R_{in} = \frac{A^2}{4\sigma_\theta^2 \Delta t \Delta B} \tag{5}$$

When the array size $N \to \infty$, the array output SNR can be defined as

$$R_{out}^{\infty} = \frac{|\langle E[\mathrm{y}_i(\mathrm{t})]\exp(-i2\pi t/T)\rangle|^2}{\langle E[\mathrm{y}_i(\mathrm{t})\,\mathrm{y}_j(\mathrm{t})] - E^2[\mathrm{y}_i(\mathrm{t})]\rangle H(1/T_s)\Delta B} \tag{6}$$

3. Experiment Results

In thissection, we consider a dynamical saturating nonlinearity with second-order as Eq.(7)

$$\frac{dx^{2}}{dt^2} = -\frac{dx}{dt} - x_i(\mathrm{t}) + C\tanh[\omega x_i(\mathrm{t})] + s(\mathrm{t}) + \theta(\mathrm{t}) + \alpha_i(\mathrm{t}) \tag{7}$$

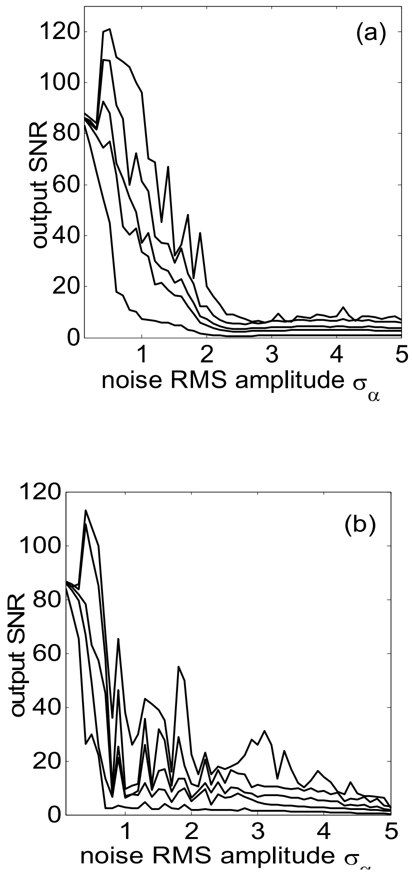

Fig. 2. Output SNR as a function of the RMS amplitude σ_α of the array noise α_i(t) .The self-coupling coefficient C=1 in (a) and C=2 in (b).

where C is the self-coupling coefficient and ω as a slope parameter. Here, $s(\mathrm{t}) = 0.2\sin(2\pi\,\mathrm{t}/\mathrm{T})$ is a deterministic sinusoid with period T. The component θ(t) is the external noise and it is the zero-mean generalizedGaussian noise,and some general cases such as Gaussian noiseare contained in the class. The PDF of the generalized Gaussian noise θ(t) is defined as

$$f_\theta(\mathrm{x}) = \frac{c_1}{\sigma_\theta}\exp(-\mathrm{c}_2 \,|\frac{x}{\sigma_\theta}|^\mu) \qquad (8)$$

where c_1 and c_2 is defined as Eq.(9) and Eq.(10)

$$\mathrm{c}_1 = \frac{\mu}{2}\Gamma^{\frac{1}{2}}(3\mu^{-1}) / \Gamma^{\frac{3}{2}}(\mu^{-1}) \qquad (9)$$

$$\mathrm{c}_2 = [\Gamma(3\mu^{-1}) / \Gamma(\mu^{-1})]^{\frac{\mu}{2}} \qquad (10)$$

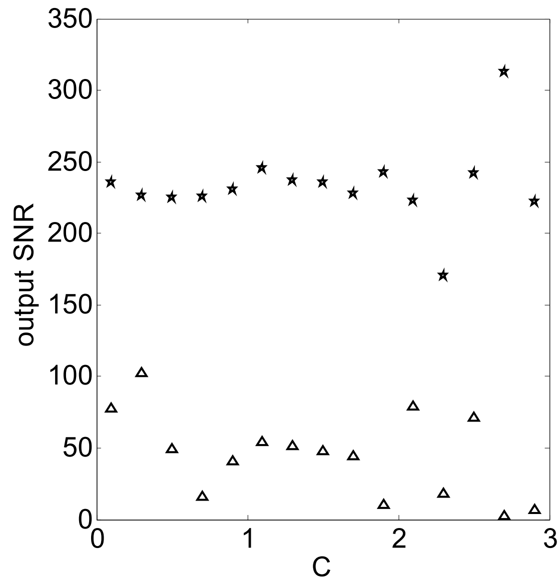

Fig. 3.Output SNR as a function of the self-coupling coefficient C of Eq.(7).

The array noise terms α_i(t) are zero-mean uniformly distributed over $[-\sqrt{3}\sigma_\alpha, \sqrt{3}\sigma_\alpha]$ with RMSamplitude σ_α .

Figure 1 and Figure 2 demonstrate the output SNR of Eq.(3)as a function of the root-mean-square (RMS) amplitude σ_α .The slope parameter ω in Eq.(7) is set $\omega = 5$. The self-coupling coefficient of the subsystem of Eq.(7) takes C=0.5 in Fig.1. While C=1 in Fig.2(a) and C=2 in Fig.2(b).In Fig.1 and Fig.2, the parameter μ of Eq.(8) is set $\mu = 2$, i.e., the Gaussian noise acts as the external noise. The external noise level $\sigma_\theta = 0.3$.

The output SNR R_{out} is revealed for N=1, 5, 10, 50 and ∞ from the bottom up in Fig.1 and Fig.2.The SR effect occurs upon increasing the array noise level σ_α and the array size N . It is shown that the bell-shape behavior is obviously as the array size $N \geq 1$ in Fig.1. But the SReffect appears lightly in Fig.2 with a certain small rangeof the array noise intensity when $N > 1$ in Fig.2. The SR effect is more unstable while increasing the self-coupling coefficient C in Fig.2. By comparison, it is shown that the SR effect can be obtained by tuning the self-coupling coefficient C of the dynamical saturating nonlinearity with second-order.

Figure 3 illustrates the output SNR as a function of the self-coupling coefficient as the array size $N \to \infty$ with different external noises. The output SNR is represented by triangles when Gaussian noise acts as the external noise, while that is represented by pentagrams with external Laplaciannoise. The RMS amplitude of the external noise $\sigma_\theta = 0.3$ and the array noise intensity is set $\sigma_\alpha = 1/\sqrt{3}$. The system output with external Laplacian noise is obviously superior to that of the nonlinear array when Gaussiannoise is the external noise.

Discussion

In this paper,SR effect is investigated firstly in an uncoupled array of dynamical saturating nonlinearities with second-order for transmitting weak noisy signal. Firstly, the SR effect occurs in parallel array of dynamical saturating nonlinearities with second-order as increasing the array size and the array noise intensity. Then, the numerical results demonstrate that higher output SNR can be obtained with smaller self-coefficient. The output SNR with the Laplace noise as the array noise is superior to that with the Gaussian noise as the internal noise.The dynamical saturating nonlinearity with second-order can be applied in the field of physical systems actual signal processing.The results from the dynamical saturating nonlinearity with second-order may be beneficial to theoretical research and signal processing.

Acknowledgements

This work is partially supported by the Natural Science Foundationof China (61501276, 61573204), the China Postdoctoral Science Foundation(2016M592139), the Qingdao Postdoctoral Application Research Project(2015120).

References

1. R. Benzi, G. Parisi, A. Sutera and A. Vulpiani, Stochastic resonance in climate changes, *Tellus*.34 (1981) 10−16.
2. McNamara B, Wiensenfeld K, Theory of stochastic resonance. *Physical Review A*.39 (1989) 4854-4869.
3. J.J.Collins, C. C. Chow, T.T.Imhoff, Stochastic resonance in neuron models, *Physical Review E*. 1995, 52: 3321-3324.
4. N. G.Stocks, Suprathreshold stochastic resonance in multilevel threshold systems, *Physical Review Letters*, 84 (2000) 2310–2313.
5. M.D. Mcdonnell, P. O. Amblard, N. G. Stocks, Stochastic Pooling Networks, *Journal of Statistical Mechanics Theory & Experiment*. 1 (2009) P01012.
6. M. Perc, Stochastic resonance on weakly paced scale-free networks via a pacemaker, *Physicsl Review E*. E 76 (2007) 066203.
7. P. Matja, stochastic resonance on excitable small-world network via a pacemaker, *Physical Review E*. 76 (2007) 066203.
8. Z. Lai and Y. Leng, Weak-signal detection based on the stochastic resonance of bistable Duffing oscillator and its application in incipient fault diagnosis, *Mechanical System and Signal Processing*. 81 (2016) 60-74.
9. F. Guo, C. Zhu, X. Cheng and H. Li, Stochastic resonance in a fractional harmonic oscillator subject to random mass and signal-modulated noise, *Physica A*. 459 (2016) 86-91.
10. P. Shi, Q. Li and D. Han, Stochastic resonance in a new asymmetric bi stable system driven by unrelated multiplicative and additive noise, *Chinese Journal of Physics*. 54 (2016) 526-532.
11. Y. Ma,F. Duan, F. Chapeau-Blondeau and D. Abbott, Weak-Periodic Stochastic Resonance in a Parallel Array of Static Nonlinearities, *PLoS ONE*. 8(3) 2013 e58507.
12. B. Lindner, J. Garcia and A. Neiman, Schimansky-Geier L. Effects of noise in excitable systems, *Physics Reports*. 392 (2004) 321-424.
13. F. Chapeau-Blondeau, Noise improvements in stochastic resonance: from signal amplification to optimal detection, *Fluctuation and Noise Letters*, 2(3)(2002) L221.
14. L. Gammaitoni, P. Hänggi, P. Jung and F. Marchesoni, Stochastic resonance, Reviews of ModernPhysics. 70(1) (1998) 233-287.
15. F. Chapeau-Blondeau and X. Godivier, Theory of stochastic resonance in signal transimission bystaticnonlinear systems, *Physical Review E*. 55 (1997) 1478-1495.
16. B. Chen, Y. Zhu, J. Hu and M. Zhang, Weak signal detection: Condition for noise induced enhancement,*Digital Signal Processing*. 23(2013)1585-1591.
17. H. Droogendijk, M. J. de Boer, R. G. p. Sanders and G. J. M. Krijnen, Stochastic Resonance in aVoltage-ControlledMicromechanical Slider,*Microelectromechanical Systems*. 24(3) (2015)651-660.
18. T. Djurhuus and V. Krozer, A Generalized Model of Noise Driven Circuits with Application toStochasticResonance, *Circuits and Systems I: Regular Papers, IEEE Transactions on*. 62(8) (2015)1981-1990.

Playware ABC: Engineering Play for Everybody

Henrik Hautop Lund
Center for Playware, Technical University of Denmark, Building 326, 2800 Kgs. Lyngby, Denmark

E-mail: hhl@playware.dtu.dk
www.playware.elektro.dtu.dk

Abstract

This paper describes the Playware ABC concept, and how it allows anybody, anywhere, anytime to be building bodies and brains, which facilitates users to construct, combine and create. The Playware ABC concept focuses engineering and IT system development on creating solutions that are usable by all kinds of users and contexts. The result becomes solutions, often based on modular technologies that are highly flexible and adaptable to different contexts, users, and applications.

Keywords: Playware, user-friendly, modular robots, playful robotics and intelligent systems.

1. Introduction

Play is a free and voluntary activity that we do for no other purpose than play itself. When we play, we experience a joyful feeling and being free to express ourselves. There is no product or end-goal with play, but it holds a life-fulfilling sensation of freedom and expression of yourself when in play. As is described in the UN Convention on the Rights of the Child, article 31 [1], every child has the right to play and leisure. Even, there exists organisations such as UNICEF, Right To Play and Playright Children's Play Association, which worldwide promote children's right to play. For instance, Right To Play work with the idea that "play is a powerful tool to change the world. It can inspire individuals and bring together entire communities. A game of football can educate children about tolerance and peace, and a game of tag can teach about malaria. When children play, they develop skills like cooperation, confidence and leadership–all important life lessons. Play provides a retreat from everyday hardships and brings joy and laughter, allowing kids to be kids." [2]

Play is for everyone, as described in work on play for the elderly [3]. Though society has often viewed play as a childish and frivolous activity, we all engage in play over our entire lifespan, and engage in such play activities in which we forget about time and place just for the enjoyment and pleasure of play itself. Games, sport, art, sex, and scientific research activities can in many cases be described as playful activities in which the subject performs an ontological shift forgetting about time and place, and in which the activity has its own course and meaning. The play activity provides life fulfilling enjoyment and meaning to the player. The player can be of all ages. It appears limiting and exclusive to define such life fulfilling enjoyment as an activity for children and youth alone. Play is, for everybody, a fundamental activity submitted to free will. In the act of playing, we manage our lives at our own choice, as we create the special form of lived life outside the "regular" life where (lust for) life and happiness as the essence of play rules. When we play we become, in the words of the philosopher Friedrich Schiller, "a whole and complete human being" [4].

Further, scientific studies [3, 5] have shown the collateral effect of play. We may observe certain effects of play. For the one who plays, these effects are not the primary reason to engage in play. Therefore, we term such effects the *collateral effects of play*. The collateral effects of play can be educational achievements, motor skill enhancement, cognitive and physical rehabilitation, etc. These collateral effects of play can be significant and important [5].

If we agree that everybody has the right to play, we also have the responsibility to ensure that we facilitate such play for everyone in the development of our society. It seems valid to ask if play happens only when you have the economical freedom to play and time to spend on play? If that is so (even if it is only so to some degree), then such wealth requirements may limit the possibilities of play, including the derived creative possibilities, for part of the global population. Further, since the development of modern technology to a large degree is a development, which defines our global society, we need to ask if the technology development allow everybody to participate, or does the technology development actually provide a further division in our global society between the technology savvy who have been brought up with technology as part of their daily life, and the non-tech population who have not had such a tech-filled upbringing? With the penetration of technology into all kinds of aspects of our lives and society (including play), there is a risk that opportunities are further polarized between the experts and non-experts of such technology, unless technology developers are consciously taking the task upon themselves of making technology, which can be easily implemented, understood and used in all kinds of contexts globally.

Therefore, in this work, we outline a concept for how it is possible to develop playful technology, which can be used creatively by anybody, anywhere, anytime. By concrete examples, we will describe the collateral effects of play with such playful technology.

2. Playware ABC

Playware is defined as intelligent hardware and software, which creates play and playful experiences for users of all ages [6, 7]. Often, it is believed that such playware can mediate other actions, for instance actions such as social interaction and physical movement. It has been outlined how the playware may act as a play force that pushes the user into play dynamics [3]. The playware is a mediator, which acts like a play force. The user is drawn into making interaction with the (playware) technology, and by acting as a play force, the playware pushes the user into a play dynamics. When you are in such play dynamics, you may feel transformed from the normal state of being and feel as if forgetting about time and place. Sometimes we may feel being able to perform more or better when in play, which is interesting if such performance may have a desired collateral effect. Indeed, Vygotsky puts it like “Play creates a zone of proximal development in the child. In play, the child always behaves beyond his average age, above his daily behavior; in play it is as though he were a head taller than himself. As in the focus of a magnifying glass, play contains all developmental tendencies in a condensed form and is itself a major source of development.” [8].

We believe that this quality of play may translate to many different groups of people. The vision of providing this quality of play and its collateral effects on many different groups of people imposes a design challenge on the playware to facilitate interaction by anybody. The *Playware ABC* concept addresses this issue. The Playware ABC concept if formed by:

A: Anybody, Anywhere, Anytime
B: Building Bodies and Brains
C: Construct, Combine, Create

The Playware ABC concepts works for creating technology solutions for *anybody, anywhere, anytime* by using embodied artificial intelligence *building bodies and brains*, which facilitates that users can themselves manipulate with the technology solutions to *construct, combine and create* their own solutions.

Often, engineering and IT system design takes it’s starting point from solving a given challenge with any technology solution available in order to achieve optimal performance under a given circumstance. This often results in systems with high performance, but with a complex installation process, which demands a large infrastructure. The Playware ABC concept suggest that such infrastructure and installation demands may be avoided to a large degree when the starting point of the engineering and IT system design is transformed from the optimal system performance to become a focus on creating a solution that can be used by *anybody, anywhere, anytime*. A demand for anybody, anywhere, anytime on the technology design should be the starting point, which forces us to find flexible solutions that can be used easily and in a flexible manner in all kinds of contexts. Fortunately, high performance and robustness of the engineered IT solution also derives from this focus on anybody, anywhere, anytime, since such performance and robustness is critically important to allow anybody to understand interacting with the solution, and to apply it anywhere.

A solution for allowing anybody, anywhere, anytime to understand and interact with the technology may be to use a modular approach derived from modern artificial intelligence, namely from embodied artificial intelligence [9]. In embodied artificial intelligence, focus is on understanding intelligence by building complete agents (robotic systems) interacting in the real environment. As opposed to good old-fashioned artificial intelligence, which to a large degree imposed a division between the body (hardware) and the brain (AI software) for instance with symbol-processing systems and expert systems, embodied artificial intelligence states that there is an intimate relationship between the body and the brain. A modular system of physical modules with processing power allows us to be *building bodies and brains* [10]. As the physical structure (body) is being built, the processing structure (brain) is made with those same building actions.

By using this concept of building bodies and brains, the abstract cognitive challenge of programming is transformed for the user to become physical actions of building. Essentially, the representation for a cognitive challenging problem is transformed to a physical representation. In a sense, this is similar to instructing small children to count numbers and make addition with their fingers: instead of using the cognitive challenging abstract representation of the numbers and addition operator, they are instructed to make a physical representation, which transforms the cognitive challenge. In this manner, engineering systems of modules may allow anybody to construct technology solutions by building bodies and brains.

By designing, engineering and testing the modules in the right manner, so that they facilitate that anybody, anywhere, anytime can be building bodies and brains, we facilitate that these users can essentially *construct, combine, and create*. The users will construct and de-construct with the modules by making different combinations and physical structures with the modules (which results in different bodies and brains). By constructing and combining with the modules, the users create their different solutions. Different modules combinations will give different results in terms of physical layout and processing result.

By playing with modules, the users should easily understand the content and the construction possibilities. Therefore, the engineering design must ensure a seamless interaction and understanding for anybody. This demands focusing on such seamless interaction and understanding for anybody in the engineering design of the modules, their content, their affordance and transparency, etc. The Playware ABC offers this focus in the engineering design process.

3. Playware ABC implementation

Based Utilising the Playware ABC concept, we can design modules that allow anybody, anywhere, anytime to be building bodies and brains, which facilitate that anybody can construct, combine, and create. The form, content, and interaction modalities will be defined by the application area, and will vary dependent on this, as exemplified in Fig. 1. Fig. 1 shows examples of modular playware systems, which we designed according to the Playware ABC. They include (a) ATRON self-reconfigurable modular robot, (b) I-Blocks in LEGO Duplo e.g. used in primary schools in Tanzania, (c) Light&Sound Cylinders and Rolling Pins for elderly dementia patient therapy in multi-sensory room, (d) modular interactive tiles for rehabilitation of stroke and cardiac patients, (e) modular interactive tiles for rehabilitation of mentally and physically handicapped children in Africa, (f) Fable user-configurable modular robot, (g) Fatherboard modular robotic wearable, (h) modular interactive tiles for soccer and playgrounds, (i) Music I-Blocks, (j) MusicTiles magic matchboxes, (k) MusicTiles magic cubes for the Roskilde Festival.

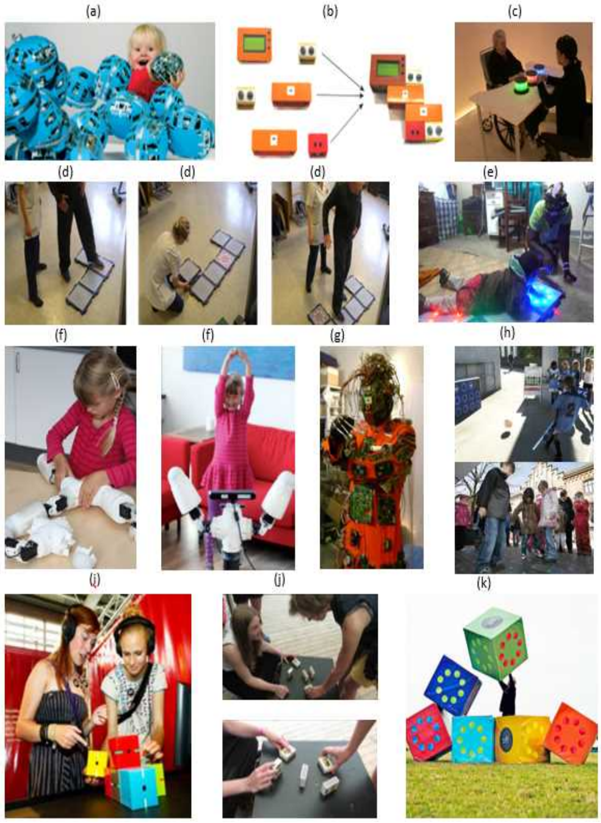

Fig 1. Examples of modular playware systems with user interaction: (a) ATRON self-reconfigurable modular robot, (b) I-Blocks in LEGO Duplo, (c) Light&Sound Cylinders and Rolling Pins for elderly dementia patient therapy in multi-sensory room, (d) modular interactive tiles for rehabilitation of stroke and cardiac patients, (e) modular interactive tiles for rehabilitation of mentally and physically handicapped children in Africa, (f) Fable user-configurable modular robot, (g) Fatherboard modular robotic wearable, (h) modular interactive tiles for soccer and playgrounds, (i) Music I-Blocks, (j) MusicTiles magic matchboxes, (k) MusicTiles magic cubes.

In the shown examples, the modules were designed based on the Playware ABC concept, so there is no need for any complex infrastructure or installation. Instead, the modules can easily be used anywhere on any continent of the world within minutes. Users ranging from small children with mental retardation in Africa, over professional football players in Europe, to older dementia patients in Asia can use the technology immediately.

4. Discussion and Conclusion

We developed the Playware ABC concept to focus engineering and IT system development on creating solutions that are usable by all kinds of users and contexts in our globalized society. The Playware ABC should result in systems that allow anybody, anywhere, anytime to be building bodies and brains, which facilitates users to construct, combine and create. The concept was exemplified with numerous examples of systems based on the Playware ABC concept, which allow use by mentally disabled children, users in developing countries, elderly stroke patients and dementia patients, etc., along with professional musicians, footballers, etc. In future, we will investigate further the adaptation, contextualisation and implementation of such Playware ABC derived technology solutions in different contexts.

References

1. http://www.unicef.org/crc/files/Rights_overview.pdf
2. http://www.righttoplay.com/Learn/ourstory/Pages/default.aspx
3. H. H. Lund, "Play for the Elderly - Effect Studies of Playful Technology," in Human Aspects of IT for the Aged Population. *Design for Everyday Life*. (LNCS Vol. 9194, pp 500-511, Springer-Verlag, 2015)
4. F. Schiller, *Letters Upon The Aesthetic Education of Man*, 1795.
5. H. H. Lund, and J. D. Jessen, "Effects of short-term training of community-dwelling elderly with modular interactive tiles," GAMES FOR HEALTH: *Research, Development, and Clinical Applications*, 3(5), 277-283, 2014.
6. H. H. Lund, and C. Jessen, "Playware - Intelligent technology for children's play," *Technical Report TR-2005-1, June, Maersk Institute*, University of Southern Denmark, 2005.
7. H.H. Lund, T. Klitbo, and C. Jessen, "Playware Technology for Physically Activating Play", *Artificial Life and Robotics Journal*, 9:4, 165-174, 2005
8. L. S. Vygotsky, *Mind in society: The development of higher psychological processes*. Harvard university press, 1980.
9. R. Pfeifer, and C. Scheier. *Understanding intelligence*. MIT press, 2001.
10. H. H. Lund, "Building bodies and brains," *Adaptive Behavior*, vol 22, no. 6, pp. 392-395, 2014.

Playware ABC 2: a Disruptive Technology for Global Development

Henrik Hautop Lund
Center for Playware, Technical University of Denmark, Building 326, 2800 Kgs. Lyngby, Denmark

E-mail: hhl@playware.dtu.dk
www.playware.elektro.dtu.dk

Abstract

The Playware ABC concept is used to create solutions that are usable by all kinds of users and contexts in our globalized society. In this paper, the Playware ABC can be exemplified with the development of the modular interactive tiles for health prevention and rehabilitation of anybody, anywhere, anytime. The paper gives examples of how playware becomes a disruptive technology for global development, for instance in the health sector. For instance, in Tanzania doctors and community-based rehabilitation workers are constructing and combining modular playware tiles to easily create the right kind of intervention for their patients in both urban and deep rural areas in Tanzania.

Keywords: Playware, user-friendly, modularity, development, playful robotics and intelligent systems.

1. Introduction

We outlined in [1] that when people get into play-dynamics, there can be certain effects of play which we termed the *collateral effects of play*. The collateral effects of play can be educational achievements, motor skill enhancement, cognitive and physical rehabilitation, etc. In the following, we will exemplify such collateral effects of play in the area of health [2].

If it is true that the collateral effects of play on playware may lead to significant and important health improvements, then it also becomes mandatory to investigate the engineering principles, which may facilitate a distribution of playware to everybody regardless of their skills, societal context, etc. We address this issue with the *Playware ABC* concept, which is based on:

A: Anybody, Anywhere, Anytime
B: Building Bodies and Brains
C: Construct, Combine, Create

Indeed, the Playware ABC concepts works for creating technology solutions for *anybody, anywhere, anytime* by using embodied artificial intelligence *building bodies and brains*, which facilitates that users can themselves manipulate with the technology solutions to *construct, combine and create* their own solutions.

2. Moto tiles for Health

The Playware ABC can be exemplified with the development of the modular interactive tiles for health prevention and rehabilitation of anybody, anywhere, anytime. In this context, play as a free and voluntary activity, which is performed for the personal enjoyment, may result in highly motivated patients, if the technology can mediate such playful engagement. At the same time, it may be possible to observe the *collateral effects of play* in the form of quantifiable health effects that exceeds the effects measured with traditional health intervention methods [2, 3].

Therefore, based on the Playware ABC, we developed modular playware in the form of the modular interactive tiles, now called Moto tiles (www.mototiles.com). The Moto tiles activates the user to perform playful interaction with play and games on the tiles that light up in different colors and registers when users step on them.

These Moto tiles are based on various generations of prototypes of modular interactive tiles, which we developed over the last decade [4, 5]. Each tile has a ring of 8 RGB LEDs, a sensory system to register step on the top surface, its own processor and rechargeable lithium battery. As a consequence of the design based on the Playware ABC concept, these Moto tiles can be easily transported to be set-up and used anywhere within a minute.

The new Moto tiles are connected to a tablet with the ANT+ radio protocol. On the tablet, the user can select between numerous games that challenge both the physical and cognitive abilities of the user. Further, the tablet shows the score in each games, shows statistics for the user, and make automatic documentation of effect.

Fig. 1. Moto tiles and app interface (www.mototiles.com)

Scientific studies of effect among community-dwelling elderly who perform group play on the modular tiles once per week show highly statistical significant effect on functional abilities of the elderly. Especially, the balancing abilities of the elderly (avg. 83 years of age) increase by more than 60% after merely 13 training sessions [3]. Also, all other measured functional abilities (strength, mobility, agility, and endurance of the elderly) improved with statistical significant effect.

Qualitative studies suggest that the high health effect from playing with the Moto tiles arises since the Moto tiles act as a play force, which pushes the participants into a play-dynamics, in which they forget about time and place, and thereby perform more than they would normally do. In play, they may forget about their fears of falling and forget about their perceived physical and cognitive limitations.

With such quantifiable health effect results of play, playware technology may disrupt certain areas of the health sector. Already, the Moto tiles are used in the health sector for the benefit of cardiac patients, stroke patients, elderly citizens at risk of falling, dementia patients, children with cerebral palsy, and in special schools in three continents. This disruptive technology for the health sector is a result of the Playware ABC with the possibility for the end-user to easily adapt to different tasks and practices, e.g. for different kinds of patients.

Fig 2. Modular interactive tiles for rehabilitation of mentally and physically handicapped children in Tanzania.

Indeed, the modular interactive tiles can be used by anybody, anywhere, anytime, as it does not demand any particular knowledge of the user, and it does not demand any infrastructure. Hence, it is used as a playful technology solutions for rehabilitation of children with cerebral palsy, mental retardation, etc. in deep rural sub-Saharan Africa [6, 7]. This derives from the Playware ABC, which here results in a highly mobile, modular and energy efficient technology, which can be set up and used anywhere and anytime. In Tanzania, we are forming a national partnership for sustainable implementation, comprising a governmental representative, national hospital, national health university department, regional hospitals, Living Labs and NGOs performing community-based rehabilitation.

Fig. 3. Playful rehab of meningitis affected child in Iringa Regional Hospital, Tanzania.

The users such as doctors in the hospitals or health workers in community-based rehabilitation programs are constructing and combining the modular tiles to easily create the right kind of intervention for their patients. The battery-powered tiles present a vast number of opportunities for games and can be used for many different purposes. Due to the modularity, it is very easy to co-design and adapt the modular tiles system to different contexts, different intervention areas, and different levels of competencies.

This can have an important impact in rehabilitation of disabled, stroke, and cardiac patients in parts of the world where a large part of the population lives in remote and rural areas. Here, potential health technology solutions often face problems of scarce availability of electricity, of technology professionals, and of health personnel. Further, due to the relatively low amount of health spendings and of health workers e.g. in sub-Saharan Africa compared to high-income countries, the individual health worker will typically need to treat a vast array of health problems compared to the high degree of specialization to single health problems amongst health workers in high-income countries. Hence, to be effective in low-income regions such as sub-Saharan Africa, there is a need for health technology solutions, which facilitate treatment of people with various diagnoses.

Through the Playware ABC, we address this challenge with the modular interactive tiles, which aim at motivating patients to perform rehabilitative actions. By taking advantage of the flexibility and easy approach to personalization inherent in the modularity, the proposed modular approach possesses the potential of becoming particularly helpful in addressing both the technological challenges and health challenges in low-income communities. With the high prevalence of disability, stroke and coronary heart cases in sub-Saharan Africa countries, it is of paramount importance to investigate how this kind of an approach can provide an eHealth solution flexible enough to adapt to the needs of patients. Based on the Playware ABC, we therefore aim at refining and contextualising modular interactive tiles to allow a local community to have one modular solution that any community rehabilitation worker can easily adapt to the individual patient and his/her needs.

Fig. 4. Modular interactive tiles for rehabilitation at Muhimbili National Hospital, Dar Es-Salaam, Tanzania.

3. Conclusion

We developed the modular interactive tiles as an exemplification of Playware ABC to allow anybody, anywhere, anytime to be building bodies and brains, which facilitates users to construct, combine and create. Indeed, in health institutions in Sub-Saharan Africa, doctors and health care workers are now utilizing the modular interactive tiles for a variety of interventions for mentally disabled children, elderly stroke patients, etc.

In future, we will investigate further the adaptation, contextualisation and implementation of such Playware ABC derived technology solutions in different contexts, including in areas of development. Especially for the health area, we will investigate with different rehabilitation methods and centres, including hospitals both in a city centres and in a rural area, NGO's performing community based rehabilitation, and rehabilitation centres [6].

Acknowledgements

The author would like to thank colleagues at the Center for Playware, Technical University of Denmark.

References

1. H. H. Lund, "Playware ABC: Engineering Play for Everybody" ibid.
2. H. H. Lund, "Play for the Elderly - Effect Studies of Playful Technology," in Human Aspects of IT for the Aged Population. *Design for Everyday Life*. (LNCS Vol. 9194, pp 500-511, Springer-Verlag, 2015)
3. H. H. Lund, and J. D. Jessen, "Effects of short-term training of community-dwelling elderly with modular interactive tiles," GAMES FOR HEALTH: *Research, Development, and Clinical Applications*, 3(5), 277-283, 2014.
4. H.H. Lund, T. Klitbo, and C. Jessen, "Playware Technology for Physically Activating Play", *Artificial Life and Robotics Journal*, 9:4, 165-174, 2005
5. H. H. Lund "Modular Robotics for Playful Physiotherapy", in *Proceedings of IEEE International Conference on Rehabilitation Robotics* (IEEE Press, 571-575, 2009)
6. H. H. Lund, L. S. D. Jensen, Y. Ssessanga, S. Cataldo & K. I. Yahya-Malima, "An Approach for a National eHealth Implementation – the Case of Modular Interactive Tiles for Rehabilitation," in P Cunningham & M Cunningham (eds), *IST-Africa 2015 Conference Proceedings*, 10.1109/istafrica.2015.7190552
7. H. H. Lund, L.S.D. Jensen, Y. Ssessanga, R. Abdalahman. "Implementing Modular Interactive Tiles for Rehabilitation in Tanzania – a Pilot Study", in *IST-Africa 2014 Conference Proceedings*, P Cunningham and M Cunningham (Eds), IIMC International Information Management Corporation, 2014, ISBN: 978-1-905824-43-4

The future of Robotics Technology

Luigi Pagliarini [1,2] Henrik Hautop Lund [1]

[1] Centre for Playware, Technical University of Denmark, 2800 Kgs. Lyngby, Denmark
[2] Academy of Fine Arts of Macerata, Via Berardi, 6, 405111 Macerata, Italy

luigipagliarini@gmail.com

Abstract

In the last decade the robotics industry has created millions of additional jobs led by consumer electronics and the electric vehicle industry, and by 2020, robotics will be a $100 billion worth industry, as big as the tourism industry.. For example, the rehabilitation robot market has grown 10 times between 2010 and 2016, thanks to advancements in rehab/therapy robots, active prostheses, exoskeletons, and wearable robotics. In short, the very next decade robotics will become vital components in a number of applications and robots paired with AI will be able to perform complex actions that are capable of learning from humans, driving the intelligent automation phenomenon. Therefore, in this paper we try to depict the direction and the fields of application of such important sector of future markets, and scientific research.

Keywords: Playware, user-friendly, modular robots, playful robotics and intelligent systems.

1. Introduction

Most certainly, in near future, and as for biological systems, Robotics will be submitted to a selective pressure under which most of its branches and authors will change. All of that will happen because of several factors: the enormous costs of production and maintenance of such machines; because of the ecosystemic and energetic costs of the robots, which are similar if not higher than any other machine; likely due to the saturation of an already seemingly fragile market. Because of that, it is quite important to try to predict the future of intelligent machines in order to focus one's efforts on the appropriate field.

In the beginning of the millennium indeed, scientists and enterprises started to apply the binomial Robot/AI to almost all of the possible domains with the "naïve" conception that the emerging technologies could have dealt with any task. Which is, in part, true. Nevertheless, on the other side, it slowly becomes self evident that there is a set of bottlenecks which are quite hard to pass. To put it in a practical way, there are at least three sets of problems, which relegate both efficiency, and functionality of such machines to a limited domain, largely excluding the dream of a "polyfunctional" robot. Such limits are (1) Mechanical, (2) Energetic and (3) Computational. Indeed, robots' mechanics tends to reach an unsustainable degree of complexity moving from a limited to a larger set of outputs. In the very same way, the energy consumption rises in parallel to the increasing of degree of freedom of any mechanics, making the energetic battery life span of a machine quite harder, up to the a critical level of inadequacy. Finally, the Computational resources of AI have largely demonstrated to be very good at solving a single task while, on the contrary, getting proportionally less efficient when handling a larger number of possible outputs. Therefore, the goal of multi-purpose robot is to be considered unreal and, oppositely, researchers and businessmen are going for a Robotics that is pretty specialized in a single task, if not a single subtask.

Given that, it happens that the number of artefacts - that we call Robots - has been exploited to such a number that both the scientific and the business markets cannot actually absorb and, as a consequence, we are about to face a phase in which selection will become necessary.
Therefore, let's now see which are the largest and maybe more promising fields, trying to distinguish their

domain of competences with their domains of application, since the two things that are not necessarily the same.

2. Robotics Fields

At the moment being, the number of robotics fields is nearly uncatchable, since robot technology is being applied in so many domains that nobody is able to know how many and which they are. Such an exponential growth cannot be fully tracked and we will try to identify and discuss upon the most evident fields of application, which, as far as we, comprehend are:

- **Healthcare Robotics**; Robotics used in the context of patient monitoring/evaluation, medical supplies delivery, and assisting healthcare professionals in unique capacities as well as, Collaborative robots and robotics used for Prevention (1,2,3).
- **Medical and Surgery Robotics**; Devices used in hospitals mostly for assisting surgery since they allow great precision and minimal invasive procedures (4,5).
- **Body-machine interfaces** help amputees to feed-forward controls that detect their will to move and also receive sensorial feedback that converts digital readings to feelings (6).
- **Telepresence Robotics**; Act as your stand-in at remote locations it is meant to be used in hospitals and for business travellers, with the idea of saving both time and money (7).
- **Cyborgs, Exoskeletons, and Wearable Robotics.** Allow users to augment their physical strength, helping those with physical disabilities to walk and climb (8).
- **Humanoids**. Combine artificial intelligence and machine learning technologies to give robots human-like expressions and reactions (9).
- **Industrial.** Arms, grippers and all of the warehouse robotics used for automation of industrial processes. They are used both for saving manoey and speed up the productions (10).
- **Housekeeping.** Floors, Gardens Pools and all the Robot Cleaners (11).
- **Collaborative Robots.** Recently the market has been opened to Domotics and other Home and Public Spaces (e.g. Shops) Automation coordinators (12).
- **Military Robotics.** Drones, Navigators, Researchers, Warriors and all of the possible robotics extensions which are to be applied in spying operations and battle fields (13).
- **Underwater, Flying and Self -Driving Machines.** All the Robotics that deals with self-piloting in all circumstances, on earth, air and water (13).
- **Space Robots.** All of the Robotics used in Space missions, therefore highly resistant, expert in exploration and material data collection (14).
- **Entertainment.** Toys, Games and Interactive Robotics for children (15).
- **Art.** Most creative robotics, which don't aim at a specific functionality but follows criteria of beauty and conceptual inspiration (16).
- **Environmental and Alternately powered robots** use sources like solar, wind and wave energy to be powered indefinitely and open up applications in areas that are off-grid (17).
- **Swarm and Microbots** allow emergency responders to explore environments that are too small or too dangerous for humans or larger robots; deploying them in "swarms" compensates for their relatively limited computational ability (18).
- **Robotic networks** emerge and allow robots to access databases, share information and learn from one another's experience.
- **Modular Robotics.** Robots that can arrange themselves in pre-set patterns to accomplish specific tasks (19).

3. Analysis

Let us now look at all of these branches distinguishing them on two different scales.

Robotics that mainly belongs to the *research* domain from those that aim at *application*, therefore, market oriented. Fields that are proficient and uprising from those that seem declining or apparently stuck in a bottle neck.

- **The Market.**

Looking at the market, the richest applications are those that belong to industrial robotics, where automation of processes is requiring more and more clever and fast robots for assembling any kind of product. No comparison, this is and apparently will be the most important robotics field for quite a while, at least. Following that, there are at least few very promising fields, Entertainment, Medical, Surgery and Housekeeping Robotics. With a completely different philosophy – few expensive vs. lots of cheap sells - they established themselves into the market in a quite persistent way. Nevertheless, even if those market slices are not saturated yet, we would say they are getting close to it, leaving little space for future improvement. We cannot say the same for Industrial Robotics.

- **The Research.**

At the moment, researchers are keen on a set of fields that are very interesting under the scientific point of view but, oppositely, pretty poor as market chances. They are Humanoids, Telepresence, Swarm, Microbots, Robotic Networks, Modular Robotics, and Body-Machine Interfaces. Such fields are crucial for basic-research and, probably, something exceptional will come out of all these investigations, but for the moment being, we can't foresee a single reasonably profitable application from all of them. On the contrary, Underwater, Self -Driving Machines and, in particular, Flying Robots (e.g. Amazon's Drones, etc.) are moving towards a promising number of vends and who's impact can be more than consistent in the next decade.

- **The Exceptions.**

An odd man out seems to be both Space and Military Robotics. For these two quite rich fields - where the concept of research and application tend to melt – there is still a large margin of exploration and exploitation. Of course, besides any further consideration, both Space and Military application can be considered, under the economical point of view, self-sustaining since they both produce and consume for their own market.

- **The Upcoming.**

There are few promising fields of robotics for the early future. They are Exoskeletons, Wearable Robotics, Healthcare and Collaborative Robotics. There is, indeed, a flow of investments both from Medical and Fashion Houses that are trying to sustain the research in these fields. Investments are motivated by marketing reasons and, sometime, by a real intent of generating a new trend in their consumers market.

- **Out of trend**

In its short history, Robotics is already producing leftovers. Indeed, few branches of past pretty popular Robotics are getting out of trend. They are Humanoids, Geminoids, Cyborgs, etc. Their appeal and impact on the public (and on a big slice of researchers) seems to be fading away, as if both the experimentation and the public imaginary had been saturated.

- **Innovations.**

At the moment, the most innovative branch is Environmental and Alternately Powered Robotics that is attracting interests from different Institutes and Industries. Anyway, few are the existing application (i.e.: toys, navigation, etc.) and they do not represent a valuable set by which we could evaluate their effective potentialities. Nevertheless, they theoretically represent a quite important goal since a big obstacle in this machine-driven society is around the energy costs, and renewable energies in Robotics, as in all other applications seems to be the unique answer.

An important answer to the energy consumption question may also be found in the branch of Neurorobotics (20) which exploits Neuromorphic computing. Here, Research is investigating the use of processes similar to (human) brain processes, which offer large scale computation at a much lower energy consumption than is currently known in any computational/robotic device.

4. Conclusions

In the last two decades Robotics has literally exploded, both in terms of research and applications. It has invaded the people's imaginary and almost all of the existing markets, up to the point that, on one side, we can spot at robotics news each single day and, on the other, Robotics is about to reach a market slice of 100 Billions dollars. In this paper we tried to summarize and analyse which are the most profitable and promising branches and where to look for new horizons. It appears that Industries' Automation is the leader of such a world while a number of applications are consolidating themselves or about to emerge and to play a consistent role in Robotics research and production. They are Healthcare, Surgery, Housekeeping, Autonomous Vehicles and, in part, Entertainment. We also underlined which are the branches that seem to lose affection of markets and researches, as for example Humanoids, and those who are gaining interests, as for example Alternately Powered Robotics. It is our belief that our analysis can provide a wider view on the world of Robotics and how to approach it in the early future.

References

1. H. H. Lund, "Play for the Elderly - Effect Studies of Playful Technology," in Human Aspects of IT for the Aged Population. *Design for Everyday Life.* (LNCS Vol. 9194, pp 500-511, Springer-Verlag, 2015)
2. H. H. Lund, and J. D. Jessen, "Effects of short-term training of community-dwelling elderly with modular interactive tiles," GAMES FOR HEALTH: *Research, Development, and Clinical Applications*, 3(5), 277-283, 2014.
3. A. Okamura, M. Mataric, & H. Christensen - Panels. CCC/CRA, Roadmapping for Robotics Workshop: A Research Roadmap for Medical and Healthcare Robotics. [Online] Available at: http://www.us-robotics.us/medical-ws.html (2008).
4. M. Sood, S. W. Leichtle. *Essentials of Robotic Surgery*, Spry Publishing LLC, Mar 1, 2013
5. T. Lendvay, (2008). Robotic Surgery Simulation: An Unintuitive Reflection. *Medical Robotics Magazine*. [Online] Available at: http://medicalrobotics.blogspot.com/2008/10/robotic-surgery-simulation-unintuitive.html .
6. T. D. Coates, *Neural Interfacing, Forging the Human-Machine Connection*. Morgan & Clayton Publishers. John D. Enderle Series Editor, (2008).
7. I. R. Nourbakhsh, *Robot Futures*. The MIT Press, Cambridge Massachusetts, London England (2013).
8. J. L. Pons. Wearable Robots: *Biomechatronic Exoskeleton*s. John Wiley & Sons Ltd. (2008).
9. S. Kajita, H. Hirukawa, K. Harada, K. Yokoi, *Introduction to Humanoid Robotics*. Springer (2014).
10. S. Y. Nof, *Springer Handbook of Automation*. Springer-Verlag (2008).
11. R. Siegwart, I. R. Nourbakhsh, D. Scaramuzza. *Introduction to Autonomous Mobile Robots*.The MIT Press, Cambridge Massachusetts, London England (2004).
12. J. Gerhart, *Home Automation and Wiring*, McGraw Hill Professional (1999).
13. P. J. Springer, *Military Robots and Drones*: A Reference Handbook. ABC-CLIO Editor (2013).
14. R. D. Launius, H. E. McCurdy. *Robots in Space: Technology, Evolution, and Interplanetary Travel*. The Johns Hopkins University Press, Baltimore. (2008).
15. R. Malone. *Ultimate Robot*. DK Pub., 2004.
16. L. Pagliarini, H. H. Lund. The Development of Robot Art. AROB, *13th International Symposium on Artificial Life and Robotics*, Oita, Japan, January 31–February 2, 2008.
17. R. Hanson. The Age of Em: *Work, Love, and Life when Robots Rule the Earth*. Oxford University Press. (2016).
18. S. Kernbach. *Handbook of Collective Robotics: Fundamentals and Challenges*. Pan Stanford Publishing. (2013).
19. K. Stay, D. Brandt, D. J. Christensen. *Self-reconfigurable Robots. An Introduction*. MIT Press, (2010).
20. P. Artemiadis. *Neuro-Robotics: From Brain Machine Interfaces to Rehabilitation Robotics*. Springer (2013).

A Combination of Machine Learning and Cerebellar Models for the Motor Control and Learning of a Modular Robot

Ismael Baira Ojeda
Center for Playware, Department of Electrical Engineering, Technical University of Denmark, Elektrovej Building 326 Kongens Lyngby, 2800, Denmark

Silvia Tolu, Moisés Pacheco, David Johan Christensen, and Henrik Hautop Lund
Center for Playware, Department of Electrical Engineering, Technical University of Denmark, Elektrovej Building 326 Kongens Lyngby, 2800, Denmark
E-mail: iboj@elektro.dtu.dk, {stolu, mpac, djchr, hhl}@elektro.dtu.dk
www.dtu.dk

Abstract

We scaled up a bio-inspired control architecture for the motor control and motor learning of a real modular robot. In our approach, the Locally Weighted Projection Regression algorithm (LWPR) and a cerebellar microcircuit coexist, forming a Unit Learning Machine. The LWPR optimizes the input space and learns the internal model of a single robot module to command the robot to follow a desired trajectory with its end-effector. The cerebellar microcircuit refines the LWPR output delivering corrective commands. We contrasted distinct cerebellar circuits including analytical models and spiking models implemented on the SpiNNaker platform, showing promising performance and robustness results.

Keywords: Motor control, cerebellum, machine learning, modular robot, internal model, adaptive behavior.

1. Introduction

Understanding the human brain is one of the greatest and most appealing challenges facing scientific research. Therefore, initiatives such as the Human Brain Project[1] (HBP) were conceived to encourage the delivery of beneficial breakthroughs for society and industry. The HBP unites the effort of numerous research centers and universities involving multiple disciplines and goals in the form of 12 subprojects. In particular, our group is framed within the subproject 10 focused on neurorobotics.

Robots lack the adaptability and precision of human beings towards uncertain or unknown environments. In contrast, the brain accomplishes tasks in an admirable way allowing smooth movements with a low power consumption. As a result, studying how we control our bodies in uncertain or unknown environments, how we coordinate smooth movements and the mechanisms of motor control and motor learning of the central nervous system (CNS) has become of interest towards the development of bio-inspired autonomous robotic systems.

1.1. *The cerebellum*

Among the distinct parts of the brain, the cerebellum stands out due to its key role in modulating accurate, complex and coordinated movements, acting as a universal learning machine[2]. Its contributions include the neural control of bodily functions, such as postural positioning, balance or coordination of movements over time[3]. Thus, understanding and mimicking the cerebellar mechanisms through bio-inspired architectures are interesting processes in the development of innovative

robotic systems capable of carrying out complex and accurate tasks in varying situations (See Refs. 4-6).
Following this motivation, we took inspiration from the cerebellum for the motor control and learning of a real modular robot. For this purpose, we used a bio-inspired control architecture which combines machine learning and a cerebellar microcircuit. The cerebellar models were simplifications of the real biological microcircuit including only the Purkinje, granule and deep cerebellar nuclei cells, and the parallel, mossy and climbing fibers. Moreover, we considered three cerebellar models, including spiking and non-spiking approaches, aiming at enlightening when to use which model and establishing the grounding for our future research. The result was a compliant robot module that by means of a bio-inspired approach was able to learn how to trace out a circular trajectory with its end-effector.

2. Material and Methods

In this section, we address the modular robot, our modular control approach and the Machine Learning technique utilized.

2.1. *The modular robot: Fable*

The target robotic platform is the modular robot called Fable[7]. Fable is based on the combination of self-contained modules which can work independently or collaborate in modular configurations. Due to a low lag radio communication link to the modules the user can program the distributed robot modules at different levels of abstraction as if they were centralized and connected directly to the computer. To do so, the communication is done via a radio dongle addressing each module with an ID and a radio channel.

Fig. 1. The robot Fable. An example of a modular configuration comprising four actuated modules and a head module endowed with ultrasound sensors.

2.2. *The modular approach*

Scientific research studies on the cerebellum such as Refs. 8-9, describe it as a set of adaptive modules, called microcomplexes, which represent the minimal functional unit and show a uniform almost crystalline microcircuitry[10]. Thus, we decided to use its structure to control a robot module in a generic manner.
Two microcomplexes were used to command the joints of a 2-DoF module. Each cerebellar output was linked to one joint as it happens in our body, where one motor cell commands one motor unit.

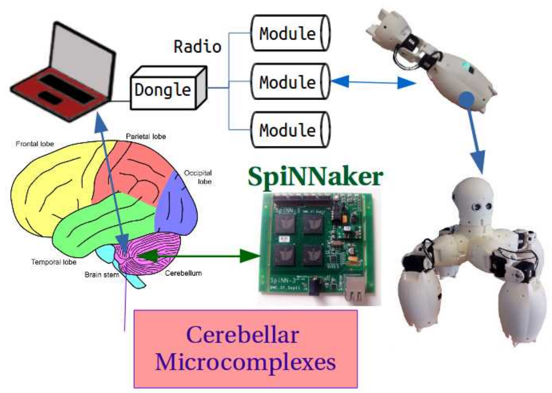

Fig. 2. Modular scheme of the connections between the computer, the modular robot Fable and the neuromorphic SpiNNaker platform, which was used for the implementation of the spiking cerebellar model.

2.3. *The bio-inspired modular control architecture*

In order to perform the motor control and learning of a Fable module, we chose the Adaptive Feedback Error Learning (AFEL) architecture[4] shown in Fig. 3.
The trajectory generation block generates the desired joint angles and velocities $(Q_d, \dot{Q}_d)$ by inverse kinematics.
On the one hand, the AFEL scheme guarantees the stability of the system by means of a control loop in which a Learning Feedback (LF) controller[4] is implemented. The LF overcomes the lack of a precise robot morphology dynamic model ensuring stability and adjusting its output torque through a learning rule after consecutive iterations of the same task. Its gains were heuristically tunes to $K_p = 7.5$, $K_v = 6.4$ and $K_i = 1$ for the Fable module.
On the other hand, the AFEL architecture is endowed with a ULM, comprised by the LWPR algorithm and a cerebellar circuit. The ULM performs a feedforward control of the robot module. The LWPR is in charge of abstracting the internal model of the robot, while the cerebellar microcircuit refines the output delivering corrective torques.

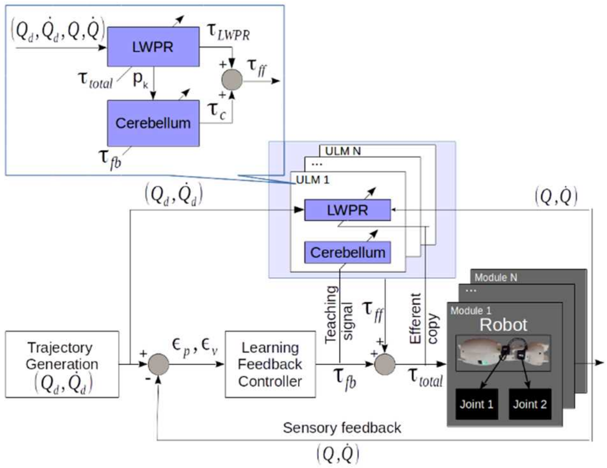

Fig. 3. The AFEL control architecture. The AFEL control architecture embeds a ULM which acts as a feed-forward controller while it abstracts the internal model of the robot module.

The cerebellar microcircuitry considered three cases. Case 1, based on Ref. 4, included only the Purkinje cells whose learning rule is based on the heterosynaptic covariance learning rule[11] in the continuous form and adjusted by an error signal τ_{fb}. In Case 2 we included the Deep Cerebellar Nuclei (DCN) cells, adding two extra synaptic plasticities whose learning rules were inspired by Ref. 12.
In case 3 we implemented a simplified spiking cerebellar model using the neuromorphic platform SpiNNaker[13], consisting of Purkinje cells and DCN cells but without considering recurrent or inhibitory synapses.

2.4. *The LWPR algorithm*

The LWPR algorithm[14] creates and combines N linear local models and feeds the sensorimotor inputs $(Q_d, \dot{Q}_d, Q, \dot{Q})$ of the robot including desired and real values to them. Thereafter, the LWPR incrementally divides this sensorimotor input space into a set of receptive fields (RFs) performing an optimal function approximation. The RFs are represented by a Gaussian weighting kernel (Eq. 1) which computes a weight in each *k-th* local unit, for each x_i data point according to its distance to the c_k center of the kernel.

$$p_k = e^{-\frac{1}{2}\left((x_i - c_k)^T D_k (x_i - c_k)\right)} \qquad (1)$$

The weight measures how often an item x_i of the data falls into the validity region of each linear model, characterized by a positive definite matrix D_k, called distance matrix.
The LWPR conveys the weights to the cerebellar circuit and at the same time, it delivers a torque output computed as the weighted mean average of the linear local model's contributions.
We chose the LWPR algorithm for three reasons: to optimize the input space to enhance learning speed and accuracy; since it can substitute and optimize the role of a certain group of cells of the cerebellum, called granule cells; and due to its capability of learning incrementally on-line.

3. Results

We tested the control architecture using the three cerebellar model cases described in Section 2.3 by commanding the robot to trace out a circular trajectory with its end-effector. The tests considered the normalized mean square error (nMSE) of the position of the joints with respect to the desired positions. First, the performance test consisted in following a circular trajectory with constant amplitude and spin frequency (see Fig. 4).

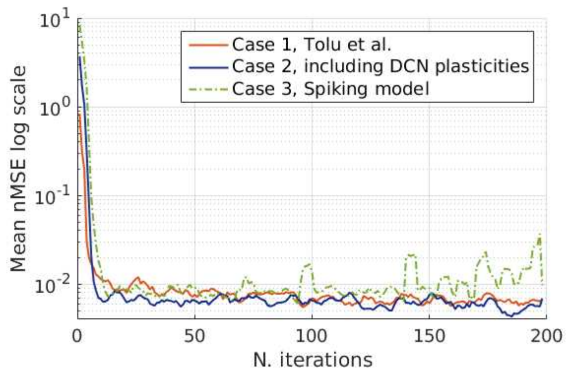

Fig. 4. Performance test: Circular trajectory with constant amplitude and spin frequency.

Secondly, we carried out two robustness tests (see Figs. 5 and 6) where we considered trajectories that varied they amplitude keeping the spin frequency constant, and thereafter, trajectories that kept the amplitude constant but varied their spin frequency (0.5-1Hz).

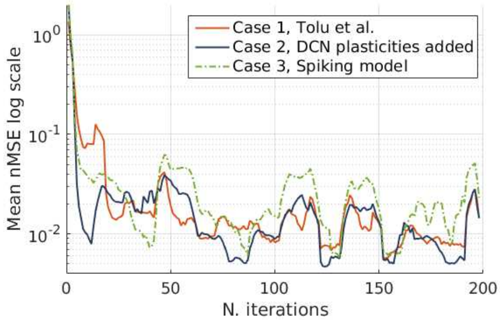

Fig. 5. Robustness test: Using three distinct amplitude values.

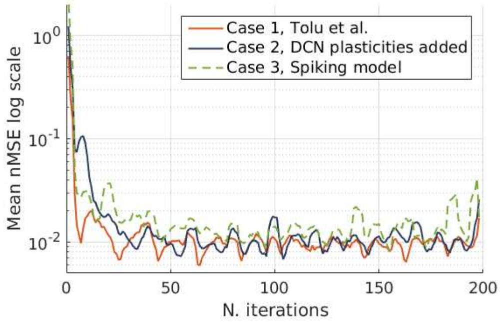

Fig. 6. Robustness test: Varying spin frequency (0.5-1Hz).

4. Conclusions

We combined the LWPR algorithm and a cerebellar circuit for the motor control and learning of a real robot module. Furthermore, we implemented three distinct cerebellar models: two non-spiking and one spiking using the neuromorphic SpiNNaker platform.

Compared to Case 1, Case 2 showed better results in the performance test while keeping similar results in both robustness tests. Case 3 did not show improvements with respect to the non-spiking models, but since its circuitry was quite simple there is much room for promising further research. Future research will exploit the potential of more detailed spiking models where inhibitory and recurrent synapses will take place and explore the control of several robot modules using SpiNNaker.

Acknowledgements

This scientific work has received funding from the European Union Horizon 2020 Programme under the grant n. 720270 (Human Brain Project SGA1). A special thank is expressed to the University of Manchester for the SpiNNaker board.

References

1. Ailamaki, A., A. Alvandpour, K. Amunts, W. Andreoni, J. Ashburner, M. Axer, M. Baaden, and R. Badia. "The Human Brain Project: A Report to the European Commission”. *Lausanne: The HBP-PS Consortium* (2012).
2. Ito, Masao. “Control of mental activities by internal models in the cerebellum”. *Nature Reviews Neuroscience* 9, no. 4 (2008): 304-313.
3. Ito, Masao. “Cerebellar circuitry as a neuronal machine.” *Progress in neurobiology* 78, no. 3 (2006): 272-303.
4. Tolu, Silvia, Mauricio Vanegas, Niceto R. Luque, Jesús A. Garrido, and Eduardo Ros. “Bio-inspired adaptive feedback error learning architecture for motor control.” *Biological cybernetics* 106, no. 8-9 (2012): 507-522.
5. Lepora, Nathan F., Paul Verschure, and Tony J. Prescott. “The state of the art in biomimetics.” *Bioinspiration & biomimetics* 8, no. 1 (2013): 013001.
6. Bologna, L. L., J. Pinoteau, J. B. Passot, J. A. Garrido, Jörn Vogel, E. Ros Vidal, and A. Arleo. “A closed-loop neurobotic system for fine touch sensing.” *Journal of neural engineering* 10, no. 4 (2013): 046019.
7. Pacheco, Moises, Rune Fogh, Henrik Hautop Lund, and David Johan Christensen. “Fable: A modular robot for students, makers and researchers.” *In Proceedings of the IROS workshop on Modular and Swarm Systems: from Nature to Robotics.* 2014.
8. Dean, Paul, John Porrill, Carl-Fredrik Ekerot, and Henrik Jörntell. “The cerebellar microcircuit as an adaptive filter: experimental and computational evidence.” *Nature Reviews Neuroscience* 11, no. 1 (2010): 30-43.
9. Verduzco-Flores, Sergio O., and Randall C. O'Reilly. “How the credit assignment problems in motor control could be solved after the cerebellum predicts increases in error.” *Frontiers in computational neuroscience* 9 (2015).
10. Ruigrok, Tom JH. “Ins and outs of cerebellar modules.” *The cerebellum* 10, no. 3 (2011): 464-474.
11. Sejnowski, Terrence J. “Storing covariance with nonlinearly interacting neurons.” *Journal of mathematical biology* 4, no. 4(1997): 303-321.
12. D’Angelo, Egidio, Lisa Mapelli, Claudia Casellato, Jesus A. Garrido, Niceto Luque, Jessica Monaco, Francesca Prestori, Alessandra Pedrocchi, and Eduardo Ros. “Distributed circuit plasticity: new clues for the cerebellar mechanisms of learning.” *The Cerebellum* 15, no. 2 (2016): 139-151.
13. Furber, Steve B., Francesco Galluppi, Steve Temple, and Luis A. Plana. “The spinnaker project.” *Proceedings of the IEEE* 102, no. 5 (2014): 652-665.
14. Vijayakumar, Sethu, Aaron D’souza, and Stefan Schaal. “Incremental online learning in high dimensions.” *Neural computation* 17, no. 12 (2005): 2602-2634.

Image Compression Using Hybrid Evolution Based Takagi-Sugeno Fuzzy Neural Networks

Chia-Nan Ko
Department of Automation Engineering, Nan Kai University of Technology
t105@nkut.edu.tw

Ching-I Lee
Department of Automation Engineering, Nan Kai University of Technology
lcy@nkut.edu.tw

Abstract

This article proposes a model of hybrid evolution-based Takagi-Sugeno fuzzy neural networks (TSFNNs). The model is to research and analyze how to improve the efficiency of image compression. In the proposed model, the hybrid evolution method integrates the advantages of improved quantum-behaved particle swarm optimization, adaptive annealing learning, and mutation operation to train Takagi-Sugeno fuzzy neural networks. The proposed hybrid evolution-based quantum-behaved particle swarm optimization Takagi-Sugeno fuzzy neural networks (HEQPSO-TSFNNs) can improve the coding result around boundaries to enhance the coding efficiency of the lossless compression of images.

Keywords: Takagi-Sugeno fuzzy neural networks, Quantum-behaved particle swarm optimization, Image compression, adaptive annealing learning

1. Introduction

Image is usually the source of data, via different transmitting and compressing procedure, data receive different compressed results. Recently, some image compression techniques have already been proposed.[1,2] Artificial intelligence methods adopted to compress image are issued successively.

How to improve compress efficiency to reach the topic that the high-quality image stores and transmits is the research issue. Recently, some methods about losing the image code and compress have already been proposed successively.[3,4] However, it is computation consuming work. To overcome this problem, some authors utilize fuzzy logic concept and neural networks to design the non-linear predictor.[5,6]

Authors proposed Takagi-Sugeno fuzzy neural networks (TSFNNs) to carry out the non-linear predictor. The neural network of Takagi-Sugeno fuzzy type has parallel computing ability.[7] In this study, we adopt the hybrid evolution approach integrating quantum-behaved particle swarm optimization (HEQPSO), adaptive learning algorithm, and mutation operation to search optimal TSFNNs (HEQPSO-TSFNNs). The HEQPSO-TSFNNs are adopted to perform image compression.

2. Takagi-Sugeno Fuzzy Neural Networks

This study built an image compression system using TSFNNs. The appropriate Takagi-Sugeno fuzzy neural networks can improve the efficiency of image compression.

2.1. *Frame of TSFNNs*

In this article, we adopted TSFNNs to construct the predictor of image codes. The TSFNNs can perform the non-linear model which describes high complexity with less fuzzy rules.[8,9] The R_i fuzzy rule can be expressed as follows:

$$R_i \ : \ \textit{If} \ \ z_1 \in F_{1i} \ \ \textit{and} \ \ z_2 \in F_{2i} \ , \ \textit{then} \quad y_i = \alpha_i(\boldsymbol{A}_i\boldsymbol{x} + \boldsymbol{B}_i\boldsymbol{u}), \ i = 1,2,\ldots,9 \tag{1}$$

where z_1 and z_2 denoted input variables. F_{1k} and F_{2k} denoted fuzzy sets. $y_i \in R^1$ is the output of the *i*th fuzzy rule and $A_i \in R^{1\times 6}$, $x \in R^6$, $B_i \in R^{1\times 2}$, $u \in R^2$. The frame of TSFNNs is described as follows:

***Layer* 1** (input layer): This layer includes two inputs z_1 and z_2 which are transmitted to layer 2. z_1 and z_2 are defined as (2).

$$z = [z_1, z_2]^T = [x_1 - x_3, x_2 - x_3]^T \tag{2}$$

where z_1 and z_2 are represented horizontal offset and vertical offset, respectively.

***Layer* 2** (membership function layer): In this layer, the membership values specifying the degree to which an input value belongs to a fuzzy set is calculated. To describe the linguistic terms, Gaussian function representing fuzzy membership functions is adopted as

$$\mu_{ij}(z_i) = \exp\left(-\frac{(z_i - c_{ij})^2}{2s_{ij}^2}\right) \ \text{for} \ i = 1,2, j = 1,2,3 \,, \tag{3}$$

where c_{ij} and s_{ij} denoted the center and width for the *i*th input and the *j*th membership function.

***Layer* 3** (inference rule layer): Product inference method is used to determine the firing strength of each node. Each inference rule can be expressed as

$$\alpha_i = \mu_{1p} * \mu_{2q} \ \text{for} \ p = 1,2,3, q = 1,2,3 \,, \tag{4}$$

***Layer* 4** (output layer): Each node represents an individual output of the TSFNNs by using a simple weighted summation. The connection weight w_i of the *i*th neuron in inference rule layer is defined as follows:

$$w_i = A_i x + B_i u \tag{5}$$

where $x = [x_1, x_2, ..., x_6]^T$ denoted coding pixel. $A_i = [a_i^1, a_i^2, ..., a_i^6]^T$ can be regarded as predictor coefficients. $u = [u_1, u_2]^T = [x_1 - x_3, x_2 - x_3]^T$ is used for horizontal and vertical edge detection. $B_i = [b_i^1, b_i^2]^T$ is the weighting coefficients associated with the *i*th rule for the vector $\boldsymbol{u}$.

The output, y, of the predictor is a linear combination of the consequent part. The weighted summation of output y is given by

$$y_i = \sum_{i=1}^{9} \alpha_i w_i = \sum_{i=1}^{9} \alpha_i (A_i x + B_i u) \tag{6}$$

From (6), the output of the proposed TSFNNs-based predictor is evaluated in an un-normalized manner.

2.2. *Optimization of TSFNNs*

In the evolution procedure of designing optimal TSFNNs, a hybrid evolution technique is adopted to find appropriate parameters combinations. Each particle $\varphi_i(k)$ can be denoted as (7).

$$\varphi_i(k) = \lfloor A_i, B_i, c_{ij}, s_{ij} \rfloor \tag{7}$$

To adapt the parameters of the proposed TSFNNs during the coding process, a fitness function is defined as (8).

$$I = \sum_{j=1}^{n} |d - y|^2 \tag{8}$$

where d is the desired output and y is output of TSFNNs.

3. Hybrid Evolution-Based QPSO

In the PSO algorithm, each particle keeps trajectory of its coordinates in the problem space. The coordinate of each particle is related to its own best position (local best position) and the global best position achieved so far.

From the view of classical dynamics, to avoid explosion and guarantee convergence, particles must be bounded and fly in an attractive potential field. Clerc and Kennedy[10] have proved that if these coefficients are properly defined, the particle's position p_i will converge to the center of potential field, $pf^c = [pf_1^c, pf_2^c, \cdots, pf_n^c]$, and is defined as:

$$pf_i^c = \frac{(c_1 \cdot r_1 \cdot p_i^l + c_2 \cdot r_2 \cdot p^g)}{(c_1 \cdot r_1 + c_2 \cdot r_2)}, \ i = 1,2,\cdots,n \,. \tag{9}$$

where p_i^l and p^g are the best position of the *i*th particle and the global best position

Inspired by the behavior that particles move in a bounded state and preserve the global search ability, Sun et al.[11,12] proposed the QPSO algorithm. In the QPSO model, particles move in a quantum multi-dimensional space, the state of particles is usually depicted by a normalized wave function. That is, a single particle with *m* mass is subjected to the influence of a potential field in quantum space and the wave function of this particle is governed by the Schrödinger equation.[12] The solution of time-independent Schrödinger equation for this system in one dimensional space can be expressed as:[12]

$$p_i = pf_i^c \pm \frac{L}{2} \cdot \ln\left(\frac{1}{\lambda}\right), \qquad (10)$$

where λ is a random number uniformly distributed on [0, 1] and L is the characteristic length of delta potential well (called "Creativity" of particles) which specifies the search scope of a particle. In order to improve performance, Sun et al.[13] employ a mainstream thought point to evaluate the parameter. The mainstream thought point and can be expressed as the following forms:

$$mbest = \left[\sum_{i=1}^{n} \frac{p_{i,1}}{n}, \sum_{i=1}^{n} \frac{p_{i,2}}{n}, \cdots, \sum_{i=1}^{n} \frac{p_{i,n}}{n}\right],\ i = 1,2,\cdots,n, \qquad (11)$$

$$L = 2 \cdot \beta \left| mbest - p_i \right|, \qquad (12)$$

The creative coefficient β with adaptive annealing learning mechanism according to the change rate of optimal estimation has the form:

$$\beta = \beta_{\max} - \Delta\beta \cdot (\Delta fit)^{\gamma}, \qquad (13)$$

$$\Delta fit = \left| p^g - p_i^l \right|, \qquad (14)$$

where $\Delta\beta$ is step length of β, Δfit is the change rate of optimal estimation so far.

4. Experimental Results

In this article, the encoded image quality of HEQPSO-TSFNNs was evaluated using the peak signal-to-noise (PSNR) and computational time (CPU-T). The definition of PSNR is expressed as follows:

$$PSNR = 20\log\left(\frac{255}{RMSE}\right) \qquad (15)$$

where

$$RMSE = \sqrt{MSE} \qquad (16)$$

$$MSE = \frac{1}{N^2} \sum_{m,n=1}^{N} \left[f(m,n) - \hat{f}(m,n)\right]^2 \qquad (17)$$

and $f(m,n)$ and $\hat{f}(m,n)$ denote the original and reconstructed images, respectively.

Two typical 512×512 images named "LENA" and "BASKET" with pixel amplitude resolution of 8 bits are given to evaluate the HEQPSO-TSFNNs. Different codebooks with size 512 are implemented. We compare HEQPSO with TVACPSO (particle swarm optimization with time-varying acceleration coefficients).[14]

In experiments, the two algorithms are implemented and then executed 10 times. The image compression and reconstruction are shown in Figs. 1-2. Meanwhile, Table 1 showed the average PSNR and CPU-T values using HEQPSO-TSFNNs and TVACPSO-TSFNNs. From the Table 1, the superiority of the proposed HEQPSO-TSFNNs for image compression was confirmed.

Table1 The average values of PSNR and CPU-T using HEQPSO-TSFNNs and TVACPSO-TSFNNs.

image	Codbook size	TVACPSO-TSFNNs		HEQPSO-TSFNNs	
		PSNR	CPU-T(sec)	PSNR	CPU-T(sec)
LENA	256	28.82	72.69	29.02	64.80
BASKET		24.29	67.06	24.77	66.20
LENA	512	30.02	122.66	30.06	120.89
BASKET		25.34	110.31	25.79	105.35

Fig. 1. LENA image: (a) Original image, (b) Low frequency image, (c) Vector quantization image, (d) Reconstructed image.

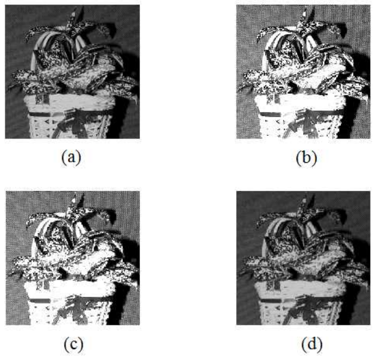

Fig. 2. BASKET image: (a) Original image, (b) Low frequency image, (c) Vector quantization image, (d) Reconstructed image.

Acknowledgements

This work was supported in part by the Ministry of Science and Technology, R.O.C., under grants MOST 105-2221-E-252-002.

References

1. H. Veisi and M. Jamzad, A complexity-based approach in image compression using neural networks, *Signal Processing*, **5**(2009) 82–92.
2. D. Salomon and A Concise, *Introduction to Data Compression*, (Springer, New York, 2008).
3. K. Sayood, *Introduction to Data Compression*, 4th edn. (Morgan-Kaufmann, New York, 2012).
4. L. J. Kau and Y. P. Lin, Least squares-based switching structure for lossless image coding, *IEEE Transactions on Circuits and Systems I*, **54**(7)(2007) 1529–1541.
5. S. Sahami and M. G. Shayesteh, Bi-level image compression technique using neural networks, *IET Image Processing*, **6**(5)(2012) 496–506.
6. B. Aiazzi, L. Alparone and S. Baronti, Fuzzy logic-based matching pursuits for lossless predictive coding of still images, *IEEE Transactions on Fuzzy Systems*, **10**(4)(2002) 473–483.
7. C. H. Lee and M. H. Chiu, Adaptive nonlinear control using TSK-type recurrent fuzzy neural network system, *Lecture Notes in Computer Science*, **4491**(2007) 38–44.
8. T. Takagi and M. Sugeno, Fuzzy identification of systems and its applications to modeling and control, *IEEE Transactions on System Man and Cybernetics*, **15**(1985) 116–132.
9. K. Tanaka and H. O. Wang, *Fuzzy Control Systems Design and Analysis: A Linear matrix inequality approach*, (John Wiley & Sons, Inc., New York, 2001).
10. M. Clerc and J. Kennedy, The particle swarm: explosion, stability, and convergence in a multidimensional complex space, *IEEE Transactions on Evolutionary Computation* **1** (2002) 68–73.
11. S. M. Mikki and A. A. Kishk, Quantum Particle Swarm Optimization for Electromagnetics, *IEEE Transactions on Antennas and Propagation*, **54** (2006) 2764–2775.
12. Y. Fu, M. Ding, and C. Zhou, Phase angle-encoded and quantum-behaved particle swarm optimization applied to three-dimensional route planning for UAV, *IEEE Transactions on Systems, Man and Cybernetics, Part A: Systems and Humans* **42** (2012) 511–526.
13. J. Sun, B. Feng and W.B. Xu, Particle swarm optimization with particles having quantum behavior, *In: Proceedings of IEEE Congress on Evolutionary Computation*, (2004) 325–331.
14. A. Ratnaweera, S. K. Halgamuge and H. C. Watson, Self-organizing hierarchical particle swarm optimizer with time-varying acceleration coefficients, *IEEE Transactions on Evolutionary Computation*, **8**(2004) 240–255.

MQPSO Algorithm Based Fuzzy PID Control for a Pendubot System

Li-Chun Lai
Computer and Intelligent Robot Program for Bachelor Degree, National Pingtung University

Yu-Yi Fu
Department of Automation Engineering, Nan Kai University of Technology
t098@nkut.edu.tw

Chia-Nan Ko
Department of Automation Engineering, Nan Kai University of Technology
t105@nkut.edu.tw

Abstract

In this study, a modified quantum-behaved particle swarm optimization (MQPSO) approach is proposed to design an optimal fuzzy PID controller for asymptotical stabilization of a pendubot system. In the fuzzy PID controller, parameters are determined by using MQPSO algorithm. The MQPSO method and other PSO methods are then applied to design an optimal fuzzy PID controller in a pendubot system. Comparing the simulation results, the feasibility of the MQPSO is verified.

Keywords: modified quantum-behaved particle swarm optimization, fuzzy PID controller, pendubot system

1. Introduction

Most industrial processes nowadays are still controlled by PID controllers. However, a conventional PID controller may have poor control performance for nonlinear and/or complex systems that have no precise mathematical models. In Keel et al[1] and Cervantes et al[2], how to tune the PID controller based on mathematical models is proposed, but complex mathematical computation is generally required in tuning procedures. For the methods in Whidborne and Istepanian[3] and Lin et al,[4] since the PID gains are fixed, the main disadvantage is that they usually lack in flexibility and capability.

Fuzzy controllers provide reasonable and effective alternatives for conventional controllers. Many researchers attempted to combine conventional PID controllers with fuzzy logic.[5] Despite the significant improvement of these fuzzy PID controllers over their classical counterparts, it should be noted that they still have disadvantages.

The PSO algorithm possesses the ability of high convergent speed, easily falling in some local optima is its fatal defect. Many researchers have presented revised PSO algorithms and obtained good results.[6] Another improvement on traditional PSO algorithm is quantum-behaved particle swarm optimization (QPSO).[7] However, in QPSO, particles fall into local optimal state in multimode optimization problems and cannot find any better state. To overcome the premature phenomenon in QPSO, a modified quantum-behaved particle swarm optimization (MQPSO) is proposed to find an optimal PID fuzzy controller. To show the flexibility and capability of the proposed method, an underactuated pendubot system is adopted as an illustrative example.

2. Fuzzy PID Controllers

In the proposed fuzzy PID controller, the input variables of the fuzzy rules are the error signals and their derivatives, while the output variables are the PID gains. Asymmetric Gaussian functions are used as the antecedent fuzzy sets in this paper. This means that input membership functions are represented as

$$X_k^{m_k}(x_k)=\begin{cases}\exp\left[-\left(\dfrac{x_k-\rho_k^{m_k}}{\sigma_{kl}^{m_k}}\right)^2\right] & if \quad x_k\le\rho_k^{m_k}\\ \exp\left[-\left(\dfrac{x_k-\rho_k^{m_k}}{\sigma_{kr}^{m_k}}\right)^2\right] & if \quad x_k>\rho_k^{m_k}\end{cases}$$

for $k=1,2,\ldots,4$, $1\le m_1\le n_1, 1\le m_2\le n_2, 1\le m_3\le n_3, 1\le m_4\le n_4$ (1)

where x_k represents the input linguistic variables, $\rho_k^{m_k}$, $\sigma_{kl}^{m_k}$, and $\sigma_{kr}^{m_k}$ denote the values of the centers, the left widths, and the right widths of the input membership functions, respectively. For the output membership functions, singleton sets are adopted. In the defuzzification process, Wang used the center of gravity method to determine the output crisp values.[8] Then, if the PID control law is used, the control signal is determined as

$$\begin{aligned}u(t)&=k_{p1}e_1(t)+k_{I1}\int e_1(t)dt+k_{D1}\dot{e}_1(t)\\&+k_{p2}e_2(t)+k_{I2}\int e_2(t)dt+k_{D2}\dot{e}_2(t)\end{aligned} \tag{2}$$

From the above description, one can find that the gains of the fuzzy PID controller are adaptive such that the controller should have more flexibility and capability than the conventional ones. The MQPSO method is proposed to search for the optimal values of these parameters simultaneously.

3. Modified Quantum Particle Swarm Optimization

From the view of classical dynamics, to avoid explosion and guarantee convergence, particles must be bounded and fly in an attractive potential field. Clerc and Kennedy[6] have proved that if these coefficients are properly defined, the particle's position p_i will converge to the center of potential field, $pf^c=[pf_1^c,pf_2^c,\cdots,pf_n^c]$, and is defined as:

$$pf_i^c=\frac{(c_1\cdot r_1\cdot p_i^l+c_2\cdot r_2\cdot p^g)}{(c_1\cdot r_1+c_2\cdot r_2)},\ i=1,2,\cdots,n. \tag{3}$$

where p_i^l and p^g are the best position of the ith particle and the global best position; c_1 and c_2 are cognitive and social constriction coefficients, respectively; r_1 and r_2 are random numbers between 0 and 1.

Inspired by the behavior that particles move in a bounded state and preserve the global search ability, Sun et al.[9] proposed the QPSO algorithm. In the QPSO model, the solution of time-independent Schrödinger equation for this system in one dimensional space can be expressed as:[10]

$$p_i=pf_i^c\pm\frac{L}{2}\cdot\ln\left(\frac{1}{\lambda}\right), \tag{4}$$

where λ is a random number uniformly distributed on [0, 1] and L is the characteristic length of delta potential well (called "Creativity" of particles) which specifies the search scope of a particle. The mainstream thought point and can be expressed as the following forms:[8]

$$mbest=\left[\sum_{i=1}^{n}\frac{p_{i,1}}{n},\sum_{i=1}^{n}\frac{p_{i,2}}{n},\cdots,\sum_{i=1}^{n}\frac{p_{i,n}}{n}\right],\ i=1,2,\cdots,n, \tag{5}$$

$$L=2\cdot\beta\left|mbest-p_i\right|, \tag{6}$$

The creative coefficient β with adaptive annealing learning mechanism according to the change rate of optimal estimation has the form:

$$\beta=\beta_{\max}-\Delta\beta\cdot(\Delta fit)^{\gamma}, \tag{7}$$

$$\Delta fit=\left|p^g-p_i^l\right|, \tag{8}$$

where $\Delta\beta$ is step length of β, Δfit is the change rate of optimal estimation so far. The mechanism of adaptive annealing learning can overcome the stagnation problem to accelerate the convergent speed.

4. An Simulation Example

4.1. *The Pendubot System*

The general dynamic model of underactuated mechanisms with m actuated joints from a total of n joint can be expressed as follows (Spong and Vidyasagar):[11]

$$\boldsymbol{M}(\boldsymbol{q})\ddot{\boldsymbol{q}}+\boldsymbol{C}(\boldsymbol{q},\dot{\boldsymbol{q}})\dot{\boldsymbol{q}}+\boldsymbol{G}(\boldsymbol{q})=\boldsymbol{\tau} \tag{9}$$

where $\boldsymbol{q}\in R^n$ is the position vector indicating link angles, $\boldsymbol{M}(\boldsymbol{q})$ denotes the inertia matrix, $\boldsymbol{C}(\boldsymbol{q},\dot{\boldsymbol{q}})\dot{\boldsymbol{q}}\in R^n$ is the vector of damping, coriolis, and centrifugal torques, $\boldsymbol{G}(\boldsymbol{q})\in R^n$ represents the gravitational term and $\boldsymbol{\tau}\in R^n$ is the vector of control torque which has $(n-m)$ zero components.

For the pendubot system in Fig. 1, let m_1 and m_2 denote the distributed mass of the actuated link (called link 1) and the unactuated link (called link 2), respectively. Meanwhile, let q_1 and q_2 denote the angles of the two links, l_1 and l_2 denote the lengths of the two links, and l_{1c} and l_{2c} denote the distances to the center of masses, respectively.

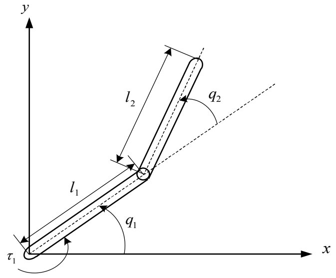

Fig. 1. Dynamics of the pendubot system

When the configuration is at equilibrium state; that is, pendubot balances at a state $\dot{q}=0$ and $\ddot{q}=0$, the following can be derived from (10).

$$(m_1 g l_{c1} + m_2 g l_1)\cos q_1 + m_2 g l_{c2}\cos(q_1+q_2) = \tau_1 \qquad (10)$$

$$m_2 g l_{c2}\cos(q_1+q_2) = 0 \qquad (11)$$

4.2. MQPSO tuning Fuzzy PID Controller

In the pendubot system, the desired value of $q_1(t)$ and $q_2(t)$ are denoted by q_{1d} and q_{2d}. If the PID control law is employed, then the input-output relation of the pendubot system is expressed as

$$\begin{aligned}\tau(t) &= k_{P1}e_1(t) + k_{I1}\int e_1(t)dt + k_{D1}\dot{e}_1(t)\\ &+k_{P2}e_2(t) + k_{I2}\int e_2(t)dt + k_{D2}\dot{e}_2(t)\end{aligned} \qquad (12)$$

where $e_1(t) = q_{1d} - q_1(t)$, $e_2(t) = q_{2d} - q_2(t)$, $\dot{e}_1(t) = \dot{q}_{1d} - \dot{q}_1(t)$, and $\dot{e}_2(t) = \dot{q}_{2d} - \dot{q}_2(t)$.

4.3. *Fitness*

In designing the fuzzy PID controller, the primary goal is to drive a pendubot system from the given initial state to the desired final state. The performance criteria can be included in the fitness as follows:

$$f = \int t\left[e_1^2(t) + e_2^2(t)\right]dt \qquad (13)$$

From the definition (14), the fitness value can be calculated to evaluate the performance of the fuzzy PID controller and a lower fitness value denotes a better performance.

5. Simulation Results

The parameters of the pendubot system shown in Fig. 1 are chosen as $m_1 = 2.0\,\text{kg}$, $m_2 = 1.5\,\text{kg}$, $l_1 = 0.3m$, $l_2 = 0.5m$, $l_{1c} = 0.15m$, $l_{2c} = 0.25m$, and $g = 9.8\ \text{m/s}^2$. The initial state and the desired final state of the pendubot system are $[q_1, \dot{q}_1, q_2, \dot{q}_2] = [-\pi/2,\ 0,\ 0,\ 0]$ and $[q_1, \dot{q}_1, q_2, \dot{q}_2] = [\pi/2,\ 0,\ 0,\ 0]$. Meanwhile, the input torque $\tau(t)$ of the motor is assumed to be within the range $[-10\ \text{Nm}, 10\ \text{Nm}]$.

In the proposed algorithm, the population size, the maximal iteration number, the crossover rate, and mutation rate are chosen to be 20, 10000, 0.8, and 0.2, respectively. Moreover, it is assumed that the values of the singletons of the output linguistic variables are all chosen as real numbers in the range $[-10, 10]$.

In PID tuning techniques, we proposed MQPSO method to design a fuzzy PID controller to asymptotically stabilize the pendubot and maintain the equilibrium state over all control processes. From Figs. 2 and 3, the illustration results demonstrate the proposed MQPSO fuzzy PID controller has good performance for asymptotical stabilization of the pendubot system.

6. Conclusions

In PID tuning techniques, the PID gains are difficult to obtain the optimal values for stabilizing a pendubot system. In this paper, we proposed MQPSO to design a fuzzy PID controller to asymptotically stabilize the pendubot and maintain the equilibrium state over all control processes. From the simulation results, one demonstrates the proposed fuzzy PID controller has good performance for asymptotical stabilization of the pendubot system.

Acknowledgements

This work was supported in part by the Ministry of Science and Technology, R.O.C., under grants MOST 105-2221-E-252-002.

References

1. L. H. Keel, J. I. Rego and S. P. Bhattacharyya, A new approach to digital PID controller design, *IEEE Transactions on Automatic Control* **48**(4)(2003) 687-692.
2. I. Cervantes, R. Garrido and A. R. Jose, et al, Vision-based PID control of planar robots, *IEEE Transactions on Mechatronics* **9**(1)(2004) 132-136.
3. J. F. Whidborne and R. S. H. Istepanian, Genetic algorithm approach to designing finite-precision controller structures, *IEE Processing of Control Theory Applications* **148**(5)(2001) 377-382.
4. L. Lin, H. Y. Jan and N. C. Shieh, GA-based multiobjective PID control for a linear brushless dc motor, *IEEE Transactions on Mechatronics* **8**(1)(2003) 56-65.

5. C. W. Tao and J. S. Taur, Robust fuzzy control for a plant with fuzzy linear model, *IEEE Transactions on Fuzzy Systems* **13**(1)(2005) 30-41.
6. A. Ratnaweera, S. K. Halgamuge, and H. C. Watson, Self-organizing hierarchical particle swarm optimizer with time-varying acceleration coefficients, *IEEE Transactions on Evolutionary Computation* **8** (2004) 240-255.
7. M. Clerc and J. Kennedy, The particle swarm: explosion, stability, and convergence in a multidimensional complex space, *IEEE Transactions on Evolutionary Computation* **1** (2002) 68-73.
8. L. X. Wang, *A Course in Fuzzy Systems and Control*, (Prentice-Hall, New Jersey, 1997).
9. J. Sun, B. Feng and W.B. Xu, Particle swarm optimization with particles having quantum behavior, *In: Proceedings of IEEE Congress on Evolutionary Computation*, 2004. pp. 325-331.
10. C. N. Ko, Y. M. Jau and J. T. Jeng, Parameter Estimation of Chaotic Dynamical Systems Using Quantum-behaved Particle Swarm Optimization Based on Hybrid Evolution, *Journal of Information Science and Engineering* **31**(2) (2015) 675-689.
11. M. W. Spong and M. Vidyasagar, *Robot dynamics and control*, (Wiley, New York, 1989.)

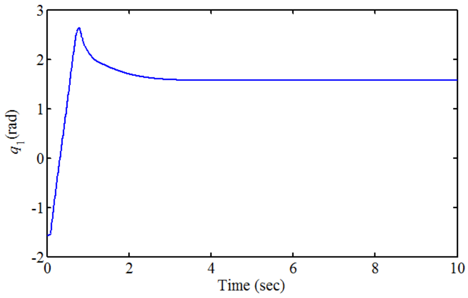

Fig. 2. Plot of angle $q_1(t)$ of the pendubot system.

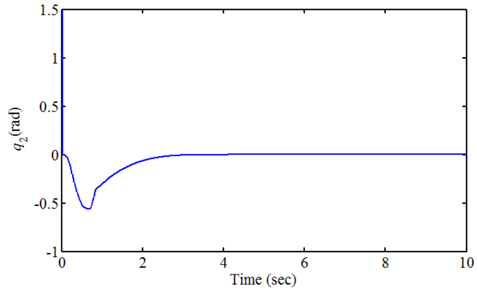

Fig. 3. Plot of angle $q_2(t)$ of the pendubot system.

A Sensor-less Ultra-high Speed Motor Driver

Chung-Wen Hung*, Yan-Ting Yu, Bo-Kai Huang and Wei-Lung Mao
Department of Electrical, National Yunlin University of Science and Technology
123 University Road, Section 3, Douliou, Yunlin 64002, Taiwan, R.O.C.
*wenhung@yuntech.edu.tw
www.yuntech.edu.tw

Abstract

An ultra-high speed motor is important in machine tools. A speed sensor-less ultra-high speed motor driver is proposed in this paper. Due to cost, only few drivers build up a closed-loop control, which could improve driver's performance. Therefore, a sensor-less speed estimation for ultra-high speed motors is developed. The design and implementation of the driver and feedback circuits are detailed in this paper. And experimental results show that the proposed system is workable.

Keywords: Ultra-high Speed Motor, Speed sensor-less Control, Motor Driver, VVVF Control

Introduction

Ultra-high speed motors are important in machine tools, and most motors are induction motor, IM, because of its high reliability and low cost. There are some studies discussed about driver method, such as variable voltage variable frequency, VVVF, and vector control; and some focused on control method including proportional-integrated (PI) control, fuzzy control and neural network. Due to cost, only few drivers build up a closed-loop control, which could improve driver's performance. Therefore, a sensor-less speed estimation for ultra-high speed motors is developed.

However, only few literatures discussed about ultra-high speed motors. [1] optimized the best driver efficiency based on the total harmonic distortion (THD) of motor current with auto-adjust driver voltage. In [2], an ultra-high speed soft switch inverter was developed to improve driver efficiency. Both proposed new driver methods. Conventional IM driver methods are open-loop scalar control, VVVF, due to easy implement. However, some papers tried to use closed-loop control. [3] used fuzzy rules to determine the VVVF command and increased efficiency. [4] proposed a slip frequency compensation method to decrease the speed error. [5] discussed two vector control methods: field orientation control, FOC, and direct torque control, DTC. The torque responds of both controls are better than scalar control. Complex calculations are necessary in above controls, so they are not suitable for ultra-high speed motor. For speed estimation, [6] described two methods. Model Reference Adaptive System, MRAS, could be used wider speed range but too sensitive to motor parameters. Another method, Least Square Method, LSM, calculated speed by iteration, but only suitable for narrow speed range. In this paper, an easier speed estimation method is used: the motor slip speed is calculated with the motor model, and then motor speed is estimated by taking induction magnetic field speed to minus the slip angle.

Slip speed estimation

The calculation of slip speed is based on rotor flux field orientation control. It can simplify the motor model by referring to rotor flux filed. The derivation is described as (1) - (5). The equation of calculating the slip, (4), can be derivate by substituting that flux on the q-axis is zero into (3). In (4), there is a variable flux on d-axis. It can be calculate by (5) using the current on d-axis.

$$\left.\begin{aligned} &\phi_r^r = L_m i_s^r + L_r i_r^r. \\ &\rightarrow i_r^r = \frac{1}{L_r}(\phi_r^r - L_m i_s^r). \end{aligned}\right\} \quad (1)$$

$$\left.\begin{aligned} &V_r^r = 0 = R_r i_r^r + \frac{d}{dt}\phi_r^r + j\omega_{sl}\phi_r^r. \\ &\rightarrow \frac{d}{dt}\phi_r^r = \frac{L_m}{L_r} R_r\, i_s^r - (\frac{R_r}{L_r} + j\omega_{sl})\phi_r^r. \end{aligned}\right\} \quad (2)$$

$$\left.\begin{aligned} &\frac{d}{dt}\phi_{dr}^r = \frac{Lm}{L_r} R_r i_{ds}^r - \frac{R_r}{L_r}\phi_{dr}^r + \omega_{sl}\phi_{qr}^r. \\ &\frac{d}{dt}\phi_{qr}^r = \frac{L_m}{L_r} R_r i_{qs}^r - \frac{R_r}{L_r}\phi_{qr}^r - \omega_{sl}\phi_{dr}^r. \end{aligned}\right\} \quad (3)$$

$$\left.\begin{aligned} &\frac{d}{dt}\phi_{qr}^r = \frac{L_m}{L_r} R_r i_{qs}^r - \frac{R_r}{L_r}\phi_{qr}^r - \omega_{sl}\phi_{dr}^r. \\ &\rightarrow 0 = \frac{L_m}{L_r} R_r i_{qs}^r - \omega_{sl}\phi_{dr}^r. \\ &\rightarrow \omega_{sl} = \frac{L_m R_r}{L_r}\frac{i_{qs}^r}{\phi_{dr}^r}. \end{aligned}\right\} \quad (4)$$

$$\left.\begin{aligned} &\frac{d}{dt}\phi_{dr}^r = \frac{L_m}{L_r} R_r i_{ds}^r - \frac{R_r}{L_r}\phi_{dr}^r + \omega_{sl}\phi_{qr}^r. \\ &\rightarrow \frac{d}{dt}\phi_{dr}^r = \frac{L_m}{L_r} R_r i_{ds}^r - \frac{R_r}{L_r}\phi_{dr}^r. \\ &\rightarrow \frac{\phi_{dr}^r}{i_{ds}^r} = \frac{L_m}{\frac{L_r}{R_r}s + 1}. \end{aligned}\right\} \quad (5)$$

where

ϕ_r^r	:	rotor flux refer rotor field	ϕ_{dr}^r	:	flux on the d-axis refer rotor field
ϕ_{qr}^r	:	rotor flux on the q-axis refer rotor field	R_r	:	rotor resistor
L_m	:	mutual inductance	L_r	:	rotor inductances
ω_{sl}	:	slip speed	V_r^r	:	rotor voltage refer rotor field
i_s^r	:	stator current on rotor flux	i_r^r	:	rotor current refer rotor field
i_{ds}^r	:	stator current on d-axis refer rotor field flux	i_{qs}^r	:	stator current on q-axis refer rotor field flux

The block diagram of estimator the slip speed is shown in Fig 1. The $\theta_{\phi r}$ is calculated by (6). And the σ is defined as (7). In Fig 1, (4) and (5) are performed to estimate slip speed and the rotor flux on d-axis. The inputs of these two blocks are stator current referring the rotor flux.

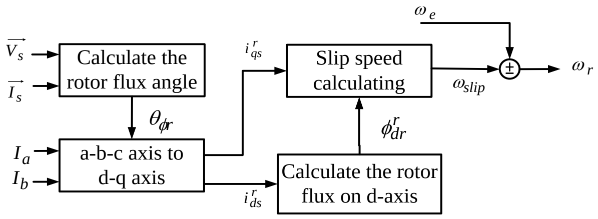

Fig 1. Block of slip speed estimator

$$\phi_r = \int \frac{L_r}{L_m}(V_s - R_s i_s - \sigma L_s \frac{d}{dt} i_s)dt. \quad (6)$$

$$\sigma = 1 - (\frac{L_m^2}{L_s L_r}). \quad (7)$$

where

ϕ_r	:	rotor flux	V_s	:	stator voltage
i_s	:	stator current	L_s	:	stator inductance

Scalar control

Scalar control drives motor by suitable waveform. In Fig 2, the curve of speed to voltage for a 200Krpm motor is provided by the motor manufactory. To drive motor in 30Krpm, the inverter should provide a three-phase sinusoidal 57 volts and 500Hz wave. However, the real rotor speed is different to the driving speed due to slip speed. Therefore, a PI controller is used in the proposed system to compensate the speed error caused by slip speed. As shown in Fig 3, the input of controller is the speed error, and the output is the index of the VVVF table to set inverter.

Motor parameter measurement

The IM's electric parameters are a key in slip speed estimation. Three parameter measuring tests are used in this paper. First, DC test is used to measure the stator resistor. Second, stall test could measure the sum of stator and rotor resistor, and the sum of stator and rotor leakage inductance. Then the rotor resistor can be got, and the stator and rotor leakage inductances, L_{ls} and L_{lr}, are assumed equal. Third, no load test is adopted for the stator inductance, and then the mutual inductance could be derived. A virtual stall test is adopted, because a traditional stall test is not convenient due to extra stalling equivalent. Fig 4 is the wiring diagram of virtual stall test.

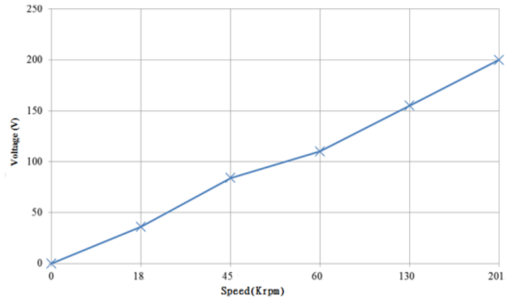

Fig 2. Speed-Voltage characteristic curve of 200Krpm motor

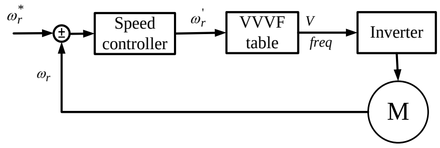

Fig 3. Block of scalar control

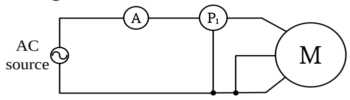

Fig 4. Wiring diagram of virtual stall test

In this paper, two ultra-high speed motors are installed in experiments. The parameters of 200Krpm and 300Krpm motors are measured and shown in table 1.

Table 1. Parameters of 200Krpm and 300Krpm motor

Motor	R_S	L_{ls}	R_r	L_{lr}	L_m
200K	1Ω	0.43mH	2.84Ω	0.43mH	5.22mH
300K	1.78Ω	0.21mH	4.33Ω	0.21mH	2.99mH

System architecture and hardware implementation

The control block diagram of system is shown in Fig 5. Scalar control is used in the speed controller. A PI controller is adopted to create the speed command which is the index of the voltage-frequency curve. Here, lookup table and interpolation method is used to index the suitable voltage and frequency commands for the inverter. And, the feedback speed is calculated by speed of synchronization field and the slip speed computed from current and voltage.

Fig 6 presents the system architecture diagram. The feedback circuit is used to sense the motor current and DC BUS states for speed estimation. The microcontroller is applied to speed estimation and speed control, and generate driving signals for the inverter circuit. The inverter circuit converts DC voltage to AC driving waveform.

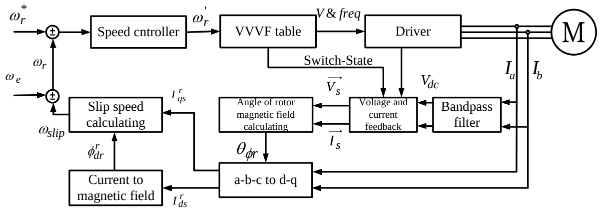

Fig 5. Control block diagram of system

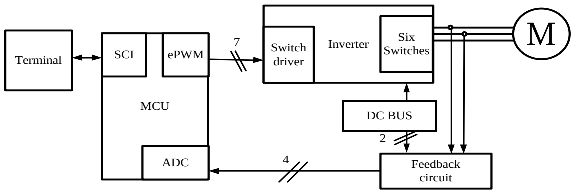

Fig 6. System architecture diagram

Fig 7 is the photo of the system proposed in this paper. At upper left corner is TMS320F28335, lower left corner is an isolated power board, middle is inverter, lower middle is the current feedback circuit and lower right corner is the DC BUS feedback circuit.

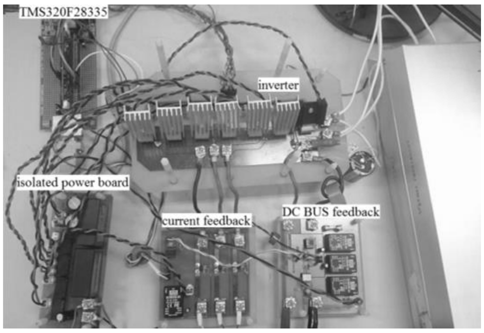

Fig 7. System photo

Experimental results

Two experiments are shown in this paper: step and ramp acceleration. Drilling function is performed when the motor achieves the rated speed, but no more speed control, due to the fast working moment. Controller is mainly used to accelerate. The experimental power supply is limited, so step range and ramp acceleration of

Table 2. Step and ramp acceleration of 200Krpm motor

	Step			Ramp acceleration		
Speed command(rpm)	40000	50000	60000	100000	120000	160000
Improved speed error(rpm)	44	94	132	940	1600	4900
Percentage error(%)	0.11	0.18	0.22	0.94	1.33	3.06
Improved stability time(s)	0.281	0.228	X	0.34	0.9	1.43

speed are limited. Fig 8 shows the experimental results under 100Krpm ramp command.

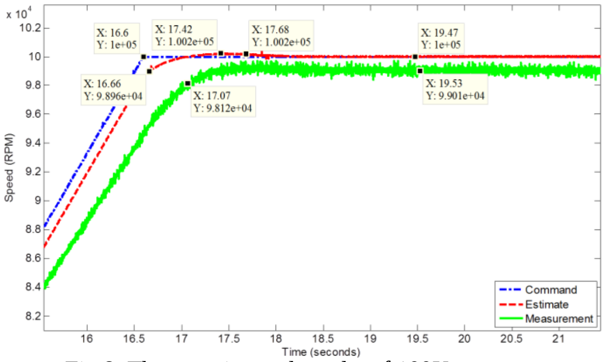

Fig 8. The experimental results of 100Krpm ramp

The experimental results are shown in table 2, and the improved numbers of the proposed controller are compared with an open-loop driver. The speed error is reduced and proportional to speed command, and then stability time is improved in 0.2 to 1 seconds. Note, proposed controller experimental results of the 60Krpm step are not shown in this table, because the required inrush current is over the capability of power supply.

In order to verify the proposed method is suitable for different motors, the other motor, rated 300Krpm, is adopted in the experiment. The speed errors of different commands in a 200Krpm motor are shown in Fig 9 and 300Krpm motor in Fig 10. Though the errors of 300Krpm motor are bigger than 200Krpm'motors, but the trends in two figures are the same. And error rate of 200Krpm motor is low than 1.5%, the same as 300Krpm motor is low than 3.5%.

Conclusion

As shown in experimental results, the motor with the proposed ultra-high speed motor driver can fast run stability. Though speed error is proportional to speed command, speed estimator can effectively estimate motor speed and react load fluctuation, and speed error rate is low than 1.5%. Closed-loop controller actually improves system responding time by low cost feedback circuit. The controller proposed in this paper is also suitable for different motors.

Acknowledgment:

This work is partially supported by the Ministry of Science and Technology, ROC, under contract No. MOST 105-2221-E-224-024 and 104-2622-E-224-016 -CC3.

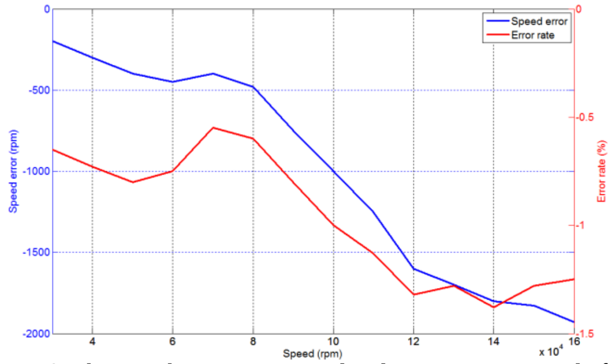

Fig 9. The error between estimated and measurement speed of 200Krpm motor

Fig 10. The error between estimated and measurement speed of 300Krpm motor

Reference

[1] C. H. Yang, "The automatically switching hybrid modulation driver for an ultra-high speed motor", *National Digital Library of Theses and Dissertations* in Taiwan, 2013.

[2] B. F. Li, "The Research and Implementation of an Ultra-high Speed Soft Switch Inverter", *National Digital Library of Theses and Dissertations* in Taiwan, 2014.

[3] J. Li and Y. R. Zhong, "Efficiency Optimization of Induction Machines Based on Fuzzy Search Controller", *IEEE International Conference on Machine Learning and Cybernetics*, Vol. 4, pp. 2518 – 2522, Aug. 2005.

[4] M. Tsuji, S. Chen, S. Hamasaki, X. D. Zhao and E. Yamada, "A Novel V/f Control of Induction Motors for Wide and Precise Speed Operation", SPEEDAM 2008 International Symposium on Power Electronics, Electrical Drives, *Automation and Motion*, pp. 1130 - 1135, Jun. 2008.

[5] J. A. Santisteban and R. M. Stephan, "Vector Control Methods for Induction Machines: An Overview", *IEEE Transactions on Education*, Vol. 44, pp. 170 – 175, Aug. 2002

[6] M. Bodson and J. Chiasson, "A Comparison of Sensorless Speed Estimation Methods for Induction Motor Control", *American Control Conference on Proceedings*, Vol. 4, pp. 3046 - 3081, May 2002

Android-Based Patrol Robot Featuring Automatic Vehicle Patrolling and Automatic Plate Recognition

Chian C. Ho*, Shih-Jui Yang, Jian-Yuan Chen, Chang-Yun Chiang, and Hsin-Fu Chen
Department of Electrical Engineering, National Yunlin University of Science and Technology
Douliou, Yunlin 64002, Taiwan
*E-mail: futureho@yuntech.edu.tw**
www.yuntech.edu.tw

Abstract

This work develops an Android-based patrol robot featuring Automatic Vehicle Patrolling (AVP) and Automatic Plate Recognition (APR). The AVP feature integrates 3 novel methods, wheel-wheelcover-based AdaBoost wheel detection, contour-wheel-oriented vehicle approaching, and Ad-Hoc-based remote motion control. The APR feature integrates 4 novel methods, Wiener-deconvolution vertical edge enhancement, AdaBoost plus vertical-edge plate detection, vertical-edge horizontal-projection histogram-segmentation stain removal, and customized optical character recognition. Implementation results show the vehicle detection rate and plate recognition rate of the Android-based patrol robot are over 96% and over 94%, respectively, under various scene conditions. On the other hand, the average execution time of AVP and APR of the Android-based patrol robot takes at most 8 second per round and at most 0.8 second per frame, respectively.

Keywords: Android, robot, automatic vehicle patrolling, automatic plate recognition.

1. Introduction

With the ever-increasing demand of anti-terrorism and public security worldwide, the global law enforcement has severely been fighting against stolen vehicles or vehicles hung with stolen vehicle plates so far. Because these vehicles, both automobiles and motorcycles, are most likely used for terrorist activities or criminal vehicles. In addition, these vehicles are always parking in or running from unimaginable corners. It is necessary for the global law enforcement to carry out the vehicle plate investigation anywhere, anytime, even under exhausted manpower condition. Therefore, the automatic patrol robot equipped with Automatic Plate Recognition (APR) functionality can satisfy the growing demand and gain the expanding attention.

On the other hand, global digital video surveillance manufacturers are unexceptionally interested in the mobile robotic APR technology so as to evolve the existing fixed APR systems to portable embedded ones

Fig. 1. Mechanism of Android-based patrol robot featuring AVP and APR.

or mobile robotic ones. Thus this work develops the Android-based patrol robot offering accurate APR and reliable Automatic Vehicle Patrolling (AVP) motion control for this emerging demand. It is composed of an Android-based smartphone platform and an Ad-Hoc-based mobile robot as shown in Fig. 1, and the Android-based smartphone platform as the host is steadily mounted onto the Ad-Hoc-based mobile robot.

In this work, the motion control of the Ad-Hoc-based mobile robot is actually steered by the Android-based smartphone platform through peer-to-peer Ad Hoc networking, while the AVP feature is routinely began by the Ad-Hoc-based mobile robot. As soon as the Android-based smartphone platform detects the vehicle contour, vehicle wheel, or vehicle plate, the Ad-Hoc-based mobile robot will be remotely controlled to approach the vehicle and further approach the plate. As for the APR feature, it is still performed by the Android-based smartphone platform, especially by the built-in auto-focus camera and low-power embedded processor, for long-endurance and cost-effective requirements. Besides, it is also a critical consideration that plenty of open-source computer vision libraries, like OpenCV Tesseract OCR, etc., are increasingly ported and supported on Android operating system [1].

This work can meet both specifications of portable embedded and mobile robotic APR systems, and it can be further transformed into any ubiquitous and diverse devices. This work not only can be applied to stolen vehicle plate tracking and roadside inspection, but also can be extensively applied to parking lot patrolling, container logistic investigation, or automotive manufacturing management.

Fig. 2 illustrates the overall algorithm flowchart of the developed Android-based patrol robot featuring AVP and APR. The flowchart in Fig. 2 is made up of 2 main stages. 1) Automatic Vehicle Patrolling (AVP) and 2) Automatic Plate Recognition (APR). Referring to Fig. 2, the organization of this paper is as follows. Sections 2 and 3 describe AVP feature and APR feature, respectively, in detail. Here, Section 2 is divided into 3 subsections: wheel-wheelcover-based AdaBoost wheel detection, contour-wheel-oriented vehicle approaching, and Ad-Hoc-based remote motion control. Section 3 is divided into 4 subsections: Wiener-deconvolution vertical edge enhancement, AdaBoost plus vertical-edge plate detection, vertical-edge horizontal-projection histogram-segmentation stain removal, and customized

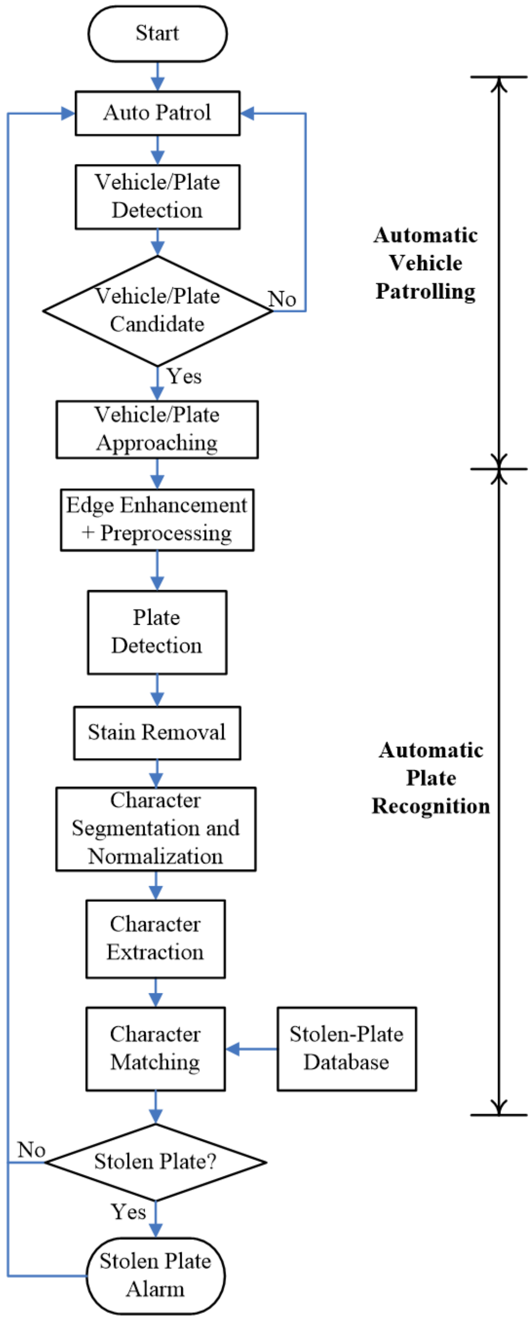

Fig. 2. Algorithm flowchart of Android-based patrol robot featuring AVP and APR.

Optical Character Recognition (OCR). Implementation results about the vehicle detection rate and the plate recognition rate improved by these proposed methods in Sections 2 and 3 are also exhibited, and so is the execution time of the overall implementation. Finally, Section 4 draws conclusions and future work.

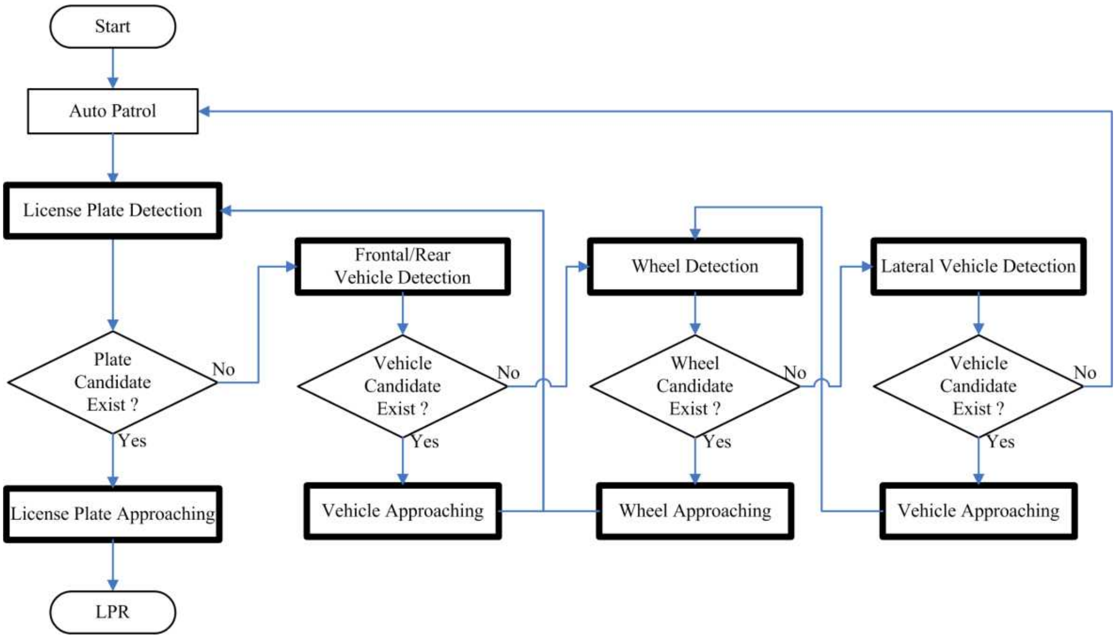

Fig. 3. Algorithm flowchart of developed AVP feature.

2. Automatic Vehicle Patrolling Feature

As shown in upper half part of Fig. 2, in the stage of AVP, autonomous patrol is initially launched by the mobile robot according to the predefined patrolling point and path planning. Next, the Android-based smartphone platform keeps working on the vehicle/plate detection to search the vehicle/plate candidates. Once one or more vehicle/plate candidates are found, the Android-based smartphone platform will evaluate the relative distance and the visual pose angle of the nearest vehicle/plate candidate, and will drive the mobile robot through Ad Hoc networking to approach the nearest vehicle/plate until the plate is close enough, that is, the character on the plate is clear enough to be recognized.

Because reliable AVP is the fundamental step toward the developed Android-based patrol robot, especially when vehicle/plate patrolling, searching, and approaching are proceeding under various conditions of illumination, scene, perspective, etc. This work proposes 3 novel methods for vehicle/plate detection and approaching, and implements peer-to-peer Ad Hoc networking mode for remote motion control [2]. The proposed 3 novel methods are summarized as follows.

2.1. *Wheel-wheelcover-based AdaBoost wheel detection*

This work develops an accurate and reliable AVP to approach the vehicle and further approach the plate closely enough, as shown in Fig. 3, whether the Android-based patrol robot is located on the frontal/rear side of the vehicle or lateral side of the vehicle. When the robot is on the frontal/rear side of the vehicle, the plate detection or frontal/rear vehicle detection is easy and straightforward. However, when the robot is on the lateral side of the vehicle, no plate can be detected, and lateral vehicle detection depends upon nothing but ambiguous features of wheel or lateral vehicle contour. Thus, this work proposes Wheel-wheelcover-based AdaBoost wheel detection based on wheel feature and unique wheelcover feature, and verifies the proposed wheel detection achieves better detection rate than conventional wheel detection methods, like Hough Transform wheel detection [3]-[5], Histogram of Oriented Gradients (HOG) wheel detection [6], [7], and AdaBoost wheel detection [8], [9].

2.2. *Contour-wheel-oriented vehicle approaching*

Once the Android-based patrol robot can smoothly detect vehicle plate or frontal/rear vehicle contour, the robot simply moves ahead to approach the vehicle/plate. But, if the Android-based patrol robot detects the vehicle wheel/wheelcover or lateral vehicle contour, it must move ahead and turn around to face the frontal/rear vehicle side, and then must go through the aforementioned steps of the frontal/rear vehicle side again for approaching the vehicle and further approaching the plate, illustrated as shown Fig. 3.

2.3. *Ad-Hoc-based remote motion control*

At first, the WiFi driver of the Android-based smartphone platform is elaborately switched from Access Point mode to Ad Hoc mode. Then, the WiFi mode of the mobile robot is also switched from Access Point mode to Ad Hoc mode, and makes the mobile robot log into the Ad Hoc network whose Service Set IDentifier (SSID) is broadcasted by the Android-based smartphone platform. Finally, after the mobile robot registers an IP address to the Ad Hoc networking gateway on the Android-based smartphone platform successfully, the Android-based smartphone platform can request any motion control commands to steer the Ad-Hoc-based mobile robot remotely.

3. Automatic Plate Recognition Feature

After approaching some nearest vehicle and plate quite closely, APR feature is engaged in detecting and recognition the vehicle plate, as shown in lower half part of Fig. 2. this work proposes 4 novel methods, Wiener-deconvolution vertical edge enhancement, AdaBoost plus vertical-edge plate detection, vertical-edge horizontal-projection histogram-segmentation stain removal, and customized OCR, for better plate detection rate and character recognition rate. These 4 novel methods are clarified in order as below.

3.1. *Wiener-deconvolution vertical edge enhancement*

In general, most vehicle plate detection systems make use of the vertical edge density feature to discriminate the vehicle plate candidate region from the background of the scene image, because most characters on the vehicle plate have higher vertical edge density than the background. If some vertical edge enhancement preprocessing method is put on the original scene image in advance, vehicle plate detection will work better. Because Wiener convolution is originally used for image blurring, this work proposes to deconvolute the scene image with a horizontal-direction Wiener filter for vertical edge enhancement. The experimental result shows the vertical edge density and intensity of the vehicle plate are strengthened by a horizontal-direction Wiener deconvolution method, and those of the background, like radiator grilles, are simultaneously weakened.

3.2. *AdaBoost plus vertical-edge plate detection*

Although AdaBoost cascaded classifier with proper and adequate training of vehicle plate patterns is almost feasible for exact plate detection, this work proposes two auxiliary methods to make plate-based AdaBoost plate detection more accurate and more reliable under various scene conditions. One method is character-based AdaBoost plate verification to filter out the false positive outcomes of plate-based AdaBoost plate detection by polling, and the other method is vertical-edge-based alternative plate detection which is activated when no plate candidate can be found by plate-based AdaBoost plate detection and character-based AdaBoost plate verification.

3.3. *Vertical-edge horizontal-projection histogram-segmentation stain removal*

The localized vehicle plate candidate is inevitably accompanying with some border stains, so the subsequent OCR procedure tends to misunderstand border stains as characters and is prone to make recognition mistakes. It is easier to remove interior stains on the vehicle plate because interior stains are similar to salt, and pepper noise can be easily eliminated by mathematical morphology. But it is quite harder to remove trapezoid border stains residing at the right side and left side, and interlinking border stains at the upside and downside. In this work, vertical-edge horizontal-projection histogram-segmentation stain removal based on fill-in and connected component labeling is proposed to effectively remove trapezoid border stains at the right side and left side, and interlinking border stains at the upside and downside.

3.4. *Customized optical character recognition*

Because Tesseract OCR open-source library is originally used for OCR of general documents, not for OCR of vehicle plates, this work elaborately retrains the font characteristics of each character on real Taiwanese vehicle plate into the character dictionary of Tesseract OCR [10]. Then, through Java Native Interface (JNI) technique, this work ports vehicle-plate-customized

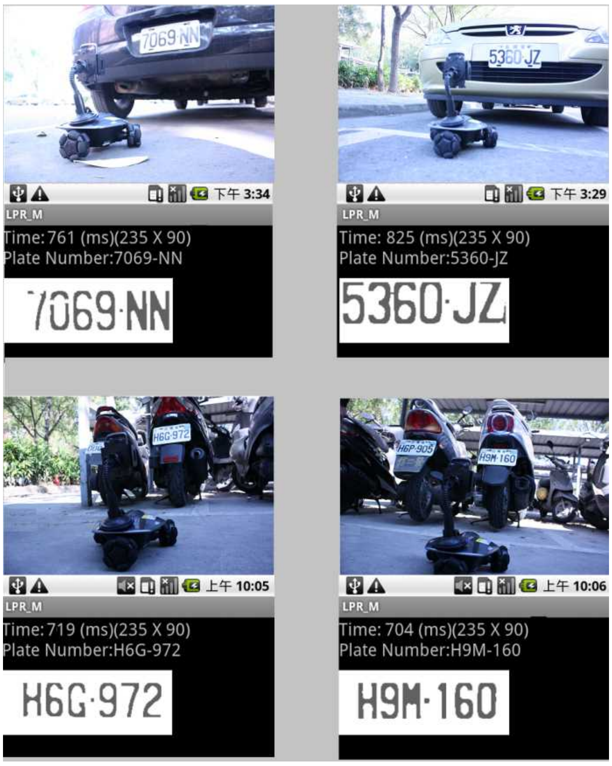

Fig. 4. field trial about OCR results of the developed Android-based patrol robot featuring AVP and APR.

Tesseract OCR onto the Android-based smartphone platform as a plug-in module of Android operating system. In addition, this work also proposes to adjust hybrid-pitch character segmentation of Tesseract OCR for the font characteristics of Taiwanese vehicle plate.

Fig. 4 demonstrates the field trial about OCR results of the developed Android-based patrol robot featuring AVP and APR. In Fig. 4, the upper row demonstrates AVP and APR results of automobile cases, and the lower row demonstrates those of motorcycle cases. The field trial result with the document recognition rate of over 99% and the plate recognition rate of over 98% verifies that Tesseract OCR can perform well on APR in Taiwan or elsewhere by customizing its character dictionary elaborately. Besides, Fig. 4 also demonstrates the vehicle detection rate and plate recognition rate of the Android-based patrol robot are over 96% and over 94%, respectively, under various scene conditions. On the other hand, the average execution time of AVP and APR of the Android-based patrol robot takes at most 8 second per round and at most 0.8 second per frame, respectively. Here, the clock frequency of the processor on Android-based smartphone platform is simply 1 GHz.

4. Conclusions and Future Work

In this work, the Android-based patrol robot featuring mobile AVP and real-time APR already can work well. In the near future, more smart AVP features and efficient APR features will continuously be developed and integrated into the Android-based patrol robot.

References

1. Google, Android Developers, [Online]. Available: http://developer.android.com/index.html
2. WowWee, API Specification for Rovio Version 1.˘3, [Online]. Available: http://breckon.eu/toby/teaching/dip/rovio/Rovio_API_Specifications_v1.3.pdf
3. F. Tan, L. Li, B. Cai and D. Zhang, Shape Template Based Side-View Car Detection Algorithm, *Proceedings of International Workshop on Intelligent Systems and Applications (ISA)*, pp. 1-4, 2011.
4. V. Vinoharan, A. Ramanan and S. R. Kodituwakku, A wheel-based side-view car detection using snake algorithm, *Proceedings of IEEE International Conference on Information and Automation for Sustainability*, pp. 185-189, 2012.
5. G. Xu, J. Su, H. Pan and D. Zhang, A Novel Method for Wheel Rim Recognition, *Proceedings of International Symposium on Electronic Commerce and Security*, pp. 1051-1054, 2008.
6. R. Brehar, S. Nedevschi and L. Dăian, Pillars detection for side viewed vehicles, *Proceedings of IEEE International Conference on Intelligent Computer Communication and Processing*, pp. 247-250, 2010
7. L. Liu, F. Zhou and Y. He, Vision-based fault inspection of small mechanical components for train safety, *IET Intelligent Transport Systems*, vol. 10, no. 2, pp. 130-139, Feb. 2016.
8. D. Dooley, B. McGinley, C. Hughes, L. Kilmartin, E. Jones and M. Glavin, A Blind-Zone Detection Method Using a Rear-Mounted Fisheye Camera With Combination of Vehicle Detection Methods, *IEEE Transactions on Intelligent Transportation Systems*, vol. 17, no. 1, pp. 264-278, Jan. 2016.
9. L. Liu, F. Zhou and Y. He, Automated Visual Inspection System for Bogie Block Key Under Complex Freight Train Environment, *IEEE Transactions on Instrumentation and Measurement*, vol. 65, no. 1, pp. 2-14, Jan. 2016.
10. Tesseract OCR, Core Developers, [Online]. Available: http://code.google.com/p/tesseract-ocr/

Adaptive CMAC Filter for Chaotic Time Series Prediction

Wei-Lung Mao, Suprapto, Chung-Wen Hung
Department of Electrical Engineering and Graduate School of Engineering Science and Technology, National Yunlin University of Science and Technology, No. 123, University Road, Section 3, Douliou, Yunlin 64002, Taiwan, ROC.

E-mail: wlmao@yuntech.edu.tw, d10210035@yuntech.edu.tw, wenhung@yuntech.edu.tw
www.yuntech.edu.tw

Abstract

Chaotic signal is a natural phenomenon exhibiting in every condition of dynamical system. Chaotic signals are almost unpredictable, noise-like, uncertain and irregular behavior, yet they are very useful in numerous applications of signal processing. Due to their behaviors, the quest of a good method to model and analyze of the chaotic signal is very crucial. This paper present a novel strategy to analyze chaotic signal using the cerebellar model articulation controller (CMAC) network combined with evolutionary algorithms (EAs) such as biogeography-based optimization (BBO), genetic algorithm (GA) and particle swarm optimization (PSO). Mackey-glass chaotic signal time series is tested and demonstrated by the conventional and the proposed algorithms. They are compared with each other to determine the optimal filtering and prediction. The result demonstrated that the CMAC combined with EAs could filter, predict and estimate chaotic signal time series well rather than the conventional methods. The best result of the algorithms tested for chaotic signal time series is the CMAC combined with BBO algorithm.

Keywords: Chaotic signal, Mackey-glass time series, signal prediction, evolutionary algorithm (EA), biogeography-based optimization (BBO), cerebellar model articulation controller (CMAC).

1. Introduction

A chaotic signal is a natural phenomenon exhibiting in every condition of a dynamical system. The chaotic signal has become an attractive issue for many researchers in recent year. Some methods have been developed to obtain the meaning of the chaotic signal. One of the common techniques to predict the value of the chaotic signal is time delays and an embedding dimension [1]. To realize this method, a predictor design involves a neural network to obtain a better result.

A kind of neural networks imitating the human cerebellum is cerebellar articulation model controller (CMAC). The CMAC has advantages, such as low computation, good generalization capability and easy implementation [2]. Due to some advantages, the CMAC can be applied as a filter to predict the chaotic signal series. A time windowing strategy called Time-division CMAC or CMAC filter is an appropriate to tackle the prediction problem. The CMAC filter is a modified classical CMAC networks for predicting chaotic signal series [3].

To achieve a good prediction result, training process is an important part in the neural network. Some evolutionary algorithms (EAs) are employed to enhance the learning system capability. There are biogeography-based optimization (BBO), genetic algorithm (GA) and particle swarm optimization (PSO).

2. CMAC Filter

The structure of the CMAC, comprises two input states, association cells ($\boldsymbol{a}_i$), memory cells, and an output state (y). In Figure 1(a), the simple example shows a memory structure of the CMAC, which each layer is mapped into three blocks. Each layer has nine areas labeled as hypercube Aa, Ab, Ac, …, and Cc. The hypercubes would be used as memory cell, which the active cell is addressed by an association cell. The actual CMAC output comes from the summation of the weights stored in the memory of each layer.
The structure of the CMAC filter design involves some basic CMACs. The prediction output can be obtained by the equation (1):

$$y(i) = \mathbf{a}_i^T \mathbf{w} = \sum_{i=1}^{d} \sum_{j=1}^{M_d} a_{ij} w_{ij} \tag{1}$$

where M_d is the memory size, $\boldsymbol{w}$ is the weight vector, and d is the number of delays. The equation for the learning phase can be written as follows:

$$\mathbf{w}(i) = \mathbf{w}(i-1) + \frac{\beta}{d * N_e} \mathbf{a}_i (y_{des} - y(i)) \tag{2}$$

where y_{des} is the desired output, $y(i)$ is the actual output, $\boldsymbol{w}(i)$ is the weight vector, β is the learning rate, and N_e is the number of activated memories.

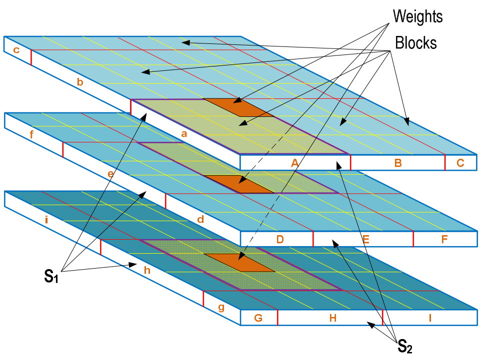

(a)

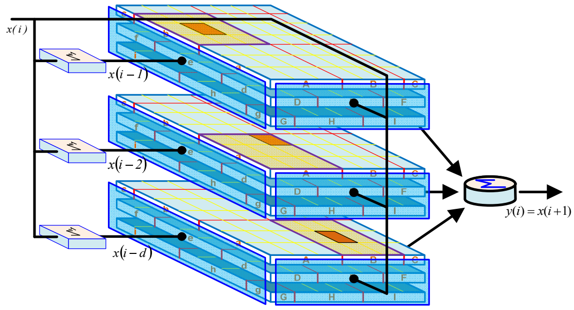

(b)

Figure 1. (a) memory structure of the CMAC, (b) memory structure of CMAC filter

3. Evolutionary Algorithms (EAs)

3.1. *Biogeography-based Optimization (BBO)*

Biogeography is the study of biology as it relates to the geographical distribution of species over time and space. The emigration rate (μ) and the immigration rate (λ) determine the BBO algorithm. In Figure 2(a), the BBO depicts emigration and immigration curves by straight lines. The equilibrium point of species S_0 occurs when the immigration and emigration rates are equal. It occurs temporarily, as conditions continually vary. The equilibrium point of migration can be written by equation (3):

$$\lambda_k = \mu_k . \tag{3}$$

The immigration and emigration rates can be written by equation (4) and (5):

$$\mu_k = \frac{Ek}{a} \tag{4}$$

$$\lambda_k = I\left(1 - \frac{k}{a}\right) \tag{5}$$

where I is the maximum immigration rate, E is the maximum emigration rate, k is the number of species, and a is the largest number of species. The mutation rate can be expressed as follows:

$$m(s) = m_{max}\left(1 - \frac{P_s}{P_{max}}\right) \tag{6}$$

where m_{max} is the value defined by the user, P_s is the mutation probability, and P_{max} = argmax(P_n) for n=1,2,…,N. A species living in a habitat can be calculated using P_s , which changes time t to time (t+Δt), and is given as follows:

$$P_s(t+\Delta t) = [P_s(t)(1-\lambda_s \Delta t - \mu_s \Delta t)] + [P_{s-1} - (t)\lambda_{s-1} - \Delta t] + [P_{s+1} - (t)\mu_{s+1} - \Delta t] \tag{7}$$

where $P_s(t)$ is the probability that a habitat contains S species, S is the species at time t without migration, S-1 is the species at time t with one species immigrating, and S+1 is the species at time t with one species emigrating.

3.2. *Genetic Algorithms (GAs)*

Genetic algorithms are population-based modeled by biological evolution based on Charles Darwin's theory of natural selection. The principle of the GA is the movement from one population of chromosomes to a new population using crossover, mutation, and selection [4]. To find a good solution, GA involves the chromosomes represented by strings of bits, the manipulation operation string, and the selection to their fitness. In one evolution cycle of the genetic algorithm, there are some steps such as evaluating the fitness of all the individuals, creating a new population, replacing the old population and iterating again using the new population.

The crossover operation is swapping one segment of one chromosome with the segment on another chromosome at a random position. The mutation can be obtained by flipping the selected bits randomly and usually has small probability. The objective of mutation is to increase the various populations. Fitness reproduction or elitism is achieved by the selection of an individual in a population. Diagram of crossover and mutation can be depicted in Figure 2(b) and 2(c).

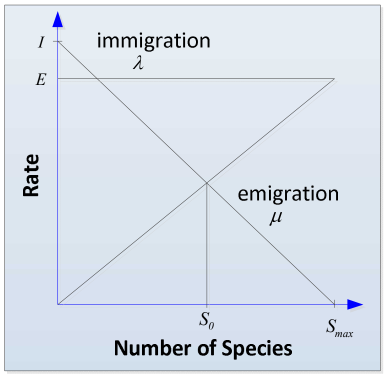

(a)

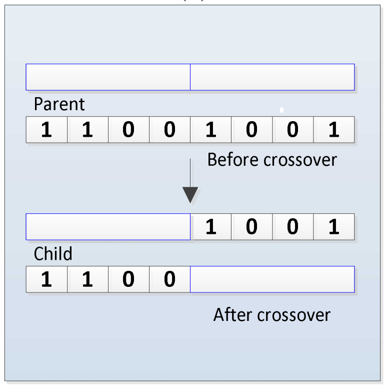

(b)

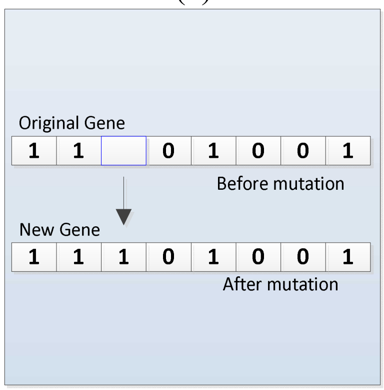

(c)

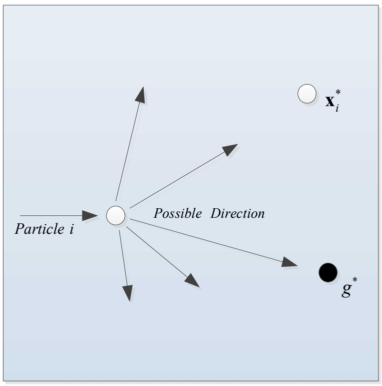

(d)

Figure 2. (a).Migration curve of species of a single habitat; (b).Diagram of crossover; c).Diagram of mutation; (d).Representation of the motion of particle *i*.

3.3 *Particle Swarm Optimization (PSO)*

The concept of PSO algorithm is the movement to search new space of swarm behavior toward an objective function by adjusting the trajectories of particles [5]. Each particle moves to a new location determined by a velocity term, which represents the attraction of global best (g^*) and its best location x_i^* in the history of the particle and random coefficient. If the location of the particle is better than any previously found location, updates such location as new current best for particle *i*.

The purpose of this algorithm looks for the global best among all the current best solution for particles. A description of the movement of the particle is represented in Figure 2(d). The global best comes from the minimum value of function $f(x_i)$ for $i=1,2,\ldots,n$. Let $\mathbf{x}_i=(x_i^1, x_i^2,\ldots,x_i^d)$ be the position vector and $\mathbf{v}_i=(v_i^1,v_i^2,\ldots,v_i^d)$ be the velocity for the particle *i*. Particle updating to obtain the new velocity vector is specified by Equation (8)

$$\mathbf{v}_i^{(t+1)} = w\,v_i^{(t)} + c_1\varphi_1(g^* - x_i^{(t)}) + c_2\varphi_2(x_g^{*(t)} - x_i^{(t)}) \tag{8}$$

$$\mathbf{x}_i^{(t+1)} = \mathbf{x}_i(t) + \mathbf{v}_i^{(t+1)} \tag{9}$$

where φ_1 and φ_2 are two random vectors, c_1 and c_2 are the learning parameter, w is the inertia weight, and $\mathbf{v}_i^{(t+1)}$ is the new position.

4. Simulation Results

In this paper, the parameter values for the CMAC filter have two inputs, s_1 and s_2, in which the number of layers is five, the width is ten, and the number of delays is three. The learning parameter values are configured as follows: the same parameters of BBO, GA and PSO have population: 15, chromosome: 10, mutation: 1%, and elitism: 2. The parameters for each EAs can be configured as follows: habitat probability of BBO is 1, λ_{upper} is 1 and λ_{upper} is 0; crossover probability and crossover type of GA is one; and initial w, c_1, and c_2 of PSO are 0.03, 1, and 1, respectively. The Mackey-glass is generated by a time-delay differential equation, such as that shown in Equation (10):

$$\dot{x}(t) = \frac{\alpha x(t-\tau)}{1+x^{\gamma}(t-\tau)} - \beta x(t) \tag{10}$$

where $\alpha = 0.2$, $\beta = 0.1$, $\gamma = 10$, and $\tau = 17$. In this paper, 400 and 100 data points are employed for training and testing. Figure 3(a) shows the prediction curves of the output. In Figures 3(b) and 3(c), the curves show the mean square error (MSE) and mean absolute percentage error (MAPE) values.

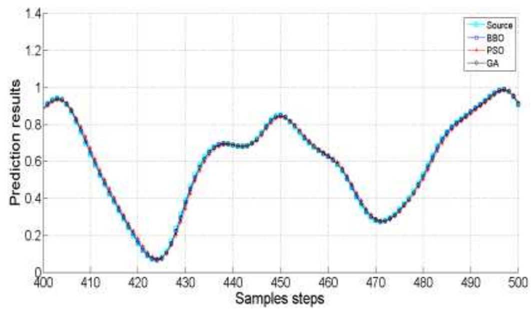

(a)

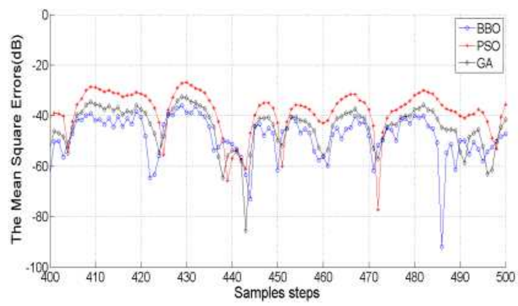

(b)

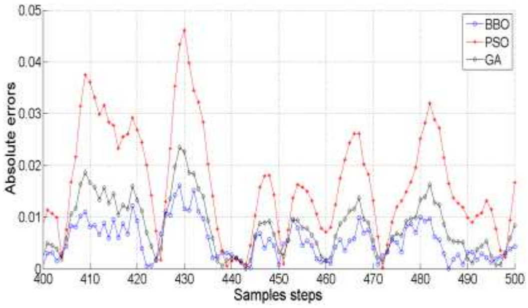

(c)

Figure 3. (a) prediction outputs, (b) MSE (dB) prediction indexes, (c) Absolute prediction errors

In Figure 3, the predictor employs the chaotic data series. The CMAC filter using BBO, GA or PSO learning system is employed to predict the chaotic signal data series. The comparative of Mackey-glass prediction results are presented in Table 1.

Table 1. The results of MSE, MAPE, and ARV

Error	Methodology		
	PSO	GA	BBO
MSE	3.9647e-04	9.6950e-05	4.2610e-05
MAPE	4.3233e-02	2.1219e-02	1.4106e-02
ARV	9.6198e-03	3.5797e-03	2.2484e-03

The MSE, MAPE, and ARV evaluate the output of the CMAC filter. The prediction results are compared with those of algorithms to identify the algorithm with the best performance. Based on the error results listed in Table 1, the learning process using BBO algorithm improves the performance of the CMAC filter. The CMAC filter using BBO learning process has the smallest MSE, MAPE, and ARV. They are 4.2610e-05 for MSE, 1.4106e-02 for MAPE, and 2.2484e-03 for ARV. Based on these errors and curves, the best prediction was made by the BBO algorithm.

5. Conclusion

This paper presents a novel filter using CMAC network to predict chaotic data time series, in which generated by Mackey-glass chaotic signal time series equations. The proposed CMAC filter is employed using EAs learning system to obtain a good performance. The EAs are BBO, GA, and PSO algorithm. The prediction results are compared with each other to determine the optimal filtering and prediction. Based on the result, the CMAC filter combined with EAs could filter, predict and estimate chaotic signal time series well. The best result of the algorithms tested for chaotic signal time series is the CMAC filter combined with BBO algorithm.

Acknowledgements

The authors would like to thank the Ministry of Science and Technology of the Republic of China, Taiwan, for financially supporting this research under Contract No. MOST 105-2622-E-224 -010 –CC, MOST 105-2221-E-224-024, and MOST 105-2218-E-150 -004 -.

References

1. P. Zhao, L. Xing, J. Yu, Chaotic time series prediction: From one to another, Physics Letters, A373, (2009) 2174-2177.
2. S. H. Lane, D.A. Handelman, J. J. Gelfand, Theory and development of higher-order CMAC neural networks, IEEE Control Systems Magazine, 12, (1992) 23-30.
3. M. Abbaspour, A. M. Rahmani, M. Teshnehlab, Carbon monoxide prediction using novel intelligent network, International Journal of Environmental Science & Technology, 1(4) (2005) 257-264
4. M. Mitchell, An Introduction to genetic algorithms (MIT Press, 1999).
5. Xin-She Yang, Nature-inspired optimization algorithms 1st edition (Elsevier 2014).

Surface defect detection for anodized aluminum tube based on automatic optical inspection

Hsien-Huang P. Wu and Hsuan-Min Sun
Department of Electrical Engineering, National Yunlin University of Science and Technology
Douliou, Yunlin, Taiwan R.O.C.

Runzi Zhao
Straits College of Engineering, FuJian University of Technology
#3 Xueyuan Rd, Gulou, Fuzhou Shi, Fujian Sheng, China

E-mail: wuhp@yuntech.edu.tw, m10312026@yuntech.edu.tw
http://el404.ee.yuntech.edu.tw/

Abstract

This paper proposed using the automated optical inspection (AOI) technology to develop a system which can automatically detect and classify defects for the shock absorber tube (SAT) made with steel. It is a high economic product which requires high-quality even under mass production. Nevertheless, the current manual quality-inspection is not only error-prone but also very manpower demanding. Due to the strong reflective property of the surface, as well as its various sizes and subtle flaws, it is very difficult to take good quality image for automatic inspection. However, based on the surface properties and shape of the SAT, lighting and proper structure combined with line scan camera have been designed to acquire image with good quality. Methods were proposed to detect various kinds of defects, and experimental results show that all the defects can be detected in real time. We believe the proposed system can greatly increase the efficiency and accuracy of defect detection and decrease the cost of manual labor.

Keywords: Automated Optical Inspection, surface defect detection, shock absorber tube (SAT), strong reflectivity surface

1. Introduction

In recent years, due to the ups and downs of oil prices, the idea of energy saving and carbon reduction prevails and the concept of healthy living gradually rises. Therefore, it becomes more common for people to ride bicycles. Furthermore, the bike lane planning and design is also gaining more attention, which makes the bike become not only a tool for travel but also an instrument for recreation. The shock absorber is the key component for the comfort of riding a bike, where the shock absorber tube (SAT) is the main body and is the most important part inside the absorber. When the surface of the SAT is defective, it can cause air leakage, oil leakage and loss of the suspension function. Thus, the finished SAT products must be inspected to detect any defects that might exist in it before shipping. This is currently done by human visual inspection which is error-prone, inefficient and costly. AOI technology has been successfully applied in various fields for product inspection. For examples, several methods have proposed using AOI for the inspection of cylindrical objects .[1,2] It is also used in some of the traditional industrial line for inspecting the defects for the bearing column[3] and iron bars.[4,5] For the inspection of metal surface, a variety of different methods of defect identification have been used.[6,7] In Ref. 8, iterative approximation threshold method was used to detect defective areas on metal surfaces. These literatures show that for different material of metal surface, one can utilize various method to detect the defects. However, the other approach is to properly design the lighting and select correct camera[9,10] to let the defects emerge from the background and simplify the process of defect detection. In this paper, lighting, camera and imaging structure have been properly designed to generate good quality image which makes the detection process become very easy.

2. Hardware for AOI System

To inspect a cylindrical object like SAT (200mm of length), as shown in Fig. 1, we need equipment with an axis to rotate it in order to inspect the whole surface. Given its round shape, a line scan camera and a line light for illumination is the suitable to acquire the image. The overall system setup is illustrated in Fig.2 and in the following subsections, we will describe these system components respectively.

2.1. *Line scan camera*

Line-scan camera accumulates many lines to form the length of the image and has the advantage of fast speed and wide FOV (field of view). The camera we used is SUFi74 (7.4k pixels/line) with F-mount lens (F1.8 and

Fig. 1. Left: The shock absorber tubes under inspection by AOI. Right: SAT inside the absorber chamber.

50mm focal length).

2.2. *Illumination*

The lighting for the line-scan camera are mostly based on line light source, which is very bright and provides very narrow stripe of illumination. Not like the golf club [10], the body of SAT is straight enough to provide stable rotation while it is rotated for image taking. The lighting we used is IDBB-LSR300W (300mm of length) manufactured by KKIMAC. The angle of illumination must be carefully setup in order to obtain useful images for inspection, and this needs experiments and experience.

2.3. *Rotatory mechanism*

The line scan camera demands a very stable rotation which depends on the stability of the rotary mechanism and the straightness of the SAT itself. This is because the line-scan camera only focuses on one thin line area of the object, and slight deviation of the rotation could miss or

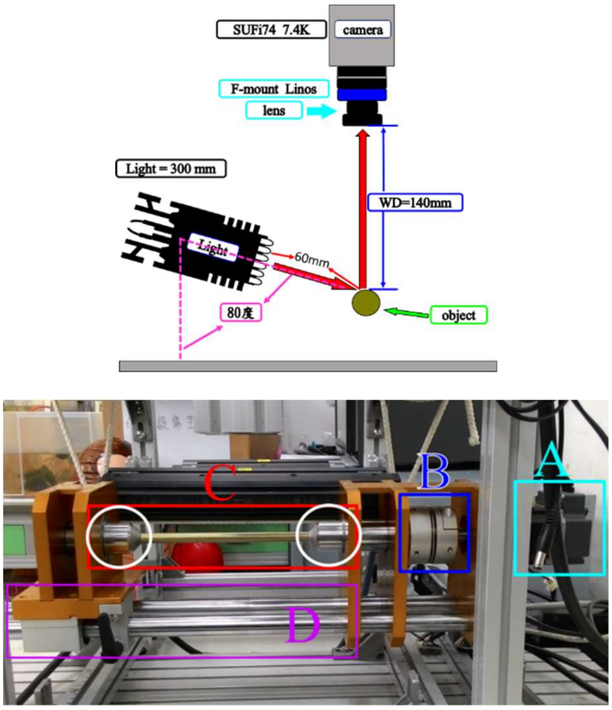

Fig. 2. Top: Sketch of the AOI system setup. Bottom: the implementation of the rotary mechanism.

degrade image acquisition of the line. The rotatory mechanism we built is shown in bottom of Fig.2, where **A** is the servo motor and encoder for controlling the position and speed of rotation (180rpm), **B** is the coupling for connecting axes of two different rotating objects to achieve concentric rotation, **C** is the measuring fixture to hold the SAT for rotation, and **D** is a slide bushing structure which can be adjusted to fit different length of the SAT.

3. Methods of Defect Detection

When the SAT is placed on the rotating mechanism to rotate with proper side lighting, the bright field is the area to be acquired for image. After the camera and motor parameters are set, the camera is controlled via the trigger signal and synchronized to the speed of the rotary mechanism to capture the full-circle image. After the whole SAT surface is acquired, the image is ready for defect detection process. Two simple methods are used to verify the suitability of the proposed approach.

3.1. *Filtering method*

Because texture of the tube can cause obvious horizontal stripes in the image, it will interfere with the judgment of the defect. It can be eliminated by ROI filtering to remove the high-frequency periodic pattern. The filtered image is first binarized to find the darker gray-scale region, and then expanded by morphological close operation to piece up the broken defect. Finally, each candidate region is discriminated as defect if its size is larger than a predefined threshold. Some of the detection results are shown in Fig.3. The disadvantage of this approach is that when the defect appears as horizontal line, it will be filtered out with the background texture, which is shown as missed detection SAT-3 in Fig. 3.

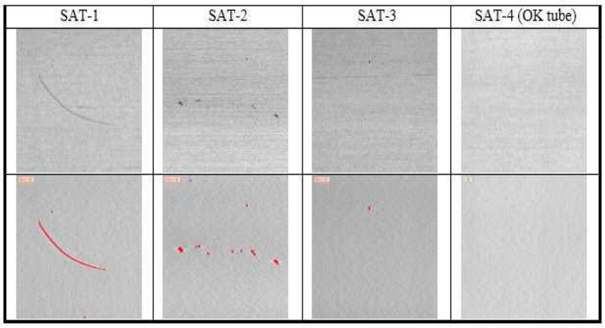

Fig. 3. The defect detection results based on filtering method. Top: acquired image, Bottom: defect detection (defect in red).

3.2. *Image difference method*

This method is to put the original image through both Gaussian filtering and mean filtering first. The two output images are then subtracted each other to obtain an image with much less texture and noise, which can greatly simplify the follow-up treatment of thresholding, morphological operation and classification. The flaw detection results are shown in Fig. 4. As we can see from the figure (SAT-3), this method can detect long-thin flaws with much less broken defect feature.

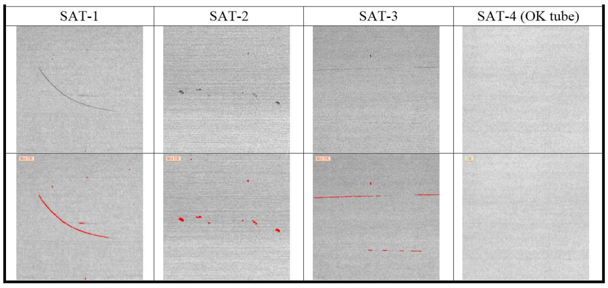

Fig. 4. The defect detection results based on image difference method. Horizontal defect (in SAT-3) can now be detected.

4. Experimental Results and Discussion

Some of the flaws on the SATs under test can be recognized by the naked eye, but some cannot. These subtle defect needs to be inspected visually using magnifying glasses or to be imaged by the proposed system. The acquired image by the system has very high resolution such that the defects can then be visually identified on the computer screen or automatically detected by machine vision method. In this evaluation phase, we put our proposed system and detection method for an on-line test to automatically identify the defects using 13 SATs provided by the manufacturer. The software is developed under C#/emgu environment, and the results are shown in Table 1. The smaller size image (1000×1000) was used for verifying detection method which only processed the region around defects. The larger size image (7392×2500) covers the actual FOV of the camera and acquired the region inside the FOV. One example is illustrated in Fig. 5 to show the detection results. Note that the darker regions on the left and right boundaries of the image might be caused by the light source or rotatory mechanism, but it does not interfere the detection. Given processing time of 550~600ms by using multithread (image difference method), it can achieve real-time to inspect the whole tube on line.

Table 1. The evaluation results conducted for 13 SATs.

Method	Image size (pixels)	Processing time (ms)	Detection rate
Image Difference	1000×1000	60 ~ 80	100%
	7392×2500	550 ~ 600	100%
Filtering Method	1000×1000	110 ~ 130	100%
	7392×2500	1700 ~ 2000	80%

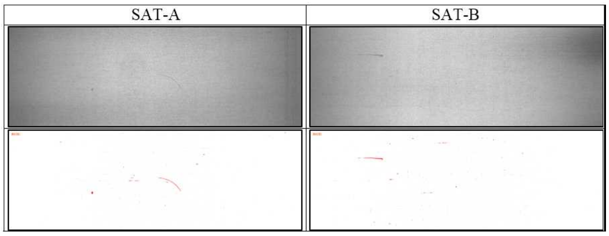

Fig. 5. The defect detection results based on image difference method with image size 7392×2500.

5. Conclusions

In this study, we used the oblique light with a proper angle to highlight the defects, so as to simplify the defect detection process and improve the detection rate. One detection method can successfully detect most of the defects on the tube surface and the other method can detect all the defective tubes with 100% detection rate. Because the manufacturer-defined defect-free SAT tubes also have been identified as defective (false alarm), there is still room for discussion between human and machine inspection. Manually visual inspection of SAT defects is not only less efficient but also less stable, we anticipate the AOI technology will soon replace the manual inspection to improve the efficiency and stability and reduce the cost.

Acknowledgements

The authors wish to express their appreciation for the financial support of the Ministry of Science and Technology under project MOST 105-2221-E-224-064. The SATs used in the experiments were kindly supplied by Jinyun Cheng Enterprise Co., Ltd., Taiwan. Their generous support is greatly appreciated.

References

1. X. C. Luo, A hybrid SVM-QPSO model based ceramic tube surface defect detection algorithm. *IEEE 5th Int. Conf. on Intelligent Systems Design and Engineering Applications (ISDEA)* (Zhangjiajie, China, 2014), pp. 28–31
2. Y. C. Chiou, and W. C. Li, Flaw detection of cylindrical surfaces in PU-packing by using machine vision technique, *Measurement*, **42**(7) (2009) 989–1000.
3. F. Pernkopf and P. O'Leary, Visual inspection of machined metallic high-precision surfaces, *EURASIP Journal on Applied Signal Processing*, 7(2002) 667–678.
4. J. P. Yun, et al., Real-time vision-based defect inspection for high-speed steel products, *Optical Engineering*, 47(7) (2008) 077204-077204-8.
5. W. B. Li, C. H. Lu, and J. C. Zhang, A local annular contrast based real-time inspection algorithm for steel bar surface defects, *Applied Surface Science*, 258(16) (2012) 6080-6086.
6. M. Mansano, et al. Inspection of metallic surfaces using local binary patterns. *IECON 2011- 37th annual conf. of IEEE Industrial Electronics Society* (Melbourne, Australia, 2011) pp. 2227–2231
7. X. Q. Huang, and X. B. Luo. A real-time algorithm for aluminum surface defect extraction on non-uniform image from CCD camera, *IEEE Int. Conf. on Machine Learning and Cybernetics* (Lanzou, China, 2014), pp. 556–561
8. M. Senthikumar, V. Palanisamy, and J. Jaya, Metal surface defect detection using iterative thresholding technique, *IEEE 2nd Int. Conf. on Current Trends in Engineering and Technology (ICCTET)*, pp. 561-564
9. H. H. Wu, J. W. Su, and C. L. Chen, Automatic optical inspection system design for golf ball, *Proc. SPIE 9971, Applications of Digital Image Processing XXXIX* (San Diego, California, USA, 2016).
10. H. P. Wu and H. Y. Guo, Automatic Optical Inspection for Steel Golf Club, *12th Int. Conf. on Fuzzy Systems and Knowledge Discovery (FSKD'15)*, (Zhangjiajie, China, 2015), pp.2378–2382.

Develop low cost IoT module with multi-agent method

Jr-Hung Guo *
Department of Electrical Engineering, National Yunlin University of Science & Technology, 123 University Road, Section 3,Douliou, Yunlin 64002, Taiwan

Kuo-Hsien Hsia
Department of Electrical Engineering, Far East University, No.49, Zhonghua Rd., Xinshi Dist., Tainan City 74448, Taiwan

Kuo-Lan Su
Department of Electrical Engineering, National Yunlin University of Science & Technology, 123 University Road, Section 3,Douliou, Yunlin 64002, Taiwan

E-mail: g9710801@yuntech.edu.tw, khhsia@cc.feu.edu.tw, sukl@yuntech.edu.tw

Abstract

Internet of Thing (IOT) is a very hot topic recently, many of the important issues in the field of research. But to the conventional apparatus or systems and network connections, sometimes we need complex modifications or expensive costs. Therefore, this paper using the MCS-51 series single-chip integration of analog, digital signal input, and ETHERNET, WIFI and other communication interface, to develop general-purpose IOT modules. This module can be used to replace existing equipment or devices, or combination use with the original device. We also use the module in a Multi-Agent Method, we can ensure that the module in signal capture or communication failure can be replaced or assisted by other modules. Finally, we can use these modules to build the sensor network.

Keywords: Internet of Thing (IOT), single-chip, Multi-Agent Method, sensor network.

1. Introduction

Internet of things technology (IOT) is a very popular research topic recently, because this technology can make people's life more convenient. For example, Gubbi, Jayavardhana, et al. [1] put forward many examples and visions for the application and future of this technology. In addition, He, Wu et al. [2] proposed an intelligent parking cloud service and a vehicular data mining cloud service. From this example we can know that the IOT technology is also the basis of cloud computing and big data. And [3] Yang, Geng, et al. Put forward the application of IOT in home care. In addition to these applications related to people's daily lives, IOT is also the basis of industrial 4.0 and intelligent factories [4].

From the above example we can know that the IOT technology for future life have a great impact. But IOT technology still has many problems to be solved. For example, many devices simultaneously communication problems, different devices connected, and IOT module costs higher etc. In this paper, we use the lower cost single chip as the core, integrating many communication interfaces. As well as multi-channel A / D and digital I / O, to development of a low-cost IOT module. This module can operate independently, and can be operated directly with the browser. In addition, modules can be grouped according to the communication interface or function. Grouping mechanism can be manual; we can also use multi-agent method to automatically create a group module. Finally, we have also developed a monitoring system for the management of all modules and data collection. This constitutes a complete system, and let the paper developed by the module in the use of more flexible.

2. System Architecture

The IOT module developed in this paper is based on MCS-51 series of single-chip-based controller. Because this module is IOT applications as the main purpose, so in the communications we have integrated Ethernet and WIFI interface. In addition the module also has UART (Universal Asynchronous Receiver / Transmitter), this interface can be converted into RS232 / 422/485 interface. So that modules can be connected with many traditional devices or devices. Finally, we also provide a 433/868/915 MHz triple-frequency, 170-channel RF interface. This module allows communication even more complete and powerful.

The IOT module in addition to powerful communications features also has a digital and analog interface. In the analog interface section, the module has eight 10-bit A / D channels, and in the digital I / O section, the module has 10 channels. When necessary or when the application is not used to the A / D, it can also be changed to digital I / O, so this module can have a maximum number of 18-bit I / O channels. In addition the IOT module also has a 1280Byte eeprom, which can be used to record the A / D data. This allows IOT module can calculate preliminary data, so that IOT module has certain decision-making analysis capability. In addition, this function can also be used in case of communication failure, as temporary storage of data. This IOT module structure is shown in Figure 1.

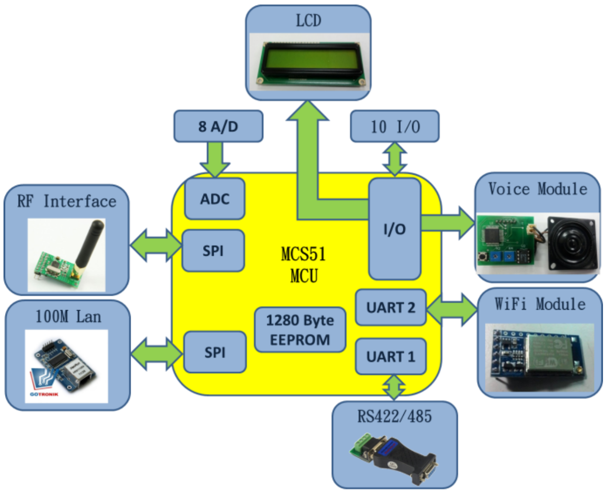

Fig. 1. IOT module Architecture

In order to make the communication module more efficient, we designed a communication protocol, the communication protocol structure shown in Table 1.

Table 1. Communication Protocol.

<table>
<tr><td>Byte 0</td><td>Byte 1</td><td>Byte 2</td><td>Byte 3</td><td>Byte 4</td></tr>
<tr><td>35H</td><td>ID</td><td>Sensor Kind</td><td>Module</td><td>State</td></tr>
<tr><td colspan="4">4N(N=1~16)</td><td>Checksum</td></tr>
<tr><td colspan="4">Data/Parameter</td><td>SUM(all byte)</td></tr>
</table>

3. Multi-agent Method

We designed the IOT module can operate independently, and from our design of the communication protocol, our system can have up to 65,536 devices. If using IPV4 protocol, so much the device will need 256 Class C network segment. So the device for the communication and management will cause great distress. Therefore, we use the structure of the group, so that modules can be grouped in accordance with the function or task group approach. Group communication, is handled by the group manager, the group has two ways.

(1) Based on Sensor Kind: This approach is based on the module preset Sensor Kind grouped, which is based on modules grouped categories.

(2) Grouped by task: This approach is by the user, depending on the task, such as fire detection, gas detection, and greenhouse control and so on. The

user can freely set the task type and the task type to which the module belongs.

The group manager in the group is generated in the following way. Each communication interface is set with different weights as shown in Table 2. Usually we first manner of communication create a group, and we have three modules while communication interface work. So the weights are the sum of the weights of the three communication interfaces. If one of the interfaces fails, the weight of that interface will be set to 99. So all the normal network communication module, the probability of a group manager will be higher. The number of connected modules of the module manager will also affect the weight, the impact of which is shown in Table 3.

Table 2. Interface Weight

Interface	w_1
Ethernet	1
WIFI	1
RF	2
UART	3

Table3. Conn. Weight

Conn. Number	w_2
1	1
2	2
⋮	⋮
15	15

Finally, the module is wired to the module manager's algorithm. We use the A* algorithm, because the algorithm is simpler, so the IOT module can calculate itself, without the need to pass through the monitoring system. In addition, if the IOT module has the ability to locate or set location information, this algorithm can also be used to find the shortest secure path. This algorithm is shown in Equation 1.

$$F(n)=G(n)+H(n) \tag{1}$$

F(n) is the movement cost of any path point. G(n) is the cost of movement from the starting point to any point on the path. H(n) is predicts the cost of moving from any point on the path to the end.

We are based on the IOT module Sensor Kind and Module as coordinates. Therefore, when we create a group in mode 1, the modules of the same type can quickly become a group. And group Module smallest value becomes higher probability of a group of managers. When using a task to create a group, Sensor Kind changes to the task number set by the user. These same task modules to quickly create groups.

Because of our communication interface, and the number of modules connected modules are set weights so that the total weight was W:

$$W=w_1+w_2 \tag{2}$$

Therefore, we can rewrite Equation 1 as.

$$F(n)=G(n)+(H(n)+W) \tag{3}$$

This allows the module to quickly create groups, and when the group is abnormal, the module can quickly re-establish the group, so that the entire system management communication more efficient.

4. Experimental Results

We use MCS-51 series of single-chip, combined with Ethernet, WIFI, RF and other communication interface to complete a low-cost IOT module. This module is modular design, all the communication interface, can be installed in accordance with demand, and can have three communication interface work at the same time. And all the A / D and I / O can allow users to determine their own functions, so that the use of the entire IOT module more flexible. Each IOT module can operate independently, when necessary, between the modules can also use multi-agent method to form groups. Module between groups can function in accordance with the communication priority or function priority setting, when the group manager failure, the group well automatically re-generate the manager module. The use of such a mechanism, to ensure that data communication between the transfer modules will not be interrupted. In this way, when use of Ethernet or WIFI communication, it also to reduce IP use and collision, improve the efficiency of the entire system. Figure 2 is some example of a group of modules. We also designed a management software as shown in Figure 3, this system can immediately manage and monitor all modules of the situation and information, so that the whole IOT system more convenient. Finally, in order to make it easier to use, we make all the IOT module has WEB server function, so all of the IOT module can operation directly with a browser. Do not need to through other management software or WEB server, the results shown in Figure 4. This makes our IOT module system more complete.

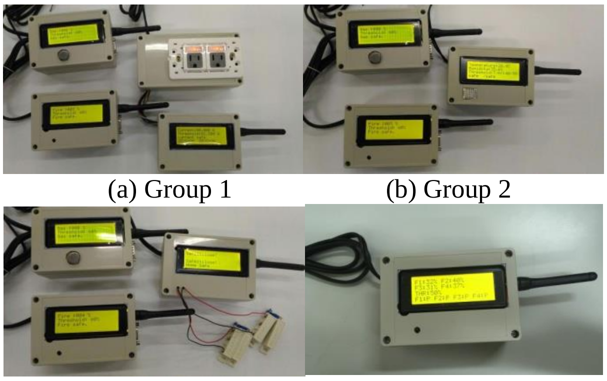

(a) Group 1 (b) Group 2

(c) Group3 (d) Group4

Fig. 2. IOT Module Group Sample.

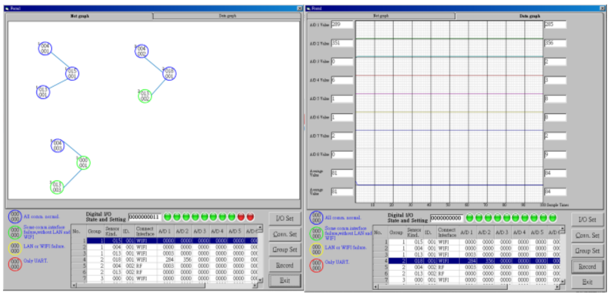

Fig. 3. User Interface.

(a) IOT Web server 1 (b)IOT Web server 2

Fig. 4. IOT Module Web Server example.

5. Conclusion Tables

We have developed a MCS-51 single-chip-based IOT module, the module has Ethernet, WIFI, RF and other communication interface. This module can operate directly in the browser, but the overall cost only about US $ 30. Therefore, the IOT module developed in this thesis is powerful and inexpensive, which will be very helpful for the application and development of IOT system.

In the future we will continue to improve the function of our development module. For example, let the number of connections for each module is capable of more, let IOT module can support IPV6, and let the volume IOT module smaller, more power saving. Finally be able to develop into a wearable device, so this paper developed modules can be applied in more fields.

References

1. Gubbi, Jayavardhana, et al. "Internet of Things (IoT): A vision, architectural elements, and future directions." *Future Generation Computer Systems* 29.7 (2013): 1645-1660.
2. He, Wu, Gongjun Yan, and Li Da Xu. "Developing vehicular data cloud services in the IoT environment." *IEEE Transactions on Industrial Informatics* 10.2 (2014): 1587-1595.
3. Yang, Geng, et al. "A health-IoT platform based on the integration of intelligent packaging, unobtrusive bio-sensor, and intelligent medicine box." *IEEE transactions on industrial informatics* 10.4 (2014): 2180-2191.
4. 4. Wang, Shiyong, et al. "Implementing smart factory of industrie 4.0: an outlook." *International Journal of Distributed Sensor Networks* 2016 (2016): 7.

Based on Short Motion Paths and Artificial Intelligence Method for Chinese Chess Game

Chien-Ming Hung
Department of Power Mechanical Engineering, Army Academy R. O. C., Jhongli, City, Taoyuan 32092, Taiwan

Jr-Hung Guo
Department of Electrical Engineering, National Yunlin University of Science & Technology, 123 Sec. 3, University Road Douliou, Yunlin 64002, Taiwan

Kuo-Lan Su*
Department of Electrical Engineering, National Yunlin University of Science & Technology, 123 Sec. 3, University Road Douliou, Yunlin 64002, Taiwan
E-mail: tpemail77@yahoo.com.tw, g9710801@yuntech.edu.tw, sukl@yuntech.edu.tw

Abstract

The article develops the decision rules to win each set of the Chinese chess game using evaluation algorithm and artificial intelligence method, and uses the mobile robot to be instead of the chess, and presents the movement scenarios using the shortest motion paths for mobile robots. User can play the Chinese chess game according to the game rules with the supervised computer. The supervised computer decides the optimal motion path to win the set using artificial intelligence method, and controls mobile robots according to the programmed motion paths of the chesses moving on the platform via wireless RF interface. We use enhanced A^* searching algorithm to solve the shortest path problem of the assigned chess, and solve the collision problems of the motion paths for two mobile robots moving on the platform simultaneously. We implement a famous set to be called "wild horses run in farm" using the proposed method. First we use simulation method to display the motion paths of the assigned chesses for the player and the supervised computer. Then the supervised computer implements the simulation results on the chessboard platform using mobile robots. Mobile robots move on the chessboard platform according to the programmed motion paths and is guided to move on the centre line of the corridor, and avoid the obstacles (chesses), and detect the cross point of the platform using three reflective IR modules.

Keywords: Evaluation algorithm, artificial intelligence method, wireless RF interface, enhance A* searching algorithm

1. Introduction

Chinese chess game is one of the most popular games, and is similar to Western chess to be a two-player game with a complexity level, and is classified red side and black side. In the recent, the Chinese chess game has gradually attracted many researchers' attention, and many evolutionary algorithms to be proposed. Darwen et al. proposed the co-evolutionary algorithm to solve problems where an object measure to guide the search process is extremely difficult to device [1].

In the paper, we use the multi-robot system to present the scenario of the Chinese chess game, and uses enhance A* searching algorithm to program the shortest path for mobile robots (chesses) moving to the target points. Player moves the chess to the assigned location or takes the chess of the supervised computer. Then there are two chesses (robots) moving in the platform simultaneously. The assigned two robots may collide on the programmed motion paths. The proposed algorithm can solve the collision condition of two mobile robots and improve the shortest motion path using enhance A* searching algorithm [2, 3].

In some condition, the mobile robot must programs the shortest path and avoids the other chess moving to the next position. A^* heuristic function is introduced to improve local searching ability and to estimate the forgotten value [4]. Flavio et al. presented a multi-robot exploration algorithm that aims at reducing the exploration time and to minimize the overall traverse distance of the robots by coordinating the movement of the robots performing the exploration [5].

2. System Architecture

The system architecture of the Chinese chess game system is shown in Fig. 1. The system contains a supervised computer, some wireless RF modules, a grid based platform, thirty-two mobile robots and some wireless modules. The game is classified red side (User) and black side (The supervised computer), and belongs to two players. Each side includes sixteen chesses. Player moves chess using the mouse on the user interface, or takes chess of the other side. The chess game will be ending until the king of each side to be taken by another side.

We want to increase the entertainment function using mobile robots to present the movement scenarios of the chesses. The supervised computer is a player to compete with the user, and programs the shortest motion path using enhance A* searching algorithm and transmits the ID code and motion command to the assigned mobile robots. The assigned mobile robots receive the self-ID code and the target positions via wireless RF interface, and move to the assigned positions to avoid the collision paths according to the programmed motion paths.

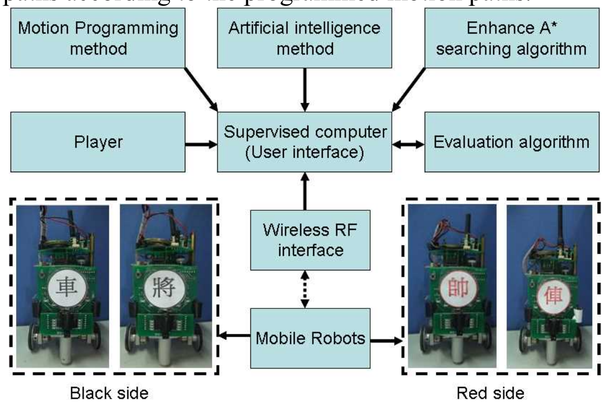

Fig. 1. System architecture

In the collision problem, player moves chess to take chess of the other side. The user interface programs two motion paths for the assigned chesses. Two mobile robots avoid collision points and paths according to the programmed motion paths moving on the platform. Players can set game time of each set and limit moving time of each step. Players don't obey the game rules to move chess using the mouse. The supervised computer can't permit and display the movement status on the user interface.

3. Motion Planning

The mobile robot has the shape of cylinder, and it's equipped with a microchip (STC12C5A60S2) as the controller, two DC servomotors and two driver devices, some sensor circuits (contain compass circuit), a voice module, three Li batteries, a wireless RF interface (2.4GHz) and three reflect IR sensor modules (One module contains two reflective IR sensors). Meanwhile, the mobile robot has four wheels to provide the capability of autonomous mobility. The structure of the mobile robot is shown in Fig. 1.

The mobile robot uses three reflective IR modules to detect the wall of each grid and obstacles. Two reflective IR sensors are fixed on the both sides of the mobile robot. The detection distance of the front side is shorter than the behind side shown in Fig. 2(a). In the both side's modules, two reflective IR sensors of the front side can detect distance to control the mobile robot moving in the centre line of the corridor shown in Fig. 2(b). Two reflective IR sensors can detect the maximum distance to be equal to the width of the corridor minuses the width of the mobile robot to be fixed on the behind side of the module shown in Fig. 2(c). The other reflective IR module is fixed on the front side, and detects the object or the mobile robot on the motion path.

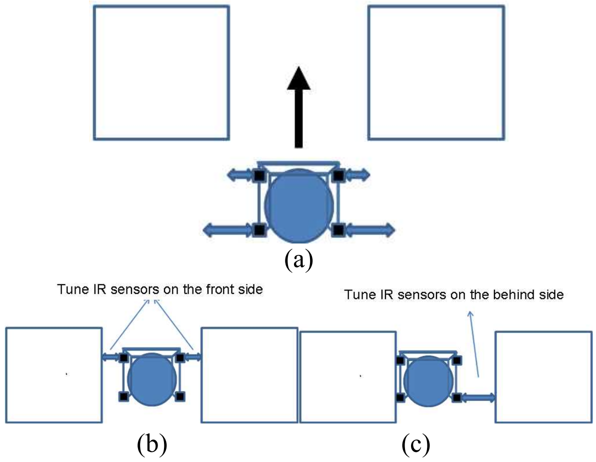

Fig. 2. The detection range for reflective IR modules

A^* searching algorithm solves the path planning problem of multiple nodes travel system. The formula of A^* searching algorithm is following

$$f(n) = g(n) + h(n) \qquad (1)$$

The core part of an intelligent searching algorithm is the definition of a proper heuristic function $f(n)$. $g(n)$ is the exact cost at sample time n from start point to the next point. $h(n)$ is the minimum cost. In this study, n is reschedules as n' to generate an approximate minimum cost schedule. The equation (1) can be rewritten as follows:

$$f(n) = g(n) + h(n') \qquad (2)$$

The A* searching algorithm can program local minimum motion path. We improve A* searching algorithm that is called enhance A* searching algorithm, and searches the shortest motion path for mobile robots [7]. In the Chinese chess game, the chesses of red side must face to the black side. In the same way, the chesses of black side must face to red side, too. The enhance A* searching algorithm can delete the turn numbers to decrease the total motion distance, and select all cross points from the programmed motion path to cut down redundant motion path in the rectangle region.

4. Experimental Result

We make an example to explain how to implement in Chinese chess game, use evaluation algorithm and artificial intelligence method to decide the moving chess with the highest evaluation score, and use enhance A* searching algorithm to program the shortest motion paths of the assigned chesses from the start positions to the target positions. There is a famous set to be called “wild horse run in farm” shown in Fig. 3.

There are eight chesses (one king, two elephants, two rooks, one horse, two pawns) in red side and nine chesses (one king, two advisors, two elephants, one rook, and three pawns) in the black side. Movement process of the set is belonging to the player and the supervised computer shown in Table.1 to be classified four steps. In the first step, the player moves red rook form (8, 5) to (8, 1). The motion path of the chess “red rook” is programmed using enhance A* searching algorithm. The movement scenario of the assigned chess is shown in left-up side of Fig. 4(a) on the user interface. The movement status of the mobile robot is instead of the assigned chess shown in Fig. 4(a). Then the computer moves the black advisor to protect the king from (5, 2) to (6, 1). The movement scenario of the assigned chess is shown in Fig. 4(b).

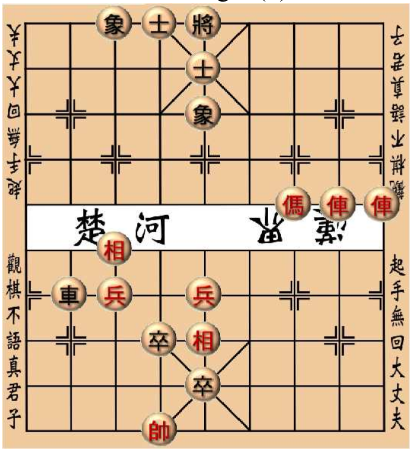

Fig. 3 A famous set “Wild horses run in farm”

The player moves the red horse to take the black king from the position (7, 5) to the position (6, 3), and the computer moves the black king from the position (5, 1) to (5, 2) in the second step. The movement process of the grid based platform is shown in Fig. 4(c) and (d). Each step of the computer must calculate the score of the moveable chesses shown in Table 1. Then the computer decides the optimal motion path of the selected chess. In the third step, the player moves the red rook from (8, 1) to (8, 2), and the computer moves the black elephant from (3, 1) to (1, 3) shown in Fig. 4(e) and (f). Then the black king will be taken by the red rook in the fourth step of the red side, and the game will be ending. The movement scenarios of two chesses (two mobile robots) are shown in Fig. 4(g). The motion paths of two mobile robots have collision problem in the case. The supervised computer must re-program the new motion paths to avoid the collision path. The black king is taken by the red rook, and moves to the assigned position 28. The set will be ending. The final arrangement positions of the remainder chesses shown in Fig. 4(h).

Table 1 Movement process of the assigned set

	Player (red side)	Computer (black side, using evaluation algorithm)	
		Movement process	Score
First step	Rook (8,5)→(8,1)	Advisor (5,2) →(6,1)	-295

Second step	Horse (7,5) →(6,3)	King (5,1) →(5,2)	-18888
Third step	Rook (8,1) →(8,2)	Elephant (3,1) →(1,3)	-19991
Fourth step	Rook (8,2) →(5,2)		
Result	Winner		

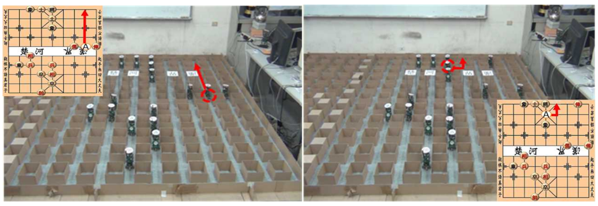

(a)The first step (player) (b)The first step(computer)

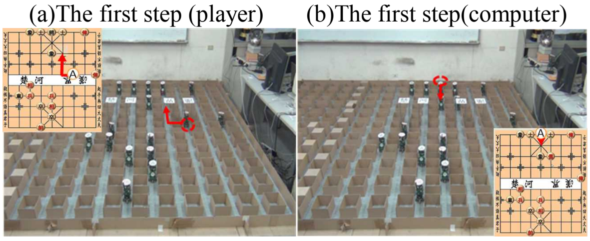

(c)The second step (player) (d)The second step (computer)

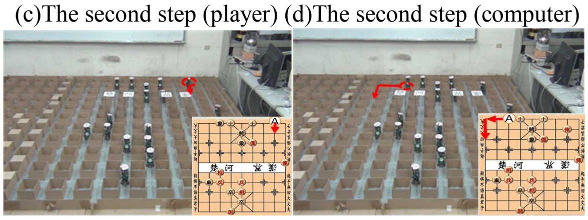

(e)The third step (player) (f)The third step (computer)

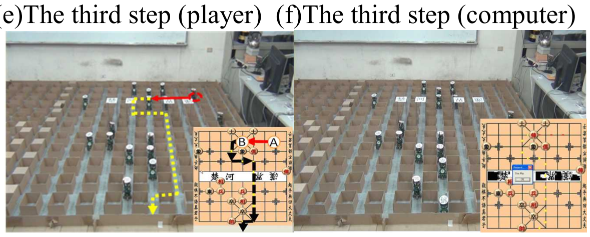

(i)The final step (player) (j)The final arrangement

Fig. 4. Moving process for the set

5. Conclusion

The Chinese chess game system contained a supervised computer with the user interface, some wireless RF modules, a chessboard platform and thirty-two mobile robots. The computer can select moveable method of the assigned chess using evaluation algorithm and artificial intelligence method. We program the shortest motion paths of assigned chesses using enhance A* searching algorithm to obey the rule of Chinese chess game. The proposed methods can program two motion paths for two chesses, and solve the collision problem for multiple mobile robots moving on the chessboard platform simultaneously. We implemented a famous set to be called "wild horses run in farm" using the proposed method. The paper used the set to implement the evaluation algorithm, artificial intelligence method and enhance A* searching algorithm. The proposed methods are not only used in the Chinese chess game, but also applied in various game, and entertainment field, and manufacture process and production management. Further the moving process of mobile robots can be used in the simultaneous war using the proposed algorithms.

Acknowledgements

This work was supported by the Ministry of Science and Technology in Taiwan, (MOST 105-2221-E-224-022).

References

1. P. Darwen and X. Yao, Coevolution in Iterated Prisoner's Dilemma with Intermediate Levels of Cooperation: Application to Missile Defense, *International Journal of Computational Intelligence Applications*, Vol. 2, No. 1, pp.83-107, 2002.
2. K. L. Su, B. Y. Li and C. Y. Chung, "Enhance A* Searching Algorithm Applying in Multiple Robot System," *Applied Mechanics and Materials*, Vol.479-480, pp.773-777, 2014.
3. K. L. Su, S. T. Su, K. H. Hsia and B. Y. Li, Implementation of the Chinese Chess Game with the Computer Using Artificial Intelligence, *International Journal of Research and Surverys, ICICExpress Letters, Part B: Applications,* Vol.7, No.6, pp.1353-1358, 2016.
4. T. Fu and H. Yin, Designing a hybrid position evaluation function for Chinese-chess computer game, *International Conference on Software Engineering and Service Science*, Beijing, China, pp.75-78, 2012.
5. Y. Saber and T. Senjyu, Memory-bounded ant colony optimization with dynamic programming and A^* local search for generator planning, *IEEE Trans. on Power System*, Vol.22, No. 4, pp.1965-1973, 2007.
6. K. L. Su, B. Y. Li, J. H. Guo and K. H. Hsia, "Implementation of The Chess Game Artificial Intelligent Using Mobile Robot," *International Conference on Soft Computing and Intelligent System*, Kitakyushu, Japan, Dec. 3- 6, pp.169-174, 2014.
7. K. L. Su, B. Y. Li and C. Y. Chung, Enhance A* Searching Algorithm Applying in Multiple Robot System, *Applied Mechanics and Materials*, Vol.479-480, 2014, pp.773-777.

Design and Implementation of the SCARA Robot Arm

Jian-Fu Weng
Graduate school Engineering Science and Technology, National Yunlin University of Science & Technology, 123 Sec. 3, University Road, Douliou, Yunlin 64002, Taiwan

Bo-Yi Li
Department of Electrical Engineering, National Yunlin University of Science & Technology, 123 Sec. 3, University Road Douliou, Yunlin 64002, Taiwan

Kuo-Lan Su*
Department of Electrical Engineering, National Yunlin University of Science & Technology, 123 Sec. 3, University Road Douliou, Yunlin 64002, Taiwan
E-mail: tpemail77@yahoo.com.tw, g9910813@yuntech.edu.tw, sukl@yuntech.edu.tw

Abstract

The article designs a four-joint SCARA robot arm using PLC-based control system. The control system (ASDA-SM) is all in one device to be produced by the DELTA Company, and contains four axis controllers and drivers. The robot arm contains four AC servomotors, four driver devices and a vision system. The PLC-based controller also programs motion commands of the gripper to finish the assigned tasks using Ladder Diagram (LG), Function Block Diagram (FBD), Sequential Function Chart (SFC), Instruction List (LL) and Structure Test (ST). Each driver has been tuned the parameters of the PID controller. The human machine interface (HMI) is a touch panel to be used for the robot arm. Users can control the motion path of any joint, and uses the DOPSoft language to design the human machine interface. In the experimental results, The SCARA robot arm catches a seal, and falls to stamp the assigned positions step by step, and identifies the precious of the robot arm, and moves eight objects to the assigned positions.

Keywords: SCARA Robot arm, PLC-based controller, AC servomotors, PID controller.

1. Introduction

How to find a fast and effective way to program the motion trajectory of the robot arm becomes an important problem. A robot arm is a mechanical device driven by some electronic motors, pneumatic devices or hydraulic actuators. A well-trained robot arm can help human to complete assigned tasks automatically. The purpose of the paper is to design and implement a four-degree-of-freedom SCARA robot arm. The robot arm is composed of four AC servomotors. In the control aspect, a PLC-based (ASDA-MS system) controller is used to control the robot arm.

There are some researches regarding the robot arm in the past. For example, Shafik et al. presented an innovative 3D piezoelectric ultrasonic actuator using flexural vibration ring transducer for machine vision and robot guidance applications [1]. Homayounzade et al. developed an observer-based impedance controller for robot arm during a constrained motion. The proposed controller required the measurements of link position and interaction force [2]. Sim et al. presented a binocular stereo vision to decide the desired location of the SCARA robot arm [3]. Kenmochi et al. proposed a motion control method based on environmental mode for a dual arm robot. By controlling mode information, particular features or trends can be given to the robot's motion. Then a distinctive complex motion can be realized [4].

In some conditions, the robot arm catches the assigned object using the feedback signal of the image system. Karthikeyan et al. presented a simple active tracking system, using a laser diode, a steering gear box setup and a photo-resistor, which is capable of acquiring two dimensional coordinate in real time without the need of any image processing technique [5]. Cao et al. designed a 5-DOF SCARA robot arm for welding, and built the model and the kinematic equations using D-H method [6].

2. System Architecture

The system architecture of the SCARA robot arm system is shown in Fig. 1. The system contains a computer, a PLC-based controller (ASDA-SM), a image system (Open CV), four AC servomotors, a solenoid and a gripper. ASDA-SM and four AC servomotors and a solenoid and a gripper integrate the SCARA robot arm. The solenoid drives the gripper to catch the assigned object.

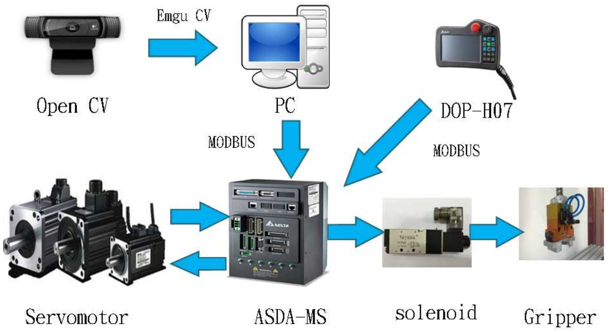

Fig. 1. System Architecture of the SCARA robot arm

The SCARA robot arm has four DOFs, (Degree of Freedom) to be shown in Fig. 1. The first and second joints rotate along the Z axis. The rotation radius of two joints is the same to be 205mm. the rotation angle of the first joint is $\pm 157^0$, and the second joint is $\pm 142^0$. The movement displacement of the third joint is 150mm. the rotation angle of the fourth joint is $\pm 180^0$. The specifications of the SCARA robot arm are shown in the table1.

The prototype of the controller (ASDA-SM) shows in the Fig. 3. We explain each function of the controller. "A" part is the communication port. The controller can use MODBUS, RS485 or RS232 interface to connect with the computer. "B" part can display the operation status and error codes. Four AC servomotors will connect with the part "C" of the controller. "D" part is the standard input and output terminal with digital signals. The limit positions of each servomotor connect with the part "E", and decide the moveable range of each joint. "F" part connect with the encoder of each motor as feedback signal and measure the real-time rotation angle. The power input is the "G" part. The arrangement method of the controller is shown in Fig. 4 with AC servomotors. The connection pin of the power system is shown in Fig. 5.

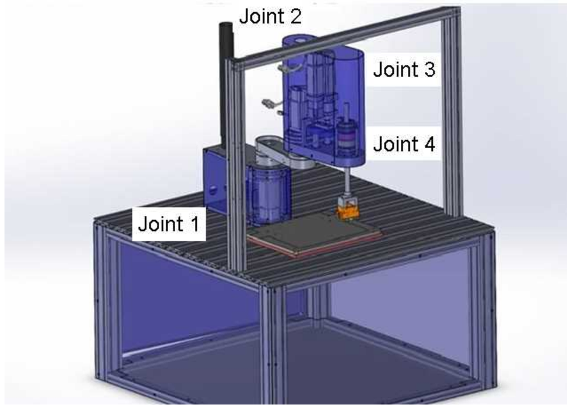

Fig. 2. Prototype of the SCARA robot arm

Table 1. Specifications of the robot arm

Functions	Joint	Range
Length of the robot arm	First joint	205mm
	Second joint	205mm
Rotation and displacement range	First joint	$\pm 157^0$
	Second joint	$\pm 142^0$
	Third joint	150mm
	Fourth joint	$\pm 180^0$

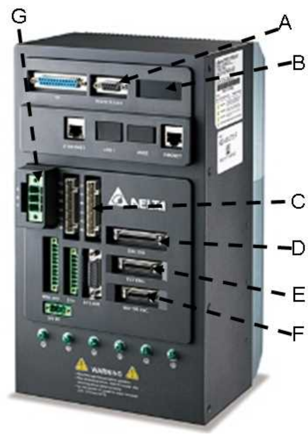

Fig. 3. The PLC-based controller(ASDA-SM)

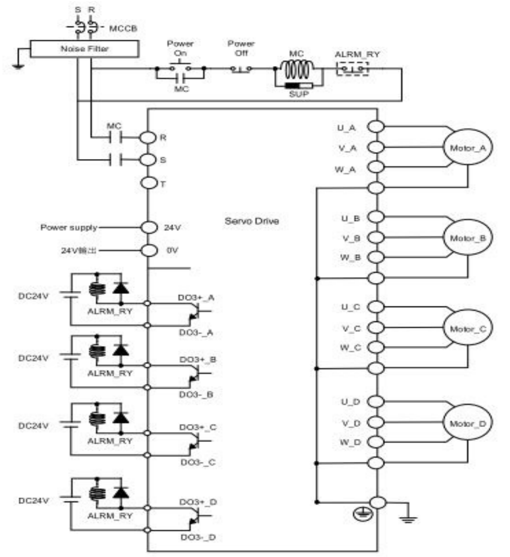

Fig. 4. Arrangement method of four servomotors

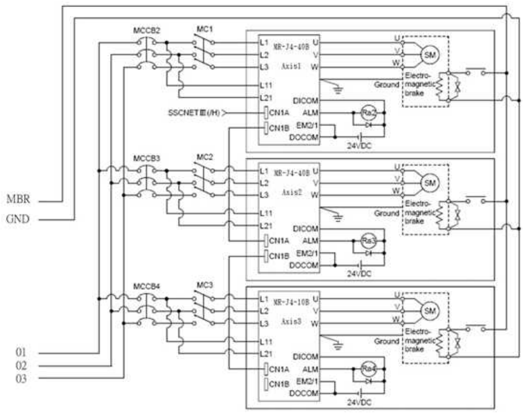

Fig. 5. The power connection method

In the assigned task, the SCARA robot arm can complete various assigned tasks such as coming and going on two points, moving multiple objects to the assigned positions and working on the multiple positions. Finally the robot arm can catch the color object moving to the assigned position according to the detection result of the image system..

3. Experimental Result

We implement the functions of the SCARA robot arm in two aspects. The robot arm catches a seal to stamp the seal on eight positions in the first experiment, and moves eight objects to the assigned positions in the second experiment.

In the first experiment, the robot arm executes catching a seal and stamps the seal on eight positions. The positions of the working space are shown in the right side of Fig. 6, and the relation distance of each working position is shown in the left side of Fig. 6. The robot arm must control the seal to stamp in the circle. The radius of the circle is 12mm. The robot arm programs a series trajectories using point to point control technology. First the robot arm moves to the initial position shown in Fig. 7(A), and catches the seal moving to the assign position "A", and falls to stamp the seal on the position shown in Fig. 7(B)-(D). Then the robot arm rises up and moves to the second position "B", and falls to stamp the seal on the assigned position shown in Fig. 7(E)-(H). The robot arm finishes the others step by step shown in Fig. 7(I)-(O). Finally the robot arm moves to the eight position, and falls to stamp the seal on the assigned position. Then the SCARA robot arm moves to the initial position and puts down the seal on the original position to stop shown in Fig. 7(P).

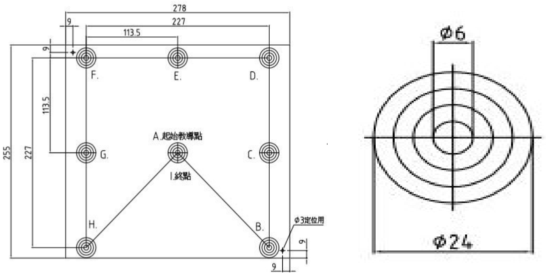

Fig. 6. The working space of the first experiment

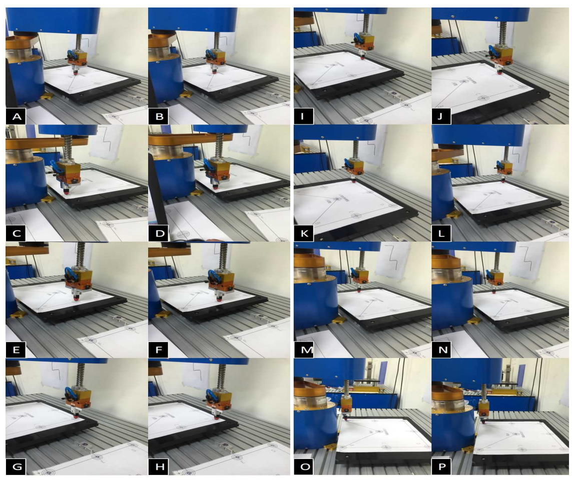

Fig. 7. The first experimental result

In the second experiment, the robot arm catches eight objects with the same size on the left side of Fig. 8, and moving to the right side with the same relation position. The size of each object is cube to be 1cm in length, width and height respectively. The robot arm programs a series trajectory using point to point control technologies, too. First the robot arm moves to the initial position shown in Fig. 9(A), and catches the first object on the right-up side. The object moves to the same position on the right side show in Fig. 9(B) and (C). Then the robot arm rises up and moves to the left-up position shown in Fig. 9(D), and catches the object moving to the assigned position shown in Fig. 9(E) and (F). And then the robot arm catches the others step by step, and moves and falls to the assigned position show in Fig. 9(M)-(Q). Finally the robot arm catches the last object on the left-down side and moves and falls on the assigned position show in Fig. 9(R) Then the robot arm moves to the initial position and stop.

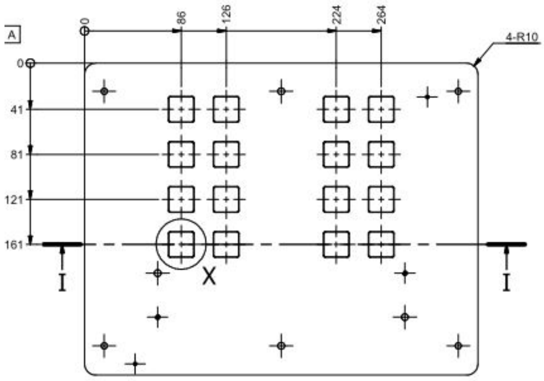

Fig. 8. The working space of the second experiment

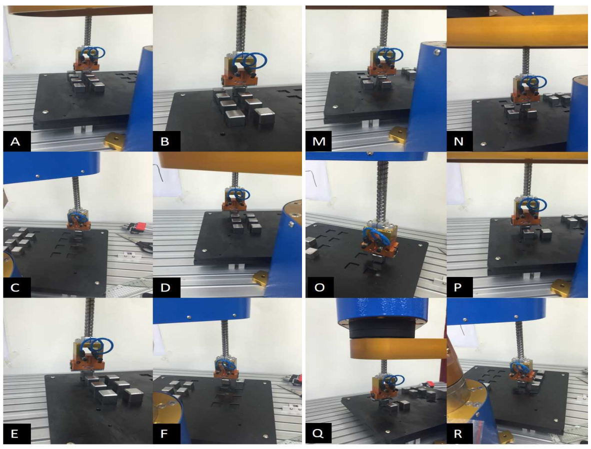

Fig. 9. The second experimental result

4. Conclusion

The papers designed and implemented a four joints SCARA robot arm, and controlled the robot arm using PLC based system. The PLC based system is ASDA-MS that is produced by DELTA Company in Taiwan. We calculated motion displacement and rotation angle of each joint from the inverse kinematic equations. In the experimental results, first the SCARA robot arm catches a seal, and falls to stamp the on eight positions one by one. Then the robot arm catches the eight objects moving to the assigned locations according to the programmed motion paths..

Acknowledgements

This work was supported by the Ministry of Science and Technology in Taiwan, (MOST 105-2221-E-224-022).

References

1. M. Shafik, B. Nyathi and S. Fekkai: An innovative 3D ultrasonic actuator with multidegree of freedom for machine vision and robot guidance industrial applications using a single vibration ring transducer, *International Journal of Engineering and Technology Innovation*, Vol. 3, No. 3(2013), pp.168-179.
2. M. Homayounzade and M. Keshmiri: Observer-based impedance control of robot manipulators, *International Conference on Robotics and Mechatronics* (2013), pp.230-235,
3. H. S. Sim, Y. M Koo, S. H. Jeong, D. K. Ahn and B. N. Cha: A study on visual feedback control of SCARA robot arm, *International Conference on Control, Automation and System* (2015), pp.1268-1270.
4. T. Kenmochi, N. Motoi, T. Shimono and A. Kawamura: A motion control method of dual arm robot based on environmental modes, *IEEE International Conference on Mechatronics* (2013), pp.458-463.
5. R. Karthikeyan, P. Mahalakshmi and N. GowriShankar: Smart laser based tracking system for robotic arm, *International Conference on Communication and Signal Processing* (2013), pp.903-907.
6. F. Cao, J. Chen, C. Zhou, Y. Z. Zhao, Z. Fu and W. X. Yan: A novel 5-DOF welding robot based on SCARA, *International Conference on Industrial Electronics and Applications* (2015), pp.2016-2019.

Transmission Power Control for Wireless Sensor Network

Kuo-Hsien Hsia
Department of Electrical Engineering, Far East University
No. 49, Zhonghua Road, Xinshi,
Tainan 74448, Taiwan (R.O.C.)

Chung-Wen Hung †, Hsuan T. Chang, Yuan-Hao Lai
Department of Electrical Engineering, National Yunlin University of Science & Technology
No. 123, Section 3, University Road,
Douliou, Yunlin, 64002, Taiwan (R.O.C.)
E-mail: khhsia@cc.feu.edu.tw, {† wenhung; htchang, m10312040}@yuntech.edu.tw
www.yuntech.edu.tw

Abstract

Wireless sensor networks can be widely applied for a security system or a smart home system. Since some of the wireless remote sensor nodes may be powered by energy storage devices such as batteries, it is a very important issue to transmit signals at lower power with the consideration of the communication effectiveness. In this paper, we will provide a fuzzy controller with two inputs and one output for received signal strength indicator (RSSI) and link quality indicator (LQI) to adjust transmission power suitably in order to maintaining a certain communication level with a reduced energy consumption. And we will divide the sampling period of a sensor node into four intervals so that the sensor node radio device does not in receiving or transmission status all the time. Hence the sensor node can adjust transmission power automatically and reduce sensor node power consumption. Experimental results show that the battery life can be extended to about 10 times for the designed sensor node comparing to a normal node.

Keywords: Transmission power control, fuzzy control, wireless sensor network, internet of thing.

1. Introduction

Sensors play an important role in a variety of intelligent applications or control systems. If a sensor cannot transmit the sensed message to the control panel, the control panel will never know what control signal to send. Thus one may say "No sensor, no control." As the development of wireless communication, a sensor module, which containing sensor unit and wireless transmission unit, can transmit the sensed information to the information center in wireless way. Such sensing modules can be distributed in different locations to form a wireless sensor network and transmit the sensed information back to the control center. Wireless sensor networks become the key technology for the IoT (internet of things) [1]. Since some of the wireless remote sensor nodes may be powered by energy-storage devices such as batteries, it is a very important issue to transmit signals at lower power with the consideration of the communication effectiveness. Researchers used TPC (transmission power control) to achieve the goal of maintaining communication quality with reduced node power consumption. Ikram et al used SINR (signal to interference plus noise ratio) and SNR (signal to noise ratio) to determine a golden receive power range of RSSI (received signal strength indicator) to ensure the success of signal transmission [2]. Ramakrishnan and Krishna developed a fuzzy logic based TPC for the consideration of energy efficiency [3]. However, only RSSI cannot guarantee a good communication in an environment with interference signals. Kim et al used LQI (link quality indicator), which is determined by signal strength and detected SNR, to determine if there is interference in the environment [4]. PER (packet error rate) is usually used as a performance index in determining an acceptable range of wireless signal transmission. Many documents showed that a system with PER over 1% may not retrieve the complete transmitted data [5-7]. So we set the allowable PER to be within 1% in our research.

2. Transmission Power Control

Maximizing the transmission power of each node in a wireless sensor network system can minimize the PER and make the transmission distance to the farthest. But this will lead to unnecessary power consumption and shorten the battery life of a wireless sensor node. Hence to control the transmission power with a certain level of communication being guaranteed is an important topic of transmit power control.

In general, the steps for controlling transmission power is as follows. At first the information about the transmission status, such as RSSI, LQI or SNR, of the node is gathered. Based on the transmission state information, the transmission power of the node is judged whether in an appropriate range or not. This range is determined by a large of experiments. If it is out of the range, then the transmission power has to be adjusted for successful communication.

The architecture of the TPC is shown in Fig. 1. It is implemented by TI CC430F6137 development board in this study. A Sub-1GHz transmission packet with the information about RSSI, LQI and CRC checking results attached will be received by the development board. RSSI, in dBm, can be used for determining whether the node transmission power is appropriately set or not. LQI represents the quality of connection in the current environment. In CC430F6137, LQI is expressed as a 7-bit positive integer. The lower the value is, the better the communication quality is. In this study, LQI will be used as a supplement. If the communication quality is too bad, then the transmission power will be added immediately to reduce the PER.

For CC430F6137, the transmission power of the Sub-1GHz is in the range of 10.7dBm to -69.2dBm. A total of

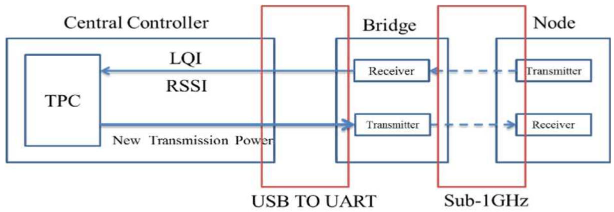

Fig. 1. Architecture of transmission power control.

121 transmission power parameters can be set. To prevent large variation of the parameters, only the transmission powers in the range of 10dBm to -34dBm are used. There are 45 emission power parameters with intervals about 1dBm in this range.

The transmission power is determined by the central controller with the RSSI and LQI at the end of a packet and then transferred to the nodes via bridge to adjust the transmission power of the nodes.

3. Fuzzy Transmission Power Controller

In order to establish the RSSI standard receiving range and the LQI threshold, a large number of experiments are needed to find out the relationship between RSSI/LQI and PER. The scenario of the experiments are described as follows:

1. There are a central controller, a bridge, and a node in our experiment. The central controller can command the node to transmitting data with a designated transmission power.
2. The initial emission power is set to 0dBm. This is the default set of CC430F6137. The distance between the node and the bridge (N-B distance) is 12m.
3. Since the RSSI value is easily disturbed by the environment and this may cause the output of the central controller variated frequently, a Kalman filter is used to eliminate the RSSI disturbance.

For the issue of RSSI, the central controller command the node to transmit a 32-byte data and extract the information of RSSI, LQI, and CRC checking result. The N-B distance varies from 1m to 12m stepping by 1m. At each distance, the node transmits 1000 data to the central controller through the bridge. The PER is defined by (1). And the resulting relationship of PER and RSSI is shown in Fig. 2.

$$PER = (\#(\text{lost package}) + \#(\text{error package}))/1000 \quad (1)$$

For the issue of LQI, an extra node transmitting noise is added to the experiments for RSSI. The N-B distance varies from 1m to 12m stepping by 1m. At each distance, the node transmits 1000 data to the central controller through the bridge in the noised environment. The PER is also defined by (1). The resulting relationship of PER and RSSI is shown in Fig. 3.

Refer to Fig. 2, the PER at RSSI equaling -81dBm is 1.1%. Hence we define the PER value as the lower threshold. Fig. 4 shows the RSSI of 500 data transmitted in 0dBm. The drift range is 9dBm. Hence the higher threshold can be set as -72dBm. The LOI threshold is set as 47 since the PER rising rapidly when LQI over 47 in Fig. 3. If the RSSI and LQI are in these ranges, the transmission power is maintained. If any one of them is out of the range, the transmission power will be adjusted by the fuzzy transmission power controller.

The membership functions of RSSI and LQI are defined in Figs. 5 and 6. The output of the controller, PAP, is an adjustment parameter. 7 fuzzy numbers of PAP are set for the controller. For the case that no power adjustment is needed, the output is AZ which is set as 0dBm. To set appropriate PAPs for the controller, we design an experiment to get the adjustment amount of node transmission power to tune the RSSI to -72dBm when RSSI is -100, -94, and -81dBm. The experimental result is shown in Fig. 7. The values marked in red are intervals from PL, PM, PS to high threshold. So we set the cores of PL, PM, and PS as 30, 22, and 7dBm, respectively. The cores of NL, NM, and NS are obtained in a similar way. The resulting membership functions are defined in Fig. 8. The control laws are as follows:

IF (LQI is PM) or (RSSI is NL) then (PAP is PL).
IF (LQI is PS) and (RSSI is not NL) then (PAP is PM).
IF (LQI is AZ) and (RSSI is not NM) then (PAP is PM).
IF (LQI is AZ) and (RSSI is not NS) then (PAP is PS).
IF (LQI is AZ) and (RSSI is not AZ) then (PAP is AZ).
IF (LQI is AZ) and (RSSI is not PS) then (PAP is NS).
IF (LQI is AZ) and (RSSI is not PM) then (PAP is NM).
IF (LQI is AZ) and (RSSI is not PL) then (PAP is NL).

Experiments show that the designed fuzzy controller can control the transmission power efficiently, and the PER can be reduced to under 1%. However, the efficiency of the battery is of no significant improvement.

4. Architecture of Time Division

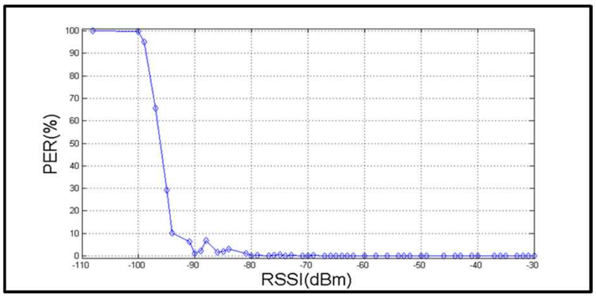

Fig. 2. Relationship of PER and RSSI.

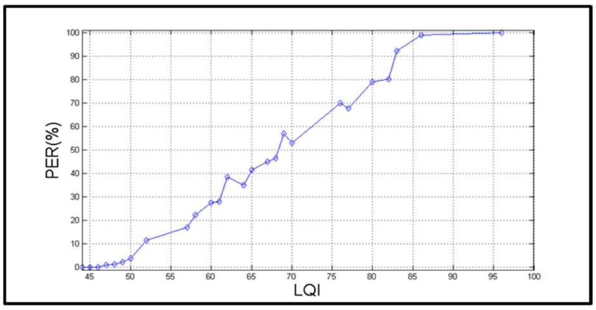

Fig. 3. Relationship of PER and LQI.

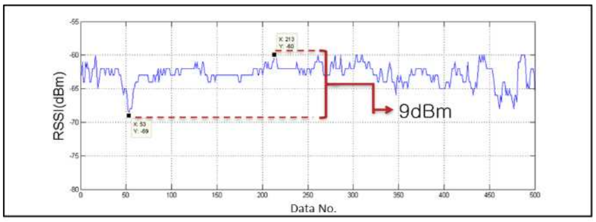

Fig. 4. Drift range of RSSI.

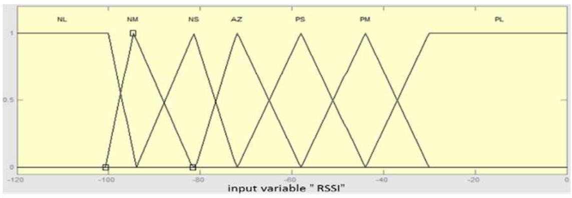

Fig. 5. Membership functions of RSSI.

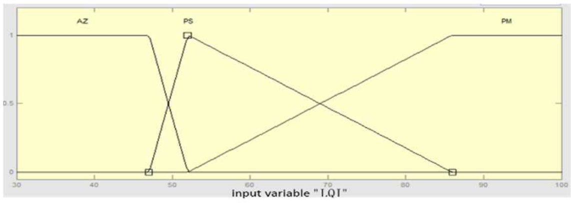

Fig. 6. Membership functions of LQI.

Time division communication is technique of preventing package collision in communication by shifting the transmission time at which each node transmitting the package. The architecture of time division of this paper is shown in Fig. 9. $T_{transform}$ is the time of a node changing status from sleep to data transmission. $T_{waiting}$ is the waiting time which is the sum the time of sensing neighboring sensors around the nodes and $T_{transform}$. T_{getN} is the data getting time for Node N. T_{acq} is the acquisition time of receiving information from all nodes.

The experimental results with battery of 1000mAh are summarized in Table 1. From Table 1, whether in short-distance or long-distance, the designed TPC controller can make PER less than 1%. If coupled with TDMA, the battery life can be increased by about 10 times.

Table 1. Experimental results of TDMA

N-B dist.	Type	#-Pack.	#-Err-Pack.	PER (%)
1 M	Normal	237072	32	0.013
	TPC	237476	56	0.024
	TDMA	2030361	185	0.009
	TDMA+TPC	2030361	311	0.015
12M	Normal	235292	8651	3.677
	TPC	234662	2087	0.889
	TDMA	2183322	52236	2.393
	TDMA+TPC	1977369	11172	0.565

5. Conclusion

We have successfully designed an energy-saving architecture of transmission power control for wireless sensor network. Battery life is important for a wireless remote sensing node. With our design, the battery life can be extend to about 10 times and also the reliability of the data transmission can be improved. It is suitable for smart home or home-security system design.

Acknowledgment:

This work is partially supported by the Ministry of Science and Technology, ROC, under contract No. MOST 105-2221-E-224-024.

References

1. International Electrotechnical Commission, *Internet of Things: Wireless Sensor Networks* (International Electrotechnical Commission, Switzerland, 2014).
2. W. Ikram, S. Petersen, P. Orten and N. F. Thornhill, Adaptive multi-channel transmission power control for industrial wireless instrumentation, *IEEE Trans. on Industrial Informatics*, **10**(2) (2014) 978-990.

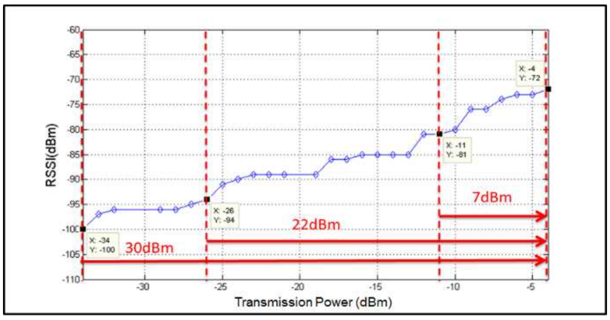

Fig. 7. Intervals of transmission power.

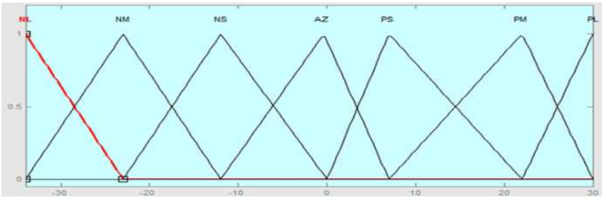

Fig. 8. Membership functions of PAP.

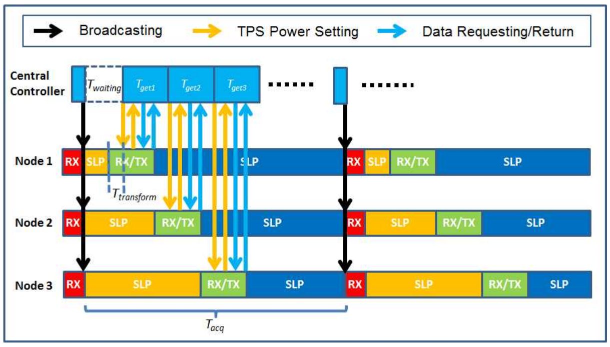

Fig. 9. Time division architecture.

3. S. Ramakrishnan and B. T. Krishna, Closed loop fuzzy logic based transmission power control for energy efficiency in wireless sensor networks, in *Proc. 2014 Int. Conf. Computer Communication and Systems*, (IEEE, 2014), pp.195-200.
4. S. K. Kim and S. H. Kim, Doo-Seop Eom, RSSI/LQI-based transmission power control for body area networks in healthcare environment, *IEEE J. Biomedical and Health Informatics*, **17**(3) (2013) 561-571.
5. S. Thodupunoori, *Reverse Link Performance of an 1xEV-DO Revision A System*, Master Thesis (University of Missouri-Kansas City, 2008).
6. S. Myneni, Application Note -- MRF89XA Radio Utility Driver Program (Microchip Technology Inc., 2010).
7. M. Petrova, J. Riihijarvi, P. Mähönen and S. Labella, Performance Study of IEEE 802.15.4 Using Measurements and Simulations, in *Proc. 2006 IEEE Wireless Communications and Networking Conf. - WCNC2006* (IEEE, 2006), pp. 487 – 492.

Mechanism of Autonomous Mowing Robot for Long Grass

Kuo-Hsien Hsia*
Department of Electrical Engineering, Far East University
No. 49, Zhonghua Road, Xinshi,
Tainan 74448, Taiwan (R.O.C.)

Yao-Shing Huang, Kuo-Lan Su and Jr-Hung Guo
Department of Electrical Engineering, National Yunlin University of Science & Technology
No. 123, Section 3, University Road,
Douliou, Yunlin, 64002, Taiwan (R.O.C.)
E-mail: khhsia@cc.feu.edu.tw, ahriman159@gmail.com, {sukl; g9710801}@yuntech.edu.tw
www.feu.edu.tw

Abstract

A land full of grass can be easily seen all over the world. For example, a golf course, a large playground, garden, waste plowed farmland and wild wasteland, all of above are full of grass. Almost all mowing work are operated by manpower, especially the long grass section. There have been some autonomous mowing robots for short grass up to now. However, there is almost no commodity for long grass mowing in the market. The main possible consideration may be the issue of safety. It is highly possible that a sharp mower blade may cause harm under the condition that the mower is not operated directly by a skilled person. In this paper, we will focus on the mechanism design for an autonomous mowing robot that can cut long grass safely. We will also outline the safety requirements for an autonomous mowing robot for long grass.

Keywords: Long grass, mowing robot, autonomous, agricultural machinery.

1. Introduction

A land full of grass can be easily seen all over the world. For example, a golf course, a large playground, courtyard, garden, waste plowed farmland and wild wasteland, all of above are full of grass and a mowing machine is needed for trimming. Almost all mowing work are operated by manpower, either carrying or driving, especially the long grass section. There have been some autonomous mowing robots for short grass up to now. However, it is now common in countries that the rural population is declining, while the cost of labor is increasing year by year. Therefore, if the mower can be working automated and unmanned, and allowed to adapt to different sizes of the work area, we believe that it should be considerable development and market size in the future.

Mowing machine is a kind of agricultural machinery. The trend of agricultural machinery industry are: (1) needs of automation since the aging of agricultural manpower and rural manpower reduction; (2) miniaturization, functional diversification and low prices; (3) environmental awareness resulting the regulatory requirements or need on the reduction of the relevant emissions, noise and energy consumption [1]. Therefore, it is important to co-ordinate products that meet market needs in response to this trend. Since autonomous robots must be able to operate autonomously in unattended situations, the primary consideration for autonomous mowing robots is the issue of safety. In this paper, we will focus on the mechanism design for an autonomous mowing robot that can cut long grass safely.

2. Overview of Mowing Machine

Generally, there are four kinds of mowing machine.

(1) Portable lawn mower, as shown in Fig. 1(a) [1]: This is the most popular kind of mowing machine. It is carried by a person and operated manually and cuts the grass by rotating the blade at the front end. It is suitable for a non-smooth terrain or a hillside. But it is dangerous since the blade is exposed and the mowing efficiency is poor. And it usually has the drawbacks of noise and air pollution because of fuel-engine driven. Hence some manufacturer replace the blade by a tendon rope or the fuel-engine by a motor, as shown in Fig. 1(b) [2].

(2) Self-propelled lawn mower, or push-type lawn mower, as shown in Fig. 1(c) [3]: This lawnmower is usually pushed by hand and cuts the weeds with the blades below the fuselage. The blade is mounted below the lawn mower, thus providing better safety. But for longer grass, there will be problems due to the mechanism. Most of its power source is by fuel engines, hence the noise and exhaust are still inevitable.

(3) Driving lawnmower, as shown in Fig. 1(d) [4]: This lawn mower is of a large body with a rotating blade below the fuselage. The operator can sit on it and control it like driving a car. This type of mower is more suitable for large and flat land, usually park, stadium, or large squares.

(4) Automated lawnmower, as shown in Fig. 1(e) [5]: The aforementioned lawn mowers need to be operated by people. This lawnmower basically uses the concept of sweeping robots, with the cleaning component replaced by a blade for mowing weed. It can be regarded as an autonomously moving robot. However, due to safety considerations, the blade must be completely hidden in the body, so it can only be used to cut the short grass. In addition, due to the characteristics of its institutions, it can only be applied to flat grass.

Fig. 1. Different types of mowing machine.

For the 4 types of mowing machine, only the portable lawn mower is suitable for long grass. However, it must be carried by a staff to operate, and it is very dangerous due to the exposed blade.

In a wasteland covered with long grass, it is likely to lurk some danger. Operating a lawn mower to finish a large grassy field of long grass requires a lot of manpower and time. In these cases, if one can have the help of autonomous mower, he will be able to avoid the dangerous and save much time.

3. Safety Requirement for Autonomous Robot

Machines or robots are working for people to save time and manpower, and to avoid dangerous. However, the safety should be the first and most important consideration on designing the manpower workings by robot workings. Almost all automatic or autonomous facilities (including systems) have to meet some safety requirements. For example, ISO 13482 is an international standard on the safety of personal care robots (life support robots) [6]. Hence all personal care robots have to meet the requirements of ISO 13482. Ni and Leung suggested some safety and liability of autonomous vehicle technologies [7]. ISO 26262 [8] is an international standard of safety-related features of electrical and electronic systems for the cars with total weight less than 3.5 tons and less than 8 passenger-seats. In our opinion, a safe autonomous long-grass mowing robot should meet the following regulations:

1. It will not make people hurt, especially by the blade.
2. The blade will not be broken by hard objects.
3. It can cut the long grass successfully.
4. It does not need to be driven by people.
5. It can move autonomously.
6. It can be commanded.
7. It can be stopped in emergency.
8. It has the ability of obstacle avoidance.
9. It can avoid falling into a hole or falling down due to terrain.
10. It can be programmed on moving.

The first regulation, which is the most important regulation, is to prevent people working or moving around the mowing robot to get injury in accident. The third regulation is the main function of the robot.

4. Possible Mechanism of Autonomous Mowing Robot

The simplest design of a mowing robot is to cut the grass with a high-speed rotating blade or tendon, just as people cutting the grass with a sickle in hand. But this will have a high chance of accidental injury to people nearby. In addition, because of the softness and flexibility of the stems and leaves of grass, if the blade rotation speed is not fast enough, the long grass cannot be cut smoothly.

Our design of the autonomous mowing robot contains four parts: (1) grasping part, (2) cutting part, (3) motion part, and (4) sensing part, as shown in Fig. 2. All parts are controlled by a central control unit. The motion part can be wheels or tracks. The sensing part may contain infrared, ultra-sonic, or laser distance sensors, force-feedback sensors, limit sensors, thermal sensors, cameras, or other sensors.

The grasping part and the cutting part work in close cooperation. The grasping part is responsible for the long grass caught up, and then the cutting part cuts the grasped

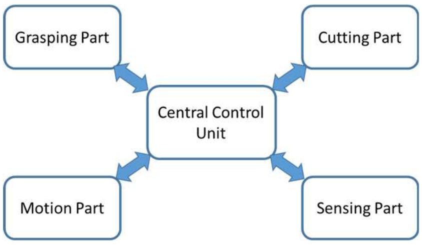

Fig. 2. Parts of the designed autonomous mowing robot.

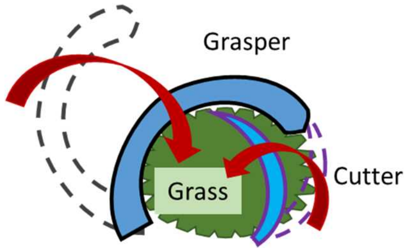

Fig. 3. Grasping and cutting parts work in cooperation.

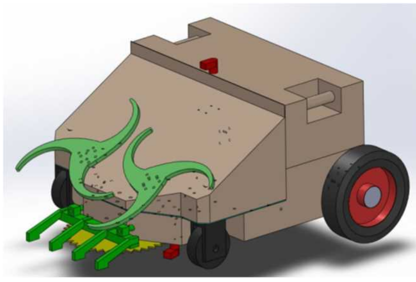
Fig. 4. Our design of the autonomous mowing robot.

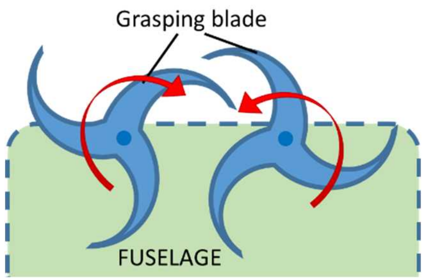

Fig. 5. Our design of the grasping part.

grass, as shown in Fig. 3. This mowing method is similar to the way people cut long grass. The cutting part can be a sickle, a gear saw, a chain saw, or clipping blades.

Fig. 4 is our design of autonomous mowing robot. It has four wheels for moving. The cutting part is a gear saw below the fuselage with a fence-type security mechanism. Anything touch the fence while the robot moving forward will cause the robot stop the gear saw immediately for safety. The grasping part is composed of two 3-arm rotating plate like shuriken in opposite direction and with phase angle difference 60°, as shown in Fig. 5. This phase angle difference is to ensure that the arms of these two grasping blades never collide with each other during rotation. Hence this mechanism can grasp the grass 6 times in one period. The grasped grass will be cut by the gear saw below the fuselage.

5. Discussion and Conclusion

A general self-propelled mower can only mowing short grass. For long grass cutting, only the portable lawn mower can deal with. Mowing with this type of mowing machine is not only hard but also of some potential dangers. In this paper, we have designed a new way for cutting long grass like the way of human cutting. Also the designed mowing robot can cut long grass in a safe way. This mowing robot without sensing part has been verified that it can successfully cut long grass. We will integrate software design and sensing systems to enable the design of the robot for autonomous moving with programmed route. We believe that an autonomous mowing robot for long grass will be commercially available in the market in the near future.

Acknowledgment:

This work is partially supported by the Ministry of Science and Technology, ROC, under contract No. MOST 105-2622-E-269-004-CC3.

References

1. http://www.jorco.com.tw/webc/html/product/02.aspx?kind=456
2. Energy - saving lithium battery mower, https://www.facebook.com/comlink.com.tw
3. http://www.jorco.com.tw/webc/html/product/02.aspx?kind=270
4. http://www.jorco.com.tw/webc/html/product/show.aspx?num=141&kind=117&page=1
5. http://detail.1688.com/offer/524607039492.html?spm=a261b.2187593.1998088710.109.xx
6. T. Jacobs and G. Singh Virk, ISO 13482 - The new safety standard for personal care robots, in *Proceedings of 41st International Symposium on Robotics (ISR/Robotik 2014)*, (IEEE, 2014), pp. 1-6.
7. R. Ni and J. Leung, *Safety and Liability of Autonomous Vehicle Technologies*, Massachusetts Institute of Technology (MIT): Boston, MA (2014).
8. ISO 26262-1:2011(en) Road vehicles — Functional safety — Part 1: Vocabulary, available at: https://www.iso.org/obp/ui/#iso:std:iso:26262:-1:ed-1:v1:en.

Design of Optimal Position Controller for Three-Phase Brushless DC Motor Applying Adaptive Sliding Mode Control

Tai-Huan, Tsai
Department of Mechatronic Engineering, National Taiwan Normal University,
162 Section 1 Heping E. Rd., Taipei City 106, Taiwan

Mei-Yung, Chen
Department of Mechatronic Engineering, National Taiwan Normal University,
162 Section 1 Heping E. Rd., Taipei City 106, Taiwan
E-mail: storyq29804@gmail.com, cmy@ntnu.edu.com.tw
www3.ntnu.edu.tw

Abstract

In this paper, we design an adaptive sliding mode controller which is applied to optimal position tracking of three-phase brushless DC motor. Considering the uncertainties and external disturbances of a three-phase brushless DC motor, we choose the sliding mode control (SMC) to be the major one. Normally we can't figure out the motor's uncertainty, so we propose an adaptive control to tune the motor's uncertainty. The adaptive control could be able to handle the unknown uncertainties and disturbances. Then we proved the stability of system by Lyapunov function, and the simulate results showed that it has excellent performance.

Keywords: adaptive control, sliding mode control, three-phase brushless DC motor.

1. Introduction

As we all know, the motor plays an important role in the automation industry. The motor can drive a lot of difference external load of mechanical structure. And the three-phase DC motor is better than the traditional motor. Because the operation of three-phase DC motor has no friction between the brush and the shaft, it has high durability and it is quiet. And because the three-phrase DC has no friction this characteristic, it can work on high speed and avoid to maintain. The three-phase brushless DC motor has gradually replaced DC motor in the automation industry. The three-phase brushless DC motor is a very good drive device, it can be used in many different mechanical structure and has good stability and controllability. In this study, we design a position controller with three-phase DC motor to let the motor get an optimal position and contribute in the automation industry.

2. The Mathematical Model of Three-Phase Brushless DC Motor

Brushless motors can be constructed in several different physical configurations: In the conventional configuration, the permanent magnets are part of the rotor. Three stator windings surround the rotor. In the outrunner configuration, the radial-relationship between the coils and magnets is reversed; the stator coils form the center of the motor, while the permanent magnets spin within an overhanging rotor which surrounds the core.

Three-phase DC motor's equivalent circuit diagram:

The equation is follow as:

$$\begin{bmatrix} v_u \\ v_v \\ v_w \end{bmatrix} = \begin{bmatrix} R & 0 & 0 \\ 0 & R & 0 \\ 0 & 0 & R \end{bmatrix}\begin{bmatrix} i_u \\ i_v \\ i_w \end{bmatrix} + \frac{d}{dt}\begin{bmatrix} L & M & M \\ M & L & M \\ M & M & L \end{bmatrix}\begin{bmatrix} i_u \\ i_v \\ i_w \end{bmatrix} + \begin{bmatrix} e_u \\ e_v \\ e_w \end{bmatrix} \quad (1)$$

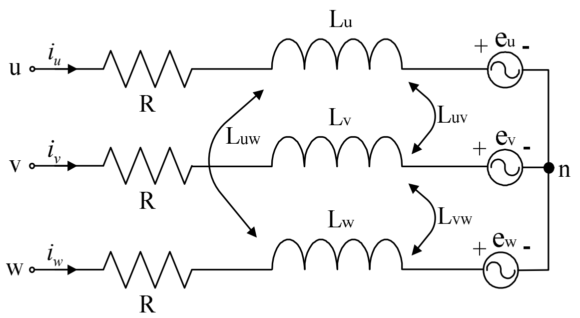

Fig. 1. Equivalent circuit diagram

The electromagnet torque and the dynamic mechanical equation is follow as:

$$T_e = \frac{(e_u i_u + e_v i_v + e_w i_w)}{\omega_r} \quad (2)$$

$$\frac{d\omega_r}{dt} = \frac{(T_e - T_L - B\omega_r)}{J} \quad (3)$$

3. Design Adaptive Sliding Mode Control

In this study, we design a sliding mode control to be the main controller because it has robustness. And we add the adaptive controller to estimates the unknown term.

3.1. *Sliding mode control*

An upper bound should be designed in a SMC and the parameter should be greater than other unknown parameters. First, we define switching function as $\sigma = \dot{e} + \lambda e$. And the error defined as $e = \theta - \theta_d$. θ is motor's current position, and θ_d is motor reference. The control law of SMC is shown as

$$u = B\omega_r + J\ddot{\theta} + J\lambda\dot{e} - k\,\mathrm{sgn}(\sigma) \quad (4)$$

3.2. *Adaptive Control*

In the system, the load and the disturbance of the motor is unknown. In this study, to let the controller have more robustness, the load of the motor is adjusted by adaptive method.

So, we define the load estimation as $\hat{T}_L$, and the current load as T_L. And we can get the equation and the adaptive control law as:

$$\hat{T}_L - T_L = \tilde{T}_L \quad (4)$$

$$u_{adap} = \hat{T}_L \quad (5)$$

The adaptive sliding mode control law is follow as:

$$u = B\omega_r + J\ddot{\theta} + J\lambda\dot{e} - k\,\mathrm{sgn}(\sigma) + u_{adap} \quad (6)$$

In steady state, this meets the design of the original parameter.

4. Stability Analysis

To prove the controller is stability, we need to define the Lyapunov function as:

$$V = \frac{1}{2}\sigma^2 + \frac{1}{2J}\tilde{T}_L^{\,2} \quad (7)$$

$$\dot{V} = \frac{\sigma}{J}\tilde{T}_L + \frac{1}{J}\tilde{T}_L\dot{\tilde{T}}_L - \frac{\sigma}{J}k\,\mathrm{sgn}(\sigma) \quad (8)$$

And we define $\dot{\tilde{T}}_L = -\sigma$, so we can get the Lyapunov function $\dot{V}$ as:

$$\dot{V} = -\frac{\sigma}{J}k\,\mathrm{sgn}(\sigma) = -\frac{k}{J}|\sigma| < 0 \quad (9)$$

5. Conclusion

This study proposed an adaptive sliding mode controller, and successfully used on the three-phase DC brushless motor. It has been clearly shown that a good transient response.

References

1. Zhi-Xiang Yang and Mei-Yung Chen, *Using Adaptive Sliding Mode Control with an Exponential Reaching Law to Improve the Response Time of Positioning of Robot Arm* (Taipai, Taiwan, 2014).

2. Bing-Hua Chou, Tian-Hua Liu and Cheng-Kai Lin, *Design and Implementation of Adaptive Sliding-Mode Controller for Synchronous Reluctance Motor Drive System*, (Tainan, Taiwan, 2010).
3. J. L. Shi, T. H. Liu, and Y. C. Chang, *Adaptive controller design for a sensorless IPMSM drive system with a maximum torque control* (Taipei, Taiwan, 2006), pp. 823–833.
4. L. K. Wong, H. F. Leung and Peter K. S. Tam, *A Fuzzy Sliding Controller for Nonlinear System*(Kowloon, Hong Kong, 2001)

Virtual surgery system with realistic visual effects and haptic interaction

Vlada Kugurakova
Digital Media Lab, Kazan Federal University, Kazan, Russia

Murad Khafizov
Ruslan Akhmetsharipov
Alexei Lushnikov
Diana Galimova
Vitaly Abramov
Digital Media Lab, Kazan Federal University, Kazan, Russia

Omar Correa Madrigal
University of Informatic Sciences, Havana, Cuba

E-mail: vlada.kugurakova@gmail.com, murkorp@gmail.com, ahmetsharipov.ruslan@gmail.com, alexkennyy@gmail.com, diana.lokiana@gmail.com, ivitazour@gmail.com, ocorreamadrig@gmail.com
www.kpfu.ru

Abstract

Currently, educational processes in medical surgery field involve not only theoretical in-class studies that are immediately followed by practical lessons in mortuaries and hospitals, but also involve simulations of various levels of reality. This paper describes our current progress in Virtual Surgery System development, which is targeted to support educational processes in medical surgery. With this system all surgery operations are performed using a virtual reality headset and haptic manipulators with force feedback. The main feature of our approach is applying a voxel data structure of a human body that provides an opportunity to simulate realistic behavior of the body. Thus, cutting, sewing, and welding of human tissues processes become realistic and, together with providing a realistic surgery scene, these will significantly speed up educational processes.

Keywords: Virtual surgery, virtual simulation, soft tissue mechanics

1. Use of VR in surgery simulations

As the presence of virtual reality in our daily lives increases, the educational system -- from the kindergarten and all the way to the college -- must respond to this new challenge. Naturally, medical surgical education is one of the top candidates for virtual reality technologies usage, as it can save many reagents and laboratory supplies, and overall reduce monetary spending[1]. This comes with a price of possible lack of proper experience with real-life operations and reduced realism of the simulation, which in surgery case can very well be downright lethal. We can, therefore, conclude that the field of virtual surgery has requirements much stricter than any other application of VR. What are those restrictions exactly?

- Highly-quality graphics, which can give the operating person a good idea of how the real thing looks;
- Realistic physics of human tissues and fluids, their proper response to various surgical procedures;
- Haptic and force feedback for user's hands according to situations in all processes;
- High level of user immersion.

As sad it might be to admit, none of currently existing virtual surgery solutions are capable of matching these criteria. This leads us to the point of this paper: we propose a complex of technological solutions for virtual surgery simulators. Among these technologies are:

- Implementation of soft tissue physics via triangulated mesh;
- Destruction and deformation of said mesh;
- Information collecting;
- Cloud storage of points necessary for rendering of multi-polygonal net;
- UV-less texturing;
- Manual interaction and haptic feedback using Glove One.

Following is description of how each of these technologies was implemented.

2. Soft tissue implementation with triangulated mesh

Proper simulation and rendering of physically realistic destructible soft tissue are costly both in resources needed to implement them and in computing power required for satisfactory performance. Hence, the choice of methods to use for this purpose is not to be taken lightly. After some deliberation of existing solutions with the functionality required for our project in mind, we settled on the triangulated mesh approach.

Following algorithms were used to implement functionality and physics of soft tissue with polygonal mesh.

2.1 *Tissue cutting*

To cut the mesh is to split the polygons located on the cutting line in half. This is accomplished by adding more edges and vertices.

Step 1. At the beginning of the process, we put a new vertex at the starting point of the cut line within the first triangle. From this vertex, we draw new edges to every other apex of this triangle, creating three new triangles as a result.

Step 2. Now, starting from this point, we start moving in the direction of the cutting tool, creating new vertices on every edge we cross. Old edges are replaced with a new one that are connected by the new apex, and extra edges are added to avoid creating quads.

Step 3. At the end of the cut, we repeat the process of the first step: splitting the last triangle into three parts.

We should note, that in this algorithm we limit the movement of the cutting tool to the straight line between two points on the triangle's edges. Because of this, the precision of the cut is in inverse relationship with the average size of triangle, and some of the more complex curves cannot be implemented into the cuts. One workaround for this is to add new vertices with predefined time intervals.

2.2 *Tissue tension*

We can implement the tissue tension by moving some vertices of the mesh, with movement gradually decreasing for vertices located further away from the initial point in which the force applies. The are several possible solutions for this.

The simplest one is to move all of the vertices within the given area. The amount of the movement would be inversely related to the distance between the moving vertex and the initial point to which force was applied. One critical flaw of this solution is, of course, the fact that it may end up moving the vertices not directly connected to the ones we were meaning to move.

The way the transformation affects an edge in the mesh depends on the angle between the edge and the direction of movement -- the acuter the angle, the greater would be the movement of the vertices adjacent to the edge. The spread of vertices movement further continues recursively, each one passing less movement to another one. This method allows us to simulate physics of tissue tension with satisfying accuracy. It is also advised to take the distance between vertices into account to reduce the number of visual artifacts.

2.3 *Tissue stitching*

To cut the mesh is to split the polygons located on the cutting line in half. This is accomplished by adding more edges and vertices.

There are two possible ways of implementing tissue stitching.

a. "Stapler-like" binding, in which specified vertices are bounded on the transformation level, passing each other information about their movement and acting in unison. In this case, we need to visibly mark the binding so it would be visible to player.

b. Stitching of the mesh. This method involves connecting two different meshes together with new edges and vertices, with triangles next to the seam being replaced to absorb the edges that are both adjacent and being stitched together.

3. Implementation of blood

Many mathematical blood flow models had been proposed by the researchers around the world, such as the ones described in Ref. 2, and we shall notice that the choice of the model is very strictly dependent on the purposes for which those model will be used. In the virtual surgery, the choice is affected by the specific operation, as blood may behave differently in different conditions. For now, we have settled on the general and all-purpose models for demonstration purposes.

While it is possible to implement blood as a system of particles each with its own form and textures, it is usually not recommended for most projects, as the computational complexity increases sharply. Physical interactions between each particle and surrounding tissue as well as surgery tools are very costly to compute and, as a result, lead to frame rate dropping. Visual artifacts in which particles "seep" through supposedly solid mesh are also not unheard of.

In our project, we used the Screen Space Fluids system. This system somewhat resembles the one we have described above but demands significantly less computational power. There is no need for a separate mesh or any other game objects in SSF implementation since all of the computing is done inside of the shaders. This greatly speeds up the whole process.

4. Digitalizing the human body

The soft tissue is merely one of the many building blocks of the human body, and of course, those blocks do not just float in the vacuum, separated from any other influences. In fact, the opposite is true -- human body is complex with so many systems of organs tightly intertwined it is almost impossible to seclude just a part of it for surgery processes least we want to sacrifice the realism of simulated operation. And yet, this is what we have to do. Our prime task, therefore, is to limit the consequences of separating the part of the body.

This is, however, not the only one issue we encounter. Recreation of even a separate part of the human body is a tedious process in itself. It's not only the physical properties of tissues and their biological purposes that are uneasy to properly implement -- the sheer size of the information we need to store is alarming by itself.

4.1 *Storing the information*

The data structure we choose directly affects the speed of information retrieval, recording and more. A good data structure can also spare us a lot of time and computational power, as we won't need to check every triangle sequentially to see if a collision has occurred. True, collision detection is one of the most essential things in any virtual simulation, and in a project where precision is literally a matter of life and death, extra effort should be put to ensure optimal performance.

A Bounding Volume Hierarchy may be used for this purpose -- a data structure which allows fast collision check, essentially a tree structure for sets of vertices[3, 4].

5. Conclusion

This concludes our report on the implementation of soft tissue physics. Naturally, this is the only beginning of the extensive research of the matter of virtual surgery and its possible applications for education. After the basics are properly implemented, we shall now focus on the creation of the realistic surgery simulation, which will consist of thoroughly recreated surgical operation -- appendix removal.

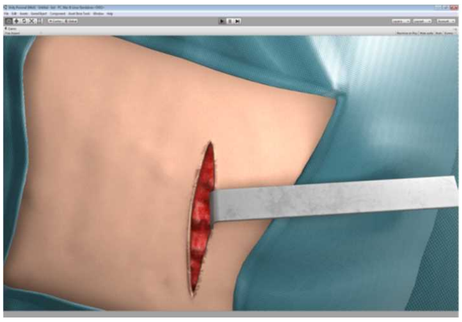

Fig. 1. Exampled of tissue cut rendered in real time

Acknowledgements

This work was funded by the subsidy of the Russian Government to support the Program of competitive growth of Kazan Federal University among world-class academic centers and universities.

References

1. V. Abramov, V. Kugurakova, A. Rizvanov, M. Abramskiy, N. Manakhov, M. Evstafiev and D. Ivanov. Virtual Biotechnological Lab Development. *BioNanoScience* 2016

2. O. Voropaeva, Y. Shockin. Numerical modeling in the medicine: goal setting and the results of the computations. *Computational technologies* (2012) pp 29-55

3. Samet, H. (1989, July). *Hierarchical spatial data structures. In Symposium on Large Databases* (pp. 191-212). Springer Berlin Heidelberg.

A. Baerentzen. Octree-based volume sculpting. In *IEEE Visualization*, 1998

A Human Reaching Movement Model for Myoelectric Prosthesis Control

Go Nakamura*, Taro Shibanoki†, Yuichiro Honda*, Akito Masuda‡, Futoshi Mizobe§, Takaaki Chin* and Toshio Tsuji**
**Robot Rehabilitation Center in The Hyogo institute of Assistive Technology, †Ibaraki University,*
*‡Kinki Gishi Corporation, §Hyogo Rehabilitation Center Hospital, **Hiroshima University*
E-mail: g_nakamura@assistech.hwc.or.jp

Abstract

This paper proposes a reaching movement model for the generation of desired trajectories within a myoelectric prosthesis training system. First, an experiment was performed to observe reaching movements with a non-impaired subject and a myoelectric prosthesis user. Reaching movements made by the prosthesis user were then adopted to construct a model based on a logistic function. The proposed model can be used to generate three trajectory types with a bell-shaped speed profile with the adjustment of only a few parameters.

Keywords: Myoelectric prostheses, Motion planning, Logistic function

1. Introduction

The prescription of myoelectric prostheses to upper-limb amputees supports everyday living and opens up new possibilities for rehabilitation. However, months of training is needed until such prescription can be made. Before being able to use a myoelectric prosthesis, patients must learn the skills necessary to perform tasks with natural posture (e.g., the direction of grasping approach and the manner of forearm usage) in addition to smooth hand opening/closing [1]. However, there is currently no quantitative evaluation method or training system for prosthesis control with natural posture. Against such a background, the authors sought to support myoelectric prosthesis prescription by developing a training system (Fig. 1). The establishment of an evaluation method and such a system requires the construction of a model capable of generating human reaching movement trajectories. A clinically applicable training system with such a model requires the following features: (1) high adaptability for generation of optimized and other trajectories (as myoelectric prosthesis users do not have the reaching movement of non-impaired people due to wrist-related limitations); (2) adjustability of hand velocity (movement time) in consideration of individual differences and variations in trainees' operational ability; (3) easy and intuitive trajectory adjustment for use in clinically applicable training; and (4) real-time trajectory generation for use in training. A number of studies on human reaching movement have been conducted [2] – [4] to clarify the human motor planning mechanism. By way of example, the minimum-jerk model [2], the minimum torque-change model [3] and the minimum-variance model [4] have all been proposed and found to be capable of generating human trajectories accurately. However, the trajectories in these studies were determined via optimization calculation; it is difficult to generate trajectories in real time. For control of machinery such as manipulators and vehicles, real-time trajectory generation models have been proposed [5] – [7]. As an example, Tsuji *et al*. proposed a real-time trajectory generation model based on an artificial potential field and a time base generator (TBG) involving a scalar signal with a controllable finite duration and a bell-shaped velocity profile. However, these models are accompanied by problems such as the difficulty of adjusting the many related parameters, which are determined by trial and error.

This paper proposes a human reaching movement model for myoelectric prosthesis control training. The model has high adaptability and can be used to generate three hand trajectory types (straight-line paths, circular-arc paths and S-shaped paths) with a bell-shaped speed profile in near-real time with the adjustment of only a few parameters.

2. Human Reaching Movement for Myoelectric Prostheses

2.1. *Experimental conditions*

A monitoring experiment was conducted with a non-impaired subject (25 years old, male) and an experienced myoelectric prosthesis user (49 years old, male; MyoBock hand) toward the development of a reaching movement model for myoelectric prosthesis control. The prosthesis user was a right upper-limb amputee (amputation site: 14 cm below the elbow), and had used a myoelectric prosthesis for 14 years. His average score for the Box and Block Test [8] was approximately 40 blocks, which exceeds the average of normal-level users. His performance was more efficient than that of most myoelectric prosthesis users.

The subjects were asked to sit on a chair and pick up a cup from one of nine locations on a table, lift it to their mouth and return it to its original location. Each task

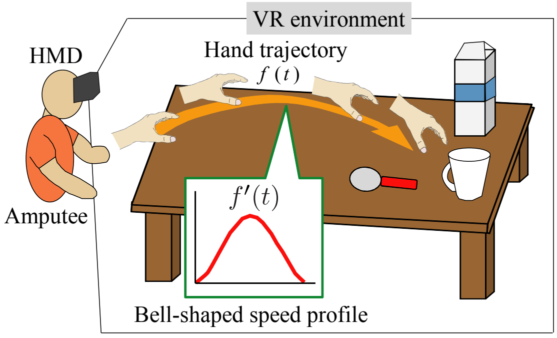

Fig. 1. Concept of the training system for myoelectric prosthesis control using the prosthetic arm trajectory model

was repeated five times. A 3D position sensor (Isotrak II, Polhemus Corp.) was attached to the right cubital fossa of each subject, and their elbow positions $\boldsymbol{P}_{\rm elbow}(t) = [x, y, z]^{\rm T}$ (accuracy: ± 2.4 mm) and postures (Eulerian angle) $\boldsymbol{\theta}_{\rm elbow}(t) = [\alpha, \beta, \gamma]^{\rm T}$ (accuracy: ± 0.75 °) were measured at 60 [Hz]. The hand trajectories and hand velocity were evaluated by calculating the hand position $\boldsymbol{P}_{\rm hand}(t)$ from the measured elbow position and posture. The hand position $\boldsymbol{P}_{\rm hand}(t)$ is defined as follows:

$$\boldsymbol{P}_{\rm hand}(t) = \boldsymbol{P}_{\rm elbow}(t) + A \begin{bmatrix} \cos\beta \sin\gamma \\ \sin(-\beta) \\ \cos\beta\cos\gamma \end{bmatrix} \quad (1)$$

Here, A is the forearm length as determined in advance. However, the two subjects had different degrees of freedom in the wrist because the wrist joint of a myoelectric prosthesis is fixed, making evaluation on a level playing field difficult. Accordingly, the location of the wrist joint was defined as the hand position. Hand velocity was estimated using a second order Butterworth low-pass filter (cut-off frequency: 10 [Hz]), and was then calculated using a low-pass differential filter. As the study focused on reaching for and picking up a cup, a two-dimensional trajectory model was constructed as a first step.

2.2. *Results*

Figures 2 shows scenes of reaching tasks for the non-impaired subject and the myoelectric prosthesis user, respectively. Figure 3 shows trajectories observed in reaching for the cup, with origin coordinates based on the initial hand position. The trajectories represent the average of five trials for each subject. The dashed lines represent the standard deviation for five sessions. The figure shows linear trajectories for both subjects. The trajectories of the skilled myoelectric prosthesis user exhibit characteristics similar to those of the non-impaired subject, but several distinctive differences such as different end points are also observed. The myoelectric prosthesis user also approached the cup placed in the nearest row (lower right, bottom and lower left) after pulling back his elbow, and the trajectories show downward movement. This can be attributed to the fixed wrist joint of the myoelectric prosthesis, which meant that the end points and trajectories for the cup in the nearest row were affected by wrist flexion/extension limitations. The two subjects exhibited different wrist postures at the time of grasping (Fig. 2).

Figure 4 shows hand velocity results based on averages of five trials for each subject. Velocity for the myoelectric prosthesis user was lower than that for the non-impaired subject, but both exhibit bell-shaped velocity profiles. This is because the myoelectric prosthesis user was able to approach the target while opening his hand within the series of motions, and performed the tasks without reducing hand velocity. Figure 2 shows that the myoelectric prosthesis user opened the hand at the start of the approach. These results indicate that the myoelectric prosthesis user performed the tasks with smooth control and hand velocity similar to that of the non-impaired subject.

The hand position and posture data are characterized by a monotonously increasing/decreasing function or a combination thereof, and a similar tendency for all data was observed. The next step in the study was to construct a human reaching movement model using a logistic function.

3. Trajectory Generation Model for Myoelectric Prostheses

The proposed model is designed to highlight the appropriate trajectory to a target in a training system. As this study focused on accurately reproducing measured hand trajectory and velocity, the model was not based on the human movement mechanism.

3.1. *Logistic function*

The study involved the proposal of a human reaching movement model using a logistic function.

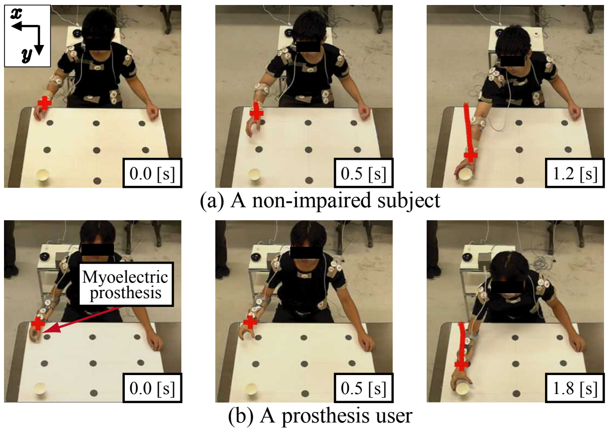

Fig. 2. Subjects approaching the cup with upper-right placement

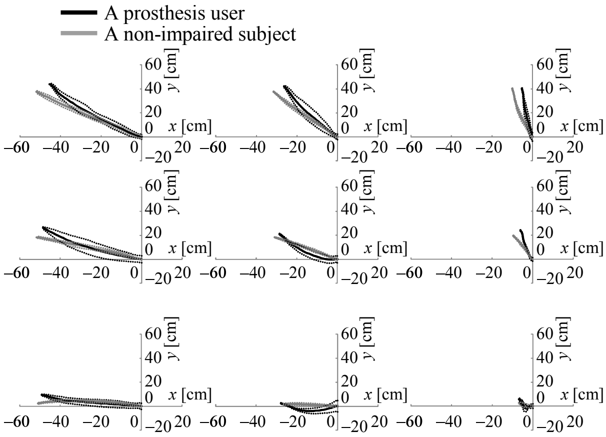

Fig. 3. Measured hand trajectories for the non-impaired subject and myoelectric prosthesis user

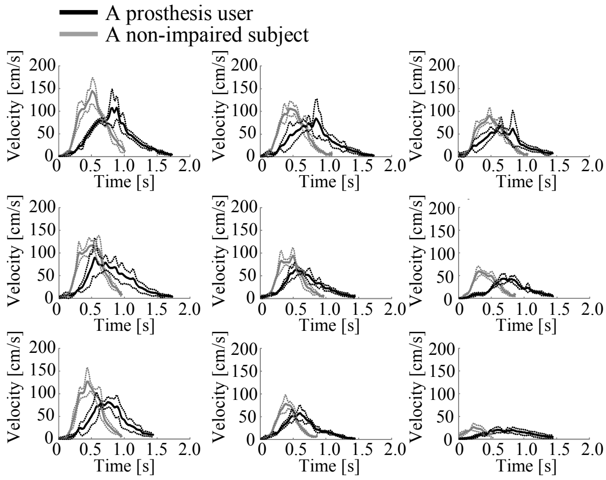

Fig. 4. Measured hand velocities for the non-impaired subject and myoelectric prosthesis user

$$f(t) = \frac{l_r}{1 + A_r(e^{-a_r t})} \tag{2}$$

$$l_r = p_r^{\text{end}} - p_r^{\text{start}} \tag{3}$$

Here, $r = (x, y, z, \alpha, \beta, \gamma) \in \boldsymbol{R}^6$, p_r^{start} is the start point and p_r^{end} is the end point. A_r is defined as $A_r = e^{a_r t_r}$. l_r, a_r and t_r are parameters determining function behavior.

3.2. *Spatial trajectory model*

The study involved the proposal of a human reaching movement model using a logistic function.
$x(t)$ and $y(t)$ are defined as

$$\begin{cases} x(t) = \frac{l_x}{1+A_x(e^{-a_x t})} & (4) \\ y(t) = \frac{l_y}{1+A_y(e^{-a_y t})} & (5) \end{cases}$$

To derive an equation for trajectory on the XY plane, the parameter t for (4) and (5) is eliminated. The trajectory on the XY plane can be represented as

$$y = \frac{l_y}{1 + A_y \left| \frac{l_x - x}{A_x x} \right|^k} \tag{6}$$

Here, k is defined as $k = \frac{a_y}{a_x}$.
To prevent the denominator from being 0, (6) can be transformed by multiplying the numerator and denominator by $|A_x x|^k$:

$$y = \frac{l_y |A_x x|^k}{|A_x x|^k + A_y |l_x - x|^k} \tag{7}$$

Here, the condition is given by $0 \leqq x \leqq l_x$.

The proposed model can be used to generate three hand trajectory types (straight-line paths, circular-arc paths and S-shaped paths) featuring a bell-shaped speed profile with the adjustment of only the two ratios of a_y/a_x and t_y/t_x.

Straight line paths can be generated by setting l_x and l_y under the conditions of $a_x = a_y$ and $t_x = t_y$. Figure 5 shows time histories of spatial trajectory based on the parameters l_x and l_y.

For circular arc paths, trajectories are generated under the conditions of $a_x = a_y$ and $t_x \neq t_y$. These paths can be controlled by adjusting only the ratio of t_y/t_x with $a_x = a_y$ maintained. Figure 6 shows time histories of spatial trajectory based on the parameters t_y/t_x. The curvature gradually increases the farther the ratio of t_y/t_x is from 1.0.

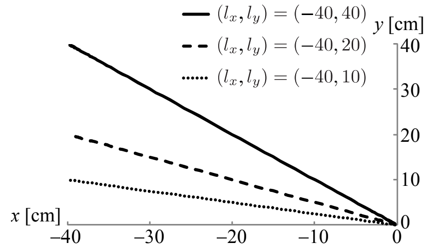

Fig. 5. Straight-line path dependence on the parameters l_x and l_y

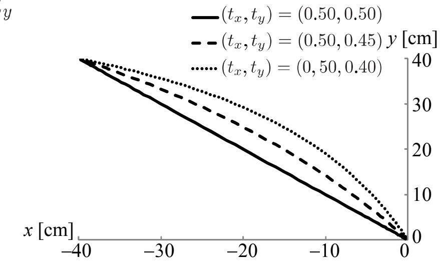

Fig. 6. Circular-arc path dependence on the parameters t_y/t_x

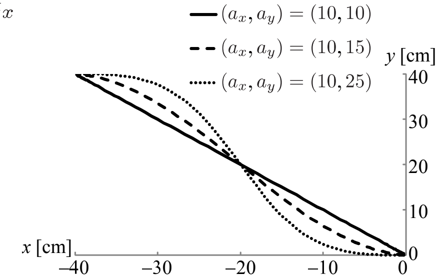

Fig. 7. S-shaped path dependence on the parameters a_y/a_x

For S-shaped paths, trajectories are generated under the conditions of $a_x \neq a_y$ and $t_x = t_y$. These paths can be controlled by adjusting only the ratio of a_y/a_x with $t_x = t_y$ maintained. Figure 7 shows time histories of spatial trajectory based on the parameters a_y/a_x. The curvature gradually increases the farther the ratio of a_y/a_x is from 1.0.

3.3. *Bell-shaped velocity profiles*

The proposed model can be used to generate bell-shaped velocity profiles. Single-peaked (unimodal) profiles, double-peaked (bimodal) profiles and other types can be expressed only with adjustment of a_y/a_x and t_y/t_x.

Unimodal profiles can be generated under the conditions of $t_x = t_y$. These profiles can be controlled by adjusting only the ratio of a_y/a_x with $t_x = t_y$ maintained. Figure 8 shows time histories of spatial trajectory based on the parameters a_y/a_x. Kurtosis gradually increases the farther the ratio of a_y/a_x is from 1.0.

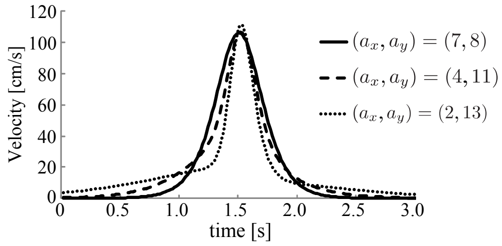

Fig. 8. Unimodal profile dependence on the parameters a_y/a_x

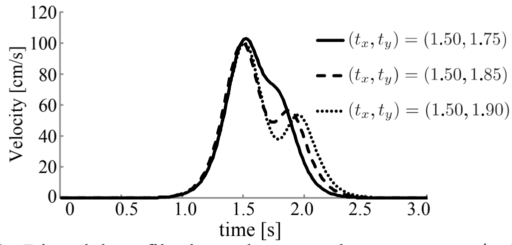

Fig. 9. Bimodal profile dependence on the parameters t_y/t_x

Bimodal profiles can be generated under the conditions of $t_x \neq t_y$. These profiles can be controlled by adjusting only the ratio of t_y/t_x. Figure 9 shows time histories of spatial trajectory based on the parameters t_y/t_x. The inter-peak distance gradually increases the farther the ratio of t_y/t_x is from 1.0.

3.4. *Adjustment of movement time*

This subsection outlines how movement time for the proposed model is adjusted. For the logistic function, it is difficult to specify the convergence time because it is not necessarily a finite period. To address this problem, a small arbitrary positive constant ϵ was set. The movement time is defined as t_f , and the logistic

$$f(t_f) = \frac{l_r}{1 + A_r(e^{-a_r t_f})} = l_r(1 - \epsilon) \tag{8}$$

functions $f(t)$ at $t = t_f$ can be expressed as

Solving (8) gives the parameters a_r and t_r , which specify the movement time. The issue of their mutual dependence is solved by fixing t_r as the time at which the function is $l_r/2$. t_r can then be easily estimated from measurement values. In addition, a rational value for t_r can be obtained because $t_r = t_f/2$ even when it is difficult to obtain a measurement value. Accordingly,

$$a_r = \frac{1}{t_f - t_r} \log \left| \frac{1 - \epsilon}{\epsilon} \right| \tag{9}$$

t_r is fixed in advance and a_r is calculated as

Here, the condition is given by $t_r < t_f$ and $0 < \epsilon < 1$. Specifying t_f allows setting of the desired movement time.

4. Simulation Experiment

A simulation experiment was conducted to evaluate the proposed model's propensity for hand trajectory generation. t_x and t_y were set as the times at which the observation values of $x(t)$ and $y(t)$ were nearest to $l_x/2$ and $l_y/2$, respectively. The parameter t_f was the measured movement time, and a_x and a_y were given using (9). ϵ was set as $\epsilon = 0.01$.

Figures 10 and 11 show reaching hand trajectories and hand velocity for each subject, respectively. Solid lines represent hand velocity based on the averages of five trials for observation and generation using the proposed model, and dashed lines represent the standard deviation for five sessions. Although approximation errors are seen with the reaching hand trajectories and hand velocity of the myoelectric prosthesis user for the cup placed in the nearest row, the simulated hand trajectories and hand velocity both correspond to the observations, and the simulated and observed lines are almost identical. Approximation error for the nearest row arises because that the observed time-series data are a combination of an increasing/decreasing function, and the proposed model based on a monotonously increasing/decreasing function was not capable of accurate replication. With this in mind, the authors plan to introduce methods for appropriate combination with the proposed model. From these results, it can be concluded that the proposed model is capable of generating hand trajectories and hand velocity data both for non-impaired subjects and for myoelectric prosthesis users.

5. Conclusion

This paper proposes a human reaching model for myoelectric prosthesis control. In the study, the authors performed an experiment to observe reaching movements with a non-impaired subject and a myoelectric prosthesis user. The distinctive characteristics of reaching movements made by the prosthesis user were identified and adopted to support the construction of a model. A simulation experiment was also performed, with results indicating that the proposed model was capable of successfully generating hand trajectories for both subjects.

In future work, the authors plan to introduce methods for combination with the proposed model and expand it model will also be applied for use with a training system.

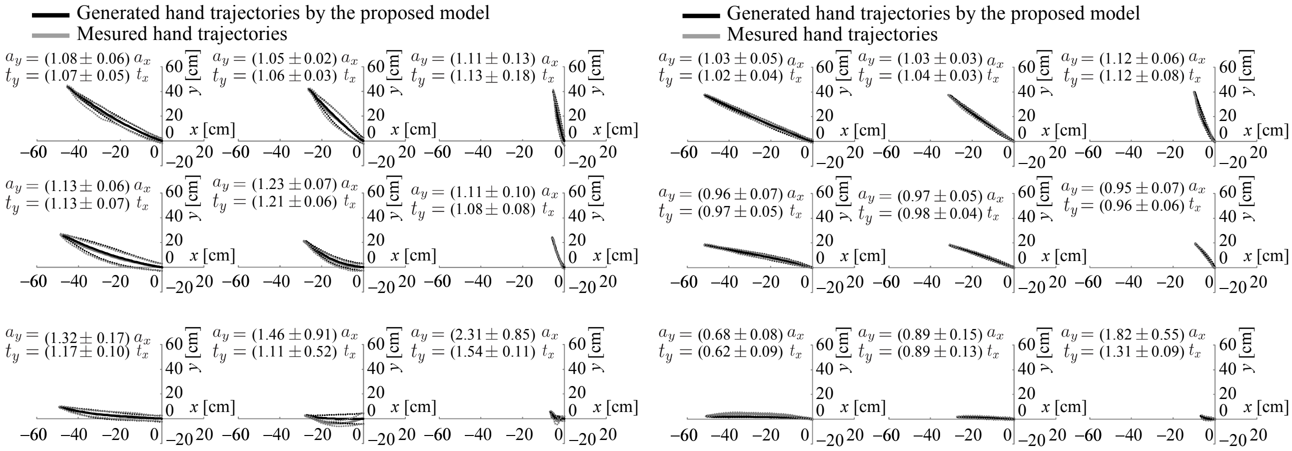

(a): A prosthesis user (b): A non-impaired subject

Fig. 10. Observed and simulated hand trajectories for the myoelectric prosthesis user and the non-impaired subject

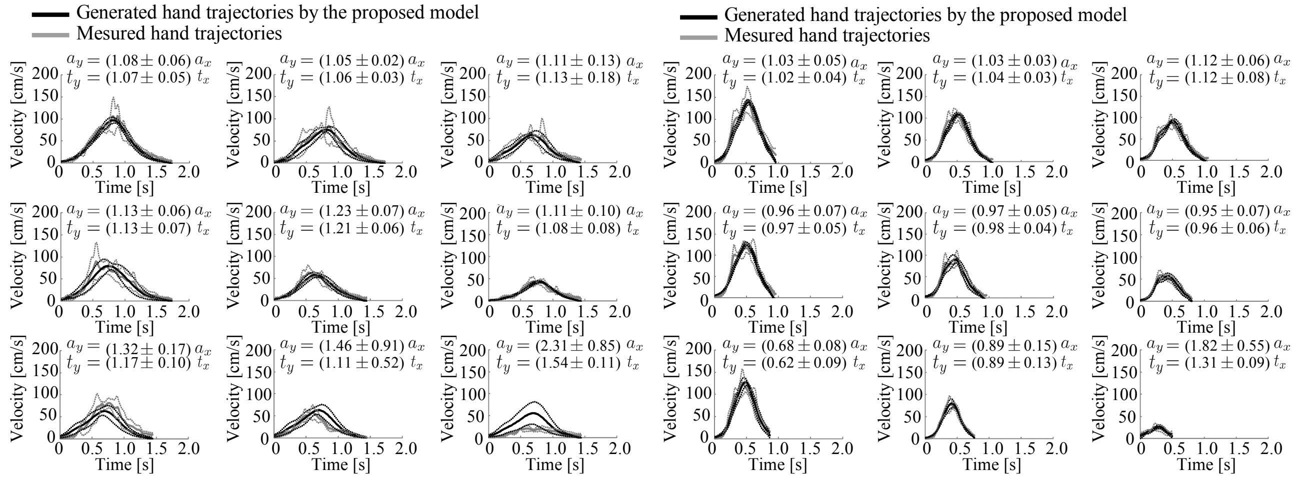

(a): A prosthesis user (b): A non-impaired subject

Fig. 11. Observed and simulated hand velocity for the myoelectric prosthesis user and the non-impaired subject

Acknowledgements

This work was partially supported by a Grant-in-Aid for Young Scientists B Number 26730111.

References

1. T. Chin, *Kinden Gishiyu Kunren Maniyuaru*, All-Japan Hospital Publication Association Ltd. (2006), p. 83. (in Japanese).
2. T. Flash and N. Hogan, The Coordination of Arm Movements: An Experimentally Confirmed Mathematical Model, *Journal of Neuroscience* **5** (7) (1985) 1683–1703.
3. Y. Uno, K. Kwato and R. Suzuki, Formation and Control of Optimal Trajectory in Human Multi-joint Arm Movement, *Biol. Cybern.* **61** (1989) 89–101.
4. C. M. Harris and D. M. Wolpert, Signal-dependent Noise Determines Motor Planning, *Nature* **394** (1998) 780–784.
5. P. Morasso, V. Sanguineti and T. Tsuji, A Dynamical Model for the Generator of Curved Trajectories, *Proceedings of the International Conference on Artificial Neural Networks* (1993) 115–118.
6. T. Tsuji, Y. Tanaka P. Morasso, V. Sanguineti and M. Kaneko, Bio-mimetic Trajectory Generation of Artificial Potential Field with Base Generator, *IEEE Transaction on Systems, Man and Cybernetics* **32** (4) (2002) 426–439.
7. T. Tanaka and T. Tsuji, Bio-mimetic Trajectory Generation Using a Neural Time-base Generator, *The Journal of Robotic Systems* **22** (1) (2005) 625–637.
8. V. Mathiowetz, G. Volland, N. Kashman and K. Weber, Adult Norms for the Box and Block Test of Manual Dexterity, *The American Journal Occupational Therapy.* **39** (6) (1985) 386–391.

Re-creation of a membrane puncture's sense of an object constituted of liquid and an outer membrane by a haptic device and a deformation simulation of the virtual objects

Takahiro Okada
Graduate School of Computer Science
and System Engineering
Kyushu Institute of Technology
680-4, Iizuka City, Fukuoka, Japan, 820-8502
okada@mmcs.mse.kyutech.ac.jp

Eiji Hayashi
Department of Mechanical Information
Science and Technology
Kyushu Institute of Technology
680-4, Iizuka City, Fukuoka, Japan, 820-8502
haya@mmcs.mse.kyutech.ac.jp

Abstract

The purpose of this research is to develop a combined sense system that uses both force feedback and visual feedback on a deformation simulation. We constructed a haptic device that gives a sense of that force to the operator when touching the sample on a computer. We focused on a way to recreate a membrane puncture's sense of salmon roes.

Keywords: force feedback, haptic interface, simulation

1. Introduction

Technologies that can accurately perform minute work are now being sought for medical treatment and bio technology field. Such minute work is improved by using micromanipulators, but their operation is difficult because the operator has no sense of force. He or she relies only on sight through a microscope. As a result, a person skilled in the use of this technology is needed for all minute work. The efficiency of minute work would be improved if the operator is able to have a sense of force while using a manipulator.

Here we describe the development of a more efficient system for minute operations. Our aim is to develop a system using not only the sense of sight through a microscope but also a sense of force from the manipulator. For this research, focus on to recreate reaction force of puncture against an object which constituted of liquid and an outer membrane. Among them, salmon rows were handled in this research.

1. System Structure

The system structure is shown in Fig. 1. This system consists of the haptic device for generating reaction force, a microcomputer for controlling the haptic device, simulation for showing virtual objects and microscope for measuring dynamic characteristics.

Fig. 2 provides a diagram of the haptic device. It consists primarily of a rotor, a laser, and a position-sensitive detector (PSD). The angle of the rotor can be measured by the laser and the PSD. The haptic device has a coil on the rotor with a polarity magnet. When current flows through the coil, the coil experiences a force (Lorentz force) perpendicular both external magnetic field and to the direction of the current flow. The rotor is able to stable follow an input waveform less than the frequency 36 Hz.

Fig. 3 shows the connection between the haptic device and a microcomputer. The haptic device is controlled by command signals from the microcomputer process.

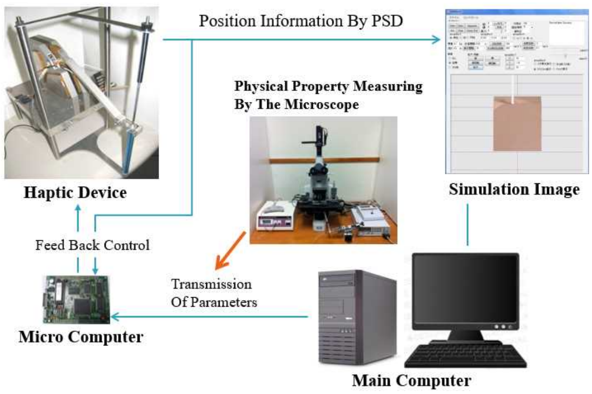

Fig.1. The system structure.

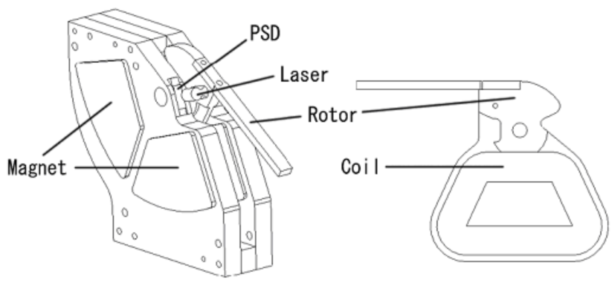

Fig.2. The structure of the haptic device.

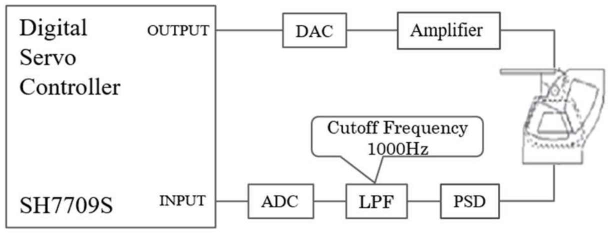

Fig.3. The connection between the haptic device and a microcomputer.

2. Force modeling for sensing a membrane puncture.

This section describes the modeling of a membrane puncture's sense of an object constituted of liquid and an outer membrane. The object is assumed salmon rows. Because salmon rows are easy to get and tractable.

Fig.4 shows the relation between the pushing amount of needle and the reaction force. The reaction force by deformation before puncture is modeled by the Voigt's model. When the pushing amount exceeds the puncture point, Transition to Maxwell's model that is expressed as a viscous resistance of a liquid. At this moment, operators can feel the puncture sense by caused the sudden fall of the reaction force. Fig.5 shows each model, and Table.1 shows characteristics of each model.

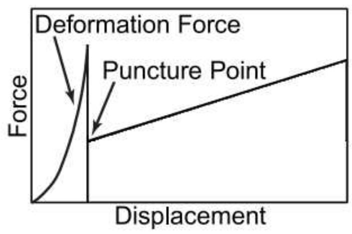

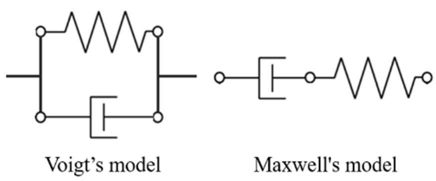

Fig.4. The relation between the pushing amount of needle and the reaction force.

Fig.5. Voigt's model and Maxwell's model.

Table.1. Characteristics of each model.

Item \ Model	Maxwell's model	Voigt's model
Combination of spring and damper	Serial	Parallel
Viscoelasticity	Liquid-like	Solid-like
Step input of stress Step input of strain	A moment elasticity Stress relaxation	A delay elasticity Creep

3. **Deforming the sample in simulation**

In this study, we attempted to build a working system using a microscope, a haptic device, and a simulation. A fundamental element was simulating the deformation of a minute object. Fig.6 shows the graphical user interface (GUI) of the simulator. A graphic tool was created using OpenGL to draw the object and to choose the shape of the sample, for instance, a cube or sphere. The dynamic model of the sample consisted of a spring-mass array of mass points in both the vertical and horizontal directions. An example of the arrangement of mass points is shown in Fig. 7 When a force was applied at a mass point, the simulation calculated the speed of all mass points that had been affected. The image was renewed after every ten calculations.

We defined a spring as having a size but no weight, and a mass point as having a size, a weight, and a rigid body. An arbitrary mass object can be placed on a spring on a bitmap (Fig. 8). In addition, a sample can be seen from various viewpoints, and the deformation of the sample, which is impossible to observe by microscope, can be checked. The shape of this object can be either a cube or a sphere, and any point may be selected as a fixed point or an operating point.

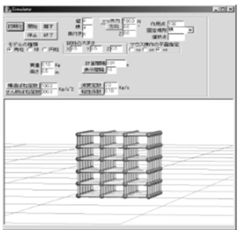

Fig.6. Simulator.

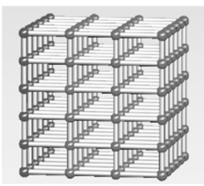

Fig.7. Arrangement of mass points

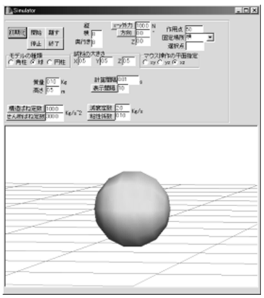

Fig.8. Placing an arbitrary object on a bitmap.

4. **Characteristic measurements and a reappearance experiment for an object**

Dynamic characteristics of the object were measured and then recreated using the haptic device as reaction force before puncture. The object used this time was salmon roe. We measured the response of salmon roe and showed the displacement of its surface a figure. Fig. 9 shows the response of the salmon roe.

Salmon roe is 6 millimeters in diameter and we cannot precisely feel the sense of touch. Hence values in the figure are multiplied by 68 so that human can feel the sense of salmon roe's touch. Fig. 10 shows that response of the salmon roe and haptic device. Table.2 shows the frequency, constant of spring, and damping coefficient in each ectopic focus.

In this experiment, there was a tendency to create a touch feeling that resembles a real and big salmon roe when characteristic was recreated.

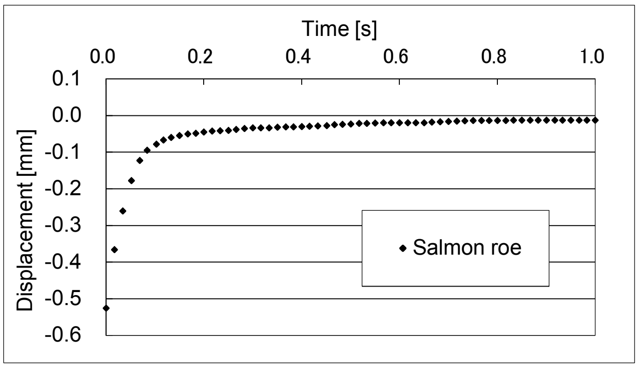

Fig.9. Time response of Salmon roe

Table.2. Haptic device parameter of dynamic characteristic

Displa cement [mm]	Frequency [Hz]	Spring constant [N/mm]	Damping ratio
0～6	6	0.072	2.6
6～35	6	0.072	1.0

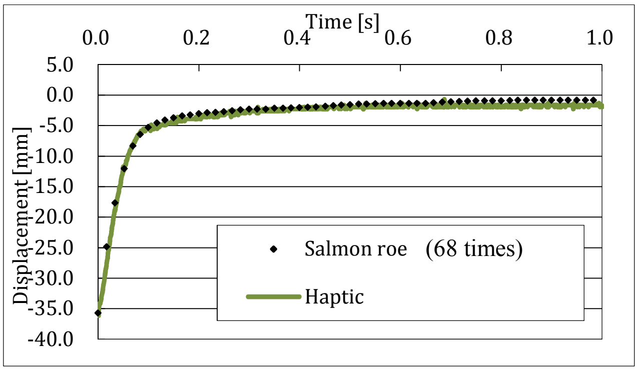

Fig.10. Time response of Salmon roe and haptic device

Next, a viscosity was measured in order to recreate the liquid viscosity of salmon rows. Fig.11 shows the conditions of an experiment. The moving part of the haptic device was sunk and then the moving part was vibrated constant parameters. Then, the vibration was damped to compare the case of not touched liquid because of viscosity. The damping difference between touched liquid and not.

In this experiment, Sodium alginate aqueous solution 1% weight ratio was used. Because the viscosity of liquid is similar to salmon roes and also use in artificial salmon roes.

Fig.12 shows the relation between the difference of damping ratio and lateral area of under the liquid. As a result, the bigger the lateral area of under the liquid of moving part, result in the bigger the damping ratio.

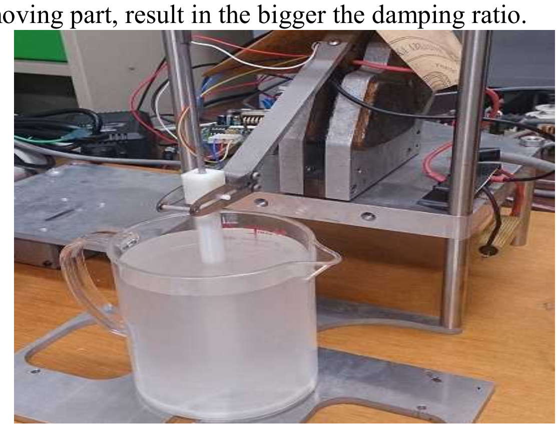

Fig.11. Experiment of measurement of viscosity.

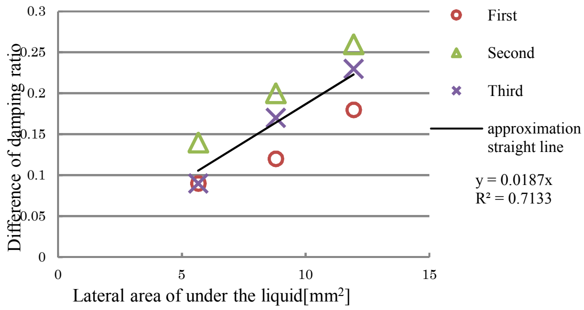

Fig.12. the relation between the difference of damping ratio and lateral area of under the liquid.

5. Conclusion

The reaction force from puncturing an object which consists of the liquid and an outer membrane was recreated by Voigt model and Maxwell model. Operators can feel the puncture sense by caused the sudden fall of the reaction force when changing the controlling model.

Future research should focus on building a system that allows a reaction force to be detected and shown more precisely. Such a system would make it possible to test smaller samples.

6. Acknowledgement

This research was partially supported by the Ministry of Education, Science, Sports and Culture, Grant-in-Aid for Scientific Research, 2012.

7. References

1. T.DOMOTO (2012) Construction of a sense of force feedback and vision for micro-objects: Recreate the response and a sense of force of objects. Kyushu Institute of Technology. *Proceedings of the 15th International Symposium on Artificial Life and Robotics*, Beppu, Oita, Japan, 2012
2. Y.ISHII (2016) Construction of a sense of force feedback and vision for micro-objects: Development of a haptic device. Kyushu Institute of Technology. *International conference on artificial life and robotics (ICAROB2016)*, Jan 29-31, Okinawa, Japan, 2016

Exercise classification using CNN with image frames produced from time-series motion data

Hajime Itoh
Division of Production Systems Engineering, Muroran Institute of Technology, 27-1 Mizumoto-cho Muroran, 050-8585, Japan

Naohiko Hanajima
College of Design Manufacturing Technology, Muroran Institute of Technology, 27-1 Mizumoto-cho Muroran, 050-8585, Japan

Yohei Muraoka, Makoto Ohata
Steel Memorial Muroran Hospital, 1-45 Chiribetsu-cho Muroran, 050-0076, Japan

Masato Mizukami, and Yoshinori Fujihira
College of Design Manufacturing Technology, Muroran Institute of Technology, 27-1 Mizumoto-cho Muroran, 050-8585, Japan
E-mail: 15042009@mmm.muroran-it.ac.jp, hana@mondo.mech.muroran-it.ac.jp

Abstract

Exercise support systems for the elderly have been developed and some were equipped with a motion sensor to evaluate their exercise motion. Normally, it provides three-dimensional time-series data of over 20 joints. In this study, we propose to apply Convolutional Neural Network (CNN) methodology to the motion evaluation. The method converts the motion data of one exercise interval into one gray scale image. From simulation results, the CNN was possible to classify the images into specified motions.

Keywords: CNN, Gray scale image, Exercises classification, Time-series data.

1. Introduction

Population of the elderly is increasing compared with that of the young in Japan[1]. It is estimated that the number of elderly care staff will be short of approximately 680,000 in 2035[2, 3]. In order to contribute for solving this problem, exercise support systems has been developed[4]. It is expected that the elderly can become healthy by strengthening their muscles with gymnastics, and less elderly care staffs will be necessary.

Some exercise support systems have been equipped with a motion sensor to evaluate the elderly' exercise. Normally, the motion sensor provides three-dimensional time-series data of over 20 joints. In previous studies, the motion was judged by human-induced conditions, such as the height of a hand position or the angle of the arm motion[5]. However, the human-induced conditions tended to be experiential and intuition in some case. Sometimes, the judgement did not fit the human judgement[6].

In this study, we propose applying Convolutional Neural-Network (CNN) methodology to the motion evaluation. The deep learning has succeeded in integrating big data. CNNs is the oldest deep neural-network architecture and is widely used as a means of handwriting recognition[7]. In recent years, image classification has been highly succeeded with CNN[8]. However, there are few examples that are applied to time-series data, and approaches to speech recognition have been proposed[9]. In this paper, we propose to apply CNN methodology to the motion evaluation. The method converts all joints of the motion data into one gray scale image. Then, CNN learns and classifies the converted images. We first explain a method to create motion data for CNN learning in Section 2. Section 3 proposes a conversion method from the motion data to the gray scale image. After that, some case studies are explained. Finally, we show the result of learning using CNN and discuss its ability of classification.

2. Creation of motion data for training data

Learning with CNN requires a lot of training data. However, exercise by humans cannot always do the right motion every time. Therefore, we created motion data by simulating human exercises using simple formulas. They were prepared with respect to what was recorded by a motion sensor in advance[4]. The motion sensor can acquire three-dimensional position data of 20 joints. To imitate the position coordinate, we utilized sinusoidal functions like Eq. (1). Eq. (1) is an example of the coordinate in the vertical direction of a hand position P.

$$P = R + l \times \sin(\theta) + \text{rand} \qquad (0 < \theta < 2\pi) \quad (1)$$

Where R is the coordinate of the rotating joint, l is the length of the arm from the rotating joint to the hand. The function rand is a uniform random number generator with a certain value.

3. Conversion of motion data to image

CNN cannot process time-series data because there is no input unit related to producing image frame from the time. In this section, we propose the conversion method from the time-series motion data to the gray scale image. Then they are learned with CNN.

3.1. *Representation of pixels*

Fig. 1 shows the image converted from a time-series motion data. Each row expresses X-Y-Z coordinate value for each joint, and the value is converted thereby to 255 tone gray scale. Time is ordered from left to right for the column. The origin of the X-Y-Z coordinate system is placed 1200 mm downward from the joint at the center of the body, the luminance value changes every 10 mm and can express up to 2550 mm.

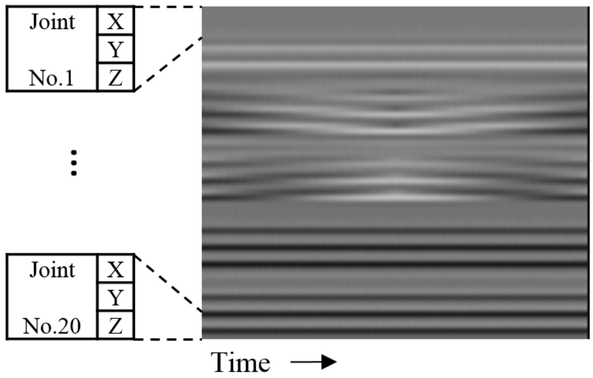

Fig. 1. The image converted from a motion data. One of the stripes represents time-series of the X-Y-Z change of each joint and it is represented in rows in order

3.2. *Arrangement of order of rows*

We can define several arrangements of order of the row. In this paper, we try two kinds of arrangement. First one is a joint oriented order as shown in Fig. 1. Second one is a coordinate oriented order, that is x_1, x_2, x_3, …, y_1, y_2, y_3, …, z_1, z_2, z_3, …, where subscript is the number of the joints.

4. Case study for learning with CNN

We chose five kinds of motion for learning experiment. They are shown in Fig.2 and their descriptions are shown as follows[4].

i. Raise and drop arms from sideways to top.
ii. No action
iii. Raise and drop your arms from front to top.
iv. Raise the left leg 90 degrees forward.
v. Bend trunk 90 degrees forward

We used Caffe to learn CNN. It is a deep learning framework developed by BVCL. The number of layers of CNN is six, the first layer has kernel size 5 and output is 32, the second layer has kernel size 5 and output is 32, the third layer has kernel size 5 and output is 64. Also, each pooling layer has kernel size 3. The number of

Table 1.

Results when processing 100 images of the motion i. As the image being processed approaches 1, the possibility is higher, and as it is closer to 0, it indicates that there is a high possibility that the image is different.

	Comparative item	i.	ii.	iii.	iv.	v.	vi.	vii.	viii.	ix.	x.
Confirmation of exercise image	Average	1	2.58E-09								
	Standard deviation	0	1.06E-11								
Learning for big motion	Average	1	1.87E-11	2.94E-19	1.39E-23	4.2E-15					
	Standard deviation	0	1.65E-13	2.80E-21	1.00E-25	3.3E-17					
Learning for small change	Average	0.999781	5.54E-17	0	1.88E-29	2.76E-44	0.000219	2.34E-22	0	1.1E-14	0
	Standard deviation	7.07E-06	1.66E-18	0	5.75E-31	8.49E-46	7.07E-06	6.9E-24	0	2.98E-16	0

output units varies depending on learning problem setting. We prepared 100 images for each kind of motion using Eq. (1). The random number contributes the variety of data set. The number of training iterations was set to 4000. We performed three kinds of case study to confirm the ability of classification of the motions using proposed method.

4.1. *Detection of exercise*

In order to confirm whether the exercise movement can be detected correctly, two kinds motions, i and ii were learned with CNN. Their images are greatly different. There are two inputs / outputs in the CNN composition.

4.2. *Classifying for large difference*

There is much difference over the prepared exercises. In order to confirm the ability to classify completely different actions, 5 kinds of exercises, i to v were learned with CNN for the classification of the exercises. There are five inputs / outputs in the CNN composition.

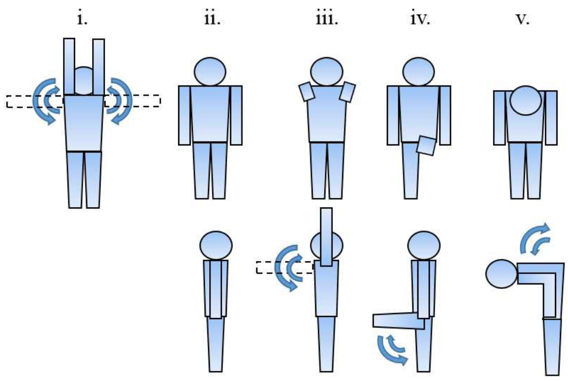

Fig. 2. Exercise to learn at CNN. The direction of the arrow indicates the movement direction, the top is the front view and the bottom is the horizontal.

4.3. *Classifying for small difference*

There is a possibility that the arm does not rise to the top because of a disorder of the body. It may cause a very small difference in the actions. To investigate ability of classification for such small difference, we prepare five additional motions, vi to x with respect to the motions, i to v. The motions, vi. and viii raise the arms to the lower position from the top by 10 degrees than the motions, i and iii. The motions, ix and x raise the legs up to 80 degrees other than the montions, iv and v. Also, the motion vii raises the arms lower by 10 degrees than the motion i. There are ten inputs / outputs in total. The small change of 10 degrees set here is an exercise that cannot actually be judged by the exercise support system. According to the exercise supervisor, the small change of 10 degrees is judged to be a bad practice, so we will verify whether it can be judged or not in this study.

5. Experimental result and discussion

After learning, classification test was performed. We prepare data set for the classification separately from the learning data, and the number of data is 100. Table 1 shows the probability and standard deviation of classification for result of each motion with test data. At first, the row was arranged for the joint oriented order.

5.1. *Detection of exercise*

It can be seen from first 2 rows in Table 1 that they are correctly classified, that is average of i is 1, and ii is almost zero. The average value of 1 shows possibility of excessive learning. The reason is considered that the kind of the motions is just two and the images used for learning are very similar.

5.2. *Classification for large difference*

From middle 2 rows in Table 1, the motion i is detected correctly. An average value of 1 was output for the motion i. It is considered that the reason is same as in Section 5.1. And, since other average values are very small, it is considered that the correct classification is achieved.

5.3. *Classification for small difference*

In classification including the small change, it is observed from bottom 2 rows Table 1 that the average value of the motion i is almost 1 and the others are quite small values. Therefore, we should say that the classification was achieved. The average of the motion i is smaller than the previous section. The average value of the motion vi is second largest in the motions. It suggests that there is some correlation between the motion i and vi. Actually, the motion vi is a variant of the motion i. These values seem to represent their relationship. Because of this, small changes in luminance values can also be regarded as feature amounts, therefore there is a high possibility of judging the difference in small change accurately.

5.4. *Rearrangement for rows in the coordinate oriented order*

Next, we show the result when the row was arranged in the coordinate oriented order. Table 2 shows a part of the result of the rearrangement for the rows order and learning with CNN.

Table 2. Result of rearranging rows of pixels. Except for the motions, i and vi, since it was less than E - 24, it is excluded in this table.

	i.	vi.
Average	0.999892	0.000108
Standard deviation	3.15E-06	3.15E-06

It is observed that there is no significant difference between two kinds of row orders. It was found that the average value of the motion i in Table 2 was slightly larger than that in Table 1. It indicates that the possibility of obtaining the feature is higher for the motion i.

6. Conclusions

In this paper, we proposed a method to apply time-series motion data to CNN. We showed that learning and classification by CNN are possible by converting the motion data of one exercise interval into one gray scale image. It was found that not only large difference but also small difference in the motion data was correctly classified. Arrangement for rows did not affect the results of classification in this case. We will apply the proposed method to analyze the human exercise data in our future work.

References

1. Cabinet office, government of Japan, *Heisei 28th edition Aged Society White Paper* (Japan, 2016), pp. 2-8.
2. Ministry of Economy, Trade and Industry, *"Study Group on Providing Long-Term Care Service According to Future Nursing Care Demand" Report* (Japan, 2016), pp. 22-39.
3. M. Kasahara et al., Relationship between One Leg Standing Time and Knee Extension Strength in Elderly Patients, *Tairyoku Kagaku*. 50(3) (2001), pp. 369–373.
4. Y. Takahashi, Study on exercise support robots providing individualized instruction, *Presentation of Graduation Theses*. (2014).
5. M. Hirano et al., Development of an Exercise Support System for the Elderly Which Use a small Humanoid Robot, *Journal of Robotics and Mechatronics* . 25(6) (2013) 939–948.
6. K. Urita et al., Precision Analysis of Center-Of-Gravity Points Estimation Based on a Motion Sensor -Comparison with a Force Plate, SICE annual conference 2014 conference proceedings, In *Ternational Conference on Instrumentation*, Information Technology and System Integration (Japan, Sapporo, 2014), pp. 2020–2024.
7. D. Ciresan et al., Multi-column Deep Neural Networks for Image Classification, In *Computer Vision and Pattern Recognition (CVPR)*, 2012 IEEE Conference on (2012), pp. 3642-3649.
8. A. Krizhevsky et al., ImageNet Classification with Deep Convolutional Neural Networks, In *Advances in Neural Information Processing System*s 25 (2012).
9. O. A. Hamid et al., Convolutional Neural Networks for Speech Recognition, *IEEE/ACM Transactions on Audio, Speech, and Language Processing*. 22(10) (2014) 1533–1545.

Proposal and Evaluation of the Gait Classification Method Using Arm Acceleration Data and Decision Tree

Kodai Kitagawa
National Institute of Technology, Kushiro Collage,
2−32−1,Otanoshike-nishi, Kushiro, Hokkaido, 084−0916, Japan
kitagawakitagawa156@gmail.com

Yu Taguchi
National Institute of Technology, Kushiro Collage,
2−32−1,Otanoshike-nishi, Kushiro, Hokkaido, 084−0916, Japan
tgcyu56@gmail.com

Nobuyuki Toya
National Institute of Technology, Kushiro Collage,
2−32−1,Otanoshike-nishi, Kushiro, Hokkaido, 084−0916, Japan
toya@kushiro-ct.ac.jp

Abstract

We have been developing a system for falling prevention to classify gait patterns based on stride length and foot clearance by arm accelerations. In this paper, we propose gait classification method using arm acceleration data and decision tree. Also, we evaluate whether decision tree using three-axis accelerations as feature quantities could classify three gait patterns. (Three gait patterns are "Normal", "High step" and "Long step".) The result showed that this method can classify three gait patterns of some subjects.

Keywords: Gait, Falling prevention, Decision tree, Arm, Acceleration, Smartphone

1. Introduction

Lately, Japan has a lot of falling accidents of elderly people. Falling accidents often lead to hospitalization on serious injuries. Hospitalization adversely affects exercise capacity and mental state. According to a survey, 86.2% of elderly people who have experienced falling accidents are afraid of falling, and 44% of them have restricted outdoor activities due to the fear of falling [1]. From these reports, it can be said that falling accidents of elderly people cause not only damages but also serious effects for daily life after accidents.

It is known that tripping is the most frequent cause of falling [1-2]. Due to decreased perceptual ability, elderly people cannot recognize that foot clearance and stride length are insufficient in gait [3]. Therefore, we have been developing a system which urges elderly people to improve of gait for falling prevention by classifying gait patterns based on stride length and foot clearance using acceleration data from sensors of a smartphone [4]. In this system, the smartphone is worn on an arm as a part at which it is easy to attach on a daily basis for users, and gait patterns are classified by arm acceleration data. In previous studies, it has been pointed out that movement of the arm is influenced by the gait in terms of dynamic stability [5].

It has been found that time waveforms of arm accelerations change by stride length and foot clearance. However, we also have found that it is difficult to classify gait patterns by only peak value and average value of time waveforms [4]. In this paper, we propose the gait patterns classification method using machine learning and arm acceleration data as feature quantities.

2. Method

In proposed method, gait patterns are classified by decision tree with three-axis acceleration and composite direction acceleration data on an arm as feature quantities. As an advantage of the decision tree, it is known that if-then rules in a tree structure for classification are readable. In addition, some algorithms of the decision tree can use continuous variables.

Gait parameters are often measured in time periods. Because elderly people are unstable in their gait cycle, there is a possibility that astandard deviation may increase in measured data. Therefore, in the proposed method, one set of arm acceleration data is measured per step by detecting the timing at which the forearm crosses the body by a proximity sensor of the smartphone.

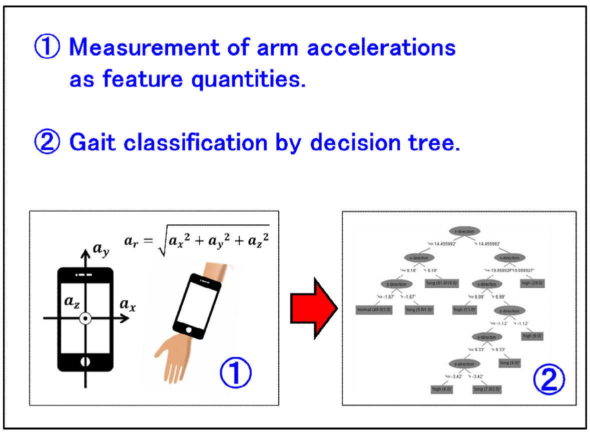

Fig. 1. Method for gait classification

3. Experiment

3.1. Data Measurement

We conducted the gait experiment on the treadmill by young people as basic examination of the proposed method. In this experiment, we instructed subjects (10 young people) three gait patterns ("Normal", "Long step ", "High step") on the treadmill. As for "Long step", we confirmed that stride lengths based on steps and gait speeds were the largest in three gait patterns during whole analysis. Also, as for "High step", we confirmed that foot clearance was rising higher than 15 cm by infrared sensors. Besides, we set gait speed which is easy to walk for each subject by treadmill.

In this experiment, as feature quantities, three-axis arm acceleration data for 60 steps per each gait pattern were measured by the smartphone. In addition, composite direction acceleration data also were calculated from three-axis acceleration data as feature quantities.

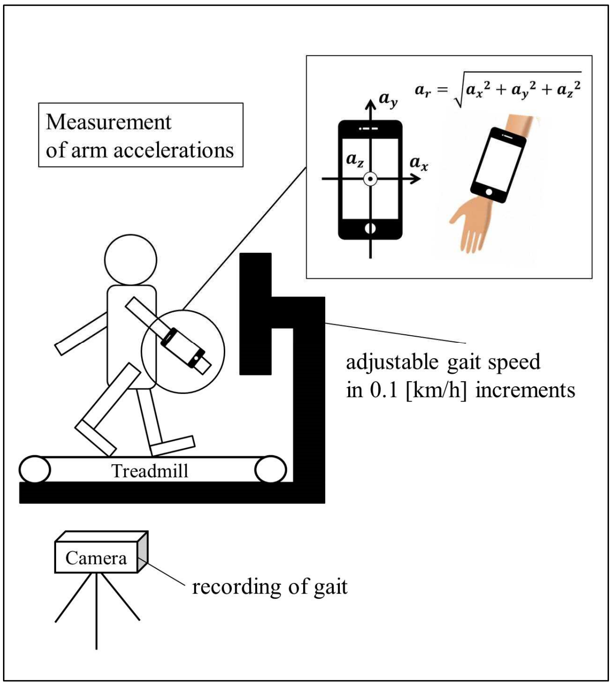

Fig. 2. Experiment system

3.2. Data Analysis

As a basic study of the proposed method, we evaluated whether decision trees using arm acceleration data as feature quantities could classify gait patterns. We used Weka and J48 algorithm for evaluation of classification performance. In the data set used for classification, arm acceleration data ("x-direction", "y-direction", "z-direction", and "composite direction") measured by the experiment were used as feature quantities, and the information of the gait patterns ("Normal", "Long step", or "High step") was added to each data as a correct answer. We calculated accuracy, precision, recall, and F-measure as evaluation index of classification performance for each subject on 5-fold cross-validation. We also analyzed if-then rules of a tree structure for each subject.

4. Results and discussions

It was found that gait patterns can be classified with accuracy more than 0.65 in 7 subjects (Table 1). This result shows the possibility that the proposed method is usable for gait classification. Comparing F-measure in each gait pattern, it was confirmed that F-measure of "Normal" was larger than other gait patterns in 6 subjects (Fig. 3). In addition, it was found that precision and recall of "Normal" was larger than other gait patterns too (Fig. 4). As the reason for these, it is assumed that "Normal" was not required an arm swing for dynamic stability, so difference of arm acceleration data appeared between "Normal" and other gait patterns.

Results of the analysis for if-then rules in the tree structures of each subject showed that threshold values of "y-direction” are larger than threshold values of "x-direction" and "z-direction" (Fig. 5). It is conceivable from these results that "y-acceleration" is dominant in "composite direction".

In addition, we examined the root node in the tree structure of each subject, and found that arm acceleration data of "x-direction" and "composite direction" are selected more frequently as the threshold variable for root node in the tree structure of high accuracy subjects (Table 1). In the decision tree, since root node is arranged so that decrease of entropy gets a maximum, root node is considered to be important for gait classification. Therefore, "x-direction" and "composite direction" which are selected more frequently as the threshold variable for root node, and "y-direction" which is dominant in "composite direction" are considered to be important in gait classification.

Table 1. Accuracy and threshold variable of root node

Subject	Accuracy	Threshold variable of root node
A	0.767	composite direction
B	0.594	composite direction
C	0.689	x-direction
D	0.7	x-direction
E	0.583	composite direction
F	0.722	composite direction
G	0.739	x-direction
H	0.378	z-direction
I	0.656	z-direction
J	0.672	composite direction

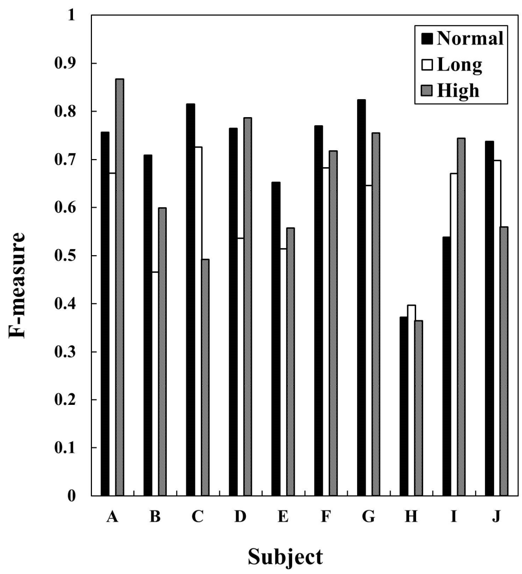

Fig. 3. F-measure of proposed method

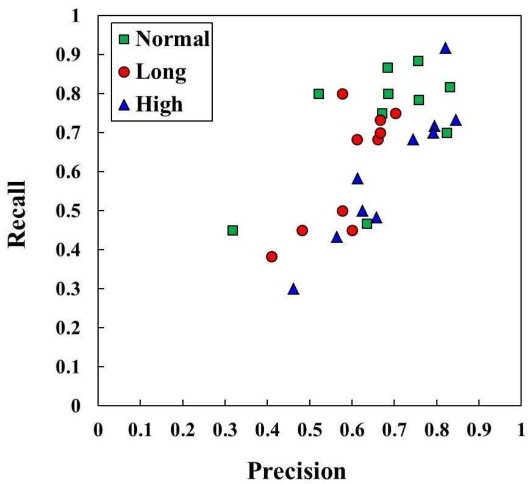

Fig. 4. Precision and recall of proposed method

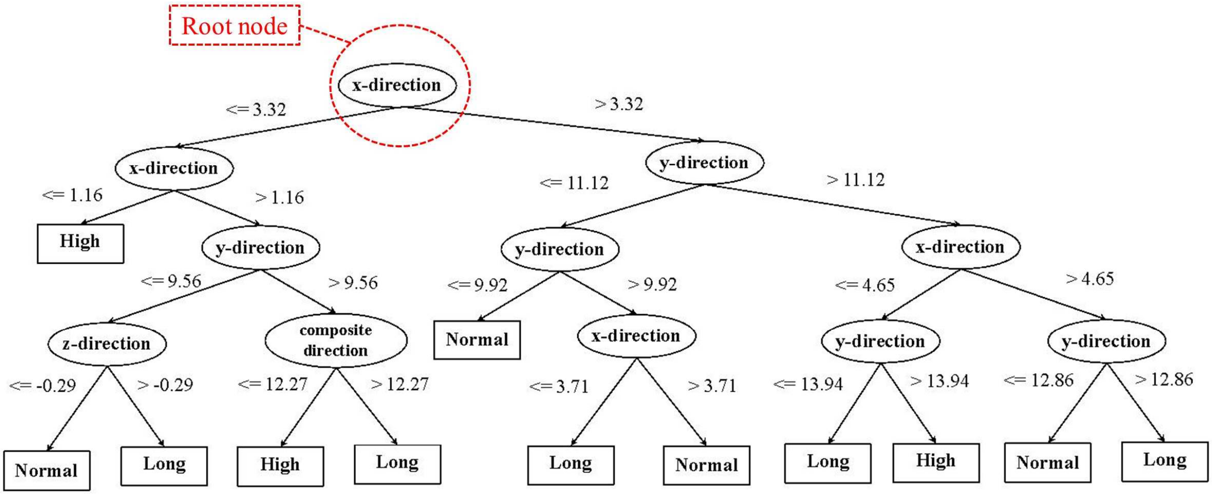

Fig. 5. Tree structure subject G

5. Conclusions

In this paper, we proposed a method to classify gait patterns by decision tree using arm acceleration data ("x-direction", "y-direction", "z-direction", and "composite direction") as feature quantities. Experimental results revealed that the proposed method could classify three gait patterns ("Normal", "Long step", and "High step") of some subjects.

Moreover, from tree structure of decision tree, we found that arm acceleration data of "x-direction" and "composite direction" were selected more frequently as the threshold variable for root node in the tree structure of high accuracy subjects. In addition, we found that "y-acceleration" is dominant in "composite direction". From these results, tree structure of decision tree showed that "x-direction", "composite direction" and "y-direction" are considered to be usable in gait classification.

In order to improve classification performance, it is considered that analysis of "two-axis" acceleration data is needed in further studies. From now on, we will examine the gait classification method using "two-axis" composite direction acceleration data from "x-direction" and "y-direction" which are considered to be important in gait classification.

References

1. K. Hunkyung, et al. , The Relationship between Fall-related Activity Restriction and Functional Fitness in Elderly Women, *Japanese Journal of Geriatrics*, 38(6)(2001), pp. 805-811.
2. P. W. Overstall, A. N. Exton-Smith, F. J. Imms, & A. L.Johnson, Falls in the elderly related to postural imbalance, *Br. Med. J.* , 29（1）(1977), pp. 261-264.
3. S. Saito, S. Muraki, Study on Tracks and Sense of Feet Position while Stepping Over an Obstacle in the Elderly, *The Japanese journal of ergonomics*, 46(2)(2010), pp. 172-179.
4. K. Kitagawa, K. Go, N. Toya, Some Discussions of Walking State Estimation Using Miniaturized Sensors for Fall Prevention, *Research Reports: Kushiro National College of Technology*, 49(2016), pp.27-30.
5. S. Tanaka, S. Murata, T. Kodama, *Effect of Upper Limbs on Walking*, Rigakuryoho Kagaku, 25(2) (2010), pp. 177-180.

A Method for Secure Communication Using a Discrete Wavelet Transform for Audio Data and Improvement of Speaker Authentication

Kouhei Nishimura, Yasunari Yoshitomi, Taro Asada, and Masayoshi Tabuse
Graduate School of Life and Environmental Sciences, Kyoto Prefectural University,
Nakaragi-cho, Shimogamo, Sakyo-ku, Kyoto 606-8522, Japan
E-mail: {yoshitomi, tabuse}@kpu.ac.jp, t_asada@mei.kpu.ac.jp}
http://www2.kpu.ac.jp/ningen/infsys/English_index.html

Abstract

We developed a secure communication method using a discrete wavelet transform. Two users must each have a copy of the same piece of music to be able to communicate with each other. The message receiver can produce audio data similar to the sending user's speech by using our previously proposed method and the given recording of music. To improve the accuracy of speaker authentication, the quantization level for the scaling coefficients is increased. Furthermore, the amount of data sent to the message receiver can be remarkably reduced by exploiting the characteristics of this data.

Keywords: Secure communication, Audio data processing, Wavelet transform, Encoding

1. Introduction

The elderly are often targets of telephone fraud. The fraudster pretends to be a grandchild of the elderly person while talking on the phone, and appeals to the elderly person to send money, for example, through a bank transfer. In the present study, we propose a method for secure communication using a discrete wavelet transform (DWT) and thus improve speaker authentication; this is an enhancement of our previously proposed method.[1] It can be used with Internet protocol (IP) telephones, and it has the potential to help prevent telephone fraud.

2. Proposed Method

2.1. *Encoding*

2.1.1. *Phenomenon exploited for the coding algorithm for audio data*

In the course of our research,[1] we found that the histogram of the scaling coefficients for each domain of a multiresolution analysis (MRA) sequence is centered at approximately zero when a DWT is performed on audio data. Exploiting this phenomenon, we have developed a secure communication method using audio data.[1]

2.1.2. *Use of five quantization levels for scaling coefficients*

(1) *Parameter setting*

In our reported study,[1] we set the following coding parameters.

The values of $Th(\text{minus})$ and $Th(\text{plus})$ in Fig. 1 are chosen such that the nonpositive scaling coefficients (S_m in total frequency) are equally divided into two groups by $Th(\text{minus})$, and the positive scaling coefficients (S_p in total frequency) are equally divided into two groups by $Th(\text{plus})$. Next, the values of *T1, T2, T3,* and *T4,* which are the parameters for controlling the authentication precision, are chosen to satisfy the following conditions:

1) $T1 < Th(\text{minus}) < T2 < 0 < T3 < Th(\text{plus}) < T4$.

2) The value of S_{T1}, which is the number of scaling coefficients in $(T1, Th(\text{minus}))$, is equal to S_{T2},

which is the number of scaling coefficients in $[Th(\text{minus}), T2)$, i.e., $S_{T1} = S_{T2}$.

3) The value of S_{T3}, the number of scaling coefficients in $(T3, Th(\text{plus})]$, is equal to S_{T4}, the number of scaling coefficients in $(Th(\text{plus}), T4)$, i.e., $S_{T3} = S_{T4}$.

4) $S_{T1} / S_m = S_{T3} / S_p$.

In the present study, the values of both S_{T1}/S_m and S_{T3}/S_p are set to 0.3, which was determined experimentally.

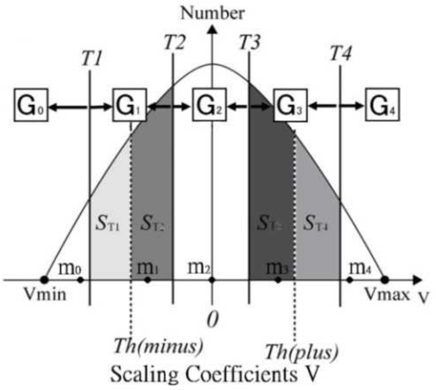

Fig. 1. Schematic diagram for demonstrating the selection of the scaling coefficients for encoding the audio data.[1]

(2) *Encoding*

In the preprocessing of the audio data prior to encoding, the scaling coefficients V of the MRA sequence are separated into five sets (G_0 to G_4), as shown in Fig.1, under the following criteria:

- $G_0 = \{V \mid V \in V^{SC}, V \le T1\}$,
- $G_1 = \{V \mid V \in V^{SC}, T1 < V < T2\}$,
- $G_2 = \{V \mid V \in V^{SC}, T2 \le V \le T3\}$,
- $G_3 = \{V \mid V \in V^{SC}, T3 < V < T4\}$,
- $G_4 = \{V \mid V \in V^{SC}, T4 \le V\}$,

where V^{SC} is the set of scaling coefficients in the audio data file.

The scaling coefficients for the MRA sequence are encoded according to the following rules, where V_i denotes scaling coefficient *i*: $V_i \in G_0$, c_i = 0; when $V_i \in G_1$, c_i = 1; when $V_i \in G_2$, c_i = 2; when $V_i \in G_3$, c_i = 3; and when $V_i \in G_4$, c_i = 4. We represent the scaling coefficient for each set, G_j, by its average value, m_j. For the formation of audio data, we use a code C, which is the sequence of c_i and m_j defined above.

2.1.3. *Use of eight quantization levels for scaling coefficients*

Here, we define eight sets of $G_{8,0}$, to $G_{8,7}$, as follows:

- $G_{8,0} = \{V \mid V \in V^{SC}, V \le T1\}$,
- $G_{8,1} = \{V \mid V \in V^{SC}, T1 < V < Th(\text{minus})\}$,
- $G_{8,2} = \{V \mid V \in V^{SC}, Th(\text{minus}) \le V \le T2\}$,
- $G_{8,3} = \{V \mid V \in V^{SC}, T2 < V < 0\}$,
- $G_{8,4} = \{V \mid V \in V^{SC}, 0 \le V \le T3\}$,
- $G_{8,5} = \{V \mid V \in V^{SC}, T3 < V < Th(\text{plus})\}$,
- $G_{8,6} = \{V \mid V \in V^{SC}, Th(\text{plus}) \le V \le T4\}$,
- $G_{8,7} = \{V \mid V \in V^{SC}, T4 < V\}$.

Again, we let the representative value for each set, $G_{8,i}$, be its average, $m_{8,i}$. For the formation of audio data, we use the code C_8, which is the sequence of $c_{8,i}$ defined for eight quantization levels for scaling coefficients in the similar manner as c_i described in Section 2.1.2, and $m_{8,j}$ as defined above.

2.1.4. *Use of 16 quantization levels for scaling coefficients*

(1) *Parameter setting*

The values of $T1m$, $T1p$, $T2m$, $T2p$, $T3m$, $T3p$, $T4m$, and $T4p$, which are the parameters for controlling the authentication precision, are chosen to satisfy the following conditions:

1) $T1m < T1 < T1p < Th(\text{minus}) < T2m < T2 < T2p < 0$
$< T3m < T3 < T3p < Th(\text{plus}) < T4m < T4 < T4p$

2) The value of $T1m$ is defined so that it equally divides the number of scaling coefficients in $[V\text{ min}, T1]$. $T1p$, $T2m$,…, $T4p$ are defined similarly to $T1m$.

(2) *Encoding*

Sixteen sets of $G_{16,0}$ to $G_{16,15}$ are defined as follows:

- $G_{16,0} = \{V \mid V \in V^{SC}, V \le T1m\}$,
- $G_{16,1} = \{V \mid V \in V^{SC}, T1m < V < T1\}$,
- $G_{16,2} = \{V \mid V \in V^{SC}, T1 \le V \le T1p\}$,
- $G_{16,3} = \{V \mid V \in V^{SC}, T1p < V < Th(\text{minus})\}$,
- $G_{16,4} = \{V \mid V \in V^{SC}, Th(\text{minus}) \le V \le T2m\}$,
- $G_{16,5} = \{V \mid V \in V^{SC}, T2m < V < T2\}$,
- $G_{16,6} = \{V \mid V \in V^{SC}, T2 \le V \le T2p\}$,
- $G_{16,7} = \{V \mid V \in V^{SC}, T2p < V < 0\}$,
- $G_{16,8} = \{V \mid V \in V^{SC}, 0 \le V \le T3m\}$,
- $G_{16,9} = \{V \mid V \in V^{SC}, T3m < V < T3\}$,
- $G_{16,10} = \{V \mid V \in V^{SC}, T3 \le V \le T3p\}$,
- $G_{16,11} = \{V \mid V \in V^{SC}, T3p < V < Th(\text{plus})\}$,

- $G_{16,12} = \{V \mid V \in V^{SC}, Th \text{ (plus)} \le V \le T4m\}$,
- $G_{16,13} = \{V \mid V \in V^{SC}, T4m < V < T4\}$,
- $G_{16,14} = \{V \mid V \in V^{SC}, T4 \le V \le T4p\}$,
- $G_{16,15} = \{V \mid V \in V^{SC}, T4p < V\}$.

As before, the value for each set, $G_{16,i}$, is represented by its average value, $m_{16,i}$. For the formation of audio data, we use the code C_{16}, which is the sequence of $c_{16,i}$ defined for 16 quantization levels for scaling coefficients in the similar manner as c_i described in Section 2.1.2, and $m_{16,j}$ defined above.

2.2. *Audio data formation using code replacement*

In this subsection, the formation of sound data is explained; for this example, we use five quantization levels for the scaling coefficient.[1] The scaling coefficient sequence for audio data A is expressed as $S(A)_k = \{x_1, x_2, x_3, \ldots, x_k\}$, where k is the total number of scaling coefficients of A at this level. Then, the sequence $C(A)_k = \{X_1, X_2, X_3, \ldots, X_k\}$ is determined, where $X_i \in \{0,1,2,3,4\}$ is the element index, which indicates to which of the five sets of scaling coefficients x_i of A belongs. Next, the audio data A' is defined as having the scaling coefficient sequence $S(A')_k$ and a value of zero for all wavelet coefficient values at every level. $S(A')_k$ is defined as $S(A')_k = \{a_1, a_2, a_3, \ldots, a_k\}$, where $a_i \in \left\{m_0^A, m_1^A, m_2^A, m_3^A, m_4^A\right\}$ is the average of the scaling coefficients of A in the range denoted by $X_i \in \{0,1,2,3,4\}$ and is obtained from A. Then, the audio data B'_A is defined as having the scaling coefficient sequence $S(B'_A)_k$ and a value of zero for all wavelet coefficient values at every level. $S(B'_A)_k$ is defined as $S(B'_A)_k = \{b_{A,1}, b_{A,2}, b_{A,3}, \ldots, b_{A,k}\}$, where $b_{A,i} \in \left\{m_0^B, m_1^B, m_2^B, m_3^B, m_4^B\right\}$ is the average of the scaling coefficients of B in the range denoted by $X_i \in \{0,1,2,3,4\}$ obtained from A. $S(B'_A)_k$ is obtained by replacing Y_i with X_i when $Y_i \ne X_i$, and then replacing b_i with $b_{A,i}$, where b_i is the average of the scaling coefficients of B in the range denoted by Y_i. Therefore, $C(B'_A)_k = C(A)_k$. As a result, B'_A is expected to be similar to A.

2.3 *Data for communication*

A sequence $D1(B'_A)_n$ is defined as $D1(B'_A)_n = \{z_1, z_2, \ldots, z_n\}$, where n is the total number of cases where $Y_i \ne X_i$, $z_p = [\![y_i]\!] \bmod 256$, and the integer p is increased from 1 to n, in steps of size 1, when $Y_i \ne X_i$.[1] Here, $[x]$ signifies the maximum integer that is not greater than x. Then, a sequence $D2(B'_A)_n$ is defined as $D2(B'_A)_n = \{Z_1, Z_2, \ldots, Z_n\}$, where n is the total number of cases for which $Y_i \ne X_i$ and $Z_p = X_i$.[1]

In communications between two users, the message sender and the receiver each have the secret key $\boldsymbol{B}$, and the sender sends $D1(B'_A)_n$ and $D2(B'_A)_n$ to the receiver.[1] Then, the receiver composes B''_A, which is defined in Section 2.4 and is expected to be similar to A.

2.4. *Audio data composition*

In this subsection, the processing of sound data formation is also explained using the case of five quantization levels, as an example, for the scaling coefficient.[1] The scaling coefficient sequence for audio data B is expressed as $S(B)_k = \{y_1, y_2, y_3, \ldots, y_k\}$, where k is the total number of scaling coefficients of B at this level . Then, a sequence $C(B)_k = \{Y_1, Y_2, Y_3, \ldots, Y_k\}$ is determined, where $Y_i \in \{0,1,2,3,4\}$ is the element index, which indicates to which of the five sets of scaling coefficients y_i of B belongs. $S(B')_k$ is defined as $S(B')_k = \{b_1, b_2, b_3, \ldots, b_k\}$, where $b_i \in \left\{m_0^B, m_1^B, m_2^B, m_3^B, m_4^B\right\}$ is the average of the scaling coefficients of B at the range denoted by $Y_i \in \{0,1,2,3,4\}$ and is obtained from B.

A sequence $D3(B)_k$ is defined as $D3(B)_k = \{z_{B,1}, z_{B,2}, \ldots, z_{B,k}\}$, where k is the total number of scaling coefficients of B at this level, and $z_{B,q} = [\![y_q]\!] \bmod 256$. B''_A is determined as follows: $S(B''_A)_k$ is calculated from $S(B')_k$ by replacing b_q with $m_{Z_p}^B$ when $z_{B,q} = z_p$, for $p = 1, \ldots, n$, then the audio data B''_A is composed using the inverse DWT (IDWT) of the scaling coefficient sequence $S(B''_A)_k$ and the value of zero for all wavelet coefficients at every level. The receiver composes B''_A from $D1(B'_A)_n$ and $D2(B'_A)_n$, which are determined by both A and B and are sent by the sender, and B, which the receiver has obtained prior to the conversation. B''_A is expected to be similar to A.

2.5. *Data reduction*

2.5.1. *Processing for* $D1$

Because $z_p = [|y_i|] \bmod 256$, z_p is in the range from 0 to 255, and thus it can be expressed using 8 bits. In our computer, an integer is represented by 32 bits. Therefore, four values for z_p, each expressed using 8 bits, can be integrated into a single value expressed by 32 bits. For $D1(B'_A)_n = \{z_1, z_2, \ldots, z_n\}$, z'_j is defined as

$$z'_j = z_{4i-3} + z_{4i-2} \times 256 + z_{4i-1} \times 256^2 + z_{4i} \times 256^3,$$

where i, j are natural numbers. As a result, we obtain a sequence for $D1'(B'_A)_m = \{z'_1, z'_2, \ldots, z'_m\}$, where

$$m = \begin{cases} [n/4] & (n \bmod 4 = 0) \\ [n/4]+1 & (n \bmod 4 \neq 0). \end{cases}$$

When $n \bmod 4 \neq 0$, $z_{4m+k-2} = 0 \; (k = 0, \ldots, |n \bmod 4 - 3|)$. Here, $[x]$ is defined as in Section 2.3. In the first case of the above formula on m, the total amount of data, $D1'$, stored in a computer is thus one quarter of that stored for $D1$. However, the total amount of data sent to a receiver depends on the way in which the data are expressed.

2.5.2. *Processing for* $D2$

(1) Case of five quantization levels

$D2(B'_A)_n = \{Z_1, Z_2, \ldots, Z_n\}$ and $D2'(B'_A)_l = \{Z'_1, Z'_2, \ldots, Z'_l\}$, where $Z'_j = Z_{13j-12} + Z_{13j-11} \times 5 + Z_{13j-10} \times 5^2 + \cdots + Z_{13j} \times 5^{12}$, are defined as described in Section 2.5.1.

(2) Case of eight quantization levels

$D2(B'_A)_n = \{Z_1, Z_2, \ldots, Z_n\}$ and $D2''(B'_A)_r = \{Z''_1, Z''_2, \ldots, Z''_r\}$, where $Z''_j = Z_{10i-9} + Z_{10i-8} \times 8 + Z_{10i-7} \times 8^2 + \cdots + Z_{10i} \times 8^9$, are defined as described in Section 2.5.1.

(3) Case of 16 quantization levels

$D2(B'_A)_n = \{Z_1, Z_2, \ldots, Z_n\}$ and $D2'''(B'_A)_s = \{Z'''_1, Z'''_2, \ldots, Z'''_s\}$, where $Z'''_j = Z_{8i-7} + Z_{8i-6} \times 16 + Z_{8i-5} \times 16^2 + \cdots + Z_{8i} \times 16^7$, are defined as described in Section 2.5.1.

3. Numerical Experiment

We applied the proposed method, using several voice recordings for A, and for B, we used two recordings of music, one classical and the other hip-hop. The music was taken from a copyright-free database.[2] In all cases, all of the produced B''_A were audible and sounded similar to A; each B''_A was made with five, eight, or 16 quantization levels. An increase in the quantization level improved the sound quality because a waveform made from B''_A with a higher quantization level was more similar to the original waveform than was one made with a lower quantization level, as shown in Fig. 2. For (1), (2), and (3) in Section 2.5.2, the data reduction for one minute of audio data at 44.1 kHz, 16 bits, a single channel, and volume of 87 KB was as follows:

(1) $D1(75\text{ KB}) \to D1'(48\text{ KB}), D2(49\text{ KB}) \to D2'(9\text{ KB})$

(2) $D1(86\text{ KB}) \to D1'(55\text{ KB}), D2(57\text{ KB}) \to D2''(21\text{ KB})$

(3) $D1(92\text{ KB}) \to D1'(59\text{ KB}), D2(65\text{ KB}) \to D2'''(29\text{ KB})$

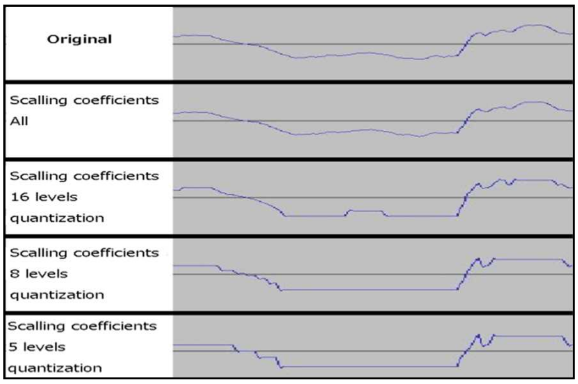

Fig. 2. Examples of waveform

4. Conclusion

We developed a secure communication method using a discrete wavelet transform for audio data; we used an increased number of quantization levels for the scaling coefficients along with a data reduction technique. The waveform produced by the proposed method was more similar to the original one than that produced by our previously proposed method.[1]

References

1. Y. Tsuda, K. Nishimura, H. Oyaizu, Y. Yoshitomi, T.Asada, and M.Tabuse, A method for secure communication using a discrete wavelet transform for audio data, *J. Robotics, Networking and Artif.* Life to appear.
2. M. Goto, H. Hashiguchi, T. Nishimura and R. Oka, RWC music database: database of copyright-cleared musical pieces and instrument sounds for research purposes, *Trans. IPSJ*, **45**(3) (2004) 728-738.

A Recipe Decision Support System Using Knowledge Information and Agent

Keita Saito, Taro Asada, Yasunari, Yoshitomi, Ryota Kato, Masayoshi Tabuse

Graduate School of Life and Environmental Sciences, Kyoto Prefectural University,
1-5 Nakaragi-cho, Shimogamo, Sakyo-ku,Kyoto 606-8522, Japan
E-mail: {yoshitomi, tabuse}@kpu.ac.jp, {t_asada, r_kato}@mei.kpu.ac.jp}
http://www2.kpu.ac.jp/ningen/infsys/English_index.html

Abstract

Abstract – We report on the development of a recipe recommendation system using collaborative filtering and impression words. As a user interface, we adopted MMDAgent. In our system, the first recommendation process using collaborative filtering is terminated based on the previously decided condition, after which the second recommendation process identifies the recipe that is most similar to past successful recommendations from recipes that have not been recommended thus far. As a final step, one recipe is selected from all successfully recommended recipes.

Keywords: Recipe recommendation, Collaborative filtering, Impression word, MMDAgent.

1. Introduction

It is sometimes bothersome to decide upon a recipe for meals because there are frequently numerous choices available. Therefore, a support system that recommends a new recipe every day could be beneficial. In this study, we developed and evaluated a new system that can be used to narrow down recipe choices to a final recommendation. In the current study, we have adopted MikuMikuDanceAgent (MMDAgent)[2] as a user interface (UI).

2. Recipe recommendation method using collaborative filtering

The recipe recommendation method[1] proposed in our current study is based on collaborative filtering, and is, in turn, based on our previously reported music recommendation method.[3] That method is explained briefly below.

We began by preparing a database composed of recipes that had been already been subjectively scored at five-levels with "5" being the most appealing to "1" being the least appealing. We then transformed the subjective scores of "1" to "3" and "4" to "5" into "0" and "1", respectively. Those scores ("0" or "1") are expressed as "evaluation scores" below.

3. Recipe recommendation method using impression words

Our recipe recommendation method also uses impression words.[1] In this study, 10 impression words pairs (see Table 1) extracted from "Sizzle Word Report 2014" were used. The method explained briefly below is also based on our previously reported music recommendation method.[3]

Each recipe prepared in advance was assigned one of seven score levels ranging from "-3" to "+3" by participating test subjects who used those impression word pairs. We then transformed these subjective scores to a three-level scale ("-3" to "-2" as "-1"", "-1" to "+1" as "0" and "+2" to "+3" as "+1"). These scores are expressed as "impression evaluation scores" below.

When a recipe not recommended to a user has the same values except "0" as that for at least one recommended recipe having a high evaluation by the user on the three-level score for at least five impression words, the recipe is treated as having a positive evaluation by the user. In contrast, when a recipe not recommended to the user has the same scores (disregarding "0") as that for another recipe just recommended to the user and having a negative evaluation by the user on the three-level score for at least seven impression words, the recipe is treated as having a negative evaluation by the user.

Table 1. Impression word pairs.

Good flavor ー Refreshing flavor
Mellow ー Spicy
Sweet ー Gentle
Addicted ー not Addicted
Rich ー Crispy
Juicy ー Scratchy
Warm ー Cool
Melty ー Chewy
Seasonal Limited ー not Seasonal Limited
Authentic ー not Authentic

4. Recipe recommendation using the collaborative filtering and impression words

Fig. 1 shows a flowchart of the proposed system, which combines collaborative filtering and impression words based on the authors' recipe recommendation method.[1] The system recommends recipes stored in the database to the user. Both the recommendation process using collaborative filtering and impression words are terminated when the number of recommended recipes reaches the pre-set upper limit (K). In our proposed system, the recommendation process using collaborative filtering is terminated when there no users in the user reference list that show the exact same evaluation for the recommended recipe as the user up to that point. The recommendation process then continues by identifying the most similar recipe, from the viewpoints of three-level scores (disregarding "0") based on impression words, to that successfully recommended among recipes not yet recommended. Just before concluding the recommendation process, the user database is updated with subjective evaluations of the recipe by adding the viewpoints of users the recipe by adding the viewpoints of users recommending the recipe.

5. Proposed system

In this section, we propose a system that narrows down recipe choices to a final recommendation using a method

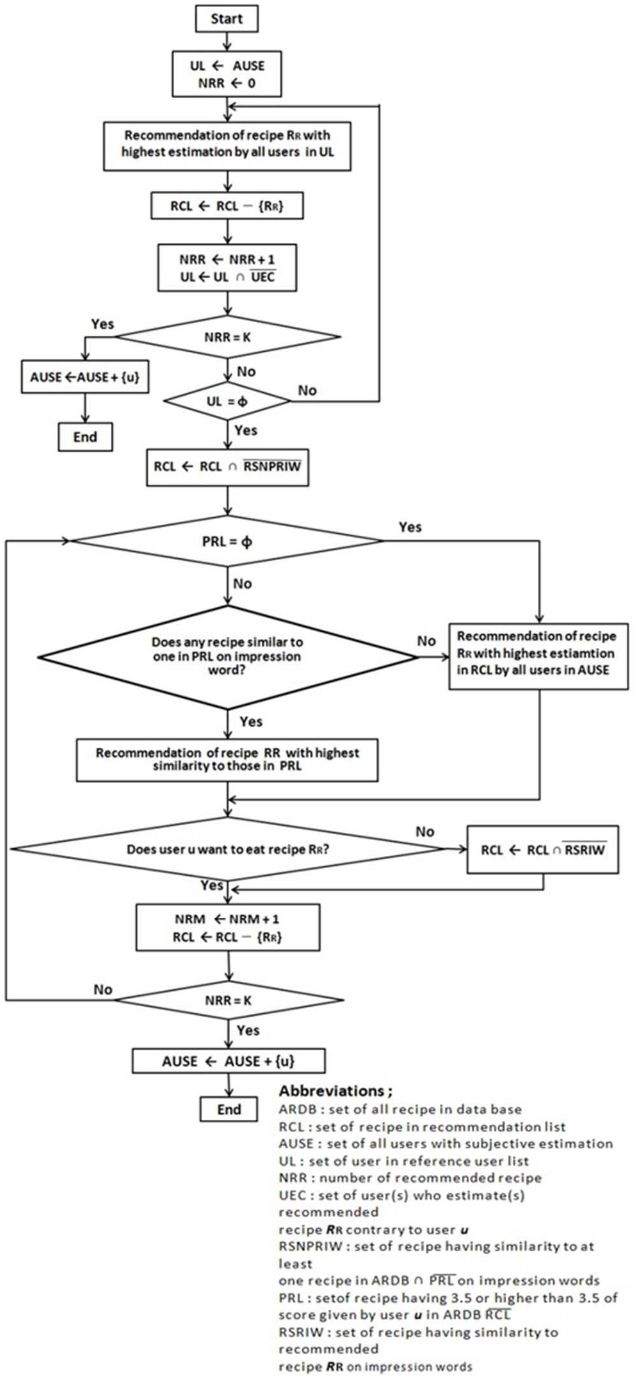

Fig. 1. Recipe recommendation using collaborative filtering and impression words.

that considers yesterday's dinner recipe in addition to the recommendation method discussed in Section 4. First, recipes in recipe groups that are similar to the recipe that user selected the day before are recommended by using the method described in Section 4. Next, recipes in recipe groups that differ from previous day's selection are also recommended by using the method described in Section 4. As in the impression word recommendation, the judgment of a recipe whose impressions are similar to yesterday's dinner recipe is based whether the "impression evaluation score" coincides with five or more of the impression word pairs of 10 items. Fig. 2 shows a recipe recommendation flowchart that considers yesterday's dinner.

6. Performance evaluations

6.1. *Conditions*

From a total of 49 recipes that exclude side dishes, soups, and arranged dishes, a main course dish that one or more user designated as "I have never tried" were extracted from the 293 entries in the "*Rakuten* recipe"[4] category for use in our evaluation. The impression words selected were four pairs of "taste expression", four pairs of "texture expression", and two pairs of "situation expression" extracted from the "Sizzle Word Report 2014".[5] Synonyms and antonyms were judged in the Weblio dictionary.[6] Similar expressions in the "expression" rankings are grouped together and chosen via the following procedure:

Step 1: The top 10 words satisfying the condition that their antonyms are within the top 25 words are chosen in each ranking.

Step 2: The words that ranked within the top 10 and their antonyms within the same ranking are chosen.

Step 3: The words ranked within the top 10 are chosen under the restriction that their antonyms are out of ranking.

Step 4: Processing repeats for words ranking below the top 10.

The proposed system recommends a recipe to 10 new participating users who were not among the 12 users who entered evaluations into the database. K was set to 15, and experiments were conducted under the following two conditions:

Recommendation accuracy = Number of recipes to which the user replied, "I want to try" / Number of recommended recipes.

Final recommendation accuracy = Number of users that recommended the recipe that the user most wants to try / Number of users.

Our experiment was performed on a Dell Inspiron 7559 personal computer (PC) equipped with Intel Core i7-6700HQ 2.60 GHz central processing unit (CPU) and 8.0 GB of random access memory (RAM). The Microsoft Windows 10 Professional operating system (OS) was installed on the PC and Microsoft Visual C++ 6.0 and Microsoft Visual C++ 2010 were used as the development languages.

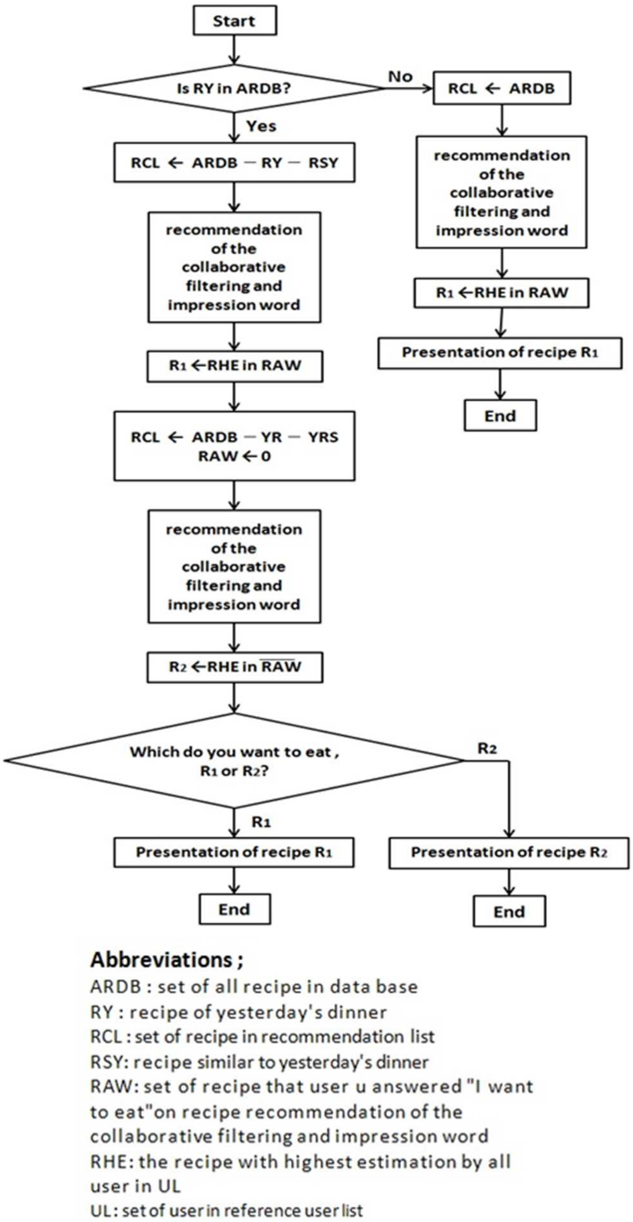

Fig. 2. Recipe recommendation considering yesterday's dinner.

6.2. *Results and discussions*

Fig. 3 shows a sample recommendation for a new user, while Fig. 4 shows the recommendation accuracy of 10 new users. The mean value of the proposed system's recommendation accuracy was 33.0%, while that of the random recommendation was 21.4%. The value of the final recommendation accuracy of the proposed system was 50.0%, while that of the random recommendation was estimated as lower than 21.4%.

The mean value (33.0%) of the proposed system's recommendation accuracy was lower than that (71.1%) by our previously reported system.[1] From this result, it is thought that a user's favorite recipes focused in our previously reported system[1] were not necessarily those that he or she wants to try, so it will be necessary to change the subjective recipe scoring system used in the this study to consider recipes the user wants to experience in the future. Since the accuracy value of our proposed system's final recommendation exceeds the value of random selection, it can be said that our proposed system has proven to be effective.

We then conducted a questionnaire survey of 10 user participants regarding the recommendations produced by our system. The four categories below were evaluated:

① Speaking ease of user to UI
② Time needed to produce recommendation

Order of recommendation	Recipe No.	Recommendation result	Evaluation matching user
1	19	○	1,2,3,4,5,7,8,9,10
2	34	○	1,3,4,5,7,8,9,10
3	18	×	ϕ
4	8	○	
5	33	○	
6	14	○	
7	21	○	
8	9	○	Recommendation using impression word
9	4	×	
10	20	○	
11	38	○	
12	40	○	
13	42	○	
14	2	×	
15	7	○	

Fig. 3. Sample new user recommendation.

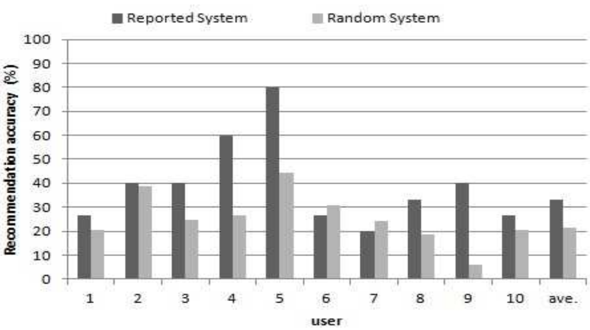

Fig. 4. Accuracy recommendations of 10 new users.

③ Naturalness of UI output as utterance
④ Dish display necessity

For the category ① results, one participant reported that the UI was "very easy to talk to", three participants said it was "somewhat easy to talk to", five said that "talking was normal", and one said it was "slightly hard to talk to". It should be noted here that no participant said the UI was "Hard to talk to". For the category ② results, no participants reported that time required to output a recommendation was "too short", "somewhat short", or "too long". Instead, seven participants said the time was "as expected," and three participants said it was "slightly excessive". For the category ③ results, one participant said the UI's utterances were "very natural", five said they were "somewhat natural", one called them "appropriate", three called them "slightly unnatural". It should be noted here that no participant said the UI utterances were "too unnatural". For the category ④ result, seven participants said visual displays were "necessary", two participants said they were "somewhat necessary", and one was "undecided". No participant said the displays were "slightly unnecessary" or "unnecessary".

7. Conclusion

In this paper, we proposed a recipe recommendation system that combines collaborative filtering and impression words and is based on our previously reported system.[1] We showed that our proposed system is more effective than random recommendations and that it has the ability to narrow down potential recipes to a single choice.

References

1. K. Saito, T. Asada, Y. Yoshitomi, R. Kato, and M. Tabuse, A Recipe recommendation System Using Knowledge Information and Agent (in Japanese), in *Proc. of Human Interface Symposium 2016* (Japan, Tokyo, 2016), pp.51 -54.
2. MMDAgent, http://www.mmdagent.jp/ Accessed 25 July 2016.
3. Yoshizaki S, Yoshitomi Y, Koro C, Asada T (2013), Music recommendation hybrid system for improving recognition ability using collaborative filtering and impression words. *J. Artif. Life and Robotics* **18**(1-2) (2013) 109-116.
4. Rakuten recipe, http://recipe.rakuten.co.jp/category/
5. Sizzle Word Report2014 Accessed 25 July 2016. http://www.bmft.jp/pdf/services/ kotoba14.pdf
6. Weblio dictionary, http://thesaurus.weblio.jp/ Accessed 25 July 2016.

A System for Analyzing Facial Expression and Verbal Response of a Person While Answering Interview Questions on Video

Taro Asada, Yasunari Yoshitomi, and Masayoshi Tabuse
Graduate School of Life and Environmental Sciences, Kyoto Prefectural University,
1-5 Nakaragi-cho, Shimogamo, Sakyo-ku, Kyoto 606-8522, Japan
E-mail: t_asada@mei.kpu.ac.jp, {yoshitomi, tabuse}@kpu.ac.jp
http://www2.kpu.ac.jp/ningen/infsys/English_index.html

Abstract

We have developed a system for analyzing facial expressions of a person while answering interview questions on a video. A video capturing the answerer is analyzed by OpenCV and the feature parameter for an eye area in addition to the mouth area focused in our reported research. Moreover, the time to utterance of the person answering just after an interview question and the fundamental frequencies of his or her voice are measured for analyzing his or her mental state.

Keywords: Facial expression analysis, Movement analysis, Mouth area, Eye area, Interview on video, OpenCV.

1. Introduction

In Japan, the average age of the population has been increasing, and this trend is expected to continue. Along with this, the number of older people with dementia and/or depression has been increasing very rapidly. To improve the quality of life (QOL) of elderly people living in a care facility or at home, we have developed a method for analyzing the facial expressions of a person who is having a conversation with another person on a videophone.[1,2] However, in our previously reported system[1,2] for analyzing the facial expression of a person during a conversation with another person, facial expression intensity was assumed to be affected by (1) the conversation topic, (2) the partner, and (3) the facial expression of the partner. In the present study, (1), (2), and (3) are fixed by using an interview video. We developed a system for analyzing the facial expressions of a person while answering the interview questions on video. The video capturing the "answerer" in an interview is analyzed by image processing software (OpenCV[3]) and the previously proposed feature parameter (facial expression intensity), which is measured for the eye area in addition to the mouth area. The mouth area was the focus of our previously reported research. Moreover, the time to utterance of the answerer just after an interview question and the fundamental frequencies of his or her voice are measured for analyzing his or her mental state.

2. Proposed System and Method

2.1. *System overview and outline of the method*

We constructed three modules in our system based on our reported research.[4] The first is a module for replaying an interviewer's video for the answerer, the second is a module for recording the answerer's response on video, and the third is a module for processing the recorded video of the answerer. The first module is a pseudo-interview. In the recorded data, the sizes of the faces are standardized, and the data are analyzed by using OpenCV for some feature parameters, as outlined below.

The Y component obtained from each frame in the dynamic image is used for analyzing the facial expressions. The proposed method is as follows: (1) the size of the lower part and the upper part of the face are standardized; (2) the mouth area in the lower part and the eye area in the upper part of the face are extracted; (3) the facial expression intensities for these two areas are measured; (4) the reference frame is selected; (5) the best positions for the mouth and the eye areas in the frame are determined; (6) the time to utterance of the answerer just after a given interview question is measured for analyzing the mental state of the answerer; (7) the feature parameters for the facial expression strengths of these two areas are calculated; and (8) the fundamental frequencies for voices of the answerer are measured by a conventional method. In the following subsections, (2) and (3) are explained in detail. For details on (1), (4), and the judgment of utterance in (6), see Refs. 1 and 2. For details on (5) of the mouth area, see Ref. 2. For details on (7) of the mouth area, see Ref. 1. The best positions for the eye areas in the frame are determined in a way similar to that for the mouth area. In addition, the feature parameters for facial expression strengths of the eye areas are calculated in a way similar way to that for the mouth area.

Fig. 1. Whole-face image (left), extracted images of the eye area (upper right) and the mouth area (lower right).

2.2. *Extraction of the mouth and eye areas*

Next, by using OpenCV, the mouth and eye areas are extracted as rectangular shapes. An example of a face image and the extracted images of the mouth and the eye areas is shown in Fig. 1.

2.3. *Measurement of facial expression intensity*

For the Y component of the selected frame, the feature vector for facial expression was extracted for the mouth and the eye areas. The extraction was performed by using a discrete cosine transform (2D-DCT) for each section of 8×8 pixels.

As the feature parameters for expressing facial expression, we selected 15 low-frequency components from the 2D-DCT coefficients, but excluded the direct current component. Next, we obtained the mean of the absolute value of each of these components in the areas of the mouth-part and the eye-part. In total, we obtained 15 values as elements of the feature vector for the areas of the mouth-part and the eye-part. The facial expression intensity is defined as the norm of the difference vector, which is a vector of the difference between the feature vector for the expressionless face and that for an observed expression. The candidate of facial expression intensity, defined as the norm of the difference vector between two feature vectors, was used for selection of the reference frame.[2]

3. Experiments

3.1. *Conditions*

The interviewer's video was made from a video recording a scene in which a psychiatrist interviewed a subject. Only the psychiatrist's voice remains in the interviewer's video. In the video, the psychiatrist asks the subject three fundamental questions generally used for a patient with potential depression. Based on a preliminary experiment for deciding the appropriate interval time, the interval time between two questions was edited by using video editing software. The experiment was performed in the following computational environment: the PC set in front of subject A was a Dell Precision T1600; CPU: Intel Xeon E31225 3.1 GHz; 8.0 GB memory; OS: Microsoft Windows 7 Professional. The development language was Microsoft Visual C++ 2008 Express Edition.

Two males (subject A in his 30s, subject B in his 20s) participated in the experiments. The subjects were interviewed by the interviewer video, which was about 40 seconds in length. As an initial condition in the experiment, the subjects were instructed to keep a neutral facial expression without utterance for about five seconds just after starting the playback of the interview video. After the initial state of the neutral facial expression was terminated, the subjects were requested to intentionally respond with three types of emotions (Experiment 1: relaxed, Experiment 2: excited, Experiment 3: depressed). The visual and audio information of the subjects in the experiments were saved as AVI files having 640×480 pixels for each frame. The AVI files were used for measuring the feature parameters of the facial expressions, the time to utterance of the subject just after an interview question was given, and the fundamental frequencies of the subject.

3.2. *Results and discussion*

The facial expression intensity for the mouth area was more sensitive than that for the eye area (Figs. 2-5). The facial expression intensity for the mouth area became high during the response to a question. On the other hand, the facial expression intensity for the eye area fluctuated widely and was almost independent of the utterance. Note that the feature parameters for facial expressions for the mouth area tended to be greater in Experiment 2 than in both Experiments 1 and 3, while those for the eye area tended to be smaller in Experiment 1 than in both Experiments 2 and 3 (Table 1). The average of the fundamental frequencies of the voice of the subjects was greater in Experiment 2 than in both Experiments 1 and 3 (Table 2). The order of increasing time to utterance of the answerer just after an interview question was terminated was Experiments 2, 1, and 3 (Table 3). The experimental results described in this subsection show the usefulness of the proposed system.

Table 1. Feature parameters for facial expressions.

Exp.		1(relaxed)	2(excited)	3(depressed)
Subject A	Mouth area	1.5	1.8	1.7
	Eye area	2.4	3.6	4.4
Subject B	Mouth area	2.2	3.5	1.4
	Eye area	3.4	4.3	3.6

Table 2. Average of fundamental frequencies of voice of the subjects for each intentional emotion in Experiments 1-3.

Exp.	1(relaxed)	2(excited)	3(depressed)
Subject A	127.97	144.61	107.03
Subject B	93.33	137.38	99.55

(Hz)

Table 3. Time to utterance of the answerer just after an interview question was terminated.

	Exp.	Q.1	Q.2	Q.3	Ave.
Subject A	1(relaxed)	2.3	1.3	0.8	1.4
	2(excited)	0.6	1.0	0.0	0.5
	3(depressed)	2.5	2.6	2.1	2.4
Subject B	1(relaxed)	1.7	1.5	1.1	1.4
	2(excited)	0.8	0.7	0.3	0.6
	3(depressed)	1.7	2.0	1.8	1.8

(s)

4. Conclusion

We developed a system for analyzing facial expressions of a person while answering interview questions in a video. Moreover, the time to utterance of the answerer just after an interview question and the fundamental frequencies of his or her voice were measured in order to analyze his or her mental state. The experimental results show the usefulness of the proposed system.

Acknowledgements

The authors would like to thank Professor J. Narumoto of Kyoto Prefectural University of Medicine for his valuable support and helpful advice in the course of this research. We would also like to thank Mr. K. Nishimura, a student of the Graduate School of Kyoto Prefectural University, for his cooperation in the experiments. This research was supported by COI STREAM of the Ministry of Education, Culture, Sports, Science, and Technology of Japan.

References

1. T. Asada, Y. Yoshitomi, R. Kato, M. Tabuse, and J. Narumoto, Quantitative evaluation of facial expressions and movements of persons while using video phone, *J. Robotics, Networking and Artif. Life* **2**(2) (2015) 111-114.
2. T. Asada, Y. Yoshitomi, R. Kato, M. Tabuse, and J. Narumoto, A System for Facial Expression Analysis of a

Person While Using Video Phone, *J. Robotics, Networking and Artif. Life* **3**(1) (2016) 37-40.
3. Open CV. http://opencv.org/ Accessed 18 November 2016.
4. T. Asada, Y. Yoshitomi, M. Tabuse and J. Narumoto, A System for Facial Expression Analysis of a Person While Answering Interview Questions on Video (in Japanese), in *Proc. of Human Interface Symposium 2016* (Japan, Tokyo, 2016), pp.679-682.

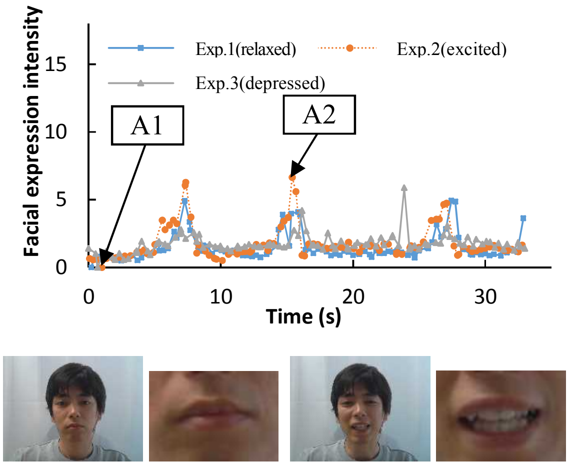

A1 A2

Fig. 2. Changes in facial expression intensity of mouth area for subject A (upper graph). Whole-face images and mouth images are shown for two moments during Experiment 2 (A1 and A2), as indicated on the graph (lower images).

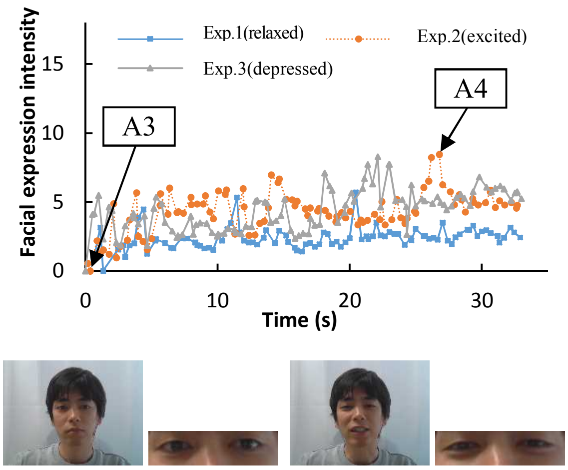

A3 A4

Fig. 3. Changes in facial expression intensity of eye area for subject A (upper graph). Whole-face images and eye-part images are shown for two moments during Experiment 2 (A3 and A4), as indicated on the graph (lower images).

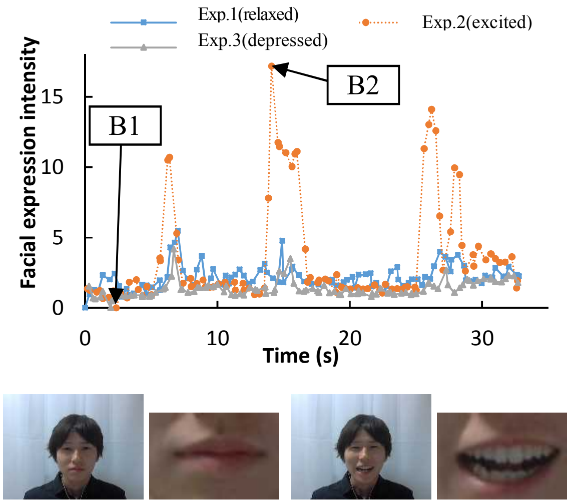

B1 B2

Fig. 4. Changes in facial expression intensity of mouth area for subject B (upper graph). Whole-face images and mouth images are shown for two moments during Experiment 2 (B1 and B2), as indicated on the graph (lower images).

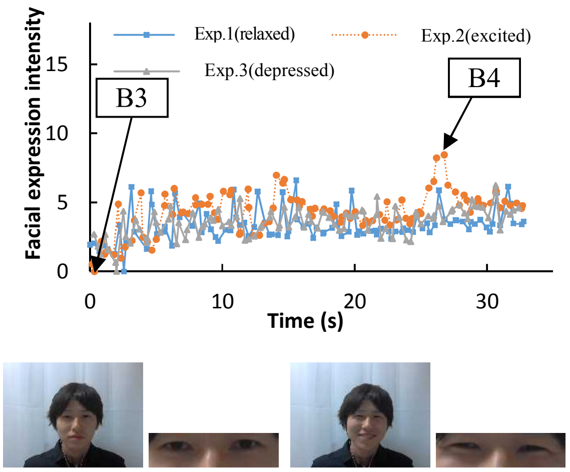

B3 B4

Fig. 5. Changes in facial expression intensity of eye area for subject B (upper graph). Whole-face images and eye-part images are shown for two moments during Experiment 2 (B3 and B4), as indicated on the graph (lower images).

Real-Time System for Horizontal Asymmetry Analysis on Facial Expression and Its Visualization

Ryoichi Shimada, Taro Asada, Yasunari Yoshitomi, Masayoshi Tabuse
Graduate School of Life and Environmental Sciences, Kyoto Prefectural University,
1-5 Nakaragi-cho, Shimogamo, Sakyo-ku,Kyoto 606-8522, Japan
E-mail: {yoshitomi, tabuse}@kpu.ac.jp, t_asada@mei.kpu.ac.jp}
http://www2.kpu.ac.jp/ningen/infsys/English_index.html

Abstract

We report on the development of a real-time system for facial expression horizontal asymmetry analysis and visualization. In our system, the image signal input from a webcam is analyzed using OpenCV, and feature parameters (facial expression intensity) are measured separately for the left and right half regions in the mouth area. Our real-time system then draws a graph expressing facial expression intensity changes. The experimental results obtained thus far suggest that this system could be useful.

Keywords: Facial expression analysis, Real-time system, Moving image, Mouth area, Visualization, OpenCV

1. Introduction

In Japan, the average age of the population has been increasing, and this trend is expected to continue into the future. We have therefore been studying ways of applying information technology (IT) to improving the medical treatment provided to elderly people with psychiatric disorders.

One of our current studies is aimed at analyzing the facial expressions of persons in a moving image captured by webcams. In this paper, we propose a real-time facial expression horizontal asymmetry analysis and visualization system. Unlike current and previously used methods[1,2] in which the moving image data are first saved in a personal computer (PC) and then analyzed, the moving image in our method is captured by a webcam and analyzed in real-time via Open Source Computer Vision (OpenCV) image-processing software[3] along with a previously proposed feature parameter (facial expression intensity) [1,2] that is based on the mouth area. The visualization method proposed in this paper is based on our reported method[4] which involves creating a graph from the OpenCV image data and then analyzing the relationship between the facial expression intensity and time. This visualization is performed concurrently with the facial expression intensity measurement.

2. Proposed System and Method

2.1. System overview and outline of the method

In this system, webcam moving imagery captured in real-time is analyzed via the following process. We constructed the modules in our system based on our reported research.[4] First the sizes of faces in the captured image data are standardized, and then analyzed using OpenCV and our proposed facial expression feature parameters.

The frames of the moving images are then changed from RGB image data into YCbCr image data, after which the Y component obtained from each frame in the dynamic image is used for facial expression analysis. The proposed method consists of (1) the extracting the mouth area, (2) measuring the facial expressions feature vectors, and (3) measuring the facial expression intensity. In (1), the mouth area is extracted from the frames by using OpenCV. In (2), for the Y component of the selected frame, facial expressions feature vectors are extracted for each 8×8-pixel section. In (3), the facial expression intensity, which is defined as the norm difference between the facial expression feature vector of the reference and target frames, is measured. These details are explained in the following subsections.

2.2. Mouth area extraction

First, moving image data are changed from RGB to YCbCr image data, after which the face area is extracted from the changed image as a rectangular shape, and the lower 40% portion of the face area is standardized. Next, the mouth area is extracted from that area. The reason the mouth area was selected for facial expression analysis is because it is where the differences between neutral and happy facial expressions appear most distinctly. An example of the moving image frame data and the extracted mouth area image is shown in Fig. 1.

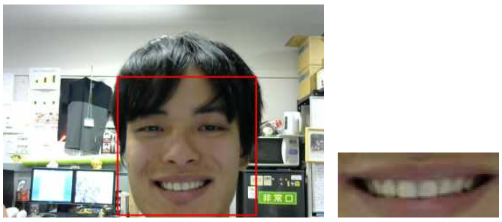

Fig. 1. Moving image frame and extracted mouth area.

In this paper, the mouth area is separated into left and right half regions, and the facial expression intensity of each region is separately measured. An example of a mouth area separated into the left and right half regions is shown in Fig. 2.

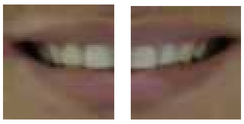

Fig. 2. The mouth area separated in the left and right half regions

2.3. Facial expression intensity measurement

For the Y component of the selected frame, the facial expression feature vector is extracted for the mouth area using a two-dimensional discrete cosine transform (2D-DCT) for each 8×8-pixel section. To measure the feature parameters of the facial expressions, we selected low-frequency components from the 2D-DCT coefficients as the facial expression feature vector elements. However, the direct current component is not included. In total, 15 feature vector elements are obtained. As mentioned above, facial expression intensity is defined the norm difference between the facial expression feature vector of the reference and target frames. The reference frame selection method is explained in next subsection.

2.4. Reference frame selection

In this subsection, we propose a new method for automatically selecting reference frames. This method was adopted because, in our new system, the moving image captured by webcam is analyzed in real-time. This means we cannot use our previous method,[1,2] which was designed for the non-real-time analysis.

In this method, the first 10 continuous frames of mouth area data successfully extracted after the webcam recording begins are treated as reference frame candidates. Then, beginning with the first reference frame candidate, the facial expression intensity of all candidate frames is measured, and the sum of all facial expression intensities is calculated. The candidate frame with the minimum value is selected as the reference frame.

2.5. Facial expression intensity visualization

Facial expression intensity is measured using our previously discussed method,[4] in which a straight line is drawn on a graph image prepared using OpenCV.

3. Experiment

The experiment was performed on a Dell OPTIPLEX 780 PC equipped with Intel Core 2 Duo E8400 3.0 GHz central processing units (CPUs) and 4.0 GB of random access memory (RAM). The Microsoft Windows 7 Professional operating system (OS) was installed on the PC and Microsoft Visual C++ 2008 Express Edition was used as the development language.

The newly proposed system display is shown in Fig. 3. We performed evaluation experiments for two test subjects (hereafter Subjects A and B) under the three conditions listed below. Furthermore, the message "SMILE, PLEASE!" was flashed on the display screen at points 20 and 40 s from the system start.

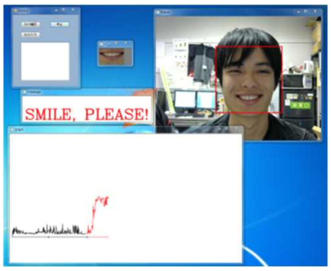

Fig. 3. Display while new system is in operation.

1. Subjects maintained neutral faces for about 60 s.
2. Subjects smiled when the above message was displayed.
3. Subjects raised the right side of their mouth when the above message was first displayed, and raised the left side of their mouth when the above message was displayed a second time.

The experimental results are shown in the following figures (Figs. 4 to 16). Arrows in each graph indicate the max point of the facial expression intensity.

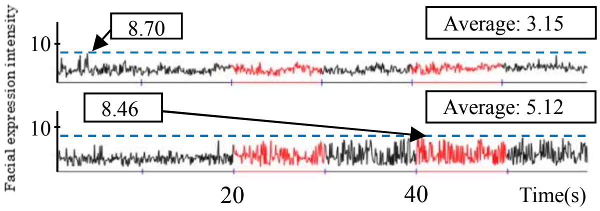

Fig. 4. Facial expression intensity of the whole mouth under experimental condition 1 (upper: Subject A, lower: Subject B).

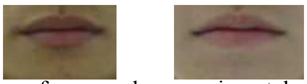

Fig. 5. Reference frame under experimental condition 1 (left: Subject A, right: Subject B).

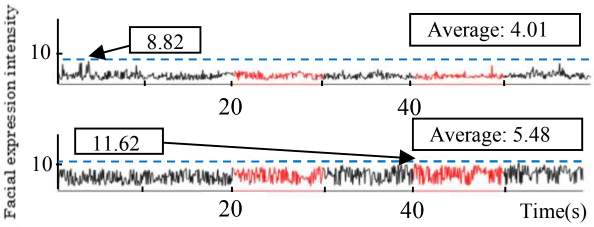

Fig. 6. Facial expression intensity of the right half region of the mouth under experimental condition 1 (upper: Subject A, lower: Subject B).

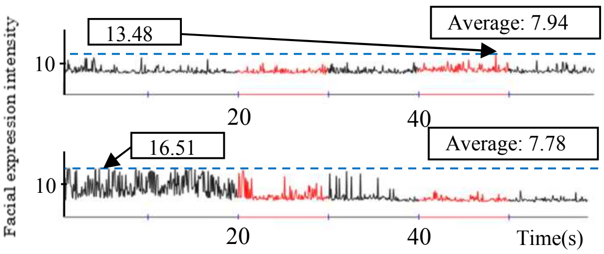

Fig. 7. Facial expression intensity of the left half region under experimental condition 1 (upper: Subject A, lower: Subject B).

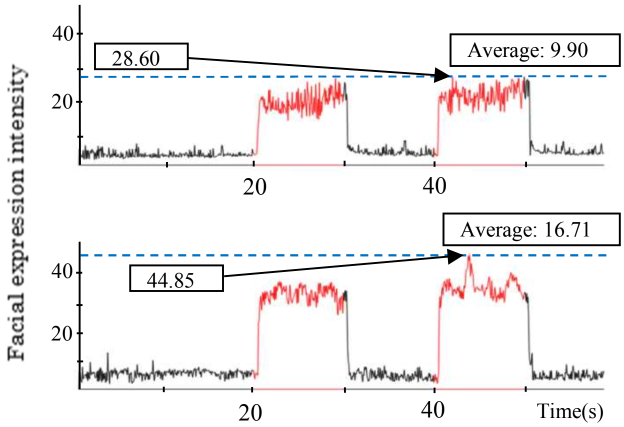

Fig. 8. Facial expression intensity of the whole mouth under experimental condition 2 (upper: Subject A, lower: Subject B).

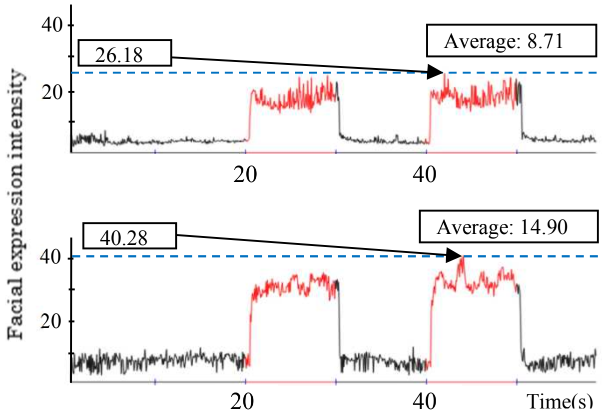

Fig. 9. Facial expression intensity of the right half of the mouth under experimental condition 2 (upper: Subject A, lower: Subject B)

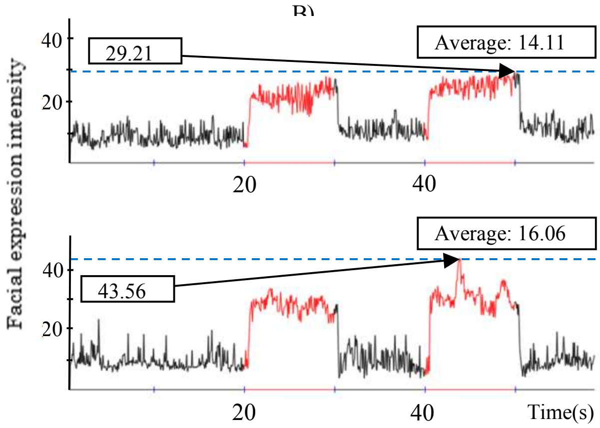

Fig. 10. Facial expression intensity of the left half region under experimental condition 2 (upper: Subject A, lower: Subject B).

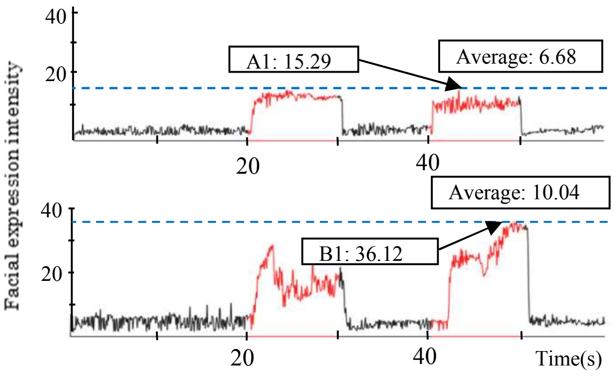

Fig. 11. Facial expression intensity of the whole mouth under experimental condition 3 (upper: Subject A, lower: Subject B).

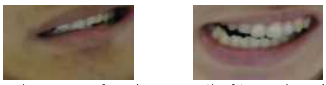

Fig. 12. Mouth area of point A1 (left) and point B1 (right).

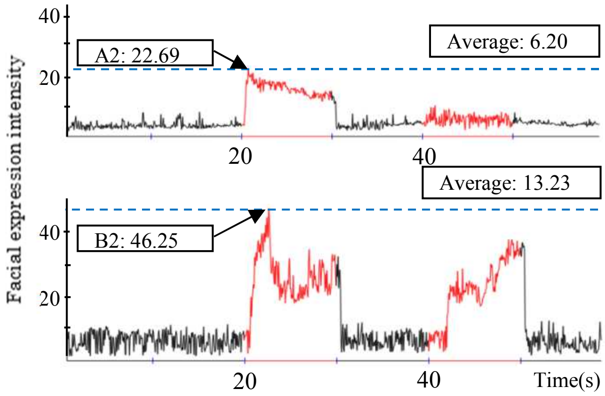

Fig. 13. Facial expression intensity of the right half of the mouth under experimental condition 3 (upper: Subject A, lower: Subject B).

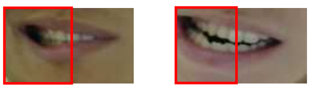

Fig. 14. Right half mouth area of point A2 (left) and point B2 (right).

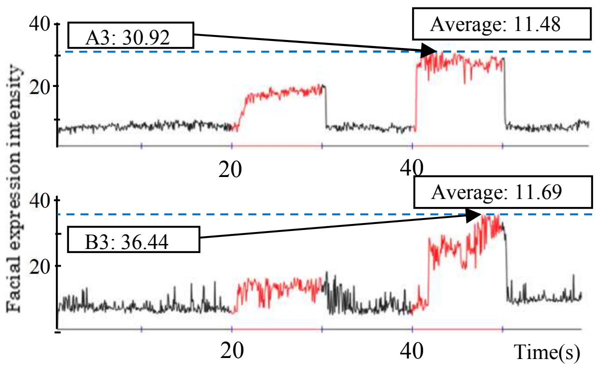

Fig. 15. Facial expression intensity of the left half region under experimental condition 3 (upper: Subject A, lower: Subject B).

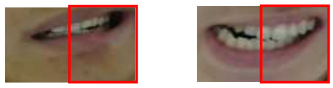

Fig. 16. Left half mouth area of point A3 (left) and point B3 (right).

The experimental results obtained thus far suggest that this system could be useful for situations where real-time reaction to facial expressions is one of the important factors. Upon examining the experimental results, some problems were discovered. Facial expression intensities on the left half of the subject's faces during neutral face recording were always higher than those of the right half, and the reason for this discrepancy is unclear.

4. Conclusion

Herein, we proposed a real-time system for facial expression horizontal asymmetry analysis and visualization and performed a number of evaluation experiments. It is believed that this system could prove useful in the treatment of psychiatric ailments such as depressive disorder and dementia, in addition to providing treatment options for persons with half side body paralysis.

Acknowledgements

The authors would like to thank Professor J. Narumoto of Kyoto Prefectural University of Medicine for his valuable support and helpful advice in the course of this research. We would also like to thank Mr. K. Nishimura, a student of the Graduate School of Kyoto Prefectural University, for his cooperation in the experiments. This research was supported by COI STREAM of the Ministry of Education, Culture, Sports, Science, and Technology of Japan.

References

1. T. Asada, Y. Yoshitomi, R. Kato, M. Tabuse, and J. Narumoto, Quantitative evaluation of facial expressions and movements of persons while using video phone, *J. Robotics, Networking and Artif. Life* **2**(2) (2015) 111-114.
2. T. Asada, Y. Yoshitomi, R. Kato, M. Tabuse and J. Narumoto, Analysis of facial expressions robust against small imperfections in mouth-part area extraction from face-images of persons while using video phone (in Japanese), in *Proc. of Human Interface Symposium 2015* (Japan, Hakodate, 2015), pp.187-190.
3. Open CV. http://opencv.org/ Accessed 1 December 2015.
4. R. Shimada, T. Asada, Y. Yoshitomi, M. Tabuse, and J. Narumoto, A real-time system for facial expression analysis and its visualization (in Japanese), in *Proc. of Human Interface Symposium 2016* (Japan, Tokyo, 2016), pp.643-646.

Development of Mouse System for Physically Disabled Person by Face Movement Using Kinect

Junpei Miyachi, Masayoshi Tabuse
Graduate School of Life and Environmental Sciences, Kyoto Prefectural University,
1-5 Nakaragi-cho, Shimogamo, Sakyo-ku, Kyoto 606-8522, Japan
E-mail:j_miyachi@mei.kpu.ac.jp, tabuse@kpu.ac.jp

Abstract

We developed a system which operates a computer by a facial movement using Kinect. Recognition of a facial movement of a person makes it possible to operate a computer. We can move a mouse cursor by changing the face direction, and we can carry out an operation of mouse click by recognizing an open mouth or a closed eye. In this paper, we evaluated the effect on operability due to the face direction and recognition rate due to distance.

Keywords: Mouse system, Kinect, Physically disabled people, Recognition of face movements.

1. Introduction

Physically disabled people cannot move their limbs freely. It is difficult for a physically disabled person to use a computer. The importance of the computer with the information society increases as a current social background. Therefore, support of the computer operation is required. The interface for them has been developed so that they can use a computer recently. There are two types of the interface. One is the contact-type which operates while attaching the device to a body. Another is the noncontact-type which operates by recognizing the movement of a body. Although the contact-type has the advantage of easy detection of body movement, the user must attach it directly during use. On the other hand, noncontact-type must adjust parameters for a user. To resolve these problems reduce a burden for the user.

One of the possible physical movements of a physically disabled person is facial movement (This means the face direction and open and closed mouth or eyes). If a computer operates with recognizing the facial movement, the physically disabled person can use it. We developed a system which operates a computer by the facial movement. Our system uses Kinect for obtaining the face direction and extracting feature points of the face. We can move a mouse cursor by changing the face direction. We can carry out an operation of mouse click by recognizing an open mouth or closed eye. This reduces the burden on the user.

2. Kinect

Kinect is a motion capture device developed by Microsoft Corporation. RGB camera, depth sensor, and microphone array is mounted in Kinect, it can obtain RGB images, depth images, and audio information. Moreover, joint positions of the whole body can be estimated from the obtained depth images.

Kinect for Windows SDK is a software development kit for using Kinect. Face Tracking is one of the functions in Kinect for Windows SDK. It can perform facial recognition and face tracking using RGB images and depth images which Kinect acquired. Furthermore, it can acquire feature points of face parts (eyes, nose, and mouth) and face direction. Face tracking algorithm is based for Active Appearance Model (AAM) with depth fitting[1]. It allows accurate and real time tracking of human faces. High definition face tracking (HD face) is also one of the functions in Kinect for Windows SDK. It is possible to extract detailed facial feature points, and there are 1347 feature points that it can extract.

3. Proposed System

3.1. *System overview*

Our system includes Kinect for operating a computer. A user moves his face towards Kinect. The movement is recognized on the basis of information acquired using Kinect. It is possible to operate a computer. Our system has three functions for a physically disabled person. Firstly, it can control a mouse cursor along face direction. Secondly, it can perform a mouse click by recognizing an open mouth. Finally, it can carry out a mouse click by judging the open or closed eyes. In the following subsections, these functions are explained in detail.

3.2. *Control of a mouse cursor by face direction*

We acquire angles of face direction using Face Tracking of Kinect for Windows SDK 2.0. The angles to use are $pitch$ and yaw which express a value of the angle (degree) for vertical and horizontal face direction. If the user turn his face toward Kinect, the values of the face direction are respectively, $pitch = 0$, $yaw = 0$. However, the user watches a monitor while using a computer. Therefore, we change the origin of face direction coordinate to the center of the monitor. We consider the difference between the angle on watching a monitor and the angle on watching Kinect. As shown in Fig. 1, the difference of the angles is expressed using the following equation:

$$\theta = \arctan\frac{y}{z} ,$$

where y denotes a length between the center of monitor and Kinect, and z denotes a distance of the depth between a face of the user and Kinect, which is obtained using Kinect. We define the face direction vector $\boldsymbol{a}$ as:

$$\boldsymbol{a} = (yaw,\ pitch - \theta) .$$

The control of a mouse cursor is operated following the face direction vector $\boldsymbol{a}$. It is moved in the same direction as the vector. The moving speed of a mouse cursor is changed according to the size of the vector. When $|\boldsymbol{a}| < 10$, we define the face is turning to the front. Accordingly, a mouse cursor isn't moved.

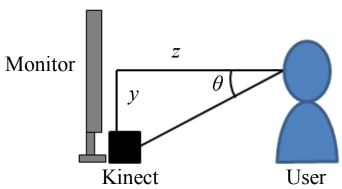

Fig. 1. Positional relation of the user and Kinect, which is looked from the side.

3.3. *Recognition of open mouth*

We extract four feature points of mouth (top, bottom, left and right) using HD face of Kinect for Windows SDK 2.0, as shown in Fig. 2. The vertical length of the mouth is found by feature point coordinates of the top and bottom. The horizontal length of the mouth is found by feature point coordinates of the left and right. The rate of the open mouth R_m is expressed as $R_m = h_m / w_m$ where h_m and w_m denote the vertical and horizontal length of the mouth. Let Th_m be the threshold for judgment of opened or closed mouth. When $R_m > Th_m$, it is recognized that the mouth is opened. In the present study, the value of Th_m is set to 0.4, which was determined experimentally.

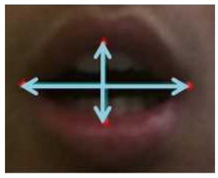

Fig. 2. Feature points of mouth extracted using Face Tracking and the vertical and horizontal length.

3.4. *Judgment of opened and closed eyes*

We extract four feature points of eyes (top, bottom, left and right) using HD face of Kinect for Windows SDK 2.0, as shown in Fig. 3. The range of X-axis is the difference of x-coordinate between the left and right, and the range of Y-axis is the difference of y-coordinate between the top and bottom. We define these ranges as eye region.

The judgment of opened or closed eye uses binary images. For the binarization, at first, the detection of the eye region is performed in a RGB image. It is converted from the RGB data to the luminance value. Next, we make the histogram of luminance values in the eye region. The threshold for judgment of opened or closed eye is decided using discriminant analysis method[2] from the histogram. Our system applies the threshold in the first frame, and it is used for the judgment after the next frame. It makes the luminance value a two level with the threshold. The binary image is made by the above procedure.

The vertical and horizontal lengths of the eye are settled from the binary image. We make the histogram of black pixels. The vertical length of the eye is the maximum on the histogram, and the horizontal length of the eye is the range of x-coordinate in the eye region. The rate of the open eye R_e is given by $R_e = h_e / w_e$ where h_e and w_e denote the vertical and horizontal length of the eye. Let Th_e be the threshold for judgment of opened or closed eye. When $R_e > Th_e$, the eye is judged to be opening state. When $R_e < Th_e$, the eye is judged to be closing state. In the present study, the value of Th_e is set to 0.3, which was determined experimentally.

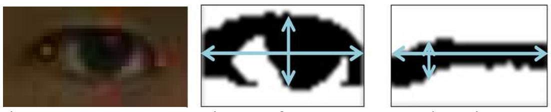

Fig. 3. Feature points of eye extracted using Face Tracking (left), and the binary image state and the vertical and horizontal length of opened eye (center) and closed eye (right).

3.5. *Mouse click processing*

Mouse click processing is performed by recognizing the intentional movement of the user. The movement is the following conditions:

- When the duration time of opening mouth state reach for *t1*,
- When the duration time of closing eye state reach for *t2*,

where *t1* and *t2*are arbitrary times. In the present study, the value of *t1* and *t2* are set to 1.0 s and 0.8 s, respectively. Mouse click processing is carried out only in the case of $|\boldsymbol{a}| < 10$.

4. Experiments

4.1. *Conditions*

The experiment was performed in the following computational environment: the PC was a HP ENVY 700-560jp (CPU: Intel(R) Core(TM) i7-4790 CPU 3.60GHz, memory: 8.00GB); the OS was Microsoft Windows 8.1 Pro; the development language was Microsoft Visual C++ 2013 Express Edition. The image was produced by Xbox One Kinect sensor which was placed in front of the PC, as shown in Fig. 4.

Fig. 4. Position of PC and Kinect during experiments.

4.2. *Method*

We conducted three kinds of experiments which ware performed by five subjects, respectively. For the first experiment, we measured times that a mouse cursor moved by face direction from a circle drawn on screen to another circle drawn in the distance of 20 cm. The subject moved to eight directions (vertical, horizontal, and diagonal), respectively. This experiment was conducted to assess the operability by difference of direction. For the second experiment, we examined the recognition rate of mouse click by open mouth. The distance between Kinect and the subjects was conducted at 0.6m, 0.8m, 1.0m, 1.5m, and 2.0m for evaluating influence to the recognition rate by the difference in distance. The subjects perform three times of opening movement for one second. The recognition rate is the proportion that click processing is carried out in fact. For the last experiment, we conducted experiment to judge opened or closed eyes. This experiment was conducted at distance of 0.6m, 0.8m, 1.0m, 1.5m, and 2.0m between Kinect and subjects for evaluating influence to the judgment accuracy by the difference in distance. We evaluate the accuracy of judgment with F-measure. F-measure is expressed the following equation:

$$F = \frac{2PR}{P + R},$$

where P, R and F denote the rate of frames which is really closing eye among frames judged as closed state, the rate of frames judged as closing state among frames which is closing eye ,and the harmonic mean of precision rate P and recall rate R. We performed judgment of closed eye by visual observation.

4.3. *Results and discussion*

4.3.1. Movement of mouse cursor by face direction

Fig.5 shows the time that took to move from a circle to another circle. From averaging of the moving time of 5 subjects, it was the movement of bottom direction to take the longest time. The second and third were the movement of bottom right and bottom left direction, respectively. It is probably due to the frame of the subject's glasses which interrupt his operation.

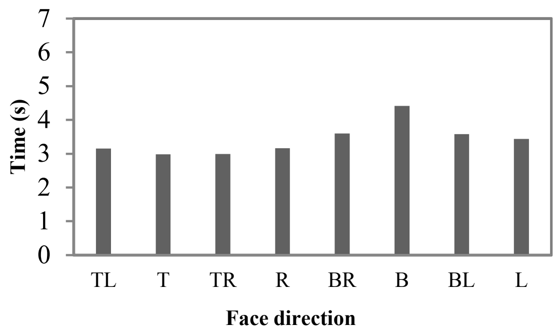

Fig. 5. Average moving time of five subjects by face direction. TL, T, TR, R, BR, B, BL, and L denote top left, top, top right, right, bottom right, bottom, bottom left, and left direction, respectively.

4.3.2. Mouse click recognition by open mouth

Fig.6 shows recognition rate of mouse click by open mouth. The recognition rate at 0.8m was 86.7%, which was the highest rate. In contrast, the recognition rate at 1.5m was 73.3%, which was the lowest rate. The cause of the recognition failure was that the rate of open mouth felt below the threshold momentarily because the subject didn't open his mouth of adequate size. Therefore, mouse click processing was carried out. It was carried out by opening mouth of adequate size for one second again.

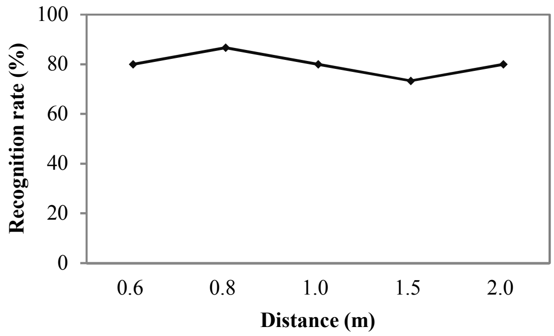

Fig. 6. Recognition rate of mouse click by open mouth .

4.3.3.Judgment accuracy of opened and closed eyes

Fig.7 shows precision rate, recall rate, and F-measure of judging opened and closed eyes. The F-measure at 0.8m was the highest value. Conversely, the F-measure at 1.5m and over greatly decreases. One of the failure cases were that the feature points extracted at 1.5m and over were out of alignment. The eye region which got out of position was not correctly judged. Moreover, there were that the shadow around a closed eye was described black in the binary image. Therefore, it was the reason that the rate of eye R_e didn't fall below Th_e.

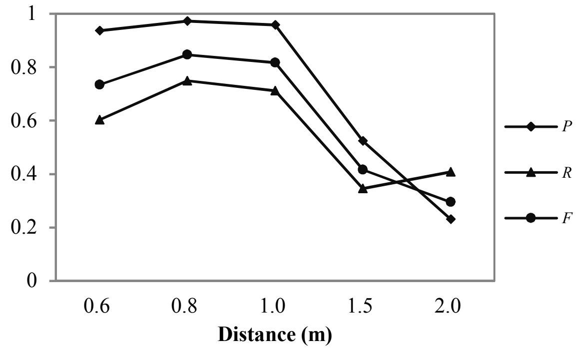

Fig. 7. Precision rate, recall rate, and F-measure in the experiment about judging opening and closing eyes.

5. Conclusion

We developed a mouse system for physically disabled people using Kinect. In this system, the user can move a mouse cursor by face direction and perform a mouse click processing by opening the user's mouth or closing the user's eye. As the results, there was not the conspicuous influence to recognition of mouse click processing by open mouth. F-measure of eye judgment decreased greatly at 1.0m over. However, because computer operation is usually performed at 1.0m or less, it can be operated by facial movement. As an area of future work, we intend to develop additional functions by recognizing other facial movements.

References

1. Nikolai Smolyanskiy, Christian Huitema, Lin Liang, and Sean Eron Anderson, Real-time 3D face tracking based on active appearance model constrained by depth data, *Image and Vision Computing*, *vol.*32 (2014) 860-869.
2. Nobuyuki Otsu, An Automatic Threshold Selection Method Based on Discriminant and Least Squares Criteria, *The IEICE Transactions*, *J63-D* (1980), 349-356.

Implementation of Multi-FPGA Communication using Pulse-Coupled Phase Oscillators

Dinda Pramanta, Takashi Morie, Hakaru Tamukoh
Graduate School of Life science and systems engineering, Kyushu Institute of Technology
2-4 Hibikino, Wakamatsu-ku, Kitakyushu 808-0196, Japan
E-mail: dinda-pramanta@edu.brain.kyutech.ac.jp, morie@brain.kyutech.ac.jp, tamukoh@brain.kyutech.ac.jp

Abstract

This paper proposes an implementation of multi-Field Programmable Gate Array (FPGA) communication using pulse-coupled phase oscillators. At first, we construct a digital phase oscillator circuit with adjustable in-phase parameters. While performing the synchronization task, the oscillators are connected into the first input and first output (FIFO) interface. The communication in-between of FPGAs will occur by enabling the following inputs and outputs on the FIFO through the Gigabit Transceiver (GTX) clock domain. Pulse-coupled phase oscillators of Winfree's model are utilized as a spike generator and we expect the ideal of model circuit will synchronize. We employ two FPGA boards of Virtex6 ML605 and implement four oscillators on a hardware level. Experimental results show that first spike synchronizing over two FPGAs takes 12.47 μsec with data bit speed stream 3.2Gbps.

Keywords: pulse-coupled oscillators, synchronization, Winfree’s model, FIFO, GTX, multi-FPGA,

1. Introduction

Pulse-coupled phase oscillator is one of the spiking neural networks. It consists of individual oscillators and a network of mutual interactions, which represented by the phase sensitivity function. [1, 2] Coupling between oscillators is determined by the timing of the spike pulse output from each oscillator. The oscillators are often assumed to be identical or nearly identical. In this case, the network reaches the *synchronization*-state where all the oscillators have the same phase. Based on the updating principles, one-bit signal line is required between oscillators for spiking the pulse. This feature is efficient for hardware implementation.[3, 4]

A field programmable gate array (FPGA) is a reconfigurable integrated circuit (IC) to perform complex interface and logic processing in a small footprint.[5] In addition, a multi-FPGA based design[5] overcomes the limitation of single FPGA resources and enables to implement large scale pulse coupled phase oscillator networks. However, communication delay between FPGAs may affect *synchronizing*-state. Therefore, high-speed communication is required to implement oscillators over the multi-FPGA and *synchronizing*-state should be verified.

In this paper, we propose an implementation of multi-FPGA communication using pulse-coupled phase oscillators. First, we design a digital circuit of pulse-coupled oscillators[3] based on the Winfree model.[2] Second, we propse a communication method between two FPGAs using the designed digital oscillator, the first input and first output (FIFO) interface and the serial connection of Gigabit Transceiver (GTX). As the multi-FPGA platform, we employ two FPGA boards and connect them by the serial connection of GTX. Experimental results show that the four oscillators network reaches to *synchronization*-state and first spike synchronizing over two FPGAs takes 12.47 μsec with data bit speed stream 3.2Gbps.

2. Pulse Coupled Oscillator model

In order to design the hardware implementation of pulse-coupled oscillator, Winfree model[2] provides an efficient ways, the fundamental of coupled phase oscillators is expressed as follows:

$$\frac{d\phi_i}{dt} = \omega_i + Z(\phi_i)Spk(t), \tag{1}$$

where ϕ_i is the i-th phase variable with 2π periodicity, ω_i is the i-th natural angular frequency, $Z(\phi_i)$ is a phase sensitivity function, which gives the response of the i-th oscillator. Inputs from other oscillators, $Spk(t)$, are assumed here pulse input as follows:

$$Spk(t) = \frac{K_0}{N}\sum_{j=1}^{N}\sum_{n=1}^{\infty}\delta(t - t_{jn}), \qquad (2)$$

where K_0 is the coupling strength, N is the number oscillators, and t_{jn} is the firing time. Mathematically, δ is a Dirac's delta function that represents the input spike pulse has a defined width Δt during which ϕ_i is updated according to the value of $Z(\phi_i)$.

2.1. *Discretized model*

In order to implement Eqs. (1) and (2) into digital hardware, oscillator is regularized into following expressions:

$$\phi_i(t+1) = \phi_i(t) + \omega_i \frac{K_0}{N}\sum_{j=1}^{N} Z(\phi_i)\mathrm{Spk}(t) \qquad (3)$$

$$Spk_j(t) = \begin{cases} 1, & if\ \ \phi_j(t) = \phi_{th} \\ 0, & otherwise \end{cases} \qquad (4)$$

The phase value of the next time step is calculated by summing the current phase value, natural angular frequency, and a product of the phase sensitivity function and input pulses. Natural angular frequency ω_i is set at a constant value. The oscillator outputs will spike the pulse when the phase variable reaches a threshold value ϕ_{th}. By the above discretization, the proposed model can be implemented with simple logic circuit.[3]

2.2. *How the oscillator works*

Basically the concept of oscillator works is based on neighbor connection between each oscillator. The model explains the local interaction only, but can generate various phenomena in the large oscillator network (in-array), based on a coupling function formula as shown in Eqs. (1) and (2).

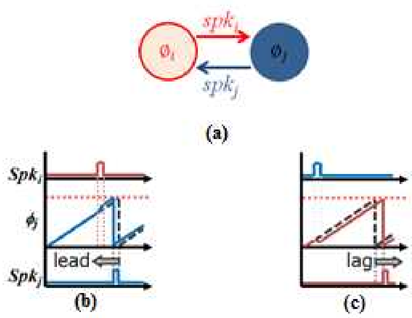

Fig. 1. Pulse-coupled phase oscillator: (a) Coupled network schematic, (b) positive update, and (c) negative update

.

Figure 1 shows a two pulse-coupled phase oscillators and their updating manner. Synchronization is occured by updating the pulse timing. There are two phases of updating the from each oscillator, which are positive updating and negative updating. Positive update will conducts whenever spike input (Spk_i) to another oscillator ϕ_j , the leading condition triggers the function $Z(\phi_j)$, which gives effect to the pulse timing for reaching the maximum value become earlier. Negative update conducts whenever Spike input (Spk_j) to another oscillator ϕ_i , the lagging condition triggers the function $Z(\phi_i)$, which gives effect to the pulse timing for reaching the maximum value become later.

3. Hardware architecture design

Hardware architecture design of a pulse-coupled phase oscillator is shown in Fig.2.(a). It consists of an oscillator circuit, a function generator circuit and an update circuit.[3] The oscillator circuit consists an n-bits counter (CNT), a spike generator (SPKGEN) and combinational circuits. The n-bit counter represents a phase variable ϕ_i and counts the clock inputs for realizing ω_i in Eq.(4). In this design, time step t in the discretized model corresponds to a clock cycle.

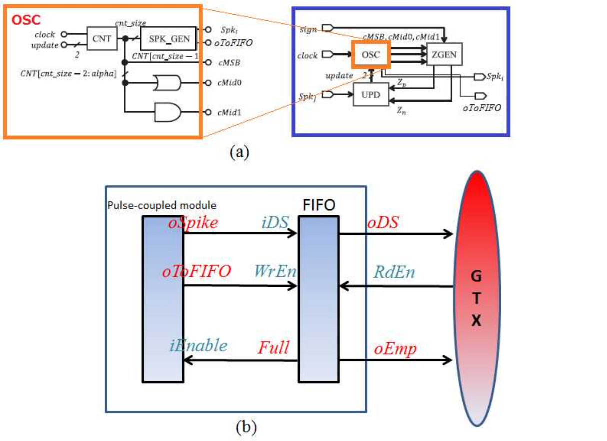

Fig. 2. Design of pulse-coupled phase oscillator circuit: (a) Properties of pulse-coupled oscillator circuit, and (b) FPGA's for each board overview.

The oscillator circuit also outputs intermediate signals *cMSB*, *cMid0* and *cMid1* which determine the shape of the function $Z(\phi_i)$ and are used in the function generator circuit. The function generator circuit combines signals *cMSB*, *cMid0* and *cMid1* into *Zp* and *Zn*. The update circuit receives *Zp*, *Zn* and spike pulses Spk_j received from other oscillators and outputs signal update.

In order to write data into the FIFO, spike output (oSpike) goes into the DataIn (iDS) and then strobe the write enable signal input WrEn high for one clock cycle as shown in Fig.2.(b). WrEn is output from oToFIFO into the FIFO's internal memory. If writing in bulk the WrEn signal can be left high while changing the data on the DataIn (iDS) for each clock cycle. When the Full flag goes high, this means that the FIFO's memory is full and will not accept any more writes (iEnable = 0) until data is read using the RdEn.

4. Experimental results

Evaluation of the proposed model of hardware design was realized. The pulse-coupled phase oscillator networks over two FPGAs through serial communication of Gigabit Transceiver (GTX) explains through subsection parts. In all experiments, respectively basic synchronizing phenomena could be observed (in-phase mode).

4.1. *In-phase three oscillators of pulse coupled spiking oscillator inside one FPGA*

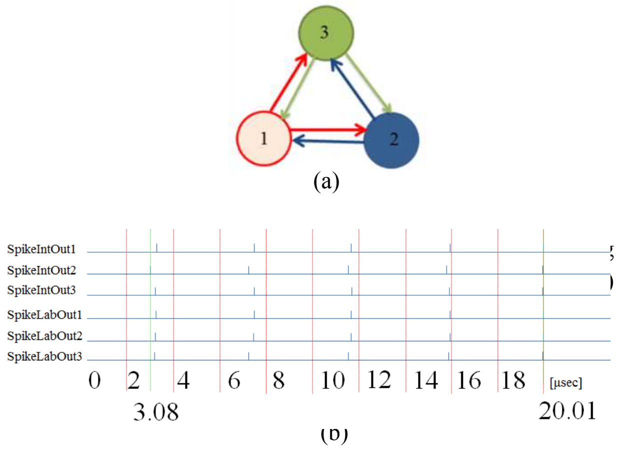

Real-time implementation results of simple *rotary* three oscillator connection are shown on Fig.3.(a). Each of oscillator has two outputs represents as label and unit. Figure 3(b) shows the condition of FPGA when running from the beginning time zero (0μsec), Δclock between sychronzing was achieved 132 clock cycles. Testing architecture was using 16-bit of data and internal max clock (200MHz) from FPGA Virtex-6 ML605. Inside the simulation part, for one second could trigger and count the counter 200 Mega cycles, in this case first spike was occurred on 3.08 μsec and reached the *synchronization*-state on 20.01 μsec. The total of data rate is equal to 16bit

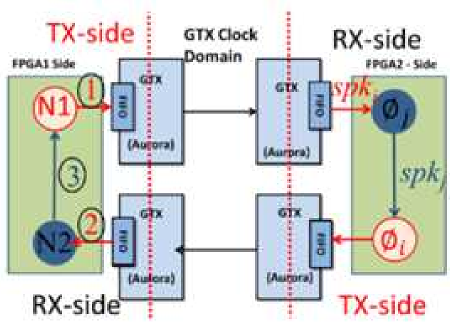

Fig. 4. Four oscillators over tow FPGAs using serial communication.

* 200 Mega counter/sec which reaches the maximum value of 3200bps or 3.2Gbps.

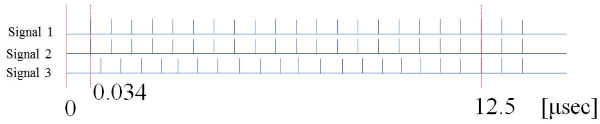

Fig. 5. Realtime result of four pulse-coupled phase oscillators over two FPGAs using *chipscope*. Signals 1, 2, 3 are corresponds to the numbers in Fig. 4.

4.2. *Four oscillators over two FPGAs using serial communication*

After we achieved with simple oscillator inside one FPGA, we employ two FPGA boards as the multi-FPGA platform. By using Virtex-6 XC6VLX240T ML605 Xilinx board design, it provides a free and open high-speed protocol for multi-FPGA communication called Aurora.[7] It is intended for serial communication between FPGAs with speeds up to and above 10 Gbps.[8]

Figure 4 shows the experimental setup using two FPGA boards of Virtex6 ML605 and implementation of four oscillators on a hardware level. Figure 5 shows the observation result of synchronization in FPGA. Here, we employed *chipscope* which is in-circuit debugger provided by Xilinx to observe spike pulses. From the result, the spike synchronization in-phase was achieved and a total time consumed around 12.47 µsec.

4.3. *FPGA design summary*

Table 1 shows the results of total usage resources of the multi-FPGA, communication using pulse-coupled phase oscillators. Four oscillators were implemented and carried out onto the hardware level with the FPGA synthesizer of Xilinx Tools. By using ISE Design Suite software information, we obtained the report of the proposed model circuit implemented with total maximum frequency 434.972MHz.

5. Conclusion

In this paper, we proposed an implementation of multi-FPGA communication using pulse-coupled phase oscillators. In the experiment, two FPGA boards were used to implement four oscillators network, and first spike synchronization over two FPGAs took 12.47 µsec with data bit speed stream 3.2 Gbps. From experimental results, we verified that the pulse-coupled phase oscillator synchronized over two FPGAs via the high-speed serial communication and the FIFO interface.

Table 1. Device utlization

	Used	Available
Slice Register	416	301440
Look-Up Tables	348	150720
IOBs	101	600

In future work, we will increase the number of FPGAs and implement large scale pulse coupled phase oscillator networks, then apply it to engineering application such as image processing.

Acknowledgements

This research was supported by JSPS KAKENHI Grand Numbers 26330279 and 15H01706.

References

1. Y. Kuramoto, *Chemical Oscillation, Waves, and Turbulence,* (Springer, Berlin, 1984).
2. A. T. Winfree, *The Geometry of Biological Time,* (Springer, NewYork, 1980).
3. Y. Suedomi, H. Tamukoh, K. Matsuzaka, M. Tanaka, and T. Morie, *Parameterized Digital Hardware Design of Pulse-coupled Phase Oscillator Networks*, Neurocomputing, **165** (2015), 54–62.
4. Kenji Matsuzaka et al, *VLSI Implementation of Coupled MRF model using pulse-coupled phase oscillators,* Electronics Letters. (2015), 46-48.
5. J. Li, Y. Atsumari, H. Kubo, Y. Ogishima, S. Yokota, H. Tamukoh, and M. Sekine, *A Multidimensional Configurable Processor Array - Vocalise*, IEICE Trans. on Information and Systems, **E98-D**(2) (2015), 313-324.
6. X. Y. Wang, A. Apsel, Pulse coupled oscillator synchronization for low power UWB wireless transceivers, in: *Proc. of 50th Midwest Symposium on Circuits and Systems* (2007) 1524–1527.
7. Xilinx Inc, *Aurora 8B/10B Protocol Specification*, (2010),http://www.xilinx.com/support/documentation/ipdocumentation/au-rora8b10bprotocolspecsp002.pdf.
8. Abhijit Athavale and Carl Christensen, *High-Speed Serial I/O Made Simple*. Xilinx,Inc., 1.0 edition, (2005), http://www.xilinx.com/publications/archives/book-s/serialio.pdf.

Multi-Valued Quantization Neural Networks toward Hardware Implementation

Yoshiya Aratani , Yeoh Yoeng Jye, Akihiro Suzuki, Daisuke Shuto, Takashi Morie, Hakaru Tamukoh
Graduate School of Life science and systems engineering, Kyushu Institute of Technology
2-4 Hibikino, Wakamatsu-ku, Kitakyushu 808-0196, Japan
E-mail: aratani-yoshiya@edu.brain.kyutech.ac.jp, yeoh-yoeng-jye@edu.brain.kyutech.ac.jp, tamukoh@brain.kyutech.ac.jp

Abstract

This paper proposes a Multi-Valued Quantization (MVQ) method of connecting weight for efficient hardware implementation of Convolutional Neural Networks (CNNs). The proposed method multiplies an input value by a multi-valued quantized weight during the forward and backward propagations, while retaining precision of the stored weights for the update process. In the both propagation processes, multipliers can be replaced with adders and shifters by setting appropriate quantized weights. We train two- to six-valued quantization CNNs with MNIST and CIFAR-10 dataset to compare the performance of them with a 32-bit floating point CNN. In the four-valued quantization, random noise is added to the quantized weight to improve the performance of generalization ability. In addition, the robustness of MVQ CNN to noise is evaluated. Experimental results show that the MVQ CNNs achieve better learning accuracy than the floating point CNN and the four-valued CNN is highly robust to the noise.

Keywords: Deep Learning, CNN, MVQ, BinaryConnect, hardware, noise

1. Introduction

Convolutional Neural Network (CNN)[1] is a kind of neural network that have proven significant improvement in image recognition and computer vision fields. Thus, the implementation of CNN in embedded system raises high expectation for real world application.

Real time processing and low power consumption are significant criteria for embedded systems. However, it is difficult to achieve them by using only software implementation. In contrast, a special purpose hardware architecture of CNN enables parallel and pipeline processing that improves processing speed and reduces power consumption. However, the repetition of matrix computation, convolution of input vectors and weights, need a lot of multipliers that require huge hardware resources. Therefore, a simplification method is desired as the limitation of hardware resources.

One of the method that simplify the processing is quantization.[2, 3] BinaryConnect is an approach to simplify neural networks by binarizing the weights.[2] By the quantization, hardware resource can be reduced by replacing multiplier with adder and subtractor. However, the recognition accuracy may drop by the quantization. Therefore, the verification of the relationship between the quantized bit rate and the accuracy of CNN is necessary in order to ensure the performance of quantization.

In this paper, we propose a Multi-Valued Quantization (MVQ) of weights for efficient hardware implementation of CNN. The recognition accuracy of CNN is compared between the proposed method with five different types (two-six quantized weights) and the conventional CNN with 32-bits floating point, using MNIST and CIFAR-10 dataset. In addition, we desire to be robust against noise in hardware implementation. Therefore, noise is applied to the MVQ-4, which shows the highest recognition accuracy among MVQs, and the change in result against noise is observed.

2. Related research

The operations of neural networks can be divided into forward propagation, backward propagation, and update process of the weight value. BinaryConnect binarizes the weight value to (+1,-1) at the forward and backward propagations while continuous-value are stored. During the update process, the update parameter is calculated through the stored continues-value. Via the binarization of the weight, the multipliers are simplified to the adder and subtraction, thus it is efficient in reducing the circuit size. Especially during propagation, the multiplier is completely removed. Moreover, the generalization performance of binarized CNN is improved and exceeded the recognition accuracy of the regular CNNs.

3. Proposed method

In this paper, we proposed the MVQ method, which extends binarization to multi value.

3.1. *MVQ*

MVQ is a method that quantizes the weights into smaller division than BinaryConnect. When the quantized bit rate is larger, the quantized weight is closer to the real valued weights, but losing the merit of simplification of calculation. It is important to balance between the quantized bit number and the computational cost. In this paper, the quantized value is changed from three-value to six-value, and the recognition accuracy results are observed.

3.2. *Quantization method*

With MVQ-4, the algorithm of the quantization is explained in detail. The quantization can be done by either stochastic or deterministic approach.[2] In this paper, the deterministic approach is employed. The original weights W are clipped to the clipping point w_range to quantize the weights into new quantized values before forward and backward propagations. The multi-valued weight W_M is formulated as in equation below.

$$W_M = \begin{cases} +w\_range & if\ W \geq \frac{w\_range}{2} \\ +\frac{w\_range}{2} & 0 \leq W < \frac{w\_range}{2} \\ -\frac{w\_range}{2} & -\frac{w\_range}{2} < W < 0 \\ -w\_range & otherwise \end{cases} \tag{1}$$

The other MVQs follow similar quantization manner as shown in Eq. (1). In this paper, we employ stochastic gradient decent (SGD) with MVQ for training CNNs and it is shown in Algorithm 1.

Algorithm 1 Stochastic Gradient Descent (SGD) training with MVQ.

---

1. Forward propagation:

$$W_M \leftarrow MVQ(w_{t-1})$$

For $k = 1$ to L, compute a_k knowing $a_{k-1}, W_M and\ b_{t-1}$

2. Backward propagation:

Initialize output layer's activations gradient $\frac{\partial C}{\partial a_L}$

For $k = L$ to 2, compute $\frac{\partial C}{\partial a_{k-1}}$ knowing $\frac{\partial C}{\partial a_k} and\ W_M$

3. Parameter update:

Compute $\frac{\partial C}{\partial W_M}$ and $\frac{\partial C}{\partial b_{t-1}}$ knowing $\frac{\partial C}{\partial a_k} and\ a_{k-1}$

$$w_t = w_{t-1} - \eta \frac{\partial C}{\partial W_M}$$

$$b_t = b_{t-1} - \eta \frac{\partial C}{\partial b_{t-1}}$$

a_k: Dot product in kth layer , L :The number of layers , Mini batch scale:10, w_{t-1} , b_{t-1} :previous parameters weights and biases, η: learning rate, C:cost function

---

3.3. *Addition of noise*

To observe for the stability and robustness to the noise, the addition of noise are also done during the experiments. The noise is generated using the uniform random number generator and insert into layers during forward propagation, backward propagation and update process, as shown below.

Noise additional position

Forward propagation's weight

$$u = \sum wx \rightarrow u = \sum (w + w_{noise})x$$

Backward propagation's error signal :δ

$$\delta = f'(u) \sum \delta w \rightarrow \delta = f'(u) \sum \delta(w + w_{noise})$$

Weight update :Δw

$$w = w - \eta\delta(w + w_{noise})$$

δ: *error signal*, w: *weight*, w_{noise}: *noise*

4. Experimental results

Experiments are carried out by modifying Tiny_CNN (now known as Tiny_DNN)[4] from the CNN header library. This library uses 32-bit floating point in usual. Here, *w_range* is set to 0.7 for all MVQs and Algorithm 1 is applied for the training.

4.1. *MNIST dataset*

MNIST dataset contains grayscale images with the size of 28x28 pixels, which has 10 different classes of handwritten number zero to nine.[5] It includes 60,000 train image data and 10,000 test image data.

The architecture of CNN is based on LeNet-5[5] as shown in Fig. 1. The result of learning is shown in Fig. 2. From the experimental results, the MVQ-4 achieved the best result of all.

4.2. *CIFAR-10 dataset*

CIFAR-10 dataset contains color images with the size of 32x32 pixels, which has 10 different classes of objects such as animals and vehicles. CIFAR-10 dataset includes 50,000 train image data and 10,000 test image data. Figure 3 shows the CNN architecture for CIFAR-10 dataset. Figure 4 shows the result of learning.

Similar to the experimental results of MNIST dataset, the MVQ-4 also achieved the highest accuracy.

4.3. *Addition of noise*

Noise addition experiments are only carried out with the MVQ-4, since it achieved the best result for both of MNIST and Cifar-10. Figure 5 shows the results of every position of noise addition. From the result, adding noise to the error during backward propagation was the best result.

To measure the noise tolerance, we increased the noise range throughout the experiment to observe the effect. As the result, the proposed method is robust to the noise up to the range around 1.0 in backward propagation. The largest value of weights in MVQ-4 is 0.999643, thus the proposed CNN seems to withstand the noise equal to the maximum of weight value.

5. Conclusion

This paper proposed the MVQ method, and investigate the relationship of the degree of multi-value to the CNN recognition accuracy. From the experimental results, the proposed method showed higher accuracy than the conventional CNN with 32-bit floating point operation, and among the different multi quantized value, MVQ-4 possessed the best result in accuracy. Furthermore, the experiment of noise addition into MVQ-4 was carried out to observe the relationship between noise position and recognition accuracy. The addition of noise during

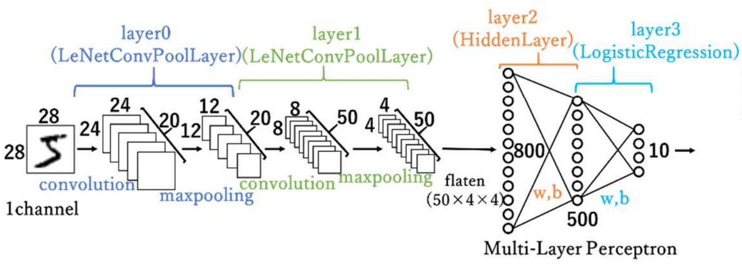

Figure 1 Construction of CNN in MNIST dataset

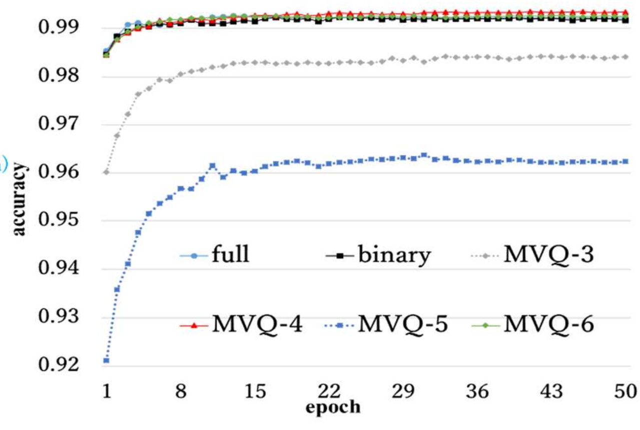

Figure 2 Results of MNIST dataset

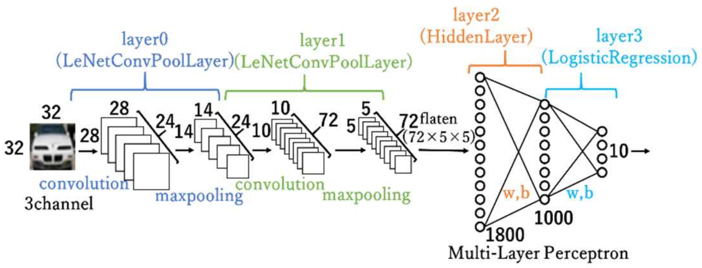

Figure 3 Construction of Tiny-cnn in CIFAR-10 dataset

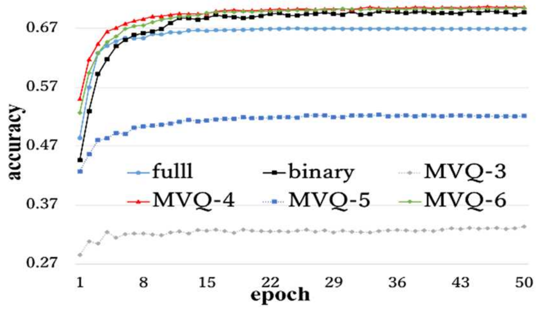

Figure 4 Results of CIFAR-10 dataset

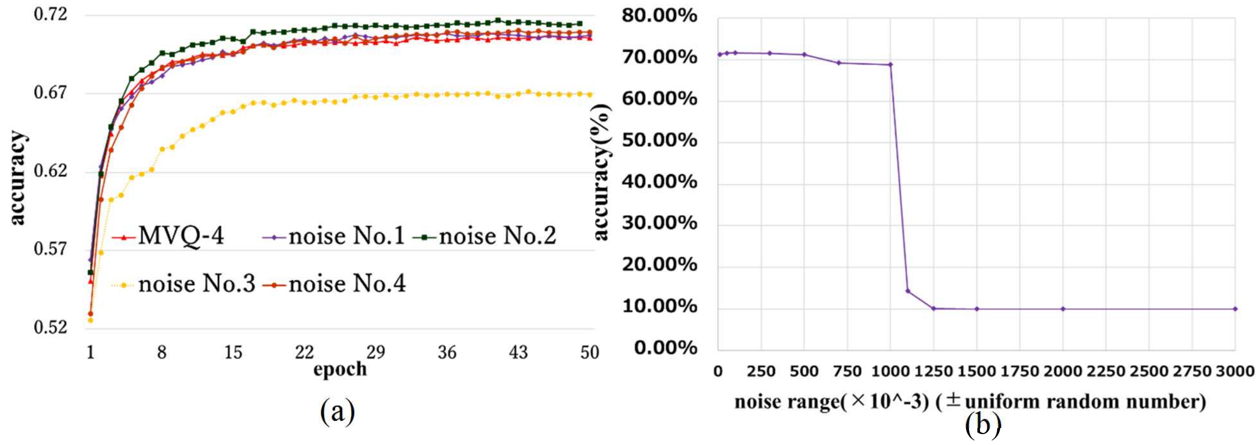

Addition of noise
noise No.1……in forward propagation only
noise No.2……in backward propagation only
noise No.3……in update only
noise No.4……noise No.1 & noise No.2

Figure 5. Results of noise addition. (a) Effect with noise range = 0.0001, (b) Noise tolerance in backward propagation.

backward propagation in MVQ-4 showed the best result compare to insertion in other positions. In addition, the robustness of proposed method to noise was verified.

In future work, we will design a special purpose hardware architecture based on the proposed method for embedded systems.

Acknowledgement

This research was supported by JSPS KAKENHI Grand Numbers 26330279 and 15H01706.

Reference

1. A. Krizhevsky, I. Sutskever, and G. E. Hinton, Imagenet classification with deep convolutional neural networks, *Advances in Neural Information Processing Systems*, **25** (2012), 1106–111.
2. M. Courbariaux, Y. Bengio, J.P. David, Binaryconnect: Training deep neural networks with binary weights during propagations, *Advances in Neural Information Processing Systems*, **28** (2015), 3105–3113.
3. M. Courbariaux, I. Hubara, D. Soudry, R. El-Yaniv, Y. Bengio, “Binarized Neural Networks: Training Deep Neural Networks with Weights and Activations Constrained to +1 or -1, *arXiv:1602.02830*, (2016).
4. Header only, dependency-free deep learning framework in C++11, http://github.com/tiny-dnn/tiny-dnn
5. Y. LeCun, L. Bottou, Y. Bengio, and P. Haffner, Gradient-Based Learning Applied to Document Recognition, *Proceedings of the IEEE*, 86(11) (1998), 2278-2324.

An Improved Parameter Value Optimization Technique for the Reflectionless Transmission-Line Model of the Cochlea

Takemori Orima and Yoshihiko Horio
Research Institute of Electrical Communication, Tohoku University
2-1-1 Katahira, Aoba-ku, Sendai, Miyagi, 980-8577, Japan
E-mail: takemori.orima.q2@dc.tohoku.ac.jp

Abstract

The passive reflectionless transmission-line model can reproduce physiological cochlear properties. We have employed an optimization technique to obtain good parameter values that give a desired cochlear property. However, we found that, in some case, it is difficult to find the sub-optimal parameter values because of complex dependencies among parameters. In this paper, we explicitly formulate some of the cochlear properties in the reflectionless transmission-line model, and improve the optimization technique using these formulae.

Keywords: cochlea, passive model, reflectionless transmission-line model, optimization technique.

1. Introduction

The physiological transmission-line model of the cochlea can reproduce the mechanical vibration of the basilar membrane well. To approximate individual human cochlear characteristics to experimental data, it is necessary to tune parameter values of the model. However, because of the large number of parameters, it is difficult to determine these values.

The passive reflectionless transmission-line model[1] (passive model) has been proposed to alleviate this problem. Although this model has less number of parameters, it can reproduce the characteristics of the cochlea well. Therefore, we proposed a design technique for this model using parameter optimization[2]. However, this method requires a long calculation time to design.

In this paper, we explicitly give approximate formulae for some key characteristics of the passive model to accelerate the calculation time. In addition, an optimization method is employed in the design technique with proposed formulae. We compare three optimization methods, and chose the best one for this design technique. Finally, we demonstrate some design examples to confirm the validity and efficiency of the proposed method.

2. The passive reflectionless transmission-line model

A minute part between x and $x + dx$ of the passive reflectionless transmission-line model[1] is shown in Fig. 1, where x is a distance from the input terminal. The parallel impedance $Z_p(x,\omega)$ in Fig. 1 is given by

$$Z_p(x,\omega) = j\omega L_p(x) + R_p(x) + \frac{1}{j\omega C_p(x)}, \qquad (1)$$

where ω is an angular frequency of the input signal.

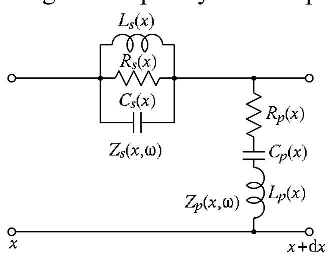

Fig. 1. A minute part between x and $x + dx$ of the passive reflectionless transmission-line model[1].

Assuming that the values of each circuit elements in $Z_p(x,\omega)$ changes exponentially with distance, they can be given as

$$R_p(x)=R_0e^{-ax},\ L_p(x)=L_0e^{ax},\ C_p(x)=C_0e^{ax}, \quad (2)$$

where R_0, L_0, and C_0 are values at $x = 0$, and a is a constant.

In Fig. 1, we further assume that the characteristic impedance $Z_0(x,\omega)$ is independent of the distance, so that

$$Z_0(x,\omega)=r, \quad (3)$$

where r is a constant. As a result, the series impedance $Z_s(x,\omega)$ in Fig. 1 can be defined as

$$Z_s(x,\omega)=\frac{r^2}{Z_p(x,\omega)}. \quad (4)$$

On the other hand, the resonance angular frequency $\omega_{res}(x)$ is given by

$$\omega_{res}(x)=\frac{1}{\sqrt{L_0C_0}}e^{-ax}. \quad (5)$$

Taking the integral of the propagation constant with respect to x yields

$$\Gamma(x,\omega)=\int_0^x\frac{r}{Z_p(x,\omega)}dx=\frac{jr}{2a\sqrt{L_0/C_0+j\omega R_0L_0}}$$
$$\times\left\{\ln\left(\frac{\sqrt{1+j\omega R_0C_0}+\omega\sqrt{L_0C_0}e^{ax}}{\sqrt{1+j\omega R_0C_0}-\omega\sqrt{L_0C_0}e^{ax}}\right)\right.$$
$$\left.-\ln\left(\frac{\sqrt{1+j\omega R_0C_0}+\omega\sqrt{L_0C_0}}{\sqrt{1+j\omega R_0C_0}-\omega\sqrt{L_0C_0}}\right)\right\}. \quad (6)$$

Finally, the transfer function is given by

$$F(x,\omega)=\frac{1}{Z_p(x,\omega)}\exp(-\Gamma(x,\omega)). \quad (7)$$

3. Explicit formulation of key characteristics of the passive model

We explicitly formulate some of the key characteristics of the passive model, the center angular frequency $\omega_c(x)$, the maximum gain $g_{\max}(x)$, and the quality factor $Q(x)$ shown in Fig. 2 as follows:

$$\omega_c(x)=\mu_c(x)\omega_{res}(x), \quad (8)$$

$$g_{\max}(x)=|F(x,\omega_c(x))|, \quad (9)$$

$$Q(x)=\frac{\omega_c(x)}{\omega_1(x)-\omega_2(x)}, \quad (10)$$

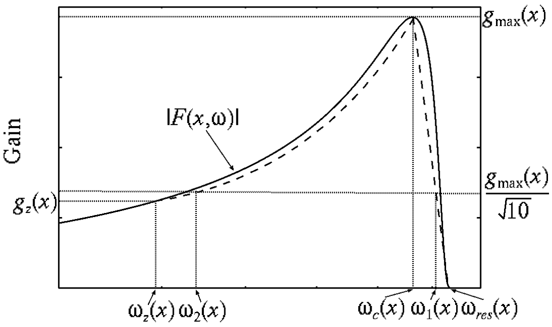

Fig. 2. The solid line: the frequency vs. gain characteristics of the original passive model obtained from Eq. (7). The dashed line: the approximation with Eqs. (13) and (14).

where $\omega_1(x)$ and $\omega_2(x)$ are the angular frequencies at $g_{\max}(x)/\sqrt{10}$ given by

$$\omega_1(x)=\frac{1}{\sqrt{10}}\omega_c(x)+\left(1-\frac{1}{\sqrt{10}}\right)\omega_{res}(x), \quad (11)$$

$$\omega_2(x)=\frac{1}{A(x)}\ln\left(\frac{1}{B(x)}\cdot\frac{g_{\max}(x)}{\sqrt{10}}\right), \quad (12)$$

where

$$A(x)=\exp\left\{\frac{\omega_c(x)\ln g_z(x)-\omega_z(x)\ln g_{\max}(x)}{\omega_c(x)-\omega_z(x)}\right\}, \quad (13)$$

$$B(x)=\frac{\ln g_{\max}(x)-\ln g_z(x)}{\omega_c(x)-\omega_z(x)}, \quad (14)$$

$$g_z(x)=|F(x,\omega_z(x))|, \quad (15)$$

$$\omega_z(x)=\mu_z(x)\omega_{res}(x), \quad (16)$$

$$\mu_z(x)=\sqrt{\frac{-v_z(x)-\sqrt{v_z(x)^2-4}}{2}}, \quad (17)$$

$$v_z(x)=\frac{C_0}{L_0}\left\{(R_0e^{-ax})^2-\left(\frac{\sqrt{10}}{g_{\max}(x)}\right)^2\right\}-2. \quad (18)$$

In addition, $\mu_c(x)$ is given by

$$\mu_c(x)=\sqrt{\frac{-v_c(x)+\sqrt{v_c(x)^2+4}}{2}}, \quad (19)$$

where

$$v_c(x)=\frac{C_0}{L_0}\left(\frac{r}{a}-R_0e^{-ax}\right)R_0e^{-ax}. \quad (20)$$

Comparisons between the original characteristics calculated numerically from Eq. (7) and approximated values from the above formulae are shown in Figs. 3 to 5, where $a = 0.288$, $R_0 = 1.5$, $L_0 = 2.385 \times 10^{-7}$, $C_0 = 2.132 \times 10^{-7}$, and $r = 5$. Equation (7) took about 0.26 sec. for calculation, in contrast, the formulae about 2.5 μsec. From these results, we can confirm validities and efficiency of the proposed formulae.

4. Design method using parameter optimization

We design the passive model using the proposed formulae to reproduce the human cochlear characteristics. We employ an optimization technique to obtain the model parameters.

First, we define the object functions as follows:

$$E_1(x) = \left| \frac{\omega_c(x) - cf(x)}{cf(x)} \right|, \tag{23}$$

$$E_2(x) = \left| \frac{g_{\max}(x) - mg(x)}{mg(x)} \right|, \tag{24}$$

$$E_3(x) = \left| \frac{Q(x) - q(x)}{q(x)} \right|, \tag{25}$$

where $cf(x)$, $mg(x)$, and $q(x)$ are the target values for the center frequency, maximum gain, and quality factor at a distance x, respectively. Then, we optimize the weighted sum of these object functions $E(x)$.

$$E(x) = \sum_{i=1}^{3} w_i E_i(x) \text{ and } \sum_{i=1}^{3} w_i = 1, \tag{21}$$

where $w_i \geq 0$ is a weight. In the following section, we design the passive model with the target parameter values

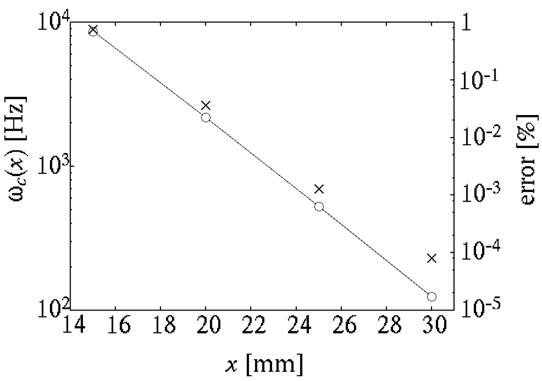

Fig. 3. The original (circles) and approximated (solid line) center frequencies $\omega_c(x)$ according to the distance x obtained from Eq. (7) and Eq. (8), respectively. The crosses: the percent errors between them.

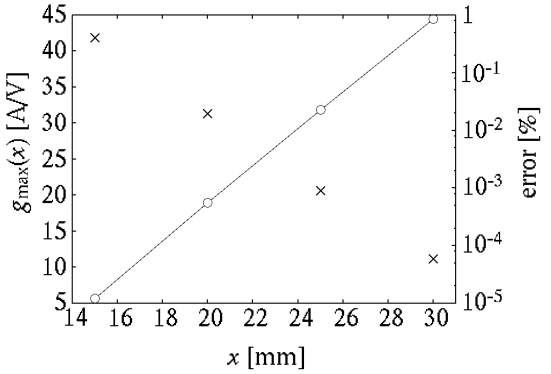

Fig. 4. The original (circles) and approximated (solid line) maximum gains $g_{\max}(x)$ according to the distance x obtained from Eq. (7) and Eq. (9), respectively. The crosses: the percent errors between them.

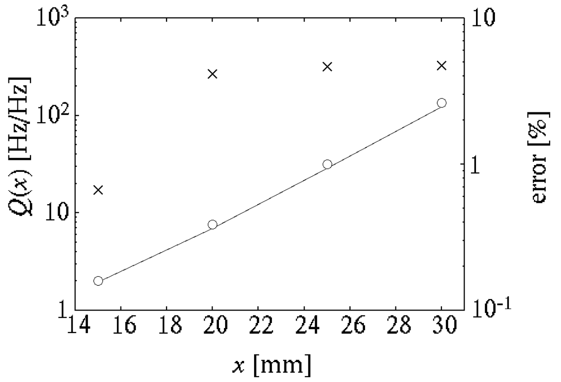

Fig. 5. The original (circles) and approximated (solid line) quality factors $Q(x)$ according to the distance x obtained from Eq. (7) and Eq. (10), respectively. The crosses: the percent errors between them.

shown in Table 1, where $cf(x)$, $mg(x)$, and $q(x)$ were estimated based on the physiological experiments[3,4].

4.1. *Optimization techniques*

We compare the downhill simplex (DHS), the genetic algorithm (GA), and the particle swarm optimization (PSO), using the design target at x = 25 mm in Table 1. The conditions of each optimization methods are

Table 1. The target design specifications.

x	15 mm	20 mm	25 mm
$cf(x)$ [Hz]	2500	1200	500
$mg(x)$ [A/V]	9.4	9.4	6.1
$q(x)$ [Hz/Hz]	3.6	2.6	1.8

summarized in Table 2. In the table, N is the number of simplexes, individuals, and particles in DHS, GA, and PSO, respectively. Note that, in the case of PSO, one iteration is counted each time as the global best is updated.

The results of the comparisons are shown in Table 3. In the table, DHS gives the smallest optimization function value. Therefore, we use DHS as the optimization method in our design.

4.2. *Design examples*

We designed the passive model specified in Table 1 using DHS. The results are shown in Table 4 and Fig. 7. From Table 4, we confirm that the designed values are almost the same as the target ones, although some errors remain due to approximation errors in the proposed formulae, in particular, Eq. (10).

5. Conclusion

We have explicitly formulated some key characteristics of the passive reflectionless transmission-line model of the cochlea to alleviate the complex calculation loads. These expressions efficiently reproduced the original characteristics.

In addition, we defined the object functions for parameter optimizations. We compared DHS, GA, and PSO as the optimization methods. As a result, we found that DHS is the best method.

We finally designed three cochlear characteristics at different distances successfully using the proposed formulae with DHS.

As a future problem, we will improve the formulae for $Q(x)$ for more precise designs.

Table 2. The simulation conditions.

	DHS	GA	PSO
N	30	30	30
Trials	30	30	30
Iterations	5000	5000	5000

Table 3. The obtained parameters and object function values with DHS, GA, and PSO for x = 25 mm.

	DHS	GA	PSO
a	0.1949	0.2299	0.2141
R_p	2.315×10^{-3}	2.596×10^{-3}	2.816×10^{-3}
L_p	4.963×10^{-9}	8.227×10^{-10}	2.122×10^{-9}
C_p	5.875×10^{-8}	1.068×10^{-8}	2.071×10^{-8}
r	2.5	2.5	2.5
E (Eq. (21))	1.47×10^{-6}	1.34×10^{-4}	6.38×10^{-2}

Table 4. The obtained center frequencies $\omega_c(x)$, maximum gains $g_{max}(x)$, and quality factors $Q(x)$ by the proposed design technique with DHS.

x	15 mm	20 mm	25 mm
$\omega_c(x)$ [Hz]	2496	1196	495
$g_{max}(x)$ [A/V]	9.408	9.417	6.133
$Q(x)$ [Hz/Hz]	3.858	2.733	1.834

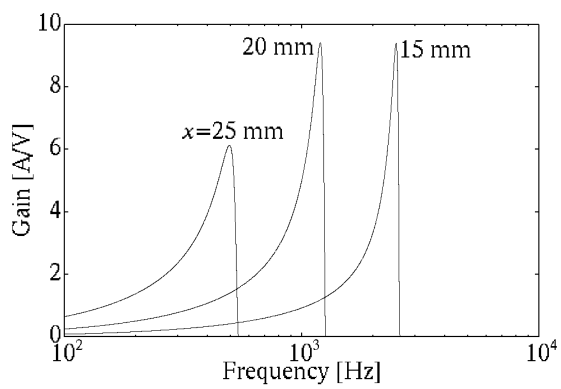

Fig. 7. The obtained frequency vs. gain characteristics at x = 15 mm, 20 mm, and 25 mm through the proposed optimization technique using downhill simplex method.

References

1. T. Kohda, T. Une, and K. Aihara, "An active, reflectionless transmission-line model of the cochlea: Revisited," in *AIP Conf. Proc.*, vol. 1403, no. 1, pp. 578–583, 2011; DOI:10.1063/1.3658152.
2. T. Orima, Y. Horio, and T. Kohda, "A parameter value optimization technique for a reflectionless transmission-line model of the cochlea," in *Proc. of Int. Symp. on NOLTA2016*, pp. 503–506, 2015.
3. G. V. Bekesy, "*Experiments in Hearing,*" McGraw-Hill Book Co., New York, 1960.
4. M. A. Ruggero and A. N. Temchin, "Unexceptional sharpness of frequency tuning in the human cochlea," *PNAS*, vol. 102, no. 51, pp. 18614–18619, 2005; DOI:10. 1073/PNAS.0509323102.

A parameter optimization method for Digital Spiking Silicon Neuron model

Takuya Nanami
The University of Tokyo, Institute of industrial Science
Tokyo, Japan

Takashi Kohno
The University of Tokyo, Institute of industrial Science
Tokyo, Japan
nanami@sat.t.u-tokyo.ac.jp, kohno@sat.t.u-tokyo.ac.jp

Abstract

DSSN model is a qualitative neuronal model designed for efficient implementation in a digital arithmetic circuit. In our previous studies, we extended this model to support a wide variety of neuronal classes. Parameters of the DSSN model were hand-fitted to reproduce neuronal activity precisely. In this work, we studied automatic parameter fitting procedure for the DSSN model. We optimized parameters of the model by a GPU-based implementation of the differential evolution algorithm in order to reproduce waveforms of the ionic-conductance models and reduce necessary circuit resources for the implementation.

Keywords: Silicon neuronal network, Spiking neuron model, Differential evolution, FPGA

1. Introduction

A wide variety of neuronal models have been used in silicon neuronal networks because of the trade-off between reproducibility of neuronal activities and computational efficiency. For example, ionic-conductance models can reproduce a neuronal activity accurately but demands enormous computational resources in large-scale implementations. In contrast, integrate-and-fire based models such as the LIF and Izhikevich models [1] can be implemented with less resource, because they approximate a spiking process by the resetting of the state variables. However, they have reduced reproducibility of complex neuronal activities. For example, these models assume fixed maximum membrane potentials during the spike process, whereas the spike intensity is nonuniform in the nervous system [2]. The DSSN model [3] is a qualitative neuronal model designed for efficient implementation in a digital arithmetic circuit. In our previous studies [4][5], we extended the DSSN models to support various neuronal activities; regular spiking, fast spiking, intrinsically bursting, low-threshold spiking, elliptic bursting, and parabolic bursting.

To reproduce a variety of spiking properties in neurons, appropriate parameter sets for neuronal models have to be found. The relationship between the values of the parameters and the behavior of the model is generally complex, and it is difficult and time-consuming to find an appropriate parameter set. Automatic parameter fitting procedures have been studied as a solution to this problem. Parameters for Hodgkin-Huxley-type models have been tuned automatically in [6] and [7]. Pospischil et al [8] reproduced regular and fast spiking neuron classes by simulated annealing based optimization method using a cost function composed of the firing rate and the adaptation time. Buhry et al. [9] developed automatic parameter estimation using a differential evolution algorithm for a Hodgkin-Huxley type model and a neuromimetic analog integrated circuit.

In this work, we studied automatic parameter fitting procedure for the DSSN model. We reproduced regular and fast spiking classes by a GPU-based implementation of the differential evolution algorithm. Regular-spiking (RS) is a most typical classes of cortical neurons and is characterized by spike-frequency adaptation; the spike frequency decreases over time in response to a constant stimulus input. Conversely, Fast-spiking (FS) neurons maintain firing at a constant frequency. Parameters were optimized to reproduce waveforms of the ionic-conductance models in [8] and reduce the circuit resource requirements for implementation.

The remainder of this paper is organized as follows. Section 2 introduces our neuron model, differential evolutional algorithm, details of our parameter optimization procedure, and GPU-based implementation. The result is shown in Section 3. Section 4 summarizes the work and suggests ideas for future.

2. Method

2.1. *Digital Spiking Silicon Neuron model*

The 3-variable DSSN model is a qualitative neuron model that can simulate several classes of neuronal activities by Euler's method with fixed point operation including RS and FS [4]. Equations for regular and fast spiking are given by

$$\frac{dv}{dt} = \frac{\emptyset}{\tau}(f(v) - n - q + I_0 + I_{stim}),$$

$$\frac{dn}{dt} = \frac{1}{\tau}(g(v) - n),$$

$$\frac{dq}{dt} = \frac{\varepsilon}{\tau}(h(v) - q),$$

$$f(v) \equiv \begin{cases} a_{fn}(v - b_{fn})^2 + c_{fn} & (v < 0) \\ a_{fp}(v - b_{fp})^2 + c_{fp} & (v \geq 0), \end{cases}$$

$$g(v) \equiv \begin{cases} a_{gn}(v - b_{gn})^2 + \mathrm{c_{gn}} & (v < r_g) \\ a_{gp}(v - b_{gp})^2 + c_{gp} & (v \geq r_g), \end{cases}$$

$$h(v) \equiv \begin{cases} a_{hn}(v - b_{hn})^2 + \mathrm{c_{hn}} & (v < r_h) \\ a_{hp}(v - b_{hp})^2 + c_{hp} & (v \geq r_h), \end{cases}$$

where v corresponds to the membrane potential, and n and q are the fast and slow variables, respectively, that abstractly describe the activity of the ion channels. Parameter I_0 is a bias constant and I_{stim} represents the input stimulus. Parameters $\emptyset$, ε, and τ control the time constants of the variables. Parameters, a_x, b_x, and c_x, where x is fn, fp, gn, gp, hn, or hp, are constants that adjust the nullclines of the variables. All of the variables and constants in this qualitative model are purely with no physical units. A cubic shaped v-nullcline is a key to replicate the spiking dynamics in qualitative models. Because multipliers are resource-consuming in a digital arithmetic circuit, the DSSN model adopts a piecewise quadratic function for the v-nullcline so that its numerical integration step requires only one multiplication between variables.

2.2. *Differential evolution algorithm*

Differential evolution (DE) algorithm [10] is a popular heuristic method to solve optimization problems using a real number function. It is characterized by its mutation process that uses geometrical location of whole population. In the following, we explain each step in the DE algorithm. We define $x_k^i(j)$ as the gene j of the i th individual of the k th generation.

- **Initialization**

We generate M-dimensional parameter vectors x_0^i ($i = 0, \ldots, \mathrm{N} - 1$), where N and M are the number of the individuals and parameters of the DSSN model. Parameter vectors are chosen randomly within the boundary constraints of the DSSN model.

- **Mutation**

We generate new parameter vector x_{mut}^i as follows:

$$\forall i = 1, \ldots, \mathrm{N}, \qquad x_{mut}^i = x_k^{r1} + F \cdot (x_k^{r2} - x_k^{r3}),$$

where r1, r2, and r3 are integer randomly chosen from [0, $\mathrm{N} - 1$]. F is usually set to 0.5.

- **Crossover**

We generate new parameter vectors x_{cross}^i that inherit genes of x_{mut}^i with a probability CR.

$$\forall i = 1, \ldots, \mathrm{N}, \qquad \forall j = 1, \ldots, \mathrm{M},$$

$$x_{cross}^i(j) = \begin{cases} x_{mut}^i(j) & if(rand \leq CR) \\ x_k^i(j) & otherwise, \end{cases}$$

where CR is usually set to 0.5.

- **Selection**

A selection is conducted by comparing the cost function values of x_k^i and x_{mut}^i, respectively, as follows:

$$\forall i = 1, \ldots, \mathrm{N},$$

$$x_{k+1}^i = \begin{cases} x_{cross}^i(j) & if\ f(x_{cross}^i) \leq f(x_k^i) \\ x_k^i & otherwise, \end{cases}$$

where $f(x)$ returns the value of the cost for parameter vector x.

A set of procedures including mutation, crossover, and selection is repeated for 10000 times, and the parameter vector that produces the lowest value in the cost function is finally adopted.

2.1. *Parameter optimization procedure*

The DSSN model for RS and FS classes has 24 parameters, exploring whose spanning space is not realistic with average computing power available to those who are not specialized in high performance computing (HPC). To reproduce the dimension of the parameter space to be explored by the DE algorithm, we first explored the parameters that control the dynamics of the fast state variables v and n to fit the spike generation mechanism. Then, the parameters related to the slow state variable q were determined to fit the adaptation of the spike-frequency.

In the DSSN model's equation, some parameters are a coefficient of a variable. In its circuit implementation, a multiplication between a coefficient and a state variable was realized by shifters and adders, and we need a larger number of couples of an adder and a shifter as the number of digits with value 1 in the fixed point representation of the coefficient increases. Parameters were optimized for not only reproducing waveforms of the ionic-conductance model but also reducing the circuit size.

In the procedure to determine the parameters that control the dynamics of the two fast variables, we fixed v-nullcline to facilitate parameter exploration while considering the dynamics of the spike generation process. It does not severely restrict the dynamical property of the model, because the relation between the v- and n- nullclines is one of the major factors that rule the dynamical structures in our neuronal model. We defined the cost function as follows:

$$f_1(x) = f_{\mathrm{w}}(x) + k_1 f_{\mathrm{b1}}(x),$$

where $f_{\mathrm{w}}(x)$ is a square error between the waveforms of the DSSN model with parameter vector x and a target waveform. The target waveform was calculated by a fast subsystem of the DSSN model in our previous study [4], which is tuned to reproduce mathematical structure of the ionic conductance model in [8]. Note that minimum and maximum values of waveforms are normalized to 0 and 1 for comparison. Function f_{b1} is a number of digits with value 1 in the binary fixed-point expression of the coefficients in x. Constant k_1 is to balance this couple of cost functions. Parameters that control the dynamics of the fast variables were determined to minimize the cost function f_1 by the DE algorithm.

The remaining parameters related to slow variable q were determined to reproduce the spike frequency adaptation. The cost function is

$$f_2(x) = f_{\mathrm{s}}(x) + k_2 f_{\mathrm{b2}}(x),$$

where $f_{\mathrm{s}}(x)$ is a square error between spike timings of the DSSN model with a parameter vector x and that of the target ionic-conductance model in response to a step stimulus. Function f_{b2} is a number of digits with value 1 in the binary fixed-point expression of the coefficients in x, and k_2 is a constant to balance this couple of cost functions.

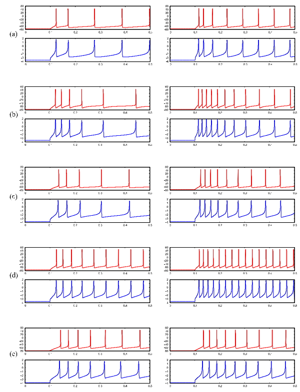

Figure 1: Waveforms of the ionic-conductance model (red) and the DSSN model (blue) in response to a weak (left) and strong (right) step stimulus input. (a)-(c) corresponds to regular spiking neuron cells. (d) and (e) corresponds to fast spiking neuron cells.

The DE algorithm is known to be compatible with parallel computation schemes because of its intrinsic parallel structure. We accelerated the calculation by the Graphic processing unit (GPU) to obtain better parameter solution by executing a larger number of DE steps in a time period. The calculation of the cost function, in which the differential equations are solved by the Euler's method for thousands of times, was parallelly processed on a GPU.

3. Result

We found five parameter sets with which the DSSN model reproduces the activities of the ionic-conductance models for three RS and two FS cells whose characteristics are slightly different from each other (Fig. 1).

We evaluated the similarity of the spiking patterns between the ionic-conductance model and the DSSN model by calculating C_V and L_v [11] that are statistics for the spike sequence while changing the stimulus intensity (Fig. 2). They are defined as follows:

$$C_V = \sqrt{\frac{1}{n-1}\sum_{i=1}^{n}(T-\bar{T})^2/\bar{T}}$$

$$L_V = \frac{1}{n-1}\sum_{i=1}^{n-1}\frac{3(T_i - T_{i+1})^2}{(T_i + T_{i+1})^2}$$

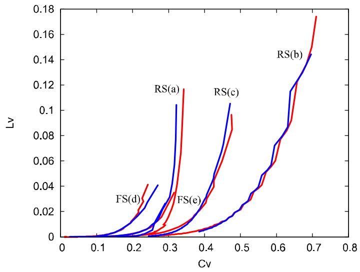

Figure 2: $C_V - L_V$ characteristics of the ionic-conductance model (red) and the DSSN model (blue).

Table. 1 : Device Utilization. The labels (a)-(e) correspond to those in Fig.1.

Name	(a)	(b)	(c)	(d)	(e)	(f)	(g)
FF	109	109	109	109	109	107	107
LUTs	697	660	624	681	631	1410	1357
DSPs	1	1	1	1	1	1	1

where T_i denotes the ith interspike interval, $\bar{T}_i$ is the average of T_i, and n is the number of spikes in the sequence. Both models have same characteristics on $C_V - L_V$ plane in each cell. The results in Figs. 1 and 2 were obtained by numerical integration with the Euler's method ($\mathrm{dt} = 2^{-13}$ s) where each variable was expressed by 18-bit fixed point with 14-bit fraction part. The same results are expected to be observed in the following FPGA implementation, because this condition is the same as our VHDL codes.

We compiled the DSSN models for Virtex-7 XC7VX690T FPGA using Xilinx Vivado Design Suite. Device utilization is listed in Table 1. In the column labeled (f) and (g), the resource usage for RS and FS settings in [4] is shown. The requirement for LUTs was reduced down to less than half in all the settings.

4. Conclusion

In this work, we developed a parameter optimization method for the DSSN model on the basis of the DE algorithm. By splitting the optimization process in 24-dimentional parameter space into two steps, we could find parameter sets with which the DSSN model reproduces the characteristics activities of RS and FS cells without using special HPC systems. Cost functions f_{bx} $(x = 1, 2)$ were introduced so that the circuit size is reduced. We also confirmed qualitative similarity between the ionic-conductance model and the DSSN model by measuring statistics for the spike timing. In our future work, we will improve this optimization method to cover above other neuron classes.

Acknowledgement

This work was partially supported by JSPS SAKURA Program and JST PRESTO and CREST.

References

1. Eugene M. Izhikevich, Simple model of spiking neurons, *IEEE Transactions on neural networks*, 14(6), pp. 1569-1572, 2003
2. Andrew A.V. et al., A Model of a Segmental Oscillator in the Leech Heartbeat Neuronal Network., *Journal of Computational Neuroscience,* Vol. 10, pp. 281-302, 2001.
3. T. Kohno and K. Aihara. Digital spiking silicon neuron: Concept and behaviors in gj-coupled network. *Proceedings of International Symposium on Artificial Life and Robotics* 2007, 2007.
4. T. Nanami and T. Kohno. Simple cortical and thalamic neuron models for digital arithmetic circuit implementation, *Frontiers in Neuroscience*, Vol. 10, No.181, pp. 1—12, 2016
5. T. Nanami, K. Aihara, and T. Kohno, Elliptic and parabolic bursting in a digital silicon neuron model, *2016 International Symposium on NOLTA*, Japan, November 27th–30th, 2016
6. Tawfik B, Durand DM, Nonlinear parameter-estimation by linear association : Application to a 5-parameter passive neuron model. *IEEE Trans Biomed Eng* 41:461–469, 1994.
7. Haufler D, Morinc F, Lacaille JC, Skinner FK, Parameter estimation in single-compartment neuron models using asynchronization-based method. *Neurocomputing* 70:1605–1610, 2007.
8. M. Pospischil et al.. Minimal Hodgkin-Huxley type models for different classes of cortical and thalamic neurons. *Biological Cybernetics*, 99(4-5):427–441, 2008.
9. L. Buhry et al., Automated parameter estimation of the Hodgkin-Huxley model using the differential evolution algorithm: application to neuromimetic analog integrated circuits, *Neural computation* 23 (10), 2599-2625, 2011.
10. R. Storn, K. Price, A Simple and Efficient Heuristic for global Optimization over Continuous Spaces, *Journal of Global Optimization*, Vol. 11, pp. 341-359, 1997.
11. Shinomoto, S., Shima, K., and Tanji, J. Differences in spiking patterns among cortical neurons. *Neural Comput.* 15, 2823–2842. 2003

A Multistage Heuristic Tuning Algorithm for an Analog Silicon Neuron Circuit

Ethan Green
Institute of Industrial Science, The University of Tokyo, 4-6-1 Komaba,
Meguro-ku, Tokyo, 153-8505, Japan

Takashi Kohno
Institute of Industrial Science, The University of Tokyo, 4-6-1 Komaba,
Meguro-ku, Tokyo, 153-8505, Japan
E-mail: green@sat.t.u-tokyo.ac.jp, kohno@sat.t.u-tokyo.ac.jp
www.u-tokyo.ac.jp

Abstract

This research looks at an ultra-low power subthreshold-operated silicon neuron circuit designed with qualitative neuronal modeling. One technical challenge to future implementation of such circuits is parameter tuning—a problem stemming from temperature sensitivity of subthreshold-operated MOSFETs and the uniqueness of individual circuits in a neuronal network due to transistor variation. This research proposes a fully automated parameter tuning algorithm that combines two heuristic approaches to search for appropriate circuit parameters over a range of temperatures. The algorithm can tune the circuit to behave as a Class I or Class II neuron.

Keywords: neuromorphic engineering, analog VLSI, silicon neurons

1. Introduction

Analog silicon neurons, electronic circuits that mimic the electrophysiological characteristics of neuronal cells, may in the future be used as fundamental building blocks of neuromorphic technologies like brain-mimetic computers. These circuits operate in continuous time, consume low power, and are expected to be implemented in massively parallel networks that are fundamentally different from digital transistor logic circuits[1]. The circuit used in this research is an ultra-low power analog silicon neuron designed with the techniques of qualitative modeling—an approach which seeks to reduce the complexity of ionic conductance models by describing the same dynamics with fewer variables[2]. Such a model allows for replication of a wide variety of spiking dynamics in neuronal cells, including Class I and Class II in Hodgkin's classification[3], with a less complex low power circuit. Power consumption is further reduced by operating the circuit's metal-oxide-semiconductor field-effect transistors (MOSFETs) in their subthreshold regime[4].

The large number of circuit parameter voltages, the temperature sensitivity of subthreshold-operated MOSFETs, and the problem of transistor variation among circuits of equivalent design means that effective parameter tuning to achieve consistent neuron-like dynamics is a significant challenge. A parameter tuning algorithm that addresses these issues will be necessary for future implementation of these circuits in large scale networks.

This research is inspired by positive results in [5] in which the Differential Evolution (DE) algorithm was used to tune the parameter voltages of a conductance-based silicon neuron circuit. The DE algorithm is an evolutionary algorithm which begins with random solution vectors, in this case vectors of circuit parameter voltages, evaluates their performance with a cost function, and passes on elements of vectors with good performance to the next generation[6].

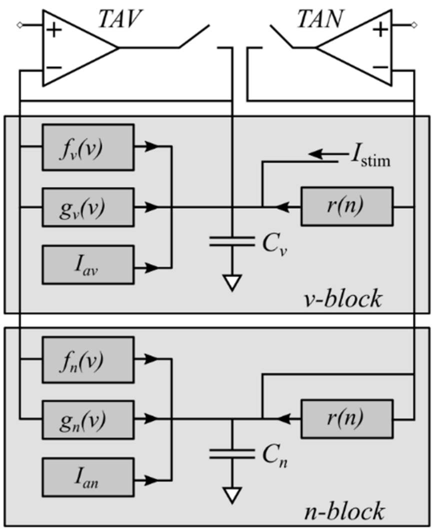

Fig. 1. Block diagram of silicon neuron circuit, reprinted from [7]

In [7], we presented a script which pairs the Spectre circuit simulator with optimization algorithms to automatically search for optimum circuit parameter voltages over a range of temperatures. Two heuristic approaches were used to improve upon a previous trial-and-error based tuning method. In this paper, we present a multistage tuning algorithm which combines those two heuristic methods with consideration given to their merits and drawbacks, and adds an additional pretuning stage to make the algorithm completely automated. Our new algorithm eliminates the need for trial-and-error, only requires input of benchmark characteristics, and can tune the circuit to behave as a Class I or Class II neuron over a range of temperatures.

2. Circuit Description

The silicon neuron circuit is divided into a v-block and an n-block which each integrate the currents from transconductance circuit components over a capacitor. Variables v and n represent membrane potential and abstracted ionic activity and are coded by subtracting the voltage over their respective capacitors from V_{dd}. The system equations are as follows:

$$C_v \frac{dv}{dt} = f_v(v) - g_v(v) + I_{av} - r(n) + I_{\text{stim}} \tag{1}$$

Table 1. Spectre Circuit Parameters (x=v,n)

Circuit	Spectre Parameter	Function
$f_x(v)$	fx_Vb	scaling
	fx_Vdlt	offset
$g_x(v)$	gx_Vm	scaling
$r(n)$	rn_Vm	scaling
I_{ax}	Iax_Vb	scaling
	Iax_Vin	adjustment

$$C_n \frac{dn}{dt} = f_n(v) - g_n(v) + I_{an} - r(n) \tag{2}$$

The current-voltage relationships for $f_x(v)$, $g_x(v)$ (x=v,n), and $r(n)$ are sigmoidal curves. A detailed description of these circuits is given in [2]. I_{ax} (x=v,n) are transconductance amplifiers used as constant current sources and I_{stim} is an externally applied stimulus current. Transconductance amplifiers TAV and TAN use a voltage clamp method to draw the nullclines—curves on which the system equations equal zero—which are used to describe the dynamics of the silicon neuron[8]. All transistors in the silicon neuron circuit are operated in their subthreshold regime, yielding desirable exponential current-voltage characteristics and power consumption as low as 3 nW.

3. Multistage Parameter Tuning Algorithm

Our algorithm requires the user to input the benchmark circuit characteristics: the nullcline structure, circuit behavior detailed in Sec. 3.3, and current-voltage curves of the I_{ax} and $r(n)$ circuits (x=v,n) at 27°C. The user then selects the target temperature that circuit parameter voltages are generated for.

Circuit simulations were conducted in the Cadence software environment with the Spectre circuit simulator on two X5570 processors (2.9 GHz, 8 threads).

3.1. *Stage I: Pretuning*

As listed in Table 1, parameter voltages Iax_Vb and rn_Vm scale the current-voltage characteristics of the I_{ax} and $r(n)$ circuits (x=v,n). The first stage of the algorithm uses Differential Evolution to find the optimum value of these parameters at the target temperature. The cost function is the mean absolute difference of the current-voltage curve resulting from a given parameter to the current-voltage curve of the circuit with benchmark settings at 27°C.

$$f(x) \triangleq \frac{1}{k}\sum_{i=1}^{k}|I_i(x) - b_i| \tag{3}$$

x is the parameter value for a given simulation, $I_i(x)$ represents each point on the current-voltage curve yielded by a given parameter value, b_i represents each point on the benchmark curve, and v = 0 V when k = 1 and v = 1 V when k = 101. The DE algorithm is used once for each of these three circuits, requiring about 1.5 minutes and 130 iterations.

3.2. *Stage II: Nullcline tuning*

The second stage of the algorithm uses the DE algorithm to tune the nullclines to match the benchmark nullclines at 27°C in the range of 300–450 mV. Spectre simulations of the silicon neuron circuit's nullcline mode are run with the input being a vector of circuit parameters gv_Vm, fn_Vb, and Iax_Vin (x=v,n). The functions of these parameters are listed in Table 1. fv_Vb, gn_Vm, and the scaling factors for the I_{ax} circuits from the pretuning stage and fv_Vb are kept constant. The $r(n)$ circuit is set to zero in the nullcline mode and is not directly evaluated.

The cost function is the magnitude of the vector of the mean absolute differences of the v and n nullclines from their respective benchmark nullclines.

$$g(\mathbf{x}) \triangleq \sqrt{\left(\frac{1}{k}\sum_{i=1}^{k}|v_i(\mathbf{x}) - b_i|\right)^2 + \left(\frac{1}{k}\sum_{i=1}^{k}|n_i(\mathbf{x}) - c_i|\right)^2} \tag{4}$$

$v_i(\mathbf{x})$ and $n_i(\mathbf{x})$ represent the points on the output v and n nullcline curves for parameter settings $\mathbf{x}$, b_i and c_i represent the points on the benchmark v and n nullclines at 27°C, and v = 300 V when k = 1 and v = 450 V when k = 151. Differential Evolution for this stage of the algorithm typically requires 7 thousand nullcline mode simulations and 4 hours of calculation time.

As reported in [7], the DE algorithm accurately replicated the benchmark nullclines at a variety of temperatures, but did not yield accurate transient behavior, suggesting the need for an additional tuning stage.

3.3. *Stage III: Tuning transient behavior*

The final stage of the algorithm uses rn_Vm from Stage I and gv_Vm, fn_Vb, and Iax_Vb (x=v,n) from Stage II as the center of a 5 × 5 search space by adding +/– 0.5 and +/–1 mV to each of these five parameter values. A brute force approach is then used to evaluate each of the 5^5 = 3125 combinations of parameters in this search space by running transient simulations of the circuit. For Class I mode, the simulation first approximates the silicon neuron's threshold current to generate a neuronal spike by sending successively stronger 500 μs pulse stimuli in intervals of 8.9 pA, 5% of the benchmark threshold current of 178.5 pA. The time v rises above 450 mV is recorded. This value roughly corresponds to the threshold current. The circuit is then subjected to 5 and 10 pA sustained stimuli and the spiking frequency is evaluated using data from an 800 ms time period.

The cost function evaluates each parameter set by calculating the magnitude of the difference vector between these three simulated circuit behaviors $\mathbf{j}(\mathbf{x})$ and their benchmark values $\mathbf{b}$, a vector calculated from simulation results with a parameter set which yields typical Class I behavior.

$$\mathbf{j}(\mathbf{x}) = \begin{bmatrix} \text{threshold index} \\ \text{5 pA stimulus response} \\ \text{10 pA stimulus response} \end{bmatrix}, \quad \mathbf{b} = \begin{bmatrix} 1.21 \\ 15.87 \\ 37.18 \end{bmatrix}$$
$$h(\mathbf{x}) \triangleq \|\mathbf{j}(\mathbf{x}) - \mathbf{b}\| \tag{5}$$

Class II neurons do not show a clear threshold to generate a neuronal spike and instead are characterized by the sudden onset of periodic spiking when subject to an adequately strong sustained stimulus. The cost function in Class II mode evaluates a vector of the circuit's frequency response to 5, 7.5, 10, and 12.5 pA sustained stimuli. $\mathbf{b}$ again was calculated from simulation results with a parameter set which results in typical Class II behavior.

$$\mathbf{j}(\mathbf{x}) = \begin{bmatrix} \text{5 pA stimulus response} \\ \text{7.5 pA stimulus response} \\ \text{10 pA stimulus response} \\ \text{12.5 pA stimulus response} \end{bmatrix}, \quad \mathbf{b} = \begin{bmatrix} 0 \\ 22.08 \\ 30.21 \\ 35.3 \end{bmatrix} \tag{6}$$

Stage III concludes with a polishing step which interpolates the optimum parameter set between the

Table 2. Algorithm results with benchmark behavior highlighted in grey. "X" indicates non-neuron-like behavior and "D" indicates decaying response.

	Temperature (°C)	2	7	12	17	22	27	32	37	42	47
Class I	I_{th}(pA)	X	X	241.0	220.5	186.0	178.5	153.0	140.0	123.0	X
	5 pA response (Hz)	X	0	13.5	12.5	16.3	15.9	18.4	19.5	21.0	X
	10 pA response (Hz)	X	22.2	32.4	36.8	35.5	37.2	37.3	37.3	37.1	X
Class II	5 pA response (Hz)	0	0	0	0	0	0	0	0	0	0
	7.5 pA response (Hz)	22.0	D	D	D	D	22.1	22.1	22.1	0	0
	10 pA response (Hz)	29.5	30.3	30.6	30.8	30.6	30.2	30.1	30.2	0	0
	12.5 pA response (Hz)	35.1	35.3	35.4	35.5	35.4	35.3	35.4	35.3	0	0

members of the original search space. This stage requires about 4 hours of calculation time to run all the transient circuit simulations. Increasing the search space exponentially increases calculation time, thus illustrating the need for nullcline tuning in Stage II.

4. Results

The algorithm was run in Class I and Class II modes for 2° to 47°C in 5° steps and the results are listed in Table 2. In Class I mode, the circuit displayed behavior closest to the benchmark in the range of 12° to 42°C. 2°, 7°, and 47° did not yield neuron-like behavior. The threshold current descended from 241 to 123 pA as temperature increased.

In Class II mode, transient behavior nearly identical to the benchmark was observable for 32° and 37°C. At 7°, 12°, and 22°C the 10 pA and 12.5 pA sustained stimuli induced spiking at a similar frequency to the benchmark, but the 7.5 pA response decayed after a few iterations. A simplified version of the algorithm which does not contain the Iax_Vb tuning step in Stage I yielded behavior nearly identical to the benchmark at 22°, suggesting that slight modifications to the algorithm may improve the decaying problem for 7–22°C.

5. Discussion

The multistage heuristic tuning algorithm considers the merits and drawbacks of the DE algorithm-based nullcline tuning and brute force transient tuning approaches as noted in [7] and combines them into a hybrid approach which in simulation can effectively tune the silicon neuron circuit to behave as a Class I or Class II neuron over a range of temperatures. The next step will be to implement a version of this algorithm with the actual silicon neuron circuit using LabVIEW or Python.

This algorithm could also be effective in dealing with issues of transistor variation in a network of silicon neurons, since it can find unique parameter sets which may yield similar nullcline structure among individual members of a network. Future silicon neuron circuits may be designed with on-chip feedback mechanisms which automatically adjust parameter voltages based on the results of a tuning algorithm.

Acknowledgements

This study was supported by JST PRESTO and CREST, and VDEC, the University of Tokyo in collaboration with Cadence Design Systems, Inc.

References

1. S. Brink, et al., "A learning-enabled neuron array IC based upon transistor channel models of biological phenomenon," *IEEE Transaction Biomedical Circuits and Systems,* vol. 7, no. 1, pp. 71-81, Feb. 2013.
2. T. Kohno and K. Aihara, "A Qualitative-Modeling-Based Low-Power Silicon Nerve Membrane," *Electronics, Circuits, and Systems* (*ICECS*), IEEE, pp. 199-202, December, 2014.
3. A. Hodgkin, "The local electric changes associated with repetitive action in a non-medullated axon," *The Journal of Physiology*, 107, 2, pp. 165-181, March, 1948.
4. S. Liu, et al., *Analog VLSI: Circuits and Principles*, MIT Press, 2002.
5. F. Grassia, et al., "Tunable neuromimetic integrated system for emulating cortical neuron models," *Frontiers in Neuroscience,* vol. 5, article 134, December, 2011.
6. K. Price and R. Storn, *Differential Evolution: A Practical Approach to Global Optimization*, Springer, 2005.
7. E. Green and T. Kohno, "Two Heuristic Approaches to Parameter Tuning for an Analog Silicon Neuron Circuit," *2016 International Symposium on Nonlinear Theory and Its Applications*, pp. 194-197, November, 2016.
8. J. Rinzel and B. Ermentrout, "Analysis of Neural Excitability and Oscillations," *Methods in Neuronal Modeling*, Massachusetts Institute of Technology, pp. 251-291, 1998.

Integral Design of Intelligent Home Equipment

Yuxing Ouyang [1], Fengzhi Dai [1*], Yiqiao Qin [1], Ce Bian [1], Bo Liu [2], Hongwei Jiao [3]

[1] College of Electronic Information and Automation,
Tianjin University of Science and Technology, China;

[2] Inner Mongolia University, China;

[3] Tianjin Technology School of Printing and Decoration, China
*E-mail: * daifz@tust.edu.cn*
www.tust.edu.cn

Abstract

The equipment is designed to household network monitoring and control. The WIFI module is used for wireless network communication to upload information of all connected smart home devices to the server, and it can be remotely controlled by the external network and monitoring of household equipment information. For simple household equipment, the control is directly taken by the built-in MCU's WIFI module, and for the complex household equipment, it is through the external MCU and WIFI module for communication control. The Airkiss distribution mode is used to connect the WIFI master module to the network, and the other WIFI module devices to adopt the ad hoc network mode for wireless networking.

Keywords: WIFI, intelligent home, ad hoc network, remote control and monitoring, Airkiss distribution network

1. Introduction

With the rapid development of the times and the rise of the Internet of things, many of the traditional home appliances have gradually developed into smart home devices, such as the intelligent sockets, intelligent clock, intelligent closestool and so on[1].

Compared to the traditional home appliances, intelligent home equipment added the function of monitoring and control equipment[2]. But each device needs to be controlled in different ways, so it is very difficult to realize the integrated control of the whole household equipment. Also, most of today's smart home equipment adopt the Bluetooth and other devices to control, or manually set the time to time control, and it cannot be achieved using the network remote control and monitoring.

Based on the above discussion, this design focuses on the integration of smart home equipment. The purpose of this design is to create a comfortable, fast and convenient intelligent home living environment, so that our smart home life can be further optimized and improved[3]. This design adopts the wireless ad hoc network mode of WIFI module. So that the local WIFI module can set up the local LAN network, and achieve the purpose of connecting all the smart home equipment[4]. The WIFI master module connects to the server through the MQTT protocol, which achieved the purpose of we control intelligent household device and monitor the information of intelligent household device. In the intelligent home life monitoring and control, the design has a very high practical value.

2. The hardware structure design

Intelligent devices are mainly responsible for the control of intelligent home appliances and data collection, so the size is better to be small. Therefore, in the design we have adopted a 10*10 PCB board to place the external MCU, WIFI main module and other modules, the rest of the WIFI submodule is directly placed inside the smart home devices.

First, the schematic is plotted using the Altium Designer software platform. Second, the PCB file is generated and the reasonable layout is designed. And finally, PCB is copper clad and sent to the factory to produce the system board[5].

PCB board is designed to make the circuit mini, intuitive, and play an important role in the optimization of electrical layout. The design of the PCB board is shown in Fig.1.

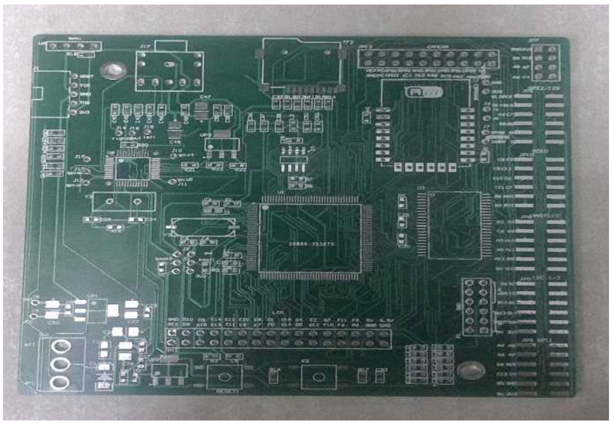

Fig.1 The design of the PCB board

2.1. ILI9341 with resistance touch screen

ILI9341 is a 320*240 resolution TFT screen, with a full color display function. It can use the 8080 timing and it can also work during -40°C to 80°C.

This design adopts the STM32 and ILI9341 to communicate through SPI timing. A series of device data information are displayed on the resistive screen and the smart home device can be manipulated by touch. ILI9341 touch screen is shown in the Fig.2.

Fig.2. ILI9341 touch screen

2.2. WIFI module

The design adopts the WIFI module of ESP8266, and it comes with a core MCU. The MCU has the built-in RAM, ROM, support RTOS, and reaches the maximum clock speed of 80 MHz. The WIFI module has the following characteristics:

- Built-in 10-bit high-precision ADC, with a complete TCP / IP protocol stack.
- Supports Cloud Server Development / Firmware and SDK for fast on-chip programming.
- Wide temperature range: -40 °C ~ 125 °C.
- Operating Voltage 3.0V ~ 3.6V.

The WIFI module is shown in Fig.3.

Fig.3. WIFI module

2.3. Main control chip

In this design, the external MCU is the STM32F103ZET6, which is the Cortex-M3 ARM core and has a 144-pin. The chip has 512KB flash memory and 64KB RAM[6]. It can through SWD or JTAG with KEIL 4 to download the program and online debugging. And it has more than 80 general-purpose IO ports, multiple timers and serial ports, which fully meet the design of the required pin and memory requirements. It has the following characteristics:

- On-chip dual RC crystal, providing 8M and 32K frequency.
- Supported peripherals: Timer, ADC, DAC, SDIO, I2S, SPI, I2C and USART.
- Operating Voltage 2.0V ~ 3.6V.
- Operating temperature range: -40 °C ~ 105 °C.

The design of the main control chip is shown in Fig.4.

Fig.4. STM32F103ZET6 chip

3. System circuit module design

In the circuit design, this design adopts a voltage stabilizing module, temperature and humidity data acquisition module and voice module. These modules greatly improve the function of the device.

3.1. *Voltage stabilizing circuit design*

The design adopts the AMS1117-5.0 voltage stabilizing chip for stable 5V design. It is a linear voltage stabilizing chip, and the input voltage is (at least) greater than the output voltage 1.3V. It has four pins, two of which are output pins, one is the input pin, and the remaining pin is the ground (GND)[7]. In the voltage stabilizing circuit, the 10uf and 100nf capacitors are added as filter capacitors.

3.2. *Design of connection circuit for temperature and humidity module*

The design adopts the temperature and humidity compound sensor DHT11. It has humidity measurement elements to measure humidity and NTC temperature measurement elements to measure temperature, and its correction factor is stored in OTP memory by program. DHT11 has four pins, one pin is the temperature and humidity data output pin, the other three pins are connected to VCC, GND and floating[8]. The DHT11 is a temperature and humidity sensor, and its measurement accuracy is very high. The accuracy of temperature measurement is about 2^{o}C, and the accuracy of humidity measurement is about 5%. Its signal transmission distance can reach to 20 meters.

3.3. *Hard-decoding circuit for speech chip*

The VS1053 chip that used in this design is the Ogg Vorbis audio decoder. The chip contains not only a low-power high-performance DSP processing core, it also has eight general-purpose IO ports, a serial port and a power amplifier interface.

The device receives the digital audio data from the STM32 micro-controller by the SPI interface, and converts the data into an analog audio signal through the chip's built-in DAC. And finally, through the amplifier interface and external speaker connection, the analog audio signal playback function is achieved.

4. Introduction of functional module

With the functional modules, we can easily control and monitor the smart home equipment.

4.1. *Wireless Ad Hoc Network Design*

This design uses a wireless Mesh network for ad hoc network communication. The Mesh network has a mesh network structure, and the number of it can be determined by the number of nodes. The relationship between the number (L) and node (N) can be expressed as:

$$L = C_N^2 = N \times (N-1)/2 \qquad (1)$$

By this way, each node can transmit data quickly and efficiently. But it is actually very difficult to achieve because it requires a large number of links to connect, which is not possible in reality. Therefore, most of the network layout is part of the Mesh network layout. For example, the internet is a part of the Mesh network layout. Therefore, most of the network layout adopt the partial Mesh network Layout mode. The paper also adopt partial Mesh network Layout mode.

This design adopts two kinds of modes for equipment connections. One is that the device node and the router is connected, and is not in the cloud server activation. The device of this connection is called the local device.

The other mode is in the cloud server activate, which is known as the network equipment. The WIFI master module is activated in the cloud server, and the other modules are locally connected through the router.

This design uses the automatic networking mode. As soon as the firmware is downloaded to the module, the WIFI master module will connect to the router, and then the routing is connected to the WAN. Other sub-modules will automatically scan around the WIFI access point (AP). The WIFI master module has the capability to receive, transmit and forward data packets, while the other sub-modules only have the capability to receive and send data packets.

4.2. Airkiss distribution network

With the mobile-phone APP WeChat, the WIFI module of this design can be carried out Airkiss distribution network, which makes WIFI module access to the Internet.

The principle of the Airkiss distribution network is through the LAN discovery and promiscuous mode to capture the way to achieve the purpose of smart configuration. Since the SDK programming and the firmware is burned to the WIFI module, the WIFI module can access to the network through the phone.

The Airkiss smart config network steps are as follows:

- Scan the two-dimensional code by WeChat.
- Fill in the SSID and password according to the pop-up window.
- WIFI master module receives the SSID and password, automatically connects to the router.

5. Testing and conclusion

By the test of the smart home devices, the following data are obtained: The Mesh network allows up to 5 hops, each mesh-non-leaf node can allow up to 4 direct child nodes to access the network, the transmission distance between nodes is best within 100 meters, the router can mount a Mesh network with a network size of 80 nodes. The above data shows that the device can basically meet the needs of smart home equipment integration.

By using DHT11 module, the indoor temperature and humidity data can be real-time transmitted to the remote client.

By using voice modules, the voice is used as the failure alarm when the touch screen is operated.

The test includes the sensitivity of the touch screen, the stability of the data transfer between the WIFI modules, and the speed and stability of the Airkiss distribution network. The test results show that the device can basically meet the user's control and monitoring of intelligent home equipment.

Acknowledgements

The research is partly supported by the Research Fund for the Doctoral Program of Higher Education of China (20131208110005). It is also supported by the Science & Technology Fund Planning Project of Tianjin Higher Schools (20120831, 20140710-1400020005).

References

1. Santing Zheng, Yanyan Bai, Xiaoxia Hu, The design and application of digital electronic clock, *Electronic Production*, 2015, 5: P90 - P91.
2. Yingang Fu, Design and implementation of information appliance control platform (Shangdong, Shandong University of Science and Technology, 2007)
3. Xiong Sun, *Smart home system based on Internet of things* (Tianjin, Tianjin University of Technology, 2013)
4. Jinrui Zhang, *Research and implementation of intelligent transportation system gateway based on Internet of things* (JlLin, Changchun University of Science and Technology, 2014)
5. Bing Xia, *Design and implementation of data acquisition and identification algorithms in an online logic chip analysis tool* (Henan, PLA Information Engineering University, 2006)
6. Wei Qin, Based on the AM2301 temperature and humidity meter design, *Hunan Agricultural Machinery*, 2012, 9: P59 - P60.
7. Qingxia Li, Wenhong Wei, Study on the structure of an extended OTIS-Mesh network, *Computer Science*, 2012, z3: P90 - P92.
8. Jean-Christophe Cuilliere, Vincent Francois, Remi LacroisLi, A new approach to automatic and a priori mesh adaptation around circular holes for finite element analysis, *Computer-Aided Design*, 2016.

Research on Underwater Robot Recognition

Binhu Song[1], Fengzhi Dai[1]*, Qijia Kang[1], Haifang Man[1], Hongtao Zhang[1], Long Li[2], Hongwei Jiao[3]

[1] *College of Electronic Information and Automation, Tianjin University of Science and Technology, China;*

[2] *Tianjin Electric Locomotive Co., Ltd, China)*

[3] *Tianjin Technology School of Printing and Decoration, China*

* *daifz@tust.edu.cn*

Abstract

The underwater robot fish needs to keep shaking the tail fin to move, but the wave of the water is very difficult to be predicted, in which the robot fish will show different shape. This paper proposes to use of Histogram of Oriented Gradient method for image feature extraction, and then use the genetic algorithm method to optimize the parameters of the support vector machine. We use the parameters optimized for the classification training of experimental images to recognition the robot fish.

Keywords: support vector machine, genetic algorithm, underwater robot fish, histogram of oriented gradient

1. Introduction

Support vector machine (SVM) belongs to the machine learning. It is a classifier for finding the maximum interval classification. It has a good effect in solving non-linear and high-dimensional pattern recognition problems[1]. Over the past few years, its importance is growing. In the use of the classifier, its performance depends on the choice of the kernel function and its parameters. In this paper, the genetic algorithm is used to optimize the parameters.

2. Histogram of oriented gradient feature extraction

2.1. Image normalization

The purpose of the normalization to image is to give the detector more robustness to illumination as the primary factor affecting the image.

2.2. Calculation of the gradient of the target image

Calculating the gradient of the target needs to be applied to the first-order differential theory, because this processing can be applied to the grayscale graphics to form a more satisfactory effect. The calculation is as follows:

$$\begin{cases} Gx = \frac{\partial \mathrm{f}}{\partial x} = f(x+1) - f(x) \\ Gy = \frac{\partial \mathrm{f}}{\partial y} = f(y+1) - f(y) \end{cases} \quad (1)$$

In order to calculate the image gradient and gradient direction better, we need to use the gradient template to calculate both the gradient of the vertical component and horizontal component[2]. The gradient template is [-1, 0, 1]. The horizontal and vertical components of the gradient can be obtained as follows.

$$\begin{cases} \mathrm{G_v}(x,y) = \mathrm{f}(x,y+1) - \mathrm{f}(x,y-1) \\ \mathrm{G_h}(x,y) = \mathrm{f}(x+1,y) - \mathrm{f}(x-1,y) \end{cases} \quad (2)$$

By the horizontal gradient component and the vertical gradient component as shown in the above expression, we can get the size of the gradient (that is, the gradient

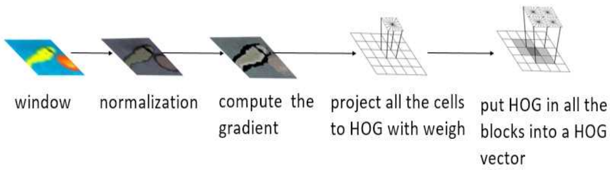

intensity), as well as the direction of the gradient, that is, the above-mentioned amplitude (magnitude) and angle (theta) values.

$$\begin{cases} \text{magnitude} = \sqrt{\text{xGradient}^2 + \text{yGradient}^2} \\ \text{theta} = \tan^{-1}(\text{yGradient}/\text{xGradient}) \end{cases} \quad (3)$$

As shown in the above equation, the edge strength is affected by the sum of the gradients of the x-direction and the y-direction, and the angle is derived from tan-1 of its ratio. According to the simplification rule proposed above, the gradient intensity formula above-mentioned can be simplified as follows

$$\text{magnitude} \approx |G_h(x,y)| + |G_v(x,y)| \quad (4)$$

The angle of the gradient is given by the following equation:

$$\text{theta}(x,y) = \begin{cases} \text{theta}(x,y) + \pi & \text{theta}(x,y) < 0 \\ \text{theta}(x,y) & \text{others} \end{cases} \quad (5)$$

A weighted projection is used in the direction of the gradient.

The goal of this step is to project the values of the pixels in the block in the gradient direction of the image. After the projection, a horizontal axis is obtained, and the histograms of our cells are aligned along this axis. With the horizontal axis, we can compute the Histogram of Oriented Gradient of all the cells in each block, and then create a histogram at each gradient angle, placing several gradient angles above the horizontal axis. There are a variety of ways to project in a gradient, not just one. But in general, the user uses a weight projection function to solve this problem. The eigenvectors of the directional gradient histograms are normalized. At the last of this step, we need to normalize each block.

$$\text{L2} - \text{norm} \qquad v \leftarrow v/\sqrt{\|v\|^2 + \varepsilon^2} \quad (6)$$

Gradient direction histogram is a very representative feature extraction method, since the emergence of this method has been shown a very powerful function in a variety of areas. Fig.1 is the basic process of HOG.

Fig.1 Basic process of HOG

2.3. Using genetic algorithms to select and optimize SVM parameters

The genetic algorithm based on model theory, applied by Professor Holland, is used most commonly so far. The general formula for the model theory is as follows[3]:

$$\text{m}(H, t+1) \geq \text{m}(H,t)\frac{\overline{f(H)}}{\bar{f}}(1 - p_c\frac{\delta(H)}{l-1} - o(H)p_m \quad (7)$$

Where H is the code of the pattern[4], t is chromosome algebra, m(H, t) is the t-generation chromosome number of strings, pc is the exchange probability, $\overline{f(H)}$ is the average fitness of the H-mode in t generation, $\bar{f}$ is the overall fitness, p_m at last is the probability of mutation. Fig.2 gives the flow chart of GA optimization to the SVM parameters.

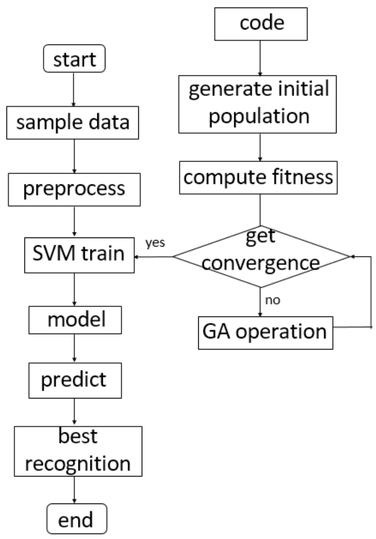

Fig.2 Flow chart of GA to optimize SVM parameters

2.4. Support vector machine

The main idea of machine learning is: there is a certain unknown dependency between the variable y and input x, which can also be understood as the variable y and input x follows an unknown joint probability F(x, y). Machine learning is based on *n* independent identically distributed observation samples $(x1, y1), (x2, y2), \ldots, (xn, yn)$. Then an optimal function $f\ (x, \omega^*)$ is obtained from a set of functions {f (x, ω)}. This optimal function can make the expected risk function

$$\text{R}(\omega) = \int L(y, f(x,\omega))dF(x,y) \quad (8)$$

have the minimum value. Here, $\{f\ (x,\omega)\}$ is a set of prediction function. Since $\omega \in \Omega$ is a generalized function parameter, theoretically $\{f\ (x,\omega)\}$ can refer to any set of functions. And $L\ (y, f\ (x,\omega))$ is the loss to predict variable y by using the set of predicting functions $\{f\ (x,\omega)\}$.

The output of the function is the codename of the sorted category. The binary output function of the problem can be simply defined as a binary function $y = (-1,1)$. With the output function, we need the loss of function output function of the forecast will result in the loss function.

$$L\big(y, f(x,\omega)\big) = \begin{cases} 0 & \text{if} \quad y = f(x,\omega) \\ 1 & \text{if} \quad y \neq f(x,\omega) \end{cases} \tag{9}$$

The support vector machine training in this experiment will be completed by the SVM toolbox in MATLAB. For feature extraction of training image, the image itself can provide accurate pixel. However, the amount of training pixel data will cause delay the experimental speed, so the application of the direction of the image gradient as a feature extraction.

2.5 Opencv for reflective compensation

In this part, we use Opencv to optimize the image of the experimental site. Experiments were taken from different periods of the experimental site of the reflective picture[5], and the obtained picture is subjected to hue saturation adjustment, get a more pure color and exposure of the image. Subsequently, the image is subjected to a grayscale operation, after all the Opencv functions have been processed, the compensation results are shown in the following Fig.3 are obtained[6].

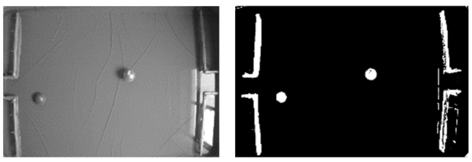

Fig.3 Before (left) and after (right) reflective compensation

3. Recognition of the underwater robot fish

3.1 Default parameters to recognize the robot fish

The recognition experiment of the underwater robot fish begins with the method of the basic support vector set. That is, it does not use any optimization means to predict and classify.

Prepare the appropriate training samples and determine the classification of labels after the start of training, the support vector machine parameters c and g were selected for the two groups to comparative experiment.

After obtaining the training result, we use several pictures to call the recognition function to classify and predict. After the prediction, we count the number of successful training samples and the number of failed samples to calculate the correctness of recognition as follows Table 1:

Table1 Standard SVM classification results

SVM parameter	c=1, g=10	c=0.5, g=0.6
accuracy	50%	52%

It can be seen that the parameters of SVM in the experiment are determined manually, the result is limited, and the result of recognition accuracy is not very high. But this kind of training method has got certain results.

3.2 Using optimized parameters to the sample training

In order to improve the accuracy of the previous SVM predictive classification experiments, the parameters of SVM are optimized by the genetic algorithm mentioned above.

First, the corresponding sample set and classification information are prepared, which includes the sample set and classification information used in the training of SVM. The parameters of SVM are optimized by using the genetic algorithm parameter optimization provided by the libSVM toolbox described above. The optimized support vector machine parameters are c = 3.4 and g = 5.7. The experimental result is shown in Table2.

Table2 SVM classification results with GA optimization

best parameter	c=0.1,g=0.4
accuracy	85%

These experiments can let us clearly see that, with the genetic algorithm to optimize participation, support vector machine training out of the classification algorithm for the recognition of the robot fish in the water is significantly more successful.

4. Conclusion

The results of the SVM-trained algorithm show that the proposed algorithm outperforms the default support vector machine, in the case of hardware and experimental environment has withstood the test.

In the future, the hardware and software will be a great development prospects, a large number of the input of training sample sets will make the training of the algorithm be more comprehensive, and the classification prediction will be more accurate.

Acknowledgements

The research is partly supported by the Research Fund for the Doctoral Program of Higher Education of China (20131208110005). It is also supported by the Science & Technology Fund Planning Project of Tianjin Higher Schools (20120831, 20140710-1400020005).

References

1. Williams C K I. Learning With Kernels, Support Vector Machines, Regularization, Optimization, and Beyond. *Journal of the American Statistical Association*, 2003, 16(462):781-781.
2. Dalal N, Triggs B, Histograms of oriented gradients for human detection. *IEEE Conference on Computer Vision & Pattern Recognition*. 2005:886-893.
3. Holland J H. Adaptation in natural and artificial systems: an introductory analysis with applications to biology, control, and artificial intelligence. *2nd ed. Cambridge*: MIT Press, 1992.
4. Tang K Z, Sun T K, Yang J Y. An improved genetic algorithm based on a novel selection strategy for nonlinear programming problems. *Computers & Chemical Engineering*, 2011, 35(4):615-621.
5. Inamura M, Toyota H, Fujimura S. Influence of the Light Reflection on Water Surface in Quantitative Remote Sensing of Water Quality and Its Removal. *Journal of the Remote Sensing Society of Japan*, 1984, 4:39-50_4.
6. Rudolph G., Convergence analysis of canonical genetic algorithms. *IEEE Trans on Neural Networks*,1994,5(1):96-101.

Design of Intellectual Vehicles with Path Memorizing Function

Yiqiao Qin [1], Fengzhi Dai [1*], Yuxing Ouyang [1], Baochang Wei [1], Simini Chen [2], Hongwei Jiao [3]

[1] Tianjin University of Science and Technology,
1038 Dagunanlu Road, Hexi District, Tianjin, 300222, China;

[2] Palace Museum, China;

[3] Tianjin Technology School of Printing and Decoration, China
*E-mail: * daifz@tust.edu.cn*
www.tust.edu.cn

Abstract

Based on the deficiencies of current intelligent vehicles, we design a new vehicle system that has a function of storing path data. It has a kind of algorithms to recognize the position and path of the vehicle that neither relies on the external positioning methods such as GPS, WIFI, etc, nor the electromagnetic rails or photoelectric rails. This system is rarely affected by the ground condition, so there is no need for any ground signs.

Keywords: intellectual vehicles, path-recognition, path-correction, MCU

1. Introduction

Nowadays there are two kinds of guided vehicles that have found an increasingly wide utilization in the short-distance transport of goods.

- Vehicles are guided by electromagnetic track.
- Vehicles are guided by photoelectronic track.

Both of them need to rely on the track on the floor, and require a good ground condition. Their limitations are as follows:

- In the factory or warehouse, the ground condition may not be optimistic. Debris, water, dust and other issues often make it difficult for photoelectric sensors to accurately detect the lane. Similarly, the electromagnetic guidance is also limited by the water, metal debris and other adverse impact.
- Before applying these two methods of guidance, workers must lay the black wire or electromagnetic wire on the ground as a "track". This is not convenient for factory to changes the product line, and it is difficult to lay "tracks" on unrepaired ground such as dirt roads and brick roads[1].

In addition to the ground track, we also could adopt wireless location technology, such as GPS and WIFI, to guided vehicles, but both GPS and WIFI have some obvious defects that are hard to overcome. GPS is vulnerable to the interference of buildings and the accuracy is poor in indoor positioning. Similarly, WIFI positioning is usually applicable to indoor space. Moreover, before positioning the vehicles, WIFI transceiver must be installed in some key locations in the room and we have to set the location information to the position system. This process generally takes a long time and is very cumbersome[2]. Also, when the indoor space changes, such as installing a new large mechanical equipment in the plant, the location information needs to be reset.

Based on the above points, it is necessary to design a transportation system that is not limited by the ground condition, and it does not rely on the GPS, WIFI or markers on the ground and can accurately transport the goods from one place to another.

Therefore, we designed a kind of intelligent vehicle with path memory function, which can record path between two locations, and quickly and accurately transport the goods from the starting point to the end point without human operation.

2. The hardware structural design

The whole hardware design consists of 9 modules: MCU, ultrasonic ranging module, communication module, speed measuring module, motor drive module, electronic compass, CCD camera, SD card and LCD module.[3] The hardware structure is shown in Fig.1.

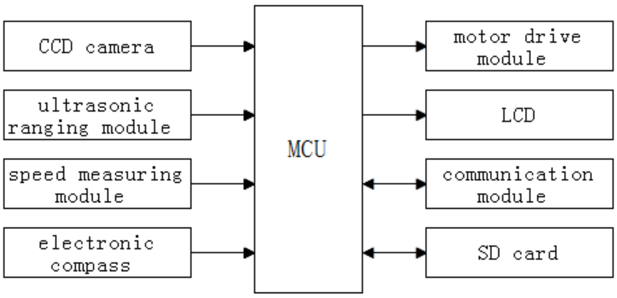

Fig.1 The hardware structural design of vehicles

The structural design of the search and rescue robots is shown in Fig.1. And the followings are some of the important details about the hardware structural design.

2.1. Ultrasonic ranging module

The ultrasonic ranging module can measure the distance between the vehicle and the surrounding obstacles to prevent the vehicle from hitting them.

Moreover, when the vehicle moves near to the end point of the transport, cooperating with the camera, the ultrasonic sensor can measures the distance between the vehicle and the marker, which is set at the end point, to eliminate the position deviation caused in the transport process, so that the vehicle can reach the destination more accurately.

2.2. Optical encoder and electronic compass

The photoelectric encoder records the vehicle traveling distance, electronic compass detects the current direction of the vehicle. With the data from both sensors, we can determine the relative position between the current vehicle and the starting point, as well as the deviation between the current vehicle and the preset travel path.

2.3. CCD camera

The camera can detect the terminal markers. With the date from optical encoder and electronic compass, if the MCU identifies that the vehicle is about to reach the terminal point, the camera will look for the terminal marker in its line of sight, and determine the relative angle to the end point. According to the relative angle and relative distance, the MCU could adjust the vehicle to reach the end point more accurately.

2.4. Vehicle body structure

As shown in Fig.2, the vehicle body has three wheels, "A" and "B" are drive wheels, "C" is a mecanum wheel.

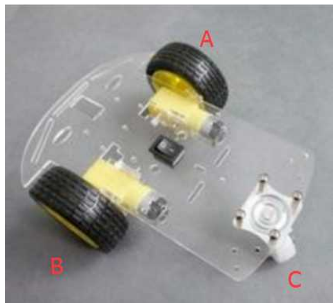

Fig.2. vehicle body structure

This kind of body has greater advantage in operation, such as the followings:

- Compared with the four-wheeled vehicle, the tricycle does not require steering gear, and its cost is lower than the four-wheeled vehicle.
- The MUC can control "A" and "B" with different speed to achieve pivot steering, while the four-wheel vehicle cannot do this. Therefore, in the adjustment of moving error, the three-wheeled body has a greater advantage[4].

3. Vehicle forward path identification algorithm

The vehicle designed in this paper can travel along the established route that is stored in the SD card. There are two sources of the established route. One is the manual input specific data, such as the distance, steering angle, etc. The other is that the vehicle is remotely controlled to move forward. At the same time, the vehicle automatically records the path in real time[5].

Therefore, it requires the vehicle to have the ability to detect the path in real time, the detailed methods are as follows:

The MCU reads the speed data from photoelectric encoders every 500ms. As we know, it is impossible that the speeds of the two drive wheels are exactly the same in the meantime. If we just integrate the average speed as vehicle's path, it will lead a large deviation. Therefore, it can be considered that in this 500ms, the vehicle moves an arc M as shown in Fig.3. We need to figure out the line distance L in the 500ms.

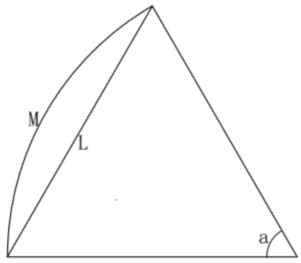

Fig.3. The calculation of line distance L

$$L = r^2 + r^2 - 2 \times r \times r \times \cos a \quad (1)$$

$$M = r \times a \quad (2)$$

$$L = M \times \sqrt{2 \times (1 - \cos a)} / a \quad (3)$$

Where, "a" is the direction difference during the 500ms, which is measured by the electronic compass. Formula 3 can be derived from the formula 1 and 2, and the line distance L can be figured out.

Assuming that the path is shown in Fig.4(a), and Fig.4(b) is the vehicle's actual travel path. The following is the algorithm to calculating the A-M straight-line distance and relate angle.

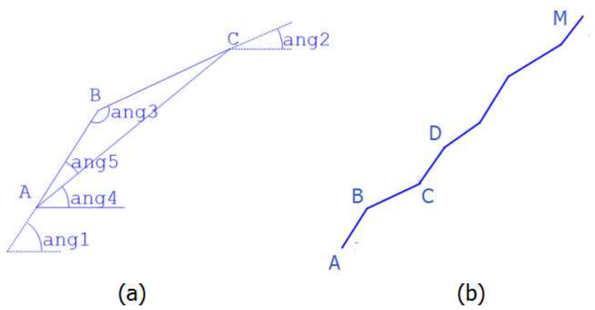

Fig.4. The algorithm to calculating the travel distance

As shown in Fig.4(a), AB, AC and Ang1, Ang2 are obtained by Formula 3 and electronic compass.

$$angle3 = 180° - (\text{ang1} - \text{ang2}) \quad (4)$$

$$AC = \sqrt{AB^2 + BC^2 - 2AC \times BC \times \cos(angle3)} \quad (5)$$

$$ang5 = \arccos[(AB^2 + AC^2 - BC^2)/(2 \times AB \times BC)] \quad (6)$$

$$ang4 = ang1 - ang5 \quad (7)$$

From Formula 4 to 7, the direction (ang4) and the distance of the path AC can be obtained. And then use the above formula again, we can get the direction and the distance of the path AD. The rest can be done in the same manner. Finally, the straight line distance and direction of path AM can be obtained.[6]

The direction and the distance of a path can be stored in the SD card as ideal path to guide the vehicle moving. In addition, by calculating the path which the vehicle has traveled in real time, error between authentic path and the ideal path can be figured out.

4. Vehicle routing correction algorithm

When the vehicle runs autonomously without operator, its real-time position and direction can be obtained by the path identification algorithm, and the ideal forward route can be obtained from the information stored in the SD card.

As shown in Fig.5, the straight line CD is the ideal forward route of the vehicle, the line AB is the distance deviation between the vehicle and the ideal forward route, and the ANG is the angle deviation between the vehicle and the ideal traveling direction.[7] The overall deviation is obtained by Formula 8.

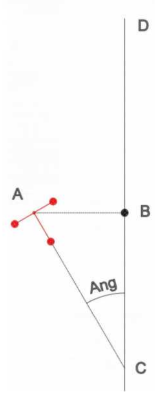

Fig.5. Calculation of distance and angle deviation

$$\text{Deviat} = \text{AB} \times \text{m} + \text{ANG} \times (1 - \text{m}) \quad (8)$$

Where, "Deviat" is the overall deviation value and is the error input of the PID algorithm. In this correction algorithm, "m" is the ratio adjustment factor of the linear deviation and the angle deviation. That is to say, when the value of m increases, the control algorithm focus much more on reducing the distance deviation. When the m decreases, the angle deviation has more affection to the control algorithm.

According to the above information, it is easily to add the PID in control algorithm.[8]

5. Testing and conclusion

We obtained the following data by testing the intelligent vehicle (the test environment is cement ground).

In the 10 times of the random tests (human remote control), the vehicle travels 10m in straight line. The maximum location error for the end point is 2.7cm and the probability of error within 2 cm is 80%.

There is a probability of 90% that the steering error of turning 90 angle is in the range of 0.3.

As shown of the routes in Fig.6, there is a probability of 90% that the error of vehicle's position in end point is less than 8cm. If adding the recognition algorithm of end point, the probability that the error that is less than 4cm will be 95%, and the probability that the vehicle does not recognize the end point is about 1.5%. It can meet the demand basically.

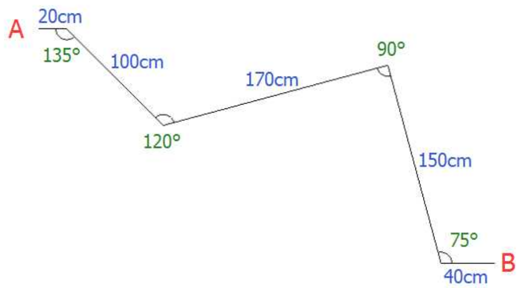

Fig.6. The test line

The functions and system advantages of the intellectual vehicle with path-memorizing function introduced in this paper are as follows:

- It can realize the transportation of goods without any signs or tracks.
- It can be applied to a variety of indoor and outdoor occasions. Even if it transports goods in the rainy days or on dirt roads, the transportation could still be proceed very well.
- It can quickly change the transport path. Thus such feature is convenient for the change of plant production line.

However, there are still some defects and shortcomings in this design, which mainly focus on the transport accuracy. Next, we will continue to improve the design on this aspect.

The path recognition algorithm of the design performs better on the ground and on the downhill path. The error is in the acceptable range when on dry dirt roads. However, in the potholes, or on muddy roads the performance is still not ideal. So we will continue to optimize the vehicle recognition algorithm and focus on improving the adaptability of the vehicle to the pavement with poor road conditions.

Acknowledgements

The research is partly supported by the Research Fund for the Doctoral Program of Higher Education of China (20131208110005). It is also supported by the Science & Technology Fund Planning Project of Tianjin Higher Schools (20120831, 20140710-1400020005).

References

1. HP Wang, Y Yang, JT Liu, Research and Development Trend of High-speed Mobile Robot. *Automation & Instrumentation*, 26 (12) (2011) 1-4.
2. HM Khoury, VR Kamat, Evaluation of position tracking technologies for user localization in indoor construction environments, *Automation in Construction*, (4) (2009) 444-457.
3. YX Wu, H Zhang, XS Wang, The Design of Intelligent Vehicle Path Recognition Based on Monochrome Camera, *Information Technology & Informatization*, 13 (2) (2009) 42-45.
4. Yonggang Wei, Yunping Fan, Guoying Meng, Comparison of Steering Performance between two wheels and four wheel Car, *Coal Mine Machinery*, 30(5) (2009) 78-80.
5. MY Fu, ZH Deng, *Intelligent vehicle navigation technology* (Beijing, Science Press, 2009)
6. Shiyong Li, *The theory of fuzzy control and intelligent control* (Harbin, Harbin Institute of Technology Press, 1999)
7. Xiong Bo, QU Shi-ru, Intelligent Vehicle's Path Tracking Based on Fuzzy Control, *Journal of Transportation Systems Engineering and Information Technology*, 10 (2) (2010) 70-75.
8. Md.Nazmul Hasan, S.M Didar-Al-Alam, Intelligent Car Control for a Smart Car, *International Journal of Computer Applications*, 14(3) (2011) 15-16.

Action recognition based on binocular vision

Yiwei Ru[1,2*], Hongyue Du[1],Shuxiao Li[2], Hongxing Chang[2]

[1].*Harbin University of Science and Technology, Harbin, China;*
[2].*Institute of Automation Chinese Academy of Sciences ,Beijing, China*

E-mail: *ruyiwei2014@ia.ac.cn

Abstract

Aimed at the problem that the recognition accuracy of the monocular camera is low, we propose a binocular vision recognition algorithm for action recognition based on HART-Net(Human action recognition networks).Firstly, the left and right views obtained by the binocular camera are matched to obtain the depth map of the human body .Then, the depth information is projected onto the three planes, the projection images of three directions are used to construct MHI (motion history image), and are combined into a new image. Finally, we use HART-Net to train a classifier for action recognition. Experimental results show that the binocular recognition algorithm is 18% more accurate than the monocular recognition algorithm.

Keywords: action recognition; binocular version; convolutional neural networks; motion history image;

1. INTRODUCTION

Since 1980s, the concept of search and rescue robot has been presented. Recognizing human activity is one of the important areas of computer vision research today[1].Its applications include video surveillance, virtual reality, human-computer interaction and others. In recent years, many human motion recognition research is based on monocular vision. Although the recognition algorithm based on monocular vision has achieved good results, but due to the monocular camera's own limitations, this approach is very sensitive to complex backgrounds, so when the background changes significantly, the accuracy of recognition will decline. In order to improve the detection accuracy of human action recognition algorithm in complex background, people use time-of-flight or structured light technology to obtain the depth map of the object. However, for some applications such active sensors are not suitable. For example, in outdoor setup or in a scenario with multiple autonomous robots whose active sensors would interfere to each other[2].

In order to solve the problem that the human action recognition algorithm is sensitive to the background under the monocular visual and cannot obtain the object depth map based on the structured light or time-of-flight technology in the outdoor environment[3], we propose an action detection algorithm based on binocular vision. In order to improve the accuracy of motion recognition in binocular vision, a novel convolutional neural networks architecture named HART-Net (human action recognition net) is presented. Firstly, the left and right views obtained by the binocular camera are matched to obtain the depth map of the human body under the camera coordinate system (O-XYZ). Then, the depth information is projected onto the three planes of O-XY, O-YZ and O-ZX respectively in the camera coordinate system[4]. In order to reflect the motion of the timing information, the projection images of three directions are used to construct MHI (motion history image), and then the three MHIs are regarded as the three channels of the image to construct a new image. We finally use CNN to train the classifier for action recognition.

2. RELATED WORK

2.1. Stereo Matching Algorithm in Binocular

Binocular stereo matching algorithm can be divided into: local matching algorithm and global matching algorithm.

(a) left image (b) right image (c) depth map

Fig1. Left-right image after line alignment, and depth map

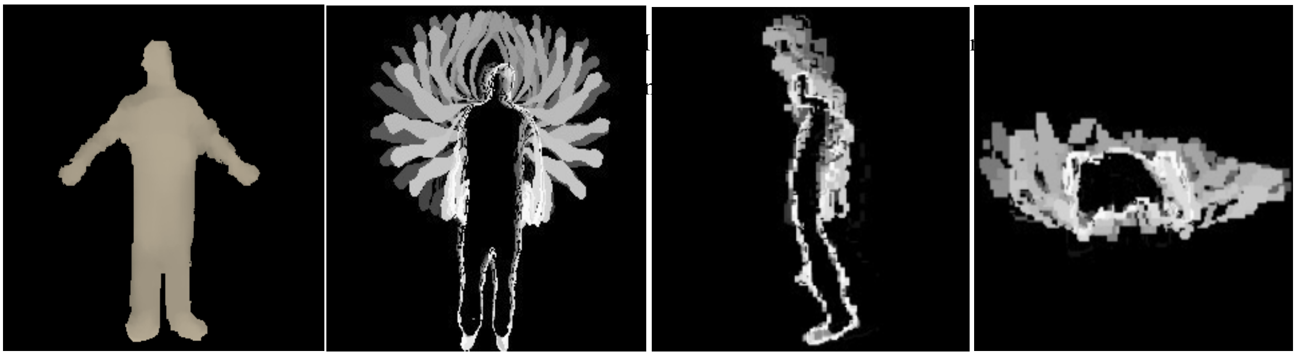

(a)Outline of the human body (b) MHI in O-XY (c) MHI in O-YZ (d)MHI in O-ZX

Fig2. Outline and MHI image

Local matching algorithm mainly compare the matching point within a certain range of loca characteristics to match. Bigone[5] et al. Used the edge information of the image as a matching feature. Marr[6] et al. Proposed to use zero-crossing as the basis, plus and continuous constraint iterations obtained after the disparity map. Nevatia and Medina[7] use line segments as matching primitives.

Global matching algorithm is generally used to scan the line or the overall consideration of the image information to be matched to solve the disparity. Boykov[8] et al. first introduced the graph-cut theory into the stereo matching algorithm. For the first time, Kolmogorov[9] incorporated the solution of the occlusion problem into the construction of the energy function. Confidence propagation was proposed by Sun Jian[10] of Microsoft Research Asia. Ohta[11] proposed an edge-characterized DP algorithm.

2.2.Action Recognition Algorithm Based on RGB and RGBD

As the RGB image is different from the RGBD image[16] which can be directly segmented out of the body region using depth information, RGB-based action recognition generally requires the use of segmentation methods to extract the contours of the human body. Ali and Aggarwal[12] define an action boundary by using a feature vector that contains three angles to the main part of the human body. Hanjalic[13] et al. used logical tale units (each of which is represented by one or several events not related to timing) to detect the motion bounds. Zhai and Shah[14] used the Markov chain Monte Carlo technique to segment the temporal scenes in various videos. Shi et al. [15] used semi-Markov model to achieve the action segmentation. For the RGBD method, the depth of the human body can be obtained by face detection or head and shoulder detection, and then the human body position can be extracted using the depth information. After the outline of the human body is obtained, the MHI[17] is used to reflect the time when the human action takes place and the time to change. The obtained MHI is used as the input picture of the classifier.

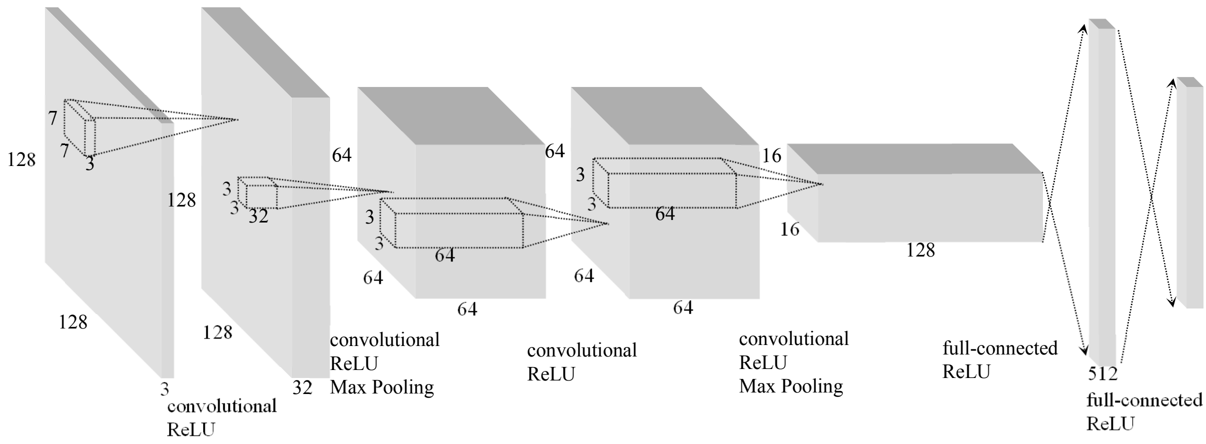

Fig3. HART-Net architecture

3. PROPOSED METHOD

3.1.Overall framework

The proposed method mainly include the following four modules:

(1) Human body region extraction. After using the camera's internal and external parameters for line alignment between the left and right images, we can get the depth image by seed pixel propagation matching algorithm, as shown in Fig 1. In order to get the location of the human body, we first use the seetaface detection algorithm to detect the face position. Then, the average depth value of the face is computed in the depth map, denoted as *D*(mm). Finally, [D-300, D+300] is used to extract the contours of the human body.

(2) Human body region refinement. As the ground and the human body is connected, the acquired human body region will contain part of the ground information. In order to remove the ground, we use RANSAC algorithm to detect plane in the picture, and then remove it from the body outline image, as shown in Fig2 (a).

(3) Get MHI images. After the human body depth map is obtained, the depth map is cropped and cut into 480 * 480. According to the position information of the human face, the human body profile is located at the middle position of the image, and the depth map is projected onto the O-XY, O-YZ, O-ZX three planes, and then the three planes were accumulated to get MHI images, as shown in Fig 2. In order to meet the different speed of movement of different people, we selected 15,20, 25, 30 images in the same sequence of motion for each action to construct MHI. Finally, the MHI of the three projection planes is merged into one image as an RGB image as shown in Fig 4.

(4) Action recognition by HART-Net. By using the MHI image as the input image of the classifier A novel convolutional neural networks architecture named HART-Net (human action recognition net) is presented in the following subsections.

3.2.HART-Net architecture

In order to meet the training needs, we propose our own convolution neural network training framework: HART-Net, as shown in Fig3. This convolutional neural network has four convolutions and two fully-connected layers. The input of the first convolution layer is 64 * 64 * 3, this layer contains 32 convolution kernel, and the convolution kernel size is 7 * 7 * 3. The second layer contains a pooling layer with max pooling. The output of the first convolution layer is the input of the pooling layer. The pooling layer contains 64 convolution kernels. The size of the convolution kernel is 3 * 3 * 32. The third layer and the fourth layer are similar to the first layer and the second layer, and the specific parameters are shown in Fig3. The output of the last fully-connected layer is fed to a soft-max layer, and the output of the soft-max layer is used as the confidence of the classifier for each class to be categorized.

Notice that, the ReLU non-linearity is applied to the output of every convolutional and fully-connected layer.

3.3.Training process

Our classification task has 8 kinds of action: Drinking, eating, making phone call, reading book, walking, waving, hand clapping, boxing. For each category, there are 1000 MHI images. For these images, we will first of all resize them to 130 * 130.For each resized picture, we randomly cut out 128 × 128 windows on these images as training samples, and then horizontally rotated all the training samples. After these transformations, our training sample is 50 times the original. Although the samples obtained from these transformations are highly dependent, training with these samples still greatly improves the training results. Because our training sample size is relatively large, limited to GPU performance, so in the course of training batch_size is general set to 16.Because the difference between the samples is relatively small, we set base_lr to 0.01 and lr_policy to "inv" where gamma is set to 0.0001 and power is set to 0.75.

4. EXPERIMENT

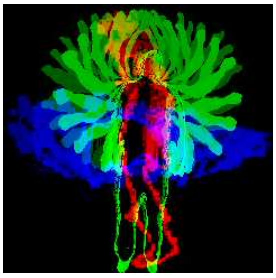

Fig4. MHI with three channels

In order to evaluate the performance of the classifier accurately, we use the self-made set, using cross-validation to test the classification of the results. The MHI is divided into five parts, one fifth is test set, three fifth is training set, and the remaining one fifth is verification set. The verification set and training set are mainly used to test the classification performance of HART-Net during training. The test set is used to test the performance of a classifier trained on RGB and RGBD samples in a real sample. For comparison, we use the projection of RGBD in the O-XY direction as a contour in the RGB.

Fig5.outline of the human body in RGB image

From the classification result of HART-Net, we can get the corresponding classification confusion matrix. Through the confusion matrix, we can see: For actions of drinking, eating, making phone call and reading book, the classifier performance trained by the RGBD sample is higher than the classifier trained by RGB by about 8%. But for actions of walking, waving, hand clapping and boxing, the classifier performance trained by RGBD is significantly better than the classifier trained by the RGB, because these three-dimensional characteristics of the action are more obvious. For RGBD, classifier training based on RGBD can get more information, so the classification performance will be better. Overall, the classifier performance training by the RGBD classification is higher than the classifier training by RGB classification by about 18%.

	Drinking	eating	making Phone C	reading book	walking	waving	hand clapping	boxing
Drinking	0.79	0.04	0.03	0.02	0.05	0.00	0.05	0.02
eating	0.03	0.83	0.02	0.04	0.02	0.01	0.03	0.02
making Phone Call	0.08	0.03	0.79	0.02	0.02	0.00	0.05	0.01
reading book	0.01	0.03	0.03	0.81	0.04	0.04	0.02	0.02
walking	0.01	0.03	0.02	0.04	0.70	0.04	0.11	0.05
waving	0.00	0.01	0.02	0.02	0.08	0.71	0.06	0.10
hand clapping	0.03	0.04	0.01	0.00	0.11	0.11	0.63	0.07
boxing	0.02	0.02	0.01	0.04	0.04	0.10	0.05	0.72

Fig7. Confusion matrix - RGBD

Fig6. Confusion matrix - RGB

	Drinking	eating	making Phone Call	reading book	walking	waving	hand clapping	boxing
Drinking	0.88	0.00	0.04	0.00	0.03	0.05	0.00	0.00
eating	0.00	0.89	0.02	0.02	0.01	0.05	0.01	0.00
making Phone Call	0.03	0.00	0.87	0.00	0.01	0.00	0.04	0.05
reading book	0.00	0.02	0.01	0.90	0.00	0.04	0.00	0.03
walking	0.03	0.02	0.04	0.02	0.83	0.01	0.03	0.02
waving	0.01	0.03	0.00	0.05	0.00	0.88	0.00	0.03
hand clapping	0.02	0.00	0.01	0.05	0.02	0.03	0.84	0.03
boxing	0.00	0.01	0.00	0.01	0.00	0.00	0.05	0.93

5. CONCLUSION

In this wok, we propose a human motion detection fork based on binocular vision. In speed, we can easily estimate the location of the human body according to face position or head and shoulder position .However, based on monocular human action recognition algorithm need to use motion information and graph cut algorithm to get the outline of human motion, so compared with monocular vision algorithm our algorithm has certain advantages in speed. In terms of applicability, our algorithm can be used outdoors, while algorithms based on structured light and time of flight can only be used indoors, and there is interference between devices, so our algorithm has the same advantage in the applicability.

REFERENCES

1. S. Birchfield. Elliptical head tracking using intensity gradients and color histograms. In *CVPR'98*, pages 232–237, Santa Barbara, CA, June 23-25, 1998.
2. M. Blank, L. Gorelick, E. Shechtman, M. Irani, and R. Basri. Actions as space-time shapes. In *ICCV'05, volume 2*, pages 1395–1402, Beijing, China, Oct. 17-21, 2005.
3. A. F. Bobick and J. W. Davis. The recognition of human movement using temporal templates. *IEEE Trans. Pattern Anal. Machine Intell.*, 23(3):257–267, Mar. 2001.
4. P. Dollar, V. Rabaud, G. Cottrell, and S. Belongie. Behavior recognition via sparse spatio-temporal features. In *VS-PETS'05*, pages 65–72, Beijing, Oct. 15-16, 2005
5. Frank Bignone, Olof Henricsson, Pascal Fua, et al. Automatic extraction of generichouse roofs fromhigh resolution aerial imagery. Proceedings of the 4th European Conference on Computer Vision: *Cambridge*, United Kingdom, Springer Verlag, 1996: 85-96
6. D. Marr, T. Poggio. Cooperative Computation of Stereo Disparity. Science，1976, 194: 209-236
7. Cordelia Schmid, Andrew Zisserman. The geometry and matching of curves in multiple views. *Proceedings of the 5th European Conference on Computer Vision*: Freiburg, Germany, Springer Verlag, 1998: 104-118
8. Boykov Y, Veksler O, Zabih R. Fast approximate energy minimization via graph cuts. *Pattern Analysis and Machine Intelligence*, *IEEE Transactions on*, 2001, 23(11): 1222-1239
9. Kolmogorov V, Zabih R. Computing visual correspondence with occlusions using graph cuts. Computer Vision, 2001 *ICCV 2001 Proceedings Eighth IEEE International Conference on. IEEE*, 2001, 2: 508-515
10. X. Sun, X. Mei, S.Jiao, et al. Stereo matching with reliable disparity propagation. *In Proc: 3DIMPVT*, 2011:132-139
11. Ohta Y, Kanade T. Stereo by intra-and inter-scan line search using dynamic programming. *Pattern Analysis and Machine Intelligence, IEEE Transactions on*, 1985, (2): 139-154
12. Ali A，Aggarwal J K． Segmentation and Recognition of ContinuousHuman Activity / / *Proc of the IEEE Workshop on Detection and Recognition of Events in Video*． Vancouver，Canada，2001: 28－35
13. Hanjalic A，Lagendijk RL，Biemond J. Automated High-LevelMovie Segmentation for Advanced Video-Retrieval Systems． *IEEE Trans on Circuits and Systems for Video Technology*， 1999， 9(4) : 580－588
14. Wang Jinjun，Xiao Jing． Human Behavior Segmentation and Recognition Using Continuous Linear Dynamic Systems / / *Proc of the IEEE Workshop on Application of Computer Vision*． Tampa， USA，2013: 61－67
15. Qinfeng Shi, Li Wang, Li Cheng，et al. Discriminative Human Action Segmentation and Recognition Using Semi-Markov Model. 2013 － 3 － 17. http: / /ieeexplore. ieee.org/stamp/ stamp.jsp? tp=＆arnumber=4587557
16. Gagalowicz A，Quah C K. 3D Model-Based Marker-Less Human Motion Tracking in Cluttered Environment / / *Proc of the IEEE 12th International Conference on Computer Vision Workshops*． Kyoto, Japan, 2009: 1042－1049
17. Bobick A F, Wilson A D. A State-Based Approach to the Representation and Recognition of Gesture. *IEEE Trans on Pattern Analysis and Machine Intelligence*, 1997, 19(12) : 1325－1337

Analysis and Control of a Novel 4D Chaotic System

Hong Niu
College of Electronic Information and Automation, Tianjin University of Science & Technology
80 Mailbox, Tianjin University of Science & Technology, No. 1038 Dagu Nanlu, Hexi District, Tianjin, China 300222
E-mail: spots@163.com
www.tust.edu.cn

Abstract

In this paper, a novel four-dimensional (4D) autonomous chaotic system is presented. For chaos control of the 4D system, a linear feedback controller only with one variable is designed via matching the variable coefficients of the Lyapunov function, so that the system is no longer chaotic or periodic but globally asymptotically converges to the equilibrium point at the origin. The numerical simulation results are given to illustrate the feasibility and effectiveness of the method.

Keywords: the novel 4D chaotic system; chaos control; Lyapunov function with variable coefficients; global asymptotic stability

1. Introduction

In 1963, Edward Lorenz developed a simplified mathematical model for atmospheric convection,[1] which is a three-dimensional(3D) autonomous system and well known as the Lorenz system. Since then, many 3D chaotic systems have been proposed, such as the unified system[2], the Qi system[3] and so on. With the wide application of chaotic characteristics in secure communication and other fields, the complexity of chaotic systems is increasing. Four and higher dimensional chaotic systems have been investigated. [4-6] In this paper, a novel 4D chaotic system is presented.

Chaos control is one of the major subjects in chaos study, and the feedback control is a common method in chaos control. [7-10] In this paper, the aim of chaos control is to design a linear feedback controller and make the novel 4D chaotic system no longer chaotic or periodic but globally asymptotically stable at the origin.

The rest of this paper is organized as follows. In Section 2, the model of the novel 4D chaotic system and its simulation phase portraits are given. In Section 3, a Lyapunov function with variable coefficients is selected to design a linear feedback controller only with one feedback variable and prove the global asymptotic stability of the controlled 4D system. Some simulation results are given to demonstrate the validity of the linear feedback controller. The conclusions are drawn in Section 4.

2. The Novel 4D Chaotic System

The dynamic equations of the novel 4D chaotic system are formulated as

$$\begin{aligned} \dot{x} &= a(y-x), \\ \dot{y} &= c(x+y)+z-xw, \\ \dot{z} &= mx-y-hz, \\ \dot{w} &= xy-bw, \end{aligned} \tag{1}$$

where $x, y, z, w \in \mathbb{R}$ are state variables, and a = 25, b = 3, c = 18, m = 19 and h = 14.

Let the initial values of the 4D system (1) be (x_0, y_0, z_0, w_0) = (1, 1, 1, 1), then the Lyapunov exponents respectively are $\lambda_1 = 2.6686 > 0$,

$\lambda_2 = 0.0003 \approx 0$, $\lambda_3 = -11.7885 < 0$ and $\lambda_4 = -14.8804 < 0$. It indicates that the system (1) is chaotic. The phase portraits of the 4D system (1) are shown in Fig. 1(a1)-(a3).

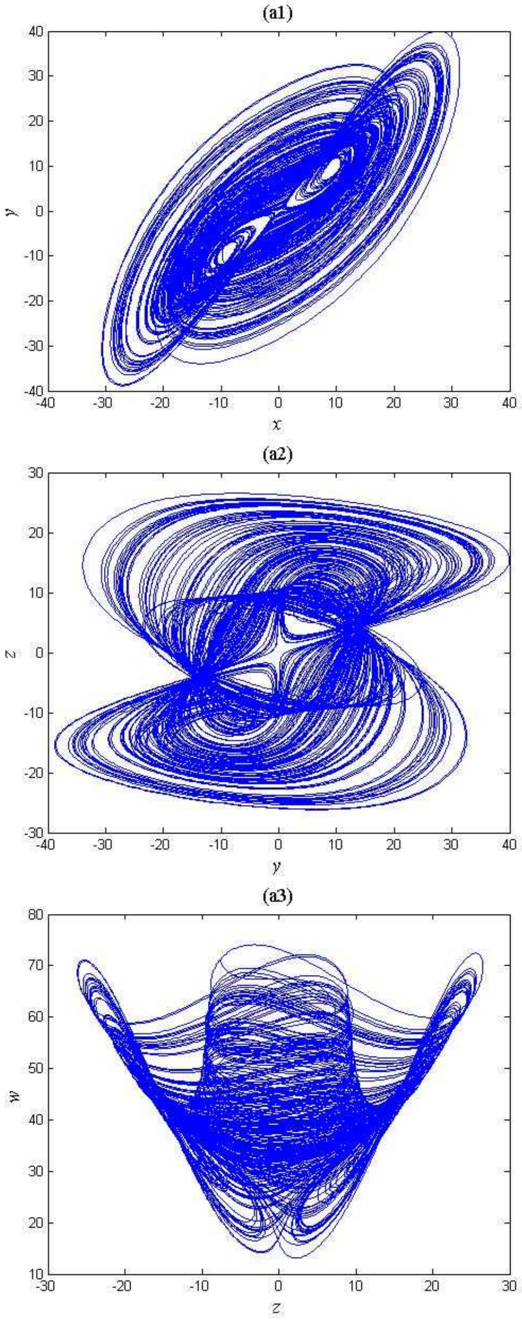

Fig. 1. Phase portraits of the novel 4D chaotic system: (a1) *x-y* (a2) *y-z* (a3) *z-w*

3. Chaos Control of the 4D Chaotic System

3.1. *Formulation of the controlled system*

Let $\tilde{\boldsymbol{X}} = \boldsymbol{X} - \mathbf{O} = \begin{bmatrix} \tilde{x} & \tilde{y} & \tilde{z} & \tilde{w} \end{bmatrix}^{\mathrm{T}}$ be the controlled state vector, where $\boldsymbol{X} = \begin{bmatrix} x & y & z & w \end{bmatrix}^{\mathrm{T}}$ is the state vector of the system (1), and $\mathbf{O} = \begin{bmatrix} 0 & 0 & 0 & 0 \end{bmatrix}^{\mathrm{T}}$ is the origin. Then, the controlled system can be represented as

$$\begin{aligned} \dot{\tilde{x}} &= a(\tilde{y} - \tilde{x}) + u_{c1}, \\ \dot{\tilde{y}} &= c(\tilde{x} + \tilde{y}) + \tilde{z} - \tilde{x}\tilde{w} + u_{c2}, \\ \dot{\tilde{z}} &= m\tilde{x} - \tilde{y} - h\tilde{z} + u_{c3}, \\ \dot{\tilde{w}} &= \tilde{x}\tilde{y} - b\tilde{w} + u_{c4}, \end{aligned} \tag{2}$$

where

$$\begin{aligned} \boldsymbol{u}_{\mathrm{c}} &= \begin{bmatrix} u_{c1} & u_{c2} & u_{c3} & u_{c4} \end{bmatrix}^{\mathrm{T}} \\ &= \begin{bmatrix} -k_1\tilde{x} & -k_2\tilde{y} & -k_3\tilde{z} & -k_4\tilde{w} \end{bmatrix}^{\mathrm{T}}, k_1, \cdots, k_4 \geq 0 \end{aligned} \tag{3}$$

is the linear feedback controller to be designed.

3.2. *Design of the controller*

Convert Eq. (2) to a state-space model which is expressed as

$$\dot{\tilde{\boldsymbol{X}}} = A\tilde{\boldsymbol{X}} + \boldsymbol{g}(\tilde{\boldsymbol{X}}), \tag{4}$$

where

$$A = \begin{bmatrix} -(k_1 + a) & a & 0 & 0 \\ c & -(k_2 - c) & 1 & 0 \\ m & -1 & -(k_3 + h) & 0 \\ 0 & 0 & 0 & -(k_4 + b) \end{bmatrix},$$

and $\boldsymbol{g}(\tilde{\boldsymbol{X}}) = \begin{bmatrix} 0 & -\tilde{x}\tilde{w} & 0 & \tilde{x}\tilde{y} \end{bmatrix}^{\mathrm{T}}$.

Take a positive definite function

$$\mathrm{V}(\tilde{\boldsymbol{X}}) = \frac{1}{2}\tilde{\boldsymbol{X}}^{\mathrm{T}} P \tilde{\boldsymbol{X}}$$

as a Lyapunov function candidate for the system (4), where

$$P = \begin{bmatrix} n_1 & 0 & 0 & 0 \\ 0 & n_2 & 0 & 0 \\ 0 & 0 & n_3 & 0 \\ 0 & 0 & 0 & n_4 \end{bmatrix}, n_1, n_2, n_3, n_4 > 0.$$

Then, the derivative $\dot{\mathrm{V}}(\tilde{\boldsymbol{X}})$ is given by

$$\dot{V}\left(\tilde{\boldsymbol{X}}\right)=\frac{1}{2}\tilde{\boldsymbol{X}}^{\mathrm{T}}\left(A^{\mathrm{T}}P+PA\right)\tilde{\boldsymbol{X}} \\ +\frac{1}{2}\left[\boldsymbol{g}^{\mathrm{T}}\left(\tilde{\boldsymbol{X}}\right)P\tilde{\boldsymbol{X}}+\tilde{\boldsymbol{X}}^{\mathrm{T}}P\boldsymbol{g}\left(\tilde{\boldsymbol{X}}\right)\right] \\ =\frac{1}{2}\tilde{\boldsymbol{X}}^{\mathrm{T}}Q\tilde{\boldsymbol{X}}+\left(n_4-n_2\right)\tilde{x}\tilde{y}\tilde{w}, \tag{5}$$

where

$$Q=\begin{bmatrix} q_{11} & q_{12} & q_{13} & 0 \\ q_{21} & q_{22} & q_{23} & 0 \\ q_{31} & q_{32} & q_{33} & 0 \\ 0 & 0 & 0 & q_{44} \end{bmatrix},$$

$$q_{11}=-2n_1\left(k_1+a\right),$$
$$q_{22}=-2n_2\left(k_2-c\right),$$
$$q_{33}=-2n_3\left(k_3+h\right),$$
$$q_{44}=-2n_4\left(k_4+b\right),$$
$$q_{12}=q_{21}=an_1+cn_2,$$
$$q_{13}=q_{31}=mn_3,$$
$$q_{23}=q_{32}=n_2-n_3.$$

Let $n_4 = n_2$, then Eq. (5) is simplified as

$$\dot{V}\left(\tilde{\boldsymbol{X}}\right)=\frac{1}{2}\tilde{\boldsymbol{X}}^{\mathrm{T}}Q\tilde{\boldsymbol{X}}.$$

For the derivative $\dot{V}\left(\tilde{\boldsymbol{X}}\right)$ to be negative definite, the leading principal minors of the matrix Q must satisfy

$$\sigma_1=-2n_1\left(k_1+a\right)<0, \tag{6}$$

$$\sigma_2=4n_1n_2\left(k_1+a\right)\left(k_2-c\right) \\ -\left(an_1+cn_2\right)^2>0, \tag{7}$$

$$\sigma_3=-8n_1n_2n_3\left(k_1+a\right)\left(k_2-c\right)\left(k_3+h\right) \\ +2mn_3\left(an_1+cn_2\right)\left(n_2-n_3\right) \\ +2n_2m^2n_3^2\left(k_2-c\right) \\ +2n_3\left(k_3+h\right)\left(an_1+cn_2\right)^2 \\ +2n_1\left(k_1+a\right)\left(n_2-n_3\right)^2<0, \tag{8}$$

$$\sigma_4=-2n_2\left(k_4+b\right)\sigma_3>0. \tag{9}$$

From Eq. (6), k_1 should satisfy $k_1 > -a$. Let $k_1 = 0$ and substitute it into Eq. (7), then k_2 should satisfy

$$k_2>\frac{\left(an_1+cn_2\right)^2}{4an_1n_2}+c. \tag{10}$$

Assume that the minimum number of the feedback variables might be equal to the number of the positive Lyapunov exponents.[11] The 4D chaotic system (1) only has one positive Lyapunov exponent and $k_2 \neq 0$ as shown in Eq. (10), so let $k_3 = 0$ and substitute $k_1 = k_3 = 0$ into Eq. (8). It is obtained that

$$\sigma_3=-8ahn_1n_2n_3\left(k_2-c\right) \\ +2mn_3\left(an_1+cn_2\right)\left(n_2-n_3\right) \\ +2n_2m^2n_3^2\left(k_2-c\right)+2hn_3\left(an_1+cn_2\right)^2 \\ +2an_1\left(n_2-n_3\right)^2<0. \tag{11}$$

Let $n_1 = n_2 = n_3$. From Eq. (11), k_2 should satisfy

$$k_2>\frac{h\left(a+c\right)^2}{4ah-m^2}+c, \tag{12}$$

so that Eq. (9) is satisfied as long as $k_4 > -b$. Hence, let $k_4 = 0$.

For $\dot{V}\left(\tilde{\boldsymbol{X}}\right)$ to be negative definite, k_2 should satisfy both Eq. (10) and Eq.(12). It means that

$$k_2>\frac{h\left(a+c\right)^2}{4ah-m^2}+c>\frac{\left(a+c\right)^2}{4a}+c,$$

when $n_1 = n_2 = n_3 = n_4$. Consequently, let $k_2 = 45$. As a result, because the derivative $\dot{V}\left(\tilde{\boldsymbol{X}}\right)$ is negative definite and the Lyapunov function $V\left(\tilde{\boldsymbol{X}}\right)$ is positive definite and radially unbounded, it can be confirmed that the controlled system (2) is globally asymptotically stable at the origin.

Substituting $k_2 = 45$ and $k_1 = k_3 = k_4 = 0$ into Eq. (3) yields

$$\boldsymbol{u}_{\mathrm{c}}=\left[u_{\mathrm{c}1}\quad u_{\mathrm{c}2}\quad u_{\mathrm{c}3}\quad u_{\mathrm{c}4}\right]^{\mathrm{T}} \\ =\left[0\quad -45\tilde{y}\quad 0\quad 0\right]^{\mathrm{T}}. \tag{13}$$

3.3. *Numerical simulation*

Substitute Eq. (13) into Eq. (2) and let the initial values still be $\left(\tilde{x}_0,\tilde{y}_0,\tilde{z}_0,\tilde{w}_0\right)=\left(1,1,1,1\right)$, then the Lyapunov exponents of the controlled system (2) respectively are $\lambda_{c1}=-3.0397$, $\lambda_{c2}=-3.7495$, $\lambda_{c3}=-15.3788$ and $\lambda_{c4}=-46.8316$, which are all negative. It implies that the controlled system (2) is no longer chaotic or periodic but stable at the origin.

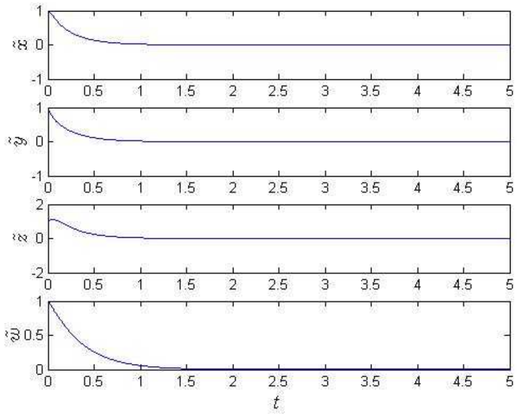

Fig. 2. Curves of the state variables of the controlled system

The curves of the state variables of the controlled system (2) are shown in Fig. 2. The horizontal axis t expresses the solution interval of differential equations, so t is a dimensionless quantity. From Fig. 2, it can be seen that the state variables $\tilde{x}$, $\tilde{y}$, $\tilde{z}$ and $\tilde{w}$ converge to zero asymptotically and rapidly. It illustrates that the controller (13) is feasible and effective for chaos control of the novel 4D chaotic system (1).

4. Conclusions

In this paper, a novel 4D chaotic system is presented. The model of the 4D system and its chaotic attractor are complex and could be applied to secure communication. For chaos control of the 4D chaotic system, different groups of the coefficients of the Lyapunov function yield different linear feedback controllers. It makes the form and parameters of the linear feedback controller flexible to select. The linear feedback controller designed in this paper only has one feedback variable, so that it is easy to implement via circuit. Furthermore, the centers of the state variables of the 4D chaotic system have been translated to the origin before the controlled system is formulated. It means that this method can be used to make the system globally asymptotically converge to any point or even some specified states via center translation. Thus, this method could be applied to chaos synchronization of the novel 4D chaotic systems. It would be discussed in another paper. The study in this paper has some engineering significance.

References

1. E. N. Lorenz, Deterministic nonperiodic flow, *Journal of the atmospheric sciences* **20**(2) (1963) 130–141.
2. J. H. Lü, G. R. Chen, D. Z. Cheng and S. Celikovsky, Bridge the gap between the Lorenz system and the Chen system, *International Journal of Bifurcation and Chaos* **12**(12) (2002) 2917–2926.
3. G. Y. Qi, G. R. Chen, S. Z. Du, Z. Q. Chen and Z. Z. Yuan, Analysis of a new chaotic system, *Physica* A **352**(2) (2005) 295–308.
4. Y. Lin, C. H. Wang, H. Z. He and L. L. Zhou, A novel four-wing non-equilibrium chaotic system and its circuit implementation, *Pramana–Journal of Physics* **86**(4) (2016) 801–807.
5. F. R. Tahir, R. S. Ali, V. -T. Pham, A. Buscarino, M. Frasca and L. Fortuna, A novel 4D autonomous 2*n*-butterfly wing chaotic attractor, *Nonlinear Dynamics* **85**(4) (2016) 2665–2671.
6. C. H. Wang, H. Xu and F. Yu, A novel approach for constructing high-order Chua's circuit with multi-directional multi-scroll chaotic attractors, *International Journal of Bifurcation and Chaos* **23**(2) (2013) 1350022–1–10.
7. J. X. Zhang and W. S. Tang, Analysis and control for a new chaotic system via piecewise linear feedback, *Chaos, Solitons & Fractals* **42**(4) (2009) 2181–2190.
8. T. Sangpet and S. Kuntanapreeda, Output feedback control of unified chaotic systems based on feedback passivity, *International Journal of Bifurcation and Chaos* **20**(5) (2010) 1519–1525.
9. C. J. Xu and Q. M. Zhang, On the chaos control of the Qi system, *Journal of Engineering Mathematics* **90**(1) (2015) 67–81.
10. H. Niu, Stability control and circuit implementation of a novel 3D chaotic system with variable coefficient, *Dynamical Systems and Control* **5**(1) (2016) 31–40.
11. B. Z. Liu and J. H. Peng, *Nonlinear Dynamics* (Higher Education Press, Beijing, 2007).

Analysis of a three-dimensional chaotic system and its FPGA implementation

Hefei Li[1], Xianghui Hu[1]

[1] Tianjin University of Science and Technology,
1038 Dagunanlu Road, Hexi District, Tianjin, 300222, China
E-mail: 1027755628 @qq.com
www.tust.edu.cn

Abstract

In this letter a three-dimensional chaotic system is implemented based on Field Programmable Gate Array (FPGA). The 3-D chaotic system has a very complex chaotic characteristic with its a real four-wing chaotic attractor. By means of numerical simulation, phase orbits, bifurcation diagram and Lyapunov exponents are given and analyzed to observe dynamic characteristics of the three-dimensional chaotic system. Numerical simulation and the results of implementation in FPGA show that this chaotic system really has many obvious characteristics of chaos.

Keywords: three-dimensional chaotic system, bifurcation diagram Lyapunov exponents, FPGA

1. Introduction

Lorenz system[1] was proposed as the first chaotic system in year 1963, which created a precedent for the study of chaotic systems. Later, scholars and researchers began to do a lot of research on the chaotic system and found and put forward many new chaotic systems. Such as Chen system[2], Lü system[3], Chua system[4] and so on. The research on chaotic characteristics can be used in many application areas, such secure communication[5], image encryption[6] and etc.

Lü system was proposed in year 2002 by Lü et.al to be a novel chaotic system with its unique chaotic characteristics different from other chaotic systems. After then, many research began to be done on Lü system. A hybrid TS fuzzy modeling was proposed approach for the newly coined chaotic Lü system in[7]. A new hyper chaotic attractor coined from the chaotic Lü system was reported by using a state feedback controller, and theoretical analyses and simulation experiments are conducted to investigate the dynamical behavior of the proposed hyper chaotic system in[8]. A new three-dimensional chaotic system, named as generalized augmented Lü system, was proposed in[9] by using the method of anti-control chaos.

In this paper, the chaotic characteristics of the integer order generalized augmented Lü system is analyzed by means of phase orbits, bifurcation diagram and Lyapunov exponents. The uniqueness of this chaotic system is that it implements a real four-wing attractor with compound structure and contains two mirrored symmetrical sub-system. A circuit is designed based on DSP Builder in FPGA to implement and observe the real four-wing chaotic attractor. Numerical simulation and the results of implementation in FPGA show that this chaotic system really has many obvious characteristics of chaos.

2. Analysis of the generalized augmented Lü system

The dynamical system of the generalized augmented Lü system is described as following,

$$\begin{cases} \dot{x} = -[ab/(a+b)]x - yz \\ \dot{y} = ay + xz \\ \dot{z} = bz + xy + cx \end{cases} \tag{1}$$

Where the system parameters a, b are negative real constants, and c is a real constant.

2.1 Chaotic attractor of the system

For the system (1), when the parameters $a = -10$, $b = -4$, $c = 1$ and the initial state $[1, 2, 3]^T$, it is chaotic and has a real three dimensional four-wing chaotic attractor as shown in Fig.1.(1)and Fig.1.(2).

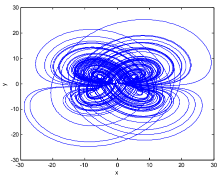

Fig.1. (1) x-y plane

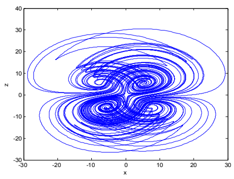

Fig.1. (2) x-z plane

Fig.1 a real four-wing chaotic attractor of system (1): the parameters $a = -10$, $b = -4$, $c = 1$ and the initial state $[1, 2, 3]^T$.

2.2 Dynamics analysis of the system

Bifurcation diagram and Lyapunov exponents can well reflect the dynamic characteristics of the system. So we mainly observe the Bifurcation diagram and Lyapunov exponents of the system to analyze the dynamic behavior of the system. As shown in the following Figs, the Bifurcation diagram and Lyapunov exponents are given varying the parameters a or b.

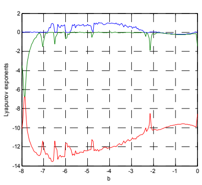

Fig.2(1)Lyapunov exponents

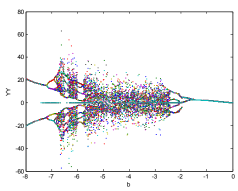

Fig.2(2)Bifurcation diagram

Fig.2 Lyapunov exponents and Bifurcation diagram of system (1): parameters value $a = -10$, $c = 1$, $b \in [-8, 0]$ and the initial state $[1, 2, 3]^T$.

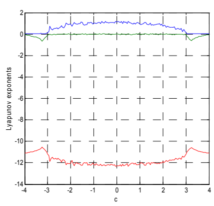

Fig.3(1)Lyapunov exponents

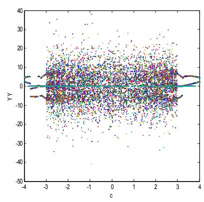

Fig.3 (2) Bifurcation diagram

Fig.3 Lyapunov exponents and Bifurcation diagram of system (1): parameters value $a = -10$, $b = -4$, $c \in [-4, 4]$ and the initial state $[1, 2, 3]^T$.

From the Lyapunov exponents shown in Fig.2(1) and Fig.3(1), there is only a single positive Lyapunov within a certain interval respectively, which shows that the system is chaotic. The corresponding Bifurcation diagram also indicates the system exists chaos. Especially, as shown in Fig. 2(1), the Lyapunov exponents is almost symmetrical on the origin. In fact, when we set $a = -10$, $b = -4$, $c = -1$, a four-wing chaotic attractor can also be obtained and it has the same topological structure with the chaotic attractor shown in Fig. 1. But the difference is that it mirrored changes in the direction of the corresponding plane through the chaotic trajectory.

3. FPGA realization of chaotic attractor

In this paper, the method of Field Programmable Gate Array is applied to implement the chaotic attractor of system (1). This is a method similar to analog circuits that the chaotic system can be shown in oscilloscope. A chaotic circuit is designed by applying the DSP Builder module based on the system (1) as shown in Fig. 4. And then, the chaotic circuit is derived as V-HDL language that will be download to FPGA development board. Here, the main chip of the FPGA development board is EP3C25Q240C8N. The adders, delays, multipliers, amplifiers and data selectors in circuit come from the DSP Builder module and the digital integrator is designed in Fig.4(1) . As shown in Fig.4(2), the obtained discrete digital signal is converted to analog signal by high speed D/A, and two of the three singles are inputted in the oscilloscope. By this method, we can obtain the chaotic attractor shown in Fig.5(1)and Fig.5(2) which are the same as the chaotic attractor shown in Fig.1(1) and . Fig.1(2).

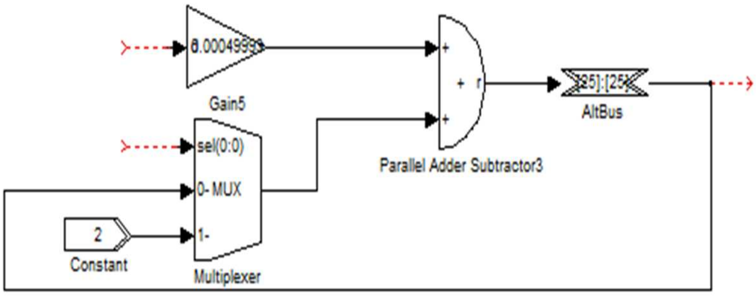

Fig.4(1) circuit of the digital integrator

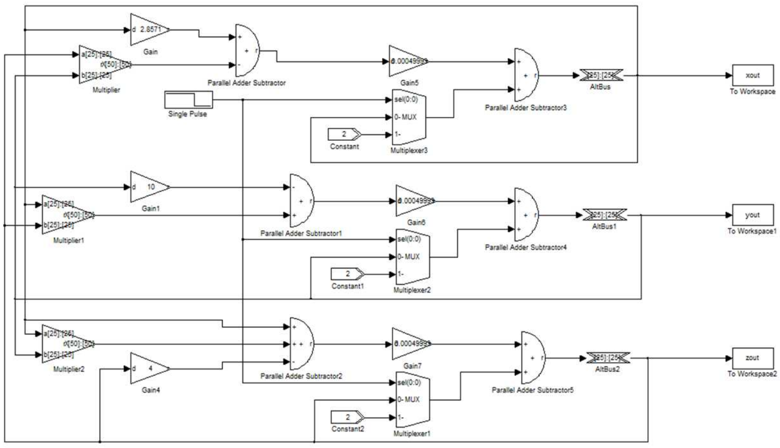

Fig.4(2) circuit of the system(1)

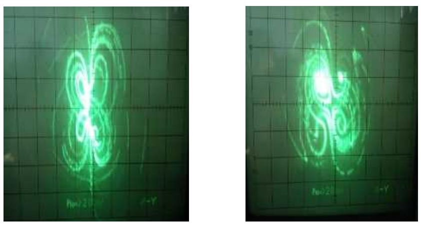

Fig.5(1)x-y plane Fig.5 (2) x-z plane

Fig.5 attractor obtained by the circuit

4. Conclusion

In this paper, the chaotic characteristics and dynamic behaviors of a three-dimensional chaotic system is analyzed by the method of bifurcation diagram and Lyapunov exponents. The oretical analysis and numerical simulation are applied to analysis the characteristics of the generalized augmented Lü system. In the last section, a method is applied based on FPGA and EDA tool to realize the chaotic attractor of the generalized augmented Lü system.The numerical simulation results and experimental results are completely consistent, showing that this method is practical and can be used in other chaotic system.

References

1. Lorenz E N, Deterministic non-periodic follow, Journal of Atmospheric Sciences. 20(2) (1963) 130-141.
2. Chen G R, Ueta T, Yet another chaotic attractor, International Journal of Bifurcation and Chaos. 9 (1999) 1465-1466.
3. Jinhu Lu, Guanrong Chen, A new chaotic attractor coined, International Journal of Bifurcation and Chaos. 12 (2002) 659-661.
4. Guanrong Chen, Yaobin Mao, Charles K. Chui, A symmetric image encryption scheme based on 3D chaotic cat maps, Chaos, Solitons and Fractals, 21 (2004) 749–761.
5. Dequan Li, TS fuzzy realization of chaotic Lü system, Physics Letters A, 356 (2006) 51–58.
6. Bocheng Bao, Zhong Liu, A Hyperchaotic Attractor Coined from Chaotic Lü System, Chinese Physics Letters, 7(25) (2008) 2396-2399.
7. Qiao XiaoHua, BaoBoCheng, Three-dimensional four-wing generalized augmented Lu system, ACTA PHYSICA SINICA, 12(58) (2009) 8152-8159.
8. Itoh Makoto, Chua, Leon O,MEMRISTOR OSCILLATORS, INTERNATIONAL JOURNAL OF BIFURCATION AND CHAOS, 11(18) (2008) 3183-3206.
9. Xiangjun Wu, Hui Wang, Hongtao Lu, Modified generalized projective synchronization of a new fractional-order hyper chaotic system and its application to secure communication. Nonlinear Analysis: Real World Applications, 13 (2012) 1441–1450.

Image Encryption Based on Fractional-order Chaotic Model of PMSM

Wei Xue*, Mei Zhang#, Shilong Liu, Xue Li
Department of Automation, Tianjin University of Science and Technology,
1038 Dagunanlu Road, Hexi District, Tianjin 300222, PR China

E-mail: xuewei@tust.edu.cn; # zhangmeifuwei@163.com*
www.tust.edu.cn

Abstract

The permanent magnet synchronous motor (PMSM) is a nonlinear system with multi-variable and significant coupling. When PMSM works in certain conditions, the chaotic behavior will occur. In this paper, the application of image encryption based on fractional-order chaotic model of PMSM is investigated. By the mean of drawing histogram, adjacent pixels correlation, key sensitivity of the cipher-text were analyzed. The results show that image encryption based on fractional-order chaotic model of PMSM have a large key space and high security.

Keywords: Fractional-order chaotic model; Permanent magnet synchronous motor（PMSM）; Image encryption; Algorithm.

1. Introduction

In the nonlinear system described by the equation of state, when motion of the system is far from the equilibrium state, with the changing of the system parameters, the dynamic behavior of the system enter into the dissipative structure state with time-space order and symmetry through bifurcation or chaotic state more disorder.[1] In recent years, many new chaotic systems have been proposed.[2-8] In 1999, the Chen system was successfully constructed by Chen et al.[3] In 2002, the Lü system was further discovered by Lü et al.[4] In 2003, Liu et al. discovered a three-dimensional continuous autonomous chaotic system of four-helical chaotic attractors, named as Liu system.[5] In 2005, a new four-wing autonomous chaotic system, the Qi system was proposed by Qi et al.[6-8] Those researches have made great progress in chaotic dynamics analysis. When the chaotic system is described by fractional-order model, the system can still show the chaotic state, it is found that the fractional-order chaotic model can accurately describe the real physical phenomena.[9-10] Some practical nonlinear systems are chaotic in the process of operation sometime. For example, there has chaotic behavior in permanent magnet synchronous motor (PMSM) when it works under certain condition.[11-12] Some scholars have studied the fractional-order chaotic model of PMSM.[13-14] As the fractional-order increases, the PMSM system enters the chaotic motion through the fixed point and quasi-periodic state.[15] In general, the existence of chaos is harmful in the actual systems, it is controlled to eliminate its chaotic behavior. But the chaotic characteristics have good effects in some aspects, we can use chaotic characteristics to achieve secure communication and image encryption.

The basic theoretical research of chaotic dynamics has been great development in the field of confidential communication and image encryption. Fractional-order chaotic system provides more key parameters for the encryption algorithm and increases the key space, in order to improve the security of the system.[16] Digital image pixel location scrambling is an important encryption method, the characteristics of the histogram are not changed, it also reflects the information system and memory the information. In addition, the nonlinearity and complexity are enhanced by the fractional-order chaotic system, which increases the key space. By the mean value of histogram, the correlation of adjacent pixels and the key sensitivity of cipher-text, the image encryption effect based on the fractional-order chaotic model of PMSM is analyzed in this paper.

2. Numerical analysis of fractional–order chaotic model of PMSM

The fractional-order PMSM chaotic model is as follow: [17-18]

$$\begin{cases} D^{\alpha} x = -x + zy \\ D^{\alpha} y = -y - xz + \gamma z \\ D^{\alpha} z = \sigma (y - z) \end{cases} \quad (1)$$

Where the dimensionless state variables x, y, z represent the stator current, the rotator current and the mechanical angular velocity respectively; σ and γ is the system parameters related to the motor damping and permanent flux; $\alpha \in (0,1]$ is the fractional order.

When $\alpha = 0.95, \sigma = 20$, and $\gamma = 300$, phase portraits are shown in Fig.1. Lyapunov exponent spectrum is shown in Fig.2.

It is showed clearly that system (1) has complex dynamic characteristics.

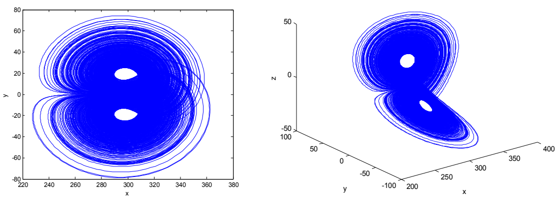

(a) (b)

Fig.1 Phase portraits of system (1) with $\alpha = 0.95, \sigma = 20$, and $\gamma = 300$: (a) $x - y$;(b) $x - y - z$.

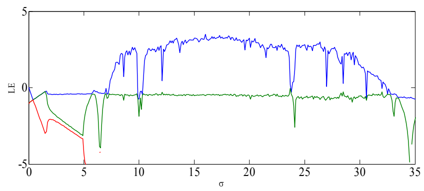

Fig.2 Lyapunov exponent spectrum of system

3. Application of fractional-order chaotic model of PMSM in image encryption

A message is called a plaintext, in order to hide content, the process of concealing messages in some way is called encryption. Encrypted messages are called cipher-text, and the process of converting cipher-text to plaintext is called decryption. Digital image pixel location scrambling change is an important document encryption method. Color images are described by R, G and B primary color, and it stores in a matrix format of $m \times n \times 3$ in computer. Fractional-order chaotic model of PMSM is a system with three state variables, the y chaotic sequence is used to perform one-dimensional time-domain scrambling sequence on the digital image. And then the three-dimensional sequence matrix is used to realize the spatial encryption algorithm by performing XOR operation. Encryption flow chart is shown in Fig.3, decryption flow chart is shown in Fig.4.

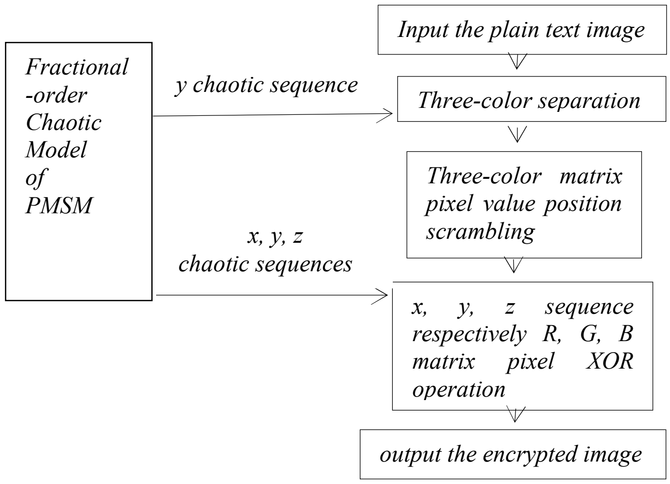

Fig.3 Encryption flow chart

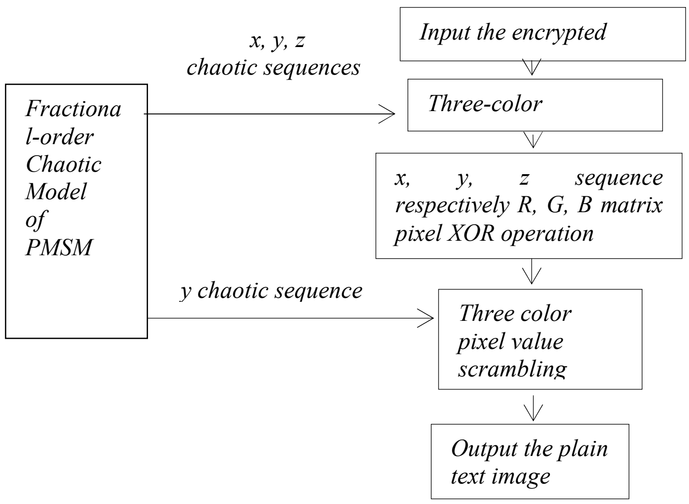

Fig.4 Decryption flow chart

3.1. Encryption process

The system (1) parameters are still chosen as $\alpha = 0.95$, $\sigma = 20$, and $\gamma = 300$,the initial states are assumed as $x_0 = 0.1$, $y_0 = 0.2$, $z_0 = 0.3$, then the digital image is encrypted. The encryption process steps are as follows:

1）The plain text is divided into three primary colors: R component image, G component image and B component image. The results are shown in Fig.5.

Fig.5 Separate images

2) The y sequence is sorted to obtain a sequence $y\_$ change, and then transform R, G, B corresponding components. After that, the R, G and B components of color image are calculated by using chaotic sequences. Due to space constraints, here only the encryption result of the G component is given. The result of the encryption of G component is shown in Fig.6.

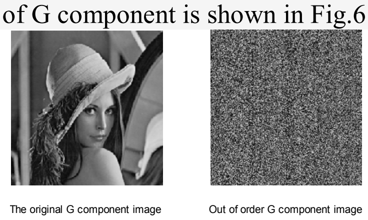

Fig.6 Spatial domain XOR results

3) The encrypted three-color matrix is used to synthesize the encrypted image. The result is shown in Fig.7.

Fig.7 Encryption results of the original image

3.2. Decryption process

The image decryption process based on system (1) is the reverse operation of its encryption. And the plaintext will not repeat. Decryption result is shown in Fig.8.

Fig.8 Decryption results of the original image

3.3. Algorithm security analysis

3.3.1. Histogram analysis

Fig.9 is the gray histogram of G component. It can be seen from the figure: Before encryption, the pixel distribution is obvious in each gray level, the difference between the highest point and the lowest point is very large; after encryption, the number of pixels is almost the same, and the frequency of the pixels is basically the same in each gray level. The pixel distribution of the original image is hidden in a large degree, which can be a good resistance to the statistic.

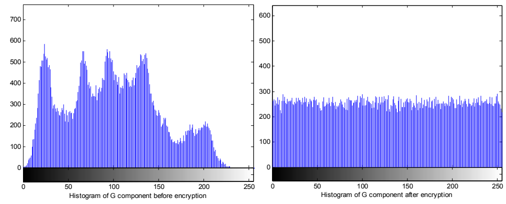

Fig.9 Each color component histogram

3.3.2. Adjacent pixel correlation analysis

One row and one column of pixels are selected from the original image and the encrypted image. The correlation coefficients of its adjacent pixels are calculated in Tab.1. The encryption algorithm of this method has good performance of diffusion and aliasing, and the encryption algorithm of fractional-order chaotic model of PMSM has better security for statistical analysis attacks.

Tab.1 The correlation of adjacent pixels

Different directions / Different images	Horizontal direction	Vertical direction
The original image R pixel matrix	0.97303	0.97327
Encrypted image R pixel matrix	0.0025357	0.00088599
The original image G pixel matrix	0.9753	0.97538
Encrypted image G pixel matrix	0.00036788	0.00060489
The original image B pixel matrix	0.98807	0.98861
Encrypted image B pixel matrix	0.00068514	0.00061357

3.3.3. Key sensitivity analysis

Given the system (1) parameter: $\alpha = 0.95, \sigma = 20$, and $\gamma = 300$. When the initial states are assumed as $x_0 = 0.1$, $y_0 = 0.2$, $z_0 = 0.3$ to the system key, the image is encrypted. When the correct key is input, the decrypted image can be obtained successfully. If we change the initial value as $x_0 = 0.100000000001$ and the other parameter values are unchanged, the image decryptions fail. Unsuccessful decryption results are shown in Fig.10. As long as the key changes, the original figure can not be decrypted. This shows that the sensitivity of the encryption system on the key requirements is high.

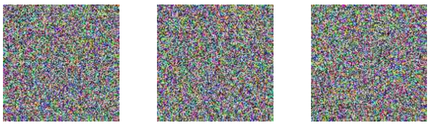

Fig.10 Decryption results of the wrong key

4. Conclusion

In this paper, the fractional-order chaotic model of PMSM is used as the key to encrypt the digital image. The phase trajectories and Lyapunov exponent spectrum of fractional-order chaotic model of PMSM are drawn. Furthermore, the chaotic model is applied to image encryption, and the flow chart of image encryption and decryption process are given. By means of histogram, adjacent pixel correlation and key sensitivity, the cipher-text is analyzed. The results show that the digital image encryption algorithm based on the fractional-order chaotic model of PMSM has the characteristics of large key space and high security, and indicates that it is feasible and effective to use the model for image encryption.

5. Acknowledgement

This work is supported by the Young Scientists Fund of the National Natural Science Foundation of China (Grant No.11202148).

6. References

1. Wang Lidong, Xing Xiuying, Chu Zhenyan. On definitions of chaos in discrete dynamical system. *Hunan: IEEE computer society*, 2008:2874-2878.
2. Chen G, Lai D. Feedback control of Lyapunov exponents from discrete-time dynamical systems. *Int. J. Bifurcation and Chaos*, 1996, 6(7):1341-1349.
3. Chen G R and Ueta T. Yet another chaotic attractor. *Int. J. Bifurcation and Chaos*, 1999,9 (7):1465−1466.
4. Lü J G. Chaotic dynamics of the fractional order Lü system and its synchronization. *Physics Letters A*. 2006, 59(4): 305-311.
5. Lü Jinhu, Chen Guangrong. A new chaotic attractor coined. *International journal of bifurcation & Chaos*, 2002, 12(3):659-661.
6. Qi G, Du S, Chen G, et al. On a 4-dimensional chaotic system. *Chaos Solitons & Fractals*, 2005, 23(5): 1671-1682.
7. Qi G, Du S, Chen G, Zhang Y. Analysis and circuit implementation of a new 4-D chaotic system. *Physic Letters A*, 2006, 352(4):386-397.
8. Qi G, Chen G, Li S, Zhang Y. Four-wing attractors: from pseudo to real. *International Journal of Bifurcation & Chaos*, 2006, 16(4): 859-885.
9. Lü J H, Chen G R. A new chaotic attractor coined. *International Journal of Bifurcation and Chaos*, 2002, 12(3):659-661.
10. Liu C X, Liu L, Liu T et al. A new butterfly-shaped attractor of Lorenz-like system. *Chaos, Solitons and Fractals*, 2006, 28(5):1196-1203.
11. Zhang Bo, Li Zhong, Mao Zongyun, Pang Minxi. A primary study on an erratic behavior and chaotic phenomena of electric machine drive systems, *Proceedings of the CSEE*, 2001, 21(7):40-45.
12. Zhang Bo, Li Zhong, Mao Zongyun, Pang Minxi. The chaotic model and hope bifurcation of a type of permanent magnent synchronous motor, *Proceedings of the CSEE*, 2001, 21(9):13-17.
13. Chen J H, Chau K T, Chan C C, Chaos in voltage-mode controlled Dc drive system. *Int J Electr*, 1999, 86 (7): 857-874.
14. Zhu J J, Chang Y, Chen G R. Complex dynamics in permanent-magnet synchronous motors model. *Chaos Solitons & Fractals*, 2004, 22(2):831-848.
15. Z. Li, et al. Bifurcations and chaos in a permanent-magnet synchronous motor, *IEEE Transaction on circuits system*. 2002, 49(3):383-387.
16. Wang Yaqing, Zhou Shangbo. Image encryption algorithm based on fractional-order Chen chaotic system, *Journal of Computer Applications*, 2013, 33(4):1043-1046.
17. Xue Wei, Li Xue. Synchronization of the Fractional-order Permanent Magnet Synchronous Motor, *International Conference on Artificial Life and Robotics* 2016, 264-267.
18. Xue Wei, Li Yongli, Cang Shijian, Jia Hongyan, Wang Zenghui. Chaotic behavior and cirxuit implementation of fractional-order permanent magnet synchronous motor model. *Journal of the Franklin Institute*, 2015, 352(7):8149-8151.
19. Wei Xue, Hui Xiao, Xu Jinkang, Jia Hongyan. A Fractional-order Hyper-chaotic System and its Application in Image Encryption, *Journal of Tianjin University of Science & Technology*, 2015, 30(5):67-71.
20. Y. K. Chin, J. Soulard, Modeling of iron losses in permanent magnet synchronous motors with field-weakening capability for electric vehicles, *International Journal of Automotive Technology*, 2003, 4(2):87-94.
21. Gao Yuan, Fan Jianwen, Luo Wenguang, Li Zhongfu. Chaos in the fractional order permanent magnet synchronous motor and its control. *Journal of Wuhan University of Technology*, 2012.
22. Li Chunlai, Yu Simin, Luo Xiaoshu. Fractional-order permanent magnet synchronous motor and its adaptive chaotic control. *Chinese Physics B*, 2012(10):168-173.

The Application of a Novel Fractional-order Hyper-chaotic System in Image Encryption

Wei Xue, Shilong Liu, Mei Zhang, Xue Li
Department of Automation, Tianjin University of Science and Technology,
1038 Dagunanlu Road, Hexi District, Tianjin 300222, PR China

E-mail: xuewei@tust.edu.cn, 16851911@mail.tust.edu.cn
www.tust.edu.cn

Abstract

In this paper, a novel fractional-order hyper-chaotic system is proposed. By drawing the phase trajectory and Lyapunov exponent spectrum, its dynamic characteristics are analyzed. The simulation results show that the fractional-order hyper-chaotic system has hyper-chaotic characteristic. Then, image encryption implementation based on the fractional-order hyper-chaotic system is investigated. And, a three-color separation and scrambling the image pixel location, the histogram, key space, pixel distribution, correlation coefficient and key sensitivity of cipher-text in color pictures are tested and analyzed. The results show that the algorithm has good security and practicability.

Keywords: Fractional-order; hyper-chaotic system; Numerical simulation; Image encryption; algorithm.

1. Introduction

In 1963, Lorenz E N delivered a paper on "deterministic a periodic flow", which reveals a series of properties of chaotic motion, such as deterministic aperiodicity, extreme sensitivity to initial values, long-term behavior unpredictability, and so on.[1] His work guides the direction for chaos theory research and development in chaotic systems, such as Chen system, [2] Lü system, [3] Liu system, [4] Qi system, [5] and so on, which make chaotic dynamics theory and applied research get rapid development. In recent years, because of the unpredictability of the chaotic system and the extreme sensitivity of the system parameters, [6] coupled with the rapid development of fractional calculus theory, the fractional-order calculus and chaotic system are integrated by scholars. [7] The calculus operator which added to the chaotic system is studied.[8] It is found that the fractional-order system can still exhibit the chaotic state sometime, and the application of the fractional-order chaotic system has a better practical value. [9] Therefore, the fractional-order chaotic systems have aroused great enthusiasm of scholars.

With the rapid development of Internet technology, much of information is released and transmitted quickly through internet. Therefore, information security issues become a focus of people's attention. Image encryption based on chaotic system processes digital image, which makes the cipher-text image disorder to cover the plaintext information and to achieve the effect of image encryption.[10] In early 1990, Matthews applied the chaotic system to the image encryption algorithm. [11] In the early stage, the low dimensional chaotic system is applied to image encryption. Although the low-dimensional chaotic system was designed easily, the random sequence acquired was fast. Because of low security and low complexity, it is easy to be deciphered. The hyper-chaotic system has four state variables so that the system complexity is relatively high, the key space is larger than chaotic system. The initial conditions are extremely sensitive, and the overall system security is high. With further studies of fractional-order chaotic systems, it is found that fractional-order chaotic system not only has characteristics of sensitivity to initial values and pseudo-randomness, but also can reflect the historical information of the system, which has the strong historical memory. [12] In addition, the fractional-order chaotic system enhances nonlinearity and complexity of system researched, which increases key space of encryption algorithm.[13] The existing integer-order chaotic system can not predict and enhance the security of communication. Based on the literature,[14] a novel fractional-order hyper-chaotic system is proposed in this paper, and the application of this fractional-order chaotic system in digital image encryption is studied by numerical simulation.

2. Numerical Analysis of a Novel Fractional-order Hyper-chaotic System

In this paper, a novel fractional-order hyper-chaotic system is constructed on the basis of literature. [14] The mathematical model as follows:

$$\begin{cases} \dfrac{d^q x}{dt^q} = -a(x+y) - yz \\ \dfrac{d^q y}{dt^q} = bx + y + xz \\ \dfrac{d^q z}{dt^q} = -dz + cy^2 \\ \dfrac{d^q w}{dt^q} = -ex \end{cases} \quad (1)$$

The system parameters are a = 33.2, b = 10, c = 18, d = 15, e = 26. The calculous order of the system (1) is q, and $q \in (0,1)$, where q = 0.95. The phase trajectory of the novel fractional-order hyper-chaotic system is shown in Fig. 1:

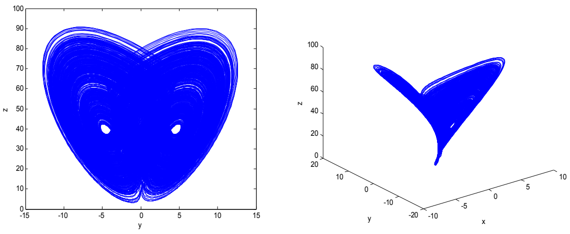

Fig.1 Phase portraits of system (1)

The Lyapunov exponent can characterize the motion characteristics of the system. Its positive and negative values and size in one direction, denotes the degree of divergence or convergence of the adjacent orbits in the attractors for a long time. [15] For the hyper-chaotic system, there must be two or more positive Lyapunov exponents. The Lyapunov exponent spectrum of system (1) is shown in Fig.2. When a =33.2, they are L_1 =4.1476, L_2 =0.7313, L_3 =-10.8891, L_4 =-36.1858, respectively, the system (1) is hyper-chaotic.

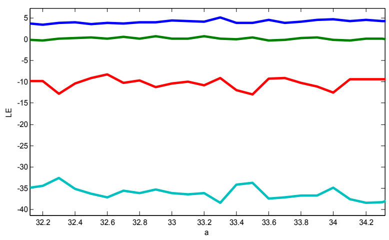

Fig.2 Lyapunov exponent spectrum of system (1)

3. The application of fractional-order hyper-chaotic system in image encryption

3.1. Image encryption and decryption process

Each color image is composed of R, G, B, which belongs to three primary colors. Different tricolor distributions make up different images. Image encryption is to scramble each color dot. The novel fractional-order hyper-chaotic system proposed in this paper adopts one-dimensional time-domain out-of-order at first, and then the other three-dimensional sequence matrix is used to realize the spatial encryption algorithm by performing XOR operation, to achieve the purpose of disorder. Decryption process is the inverse of the encryption process, the specific flow chart is shown in Fig.3:

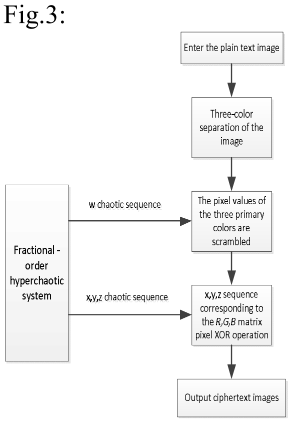

a) Encryption

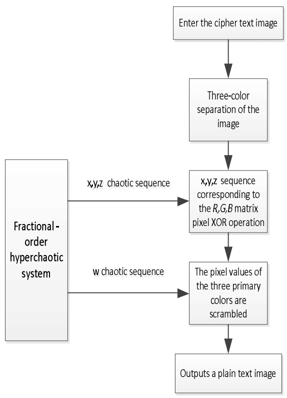

b) Decryption

Fig.3 Flow chart of encryption and decryption

The specific steps of the encryption scheme as follows:

1) The original image of R, G, B three primary colors is separated from the corresponding gray-scale image, the results are shown in Fig.4:

Fig.4 The image of original and each component

2) Firstly, the chaotic sequences of w series is used to scramble the components. And then use x, y, z sequence respectively on the R, G, B matrix to perform XOR operation to achieve spatial domain encryption. The results of the encryption of each component are shown in Fig.5:

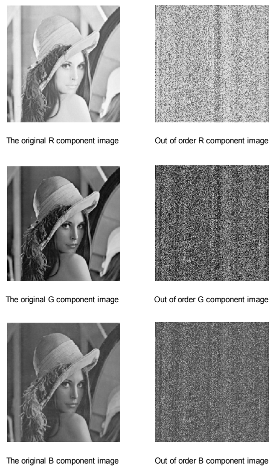

Fig.5 Spatial domain XOR results

3) After scrambling, the three-primary color matrix are synthesized for encryption, the original image encryption results are shown in Fig.6:

Fig.6 Encryption results of the original image

4) Decrypting the ciphertext image is the inverse process of the encryption operation. First of all, the three primary colors of the image are separated. Then, use R, G, B matrix components that were separated out to perform XOR inverse according to x, y, z sequences. And then in accordance with the w chaotic sequence, each pixel is anti-scrambled. And finally, the original image is obtained. Decryption results are shown in Fig.7:

Fig.7 Decryption results of the original image

3.2. Algorithm security performance analysis

3.2.1 Key sensitivity analysis

Given system parameters a = 33.2, b = 10, c = 18, d = 15, e = 26, q = 0.95. When set the system initial value $x_0 = y_0 = z_0 = w_0 = 0.1$ as the system key, the image is encrypted. When you enter the correct key, you can successfully decrypt to get the correct image. If we change the initial value as x_0 = 0.100000000001, other initial values and parameter values are unchanged, the image decryption fail. The result is shown in Fig.8. It can be seen that slightly small key changes cannot decrypt the cipher-text image. System (1) has higher key sensitivity.

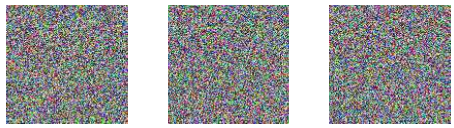

Fig.8 Decryption result of the wrong key

3.2.2 Histogram analysis

Fig.9 is a gray histogram of the B component before and after encryption, which describes the number of pixels in each gray level. It can be seen from Fig.9 that the number of pixels on each gray level before encryption is not uniform and the fluctuation is relatively large. The difference in the number of pixels between wave crests and troughs is relatively large, and the image distribution is obvious. After the encryption, the number of pixels in each gray level is relatively uniform, almost no fluctuations, a large degree of hiding the pixel distribution of the original image, which can be a good resistance to the statistical analysis of the decipher.

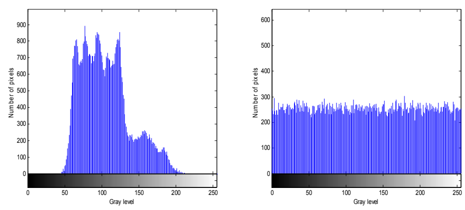

Fig.9 Histograms before and after image encryption

3.2.3 Adjacent pixel correlation analysis

One row and one column of pixels are selected from the original image and the encrypted image. The correlation coefficients of its adjacent pixels are calculated in Tab. 1. Observation of the data in Tab.1 can be drawn: the correlation coefficients of the original image adjacent pixels are close to 1, the correlative performance is relatively high. In addition, the correlation coefficients of the adjacent pixels of the encrypted image is close to zero, and the adjacent pixels are almost irrelevant. Therefore, the encryption algorithm based on system (1) has higher resistance to attack.

4. Conclusion

In this paper, a novel fractional-order hyper-chaotic system is proposed and its dynamical properties are analyzed. Firstly, the phase trajectories and Lyapunov exponent spectrum are gained, which verify that the fractional-order system has hyper-chaotic attractors. Then, this system is applied to the digital image encryption. Algorithm based on the one-dimensional time-domain chaotic sequence, and three-dimensional spatial re-encryption is used to encrypt and decrypt the color image. Finally, the key sensitivity, histogram characteristics and correlation coefficients of adjacent pixels are analyzed. The analysis results show that the encryption algorithm based on a novel fractional-order hyper-chaotic system proposed has advantages of high sensitivity and reliability.

Tab.1 The correlation of adjacent pixels

Different directions / Different images	Horizontal direction	Vertical direction
The original image R pixel matrix	0.97757	0.9555
Encrypted image R pixel matrix	0.0011284	0.00056923
The original image G pixel matrix	0.97161	0.94387
Encrypted image G pixel matrix	0.0016781	0.0027984
The original image B pixel matrix	0.95435	0.92538
Encrypted image B pixel matrix	0.0036514	0.0070632

5. Acknowledgement

This work is supported by the Young Scientists Fund of the National Natural Science Foundation of China (Grant No.11202148).

6. References

1. Lorenz E N. Deterministic non-period follow. *Atoms Sci.* 1963, 20(2): 130-141.
2. Chen G R, Ueta T. Yet another chaotic attractor. *International Journal of Bifurcation and Chaos*. 1999, 9(7): 1465-1466.
3. Lü J H, Chen G R. A new chaotic attractor coined. *International Journal of Bifurcation and Chaos*. 2002, 12(3): 659-661.
4. Liu C X, Liu L, Liu T etal. A new butterfly-shaped attractor of Lorenz-like system. *Chaos, Solitons and Fractal*. 2006, 28(5): 1196-1203.
5. Qi G Y, Chen G R, van Wyk M A, et al. A four-wing chaotic attractor generated from a new 3-D quadratic autonomous system. *Chaos, Solitons and Fractals*. 2006, 28(5): 1196-1203.
6. Jia H Y, Chen Z Q, Xue W. Analysis and circuit implementation for the fractional-order Lorenz system. *Acta Physica Sinica*. 2013, 62(14): 14503-1–140503-7.
7. Huang L L, Xin F, Wang L Y. Circuit implementation and control of a new fractional-order hyperchaotic system. *Acta Physica Sinica*. 2011, 60(1): 010505-1–010505-9.
8. Grigorenko I, Grigorenko E. Chaotic dynamics of the fractional Lorenz system. *Physical Review Letters*. 2003, 91(3): 034101-1–034101-4.
9. Li C P, Peng G J. Chaos in Chen's system with a fractional order. *Chaos, Solitons and Fractals*. 2004, 22(2): 443–450.
10. Zhu Cong Xu, Sun Ke Hui. Cryptanalysis and improvement of a class of hyperchaos based image encryption algorithms. *Chinese Journal of Theoretical Physics*. 2012, 61(12): 120503-1–120503-12.
11. Matthews. On the Derivation of a "Chaotic" encryption algorithm. *Cryptologia*. 1989, 13(1): 29-42.
12. Wang Q Y, Zhou S B. Image encryption algorithm based on fractional-order Chen chaotic system. *Journal of Computer Applications*. 2013, 33(4): 1043-1406.
13. Wu X, Wang H, Lu H. Modified generalized projective synchronization of a new fractional-order hyperchaotic system and its application in secure communication. *Nonlinear Analysis: Real World Applications*. 2012, 13(3): 1441–1450.
14. Li Xue, Xue Wei. Analysis and unidirectionally coupled synchronization of a novel chaotic system. *The 2016 International Conference on Artificial Life and Robotics*. 2016, 412-415.
15. Xue Wei, Xiao Hui, Xu Jinkang, Jia Hongyan. A fractional-order hyper-chaotic system and its application in image encrption. *Journal of Tianjin University of Science & Technology*. 2015, 30: 01-05.

A Method of Detecting Abnormal Crowd Behavior Events Applied in Air Patrol Robot

Huailin Zhao
School of Electrical and Electronic Engineering ,Shanghai Institute of Technology, Shanghai, China

Shunzhou Wang
School of Electrical and Electronic Engineering ,Shanghai Institute of Technology, Shanghai, China

Shifang Xu
School of Electrical and Electronic Engineering ,Shanghai Institute of Technology, Shanghai, China

Yani Zhang
School of Computer Science and Information Engineering ,Shanghai Institute of Technology, Shanghai, China

Masanori Sugisaka
Alife Robotics Corporation LTD, Oita, Japan
zhao_huailin@yahoo.com

Abstract

When the ground or air patrol robot monitors a certain area, one of the important intelligent functions is to estimate the crowd density of the monitored area. This paper analyzes the crowd density estimation algorithm, and use a Gaussian process regression model for crowd density estimation. Through the crowd density estimation and changes, we can detect abnormal behavior events of the crowd. The method can not only estimate the population density of the specified area, but also analyze and detect the abnormal behavior events of the crowd. This application provides an important technical support for enhancing the patrol robot monitoring effect.

Keywords: Air Patrol robot, Abnormal event detection, Gaussian process regression

1. Introduction

It is an important research topic to monitor the emergent events in large public places. With the development of robotics technology in recent years[1,2,3,4], unmanned aerial vehicles (UAVs) play a more and more important role in the field of intelligent monitoring. In this paper, an unmanned aerial vehicle (UAV) is used to monitor the abnormal event of public area. By monitoring the number of people in the specific area, it can alarm in a short time when abnormal number change happens.

A lot of works on the crowd counting algorithm have been studied. The crowd counting algorithm is currently divided into three categories: counting the number of people in the video[5,6,7,8], counting the number of people in a single image[9], and counting the number of people based on the deep learning[10,11]. The method of counting the number of people in the video is generally divided into three steps: 1) foreground segmentation 2) feature extraction 3) crowd regression. The method of counting the number of people in a single image generally split the image into patches, and then extract the feature of each patch, and sum the number of each patch to get the total number of the picture. The crowd counting work based on the deep learning usually use the population density map of the picture as the supervisory information, and design the convolutional neural network to return the density map. The prediction of density map can be integrated to get the number of people in the frame.

Considering the requirements of the performance of real-time and computational resource constraints, we adopt the video-based crowd counting algorithm of Ref.4, and its prediction results are used as the criteria for UAV monitoring abnormal time.

2. Design of the Whole System

The flowchart of air patrol robot monitoring abnormal event in crowded public area is shown in Fig.1. Unmanned aerial vehicles monitor the large public places, the collected images are real-time transmit to remote monitoring terminal. The monitoring terminal use the crowd counting algorithm to count the images from unmanned aircraft real-time, and record the number of changes over time. When the crowd number changes dramatically in a short term, the monitoring terminal remind the management that the region have abnormal immediately.

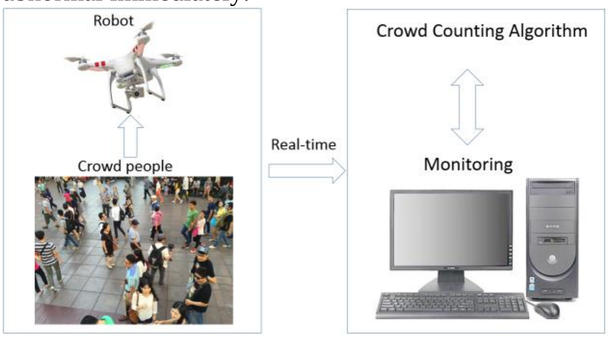

Fig.1. The flowchart of air patrol robot monitoring abnormal event in crowded public area

3. Crowd Counting Algorithm Based on Video Segmentation and Traditional Machine Learning

Video-based population counting algorithm is generally divided into three steps: 1) foreground segmentation; 2) feature extraction; 3) regression. In this paper, the method in Ref.4 is used, the whole algorithm is shown in Fig.1.

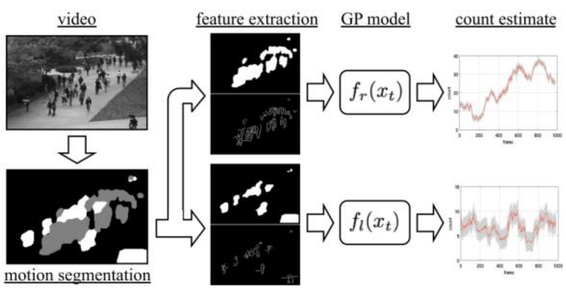

Fig.1. Monitoring video crowd counting system[5]

3.1 Foreground segmentation

The purpose of segmentation is to segment the crowd people from the image to facilitate the subsequent step feature extraction. The performance of the segmentation is directly related to the final count precision, so it is an important factor limiting the performance of crowd counting algorithms. Commonly used segmentation algorithms are Optical Flow, Mixture of Dynamic Textures[6], Wavelets and so on. The disadvantage of this motion-based foreground segmentation algorithm is obvious. If the person does not move in the video, the stationary person will be divided into the background, which affects the performance of the crowd counting. In this paper, we use the Mixture of Dynamic Textures[6] to process the foreground segmentation on the UCSD dataset and PETS2009 dataset respectively. The concrete process is shown in Fig.2.

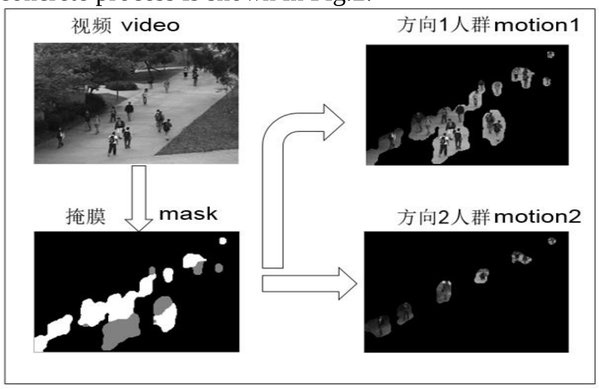

(a)

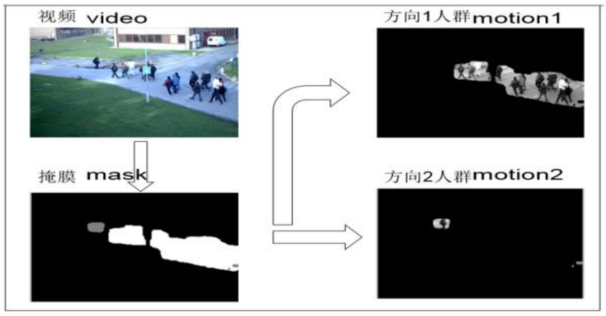

(b)

Fig. 2. Foreground segmentation based on mixture of dynamic textures(a)UCSD dataset (b)PETS2009 dataset

3.2 Perspective normalization

Due to the perspective of view, people who are close to the camera take more pixels in the image than those who are away from the camera. We use two different perspective normalization method to two different datasets. The perspective normalization is shown in Fig.3.

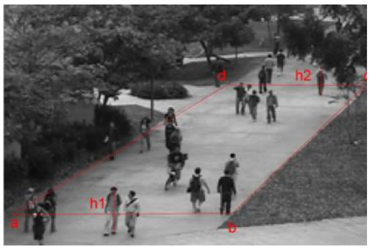

(a)

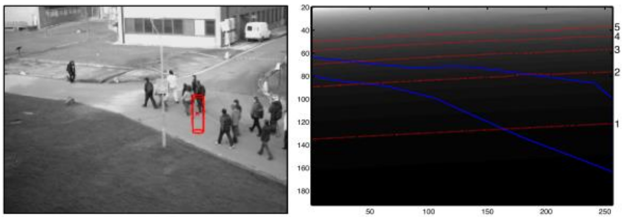

(b)

Fig.3. Perspective normalization (a)UCSD dataset(b)PETS2009dataset

On the UCSD dataset, we make a ground plane[5], which is scaled to measure the height h_1 of the person at ab and the height h_2 of the person on the cd .We can see the ground plane as in Figure 3a. The weight of the middle pixel is obtained by multiplying the pixels on ab and cd by the weights 1 and $\frac{h_1|\overline{ab}|}{h_2|\overline{cd}|}$ respectively, and the middle pixel weight is obtained by the linear interpolation between the two lines.

On the PETS2009 dataset, the perspective map is approximating a person moving in a 3-D scene to a cylinder with a height of 1.75 m and a radius of 0.25 m.[6] For each pixel (x, y) in the 2-D camera view, the cylinder is positioned in the 3D scene so that the center of the cylinder is projected to (x, y) in the 2-D view as shown in Figure 3(b), which is shown on the left. The total number of pixels used to fill the cylinder is expressed as c (x, y). The perspective is then calculated as $M(x, y) = c(230,123)/c(x, y)$, where the coordinates (230,123) correspond to the reference person on the right side of the sidewalk. Figure 3(b) is a perspective view with the contour line (red) which is indicated that the pixel weight at that location is {1, ..., 5}.

The mean absolute error (MAE) and the mean square error (MSE) are commonly used to measure the performance of the algorithm.

$$MAE = \frac{1}{N}\sum_1^N |z_i - \hat{z}_i| \quad (1)$$

$$MSE = \sqrt{\frac{1}{N}\sum_1^N (z_i - \hat{z}_i)^2} \quad (2)$$

Where N is the number of pictures to be tested (number of video frames). z_i is the number of the i-th frame. $\hat{z}_i$ is the estimated number of the algorithm.

3.3 Feature extraction

After completion of the foreground segmentation, a variety of low-level features are extracted from the foreground (population) obtained from the segmentation. Common features are: Area and Perimeter of Crowd Mask, Edge Count, Edge Orientation, Texture Features, Minkowski Dimension, and so on. In this project, two datasets are tested respectively, and the feature of each image is saved as a feature vector. There are 29 features in each feature vector of the UCSD dataset[5]. Each feature vector of the PETS2009 dataset has 30 features[7].

4. Experiments

In this part, we repeat the reference papers Ref.4 and Ref.6 experiments. We use the regression model to regress the feature extracted in the previous step to the number of people in the image. The regression can be a simple linear regression, or a complex nonlinear regression. Commonly regression methods are Linear Regression, Piecewise Linear Regression, Ridge Regression, Gaussian Process Regression, and so on. We use Gaussian process regression to predict the number of people in the image of UCSD dataset and PETS2009 dataset. The prediction result is shown as in Fig.4.

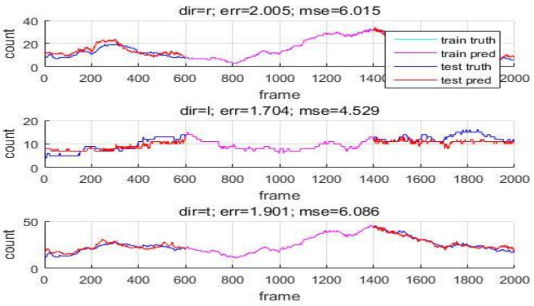

(a)

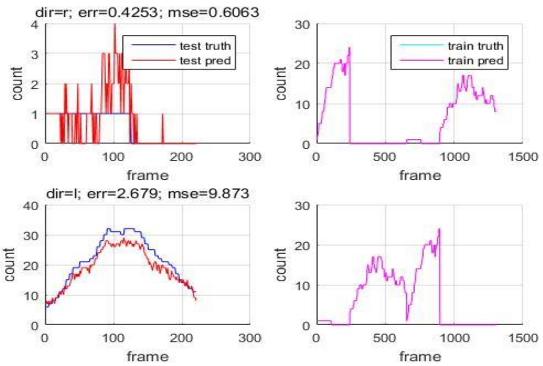

(b)

Fig.4. Crowd counting method employed in (a)UCSD dataset and (b)PETS2009 dataset

For the UCSD dataset, 800 pictures are used as the training set, and the remaining 1200 pictures are used as test set. The output of the Gaussian process regression is rounded to the nearest integer to generate a population count and record the mean square error (MSE) and the mean absolute error between the estimate and the true value. The results of the crowd counting algorithm for counting the UCSD dataset are shown in Figure 4(a)

The MSE of the two groups were 6.015 and 4.529, respectively. The accuracy of the algorithm basically meet the design requirements.

The whole area of scene S1.L1 of PETS2009 dataset was tested by the crowd counting algorithm, and 1308 images are used as training set and the video 13-57, 13-59F, 13-59F, 14-03,14-03F, 221 images are used as a test set. The output of the Gaussian process regression is rounded to the nearest integer to generate a population count and record the mean square error (MSE) and the absolute error between the estimate and the true value. The population count algorithm for the PETS2009 data set scene S1.L1 count results shown in Figure 4b), the MSE of the two groups of people counting are 0.6063 and 9.873, the accuracy of the crowd counting algorithm basically meet the design requirements.

5. Conclusion

In this paper, we design a monitoring function of patrol robot to detect the abnormal crowd behavior events applied in the monitoring area with the changes of crowd counting results. We analyze the crowd counting algorithm and select the typically machine learning method rather than convolution neural network to apply in this specific filed due to the real-time performance and the computation of the algorithm. We repeat the reference papers experiment and the prediction result of the crowd counting algorithm is not the state of the art, but can basically meet the design purposes. In the future, we will design a new crowd counting algorithm to increase the accuracy and attempt to apply deep learning in the patrol robot monitoring function.

6. References

1. Shunzhou Wang, Huailin Zhao, Xuyao Hao. Design of An Intelligent Housekeeping Robot Based on IOT. *Proceedings of 2015 International Conference Intelligent Informatics and BioMedical Sciences (ICIIBMS2015)*, 2015.11, p197-200.
2. Huailin Zhao, Lin Wang, Bei Wang, Masanori Sugisaka, "System development of an artificial assistant suit", *Artificial Life and Robotics* (ISSN1433-5298), Vol.17, 2013, No.3-4, p331-335.
3. Huailin Zhao, Bei Wang, "Configuration of the Mckibben Muscles and Action Intention Detection for an Artificial Assistant Suit", *International Journal of Advanced Robotic Systems* (ISSN 1729-8806), Vol. 9, 2012, p1-7.
4. Huailin Zhao, Masanori Sugisaka, "Simulation study of CMAC control for the robot joint actuated by McKibben muscles", *Applied Mathematics and Computation* (ISSN0096-3003), Vol.203, 2008, p457-462
5. Chan A B, Liang Z S J, Vasconcelos N. Privacy preserving crowd monitoring: Counting people without people models or tracking[C]. *Computer Vision and Pattern Recognition, 2008. CVPR 2008. IEEE Conference on. IEEE*, 2008: 1-7.
6. Chan A B, Vasconcelos N. Modeling, clustering, and segmenting video with mixtures of dynamic textures[J]. *IEEE Transactions on Pattern Analysis and Machine Intelligence*, 2008, 30(5): 909-926.
7. Chan A B, Morrow M, Vasconcelos N. Analysis of crowded scenes using holistic properties[C].*Performance Evaluation of Tracking and Surveillance workshop at CVPR*. 2009: 101-108.

8. Fengzhi Dai, Huailin Zhao, Resonance algorithm for image segmentation, *Computer Engineering and Design* (ISSN1000-7024), Vol.28 (No.23), 2007, p5657-5660.
9. Idrees H, Saleemi I, Seibert C, et al. Multi-source Multi-scale Counting in Extremely Dense Crowd Images[C]. *IEEE Conference on Computer Vision and Pattern Recognition. IEEE Computer Society*, 2013:2547-2554.
10. Zhang C, Li H, Wang X, et al. Cross-scene crowd counting via deep convolutional neural networks[C]. *Proceedings of the IEEE Conference on Computer Vision and Pattern Recognition*. 2015: 833-841.
11. Zhang Y, Zhou D, Chen S, et al. Single-image crowd counting via multi-column convolutional neural network[C]. *Proceedings of the IEEE Conference on Computer Vision and Pattern Recognition*. 2016: 589-597.

Design of the Multi-Car Collaboration System

Huailin Zhao[1], Yangguang Guo[1], Masanori Sugisaka[2]

1. Schol of Electrical and Electronic Engineering,
Shanghai Institute of Technology, Shanghai , China
2. Alife Robotics Corperation LTD, Oita, Japan
zhao_huailin@yahoo.com
www.sit.edu.cn

Abstract

With the development of the computer and electronical technology, it is an irresistible trend to make the multiple intelligent agents cooperate with each other to complete a specific complex task. Due to the high cost of real vehicles, most of the researches are based on simulation softwares. In our project, a few real small smart cars are used, and the design of multi-car cooperation system is completed. A system platform of the small smart cars is established, which can simulate the behavior such as positioning, formation and so on. In the experiment field, a global camera is used to achieve global synchronical positioning. The simulation results show that the multiple smart cars can get collaborating.

Keywords: Multi agent; Simultaneous localization; Robot formation;

1. Introduction

For multi agent cooperative system, some universities and research institutions in developed countries have studied the related aspects of multi-agent collaboration system. For example, the European Regional intelligent transportation CyberCars-2 project, the Collective Robotics experimental system was developed by the research team in Alberta university of Canada, the research team which led by Professor T.Fukuda in Nagoya University of Japan develop the CEBOT (Cellular Robotic System). In recent years, Shanghai Institute of Technology has designed some special robots[1,2,3]. They have developed some useful control algorithms[4,5,6], and going to establish the collaboration system based on them[7,8,9]. Because of the cost of the above research, this paper designed a low-cost platform to facilitate the research. The main contents of this paper are the overall design of the car hardware, the software design of the car and the design of the car formation algorithm. Firstly, according to the structure, function and characteristic of the real intelligent vehicle, the intelligent vehicle which can imitate the real vehicle is designed. Secondly, the software system is designed to realize the control function of the intelligent vehicle. Finally, aiming at the problem of cooperative control of multi intelligent vehicles in the experimental environment, this paper designs a control algorithm of formation control based on the travel mode.

2. Integrated design of multi vehicle cooperative system

The integrated scheme of multi vehicle cooperative system is shown in Fig.1.

The whole system includes a PC machine, a global camera and three independent design of the car. The car to get the location information as shown in Figure 2 and Figure 3, PC machine running global positioning algorithm, real-time access to three cars by the global camera position, so as to establish the corresponding coordinate positioning, and every car smart car range. The decision-making process of each intelligent vehicle is shown in Figure 4. Position data is transmitted to each car via a host. Three car can read the location of the other car information, and through the car's own processor to make decisions, and then send the results to the car around the motor, real-time control of the car's work.

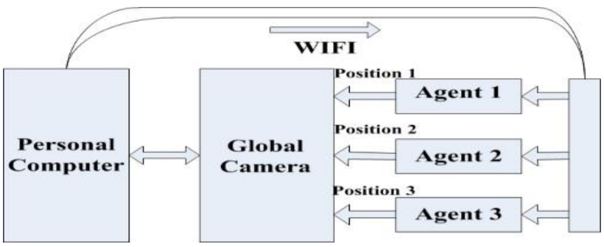

Fig.1 The overall system design

Fig.2 Global Positioning camera car diagram (front view)

Fig.3 Global positioning camera car schematic (platform)

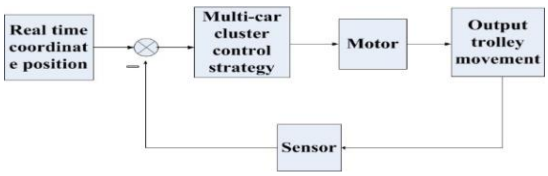

Fig.4 Single car control flow chart

3. The hardware design of control system

The hardware system structure of the intelligent car is shown in Figure 5, there are three main function modules. Respectively is the motor drive module, speed sensor module and communication module. Smart car by driving the processor module to send PWM[1] to the motor wave to realize the motor control; speed sensor is used in integrated photoelectric encoder on the motor, the encoder interface will speed by the speed of the data passed to the small processor; wireless communication module can realize communication workshop installation trolley car.

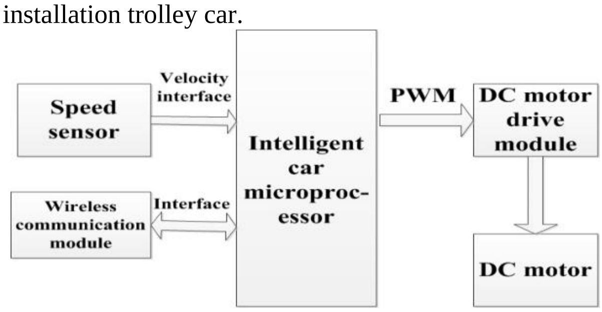

Fig.5 Intelligent Vehicle Hardware Architecture

4. The design of software system

As shown in Figure 6, on the basis of the software system for the realization of intelligent vehicle control functions, the system will be divided into 3 groups. The first time, should be in the detection of measuring magnetic sensor and speed sensor; second, software project management system should also be in this piece of the signal as the navigation and rate control; third, the software system should also be in the management of the implementation of communication signal block management and control command analysis project.

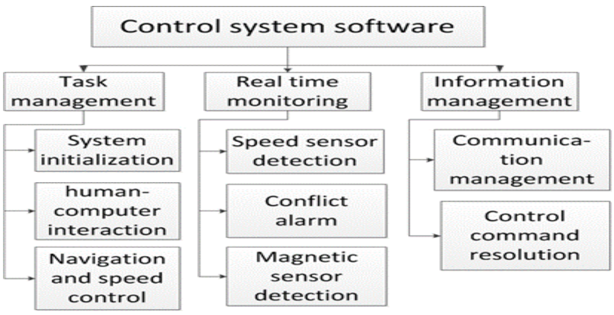

Fig.6 The basic functions of the software system

The software should not only ensure timeliness, but also to complete a wealth of difficult projects. Several levels of software architecture for intelligent vehicle control system is shown in Figure 7.

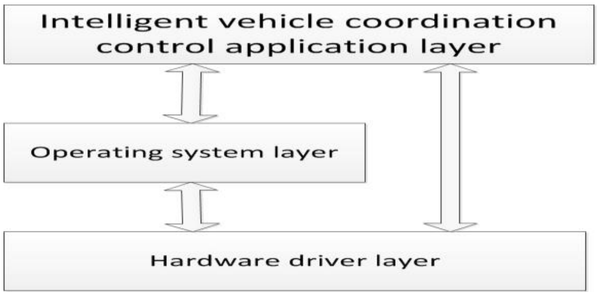

Fig.7 Software architecture

5. The Formation control algorithm of multi vehicle cooperation

Our approach relies on two key ideas[10,11,12]. The first is the use of dynamical systems as a paradigm for understanding information exchange between vehicles, and the design of a dynamical system which enables the vehicles to achieve consensus on the formation center. The second is the use of feed-forward compensation to render the sensed and transmitted information timely.

5.1 *The equation of state for the control system of a single vehicle is expressed as:*

$$\dot{x} = AX + Bu \qquad y = Cx \tag{1}$$

A single control system (one agent) becomes multiple agents:

$$\dot{x}_i = Ax_i + Bu_i \tag{2}$$

Where, $x_i \in R^n$, $u_i \in R^m$ are the vehicle states and controls, and *i* is the index for the vehicles in the flock. Each vehicle receives the following measurements:

$$y_i = C_1 x_i \qquad z_{ij} = C_2(x_i - x_j),\ j \in J_i \tag{3}$$

Where the set $J_i \subset [1, N] \setminus \{i\}$ represents the set of vehicles which vehicle can sense. Thus, $y_i \in R^k$ represents internal state measurements, and $z_{ij} \in R^l$ represents external state measurements relative to other vehicles. We assume that $J_i = \varnothing$, meaning each vehicle can sense at least one other vehicle. Note that a single vehicle cannot drive all the $z_{ij} \in R^l$ terms to zero simultaneously; the errors must be synthesized into a single signal. For simplicity, and without loss of generality, we assume that all relative state measurements are weighted equally to form one error measurement

$$Z_i = \frac{1}{|J_i|} \sum_{j \in J_i} z_{ij} \tag{4}$$

Where $|J_i|$ is the cardinality of the set J_i. The choice of weighting does not impact the results, as long as the weights for a given vehicle sum to one. We also define a decentralized control law *K* which maps y_i to z_i and has internal states u_i, represented in state-space form by

$$\dot{v}_i = K_A v_i + K_{B1} y_i + K_{B2} z_i \qquad u_i = K_C v_i + K_{D1} y_i + K_{D2} z_i \tag{5}$$

This is 2nd system for x_i. It is based on the observations of the other agents and is used to determine the input to agent *i*.

Dynamic model design of intelligent vehicle:

$$\dot{x}_i = A_{veh} x_i + B_{veh} u_i \quad i = 1, \ldots, N \tag{6}$$

$$A_{veh} = \begin{bmatrix} 0 & 1 \\ a_{21} & a_{22} \end{bmatrix}, B_{veh} = \begin{bmatrix} 0 \\ 1 \end{bmatrix}, x_i = \begin{bmatrix} x_p \\ x_v \end{bmatrix}$$

State variable of N vehicle:

$$\dot{x}_i = \begin{bmatrix} x_v \\ x_a \end{bmatrix}, x_a = a_{21} x_p + a_{22} x_v + u_i \tag{7}$$

For the information from other agents, we set j_i, set of agents that can be observed by agent *i*.

$$z_i = \sum_{j \in J_i} \left((x_i - h_i) - (x_j - h_j) \right) \qquad L_G = D - Q \qquad L = L_G \otimes I_2 \qquad z = L(x - h) \tag{8}$$

5.1. *Feedback Equation*

By using feedforward compensation, the sensing and transmission of information are obtained in a timely manner, and the feedback equations are as follows:

$$\dot{x} = Ax + BFL(x - h) \qquad \dot{x} = I_N \otimes A_{veh} x + L_G \otimes B_{veh} F_{veh} (x - h) \tag{9}$$

Dimensions

$\dot{x} : 2N \times 2, F_{veh} : 2 \times 1, B_{veh} : 2 \times 1, L_G : 2N \times 2$

$I_N \otimes A_{veh} : 2N \times : 2N, L_G \otimes B_{veh} F_{veh} : 2N \times : 2N$

6. Experiment simulation

Problem：

-Get three agents to move into a triangular formation

-Each agent starts with a certain position and
Velocity.

Assumptions:

- Same dynamics for each agent

-The internal system of each agent is decoupled from the others

-Each agent can observe the positions of the other two and then adjust its own velocity accordingly

-No agent can directly change the velocity of another

Simulation result

Simulation results are shown in Figure8

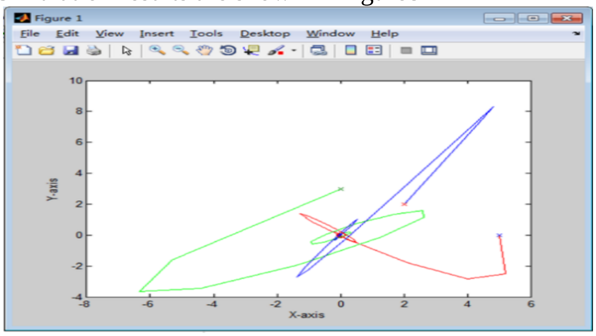

Fig.8 Three cars brought together a little

The red line represents the moving track of the trolley, and the green represents the track of the trolley. The blue represents the track of the car. The initial location of the three vehicles (5,0), (2,2), (0,3), the convergence point is (0,0). This experiment through the global real-time camera reads three car position, so as to establish the corresponding coordinate positioning, and every car intelligent vehicle location and location information will be sent to the car, the car intelligent formation algorithm makes the three
utual cooperation, from the initial position of the respective converge at a point.

7. Conclusion

This experiment through the global real-time camera reads three car position, so as to establish the corresponding coordinate positioning, and every car intelligent vehicle location and location information will be sent to the car, the car intelligent formation algorithm makes the three mutual cooperation, from the initial position of the respective converge at a point.

Multi-Agent Systems: multiple agents working together to achieve a common goal. Multi Agent Systems are often a more natural model for problems, such as Autonomous highway driving, Swarm robotics and so on.

Reference

1. Shunzhou Wang, Huailin Zhao, Xuyao Hao. Design of An Intelligent Housekeeping Robot Based on IOT. *Proceedings of 2015 International Conference Intelligent Informatics and BioMedical Sciences (ICIIBMS2015)*, 2015.11, p197-200.
2. Huailin Zhao, Lin Wang, Bei Wang, Masanori Sugisaka, "System development of an artificial assistant suit", *Artificial Life and Robotics* (ISSN1433-5298), Vol.17, 2013, No.3-4, p331-335.
3. Huailin Zhao, Bei Wang, "Configuration of the Mckibben Muscles and Action Intention Detection for an Artificial Assistant Suit", *International Journal of Advanced Robotic Systems* (ISSN 1729-8806), Vol. 9, 2012, p1-7.
4. Huailin Zhao, Wei Ren, Consensus Problem of Distributed Multi-agent Systems, *Proceedings of the 2015 International Conference on Artificial Life and Robotics (ICAROB 2015)*, 2015.01, p201-206.
5. Huailin Zhao, Masanori Sugisaka, "Simulation study of CMAC control for the robot joint actuated by McKibben muscles", *Applied Mathematics and Computation* (ISSN0096-3003), Vol.203, 2008, p457-462.
6. Huailin Zhao, Masanori Sugisaka, "A Model of the Mckibben muscle actuator based on experiment", *Systems Science* (ISSN0137-1223), Vol.34, No.2, 2008, p83-88.
7. Huailin Zhao, Masanori Sugisaka, Leilei Cui, Guanglin Shi, "Research on the intelligent control algorithm for a soft joint actuated by Mckibben muscles", *Artificial Life and Robotics* (ISSN1433-5298), Vol.14, No.1, 2009, p85-88.
8. Huailin Zhao, Xiaoqing Jia, Masanori Sugisaka, "Some thought for the Mckibben muscle robots", *Proceedings of the 16th International Symposium on Artificial Life and Robotics (AROB 16th '2011)*, p533-536.
9. Huailin Zhao, Yulong Xia and Yi Liu, "A Jacket Robot and Its Human-Robot Interacting Technology", *Lecture Notes in Electrical Engineering* (ISSN18761100), Vol.255(2013), Chapter 92, p1-7
10. Lin R, Du Z, Sun L. Moving object tracking based on mobile robot vision[C]// *International Conference on Mechatronics and Automation*. 2009:3625-3630.
11. Fax J A, Murray R M. Information flow and cooperative control of vehicle formations[J]. *IEEE Transactions on Automatic Control*, 2002, 35(1):115-120.
12. Huailin Zhao, Datai Yu, Guo Li, A humanoid joint actuated by Mckibben muscles, *Journal of University of Science and Technology Beijing* (ISSN1001-053X), Vol.28 (No.11), 2006, p1096-1100.

Research on a Method of Character Recognition for Self-learning Errors

Huailin Zhao[1], Yawei Hou[1], Shifang Xu[1], Congdao Han[1], Masanori Sugisaka[2]

[1]Schol of Electrical and Electronic Engineering
Shanghai Institute of Technology, Shanghai , China
[2]ALife Robotics Corperation LTD, Oita, Japan
E-mail:hyw_2016@163.com,zhao_huailin@yahoo.com
www.sit.edu.cn

Abstract

Due to the different writing habits, the handwritten numeral is difficult to identify. No matter what kind of network, the computer can not judge the output of the network. This reduces the recognition rate of the network. In order to improve the recognition rate, this paper proposes a method of character recognition for self-learning errors. Finally, on the matlab simulation platform, it is proved that the method proposed in this paper can improve the recognition accuracy.

Keywords: probabilistic neural network; handwritten numeral recognition; self-learning; matlab;

1. Introduction

The optical character recognition technology includes the handwritten character recognition and printed characters recognition. As a part of handwritten character recognition, handwritten numeral recognition is a very important research direction. In recent years, with the development of computer and pattern recognition technology, character recognition technology has been widely used in postal code, financial amount and robot[1,2], artificial assistant suit[3,4]. Although the classification of the classifier has been further enriched, but the researchers still can not find an algorithm to achieve the perfect effect.

The artificial neural network with strong self-learning ability, self-adaptability, classification ability, fault-tolerance and fast recognition has attracted much attention, and it has been widely used in character recognition[5]. Common neural networks have BP neural network, CMAC neural network[6]. Neural networks can be combined with other intelligent controls, such as fuzzy neural networks[7]. In this paper, the probabilistic neural network is selected in the research of handwritten numeral recognition, and the recognition rate of characters is improved by using the method of re-recognition. By using the data of MNIST database, it is proved that the recognition rate can be improved when the self-learning error recognition method is used.

2. Fundamentals of Probabilistic Neural Networks

The theoretical basis of probabilistic neural networks is the Bayesian minimum risk criterion. The theoretical basis of probabilistic neural networks is the Bayesian minimum risk criterion. The basic principle of Bayesian classifier: Under the condition of prior probability, according to the prior probability of an object, the Bayesian formula can get its posterior probability. Finally, the class with the largest posterior probability is chosen as The class to which the object belongs [8].

For ease of analysis, it is assumed that the classification to be made as $c = c_1$ or $c = c_2$. The prior probability is

$$h_1 = p(c_1), h_2 = p(c_2), h_1 + h_2 = 1. \quad (1)$$

$x=[x_1, x_2, ..., x_n]$ as the input vector and is classified according to Eq.(2)

$$c = \begin{cases} c_1, p(c_1|x) > p(c_2|x) \\ c_2, otherwise \end{cases}. \quad (2)$$

$p(c_1|x)$ is the posteriori probability of class c_1 in the case of x. According to the Bayesian formula, the posterior probability is equal to

$$p(c_1|x) = \frac{p(c_1)p(x|c_1)}{p(x)}. \quad (3)$$

But the actual situation should also consider the loss and risk issues. The samples belonging to c_1 may be assigned to c_2, the samples belonging to c_2 may be assigned to c_1, this will cause losses, so the classification rules should be adjusted.

The adjusted Bayes decision rule becomes:

$$c = \begin{cases} c_1, R(c_1|x) < p(c_2|x) \\ c_2, otherwise \end{cases}. \quad (4)$$

Where $R(c_1|x)$ is the expected risk that the input is classified as c_1.

It is found that the training of probabilistic neural network is simple and fast convergence, which can be fully realized in real-time processing, and the network has better performance.

3. Implementation of handwritten numeral recognition system

The handwritten numeral is generally provided in the form of picture in its practical application. The original image can be obtained by the input device, and then handwritten numeral recognition is started after pre-processing, character segmentation, feature extraction and classifier selection [9].

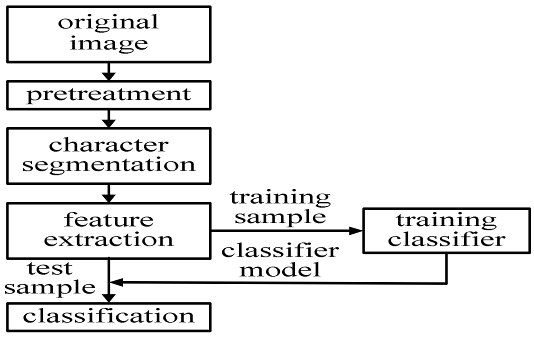

Fig. 1. The process of handwritten numeral recognition

3.1. *Pretreatment*

Pretreatment can improve the final recognition rate, so preprocessing is very important. Mainly for denoising, filtering and other operations. The digital image which be used in digital identification needs to be binarized. For image analysis, image segmentation is necessary[10]. The data used in this article from the MNIST database which is not pretreatment, but directly using the data from the database experiments.

3.2. *Feature extraction*

The importance of feature extraction[11] in image recognition is self-evident. Commonly used handwritten digital features are: structural features and statistical characteristics. In order to get better results, this paper uses the combination of the two characteristics of the image feature extraction, and obtain the 14-dimensional feature. There are eight structural features and six statistical characteristics in it. Constitute a feature vector with 14 values, each digital image is represented by the feature vector.

3.3. *Implementation of handwritten numeral recognition*

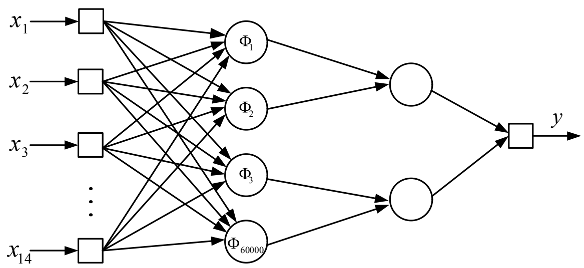

Fig. 2. The probabilistic neural network in experiments

It can be seen from Fig. 2 that the probabilistic neural network used in the experiment consists of 14 inputs. Since the training data used MNIST's data set, it contains 60000 training samples and 10000 test samples. In this paper, we don't select the 60000 training samples. All the training samples are directly used. Therefore, there are 60000 neurons in the hidden layer. As to identify the number zero to nine, so the Summation layer have ten neurons. The final result of classification is only one, the network output layer is a neuron.

4. The experimental results and improvements

The selected MNIST datasets[12] consisted of 60000 training samples and 10000 test samples. All the training samples were used to train the network, and then 10000 test samples were tested. Table 1 shows the recognition results at different network diffusion rates.

Table 1. the recognition rate of the system at different diffusion rates

Network diffusion speed	Sample number	Recognition rate
0.1	60000	80.51%
0.2	60000	80.33%
0.3	60000	73.86%
0.4	60000	68.29%
0.5	60000	64.16%

In order to improve the recognition rate of the network, this paper proposes a recognition method of self-learning errors.

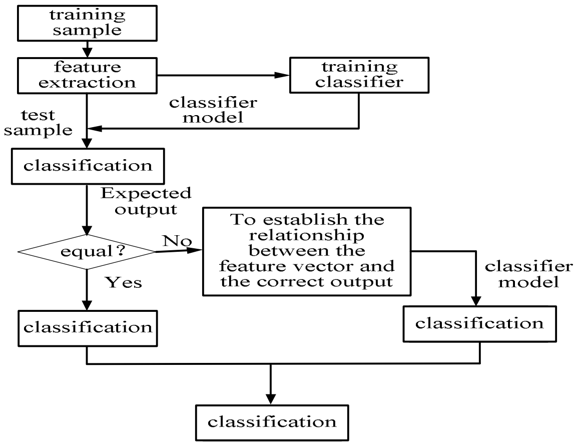

Fig. 3. The block diagram of improved system

The number of individual digits in the selected test samples is known, so we can create a matrix which has 1 row and 10000 columns. If the test samples is number 0, then it is marked as 1, and so on. As shown in Table 2 .

Table 2. The expected output of test samples

Image ID	1	2	3	...	9998	9999	10000
Expected output	1	1	1	...	10	10	10

In the experiment, the recognition rate obtained through the network training at different diffusion speed is shown in Table 1. When the diffusion speed of the network is 0.1, the recognition effect of the network is the best. In order to improve the recognition rate, the network can make up for the wrong knowledge by learning errors. Compare the results of the network with the expected output of the test samples, we can obtain a comparison result. If the comparison results are the same, the network output the results of recognition. If the results are different, the network is misidentification. According to the desired output, we should establish a matrix which contains the number of false images and the corresponding expected output. Through statistical data, it is find that there are altogether 1949 images which are not recognized correctly. There are some of the values shown in Table 3.

Table 3. A partial misrecognition of the image number and the corresponding expected output result

Image ID	30	38	...	9994	10000
Expected output	1	1	...	10	10

Select the eigenvectors of the error image and the corresponding expected output to train the error. The final recognition rate of the network is the sum of the two recognition results. Through the MATLAB simulation platform, we can get the final recognition rate which is shown in Table 4.

Table 4. The improved network recognition rates at different diffusion speed

Network diffusion speed	Sample number	Recognition rate
0.1	60000	100%
0.2	60000	99.57%
0.3	60000	94.35%
0.4	60000	87.46%
0.5	60000	81.90%

By analyzing Table 1 and Table 4, it can be seen that the method of using self-learning error can improve the recognition rate of the network. When the network diffusion speed is 0.1, the final recognition rate is 100%, which is nearly 20% higher than before.

In practice, the computer can’t establish the desired output corresponding to the image to be recognized in advance. In order to solve the problem, this paper designs a method to set up the expected output corresponding to the image to be recognized by the computer. In order to enable the computer to quickly compare the test data with the training data, the contrast data used in this paper are the feature vectors obtained by the feature extraction which proposed in the preceding paper. The Euclidean distance between the two sets of vectors is compared by distance-based method to judge the similarity.

For the two n-dimensional sample points a $(x_{11},x_{12},...,x_{1n})$ and b $(x_{21},x_{22},...,x_{2n})$, the Euclidean distance is

$$d_{12} = \sqrt{\sum_{k=1}^{n} \left(x_{1k} - x_{2k}\right)^2}. \quad (5)$$

It can also be expressed in the form of vector operations:

$$d_{12} = \sqrt{(a-b)(a-b)^T}. \quad (6)$$

Where a and b represent two vectors.

Through the analysis, we can seen that the Euclidean distance between the two vectors is smaller, the similarity between the two vectors is larger. Therefore, the characteristic vectors of each test samples are calculated by Euclidean distance with the characteristic vectors of the 60000 training samples, and the number of the training samples with the smallest Euclidean distance from the test samples is calculated.

Using Euclidean distance as a condition of similarity judgment has some misconceptions. In order to reduce the error, we use the network recognition result to modify the expected output to get the final expected output of the test samples.

According to the above description, the network is simulated and the recognition rate of the network is 86.32%. The recognition rate is improved by 6% compared with the network before the improvement.

5. Conclusion

In this paper, the probabilistic neural network is deeply analyzed. The feasibility and validity of handwritten numeral recognition of probabilistic neural network are explored. An automatic learning error recognition method is designed to improve the probabilistic neural network. If the expected output of the test samples can be obtained, the recognition rate of the network can reach 100%. But the expected output of the test samples is not easy to obtain. The recognition rate of the network can increased by 6%. The establishment of the expected output still need to conduct in-depth study.

References

1. Huailin Zhao, Xiaoqing Jia, Masanori Sugisaka, “Some thought for the Mckibben muscle robots”, *Proceedings of the 16th International Symposium on Artificial Life and Robotics (AROB 16th ’2011)*, p533-536.
2. Huailin Zhao, Masanori Sugisaka, “A Model of the Mckibben muscle actuator based on experiment”, *Systems Science* (ISSN0137-1223), Vol.34, No.2, 2008, p83-88.
3. Huailin Zhao, Lin Wang, Bei Wang, Masanori Sugisaka, “System development of an artificial assistant suit”, *Artificial Life and Robotics* (ISSN1433-5298), Vol.17, 2013, No.3-4, p331-335.
4. Huailin Zhao, Bei Wang, “Configuration of the Mckibben Muscles and Action Intention Detection for an Artificial Assistant Suit”, *International Journal of Advanced Robotic Systems* (ISSN 1729-8806), Vol. 9, 2012, p1-7.
5. Impedovo S, Pirlo G, Modugno R, et al. Zoning Methods for Hand-Written Character Recognition：An Overview[C]. *International Conference on Frontiers in Handwriting Recognition. IEEE Computer Society*, 2010：329-334.
6. Huailin Zhao, Masanori Sugisaka, “Simulation study of CMAC control for the robot joint actuated by McKibben muscles”, *Applied Mathematics and Computation* (ISSN0096-3003), Vol.203, 2008, p457-462.
7. Huailin Zhao, Masanori Sugisaka, Leilei Cui, Guanglin Shi, “Research on the intelligent control algorithm for a soft joint actuated by Mckibben muscles”, *Artificial Life and Robotics* (ISSN1433-5298), Vol.14, No.1, 2009, p85-88.
8. Jianju Xing, Jun Li, Zanfu Xie. Application of PNNin handwritten numeral recognition[J]. *Modern Computer*, 2016(08):20-23.
9. Sanping Li, Zhenjun Yue. Realization of Handwritten Numeral Recognition System Based on Probabilistic Neural Network [J]. *Military Communication Technology*, 2005,26 (1): 54-57.
10. Fengzhi Dai, Huailin Zhao, Resonance algorithm for image segmentation, *Computer Engineering and Design* (ISSN1000-7024), Vol.28 (No.23), 2007, p5657-5660.
11. N. Das, S. Basu, R. Sarkar, M. Kundu, M. Nasipuri, D. kumar Basu. *An Improved Feature Descriptor for Recognition of Handwritten Bangla Alphabet*, Jan, 2015.
12. Qiong Li, Li Chen, Weihu Wang. Study on handwriteen numeral rapid identification based on SVM[J]. *Journal of Computer Technology and Development*, 2014, 24(2): 205-208.

An Improved Method of Power System Short Term Load Forecasting Based on Neural Network

Shunzhou Wang
School of Electrical and Electronic Engineering
Shanghai Institute of Technology, Shanghai, China

Huailin Zhao
School of Electrical and Electronic Engineering
Shanghai Institute of Technology, Shanghai, China

Yani Zhang
School of Computer Science and Information Engineering
Shanghai Institute of Technology, Shanghai, China

Peng Bai
School of Electrical and Electronic Engineering
Shanghai Institute of Technology, Shanghai, China

E-mail: wangszvision@qq.com

Abstract

Load forecasting is an important content of planning and operating power system. It is the prerequisite to ensure the reliable power supply and economic operation. In this paper, an improved method of short-term load forecasting for load data of two different regions is proposed. Firstly, we analyze the relationship between weather factors and load, and then the greatest impact on load of weather factors are selected. The Elman neural network is used to predict unknown one-week load data taking into account without whether factors situation and whether factors situation. In the predicting situation of considering whether factors, the multi-weather factors are integrated with the temperature and humidity index , which are used as the neural network input training samples. The prediction result is good.

Keywords: Load forecasting , Elman neural network, Temperature and humidity index

1. Introduction

Short-term load forecasting is an important part of load forecasting, which is of great significance for economic dispatch, electrical market transactions and so on.

In the load forecast theory and methods field, academia and industry have done a lot of research and have made fruitful progress. In recent years, experts and scholars have proposed a variety of methods. These methods include: single consumption method, elasticity coefficient method, partitioned load density method[1], time series method[2], trend extrapolation method[3], regression analysis method[4] and gray model method[5], artificial neural network method[6,7], expert system method[8], wavelet analysis[9], genetic algorithm[10] and support vector machine[11]and so on

Short-term load forecasting is becoming more and more important. In recent years, the maximum load of power supply increased year by year, which constitute the peak load of electricity. The load is very sensitive to meteorological changes, and the impact of meteorological factors is growing[12]. Although many models have taken into account the effect of weather on power load, most of these models only consider temperature as a single meteorological factor[13,14,15]. However, relative humidity, air pressure, wind speed, radiation and other meteorological factors will have a great impact on power load.

Most of the neural network for short-term power load forecasting requires a large number of data samples, and only forecast the power load of one day, and there is little work to predict the unknown one-week load[16,17,18]. In this paper, an improved short-term load forecasting algorithm based on Elman neural network is proposed, which can predict unknown power load data with a small amount of known load data, and achieves good results by combining the characteristics of temperature and humidity meteorological factors.

2. Short Term Load Forecasting

The feedback neural network is suitable for power system load forecasting because of input delay. According to the historical data of load, the input and output nodes of feedback neural network are selected to reflect the inherent law of power system load operation, so as to forecast the load of future time. Therefore, the primary problem of the artificial neural network for power system load forecasting is to determine the neural network input and output nodes, so that it can reflect the power load operation law.

2.1Data sample preprocessing

2.1.1. *Processing of abnormal data*

The power load has a clear weekly change characteristics, working days Monday to Friday high, weekends low. This is due to weekend industrial electricity load reduction reasons. In addition, some holidays load, such as International Labor Day, National Day, the New Year, the Spring Festival, compared with usual day is significantly lower, which is due to the holiday industry caused by a substantial reduction in electricity. Therefore, the weekday and holiday electricity load is removed from the data sample, and only the electricity load of the working day is chosen as the historical data to improve the accuracy of the prediction result.

2.1.2. *Data sample normalization*

If the neural network directly use the original data as input, it will make the neuron training saturation. Therefore, before the network training, the data must be normalized to the same number level, so that the neural network can be converged. Finally, we can get the real load through the anti-normalization process[19]. Commonly the normalization means [0,1] is used, the formula is as follows:

Normalization：

$$y_i = \frac{x_i - x_{min}}{x_{max} - x_{min}} \tag{1}$$

Anti-normalization：

$$x_i = (x_{max} - x_{min})y_i + x_{min} \tag{2}$$

2.2 The framework of the neural network

This paper aims to predict the two regions total of 7 unknown days load data from January 11, 2015 to January 17, 2015, based on the historical load data. We select the load data from December 25, 2014 to January 2015 10 , a load data of 17 days to be as a training sample, excluding large fluctuations changes in relatively data: the region 1 December 28, December 31, January 1 data and the region 2 December 30, December 31 Day, January 1 data. After removing the abnormal data, a total of 8 days of data from December 25, 2014 to January 4, 2015 were selected as the training samples of the network. The load is used as the input vector every 3 days and the load on the 4th day as the target vector. Thus, five sets of training samples can be obtained. A total of six days of data ,January 5, 2015 to January 10, 2015 can be as a network of test samples to verify the network reasonably predict the day's load data or not. As the daily load data are 96 points, three days of load data is as a set of input, the day's load data is as the output, so the input variable is 288 variables, the output variable is 96 variables.

The number of hidden layers is two layers, the number of the first layer nodes is 11, the number of the second layer nodes is 5, the practice effect is better.

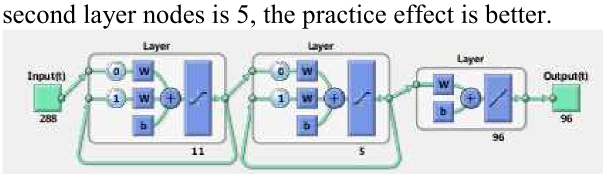

Fig. 1. The framework of the neural network for short term load forecasting

3. Short Term Load Forecasting Based on Weather Factors

The relationship between temperature, humidity and rainfall is analyzed[19]. The influence of humidity factor on the load is more significant. Based on the above, the short-term load model based on Elman neural network is established in this section considering the effect of meteorological factors on load forecasting.

3.1 Comprehensive meteorological factors

It has been pointed out that the change of the electric load is affected by various meteorological factors, and the meteorological factors also have some coupling effect. Therefore, it can not be evaluated on the basis of single temperature or other meteorological factors. It is an important content of short-term load forecasting how to use all meteorological factors reasonably and effectively to reduce the input judgment amount and improve the prediction precision. Fig.2. shows the influence of various meteorological factors on the power load.

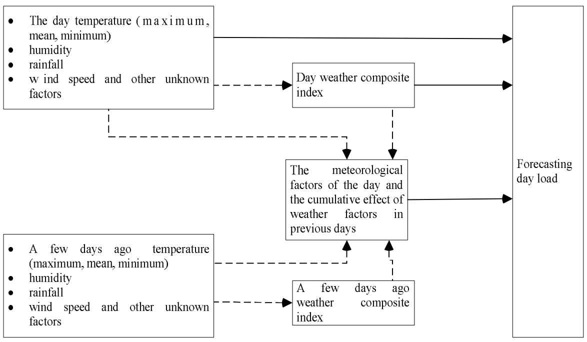

Fig. 2. The influence of various meteorological factors on the power load daily prediction

In practice, although the rainfall has a certain impact on the load forecast. However, since the rainfall mainly concentrates at a certain time of the day, the study of rainfall should be carried out for the time period during when rainfall occurs, and should not be added to each point throughout the day in a general manner. In this way, a comprehensive temperature and humidity index (Temperature and Humidity Index) is derived[19], which is derived from the effective temperature formula established by the well-known Russian scholar, and can be well described the effect of temperature and humidity on the power load. The formula is as follows.

$$THI = T_H - (0.55 - 0.55H_L) * (T_H - 58) \quad (3)$$

where, T_H is Fahrenheit, it is necessary to convert the given temperature data firstly.

Considering the correlation of meteorological factors and short-term load forecasting model based on historical load data, In this paper, the neural network input is mainly selected temperature and humidity meteorological factors, and then on the basis of the previous model this paper build a meteorological factors in the load forecasting model.

3.2 The load prediction algorithm flowchart

In this paper, the temperature and humidity index is added to each input sample of the Elman neural network (the temperature and humidity index has been normalized). Firstly, the neural network model is trained with the known date load data and the temperature humidity index. Then, when the load data of January 11, 2015 is forecasted, the actual temperature humidity index THI (1) replaces the neural network prediction THI (1), which is added to the training and iteration of the neural network. The actual temperature humidity index THI (2) of January 12 is instead of the neural network predictive THI (2) to train and iterate the neural network. Until the data of January 17 is predicted. The flow chart of the whole algorithm is shown in Fig.3.

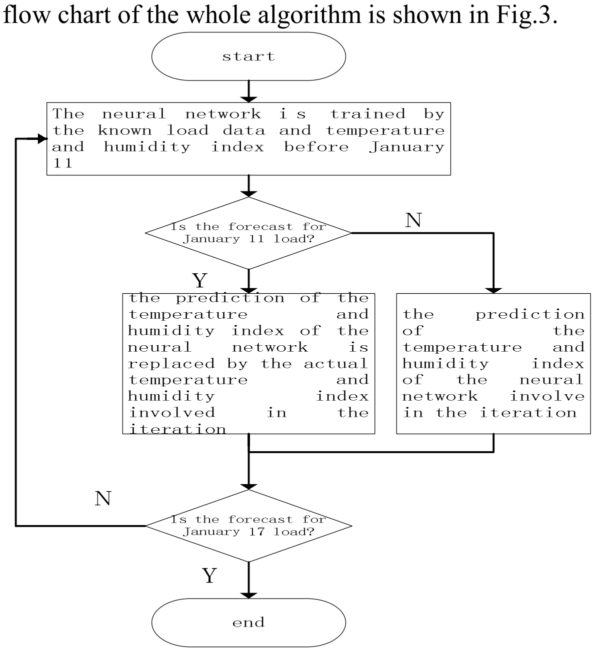

Fig. 3. Flow chart of load forecasting algorithm with meteorological factors

3.3 Experiment results

In order to test the accuracy of the forecasting model, the paper first calculates the power load of the area 2 from January 5, 2015 to January 10, 2015 (576 points) ,by taking account of the meteorological factors. The predicted results are shown in Fig. 4, and the resulting prediction errors are shown in Fig. 5.

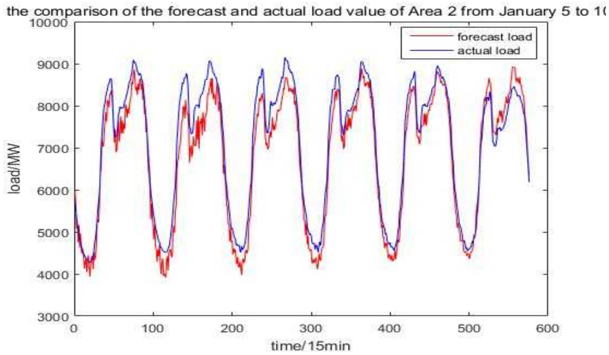

(a)

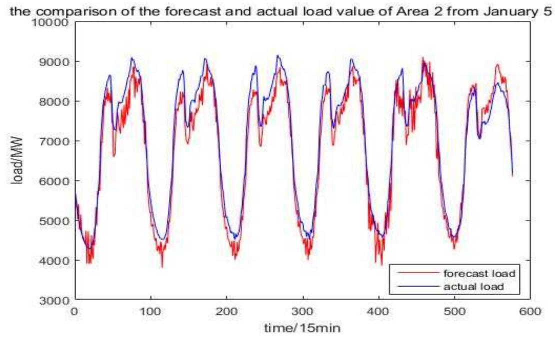

(b)

Fig.4. The forecasting result of area 2 load from from January 5, 2015 to January 10, 2015 (a) the prediction result without consideration the Meteorological Factors (b) the prediction result with consideration the Meteorological Factors

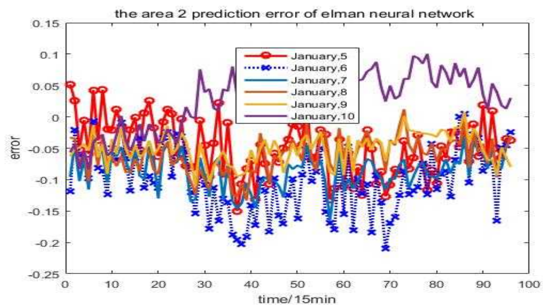

(a)

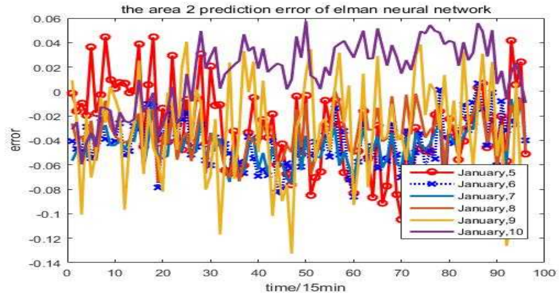

(b)

Fig.5. The prediction error of area 2 load from January 5,2015 to January 10,2015 (a)the prediction without consideration the Meteorological Factors (b) the prediction error with consideration the Meteorological Factors

In Figure 4, the difference between the predicted results in the two cases is not obvious, but it is clear from Fig. 5 that the error of the prediction result of the region 1 is greatly reduced by meteorological factors, and controlled to half of the error without considering meteorological factors, the precision of the prediction is greatly improved. In order to show the superiority of the forecasting with the meteorological factors, the power load from January 11 to 17, 2015 (672 points) is forecasted without meteorological factors. The predicted results for region 2 are shown in Fig.6.

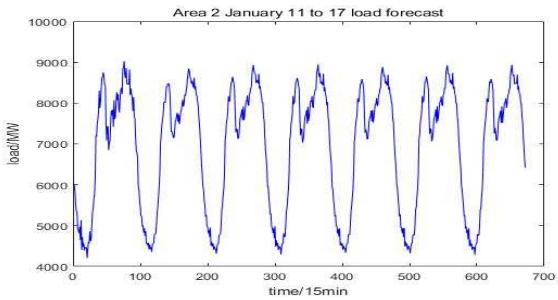

(a)

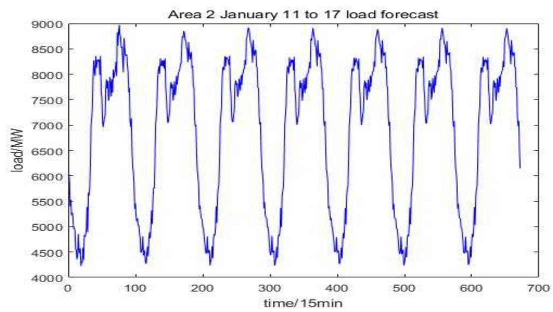

(b)

Fig.6. The forecasting result of area 2 load from January 11, 2015 to January 17, 2015 a)the prediction result without consideration the Meteorological Factors (b) the prediction result with consideration the Meteorological Factors

Based on the comparison of forecasting error and meteorological factors between meteorological factors and meteorological factors in the above two regions, it is clear that the prediction accuracy has been significantly improved with the meteorological factors. In this way, the result, which prediction model based on the Elman neural network and meteorological factors is used to forecast the load of the two regions in the period from January 1 to 17, 2015, is valuable.

4. Conclusion

In this paper, we have proposed an improved power system short term load forecasting method. We analyze the factors affect the power load and use the temperature and humidity index to be as an input sample of Elman neural network. To validate the method effectively, we use the neural network to predict two different area load data .We only use a few history load data to predict an unknown week load. The prediction result is reasonable and prediction error is small. Our method will help the manager to analyze and plan weekly load data.

5. References

1. Li Yu-mei, “The Utility of Combination Forecasting Method in Mid-long Term Load Forecasting ”, *M.S. Thesis, Sichuan University*, Sichuan province, SW, China, 2006
2. Soliman S A, Persaud S, El-Nagar K, et al. Application of least absolute value parameter estimation technique based on linear programming to short-term load forecasting. *Canadian Conference on Electrical & Computer Engineering*, 1996, 2(3):529 - 533.
3. Jinying Li, Dongxiao Niu. Study On Gray Combined Forecasting of Nonlinear Seasonal. *Power Load Power System Technology*, 2003, 27(5):26-28.
4. Chongqing Kang, Qing Xia, Mei Liu. Special Problems in Regression Analysis Applied to Load Forecasting *Automation of Electric Power Systems*, 1998(10):38-41.
5. Dahai Zhang, Yanqiu Bi, Yanxia Bi.etc. Power Load Forecasting Method Based on Series Gray Neural Network. *System Engineering Theory and Practice*. 2004, 24(12):128-132.
6. Huailin Zhao, Masanori Sugisaka, Leilei Cui, Guanglin Shi, “Research on the intelligent control algorithm for a soft joint actuated by Mckibben muscles”, *Artificial Life and Robotics* (ISSN1433-5298), Vol.14, No.1, 2009, p85-88.
7. Huailin Zhao, Masanori Sugisaka, “Simulation study of CMAC control for the robot joint actuated by McKibben muscles”, *Applied Mathematics and Computation* (ISSN0096-3003), Vol.203, 2008, p457-462.
8. Wei Wei, Dongxiao Niu, Zheng Chang. New Development of Load Forecast Technology. *Journal of North China Electric Power University*, 2002, 29(1):10-15.
9. Bi Y, Zhao J, Zhang D. Power Load Forecasting Algorithm Based on Wavelet Packet Analysis. *International Conference on Power System Technology, 2004. Powercon. 2004*:987-990 Vol.1.
10. Zhengyuan Jia, Dongxiao Niu. Genetic Neural Network Model Research for Power Load Forecasting. *Operations Research and Management Science*, 2000(2):31-36.
11. Xuegong Zhang. Introduction to Statistical Learning Theory and Support Vector Machines. *Acta Automatica Sinica*, 2000, 26(1):32-42.
12. Xiping Zhao, Dai Song, Guoqing Zhang, Xinyang Han, Zhaoguang Hu. Research on Correlativity Among Air Temperature, Maximum Load and Power Consumption in Shandong Power Grid. *Power System Technology*, 2004(17).
13. LI Ran, LIU Yu, LI Jing-hua.etc.Study on the Daily Characteristic Load Forecasting Based on the Optimizied Algorithm of Decision Tree[J] *Proceeding of the CSEE*, 2005, 25(23):36-41.
14. LI Yang, WANG Zhi-hua, LU Yi.etc. Characteristic Analysis of Summer Air Temperature Daily Peak Load in Nanjing. *Power System Technology*, 2001,25(7):63-66.
15. WANG Zhi-hua, LI Yang, ZHAO Cui-yu,etc. Study on Summer Temperature Sensitive Load in Nanjing. *Automation of Electric Power Systems*, 2002, 26(3):60-63.
16. Guo Jiao-jiao. “The Short-term Power Load Forecasting Based on Improved Elman Neural Network”, M.S. Thesis, Liaoning University of Technology, NE, China,2015
17. REN Lina. “Research on Medium-Term Electrical Load Forecasting Model Based on Elman Neural Network”, *M.S. Thesis*, *Lanzhou University of Technology*, NW,China,2007
18. HU Chang-hong, “Research on Short-term Load Forecasting Based on Hourly Weather Factors”, *M.S. Thesis, Zhejiang University*, Zhejiang province, EC, China, 2010

19. Rong Liu. “Short Term Load Forecasting Based on Elman Neural Network”, *M.S. Thesis, Zhejiang University*, Zhejiang province, EC, China, 2013

Improvement on LEACH Agreement of Mine Wireless Sensor Network

Liu Yun-xiang
Computer and Information Engineering College
Shanghai Institute of Technology, Shanghai, China

Zhang Wei
Computer and Information Engineering College
Shanghai Institute of Technology, Shanghai, China

Zhou Lan-feng
Computer and Information Engineering College
Shanghai Institute of Technology, Shanghai, China
E-mail: yxliu@sit.edu.cn

Abstract

Based on the characteristics of wireless sensor network communication in mine, LEACH protocol clustering is optimized, and the factors of energy and distance are considered fully. The selection of cluster head nodes is optimized, and a routing algorithm based on K-means ++ clustering is proposed. The problem of uneven distribution of cluster head nodes, uneven energy consumption and network stability in LEACH algorithm is improved effectively. Simulation results show that the proposed algorithm can improve the energy consumption of the whole network and improve the energy utilization rate, extending the network life cycle effectively.

Keywords: Wireless sensor networks, LEACH agreement, K-means++ algorithm, Mine

1. Introduction

Wireless Sensor Network is composed of a large number of data acquisition, data processing and communication capabilities of Sensor nodes to be self-organization formed a dynamic Network topology [1-3]. Which has a strong anti-destruction, self-adaptable and capable of rapid deployment and other advantages, it is widely used in important areas of industrial control, environmental monitoring, traffic control, health care, military and other [4-5]. Coal mining operations mainly in downhole and before the wireless sensor network has not been popular in the mine the wireline communication device is still in use. Wired communication there are some drawbacks, unable to pinpoint the underground site of the incident and the staff position when a security incident, coal ground personnel could not get the downhole specific information timely and accurately, it is not conducive to the underground work and security management. By using wireless sensor networks to achieve downhole communications and wireless security system to improve the mine mobile communication system, and to strengthen the safety management of the mine.

According to the characteristics of the coal mine tunnel, the network topology is banded, and the communication environment is relatively poor. Same as the general wireless communications networks, the nodes work in some of the unmanned monitoring area, not easy to maintain and are limited and not renewable energy, so efficient, stable, energy-efficient routing protocol for the entire wireless sensor network is very important. Low Energy Adaptive Clustering Hierarchy (LEACH) protocol is widely used at present hierarchical routing, which can be applied to the general working environment. But for the special conditions in the mine under, LEACH protocol can’t meet their requirements, therefore in this paper, we propose a route-based K-means++ clustering algorithm named LEACH-KPPE, to enable it efficient and stable to work in the mine environment. The clustering algorithm is optimized by K-means clustering algorithm, and fully consider the factor of energy and distance to control the selection of cluster head nodes. The problem of uneven distribution of cluster head nodes, uneven energy consumption and network stability in LEACH algorithm is effectively improved.

2. LEACH Protocol

LEACH protocol is the wider application of a hierarchical routing protocol in wireless sensor networks, the workflow is divided into two steps: generation and transmission of data clusters. The whole process will be repeated periodically, so that the process can be called a period of "round" . In each round several more suitable node will be selected as a cluster head node from the network nodes randomly, before selecting cluster head, LEACH algorithm is given a pre-defined threshold value T(n), the threshold value is calculated as:

$$T(n) = \begin{cases} \frac{p}{1-p*\left(r \bmod \frac{1}{p}\right)}, & n \in G \\ 0, & \text{others} \end{cases} \quad (1)$$

Wherein p is the networks cluster head node proportion accounted for all the expectations, r is the current cycle of the number of rounds selected cluster head, G is a collection of which is not a cluster head node.

After completing the clustering work, the wireless sensor network begins to work. The nodes in the cluster begin to collect the required information, and then send the collected data to the head node within their cluster.

3. LEACH-KPPE Protocol

3.1 LEACH-KPPE algorithm basic idea

In this paper, a new LEACH-KPPE protocol is proposed based on the LEACH protocol for some defects of traditional LEACH applications in coal mines. LEACH-KPPE agreement in the main work process is same with the original LEACH basically, they are also cyclical round of reconstruction, and each round also includes two stages of the establishment of clusters and stable data transmission. In the cluster stage, the nodes in the whole network send their own position information and residual energy information to the base station. After the base station integrates the data, the K-means ++ algorithm is used to cluster the nodes within the network area. After the K-means ++ algorithm clustering processing, the clustering is complete. Next according to the quantity of the node residual energy and location information to decide the optimal cluster head nodes. After the completion of the establishment of clusters and the choice of cluster head there will be going on stable data transmission phase. In the LEACH-KPPE protocol not only retain the original single-hop communication, also joined the multi-hop communication.

Considering the correlation of meteorological factors and short-term load forecasting model based on historical load data, In this paper, the neural network input is mainly selected temperature and humidity meteorological factors, and then on the basis of the previous model this paper build a meteorological factors in the load forecasting model.

3.2 LEACH-KPPE algorithm implementation

3.2.1 The optimal number of cluster nodes

In this paper, by analyzing the traffic and energy consumption in the network, the optimal number of cluster head nodes can be obtained. There are M nodes in the erected wireless area, and they all be distributed in the N×N area. The number of cluster nodes is k, the whole network is divided into k clusters, each cluster has M/k-1 nodes, so the number of common nodes in each cluster is M/k-1. Multipath fading is used here, so the energy consumption of each cluster head nodes including receiving the rest of the nodes within cluster data information of power consumption, energy consumption of the data fusion and sends the data to base station:

$$E_{CH} = E_{elec}\left(\frac{M}{k} - 1\right)b + E_{DC}\frac{M}{k}b + \varepsilon_{amp}{d_{CB}}^{4} \quad (2)$$

Where E_{elec} is the energy consumption of transmitting or receiving 1bit data, b is the number of transmitted data, ε_{amp} is constant and associated with hardware, E_{DC} is the energy consumption of cluster head node fusion data, d_{CB} is the distance between cluster head node and the base station.

When the communication between a member node in a cluster and cluster head node, the member node is similar to the cluster head node, then use the free space model, then the energy consumption with a member of the cluster node in a round of work is:

$$E_{CM} = E_{elec}\, b + \varepsilon_{amp}{d_{CM}}^{2}b \quad (3)$$

Where: E_{elec}、 b and ε_{amp} as above, d_{CM} denotes the distance between the member node and the cluster head node.

Assuming that the whole $N \times N$ area are circular and divided into k clusters, then the radius $\mathrm{R} = N/\sqrt{\pi k}$. Assuming that the probability density of nodes in a cluster is ρ *(x, y)*, then:

$$E\left[{d_{CM}}^{2}\right] = \iint (x^2 + y^2)\,\rho(x,y)\,dx\,dy \quad (4)$$

$E\left[{d_{CM}}^{2}\right]$ is the expectation of the square of the distance between the cluster member node and the cluster head node, by the radius $R = N/\sqrt{\pi k}$ available:

$$E\left[{d_{CM}}^2\right] = \int_{\theta=0}^{2\pi}\int_{r=0}^{N/\sqrt{\pi k}} \rho\, r^3\, dr\, d\theta = \frac{N^2}{2\pi k} \quad (5)$$

By the above calculation, in each round of energy consumption of each cluster are as follows:

$$E_T = E_{CH} + (M/k - 1)E_{CM} \quad (6)$$

At this point the whole network has a total of k clusters, and the energy consumption in each round of E as follows:

$$\begin{aligned} E = kE_T &= kE_{CH} + (M - k)E_{CM} \\ &= \Big(2ME_{elec} + ME_{DC} + k\varepsilon_{amp}{d_{CB}}^4 + \\ &\qquad M\varepsilon_{amp}\frac{N^2}{2\pi k} - 2kE_{elec} - \varepsilon_{amp}\frac{N^2}{2\pi}\Big)\, b \end{aligned} \quad (7)$$

Because E_{elec} , E_{DC} and ε_{amp} is constant and independent of the k, so derivative the type (7) can get the extreme value of k with k_{opt} as follows:

$$k_{opt} = N\sqrt{\frac{M}{2\pi({d_{CB}}^4 - 2E_{elec}/\varepsilon_{amp})}} \quad (8)$$

In this way, the optimal number of cluster heads k_{opt} in the $N{\times}N$ region is obtained, that is the number of cluster centers k to be used by the K-means ++ algorithm.

3.2.2 Establish cluster stage

When building cluster, the information of location and residual energy of all the nodes in the area will be sent to the base station first, then use the K-means++ algorithm to cluster the nodes within the network. Its main working process is as follows:①The number k of optimal cluster centers is obtained by the above; ②For each node x within the region, to calculate the distance D(x) with the nearest cluster center;③Choose a new node as a new cluster center,;④Repeat ② and ③ until the election of the k cluster centers;⑤Calculate the dissimilarity of k cluster centers in the rest of the nodes; ⑥Re-update the k cluster centers by calculating dimension of all the nodes in each cluster;⑦Repeat steps ⑤ and ⑥ until the criterion function began to convergence. Establish the cluster of flow chart shown in figure 1

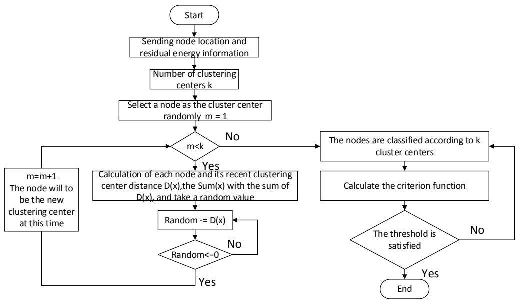

Fig. 1. This is the caption for the figure. If the caption is less than one line then it is centered. Long captions are justified manually.

3.2.3 Stable data transmission phase

After the cluster head node selection and cluster work of the whole area is completed, the data transmission is started. Single-hop communication cannot meet the requirements of communications in coal mines, this paper based on single-hop communication and then use multi-hop mode for data transmission. Figure 2 and Figure 3 compare the LEACH and LEACH-KPPE inter-cluster communication.

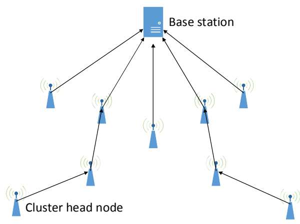

Fig.2. LEACH inter-cluster communication

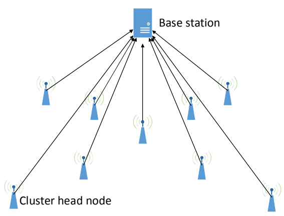

Fig.3. LEACH-KPPE inter-cluster communication

4. Simulation and Result Analysis

In this paper, the traditional LEACH protocol and the improved LEACH-KPPE protocol are simulated and analyzed in MATLAB platform. In this paper, $M = 100$ sensor nodes are distributed in the $100\times$

$100m^2$network area. The parameters in the simulation are shown in Table 1.

Table 1 Simulation parameters

Parameter Name	Parameter Value
Base station location B	(50,120)
Node initial energy E_0	1 J
Transmit/Receive circuit energy E_{elec}	50 nJ • b^{-1}
Power amplification factor ε_{amp}	0.0013 pJ • $(b \cdot m^2)^{-1}$
Data fusion energy consumption E_{DC}	5 nJ • b^{-1}
Packet length b	4000 b

From the above parameters, we can see that the distance between the cluster head node and the base station of d_{CB} is in the range of $50-130$, then we can know from formula (8) that the optimal cluster head number is related to the value of d_{CB}. The number of values ranges from $1 \le k_{opt} \le 4$. According to the parameters in Table 1, the relationship between the average energy consumption and the number of cluster head nodes k in the network is shown in Figure 4.

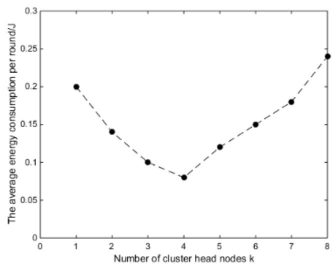

Fig.4. Relationship between cluster head node number and network energy consumption

Figure 5 shows the clustering simulation results of LEACH and LEACH-KPPE in one round. In Figure 5 (a) and (b), x represents the cluster center or the corresponding candidate node.

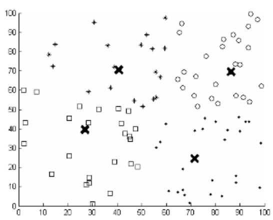

(a) LEACH-KPPE clustering results

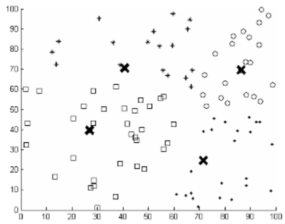

(b) LEACH clustering result

Fig.5. The clustering simulation results of the two algorithms

Figure 6 shows the relationship between the total energy consumption of the entire network and its operating time, which is represented by the number of rounds.

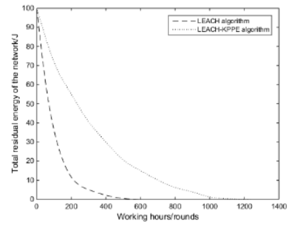

Fig.6. Network energy consumption curve

Figure 7 shows the relationship between the number of remaining nodes and their working time.

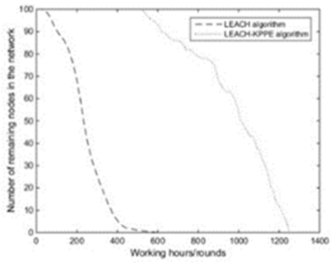

Fig.7. Network remaining node relationship diagram

5. Conclusion

In this paper, the K-means ++ clustering algorithm is used to improve the traditional clustering method of LEACH protocol, and the cluster head selection is optimized based on the energy of node and multi-hop mode is used between some cluster heads and base stations. LEACH-KPPE routing protocol, making it more suitable for wireless communications in coal mines. The simulation results show that the improved protocol has a significant improvement in terms of clustering results, energy consumption and node survivability compared with the traditional LEACH protocol, thus improving the network life cycle effectively and stability.

6. References

1. Sun liming, Li jianzhong. Wireless Sensor Networks [M]. Beijing: *Tsinghua University Press*, 2005.
2. Wang Shu, Yang Yujie, Hu Fuping et. Theory and application of wireless sensor networks [M]. Beijing: *Beijing University of Aeronautics and Astronautics*, 2007.
3. Zhang Haiyan, Liu Hong. Energy consumption balanced routing algorithm for WSN based on K-means clustering [J]. *Chinese Journal of Sensors and Actuators*,2011, 24(11):1639-1643.
4. Lin nan, Shi weihang. Optimization and Simulation of Wireless Sensor LEACH Algorithm [J] .*Computer Simulation*, 2011,28 (1): 178-182.
5. Zhao xiulan, Xu xiulan, Li keqing. Different Clustering Routing Algorithm Based on LEACH [J]. *Application Research of Computers*, 2013,30 (3): 866-868.

A New Four-Wing Chaotic System Generated by Sign Function

Hongyan Jia, Shanfeng Wang

Department of Automation, Tianjin University of Science and Technology,

1038 Dagunanlu Road, Hexi District, Tianjin300222, PR China

E-mail: jiahy@tust.edu.cn

www.tust.edu.cn

Abstract

In the paper, a new chaotic system is obtained by adding a Sign Function to a three-dimensional chaotic system. Its some basic characteristics including the equilibrium point, phase trajectory, bifurcation diagram, Lyapunov exponents and so on, are subsequently calculated. Moreover, the dynamic characteristics of the new chaotic system is also analyzed with the variation of the system parameters. In the end, the paper design an analog circuit to implement the chaotic system, the results from the circuit are consistent with those from the numerical analysis, and thus the chaotic characteristics of the new system is verified physically. The new chaotic system can provide a new model for engineering applications.

Keywords: four-wing chaotic system; sign function; dynamic characteristics

1. Introduction

Chaos is a new discipline developed over the past half a century, the phenomenon of chaos is ubiquitous in our nature. In 1963, Lorenz, a famous meteorologist, found a phenomenon of chaos when he studied meteorological changes. Then, he published a paper named "Deterministic nonperiodic flow" [1]. And the curtain of the chaotic phenomenon slowly began to open. After more than 10 years of development, many landmark papers have been published. For example, the concept of strange attractors was proposed by French physicist Ruell and Dutch mathematician Takens[2]. The theory of "Period three implies chaos" has also been proposed by the Chinese-American Tianyan Li and American mathematician Yorke[3]. The scalability and universal constants in the phenomenon of double-periodic bifurcations are found by Feigenbaum[4]. All these important discoveries have made important contributions to the development of chaos research.

With the deepening of the research on chaotic theory, it is gradually realized that the characteristics of the multi-wing chaotic systems are more complicated than ones of the single-wing or two-wing chaotic systems, and multi-wing chaotic systems have a wide range of applications. So, there are many different research which dedicate to construct some multi-wing chaotic systems, and they present some different methods such as the absolute value [5], the triangular wave sequence [6] and so on.

The multi-wing chaotic systems may be obtained by adding the multi-pulse function with the sign function to some one-wing or two-wing chaotic systems. In the paper, a new multi-wing chaotic system is firstly constructed by adding the multi-pulse function to a three-dimensional chaotic system. Then chaotic characteristics of the new system is showed by analyzing phase trajectory diagram, bifurcation diagram, equilibrium point and Lyapunov exponent approach. Finally, the new chaotic system is studied by the real analog circuit. All the results verify that the chaotic characteristics exist in the new system.

2 A New Four-Wing Chaotic System

2.1 Sign Function

Generally, sign function can be described by

$$\mathrm{f(x)} = \begin{cases} = 1 & x > 0 \\ = 0 & x = 0 \\ = -1 & x < 0 \end{cases} \tag{1}$$

where $x \in R$.

The sign function is a continuous function except for the only jump break point $\mathrm{x} = 0$[7] . Because $\mathrm{sgn(-x)} = -\mathrm{sgn(x)}$, the sign function is an odd function.

The multi-pulse function $\mathrm{p(x)}$ adopted in the paper is

$$p(\mathrm{x}) = \mathrm{m} * [\mathrm{sgn}(\mathrm{x} + B_1) - \mathrm{sgn}(\mathrm{x} - B_1) + \mathrm{sgn}(\mathrm{x} + B_2) - \mathrm{sgn}(\mathrm{x} - B_2) - 4] \tag{2}$$

where m, $\mathrm{B_1} = 0.8$ and $B_2 = 1.17$ is positive parameter. It will be used to generate multi-wing chaotic attractors in this paper.

2.2 A New Chaotic System

The fourth term of the 4D hyper-chaos system in Ref [8] is firstly removed to constitute a 3D chaotic system. As follows:

$$\begin{cases} \dot{x} = ax + byz \\ \dot{y} = cy + dxz \\ \dot{z} = kz + exy \end{cases} \tag{3}$$

And then add the multi-pulse function $\mathrm{p(x)}$ in the second term of system (3), and finally a new chaotic system with sign functions is obtained. As follows:

$$\begin{cases} \dot{x} = ax + byz \\ \dot{y} = cy + dxz + p(x) \\ \dot{z} = kz + exy \end{cases} \tag{4}$$

where a, b, c, d, e and k are system parameters, x, y and z are variables, and $p(x)$ is the multi-pulse function(2). the new system exhibits the characteristics of the four-wing chaotic attractor, when the initial value is (1,1,1) and $\mathrm{a} = 8, \mathrm{b} = -1, \mathrm{c} = -40, \mathrm{d} = 1, \mathrm{e} = 1$, $\mathrm{k} = -14$.

The corresponding changes of multi-pulse function $\mathrm{p(x)}$ will happen when selecting different free variables m. So, in the paper, some characteristics of the new chaotic system will be discussed when free variable m changes.

3 The Dynamics Of The New Four-Wing Chaotic System

3.1 Equilibrium point analysis

The multi-pulse function (2) with sign function is segmental function. So, the method of segment calculation is used to analyze the equilibrium point of the new chaotic system. The interval of x is as follows:

$$\mathrm{D_1} = \{(x, y, z) | x < -1.17\}$$

$$\mathrm{D_2} = \{(x, y, z) | -1.17 < x < -0.8\}$$

$$\mathrm{D_3} = \{(x, y, z) | -0.8 < x < 0.8\}$$

$$\mathrm{D_4} = \{(x, y, z) | 0.8 < x < 1.17\}$$

$$\mathrm{D_5} = \{(x, y, z) | 1.17 < x\}$$

The values of multi-pulse function $\mathrm{p(x)}$ in every interval of x is follow:

$$\begin{aligned} p(\mathrm{x}) &= \mathrm{m} * [\mathrm{sgn}(\mathrm{x} + 0.8) - \mathrm{sgn}(\mathrm{x} - 0.8) + \mathrm{sgn}(\mathrm{x} + 1.17) - \mathrm{sgn}(\mathrm{x} - 1.17) - 4] \\ &= \begin{cases} -4m & x < -1.17 \\ -2m & -1.17 \le x < -0.8 \\ 0 & -0.8 \le x < 0.8 \\ -2m & 0.8 \le x < 1.17 \\ -4m & 1.17 \le x \end{cases} \end{aligned} \tag{5}$$

And thus equilibrium points of the system (4) are shown in Table 1.

Table 1 The equilibrium point of equation (4)

X	p(x)	Equilibrium point
$\mathrm{D_1}$	-4m	$E_1\left(0, -\frac{m}{10}, 0\right)$ $E_2\left(\frac{7\left[\frac{8\sqrt{7}m}{7}+320\right]^{\frac{3}{2}}}{16m} - \frac{140\sqrt{\left[\frac{8\sqrt{7}m}{7}+320\right]}}{m}, 4\sqrt{7}, \sqrt{\frac{8\sqrt{7}m}{7}+320}\right)$ $E_3\left(\frac{140\sqrt{\left[\frac{8\sqrt{7}m}{7}+320\right]}}{m} - \frac{7\left[\frac{8\sqrt{7}m}{7}+320\right]^{\frac{3}{2}}}{16m}, 4\sqrt{7}, -\sqrt{\frac{8\sqrt{7}m}{7}+320}\right)$ $E_4\left(\frac{7\left[320-\frac{8\sqrt{7}m}{7}\right]^{\frac{3}{2}}}{16m} - \frac{140\sqrt{\left[320-\frac{8\sqrt{7}m}{7}\right]}}{m}, -4\sqrt{7}, \sqrt{320-\frac{8\sqrt{7}m}{7}}\right)$ $E_5\left(\frac{140\sqrt{\left[320-\frac{8\sqrt{7}m}{7}\right]}}{m} - \frac{7\left[320-\frac{8\sqrt{7}m}{7}\right]^{\frac{3}{2}}}{16m}, -4\sqrt{7}, -\sqrt{320-\frac{8\sqrt{7}m}{7}}\right)$
$\mathrm{D_2}$	-2m	$E_1\left(0, -\frac{m}{20}, 0\right)$ $E_2\left(\frac{7\left[\frac{4\sqrt{7}m}{7}+320\right]^{\frac{3}{2}}}{8m} - \frac{280\sqrt{\left[\frac{4\sqrt{7}m}{7}+320\right]}}{m}, 4\sqrt{7}, \sqrt{\frac{4\sqrt{7}m}{7}+320}\right)$ $E_3\left(\frac{280\sqrt{\left[\frac{4\sqrt{7}m}{7}+320\right]}}{m} - \frac{7\left[\frac{4\sqrt{7}m}{7}+320\right]^{\frac{3}{2}}}{8m}, 4\sqrt{7}, -\sqrt{\frac{4\sqrt{7}m}{7}+320}\right)$

		$E_4\left(\frac{7\left[320-\frac{4\sqrt{7}m}{7}\right]^{\frac{3}{2}}}{8m}-\frac{280\sqrt{\left[320-\frac{4\sqrt{7}m}{7}\right]}}{m},-4\sqrt{7},\sqrt{320-\frac{4\sqrt{7}m}{7}}\right)$ $E_5\left(\frac{280\sqrt{\left[320-\frac{4\sqrt{7}m}{7}\right]}}{m}-\frac{7\left[320-\frac{4\sqrt{7}m}{7}\right]^{\frac{3}{2}}}{8m},-4\sqrt{7},-\sqrt{320-\frac{4\sqrt{7}m}{7}}\right)$
D_3	0	$E_1(0,0,0)$, $E_2(4\sqrt{35},4\sqrt{7},8\sqrt{5})$, $E_3(-4\sqrt{35},-4\sqrt{7},8\sqrt{5})$, $E_3(4\sqrt{35},-4\sqrt{7},-8\sqrt{5})$, $E_2(-4\sqrt{35},4\sqrt{7},-8\sqrt{5})$
D_4	-2m	The same as D_2
D_5	-4m	The same as D_1

3.2 Phase trajectory

Here, When $a=8,\ b=-1,\ c=-40,\ d=1,\ e=1$ and $k=-14$. The phase trajectory of equation (3) is shown in Fig 1.

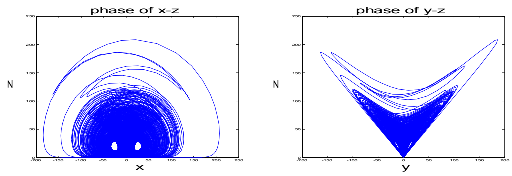

Fig 1 The phase trajectory of equation (3)

When $a=8,\ b=-1,\ c=-40,\ d=1,\ e=1,\ k=-14$ and $m=8$, the phase trajectory of equation (4) is shown in Fig 2.

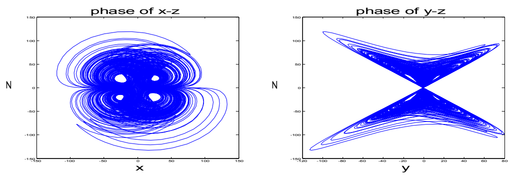

Fig 2 The phase trajectory of equation (4)

Comparing chaotic attractors in Fig 1 with ones in Fig 2, a conclusion will be obtained that multi-wing chaos can be generated by adding multi-pulse function with sign function to equation (3).

3.3 Bifurcation diagram

Bifurcation diagram can indicate the performance of chaotic system with the variation of parameter. The bifurcation diagram of equation (4) is shown in Fig 3.

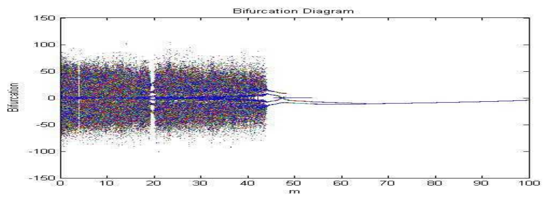

Fig 3 The bifurcation diagram of equation (4)

In the Fig 3, the bifurcation diagram start to enter into much sparse condition when $m=45$. That is, the bifurcation gradually varies from dense points to several lines, from several lines to one line, respectively. Generally, the system will be chaotic when points in bifurcation diagram are dense. To the contrary, the system is quasi periodicity or cycle when points in bifurcation diagram is several lines or one line.

3.4 Lyapunov exponent

The characteristic of chaotic motion is always analyzed by calculating lyapunov exponent. Therefore, The laypunov exponents of equation (4) is also computed and shown in Fig 4.

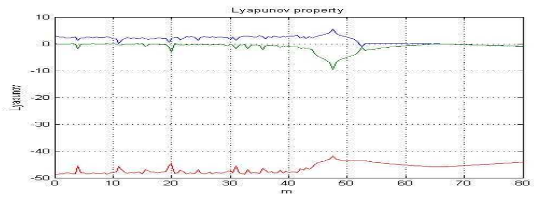

Fig 4 Lyapunov exponent of equation (4)

If the biggest one of lyapunov exponents is larger than zero, the equation will show the character of chaos. So, in Fig 4, chaotic dynamics of system (4) can be observed when $m \in (0,44)$, and periodic dynamics of system (4) can be obtained when $m > 44$. The phenomenon can also be described by phase trajectory, as shown in Fig 5-6.

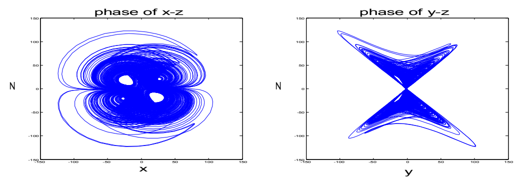

Fig 5 Chaotic dynamics of equation (4), $m=25$

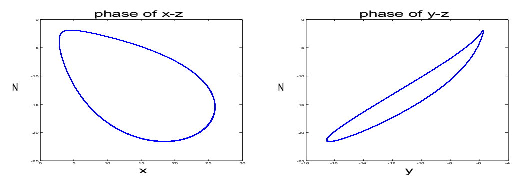

Fig 6 Periodic dynamics of equation (4), $m=55$

4 Analog Circuit for The New Chaotic System

The analog circuit for the new chaotic systems is designed by operational amplifier, multiplier, resistor and capacitance, as showed in Fig 7. The analog circuit for multi-pulse function is consisted of operational amplifier and resistor, as showed in Fig 8. The experiment results is obtained, as showed in Fig 9. The results are in agreement with the results of the numerical analysis, which physically proves the system (4).

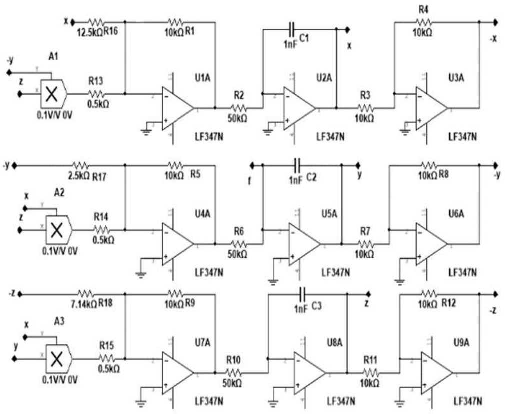

Fig 7 The analog circuit for system (4)

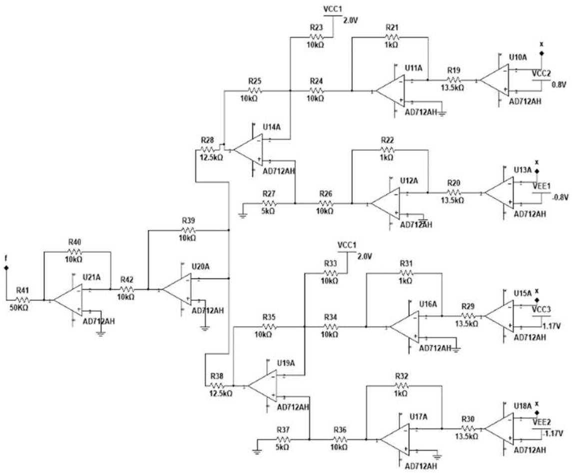

Fig 8 The analog circuit for multi-pulse function

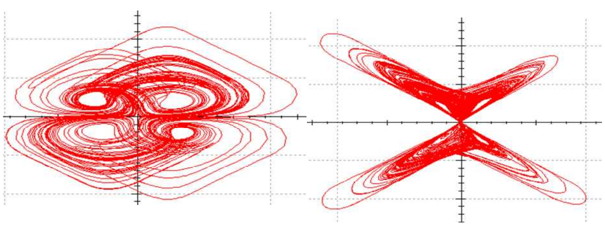

(a) (b)

(a) $x-z$ phase plane, (b) $y-z$ phase plane.

Fig 9 Experimental results by using the Multisim.

5 Conclusion

In the paper. Firstly, the basic properties of the sign function is introduced. Secondly, a multi-pulse function p(x) is made up of sign function, and the new chaotic system with multi-pulse function is designed. Third, by analyzing the dynamic characteristics of the system such as phase trajectory, bifurcation diagram and Lyapunov exponent, the chaotic characteristics of the new system are verified. Finally, it can be concluded that the multi-pulse function can produce four-wing chaotic attractor in the chaotic system. Because the chaotic system with sign function can generate complex character of chaos, it is meaningful for the chaotic system with sign function to be used in encryption communication.

References

[1] Lorenz E N. Deterministic nonperiodic flow. *Journal of the Atmospheric Sciences*, 1963, 20(2): 130-141.

[2] Ruell D, Takens F. On the nature of turbulence. *Communications in Mathematical Physics*, 197 1, 20(3): 1 67-192.

[3] Li T Y, Yorke J A, Period three implies chaos. *American Mathematical Monthly*, 1975, 82(10): 985-992.

[4] Feigenbaum M J. Quantitative universality for a class of nonlinear transformations. *Journal of Statical Physics*, 1978, 19(1): 25-52.

[5] Liu Jin-mei1, Qiu Shui-sheng2. A New Three-Dimension Chaotic System with an Absolute Item. *Journal of South China University of Technology*, 2013, 04(4): 137-141.

[6] Yu Si-Min. Circuit implementation for generating three-dimensional multi-scroll chaotic attractors via triangular wave series. *ACTA PHYSICA SINICA*, 2005, 04 (4): 1500-1509.

[7] Lü Ensheng, Sun caiyun. Design of Chua's circuit based on sign function and application thereof. *Chena science paper*, 2014, 1, 9(1): 37-39.

[8] Zhan Kai, Jiang Wengang. A novel four-wing hyper-chaos system and its application in image encryption. *Computer Engineering and Applications*, 2016, 3.

A three-dimensional chaotic system generating single-wing and two-wing chaotic attractors

Hongyan Jia, Yongjun Wu
Department of Automation, Tianjin University of Science and Technology,
1038 Dagunanlu Road, Hexi District, Tianjin300222, PR China

E-mail: jiahy@tust.edu.cn
www.tust.edu.cn

Abstract

In this paper, a three-dimensional chaotic system is proposed based on a simple 3-D autonomous system by adding a linear piecewise function. It is very interesting that the new three-dimensional chaotic system can generate single-wing or two-wing chaotic attractor with variation of parameter. Several basic characteristics of the system, such as bifurcation diagram, phase orbits, and Lyapunov exponents are given to investigate different chaotic motions for the new system. The new system is found to be chaotic in a wide parameter range, and to show many complex dynamical behaviors. That is, the results obviously show the system is chaotic and its dynamics are very complex.

Keywords: autonomous system; single-wing attractor; two-wing attractor; Lyapunov exponents; bifurcation diagram.

1. Introduction

In recent decades, many chaotic systems have been proposed since Lorenz discovered a simple three-dimensional smooth autonomous chaotic system in 1963 [1]. It is well known that chaotic systems can show complex dynamic characteristics that can be used in many application fields such as engineering [2], image encryption [3], secure communications [4] etc. Therefore, many scholars and researchers proposed and studied some chaotic systems, such as Chen system [5], Lü system [6], Qi system [7], and so on [8,9].

Generally, the structure and characteristics of the chaotic systems can be changed when introducing linear piecewise function. Therefore, by the method of introducing linear piecewise function, researchers have designed many complex chaotic systems. For example, in [10], the paper introduced the method of designing chaotic system by using piecewise linear function, and discussed the computer simulation and circuit implementation in detail. In addition, the application of the nondominated sorting genetic algorithm to optimize two characteristics of multi-scroll chaotic oscillators was introduced in [11]. Where the linear piecewise function is used to generate the two multi-scroll chaotic oscillators.

In this paper, a new chaotic system is designed by adding a linear piecewise function to the second equation of a simple 3-D autonomous system [12]. This system can show some very complex dynamic characteristics generating single-wing or two-wing chaotic attractor when varying the system parameters. In the following sections, bifurcation diagram, phase orbits, and Lyapunov exponents of the system are calculated to analyze the dynamic characteristics of the system. The numerical results analysis clearly show that this system is chaotic and its dynamics are very complex.

2. The 3-D chaotic system

Considering the simple three-dimensional autonomous system [12]:

$$\begin{cases} \dot{x} = -ax + y + byz \\ \dot{y} = cy - xz + z \\ \dot{z} = dxy - hz \end{cases} \tag{1}$$

Where the parameters a, b, c, d and h are real constants.

Here, a linear piecewise function is introduced to the three-dimensional autonomous system above. This piecewise function will substitute for the linear term z of the second equation, and the new chaotic system is obtained as following.

$$\begin{cases} \dot{x} = -ax + y + byz \\ \dot{y} = cy - xz + f(z) \\ \dot{z} = dxy - hz \end{cases} \tag{2}$$

Where $f(z)$ is the linear piecewise function described as formula (3):

$$f(z) = m_N z + 0.5 \sum_{i=1}^{N} (m_{i-1} - m_i)(|z + E_i| - |z - E_i|) \tag{3}$$

$$E_n = \left(1 + 2\sum_{i=1}^{n-1} \frac{|m_0|}{|m_i|}\right) E_1 \tag{4}$$

Where $m_0 = -m_1$, $N = 0, 1, 2, \cdots$, $i = 0, 1, 2, \cdots$, $n = 1, 2, \cdots$, equation (4) is the turning points formula of the linear piecewise function. Here, we set $N = 1, n = 1, E_1 = 0.5$, so the linear piecewise function can be simplified as equation (5).

$$f(z) = m_1 z - m_1(|z + 0.5| - |z - 0.5|) \tag{5}$$

3. Dynamical characteristics of the chaotic system

For the chaotic system (2), when the parameters *a, b, c, d, h* and m_1 are taken different values, the system can show different kinds of chaotic states. By analyzing, the system is found to show a single-wing chaotic attractor when the parameters $a = 37$, $b = 25$, $c = 13$, $d = 6$, $h = 8$, $m_1 = 2$ and two-wing chaotic attractor when the parameters $a = 37$, $b = 25$, $c = 16$, $d = 6$, $h = 8$ and $m_1 = 0.5$, respectively, as shown in Fig.1 and Fig.2. In the following section, the Lyapunov exponents and the corresponding bifurcation diagram of system (2) are given to analysis the complex chaotic dynamics.

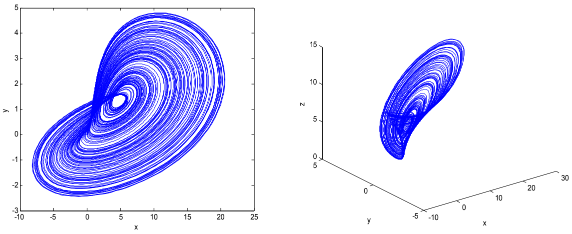

(a) x-y plane (b) x-y-z plane

Fig.1 Single-wing attractor of system (2)

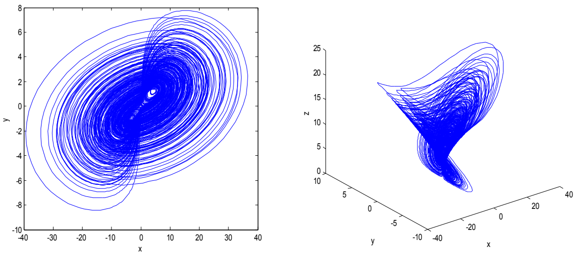

(a) x-y plane (b) x-y-z plane

Fig.2 Two-wing attractor of system (2)

4. *Lyapunov exponents and bifurcation diagram analysis*

Now let $a = 37$, $b = 25$, $c = 16$, $d = 6$, $h = 8$, and select $m_1 = 2$, and $m_1 = 0.5$, the chaotic dynamics of this system are investigated by means of Lyapunov exponents analysis and bifurcation diagram analysis, respectively.

4.1 Lyapunov exponents and bifurcation diagram analysis when $m_1 = 2$

Here, dynamics analysis of the system (2) is firstly done when the parameters $a = 37$, $b = 25$, $m_1 = 2$, $d = 6$, $h = 8$ and vary c.

The Lyapunov exponents and the corresponding bifurcation diagram of the system with variation of parameter *c* are shown in Fig.3 (a) and Fig.3 (b), where $a = 37$, $b = 25$, $d = 6$, $h = 8$, $m_1 = 2$ and $c \in [0, 30]$. The basic dynamics of the chaotic system (2) can be summarized by the Lyapunov exponents and bifurcation diagrams. By analyzing Lyapunov exponents in the Fig.3 (a), when $c \in [1.8, 9.3)$, the system (2) exhibits periodic dynamics with the biggest Lyapunov exponent of the system (2) being zero. when $c \in [9.3, 25.2)$, the biggest Lyapunov exponent of the system (2) is found to positive, implying that the system is chaotic.

In addition, by analyzing the corresponding bifurcation diagram in Fig.3 (b), the system (2) also exhibits periodic dynamics when $c \in [1.8, 9.3)$, here, a period-2 orbit is given to show its periodic dynamics when $c = 8$, as shown in Fig.4 (a) and Fig.4 (b). And this system also becomes chaotic when $c \in [9.3, 25.2)$, and its dynamics very complex. A single-wing chaotic attractor is found when the parameter $c = 16$, as shown in Fig.4 (c) and Fig.4 (d). And a double-wing chaotic attractor is observed when the parameter $c = 20$, as shown in Fig.4 (e) and

Fig.4 (f). Moreover, when increasing c in the range of $c \in [25.2,\ 30)$, there are just several or two lines in the bifurcation diagram. The system (2) shows period-2 orbit when $c = 27$, as shown in Fig.4 (g) and Fig.4 (h).

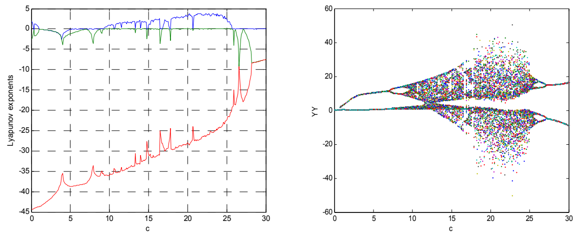

(a) Lyapunov exponents (b) bifurcation diagrams

Fig.3 Lyapunov exponents and bifurcation diagrams of system (2) with $a = 37,\ b = 25,\ d = 6,\ h = 8,\ m_1 = 2$ and $c \in [0,\ 30]$.

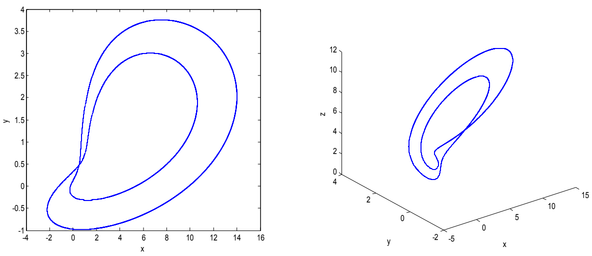

(a) x-y plane (b) x-y-z plane

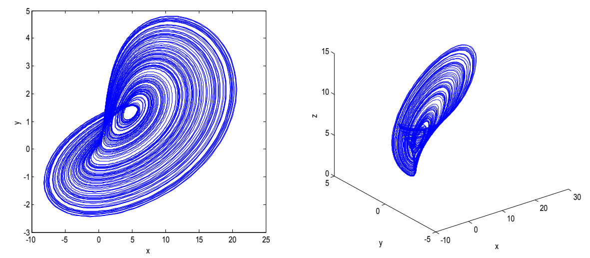

(c) x-y plane (d) x-y-z plane

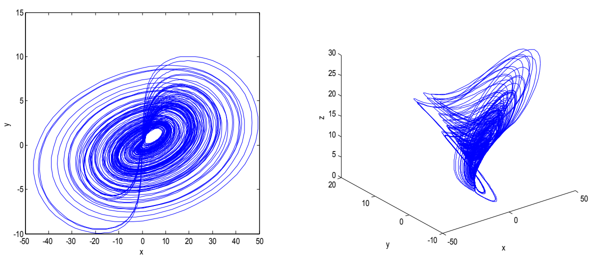

(e) x-y plane (f) x-y-z plane

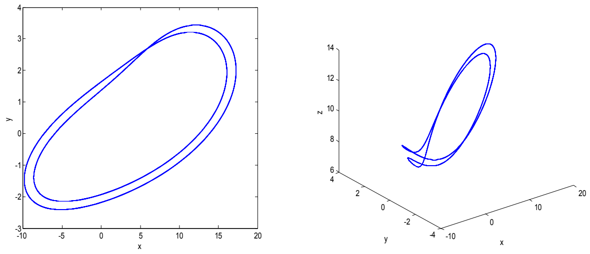

(g) x-y plane (h) x-y-z plane

Fig.4 The orbital modes of system (2) with $a = 37,\ b = 25,\ d = 6,\ h = 8,\ m_1 = 2$. (a) period-2 orbit when $c = 8$, (b) period-2 orbit when $c = 8$, (c) single-wing chaotic attractor when $c = 16$, (d) single-wing chaotic attractor when $c = 16$, (e) double wing chaotic attractor when $c = 20$, (f) double wing chaotic attractor when $c = 20$, (g) period-2 orbit when $c = 27$, (h) period-2 orbit when $c = 27$.

4.2 Lyapunov exponents and bifurcation diagram analysis when $m_1 = 0.5$

Next, the dynamics behavior of the system (2) is analyzed when the parameters $a = 37,\ b = 25,\ m_1 = 0.5,\ d = 6,\ h = 8$ and vary c.

When varying parameter c, the Lyapunov exponents and the corresponding bifurcation diagram of the system (2) are shown in Fig.5(a) and Fig.5(b), where $a = 37$, $b = 25,\ d = 6,\ h = 8,\ m_1 = 0.5$ and $c \in [0,\ 30]$. By analyzing the Lyapunov exponents in Fig.5(a), it is found that the system shows periodic dynamics when $c \in [0,\ 4.5)$. And in the regions $c \in [4.5,\ 21.8)$ and $c \in [22.2,\ 25.5)$, the system (2) exhibits chaos with just one positive Lyapunov exponent. When $c \in [25.5,\ 30]$, the system shows periodic motion again with the biggest Lyapunov exponent of the system (2) being zero.

Considering the bifurcation diagram in Fig.5(b), in the region $c \in [0,\ 4.5)$, the system shows the characteristic of period orbit and it shows a period-2 orbit when $c = 28$, as shown in Fig.6(a) and Fig.6(b). When $c \in [4.5,\ 21.8)$ and $c \in [22.2,\ 25.5)$, the system (2) exhibits complex chaotic characteristics. In this case, a two-wing chaotic attractor is found when $c = 16$ and it is given in Fig.6(c) and Fig.6 (d). As c increases in the region $c \in [25.5,\ 30]$, the system enters into periodic dynamics and it exhibits period-1 orbit when $c = 29$, as shown in Fig.6(e) and (f).

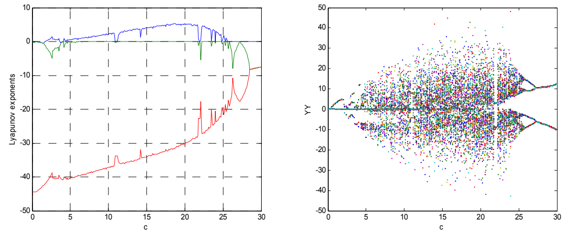

(a) Lyapunov exponents (b) bifurcation diagrams

Fig.5 Lyapunov exponents and bifurcation diagrams of system (2) with $a = 37,\ b = 25,\ d = 6,\ h = 8,\ m_1 = 0.5$ and $c \in [0,\ 30]$.

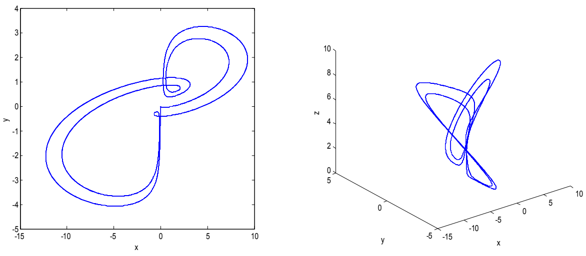

(a) x-y plane (b) x-y-z plane

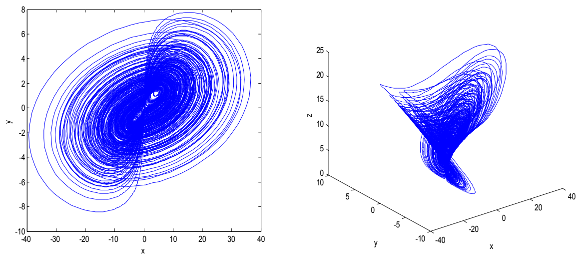

(c) x-y plane (d) x-y-z plane

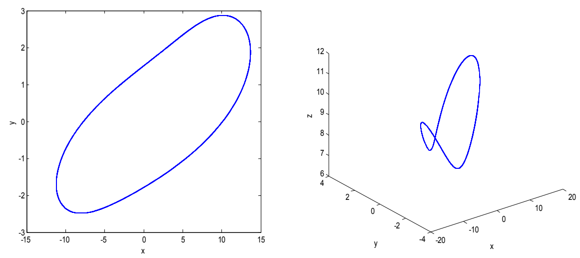

(e) x-y plane (f) x-y-z plane

Fig.6 The orbital modes of system (2) with $a = 37,\ b = 25,\ d = 6,\ h = 8,\ m_1 = 0.5$. (a) period-2 orbit when $c = 28$, (b) period-2 orbit when $c = 28$, (c) two-wing chaotic attractor when $c = 16$, (d) two-wing chaotic attractor when $c = 16$, (e) periodic orbit plane when $c = 29$, (f) period-1 orbit when $c = 29$.

5. Conclusion

In this paper, a three-dimensional chaotic system is designed by introducing a linear piecewise function. It is found that the system can generate a single-wing chaotic attractor or two-wing chaotic attractor by varying parameter m_1. Some basic properties of the chaotic system were analyzed by means of Lyapunov exponents and bifurcation diagrams analysis in detail. The numerical results confirm that this chaotic system is chaotic and it can show complex dynamic characteristics.

References

1. Lorenz E N, Deterministic non-periodic follow, *Journal of Atmospheric Sciences*. 20(2) (1963) 130-141.
2. Ihsan Pehlivan, Akif Akgul, Irene Moroz, Sundarapandian Vaidyanathan, A new four-scroll chaotic attractor and its engineering applications. *Optik*, 127 (2016) 5491–5499.
3. Leyuan Wang, Hongjun Song, Ping Liu, A novel hybrid color image encryption algorithm using two complex chaotic systems. *Optics and Lasers in Engineering*, 77 (2016) 118–125.
4. Xiangjun Wu, Hui Wang, Hongtao Lu, Modified generalized projective synchronization of a new fractional-order hyperchaotic system and its application to secure communication. Nonlinear Analysis: *Real World Applications*, 13 (2012) 1441–1450.
5. Chen G R, Ueta T, Yet another chaotic attractor, *International Journal of Bifurcation and Chaos*. 9 (1999) 1465-1466.
6. Jinhu Lu, Guanrong Chen, A new chaotic attractor coined, *International Journal of Bifurcation and Chaos*. 12 (2002) 659-661.
7. Guoyuan Qi, Guanrong Chen, M. A. van Wyk, B. J. van Wyk, A four-wing chaotic attractor generated from a new 3-D quadratic autonomous system. *Chaos, Solitons and Fractals. 38 (2008) 705-721.*
8. *Itoh, M*akoto, Chua, Leon O, Meristor oscillators, *International journal of bifurcation and chaos*, 11(18) (2008) 3183-3206.
9. Guoyuan Qi, Barend Jacobus van Wyk, Michael Antonie van Wyk, A four-wing attractor and its analysis, *Chaos, Solitons and Fractals*, 40 (2009) 2016–2030.
10. Jinhu Lu, Guanrong Chen, Generating multiscroll chaotic attractors: Theories, methods and applications. *International Journal of Bifurcation and Chaos*, 4(16) (2006) 775-858.
11. Luis Gerardo de la Fraga · Esteban Tlelo-Cuautle, Optimizing the maximum Lyapunov exponent and phase space portraits in multi-scroll chaotic oscillators, *Nonlinear Dyn*, 76 (2014) 1503–1515.
12. Sara Dadras, Hamid Reza Momeni, A novel three-dimensional autonomous chaotic system generating two, three and four-scroll attractors. *Physics Letters A*, 373 (2009) 3637-3642.

Circuit Implementation of a New Fractional-Order Hyperchaotic System

Xuyang Wu, Hongyan Jia, Ning Bai, Weibo Jia

Department of Automation, Tianjin University of Science and Technology,

1038 Dagunanlu Road, Hexi District, Tianjin 300222, PR China

E-mail: jiahy@tust.edu.cn

www.tust.edu.cn

Abstract

In the paper, some basic dynamic properties of a new fractional-order hyperchaotic system were firstly investigated, such as the phase trajectory, bifurcation diagram, Lyapunov exponent etc. Then the paper designed an analog circuit to implement the fractional-order hyperchaotic system. The results from the circuit were consistent with those from the numerical analysis, and thus the hyperchaotic characteristics of the new fractional-order system are verified physically. It is very important to implement fractional-order hyperchaotic systems with more complicated dynamics for theoretical research and practical application. The new hyperchaotic system will provide a new model for engineering applications.

Keywords: fractional-order; hyperchaotic; circuit implementation; dynamical characteristics

1. Introduction

In the last century, Rössler proposed the first hyperchaotic system [1]. Since then, the hyperchaotic system has attracted more and more attention owning to its abundant and complex dynamic characteristics. Extensive and in-depth researches have been carried out, such as the modified hyperchaotic system, circuit implementation of hyperchaotic systems [2-4], especially in synchronous control [5-7].

In 1995, Hartley studied the fractional-order Chua system in which the chaotic attractor was found [8]. Soon chaotic attractors in the fractional-order Lorenz system were also confirmed [9] and then fractional-order systems have been investigated and developed in more and more fields [10-13].

At present, most researchers focus on the low-dimensional chaotic system, while there are few researches on the higher-dimensional and hyperchaotic system. However, many real systems in nature and society often are higher-dimensional and hyperchaotic. Therefore, it is very interesting to study fractional-order hyperchaotic systems with more complicated dynamics for theoretical research and practical application.

For the fractional-order differential equation, numerical methods used commonly are the frequency domain approximation or Adams-Bash-Moulton algorithm. In this paper, with the frequency domain approximation, we study some basic dynamical characteristics of a four-dimensional hyperchaotic system, such as the phase trajectory, Lyapunov exponent and bifurcation diagram. And then we design a circuit to implement the four-dimensional fractional-order hyperchaotic system. These will provide technical support for engineering applications.

2. Four-Dimensional Hyperchaotic System

Recently, a new four-dimension integral-order hyper-chaotic system [14] based on the Dadras-Momeni （D-M）system [15] was proposed by Nik, Van Gorder et al. which is given by

$$\begin{cases} \dot{x} = y - ax + byz, \\ \dot{y} = cy - xz + z - \omega, \\ \dot{z} = dxy - hz, \\ \dot{\omega} = px + k, \end{cases} \tag{1}$$

where x, y, z, ω are state variables and $a, b, c, d, \ h, p, k$ are system parameters.

When the parameters are chosen as:

$$\begin{cases} a = 36, \\ b = 0.4, \\ d = 1, \\ h = 5.07, \\ p = 5, \\ k = 0.4, \end{cases}$$

the system is hyperchaotic and the hyperchaotic strange attractor is shown in Fig.1.

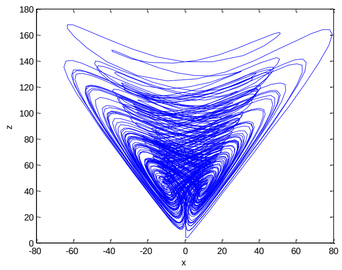

Figure 1 Hyperchaotic attractor of the system (1).

3. Fractional-Order Four-Dimensional Hyperchaotic System

Basing on the integer-order system mentioned above, we introduce a fractional-order hyperchaotic H-M system:

$$\begin{cases} \frac{d^\alpha x}{dt} = y - ax + byz, \\ \frac{d^\alpha y}{dt} = cy - xz + z - \omega, \\ \frac{d^\alpha z}{dt} = dxy - hz, \\ \frac{d^\alpha \omega}{dt} = px + k, \end{cases} \tag{2}$$

where x, y, z, ω are state variables and $a, b, c, d, \ h, p, k$ are system parameters.

We utilize the Riemann-Liouville definition of fractional-order differentiation:

$$\frac{d^\alpha f(t)}{dt} = \frac{1}{\Gamma(n-\alpha)} \frac{d^n}{dt^n} \int_0^t \frac{f(\tau)}{(t-\tau)} d\tau, \tag{3}$$

its Laplace transform is:

$$L\left[\frac{d^\alpha f(t)}{dt^\alpha}\right] = s^\alpha L[f(t)]. \tag{4}$$

Reference [1] provides an approximation of $1/s^{0.9}$ with an error of about 2 dB as follows:

$$\frac{1}{s^{0.9}} \approx \frac{2.2675(s+1.292)(s+215.4)}{(s+0.01292)(s+2.154)(s+359.4)} \ . \tag{5}$$

We use the approximation to analyze the system (2) by using the Matlab. Fig.2 shows the fractional-order hyperchaotic phase diagram with

$$\begin{cases} a = 36, \\ b = 0.4, \\ d = 1, \\ h = 5.07, \\ p = 5, \\ k = 0.4, \end{cases}$$

which indicates clearly that hyperchaotic behaviors exist in the above fractional-order system.

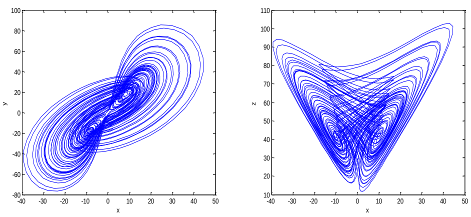

Figure 2 Attractors in fractional-order system (2). (a) $x - y$ phase plane, (b) $x - z$ phase plane.

In order to further study the chaotic characteristics of the system (2), we obtain a bifurcation diagram by altering parameter h, which is shown in Fig.3. It can be seen from the figure that the system discretization is most obvious when h is in the range of 5-12.

In addition, we further consider the Lyapunov exponents of the system (2), which is shown in Fig.4. The result shows that the biggest two Lyapunov exponents are positive, which satisfies the necessary conditions for the hyperchaotic system.

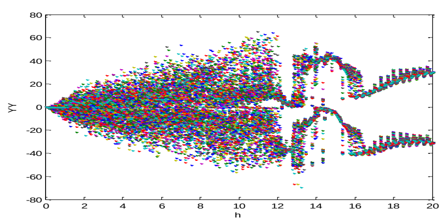

Figure 3 Bifurcation diagram of the system (2).

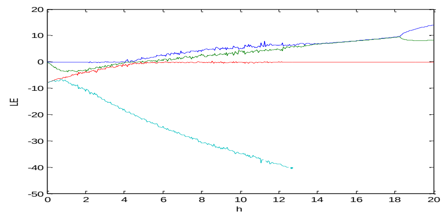

Figure 4 Lyapunov exponents of the system (2)

4. Circuit Design of the Fractional-Order System

In this section, utilizing the frequency domain approximation, we design the circuit of the system (2) by using the resistance, capacitance, analog operational amplifier LF347BN and multiplier AD633JN. The amplitude of voltage operational amplifier is ± 13.5V that is significantly less than the range of the system. Therefore, we make the voltage to be one tenth of the value that is a normal value in the system. We choose $c_1 = c_4 = c_7 = c_{10} = 0.52\mu F$, $c_2 = c_6 = c_9 = c_{12} = 0.73\mu F$, $c_3 = c_5 = c_8 = c_{11} = 1.1\mu F2$, $R_2 = R_5 = R_6 = R_{14} = R_{15} = R_{16} = R_{17} = R_{22} = R_{23} = R_{25} = R_{26} = R_{31} = R_{32} = R_{37} = R_{38} = 10K\Omega$, $R_{18} = R_{24} = R_{30} = R_{36} = 20K\Omega$, $R_{19} = R_{27} = R_{33} = R_{39} = 1.5M\Omega$, $R_{20} = R_{28} = R_{34} = R_{40} = 61.54K\Omega$, $R_{21} = R_{29} = R_{35} = R_{41} = 2.5K\Omega$, $R_1 = 0.278K\Omega$, $R_3 = 0.25K\Omega$, $R_4 = 0.5K\Omega$, $R_7 = R_9 = 0.1K\Omega$, $R_8 = 1.9K\Omega$, $R_{10} = 2K\Omega$, $R_{11} = 250K\Omega$, $R_{12} = 14K\Omega$, $R_{13} = 1K\Omega$. The circuit design of the system is shown in Fig. 5.

This circuit is designed to implement the system (2), and the experimental results obtained by the Multisim are shown in Fig.6. Obviously, the experimental results are consistent with the results of the numerical analysis, which physically proves the system (2).

5. Conclusions

In this paper, we proposed a fractional-order hyperchaotic H-M system based on the integer-order H-M system. Some basic dynamical characteristics of the proposed system, such as the phase trajectory, Lyapunov exponent, and bifurcation diagram, were analyzed respectively by using the Matlab. The results show that the system has more complicated dynamic characteristics, which will enrich the research content of the fractional-order hyperchaotic system. What's more, an analog circuit was designed to realize the four-dimensional fractional-order hyperchaotic system, and the experimental results are in agreement with the numerical analysis, which further confirms the existence of the four-dimensional fractional-order hyperchaotic system. The work in this paper may offer a model for engineering applications.

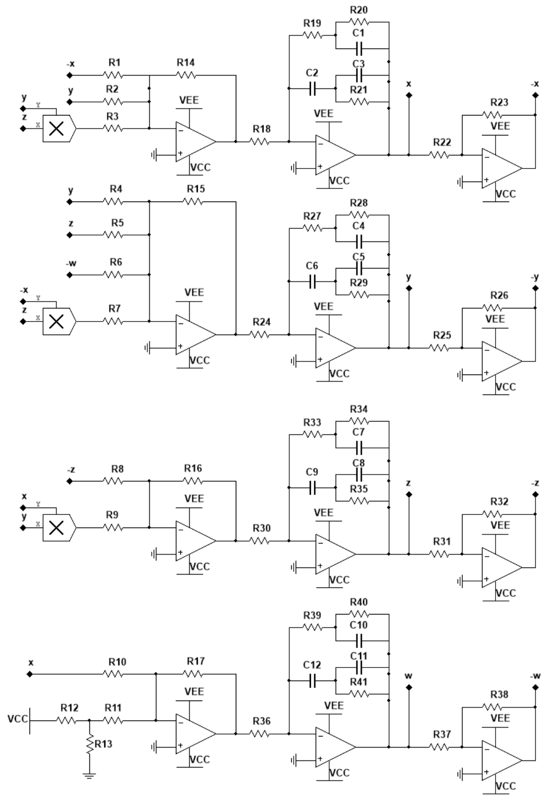

Figure 5 Circuit implementation of the system (2)

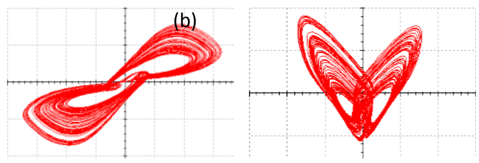

Figure 6 Experimental results by using the Multisim. (a) $x-y$ phase plane, (b) $x-z$ phase plane.

Acknowledgements

This work was supported by the Undergraduate Training Program for Innovation and Entrepreneurship of Tianjin (201610057058).

References

1. Rössler, An equation for hyperchaos, *Phys. Lett. A.* 71(2-3)

(1979) 155-157.
2. G Wang, X Zhang, Y Zheng, Y Li, A new modified hyperchaotic Lü system, *Phys. A*. 371(2) (2006) 260-273.
3. G Y Qi, M A V Wyk, B J V. Wyk, G R Chen, A new hyperchaotic system and its circuit implementation, *Chaos Soliton. Fract*. 40(5) (2009) 2544-2549.
4. Zarei A, Tavakoli S, Hopf bifurcation analysis and ultimate bound estimation of a new 4-D quadratic autonomous hyper-chaotic system, *Appl. Math. Comput.* 291 (2016) 323-339.
5. S Zheng, G G Dong, Q S Bi, A new hyperchaotic system and its synchronization, *Appl. Math. Comput*. 215(9) (2010) 3192-3200.
6. S Q Pang, Y J Li, A new hyperchaotic system from the Lü system and its control, *I. ComDut. ADDl. Math.* 235(8) (2011) 2775-2789.
7. Luo RZ, Zeng YH, The control and synchronization of a class of chaotic systems with output variable and external disturbance, *J.Comput. Nonlin. Dyn*. 11(5) (2016) 051011.
8. Hartley T T, Lorenzo C F, Qammer H K, Chaos in a fractional order Chua's system, *IEEE Trans. Circuits Syst. I: Fundamental Theory and Applications*. 42(8) (1995) 485-490.
9. Grigorenko I, Grigorenko E, Chaotic dynamics of the fractional Lorenz system, *Phys. Rev. Lett*. 91(3) (2003) 034101/1-034101/4.
10. Yang Q G, Zeng C B, Chaos in fractional conjugate Lorenz system and its scaling attractors, *Commun. Nonlinear. Sci*. 15(12) (2010) 4041-4051.
11. Jia H Y, Chen Z Q, Xue W, Analysis and circuit implementation for the fractional-order Lorenz system, *Acta Phys. Sin*. 62(14) (2013) 140503/1-140503/7 (in Chinese)
12. Yang JH, Sanjuan, MAF , Liu HG, Cheng G, Bifurcation transition and nonlinear response in a fractional-order system, *J. Comput. Nonlin. Dyn*. 10(6) (2015) 061017.
13. Boulkroune A, Bouzeriba A , Bouden T, Fuzzy generalized projective synchronization of incommensurate fractional-order chaotic systems, *Neurocomputing*. 173 (2016) 606-614.
14. Dadras S, Momeni HR, A novel three-dimensional autonomous chaotic system generating two, three and four-scroll attractors, *Phys. Lett. A*. 373(40) (2009) 3637-3642.
15. Nik HS, Van Gorder RA, Gambino G et al. The chaotic Dadras-Momeni system: control and hyperchaotification, Ima. J. Math. Control I. 33(2) (2016) 497-518.

Estimation and Categorization of Errors in Error Recovery Using Task Stratification and Error Classification

Akira Nakamura, Kazuyuki Nagata
Intelligent Systems Research Institute
National Institute of Advanced Industrial Science and Technology (AIST)
Central 2, 1-1-1 Umezono, Tsukuba, Ibaraki, 305-8568 Japan

Kensuke Harada
Robotic Manipulation Research Group
Systems Innovation Department
Graduate School of Engineering Science, Osaka University
1-3 Machikaneyama, Toyonaka 560-8531, Japan

Natsuki Yamanobe
Intelligent Systems Research Institute
National Institute of Advanced Industrial Science and Technology (AIST)
Central 2, 1-1-1 Umezono, Tsukuba, Ibaraki, 305-8568 Japan

E-mail: a-nakamura@aist.go.jp, k-nagata@aist.go.jp,
harada@sys.es.osaka-u.ac.jp, n-yamanobe@aist.go.jp
www.aist.go.jp

Abstract

We have proposed an error recovery method using the concepts of task stratification and error classification in which errors are classified based on an estimated cause into several categories such as modeling errors and planning errors. When an error is classified correctly, the possibility increases that the most suitable recovery will be performed. This paper describes our procedure for the categorization of errors.

Keywords: error recovery, task stratification, error classification, manipulation, planning

1. Introduction

Error recovery is an important research theme for the manipulation tasks of plant maintenance and industrial production robots.[1-4] However, systematical methods of error recovery have not yet appeared. We have proposed an error recovery method using the concepts of task stratification and error classification.[5, 6] A highly reliable system expression is derived by an analysis of an error and an estimate of the cause in our error recovery technique, and the task is continued based on the expressions of the corrected system.

In error recovery, judgment of an error is performed during the execution of a process by the system. In our method, classification of errors that have occurred is performed based on an estimated cause. Specifically, errors are classified into several categories such as sensing errors, modeling errors, planning errors and execution errors. When an error is classified correctly, the possibility increases that the most suitable recovery will be performed. In this paper, we describe a procedure for the categorization of errors.

A concept of error recovery is described in Section 2. A method of error classification and the recovery process in which the classification is used are proposed in Section 3 and 4, respectively.

2. Concept of Error Recovery

The basis of the error recovery technique we use is described in this section. The target tasks are robot applications in industrial factories and power generation facilities that mainly involve assembly and parts replacement. In recent years, as robots have been playing increasingly active roles in the daily life of humans, such tasks as cleaning, washing and cooking have also become a target of our error recovery system.

In this paper, our technique of error recovery with the concepts of both task stratification and error classification as shown in Ref. 5 is used. We proposed a new type of error recovery using both forward and backward pass in Ref. 6.

Figure 1 shows the basic concept of our error recovery method. The main part comprises tasks performed by the robot that are basically elements with sequences of sensing, modeling, planning and execution. This main part is hierarchized from the main work objective to a bottom layer in our method, but is composed of process flows of sensing, modeling, planning and execution for each hierarchy.

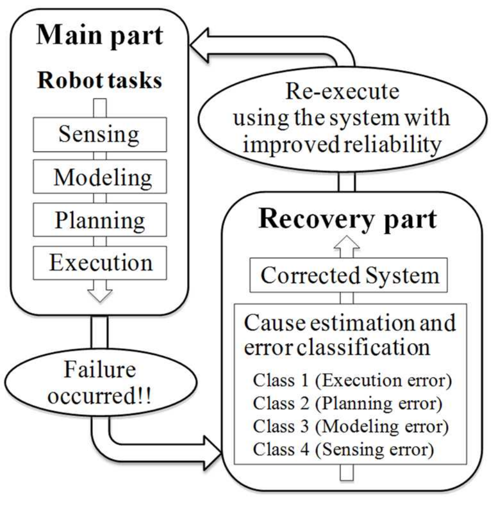

Fig. 1 Robot task system with an error recovery function

If a failure occurs in this main part, the process advances to the recovery part (Fig. 1). The basic flow in this recovery part is as follows: the cause of the error is estimated, the error is classified, the system is corrected, and re-execution is performed using the corrected system with improved reliability.

3. Cause of Error

We have explained that the tasks of the robot consist of the process flows of sensing, modeling, planning and execution. Therefore, the following four types of errors are considered and the Class number is assigned respectively. For simplification, the cause of the error is set to only one in this paper.

(Class 1) Execution Error

This error occurs from a problem with the machine and the task can be achieved without failing usually if the same execution is repeated many times. When a problem with a mechanism is indicated specifically, the cause of the most typical error is a backlash of a gear. The clearance is altered by abrasion. There are many causes such as changes in temperature and humidity, vibration, bending, aged deterioration, and decreased lubricant. It is desirable to identify the cause through experience and artificial intelligence.

(Class 2) Planning Error

This error occurs when the expression of the system used in the computer software does not express a real system strictly. The cause of the error is mostly a setting mistake of a threshold and a parameter in planning, and when that mistake is corrected, the task should succeed. A correct system expression is also derived by specifying the part to be corrected from an analysis of the error.

(Class 3) Modeling Error

This error occurs when the geometry model used in the computer software does not express the real object exactly. Therefore, the task may succeed if the model is corrected and the task is performed again. When the model used is a simplification of the real object, the necessary part is changed to express the model more exactly. A model appropriate for performing a more accurate task should be derived by performing it repeatedly.

(Class 4) Sensing Error

This error occurs due to an error in sensing and insufficient calibration, and when that is corrected and the task is re-executed, the task should succeed. A camera parameter will be generally corrected. In many cases, it becomes necessary to stop the execution task and make the correction.

The correction is performed based on the cause of the error specified by the classification, and the task is performed again using the corrected system with improved reliability as shown in the flow chart (Fig. 2) depicting a task of loosening a screw using screwdriver as an example.

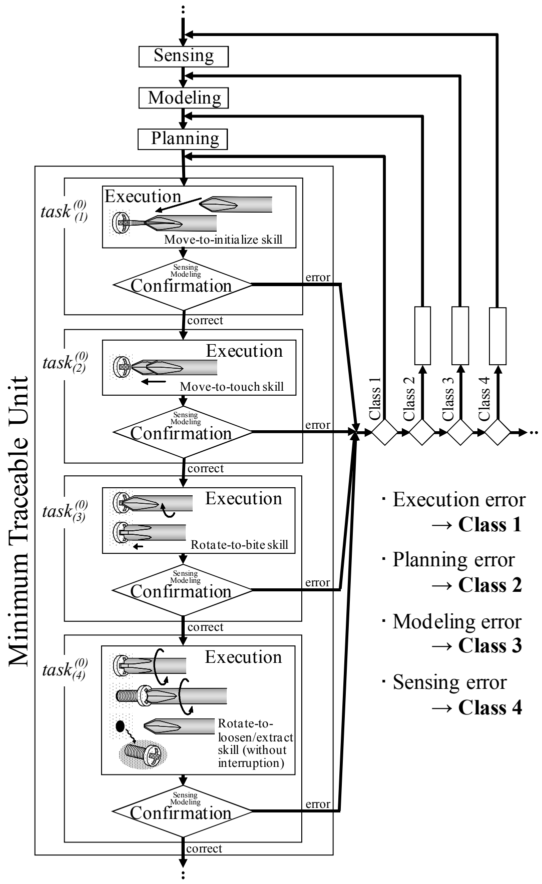

Fig. 2 Process flow with error recovery in skill sequence of loosening a screw using a screwdriver

4. Process of Error Recovery

In this section, we will consider how to take passes based on the possibility of the error classification.

(Case 1) Estimation of the cause of the error is not possible.

The error recovery is performed by completely regarding the error cause as a virtual one. In this case, as shown in the process of the recovery in the flow chart in Fig. 3, the cause is first regarded as an execution error of (Class 1) and the task is merely repeated. When the error status continues even after repeating more than one time, the error is then regarded as a planning error of (Class 2). When numerical values for various parameters are changed, it is possible that something to improve may be found. When that is found and corrected, the task is performed and the error status is checked. When the error status is removed, it is possible to assume that a planning error was the cause. If the error recovery does not succeed, the cause is estimated as (Class 3) and (Class 4) and a similar procedure is performed successively.

(Case 2) Estimation of the cause of the error is possible to some extent.

In this case, the cause is narrowed down to some extent from experience and it can be chosen from those

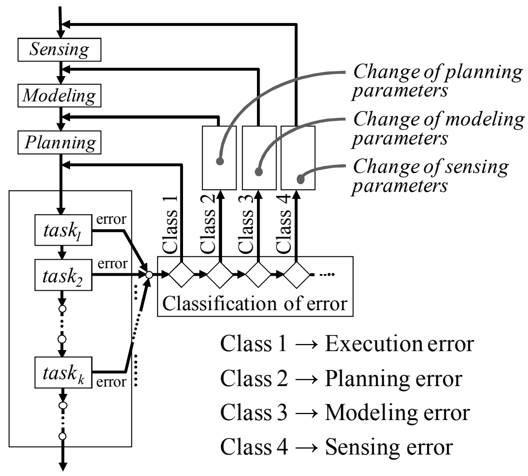

Fig. 3 Fundamental process flow with error recovery

in a list. The error cause is sorted by the order in which it tends to occur and the recovery flow chart (Fig. 3) is changed. For example, when the priority of the error cause is the following,

(i) Error 1 (Class 1)
(ii) Error 2 (Class 3)
(iii) Error 3 (Class 2)
(iv) Error 4 (Class 3)
(v) Error 5 (Class 2)
(vi) Error 6 (Class 4)

the flow chart of the recovery becomes as shown in Fig. 4. The cause is specified from the error conditions, the task when the error occurred, and the process up to that point. The system is corrected and the task is re-executed by the system with improved reliability.

5. Conclusion

We have shown a method for classifying the cause when an error occurs and how to process the recovery for the case in question. The accuracy of the estimated cause

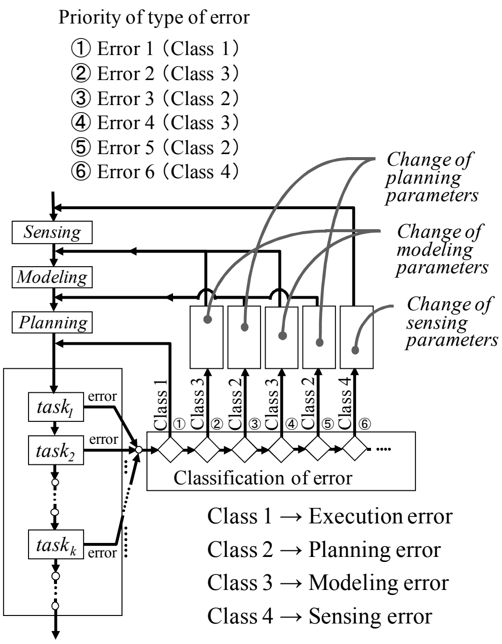

Fig. 4 Corrected process flow with error recovery

of the error depends on the degree of experience with the task. We presented and described the estimation in two ways: with experience and without experience. In addition, we described the route that approximated the true cause in each category of the error cause. When the cause can be identified correctly, the expression of the system becomes correct. Therefore, the probability that the error will occur in the execution of a later task will decrease. Our future studies will include the applicability of our method to an actual system and a search for a method that can derive the cause more accurately even when there is little experience.

Acknowledgement

This work was supported by JSPS KAKENHI Grant Number 15K00370.

References

1. B. R. Donald, Planning multi-step error detection and recovery strategies, *Int. J. Robot. Res.*, 9(1) (1990) 3-60.
2. E. Z. Evans and C. S. George Lee, Automatic generation of error recovery knowledge through learned reactivity, in *Proc. IEEE Int. Conf. Robot. Autom.,* (San Diego, USA, 1994), 2915-2920.
3. C. M. Baydar and K. Saitou, Off-Line error prediction, diagnosis and error recovery using virtual assembly systems, in *Proc. IEEE Int. Conf. Robot. Autom.,* (Seoul, Korea, 2001), 818-823.
4. C. W. Moon and B. H. Lee, A model-based error recovery scheme for a multi-robot system, *Robotica,* Cambridge Univ. Press, **19**(4) (2001) 371-380.
5. A. Nakamura and T. Kotoku, Systematization of error recovery in skill-based manipulation, Artificial Life and Robotics, Springer, **14**(2) (2009) 203-208.
6. A. Nakamura, K. Nagata, K. Harada, N. Yamanobe, T. Tsuji, T. Foissotte and Y. Kawai, Error recovery using task stratification and error classification for manipula-tion robots in various fields, in *Proc IEEE/RSJ Int. Conf. on Intell. Robots Syst.,* (Tokyo, Japan, 2013), 3535-3542.

The Suitable Timing of Visual Sensing in Error Recovery Using Task Stratification and Error Classification

Akira Nakamura, Kazuyuki Nagata
Intelligent Systems Research Institute
National Institute of Advanced Industrial Science and Technology (AIST)
Central 2, 1-1-1 Umezono, Tsukuba, Ibaraki, 305-8568 Japan

Kensuke Harada
Robotic Manipulation Research Group
Systems Innovation Department
Graduate School of Engineering Science, Osaka University
1-3 Machikaneyama, Toyonaka 560-8531, Japan

Natsuki Yamanobe
Intelligent Systems Research Institute
National Institute of Advanced Industrial Science and Technology (AIST)
Central 2, 1-1-1 Umezono, Tsukuba, Ibaraki, 305-8568 Japan

E-mail: a-nakamura@aist.go.jp, k-nagata@aist.go.jp,
harada@sys.es.osaka-u.ac.jp, n-yamanobe@aist.go.jp
www.aist.go.jp

Abstract

Judgment of errors for recovery is performed during execution of the system. Ideally, it is desirable for the judgment to be performed at several times. However, in that case, many sensors would be needed and it would lead to disturbing the workflow. Therefore, it is important to be able to judge an error efficiently in the most suitable timing and within a few attempts. This paper describes a method for efficient timing of visual sensing for error recovery.

Keywords: error recovery, task stratification, error classification, manipulation, sensing timing

1. Introduction

In the manipulation tasks performed by robots involved in industrial production and household chores, error recovery techniques are important since robots need to perform complicated tasks.[1-6] We have proposed an error recovery method using the concepts of task stratification and error classification.[7, 8]

In a robot system with error recovery capability, sensing is performed by using vision systems for the judgment of errors mainly at important points. For the purpose of evading errors as much as possible, it is desirable to perform visual sensing for error judgments at several times. However, it is difficult practically since a large number of sensors would be necessary for the hardware and execution system, and the interruption of the workflow and time limitations are also problems. In this paper, a method to derive efficient timing for visual sensing during error recovery is proposed.

Section 2 shows the significance of visual sensing in error recovery. Classification of visual sensing is described in Section 3. Efficient timing for visual sensing is shown in Section 4.

2. Significance of Visual Sensing in Error Recovery

The robot tasks targeted for this paper are mainly assembly, disassembly, inspection, and parts replacement in industrial factories and power plants. Tasks such as bed-making, cooking and washing performed by robots assisting humans in daily life are also our target.

We proposed a method of error recovery for a manipulation robot system in Ref. 7 and proposed a new method of error recovery in Ref. 8. These methods are based on the concepts of task stratification and error classification.

The robot tasks that we consider basically consist of sequences of sensing, modeling, planning and execution. We consider the sequences to achieve the completion of the main task using a hierarchy, but the robot system is composed of sequences basically for each layer. After execution of the task, the error judgment is performed. That is to say, after execution of the sequence of sensing, modeling, planning and execution for each task, sensing is performed once again to check for an error. A check of whether the objective of the given task has been accomplished is performed in the top layer. In addition, a check of whether the goals of the sub-tasks have been achieved is performed in each layer. Usually, visual sensing is used for judgment of the error status in all layers. Sensing based on vision is performed for the most part in manufacturing processes and in tasks providing human life assistance in particular. Therefore, we also considered the checking of errors by visual sensing in this paper.

There are various methods of checking errors using data obtained by sensing. For example, there are methods using judgment based on raw data, using geometric models derived from the original data, and so on.

3. Classification of Visual Sensing

There are many kinds of visual sensors. In our method, visual sensors from which three-dimensional data can be obtained are needed. Depending on the kind of visual sensor used, the visual data obtained will differ as follows.

(a) Visual sensor from which three-dimensional data can be obtained for moving objects

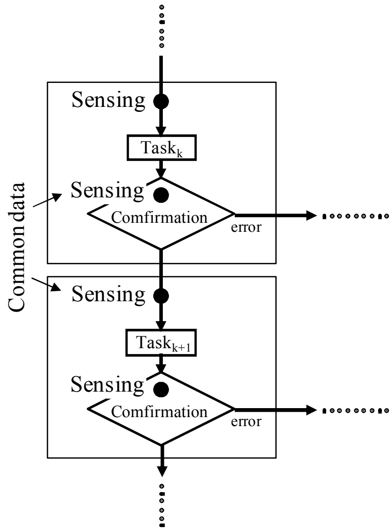

Fig. 1 Common data in successive sub-tasks in (Case 1)

This is a high-speed three-dimensional data acquisition device such as high-speed stereovision equipment. However, this is not applicable for this paper because such equipment is expensive and unrealistic for general-purpose applications.

(b) Vision sensor for stationary object use only

This is a three-dimensional data acquisition device of the normal-speed stereovision that is inexpensive passive stereovision equipment. The laser range finder of active stereovision is this type, too. For this paper, this is the type of sensor we considered. In addition, a stationary object is ideal for data acquisition. When an object is not stationary, the acquired data may include errors.

4. Timing of Efficient Visual Sensing

In this section, we will consider a case in which data is acquired in a stationary state such as (b) of Section 3. In our method, sequences composed of sensing, modeling, planning and execution are performed in each layer derived by stratification, but it is difficult to perform sensing to obtain visual data at all sensing points. It is the cause that it takes time, with computational complexity becoming extensive and task motion interruptions increasing. Therefore, it is desirable to keep the timing of data acquisition to a minimum. For this reason, we will explain desirable sensing timing in detail.

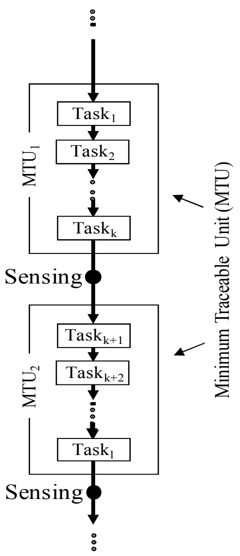

Fig. 2 Sensing points in (Case 2)

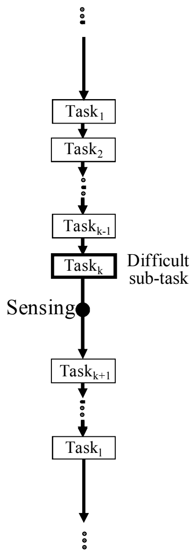

Fig. 4 Sensing point in (Case 4)

(Case 1) Use of sensing data for an error check in the next sub-task

It is sometimes possible that the sensing data acquired for the error check in a sub-task can be used for the data needed first in the next sub-task. If the necessary conditions of both data are the same in the range and precision of the three-dimensional data, they can be used as common data (Fig. 1).

(Case 2) Use of sensing on the basis of a minimum traceable unit

Next, we will show visual sensing on the basis of a minimum traceable unit (MTU), which means the smallest unit in which it is necessary to return to the first node of a motion primitive sequence if an error occurs. Visual sensing is performed just after an MTU, and a check of the error status is performed (Fig. 2).

(Case 3) With consideration for the ease of performing a recovery task

When the place where a recovery task is easy to do is known in advance, a check of whether or not an error has occurred is performed at that point (Fig. 3). When the emphasis is on the ease of the task, this method is effective.

(Case 4) With consideration for the difficulty of accomplishing a sub-task

When the place where a sub-task tends not to achieve the sub-goal or where a failure tends to occur is known in advance, a check of whether or not an error has occurred is performed at that point (Fig. 4). When the emphasis is on the achievement of the sub-task, this method is effective.

(Case 5) With consideration for a change in the range or accuracy of sensing

When the range of sensing varies from the local domain to a wider domain (or the reverse) or when the accuracy of sensing varies from precise to rough (or the reverse), a check of whether or not an error has occurred is performed at that point. For example, local range sensing is performed for manipulator operations and global range sensing is performed for transfer of objects by manipulator (Fig. 5). When a camera parameter changes due to the place or the area of the space, this method is effective.

We have shown guidelines where the sensor timings can be placed to reduce the number of sensing executions.

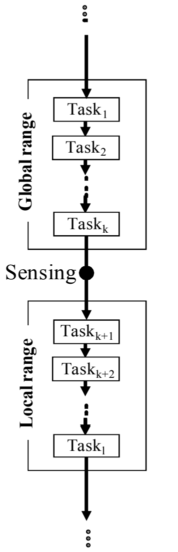

Fig. 5 Sensing point in (Case 5)

5. Conclusion

We have shown guidelines for effective timing for visual sensing in a manipulation system with error recovery capability. It is possible to reduce the number of vision sensors and the calculation workload of the software according to the guidelines we suggested. Our future studies will include applicability of this technique to an actual system, derivation of effective sensing timing for a moving manipulation system, error estimation using non-vision sensors, and so on.

Acknowledgement

This work was supported by JSPS KAKENHI Grant Number 15K00370.

References

1. L. Seabra Lopes and L. M. Camarinha-Matos, A machine learning approach to error detection and recovery in assembly, in *Proc. IEEE/RSJ Int. Conf. on Intell. Robots Syst.*, (Pennsylvania, USA, 1995), vol. 3, 197-203.
2. T. Fukuda, M. Nakaoka, T. Ueyama and Y. Hasegawa, Direct teaching and error recovery method for assembly task based on a transition process of a constraint condition, in *Proc. IEEE Int. Conf. Robot. Autom.,* (Seoul, Korea, 2001), 1518-1523.
3. K. Yamazaki, M. Tomono, T. Tsubouchi and S. Yuta, Motion planning for a mobile manipulator based on joint motions for error recovery, in *Proc. IEEE/RSJ Int. Conf. on Intell. Robots Syst.,* (Beijing, China, 2006), 7-12.
4. M. Scheutz and J. Kramer, Reflection and reasoning mechanisms for failure detection and recovery in a distributed robotic architecture for complex robots, in *Proc. IEEE Int. Conf. Robot. Autom.*, (Roma, Italy, 2007), 3699-3704.
5. J. C. Himmelstein, E. Ferre and J.-P. Laumond, Teleportation'-Based Motion Planner for Design Error Analysis, in *Proc. IEEE Int. Conf. Robot. Autom.*, (Kobe, Japan, 2009), 914-920.
6. P. Pastor, M. Kalakrishnan, S. Chitta, E. Theodorou and S. Schaal, Skill learning and task outcome prediction for manipulation, in *Proc. IEEE Int. Conf. Robot. Autom.*, (Shanghai, China, 2011), 3828-3834.
7. A. Nakamura and T. Kotoku, Systematization of error recovery in skill-based manipulation, *Artificial Life and Robotics*, Springer, **14**(2) (2009) 203-208.
8. A. Nakamura, K. Nagata, K. Harada, N. Yamanobe, T. Tsuji, T. Foissotte and Y. Kawai, Error recovery using task stratification and error classification for manipula-tion robots in various fields, in *Proc IEEE/RSJ Int. Conf. on Intell. Robots Syst.*, (Tokyo, Japan, 2013), 3535-3542.

Hexapod Type MEMS Microrobot Equipped with an Artificial Neural Networks IC

Kazuki Sugita
Graduate School of Precision Machinery Engineering College of Science and Technology, Nihon University, 7-24-1, Narashinodai, Funabashi, Chiba, 274-8501, Japan

Taisuke Tanaka, Yuya Nakata, Minami Takato, Ken Saito, Fumio Uchikoba
Department of Precision Machinery Engineering College of Science and Technology, Nihon University, 7-24-1, Narashinodai, Funabashi, Chiba, 274-8501, Japan
E-mail: cska15018@g.nihon-u.ac.jp, takato@eme.cst.nihon-u.ac.jp, kensaito@eme.cst.nihon-u.ac.jp, uchikoba@eme.cst.nihon-u.ac.jp

Abstract

This paper proposes a hexapod type microrobot controlled by an artificial neural networks IC. The structural component of the microrobot is produced by micro electro mechanical systems (MEMS) process. The rotary actuator inside the robot is composed of the artificial muscle wire of shape memory alloy (SMA) material. The artificial neural networks IC includes cell body models, inhibitory synaptic models and current mirror circuits. By reducing the heat capacity of the actuator and the length of electrical wire to the actuator, the walking speed achieved 12 mm/min.

Keywords: Microrobot, MEMS, Artificial neural networks, SMA, Artificial muscle wire

1. Introduction

Several studies have reported the miniaturization of robots1-2. Microrobots are suggesting possibility of activities in a small space. However, the miniaturization and high functionalization of microrobots have not been sufficiently achieved yet.

In heading toward the implementation of more sophisticated microrobots, biomimetics, a technology that imitates living organisms, is attracting attention3. Insects have the compact walking mechanisms and the excellent flexible control systems using biological neural networks. Hence, the realization of small walking systems with the size of an insect is valuable. However, the processing of the miniature component as small as the insect is difficult only by the conventional mechanical machining. One of the solutions is micro electro mechanical systems (MEMS). The MEMS process is based on the integrated circuit (IC) production process, which applies photolithography on a silicon wafer.

Some studies have considered artificial neural networks as a new alternative control method for robots4. The study of the artificial neural networks is roughly divided into software models and hardware models. The software model is a numerical simulation method using a computer system. To achieve the fabrication of large-scale neural networks using software models, processing in continuous time is difficult. The hardware model is imitating the neural networks using electronic circuits. The nonlinear operation of an electronic circuit can be performed at a high speed and processed in continuous time. Therefore, the hardware neural networks can obtain an output in real time, even if the circuits scale increases.

Previously, we developed the microrobot that imitates the hexapod walking motion of insects using MEMS technology. We fabricated small walking systems equipped with the actuator using artificial muscle wires based on shape memory alloy (SMA). The lead wires electrically connecting the microrobot and artificial neural networks IC were exposed outside the microrobot. This wire connection was harmful for the robot balance. This microrobot walked at a locomotion speed of 2.8 mm/min.

In this study, we report that the faster walking motion of the hexapod-type MEMS microrobot. The miniaturization of rotor parts was performed to reduce its heat capacity. The electrical wires were leaded inside the microrobot. It improved the weight balance of the microrobot. As a result, the microrobot could achieve the walking speed at 12 mm/min.

2. Mechanism of the MEMS Microrobot

The microrobot that we manufactured is shown in Fig. 1. The microrobot is a hexapod walking robot with a total length of 5 mm or less. The components of the microrobot are the frame, the rotary actuator, the shaft, and six legs. The each part is fabricated from silicon wafers using MEMS process. We used link mechanism and the artificial muscle wire to achieve the further advanced miniaturization required for a small walking system. As the material of the artificial muscle wire itself has the function of generating the displacement, this is suitable for the miniaturization of the microrobot.

Artificial muscle wires and a ground (GND) wire are electrically and mechanically connected to the rotor part through the silver conductive paste. The displacement of the artificial muscle wires changed by successively applying an electrical current to generate joule heat. Previously, we applied a circle-type rotor for the rotary actuator as shown in Fig. 2 (a). This circle-type rotor was completely over-coated with the silver conductive paste. On the contrary, the two-hole-type rotor in this paper can fix the artificial muscle wire firmly by the hole. So, the amount reduction of the silver conductive paste was achieved (see Fig. 2 (b)).

We compared the heat capacity calculated based on the weight of two-type rotors. The weight of silicon parts of the circle-type rotor and two-hole-type rotor were 52.4 μg and 18.1 μg, respectively. The weight of silver conductive paste were 1.18 mg and 139 μg, respectively.

In terms of the two-type-rotors, the calculated heat capacity is shown in Table 1. As a result, the two-hole-type rotor is expected to shorten the revolving period because new design can suppress the heat capacity. Also, we installed the lead wire inside the microrobot to reduce the harmful element of the weight balance.

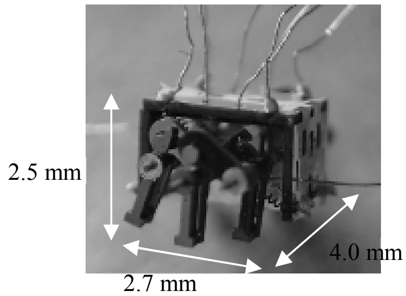

Fig. 1. Hexapod type microrobot.

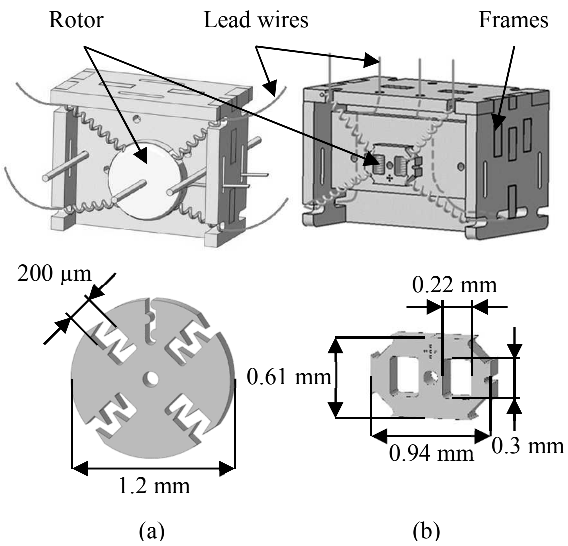

Fig. 2. Structure of the microrobot.

Table 1. Heat capacity of two-type rotors

	Circle-type rotor	Two-hole-type rotor
Heat capacity of rotor part [μJ/K]	38.8	13.4
Heat capacity of conductive paste [μJ/K]	277	32.7

2.1. *Walking mechanism*

We employed a link mechanism that converts the rotary motion of the actuator to walking motion. The link mechanism connects the middle leg to the front and rear legs. The locomotion pattern generates a 180° phase shift on each side. Therefore, the microrobot performs a hexapod walking by grounding the three legs like an insect (see Fig. 3).

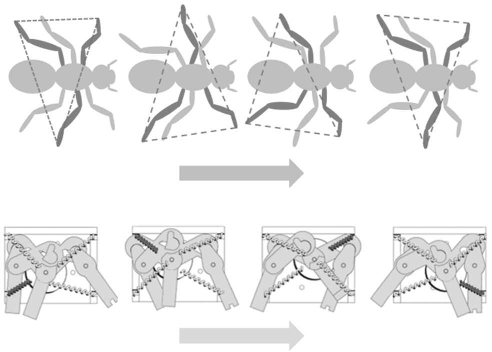

Fig. 3. Locomotion diagrams of the microrobot.

3. Artificial Neural Networks

The neural networks present in their brains consist of cell bodies, dendrites, axons and synapses. The cell body fires electrical pulses by changing the membrane potential. The signals for electrical pulses are transmitted to the dendrites of another neuron through the axon. The synapses change signals for electrical pulses by inhibit or promote transmitting of electrical pulses.

In this study, we modeled the cell body and the inhibitory synapse as shown in the Fig. 4 and Fig. 5. The cell body model has a refractory period, an analog characteristic for the output pulse, and time varying negative resistance characteristics. The circuit parameters for the cell body model were $V_A = 2.8$ V, M_{C1}, M_{C2}: $W/L = 10$, M_{C3}: $W/L = 0.1$, M_{C4}: $W/L = 0.3$, $C_G = 4.7\mu$F, $C_M = 1.0\mu$F. A cell body model connected by an inhibitory synaptic model causes anti-phase synchronization. The circuit parameters for the inhibitory synaptic model were $V_{ISDD} = 2.8$ V, $C_{IS} = 1$ pF, M_{IS1}, M_{IS2}, M_{IS3}, M_{IS11}, M_{IS12}: $W/L = 1$.

We used the four cell body models that coupled inhibitory mutually using 12 inhibitory synaptic models as shown in the Fig. 6. The artificial neural networks and the current mirror circuit for obtaining a driving current of the actuator were constructed on an IC. The layout pattern of the IC is shown in Fig. 7. The design rule of the IC was 4 metal 2 poly CMOS 0.35 μm. The chip size was 2.45 mm square.

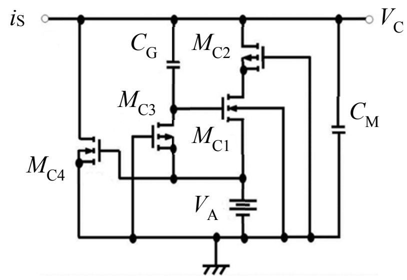

Fig. 4. Circuit diagram of the cell body model.

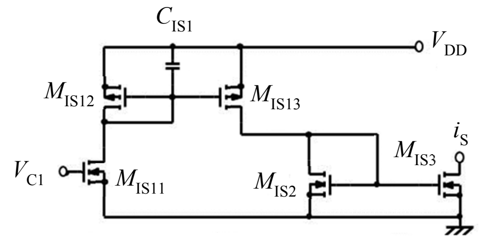

Fig. 5. Circuit diagram of the inhibitory synaptic model.

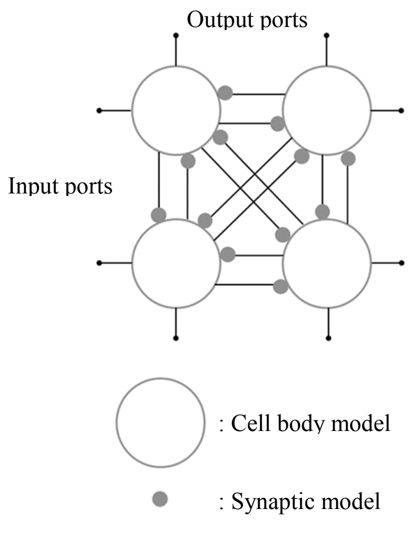

Fig. 6. Connection diagram of the artificial neural networks.

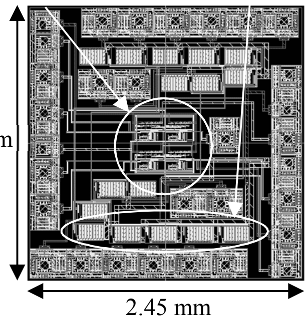

Fig. 7. Layout pattern of the artificial neural networks IC.

4. Results

Fig. 8(a), (b) shows the microrobots equipped the artificial neural networks IC. The side, the end, and height dimensions of the microrobot include the whole circuit were 4.0, 2.7, and 5.0 mm, respectively. Only power sources were connected externally. While the previous microrobot had lead wires outside the microrobot, in this case, we installed the lead wire inside the microrobot. As a result, the internal wiring achieved excellent weight balance and structurally stable performance of the microrobot.

The hexapod walking locomotion of the microrobot was achieved as shown in fig. 9. Previously, the input pulse duration was a 0.5 s, and cycle period was 2.0 s. The new two-hole-type rotor was possible to accelerate the revolving frequency of the actuator. Therefore, we could shorten the input pulse width and cycle period to 0.3 s and 1.2 s, respectively, and consequently increased the rotation speed of the rotary actuator. The locomotion speed of the microrobot accelerated from 2.8 mm/min to 12 mm/min.

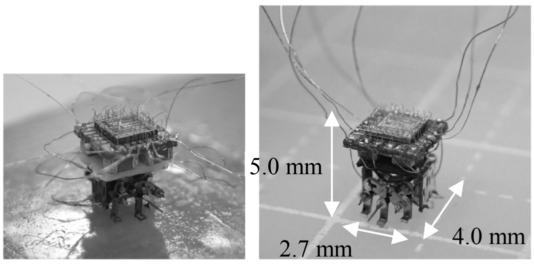

(a) Previous robot with outside wire

(b) Present robot with inside wire

Fig. 8. Fabricated microrobot equipped driving circuit.

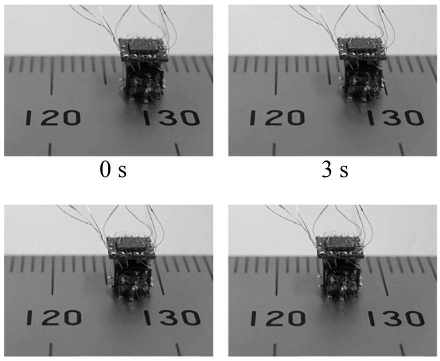

Fig. 9. Walking locomotion of the microrobot.

5. Conclusion

In this study, we proposed the hexapod type MEMS microrobot controlled by the artificial neural networks IC. We designed two type actuators using artificial muscle wires. The new two-hole-type rotor was possible to reduce the thermal capacity of the rotor by reducing the size and the amount of the conductive paste. The new microrobot had lead wires inside of the microrobot, and achieved the better weight balance. It was possible to mount a driving circuit on the microrobot by using a bare chip IC. As a result, the speed of the hexapod type microrobot increased to 12 mm/min. The microrobot equipped all of constituent elements except the power source.

References

1. T. Shibata, Y. Aoki, M. Otsuka, T. Idogaki, and T. Hattori, Microwave Energy Transmission System for Micro-robot, *IEICE Trans. ELECTRON.* Vol. E80-C,NO.2, pp. 303–308, Feb. 1997.
2. M. K. Habib, Innovations and robotics, *International Journal of Mechatronics andManufacturing Systems*, 4(2),1993, pp. 123–135.
3. A. T. Baisch, P. S. Sreetharan and R. J. Wood, E. H. Miller, Biologically-inspired locomotion of a 2g hexapod robot, in *Proc. Int. Conf. on Intelligent Robots and systems,* Taipei, Republic of China, 2010, pp. 5360–5365
4. S.A. Vukosavljev, D. Kukolj, I. Papp, and B. Markoski, Mobile robot control using combined neural-fuzzy and neural network, in *Proc. 12th IEEE Int. Symposium on Computational Intelligence and Informatics (CINTI 2011)*, Budapest, 2011, pp. 351–356.

Heat Distribution of Current Output Type Artificial Neural Networks IC for the MEMS Microrobot

Taisuke Tanaka, Yuya Nakata, Kazuki Sugita, Minami Takato, Ken Saito, Fumio Uchikoba
Department of Precision Machinery Engineering College of Science and Technology, Nihon University,
7-24-1, Narashinodai, Funabashi, Chiba, 274-8501, Japan
E-mail: csta13083@g.nihon-u.ac.jp, takato@eme.cst.nihon-u.ac.jp, kensaito@eme.cst.nihon-u.ac.jp,
uchikoba@eme.cst.nihon-u.ac.jp

Abstract

Heat distribution of the artificial neural networks IC developed for controlling microrobots is described in this paper. We measured the temperature distribution of the designed IC using thermography. As a result, it is found that the major heat source is the current mirror part on the IC. However, it was observed that the part of the artificial neural networks also generated the heat. The heat contribution of the artificial neural network part was evaluated. As a result, the temperature rise of the artificial neural networks part on the IC was calculated to be 0.0535°C per second.

Keywords: Microrobot, Artificial neural networks, MEMS, IC

1. Introduction

Insects inhabit the earth from about 300 million years ago. During that process, insects have experienced many environmental changes and have developed biological functions[1]. The insect has excellent form and function. Therefore, if it is possible to produce micro robots having functions equivalent to those of the insect, it is considered to be possible that the robot deal with various situations and application in various fields[2]. For example, in the medical field, the microrobot that mimics the peristaltic movement of the insect has been studied[3].

The Insect has a flexible control system with a compact moving mechanism and neural networks of the brain. In order to imitate this, we are applying micro electro mechanical systems (MEMS) technology to create the movement mechanism of the microrobot. MEMS technology is based on the integrated circuit (IC) production process. Also, the conventional program control used as a robot control makes it difficult to deal with unknown situations. Therefore, the control method using the artificial neural networks has been expected as an alternative method of the program control[4]. Neurons of the brain in the living organisms are connected to each other and form networks. By carrying out information transmission using those, the flexible information processing can be performed. By modeling the neuron of the living organism and constructing the artificial neural networks, the robot can judge and execute the required process by themselves like the living organism. We have integrated simple artificial neural networks into a IC and used it as a controlling circuit of the MEMS microrobot[5]. We designed a current output type artificial neural networks IC to drive the MEMS microrobot using shape memory alloy (SMA) for the actuator. In this paper, focusing on heat generation of the artificial neural networks IC, its heat distribution was measured by thermography. We considered the source of the heat generation from the results.

2. Walking control of microrobot

Artificial muscle wires based on SMA are used in the actuator of the robot. The wire shrinks by joule heat of current flow and extends by cooling. Fig. 1 shows the walking mechanism of the microrobot. The walking motion of the microrobot is generated by the rotational motion of the rotor attached with 4 helical artificial muscle wires. The rotational action of the actuator is obtained from current flows through the artificial muscle wire in the order of A to D. Therefore, the rotor rotates and transmits to the link mechanism of the leg portion.

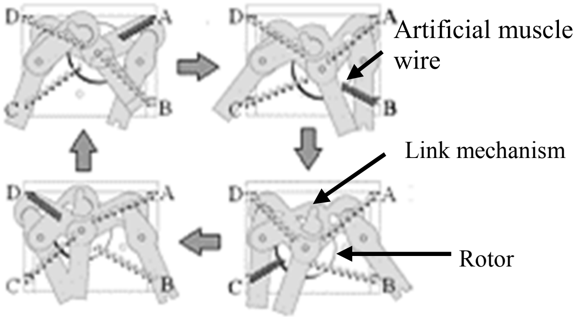

Fig. 1. Walking mechanism of the microrobot.

3. Artificial neural networks

An artificial neural circuit mimics the function of a neural circuit of the living organism with analog electronic circuits. The neural circuits of the living organism is mainly composed of cell bodies, dendrites, axons and synapses. We modeled the cell body and the synapse.

3.1. *Cell body model*

Fig. 2 shows the circuit diagram of the cell body model. V_C in Fig. 2 is the output voltage. The cell body model consists of a capacitor C_G and a membrane potential capacitor C_M, MOSFETs M_{C1}, M_{C2}, M_{C3} and M_{C4}. The cell body changes the membrane potential using external stimulation and fires electrical pulses. The cell body model has a refractory period, an analog characteristic for the output pulse, and time varying negative resistance characteristics. The circuit parameters for the cell body model were V_A = 3V, M_{C1}, M_{C2}: W/L = 10, M_{C3}: W/L = 0.1, M_{C4}: W/L = 0.3, C_G = 4.7μF, C_M = 1.0μF.

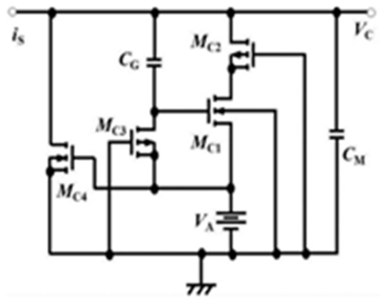

Fig. 2. Circuit diagram of the cell body model.

3.2. *Synaptic model*

Fig. 3 shows a circuit diagram of an inhibitory synaptic model. When a multiple of cell body models are connected by the synapse model, a synchronization phenomenon occurs at the oscillation timing of the cell body model. The inhibitory synaptic model, particularly, causes anti-phase synchronization. We used the inhibitory mutual coupling to generate driving pulses of the microrobot. The circuit parameters for the inhibitory synaptic model were V_{DD} = 3V, C_{IS1} = 1 pF, M_{IS1}, M_{IS2}, M_{IS3}, M_{IS4}: W/L = 1.

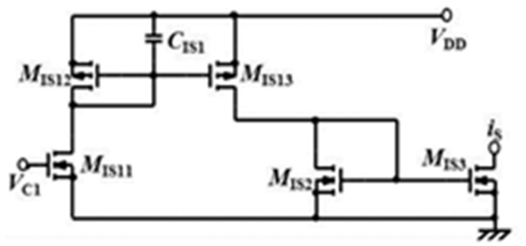

Fig. 3. Circuit diagram of the inhibitory synaptic model.

3.3. *Pulse- type hardware neural networks*

Fig. 4 shows the pulse-type hardware neural networks mimic a central pattern generator of the living organism. The central pattern generator is known as basic rhythm generator of the living organism. As shown in Fig. 4, four cell body models are inhibitory mutually coupled using 12 inhibitory synaptic models. As a result, a four-phase anti-phase synchronous waveform is generated.

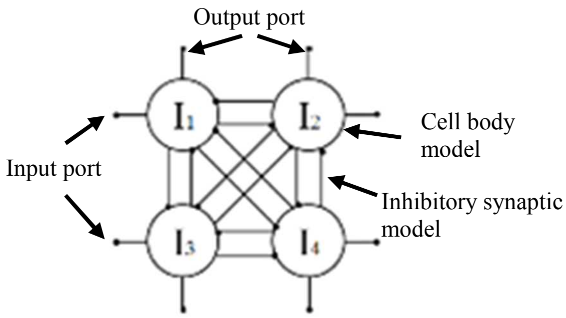

Fig. 4. Pulse-type hardware neural networks.

3.4. *Current mirror circuit*

Fig. 5 shows a circuit diagram of the current mirror circuit. The shape memory alloy actuator requires the electrical current to generate movement. Therefore, the current mirror circuit is connected to the pulse type hardware neural networks in order to convert the voltage into the current. The circuit parameters for the current mirror circuit were V_{DD} = 4V, M_{S1}: W/L = 40, M_{S2}: W/L = 1, MON: W/L = 66. The number of stages of the current mirror varied by the designed IC.

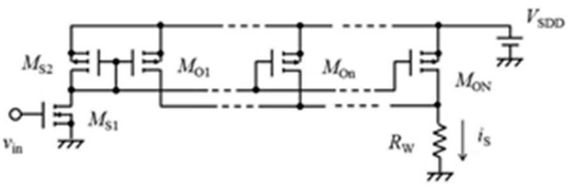

Fig. 5. Circuit diagram of the current mirror circuit.

3.5. *Artificial neural networks IC*

We designed an IC that constructed pulse-type hardware neural networks. Fig. 6 shows the layout pattern of the designed IC. The design rule of the IC was 4 metal 2 poly CMOS 0.35μm. The sizes of the capacitors C_G, C_M of the cell body model were too large to pattern on the IC. Therefore, it was added on the peripheral circuit. Fig. 7 shows an IC mounted on the circuit board. Fig. 8 shows an example of output waveform of the pulse-type hardware neural networks IC.

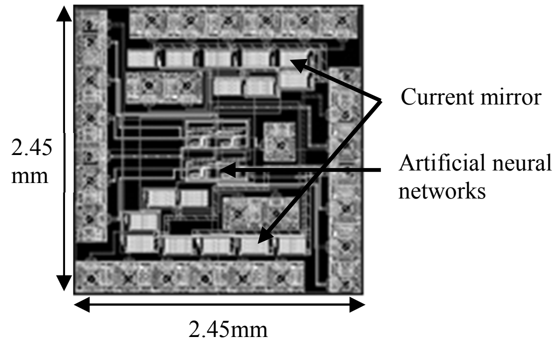

Fig. 6. Layout pattern of Artificial neural networks IC.

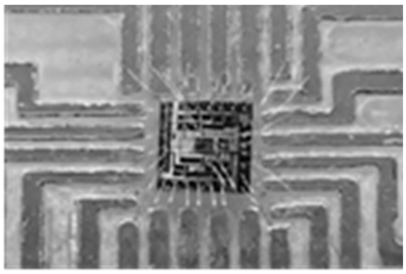

Fig. 7. ICs mounted on the circuit board.

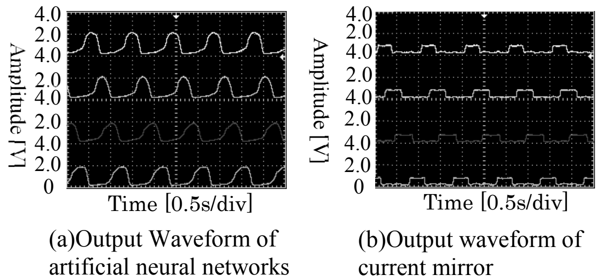

Fig. 8. Example of the output waveform of the pulse type hardware neural networks IC

4. Measurement of heat generation

4.1. *Measurement condition*

3V was applied to the artificial neural networks using a power source and 4V was applied to the current mirror. A 12Ω load resistance was connected as output instead of SMA. The measurement was carried out for about 30 seconds after the voltage input. The room temperature was 20°C.

4.2. *Measurement result*

Fig. 9 shows measurement results. Mainly two high temperature areas are confirmed. The two areas are the artificial neural networks and the current mirror. In the IC shown in Fig. 9, it was confirmed that the maximum temperature in the artificial neural network was 100.4°C and the maximum temperature in the current mirror was 100.1°C.

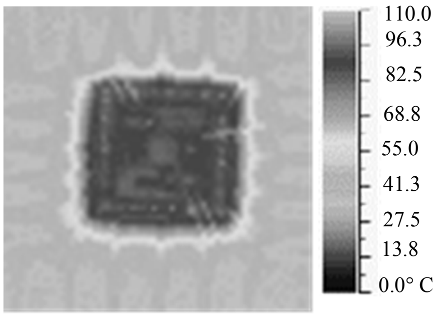

Fig. 9. Temperature distribution measurement on ICs with 12Ω load.

4.3. *Measurement result with reduced influence of current mirror*

We focused on the heat generation in the artificial neural networks. In order to confirm that the artificial neural network was generating heat, the load resistance was increased from 12Ω to 110Ω. Fig. 10 shows the measurement result. Load resistance of 110Ω was the highest resistance the IC output the stable pulse. In the IC shown in Fig. 10, it was confirmed that the maximum temperature in the artificial neural networks was 39.1°C and the maximum temperature in the current mirror was 39.3°C.

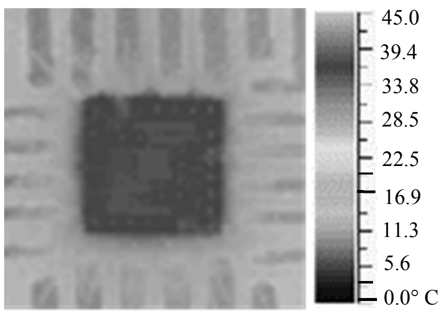

Fig. 10. Temperature distribution measurement on ICs with 110Ω load.

The measurement was performed without applying the power source of the current mirror. In the IC shown in Fig. 11, it was confirmed that the maximum temperature in the artificial neural networks was 29.2°C. Fig. 12 shows the measurement result of the temperature rise at the representative points of the artificial neural networks. The temperature rise in the artificial neural network was confirmed.

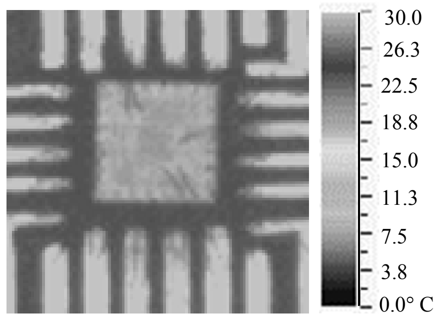

Fig. 11. Measurement of heat distribution of IC without input of current mirror.

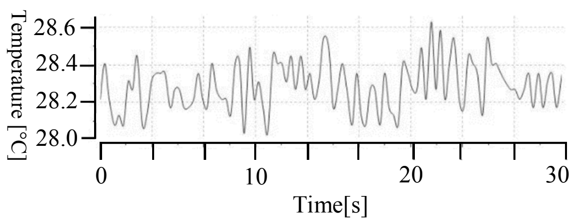

Fig. 12. Measurement result of temperature rise of artificial neural networks.

5. Discussion

5.1. *Heat generation in artificial neural networks IC*

From these results, it is found that the major heat source is current mirror part because the temperature decreased with increasing of the load resistance. However, the high temperature areas of the IC are corresponding to the not only the current mirror but also the artificial neural networks. The temperature of the artificial neural networks portion was higher than that of the neighbor area. Also, we confirmed the heat generation of the artificial neural network even when the power supply of the current mirror is stopped. The temperature rise almost corresponded to the pulse timing. So, it is suggested the artificial neural networks also generates the heat to some extends.

5.2. *Evaluation of temperature rise per second of artificial neural networks*

In the cell body model, when a voltage of V_A is applied, the charge accumulates in C_G, and the potential difference between MOSFETs M_{C1} and M_{C2} disappears. Then, M_{C2} conducts, the charges of C_G and C_M are extracted, applied to the M_{IS3} of the inhibitory synapse model, and flow to GND. It is thought that the heat is generated by the charges extracted from C_G, C_M. We evaluated the calculated value of the temperature rise per second from the power consumption of the capacitors C_G, C_M, the mass of the heat generation part, and the specific heat of silicon. The power consumption due to charges extracted from C_G and C_M can be obtained by equation (1).

$$W = \frac{1}{2} CV^2 [J] \tag{1}$$

C_G and C_M are 4.7μF and 1.0μF respectively. It is assumed that 0.5 V is applied to C_G and 1.5 V is applied to C_M. Therefore, power consumption of 0.587μJ and 1.13μJ are obtained on each capacitor. Because the artificial neural networks is composed of four cell body models, then, the one cycle power consumption of the whole artificial neural networks is calculated as 6.87μJ. The duration of one cycle is 1.1 seconds. Therefore, the total power consumption per second is 6.25μW. The temperature rise of the artificial neural networks per second can be obtained by equation (2).

$$\Delta T = \frac{P}{\rho V C_V} [° \boldsymbol{C}] \tag{2}$$

C_V is the specific heat of silicon, 0.73J/gK. V is the volume of heated area. Those are derived from the temperature distribution of the ICs, 6.88×10-5cm3. ρ is the density of the silicon, 2.33g/cm^3. From these, it is calculated that an artificial neural networks increases 0.0535°C per second. Compared with the calculation result and the measurement result of Fig. 12, the calculated value follows the tendency of the measured value.

6. Conclusion

The heat distribution of the artificial neural networks IC developed to controlling the microrobot was described in this paper. As a result, heat generation was observed with the artificial neural networks and the current mirror parts. It was found that major heat source was the current mirror part. Focusing on the heat generation of artificial neural networks, we thought that heat generated by charges extracted from C_G and C_M of the cell body model. The temperature rise per second was evaluated using the power consumption of C_G and C_M. As a result, it was calculated that the temperature rises of 0.0535°C per second for the IC.

7. References

1. H. Hugo, 2008, *People learn-Insect wisdom*, Tokyo: Tokyo Agricultural University Press Publications
2. A. T. Baisch, P. S. Sreetharan and R. J. Wood, E. H. Miller, Biologically-inspired locomotion of a 2g hexapod robot, in *Proc. Int. Conf. on Intelligent Robots and systems*, (Taipei, Republic of China, 2010), pp. 5360–5365
3. Y. Sonobe, Y. Arai, Y. Nakazato, Development of In-pipe Micro Robot Moving in the Blood Vessel, *Welfare Engineering Symposium Presentation Papers* 2007, (japan,2007), pp. 231-232
4. A. Iwata, Y. Amemiya, 1995, Neural network LSI, Tokyo: Institute of Electronics, *Information and Communication Engineers*
5. K. Saito, Y. Ishihara, K. Okane, H. Oku, Y. Asano, K. Iwata, M. Tatani, M. Takato, Y. Sekine and F. Uchikoba, Artificial Neural Circuit Integration for MEMS Microrobot System, in *Proc. 2015 Int. Conf. Advanced Intelligent Mechatronics*, (Busan, Korea, 2015), pp.1055-1060.

AGV with Mind and its production simulation for autonomous decentralized FMS

Masato Chikamatsu
Human and Information System Division, Gifu University,
1-1, Yanagido, GifuCity, GifuPref 501-1193, Japan

Hidehiko Yamamoto
Department of Mechanical Engineering,
1-1, Yanagido, GifuCity, GifuPref 501-1193, Japan

Takayoshi Yamada
Department of Mechanical Engineering,
1-1, Yanagido, GifuCity, GifuPref 501-1193, Japan

E-mail:u3128017@edu.gifu-u.ac.jp, yam-h@gifu-u.ac.jp, yamat@gifu-u.ac.jp
www1.gifu-u.ac.jp/~yamlab/

Abstract

This study controls Automated Guided Vehicle (AGV) moving by using a mind model in order to avoid AGVs' interference. The mind model can avoid the interference by repeating the two types of mind changes. By applying the mind to several FMSs, the production simulations were carried out. As a result, AGV could avoid the interference flexibly even if the shape of the production floor was changed, and it is ascertained that the mind model could control the AGV actions.

Keywords: Autonomous Decentralized FMS, AGV control, AGV mind, Production simulation

1. Introduction

We have developed an autonomous decentralized FMS factory. We need to avoid collisions among AGVs when we use the autonomous decentralized FMS. Although some rules to avoid collisions are considered, these rules are not enough to control when many AGVs are used. Therefore, we try to control the behavior of AGVs by using a mind model. In this study, we apply AGV with the mind model to plural FMSs and examine whether AGVs can avoid the path interferences flexibly even if the shape of the production floor is changed. Moreover we examine the influence on production efficiency.

2. Mechanism of autonomous decentralized FMS

2.1. Overview of autonomous decentralized FMS

Fig.1 illustrates an autonomous decentralized FMS factory scheme. As Fig.1 shows, the factory floor is divided into grid patterns and AGVs are moving along these lines to carry parts to the warehouse and machining centers. The autonomous decentralized FMS does not have a management mechanism to integrate the entire system, such as machining centers, AGV, product warehouse and parts warehouse. Each agent that configures the system autonomously determines the act by recognizing the purpose of the system by cooperating and negotiating to other agents

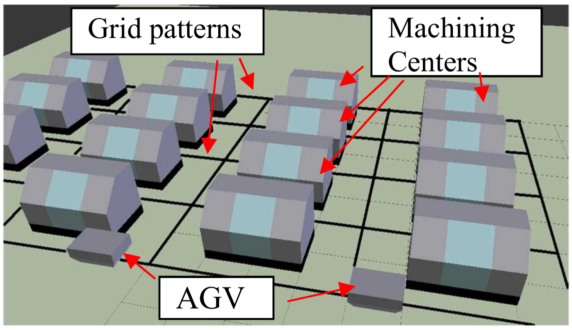

Fig.1. Example of autonomous decentralized FMS

2.2. Model of mind and behavior of AGVs

In autonomous decentralized FMS, each AGV determines the behavior autonomously. Therefore, AGVs often cause path interferences. In our previous studies, we used control rules to avoid path interferences. However, in the control rules, it was not able flexibly to adapt the environmental changes including the changes of the number of AGVs and the changes of the shape of production floor.

Therefore, in this study, we apply the AGV mind to solve the problem and realize the autonomous movement control not to produce path interferences of AGVs.

AGVs' mind is expressed two kinds of an arrogant mind and a modest mind. Specifically, (1) AGV with an arrogant mind takes the action forcibly to approach the destination. (2) AGV with a modest mind takes the action to make way for other AGVs.

AGVs take three actions by changing the two kinds of mind.

- If AGV with an arrogant mind and AGV with a modest mind run on the same line at the same time, AGV with a modest mind takes the action to give way and AGV with an arrogant mind takes the action to approach the destination forcibly.
- If the two AGVs with an arrogant mind run on the same line at the same time, one of the AGVs changes its mind to a modest mind and gives way for the other AGV.
- If the two AGVs with modest mind run on the same line at the same time, one of the AGVs changes its mind to an arrogant mind and the other gives way for the AGV just changed to an arrogant mind.

We use the mind model as shown in Fig.2 to express the mind. In the study, we call it Minimum Unit of Mind (MUM). In Fig.2, A1 and A2 is a unit, X is a load, and an arrow is a stimulation vector. The threshold is determined by the unit. When the internal value reaches the threshold, we call the mind situation as excited and if it does not reach, normal.

The functions of each component of MUM are as follows.

・Unit: When a signal is sent to the unit, it sends a signal to the direction of the arrow when excited, and it is not sent when normal.
・Load: Load has the function to change the internal value of the unit. When the signal is sent to the load, the value of unit is decreased by the value of X.
・Stimulation vector: Stimulation vector is a line connecting the load and the unit. It gives a signal to the load or unit when the signal comes.

When A1 keeps exited, we call a modest mind, and when normal, we call an arrogant mind.

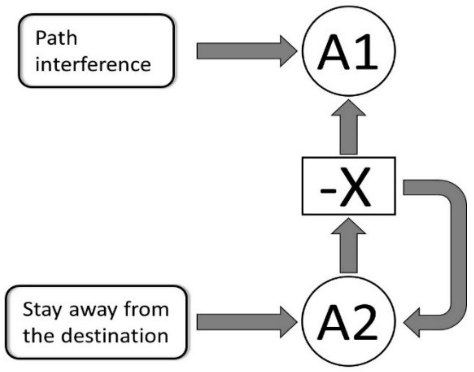

Fig.2. Model of mind (MUM)

Next, we describe the internal functions of MUM by the following ① to ③.

① When the AGV with an arrogant mind encounters a path interference, the value of A1 is increased by 1. Keeping the situation of the interference, the value of A1 will increase and soon becomes the threshold value. As soon as the value becomes the threshold value, the AGV mind is changed to a modest mind.
② When AGV with a modest mind keeps giving way, the value of A2 is increased by 1. When the situation is repeated an optional time and A2 becomes exited, the signal is sent to a load.
③ The load received the signal from A2 decreases the value of units A1 and A2 by an optional value. Because of this, A1 and A2 return to normal and AGV with a modest mind is changed to AGV with an arrogant mind.

In this way, by changing minds from arrogant to modest or from modest to arrogant repeating ① to ③, the mind change is realized.

3. Target production line

We performed the production simulations of autonomous decentralized FMS using the production floors of two different shapes.

One is the integrated production floor that parts warehouse and products warehouse are next to each other as shown in Fig.3 and are contiguous with one production floor.

The other is the split production floor shown Fig.4 that the floor of Fig.3 is split into the production floor connected parts warehouse and production floor connected products warehouse. AGVs come and go between the two floors.

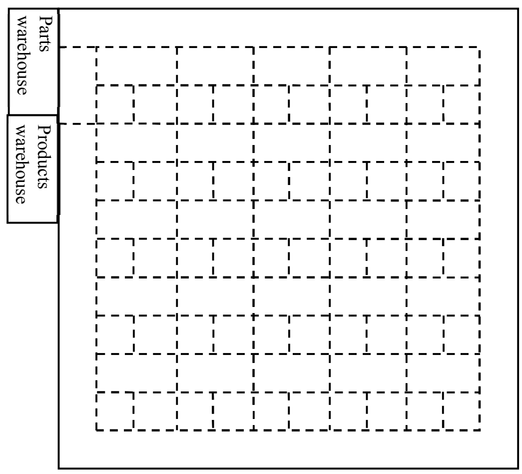

Fig.3 Integrated production floor

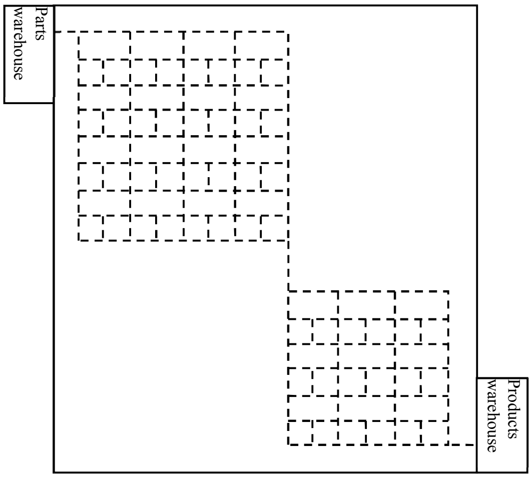

Fig.4 Split production floor

We carried out the production simulation by using these two kinds of production floors and compared the production outputs and the number of path interferences of AGVs.

The initial internal value of MUM unit A1, A2 is 0 and the threshold values are chosen as random. Therefore, all AGVs keep arrogant minds for the first time.

4. Simulation results

We investigated parameters changing number of AGVs and simulation times in each integrated production floor and split production floor.

Condition 1(number of AGV: 5 units, simulation time: 8 hours)

Condition 2(number of AGV: 5 units, simulation time: 40 hours)

Condition 3(number of AGV: 8 units, simulation time: 8 hours)

Table.1, 2, 3 and Fig.5, 6 are the acquired number of production outputs and the acquired number of path interferences in each condition.

Table.1. Simulation result of condition 1

	Production Outputs	Number of path interference
Integrated production floor	186	769.6
Split production floor	134.6	911.8

Table.2. Simulation result of condition 2

	Production Outputs	Number of path interference
Integrated production floor	971	3190.8
Split production floor	712.2	3752

Table.3. Simulation result of condition 3

	Production Outputs	Number of path interference
Integrated production floor	238	1507.6
Split production floor	165.4	2507.6

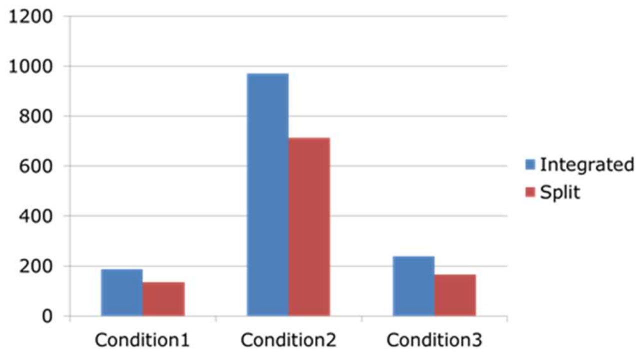

Fig.5 Comparison of Production Outputs

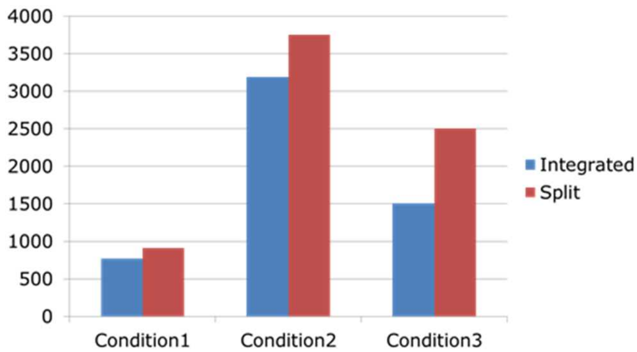

Fig.6 Comparison of Number of path interference

Fig.5 shows that the integrated production floor acquired more production outputs than the split production floor in any conditions. In condition 1 and 2, the production outputs are proportional at simulation time. In condition 1 and 3, condition 3 manufactured more production outputs than condition 1. Therefore, the more number of AGVs becomes, the more production outputs.

Fig.6 shows that the split production floor gets more path interferences than the integrated production floor in any conditions. Comparing condition1 and condition 2, 3, it is proved that the more simulation time and the number of AGVs, the more the path interferences. The split production floor gets much more path interferences than the integrated production floor in condition 3.

Table.4, 5, 6 indicate the percentage of each places (periphery of parts warehouse, products warehouse and the route connecting two floors) in the total places caused path interference in each condition. Fig.7, 8, 9 are the plots of path interference places of the split production floor.

Table.4. Path interference place of condition 1

	Parts warehouse	Products warehouse	Route connecting two floor
Integrated production floor	21%	8.4%	-
Split production floor	12.7%	3%	37%

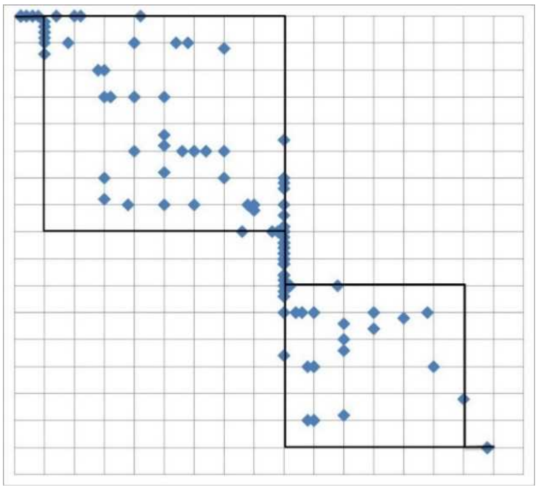

Fig.7 Path interference place of condition 1

Table.5. Path interference place of condition 2

	Parts warehouse	Products warehouse	Route connecting two floor
Integrated production floor	17.2%	10%	-
Split production floor	8%	4.5%	43.3%

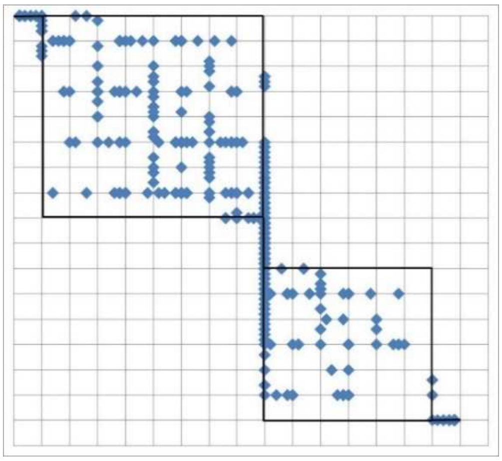

Fig.8 Path interference place of condition 2

Table.6. Path interference place of condition 3

	Parts warehouse	Products warehouse	Route connecting two floor
Integrated production floor	19.3%	5.6%	-
Split production floor	11.2%	1.7%	56%

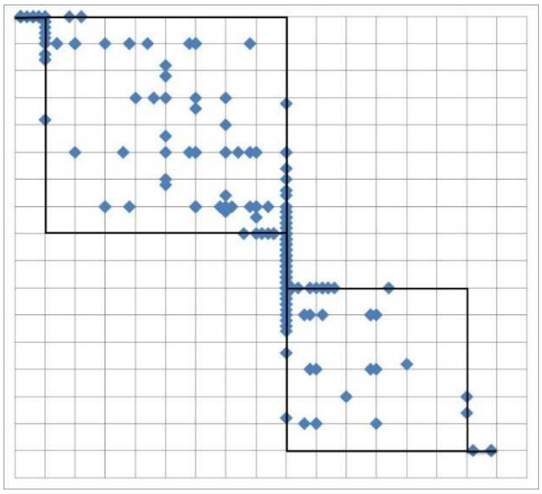

Fig.9 Path interference place of condition 3

Table.4, 5 and 6 shows that the split production floor has much more path interferences on route connecting two floors. For this reason, it is assumed that the path interferences increase in the split production floor. As a result, it is assumed that the integrated production floor has more production outputs than the split production floor. Comparing condition 1 and condition 2, 3, the path interference percentage increased a little in condition 2 and the path interference percentage much increased in condition 3 on the route connecting two floors. From Table.4, 5 and 6, it is assumed that the reason for condition 3 acquired much path interferences on the route connecting two floors than condition 1 or 2. From this, the number of AGVs have a great influence on congestion of the route connecting two floors in split production floor.

5. Conclusions

With AGV minds, even if a different shape production floor is adopted, AGV was able to avoid path interferences flexibly in autonomous decentralized FMS. In the split production floor, AGV was crowded very much near the route connecting two floor. However, it was able to finish the simulation without freezing and it is ascertained that the results of the production simulation becomes proper. Therefore, we were able to control actions of AGVs by using AGV mind.

UNARM System to Decide Units Locations of Cell-type Assembly Machines with Robots Arms

Hirotaka Moribe
Department of Human Information Systems, Gifu University, Yanagido 1-1, Gifu, Gifu 501-1194, JAPAN

Hidehiko Yamamoto
Department of Mechanical Engineering, Gifu University, Yanagido 1-1 Gifu, Gifu 501-1194, JAPAN

Takayoshi Yamada
Department of Mechanical Engineering, Gifu University, Yanagido 1-1 Gifu, Gifu 501-1194, JAPAN

E-mail: u3128029@edu.gifu-u.ac.jp, yam-h@gifu-u.ac.jp, yamat@gifu-u.ac.jp

Abstract

This study develops the system called UNARM which assists the unit placement decision of the automatic assembling equipments to assemble efficiently. The unit is a part supply or a robot hand constituting assembling equipment. It is the system which decides these units placement where of the assembling equipment you place the interference of the both arms of the robot using reinforcement learning in spite of being a guard.

Keywords: Reinforcement Learning, Unit placement decision, Double arm robot, Assembly machine

1. Introduction

In recent years, automations of the assembly works with robots have been performed in the production area. As for the automatic assembly machine with robots, the production efficiency changes by the placement of each unit. However, because the placement of units is determined by the experience of engineers in many factories, it is questionable whether the determined placement is good or not. To solve the problem, we develop the system, Units-layout Nomination for Assembly with Robot Mechanism (UNARM), to assist the unit placement decision of the assembly machine with robots. In addition, we apply UNARM to a cell type assembly machine with robot both arms and ascertain the usefulness of UNARM.

2. UNARM

UNARM is the system to decide each unit placement of the assembly machine using reinforcement learning. For the placement place of each unit chosen by every learning, UNARM calculates the assembly time and improves the unit placement using machine learning and the calculate time.

2.1. *Structure of UNARM*

UNARM consists of two modules, (i)the conditions making module and (ii)the learning module as shown in Fig.1.

After the condition making module reads the work data and the possible area of unit placements, the module gets ready to learn in a learning module based on it. The work data means the time between chuck and unchuck, the coordinates that both arms move and the work sequence. The learning module uses reinforcement learning based on values and repeats the four processes, ①to choose the tentative placements, ②to calculate the working time, ③to evaluate the acquired cycle time, and ④ to repeat the four reward distribution operations. Finally, the most suitable placement of the units can be decided.

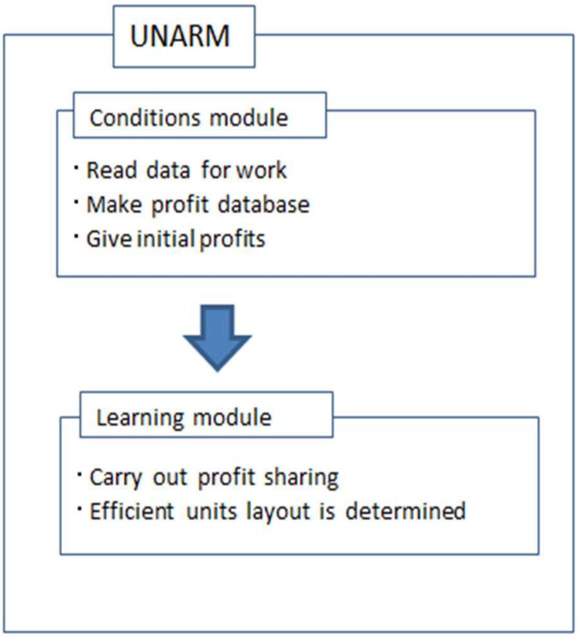

Fig. 1. System construction of UNARM.

2.2. *Condition making module*

The condition making module carries out the following processes.
Step1. Read each work data of the robot two arms.
Step2. Read the possible area of each unit placement.

As shown in Fig.2, the possible area of each unit placement is divided as a lattice and the center of each lattice becomes the center of the candidate place.
Step3. Give initial values to the candidate place created in Step2.

2.3. *Learning module*

The learning module carries out the following processes.

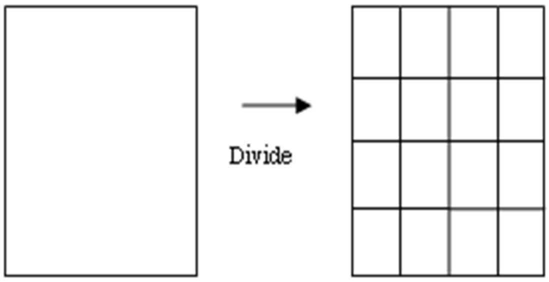

Fig. 2. Divided placements.

10	10	10	10
10	10	10	10
10	10	10	10
10	10	10	10

Fig. 3. Distributions of values.

Step1. Make an initial values of the values.
Step2. Decide the placement of the unit by a roulette selection.
Step3. Calculate the coordinates of each part.
Step4. Calculate the moving distances of the robot arms.
Step5. Calculate the working time of the robot arms.
Step6. Compare the calculated working times with the standard value.
Step7. If the time is smaller, give the reward.
Step8. If the working time is smaller, update the standard value.
Step9. Repeats Step2 from Step8 till a decided reputation times.

We adopt the concept of waiting time not to produce arm interferences because the two arms move at the same time in Step5. In step6, the concept chooses the longer working time as the next evaluation time.

3. Moving method of robot arms

To calculate the working time of the robot arms in Step5, the robot arm moving speed is necessary to calculate.

Therefore we define the arm moving locations as follows, Apprpach-1: the upper point of the part that a robot will take, Approach-2: the upper point closer to Approach-1 and Chuck point: the point that the arms chuck, unchuck or put a part. We also define the arm moving speed among the upper three points. The speed between Approach-2 and Approach-2 is defined a feet speed. The speed between Approach-2 and Approach-1 as approach speed I, the speed between Approach-1 and chuck point as approach speed II. In addition, as these three kinds of speed have different speeds whether the arm grasp a part or not, the six kinds of speed value definitions in total must be chosen. In this study, we adopt that the robot arms always move by regular linear motion.

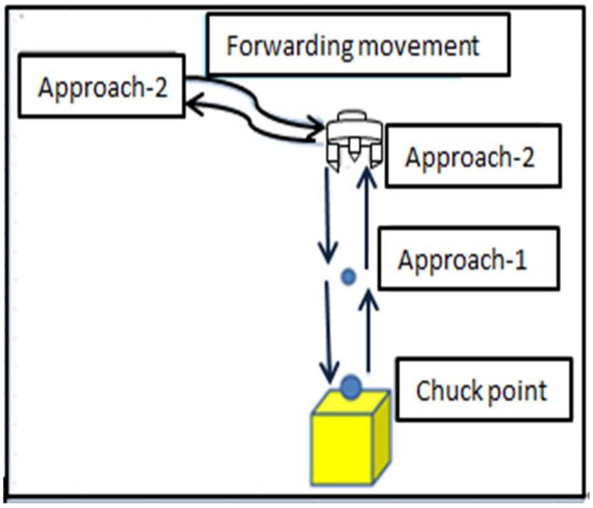

Fig. 4. Robot arm movements.

4. Concept of waiting time

The robot of this study has both arms. When we use the both arms, the most difficult point is to interfer both arms each other. In other words, it is necessary to decide the work sequence not to make the interference of the right arm and the left. Therefore we adopt the concept, the waiting time, to prevent arm interferences in calculating working times of one cycle in Step5. in the learning module. For example, the assembly sequence exists that the assembly work A must be set after the completion of the assembly work X. In this case, when one of the two arms performs assembly work A, the other arm must confirm the completion of assembly work X. In other words, the assembly work A must start after the completion of assembly work X. We define this time lag as the waiting time.

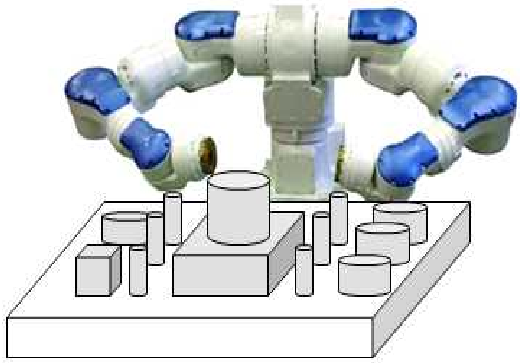

Fig. 5. Both arms of robot.

The following shows the waiting time.We define the two flags, Lp and P.

Lp(Look at Point): Job that starts to need the waiting time.
P(Point): Work corresponding to the waiting time of Lp.

In order not to make arm interferences, the works that need the waiting time are given Lp and the corresponding works are given P.

For example, as shown in Fig.6, when the left arm starts Lp, the left arm can continue the work as the right arm still finished P. This is because waiting time is not given to the left arm.

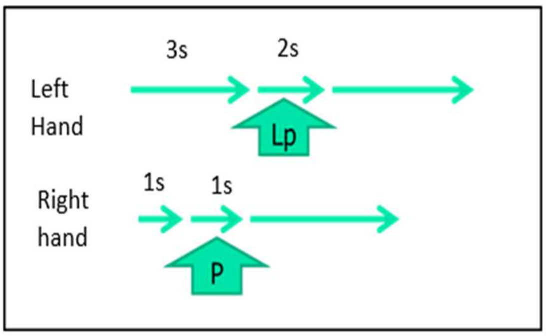

Fig. 6. No waiting time.

On the contrary, in the case of Fig.7, when the left arm starts Lp, the work of P of the right arm is not finished. This is because the left hand has to wait seven seconds to start Lp. The seven seconds correspond to waiting time.

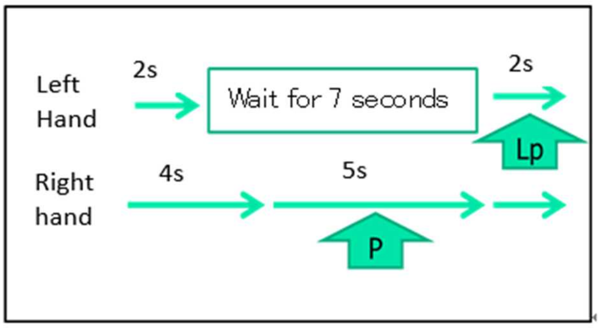

Fig. 7. Waiting time.

5. Simulation applications

We applied UNARM to the cell type assembly machine with the both arms of the robot to ascertain the usefulness of UNARM. The application example adopted eight units (two of the eight are trays that many parts were put), 10 initial values, 10 reward levels, 600,000 times learning number, 36 left arm assembly processes and 40 right arm assembly processes. Table 1 shows the moving speed of the robot arms. In addition, in order to compare the learning results, the simulations randomly to choose unit placements were also carried out.

Table 1. Moving patterns of arms.

	Without part	With part
Approach-2—Approach-2	770mm/s	380mm/s
Approach-2—Approach-1	400mm/s	250mm/s
Approach1—Chuck point	25mm/s	50mm/s

5.1. *Simulation results*

We carried out ten times simulations for each condition and showed the mean and the minimum of two kinds simulations in Table2.

Table 2. Simulation results.

	UNARM(s)	Random(s)
Average time	237.4228	243.9498
The smallest time	237.2925	241.9623

Acquired placements of the minimum evaluation time are shown in Fig.8. The placements acquired by random selections are shown in Fig.9.

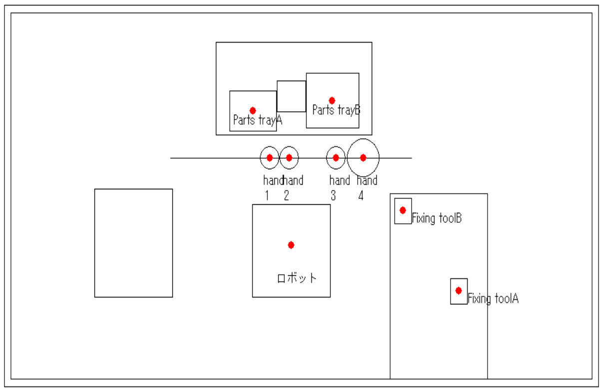

Fig. 8. Placements of the minimum.

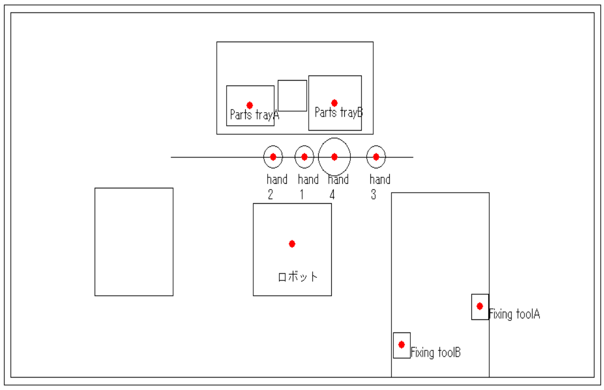

Fig. 9. Placements by a random method.

Comparing the results of Table2, UNARM's evaluation times are better than the random ones. Especially, the mean evaluation time is shorter six seconds. It is said that UNARM can continuously acquire the better assembly cycle time corresponding to the efficient units placement.

6. Conclusions

In this study, we developed UNARM system which finds the better unit placements and prevents the interferences of both arms. To do this, UNARM adopted the concept of waiting time. By applying UNARM to the cell-type assembly machine that includes the both arms robot, UNARM acquired the good unit placements. I t is ascertained that UNARM is useful.

Development of a Hydraulic Underwater Manipulator for Deep-Sea Survey AUV

Takashi Sonoda
Dept. of Human Intelligence Systems, Kyushu Institute of Technology,
2-4 Hibikino, Wakamatsu, Kitakyushu, Fukuoka, Japan
E-mail: t-sonoda@brain.kyutech.ac.jp

Amir Ali Forough Nassiraei
Dept. of Human Intelligence Systems, Kyushu Institute of Technology,
2-4 Hibikino, Wakamatsu, Kitakyushu, Fukuoka, Japan
E-mail: nassiraei@brain.kyutech.ac.jp

Ivan Godler
Twist Drive Technologies, Inc.,
967-3 Ueki, Nogata, Fukuoka, Japan
E-mail: ivan.godler@twistdrive.co.jp

Tharindu Weerakoon
Dept. of Human Intelligence Systems, Kyushu Institute of Technology
2-4 Hibikino, Wakamatsu, Kitakyushu, 808-0196, Japan
E-mail: weerakoontharindu@brain.kyutech.ac.jp

Kazuo Ishii
Dept. of Human Intelligence Systems, Kyushu Institute of Technology
2-4 Hibikino, Wakamatsu, Kitakyushu, 808-0196, Japan
E-mail: ishii@brain.kyutech.ac.jp

Abstract

We are developing a group of AUVs whose mission is to capture underwater creatures or acquire in-situ biological samples in the deep sea. The AUV under developing has a hydraulic manipulator to capture the target creature, and sends underwater images that provide biologists (operators) with information to determine which creatures should be targeted and captured during the operation. In this paper, the concept and design of hydraulic actuator for 5-axis manipulator, and the mechanics of manipulator is proposed, and the experimental results of manipulator control at 10 and 20 M Pa pressure are shown.

Keywords: Underwater Manipulator, Hydraulic Actuator, AUV

1. Introduction

New discoveries of mineral resources, energy resources and marine lives in the deep-sea have big potential to give deep impacts on our society. However, we are still unable to get detailed information about the mechanism of ecological system of dep-sea because of special features, high pressure, darkness and radio attenuation. Recently, underwater robots are employed to observe deep-sea floor as useful tools[1-5], and they are mainly classified as Human Occupied Vehicle (HOV), Remotely Operated Vehicle (ROV) and Autonomous Underwater Vehicle (AUV) depending on the extent of autonomy and mounted facilities. We have been developing a group of AUV systems whose mission is to capture underwater creatures or acquire in-situ biological samples like DNA from various types of creatures in the deep sea. Although the final goal is to get the sample of wide variety of fish and marine creatures, considering the state of the arts of AUVs, our first target is to catch a creature, which moves slowly like a small crab or marine benthos.

The AUV under developing[6] has a hydraulic manipulator to capture the target creature, and sends underwater images that provide biologists (operators) with information to determine which creatures should be targeted and captured during the operation. These images are to be sent from the AUV to the surface support vessel where the biologist are checking monitors to determine his/her desirable target creature and the transmission of image information data is carried out through an ultrasound communication.

The operation is illustrated in Fig.1. There exist a lot of issues to realize underwater sampling AUV such as navigation, control, image processing, actuators, sensory systems. In this paper, we introduce an underwater manipulator for a deep-sea survey and sampling AUV. Firstly, we introduce our project that aims to develop an observation and capturing system of marine creatures using multiple underwater robots composed of cruising and manipulator mounted AUVs. Next, we introduce the concept and design of hydraulic actuator for 5-axis manipulator, and the mechanics of manipulator to change the linear motion to rotational motion using cams, and the experimental results of manipulator control at 10 and 20 M Pa pressure.

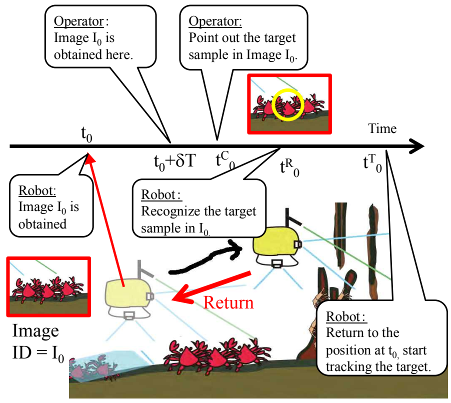

Fig.1 Concept of AUV sampling system

2. Hydraulic Underwater Manipulator

The manipulator is supposed to have minimum 3 degrees of freedom (DOF) in the same plane for positioning (2 DOF) and orientation (1 DOF) of the arm tip, and 1 DOF for open-close of a gripper.

Basic requirements are:

- arm length ~ 600 mm
- payload ~ 0.5 kg (max)
- external pressure 20 MPa (max)

The manipulator should be able to operate in the salty water at neutral buoyancy, and is actuated by a set of stepping motors, ball screws and hydraulic cylinders that generates hydraulic pressure to move cylinders on the manipulator links. In order to convert the linear motion of cylinder into rotation, a special cam mechanism was introduced. The variation of linear motion is 50 mm and converted to 180 degree rotation. The criterion for the cam design is to achieve minimal, possibly small lateral force on the piston rod during the motion.

The problem to minimize lateral force on the piston rod is the same as to orient the hydraulic cylinder in the normal direction to the cam shape. We assume that the cylinders are aligned with the direction of the robotic arm length; therefore, the problem is translated into finding a cam shape r (φ), which satisfies the cylinder direction to be normal to the cam. For this we need to derive the equations that consider the offset angle between the cam shape angle parameter φ and the arm rotation angle θ, which is cause by the initial offset angle θ_0 of the cylinder towards the cam radial direction.

The constraint to the solution here is linear motion of the piston Kθ that is proportional to the rotational angle of the arm θ. The parameters and obtained cam shape are shown in Fig. 2.

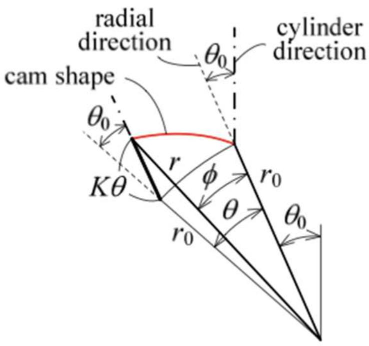

(a) Cam design parameters

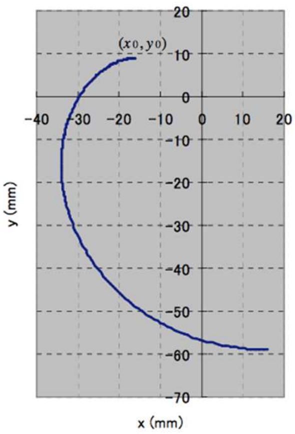

(b) Results of Cam calculation

Fig.2 Parameters for cam design and obtained cam shape.

The hydraulic underwater manipulator is composed of dual-oil system as shown in Fig. 3. The oil in the main cylinder is pushed to the arm cylinder whose shaft pushes the cam, then the arm rotates. The other side of arm cylinder is connected to the back side of main cylinder.

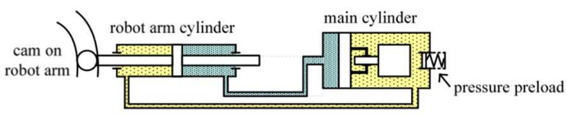

Fig. 3 Concept of manipulator system.

The developed manipulator is shown in Fig.4. The structure is made of MC-nylon and the pressure hull is made aluminum with coating.

Fig.4 Underwater manipulator for deep-sea

3. Experiments in the Pressure Tank

The experimental results at pressure 10 to 20 MPa in test tank are shown in Fig.4. Pressure change (increase, decrease) was performed in 12 minutes, and the pressure was kept constant for 12 minutes to do the measurements. During the measurements, each joint was moved separately. Joint angles were measured by RLS 12bit absolute angle magnetic sensor RMD08. A video was also recorded during each measurement. Each main piston of each joint was moved for 4 mm: that is joint angles 23.59 degrees for DOF1, 36.86 degrees for DOF2, and 73.72 degrees for DOF3.

Although hysteresis of about 3 degrees (from 3 to 3.5 degrees) in DOF1, about 3 degrees (2.7 to 3 degrees) in DOF2, and about 9 degrees (8 to 9.5 degrees) in DOF3 can be observed in the results independently of the pressure, the manipulator showed good performance in deep-sea pressure.

4. Conclusion

In this paper, the concept and design of hydraulic actuator for 5-axis manipulator, and the mechanics of manipulator is proposed, and the experimental results of manipulator control at 10 and 20 MPa pressure are evaluated. It is shown that the developed manipulator is enough small to be mounted on AUV, and can be actuated under the deep-sea pressure.

Acknowledgement

This research is supported by JST CREST "Establishment of core technology for the preservation and regeneration of marine biodiversity and ecosystems".

References

1. Y. Junku, T. Ura , G. Bekey, *Underwater robots*, Springer Science & Business Media, (2012)
2. Whitcomb, Underwater robotics: Out of the research laboratory and into the field, *Proc. of IEEE/ICRA'00*, (2000)
3. Y. Nishida, T. Ura, T. Sakamaki, J. Kojima, Y. Ito , K. Kim, "Hovering Type AUV "Tuna-Sand" and Its Surveys on Smith Caldera in Izu-Ogasawara Ocean Area, *Proc. of IEEE/OCEANS2013*, (2013)
4. T. Maki, Y. Sato, T. Matsuda, R. T. Shiroku , T. Sakamaki, "AUV Tri-TON 2: An intelligent platform for detailed survey of hydrothermal vent fields," *Proc. of IEEE/AUV2014*, (2014)
5. Y. Nishida, K. Nagahashi, T. Sato, A. Bodenmann, B. Thornton, A. Asada, T. Ura, Development of an autonomous underwater vehicle for survey of cobalt-rich manganese crust, *Proc. of IEEE/OCEANS2015*, (2015)
6. Y. Nishida, T. Ura, T. Nakatani, T. Sakamaki, J. Kojima, Y. Itoh and K. Kim, Autonomous Underwater Vehicle "Tuna-Sand" for Image Observation of the Seafloor at a Low Altitude, *Journal of Robotics and Mechatronics*, Vol.26, No.4, pp.519-521, 2014

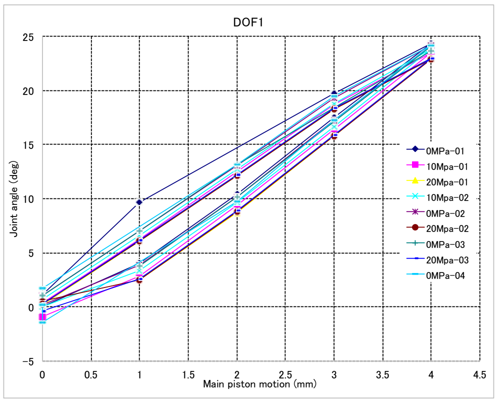

(a) First Joint Angle

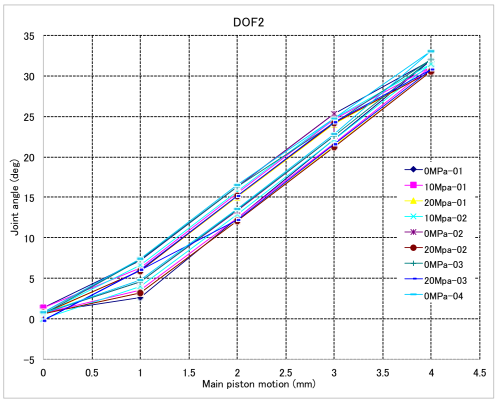

(b) Second Joint Angle

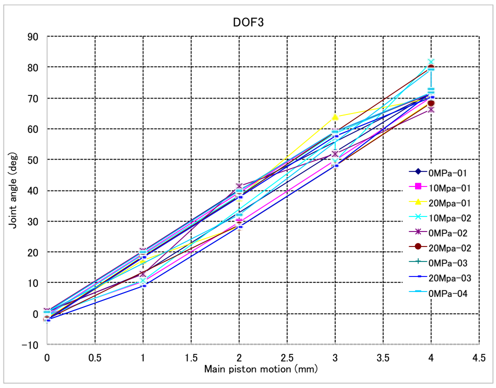

(c) Third Joint Angle

Fig.4 Experimental results in the pressure tank.

Floating LBL concept for underwater position detection

Keisuke Watanabe
Dept. of Navigation and Ocean Engineering, Tokai University,
3-20-1 ORido Shimizuku, Shizuoka, Shizuoka, Japan
E-mail: keisukejapan@gmail.com

Kazuo Ishii
Dept. of Human Intelligence Systems, Kyushu Institute of Technology
2-4 Hibikino, Wakamatsu, Kitakyushu, 808-0196, Japan
E-mail: ishii@brain.kyutech.ac.jp

Abstract

Determination of underwater coordinates is important in such activities like underwater vehicle operation, installation of underwater structure and so on. The determination methods are using LBL, SSBL or an inertia navigation sensor, which are all very expensive. In some scientific or academic operations, the cost of position determination of an underwater structure or a vehicle is too expensive to realize in the sea experiments and a low cost position detection system should be developed. In this paper, a floating LBL concept is presented. The LBL system consists of at least three floating buoys each of which has a GPS, a pair of ultrasound transmitter and receiver, wireless communication device and a microcomputer board which controls the total procedure. We will introduce and explain about each module of the buoy system, ultrasound transmitter/receiver.

Keywords: Underwater position detection, floating LBL, subsea installation

1. Introduction

Determination of underwater coordinates is important in such activities like underwater vehicle operation, installation of underwater structure and so on. The determination methods are using LBL, SSBL or an inertia navigation sensor, which are all very expensive. In some scientific or academic operations, the cost of position determination of an underwater structure or a vehicle is too expensive to realize in the sea experiments and a low cost position detection system should be developed. One example supposed in our laboratory is position detection of a ROV in the coral reef monitoring operation. In this operation, we need to take underwater pictures of coral reefs to record and monitor the condition of the reefs, where we need underwater coordinates of the picture taken to make a map of the total reef condition in the supposed area. The price of ROVs or underwater cameras is becoming cheaper and it seems ridiculous to use SSBL whose price is almost from five to ten times of ROV itself. Another supposed operation is installation of underwater devices or structures. To put the structure down on the desired position of the seabed, we need to monitor the coordinate of the structure during its installation operation. If the project is related to oil/gas development, this coordinate detection cost is relatively small compared to the total project investment. However, if the project is related to an academic research like settling a seismic sensor down on the seafloor, the cost of position detection must be much cheaper.

In this paper, a floating LBL concept is presented. The LBL system consists of at least three floating buoys each of which has a GPS, a pair of ultrasound transmitter and receiver, wireless communication device and a microcomputer board which controls the total procedure. We will introduce and explain about each module of the buoy system, ultrasound transmitter/receiver.

2. Floating LBL system

The floating LBL system consists of at least 3 buoys each of that has a pair of ultrasound receiver and transmitter. A buoy also has a set of Xbee wireless communication device to make a serial communication link with a master computer.

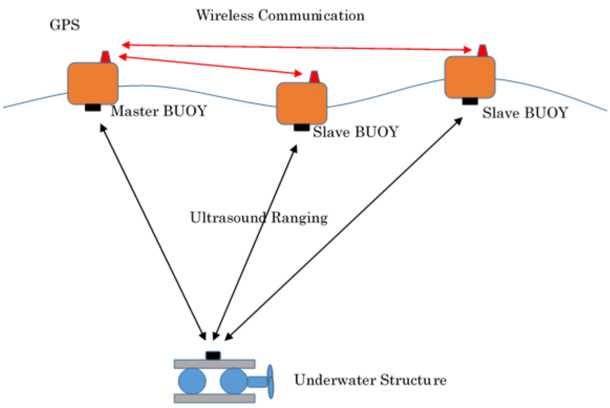

Fig.1 The concept of floating LBL system

A GPS unit is attached on each buoy. The master buoy is the origin of the coordinate and controls the total system. The procedure of the coordinate calculation of underwater structure is as follows.

(1) The master buoy transmits the start signal to slave buoys using Xbee module. At the same time, the master buoy transmits the ultrasound signal to underwater structure. The timer of the master buoy is cleared and set zero.

(2) As soon as a slave buoy receives the start signal, it clears its own clock and set zero. At the same time, the ultrasound receiver of the slave buoy goes waiting mode.

(3) The underwater structure receives the transmitted signal from the master buoy and responds back the ultrasound signal toward water surface where each buoy is floating.

(4) The buoys receive the ultrasound signal from the underwater structure. Each buoy stops the timer and records the GPS (N,E) coordinate at the same time.

(5) If the master buoy receives the returned signal from the underwater structure, it stops its timer and records the time as well as its GPS position values.

(6) The master buoy calls to the slave buoy No.1 through Xbee and the slave No.1 calls back its timer count value and GPS coordinate through Xbee communication to the master buoy.

(6) The slave buoy No.2 calls back according to the request from the master buoy.

(7) The master buoy calculates the distance between the master and the slave respectively using the GPS coordinate values gotten from slaves.

(8) The master calculates the distance between each buoy and the underwater structure using the timer values gotten from slaves and its own.

(9) Using the distances mentioned above, the master can calculate the underwater coordinate of the structure.

(10) This procedure will be repeated periodically in the given interval time.

3. An example of underwater structure motion

As an example of the application of the floating LBL system, we considered a hanged underwater structure from a crane on the vessel. The offset angle from the vertical axis is a parameter of the nonlinear pendulum motion of the structure as shown in Fig.2.

It is assumed that the crane cable is paid out from the initial length l_0 with v m/s speed. The initial length corresponds to the height from the initial submerged point of the structure to the hanging point of the top of the crane arm.

Considering the added mass and fluid resistance force, the equation of motion of the pendulum system is,

$$(1 + C_m)m\, l^2\, \ddot{\theta} + \left(2mlv + \frac{1}{2}\rho C_d A l\right)\dot{\theta} + mgl\sin\theta = f$$

, where, f is control force, Cm is added mas coefficient, m is the mass of the structure, theta is the angle of the cable, l is the length of the cable, v is the speed of the cable pay out, Cd is the drag coefficient, A is the effective area of the structure.

The simulation is executed using next parameters. The structure size is 5m wide 5m long 4m height. The mass is assumed 50tf. The water depth is assumed as 2500m.The initial offset angle is 20 deg. The paid out rate of the cable are 2 cases, which is 1m/s and 0.5 m/s. Added mass coefficient is assumed 1.0, whereas drag force coefficient is assumed as 3.0.

The simulation result of the paid out rate is 1.0m/s is shown in Fig.3. The horizontal displacement which means the fluctuation from the desired installation point is shown in Fig.4. As Fig.3 shows, the offset angle is decreasing according to time, which is due to damping effect of fluid resistance force. However, as the crane cable length is increasing, the horizontal offset from the desired point is developing as shown in Fig.4. I assumed the drag coefficient higher assuming that some damping device is attached to the structure. But from the result shown in Fig.4, it shows very difficult to reduce the offset vibration amplitude only using passive fluid damping force. So the active control method should be employed to reduce the vibration of the structure. For the active control of the structure, we need to detect the underwater position, so the floating LBL system should be developed.

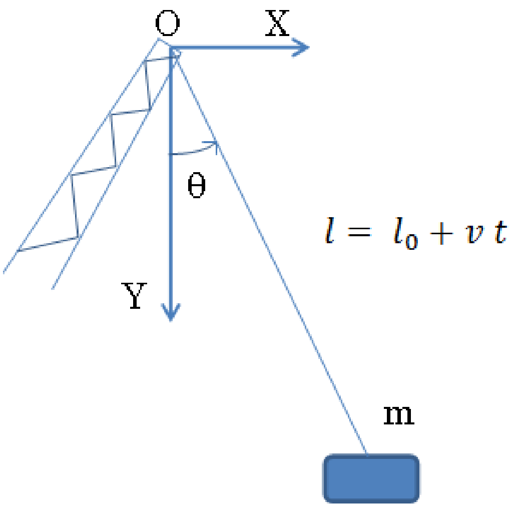

Fig. 2 Sand captured by the blocks

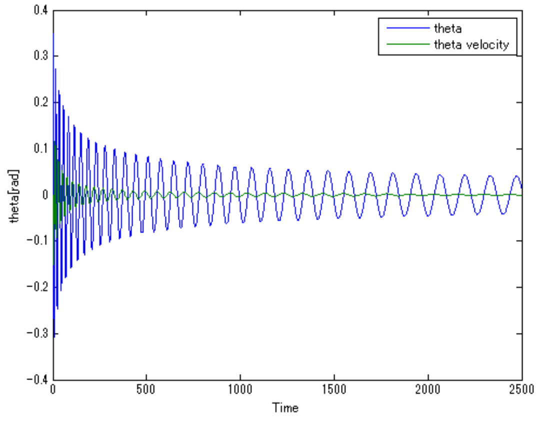

Fig.3 Vibration angles of the cable of the structure

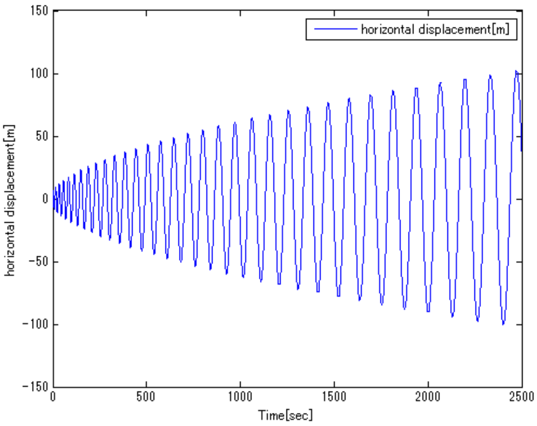

Fig. 4. The horizontal displacement of the structure

4. Ultrasound transmitter/receiver

Ultrasound receiver/transmitter is expensive in general. So we are developing a set of ultrasound receiver/transmitter for this experiments. Fig.5 shows the sea trial of our ultrasound receiver/transmitter. We succeeded more than 20m distance measurement, however, we found that the directivity of the sensor probe is too narrow so we need to improve it to realize the sea experiments. Through this experiments we realized the delivery of the master and slave buoys on the sea surface is very hard task. So we modified a UAV drone to be floatable and watertight to bring the buoys from the support vessel to the desired sea surface.

5. Conclusion

In this paper, we presented our floating LBL concept for the detection of the coordinate of the underwater structures. Using Xbee wireless communication and ultrasound ranging system, we can constitute a set of LBL much cheaper than the traditional LBL system that needs very expensive setup for seafloor baseline installation. To put the buoys on the desired surface position from the support vessel, we also modified a UAV drone to deliver the buoy system from the vessel to the sea.

Fig.5 Distance detection experiments at sea

Acknowledgement

This research is supported by KAKANHI, Grant-in-Aid for Challenging Exploratory Research, JSPS JP26630230.

References

1. K. Watanabe, "A Possibility of Active Controlled Installation for Deep Water Subsea Production Modules", *Proceedings of ICETET2012*, IEEE
2. Y. Watanabe, K. Watanabe, F. Yuasa, " A self-walking vertical mining system concept using DTH for seafloor mining and its preliminary design", *OTC27003-MS*, 2016
3. K. Watanabe, Y. Watanabe, F. Yuasa, "A vertical mining system concept using DTH for seafloor mining", *OTC25825-MS*, 2015

Experiments of Floatable UAV Drone for Wave Dissipating Block Inspection

Keisuke Watanabe
Dept. of Navigation and Ocean Engineering, Tokai University,
3-20-1 ORido Shimizuku, Shizuoka, Shizuoka, Japan
E-mail: keisukejapan@gmail.com

Koshi Utsunomiya
Dept. of Navigation and Ocean Engineering, Tokai University,
3-20-1 ORido Shimizuku, Shizuoka, Shizuoka, Japan
E-mail: bebop0911@gmail.com

Kazuho Mitsumura
Dept. of Navigation and Ocean Engineering, Tokai University,
3-20-1 ORido Shimizuku, Shizuoka, Shizuoka, Japan
E-mail: kazuho.rc@gmail.com

Shiyun Takasaki
D Dept. of Navigation and Ocean Engineering, Tokai University,
3-20-1 ORido Shimizuku, Shizuoka, Shizuoka, Japan
E-mail: 4bkw1105@tokai-u.ac.jp

Abstract

In this paper, we present our modification experience of making a UAV drone watertight and floatable. Then we present several experiments on taking pictures considering ocean monitoring in the sea near our campus. The watertight experiments are done from our school's pier. In these experiments, we repeated to start flying the drone from the sea surface and fall it down into the water several times. Using this UAV drone, we tested several experiments to take pictures of wave dissipating blocks at MIHO Island where beach line erosion is critical and many blocks are arranged to prevent waves from washing the shore. We can see the shoreline very clearly from more than 200m high as a macro image and also we can inspect the blocks looking around its stacks as well as approaching near the sea surface where waves break and wave splash washes the drone.

Keywords: UAV drone, environmental monitoring, coastal erosion, offshore structure monitoring

1. Introduction

A UAV drone is an effective low cost photographing apparatus for ocean environment monitoring. Taking images is essential for these environment monitoring such as coastal line monitoring where beach erosion is severe, inspection of offshore structures like wind power stations or coral reef observation etc. Usually the UAV drone flies high above the water surface, however, it is possible that the drone happens to fall down into the water due to operator's control mistake or malfunction of itself. In addition, in some operations, it is desirable for the drone to be able to float on the water surface to save energy consumption. In those cases, we need to make the drone watertight and floatable.

As shown in Fig.1, while the MIHO Island in Shizuoka prefecture is designated as a World Heritage Site, rapid and massive beach erosion of the island is one of the critical issues. It is said that UNESCO is warning if the wave dissipating blocks will not be removed, they will cancel the WHS designation because the blocks damage the beauty of the landscape of the coastline of the island. However, the wave dissipating blocks are essential to keep shore sand from being washed away by waves or currents. There is a very important road Route 150 that faces the shore and the most important role of these blocks is protecting the road from caving or depression due to road foundation washing away.

So it is very important for us to monitor the shoreline as well as the condition of those blocks widely viewed for some long term constantly. Using watertight UAV drones are one of the possible solutions for this problem.

2. UAV drone modification for watertight

To realize the UAV drone monitoring system, we firstly need to examine how to make it watertight and floatable. The electrical components that are vulnerable to water are GPS module, wireless communication system, motor drivers, batteries and motors for propellers. We packed those systems inside a watertight container as shown in Fig.2.

Fig.1 Coastal shore erosion and wave dissipating blocks

Fig.2 Electrical component in a watertight container

Fig.3 UAV watertight experiment in the sea

We tested in our tank to check whether this method is available or not. At first, we experienced some troubles, for example, one of the wire connectors of motors are detached by the impact of falling down to the water surface, which capsized the drone due to the flying force unbalance. Through these experiences we modified the drone to be able to use on the water surface.

As the motors for the propeller are brushless motors and if we wash those motors with fresh water soon after we use them, they can be used even if we put the drone into seawater as shown in Fig.3 and Fig.4.

3. Monitoring of wave dissipating blocks

After we confirmed our watertight method is available, we took several experimental pictures of the wave dissipating blocks at MIHO Island.

Fig.5 shows one area of those blocks from the height of around 100m. From this picture, we can see the blocks captured some sand that is put by using many dumper trucks to fill the eroded shore to recover. However, it also shows at the edge of the lined blocks, there seems another erosion started as shown in the upper left of Fig.5. Fig. 6 shows that shore erosion proceeds in between two block areas. As we can see from the picture, the shore line vanished clearly between the two block areas. From the different colors of the water, we can see the sand flow in the sea. As the lower part of the Fig.6 shows we can notice a kind of vortex flow which surrounds the edge of blocks where water color is rather green than blue compared to the left side of the picture. This implies a mountain of blocks can keep some sand around its area, however, the effect of accumulation is quite limited. For more than 20 years, hundreds of dumper trucks transported sand to fill the shore and put tons of sand into water, the shore line has not recovered yet. From the pictures taken this time, we confirmed our feeling that sand put into water never recover shoreline, instead, waves wash away sand. This picture indicates if we monitor the same point for a long term and trace changes of the landscape, we can estimate the amount of washed away sand as well as find more effective arrangements of the blocks to capture sand put by the dumper trucks everyday.

Fig.7 shows the closer look of the blocks where the island of blocks are sagged. From the picture, we find the sagging downward of the blocks are where those blocks are not old but newly put into the shore. The reason why this area is sagged downward is not clear, however, several blocks underwater are destroyed. To find the reason, we inspected the blocks further by taking many pictures.

As shown in Fig.8, we found a broken block that looks newly put judging from its surface condition that there are few seaweeds on the surface of the block. We can find several broken blocks like this, and the reason of sagging downward shown in the Fig.5 seems due to this kind of collapse. We need to investigate further to find the exact reason of this kind of collapse of a block.

Fig.4 UAV floating experiment on the seasurface

Fig. 5 Sand captured by the blocks

Fig.6 Erosion proceeds between block areas

Furthermore, we found the evidence of wave abrasion of the block as shown in Fig.9. This is because the water around the mountain of blocks contain sand as I mentioned in Fig.6. From Fig.9, we guess sand mixed water abrades the block faster compared to normal sea water, though we need to investigate further from this view point.

4. Conclusion

In this paper, we modified the UAV drone to be able to use on the sea. We packed the electrical components into a watertight container and checked the brushless motors of propeller can be used with no special fabrication if we maintenance them correctly. Using this watertight and floatable UAV drone, we tried monitoring of wave dissipating blocks at MIHO shore. We found out several new things related to collapse of blocks and shore line erosion from observation using this UAV drone.

Acknowledgement

This research is supported by KAKANHI, Grant-in-Aid for Challenging Exploratory Research, JSPS JP26630230.

References

1. K. Nihiguchi, S. Sato, T. Sakashita, Y. Tajima, Y. Sekiguchi, K. Tsuchihashi, "Beach Erosion Mechanism by a Structure Protruding from Shoreline and the Performance of a Sand-packed Jetty against Beach Erosion", *Journal of JSCE*, Vol.68, No.2 (2012)
2. K. Kimura, K. Nemoto, Y. Nagahama, O. Nishimura, "Characteristics of Beach Erosion and Effect of the Beach Erosion of the Habitat of Macrobenthos in MIHO Beach", *Journal of JSCE*, Vol.21, pp.229-234, (2005)

Fig.7 Downward sagging area of the blocks

Fig.8 Broken blocks which are relatively new

Fig.9 Wave sand abraded block

Development of Self-Diagnosis System of an Autonomous Underwater Vehicle Tuna-Sand 2

Takashi Sonoda
Dept. of Human Intelligence Systems, Kyushu Institute of Technology
2-4 Hibikino, Wakamatsu, Kitakyushu, Fukuoka, 808-0196, Japan
E-mail: t-sonoda@edu.brain.kyutech.ac.jp

Naoya Fujii
Dept. of Human Intelligence Systems, Kyushu Institute of Technology
2-4 Hibikino, Wakamatsu, Kitakyushu, Fukuoka, 808-0196, Japan
E-mail: t-sonoda@edu.brain.kyutech.ac.jp

Yuya Nishida
Dept. of Human Intelligence Systems, Kyushu Institute of Technology
2-4 Hibikino, Wakamatsu, Kitakyushu, Fukuoka, 808-0196, Japan
E-mail: ynishida@lsse.kyutech.ac.jp

Kazuo Ishii
Dept. of Intelligence Systems, Kyushu Institute of Technology,
2-4 Hibikino, Wakamatsu-ku, Kitakyushu, Fukuoka, Japan
E-mail: ishii@brain.kyutech.ac.jp

Abstract

For autonomous underwater vehicle (AUV), high autonomy is required in order to accomplish mission such as inspection, observation, manipulation under extreme environments, deep-ocean. One of necessary function for AUV is the self-diagnosis system to detect the abnormality can be said to be an important feature. In this paper, we propose a self-diagnostic system using the dynamical model of Sampling-AUV "TUNA-SAND2", where the fault device detection is carried out using the model, and evaluated through tank tests.

Keywords: AUV, Self-Diagnosis System .

1. Introduction

Underwater robots have attracted attention as useful tools[1-6] to observe deep-sea floor. Especially, Autonomous Underwater Vehicle (AUV) can move wide area freely not having tethered cable with support vessel. On the other hand, for AUV, high autonomy is required in order to accomplish mission such as inspection, observation, manipulation under extreme environments, deep-ocean. One of necessary function for AUV is the self-diagnosis system to detect the abnormality can be said to be an important feature.

As a previous study, Takai[7] et al. proposed a self-diagnosis system utilizing a dynamic model by a neural network (NN) However, NN cannot prove the stability of the model theoretically.

In this paper, we propose a self-diagnostic system using the dynamical model of Sampling-AUV "TUNA-

SAND2[8]", where the fault device detection is carried out

using the model, and evaluated through tank tests.

Fig.1 Newly Developed AUV "TUNA-SAND 2"

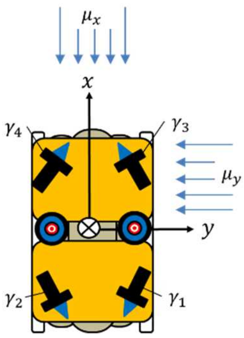

Fig. 2 Thruster Arrangement in Horizontal Plane.

2. Dynamic Model of AUV

Depending on the mission objectives, AUV has mounted different sensors and thrusters, so the mathematical model also changes. Therefore, a hovering type AUV "TUNA-SAND2" jointly developed by the University of Tokyo and Kyushu Institute of Technology was set as target robot. We assume two abnormalities to be detected are (1) tidal disturbance and (2) low thruster output.

TUNA-SAND 2 has six thrusters, as shown in Fig. 2, it has a redundant drive system using four thrusters for the horizontal movement of the three DOF of Surge, Sway and Yaw. In order to develop an algorithm to solve this redundancy, AUV models the horizontal plane movement in diagnosing the failure of the thruster.

Based on the above condition setting, we define the equation of motion of AUV[9] in eq. (1) and the current consumption of AUV in eq.(2).

$$\dot{\boldsymbol{v}}_t = \boldsymbol{M}^{-1}\{-\boldsymbol{C}(\boldsymbol{v}_{t-1}-\boldsymbol{\mu})|\boldsymbol{v}_{t-1}-\boldsymbol{\mu}| + \boldsymbol{B}(\boldsymbol{I}-\boldsymbol{\gamma})\boldsymbol{\tau}_{t-1}\} \quad (1)$$

$$I_t = I_0 + e_\tau \sum(1-\gamma_l)\tau^l_{t-1} \quad (2)$$

Here, $\boldsymbol{v}_t = [v_t^x\ v_t^y\ \omega_t^z]^T$ means the velocity vector of AUV, $\boldsymbol{\tau}_t = [\tau^1_t\ \tau^2_t\ \tau^3_t\ \tau^4_t]^T$ is the thruster control signal vector, $\boldsymbol{M} \in \mathrm{R}^{3\times3}$ is the mass and inertia moment including additional mass, $\boldsymbol{C} \in \mathrm{R}^{3\times1}$ is the hydraulic coefficient, $\boldsymbol{B} \in \mathrm{R}^{3\times4}$ is the inverse kinematics transfer thruster output to the force to the center of gravity of AUV. Regarding eq. (2), I_t is the total consumption current of AUV, I_0 is the steady consumption current of CPU and others excluding thrusters, e_τ is the conversion coefficient from command thrust to thruster consumption current. Also, $\mu = [\mu_x\ \mu_y\ 0]^T$, $\gamma = diag\ \{\gamma_1, \gamma_2, \gamma_3, \gamma_4\}$ are the ambient power flow rate to be diagnosed, the power reduction rate of each thruster (0 to 100 [%]) .

State vector $\boldsymbol{x}_t$, observation vector $\boldsymbol{y}_t$, manipulation vector $\boldsymbol{u}_t$, abnormal variable β to be diagnosed as in equations (3) - (6).

$$x_t = [\dot{v}_t^x\ \dot{v}_t^y\ \dot{\omega}_t^z\ v_t^x\ v_t^y\ \omega_t^z\ I_t\ ]^T \quad (3)$$

$$y_t = [v_t^x\ v_t^y\ \omega_t^z\ I_t\ ]^T \quad (4)$$

$$u_t = [\tau_t^1\ \tau_t^2\ \tau_t^3\ \tau_t^4]^T \quad (5)$$

$$\beta = [\gamma_1\ \gamma_2\ \gamma_3\ \gamma_4\ \mu_x\ \mu_y\ ]^T \quad (6)$$

$\boldsymbol{y}t$, the translational speed, angular velocity, current consumption, can be observed from the velocity sensor, the inertial navigation device and the current sensor. Using eqs. (1) to (6), the state equation motion is in (7) and observation equation is in (8) .

$$\boldsymbol{x}_t = \boldsymbol{F}(\boldsymbol{x}_{t-1}, \boldsymbol{u}_{t-1}, \boldsymbol{\beta}) \quad (7)$$

$$\boldsymbol{y}_t = \boldsymbol{G}\boldsymbol{x}_t = [\boldsymbol{O}^{4\times3}\ \ \boldsymbol{I}] \cdot \boldsymbol{x}_t \quad (8)$$

3. Self-Diagnosis System

The basic concept of self-diagnosis system is shown in Fig. 2. Based on the time series data of the manipulated variable $\boldsymbol{u}_t$ and observation variable $\boldsymbol{y}_t$ of AUV, the observer to estimate β is constructed.

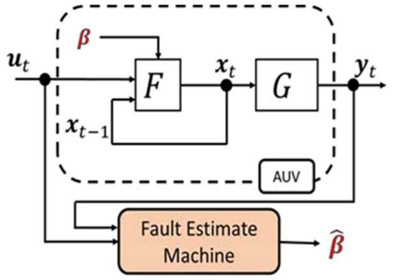

Fig. 3 The concept of self-diagnosis system

First, the diagnostic data is the time series of data in time $[t,\ k\text{-}t]$. The initial state in the diagnosis at time t is $\boldsymbol{x}_{t\text{-}k}$ and the manipulated variable are $\boldsymbol{u}_{t\text{-}k},\ldots,\ \boldsymbol{u}_{t\text{-}1}$. By substituting these into the eqs. (7) and (8), the observations $\hat{y}_{t-k}(\boldsymbol{\beta})$ to $\hat{y}_{t-1}(\boldsymbol{\beta})$ are estimated. Here, the estimation error RSS(β) is calculated in eq. (9).

$$RSS(\boldsymbol{\beta}) = \sum_{m=1}^{M}\sum_{i=t-k}^{t-1}\varepsilon^m(\hat{y}_i{}^m(\boldsymbol{\beta}) - y_i{}^m(\boldsymbol{\beta})) \quad (9)$$

Here, M is the dimension number of the observation vector, ε is the weighting parameter, and *RSS* (β) shows the error between the proposed model and the measured value. By finding the optimal solution β that minimizes this function *RSS* (β), the model estimates the current defaults. The steepest descent method was used for searching for the optimal solution β (see Fig.4).

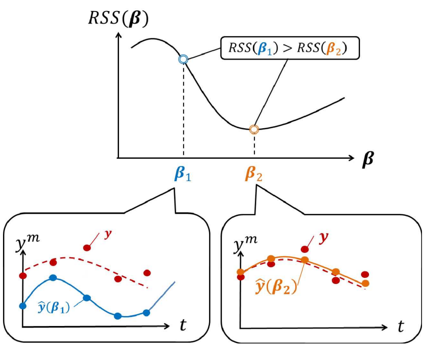

Fig.4 Parameter search by changing β.

4. Evaluation of Proposed System

4.1. *Simulation*

The simulations are carried out supposing that defaults and disturbances happen during the cursing at 0.2 m/s in forward direction as shown in Table 1.

Table 1 Simulation Condition for Observer Evaluation

ID	Time[s]	Condition	Parameters
-	0 - 5	Normal	-
1	10 - 25	Thruster 1 stop	$\gamma_1 = 1$
-	25 - 50	Normal	-
2	50 - 75	Thruster 1&3 50% down	$\gamma_1, \gamma_3 = 0.5$
3	75 - 100	All thruster 50% down	$\gamma_{1-4} = 0.5$
4	100-125	Current	μ_x=0.2

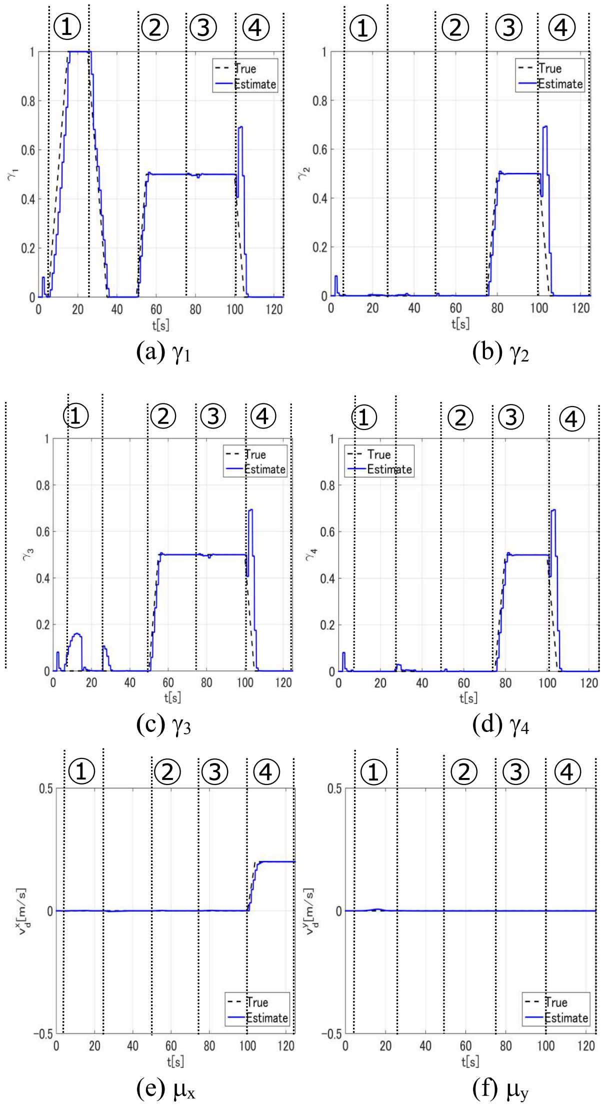

(a) γ_1 (b) γ_2 (c) γ_3 (d) γ_4 (e) μ_x (f) μ_y

Fig.5 Performance Evaluation by Simulations.

We evaluated the diagnostic performance by simulation as shown in Fig.5, assuming the case where four kinds of defaults occurred. The solid line means the estimated defaults and dot line true value. In the simulations, the observer can estimate the defaults and disturbances.

4.2. *Experiments*

We had evaluation experiments using AUV TUNA-SAND2, where the AUV is cruising at 0.2 m/s in surge direction and all thrusters outputs become half after 10 seconds passed. The evaluation results are shown in Fig.6. The estimation of reduction percentage is over-estimated than commanded values, thrusters' defaults are detected.

5. Conclusions

In this research, we proposed a model based faults detection system for diagnosis of AUV. The system is evaluated by simulations and experiments using AUV TUNA-SAND2, and the results show good performance and detect the faults.

Acknowledgement

This research is supported by JST CREST "Establishment of core technology for the preservation and regeneration of marine biodiversity and ecosystems".

References

1. Y. Junku, T. Ura , G. Bekey, Underwater robots, Springer Science & Business Media, (2012)
2. Whitcomb, Underwater robotics: Out of the research laboratory and into the field, *Proc. of IEEE/ICRA'00*, (2000)
3. Y. Nishida, T. Ura, T. Sakamaki, J. Kojima, Y. Ito , K. Kim, "Hovering Type AUV "Tuna-Sand" and Its Surveys on Smith Caldera in Izu-Ogasawara Ocean Area, *Proc. of IEEE/OCEANS2013*, (2013)
4. T. Maki, Y. Sato, T. Matsuda, R. T. Shiroku, T. Sakamaki, "AUV Tri-TON 2: An intelligent platform for detailed survey of hydrothermal vent fields," *Proc. of IEEE/AUV2014*, (2014)
5. Y. Nishida, K. Nagahashi, T. Sato, A. Bodenmann, B. Thornton, A. Asada, T. Ura, Development of an autonomous underwater vehicle for survey of cobalt-rich manganese crust, *Proc. of IEEE/OCEANS2015*, (2015)
6. Y. Nishida, T. Ura, T. Nakatani, T. Sakamaki, J. Kojima, Y. Itoh and K. Kim, Autonomous Underwater Vehicle "Tuna-Sand" for Image Observation of the Seafloor at a Low Altitude, *Journal of Robotics and Mechatronics*, Vol.26, No.4, pp.519-521, 2014M.
7. Takai, T. Ura, Development of a system to diagnose autonomous underwater vehicles, *International Journal of Systems Science*, 30(9), (1999) 981-988.
8. Y. Nishida, T. Sonoda, S. Yasukawa, J. Ahn, K. Nagano[*2], K. Ishii and T. Ura, Development of an Autonomous Underwater Vehicle with Human-aware Robot Navigation, *Proc. IEEE/OCEANS2016*, (2016) 4 pages.
9. Thor I. Fossen, *Guidance and Control of Ocean Vehicle* , John wiley & sons, (1995)

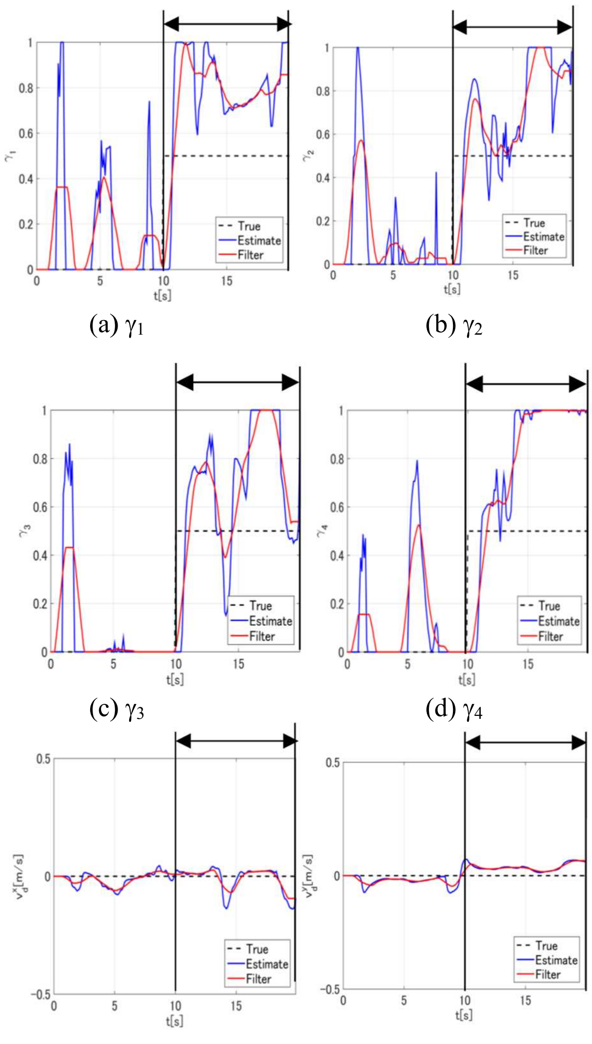

(a) γ_1 (b) γ_2

(c) γ_3 (d) γ_4

(e) μ_x (f) μ_y

Fig. 6 Evaluation Using TUNA-SAND2.

Development of Underwater Wireless Power Supply System Using Resonant Energy Transfer

Shota Hidaka
Dept. of Human Intelligence Systems, Kyushu Institute of Technology
2-4 Hibikino, Wakamatsu, Kitakyushu, Fukuoka, 808-0196, Japan

Kazuo Ishii
Dept. of Intelligence Systems, Kyushu Institute of Technology,
2-4 Hibikino, Wakamatsu-ku, Kitakyushu, Fukuoka, Japan
E-mail: ishii@brain.kyutech.ac.jp

Keisuke Watanabe
Dept. of Navigation and Ocean Engineering, Tokai University,
3-20-1 ORido Shimizuku, Shizuoka, Shizuoka, Japan
E-mail: keisukejapan@gmail.com

Abstract

Autonomous Underwater Vehicles (AUV) is one of the key technologies for deep ocean research. However AUV cannot work for long time due to the limitation of battery capacity. To solve this problem, a noncontact wireless power supply is required for AUV to conduct observations for long period. In this study, we developed a resonant energy transfer system, which is mounted into a small AUV "DaryaBird" and the simulations and evaluation tests are carried out in the test tank.

Keywords: AUV, Wireless Power Supply .

1. Introduction

Japan possesses a vast ocean area, seabed resources such as abundant energy resources and minerals have been found in the deep-sea. However, the deep-sea is one of extreme environments that human cannot access directly. Therefore, Underwater robots have attracted attention as useful tools[1-6] to observe deep-sea floor. Especially, Autonomous Underwater Vehicle (AUV) can move wide area freely not having tethered cable with support vessel. However, AUV has the disadvantage of a short operation time. In order to realize long-term operation of the AUV, a wireless battery charging system on the underwater observation station is necessary.

In the conventional electromagnetic induction system for wireless power supply, the transmission distance between power supply and receive coil should be short. Thus, AUVs are required to have highly accurate docking with the underwater stations. Ura[7] et. al developed a wireless power supply system using Electromagnetic induction system, and accomplish 3-days operation.

The purpose of this research is to perform underwater wireless power supply using magnetic resonance method. It is possible to feed in a wide range stronger than the conventional methods even if the large gap of coils and the coil center axis exit. Measurements of the transmission efficiency in the underwater environment using the magnetic field resonance method are carried out, and the changes in the transmission efficiency due to the size and position deviation of the coil are evaluated. Transmission range do the actual experiment using the AUV "DaryaBird". The comparison of electromagnetic induction method and magnetic resonance method is shown in Table 1. The advantage of electromagnetic induction method is high efficiency, however the needs accurate coil setting. The magnetic resonance method can transfer longer distance, and the disadvantage is the difficulty of the design of resonance circuit. The concept of magnetic resonance method is shown in Fig.1.

In this study, we developed a resonant energy transfer system, which is mounted into a small AUV "DaryaBird" and the simulations and evaluation tests are carried out in the test tank.

Table 1. The comparison of wireless supply methods.

	Electromagnetic Induction	Magnetic Resonance
Transfer Distance	~ 10 cm	~ 1 m
Frequency	100 kHz order	~ MHz
Efficiency	70 ~ 90 %	40~ 60 %
Size	~ 3 cm	~ 30 cm

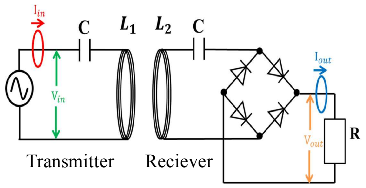

Fig. 1 The concept of magnetic resonance method.

2. Basic Property of Magnetic Resonance

As the performance evaluation experiments in the magnetic field resonance method, transmission efficiency by changing environment (air, pure water and salty water) is compared, and the result is shown in Fig. 2. In all environments, we could not find the distinguish differences.

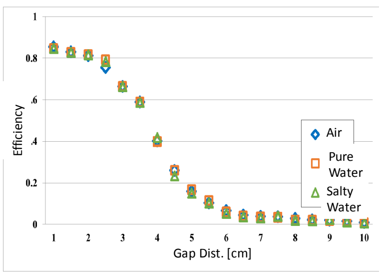

Fig.2 Comparison by Operation Environments

Next, the changes in transmission efficiency caused by winding number of the coil is evaluated. The radius of coils are 30, 40 and 50 mm, respectively (see Fig.2). The specification of each coil is in Table 2.

Table 2. The specifications of coils.

r [mm]	30	40	50
Outer Diameter [mm]	64	83	112
Winding Number	9	13	16
Inductance [μH]	38.3	51.2	78.1

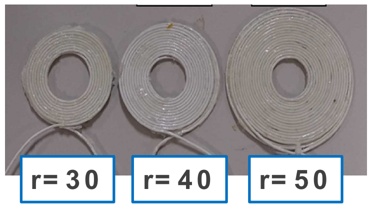

Fig.2 The coils for performance evaluation.

The results are shown in Fig. 3. The bigger coil is more efficient that small one, and small gap distance shows the better performance.

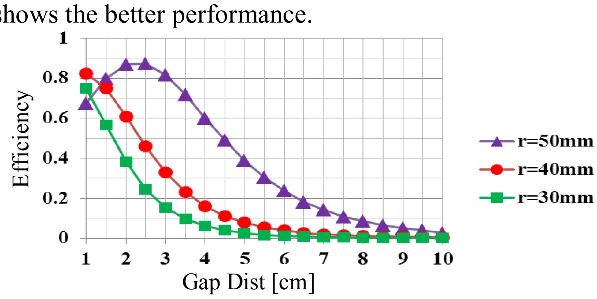

(a) Results of Simulations

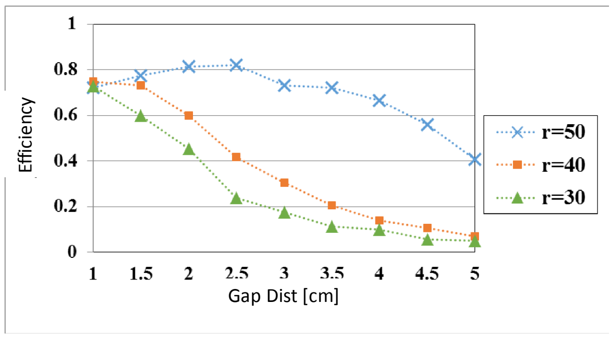

(b) Results of Experiments

Fig. 3 The comparison of efficiency by changing the size of coil and gap distance.

Then, the influence of position alignment of coils centers of transmitters and receivers are evaluated. It is shown that the big diameter coil is more robust than the small coil in center difference.

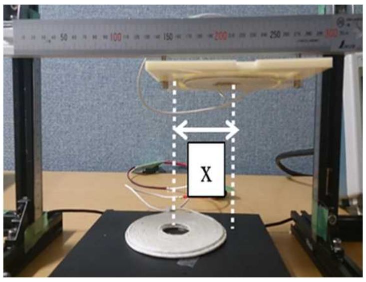

(a) Experimental setup. X is the gap of two coils.

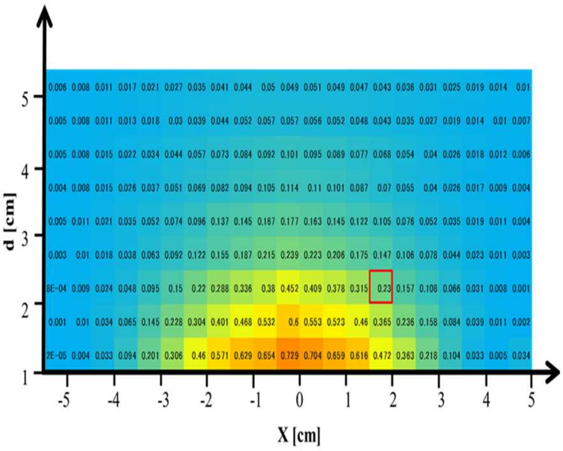

(b) Efficiency of r = 30 mm

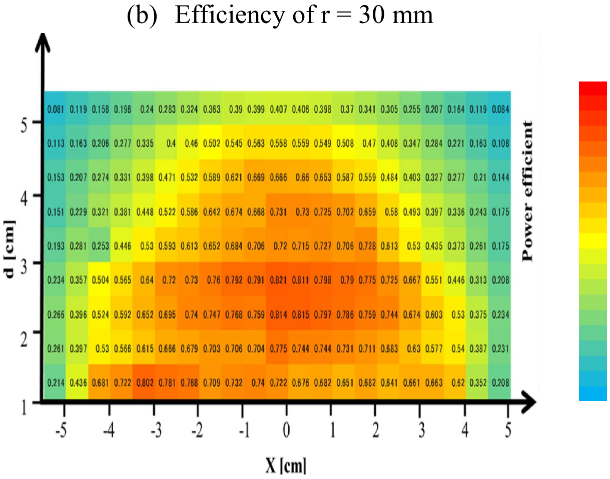

(c) Efficiency of r = 50 mm

Fig.4 The comparison by position alignment of coil centers.

3. Development of Wireless Power Transfer System for AUV

The wireless power supply system is developed under the following conditions from the specification of the target AUV.

(1) mounting position of the receiving coil is with the bottom surface of the AUV to adopt the landing system.

(2) the maximum diameter of the coil as long as it can be installed in AUV considering the axial misalignment between coils.

(3) the optimal position for maximum power transmission efficiency exits, so it is necessary to adjust the gap length between the charging station receiving coil.

Under the above conditions, the wireless power transmission system was developed, whose maximum efficiency was 81% at the time of the gap length 8.5cm. Also regarding positional displacement of the coils has resulted in power can be supplied in a range of -6cm ~ 7.5cm.

The wireless power supply system was mounted for charging experiment to AUV "DaryaBird". Figure 5 shows the block diagram of the system, and Figure 6 shows the arrangement of AUV and charging system. The voltage of the battery is monitored while charging the battery, and when the voltage comes to charging termination voltage, the system cut off the power supply automatically. The experiments were carried out with the positional gaps of coils 0 cm, 3 cm, at 6 cm, and each charging time were 40.8 min., 61 min. and 137.5 min. Figure 7 shows the results at the time of 0cm.

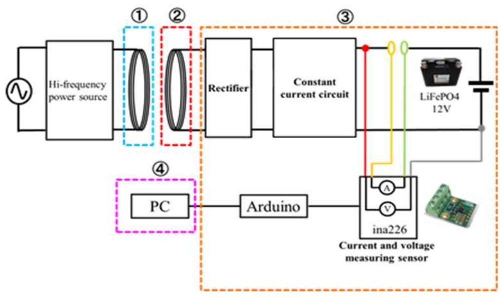

Fig. 5 The Block diagram of wireless power supply system.

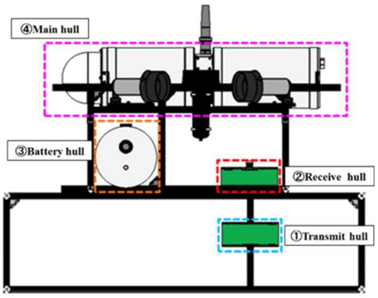

Fig. 6 The arrangement of power transmission system and AUV.

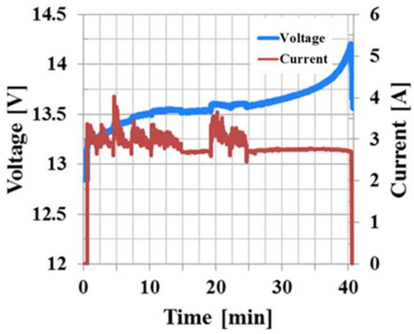

Fig. 7 The results of power supply.

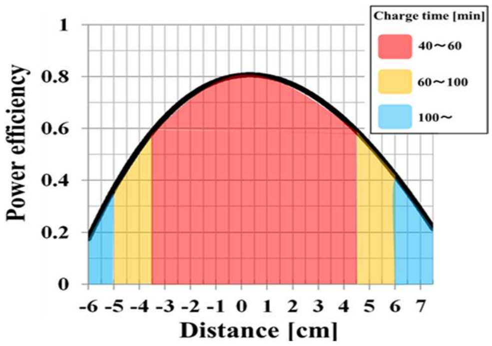

Fig. 8 The relation between charging time and gap of coils' center.

4. Conclusions

In this research, we proposed a wireless power supply system of AUV. The system is evaluated by simulations and experiments using AUV, and the results show good performance and detect the faults. Using magnetic resonance method, the chargeable range and the expected charging time of the battery in the underwater wireless power supply system created are shown in Fig.8. Assuming that the charging efficiency is more than 60% and charging time is 1 hour, the positional gap of 3.5 [cm] to 4.5 [cm] is acceptable.

References

1. Y. Junku, T. Ura , G. Bekey, *Underwater robots*, Springer Science & Business Media, (2012)
2. Whitcomb, Underwater robotics: Out of the research laboratory and into the field, *Proc. of IEEE/ICRA'00*, (2000)
3. Y. Nishida, T. Ura, T. Sakamaki, J. Kojima, Y. Ito , K. Kim, "Hovering Type AUV "Tuna-Sand" and Its Surveys on Smith Caldera in Izu-Ogasawara Ocean Area, *Proc. of IEEE/OCEANS2013*, (2013)
4. T. Maki, Y. Sato, T. Matsuda, R. T. Shiroku, T. Sakamaki, "AUV Tri-TON 2: An intelligent platform for detailed survey of hydrothermal vent fields," *Proc. of IEEE/AUV2014*, (2014)
5. Y. Nishida, K. Nagahashi, T. Sato, A. Bodenmann, B. Thornton, A. Asada, T. Ura, Development of an autonomous underwater vehicle for survey of cobalt-rich manganese crust, *Proc. of IEEE/OCEANS2015*, (2015)
6. Y. Nishida, T. Ura, T. Nakatani, T. Sakamaki, J. Kojima, Y. Itoh and K. Kim, Autonomous Underwater Vehicle "Tuna-Sand" for Image Observation of the Seafloor at a Low Altitude, *Journal of Robotics and Mechatronics*, Vol.26, No.4, pp.519-521, 2014M.
7. J. Han, A. Asada, T. Ura, Noncontact power supply for seafloor geodetic observing robot system, *J. Marine Science and Technology*, (2007) 12:183-189

Development of End-effector for Sampling-AUV “TUNA-SAND2”

Kazuo Ishii
Dept. of Intelligence Systems, Kyushu Institute of Technology,
2-4 Hibikino, Wakamatsu-ku, Kitakyushu, Fukuoka, Japan
E-mail: ishii@brain.kyutech.ac.jp

Atsushi Nishijima
Dept. of Human Intelligence Systems, Kyushu Institute of Technology
2-4 Hibikino, Wakamatsu, Kitakyushu, Fukuoka, 808-0196, Japan

Takashi Sonoda
Dept. of Intelligence Systems, Kyushu Institute of Technology,
2-4 Hibikino, Wakamatsu-ku, Kitakyushu, Fukuoka, Japan
E-mail: t-sonoda@brain.kyutech.ac.jp

Keisuke Watanabe
Dept. of Navigation and Ocean Engineering, Tokai University,
3-20-1 ORido Shimizuku, Shizuoka, Shizuoka, Japan
E-mail: keisukejapan@gmail.com

Abstract

UV requires high autonomy to accomplish various deep-ocean observation missions, and the next AUV is expected to have sampling function of marine benthos, that is, the end-effector to catch and bring back marine creatures. However, sampling is not easy task for AUV as the shape, size, motion of targets differs. One of the effective end-effectors is the slurp-gun type device to absorb the target with water.
In this research, we had developed a sampling device for deep-ocean observation and sampling AUV, Sampling-AUV TUNA-SAND2 in order to inspection of marine ecosystem.

Keywords: AUV, Sampling, End-Effector .

1. Introduction

In recent years, marine survey and development has been carried out in various fields for the purpose of mineral resources, sea floor biological sampling etc. A wide variety of organisms live in the vast ocean and it can be said that the ocean is the largest biosphere on Earth with diverse organisms ranging from microorganisms to whales and huge algae. Investigation of the deep ocean and ecosystems has big contributions for elucidation of biological diversity such as ensuring marine life, predicting ecological changes after marine resource mining, biological strains, and life history. The ocean around Japan is the one of most biodiversity area in the world, which is an irreplaceable resource of Japan.

In this research, we will develop a sampling device of underwater robot for collecting living organisms for the purpose of technical contribution to investigation of ecosystem in the deep ocean floor. In order to elucidate the diversity of marine life, biological sampling is planned using an autonomous underwater robot[1-6] (hereafter AUV). However, sampling by AUV is different from the remote-operated underwater robot (hereafter ROV), fine operation by human and marine surveys without instruction, and the collection of a precise path plan is required. Figure 1 is the histogram to show which kind methods are used for underwater sampling based on JAMSTEC database[7]. As a first step, we studied the suction type capturing method like a slurp gun, and developed a sampling device that can capture small crabs or shells, and propose the combination of slurp gun and gripper for performance evaluation.

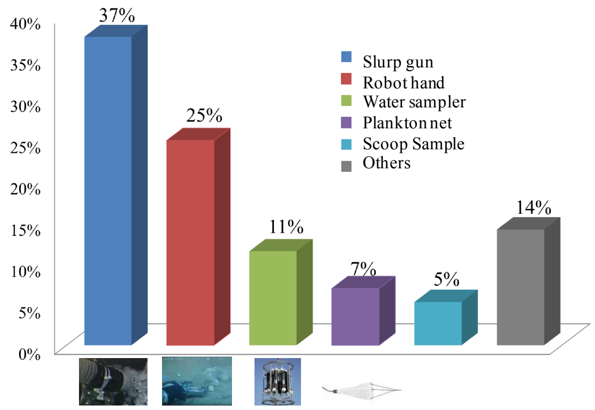

Fig. 1 Classification of sampling method based on JAMSTEC biological database[7].

2. Development of Sampling Device

2.1. *Concept of Device*

The slurp gun developed in this research is a device that brings the nozzle closer to the target object to be aspirated, sucks the sea floor organisms together with the seawater, and preserves the organisms in a storage container called a canister after collection. Figure 2 shows the prototype of Slurp gun.

One of our target benthos is Shinkaia crosnieri, which is a species of squat lobster in a monotypic genus[8] in the family Munidopsidae[9]. The target weight in water is 100g, and size is below 10 cm.

2.2. *Suction Force Evaluation*

The suction force experiment was conducted as performance evaluation of developed sampling equipment. In the experiment, it was investigated whether the target moves to the canister while leaving the nozzle tip a certain distance from the suction target. Then aspirated and up to 10cm while away the distance from the center of the nozzle for each 2cm, to measure the suction force. It was a ping-pong ball (in water weight 10 ~ 100g) as a suction target. Prototype maximum suction amount was 100g. The specifications are follows: Pump power is 90 W, the diameter of nozzle is 9.4 cm, the length of pipe is 1 m, water flow is about 350 litter/sec.

Fig.2 The slurp gun prototype for performance

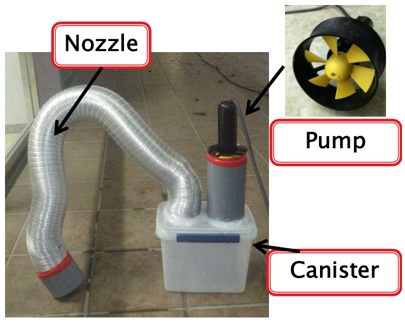

evaluation.

The experimental variables are shown in Fig. 3, and the experimental result is in Fig. 4.

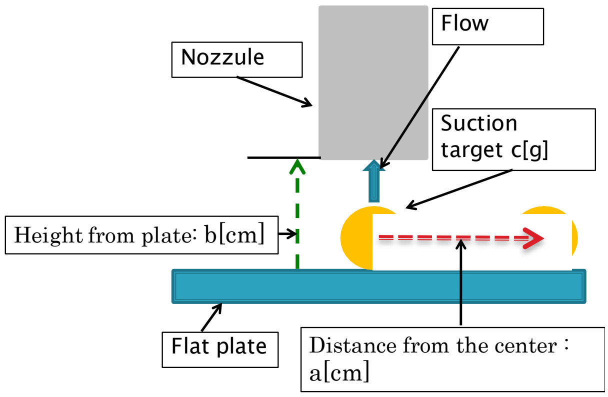

Fig.3 Experimental condition and parameters.

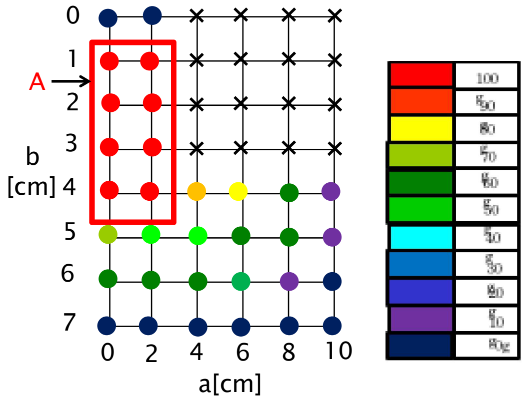

Fig.4 Results of suction force evaluations.

2.3. *Slurp gun with Gripper*

Biological capture around the nozzle is important to improve the capture rate of organisms. Therefore, we developed a suction gripper that attracts organisms around the nozzle into the nozzle diameter. Also, it was placed streamlined to suppress the fluid resistance portions attract. Fig. 5 shows the state of the opening and closing of the gripper in, Fig.6 shows the combination of slurp gun and gripper.

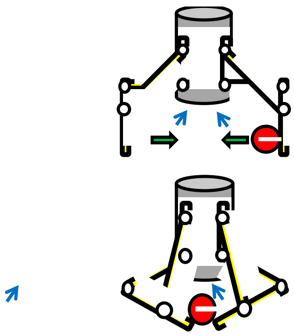

Fig. 5 The concept of the gripper.

Fig.6 The combination of slurp gun and gripper.

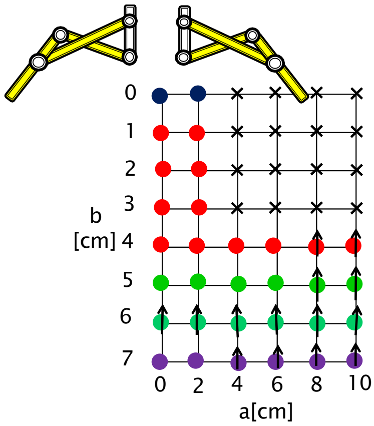

Fig.7 Results of suction force evaluations with slurp gun and gripper.

The combination of slurp gun and gripper has been successful in suction pulls the suction target of 100g at a distance of a=10 cm from the center of the nozzle, which could not be suction with only slurp gun. The developed end-effector is shown in Fig. 8.

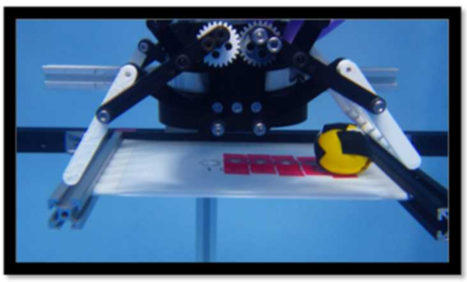

Fig. 8 The developed end-effector.

3. Conclusions

In this research, we developed the sampling device for seabed biological sampling and evaluated its performance. It is assumed that the undersea organism is assumed to be close to the neutral buoyancy, therefore the developed end-effector has sufficient suction power for undersea biological collection. Aspiration around the nozzle which was difficult with conventional slap gun was also possible by attaching gripper. As a result, capture of living organisms is improved and harvesting is expected.

Acknowledgement

This research is supported by JST CREST "Establishment of core technology for the preservation and regeneration of marine biodiversity and ecosystems".

References

1. Y. Junku, T. Ura , G. Bekey, Underwater robots, Springer Science & Business Media, (2012)
2. Whitcomb, Underwater robotics: Out of the research laboratory and into the field, *Proc. of IEEE/ICRA'00*, (2000)
3. Y. Nishida, T. Ura, T. Sakamaki, J. Kojima, Y. Ito , K. Kim, "Hovering Type AUV "Tuna-Sand" and Its Surveys on Smith Caldera in Izu-Ogasawara Ocean Area, *Proc. of IEEE/OCEANS2013*, (2013)
4. T. Maki, Y. Sato, T. Matsuda, R. T. Shiroku, T. Sakamaki, "AUV Tri-TON 2: An intelligent platform for detailed survey of hydrothermal vent fields," *Proc. of IEEE/AUV2014*, (2014)
5. Y. Nishida, K. Nagahashi, T. Sato, A. Bodenmann, B. Thornton, A. Asada, T. Ura, Development of an autonomous underwater vehicle for survey of cobalt-rich manganese crust, *Proc. of IEEE/OCEANS2015*, (2015)
6. Y. Nishida, T. Ura, T. Nakatani, T. Sakamaki, J. Kojima, Y. Itoh and K. Kim, Autonomous Underwater Vehicle "Tuna-Sand" for Image Observation of the Seafloor at a Low Altitude, *Journal of Robotics and Mechatronics*, Vol.26, No.4, pp.519-521, 2014.
7. http://www.jamstec.go.jp/e/database/
8. K. Baba, E. Macpherson, G. C. B. Poore, Shane T. A., A. Bermudez, Patricia C., Chia-Wei Lin, M Nizinski, Celso Rodrigues and K. E. Schnabel, *Catalogue of squat lobsters of the world* (Crustacea: Decapoda: Anomura – families Chirostylidae, Galatheidae and Kiwaidae) Zootaxa. 1905: (2008),1–220.
9. S. T. Ahyong, K. Baba, E. Macpherson & Gary C. B. Poore, *A new classification of the Galatheoidea* (Crustacea: Decapoda: Anomura), Zootaxa. (2010), 2676: 57–68

Development of a Tool for Extended Place/transition Net-Based Mutation Testing

Tomohiko Takagi
Faculty of Engineering, Kagawa University
2217-20 Hayashi-cho, Takamatsu-shi, Kagawa 761-0396, Japan

Shogo Morimoto
Faculty of Engineering, Kagawa University
2217-20 Hayashi-cho, Takamatsu-shi, Kagawa 761-0396, Japan

Tetsuro Katayama
Faculty of Engineering, University of Miyazaki
1-1 Gakuen-kibanadai nishi, Miyazaki-shi, Miyazaki 889-2192, Japan
E-mail: takagi@eng.kagawa-u.ac.jp, s13t270@stmail.eng.kagawa-u.ac.jp, kat@cs.miyazaki-u.ac.jp

Abstract

This paper shows a tool for EPN (Extended Place/transition Net)-based mutation testing to evaluate and improve the quality of a test suite for concurrent software. The tool includes functions for (1) construction of an original EPN that represents the expected behavior of concurrent software under test, (2) construction of mutant EPNs by applying mutation operators to the original EPN, (3) execution of a test suite on each mutant EPN in order to calculate its mutation score, and so on.

Keywords: Software Testing, Mutation Testing, Model-Based Testing, Vienna Development Method

1. Introduction

The techniques to create a test suite (a set of test cases) based on formal models that represent specifications of SUT (Software Under Test) is called MBT (Model-Based Testing),[1] and they can be introduced into a software testing process in order to systematically evaluate and improve the reliability of large SUT. The effects of MBT depend on the quality of a test suite, that is, the capacity of a test suite to find possible failures in SUT. MBMT (Model-Based Mutation Testing) was proposed as a technique to evaluate and improve the quality of a test suite of MBT.

In MBMT, mutant models are created by inserting an intentional failure into a formal model of SUT, and then the ratio of killed mutant models (that is, mutant models whose failures have been found by a test suite) is calculated to evaluate the quality of the test suite. The ratio is called a mutation score, and it can be improved by modifying the test suite based on mutant models that have not been killed.

For example, some studies showed MBMT using directed graphs or automata as their formal model.[2] On the other hand, we have been discussing PNBMT (PN-Based Mutation Testing), that is, MBMT using a PN (Place/transition Net) that can represent concurrent behavior of SUT.[3-5] However, a PN cannot represent actions (data processing that should be executed with state transitions of SUT) and guards (conditions to get transitions fireable). The actions and guards play an important part especially when MBMT (also MBT) is applied to SUT including complex data processing.

In this paper, we propose an EPN (Extended Place/transition Net), that is, a PN that is extended by introducing VDM++ (a formal specification description language for VDM (Vienna Development Method))[6] in order to define actions and guards, and then, we show a tool that we have been developing to support EPNBMT (EPN-Based Mutation Testing). The tool is supposed to be used by test engineers. This study is based on the idea that the effectiveness of PNBMT will be improved by achieving (a) the higher representation power of a PN by actions and guards, and (b) the semi-automation by our tool.

The rest of this paper is organized as follows. In section 2, we propose an EPN. Section 3 shows the principal functions of our tool according to the procedure of EPNBMT. Section 4 gives a conclusion and future work.

2. EPN (Extended Place/transition Net)

In this section, we propose an EPN, that is, a PN that is extended by introducing VDM++ (a formal specification description language for VDM) in order to define actions and guards.

An EPN consists of a PN and VDM specifications. The PN is a traditional formal model suitable for representing expected state transitions of SUT including concurrent behavior. It consists of places to represent the states of components of SUT, transitions and arcs to represent the change of states of SUT, and tokens to represent current states or resources of the components. The VDM specifications are a set of VDM++ codes to represent actions and guards that are given to transitions of the PN if necessary. The actions can represent data processing that should be executed with state transitions of SUT, and the guards can represent conditions to get transitions fireable.

In an EPN, a state of SUT corresponds to a set that consists of a marking (that is, a distribution of tokens on a PN) and values of instance variables (that is, variables that are defined in VDM specifications and are used in actions and guards), and a state transition of SUT corresponds to the change of a marking and values of instance variables that results from the firing of a transition of a PN.

A simple example of an EPN is shown in Fig. 1. The initial marking of the EPN is expressed as [0,1,1,0], since the numbers of tokens in the places p_1, p_2, p_3, p_4 are 0, 1, 1, 0, respectively. Also, the instance variable v is initialized to 0, and therefore the initial state of the EPN

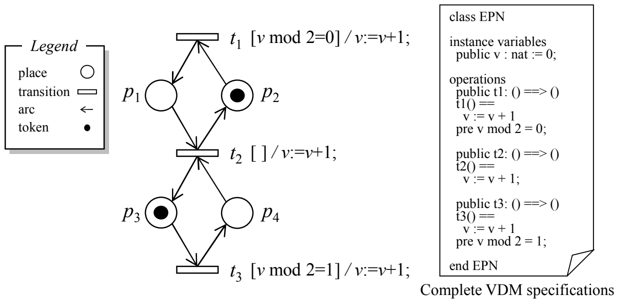

Fig. 1. Simple example of an EPN (initial state).

is expressed as {[0,1,1,0], v=0}. The action "v:=v+1;" is attached to the transitions t_1, t_2, t_3, and it is executed by the firing of each transition. Additionally, the guards "v mod 2=0" and "v mod 2=1" are attached to t_1 and t_3, respectively. t_1 and t_3 can be fired, when there are tokens for their ingoing arcs and their guards are satisfied. For example, only t_1 is fireable in the initial state of the EPN of Fig. 1.

3. Tool for EPNBMT (Extended Place/transition Net-Based Mutation Testing)

This section shows the functions of the tool that we have been developing to support EPNBMT, according to the procedure of EPNBMT. The functions (the procedure) consist of (1) construction of an original EPN, (2) construction of mutant EPNs, (3) conversion of a test suite, and (4) execution of a test suite.

3.1. *Construction of an original EPN*

First, test engineers need to construct an original EPN based on specifications of SUT. The original EPN is an EPN that represents the expected behavior of SUT; it is called "original" in order to distinguish it from mutant EPNs that will be constructed on the next step. The EPN has been discussed in the previous section.

Our tool provides the function to construct an original EPN. Fig. 2 gives the screen image in the execution of the function. The GUI (Graphical User Interface) for the function consists of (A) a pane to edit a PN and (B) a pane to edit VDM specifications for actions and guards. Additionally, (B) consists of five code editors to edit values, types, instance variables, operations, and functions of the VDM specifications, and one of them can

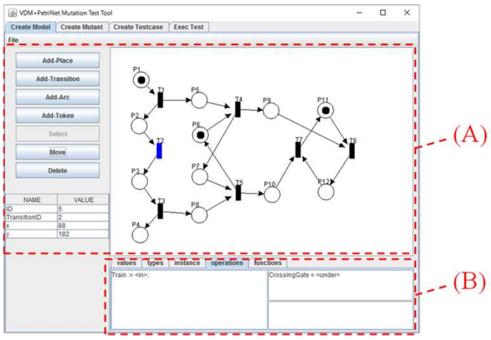

Fig. 2. Screen image of the tool in constructing an original EPN.

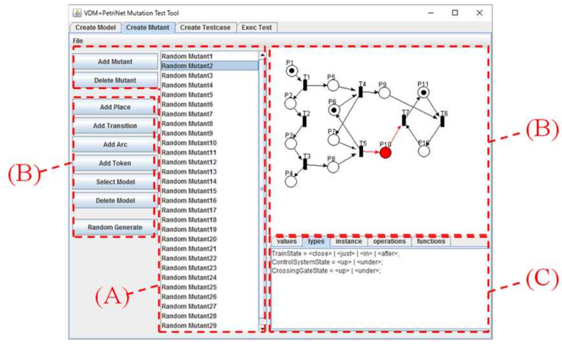

Fig. 3. Screen image of the tool in constructing mutant EPNs.

be selected by a tab. Test engineers can define not only the PN of an original EPN but also the actions and guards of an original EPN.

3.2. *Construction of mutant EPNs*

After completing constructing an original EPN, test engineers need to construct mutant EPNs. The mutant EPN is an EPN that intentional failure(s) has been inserted into by the use of mutation operators. In this study, the following mutation operators are supposed to be utilized.

- Model-based mutation operators: the addition and deletion of an element of a PN (that is, a place, a transition, an arc, or a token) can be performed in order to insert an intentional failure. They were proposed in our previous study.[3]
- Code-based mutation operators: the grammar of VDM++ is somewhat similar to those of general procedural programming languages. Therefore, in order to insert an intentional failure, traditional code-based mutation operators (for example, replacement of operators, variables, and constants) can be applied to actions and guards that have been implemented as VDM specifications.

Our tool provides the function to construct mutant EPNs. Fig. 3 shows the screen image in the execution of the function. The GUI for the function consists of (A) a list of mutant EPNs that have been constructed, (B) a pane to edit a PN of a mutant EPN by the use of model-based mutation operators, and (C) a pane to edit VDM specifications for actions and guards by the use of code-based mutation operators.

(A) enables test engineers to select one of existing mutant EPNs and show it on (B) and (C). Additionally, it enables to add and remove a mutant EPN. (B) highlights a part that a mutation operator has been applied to in order that test engineers can easily confirm a result of application of a mutation operator. (B) also gives test engineers the way of manual and automatic construction of a mutant EPN. When performing manual construction, test engineers select a model-based mutation operator from the menu, and then specify a part of a PN that it should be applied to. When executing automatic construction, a model-based mutation operator is randomly selected, and then a part that it will be applied to is randomly determined by our tool. (C) consists of five code editors to edit values, types, instance variables, operations, and functions of VDM specifications, and one of them can be selected by a tab. These code editors enable test engineers to manually apply a code-based mutation operator.

3.3. *Conversion of a test suite*

After the construction of an original EPN, a test suite to be evaluated needs to be converted to execution paths (that is, sequences of successive markings, transitions, and values of instance variables) on the original EPN. It is a preparation for automatic execution of the test suite in the next step. Our EPNBMT accepts an arbitrary format and design technique of the test suite.

Our tool provides the function to manually convert an arbitrary test suite to execution paths on an original EPN. Fig. 4 shows the screen image in the execution of the function. The GUI for the function consists of (A) a list of test cases that a test suite consists of, (B) a list to edit

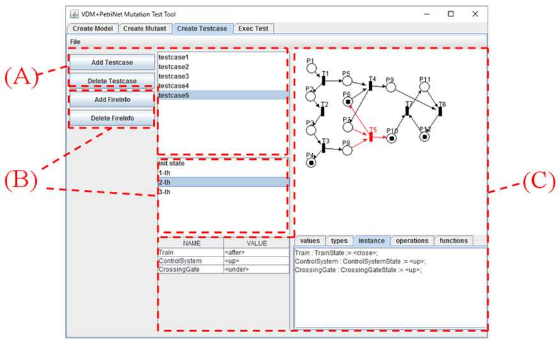

Fig. 4. Screen image of the tool in converting a test suite.

transitions of a test case selected on (A), and (C) a pane to show an original EPN and edit a test case.

(A) enables test engineers to select one of existing (already converted) test cases and show its execution path representation on (B) and (C). (C) highlights a transition that is selected on (B), and shows a marking and values of instance variables just after the firing of the transition. Additionally, (A) enables to add and remove a test case. When adding a test case (converting a test case and entering it into our tool), test engineers input required information (successive markings, transitions, and values of instance variables) via (B) and (C). (B) enables to add and remove a transition of a test case selected on (A). When a new transition is added, (C) can highlight fireable transitions based on a current marking and values of instance variables, and then selecting a highlighted transition brings the automatic updating of the current marking and values of instance variables, which will save test engineers' labor.

3.4. *Execution of a test suite*

Finally, test engineers need to apply the converted test suite to all of the constructed mutant EPNs, and then calculate a mutation score as the ratio of killed mutant EPNs to all of the constructed mutant EPNs. If the mutation score is not good, the test suite can be improved based on mutant EPNs that have not been killed.

Our tool provides the function to execute a test suite. Fig. 5 shows the screen image in the execution of the function. The GUI for the function consists of (A) a control panel to start executing a test suite, (B) a list of mutant EPNs with the results of testing, (C) a list of test cases with the results of their application to a mutant EPN selected on

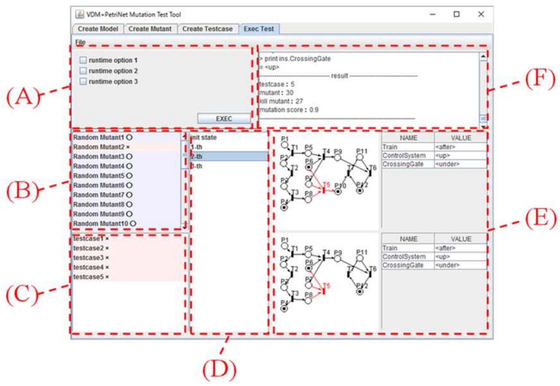

Fig. 5. Screen image of the tool in executing a test suite.

(B), (D) a list of transitions of a test case selected on (C), (E) a pane to show markings and values of instance variables of an original EPN (the upper part) and the selected mutant EPN (the lower part) just after the firing of the selected transition in the selected test case, and (F) a pane to show a detailed log of test suite execution, including a mutation score. (B)-(F) enable test engineers to easily confirm the result of test suite execution invoked by (A).

Each test case is executed as follows:

- (i) A mutant EPN is initialized based on an initial marking and initial values of instance variables of a test case.
- (ii) In the mutant EPN, transitions are fired from the top of the test case. Each of firings is performed by the following (a)-(c).
  - (a) The pre-conditions to fire a transition, that is, the existence of tokens for ingoing arcs of the transition, and the guard of the transition are checked. When they are not satisfied, it is found that the mutant EPN is killed by the test case.
  - (b) The transition is fired, and the action attached to the transition is executed. As a result, a current marking and values of instance variables are updated.
  - (c) If the transition includes post-conditions, and they are not satisfied, it is found that the mutant EPN is killed by the test case.
- (iii) When the firing of the final transition of the test case has been completed, the test result (that is, a final marking and values of instance variables in the mutant EPN) is compared with the expected result

included in the test case (that is, a final marking and values of instance variables in the original EPN). If there are differences between the test result and the expected result, it is found that the mutant EPN is killed by the test case.

4. Conclusion and Future Work

This paper has shown a tool for EPNBMT (Extended Place/transition Net-Based Mutation Testing) to evaluate and improve the quality of a test suite for software including concurrent behavior. The EPN proposed in this paper is a PN extended by introducing a formal specification description language for VDM, in order to represent actions and guards. The tool consists of the following four functions: (1) an original EPN can be created to define the expected behavior of SUT, (2) mutant EPNs including intended failures can be created by applying mutation operators to the original EPN, (3) an arbitrary test suite to be evaluated can be converted to execution paths on the original EPN, and (4) a mutation score can be calculated by applying the converted test suite to all the mutant EPNs. If the mutation score is not good, the test suite can be improved based on mutant EPNs that have not been killed.

In the tool, model-based mutation operators are automatically applicable, but code-based mutation operators are only for manual application. The latter will be automated in order to save test engineers' labor in our future work. Additionally, if the tool can generate mutant EPNs intensively including failures that are possible in operational environments, a degree of precision of a mutation score would be improved. Thus we will plan to develop the techniques for modeling of actual failures and for strategical application of mutation operators based on the model.

Another approach to improve the degree of precision of a mutation score is to utilize fault-proneness information that can be derived from software metrics, in order to adjust a mutation score. In the previous study, we proposed a technique in which the weights based on fault-proneness information and usage distributions are given to a PN in order to calculate an adjusted mutation score[5]. Extending this technique for EPNs is also included in our future work.

Acknowledgements

This work was supported by JSPS KAKENHI Grant Number 26730038.

References

1. M. Utting, A. Pretschner, and B. Legeard, A taxonomy of model-based testing approaches, *Software Testing, Verification and Reliability*, Vol.22 (2012), pp.297-312.
2. F. Belli, C.J. Budnik, E. Wong, Basic Operations for Generating Behavioral Mutants, in *Proc. 2nd Workshop on Mutation Analysis in conjunction with ISSRE'06* (Nov. 2006), pp.9.
3. T. Takagi, R. Takata, Z. Furukawa, F. Belli, M. Beyazıt, Metrics for Model-Based Mutation Testing Based on Place/Transition Nets, in *Proc. of Joint Conf. of 21st Int. Workshop on Software Measurement and 6th Int. Conf. on Software Process and Product Measurement (IWSM-MENSURA)* (Nov. 2011), pp.7-10.
4. T. Takagi, T. Arao, "Overview of a Place/Transition Net-Based Mutation Testing Framework to Obtain Test Cases Effective for Concurrent Software", in *Proc. of 16th Int. Conf. on Software Engineering, Artificial Intelligence, Networking and Parallel/Distributed Computing* (June 2015), 3 pages.
5. T. Takagi, T. Teramoto, Extended Mutation Score Based on Weighted Place/Transition Nets to Evaluate Test Suites, in *Proc. of 15th Int. Conf. on Computer and Information Science (ICIS)* (June 2016), pp.959-961.
6. J. Fitzgerald, P.G. Larsen, P. Mukherjee, N. Plat, M. Verhoef, *Validated Designs for Object-Oriented Systems*, (Springer-Verlag London, 2005).

Improvement of Decision Table Automatic Generation Tool VDTable for let in Statement

Yinuo Huang*, Teturou Katayama* Yoshihiro Kita†,
Hisaaki Yamaba*, and Naonobu Okazaki*
University of Miyazaki, 1-1 Gakuen-kibanadai nishi, Miyazaki, 889-2192 Japan
†Tokyo Institute of Technology, 1404-1 katakura, Hachioji, 192-0914 Japan
E-mail: kouitsudaku@earth.cs.miyazaki-u.ac.jp, kat@cs.miyazaki-u.ac.jp,
kitayshr@stf.teu.ac.jp, yamaba@cs.miyazaki-u.ac.jp, oka@cs.miyazaki-u.ac.jp

Abstract

This research has expanded the applicable range of VDTable. VDTable is a tool of decision table automatic generation tool using VDM++ specification which is the lightweight formal methods VDM. We have improved VDTable to be able to correspond to let in statement, which is one of the VDM++ syntax, that the existing VDTable doesn't support. We applied an application example to improved VDTable. From the result of the application example, the applicable range of VDTable has been expanded.

Keywords: VDM++, automatic generation, decision table, formal specification, VDTable, let in statement.

1. Introduction

Formal methods[1], in software development, is one of the means to describe the specification strictly. On the other hand, the decision table[2] is one of the testing techniques to exhaustively represent the logical combination included in software. But, for generating a decision table, it is necessary to understand the description content of the target system or specification. In extracting conditions and actions manually from specifications, it takes time and errors are prone to occur.

Therefore, our laboratory developed a VDTable[3] (VDM Decision Table) to reduce this labor and time. VDTable can automatically generate the decision table, from the specification written in specification description language VDM++ (VDM++ specification). But, the VDTable, since many VDM++ syntax is not corresponded, its usefulness is limited.

To improve the usefulness, this paper expands VDTable. Specifically, VDTable is improved to be able to correspond to let in statement, which is one of the VDM++ syntax, that the existing VDTable does not support.

2. Introduction of existing VDTable

The flow of processing of VDTable is shown in Fig.1. VDTable consists of three parts: Parser, Converter, and DT-Generator.

Parser uses VDMJ[4] to parse the VDM++ specification and outputs a parsing data. The parsing data has an abstract syntax tree. The abstract syntax tree holds analysis information such as the definition block type, argument, definition name and expression for each class definition. The parsing data to be used as input in the Converter.

Converter converts the parsing data outputted by Parser into internal expression data for analysis in order to facilitate extraction of conditions and actions and creation of truth values, which are necessary in generating a decision table. The internal expression data

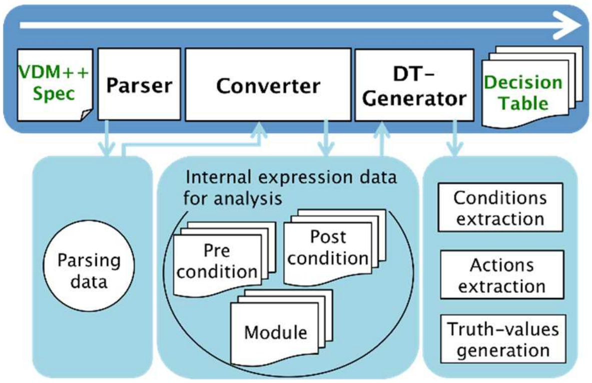

Fig. 1. Process flow of VDTable

for analysis is data obtained by dividing the parsing data in module units and expressing the expression of the definition main for each token as the minimum unit of the syntax.

DT-Generator defines extraction rules of conditions and actions. Firstly, it extracts conditions and actions, when its matching the condition extraction pattern or actions extraction pattern from the analysis internal expression data, and extracts String type array (condition array and action array), respectively. Next, DT-Generator stores conditions and actions in an array of String type. DT-Generator makes CA-Table (Condition Action Table), when DT-Generator extracts conditions and actions. CA-Table is a table which is correspondence of conditions and actions. CA-Table is three columns of condition index, token and action index. And then, DT-Generator generates truth-values based on this CA-Table. Finally, DT-Generator generates a decision table from the created condition and action, and the truth-values of the condition and action.

3. Improvement of VDTable

To correspond to let in statement, we extend Converter and DT-Generator. Specifically, we conduct the following three items.

- Proposal of data conversion rules for converting parsing data of let in statement to internal expression data for analysis
- Proposal of condition extraction rules and action extraction rules of let in statement

Table 1. Condition extraction rules and action extraction rules of let in statement.

Condition extraction pattern	Action extraction pattern
Let condition 1 in condition 2	Name action

Table 2. Example of creating a String type two-dimensional array that stores truth-values

Condition 1	-	-
Condition 2	-	-
Action	-	-

- Proposal of truth table generation rules of let in statement

3.1. *Proposal of data conversion rules for converting parsing data of let in statement to internal expression data for analysis*

To parse let in statement, we use the Parser of the existing VDTable as it is. In VDTable, Converter converts parsing data of let in statement into internal expression data for analysis. In order to realize this, we propose data conversion rules of let in statement.

- In the data conversion of let in statement, when matching the token "let" from the parsing data, three items of "from immediately after ‘let’ to before ‘in’", "in", "immediately after ‘in’ to the last" are extracted.
- The part of name is extracted as one item.

These are saved as String type as internal expression data for analysis of let in statement.

3.2. *Proposal of condition extraction rules and action extraction rules of let in statement*

We propose condition extraction rules and action extraction rules of let in statement. Table 1 shows the condition extraction rules and action extraction rules of let in statement proposed in this paper. In the internal expression data for analysis, let the line above "in" be the condition 1, the line next to "in" be the condition 2, and let it be the condition extraction pattern. Also, the part after "name" is taken as the action extraction pattern.

```
class MyersTriangle

 functions
 public triangle : int * int * int -> bool
      triangle(A,B,C) ==
           let perimeter = A+B+C in
           perimeter>(2*A) and  perimeter>(2*B) and perimeter>(2*C);

 public Shape_judgment: int*int*int -> seq of char
      Shape_judgment(A,B,C) ==
          if triangle(A,B,C) then
            if(A=B and B=C) then
                        "equilateral triangle and isosceles triangle"
              elseif (A=B or B=C or C=A) then
                        "isosceles triangle"
              else
                        "scalene triangle"
         else
                 "Non-triangular"

end MyersTriangle
```

Fig. 2. Specification of shape judgment of the triangle

```
access#public
location#in 'C:\Users\kat\Desktop\triangle.vpp' at line 4:9
name#triangle
scope#GLOBAL
pass#DEFS
type#(int * int * int -> bool)
kind#explicit function
body#public triangle: (int * int * int -> bool)
        triangle(A, B, C) ==
let perimeter = ((A + B) + C) in ((perimeter > (2 * A)) and ((peri
meter > (2 * B)) and (perimeter > (2 * C))))
```

Fig. 3. Specification parsing data of shape judgment of the triangle

3.3. *Proposal of truth table generation rules of let in statement*

We propose truth table generation rules of let in statement. The proposed the values of the truth table generation method is as follows.

(1) “Generate an array that stores the values of the truth table”
(2) “Extract conditions”
(3) “Extract actions”
(4) “Store truth values in the array”

First, in order to store the values of the truth table, a two-dimensional array of String type is prepared. Describe the conditions and actions in the elements of vertical first column, and describe the truth-values information in the horizontal element. An example of creating an array is shown in Table 2.

Next, DT-Generator extracts each condition according to the condition extraction rules. Then, DT-Generator extract actions according to the action extraction rules.

Finally, DT-Generator store the values of the truth value. In the proposed the truth table generation rules, it is assumed that when let in statement is described as "let condition 1 in condition 2", "if condition 1 and condition 2 are true (stores" Y "), the action is established (stores" X ")", " when Condition 1 is true (stores" Y "), condition 2 is false (stores" N "), action is not established (stores" -"). The reason is the movement of let in statement in the VDM specification is such that the condition 1 part is assigned to the condition 2. So, for condition 2, the condition 1 is always true. Therefore, when generating the truth table of let in statement, it is assumed that the condition 1 is always true, and when the condition 2 is true or false, the operation is determined or established.

The DT-Generator generates a decision table based on the extracted conditions and actions, and the truth values of the generated conditions and actions.

4. Application Example

The specification used for an application example is the specification described using VDM ++ for triangle shape determination, and it is determine whether triangle by using let in statement. The specifications of shape judgment of the triangle is shown in Fig. 2. The result of parsing this specification with Parser is shown in Fig. 3.

Fig. 4 shows the result of converting the content of let in statement in the specification from the syntax analysis data in Fig. 3 to the analysis internal expression data. Condition 1 and condition 2, and contents of let in statement including action are saved as String type. It is understood that let in statement is correctly converted to the internal expression data for analysis.

Fig. 5 shows the result of applying the VDM++ specification of the application example to the improved VDTable. From the decision table of Fig. 5, it can be seen from Fig. 4 that the line before the token "in" is correctly extracted as condition 1 and the line following "in" as condition 2. Also, from Fig. 5, it can be seen that the portion after "name" is correctly extracted as an operation. Finally, from the truth table of the decision table of Fig. 5, when the decision table shows the condition 1 and the condition 2 are true (stores "Y"), the action is established

```
perimeter = ((A + B) + C)
in
((perimeter > (2 * A)) and ((perimeter > (2 * B))
and (perimeter > (2 * C))))
name triangle
```

Fig. 4. Analysis internal representation data of the of shape judgment of the triangle

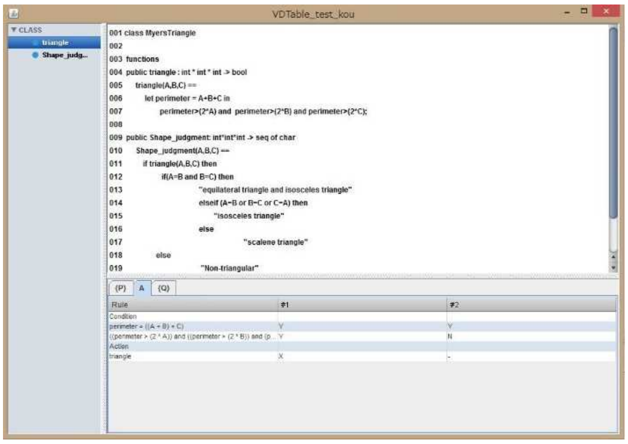

Fig. 5. The result of applying the specification to VDTable

(stores "X"), When the condition 1 is true (stores "Y"), when the condition 2 is false (stores "N"), the action is not established (stores "-"). Hence, it is understood that the truth table is correctly generated.

5. Related work

Currently, there are few cases where test design was done from formal specifications. CEGTest[5] is available as a tool to support the generation of decision tables. CEGTest automatically generates a decision table from the cause result graph created by the user. So the user must make a cause effect graph created, manually. For this reason, when creating a decision table it is troublesome and time-consuming to understand the contents and to extract conditions and actions, and input errors are likely to occur.

In contrast, VDTable can automatically get a decision table from a formal specification inputted by a user.

6. Conclusion

In this research, VDTable has been improved for the purpose of expanding the application range of VDTable, an automatic generation tool for decision tables using the VDM++ specification. Specifically, we propose data conversion rules of let in statement, propose a condition extraction rules and action extraction rules of let in statement, and propose truth table generation rules of let in statement.

We confirmed that the improved VDTable is applied to the triangle judgment VDM ++ specification including a let in statement to correctly generate the decision table. From the above, it can be said that the application range of the VDTable improved in this paper has expanded, and its practicality has improved.

Future issues are as follows.

- Extension of scope
- Dealing with compound conditional expressions
- Improvement of readability
- Correspondence to functions including multiple syntax

Acknowledgements

This work was supported by JSPS KAKENHI Grant Number 24220001

References

1. John Fitzgerald, Peter Gorm Larsen, Paul Mukherjee, Nico Plat, Marcel Verhoef, Validated Designs for Object-Oriented Systems, Springer (2005).
2. ISO 5806, Specification of single-hit decision tables.
3. Kenta Nishikawa, Tetsuro Katayama, Yoshihiro Kita, Hisaaki Yamaba and Naonobu Okazaki, Proposal of a Supporting Method to Generate a Decision Table from the Formal Specification, *International Conference on Artificial Life and Robotics*, 222-225(2014).
4. VDMJ. http://sourceforge.net/projects/vdmj/ (accessed November 30, 2016).
5. CEGTest, http://softest.jp/tools/CEGTest/ (accessed November 30, 2016).

Prototype of Test Cases Automatic Generation Tool BWDM Based on Boundary Value Analysis with VDM++

Hiroki Tachiyama*, Tetsuro Katayama* Yoshihiro Kita†,
Hisaaki Yamaba*, and Naonobu Okazaki*
**University of Miyazaki, 1-1 Gakuen-kibanadai nishi, Miyazaki, 889-2192 Japan*
†Tokyo University of Technology, 1404-1 Katakura, Hachioji, 192-0914 Japan
E-mail: tachiyama@earth.cs.miyazaki-u.ac.jp, kat@cs.miyazaki-u.ac.jp,
kitayshr@stf.teu.ac.jp, yamaba@cs.miyazaki-u.ac.jp, oka@cs.miyazaki-u.ac.jp

Abstract

For software development using Formal Methods, we have developed a prototype of the boundary value test case automatic generation tool BWDM. The main two topics of our tool are (1) automatically generation of test cases and (2) boundary value analysis. Our tool improves the efficiency of software testing process in using VDM++ that is one of the Formal Methods. In this research, we show the composition of our tool, application example, evaluation of the usefulness, relative research, and future issues.

Keywords: Software Testing, Boundary Value Analysis, Formal Methods, VDM++

1. Introduction

A cause of coming into bugs in software is using natural languages in process of software design. Natural languages are ambiguous. And this causes misunderstanding of a programmer in designing documents. Finally, he implements software based on the misunderstanding, and the software will have bugs.

As one method to solve this problem, Formal Methods are suggested that used in upstream process of software development. In developing process of using formal methods, specification is described what characteristic of development target, by using not natural languages but formal specification languages what based on mathematical logic. For that reason, unlike conventional development, specification can be proved its correctness of description contents by arithmetical theorem proofs, mechanical inspection, etc. In other words, it is possible to write strict specification document which is excluded ambiguous description.

On the other hand, either way designed using natural languages or formal specification languages, it needs software testing after implementation of software. In order to test software, it is necessary to design test cases, but it takes much time and effort to design them manually. Therefore, by efficiently designing test cases, it is possible to improve the efficiency of the testing process. It is also important to design test cases focused on places where bugs can be hidden, in order to improve the efficiency of executing of software testing.

Therefore, in this research, we develop a prototype of test case automatic generation tool BWDM (Boundary Value/Vienna Development Method) for the purpose of improving the efficiency of the test process in software development using formal methods. We use Boundary Value Analysis[1] for test cases designing. We use the "boundary value test case" what means the test case designed based on boundary value analysis.

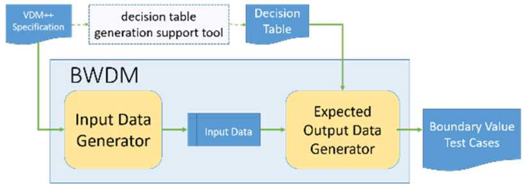

Fig. 1. The flow of BWDM processing

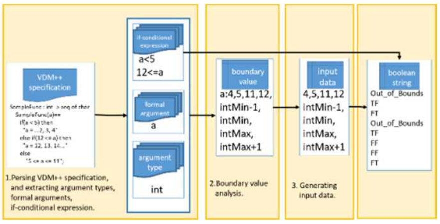

Fig. 2. The flow of input data generator processing

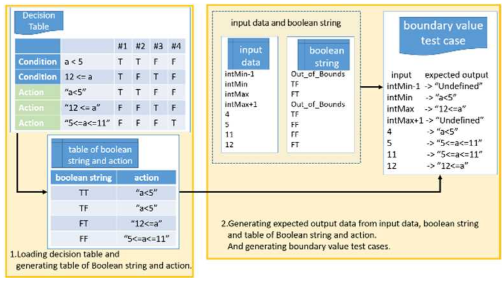

Fig. 3. The flow of expected output data generator processing

2. Boundary Value Test Case Automatic Generation Tool BWDM

BWDM analyzes boundary values of function definitions that described in VDM++ specification, and automatically generates boundary value test cases. Figure 1 shows the flow of BWDM processing. Note that VDM is a formal method devised at the IBM Vienna Research Institute in the 1970s, and VDM++ is an object-oriented extension of VDM-SL[2] which is formal specification language of VDM.

BWDM consists of input data generator and expected output data generator. In process of expected output data generator, the decision table is used, what is generated by decision table generation support tool developed in our laboratory[3]. The inputs into BWDM are VDM++ specification and decision table. Here, we implement BWDM in Java language.

2.1. *Process of input data generator*

Figure 2 shows the flow of processing of input data generator. The input is VDM++ specification file. And this unit generates input data based on boundary value analysis.

2.2. *Process of expected output generator*

Figure 3 shows the flow of processing of expected output data generator. This unit generates expected output data when input data is input to a function that is written in the VDM++ specification. And it outputs test cases that consists of input data and expected output data.

3. Application Example

We apply the formal specification that mixed inequality expression and surplus expression to BWDM. And we check 3 items.

(i) BWDM is operated correctly.

(ii) The boundary value is correctly extracted from the VDM++ specification.

(iii) BWDM outputs the input data and the expected output data correctly as the boundary value test case.

Figure 4 shows formal specification that we apply to BWDM. This specification judges whether the first argument is even or odd, and whether the second argument is a positive number or a negative number. Figure 5 shows the generated test cases by applying the formal specification of Figure 4 to BWDM.

The boundary values generated from the argument arg1 of the specification in Fig. 4 are natMin-1, natMin, natMax, natMax+1, 1, 2, and 3. And from the argument arg2, intMin-1, intMin, intMax, intMax+1, -1, and 0 are generated. Here, “natMin-1” means a value which is one less than the minimum value of the natural type. BWDM generates all combinations of boundary values of each of the two variables as input data. Therefore, the number of test cases generated from this specification is 7 * 6 = 42 (cases). By Fig. 5, we can check test cases from No. 1 to No. 42. From this, it is clear that BWDM outputs correct test cases from the formal specification. Also, we can check that both of extracting boundary values from VDM++ specification and outputting boundary value test

```
class MixSpecification

functions

  mix: nat * int -> seq of char
    mix( arg1 , arg2 ) ==
      if( arg1 mod 2 = 0) then
        if (0 <= arg2 ) then
          " arg1:even arg2:positive"
        else
          " arg1:even arg2:negative"
      else
        if( arg2 < 0) then
          " arg1:odd arg2:negative"
        else
          " arg1:odd arg2:positive";

end MixSpecification
```

Fig. 4. The formal specification that mixed inequality expression and surplus expression

cases that consist both of input data and expected output data are correct as well.

4. Discussion

In this research, for the purpose of improving the efficiency of the test process in software development using formal methods, we have developed a prototype of boundary value test case automatic generation tool BWDM. The inputs to BWDM are VDM++ specification and decision table, and the test case automatic generation and the boundary value analysis to the function definition in the specification are performed. Therefore, this tool improves the efficiency both of designing of test case and conducting of testing. In the followings, we consider BWDM.

4.1. *Evaluation of usefulness*

To consider BWDM usefulness, we used 3 specifications. We measured the time to generate test cases. Table 1 shows conclusion of measuring. Within the three specification, the if-conditional expressions of inequalities are described. The specification 1 has 5 if-conditional expressions, specification 2 has 10 expressions and specification 3 has 15 expressions. To measure execution time, we used System.nanoTime[4] method of Java. We measured the time that is to give the VDM++ specification and the decision table as an input to the BWDM and to finish outputting the test cases. The unit of time was millisecond, and measurements were made five times for each specification, and we calculated the average of 5 measuring as well. Here, we don't consider the time to prepare the VDM++ specification and the decision table.

```
The number of arguments:2

argument type:  argument1:nat   argument2:int

No.     input data      -->     expected output data
No.1    natMin-1        intMin-1        -->     Undefined Action
No.2    natMin-1        intMin          -->     Undefined Action
No.3    natMin-1        intMax          -->     Undefined Action
No.4    natMin-1        intMax+1        -->     Undefined Action
No.5    natMin-1        0               -->     Undefined Action
No.6    natMin-1        -1              -->     Undefined Action
No.7    natMin          intMin-1        -->     Undefined Action
No.8    natMin          intMin          -->      arg1:even arg2:negative
No.9    natMin          intMax          -->      arg1:even arg2:positive
No.10   natMin          intMax+1        -->     Undefined Action
No.11   natMin          0               -->      arg1:even arg2:positive
No.12   natMin          -1              -->      arg1:even arg2:negative
No.13   natMax          intMin-1        -->     Undefined Action
No.14   natMax          intMin          -->      arg1:odd arg2:negative
No.15   natMax          intMax          -->      arg1:odd arg2:positive
No.16   natMax          intMax+1        -->     Undefined Action
No.17   natMax          0               -->      arg1:odd arg2:positive
No.18   natMax          -1              -->      arg1:odd arg2:negative
No.19   natMax+1        intMin-1        -->     Undefined Action
No.20   natMax+1        intMin          -->     Undefined Action
No.21   natMax+1        intMax          -->     Undefined Action
No.22   natMax+1        intMax+1        -->     Undefined Action
No.23   natMax+1        0               -->     Undefined Action
No.24   natMax+1        -1              -->     Undefined Action
No.25   2               intMin-1        -->     Undefined Action
No.26   2               intMin          -->      arg1:even arg2:negative
No.27   2               intMax          -->      arg1:even arg2:positive
No.28   2               intMax+1        -->     Undefined Action
No.29   2               0               -->      arg1:even arg2:positive
No.30   2               -1              -->      arg1:even arg2:negative
No.31   1               intMin-1        -->     Undefined Action
No.32   1               intMin          -->      arg1:odd arg2:negative
No.33   1               intMax          -->      arg1:odd arg2:positive
No.34   1               intMax+1        -->     Undefined Action
No.35   1               0               -->      arg1:odd arg2:positive
No.36   1               -1              -->      arg1:odd arg2:negative
No.37   3               intMin-1        -->     Undefined Action
No.38   3               intMin          -->      arg1:odd arg2:negative
No.39   3               intMax          -->      arg1:odd arg2:positive
No.40   3               intMax+1        -->     Undefined Action
No.41   3               0               -->      arg1:odd arg2:positive
No.42   3               -1              -->      arg1:odd arg2:negative
```

Fig. 5. The test cases generated by applying the formal specification of Figure 4 to BWDM

For the average time in each specification, specification 1 and specification 2 were less than 0.5 seconds, and specification 3 was less than seven seconds. The number of rules on the decision table for specification 1 (number of columns in the decision table) is 32, specification 2 is 1024 and specification 3 is 1048576. These represent the number of states that the function can take, depending on the Boolean value in the if-conditional expression. When constraint conditions such as preconditions are described in the specification, the number of states actually taken by the function is less than this number. However, it is troublesome and time consuming to manually design test cases for functions that can have as many states as possible. On the other hand, BWDM can automatically generate boundary value test cases in several seconds if the specification is up to condition number 15.

Hence, we think that BWDM is usefulness when testing software that implemented from VDM++ specification.

4.2. *Related research*

TOBIAS[5] is a test cases automatic generation tool for testing the VDM++ specification. TOBIAS automatically generates test cases according to a test pattern input to TOBIAS. The test pattern is defined by

Table 1. Generation time of test cases from three specifications

Times	Specification1	Specification2	Specification3
1st time	325	316	6277
2nd time	283	389	5321
3rd time	500	371	6236
4th time	291	334	5070
5th time	269	371	5700
Average	334	356	5720

test designer using a regular expression to output a test case.

Both TOBIAS and BWDM support the testing phase of software development using VDM++. TOBIAS supports testing the VDM++ specification. In contract, BWMD supports testing actually implemented software.

This is what the difference of between two tools. Therefore, when you need to test implemented software, BWDM is superior.

5. Conclusion

In this research, we have developed a prototype of test cases automatic generation tool BWDM based on boundary value analysis targeting the VDM++ specification with the aim of streamlining the testing process in software development using formal method.

We applied the VDM++ specification that mixed inequality expression and surplus expression into BWDM, and our tool analyzed boundary value of the specification correctly. Finally, BWDM outputs boundary value test cases that consist both of input data and expected output data correctly. Furthermore, as a result of applying three kinds of VDM++ specifications including up to 15 if-conditional expressions to BWDM, it generated test cases within about seven seconds. Therefore, BWDM improves the efficiency of designing test cases.

In conclusion, by using BWDM, it is expected to improve the efficiency of the test process in software development using formal methods. Moreover, by conducting test design and test process based on the VDM++ specification, improvement both of productivity and quality of developed software is expected.

Future works are as follows.

- Generation of boundary values not appearing in the specification description

  Although it does not appear as a concrete numerical value in the specification description, there are boundary values that occur when two or more if-conditional expressions are related, and the current BWDM cannot generate those values as input data. It is necessary to modify the current process to generate boundary values.

- Responding to various environments

  Current BWDM, boundary value analysis of argument types of function definition cannot cope with various environments (bit number and development language) used for actual development. It is necessary to implement a function to allow users to set information about test cases what they want.

Acknowledgements

This work was supported by JSPS KAKENHI Grant Number 24220001.

References

1. Blake Neate, Boundary value analysis, http://www.cs.swan.ac.uk/~csmarkus/CS339/docs.htm, (accessed November 30, 2016).
2. International Organization for Standardization, ISO/IEC JTC 1/SC 22/WG, Information technology--Programming languages, their environments and system software interfaces--Vienna Development Method--Specification Language--Part 1: Base language (1996)
3. Kenta Nishikawa, Tetsuro Katayama, Yoshihiro Kita, Hisaaki Yamaba and Naonobu Okazaki, Proposal of a Supporting Method to Generate a Decision Table from the Formal Specification, *International Conference on Artificial Life and Robotics*, 222-225 (2014)
4. Java System class, https://docs.oracle.com/javase/ja/6/api/java/lang/System.html, (accessed November 30, 2016).
5. Olivier Maury, Yves Ledru, Pierre Bountron and Lydie du Bousquet, Using TOBIAS for the automatic generation of VDM test cases, http://vasco.imag.fr/Tobias/Papers/vdm02tobias.pdf, (accessed November 30, 2016).

Prototype of Refactoring Support Tool MCC Focusing on the Naming of Variables

Satoshi Tanoue[*], Teturou Katayama[*] Yoshihiro Kita[†],
Hisaaki Yamaba[*], and Naonobu Okazaki[*]
[*]*University of Miyazaki, 1-1 Gakuen-kibanadai nishi, Miyazaki, 889-2192 Japan*
[†]*Tokyo University of Technology, 1404-1 Katakura, Hachioji, 192-0914 Japan*
tanoue@earth.cs.miyazaki-u.ac.jp, kat@cs.miyazaki-u.ac.jp,
kitayshr@stf.teu.ac.jp, yamaba@cs.miyazaki-u.ac.jp, oka@cs.miyazaki-u.ac.jp

Abstract

This research has implemented a prototype of refactoring support tool MCC(Make Clean Coder) which focuses on the naming of variables. This prototype helps to describe a clean code by static analysis for the source code written in C language. And, it can help to reduce factors that prevent programmers understanding the source code when they modify it by pointing out improper variable names. Programmers can lower the possibility of embedded bugs, and decrease the time required to add new functions.

Keywords: Static Analysis, Refactoring, Clean Code, Variable Name

1. Introduction

In recent years, along with the evolution of ICT, the role of information systems in society is gradually increasing. As a result, economic and social impacts caused by system failures and software malfunctions are immeasurable. Against such a background, high-quality systems have become more important.

There is refactoring as a method to maintain and improve the quality of the system[1]. Refactoring is to improve the source code so that it is easy to understand while maintaining external behavior. If there is an unknown variable name, it becomes hard to understand what kind of processing[2]. In modifying the source code, a programmer may delete the necessary processing and use variables and functions differently from intended usage. Therefore, the programmer may embed bugs in the source code.

In this research, a prototype of refactoring support tool MCC (Make Clean Coder) has been developed for the purpose of supporting improvement of code quality. This prototype helps to describe a clean code by static analysis for the source code written in C language. And, it can help to reduce factors that prevent programmers understanding the source code when they modify it by pointing out improper variable names. The Improper variable names are one character or the variable name is not included in a dictionary. For the dictionary data, MCC uses the Dejizo Web Service[3] which is a dictionary published for experiments. By using this prototype, because it can reduce the time to understand the source code, programmers can shorten the coding time, lower the possibility of embedded bugs, and decrease the time required to add new functions.

2. Overview of MCC

Fig. 1 shows an overview of the prototype MCC. MCC consists of the MenuBar, EditArea, and DisplayArea. Each is explained below.

2.1. *MenuBar*

A user can use the function of the MCC by selecting each menu item on the MenuBar. When “File” is selected, the file menu is displayed. He can use the following two functions from the file menu.

- Open File
- Save File

When “Edit” is selected, the edit menu is displayed. He can use the following two functions from the edit menu.

- Clear DisplayArea
- Clear EditArea

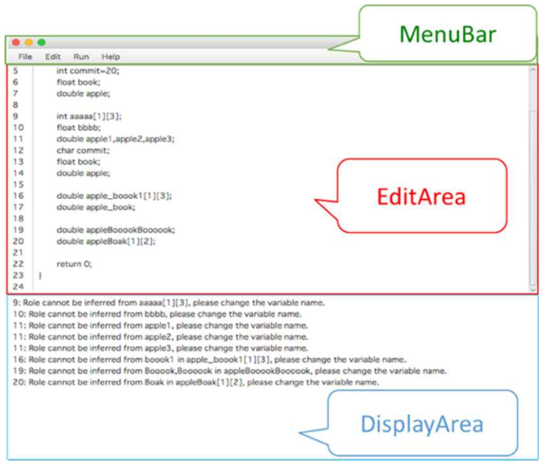

Fig. 1. An overview of MCC

When "Run" is selected, the run menu is displayed. He can use the following a function from the run menu.

- Analyze variable names

2.2. *EditArea*

EditArea is an area for editing the source code. MCC opens the file and displays the code in EditArea. EditArea has a simple editor function and can edit the source code.

2.3. *DisplayArea*

DisplayArea is an area for displaying the analysis result. MCC selects "Run" on the menu bar and selects "Analyze variable names" for the menu item to display the analysis result.

3. MCC Functions

The MCC has the following five functions.

- Open File
- Save File
- Analyze Variable Names
- Clear EditArea
- Clear DisplayArea

We explain the "Analyze Variable Names" function which is one of the functions of MCC. The variable name is analyzed by static analysis for the variable declaration part in the source code. In case of an inappropriate variable name, a warning is displayed in the display area as "the line number: Role cannot be inferred from ~, please change the variable name.". When the variable name is a snake case or a camel case, each word which is a compound word is searched with the dictionary. In the case of an inappropriate variable name, a warning is displayed in the display area as "Line number: Role cannot be inferred from ~ in ~, please change the variable name." .

```
valiableDeclaration::= <type> <name> <expr> (',' <name> <expr>)* ';'
name::= <camellCaseName> | <snakecaseName> | <commonName>
camellCaseName ::= <commonName>(<largeLiteral><commonName>)+
snakecaseName::= <commonName>('_'<commonName>)+
commonName::= (<smallLiteral>(<digits>)?)+
expr ::=(<array>)*('='<digits>)?
array::='['(<smallLieral>|<digits>|(<largeLiteral>)+)?']'
type::="double"|"float"|("unsigned")? ("int"|"long"|"short"|"char")
smallLieral::= ['a'-'z']+
largeLiteral::= ['A'-'Z']
digits ::=['0'-'9']+
```

Fig. 2. The definition of the syntax analyzed by MCC written in ENBF

4. Implementation

Analysis Variable Names, which is one of the functions of MCC, is implemented by combining a parser generated using JavaCC[4] and the dictionary by Web service[3]. A variable name is acquired using a parser, and it is judged whether a variable name is appropriate by the dictionary. Each is explained as the followings.

4.1. *Get the variable name*

When writing syntax rules in EBNF (Extend Backus Naur Form) with JavaCC grammar, JavaCC automatically generates code to perform syntax analysis written in Java. The definition of the syntax analyzed by MCC written in ENBF is shown in Fig. 2. We implement the parser by describing it according to the grammar of JavaCC and add actions. And can we get the variable name with this parser.

4.2. *Determining whether variable names are appropriate*

Whether variable names are appropriate is determined by using the dictionary[3]. If the variable name does not exist in the dictionary, it is dealt with an inappropriate variable name. Here, if the variable name is 1 character, do not

```xml
<SearchDicItemResult xmlns:xsi="http://www.w3.org/2001/XMLSchema-instance"
   xmlns:xsd="http://www.w3.org/2001/XMLSchema"
   xmlns="http://btonic.est.co.jp/NetDic/NetDicV09">
  <ErrorMessage/>
  <TotalHitCount>1</TotalHitCount>
  <ItemCount>1</ItemCount>
  <TitleList>
    <DicItemTitle>
      <ItemID>027022</ItemID>
      <LocID/>
      <Title>
        <span xmlns="" class="NetDicTitle">name</span>
      </Title>
    </DicItemTitle>
  </TitleList>
</SearchDicItemResult>
```


Fig. 3. The obtained XML file

search the dictionary and make it an inappropriate variable name.

As an example of dictionary search using Dejizo Web Service, search of “name” is shown. As request URL in MCC, http://public.dejizo.jp/NetDicV09.asmx/SearchDicItemLite?Dic=EJdict&Word=name&Scope=HEADWORD&Match=EXACT&Merge=AND&Prof=XHTML&PageSize=20 & PageIndex = 0 is used. As request parameters, assign EJdict to Dic, Word to Word, Scope to HEADWORD, Match to EXACT, Merge to AND, Prof to XHTML, PageSize to 20, PageIndex to 0. “name” is searched, and the obtained XML file is shown in Fig.3. We parse this XML file using Java XMLParser and get the value of TotalHitCount. When the value of TotalHitCount is 1 or more, it is registered in the dictionary. When the value of TotalHitCount is 0, it is not existed in the dictionary. That is, by the value of TotalHitCount, we can know whether or not it is registered in the dictionary.

5. Application Example

In order to verify that the MCC works properly, it was applied to source code written in C language. The results of the application are shown in Fig. 4. In line 41 of the edit area, the variable name is “r_num[50]”. Since “r” is one character and “num” does not exist in the dictionary, it is judged as an inappropriate variable name and a warning is displayed in the display area as “41: Role cannot be inferred from r,num in r_num[50], please change the variable name.”

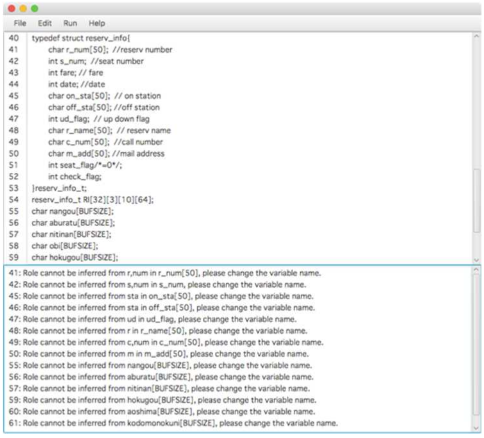

Fig. 4. The results of the application

Similarly, since there are variable names that are not appropriate for 42, 45, 46, 47, 48, 49, 50, 55,56, 57,59 lines of the editing area, a warning is displayed in the display area as “line number: Role cannot be inferred from ~, please change the variable name.”.

Therefore, it can be confirmed that MCC can correctly analyze.

6. Discussion

We describe the evaluation and related researches of MCC developed in this paper.

6.1. *Evaluation*

MCC developed in this paper reads the source code written in C language and performs static analysis. It can be judged by using a dictionary whether or not each variable name is appropriate. This makes it easy to find out where a word is not included in the dictionary. In addition, in the case of snake case or camel case, it is possible to judge each part of the compound word is not in the dictionary. With these functions, it is possible to find variable names named by one letter and words not included in the dictionary. The source code can be edited and saved.

By using MCC with these functions, it is possible to reduce the factor that hinders understanding in modifying the source code. This reduces the time required for understanding the source code, shortening the coding time, decreasing the possibility of embedding bugs, and reducing the time required to add new functions.

6.2. *Related Research*

Static analysis tool for C language, a lot of researches and development has been carried out.

Splint[5] is a tool for statically checking C programs for security vulnerabilities and coding mistakes. Splint performs static analysis such as unused declaration, type mismatch, use before definition, unreachable code, ignoring return value, execution path without return, possibility of infinite loop, and so on.

AdLint[6] can output a warning message about parts of lack of reliability or portability in the source code and can simultaneously measure various quality metrics. As quality metrics, you can measure the number of sentences in a file, the number of statements in a function, the number of goto statements, and so on.

On the other hand, the MCC can use a dictionary to decide whether it is properly named. Since it can be determined whether the variable name is properly named, it is possible to reduce variables that impede the understanding of the programmer.

7. Conclusion

In this research, a prototype of refactoring support tool MCC has been developed for the purpose of supporting improvement of the source code quality. MCC is a tool that performs static analysis on the source code written in C language and supports description of clean code, focusing on the naming of variable names. The MCC has the following five functions.

- Open File
- Save File
- Analyze Variable Names
- Clear EditArea
- Clear DisplayArea

In static analysis, it is judged whether each variable name is properly named by using a dictionary. If the variable name is not appropriate, MCC displays a warning for the line number and the variable name. In addition, MCC has the source code editing function.

We have confirmed that MCC works correctly by applying the example of source code written in C language to MCC. MCC can point out variable names that are not naming properly. This reduces the time to understand the source code, shortens the coding time, reduces the possibility of bug contamination, and reduces the time required for function addition. From the above, it can be considered that by using MCC developed in this paper, it is possible to support improving the quality of the source code.

The future issues are shown below.

- Correspondence to variable names that exist in multiple lines

If variable names extend over multiple lines, it can not be parsed. MCC hands the source code to the parser one line at a time. Passing variable names that exist multiple lines will cause ParseExecption when there is a C language syntax that is not supported. It can be solved by making it possible to analyze the syntax of all C languages.

- Correspondence to variable names that are not supported.

MCC can not parse pointer variables and variable names of types defined in the structure. It can be solved by adding syntax to the definition of the syntax analyzable by MCC.

- Correspondence to function names.

MCC can not judge whether function names are properly named. It can be solved by adding syntax to the definition of the syntax analyzable by MCC.

- Correspondence to the case where the variable name is not appropriate when existing in a dictionary.

Even if it exists in a dictionary, the variable name may not be appropriate. For example, word_word is the case. Such variable names are inappropriate because a programmer do not know the meaning. It is necessary to modify MCC so that it can judge whether variable names are appropriate names in consideration of the order of the variable names.

References

1. Martin Flower et al. (eds.), *Refactoring Improving the Design of Existing Code*, 1nd edn. (Pearson Education,1999).
2. Dustin Boswell and Trevor Foucher, *The Art of Readble Code* (O'Reilly Media 2012).
3. Dejizo Web Service, http://dejizo.jp/dev/index.html.
4. JavaCC, *JavaCC Home*, https://javacc.java.net/.
5. Split, *Splint Home Page*, http://www.splint.org/.
6. AdLint, *Adlint::AdvancedLint*, http://adlint.sourceforge.net/.

Improvement of Transitions and Flow Visualization TFVIS for Exception Handling

Takuya Sato*, Tetsuro Katayama*, Yoshihiro Kita†, Hisaaki Yamaba*, and Naonobu Okazaki*

[*]University of Miyazaki, 1-1 Gakuen-kibanadai nishi, Miyazaki, 889-2192 Japan

† Tokyo University of Technology, 1404-1 Katakuramachi, Hachioji City, Tokyo 192-0982, Japan

sato@earth.cs.miyazaki-u.ac.jp, kat@cs.miyazaki-u.ac.jp, kitayshr@stf.teu.ac.jp, yamaba@cs.miyazaki-u.ac.jp, oka@cs.miyazaki-u.ac.jp

Abstract

It takes much time in debugging process. To find bugs effectively, it's important to understand the dynamic behavior of programs. To support understanding the dynamic behavior, we developed TFVIS(transitions and flow visualization). It provides visualization of data transitions and data flow of Java programs. But it visualizes only some control structures and expression. Therefore, we newly corresponded to Exception-handling. This improves the usefulness of TFVIS as a tool to support the understanding of the dynamic behavior of programs.

Keywords: Debugging, Visualization of program, dynamic analysis, Exception-handling, Java

1. Introduction

In software development, it takes much time in debugging process[1]. To find bugs in a program effectively, it's important to understand the dynamic behavior of the program. But it's difficult since the dynamic behavior of the program is generally invisible[2,3].

To solve this problem, we developed TFVIS(transitions and flow visualization)[4], which can visualize the dynamic behavior of Java programs.

It provides visualization of data transitions in each method and flow of the whole program. It has another feature which can show the data transitions with arrows. This makes it easy to follow a defect from the incident. But it's not useful because it visualizes only some control structures and expressions.

We aim at the improvement of the usefulness by corresponding an unsupported structure. This paper focuses on Exception-handling, which is one of features of Java programs and especially corresponds to Try Catch syntax.

2. TFVIS

Figure 1 shows an example of visualization by TFVIS.

TFVIS generates a data transition diagram. It shows the behavior at the time of program execution in detail. It is based on structural information obtained by analyzing the program structure and executional information at the time of execution.

The data transition line can visualize data transitions. When the user finds a suspicious value of a variable on the data transition diagram, by using the data transition line, it becomes easy to specify the cause of generating the suspicious value.

TFVIS visualizes the flow of the whole program by the execution flow diagram based on the UML sequence diagram. The execution flow diagram shows the usages of a method of each class and relation of a method call.

Figure 2 shows the structure of TFVIS. It consists of Analyzer and Visualizer, and Analyzer consists of Structural Analyzer, Probe File Generator, and Dynamic Analyzer.

Structural Analyzer analyzes the structure of the program and outputs the analysis result as structural

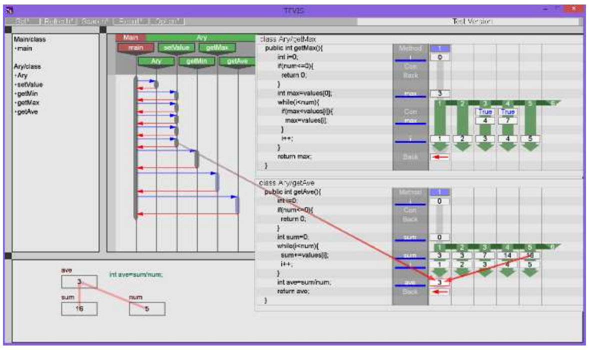

Fig. 1. Example of visualization by TFVIS

information to the file. The structural information is used for deciding the insert position of probes in Probe File Generator and for generating diagrams in the Visualizer. Further, Structural Analyzer obtains events occurring in each line of the source code. The events are a specific process as a standard of visualization, and each event has a value of an event type.

Based on the structural information, Probe File Generator generates a probe file, which embedded probes in the target source code. The probe outputs information on the behavior at program execution. The probe outputs information on the behavior at program execution. There are several kinds of probes, and Probe File Generator selects probes to be inserted for each event that occurs in each line of the source code.

Dynamic Analyzer analyzes the behavior at the time of execution from the probe file and outputs the analysis result as executional information.

Visualizer visualizes the behavior at the time of program execution based on the structural information and the executional information outputted by the Analyzer.

3. Improvement of TFVIS

In this section, we describe the improvement of TFVIS for corresponding to Try Catch syntax. We describe the changes of each part to correspond to Try Catch syntax and then show the data flow of TFVIS after the improvement.

3.1. *Improved points of each division*

The improvement to correspond to Try Catch syntax is as below.

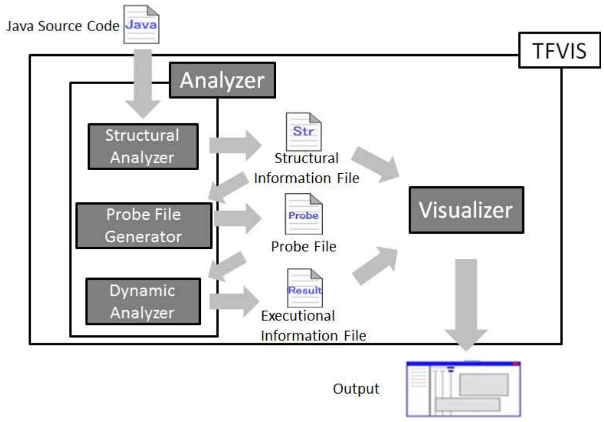

Fig. 2. Structure of TFVIS

- Definition of values of new event types in Structural Analyzer
- Definition of new probes for Try Catch syntax in Probe File Generator
- Insertion of the probes for Try Catch syntax in Probe File Generator
- Visualization of events of Try Catch syntax in Visualizer

3.1.1. *Definition of values of new event types in Structural Analyzer*

In Structural Analyzer, we newly define the values of the event types for Try Catch syntax.

The values of the defined event types are the value of the start of the Try block (380), the value of the end of the Try block (382), the value of the start of the Catch block (390), and the value of the end of the Catch block (392).

3.1.2. *Definition of new probes for Try Catch syntax in Probe File Generator*

In Probe File Generator, we newly defined probes to be inserted for the event of Try Catch syntax.

The probe for the event of the Try block defines as Try Detection Probe. This probe takes as arguments the instance ID, method ID, method execution number, and line number at the time of execution. And, to visualize it, outputs try event ID (380), instance ID, method ID, method execution number, and the line number to the Executional Information File.

In a similar way, the probe for Catch block defines as Catch Detection Probe. In this probe, the arguments are

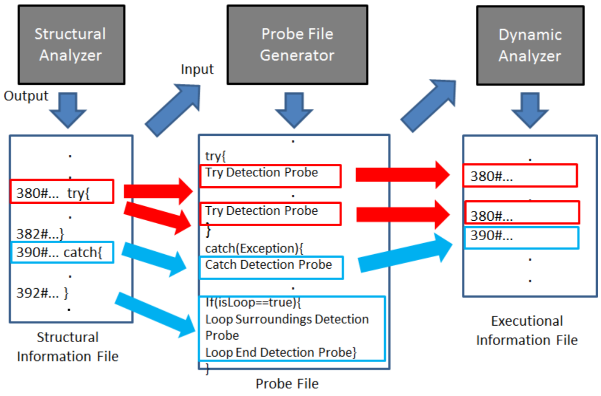

Fig. 3. Data Flow of TFVIS

the same as Try Detection Probe, but the output is the Catch event ID (390) instead of the Try event ID (380).

3.1.3. *Insertion of the probes for Try Catch syntax in Probe File Generator*

In the Probe File Generator, the newly defined probes are inserted for the event of the Try Catch syntax.

Try Detection Probe is inserted just preceding every line from the start of the Try block to the end of the Try block. At this time, the value of the line number obtained by the probe is the line number of the immediately following statement. Also Catch Detection Probe is inserted immediately following the Catch event.

When a Catch block is executed during Loop, there is such a process as to break out of Loop. To correspond to this, insert a boolean type variable ("isLoop") definition indicating whether it is in a Loop at the start of method. We change Probe File Generator so that "isLoop" becomes true if it is in the Loop, and false otherwise. If "isLoop" is true when an event of the end of Catch block occurs, existing Loop Surroundings Detection Probe and Loop End Detection Probe are executed on the immediately preceding line.

3.1.4. *Visualization of events of Try Catch syntax in Visualizer*

When an Exception-handling event occurs, a box describing "Catch" in red font is placed in the execution place immediately preceding the data transition diagram. Also, a red arrow that connects the occurrence part of Exception- handling and the execution part is drawn.

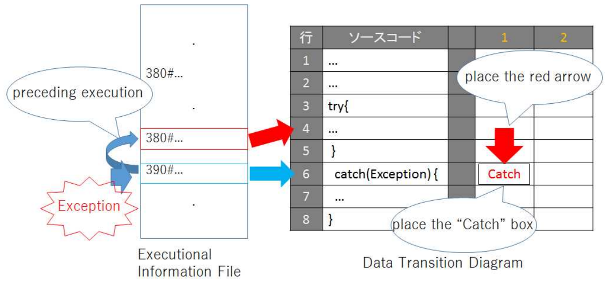

Fig. 4. Flow of Visualization

3.2. ***Data flow of TFVIS after improvement***

3.2.2. *Data flow in Analyzer*

Figure 3 shows the flow of data in which a program including a Try Catch syntax is applied to TFVIS after the improvement.

By improving of Structural Analyzer, we can obtain events on Try Catch syntax. From Figure 3, we can see that structural information file has value of the start of the Try block (380), the value of the end of the Try block (382), the value of the start of the Catch block (390), and the value of the end of the Catch block (392).

By the events of Try Catch syntax obtained by Structural Analyzer, Probe File Generator inserts the newly defined probes. From Figure 3, we can see that Try Detection Probes are inserted just preceding each statements in Try block, Catch Detection Probe is inserted just following start of Catch block, and an if statement that executes Loop Surroundings Detection Probe and Loop End Detection Probe if it is in a loop.

By executing the probe file in which the probes are embedded by the Dynamic analyzer, we obtain executional information.

3.2.3. *Flow of Visualization in Visualizer*

Figure 4 shows the flow of visualization when applying a program including Try Catch syntax.

Based on the structural information, the data flow diagram and source code on data transition diagram are drawn. Based on the executional information, the data transition diagram is drawn.

When Visualizer reads execution information having a Catch event ID, the execution of the event immediately

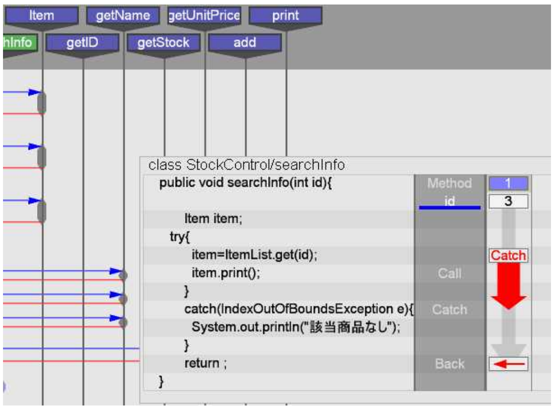

Fig. 5. Visualization of SearchInfo method

preceding is referred as the point occurred Exception-handling.

4. Application Example

By the improvement of TFVIS, we confirm that programs including Try Catch syntax can be visualized correctly. As an application example, we show that TFVIS correctly visualizes the method including Try Catch syntax by using “inventory management program” written in Java.

Figure 5 shows a data transition diagram that visualizes the SearchInfo method, including a Try Catch syntax. This method requires “ID” as an argument, and displays instance’s “ID”, “name”, “number of stock”, and “unit price”. Since there were only 3 instances generated as inventory, and stored in the list. At this time, assuming that the user inputs “ID” 3, it refers to the fourth in the list, and an exception of “IndexOutOfBoundsException” occurs.

From Fig 5, we can see that the box “Catch” in the line referring to the list and a red arrow from the box to the line of Exception-handling which occurred is drawn. From this, it can be seen that the occurrence of Exception-handling is correctly visualized on the data transition diagram.

5. Discussion

In this research, we aimed to improve the usefulness of TFVIS by corresponding to Try Catch syntax. In this section, we first describe the evaluation of the improvement of TFVIS. Next, we describe relation works.

5.1. *Evaluation*

If the program to be applied contains Try Catch syntax, a compile error occurs and visualization cannot be executed in existing TFVIS.

In order to visualize a program containing a Try Catch syntax, firstly, we improved Structural Analyzer to obtain the events by using newly defined values of event types for the Try Catch syntax.

Secondly, we improved Probe File Generator to insert the newly defined probes which output executional information for Try Catch syntax.

Finally, we improved Visualizer to draw the box written “Catch” in red and red arrow that connects the occurrence part of Exception-handling and the execution part.

TFVIS after the improvement can visualize the program containing Try Catch syntax. From this, it can be said that the usefulness of TFVIS has been improved by corresponding to Try Catch syntax.

5.2. *Relation works*

- Breakpoint debugging

  Breakpoints are one of the most frequently used debugging support approaches[6]. With debugging using breakpoints, program execution can be stopped at arbitrary points. Then, you can refer to the execution status of the program, such as values of each variable at the time of stoppage.

  Breakpoint debugging has a problem that it is difficult to select the installation point of the breakpoint. Selection of an appropriate breakpoint location requires user’s knowledge and experience[7]. TFVIS is useful in that it can obtain information only by selecting a method having information desired by the user and therefore does not depend on the user’s ability.

  Moreover, visualization by TFVIS can overlook the flow of the whole program and the flow of method process. By using the data transition line, it is also possible to grasp the dependency relationship between the variables. In comparison with breakpoint debugging, these functions are superior in that it is easier to find out how the certain variable is defined.

- JIVE

JIVE[8](Java Interactive Visualization Environment) is a tool visualizing execution of Java programs.

JIVE has the function of generating UML object diagrams and sequence diagrams from process at the time of program execution. In addition, it supports inquiries by queries, for example, it is possible to make an inquiry such as "Where is the method "func" returning NULL to the return value?". The process found by the inquiry is highlighted on the sequence diagram and helps to grasp the behavior at the time of execution.

When comparing JIVE and TFVIS, JIVE does not have a function to indicate the dependency between variables like data transitions. Inquiries about variable updating are possible, but when examining dependencies such as data transitions, it is necessary to repeat inquiries. Therefore, TFVIS is more effective for tasks such as searching for the cause when a suspicious value is found.

6. Conclusion

In this research, we aimed to improve the usefulness of TFVIS by corresponding to unsupported structure. TFVIS shows behavior at the time of program execution by data transition and data flow visualization. The visualization of TFVIS makes it easy to grasp the behavior at the time of execution of the program including the defect, and it becomes possible to efficiently specify the defect.

However, there are programs that cannot be visualized with existing TFVIS. The fact that programs containing basic syntax of Java programs cannot be visualized means lacking usefulness.

In this research, we improved TFVIS so that it can visualize a program containing Try Catch syntax. It can be said that the usefulness of TFVIS has been improved by this improvement.

The future issues are shown below.

- Correspondence to programs including occurrence of input wait state

TFVIS does not have the function of receiving input from the user. Therefore, when a program including occurrence of an input wait state is applied to TFVIS, since the execution of the analysis section is not completed, execution information cannot be obtained and visualization cannot be performed.

- Implementation of inquiry function

TFVIS has no inquiry function. This problem becomes more troublesome as the process of the program to be visualized increases. Therefore, we think that it is necessary to implement the inquiry function so that the user can easily find a process satisfying a specific condition.

- Support for multithread programs

TFVIS cannot visualize multithreaded programs. In multithread programs, process becomes complicated easily because data is exchanged between threads. If we can visualize a complicated process by multithreading, the usefulness of TFVIS will be improved.

References

1. Thomas D. LaToza, Gina Venolia, and Robert DeLine: Maintaining mental models: a study of developer work habits, *Proceedings of the 28th international conference on Software engineering,* pp.492-501 (2006).
2. Roger S. Pressman: *Software Engineering A Practitioner's Approach*, McGraw-Hill Science (2001).
3. Jonathan Sillito, Gail C. Murphy, and Kris De Volder: Asking and Answering Questions During a Programming Change Task, *IEEE Transactions on Software Engineering*, Vol.34, No.4, pp.434-451 (2008).
4. Hiroto Nakamura, Tetsuro Katayama, Yoshihiro Kita, Hisaaki Yamaba, Kentaro Aburada and Naonobu Okazaki: TFVIS: a Supporting Debugging Tool for Java Programs by Visualizing Data Transitions and Execution Flows, *The 2015 International Conference on Artificial Life and Robotics*, pp.376-379 (2015).
5. Gail C. Murphy, Mik. Kersten and Leah Findlater: How Are Java Software Developers Using the Eclipse IDE?, Software, *IEEE*, Vol.23, No.4, pp.76-83 (2006).
6. Gail C. Murphy, Mik. Kersten and Leah Findlater: How Are Java Software Developers Using the Eclipse IDE?, Software, *IEEE*, Vol.23, No.4, pp.76-83 (2006).
7. Cheng Zhang, Juyuan Yang, Dacong Yan, Shengqian Yang and Yuting Chen: Automated Breakpoint Generation for Debugging, *Journal of Software*, Vol.8, No.3, pp.603-616 (2013).
8. Demian Lessa, Bharat Jayaraman and Czyz Jeffrey: JIVE: A Pedagogic Tool for Visualizing the Execution of Java Programs. *Technical Report* 2010-13, Department of Computer Science and Engineering, University at Buffalo (2010).

Automatically Business Decision Making System for Software Development by using CMMI

Hnin Thandar Tun†, Tetsuro Katayama*, Kunihito Yamamori*, and Khine Khine Oo†
**University of Miyazaki, 1-1 Gakuen-kibanadai nishi, Miyazaki, 889-2192 Japan*
† University of Computer Studies, Yangon, No. (4) Main Road, Shwe Pyi Thar Township, Yangon, Myanmar
thandar123@ucsy.edu.mm, kat@cs.miyazaki-u.ac.jp, yamamori@cs.miyazaki-u.ac.jp, k2khine@gmail.com

Abstract

The automatic business goals are effectively to provide in the software development system. In this research, the senior level management will define goals based on previous data. We focus to generate all of the business goals based on Capability Maturity Model Integration (CMMI) applied by Goal Question Metric (GQM) approach. According to the GQM approach, the system will check estimated data for future and come out possible goals automatically alignment on defined future goals by senior level management.

Keywords: CMMI, GQM approach, Project Monitoring and Control, MySQL database, Java

1. Introduction

In the current software development, business decision-making system is important process to support the automatic business goals. In this research, we proposed to make a decision model that is Capability Maturity Model Integration (CMMI) [1].

We cannot suggest automatic goals only used to CMMI model. Therefore, we applied the GQM approach, which is a good measurement process to provide business goals better and timelier decision. Thus, this approach will support to define goals by senior management based on CMMI model[2, 3].

The system will check the defined goals of metric data plan by senior level management. If defined goals by senior management will match with the resources data, the system will be operated automatically. If the resources will not match with the required goals, the system will realign production goals, which will be match with the actual goals of processing.

Additionally, the metric program framework used to generate a complete metric plan, which includes GQM analysis, to monitor and control measurements of defined goals. The GQM approach has three levels of measurement of defined goals system, such as (1) conceptual level, (2) operation level, and (3) quantitative level. In the GQM analysis, the metric plan will define specific goals according to the project monitoring and control measurements in the software development.

Therefore, the research paper focused measurement approach of GQM analysis to define all of the business goals and measurable index to perform business operation functionality[4]. For application concerned, the model developed in this paper is used for dairy farms milk production procedure. By constructing milk production database, the proposed is able to monitor targets of each unit to achieve goals schedule (daily, weekly, monthly and quarterly). Then the senior level management will be confirmed and the system will assign automatically decision goals alignment and control all of the future resources of performance.

For technical construction, we collect data by using excel data collection tool to import data in MySQL database first. Moreover, the system will report business goals to senior management showed by graphical interface as a result for the future target. The test result will perform the automatic business goals for future target that are reporting in step by step to the senior management.

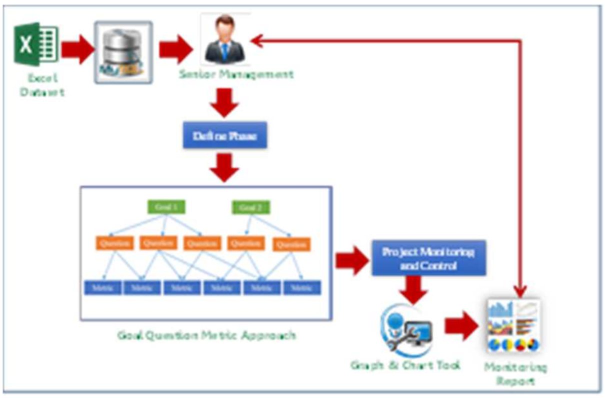

Fig. 1. Overview of the business goals decision-making system

2. Framework of the CMMI model applied with GQM approach

In this research, CMMI model applied the GQM approach, which is an approach of metric data analysis used to monitor business decision goals in the software development.

It is related the metric plan with the key process area of Project Monitoring and Control measurements.

2.1. *Applying GQM approach based on CMMI*

Figure 1 shows how to perform business goals decision-making system of the CMMI model.

This paper is concerned with a generating of business goals by CMMI model. In doing so, this model applied or adapted the Goal Question Metric (GQM) approach. It is used to evaluate the defined goals by senior level management that can monitor and control measurements for the progressive measurements systematically.

This research identifies the general measures for the specific goals and its specific practices related to the process area of CMMI. Monitoring and control measurements provide business goals with progressive measurable index to align directly with the GQM approach. This approach is defined to align all of the business goals at the levels of the organization. Moreover, it will make to control success or failure through progressive measurement and key performance indication of metric definition for improvement decisions[5]. Therefore, the GQM approach is an excellent metric approach to be uses everywhere better than similar approaches that do not take into all business operation levels.

2.2. *Metric data decision of GQM approach*

Metric framework that is used to generate the metric plan is described, followed by a complete metric plan.

The process metric plan is established by the business decision based on the actual progress in terms of GQM approach according to the business goals. The metric plan contains goals and scope of implementation metrics[6]. The metric plan includes data collection, data analysis, data reporting and metric decision making. This section defines the metric plan based on monitoring and control measurements for developing metric steps are:

1. Define the measurement goals by senior management and obtain the objectives/goals for the future target.
2. Utilize the GQM approach and determine the business goals progressive measurements to monitor.
3. Review measurement practices and the target of business processes in specified areas.
4. Establish reporting and monitor key performance indicator of metric units.
5. Align with the business operation for monitoring results per all units (daily, weekly, monthly, quarterly, and yearly).

Therefore, this paper presents the key process area of CMMI model that is necessarily to support on business effective process improvement, needs design implementation, needs decision tools for achieving goals for future target systematically. According to the illustration propose, we need to define the actual business goals by senior level management aligned with the resources of business data.

3. Implementation of metric analysis approach

In this section, we consider to implement the metric data that is used to define the actual milk production diary.

According to the defined phase, the milk production diary consists of four collection records such as production collection records, milk storage units collection, own farmer collection records and other farmer contract units. In this collection procedure, own farm and other farmer contract collection will provide as

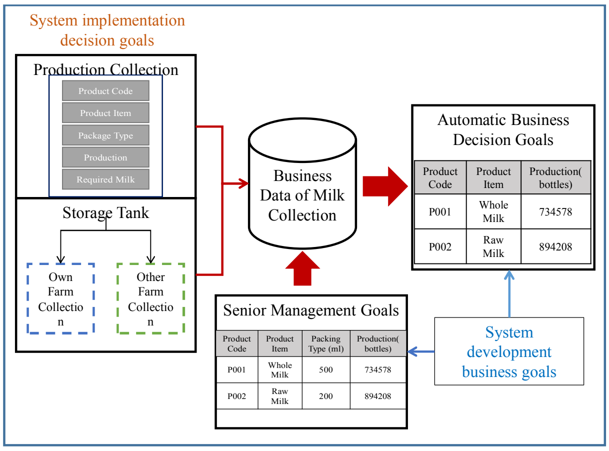

Fig. 2. Implementation of metric data flow

an input to the storage tank collection. Among them, the systematic collection form involve product code, product item, packing type, production amount of metric units, usage amount of collection, usage amount of production and the remaining amount of milk data to support operation target (business goals) smoothly. This section has to discuss two divisions such

3.1. *Metric data collection procedure*

Based on the GQM approach, we need to store the specific goals of metric data as a previous data collection.

The collection data refer to the milk diary production such as milk production units, milk storage units' collection. The storage collection is provided by the own farm collection records and other farmer contract units as an input to become the milk resources.

Figure 2 shows the implementation of the approach of metric data flow. In this operation, we describe how to implement the milk production diary.

3.1.1. *Create the production collection records*

We define the business goals of production units in the milk production system.

This system apply the production code, product item, packing type of each product item, amount of production per milk bottle, required milk liter per each of product item and usage of milk liters which are able to support operation target (defined goals by senior management) smoothly. All of the productions units are stored in the metric database of the milk production system.

3.1.2. *Create the storage units collection*

In storage collection, we store the received data from own farm and other farmer collection, amount of production usage data, amount of remaining balance production units.

They are related to each other to align the defined goals of production by senior management level based on previous data.

3.1.3. *Define goals by senior level management*

Based on previous data results, senior level management defines goals for future target of production.

Moreover, the system will check estimated milk production collection for future and come out possible goals automatically alignment on defined future goals by senior level management.

3.2. *Monitoring progress of auto suggestive goals*

The senior level management specifies business goals of the future target to compare the previous data.

As a metric data flow, all databases are used to make suggestion goals for future target. The system will assume that senior management last input results which must be approximately they want to product for appropriate products. As per previous data result, the system will auto align with the senior management last input results. If the resources of milk production are not matched with the suggestive goals by senior management, the system will realign the production goals per each product items, which will be matched with the actual milk collection data in storage.

Based on daily actual results, weekly, monthly, quarterly, yearly data will realign the goals systematically and report in systematically to senior level management.

3.3. *System Implementation of milk production*

This system presents evaluation of the automatic goals for window application that is developed in Java.

Database in window application is MySQL database that are connect to the graphical interface by using JFreeChart tool. In the evaluation process, it is performed the metric parameters of the milk production system by graphically. Milk production system shows the automatic

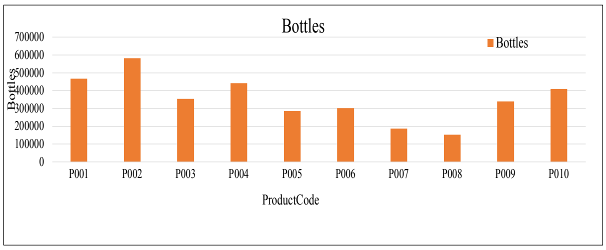

Fig. 3. Yearly data progress of milk production units

decision goals of that are implemented in window application.

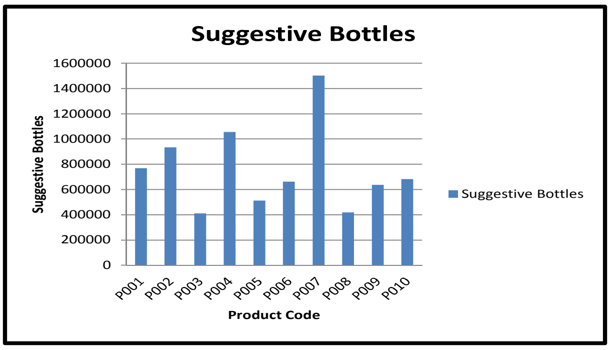

Fig. 4. Suggestive goals for milk production target

4. Performing results of business goals

In the research application, the performing results are classified into three phases to suggest the automatic business goals as follow as.

Phase 1: Collection of the business goals is supported to define the business for future target by senior level management. The amount of collection units displays the milestone review of the production resources that are calculated by using packing type as required milk bottles as shown in Figure 3.

Phase 2: According to the phase 1, the production of business goals are stored in the milk production database. The production data is used for future target of business goals defined by senior level management. Based on the previous data results, the senior management defines the production of goals described as a decision-making goal for future target.

Phase 3: The system will accept auto suggestive goals for production units matched with the storage data resources if the storage tank units are greater than requirement of milk calculation. Then, the system will be realigned by suggestive goals based on the storage unit resources. In addition, the system will monitor targets of business goals to achieve business goals timely (daily, monthly, and yearly). During the system implementation, the auto suggestive goals will come out to specific indicators of milk products by using graphical interface tool. Figure 4 shows the evaluation of the auto suggestive goals for the future target.

5. Conclusion

In this system, GQM approach is modeled as a metric plan for measuring the performance of milk production units. GQM approach can easily tested to calculate and align the metric of milk production units.

Therefore, the system can perform the auto suggestive goals by systematically for the defined goals by senior level management.

In the future issue, the research is used to refine the proposed method that can evaluate the quality of metrics applying more kinds of metrics to link to the GQM approach. The system will implement GQM plugin and monitoring tools flexible approach to improve the quality.

References

1. V.Basili, G. Caldiera and D. Rombach: *Goal Question Paradigm*, (Marciniak,J.J., editor), Vol.1, pp.528-532 (1994).
2. R.Van Soligen and E. Berghout: *the Goal Question Metric Method: A Practical Guide for Quality Improvement of Software Development*, McGraw-Hill, (1999).
3. M. Chrissis, M. Konrad, S. Shrum: *CMMI® Guidelines for Process Integration and Product Development*, Addion-Wesley (2007).
4. R. Xu, Y. Xue, P.Nie, Y.Zhang and D. Li: Research on CMMI based Software Process Metrics, *the First International MultiSymposiums on Computer and Computional Science*, IMSCCS (2006).
5. S.Wanapasim, T. Suwannasari, and A. Methawachananont: An Approach for Monitoring Software Development using Timesheet and Project Plan, *International MultiConference of Engineering and Computer Scientists*, Vol.1, (2013).
6. Hnin Thandar Tun, Tetsuro Katayama, Kunihito Yamamori and Khine Khine Oo: Business Goals Monitoring and Control Measures in CMMI, *IEEE 5th Global Conference on Consumer Electronics* (GCCE), pp. 376-378 (2016).

An Application of Collaborative Filtering in Student Grade Prediction

Chaloemphon Sirikayon[1] **and Panita Thusaraon**[2]

College of Innovative Technology and Engineering
Dhurakij Pundit University
Bangkok, Thailand
E-mail: chaloemphon.sir@dpu.ac.th, panita.thu@dpu.ac.th
www.dpu.ac.th

Abstract

This research presents the process of student performance prediction by using the collaborative filtering (CF). The benefit of this research includes assist instructor to identify student performance, personalized advising, and student degree planning. The CF technique composes of similarity calculation and prediction. In our experiments, a prior course clustering with heuristic knowledge is adopted and different techniques of similarity calculation are compared. The performance of each student has been predicted by using existing grades available at that time.

Keywords: grade prediction, collaborative filtering, educational data mining

1. Introduction

Student performance prediction in future course is important as it provides valuable information to facilitate student success. In this paper, we present the process of student performance prediction by using the collaborative filtering: CF [1], which is one of the most popular techniques wildly used for student performance prediction. The performances that students achieved in the earlier courses are used to predict grade that they will obtain in future courses. The algorithm is based on the idea of finding the most similar students. We have performed various methods to calculate students' similarity, i.e. Pearson correlation, cosine similarity, and Euclidian distance. The performance of each method is experimentally evaluated on a dataset obtained from Dhurakij Pundit University with enrollments of 200 undergraduate students between 2012 and 2016 from the Faculty of Information Technology. Our experiments shows that finding students' similarity with Pearson correlation achieves the lowest prediction error and a prior course clustering with heuristic knowledge can enhance predictability.

The rest of this paper is organized as follows: related work and fundamental concept is given in Section 2. The proposed method is described in Section 3. Experiments are conducted in Section 4. Conclusions are summarized in Section 5.

2. Preliminaries

This section summarizes related work and briefly defines the fundamental concept needed to facilitate the presentation of the proposed algorithm.

2.1. *Related work*

Different models have been developed in order to predict student's performance and many approaches rely on collaborative filtering methods. The similarities of students are calculated utilizing their study results, represented by the grades of their previously passed courses. A recommendation tool called the personalized Grade Prediction Advisor (pGPA) was proposed in [3]. The system allows user to set parameters such as number of similarity students used for prediction. Another course recommender system for University College Dublin's on-line enrolment application was proposed in [2]. The system recommends elective modules to students based on the core modules that they have selected by using item-based collaborative filtering.

On the other hand, [5] presented future course grade prediction methods that utilize approaches based on linear regression and matrix factorization. Hybrid methods and content features are also used in [6].

2.2. *User-based collaborative filtering*

Collaborative Filtering algorithm is based on the main idea that people have similar preferences and interests. One user's behavior is compared with other user's behavior to find his/her nearest neighbors, and according to his/her neighbor's preferences or interest to predict his/her preferences or interest. Suppose that U = {u_1, u_2,..., u_m} is a list of m users and I = {i_1, i_2,..., i_n} is a list of n items. Each user U_i gives rating scores for a list of items I_{ui}. The prediction problem is to predict the rating active user U_a will give to an item I_{ua} from the set of all items that U_a has not yet rated. The CF technique composes of 3 steps as follows: 1) users similarity calculation 2) top N nearest neighbors selection and 3) prediction.

2.2.1. *Similarity and distance*

Various methods can be used to find similarity between users such as Pearson correlation and cosine similarity. On the other hand, dissimilarity calculation, i.e. Euclidean distance can be converted to similarity.

2.2.1.2 *Pearson correlation*

Let the set of items rated by both users u and v be denoted by I, then similarity coefficient $sim(u,v)$ between them is calculated as

$$sim(u,v) = \frac{\sum_{i \in I_u \cap I_v} (r_{u,i} - \bar{r}_u)(r_{v,i} - \bar{r}_v)}{\sqrt{\sum_{i \in I_u \cap I_v} (r_{u,i} - \bar{r}_u)^2} \sqrt{\sum_{i \in I_u \cap I_v} (r_{v,i} - \bar{r}_v)^2}} \quad (1)$$

Here $r_{u,i}$ denotes the rating of user u for item i , and $\bar{r}_u$ is the average rating of all items given by user u. Similarly, $r_{v,i}$ denotes the rating of user v for item i, and $\bar{r}_v$ is the average rating of all items given by user v.

2.2.1.2 *Cosine similarity*

The similarity $sim(u,v)$ between user u and v is calculated as

$$s(u,v) = \frac{r_u \cdot r_v}{\| r_u \|^2 \| r_v \|^2} = \frac{\sum_i r_{u,i} r_{v,i}}{\sum_i r_{u,i}^2 \sum_i r_{v,i}^2} \quad (2)$$

where $r_{u,i}$ denotes the rating of user u for item i , and $r_{v,i}$ denotes the rating of user v for item i.

2.2.1.3 *Euclidean distance*

Euclidean distance for two user u and v is calculated by

$$d(u,v) = \sqrt{\sum_{i \in I_u \cap I_v} (r_{u,i} - r_{v,i})^2} \quad (3)$$

Here $r_{u,i}$ denotes the rating of user u for item i , and $r_{v,i}$ denotes the rating of user v for item i . Then, obtained distance scores are converted to similarities by

$$sim(u,v) = \frac{1}{1 + d(u,v)} \quad (4)$$

2.2.2. *Prediction*

Once similarities are calculated, a set of top-k users most similar to the active user u are selected and their rating scores are used for the prediction $P_{u,i}$ of the specific item i for user u as follow:

$$P_{u,i} = \bar{r}_u + \frac{\sum_{v \in N} s(u,v)(r_{v,i} - \bar{r}_v)}{\sum_{v \in N} | s(u,v) |} \quad (5)$$

3. Dataset and Method

For each student whose grade needs to be predicted, a set of similar students are identified by using their grades from courses that they have already taken. The data used for this study obtained from Dhurakij Pundit University with enrollments of 200 undergraduate students between 2012 and 2015 from the Faculty of Information Technology. The dataset comprised of 200 students and their 12,000 grades. The A-F letter grades were converted to the 4–0 scale. The performance of each student who enrolled in semester 2, 2015 has been predicted by using grades available at that time.

3.1. *Prediction without prior courses clustering*

Our study have comprised of 3 steps in user-based CF to make a prediction for each student as follows:

Step 1: Calculate similarity between the active student S_a and every other user by using Pearson correlation, cosine similarity, and Euclidian distance.

Step 2: Based on their similarity scores, various set of k students, most similar to active student S_a is then selected.

Step 3: Prediction for grade student S_a will receive from the course i is generated by using grades of course i that k similar neighbors have already taken.

Table 1. Example of similarity scores for student S_1

Top N neighbors	Similarity Calculation Method		
	Pearson	Cosine	Euclidean
1	025: 0.3033	025: 0.9466	023: 0.2450
2	010: 0.2843	013: 0.9429	041: 0.2297
3	013: 0.2393	010: 0.9427	055: 0.2240
4	073: 0.2205	023: 0.9408	067: 0.2240
5	102: 0.2121	065: 0.9400	036: 0.2222
6	064: 0.2102	068: 0.9396	040: 0.2188
7	022: 0.2072	073: 0.9396	052: 0.2188
8	023: 0.2065	022: 0.9395	004: 0.2171
9	041: 0.2040	014: 0.9392	082: 0.2171
10	075: 0.2033	019: 0.9386	046: 0.2139

Table 1. shows an example of similarity scores for student S_1 obtained by various approach. The result is slightly different for Pearson correlation and cosine similarity methods. For Pearson correlation method, top 3 most similar students are student S_{25}, S_{13}, and S_{10} with similarity scores 0.9466, 0.9249 and 0.9427, respectively. The result from cosine similarity method depicts that top 3 most similar students are student S_{25}, S_{10} and S_{13}, respectively. On the other hand, top 3 most similar students form Euclidean distance are student S_{23}, S_{41}, and S_{55}.

Once similarities for each student are obtained, the performance of each student who enrolled in semester 2, 2015 has been predicted as show in Table 2.

Table 2. Example of grade prediction for student S_1 with different similarity approach

Method	Neighbors Size (N)				
	25	30	35	40	45
Subject: IS203 Real Grade: 2(C)					
Pearson	2 (1.85)	2 (1.85)	2 (1.85)	2 (1.85)	2 (1.85)
Cosine	2 (1.74)	2 (1.74)	2 (1.77)	2 (1.78)	2 (1.79)
Euclidean	2 (1.86)	2 (1.86)	2 (1.86)	2 (1.87)	2 (1.87)
Subject: IS306 Real Grade: 2.5(C+)					
Pearson	2 (1.90)	2 (1.88)	2 (1.87)	2 (1.87)	2 (1.87)
Cosine	2 (1.93)	2 (1.87)	2 (1.83)	2 (1.86)	2 (1.83)
Euclidean	2 (1.87)	2 (1.86)	2 (1.85)	2 (1.86)	2 (1.85)

3.2. *Performance evaluation*

The performance evaluations were conducted using accuracy measure and root mean square error (RMSE) obtained by Eq.(6) and Eq.(7), respectively.

$$Accuracy = \frac{\sum Corrected \quad Answer}{|Subjects| \times |Users|} \times 100 \qquad (6)$$

$$RMSE = \sqrt{\frac{1}{n}\sum_{i=1}^{n}(\hat{Y}_i - Y_i)}^{2} \qquad (7)$$

where $\hat{Y}_i$ is a predicting value of subject i and Y_i is a real value of subject i.

4. Experiment

We compared the predicted grades with the actual grades of students who enrolled in semester 2, 2015. The performance of each approach is compared as shown in Table 3. In our experiment, Pearson correlation achieves the best accuracy. There are hardly different between Pearson correlation and Euclidean distance method.

Table 3. Comparison of accuracy for each method

Similarity	Neighbors Size (N)				
Approach	25	30	35	40	45
Pearson	0.42	0.42	0.42	0.42	0.42
Cosine	0.35	0.35	0.37	0.39	0.38
Euclidean	0.42	0.42	0.41	0.42	0.42

Since the A-F letter grades were converted to the 4–0 scale, which is actually discrete. Then, the result of prediction has been compared to real performance of student which has been removed from the experiment data. However, letter grades come from marks range such as 90-100 for A, 85-89 for B+. It means that with only 1 mark different, student who has mark at 89 will get grade B+ while student with mark at 90 will get grade A. Therefore, the comparison was relaxed in the boundary of deviation error, 0, and 0.5. By

(i) Error deviation 0 means the result of prediction have to exactly match to the real performance of student, and

(ii) Error deviation 0.5 means the result of prediction will be counted as corrected if it differs from the real performance of student less than or equal to 0.5, as shown in Table 4.

Table 4. Grade converted scale with tolerance 0.5

Predicting Scale	University grade (real student performance)
0	F
1	D or D+
1.5	D or D+ or C
2	D+ or C or C+
2.5	C or C+ or B
3	C+ or B or B+
3.5	B or B+ or A
4	B+ or A

The corrected answers have been taking to calculate the average of accuracy and root mean square error, as shown in Table 5 and 6.

Table 5. Comparison of accuracy with tolerance ±0.5

Similarity	Neighbors Size (N)				
Approach	25	30	35	40	45
Pearson	0.84	0.83	0.83	0.83	0.83
Cosine	0.83	0.84	0.83	0.83	0.85
Euclidean	0.83	0.83	0.83	0.83	0.83

Table 6. Comparison of RMSE with tolerance ±0.5

Similarity	Neighbors Size (N)				
Approach	25	30	35	40	45
Pearson	0.54	0.55	0.54	0.54	0.54
Cosine	0.56	0.55	0.56	0.55	0.54
Euclidean	0.54	0.54	0.54	0.54	0.54

References

1. S. Xiaoyuan and K. M. Taghi, A survey of collaborative filtering techniques, *Advances in Artificial Intelligence archive* (2009)
2. M. P. O'Mahony and B. Smyth, A recommender system for on-line course enrolment: an initial study, *In Proceedings of the 2007 ACM conference on Recommender systems* (2007), pp. 133–136.
3. M. Sheehan and Y. Park, pGPA: a personalized grade prediction tool to aid student success. *In Proceedings of the sixth ACM conference on Recommender systems* (2012). pp. 309–310
4. H. Bydžovská, Student Performance Prediction Using Collaborative Filtering Methods. In C. Conati, N. Heffernan, A. Mitrovic, & M. F. Verdejo (Eds.), *Artificial Intelligence in Education* (2015), pp. 550–553. Springer International Publishing.
5. A. Polyzou and G. Karypis, Grade prediction with models specific to students and courses, *International Journal of Data Science and Analytics* (2016)
6. S. Mack, L. Jaime and R. Huzefa, Next term grade prediction, *Proceedings of the 2015 IEEE International Conference on Big Data* (2015), pp.970-975
7. H. Bydžovská, A comparative analysis of techniques for predicting student performance, *In Proceeding of the 9th International Conference on Education Data Mining* (2000), pp. 306–311.
8. N. Thai-Nghe, L. Drumond, A. Krohn-Grimberghe and L. Schmidt-Thieme, Recommender system for predicting student performance, 1st Workshop on Recommender Systems for Technology Enhanced Learning (2010), pp. 2811-2819.

An improved detection method for railway fasteners

Jiwu Wang[1]
School of Mechanical, Electronic and Control Engineering, Beijing Jiaotong University
Beijing 100044, China[1]

Yan Long[1]
School of Mechanical, Electronic and Control Engineering, Beijing Jiaotong University
Beijing 100044, China[1]

Sugisaka Masanori [2]
Alife Robotics Corporation Ltd, Japan and Open University, United Kingdom[2]
E-mail: jwwang@bjtu.edu.cn; ms@alife-robotics.co.jp

Abstract

Aiming at the disadvantages of low efficiency and poor stability of the existing methods of fastener detection, this paper proposes a method of fastener detection based on template matching. Firstly, the image is processed by noise reduction, this method does not need to be based on histogram can match template directly. We choose a standard fastener image as template, read template firstly, then slide the image blocks on the input image to match the template and the input image. Experimental results show that this method can effectively detect the flaw, deformation and obstacles of railway fastener occlusion. This method has a fast matching speed and a good robustness, it's detection accuracy is up to 96%

Keywords: Fastener detection, template matching, trigger device.

1. Introduction

Railway fastener is used to tightly fixed tracks to the sleepers, as an important part of the railway system, plays an important role in ensuring the high-speed running of the railway train. At present, with many kinds of literature are used as the detection method of fastener. Ça˘glar Aytekin, Yousef Rezaeitabar et al[1] using a method which fuse various methods based on pixel-wise and histogram similarities. The method has a large amount of calculation and low accuracy. Xavier Gibert, Vishal M. Patel et al[2] proposed a method of railway fastener state detection which is based on the HOG feature and PCA algorithm. This method need to calculate the histogram of each image, a large amount of calculation, and a large number of training. The efficiency of this method is not high. Liu Manhua, Yang Jinfeng et al[3] take use of directional field algorithm to extract parts of the image features, and then do the template matching. This method has higher computing speed, but higher false detection rate and low accuracy. Stella, Mazzeo et al[4]and Marino Distante et al[5] using Wavelet analysis and, Multilayer Perceptron Neural classifiers to detect hexagon Al-headed bolts (a kind of fastener reveals the presence/absence), of the fastener bolts with high detection and classification rate, but that is not applicable to our situation.

Because railway fastener has a complex background. Characteristics of fastener has a obvious difference from characteristics of track, subgrade and sleepers. distinct characteristics.

Considering the shortage of existing methods, this paper proposes a new method for fastener detection. Using image and standard template matching method. Calculate the similarity between the template and the template. When the threshold value is beyond a given threshold, the fastener can be identified as missing, deformed or blocked.

2. Fsterner detection system design

Fastener detection system is mainly composed of the bottom fastener image acquisition device and the software processing system. Fastener image acquisition device is mainly responsible for accurate, complete, clear to capture the image of each fastener. Specific devices such as figure 1:

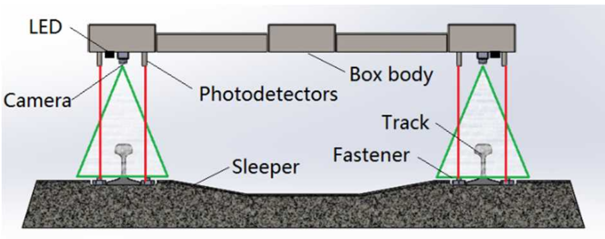

Fig 1. Fastener image collecting device

LED light source to provide the system with sufficient brightness and uniform light, reducing the impact of light and weather on the picture quality. A high speed industrial camera with a high frequency can be guaranteed to capture a clear image even in the case of a vibration. Photoelectric sensor is used as the trigger sensor of the fastener. When the train through each fastener, the sensor input a signal to the control system, the control system output a signal to the camera, shooting a pair of images. In this way, we can ensure that each image can only be collected to a complete image of the fastener. To avoid the image caused by the false detection and miss detection conditions. Main control board and circuit inside the box body.

3. Fastener detection algorithm

The method for detecting the fastener is as follows: select an image of the complete fastener on the actual line as a template, and the template is sliding from the upper left corner to the lower right corner of the image. Calculate the similarity of each location. Match The best match position is the fastener position. If the acquisition image size is W*H and the template size is w*h, the output image size is (W-w+1) * (H-h+1). The coordinates of a pixel point on the image acquisition image is (x, y), and the coordinate value of a pixel point on the template image is (x ', y'). T (x ', y') represents the position of the template (x ', y') of the pixel value. I (x ', y') representation (x ', y') to cover the pixel value of the corresponding point on the image. R (x,y) represents the final calculation results. The following algorithms are given in this paper:

SQDIFF NORMED:

$$R(x,y)=\frac{\sum_{x',y'}\left(T(x',y')-I(x+x',y+y')\right)^2}{\sqrt{\sum_{x',y'}T(x',y')^2-I(x+x',y+y')}}$$

This kind of method uses the square difference to match, the best match is 0 but if the match is bad, the match value is bigger.

CCORR NORMED:

$$R(x,y)=\frac{\sum_{x',y'}\left(T(x',y')\cdot I'(x+x',y+y')\right)}{\sqrt{\sum_{x',y'}T(x',y')^2\cdot\sum_{x',y'}I'(x+x',y+y')^2}}$$

This kind of method uses the multiplication operation between the template and the image. Therefore, the larger number of representative matching degree is higher. 0 represents the worst matching effect.

CCOEFF NORMED:

$$R(x,y)=\frac{\sum_{x',y'}\left(T'(x',y')\cdot I'(x+x',y+y')\right)}{\sqrt{\sum_{x',y'}T'(x',y')^2\cdot\sum_{x',y'}I'(x+x',y+y')^2}}$$

In the algorithm mentioned above

$$\mathrm{T}'(x',y')=T(x',y')-1/(w\cdot h)\cdot\sum_{x'',y''}T(x'',y'')$$

$$\mathrm{I}'(x+x',\ \mathrm{y}+\mathrm{y}')=I(x+x',y+y')-1/(w\cdot h)\cdot\sum_{x'',y''}I(x+x'',y+y'')$$

This method can match the relative value of the template to the average value of the template and the image to the mean value of the template. 1 epresents the perfect match result, and the -1 represents a bad match, and the 0 represents no correlation.

4. Experiments

Please provide a shortened running head (not more than four words, each starting with a Capital) for the title of your paper. This will appear with page numbers on the top right-hand side of your paper on odd pages.
Using the above three algorithms, we use 77*137 pixels of the fastener image template, 300*400 image matching, the matching effect as shown in figure:

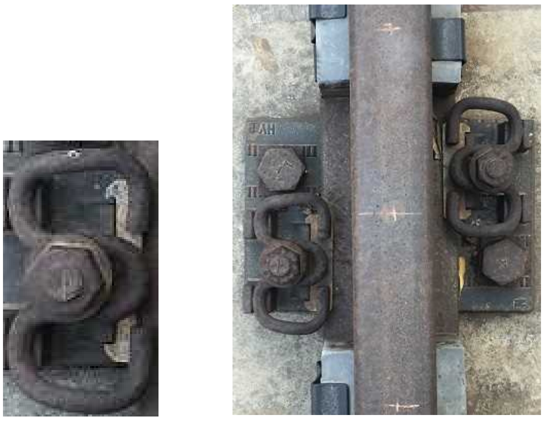

a b

Fig 2. (a) is template image, (b) is collecting image.

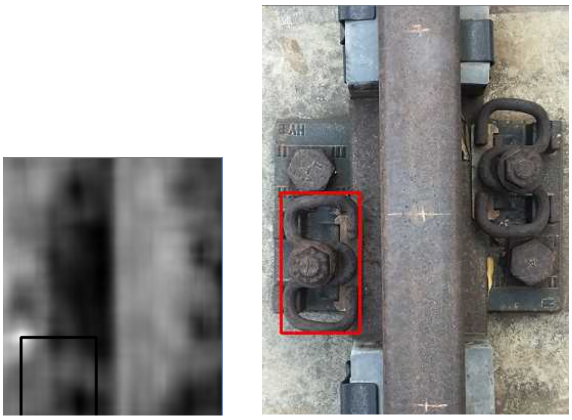

C d

Fig 3. (c) is calculation result image, (d) is matching result image

Using the above three algorithms, when the output value is close to the ideal result, we judge for the fastener is normal, when the output result is abnormal, we judge the fault or obstructions to fastener. Due to the small number of samples, we use the method of artificial judgment to judge. In the follow-up work, we will use the PCA algorithm to classify and identify, in order to achieve the most effective. This experiment for 200 pictures, including normal picture 177, abnormal picture 23, including the fastener deformation 8, lost 4, the barrier 11, the statistics of the three algorithms matching results are as follows:

Algorithm	Accuracy	False detection	Missing detection
SQDIFF NORMED	75%	9%	16%
CCORR NORMED	89%	2%	9%
CCOEFF NORMED	99%	0	1%

5. Summary

By using these three methods, template matching effect can be achieved. From the SQDIFF NORMED matching method to the CCORR NORMED matching method, and then to the CCOEFF NORMED matching method, the matching accuracy is improved, but the corresponding calculation time is also increased gradually. Due to the large size of the fasteners detecting data, we require the higher accuracy of matching result. The NORMED CCOEFF algorithm is more suitable for the detection of fasteners. We will further optimize the efficiency of the algorithm in the following work, select the high performance computer configuration, in order to improve the computational efficiency.

.

References

1. Ça˘glar Aytekin, Yousef Rezaeitabar, Sedat Dogru, and ˙Ilkay Ulusoy, Railway Fastener Inspection by Real-Time Machine Vision, *Systems, Man, and Cybernetics, Part C: Applications and Reviews, IEEE Trans.* on, 45(7):1101-1107, 2015. 7
2. Xavier Gibert, Vishal M. Patel, and Rama Chellappa, Robust Fastener Detection for Autonomous Visual

Railway Track Inspection, *IEEE Winter Conference on Applications of Computer Vision*, IEEE 2015:694-702.
3. Jinfeng Yang, Manhua Liu, Hui Zhao and Wei Tao, An Efficient Image-based Method for Detection of Fastener on Railway, *International Conference on Test and Measurement* 2010:731-737.
4. Stella, E., P. Mazzeo, et al, Visual recognition of missing fastening elements for railroad maintenance, Intelligent Transportation Systems, *IEEE 5th International Conference*, 2002 Proceedings:94-99.
5. Marino, F., A. Distante, et al, A Real-Time Visual Inspection System for Railway Maintenance:Automatic Hexagonal-Headed Bolts Detection, *System, Man, and Cybernetics, Part C: Applications and Reviews, IEEE Trans. on,* 37(3):418–428, 2007.

A New Tool to Access Deep-Sea Floor "Sampling-AUV"

Kazuo Ishii
Dept. of Intelligence Systems, Kyushu Institute of Technology,
2-4 Hibikino, Wakamatsu, Kitakyushu, Fukuoka, Japan
E-mail: ishii@brain.kyutech.ac.jp

Takashi Sonoda
Dept. of Intelligence Systems, Kyushu Institute of Technology,
2-4 Hibikino, Wakamatsu, Kitakyushu, Fukuoka, Japan
E-mail: t-sonoda@brain.kyutech.ac.jp

Yuya Nishida
Center for Socio-Synthesis, Kyushu Institute of Technology,
2-4 Hibikino, Wakamatsu, Kitakyushu, Fukuoka, Japan
E-mail: ynishida@lsse.kyutech.ac.jp

Shinsuke Yasukawa
Dept. of Intelligence Systems, Kyushu Institute of Technology,
2-4 Hibikino, Wakamatsu, Kitakyushu, Fukuoka, Japan
E-mail: s-yasukawa@brain.kyutech.ac.jp

Tamaki Ura
Center for Socio-Synthesis, Kyushu Institute of Technology,
2-4 Hibikino, Wakamatsu, Kitakyushu, Fukuoka, Japan
E-mail: ura@lsse.kyutech.ac.jp

Keisuke Watanabe
Dept. of Navigation and Ocean Engineering, Tokai University,
3-20-1 ORido Shimizuku, Shizuoka, Shizuoka, Japan
E-mail: keisukejapan@gmail.com

Abstract

Underwater robot is one of the important research tools to explore deep-sea. Especially, Autonomous Underwater Vehicles (AUVs) attract attentions as new tools because they are un-tethered and suitable for wide area observation. As the next generation AUV, we have been developing a Sampling-AUV that can dive into deep-sea and bring back marine creatures using a mounted manipulator. In the mission, the AUV transmits the deep-sea floor images to the support ship using acoustic communication, and the operator selects the marine creatures to sample and bring back them. In this talk, we introduce the new AUV, the underwater manipulator and image processing techniques for sampling.

Keywords: Sampling-AUV, Next Generation AUV, Image Processing.

1. New Tool to Survey Seafloor "Sampling-AUV"

Discoveries such as mineral resources, energy resources and marine lives in the deep-sea give deep impacts on our society and have good reasons to attract researchers in various fields. In spite of attractive discoveries, we are still unable to get detailed information about the mechanism of ecological system, because the deep-sea is an extreme environment with special features of high pressure, darkness and radio attenuation. Recently, underwater robots are employed to observe deep-sea floor as useful tools[1,2], and they are mainly classified as Human Occupied Vehicle (HOV), Remotely Operated Vehicle (ROV) and Autonomous Underwater Vehicle (AUV) depending on the extent of autonomy and mounted facilities.

Especially, AUV is expected as a new tool because they can cruise long distance without the limitation of tethered cable, suitable for wide area observation and as a stable observation platform[3-5]. However, as the disadvantages, AUV should be equipped with high autonomy and various devices such as onboard high specification computers, expensive sensory system for navigation (INS, DVL) and actuators for motion control, and special devices of mission-dependent sensors[6].

As one of the next generation missions, AUVs are required to sample deep-sea marine life such as crabs, shellfish, sea cucumber or deep-sea floor sediments which include a lot of micro-organisms. However, the sampling mission is not easy to be performed full-autonomously by the AUV, because the AUV has difficulty to decide what should be the interesting targets or situation, such as spawning to sample marine lives.

We have been developing a sampling system using AUV which incorporates the interaction between the robot and human, a man-machine system. The strategy of developing sampling system consists of several steps which are; (i) deep-sea floor image acquisition, (ii) interesting image selection, (iii) image transmission to research ship, (iv) checking image by operator, (v) sending a command to AUV to go back to the interesting target area ordered by onboard operators, (vi) sampling targets, and (vii) surfacing to bring back samples to the research ship. The mission scenario is shown in Fig.1.

We have already presented steps (i), (iii), (iv) and (v) which provides detailed discussion about image enhancement, data compression and reconstruction method, experimental study of image transmission using AUV with the aid of acoustic transmitter and receiver[7] and going back to the area where the image was taken[8]. However, AUV was not able to transmit all the taken images through acoustic communication due to narrow transmission bandwidth. Therefore, AUV has to select the interesting image which includes marine lives automatically before transmitting.

In this research, we propose the next generation AUV "Sampling-AUV".

Fig.1 The mission Scenario of Sampling-AUV

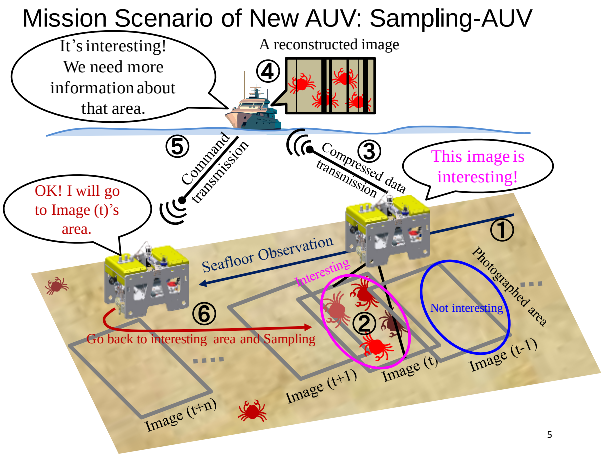

2. TUNA-SAND2

The technical issues are shown in the followings.

2.1. *Hardware*

- New AUV design for sampling
- Sampling device: Underwater manipulator & hand
- Acoustic communication device
- Camera system
- etc...

2.2. *Software*

- Motion control & navigation
- On-line image processing
- Sea-floor image enhancement
- Curious image selection
- Image compression
- Acoustic data transmission
- Sampling device control
- Visual servo for target tracking

1. etc...

2.3. *Design of TUNA-SAND2*

The developed Sampling-AUV is illustrated in Fig.2, and shown in Fig.3.

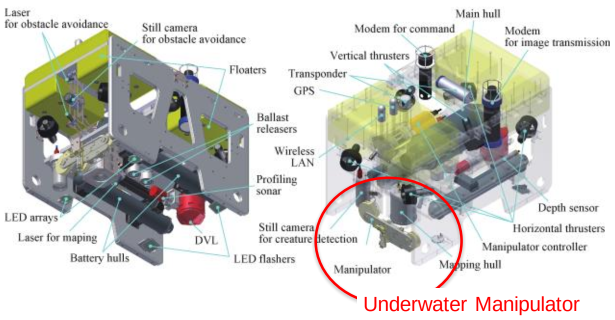

Fig.2 Overview of TUNA-SAND2.

Fig.3 The Developed Sampling-AUV
“TUNA-SAND2”

Acknowledgement

This research is supported by JST CREST “Establishment of core technology for the preservation and regeneration of marine biodiversity and ecosystems”.

References

1. Y. Junku, T. Ura , G. Bekey, *Underwater robots*, Springer Science & Business Media, (2012)
2. Whitcomb, Underwater robotics: Out of the research laboratory and into the field, *Proc. of IEEE/ICRA'00*, (2000)
3. Y. Nishida, T. Ura, T. Sakamaki, J. Kojima, Y. Ito , K. Kim, “Hovering Type AUV “Tuna-Sand” and Its Surveys on Smith Caldera in Izu-Ogasawara Ocean Area, *Proc. of IEEE/OCEANS2013*, (2013)
4. T. Maki, Y. Sato, T. Matsuda, R. T. Shiroku, T. Sakamaki, “AUV Tri-TON 2: An intelligent platform for detailed survey of hydrothermal vent fields,” *Proc. of IEEE/AUV2014*, (2014)
5. Y. Nishida, K. Nagahashi, T. Sato, A. Bodenmann, B. Thornton, A. Asada, T. Ura, Development of an autonomous underwater vehicle for survey of cobalt-rich manganese crust, *Proc. of IEEE/OCEANS2015*, (2015)
6. Y. Nishida, T. Ura, T. Nakatani, T. Sakamaki, J. Kojima, Y. Itoh and K. Kim, Autonomous Underwater Vehicle “Tuna-Sand” for Image Observation of the Seafloor at a Low Altitude, *Journal of Robotics and Mechatronics*, Vol.26, No.4, pp.519-521, 2014.

An effective method for detecting snatch thieves in video surveillance

[1]Hiroaki Tsushita and [2]Thi Thi Zin

[1]*Graduate School of Engineering, University of Miyazaki, Japan*
[2]*Faculty of Engineering, University of Miyazaki, Japan*
E-mail:hc11046@student.miyazaki-u.ac.jp, thithi@cc.miyazaki-u.ac.jp

Abstract

Nowadays, a tremendous amount of accidents and terrorisms has been occurred all over the world no exception in Japan. Thus, detection of suspicious activities in public areas such as railway stations, shopping malls and many other areas using video surveillance becomes important. However, very little has been achieved regarding real-time event recognition of two person interactions such as snatch theft events. Moreover the way of snatch theft has been increasing like using a motorcycle and so on. In this paper, we propose an effective method for detecting the snatch theft event between two persons. Specifically, the proposed method consists of several steps: pedestrian tracking, feature computation and snatch theft detection. For feature computation, shape and motion features are used. To confirm the validity of proposed method some experimental results in a various situations are shown by using some collected video sequences.

Keywords: snatching, detecting, intersection, feature extraction,

1. Introduction

In modern times, a variety of crimes have reported from the daily news. Some of news includes the events of theft and theft damages. In this paper, we have focused on "snatching" among a great number of thefts. Currently a number of surveillance cameras are installed in preparation for detecting a crime theft. Active detections of incidents are also required to reduce costs of security issues. There is a limit to the number of securities by people, and finding the suspicious behavior in the surveillance camera in real-time is leading to prevention of incidents and also to increase the event detection rate [1].

The main purpose is to detect the theft, such as snatching or pickpocketing in various situations. The human that do the criminal acts such as theft, there are some features different from the ordinary passengers.

The automatically detecting of suspicious person by using security camera has been processing practically in the environment that is not crowded. But it is a little hard for detection in case of distinguishing immediately; it is necessary to track person for a long time.

In addition, Tokyo Olympic Games will be held in 2020. We estimate that a great number of tourists come to Japan for it from all over the world. Obviously, more security measures should be taken with the aids of surveillance system for preventing and detecting various type of crimes. In such aspect, we expect that the advance of this research will be helpful of preventing snatching in crowded environments [2].

2. The Proposed Method

In this section, we propose an effective method for detecting snatch thieves. The overall system flowchart is shown in Fig.1.The system includes four components as shown in the figure. Among then we will emphasize on feature extraction process in this paper [3].

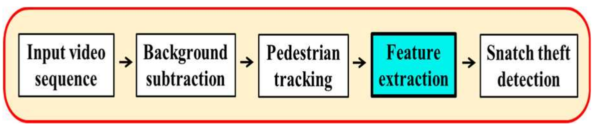

Fig.1. The overall flowchart to detect snatching

2.1. *Background subtraction*

Foreground image is made by difference between background and input image. Therefore we removed some silhouettes except for the person by determining a threshold. It is not accurately extracted if we calculate the amount of white pixel without removing of the shadow of person silhouette. That's why we cut the silhouette about 10% from the bottom of bounding box (BB). The process result is shown in Fig. 2.

2.2. *Feature extraction*

The feature extraction step is main process in our proposed system. It is possible to classify abnormal behaviors by extracting a person from input images and finding the features of person. Generally speaking, there existed two ways on what to extract features. They are appearance features and motion features. There are some contacts like intersection between two persons when the snatching has happened. An example is shown in Fig.3. We compared with the intersection events before and after, and the value of average each 15 frames before and after events was used. Then the change amount compared with before and after, is used as feature value (*FV*). Moreover these feature values are divided by height of BB for normalization [4].

(i) *Appearance feature*

We used the binary image conversed from original one, then focused on the BB of each person exists in frame. And we created histogram in terms of the silhouette (amount of white pixels) of a person in BB. As seen in Fig.4, shape of histogram is quite different before and after snatching event.

This appearance feature value (FV_A) and difference value (D_A) between before and after event can be defined by:

$$FV_A = \frac{total\ number\ of\ white\ pixel\ in\ BB}{height\ of\ BB} \quad (1)$$

$$D_A = \left| FV_A(after) - FV_A(before) \right| \quad (2)$$

(ii) *Motion feature*

We found the point of head after extract the silhouette of human. To compare with consecutive frames, it is measured the moving distance in each person by using the coordinates of head point. We figure that there is difference in moving distance between running person or riding bicycle and pedestrian. The difference between running person and pedestrian is shown in Fig.5. The person with yellow box is original position. On the other hand, the person with red box is the position after two seconds.

This motion feature value (FV_M) and difference value (D_M) between before and after event can be defined by:

$$FV_M = \frac{moving\ distance\ of\ head\ point}{height\ of\ BB} \quad (3)$$

$$D_M = FV_M(after) - FV_M(before) \quad (4)$$

(a) original image (b) after cutting 10 percent

Fig.2. Removal of the shadow of person silhouette

(a) before intersection (b) intersecting (c) after intersection

Fig.3. Flow of snatching with intersection

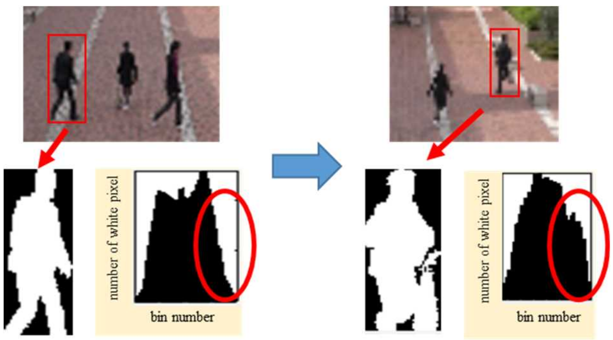

(a) before snatching (b) after snatching

Fig.4. Difference of human silhouette histogram

(a) Walking pattern (b) Running pattern

Fig.5. Difference of moving distance

2.3. *Decision method of snatching*

We used appearance features and motion features to judge that snatching happens. In this time, we found each parameter of motion feature and appearance feature by using three training videos. The parameters were used as indicator of judgement in each features. We defined that the threshold of appearance feature value is $Th_A = 10$, the threshold of motion feature value is $Th_M = 0.049$.

We extracted two feature values, appearance and motion, of each person in video, and compare with the threshold we defined. By comparing, we can confirm some actions with person happens or not.

The way of judging action is different between each features. From next section, we will consider some criterion to classify the events by using the outcomes of comparing features.

(i) *Judging way of appearance feature*

In appearance feature, the absolute value was used to classify whether something happens or not. If the feature value is more than threshold ($Th_A = 10$), it can be classified as something happens. In this case, the two persons are to be differentiated between victim and suspect depending on sign of feature value. It is shown by following equation. The flow of classification is shown in Fig.6. Then we also defined that "Something happen" is A1, and "Nothing happen" is A2 for later process.

Then we also classify which person is a victim or a suspect. After process of classification whether something happens or not, we focus on the feature value without absolute value. If the feature value of appearance takes negative value, the person can be a victim because he lost the silhouette of bag in binary image. On the other hand, if the feature value of appearance takes positive value, the person can be a suspect because he gain the silhouette of bag by snatching bag. This classification can be defined by:

$$\begin{cases} Victim & if\ FV_A < 0 \\ Suspect & if\ FV_A > 0 \end{cases} \tag{3}$$

(ii) *Judging way of motion feature*

In motion feature, we found the change of velocity of person between before and after event. If the feature value is more than the threshold ($Th_M = 0.049$), the velocity of person increases compare with before intersection. This feature was used to classify as motion feature. The flow of classification is shown in Fig.7. Then we also defined that "Speed up" is M1, and "No change" is M2 for later process.

There are some patterns by using the way is explained previous section. We estimate snatch theft by using some patterns. The overview is shown in Fig.8.

3. Experimental Result

We used two video sequences for training and four test video sequences for test in this experiment. They were taken as demonstration in our university. Two training videos are data with snatching event and without snatching event. In test video sequences, Test 1 and Test 2 have the snatching event with bicycle, and Test 3 and Test 4 have the snatching events without bicycle. If the victim with bicycle chases suspect after snatching like Test 1 and Test 2, he doesn't have much difference of feature. So these feature value estimated wrong classification. And the feature value in Test 3 does not have big change for classifying, it is false recognition. Table 1 shows the results from four test videos.

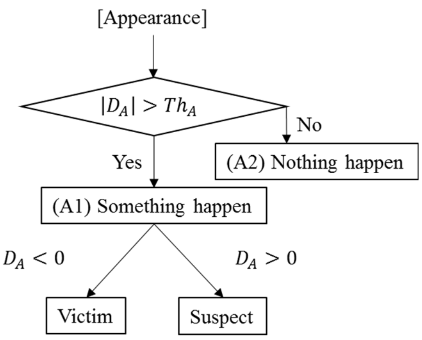

Fig.6. The flowchart of classifying of appearance feature

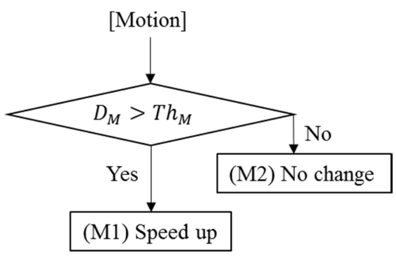

Fig.7. The flowchart of classifying of motion feature

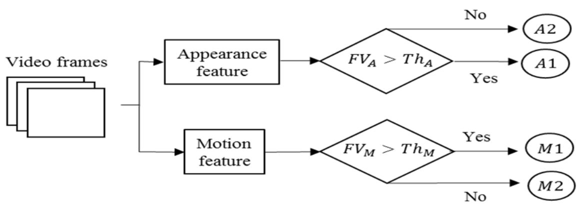

Fig.8. Overview of this method

Table 1 Result of classification on each video

Video	Victim		Suspect		Result
	Appearance	Motion	Appearance	Motion	
Test 1	○ (A 1)	× (M 2)	○ (A 1)	○ (M 1)	○
Test 2	○ (A 1)	× (M 2)	○ (A 1)	○ (M 1)	○
Test 3	× (A 2)	○ (M 1)	○ (A 1)	○ (M 1)	○
Test 4	○ (A 1)	○ (M 1)	○ (A 1)	○ (M 1)	◎

From the result of Table 1, we could get almost correct classification result in the test videos. But the result of Test 1 and 3 figure that it is just possibility that snatching has happened in sequence.

To get 100 percent of possibility that snatching has happened, we add another feature of direction which person goes into appearance features. Because the bag might be hidden to person shadow depends on the position of surveillance camera. In this case, the feature value of bag silhouette in appearance feature does not come up well. An example of this case is shown in Fig.9. (a) is the scene of before snatching, and the bag is seen from camera side. On the other hand, Fig.9 (b) is the scene of after snatching, then the bag position is opposite side from camera. So it is hidden to person shadow.

From this if the direction of moving changes other course after intersection, this feature also gets a clue to detect snatching.

4. Conclusions

In this paper we had proposed and tested an effective method for detecting an even of snatch thieves by using mainly two features, ratio of the amount of white pixels in bounding box and moving distance of head coordinates. Then we found that it needs another feature, direction of moving, to detect snatching thieves events.

Moreover the way of snatch thieves is more variety in recent times like using a bike or car. And the snatch thieves happens not only day time but also night time. Thus, our proposed method will be useful of preventing snatching in various situations and ways.

(a) before snatching (b) after snatching

Fig.9. Difference of bag position

Acknowledgements

I would like to express my sincere thanks and appreciation to all persons who contributed towards the success of this my paper. I would like to show my greatest appreciation to my supervisor Professor Thi Thi Zin whose comments and suggestions were innumerably valuable throughout my study.

References

1. Henri Bouma, Jan Baan, et al, "Automatic detection of suspicious behavior of pickpockets with track-based features in a shopping mall", *Proc. SPIE 9253, Optics and Photonics for Counterterrorism, Crime Fighting, and Defence X; and Optical Materials and Biomaterials in Security and Defence Systems Technology* XI, 92530F, Oct. 2014.
2. Surya Penmetsa, Fatima Minhuj, "Autonomous UAV for Suspicious Action Detection using Pictorial Human Pose Estimation and Classification", *Electronic Letters on Computer Vision and Image Analysis,* vol. 13, no. 1, pp.18-32, 2014.
3. Jasper R. van Huis, Henri Bouma, et al, "Track-based event recognition in a realistic crowded environment", *Proc. SPIE 9253, Optics and Photonics for Counterterrorism, Crime Fighting, and Defence X; and Optical Materials and Biomaterials in Security and Defence Systems Technology XI*, 92530E, Oct. 2014.
4. Thi Thi Zin, J. Kurohane, "Visual analysis framework for two-person interaction", *Proc. of The 4th IEEE Global Conf. on Consumer Electronics* (GCCE 2015), Osaka, Japan, pp. 519-520, 2015.

Color and Shape based Method for Detecting and Classifying Card Images

Cho Nilar Phyo[1], Thi Thi Zin[1], Hiroshi Kamada[2], Takashi Toriu[3]
[1]*Graduate School of Engineering, University of Miyazaki, Miyazaki, Japan*
[2]*Graduate School of Engineering, Kanazawa Institute of Technology, Ishikawa, Japan*
[3]*Graduate School of Engineering, Osaka City University, Osaka, Japan*
nc16004@student.miyazaki-u.ac.jp, thithi@cc.miyazaki-u.ac.jp

Abstract

This paper proposes an effective method for detecting and classifying card images by using color and shape features. We extract the card color area using color information and remove low possibility regions based on shape feature. Then, we classify the image by taking classroom size and camera distance. In order to confirm the proposed method, we conduct the experiments with our own videos. Our experimental results show that the proposed method is very promising compared to some existing methods.

Keywords: color segmentation, shape classification, interactive e-learning.

1. Introduction

In today world, the education system is rapidly changing and the video conferencing is widely used for education due to its enormous advantages. The video conferencing based e-learning system can make the classroom to be geographically limitless and reduce the travel cost and time for the lecturers. One weakness of the traditional video conferencing based e-learning system is the difficulty of getting student's feedback when it is using in enlarge classroom. The computer vision based interactive e-learning system can solve that weakness by supporting student-lecturer interaction during the lecture time which is the most important thing in teaching system. In the proposed methods, we use color and shape based color card detection and classification method for the implementation of interactive e-learning system.

We describe some related work of shape based object identification and color based segmentation in section 2 and the detail process of the proposed method in section 3. Then we describe some experimental results in section 4 and the conclusions of the proposed methods is explained in section 5.

2. Related Works

The color based object segmentation and shape based object identification are widely used in the area of computer vision research. The authors proposed[1] that pointed pattern based shape information and modified background subtraction to identify the cows for the implementation of automatic cow monitoring system. The authors implement[2] that image retrieval system for trademark images using modified shape based. The object-based retrieval in image and video databases using morphology and histogram based method is described in Ref. 3. One proposed[4] that the segmentation with morphology and relative color for robust road sign recognition.

3. Proposed System

In this system, we will use color cards images to implement the interactive e-learning system in which the students can immediately give feedback over the understanding level of the lecture. So that the e-learning system can become more active and attractive and the lecturer can find the way to explain about the lecture based on the feedback of the students. There include four main components in the proposed system as shown in Fig. 1.

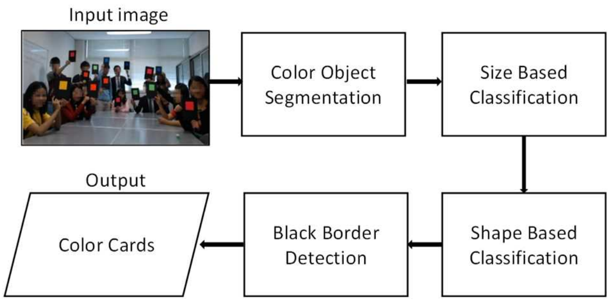

Fig. 1. Overview of the detection and classification of card images

3.1. *Color Object Segmentation*

The first component of the system is segmentation of color object. In the proposed system, we will use HSL color space in order to segment the color object under various illumination changing condition. In HSL color space, H stands for hue that measure the purity of the base color, S stands for saturation that measure the degree of white color embedded in specific color and L stands for lightness. HSL is the non-linear transformation of device-dependent RGB color model and widely used in the color picker systems of many graphical applications because of its convenience for the color perception of human being. We can simply transform HSL from RGB color space by performing the following steps:

(i) Find maximum(Max) and minimum (Min) value in R, G and B component.

(ii) Find L value as describe the following.

$$L = \frac{1}{2}(Max + Min)$$

(iii) Find S value using L value.

$$S = \frac{Max - Min}{1 - |2 * L - 1|}$$

(iv) Find H value using the following equation.

$$H = \begin{cases} \left[60 * \left(\frac{G - B}{Max - Min} \right) \right] \text{mod } 360 & \textit{if} \quad Max = R \\ \left[60 * \left(\frac{B - R}{Max - Min} \right) \right] + 120 & \textit{if} \quad Max = G \\ \left[60 * \left(\frac{R - G}{Max - Min} \right) \right] + 240 & \textit{if} \quad Max = B \end{cases}$$

2.1.1. Color Thresholding

Thresholding is the important task in color segmentation and the performance of the system is depending on the choosing of correct color threshold. In our system, we use two threshold range for defining the card color (pink, yellow, green, blue and orange), one is for day time and another is for the night time. In order to determine the suitable threshold range, we vertically divide the image into two parts and check day time or night time by using the mean intensity of the upper part. If the mean intensity is greater than some threshold, we regard as day time image because the mean intensity of day time image is greater than night time. The result color mask of the segmentation of yellow color region is as shown in Fig.2.

Fig. 2. (a) Input image, (b) Segmentation result of yellow color

3.2. Size Based Classification

The second part of the system is classification of cards object using size information which is taking according to the classroom size. We use two threshold range in order to accuracy detect the card object in both far and near from the camera. To define far and near area, we vertically divide the image into two parts and regards the upper part as far area and the lower part as near area from the camera. Then we generate the equation for finding the size threshold depend on the relationship between 3D and 2D in photograph.

3.2.1. Size Thresholding

In order to find the size threshold, we take the photograph of the card by placing it on 1 to 5 meters' distance from the camera. Then, we count the height pixels of color region as shown in Table 1. Then we generate the equation to estimate the height using the following linear equation.

$y = m * x + b$

where y is the height in pixel, x is the value 1/D, D is the 3D real world distance between the card and camera, m determines the slope of the straight line and b is the interception point of y axis. We get the value of 68 and 3 for parameter m and b. distribution of the height and the straight line equation is shown in Fig. 3. The result color mask is as shown in Fig. 4.

Table 1 Estimated height of color region

Distance (meter)	1	2	3	4	5
1/Distance	1	0.5	0.33	0.25	0.2
height (pixel)	71	37	26	20.0	17
Estimated height	71	37	25.67	20	16.6
Error	0	0	0.33	0	0.4

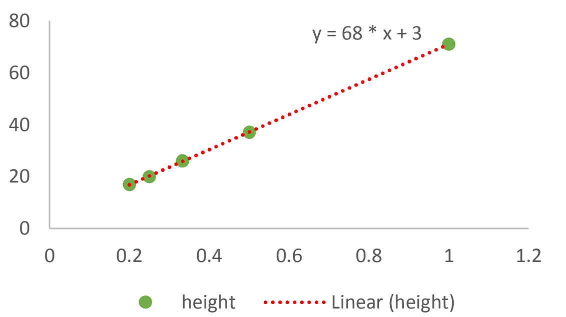

Fig. 3. Linear equation for finding the height of color region

Fig. 4. (a) Input image, (b) Color mask result of size based classification of yellow color

3.3. *Shape Based Classification*

The third component is the classification of card objects based on shape information. We will use the aspect ratio to classify the square color card object. The result of shape based classification is as shown in Fig. 5.

Fig. 5. (a) Input image, (b)Color mask of shape based classification of yellow color.

3.4. *Black Border Detection*

The fourth component of the system is the detection of black border in order to avoid the detection of the other object that have the same color and shape as the color card objects. In Figure 6 (b), we can see that size and shape based classification result blue screen monitor as color card object because the color, size and aspect ratio of monitor is matching with the threshold value. In order to solve those kind of problem, we will use the detection of black border region around the detected color objects. We make the border region of the result of detected object by applying morphological operation. Then we remove the border region whose value is not black color. The result removing non-black border region is shown in Fig. 6.

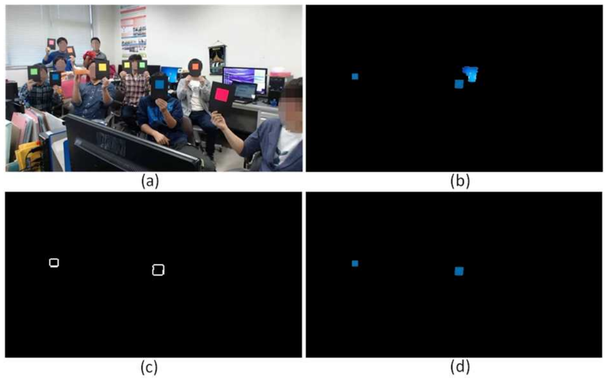

Fig. 6. (a)Input image, (b) Color mask result after size based and shape based classification for blue color, (c)Black border mask (d) Result after black border detection.

4. Experimental Results

We test the proposed system on the self-collecting data taking under the small classroom which includes over 10 students and large classroom which contains around 200 students at both day time and night time. In order to evaluate the robustness of the proposed methods, we also test on the images of complex environment which include the students whose dress's' color is the same as card colors. According to the experimental result, we can see that the proposed method can give accuracy of 100% for small classroom images, 93.46 % for large classroom (day time) images and 88.34 % for large classroom (night time) images which include highlight area. Some experimental results of the proposed method are shown in Fig. 7.

5. Conclusion

In this paper, we proposed color and shape based card images detecting and classifying method that can effectively detect and classify the various color card objects which is very useful in the implementation of the interactive e-learning system. According to experimental results, we found that the proposed methods can correctly detect and classify the card objects on both day time and night time images with accuracy over 90% and the accuracy decrease only at the highlight area of night time image due to the difficulty of segmentation which is the next challenge that will be solved in the future. By using the dynamic threshold calculation methods for finding the size threshold based on the lecture room size, the proposed method can give ubiquitous operation of interactive e-learning system which can process anytime and anywhere in the world.

Acknowledgements

This work was supported by JSPS KAKENHI Grant Number 15K01041.

References

1. K. Sumi, I. Kobayashi and T.T. Zin, Cow Identification by Using Shape Information of Pointed Pattern, *in Proc. 9th Intl. Conf. on Genetic and Evolutionary Computing.*, (Springer-Verlag, New York, 2015), pp. 273-280.
2. T. Iwanaga, H. Hama, T. Toriu, P. Tin and T.T. Zin, A Modified Histogram Approach to Trademark Image Retrieval, *Int. J. of Computer Sci. and Net. Security* **11**(4) (2011) 56-62.
3. T.T. Zin and H. Hama, A Method Using Morphology and Histogram for Object-based Retrieval in Image and Video Databases. *Int. J. of Computer Sci. and Net. Security* **7**(9) (2007) 123-129.
4. T.T. Zin and H. Hama, A robust road sign recognition using segmentation with morphology and relative color, *J. of the Inst. of Image Information and Television Engineers* **59**(9) (2005) 1333.

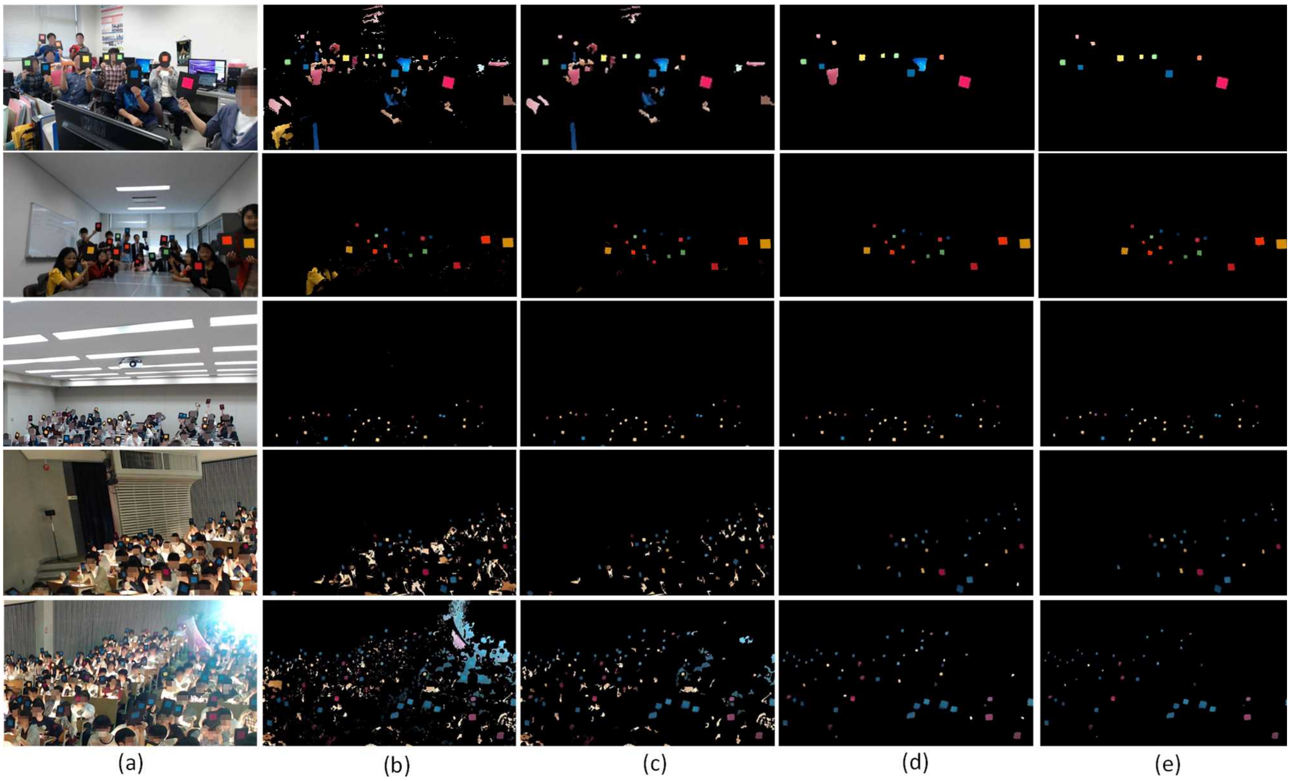

Fig. 7. Some Experimental Results [row 1~2 small class room and 3~5 large class room] (a) Input images, (b) Color segmentation result, (c) and (d) Result of size-based and shape-based classification, (e) Result of combination of color, size, shape and black border detection methods

Automatic Assessing Body Condition Score from Digital Images by Active Shape Model and Multiple Regression Technique

Nay Chi Lynn[1], Thi Thi Zin[2], Ikuo Kobayashi[3]
([1]Graduate School of Engineering, University of Miyazaki, Japan)
([2]Faculty of Engineering, University of Miyazaki, Japan)
[1]naychelynn@gmail.com, [2]thithi@cc.miyazaki-u.ac.jp, [3]ikuokob@yahoo.co.jp

Abstract

Body Condition Score (BCS) of a dairy cow is a magnificent indicator for determining energy reserves of cows. The purpose of this study is to assess BCS of dairy cattle by analyzing cows' rear-view images. In order to do so, we first model shape of cow's tailhead area by using active shape model. Then, angle features are modelled as multiple regression model for estimating scores. The experimental results show that proposed system is promising compared to some existing methods.

Keywords: Body Condition Score, Active Shape Model, Multiple Regression Analysis, Angle features.

1. Introduction

Most of the existing methods for measuring Body Condition Scores of dairy cows have been based on a subjective assessment of tissue reserves of lactating dairy cows.[1] BCS is widely considered as an important factor for management of dairy cattle due to its simplicity and repeatability. Moreover, it can evaluate body fat stores and estimate cumulative energy balance through visual or tactile inspection.[2] Svaluation of BCS is important for analyzing health problems, feed intake, and optimal time interval between calving and first insemination. For cattle, sheep and goats, the scoring systems most commonly used for BCS are numerical scales with 5-point, 6-point, 8-point or 10-point scales. For dairy cows, the BCS is normally a number in a scale that spans from 1 to 5 (0.25 increments) or from 1 to 9 (1 increment). Generally, the score range used by dairy management advisors describes thin animals with receiving lower scores and fat animals with receiving higher scores (1 represents emaciated cows, 5 represents obese cows for a 5- point system). For a certain management of farms, the BCS should be assessed. However, this task is time consuming and observed experts need considerable training and experience. Roii et al. stated[3] that automatic and objective BCS will help to ensure that the cow is in the correct condition for each stage of her annual cycle and correct any deficiencies with appropriate dietary changes.

The aim of the proposed research is to develop a system that models the body shape of a cow from the back view images and then assesses the BCS with observed angle features in score estimation. The rest of the paper is organized as follows: section 2 introduces some related works on approximations for automatic body condition scoring system, section 3 describes system overview with theoretical methods that are mainly applied in this research, section 4 explains how the experiments performed with output results, and finally in section 5, the conclusions and future works are described.

2. Some Related Works

Among the many attempts for estimating body condition scores automatically, the first attempt by Coffey et al., tested[4] using line patterns painted with laser light over the tailhead area of the cows. Some attempts apply digital images or some system used videos and an analysis of the cow's contour and shape that commonly involved. Roii et al., have taken[3] 3D images from the above view view of the cow acquisition of data automatically. Halachmi et al., have also taken[5] thermal images and they made decision that fatter cow's shape are rounder. Bewley et al., use[6] top view images, 23 points and 15 angles are extracted and show a good correlation with their expected score. Bercovich et al., also used[7] the above view images and they use Fourier descriptors method and regression method for the cow signature showing that body condition score can be automatically extracted from those images. Rafel et al. used[8] twenty-two angle features from the rear view images with the classifiers from Weka tool and they showed that their estimation is possibly comparable with difference of two human experts. Nevertheless, currently most dairy farms don't pay so much attention on automatic estimation of BCS in their dairy management. This is because some systems need to preprocess like laser paint or some systems need to install some kind of high cost camera like 3D camera, 3D Kinect camera, thermal camera despite their usefulness. Some commercial application like DeLaval- 2015 has appeared, but its accuracy was not published in a scientific publication in the statement[3]. So, this study will build the BCS estimation system of using simple 2D images by expressing observed accuracy.

3. System Overview

The proposed system for assessing BCS from digital images contains three main components. The preprocessing of the images, the segmentation of the shape and the estimation of the BCS as depicted in fig 1.

3.1. *Preprocessing*

The images for this study were collected from the web. We choose the back shape view of cow images because

Fig.1. Main components of the proposed system.

Ferguson et al., agreed[2] that the score of a cow can be assessed by a human observer with only the rear-end view of the cow.

Out of one hundred and thirty images of different cows, only seventy images are selected because of some background noise and position of the cow (e.g cluttered noise mixing with cow's color, very low resolution, too much variation of pose, etc.). Scores are assessed according to Ferguson et al., evaluation chart that one can see Ref. 3 for details. It is the common system used within the United Kingdom (UKBCS system) using a 0

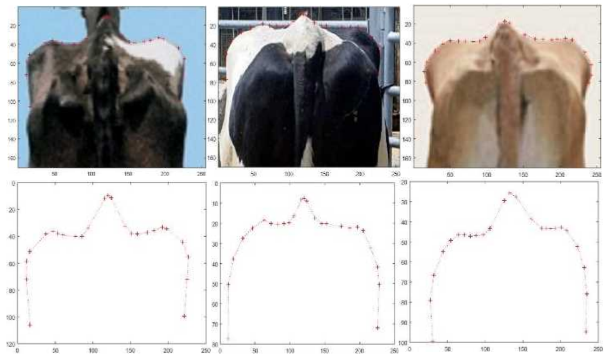

Fig. 2. Cow Images with shape (the upper) and extracted shapes from cow images.

to 5 scale with 0.25 intervals. But in this study, it is observed that scores are ranging from 1.5 to 4.5 with 0.5 increment. Moreover, most frequent scales here are 2, 2.5, 3 or 3.5. These scores are identified and collected with their corresponding cows' images for subsequent analysis. The images are then cropped to resize with the resolution of 255*170 pixels because Rafel et al., recommended[8] that most features or the rear of the cow are distinguishable with this resolution.

Table 1. Anatomical Points Description.

Point	Description
1-3	left hook start points
4	left hook midpoint
5	left hook angle point 1
6	left hook angle point 2
7	left hook angle point 3
8	left hook end point
9	left tailhead depress angle point1
10	left tailhead depress angle point 2
11	left tailhead depress angle point 3
12	tailhead peak angle point 1
13	tailhead peak angle point 2
14	tailhead peak angle point 3
15	right tailhead depress angle point1
16	right tailhead depress angle point 2
17	right tailhead depress angle point 3
18	right hook end point
19	right hook angle point 1
20	right hook angle point 2
21	right hook angle point 3
22	right hook midpoint
23-25	right hook start points

3.2. *Segmentation of the back shape of the cow*

Once we have the preprocessed cows' back view images, we need to extract the computationally manageable representation of the anatomy of the back shape of cows. A computer program written with Matlab 2015a was used in annotating of cow images from the dataset. Twenty-five anatomical points are identified. Those anatomical points according to recognizable features can influence the important information for representation of the shape. Those anatomical points with their description are depicted in the figure 1. The shapes are then aligned to endure the pose (scaling, rotation and resizing). Angles are measured according to law of cosine method using three points. There are five angles totally computed, two angles around the left and right hooks and two angles around the tailhead depression area and one angle at the peak of the tailhead as shown in figure 2.

3.3. *Analysis by Regression Method*

By using those angle features, we compute the regression coefficients in estimation of BCS. The multiple regression method is computed with the equation as follows:

$$BCS_i = b_0 + b_1Ang_1 + b_2Ang_2 + b_3Ang_3 + b_4Ang_4 + b_5Ang_5 \quad (1)$$

where BCS_i is the BCS of the i^{th} cow, Ang_1 and Ang_5 are the left and right hook angles, Ang_2 and Ang_4 are the left and right tailhead depression angles, and Ang_3 is the tailhead peak angle respectively. And b_0 is the constant or intercept and b_1, b_2, b_3, b_4 and b_5 are the slope (coefficients) of the three angles respectively. We computed the angles in radian rather than degrees to reduce the variation among values.

4. Experiments and Results

After analyzing those angle features using regression method, the computed regression coefficient and the predicted BCS values are shown in Table 1. In the experiment, we take threshold to those angle values by rounding the point value and then observed that the predicted BCS values are close and some even identical to the estimated BCS as in shown in figure 3. The residual values (which is the difference between predicted values and already estimated values) are 0, 0.5 and 1.

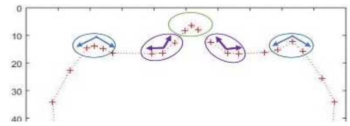

Table 2. (a) Regression coefficients (b) Some angle features with respective BCS from 10 random images out of 70, where Y= BCS and Y' = predicted BCS (c) Correlation of each angle with BCS

b_0	b_1	b_2	b_3	b_4	b_5
-9.2863	2.2450	1.0451	-0.1265	-0.3583	1.3034

(a)

Ang_1	Ang_2	Ang_3	Ang_4	Ang_5	Y	Y'
2.5491	1.4157	2.3629	2.3629	0.1212	2	2.5
2.8389	1.2727	1.8776	1.8776	0.1333	2.5	3
2.5605	1.4049	2.3836	2.3836	0.1695	2.5	2
2.4930	1.2870	2.3031	2.3031	0.1301	1.5	1.5
2.7783	1.5187	2.3119	2.3119	0.1536	3	3
2.9189	1.4515	2.5580	2.5580	0.1085	3.5	3.5
2.7980	1.5669	2.4416	2.4416	0.2446	3	3
2.7762	1.3964	2.4901	2.4901	0.0865	2.5	3
2.7088	1.2597	2.4962	2.4962	0.0948	2	2.5
2.8441	1.3426	2.2667	2.2667	0.1068	3	3

(b)

	Correlation with BCS
Ang_1	0.6090
Ang_2	0.4161
Ang_3	0.1001
Ang_4	0.2229
Ang_5	0.5446

(c)

Out of seventy images, twenty-four images have zero difference, thirty-four images have 0.5 difference and eleven images have 1 difference. We assumed the 0.5 difference is feasible because even the difference between the trained experts can have 0.5 difference in estimating the BCS. Thus, the accuracy for this experiment is 83% which is acceptable to estimate. We also computed the correlation between each angle feature with their respective BCS value as shown in Table 2(c) and we find that all these angle features have the positive correlation with the BCS. This means that if those angle have the higher value (wider angle) the BCS value is the higher value. This assumption agrees with the wider

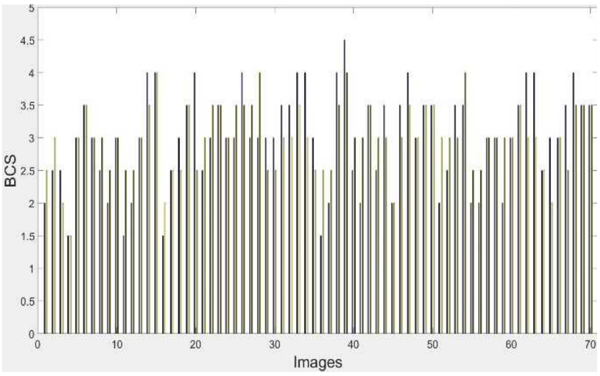

Fig. 3. Cow Images with shape (the upper) and extracted shapes from cow images.

angles indicate a rounder cow in the statement stated[5] by Halachmi et al., in their study.

5. Conclusion

In this paper, we used the back view images of cows in estimation of BCS. The BCS of the cows are estimated using the 5 point scale. Experimental results showed that this method is effective in assessing the BCS of the cow as the predicted scores are closed to the actual scores. Moreover, our experiment also hold the same impression with the assumption of the rounder shape have the higher scores. In the future, a more robust method for extraction of shape and a dataset of back view cow images useful for cattle management will be addressed.

Acknowledgement

This work was supported by JSPS KAKENHI Grant Number JP15K14844.

References

1. Sharad Mishra1, Kiran Kumari1, Ashutosh Dubey, Body Condition Scoring of Dairy Cattle: A Review, *Journal of Veterinary Sciences, 58.* RRJVS| Volume 2 | Issue 1 | March, 2016.
2. D. Ferguson, D. T. Galligan, and N. Thomsen. Principal descriptors of body condition in Holstein dairy cattle. *Journal of Dairy Science*, 77, 1994.
3. Roii Spoliansky, Yael Edan, Yisrael Parmet, and Ilan Halachmi, Development of automatic body condition scoring using a low-cost 3-dimensional Kinect camera, *J Dairy Sci 2016* Sep 16;99(9):7714-25. Epub 2016 Dec 16.
4. M. P. Coffey, G. Simm, W. G. Hill, and S. Brotherstone, "Genetic Evaluations of Dairy Bulls for Daughter Energy Balance Profiles Using Linear Type Scores and Body Condition Score Analyzed Using Random Regression," *Journal of Dairy Science*, vol. 86, pp. 2205 – 2212, 2003.
5. Halachmi, I., Polak, P., Roberts, D.J., Klopcic, M.: Cow Body Shape and Automation of Condition Scoring. *Journal of Dairy Science* (2008) 4444{4451}.
6. J. M. Bewley, A. M. Peacock, O. Lewis, R. E. Boyce, D. J. Roberts, M. P. Coffey, S. J. Kenyon, and M. M. Schutz, Potential for Estimation of Body Condition Scores in Dairy Cattle from Digital Images, *Journal of Dairy Science*, vol. 91, pp. 3439 – 3453, 2008.
7. A. Bercovich , Y. Edan , V. Alchanatis , U. Moallem , Y. Parmet , H. Honig , E. Maltz , A. Antler, and I. Halachmi, *J. Dairy Sci*. 96 :8047–8059, 2013.
8. Rafael Tedın, J. A. Becerra1, and Richard J. Duro, Ismael Mart´ınez Lede, Towards automatic estimation of the body condition score of dairy cattle using hand-held images and active shape models, *Frontiers in Artificial Intelligence and Applications* 243:2150-2159 · January 2012.
9. www.infodairy.com/infodairy_upload.../0129learn%20to %20score%20bcs-e.ppsx
10. http://www.slideshare.net/jonescoleen/beginners-guide-to-body-condition-scoring
11. http://www.slideshare.net/jonescoleen/learn-to-score-body-condition-for-dairy-cows
12. http://www.techproindia.in/wws/2013/10/understanding-dairy-terminology-and-body-condition-scoring-in-dairy-cattle.html
13. http://www.dairynz.co.nz/animal/herd-management/body-condition-scoring/bcs-visual-examples/
14. http://www.nadis.org.uk/bulletins/condition-score-(bcs)-in-beef-herds.aspx
15. http://www.agweb.com/article/achieving-optimum-dry-cow-body-condition-university-news-release/

General Image Categorization Using Collaborative Mean Attraction

Hiroki Ogihara
Department of Computer Science and Systems Engineering, University of Miyazaki,
1-1 Gakuen Kibanadai Nishi, Miyazaki, 8892191, Japan

Masayuki Mukunoki
Department of Computer Science and Systems Engineering, University of Miyazaki,
1-1 Gakuen Kibanadai Nishi, Miyazaki, 8892191, Japan

E-mail: hm13015@student.miyazaki-u.ac.jp, mukunoki@cs.miyazaki-u.ac.jp
cvlab.cs.miyazaki-u.ac.jp

Abstract

In this paper, we apply Collaborative Mean Attraction (CMA) method, which has been developed for person re-identification problem, to general image categorization problem. Experimental results using Caltech101 and Caltech256 dataset reveal that CMA shows better categorization accuracy than traditional methods, particularly in the case when the size of training data is small. Furthermore, we discuss the parameter settings for CMA through several experiments.

Keywords: Generic Object Recognition, CMA method, ImageNet, Caltech dataset

1. Introduction

Recently, studies of general object recognition have been progressed. In this paper, we address the general image categorization problem, which classifies each image into one of known categories.

In general object recognition, Deep Learning method shows great results. Deep Learning not only classify a given input image but also extract features of the image. The extracted features can be used for general purpose object recognition, and using the features we can achieve excellent recognition results. To accomplish that, Deep Learning demands a huge number of training images.

However, in general object categorization problem, there are some cases when we can give only a small number of training images. For example, when a user wants to organize his/her personal photos based on his/her personal criteria, the user can give only a small number of example images, which can be used as training images. In such cases, we need a categorization method which works fine with a small number of training images.

In this paper, we apply Collaborative Mean Attraction (CMA) method to general image categorization problem.[1] CMA has been developed for person re-identification problem. In person re-identification problem, we classify a person in query images into one of known persons in gallery (training) images. Here, since gallery images are taken while the person passes through the view area of a surveillance camera, a few gallery images can be available. CMA shows good results in person re-identification problem.

In the experiment, we apply CMA method and other comparison methods to Caltech101 and Caltech256, which are public general image categorization datasets, and discuss the characteristic of CMA method.

2. CMA method

CMA is an identification method which classifies unknown test data into one of known categories. Known categories are given as feature sets of one or more training images belonging to that category. The test data is also given as the feature of the test image, but it is possible to give a set of test images as one group and classify the group into one of known categories at once.

CMA method consists of two stages, that is, the optimization stage and the classification stage. In the optimization stage, we generate a representative of test data and approximate it with all training images. In the classification stage, we select the category that most contributed to the approximation.

2.1 Optimization stage

A representative point and its approximate point are represented by linear sums of test data and training data, respectively. In the optimization stage, the coefficients of the linear sum constituting the representative point and the approximate point are obtained.

The coefficients are determined so that the distance between the representative point and the approximate point becomes short. At the same time, the constraint is imposed that the representative point and the approximate point should be near to the average of each data so that the properties of each data are retained.

A test data matrix $\boldsymbol{Q} \in R^{m \times N_q}$ and a training data matrix $\boldsymbol{X_i} \in R^{m \times N_x^i}$ ($i \in \{1,\ldots,n\}$) are given, where m is the number of dimensions of the feature vector, N_q is the number of the test images, n is the number of known categories, N_x^i is the number of training images in *i-th* category. We denote the matrix which concatenates all the training data matrix as $\boldsymbol{X} = (\boldsymbol{X_1}\ \boldsymbol{X_2} \ldots \boldsymbol{X_n}) \in R^{m \times N_x}$, where $N_x = \sum_i N_x^i$ is the total number of training images.

Here, we obtain the coefficient vector $\boldsymbol{\alpha}, \boldsymbol{\beta} \in R^m$ by minimizing the following expression $f(\boldsymbol{\alpha}, \boldsymbol{\beta})$:

$$f(\alpha, \beta) = \|\boldsymbol{Q\alpha} - \boldsymbol{X\beta}\|^2 + \lambda_1 \left\|\boldsymbol{\alpha} - \frac{1_{N_q}}{N_q}\right\|^2 + \lambda_2 \left\|\boldsymbol{\beta} - \frac{1_{N_x}}{N_x}\right\|^2 \quad (1)$$

where 1_k is the k-dimensional vector with each element 1, $\|\cdot\|$ is the L_2 norm of the vector. $\boldsymbol{Q\alpha}$ and $\boldsymbol{X\beta}$ in Equation (1) are the representative point and approximate point, respectively.

The first term is a term for minimizing the distance between the representative and approximate point. The second term and the third term are constraint terms (regularization term) for bringing the representative and approximate point close to their respective average points. λ_1, λ_2 are weight parameters of the regularization term.

2.2 Classification stage

Using the coefficients $\boldsymbol{\alpha}$ and $\boldsymbol{\beta}$ obtained in the optimization stage, we find the category that most contributed to constructing the approximation point, and classify the test data into that category. Each dimension of the coefficient $\boldsymbol{\beta}$ corresponds to the training image. $\boldsymbol{\beta}$ can be decomposed with $\boldsymbol{\beta_i}$ as the coefficients of the training image in *i-th* category. Thus, we calculate the following formula for each category i and we classify the test data into the category which has the minimum d^i.

$$d^i = (\|\boldsymbol{Q}\|_* + \|\boldsymbol{X}_i\|_*) \cdot \left\|\boldsymbol{Q\alpha} - \boldsymbol{X_i\beta_i}\right\|^2 \|\boldsymbol{\beta}\| / \left\|\boldsymbol{\beta_i}\right\| \quad (2)$$

The smaller $\left\|\boldsymbol{Q\alpha} - \boldsymbol{X_i\beta_i}\right\|^2$ is, the better the representative point can be approximated with only *i-th* category. Similarly, when the value of $\|\boldsymbol{\beta_i}\|/\|\boldsymbol{\beta}\|$ is larger, the coefficient of *i-th* category plays a large role in the entire known categories. $\|\cdot\|_*$ is the nuclear norm of the matrix (sum of singular values of the matrix). The larger the variation of the data, the larger the nuclear norm becomes. It is used for weighting the variance of the categories.

3. Image Categorization

3.1 Dataset

We used the Caltech101 and Caltech256 dataset for evaluation.[2] The Caltech101 and Caltech256 dataset consists of images with 101 and 256 categories, respectively. The number of images per category is 31 to 800 in Caltech101, while more than 80 in Caltech256. Overall, Caltech256 is a more challenging dataset than Caltech101.

3.2 Feature extraction

For feature extraction, we use the model (bvlc_reference_caffenet)[3] that trained using the ImageNet image with Caffe,[4,5] which is a Deep Learning framework. This model was constructed using 1,000 categories of ILSVRC2012, using 1.2 million training images. The output of the coupling layer is taken as the feature of the image. The dimension of the extracted feature is 4096. For implementation, OpenCV 3.1 Deep Neural Network Module was used.

3.3 Comparison methods

To discuss the characteristics of the CMA method, we compare it with three conventional methods.

The first method is Support Vector Machine (SVM). SVM is a standard method of current pattern recognition. SVM is basically two-class classifier. In order to apply SVM to multi-class classification, we employ "one-to-one classification" approach, which constructs SVM for all 2 class combinations and classifies by the majority decision of the result. We use a linear kernel for the kernel. Since SVM basically cannot handle test data as a group, it was used only for experiments with single test data. We used libsvm for implementation.[6]

The second method is Center Point Distance (CPD). In CPD we let the distance between the average of training data of one category and the average of test data be the distance between that category and test data. The test data is classified into the category that has minimum this distance.

The Third method is Minimum Point Distance (MPD) between data. At first, we find the distance between two points for all data point combinations of training and test data. Then we let the minimum value be the distance between the category and the test data and classify the test data into the category with the minimum distance. Whereas CPD considers only the center of the group, MPD is based on individual data points, and classification result can reflect the distribution of data.

4. Experiments

4.1 Experiment for single test data

In this experiment, we give each test data from a single image and investigate that how the result of identification changes when the number of training images is changed.

We randomly extract k images from each categories in the dataset as training images, extract features and make them as training data. All of the remaining images are used as an evaluation dataset. The test data is extracted one by one from the evaluation dataset and categorized by each method. After obtaining the accuracy for the evaluation dataset for each category, we calculate the overall accuracy by averaging them for all categories. The number of training images is k=1, 2, 4, 8, 16, 30. In order to avoid the influence of the particular selected images for training, we calculate the accuracy for 8 kinds of training images, and let the average be the experimental result. In all methods, the same eight training dataset are used. The results are shown in Fig. 1.

Experimental results show that CMA shows higher accuracy than any other comparison methods in any k and in both datasets. Especially, in Caltech101, when k=1, CMA shows 12.7 points better accuracy than the comparison methods, and it can be seen that the performance is relatively higher in the range where the number of training images is small.

4.2 Experiment for group test data

Then we give the test data as a group of images. In the same way as sec. 4.1, training data is created and the rests are used as an evaluation dataset. In this experiment, plural images are extracted from the evaluation dataset as a group and used as a test data. The number of images in each group is l=2, 4, 8, 16, 30. In order to avoid the influence of the particular selected images for testing, we conduct 3 trials for each l and averaging the results. The results are shown in Fig.2.

Even in the case of group test data, CMA shows higher accuracy than the comparison methods in k=1 and 2. As a whole, as the number l of test data increases, the accuracy increases, and it is considered that there is an advantage in CMA that can apply image classification to a combined plural test data as a group. However, at k=4, 8, 16 and 30, CPD shows equal to or higher accuracy than that of CMA.

4.3 Experiment on regularization parameters

In the previous experiments, the regularization parameter λ_1 and λ_2 is set to λ_1=16, λ_2=16. In order to observe the influences of the regularization parameters, we changed the values of λ_1 and λ_2 with 32, 16, 8 and investigate how the accuracy changes. Caltech256 dataset is used in this experiment. The number of training data is k=1, 30 and the number of test images in a group is l=30. The results are shown in Table 1.

It was found that the lower the value of λ_2 is, the higher the accuracy rate is. This result suggests that since the training data contains different kinds of objects, the approximate point should not be close to the average of the training data.

Table 1 Accuracy for various parameters

λ_1	λ_2	k=1(%)	k=30(%)
32	32	53.4	97.7
32	16	55.1	98.7
32	8	**55.7**	**98.9**
16	32	54.7	97.9
16	16	55.4	98.6
16	8	**56.6**	**99.2**
8	32	54.8	98.1
8	16	55.9	98.5
8	8	**56.3**	**98.9**

5. Conclusion

In this paper, we conducted experiments to apply CMA method to general image categorization problem. Although CMA was developed for person re-identification problem, it showed higher classification accuracy in the general image categorization problem, especially when the number of training data was small.

Analysis of the parameters in CMA suggested that the difference between person re-identification and the general image categorization could be reduced by setting the parameters appropriately. The method to give the optimal parameter values is left as a future work.

References

1. Y.Wu, M.Mukunoki, M.Minoh: Collaborative Mean Attraction for Set Based Recognition, *MIRU2014*, OS3-3, 2014.
2. L.Fei-Fei, R.Fergus, P.Perona: Learning generative visual models from few training examples: an incremental Bayesian approach tested on 101 object categories, *CVPR Workshop on Generative-Model Based Vision*, 2004.
3. http://dl.caffe.berkeleyvision.org/ bvlc_reference_caffenet.caffemodel.
4. L.Fei-Fei: ImageNet: crowdsourcing, benchmarking and other cool things, *CMU VASC Seminar*, 2010.
5. Y.Jia, E.Shelhamer, J.Donahue, et al.: Caffe: Convolutional Architecture for Fast Feature Embedding, *arXiv preprint arXiv:*1408.5093, 2014.
6. C.C.Chang, et al.: LIBSVM - A Library for SVM,http://www.csie.ntu.edu.tw/~cjlin/libsvm/.

Figure 1 Accuracy for single test data

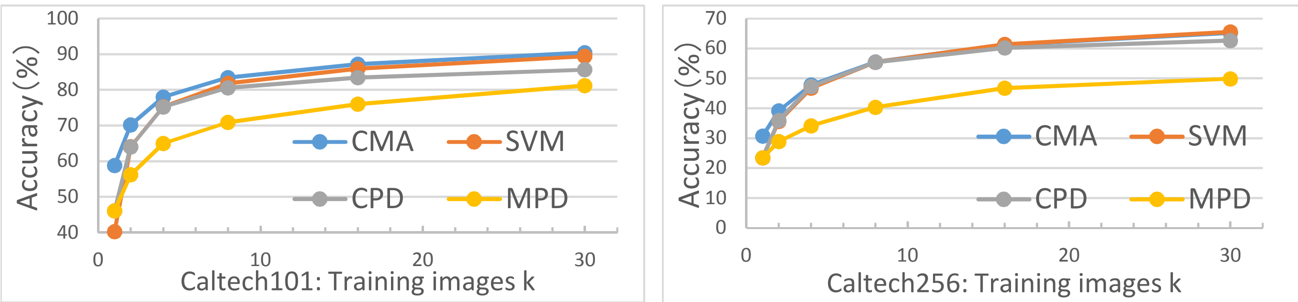

Figure 2 Accuracy for group test data

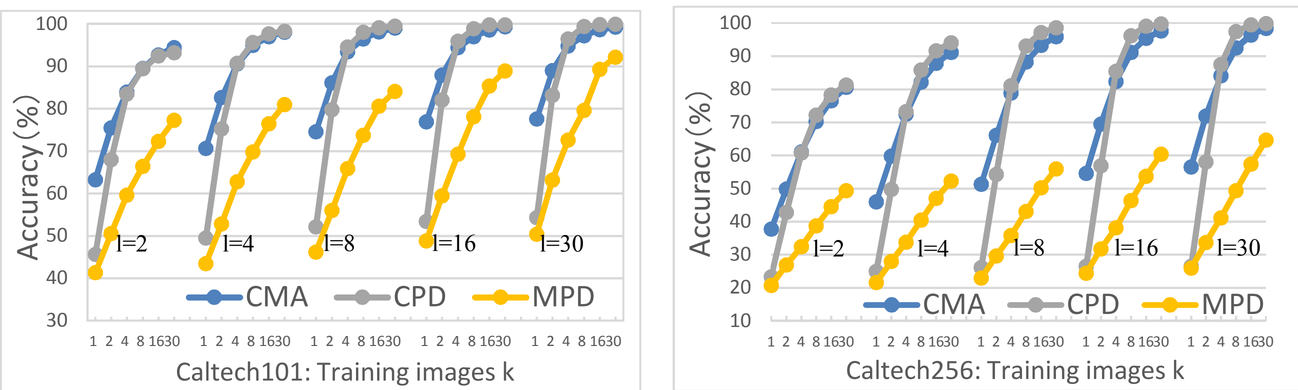

Consideration on the Photo-Realistic Rendering of Fruits by 3DCG

Haruka Tsuboi, Makoto Sakamoto[1], Sho Yamada, Kensuke Ando
Faculty of Engineering, University of Miyazaki, 1-1, Gakuen Kibanadai-nishi, Miyazaki-shi, 889-2192 Miyazaki, Japan

Sun Chongyang[2]
Graduate School of Engineering, University of Miyazaki, 1-1, Gakuen Kibanadai-nishi, Miyazaki-shi, 889-2192 Miyazaki, Japan

Makoto Nagatomo[3]
Interdisciplinary Graduate School of Agriculture and Engineering, University of Miyazaki, 1-1, Gakuen Kibanadai-nishi, Miyazaki-shi, 889-2192 Miyazaki, Japan

Koshiro Mitsuhashi[4], Yukari Kodama
Miyazaki Multimedia Academy, 2-4-37, Takachihodori., Miyazaki-shi, 880-0812, Japan

[1]sakamoto@cs.miyazaki-u.ac.jp, [2]sun_1987@ezweb.ne.jp, [3]je.suis.makoto@gmail.com, [4]koshiro@multi-m.jp

Abstract

Three-dimensional computer graphics (3DCG) is the technique of creating an image having a stereoscopic effect by converting an object in the virtual three-dimensional space into two-dimensional information. It is also possible to produce an image that cannot be distinguished from the real thing by using the 3DCG. 3DCG is expected for the application to visual representations very much. However, it is difficult to express the "freshness" of fresh food by 3DCG.Therefore, expressiveness of 3DCG is considered to be improved by overcoming this weakness. In this paper, we consider the photo-realistic rendering of fruits by 3DCG. The algorithm is implemented by using the Visual C++ 2010 and C on a personal computer. Through this trial, we hope to improve the representation in photo-realistic rendering by 3DCG.

Keywords: 3DCG, OpenGL, Blender, GIMP

1. Introduction

Today, researches and developments of three dimensional computer graphics (hereinafter referred to as 3DCG) and technologies related to 3DCG are extensively conducted. Among them, there is a field pursuing ultimate reality by making full use of rendering and bump mapping. One of them is a digital food, which is being studied for the future practical application. For digital foods, it is expected to solve problems related to food freshness management, disposal, development simulation of new products, and the like. In this thesis we will consider how to express the freshness of food as an example of cut apples [1-3].

2. Principle

In many cases, CG refers to images and images drawn with 3DCG. One of the reasons why various technologies using 3DCG technology such as AR and 3D printers are developed is high expressive power of 3DCG. However, it is difficult to express 'freshness' or 'organic coloration' of fresh foods, fresh flowers, etc. even with 3DCG expressive power.

In this research, we explore what technology is necessary to express "freshness" and "organic coloration" which 3DCG is not good at.

3. Previous study

We used OpenGL to create CG. Modeling in OpenGL is performed by designating a set of vertex data and a rule connecting vertices. Note that since the shape of the model changes depending on the order of the given vertices, the order of the vertex data must be taken care of in the consolidation rule. Also, OpenGL does not have functions to create circles or surfaces. Therefore, triangle polygons and quadrilateral polygons must be arranged and their shapes approximated.
Materials are set by mapping. Texture mapping was done to express apple skins. For the texture image, the image of the skin was cut out from the apple photograph (Fig. 1).

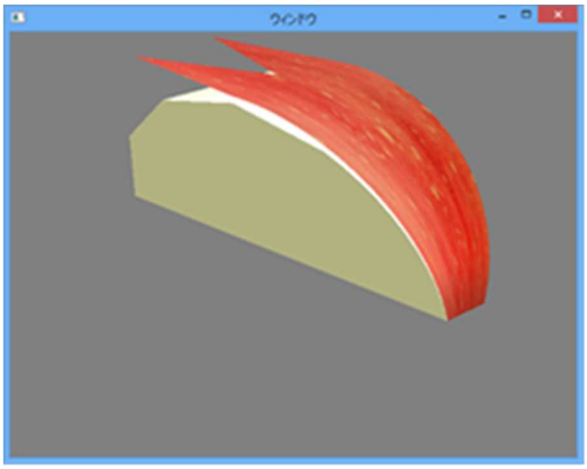

Fig. 1: Model applying texture mapping.

Bump mapping was carried out to express fine unevenness of apple fruit. The image used for bump mapping was generated using image editing / processing software called GIMP (Fig. 2).

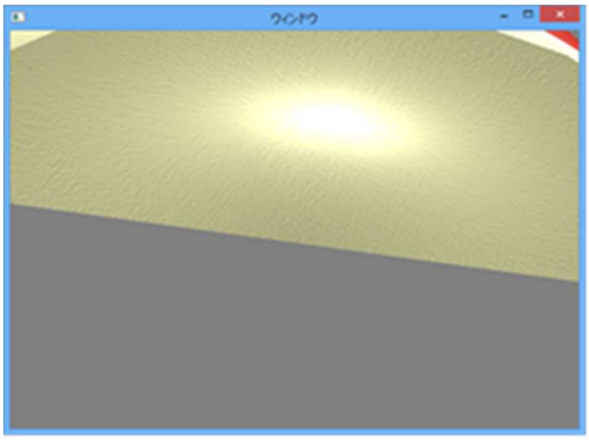

Fig.2: Model applying bump mapping.

4. Creation

This time I used Blender instead of OpenGL to create CG. Generally, creation of CG is generally not made by program only like OpenGL, but because there are many software to create sensually using GUI etc. I chose Blender because the concept is basically the same as such software.
I studied how to become more real on my own from images in previous research. Compared with actual cut apples, dense expression is not done. In addition, CG has not removed core and its expression is not done either. Overall we can not feel the freshness. Solve these problems.

4.1. Modeling

In this time we will create ordinary apple and cut apples. First, we made ordinary apples from UV spheres and edited it to make cut apples (Fig. 3). The part with the leather expresses a smooth curve by increasing the number of divisions and the number of divisions is made smaller for the cut part so that it is expressed linearly.

4.2. Material setting

Material setting is done by mapping as in previous research. In the previous study, only texture mapping and bump mapping were performed, but this time UV mapping is performed. UV mapping is a part of texture mapping, and by attaching a texture to a two-dimensional developed view of the surface of the object, the texture is stretched to the sterically wrapped part without being stretched. As a result, we were able to freely change the material and expressed it densely (Fig. 3).

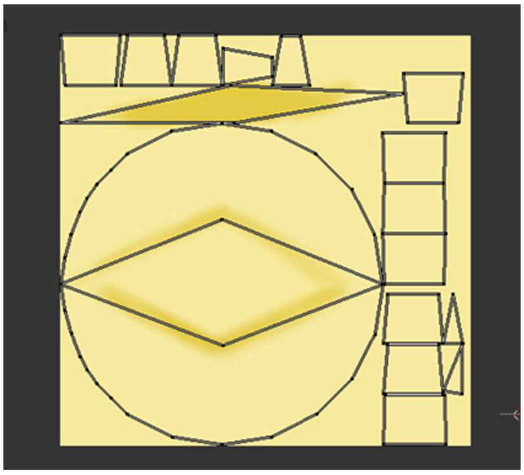

Fig.3: Fabrication of map by UV development.

5. Result

The cut apple I made is as shown in Figure 4. I think that more realistic things could be made using means not used in previous research. However, the mapping looks more beautiful in the previous research. In OpenGL, the mapping associates the vertices of the image with the vertices of the object, so it is affixed as expected, but it did not work in Blender so it did not work. Also, it is impossible to say that the expression of freshness has become a sense as it will make it just fine.

Fig.4: Finished cut apples.

Fig.5: Actual cut apple.

6. Discussion

About realistic depiction of fruits by 3DCG I have been researching with awareness of the shape and color reproduction. From now on, it is considered necessary to investigate future research and evaluation methods of algorithms that make it possible to reproduce the structure of fruits finer. Also, people are affected by many colors. Although the syrup of shaved ice has the same taste, it feels like the taste is different only by the difference in color. There is also a psychological experiment that affects appetite and hangs glasses with blue film, which makes the dish look a little tasteless (Fig.6). As you can see, I think that rather than putting emphasis on models to be created, understanding human visual information and using optical illusion will make it more realistic. It is easy but made around so that it looks more natural (Fig.7). For comparative purposes keep an apple that is not mapped next to it.

Fig.6: Blue Curry Rice.

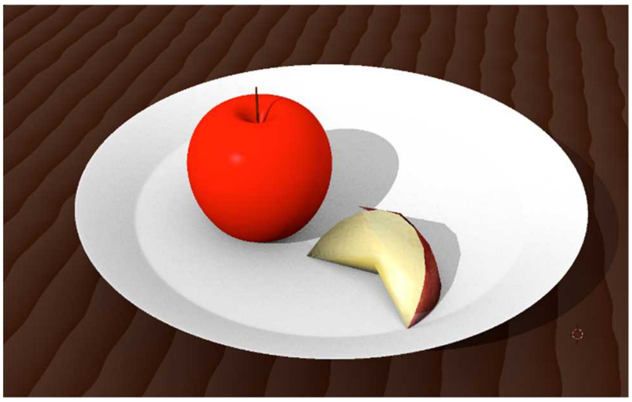

Fig.7: Apples created including surroundings.

7. Conclusion

In the expression pursuing reality, I felt that not only the solution of the technical problem of 3DCG but also the ingenuity of the production process is necessary. Since CG technology was developed, CG technology has grown rapidly, but it is a developing technique that still has many problems to be solved. In the future, as 3DCG technology advances, new technology applying 3DCG can be expected to be born. The advent of such technologies may bring big changes to our society in the future.

References

[1] Keisuke Ando, *Consideration on pursuit of reality in three-dimensional CG, graduation thesis of Information Systems Engineering*, Faculty of Engineering, Miyazaki University, 2014.
[2] Sakamoto Masato, Okaya Tetsushi, Research on Simple 3-D CG Production by Java, *Bulletin of the Faculty of Engineering*, Miyazaki University, No. 36, pp. 321-328, 2007.
[3] Sakamoto Masato, Yamada Sho, Consideration on graphical drawing of fresh foods by three-dimensional CG, *Bulletin of the Faculty of Engineering*, Miyazaki University, No. 45, pp. 239 - 242, 2015.

Consideration for the Possibility to the Tourism by the AR Technology

Masamichi Hori[1]
[1] *Department of Computer Science and Systems Engineering, University of Miyazaki, 1-1 Gakuenkibanadainishi Miyazaki-shi, Miyazaki, 889-2192, Japan*

Makoto Sakamoto[1]**, Koshiro Mitsuhashi**[2]**, Yukari Kodama**[2]**, Takeshi Tanaka**[3]**, Mihoko Fukushima**[3]**, Chikashi Deguchi**[3]**, Masahiro Yokomichi**[1]**, Masayuki Mukunoki**[1]**, Kunihito Yamamori**[1]**, Atsushi Iiboshi**[4]
[1] *Department of Computer Science and Systems Engineering, University of Miyazaki, 1-1 Gakuenkibanadainishi Miyazaki-shi, Miyazaki, 889-2192, Japan*

[2]*Miyazaki Multimedia Academy, 2-4-37 takachihodori Miyazaki-shi, Miyazaki, 880-0812, Japan*

[3]*Faculty of Regional Innovation, University of Miyazaki, 1-1 Gakuenkibanadainishi Miyazaki-shi, Miyazaki, Miyazaki, 889-2192, Japan*

[4]*Takachiho Muratabi Co., Ltd., 6604 ohazamukouyama takachiho-cho nishiusuki-gun, Miyazaki, 882-1103, Japan*

[1]*sakamoto@cs.miyazaki-u.ac.jp*, [2]*koshiro@multi-m.jp*, [3]*deguchi@cc.miyazaki-u.ac.jp*, [4]*muratabi@bz04.plala.or.jp*

Abstract

The promotion of the tourism nation became the important problem of our country, and we expect increase of the number of the foreign tourists visiting Japan. So we must contribute plain guidance information to the foreigners who cannot understand Japanese. On the other hand, AR (augmented reality) is becoming the boom recently. In this paper, when we use the AR technology for tourism and sightseeing, we inspect what kind of possibilities we have through some experiments.
Keywords: Promotion, Augmented reality, Sightseeing, Traditional culture.

1. Introduction

As of 2016, virtual technology is showing great excitement. Regarding VR technology, dedicated equipment with a slightly high threshold is needed although it has become a price range where individuals can reach out. On the other hand, AR technology has come to be seen in a wide range of fields such as advertisement, sightseeing, education and entertainment due to popularization of personal-owned devices such as smartphones and tablets [1].

This laboratory has conducted numerous research on AR technology using 3DCG in the past. We will construct a system that combines AR technology which was one of its final objectives and sightseeing which is a characteristic of Miyazaki prefecture and carries out tourism support in this research. This method aims at consumers visiting sightseeing spots to experience AR technology and to reproduce and share the experiences that we have defined it as “Omochikaeri” in any environment.

2. Background

I will talk about Takachiho-cho which is the core in this research. Takachiho-cho is located in the northernmost tip of Miyazaki prefecture and the center of Kyushu, has a scenic natural monument Takachiho Gorge is a city blessed with wonderful nature that is rich in the four seasons. Takachiho Gorge is shown in Figure 1. Also, its origin is old, it is said that the village had existed around 4000 BC [2].

Fig.1：Takachiho Gorge.

Meanwhile, it is a place of descendants of descendants, and it is regarded as a land with considerable deep connection with Japanese mythology and the birth of Japan. There accompanied the evening Kagura born from the Amanoiwato legend, and the land related to myths exist, and in recent years has attracted more attention to a wide range of power spot[3].

Especially in the Akimoto district called OkuTakachiho, efforts are focused on people living in the village, and efforts to have tourists make experiences in close contact with the village popular. It is possible to touch the shrines using regional ingredients, the environment that talks while feeling nature in an old private house inn, and the shrines and sacred trees standing in majestic nature. The Akimoto shrine is shown in Figure 2. Recently it has been selected as a good example of "Treasure of Discover Rural Mountain Fishing Village" designated by the Ministry of Agriculture, Forestry and Fisheries, and it seems that tourists will increase further in the future[4].

Therefore, in this research, tourism support that visitors who visit regardless of domestic and overseas enjoy the tourist resources as much as possible to maximize the number of repeat customers and new customers will be done.

Fig.2：Akimoto shrine.

3. Methods

I will explain the technology used in this experiment.

3.1. *CG modeling*

In this laboratory we produce applications for terminals, and we will cooperate with vocational schools in Miyazaki prefecture for 3DCG model production. Display 3DCG model with AR technology and reproduce the beautiful landscape of the night dance performers and sightseeing spots. Until the model is completed, we will develop a prototype using 3DCG of Miyazaki University's mascot character shown in Fig. 3 [5]

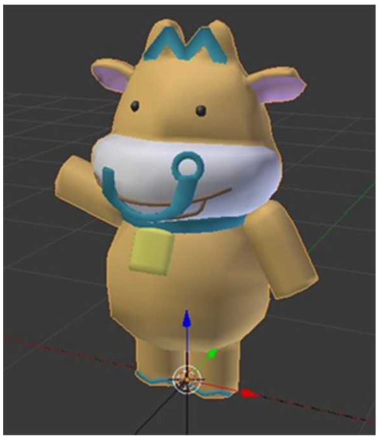

Fig.3 : Bird's eye view of Miyadaimoukun.

3.2. *Unity3D*

We chose Unity3D as a software that can produce applications for mobile [6]. Unity3D is an integrated game development environment compatible with many platforms, and a variety of plug-ins accompanying it are also present. In this time, we selected it from the viewpoint of wanting to develop applications that are not dependent on future developability and OS.

3.3. *Selection of API for AR for Unity3D*

In this time, I will concentrate on functioning only with the application itself. We aim to create markerless type location-based AR applications in that it does not break the sightseeing landscape and costs marker preparation. A markerless type SmartAR SDK [7], which corresponds to the above Unity3D and satisfies the requirements, was selected. Based on this SDK, we will add location based functions and others.

4. Experiment and Result

I will describe the results of our experiment.

4.1. *Development environment*

In this research, we made prototype application using Unity 3d and plugin. The 3DCG model used Blender. The portable terminal to use is Xperia Z3.

4.2. *Development environment*

Figure 4 shows the experimental results. I was able to display Miya Kun's 3DCG model for the natural image added to the dictionary. Once reading the natural image inside the camera, I continued to display the model even at all angles, up and down, right and left. However, when the distance gets away, the unnaturalness of the point where the model turns white and the model itself becomes conspicuous becomes conspicuous.

5. Conclusion

In this research, we tried to make an application using Unity3D. Future tasks include functions of advanced applications such as GPS functions in addition to the functions of SmartAR, creation of other models, and exploring problems for practical use. I want to improve these points and complete it as an actual application.

Fig.4 : Displaying the 3D CG model of Miyadaimoukun as AR.

6. Future plans

In addition to the function of SmartAR, GPS function,model creation, seeking problems for practical use, etc. are completed and completed as an application. In addition, I would like to expand the area beyond Takachiho focused this time. Especially in the production of models, we are currently making intensive work on Tajikarao under construction. The model under development is shown in figure 5.

Fig.5 : 3DCG model of Tajikarao.

As a concrete implementation planning function, there is a function that the performance of the 3DCG model with the palm, which is conscious of "Omochikaeri", reproduces Kagura 's dance. The situation is shown in figure6. In addition to this, we planned functions such as displaying the menu by holding the terminal in the pamphlet so that a beautiful image can be played by tapping, and displaying the 3DCG model reproducing a beautiful landscape when reading the brochure as well ing. An image diagram showing a menu from a pamphlet is shown in figure7.

Fig.6：Image dancing on hands.

Fig.7：Image showing menu from brochure.

Acknowledgements

Miyazaki multimedia vocational school people are very busy, thank you hearty thank you for your cooperation in 3DCG modeling and advice etc. Also, the Miyazaki Tourism Convention Association, Inc., abc Corporation, Inc., Phoenix Seagaia Resort Co., Ltd., people in the Akimoto district who took care of me in the interview, other prefectures within the prefecture I would like to express my gratitude to all concerned parties in each municipality.

References

1. "Idealizing AR technology" edited by *I/O editorial department. "VR" "AR" Frontline of technology*. Kohgaku-Sha Co., Ltd. 2015. pp. 20-34.
   Overview of Takachiho | Introduction / History of the town | administrative information | Takachiho cho Takachiho cho information official website. http://www.town-takachiho.jp/administration/history/outline.html. (accessed 2016/11/30).
   Myth of Takachiho | Tourist spot | Takachiho cho tourist association | Miyazaki ken Takachiho sightseeing, accommodation and event information Takachiho cho information official website. http://takachihokanko.info/sightseeing/detail.php?log=1368001475. (accessed 2016/011/30).
   Takachiho Mura Council "Treasure of Discover Rural Farm Village (Mura)" was selected. | What's New | Takachiho-cho Tourist Association Takachiho cho information official website. http://takachiho-kanko.info/news/detail.php?log=1479688433. (accessed 2016/11/30).
2. Makoto Sakamoto, Keisuke Hozumi. "Study on depiction of 3D character guiding at sightseeing spots using AR technology" *Bulletin of the Faculty of Engineering, University of Miyazaki*. Faculty of Engineering, University of Miyazaki 2016. vol.45, pp. 231-234.. .
3. Unity Technologies Japan. “Unity - Game Engine”. Unity3D Homepage http://japan.unity3d.com/. (accessed 2016/11/30). Sony Digital Network Applications Co., Ltd. "SmartAR SDK".SmartAR website. http://www.sonydna.com/sdna/solution/SmartAR_SDK.html. (accessed 2016/11/30).

Development of Cloud Action for Seamless Robot Using Backpropagation Neural Network

Wisanu Jitviriya
Faculty of Engineering, King Mongkut's University of Technology North Bangkok.
1518 Pracharat 1, Wongsawang Rd., Bangsue, Bangkok, Thailand 10800
wisanu_jitviriya@hotmail.com

Jiraphan Inthiam and Eiji Hayashi
Mechanical Information Science and Technology, Kyushu Institute of Technology.
680-4, Kawazu, Iizuka, Fukuoka, 820-8502, Japan.
jiraphan@mmcs.mse.kyutech.ac.jp and haya@mse.kyutech.ac.jp

Abstract

This paper presents the cloud action model for a five DOF Seamless robotic arm using the inverse kinematics solution based on artificial neural network (ANN). Levenberg-Marquardt method is used in training algorithm. The desired position and orientation of the end effector is defined as the input pattern of neural network. In addition, we propose the cloud action which is the movement patterns of the robotic arm. The cloud action platform is created in order to perform the basic behaviors of the Seamless robot such as "Catch", "Approach", "Interest", "Look around", "Alert" and "Avoid" actions. Experimental results show the suitable structure of artificial neural network used for solving the inverse kinematics equation, and the testing points in the robot's workspace were verified with the robotic arm.

Keywords: Inverse kinematics solution, Artificial neural network, Levenberg-Marquardt method.

1. Introduction

Nowadays, the service robot technology is developing and advancing rapidly. Therefore, our researches have concentrated on exploring and studying an artificial intelligent method to create the behavioral and emotional models of the autonomous robot [1] - [3]. The new model for our robot is the dynamic behavior selection model based on emotional states which develops from the Consciousness-Based Architecture (CBA) model combined with Self-Organizing Map (SOM) learning and Markovian model. However, it seems to be the efficient model of the autonomous robot, but we face some problems in posturing the behavior and expressing the emotion of the robot.

Consequently, in this paper, we present the cloud action which is the movement patterns of Seamless robotic arms. The cloud action platform is created in order to perform the behavior of robot smoothly. In addition, we introduce the performance of the training algorithm which is Levenberg-Marquardt learning algorithm [4] that is used for solving the inverse kinematics problem of the Seamless robotic arms.

This paper is organized as follows: Section 2 provides the kinematic modeling of Seamless robotic arm. Section 3 of the paper explains the neural network for determining the inverse kinematics solution. Section 4 describes the process of the cloud action model. Section 5 shows the experimental results of the proposed model, and finally, Section 6 concludes the paper.

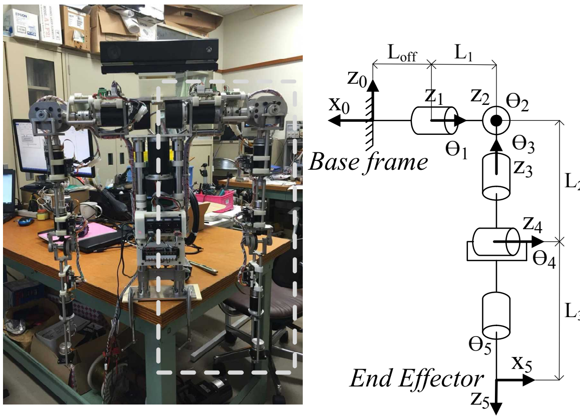

Fig.1 Seamless robotics arm (Left arm)

Table 1. The DH parameters for Seamless robotics arm (Left arm)

Joints	Θ_i	d_i	a_i	α_i
1	Θ_1	$-(L_1+L_{off})$	0	90
2	Θ_2+90	0	0	90
3	Θ_3+90	L_2	0	90
4	Θ_4	0	0	-90
5	Θ_5+90	L_3	0	0

2. Kinematics modeling of Seamless robotic arm

For this research work, Seamless robot in our robotics laboratory is being used shown in Fig.1. Actually, it has two arms, but in this case, we only present the left arm for considering and determining the forward and inverse kinematics solutions. Denavit-Hartenberg (D-H) method [5] is used to derive its kinematics. Fig.1 shows the joints and links of the left side of robotic arm, which has the base frame, shoulder, elbow, and wrist. The DH parameters of the robotic arm are listed in Table 1. According, DH method, the transformation can be formed in the chain product of five homogenous matrices ${}^{i-1}_{i}T$ as expressed by Equation (1).

$$ {}^0_5T = {}^0_1T\,{}^1_2T\,{}^2_3T\,{}^3_4T\,{}^4_5T \qquad (1)$$

Where, $\sin\theta_i = s_{\theta_i}$ and $\cos\theta_i = c_{\theta_i}$.

The homogeneous transformation matrix of Seamless robotic left arm can be shown in Equation (2).

$$ {}^0_5T = \begin{bmatrix} n_x & o_x & a_x & p_x \\ n_y & o_y & a_y & p_y \\ n_z & o_z & a_z & p_z \\ 0 & 0 & 0 & 1 \end{bmatrix} \qquad (2)$$

In Equation (2) indicates the elements of rotational of transformation matrix ($n_x, n_y, n_z, o_x, o_y, o_z, a_x, a_y, a_z$) and the elements of position vector (p_x, p_y, p_z). All elements can be solved as follows:

$$\begin{aligned}
n_x =& -c_{\theta_5+90}(c_{\theta_2+90}s_{\theta_4} - s_{\theta_2+90}c_{\theta_3+90}c_{\theta_4}) \\
& - s_{\theta_2+90}s_{\theta_3+90}s_{\theta_5+90} \\
n_y =& -c_{\theta_5+90}(c_{\theta_4}(c_{\theta_1}s_{\theta_3+90} - s_{\theta_1}c_{\theta_2+90}c_{\theta_3+90}) - s_{\theta_1}s_{\theta_2+90}s_{\theta_4}) \\
& - s_{\theta_5+90}(c_{\theta_1}c_{\theta_3+90} + s_{\theta_1}c_{\theta_2+90}s_{\theta_3+90}) \\
n_z =& -c_{\theta_5+90}(c_{\theta_4}(s_{\theta_1}s_{\theta_3+90} + c_{\theta_1}c_{\theta_2+90}c_{\theta_3+90}) + c_{\theta_1}s_{\theta_2+90}s_{\theta_4}) \\
& - s_{\theta_5+90}(s_{\theta_1}c_{\theta_3+90} - c_{\theta_1}c_{\theta_2+90}s_{\theta_3+90}) \\
o_x =& \ s_{\theta_5+90}(c_{\theta_2+90}s_{\theta_4} - s_{\theta_2+90}c_{\theta_3+90}c_{\theta_4}) \\
& - s_{\theta_2+90}s_{\theta_3+90}c_{\theta_5+90} \\
o_y =& \ s_{\theta_5+90}(c_{\theta_4}(c_{\theta_1}s_{\theta_3+90} - s_{\theta_1}c_{\theta_2+90}c_{\theta_3+90}) - s_{\theta_1}s_{\theta_2+90}s_{\theta_4}) \\
& - c_{\theta_5+90}(c_{\theta_1}c_{\theta_3+90} + s_{\theta_1}c_{\theta_2+90}s_{\theta_3+90}) \\
o_z =& \ s_{\theta_5+90}(c_{\theta_4}(s_{\theta_1}s_{\theta_3+90} + c_{\theta_1}c_{\theta_2+90}c_{\theta_3+90}) + c_{\theta_1}s_{\theta_2+90}s_{\theta_4}) \\
& - c_{\theta_5+90}(s_{\theta_1}c_{\theta_3+90} - c_{\theta_1}c_{\theta_2+90}s_{\theta_3+90}) \\
a_x =& -c_{\theta_2+90}c_{\theta_4} - s_{\theta_2+90}c_{\theta_3+90}s_{\theta_4} \\
a_y =& \ s_{\theta_4}(c_{\theta_1}s_{\theta_3+90} - s_{\theta_1}c_{\theta_2+90}c_{\theta_3+90}) + s_{\theta_1}s_{\theta_2+90}c_{\theta_4} \\
a_z =& \ s_{\theta_4}(s_{\theta_1}s_{\theta_3+90} + c_{\theta_1}c_{\theta_2+90}c_{\theta_3+90}) - c_{\theta_1}s_{\theta_2+90}c_{\theta_4} \\
p_x =& -(L_1 + L_{off}) - L_2c_{\theta_2+90} - L_3(c_{\theta_2+90}c_{\theta_4} + s_{\theta_2+90}c_{\theta_3+90}s_{\theta_4}) \\
p_y =& \ L_2s_{\theta_1}s_{\theta_2+90} \\
& + L_3(s_{\theta_4}(c_{\theta_1}s_{\theta_3+90} - s_{\theta_1}c_{\theta_2+90}c_{\theta_3+90}) + s_{\theta_1}s_{\theta_2+90}c_{\theta_4}) \\
p_z =& -L_2c_{\theta_1}s_{\theta_2+90} \\
& + L_3(s_{\theta_4}(s_{\theta_1}s_{\theta_3+90} + c_{\theta_1}c_{\theta_2+90}c_{\theta_3+90}) - c_{\theta_1}s_{\theta_2+90}c_{\theta_4})
\end{aligned}$$

3. Neural network based the inverse kinematics solution

Solving the inverse kinematics problem is one of the most important task in robot kinematics and control. The complexity of this problem is obtained from the robot's geometry and the nonlinear trigonometric equations. Therefore, there are three traditional techniques used for determining inverse kinematics problem that can be

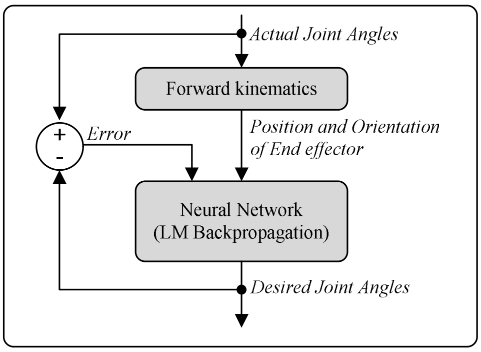

Fig.2 Neural Network based inverse kinematics solution

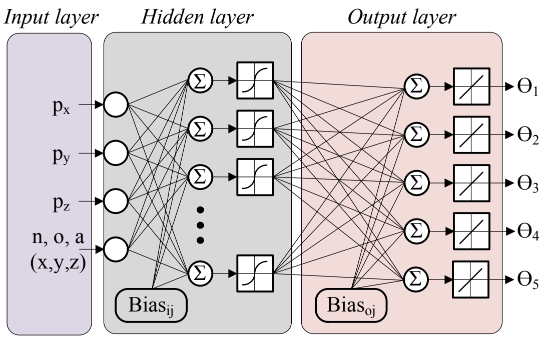

Fig.3 Multi-layered perceptron neural network structure

classified as algebraic, geometric and numerical algorithms. These methods are time consuming, incorrect initial estimation, the inverse kinematics cannot be guaranteed and heavy computational calculation. Consequently, another method can solve the inverse kinematics problems that is Neural Networks. It is possible to formulate the nonlinear mathematical model. Many researchers have verified with this approach in several works [6] - [8].

4. Cloud action of Seamless robotic arm

After solving the inverse kinematics problem base on Neural Network, We try to generate the trajectory path between the target position and the end effector position. But trajectory path of Seamless robotic arm differs from the existing trajectory paths, because Seamless robot that is used to perform the suitable behavior and express the intelligent emotion. Therefore, Cloud action model is introduced in this paper. The procedure of the Cloud action can explain by the following steps:

Table 2. Results of each Neural Network structure

In hidden layer (Hidden node)	Epoch	MSE	Regression
30	205	51.6	0.99291
32	145	51.3	0.99293
34	193	51.2	0.99295
36	238	51.3	0.99293
38	276	51.2	0.99295
40	**167**	**50.9**	**0.99296**
42	230	52.0	0.99286
44	254	52.1	0.99284

Step 1: Determine the straight line (distance) between the target object and end effector position.
Step 2: Find the center point of each behavior on the straight line. Then, the sphere of each action is created, depending on the rate action.
Step 3: Verify the response action for selecting the group action.
Step 4: Random the point in the selecting workspace based on the random distribution technique.

5. Experimental results

In this study, Seamless robotic arm was used to verify the movement of the robot based on Cloud action model. In Fig.2 shows the process of inverse kinematics solution. Levenberg-Marquardt method (trainlm) from MATLAB toolbox was used to train and update the weight and bias values, because it is the fastest back propagation neural network algorithm (Supervised learning). The designed neural network model is illustrated in Fig.3. The Multi-layered perceptron neural network model consists of 12 node inputs (the position vector and nine elements of rotation matrix), 5 node outputs and only one hidden layer. For training and testing data of neural network that was determined by the equation of each element in Equation (2). A work space data set 33880 data. While 80% of the data set was set as the training data, 10% to validation and 10% data for testing data. Table 2 shows the experiment results of the suitable structure of Neural Network based inverse kinematics solution for Seamless robotic arm. After modeling the neural network to calculate the inverse kinematics solution, the movement paths of robotics arms were verified by the Cloud action method as shown in Fig.4.

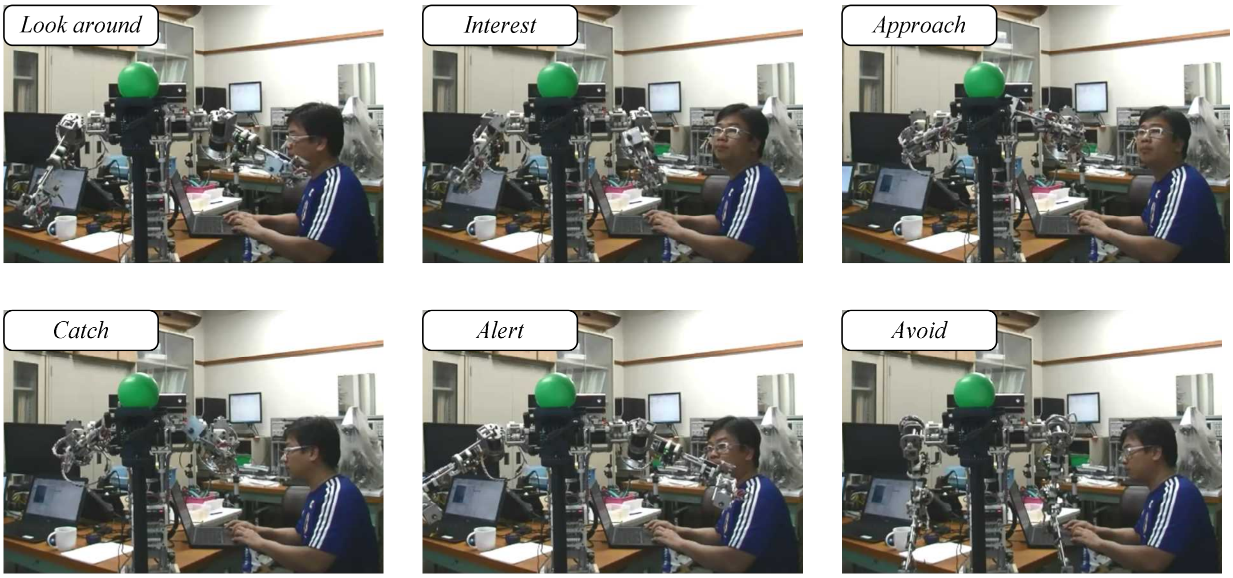

Fig.4 Results of the six actions with cloud action model

6. Conclusions

In this paper, we propose the new control system for designing and developing a 5 DOF revolute robot arm, using a backpropagation neural network and the cloud action model. Results have shown that the Seamless robot arm can move randomly in the workspace of the six basic actions. For future work, we would like to improve this model into the conventional action selection system (Consciousness-Based Architecture (CBA) model combined with Self-Organizing Map (SOM) learning and Markovian model), in order to create the intelligent service robot perfectly.

References

1. E. Hayashi, T. Yamasaki, and K. Kuroki, “Autonomous Behavior System Combing Motivation and Consciousness Using Dopamine,” Proc. of 8th Int. IEEE Symposium on Computational Intelligence in Robotics and Automation (CIRA 2009), pp. 126-131, 2009.
2. W. Jitviriya, and E. Hayashi, “Analysis of Robotic Arm’s Behavior using Self Organizing Map combined with Consciousness-Based Architecture Module,” *in Proc. 2013 IEEE/SICE International Symposium on System Integration (SII2013)*, pp. 533-538, 2013.
3. W. Jitviriya, J. Inthiam, and E. Hayashi, “Dynamic Behavior Selection Model based on Emotional States for Conbe-I robot,” *Journal of Robotics, Networking and Artificial Life (JRNAL)*, Vol.2, No.4, pp. 247-251, 2016.
4. D. Marquardt, “An algorithm for least-squares estimation of nonlinear parameters,” *SIAM Journal on Applied Mathematics*, Vol.11, No.2, 431–441, 1963.
5. Denavit J., and R.S. Hartenberg, “A Kinematic Notation for Lower- Pair Mechanism Based on Matrices,” *ASME Journal of Applied Mechanics*, pp. 215-221, 1955.
6. Guez, A., and Ahmad, Z., “A Solution to the Inverse Kinematic in Robotics Using Neural Network Processing,” *IJCNN89*, Vol. 2, pp. 299-304, 1989.
7. Oyama, E., et.al,, “Inverse Kinematics Learning by Modular Architecture Neural Networks with Performance Prediction Networks,” *Proc. IEEE Int. Conf on Robotics and Automation*, pp. 1006-1012, 2001.
8. Nguyen, L., Patel, RV., and Khorasani, K., “Neural Network Architectures for the Forward Kinematics Problem in Robotics,” *IJCNN90*, Vol. 3, pp. 393-399, 1990.

Mathematical Modelling Of Human Fear And Disgust Emotional Reactions Based On Skin Surface Electric Potential Changes

Gaisina Kristina
N.I. Lobachevsky Institute of Mathematics and Mechanics, Kazan Federal University, Kremlevskaya 35
Kazan, 420008, Russia

Gaisin Ruslan
Higher Institute for Information Technology and Information Systems, Laboratory of Neurobiology, Kremlevskaya 35
Kazan, 420008, Russia
E-mail: krictishaa@gmail.com, rusgaisin@gmail.com
http://kpfu.ru/eng

Abstract

The paper deals with skin surface electric potential data registration of a human while he / she is watching specially selected videos that are supposed to activate basic emotions of fear and disgust. We describe the selected video materials and data logging process and present human emotional reactions model, which was implemented by numerical methods. We demonstrate these experimental results of fear and disgust psycho-emotional states that were obtained from 100 respondents.

Keywords: Mathematical model of emotions, skin surface electrical potential, emotion model, numerical indicator of emotional level.

1. Introduction

The classification of human emotional reactions is normally based on the analysis of video data, psychological tests, electroencephalography data, galvanic skin response and other non-invasive methods. We propose developing a numerical model of human emotional reactions as the way to measure the level of experienced emotions, not to classify them. The main objectives of this study were to develop a hypothesis of numerical model to evaluate a person's emotional state and to compare the data obtained in the experiment with the subjective ones received from the interviews.

2. Material and Methods

During the experiment two basic emotions were analyzed, i.e. disgust and fear. We selected them because of the eight basic emotions these two are considered to be the most prominent, easily reproducible and recorded ones. 100 respondents were interviewed. As a basis we took the existing developments to register the skin surface electric potential and adapted them for the investigation. We used the SuTest Pro project source code [1] and Biopulse-TC device for the skin surface electric potential registration. The Biopulse-TC device is characterized by the maximum electric current of 40 µA, the output values are from 0 to 200 standard units, which corresponds to 0 - 50 mV with 0.01 Hz sampling frequency. During the experiment we recorded the electrical skin response in three stages: before, during and after watching a video. The rate of data logging was approximately from 8 to 10 records per second.
At the same time we had a psychological polling. For that purpose we developed a psychological test to represent

subjective emotional state in numerical form, that consisted of 41 questions: 10 neutral questions, 10 questions related to one of the basic emotions according to Tomkins [2] and remaining 3 questions for the rest basic emotions. The sequence of questions was generated randomly. The answer to the question was marked on a scale from -3 to +3, where the value of -3 meant that the emotion was not expressed and the value of +3 meant that the emotion was completely expressed at the highest rate. 100 respondents took part in the experiment.

To select the most appropriate video material (the most terrible one for fear and the most "disgusting", "hideous" one for disgust), we demonstrated each of the options to 30 respondents. We took into account personal opinions of the respondents and external reactions to the video (mimic, facial expression).

3. Results and Discussion

To analyse the data obtained, all the results were presented in graphical form. In case of disgust we noticed that all the graphs had a descending tendency. Moreover, if there was any development of action in a storyline of the video, we could find insignificant increase in indices during the most emotive parts of the video (Fig. 1).

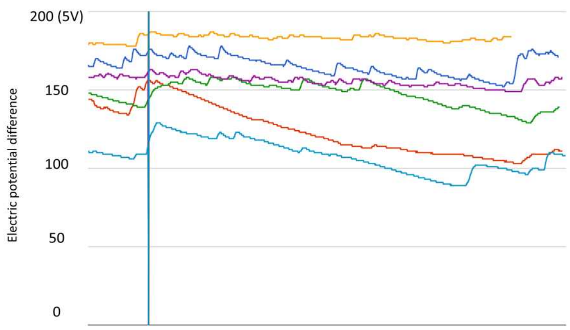

Fig. 1. Graphs for the state of disgust demonstrating descending tendency with time measured in intervals of 100 ms. The vertical line shows the beginning of watching video.

Fear expression, a peak emotional state (caused by video material), was represented by jumps in the graphs of all respondents (Fig. 2). In our research we supposed that fear and disgust dominate over all human emotions [3].

Our hypothesis regarding each indicator of numerical model (for the state of disgust) is as follows.

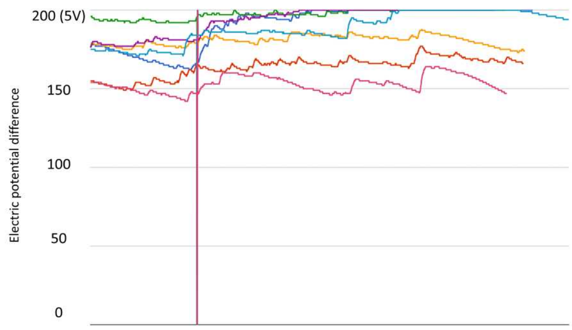

Fig. 2. Graphs for the state of fear. Time was measured in intervals of 100 ms. The vertical line shows the beginning of watching video.

The graph tendency is characterized by:

$$\bar{x}_1 - \bar{x}_2 \tag{1}$$

where $\bar{x}_1$ is arithmetic mean of initial sample (before watching the video), $\bar{x}_2$ is arithmetic mean of final sample (last seconds of watching the video). The value characterizes a common level of the experienced emotion (disgust). It is assumed that the greater the value is, the higher the level of experienced disgust.

The indicator that characterizes fluctuations intensity of the graph is:

$$\sum_{i=1}^{n} |x_i - x_{i-k}| \tag{2}$$

where n is total number of values, x_i – value, x_{i-k} – value with the step of k size. This value characterizes variability of the emotional state. It is assumed that the greater the value, the more stable the emotional state is.

The standard deviation is:

$$s = \sqrt{\frac{1}{n}\sum_{i=1}^{n}(x_i - \bar{x})^2} \tag{3}$$

where n is total number of values, x_i – value, $\bar{x}$ – arithmetic mean. This value represents the total change of the emotional state. It is assumed that the greater the value, the higher the level of experienced disgust is.

Our hypothesis regarding each indicator of numerical model (for the state of fear) is as follows.

The biggest (maximal) fluctuation:

$$\max|x_i - x_{i-k}|,\ i = \overline{1,n} \qquad (5)$$

This value represents a peak emotional state, maximal emotion expression (the state of fear). It is assumed that the greater the value, the higher the level of experienced fear is.

The maximal standard deviation of fluctuations:

$$\max s(|x_i - x_{i-k}|),\ i = \overline{1,n} \qquad (6)$$

It is assumed that this value represents a peak emotional state (the maximal emotion expression (fear)) regarding its own generalized emotional state.

The numerical model presented in our study makes it possible to distribute respondents according to the level of the experienced emotion. Thus, we built distribution for each emotional state separately for all the respondents. We made similar distribution in accordance with numerical polling data.

After comparing psychological polling data and skin electric response indicators for the same video we came to the conclusion that experienced emotional intensity distributions did not match.

The method used for subjective estimation of the emotional state cannot be used for numerical model validation.

4. Conclusions

Mismatch between psychological polling results and final indicators data needs to be investigated further.

For that purpose we suggest to take a Lövheim Cube as a basis [4]. The Lövheim Cube represents 8 basic emotions according to Tomkins, which levels depend on serotonin, dopamine and noradrenaline neuromediator values.

The validation of the proposed numerical indicators for experienced emotion intensity evaluation is possible only after measuring neuromediator levels in the brain during video watching.

We do not consider invasive ways of measurement. The only non-invasive and the most precise way to measure serotonin, dopamine and noradrenaline levels is to study subcortical systems of the brain with FMRT [5].

In case of successful validation, the resulting model will allow us to compare the level of the analysed basic emotions of fear and disgust in number. The results of the research can be used to estimate the strength of the external influence on the emotional state of a person.

Acknowledgements

This work was supported by the program of competitive growth of Kazan Federal University and the subsidy allocated to Kazan Federal University for the state assignment in the sphere of scientific activities.

References

1. Kajsa Landgren (2008). Ear Acupuncture, *Elsevier Health Sciences*, 30
2. Tomkins, Silvan S. (1962). Affect Imagery Consciousness: The Positive Affects (Vol. 1, ch. 9), New York: Springer.
3. Leukhin A., Talanov M., Sozutov I. (2016). Simulation of a fear-like state on a model of dopamine system of rat brain. *Advances in Intelligent Systems and Computing , 449,* 121-126
4. Lövheim, H. (2012). A new three-dimensional model for emotions and monoamine neurotransmitters. *Med Hypotheses*, 78: 341–348
5. Bär, K.-J., De la Cruz, F., Schumann, A., Koehler, S., Sauer, H., Critchley, H., Wagner, G. Functional connectivity and network analysis of midbrain and brainstem nuclei (2016) *NeuroImage*, 134, Pages 53-63.

Neuromorphic Robot Dream: A Spike Based Reasoning System

Alexander Toschev
Laboratory of Neurobiology, ITIS,
Department of Intellectual Robotics,
Kazan Federal University, Kazan, Russia
E-mail: atoschev@kpfu.ru

Max Talanov
Laboratory of Neurobiology, ITIS,
Department of Intellectual Robotics,
Kazan Federal University, Kazan, Russia
E-mail: max.talanov@gmail.com

Alexander Tchitchigin
Service Science and Engineering Laboratory, Innopolis University and
Laboratory of Neurobiology, Kazan Federal University, Kazan, Russia,
E-mail: a.chichigin@innopolis.ru

Salvatore Distefano
Social and Urban Computing Group, ITIS, Kazan Federal University, Kazan, Russia and
MDSLAB, University of Messina, Messina, Italy
E-mail: s_distefano@it.kfu.ru, sdistefano@unime.it

Abstract

In this position paper we propose the approach to create a reasoning system starting from brain spikes as main information medium to control a (quasi) real-time robotic system. Based on the robot dream architecture, the robot input in form of spike stimulus is provided to a simulated spiking neural network, then elaborated and fed back to the robot as specific rules. The reasoning rule-based system for intelligent spike processing transforming signals into software actions or hardware signals is thus specified.

Keywords: artificial intelligence, robotics, spikes, neurobiology, reasoning, logic.

1. Introduction

This work is a part of the Robot Dream project [1] focusing on the integration of real-time robotic system with spiking neural network simulation of a brain. One of the parts of the Robot Dream project is the translation the simulated neuron spikes into robotic system signals and the management of the robotic system using the reasoning system, based on the TU (thinking and understanding) framework described in [2]. The Robot Dream project integrates the simulated brain via spiking neural network with the robot system.

Figure 1. depicts the “wake-dream” cycle of the Robot Dream project architecture. The idea of the “wake-dream” was inspired by mammalian dream and sleep cycles. We split the computations into two phases: “wake” and “dream”. In the “wake" phase the robotic system actively interacts with the complex social environment in a

(quasi) real-time. Thus system reactions over permanently changing environment should be performed via light-weight rule-based system. The “dream” phase is responsible for processing of experience accumulated during the “wake" phase. During the “dream” phase the “dreaming brain” plays back stored experience over the part of the brain corresponding to the input channel (visual information over visual cortex, haptic information over somatosensory cortex, etc.). We call this process the direct translation.

During the reverse translation the simulated neuronal structures are consequentially transformed into the form of the logical rules of the robotic system.

The aim of this paper is to describe the system of light-weighted logical rules operating in the real-time robotic system which were obtaining during the reverse translation phase.

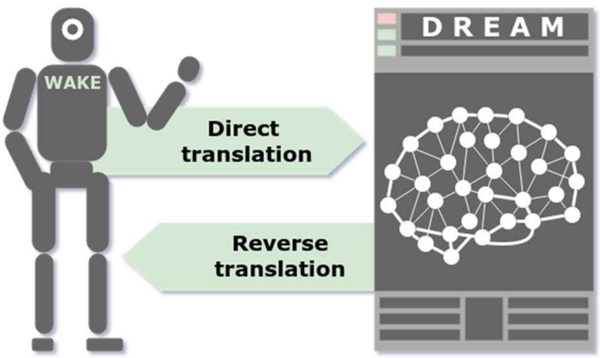

Fig. 1. The representation of “wake-dream” cycle: during “wake” phase the robotic system accumulates experience, during “dream” phase the accumulated experience is transferred from a robotic system to the “dreaming brain”. Later the “dreaming brain” updates its synaptic connections and translates the neuronal structures into the robotic system rules. Robotic system during “wake” phase operates in real-time using light-weight rules based system.

2. Robot lifecycle

The robotic system operates in the (quasi) real-time mode during the “wake” phase. If the (quasi) real-time requirement is strict the robot should use a lightweight management system. The second requirement is that the robotic system must store the input from sensors and actuation control logs in a format transferable to the “dreaming brain”, according to our bio-inspired approach basically as spikes.

Following a biologic analogy, our solution is based on spikes both in the representation of input information coming from the robot and in controlling the latter through spikes-encoded rules. This way all sensed data is stored in form of tagged spike trains. Later it is transmitted and “played back” over the simulated “dreaming brain”. We propose to use spikes as main information unit for the reasoning system instead of textual or numerical forms. Both approaches are described in detail below.

3. Rule based system

Due to the (quasi) real-time requirement we propose to use TU framework [2], based on the “Critic-Selector-Way to think” (T^3) model [3]. This framework helps us to implement the rule based system managing the robotic system. The T^3 “Critic-Selector-Way to think” triplet is inherited from the works of Marvin Minsky [4]. This approach provides an option to evaluate incoming sensory data over the stored knowledge in the knowledge base. The input information of the TU framework [2] is textual while in this work we propose to use spikes for the representation of input and processing information of the TU framework. The TU framework is based on probabilistic rules and uses logical reasoning with the 6-levels of mental activity and T^3 over spikes [4].

3.1. *Probabilistic Critic*

Probabilistic critic is the implementation of critic from the T^3 “Critic-Selector-Way to think” triplet. Spikes trigger several critics, that start inbound information processing in parallel on several levels of mental activity. Critics are grouped in contexts based on their level of mental activity and semantics of the processing information (audial, visual, tactile). The activation of one critic of the context increases the probability of triggering corresponding critics on the same context. This way every critic is a temporal probabilistic predicate that contains set of rules that are evaluated not only over the incoming information, but over current system state and context of recently processed information.

The sequence of the logical spiking information processing is depicted in Fig. 2.

The incoming set of spikes S1 triggers the pattern P1 of critics on two levels: instinctive (basic reflexes) and learned (simple-trained reactions). The pattern P1 and the next set of spikes trigger two patterns P2 on learned level and P3 on the instinctive levels. Later these two patters trigger two more patters one on each level: P4 and P5. This mechanism of spiking reasoning system is inspired by the “Hierarchical temporal memory” HTM approach [5] and in a similar way has predictive mechanism: the activation of the pattern P1 could be used as the indication of the S2 set of spikes. To use the advantages of training we propose to extend logical rules with weight value similar to confidence value in NARS [6].

3.2. *Way to think*

A way to think is a main activity to change the content of memory and perform an action [4]. A way to think runs a workflow that could trigger the hardware controller of the robotic system or change the data of the information processing context. We propose the following workflow:

1. Spike hits the system;
2. The system creates inbound context for this spike based on its attributes: source channel (visual, audial, ...), time, number of activated neurons, neurotransmitters, previously processed information, see Data Structures section for the details;
3. The system starts processing the spike;
4. Several Critics are activated by based on resulting probability of their rules;
5. Several spikes are accumulated in the system state and when their number reaches the threshold the motor reaction is triggered;
6. The critic activates a way to think;
7. The way to think generates data for controllers.

3.3. *Data structures*

According to our approach, the input from robots is encoded by spikes. A spike is an abstract object with following attributes:

1. Source channel;
2. Timing: start time, duration.
3. Semantic tag of the event to be processed.
4. Number of activated neurons.

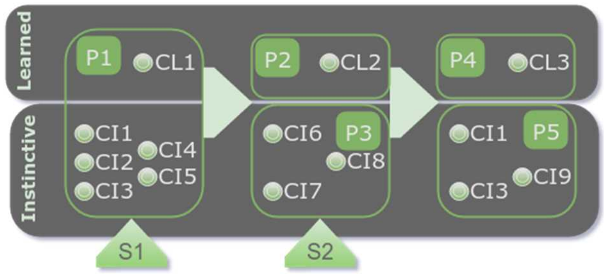

Fig. 2. Inbound set of spikes S1 trigger pattern of P1 critics CL1, CI1, CI2, CI3, CI4, CI5 on two levels: instinctive reactions and learned reactions. The pattern P1, and the spikes S2 trigger the patterns: P2 (CL2) and P3 (CI6, CI7, CI8) they in their turn trigger P4 (CL3) and P5 (CI1, CI3, CI9). This way, when P1 is triggered it could indicate that the next incoming set of spikes could most probably be S2.

5. Neurotransmitters used to generate this spike.
6. Previously processed information context.

4. The implementation of the model of six

We implement TU framework based on "Model of Six" developed by Marvin Minsky [4] as an instance of a rule-based (soft) real-time architecture.

Firstly we developed first three layers of the model: instinctive, learned and deliberative thinking. All layers process input data in parallel, the fastest one wins. This means that whatever layer selects a next action first, that action gets executed. This way simple instinctive reactions get executed much faster than long deliberative planning. Later long deliberative planning could override the fast behavior. It's useful for immediate handling of "emergency" situations. On the other hand, in the case no instinctive or learned rules match the situation the system can "take some time" to plan sequence of actions leading to a goal using deliberative thinking.

At the bottom of our layered architecture, closest to the hardware, there is the driver layer. This layer allows to use several drivers for different hardware and robotic platform configurations. Next one is hardware abstraction layer (HAL). This layer defines abstract high-level commands (like "move forward 10 cm") hardware or platform agnostic. The driver is responsible for executing these commands on a given robotic system. The third layer implements actual reasoning and control providing the system with the commands to be enforced. In our case, as stated above, it implements the Marvin Minsky's "Model of Six" [4]. The specific rules managing the system are tailored on the application running on the robotic system and subject to modifications through the feedback from the “dreaming brain”. The initial rules for an application are not generated by the inference engine ("Model of Six"). This architecture provides a relatively straightforward and flexible enough framework to experiment with and adapt to different tasks and robotic systems.

5. Conclusion

In the paper we propose the mechanism of the translation of neuron spikes into control signals for the robotic system. The TU framework is used to process reasoning life-cycle over the spikes and apply proper transformation of the brain neuronal signals (spikes) into the pseudo-neuronal activity of the robotic system. However, the system should be able to track existing signals and reactions from simulated “sleeping” brain mapping them into the robotic systems.

References

1. A. Tchitchigin and M. Talanov, *Robot dream* (Agent and Multi-Agent Systems: Technology and Applications: 10th KES International Conference, KES-AMSTA 2016 Puerto de la Cruz, Tenerife, Spain, June 2016 Proceedings 2016).
2. A. Toschev and M. Talanov (eds.), *Thinking Lifecycle as an implementation of machine understanding in software maintenance automation domain* (Agent and Multi-Agent Systems: Technologies and Applications. 9th KES International Conference, KES-AMSTA 2015 Sorrento, Italy, June 2015, Proceedings, 2015).
3. A. Toschev, Thinking lifecycle as an implementation of machine understanding in software maintenance automation domain (Smart Innovation, Systems and Technologies, pp. 301–310, 2015).
4. M. Minsky, The Emotion Machine: Commonsense Thinking, Artificial Intelligence, and the Future of the Human Mind, *Simon & Schuster.*2007.
5. J. Hawkins, HIERARCHICAL TEMPORAL MEMORY (Numenta, Inc., 2011), pp. 421–439.
6. H. Wang and M. Morales, Pedunculopontine and laterodorsal tegmental nuclei contain distinct populations of cholinergic, glutamatergic and GABAergic neurons in the rat. (The European journal of neuroscience, 2009).
7. A. Kumar and S. Rotter, Spiking activity propagation in neuronal networks: reconciling different perspectives on neural coding (Nature reviews neuroscience, 2010).
8. L. Buesing and W. Maass, Simplified rules and theoretical analysis for information bottleneck optimization and PCA with spiking neurons (Advances in Neural Information Processing Systems, 2008).
9. P. Vincent and H. Larochelle, tacked denoising autoencoders: Learning useful representations in a deep network with a local denoising criterion (Journal of Machine Learning Research, 2010).

Development of Behavioral Robot Using Imitated Multiplex Neurotransmitter System

Saji Keita and Eiji Hayashi
Mechanical Information Science and Technology, Kyushu Institute of Technology.
680-4, Kawazu, Iizuka, Fukuoka, 820-8502, Japan.
saji@mmcs.mse.kyutech.ac.jp and haya@mse.kyutech.ac.jp

Wisanu Jitviriya
Faculty of Engineering, King Mongkut's University of Technology North Bangkok.
1518 Pracharat 1, Wongsawang Rd., Bangsue, Bangkok, Thailand 10800

wisanu_jitviriya@hotmail.com

Abstract

This paper presents the design of the robot's behavior using the imitated multiplex neurotransmitter system. The major neurotransmitters of the nervous system are Dopamine, Noradrenaline and Serotonin, which are called monoamine neurotransmitter and they are related to the motivation, behavior and feeling. The proposed system is analyzed based on Lövheim's cube of emotion and Wundt's three-dimensional theory of feeling. So, Dopamine is applied as a comfort dimension, Noradrenaline is defined as a tense dimension, Serotonin is considered as an energetic dimension. In our system, three neurotransmitters are generated in each of the different factors, and then the motivation is calculated. The robot's motivation and some external information are classified into behavior and emotion maps using Self-Organizing Map learning. Finally, the robot's behavior and emotion are decided by Markov's stochastic model. The experimental results confirm the effective outcomes by comparing the conventional model with the proposed model.

Keywords: Neurotransmitter, Self-Organizing Map, Dimensions of Emotion

1. Introduction

Nowadays, the robot technology is applied to service field and developing and advancing rapidly. Domestic robot, medical robot, business robot and rescue robot are classified as service robot. These robots are necessary to work with people. Therefore, the robots need to have enough ability for user affinity. We suggest some function, comforting, attraction, and friendship in order to obtain the affinity. Therefore, the functions of animals (dog and cat) in real life, which is focused on improving our robot. We propose the development of service robot's behavior design by imitating the animal's consciousness

The new model of our robot is the dynamic behavior selection model based on emotional states which develops from the Consciousness-Based Architecture (CBA) model [1] combined with Self-Organizing Map (SOM) learning and Markovian model. CBA is based on animal's motivation system by dopamine in the brain. In this paper, we present the multiplex neurotransmitter system which simulates the generation of neurotransmitters such as serotonin, noradrenaline, and dopamine patterns. The multiplex neurotransmitter system is created to diversify the behavior factors of robot and to imitate animal's consciousness.

This paper is organized as follows: Section 2 provides the system structure of our robot and CBA model. Section 3 suggests a new method to improve the robot's behavior factors by the multiplex neurotransmitter system. Section 4 and 5 explain the approximation in applying the generation of neurotransmitters consisting of serotonin, noradrenaline, and dopamine. Section 6 shows the experimental results of the proposed model, and finally, Section 7 concludes the paper.

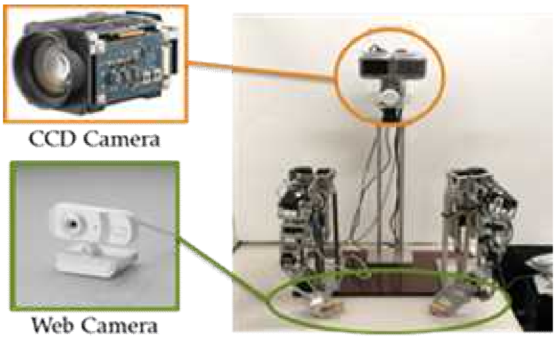

Fig.1 the system structure

2. System Structure

In this research work, the robot in our laboratory is being used as shown in Fig.1. This robot has two arms which have the base frame, shoulder, elbow, and wrist (6 DOF), and the robot head is made for acting the facial recognition and expression. The web camera is attached at the end-effector of arm that is used for recognition of an external situation and forward tracking algorithm, in order to recognize the target object. The CCD camera attached at the head that is used for recognition of user's facial emotional expressions. Fig. 2 shows the overview system of the robot. The procedure of the system can explain by the following steps:

Step1: Recognizing an external situation (the objects) by cameras and calculating the release of Dopamine and a motivation according to the circumstances.

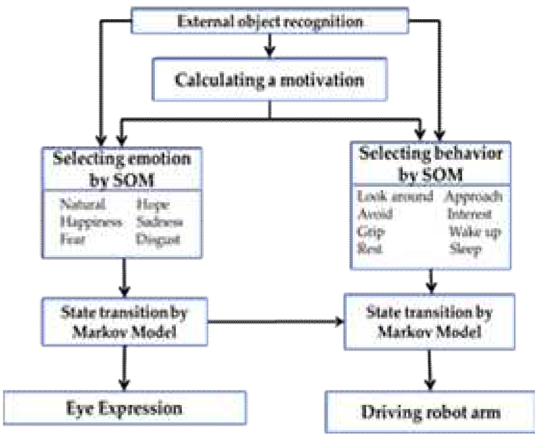

Fig.2 the overview system

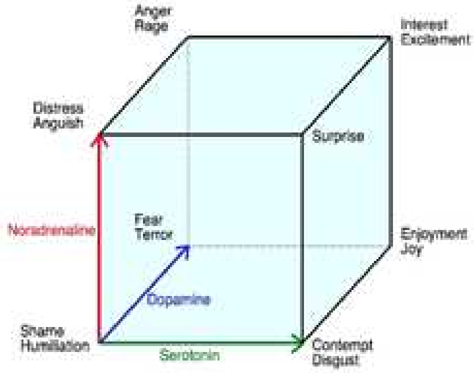

Fig.3 Lövheim's cube of emotion

Step2: Creating the maps that classified with default emotions (natural, hope, happiness, sadness, fear, disgust) and behaviors (look around, approach, avoid, etc.) using Self-Organizing Map method.

Step3: Selecting the candidate of emotion and behavior of next time step by a verification of the external situation (including the Dopamine and the motivation) and the map.

Step4: Deciding the emotion and the behavior for next time step by the results of the calculation. The state transition probability of Markov model is determined by the candidate of emotion and behavior.

Step5: The robotics arm drives the actuators according to the selected behavior, and the two displays which attached at the robot head present the eye images according to the selected emotion.

3. Imitated Multiplex Neurotransmitter system

In this paper, we suggest the imitated multiplex neurotransmitter system based on Lövheim's cube of emotion [2]. That theory is proposed theoretical model aiming at explaining the relationship between the monoamine neurotransmitters and the emotions (Fig.3). In addition, Wundt's three-dimensional theory of feeling [3] (Fig. 4), three psychological axes of feeling, pleasure-displeasure, relaxation-strain, and excitement-calm, can be applied to these neurotransmitters. In brain, Noradrenaline is known to be related to the attention and impulse, and Serotonin is known to be suppressed by fatigue substance in neuropsychology. Therefore, in this

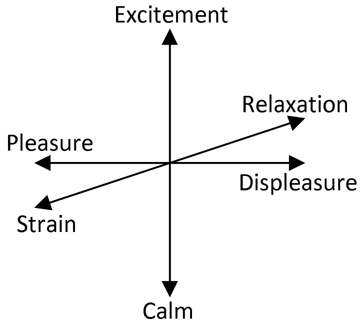

Fig.4 Wundt's three-dimensional theory of feeling

paper, Noradrenaline is fitted to relaxation-strain axes and Serotonin is fitted to excitement-calm axes.

Due to generate a motivation from different factors, the behavior factors of robot can be diversified and the system can imitate animal's consciousness based on biologically inspired artificial emotions.

4. Approximation of neurotransmitters

In this research, not only Dopamine (DA) neurotransmitter but also Noradrenaline (NE) and Serotonin (HT-5) neurotransmitters are applied because they are the element constituting the monoamine neurotransmitters. In this robot, the generating waveforms of these neurotransmitters are simulated based on the experimental results when researchers test them with the rat [3], [4] as shown in Fig.5. The generating waveform of Noradrenaline is approximated by a Gaussian Equation (1), and the generating waveform of Serotonin is approximated by Equations (2) and (3).

$$y(t) = \lambda \exp\{-\frac{(t-\mu)^2}{2\sigma^2}\} \tag{1}$$

$$y'' + 2\omega_n \varsigma y' + \omega_n{}^2 y - \omega_n{}^2 u = 0 \tag{2}$$

$$y = y_{peak} e^{-t/\tau} \tag{3}$$

5. Applying neurotransmitters

In this robot, the positive Noradrenaline is generated while the robot cannot complete some behaviors after deciding the behavior using Markov model. That means a strain, but the negative Noradrenaline is generated when the robot complete the behavior and that means a relaxation. The positive Serotonin is generated when the robot get some favorite things. That means an excitement. On the contrary, the negative Serotonin is generated when the robot moves and that means a calm. These generating waveforms are calculated using Equation (1), (2) and (3). Dopamine is generated same as the usual model.

Finally, a motivation is calculated by a second order response of the sum of all monoamine neurotransmitters.

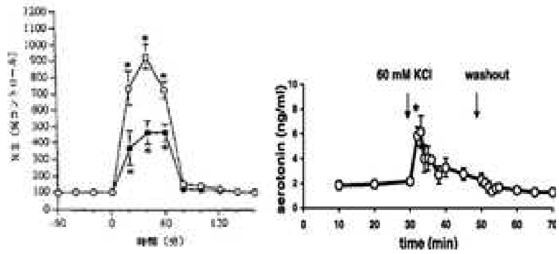

(a) Noradrenaline (b) Serotonin

Fig.5 the referenced waveforms

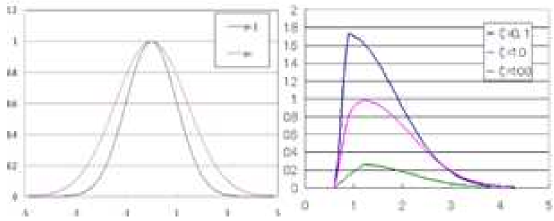

(a) Noradrenaline (b) Serotonin

Fig.6 the simulated waveforms

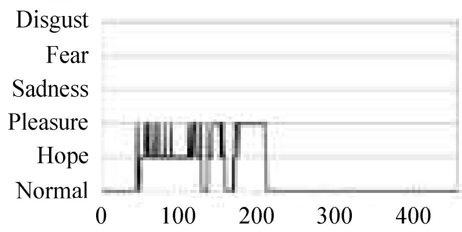

(a) Conventional model

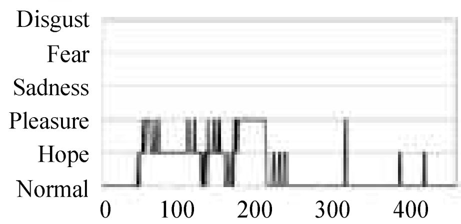

(b) Proposed model

Fig.7 the favorite object and the robot can catch target object

6. Experimental results

In this study, the multiplex neurotransmitter system is applied to CBA model. In Fig. 2 shows the process of the CBA system. In each time step, the amount of each neurotransmitter was calculated by the Equations (1), (2) and (3). Fig.7 shows the experimental results of comparison of the transition of emotion between conventional model and the model was applied with the multiplex neurotransmitter system when the robot detected a favorite object and it could complete in approaching and catching the target object.

On the other hand, Fig.8 also shows the experimental results of comparison of the transition of emotion when the robot detected a target object, but it couldn't be successful in the task.

7. Conclusions

In CBA, the generation process of motivation for emotional and behavior of the robot was improved by the multiplex neurotransmitter system. For this system, in addition to Dopamine, two neurotransmitters in brain Noradrenaline and Serotonin was applied to the generation of the motivation.

As a result of that, the improvement of diversity of emotion was confirmed and that means the behavior factor of the robot is also diversified.

References

1. E. Hayashi, T. Yamasaki, and K. Kuroki, "Autonomous Behavior System Combing Motivation and Consciousness Using Dopamine," *Proc. of 8th Int. IEEE Symposium on Computational Intelligence in Robotics and Automation* (CIRA 2009), pp. 126-131, 2009.
2. Lövheim, H (February 2012). "A new three-dimensional model for emotions and monoamine neurotransmitters". *Med.Hypotheses*.78:3418.doi:10.1016/j.mehy.2011.11.016. PMID 22153577.
3. Shahrzad Rezaie-Majd(2004), 「Increased release of serotonin from rat ileum due to dexfenfluramine」, *American Journal of Physiology – Regulatory*, Vol. 287 no. 5(2004), pp.2-4.
4. Japanese Patent, Public Patent Public Relations. Santen Pharmaceutical Co., Ltd. 6-Nitro. A pharmaceutical composition comprising norepinephrine as an active ingredient. Japanese Unexamined Patent Publication 9-227368. 1997-9-2.

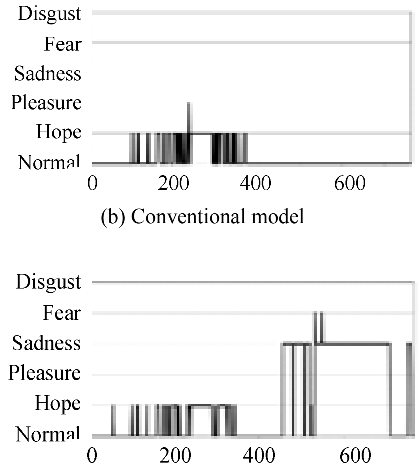

(b) Proposed model

Fig.8 the favorite object and the robot cannot catch target object

Nonlinear Estimation Strategies Applied on an RRR Robotic Manipulator

Jacob Goodman, Jinho Kim, Andrew S. Lee
Department of Mechanical Engineering, University of Maryland, Baltimore County (UMBC),
1000 Hilltop Circle, Baltimore, Maryland, USA, 21250
S. Andrew Gadsden
School of Engineering, University of Guelph,
Guelph, Ontario, Canada, N1G 2W1
Mohammad Al-Shabi
Department of Mechanical Engineering, University of Sharjah
Sharjah, UAE
E-mail: jg4@umbc.edu, umbcjhkim@umbc.edu, alee20@umbc.edu, gadsden@uoguelph.ca, malshabi@sharjah.ac.ae

Abstract

Nonlinear estimation strategies are important for accurate and reliable control of robotic manipulators. This paper studies the application of estimation theory to a simple robotic manipulator. Two estimation techniques are considered; the classic extended Kalman filter (EKF), and the smooth variable structure filter (SVSF). The EKF is included to present a basic background in estimation techniques and the SVSF demonstrates an example of the state-of-the art. We simulate the SVSF applied to a dynamically modeled three-link (RRR) robotic manipulator. The results of the paper demonstrate that nonlinear estimation techniques such as the SVSF can be applied effectively. Suggestions for future estimation and robotics research are also provided.

Keywords: Estimation theory, Kalman filter, smooth variable structure filter, robotic manipulator

1. Introduction

Accurate and predictable control of mechanical and electrical systems is often dependent on precise knowledge of system states. Accurate knowledge of these states however is rarely directly available, and instead some sort of estimate is required. Typically estimates will be made based on available measurement data as well as knowledge of the system model. Estimation theory concerns itself with the various techniques with which accurate and robust estimates can be made. Some estimators have become to be termed "filters" due their ability to effectively extract the true signal from system and measurement noise.

Many estimation strategies are well suited for linear systems in the discrete time domain. Systems can be generalized into four main categories (with physical systems only existing in the latter three): (i) linear, (ii) approximately linear systems, (iii) medium to strongly non-linear systems, (iv) systems for whom non-linearity is the main characteristic[1]. For categories i. and ii. typical estimations strategies work well. For category iii. estimation strategies can be extended with the use of linearization techniques. Category iv. systems can present a significant challenge for any estimation or control system.

Robotic manipulators have become quite ubiquitous over the last several decades. Many significant advances in manufacturing and automation are due to effective implementation of robotic manipulators. Robotic manipulators have achieved great utility in their ability to perform repetitive tasks in a highly consistent manner. As such estimation techniques necessarily play a critical role in the performance of these systems.

In this paper, we shall consider a relatively simple planer RRR robotic manipulator. The dynamics of even such a simple system are clearly nonlinear. For context we give a basic overview of the classic estimation algorithm known as the Kalman Filter, and its nonlinear variant the extended Kalman filter (EKF). We then present the relatively new estimation technique known as smooth variable structure filter (SVSF). We demonstrate the latter's application to a simple RRR manipulator and note the results. This paper is organized as follows: Section 1 is the introduction. Section 2 we present a brief background to both the EKF and SFVF with references for further review. In Section 3 we present the system dynamics and basic control loop. In Section 4 we present simulation results. In section 5 we draw our conclusions and discuss future work.

2. The Kalman Filter and Smooth Variable Structure Filter

2.1. *The Kalman Filter*

For a linear system, state dynamics can be expressed in state representation form as follows[1]:

$$x_{k+1} = Ax_k + Bu_k + w_k \quad (1)$$

$$z_{k+1} = Cx_{k+1} + v_{k+1} \quad (2)$$

In (1), x_k refers to the system states. A is the linear system matrix, B is the input gain matrix, u_k is the input vector and w_k is the system noise. In (2) z_k is the measurement vector, C is the linear measurement matrix, and v_k represents the measurement noise.

The Kalman filter assumes that the system model is well known and linear, the initial states are known, and the measurement and system noise is Gaussian with zero mean and known respective covariance matrices.[1,2] The KF works as a predictor-corrector; the system model is used to obtain an *a priori* estimate of the states, whereupon measurements combined with the Kalman Gain matrix are used to apply a correction term to create an updated *a posteriori* state estimate. Figure 2 illustrates the general concept.

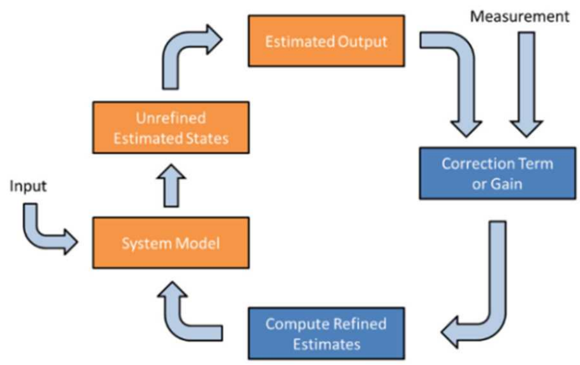

Fig 1. Predictor Estimator[1]

What makes the Kalman Filter so effective is the ability of an appropriately computed Kalman Gain matrix to optimally minimize the estimation error.
For a nonlinear system, equation's (1) and (2) become:

$$x_{k+1} = f(x_k, u_k) + w_k \quad (3)$$

$$z_{k+1} = h(x_{k+1}) + v_{k+1} \quad (4)$$

Where f and h are the nonlinear system and measurement models respectively.

The EKF follows the basic procedure of the KF. When computing the predicted and updated state error covariance matrices, where the nonlinear equations cannot be used, the strategy of the EKF is to linearize f and h around the current state estimate by means of the Jacobian. While this algorithm is effective, it does come at the price of optimality as well as robustness. Linearization can fail to account for some modeling uncertainties which can lead to instability[1]. More in depth treatment of the Kalman filter can be found in the literature.[3,4,5]

2.2. *The Smooth Variable Structure Filter*

The smooth variable structure filter is a relatively recent development, appearing in 2007. Also formulated as a predictor corrector, it is based on variable structure theory as well as sliding mode concepts.[1,6]. The basic idea is to use a switching gain to drive estimates to within a defined boundary of the true states - termed the existence subspace.[1] The SVSF can be applied to both linear and nonlinear systems. Important prerequisites of the SVSF is that the system in question be differentiable as well as observable.[7] The basic SVSF concept is illustrated in Figure 2 below. An in-depth treatment of the concepts can be found in the reference literature.[1,6,7,8,10,11,12]

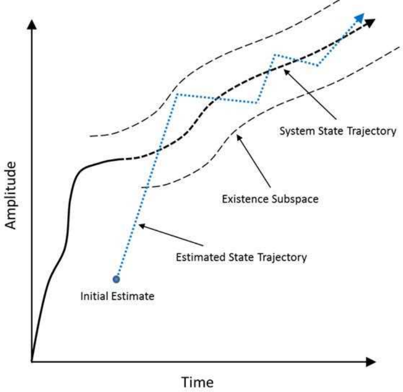

Fig. 2. SVSF Concept Diagram[1]

3. RRR Manipulator Dynamics

The basic configuration of an RRR robotic manipulator appears in Figure 3 below. Note the important parameters include the rod masses m_i, center of gravity lengths l_i, and overall lengths L_i. From these the moments of inertias J_i can be computed. θ_i are the joint variables. For all parameters i=1,2,3.

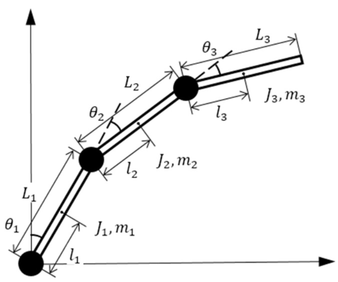

Fig. 3. RRR Planer Manipulator

The generalized equation for a frictionless robotic arm can shown to be[9]:

$$M(\boldsymbol{\theta})\ddot{\boldsymbol{\theta}} + B(\dot{\boldsymbol{\theta}}, \boldsymbol{\theta})\dot{\boldsymbol{\theta}} + G(\boldsymbol{\theta}) = \boldsymbol{u} \quad (5)$$

Where $\boldsymbol{\theta}$ refers to the joint variable matrix with n degrees of freedom. In the case of an RRR manipulator $n=3$. M is the inertia matrix, V is the Coriolis vector, G is the gravity vector, and $\boldsymbol{u}$ is the control input vector.

4. Simulation

For simulation we consider a simplified RRR manipulator with unitary masses and moments of inertia. Reference inputs are simple sinusoids. A simple PD controller is used to drive the system inputs. A SVSF filter is applied to the measurement feedback loop. In this simulation the SVSF operates with full measurements.

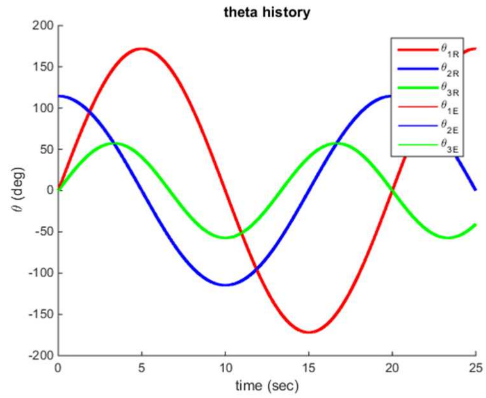

Fig. 7. Angle Input and Response

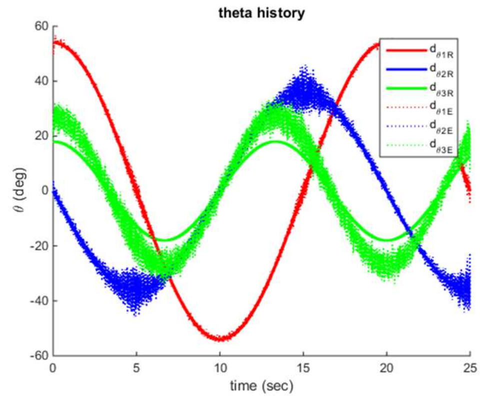

Fig. 8. Velocity Input and Response

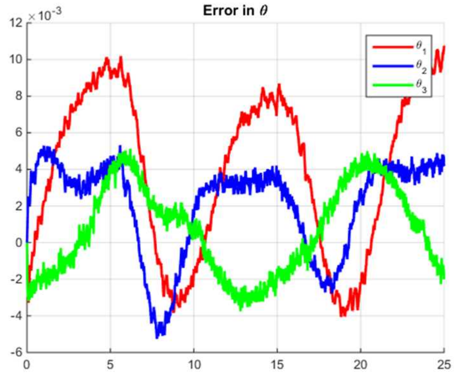

Fig. 10. Angle Errors

5. Conclusions and Future Work

Estimation theory has profound utility to a wide variety of control problems. Robotic manipulators in their requirement for precise and consistent control represent an important application of accurate and robust estimation techniques. Filters such as the SVSF are particularly suited for robotic manipulators as manipulator dynamics are by necessity almost always nonlinear. The results demonstrate that the SVSF can be effectively applied to an idealized robotic arm. For future work, more realistic model conditions can be considered, and the SVSF as well as other estimation strategies can be assessed for both robustness and accuracy.

Acknowledgements

The author wishes to thank Dr. Mohammad Al-Shabi for his generous assistance with the robotics dynamics and simulation.

References

1. J. R. Leigh, *Control Theory, 2nd Ed.* (The Institution of Electrical Engineers, London, 2004).
2. S. A. Gadsden, *Smooth Variable Structure Filtering: Theory and Applications*, (Department of Mechanical Engineering, McMaster University, Ph.D Thesis, Hamilton, Ontario, 2011).
3. R. E. Kalman, A New Approach to Linear Filtering and Prediction Problems, *J. of Basic Engineering, Transactions of ASME*, **82**, (1960), 35-45.
4. B. D. O. Anderson and J. B. Moore, *Optimal Filtering,* (Prentice-Hall Englewood, NJ, 1979).
5. A. Gelb, Applied Optimal Estimation, Cambridge, MA: MIT Press, 1974.
6. S. R. Habibi, "The Smooth Variable Structure Filter," *Proceedings of the IEEE,* **95**(2), (2007), 1026-1059.
7. M. Al-Shabi, *The General Toeplitz/Observability SVSF*, (Department of Mechanical Engineering, McMaster University, Hamilton, Ontario, 2011).
8. S. R. Habibi and R. Burton, The Variable Structure Filter, *J. of Dynamic Systems, Measurement, and Control (ASME),* **125**, (2003), 287-293.
9. F. L. Lewis, D. M. Dawson and C. T. Abdallah, *Robot Manipulator Control: Theory and Practice, 2nd Ed.*, (Marcel Dekker Inc., New York 2004).
10. S. A. Gadsden and S. R. Habibi, A New Robust Filtering Strategy for Linear Systems, *ASME Journal of Dynamic Systems, Measurements, and Control*, **135**, (2013).
11. S. A. Gadsden, Y Song, and S. R. Habibi, Novel Model-Based Estimators for the Purposes of Fault Detection and Diagnosis, *IEEE/ASME Transactions on Mechatronics*, **18**, (2013).
12. S. A. Gadsden, S. R. Habibi, and T. Kirubarajan, Kalman and Smooth Variable Structure Filters for Robust Estimation, *IEEE Transactions on Aerospace and Electronic Systems*, **50**, (2014).

Adaptive Negotiation-rules Acquisition Methods in Decentralized AGV Transportation Systems by Reinforcement Learning with a State Space Filter

Masato Nagayoshi, Simon Elderton
Niigata College of Nursing, 240 shinnan-cho
Joetsu, Niigata 943-0147, Japan
E-mail: nagayosi@niigata-cn.ac.jp, elderton@niigata-cn.ac.jp

Kazutoshi Sakakibara
Toyama Prefectural University, 5180 Kurokawa
Imizu, Toyama 939-0398, Japan
E-mail:sakakibara@pu-toyama.ac.jp

Hisashi Tamaki
Kobe University, 1-1 Rokkodai-cho, Nada-ku,
Kobe, Hyogo 657-8501, Japan
E-mail:tamaki@al.cs.kobe-u.ac.jp

Abstract

In this paper, we introduce an autonomous decentralized method for multiple Automated Guided Vehicles (AGVs). In our proposed system, each AGV as an agent computes its transportation route by referring to the static path information. route. Once potential collisions are detected, one of the two agents chosen by a negotiation rule modifies its route plan. The rules are improved by reinforcement learning with a state space filter. Then, the performance is confirmed with regard to the adaptive negotiation rules.

Keywords: reinforcement learning, AGV transportation system, negotiation rules, state space filter

1. Introduction

Recently, the problem of planning and operation are recognized as one of the most important issues in production and logistic systems. In particular, the transportation planning using Automated Guided Vehicles (AGVs) in a lot of steel production, semiconductor production and warehousing systems has been widely studied from both theoretical as well as practical viewpoints[1,2]. This paper focus on the AGV routing problem[2]. In this problem, all requests for transportation are given, but it is necessary to determine the transportation route plan in which collisions among AGVs do not occur.

In this paper, we introduce an autonomous decentralized approach for the AGV routing problem[3]. At first, each AGV as an agent creates its optimal route which satisfies the requests assigned to it. Once potential collisions are detected, one of the two agents chosen by a negotiation-rule modifies its route. A set of negotiation-rules are used at every collision avoidance. In this paper, we propose a reinforcement learning (RL)[4] approach with a state space filter[5] for improving the negotiation-rules. Furthermore, the effectiveness of the proposed approach is discussed through a computational experiment.

2. Problem Description

In this section, we describe a problem of routing AGVs to the destination, under the given rail networks and the given assignment of transportation requests as an AGV route planning problem. This problem is hard to find routing plans without collisions.

The AGV route planning problem is defined as follows: N^{V} AGVs V_i ($i = 1,\cdots, N^{\mathrm{V}}$) are available in the rail system. The rail system is represented as N^{N} nodes N_j ($j = 1,\cdots, N^{\mathrm{N}}$) and N^{A} arcs A_k ($k = 1,\cdots, N^{\mathrm{A}}$). A node represents the area for the loading and unloading points and branching points of the rail. An arc represents the path for AGVs. V_i moves to the destination node D_l which is specified by the request R_l ($l = 1,\cdots, N^{\mathrm{R}}$) assigned to V_i. R_l is given to the system at the start time t_l^{R} , and the assignment of R_l to V_i is given. These problem parameters can be summarized as follows:

(i) AGV V_i ($i = 1,\cdots, N^{\mathrm{V}}$):
+ initial node $\mathrm{P}_{i,}$

(ii) Node N_j ($j = 1,\cdots, N^{\mathrm{N}}$),

(iii) Arc A_k ($k = 1, \cdots, N^{\mathrm{A}}$),

(iv) Request R_l ($l = 1, \cdots, N^{\mathrm{R}}$):
+ occurrence time t_l^{R},
+ destination node D_l^{R}.

The following constraints should be taken into account in a planning process:

(i) All AGVs move synchronously.

(ii) The velocity of each AGV is constant.

(iii) Each AGV can travel on the arc and turn only on each node. The distance between the nodes is constant.

(iv) Each arc has a width of one AGV. Therefore, two AGVs cannot travel between the two nodes from the opposite direction simultaneously.

As for the evaluation of the routing plan, various kinds of criteria may be considered. We consider here the maximum completion time $C^{\max}$:

$$C^{\max} = \max t_i^{\mathrm{V}} \qquad (1)$$

where t_i^{V} represents the arrival time at the destination node D_l assigned to V_i.

3. Autonomous Decentralized Route Planning System

3.1. *Algorithm based on negotiation*

In this section, we introduce an autonomous decentralized planning method[3], in which each AGV as an agent repeats planning its own route and exchanging the route information with another until there is no collision. The route of each AGV is calculated by Dijkstra's method[6] on the graph representation. Once potential collisions are detected, one of the two agents chosen by a negotiation-rule modifies its route. The whole procedure of route planning is designed as follows:

(i) *Initialization* Each AGV calculates its minimum route from the start point to the destination point.

(ii) *Information Exchange* All AGVs within a certain distance d_{F} exchange their route information with each other.

(iii) *Termination* If any potential collisions are detected until a certain time step t_{L} ahead, go to stage (iv), otherwise the current set of routes are outputted and time proceeds one step.

(iv) *Negotiation and Re-planning* One of 2 AGVs involved potential collisions is chosen by a negotiation-rule and re-plans its route in order to avoid collisions. Go back to stage (ii).

In stage (iv), a new route plan is acquired by re-planning by Dijkstra's method on the network graph in such a way that the arc adjacent to the potential collision point is given 1 extra value of weight.

However, it is impossible to pass through the same node several times to avoid collisions using simply Dijkstra's method. In this route planning, it is effective to move backward into an adjacent node in order to avoid collisions. For that reason, it is necessary to pass through the same node several times.

Therefore, we enable the AGV to pass through the same node up to twice using Dijkstra's method by virtually adding one dummy node to each of the nodes, though it may be effective to pass through the same node more than 3 times. One of two AGVs re-plans route plans in this procedure. Nishi et.al[2] have proposed the agent-based AGV routing algorithms, where both of two AGVs in collision modify their route plans separately. In their approach, both AGVs might move in the same direction to avoid the collision points, and then new route plans are still infeasible. In contrast, this method is free from such oscillation phenomena.

3.2. *Structure of negotiation rules*

The AGV which re-plans its own route is determined by a negotiation rule. A negotiation rule consists of a condition-part and an action-part. The rule which matches the difference between each state of the 2 AGVs under negotiation is selected from a set of rules. As for the state parameters, we introduce three kinds of variables to represent the whole state space $\boldsymbol{S}$:

- s^{O}: The amount of incremental change in the route length after the re-creation.
- s^{R}: Route length from the collision point to the destination point.
- s^{F}: Number of nodes with 3 or more arcs.

Among the state parameters, s^{F} represents the flexibility of route creation. Then, $\boldsymbol{S}$ is divided into n^{S} portions $\boldsymbol{S}_u$ ($u = 1,\cdots, n^{\mathrm{S}}$). The action-part expresses the index of the AGV which re-plans its route.

4. A Negotiation-rules Acquisition Method by Reinforcement Learning

It is hard to design good negotiation-rules shown in Sec. 3, in advance without advanced knowledge of an object system. In this paper, the negotiation-rules are improved autonomously by reinforcement learning (RL)[4]. Specifically we use Q-learning (QL)[7] which is one of the typical RL methods, where state space and action space are constructed by the condition-parts of the negotiation-rules and by the action-parts, namely 0 or 1, respectively. It is necessary to design a positive reinforcement signal (reward) based on an evaluation of the route plans of all AGVs. In this paper, the reward is given to a RL agent only when all AGVs arrive at the destination point allowing the maximum completion time $C^{\max}$ to be evaluated.

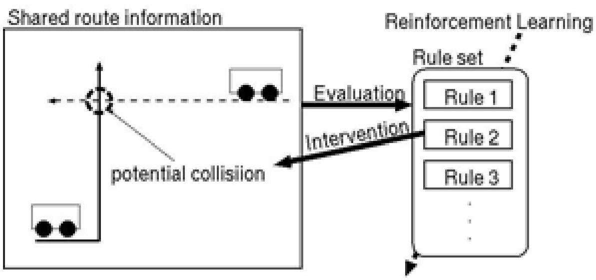

Fig. 1. A framework of rule learning using reinforcement learning.

5. Reinforcement Learning with a State Space Fitler

We have proposed a state space filter based on the entropy which is defined by action selection probability distributions in a state[5].

The entropy of action selection probability distributions using Boltzmann selection in a state $H(s)$ is defined by

$$H(s) = -(1/\log|\boldsymbol{A}|)\ \textstyle\sum_{a\in\boldsymbol{A}} \pi(a|s)\log\pi(a|s) \qquad (2)$$

where $\pi(a|s)$ specifies probabilities of taking each action a in each state s, $\boldsymbol{A}$ is the action space and $|\boldsymbol{A}|$ is the number of available actions.

The state space filter is adjusted by treating this entropy $H(s)$ as an index of a correctness of state aggregation in the state s. In particular, in case of mapping from the inner state space roughly digitized to the inner state space, a perceptual aliasing problem is happened. That is, the action which an agent should select cannot be identified clearly. Thus, the entropy may not be small in the state space should be divided. In this paper, sufficiency of the number of learning opportunities is judged using a threshold value θ_{L}.

Therefore, if the entropy does not get smaller than a threshold value θ_{H} despite the number of learning opportunities is sufficient, the state space filter is adjusted by dividing the state due to that the perceptual aliasing problem is happened.

Similarly, if the entropy is smaller than θ_{H} in a state s and a different state mapping from a transited input state s', and representative actions in each other's states are same, the state space filter is adjusted by integrating the states due to that the states is too divided. In addition, if a state s which never, not once, mapped during a certain period θ_{t} exists, then the state space filter is adjusted by integrating s and an adjacent state to s.

6. Computational Example

The effectiveness of the proposed approach is investigated in this section. We have prepared an AGV route planning problem (hereafter called ``N18"): N^{N}=18, N^{A}=26, N^{V}=8. 1 step is defined as the time step for moving to the adjacent node. The period from when all

Table 1. Parameters for Q-learning with a state space filter.

Parameter	Value
α_Q	0.1
γ	0.9
τ	0.1
θ_H	0.47
θ_L	1,000
θ_t	50 episode

AGVs are located at the start point to when all AGVs arrive at the destination point or 100 steps pass away is labeled as 1 episode. All occurrence time: $\forall l, t_l^R = 0$, the detectable time step $t_L = 2$, and the exchangeable distance $d_F = 2$ which is Manhattan distance. The least number of steps required for all AGVs to arrive at the destination point is 7 in N18.

To apply QL with a state space filter, a 3 dimensional initial state space, which is constructed by the difference between each state element of 2 AGVs which is designed so that the state space is evenly divided into 2×2×2 (hereafter called "2-2-2'"). For comparison, 3 state space constructions with 1 dimensional initial state space, which are constructed by the difference between each state element which are designed so that the state spaces are evenly divided into 2 (hereafter called "2-1-1'", "1-2-1'" and "1-1-2'"), and 1 state space construction with 1 initial state space where the size of state space is 1 (hereafter called "1-1-1").

The reward r = 10 (reward) is given to the agent only when all AGVs arrive at the destination point, the reward r = -15 (punishment) is given to the agent only when the weight of the arc is more than 100., and the reward r = 0 is given to the agent.at any other points.

Computational experiments have been done with parameters as shown in Table 1. In addition, all initial Q-values are set at 5.0 as the optimistic initial values.

The average number of steps required for all AGVs to arrive at the destination point in N18 were observed during learning over 20 simulations with different initial state space constructions, as described in Fig. 5.

It can be seen from Fig. 5 that all initial state space constructions could acquire feasible route plans within nearly the least number of required steps.

7. Conclusion

In this paper, we deal with the AGV route planning problem and introduce an autonomous decentralized route planning method. Here, we propose a reinforcement learning approach with a state space filter for improving the negotiation-rules. Through a computational experiment, it is observed that the proposed approach can acquire feasible and efficient rule-sets for the problem.

Our future projects include evaluating the effectiveness of our proposed approach under the condition that more than one request is assigned to each AGV.

References

1. Y. Seo and P. J. Egbelu, Integrated Manufacturing Planning for an AGV-based FMS, *in Int. Journal of Production Economics*, **60-61**, (1999) 473-478.
2. T. Nishi, K. Sotobayashi, M. Ando and M. Konishi, Evaluation of an Agent-Based Transportation Route Planning Method for LED Fabrication Line using Lagrangian Relaxation Technique, *in Proc. of Int. Symposium on Scheduling* (2002), 71-74.
3. K. Sakakibara, Y. Fukui and I. Nishikawa, Genetic-Based Machine Learning Approach for Rule Acquistion in an AGV Transportation System, in *Proc. of ISDA*, **3** (2008), 115-120.
4. R. S. Sutton and A. G. Barto, Reinforcement Learning (A Bradford Book, MIT Press, Cambridge, 1998).
5. M. Nagayoshi, H. Murao and H. Tamaki, A State Space Filter for Reinforcement Learning, in *Proc. of AROB 11th'06* (2006), 615-618.
6. E. W. Dijkstra, A note on two problems in connexion with graphs, *Numerische Mathematik* (1959), 269-271.
7. C. J. C. H. Watkins and P. Dayan, Technical note: Q-Learning, *Machine Learning* **8** (1992), 279-292.

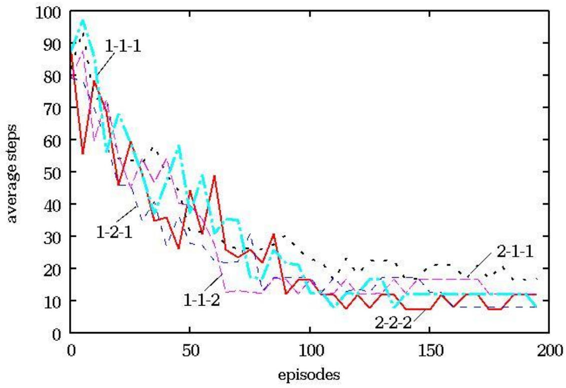

Fig. 2 Required steps for task N18 by QLs with state space filter

Modeling and Control of a Quadrotor Vehicle Subject to Disturbance Load

Jun Wang, Song Xin*, Yuxi Zhang
School of Electronics and Information Engineering, Beihang University, XueYuan Road No.37, HaiDian District Beijing, 100191, P. R. China

E-mail: wangj203@buaa.edu.cn, song.xin@buaa.edu.cn, zhangyuxi@buaa.edu.cn
www.buaa.edu.cn

Abstract

In this paper, a dynamic model of quadrotor vehicle is derived for theoretic and practical evaluation. Four transfer functions in different channels are converted from the state equations. To study the behavior of quadrotor subject to the external disturbance load, the FLC (fuzzy logic controller) is designed to compare with the PID (proportional-integral-derivative) controller. Subsequently, Liapounov function is applied for stability analysis. Finally, simulation results are presented to illustrate the performance between FLC and PID. Considering model error, the evaluation simulations are divided into two parts, which describe the ability for rejecting external disturbance, setpoint tracking and disturbance rejection respectively. The simulation scheme demonstrates the FLC method outperforms the PID control scheme.

Keywords: Disturbance load; Dynamic model; Fuzzy logic controller; PID; Quadrotor.

1. Introduction

In the recent years, quadrotor vehicle has been paid special attention due to its small size and flexible maneuverability[1]. The previously developments like PID control, Linear Quadratic control, back-stepping, slide mode control[2-3] are still used nowadays as suitable solutions for the quadrotors autonomous flying[1,4]. Considering the robust control in terms of process modeling errors and disturbance load, Lyapunov theory is introduced for the flight control design[5-7]. Back-stepping is well known and widely used in the control of nonlinear system, especially in the trajectory tracking control of the UAV[8-10].

However, the application of back-stepping depends on the actuated modeled system dynamics. Under-actuated model will dramatically decrease the control quality. In this paper, the Liapounov function and fuzzy logic controller is proposed to achieve better performance for quadrotor control.

2. Modeling of quadrotor vehicle

As shown in Fig.1, the quadrotor is an X-shaped four-rotor aircraft, with each rotor located in endpoints.

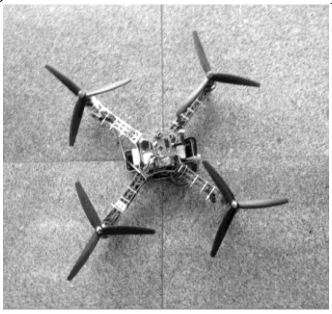

Fig. 1. Designed Quadrotor

The quadrotor drives the posture and movement depending on the rotational thrust and torque of four rotors. As shown in Fig. 2, rotors 2, 4 and 1, 3 rotate in opposite direction for eliminating the yawing torque. If the four rotors rotate at the same speed, the aircraft will produce vertical motion. Change the speeds of rotors 4, 2 and keep the speeds of rotors 1, 3, the aircraft will produce pitch movement. Similarly, roll movement result from 1, 3 rotor's speeds change. If the yawing torque in the different diagonals cannot be cancelled, the yaw movement is achieved.

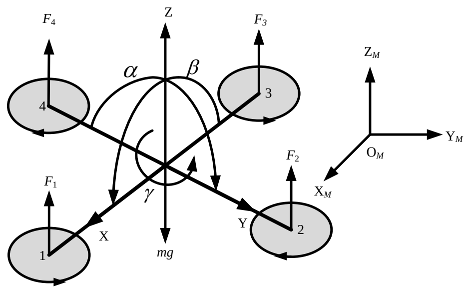

Fig. 2. The sketch map of the quadrotor

Let the vector $p=[x,y,z]^T$ denote the relative position of a quadrotor with respect to an inertial coordinate, and $q=[\alpha,\beta,\gamma]^T$ represents attitude angles of the quadrotor. Set O_M as the original point. $X_MY_MZ_M$ is the inertia coordinates and XYZ is the body fixed coordinates. The transformation matrix between the two coordinates is written as:

$$R_{\alpha\beta\gamma}=\begin{bmatrix}1&0&0\\0&\cos\alpha&\sin\alpha\\0&-\sin\alpha&\cos\alpha\end{bmatrix}\left\{\begin{bmatrix}\cos\beta&0&-\sin\beta\\0&1&0\\\sin\beta&0&\cos\beta\end{bmatrix}\begin{bmatrix}\cos\gamma&-\sin\gamma&0\\-\sin\gamma&\cos\gamma&0\\0&0&1\end{bmatrix}\right\}$$
$$=\begin{bmatrix}\cos\beta\cos\gamma&\cos\beta\sin\gamma&-\sin\beta\\-\cos\alpha\sin\gamma+\sin\beta\cos\gamma\sin\alpha&\cos\alpha\cos\gamma+\sin\beta\sin\gamma\sin\alpha&\sin\alpha\cos\beta\\\sin\alpha\sin\gamma+\sin\beta\cos\alpha\cos\gamma&-\sin\alpha\cos\gamma+\sin\beta\sin\gamma\cos\alpha&\cos\alpha\cos\beta\end{bmatrix}$$

Assume that the thrust generated by the four rotors is perpendicular to the aircraft. Therefore, in the body coordinates, the thrust is expressed as:

$$F_M=\left[0,0,\sum_{i=1}^{4}F_i\right]^T \quad (2)$$

Considering equations (1), (2), in inertial coordinate, the thrust analysis is:

$$F=\begin{bmatrix}F_x\\F_y\\F_z\end{bmatrix}=R_{\alpha\beta\gamma}F_M=\sum_{i=1}^{4}F_i\begin{bmatrix}-\sin\beta\\\sin\alpha\cos\beta\\\cos\alpha\cos\beta\end{bmatrix} \quad (3)$$

Let m denote the quality of the quadrotor. The acceleration of quadrotor in the inertial coordinate is given by:

$$\ddot{p}=\begin{bmatrix}\ddot{x}&\ddot{y}&\ddot{z}\end{bmatrix}^T=\begin{bmatrix}F_x/m&F_y/m&(F_z-mg)/m\end{bmatrix}^T \quad (4)$$

Similarly, the angular acceleration can be written as:

$$\ddot{q}=\begin{bmatrix}\ddot{\alpha}\\\ddot{\beta}\\\ddot{\gamma}\end{bmatrix}=\begin{bmatrix}r(F_4-F_2)/I_x\\r(F_1-F_3)/I_y\\(M_1-M_2+M_3-M_4)/I_z\end{bmatrix} \quad (5)$$

Where, r is the length from rotor to the center of the mass of the quadrotor. F_i denotes the thrust of *ith* rotor. I_x, I_y and I_z are the rotational inertia of the quadrotor around X, Y and Z-axis respectively. M_i is torque generated by *ith* rotor.

In terms of the equations (4), (5), the dynamic equations can be yielded:

$$T=\begin{bmatrix}\ddot{x}&\ddot{y}&\ddot{z}&\ddot{\alpha}&\ddot{\beta}&\ddot{\gamma}\end{bmatrix}^T \quad (6)$$

Let $X=(\dot{x},\dot{y},\dot{z},\dot{\alpha},\dot{\beta},\dot{\gamma},\alpha,\beta,\gamma), Y=(z,\alpha,\beta,\gamma)$, the state equations are given as:

$$\begin{aligned}\dot{X}&=AX+Bu\\\dot{Y}&=CX+Du\end{aligned} \quad (7)$$

Where,

(1)

$$A=\begin{bmatrix}0&0&0&0&0&0&0&0&0\\0&0&0&0&0&0&0&0&0\\0&0&0&0&0&0&0&0&0\\0&0&0&0&0&0&0&0&0\\0&0&0&0&0&0&0&0&0\\0&0&0&0&0&0&0&0&0\\0&0&0&1&0&0&0&0&0\\0&0&0&0&1&0&0&0&0\\0&0&0&0&0&1&0&0&0\end{bmatrix} \quad B=\begin{bmatrix}-\sin\beta/m&0&0&0\\\sin\alpha\cos\beta/m&0&0&0\\\cos\alpha\cos\beta/m&0&0&0\\0&\frac{1}{I_x}&0&0\\0&0&\frac{1}{I_y}&0\\0&0&0&\frac{1}{I_z}\\0&0&0&0\\0&0&0&0\\0&0&0&0\end{bmatrix}$$

$$C=\begin{bmatrix}0&0&1&0&0&0&0&0&0\\0&0&0&1&0&0&0&0&0\\0&0&0&0&0&1&0&0&0\\0&0&0&0&0&0&1&0&0\end{bmatrix},\quad D=0$$

The transfer function of quadrotor can be presented:

$$G(s)=C(sI-A)^{-1}B+D=\begin{bmatrix}\frac{\cos\alpha\cos\beta}{ms}&0&0&0\\0&\frac{1/I_x}{s^2}&0&0\\0&0&\frac{1/I_y}{s^2}&0\\0&0&0&\frac{1/I_z}{s^2}\end{bmatrix} \quad (8)$$

The parameters of the designed quadrotor are measured as follows:

Table 1. Parameters of the quadrotor

Item	Values
$r\ (m)$	0.245
$m\ (kg)$	1.05
$Ix*10^{-3}/(kg.m^2)$	6.2
$Iy*10^{-3}/(kg.m^2)$	6.2
$Iz*10^{-2}/(kg.m^2)$	3

3. Control design and stability analysis

3.1. *PID control method*

The PID control with simple structure has excellent stability by selecting appropriate proportion, differentiation and integration coefficients for disturbance rejection. Taking pitch channel as an example, the simulation results are conducted on the block diagram of PID control system in Fig. 3.

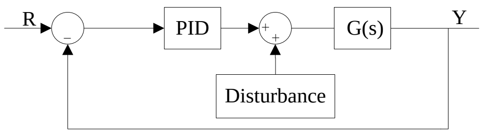

Fig. 3. Block diagram of PID control system

3.2. *Fuzzy logic modified PID control implementation*

The fuzzy logic modified PID controller (FLC) is also proposed in the same manner to compare with the performance of PID controller. A block diagram of fuzzy controller structure with a disturbance load is shown in Fig. 4.

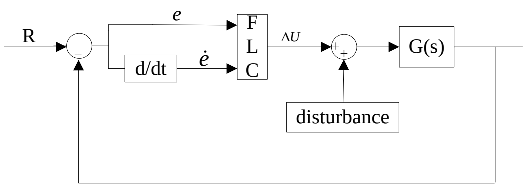

Fig. 4. Block diagram of FLC control system

The error of angle (expressed by e) and change of the angle error (expressed by $\dot{e}$) are regard as inputs of FLC; U is the control output of the FLC. As a rule of a thumb, e and $\dot{e}$ can be divided into seven grades (As shown in Fig. 5.).

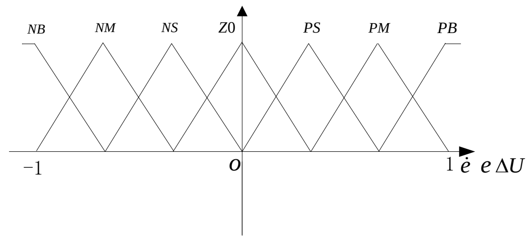

Fig. 5. Input fuzzy membership functions

Where, *NB* is negative big, *NM* is negative middle, *NM* is negative small, *Z0* is zero, *PS* is positive small, *PM* is positive middle, *PB* is positive big. For instance, if e is negative big "*NB*", $\dot{e}$ is positive big "*PB*", so the control output U is supposed to be increased so as to eliminate system error. So U should be positive big "*PB*".

3.3. *Convergence analysis*

To further illustrate quadrotor's stability, a Lyapunov function approval is introduced. In terms of the pitch motion, it can be described as:

$$\begin{aligned} e &= \alpha - \alpha_0 = x_1 \\ \dot{e} &= \dot{\alpha} - \dot{\alpha}_0 = x_2 \end{aligned} \tag{9}$$

In which, α is the measured angle, α_0 is the desired angle, we usually set α_0 =0.it is obtained:

$$\begin{aligned} \dot{x}_1 &= x_2 = \dot{\alpha} - \dot{\alpha}_0 \\ \dot{x}_2 &= \ddot{\alpha} - \ddot{\alpha}_0 = u_2 / I_x - \ddot{\alpha}_0 \end{aligned} \tag{10}$$

Assume nonlinear systems:

$$\dot{x} = f(x) = [\dot{x}_1, \dot{x}_2]^T = [x_2, \dot{x}_2]^T \tag{11}$$

is asymptotically stable on the equilibrium $x_e = [0,0]$.

The progress of looking for a Lyapunov function is organized as follows:

(1) Assume $V(x)$ is a scalar function of x, the gradient of $V(x)$ is:

$$\nabla V = \begin{pmatrix} a_{11}x_1 + a_{12}x_2 \\ a_{21}x_1 + a_{22}x_2 \end{pmatrix} = \begin{pmatrix} \nabla V_1 \\ \nabla V_2 \end{pmatrix} \tag{12}$$

Where, a_{11}, a_{12}, a_{21}, a_{22} are unknown coefficients.

(2) Then we have:

$$\begin{aligned} \dot{V}(x) &= (\nabla V)^T \dot{x} = (a_{11}x_1 + a_{12}x_2, a_{21}x_1 + a_{22}x_2)(\dot{x}_1, \dot{x}_2)^T \\ &= (a_{11}x_1 + a_{12}x_2)\dot{x}_1 + (a_{21}x_1 + a_{22}x_2)\dot{x}_2 \end{aligned} \tag{13}$$

(3) Try to choose $a_{11} = a_{22} = 1, a_{12} = a_{21} = 0$, we get

$$\dot{V}(x) = x_1\dot{x}_1 + x_2\dot{x}_2 \tag{14}$$

Recall (12), we have

$$\nabla V = \begin{pmatrix} x_1 \\ x_2 \end{pmatrix} \tag{15}$$

It is obvious to meet curl equation:

$$\frac{\partial \nabla V_1}{\partial x_2} = \frac{\partial \nabla V_2}{\partial x_1}, \text{ namely, } \frac{\partial x_1}{\partial x_2} = \frac{\partial x_2}{\partial x_1} = 0 \tag{16}$$

which indicates the parameters chosen above is rational.

(4) Therefore, the Lyapunov function can be yield as follows:

$$V(x) = \int_0^x (\nabla V)^T dx = \int_0^{x_1(x_2=0)} x_1 dx_1 + \int_0^{x_2(x_1=x_1)} x_2 dx_2$$

$$= \frac{1}{2}(x_1^2 + x_2^2) \tag{17}$$

Invoking (10), (14), we have

$$\begin{aligned} \dot{V}(x) &= x_1\dot{x}_1 + x_2\dot{x}_2 = (\dot{\alpha} - \dot{\alpha}_0)(\alpha + \ddot{\alpha} - \alpha_0 - \ddot{\alpha}_0) \\ &= (\dot{\alpha} - \dot{\alpha}_0)(\alpha - \ddot{\alpha}_0 - \alpha_0 + u_2 / I_x) \end{aligned} \tag{18}$$

To achieve the stability of the system, the condition $\dot{V}(x) \le 0$ is necessary. Due to, $\alpha_0 = 0$ we have $\dot{\alpha}_0 = \ddot{\alpha}_0 = 0$.Therefore, to achieve $\dot{V}(x) \le 0$, we just need design a fuzzy controller to adjust $\alpha, \dot{\alpha}$ for satisfying either of the following conditions:

$$\dot{\alpha} > 0 \text{ and } \alpha + u_2 / I_x < 0 \tag{19}$$

$$\dot{\alpha} < 0 \text{ and } \alpha + u_2 / I_x > 0 \tag{20}$$

From the mentioned above, we can make a conclusion that the convergence in the model can be guaranteed.

4. Simulation

In this section, the performance of PID and FLC are compared by simulations, which are mainly divided into two parts. The first part is conducted in the presence of disturbance load; the second part presents the case with modeling error.

4.1. *No modeling error*

4.1.1. *Disturbance rejection*

According to Fig. 4, the time of simulation is 20*s*. During *t*=4-4.4*s*, a pulse signal disturbance load is introduced. The simulation result is shown in Fig. 6.The PID controller responds from peak to bottom during *t*=4.4-6.59*s*, the overshoot angle in negative direction reaches -0.85°. At about *t*=16.09*s*, the angle reaches the desired value.

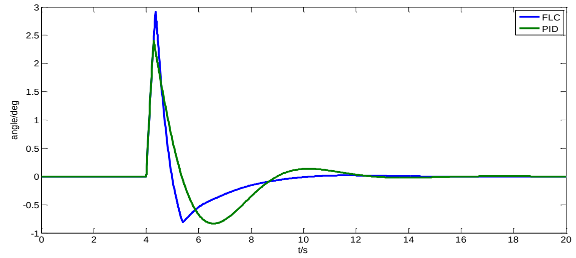

Fig. 6. Simulation results for fighting against a disturbance

For FLC, the response wave reaches peak at about t=4.37s, and reaches trough at about t= 5.41s. The overshoot angle in negative direction is -0.8°. At about t=13.86s, the controlled angle reaches 0°. The FLC has faster response speed, smaller reverse overshoot than PID. Thus, fuzzy PID control scheme has stronger ability to resist a disturbance load.

4.1.2. *Setpoint tracking*

To identify the tracking abilities of PID and FLC, set the disturbances to zero. According to Fig.3, Fig. 4, a step signal is introduced at initial time.

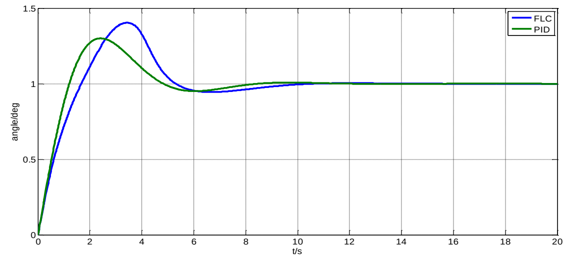

Fig. 7. Simulation results of setpoint tracking

In Fig.7, when a step signal is introduced, the two systems make response at the same time. With PID, the response is faster than that of FLC during 1s-2s. As for FLC, it reaches the desired value at 10.3s, which is slightly earlier than that of PID.

4.1.3. *Setpoint tracking& disturbance rejection*

Fig.8 shows the simulation results of the step response with a disturbance load. When a step signal is introduced at the beginning, the response of two systems just like what the Fig. 7 shows.

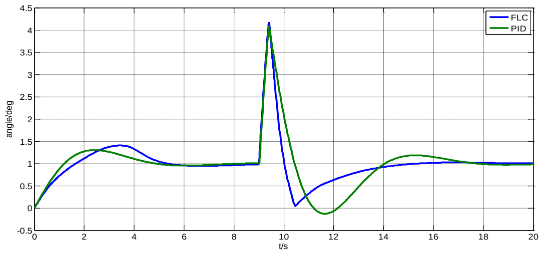

Fig. 8. Setpoint tracking & disturbance rejection

When a disturbance is introduced within t=8-8.4s, It can be observed that both of two controllers quickly moves towards the maximum in negative direction. However, the response of FLC is more sensitive to the disturbance than that of traditional PID controller. It is apparent that the system controlled by FLC reaches the desired angle quickly.

4.2. *With modeling error*

A Considering process modeling error, a third order transfer function in pitch channel is applied as follows:

$$G(s)=\frac{56.95s+4391}{s^3+105s^2+870s+4430} \tag{21}$$

4.2.1. *Setpoint tracking& disturbance rejection*

Let the gain of disturbance be zero, a step signal is given to identify the ability of setpoint tracking of the third order transfer function. Meanwhile, a disturbance is introduced during 8s-8.4s.The simulation result is presented in Fig.9.

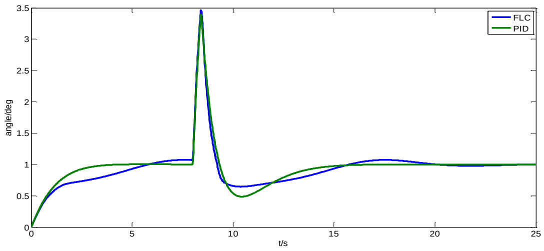

Fig. 9. Simulation of setpoint tracking & disturbance rejection of third order transfer function

The result shows the angle can be controlled to its desired value within 20s. And the overshoot angle of FLC in negative direction is smaller. Therefore, FLC provides better performance. All the simulation results mentioned above indicate that the FLC controller can efficiently respond to the outside disturbance, thus show better performances than its counterpart. The reason lies in the fact that the FLC can automatically adjust k_p, k_i, k_d in time according to the external conditions so as to maintain the stability of the control system. However, the three parameters of traditional PID is unchanged as soon as they are set in the initial time, that is to say, the traditional PID does not have the adaptive characteristics.

5. Conclusion

In the paper, a fuzzy logic modified PID (FLC) control scheme is designed to control stability of the quadrotor. Based on theoretical analysis, a Liapounov function is constructed to prove that the stability of the control system can be achieved. The difference between the actual angle and desired angle is presented as the error. The error and change-in-error are applied as inputs of the FLC. To further test the performance of the designed controller subjecting to the disturbance load, the simulation are conducted in MATLAB/ Simulink .The simulation results demonstrate that FLC response more quickly than PID control method, moreover, in terms of FLC, the angle can be controlled to its desired value within less time compared to its counterpart.

References

1. N. Michael, D. Mellinger, Q. Lindsey, and V. Kumar, “The GRASP multiple micro-UVA test bed,” IEEE Robot. Autom. Mag,Vol. 17, No. 3, pp. 56–65, 2010.
2. S. Bouabdallah, “Design and control of quadrotors with application to autonomous flying (PhD Thesis),” 2007.
3. S. Bouabdallah, A. Noth, and R. Siegwan, “PID vs LQ Control Techniques Applied to an Indoor Micro Quadrotor,” in Proceedings of 2004 IEEE/RSJ International Conference on Intelligent Robots and Systems, (IROS 2004)., 2004, pp. 2451–2456.
4. B. H. Lim, J. Park, D. Lee, and H. J. Kim, “Build your own quadrotor: open-source projects on unmanned aerial vehicles,” IEEE Robot. Autom. Mag., Vol. 19, No. 3, pp. 33–45, 2012.
5. A. Tayebi and S. McGilvray, “Attitude stabilization of a VTOL quadrotor aircraft,” IEEE Trans. Control Syst. Technol., Vol. 14, No. 3, pp. 562–571, May 2006.
6. R. Zhang, Q. Quan, and K.-Y. Cai, “Attitude control of a quadrotor aircraft subject to a class of time-varying disturbances,” IET Control Theory Appl., Vol. 5, No. 9, pp. 1140–1146, Jun. 2011.
7. D. Cabecinhas, R. Cunha, and C. Silvestre, “A nonlinear quadrotor trajectory tracking controller with disturbance rejection,” Control Eng. Pract., Vol. 26, pp. 1–10, 2014.

8. F. Kendoul, I. Fantoni, and R. Lozano, "Modeling and control of a small autonomous aircraft having two tilting rotors," in Proceedings of the 44th IEEE Conference on Decision and Control, 2005, pp. 8144–8149.
9. F. Kendoul, I. Fantoni, and R. Lozano, "Modeling and control of a small autonomous aircraft having two tilting rotors," IEEE Trans. Robot., Vol. 22, No. 6, pp. 1297–1302, 2006.
10. R. Mahony and T. Hamel, "Robust trajectory tracking for a scale model autonomous helicopter," Int. J. Robust Nonlinear Control, Vol. 14, No. 12, pp. 1035–1059, Aug. 2004.

A multithreaded algorithm of UAV visual localization based on a 3D model of environment: implementation with CUDA technology and CNN filtering of minor importance objects

Alexander Buyval, Mikhail Gavrilenkov
Department of computer science,
Bryansk State Technical University[1],7 Oktyabrya boulevard, Bryansk, 241035,Russian Federation

Evgeni Magid
Intelligent Robotic Systems Laboratory, Higher Institute for Information Technology and Information Systems (ITIS),
Kazan Federal University[2], 35 Kremlyovskaya street, Kazan, 420008, Russian Federation
E-mail: alexbuyval@gmail.com, gavrilenkov@umlab.ru, dr.e.magid@ieee.org
[1]http://iipo.tu-bryansk.ru[2] http://kpfu.ru/eng/itis

Abstract

Visual based navigation plays an important role in localization and path planning, especially in GPS-denied environments. This paper presents a visual based localization algorithm for a UAV within an indoor environment. The algorithm uses multithreaded computing CUDA technology and CNN-preprocessing filtering, which is responsible for filtering out dynamic objects. The algorithm is simulated in ROS/Gazebo environment with two different approaches – one uses CPU only and the other uses CPU and GPU - and their performance is compared.

Keywords: localization of UAV; particle filter; ROS; Gazebo, CUDA; CNN.

1. Introduction

Robot self-localization and simultaneous localization and mapping (SLAM)[1] play important role in path planning and navigation for multiple purposes, including such broad fields as service robotics, industrial robotics, search and rescue robotics, and others[2]. Within indoor environment, which are typically GPS-denied, visual localization is often a natural substitution of a GPS approach. Due to visual sensors' long range, high resolution, low energy consumption, and affordable price visual localization is often preferred over laser range finder or sonar based localization solutions. Selection of a passive visual sensor ranges from cheap and simple monocular cameras to stereo or depth cameras, like Kinect, or event-driven cameras. We may distinguish two typical subclasses of visual localization methods: the first subclass uses special visual markers with known positions and thus requires some additional marking of environment prior to its use; the second subclass uses native visual features.

This paper focuses on visual localization approach, which uses object edges as key features, and proposes several improvements to a particle filter based algorithm. The algorithm uses multithreaded CUDA technology and CNN-preprocessing filtering to exclude dynamic objects. We assume that while an initial 3D model of environment is available, the scene may undergo minor dynamical changes, e.g. new objects may appear in the scene as the time passes. The localization is performed in two steps. Initially, a neural filtering module detects new objects in the scene and filters them out. Next, a multithreaded edge-computing module processes filtered data and compares it with the initial model. The algorithm is simulated in ROS/Gazebo environment with two different approaches – one uses CPU only and the other uses CPU and GPU – and their performance is compared.

2. Basic localization algorithm

To solve a localization problem our system uses image edges as visual features. Based on location model, it compares a received from a camera real image and a simulated image of a pre-stored 3D model. The algorithm considers a number of robot position hypotheses and renders a set of images from the 3D model that correspond these hypotheses. Each image corresponds to an image that would be obtained in the estimated point under a particular hypothesis. Thus, at each algorithm iteration, we compare one image from the camera to a set of simulated images, estimate edge matching between them and a level of their similarity.

Edge features are formed from typical elements of indoor environment: conjunctions of walls, ceiling and floor, window and door frames, etc. Such edges are rather steady features. They are steady in time and, as a rule, illumination changes do not influence their perception. Experimental work showed that it is enough to consider these basic elements, which in turn significantly simplifies a 3D model of the room.

2.1. *Using a particle filter for robot localization*

For processing of images and locomotion sensory data, which are followed by localization hypotheses, we use particle filter approach that has proven to perform well in similar tasks. This approach provides a reasonable set of location hypotheses and allows for nonlinear models of the system and sensory input.

2.2. *The particle filter measurement model*

To estimate each hypothesis probability (a particle), edges from the on-board camera images are compared with edges of synthetic images from the 3D model, applying the nearest edges method. This method estimates edges' similarity using a set of line normals that are constructed from synthetic images' edges[3-5]. Figure 1 presents the result of rendering a synthetic image of a room at the position, which corresponds to a particular hypothesis. Edge features, which have been found in the synthetic image and correspond to real world edges, are shown in green; blue lines depict edges of the real world camera image, projected onto the synthetic image; line normals are shown as red segments. The algorithm uses the extracted edges to perform the following calculations:

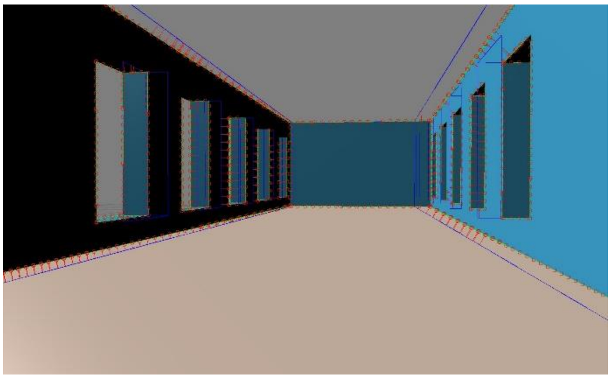

Fig. 1. Calculation of images similarity using edges.

(i) *(Each) line weight* calculated as follows:

$$g(d) = exp\left(-\frac{d^2}{2\sigma^2}\right), \quad (1)$$

where d is the normal's length, σ is the parameter that determines the weight of the normal and depends on the normal length d. Parameter σ allows to scale (to increase or decrease) the influence of long normals.

(ii) *Total weight* is calculated as follows:

$$l = \frac{\sum_{i=0}^{S} g(d_i)}{S}, \quad (2)$$

where S is the total number of lines in the simulated image.

(iii) *Total probability hypotheses* is calculated by combining the weights of each line:

$$W = \propto \cdot\, exp\left(k\,\frac{\sum_{n=0}^{m} l_n}{m}\right), \quad (3)$$

where m is the count of lines, and $\propto, k$ are empirically established parameters.

3. Particle filter implementation

The most important particle filter task is updating the particle weights. At the first stages of the algorithm, we detect edges within an image and find straight lines. We implemented the system as a robot operating system (ROS[6]) package, and a number of computer vision functions from OpenCV library were utilized. The system uses a constant number of particles, which allows static memory allocation and decreases memory management time.

3.1. *Comparative analysis of the CPU and GPU implementations*

Figure 2 presents a flowchart of particle weights calculation, which employs eq.(1-3). The main drawback of the algorithm is its complexity of $O(N*K*M)$, where N is a number of particles, K is a number of straight segments within a simulated image, M is a number of segment normals for a single straight line.

We parallelize the algorithm with NVIDIA's CUDA technology, which allows to receive a parallel computing system that works according to SIMT-principle (Single-Instruction, Multiple-Thread), when one instruction is simultaneously executed by multiple independent threads (Fig.3). We apply CUDA technology for particle weight

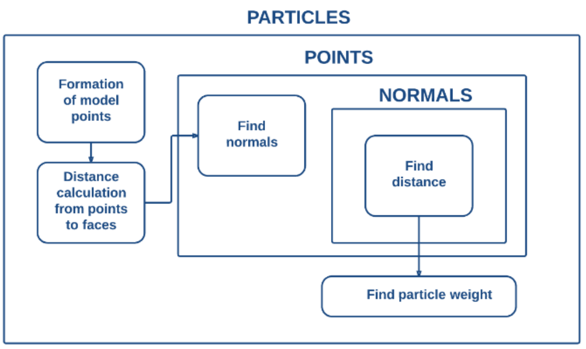

Fig. 2. The scheme of calculating the weights of the particles using a CPU only.

calculation through usage of a separate block for each particle and separate GPU core for each calculation of normal line's weight (Fig.4).

3.2. *Simulation results*

We implemented two versions of the system in ROS: one uses CPU only, while the other employs both CPU and GPU for calculations. Experiments were performed in ROS/Gazebo environment. Table 1 presents the two implementations' comparison within four different experiments: N denotes a number of the experiment, t_{CPU} and t_{GPU} denote calculation time in ms for CPU only system and CPU with GPU system implementation respectively, *ratio* denotes the ratio of t_{CPU} to t_{GPU}. The later system (CPU with GPU) demonstrated significantly

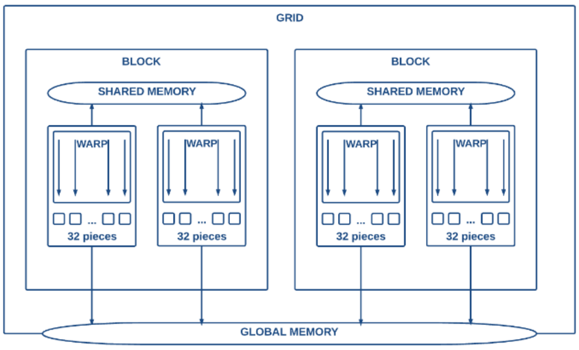

Fig. 3. CUDA threads hierarchy.

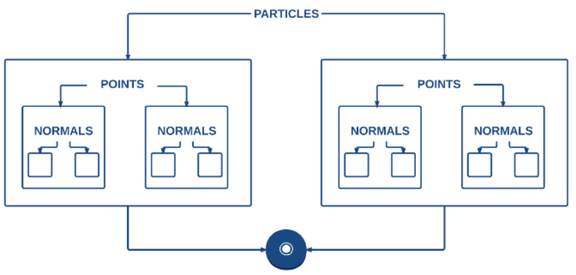

Fig. 4. The scheme of calculating the weights of the particles using a CPU together with GPU scheme.

better execution time, which surpassed the CPU-only system in almost 17 times in average.

Table 1. Performance comparison results, ms.

N	1	2	3	4
t_{CPU}	123,6	102,83	150,12	131,84
t_{GPU}	7,39	6,54	8,44	7,45
Ratio	16,7	15,7	17,7	17,6

4. Neural image filtering

The presented approach works well when a 3D model of environment is static and almost identical to the actual environment. However, in real world scenarios, most scenes are rather dynamic, i.e. new objects that were not captured during the 3D model building process appear and may even move through the actual environment (for example, the black sofa and the PC blocks in Fig.5 are new objects). To improve robot localization in such cases, all new and moving objects should be excluded from the scene analysis. Yet, if many temporary objects are excluded, too many edges (that belong to these objects) may be excluded as well and there is a risk of obtaining a very small number of detected edges.

One of the most effective ways to find objects within an image is to employ a convolutional neural network (CNN). To initialize and train, these networks use image databases, which form a dictionary with each word corresponding to a graphical image[7]. The properly adjusted and trained CNN allows finding objects and excluding them from an image in real time. At the preliminary stage, the CNN preprocesses data prior to edge detection in order to eliminate potentially dynamic objects within the environment. Next, edge detection is performed for an "empty" room, followed by robot localization. Figure 5 demonstrates CNN image preprocessing results, where the black sofa (i.e., a "dynamic" object) was properly detected. CNN returned a two-dimensional mathematical description of an object,

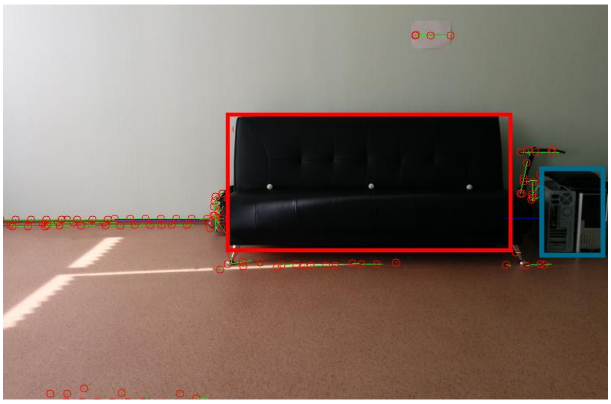

Fig. 5. Example of objects excluding by CNN: the black sofa (in red rectangular) and the PC blocks (in blue rectangular).

and the image area that belongs to the sofa object was eliminated from further processing.

Object detection and identification time is proportional to system hardware capabilities. After successful object detection, as a result of learning process, the CNN weights are redistributed. For all further appearances of the sofa object CNN performs quick identification in real time and thus localization process time decreases significantly.

Integrating such CNN module into a UAV onboard control system in addition to robot localization would allow a specific object detection, tracking a moving object[8] and other useful functionality.

5. Conclusions

This paper focuses on visual localization approach, which uses environment edges as key features. Our approach compares an obtained from a camera image with a simulated image of indoor environment's 3D model. We suggested a particle filter based algorithm improvement through CNN-preprocessing filtering, which eliminates dynamic objects from an image, and usage of GPU in UAVs localization system. Using parallel threads allowed increasing of localization system speed in almost 17 times in average. In addition, CNN filtering decreased negative influence of dynamic objects on localization process.

Acknowledgements

Part of the work was performed according to the Russian Government Program of Competitive Growth of Kazan Federal University.

References

1. A. Buyval, I. Afanasyev and E. Magid, Comparative analysis of ROS-based SLAM-related methods for autonomous indoor navigation, in *Int. Conf. on Machine Vision* (Nice, France, 2016)
2. E. Magid and T. Tsubouchi. Static Balance for Rescue Robot Navigation: Discretizing Rotational Motion within Random Step Environment, in *Lecture Notes in Artificial Intelligence*, 6472, (2010), pp. 423-435.
3. S. Nuske, J. Roberts and G. Wyeth, Outdoor visual localization in industrial building environments, in *IEEE Int. Conf. on Robotics and Automation*, (Pasadena, CA., 2008), pp. 544-550.
4. S. Nuske, J. Roberts and G. Wyeth, Robust outdoor visual localization using a three‑dimensional‑edge map, in *J. of Field Robotics* **26**(9), (2009),pp. 728-756.
5. A. Buyval and M. Gavrilenkov, Vision-based pose estimation for indoor navigation of unmanned micro aerial vehicle based on the 3D model of environment, in *IEEE Int. Conf. on Mechanical Engineering, Automation and Control Systems* (Tomsk, Russia, 2015).
6. E. Fernandez, S. Crespo, A. Mahtani and A. Martinez, Learning ROS for Robotics Programming Second Edition, (Birmingham, UK, 2015).
7. J. Redmon and S. D. Allen, You only look once: Unified, Real-Time Object Detection. arXiv preprint arXiv: 1506.02640v4 (2015).
8. G. Klein and D. Murray,Full-3D edge tracking with a particle filter, in *British Machine Vision Conference*,(UK, Edinburgh,2006).

Modelling a crawler-type UGV for urban search and rescue in Gazebo environment

Maxim Sokolov, Ilya Afanasyev
Intelligent Robotic Systems Laboratory, Robotics Institute, Innopolis University,
1 Universitetskaya street, Innopolis City, 420500, Russian Federation

Roman Lavrenov, Artur Sagitov, Leysan Sabirova, Evgeni Magid
Intelligent Robotic Systems Laboratory, Higher Institute for Information Technology and Information Systems (ITIS),
Kazan Federal University, 35 Kremlyovskaya street, Kazan, 420008, Russian Federation
E-mail: {m.sokolov, i.afanasyev}@innopolis.ru, {lavrenov, sagitov, sabirova, magid}@it.kfu.ru
http://university.innopolis.ru, http://kpfu.ru/eng/itis

Abstract

A long-standing goal of robotics is to substitute humans in unreachable or dangerous environments, and one of such environments is urban search and rescue (USAR) domain. For USAR tasks we have selected a novel Russian crawler-type robot Engineer, and this paper presents our first steps toward modelling the robot in ROS/Gazebo environment. We convert provided by robot developers CAD models into workable ROS-based 3D simulation and incorporate physical parameters of the mechanisms into the model, focusing on track simulation. Robot motion and relative interplay of its visible mechanical parts is visualized in RViz software. The proposed model is integrated into a ready-to-use ROS navigation stack and the model's behavior is thoroughly investigated while navigating through static obstacles populated scene in Gazebo environment. In this paper, we introduce an approximation of track-surface interaction of Engineer robot with modeled environment, and discuss the applicability of ROS-based "Gazebo-tracks" package for robust robot locomotion.

Keywords: USAR, ROS/Gazebo, crawler robot modelling, track simulation, system integration.

1. Introduction

Crawler-type unmanned ground vehicles (UGVs) are targeting for urban and rescue operations, especially in situations where a USAR mission deals with dangerous environments and high risk of rescuers' injury or life loss (e.g. buildings with high collapse probability, ruins after technogenic and natural disasters, etc.)[1,2]. In spite of obvious progress in crawler-type mobile robotics, our literature review demonstrated a lack of significant progress on track simulation and visualization. Although there are a number of papers, which dealt with track-type robots, considering crawler belt motion simulation[2] and mathematical modelling[3], track-surface interaction[4] or a simplified approach of contact point estimation in artificial[5,6] and natural environments[7] etc.

In our research, we employ Russian crawler robot Engineer as a USAR-oriented platform[8]. Original Engineer robot system does not contain any operator oriented robotics software. Customers can use only a client-server system to control the robot in a simple teleoperation mode, and our main purpose is to create a robot control software based on robot operating system (ROS) framework. A next essential task is to build a 3D simulation of the robot model in Gazebo simulator, using

CAD models from Engineer robot designers. ROS and Gazebo integration allows simulating Engineer robot in 3D environment, implementing navigation algorithms and providing comfortable and fast synchronization between the 3D model and the robot. To test workability of the robot's 3D model, it is exported into a ready-to-use navigation stack that was previously described by the authors[8], supporting point-to-point navigation in ROS/Gazebo/RViz simulation.

The rest of this paper is structured as follows. Section 2 describes system setup. Section 3 presents Engineer robot modelling with a focus on robot main body's tracks simulation. Section 4 summarizes our conclusions and hints on our future work.

2. Robot system setup

A crawler-type mobile robot Engineer (Fig. 1) is designed and manufactured by Russian company "Servosila" for operating in difficult terrain conditions (e.g. pipeline and tunnel inspection, underneath a suspected vehicle, etc). The robot is equipped with radiation-hardened electronics and a sensors pack, which includes 3D/2D laser scanner, an optical zoom camera, and a pair of stereo vision cameras, IMU, and GPS/GLONASS receiver. The robot is also tooled with a headlight for operations in low illumination conditions and a manipulator for grasping, pushing or pulling potentially dangerous objects or opening different doors with its gripper in teleoperated mode.

Fig. 1. "Servosila" Engineer crawler-type UGV. Courtesy of "Servosila" company.

3. Robot modelling

3.1. *Modelling in ROS*

We performed Engineer robot modelling and simulation in Gazebo 2.2.3 simulator integrated with ROS Indigo. Engineer robot 3D model consists of seven parts: a main crawler-based body, two front flippers, a clamp (which connects upper part to crawler-based body), two links of 3DoF hand-type manipulator with a gripper and a head (Fig. 2). To visualize Engineer robot model in Gazebo we used CAD models from "Servosila" company, and created: (1) step-files, applying physical parameters of robot model parts for 3D model data exchange between CAD software; (2) dae-files for ROS applications, in which all robot parts were transformed into separate files with relevant parameters. Thus, initially we modeled a main crawler-based body with tracks, then robot's upper part with the 3DoF hand-type manipulator, grippers and a head on its end-effector[8]. Using CAD models, we assembled the animated model (Fig. 2), where we connected all robot parts with ROS joints and set angle limits according to the robot specifications. In future, we are planning to use an adaptive PID controller to optimize the robot manipulator control and to damp oscillations that appear when operating the manipulator at a high speed.

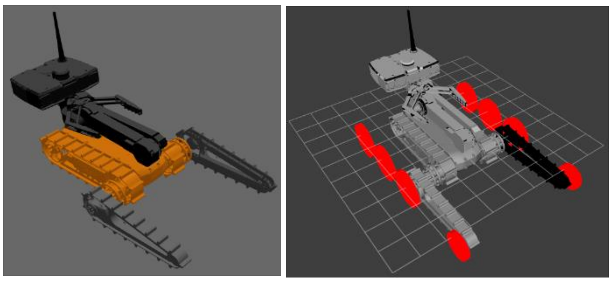

Figure 2. Simulation of Engineer robot in ROS/Gazebo (left) and in ROS\RViz (right). Imaginary pseudo wheels are marked in red.

3.2. *Track simulation*

The Engineer robot body is equipped with soft tracks, and it is a well-know problem to simulate and animate them. Moreover, to the best of our knowledge, track simulation has no standard robust solution in ROS. Modelling chain track belt-drive mechanism is a difficult task since it contains multiple details, which should be properly built into a model and animated. The difficulties in a track modeling arise because of a heterogeneous structure of a track and its supporting elements, with significantly varying properties along the track length.

One of possible solutions is based on imaginary pseudo wheels next to robot tracks (Fig. 2, right). Such simplified model does not simulate physical phenomena of track-surface contact with typical track slipping and skidding[2]. Further increase of pseudo wheels' number and decrease of their size improves the correspondence to a real crawler physics. This solution for motion animation of tracks and front flippers was implemented[8] and provided a simple wheel control with ROS request and response messages that synchronize wheels' speed. Engineer flipper wheels have different sizes, and in order to match them with chain tracks and synchronize to each other, limits on flipper wheel rotation were assigned and rotation speed control was realized with standard ROS modelling mechanisms. The simplified model was visualized with ROS\RViz software. However, our next goal is to create a realistic track simulation, taking into account physical phenomena of track-surface contact.

Currently, there is only one ROS-based package for tracks modelling - *Gazebo-tracks.* It contains a script that creates a track driven SDF model for Gazebo environment[9]. SDF model uses XML format to describe objects and environments for ROS/Gazebo; it helps defining robots, static and dynamic objects, lighting, terrain, physics, and could be further integrated into robot simulation, control, and visualization. Gazebo-tracks package supports track modelling of a system with two equal radii rollers. Thus, it could not be directly applied for Engineer robot flippers that have rollers of different radii. Gazebo-tracks takes into account a distance between tracks, a roller radius, a distance between rollers, a track chain width and thickness, a number of track chains. An example of a crawler robot prototype (main body) SDF file visualization is demonstrated in Fig. 3.

Initially, we had generated a complete Engineer robot model in Unified Robot Description Format (URDF)[8], which is also an XML format that represents a robot model in ROS/Gazebo. Unfortunately, it turned out that URDF does not support involvement of track joints in a loop closure configuration. Thus, only SDF format could be directly applied for track modelling. SDF approach with Gazebo-tracks allowed connecting modeled tracks to the robot body (Fig. 4), although the solution demonstrated a number of critical drawbacks:

- Typically, the modelled tracks are not stable and fall down not so long after the robot starts moving, which is resulted by inertial forces and accumulating shift of the tracks with regard to the rollers;
- As was previously emphasized, Gazebo-tracks package supports only two equal radii rollers and this restricts its application for Engineer flippers modelling;
- Gazebo-tracks package does not have proper ROS API, and thus rollers could not be synchronized via ROS topics and message exchange.

Therefore, we plan to develop a ROS-based approach, which generates tracks of any configuration for different number, location, and radii of track rollers.

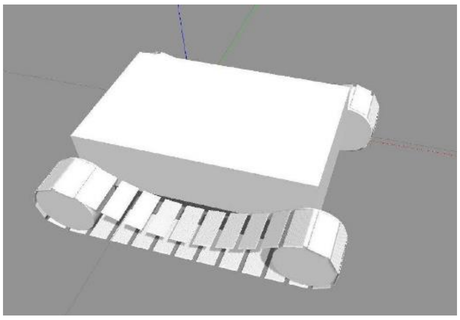

Fig. 3. Generic robot's main body tracks prototype modeling with *Gazebo-tracks package*

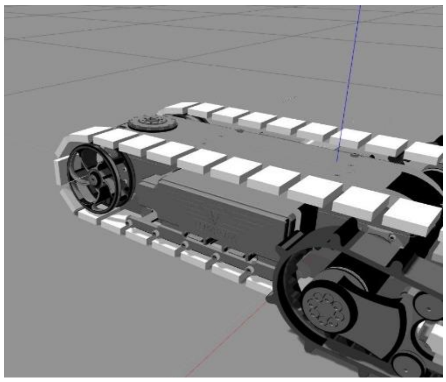

Fig. 4. The result of Engineer robot modelling with *Gazebo-tracks package* for main body tracks (shown in light grey)

4. Conclusions and future plans

Proper modelling of a crawler-type UGVs is an important task within USAR domain. In this paper, we introduced track modelling for a crawler-type UGV Engineer in ROS/Gazebo framework using original CAD data (provided by "Servosila" company) and Gazebo-tracks package. This ROS-based package was integrated into our model in trials to substitute our initial approach of modelling track-surface interaction with hidden pseudo wheels. Unfortunately, Gazebo-tracks package demonstrated a number of critical drawbacks, such as track instability due to inertial forces, strong restrictions on number and radii of track rollers, and a lack of proper ROS API, which prevents its smooth integration into a crawler robot model.

Therefore, as a part of our future work, we plan to create a novel ROS package for modelling tracks of a crawler-type UGV within ROS/Gazebo environment. The requirements for such package include robust robot locomotion, flexibility with a number, location and radii of track rollers, mechanisms for rollers synchronization, ROS API and messaging.

Our Engineer robot model and original software files are available for a download in the public domain of GitHub[10].

Acknowledgements

This work was partially supported by the Russian Foundation for Basic Research (RFBR) and Ministry of Science Technology & Space State of Israel (joint project ID 15-57-06010). Part of the work was performed according to the Russian Government Program of Competitive Growth of Kazan Federal University. Special thanks to Innopolis University and "Servosila" company (Russia).

References

1. T. Kamegawa, N. Sato, M. Hatayama, Y. Uo, and F. Matsuno, System Integration for Grouped Rescue Robots System Using Robohoc Network, in *Workshop on Robots and Sensors integration in future rescue INformation system* (ROSIN, Taipei, Taiwan, October 2010)
2. S. Kohlbrecher, F. Kunz, D. Koert, C. Rose, P. Manns, K. Daun, and O. von Stryk, Towards Highly Reliable Autonomy for Urban Search and Rescue Robots, in *Robot Soccer World Cup* (Springer International Publishing, 2014)
3. T. Inoue, T. Shiosawa, and K. Takagi, Dynamic Analysis of Motion of Crawler-Type Remotely Operated Vehicles, in *IEEE Journal of Oceanic Engineering*, 38(2), (2013), pp. 375-382
4. M. Pecka, V. Salansky, K. Zimmermann, and T. Svoboda, Autonomous flipper control with safety constraints, in *IEEE/RSJ International Conference on Intelligent Robots and Systems* (IROS, Daejeon, Korea, October 2016)
5. E. Magid, and T. Tsubouchi. Static Balance for Rescue Robot Navigation: Discretizing Rotational Motion within Random Step Environment, in *Lecture Notes in Artificial Intelligence*, 6472, (2010), pp. 423-435.
6. R. Sheh, M.W. Kadous, C. Sammut, and Hengst, B., 2007, September. Extracting terrain features from range images for autonomous random stepfield traversal, in *IEEE International Workshop on Safety, Security and Rescue Robotics* (IEEE SSRR, 2007), pp. 1-6.
7. E. Magid, T. Tsubouchi, E. Koyanagi, T. Yoshida, and S. Tadokoro. Controlled Balance Losing in Random Step Environment for Path Planning of a Teleoperated Crawler Type Vehicle, in *Journal of Field Robotics*, 28(6), (2011), pp.932–949.
8. M. Sokolov, R. Lavrenov, A. Gabdullin, I. Afanasyev, E. Magid, 3D modelling and simulation of a crawler robot in ROS/Gazebo, in *Proc. Conf. on Control, Mechatronics and Automation. MATEC Web of Conferences*. (ICCMA, Barcelona, Spain, December 2016).
9. A. Synodinos, Gazebo-tracks, ROS package repository (2013): https://github.com/progtologist/gazebo-tracks
10. M. Sokolov, Somal / Robot_Engineer, Repository with ROS package for robot Engineer, (Innopolis University, 2016), https://github.com/Somal/Robot_Engineer/

Development of Autonomous Robot for the Labor-saving Forestry
- Positioning of the Robot using IMU, GPS and Encoder -

Sho Yamana
Computer Science and Systems Engineering, Kyushu Institute of Technology.
680-4, Kawazu, Iizuka, Fukuoka, 820-8502 Japan.
Shoyamana0925@gmail.com

Eiji Hayashi
Mechanical Information Science and Technology, Kyushu Institute of Technology.
680-4, Kawazu, Iizuka, Fukuoka, 820-8502, Japan.
haya@mse.kyutech.ac.jp

Abstract

This paper presents about the positioning of the autonomous robot using IMU, GPS, and encoder devices. Using acceleration and orientation of the IMU sensor that is used to calculate the position of the robot. To locate the position, need to know the distance when the robot moved. Distance is calculated by integrating velocity function and also the velocity is considered by integrating the acceleration function. Results showed distance measurement using only IMU. It shows the difficulty of locating used only IMU. Therefore, GPS and encoder devices need to be combined into the system for position measurements.

Keywords: Positioning system for wheeled robot, IMU, GPS, Encoder.

1. Introduction

Generally, it takes a lot of time and needs much labor for managing the resources of the forest. In addition, nowadays in Japan, the population of the forestry is getting fewer and getting older. Therefore, our researches have concentrated on developing the autonomous robot for the labor-saving forest, and particularly this research focuses on developing the positioning system of the robot to collect the data in the forest.

The robot is supposed to look around in the forest and collecting the data of the forest. Therefore the robot is modeled based on ATV and some sensors and actuators are installed on it.

To look around automatically at the forest, positioning system is essential to the robot. Our positioning system is going to be composed of IMU, GPS, and Encoder devices. This paper presents about the positioning system using only IMU. The IMU can output 3-axes acceleration, 3-axes angular rate, and 3-axes magnetic field. Integrating the acceleration from IMU, and calculates velocity of the robot and integrates the velocity and calculates the distance the robot moved. Orientation of the robot is decided by the magnetometer of the IMU.

This paper is organized as follows: Section 2 provides the configuration of the robot. Section 3 of the paper explains the way calculating the distance of the robot using IMU and its problem. Section 4 shows the

Fig.1 The exterior of the robot

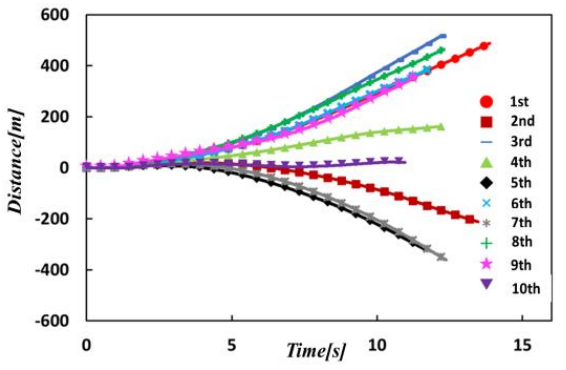

Fig.2 The results of distance using IMU device

algorithm for solving the problem. Section 5 shows experimental results with the algorithm. Section 6 concludes the paper.

2. Configuration of the Robot

Our robot developed is shown in Fig.1. KFX®90 (Kawasaki Heavy Industries Motorcycle & Engine Company) is platform of the robot to be able to run in the rugged area (the forest). For avoiding trees, 3D Depth sensor, CCD camera, and RFID antenna are installed. Motors are used for controlling the movement of the robot. IMU for positioning system of the robot. Multi blades for weeding in the forest. And three mini-computers (Intel NUCs) for controlling the all devices.

3. Measuring distance with IMU device

To measure the distance using IMU, fixed the IMU on a cart and move it 10[m] parallel to the IMU's y-axis and start to measure before cart starts and stop measure when car moves 10 [m] and stops. 10 times conducted. Fig.2 shows the distance calculated by acceleration using IMU. It shows how far it is from 10[m] and how wide its variability, and its standard deviation is 328.04. The distance and velocity are calculated by Equations (1) and (2), where, $\vec{a}$ is acceleration, $\vec{v}$ is velocity and $\vec{x}$ is distance.

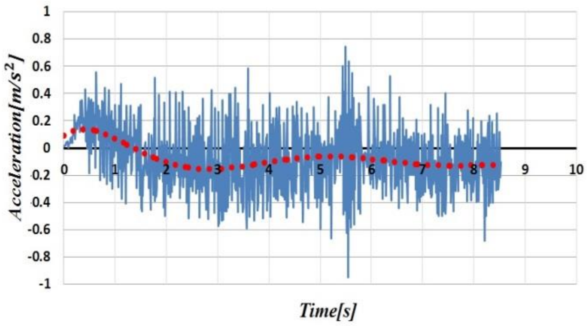

Fig.3 The acceleration and approximate line

$$\vec{v} = \int \vec{a}dt \tag{1}$$

$$\vec{x} = \int \vec{v}dt \tag{2}$$

Fig.3 shows a result of acceleration (blue line) and its approximate line (red points) in this experiment. It shows approximate line is negative ever since about 1.5[s]. It is supposed to be zero except while start moving and stopping. In addition, the value of approximate line is totally different every measurement. Therefore, the calculating approximate curve need for our system.

4. Algorithm for solving the error

To solve the problem we created following system. First, get acceleration data every 0.01 second, and decide whether the cart moves or not. If the cart moves, the acceleration data are accumulated in an array have 100 elements. When the array is full, start calculating the distance and clear all elements of the array and start accumulating from the beginning. Using moving

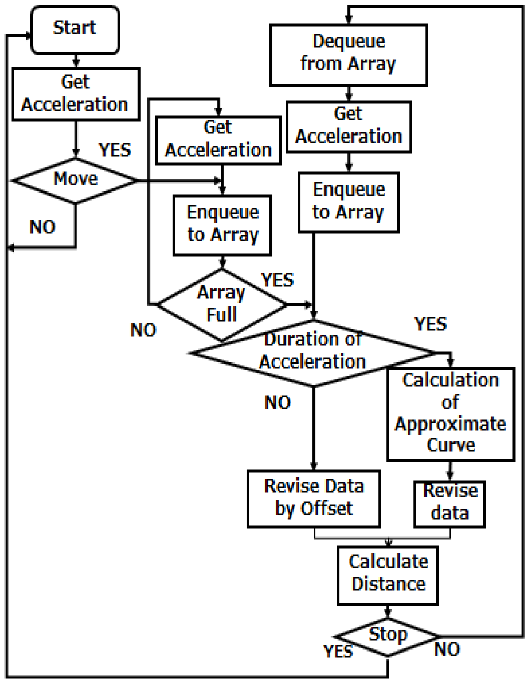

Fig.4 Flowchart of the system

average of the acceleration, determine the duration of acceleration of the cart. While duration of the acceleration, calculates distance using acceleration revises by offset is determined by average of acceleration before start moving. After the duration of acceleration, calculates approximate curve using the all elements of array, and calculates distance using acceleration subtracted by approximate curve every 0.01second. The approximate curve is updated every 1 second because the number of elements of array is 100 and get acceleration from IMU every 0.01 second. After calculating distance, decide whether cart moves or not. Fig.4 shows the flowchart.

5. Experimental results

To examine the effect of the system, conducted the experiment the same as it was mentioned in the Section3. Fig.5 shows the experimental results. Results show that accuracy of measurement was improved, and its variability is smaller than before. In fact, its standard deviation is 1.77, before it was 328.04.

Fig.6 shows a result of acceleration (blue line) and its approximate line (red points) in this experiment. It shows that the system started calculating distance after 1 second, because that need to wait accumulating data in the array. After that, duration of acceleration,

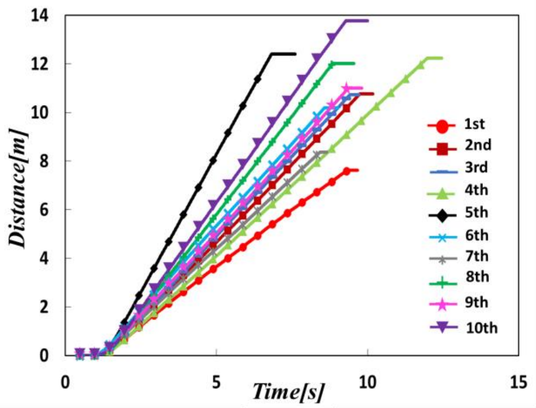

Fig.5 Experimental result (Distance)

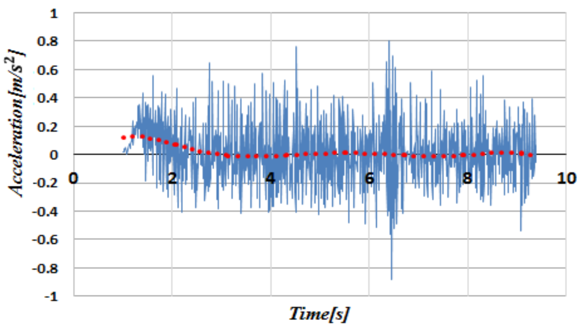

Fig.6 Experimental result (Acceleration and approximate line)

approximate line is nearly to zero. Now, the effect of this system that revising raw acceleration is verified. However, in this algorithm assume that after duration of acceleration, cart moves in accordance with uniform linear motion. Therefore, when cart motion is not uniform linear motion, this algorithm cannot be used, because revision by the approximate line clear the steep change of acceleration. For example, when cart moves forward and backward in a short term, the change of acceleration is cleared by the approximate line. Because of this, the algorithm cannot be installed with the actual robot.

6. Conclusion

The system improved the accuracy of the measurement, but the system can only be used for the specific situation and application of the system is very limited. Therefore, measuring the distance only using IMU is difficult, because the shape of the approximate line of the acceleration is completely different every time even cart moves in accordance with the uniform linear motion. Finally, the IMU can also output Euler angle based on angular rate, so it is necessary to use IMU for compensation of the system composed of Encoder and GPS.

References

1. Wataru Shinyashiki, "*Development of Sensing Robot～Design and Autonomous Control～*", Kyushu Institute of Technology, 2015
2. Naoki Tominaga, "*Development of Positioining Sytem Using Accelerometer and its evaluation*", The University of Electro-Communications, 2003
3. Jingang Yi, et.al., "Kinematic Modeling and Analysis of Skid-Steered Mobile Robots With Application to Low-Cost Inertial-Measurement-Unit-Based Motion Estimation," *Proc. IEEE Transactions on Robotics*, pp. 1087-1097, 2009.
4. G. Dissanayake, et.al., "The aiding of a low –cost strapdown inertial measurement unit using vehicle model constraints for land vehicle application," *Proc. IEEE Transactions on Robotics*, pp. 731-747, 2002.

Development of Autonomous Robot for Laborsaving of the Forestry
Detection of young plants by RGB and Depth Sensor

Nobuo Miyakawa
Department of Mechanical Information Science and Technology, Kyushu Institute of Technology
680-4, Kawazu, Iizuka-City, Fukuoka, 820-8502, Japan
Email: miyakawa@mmcs.mse.kyutech.ac.jp

Eiji Hayashi
Department of Mechanical Information Science and Technology, Kyushu Institute of Technology
680-4, Kawazu, Iizuka-City, Fukuoka, 820-8502, Japan
Email: haya@.mse.kyutech.ac.jp

Abstract

Traditional forest management and maintenance consumes excessive labor time. Particularly burdensome is the investigation and management of resource quantity (tree growth) in the forest and the elimination of weeds. Therefore, this paper proposes a prototype mechanism for an autonomous self-moving robot that promises to reduce the workload of forest management investigation. For the autonomous movement task, we installed some actuators and a three-dimensional (3D) depth sensor into an all-terrain vehicle. The trajectory path of the robot is determined from the obtained depth-sensor data via 3D conversions and a labeling process. The handle is then controlled by calculating the steering angle. In an experimental evaluation mimicking a real forest environment, the prototype achieved autonomous self-movement with successful passage through the trees.

Keywords: Autonomous Self-Moving, Depth Sensor, Forest, Image processing

1. Introduction

Seventy percent of Japan's land is occupied by forests, approximately 40% (100 billion hectares) of which comprises artificial forests. The artificial forests are planted with Hinoki and cedars at a density of 3000 trees per hectare. Both species are cultivated for construction and other projects. The time between planting and shipment is 50 years. Within this term, forestry workers must not only investigate and manage the resource quantity (tree growth) in the forest but also eliminate weeds. Such work places a large labor burden on forestry workers. Moreover, the falling employment rate has depleted the work force, causing delay of these tasks and degradation of the forest. Our laboratory is developing an autonomous self-moving robot equipped with a weeding mechanism for forest investigation. The proposed robot reduces the labor burden in forestry work.

Forest scenarios change daily under the dynamic conditions of tree and weed growth. Moreover, forests are large-area, steep-grade natural environments that are not easily patrolled by humans. For the same reasons, map information and path planning is rendered difficult in forests. Both tasks (maintenance and path planning) could be much more easily accomplished by an appropriately designed mobile robot.

This study proposes a robot that moves autonomously in forest environments. When moving, the robot must avoid the trees (resources). As mentioned above, a forest path is difficult to plan in advance, so the robot must detect its plausible trajectory from information of the equipped sensors. The final goal of this study is to develop a robot that eliminates weeds and investigates resource quality while traveling extensively through the forest. Fig. 1 shows an overview of the robot. The robot platform is an all-terrain vehicle (ATV; Kawasaki, Inc.), which can access the difficult forest terrain. The external situation is recognized by a depth sensor and a CCD camera equipped on the ATV. The brake lever, accelerator lever and steering are controlled by a motor. Weeding is performed by a multi-blade mechanism attached between the front wheels of the ATV.

Fig. 1. Overview of the robot

As a first step toward this goal, we are developing an autonomous self-moving robot. In previous studies, environment recognition and autonomous movement control have been achieved by laser range finders (LRFs) and charge-coupled device (CCD) cameras [1-2]. In this study, the external situation is recognized by a depth sensor and a CCD camera. The depth sensor is less precise than the LRF, but is considerably cheaper. In addition, it is easily introduced to the robot system because its information is easily interpretable from images. The robot always moves toward a traversable gap between the trees.

2. AUTONOMOUS SELF-MOVING SYSTEM

The main sensor that detects external situations is the depth camera. This sensor provides the information (placement, size and number) of the objects ahead of the robot. A flowchart of the robotic system is shown in Fig.2. The various processing stages are detailed below.

Recognition of external situation by depth sensor and CCD camera

The depth sensor utilized in this study is commonly called Infinisoleil (Nippon signal, Inc.). This sensor measures the depth of an object from its installation position. The horizontal and vertical components of the viewing angle are 60° and 50°, respectively. The maximum measurable depth is 15 m. The depth values in the grayscale depth image are converted to pixel values (Fig. 3a), and to a bird's eye view (x–z plane image) via three-dimensional conversions (Fig. 3b). The placement, size and number of the trees are recognized by labeling processing on the x–z plane image.

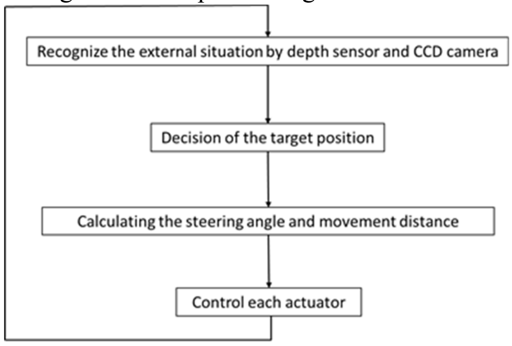

Fig. 2. Flowchart of the proposed robotic system

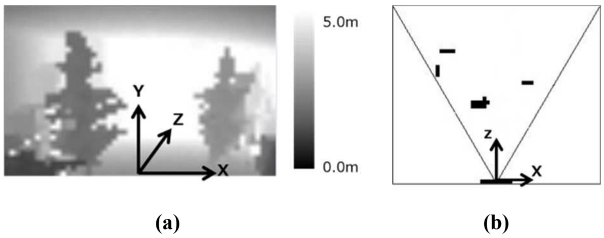

Fig. 3. Grayscale depth image and bird's eye view (x–z plane image)

B. Decision of the target position

The passable gaps through the trees and weeds are detected in the x–z plane image after the label processing. Fig. 4 shows the measuring results of the tree gaps. After selecting a passable gap, the robot sets the center point of the gap as the target point. If several passable gaps are detected, the robot selects one of these gaps (currently, the widest one). If no passable gaps are detected, the robot measures the gaps between the trees and the line of the sensor angle, then selects the left or right gap (whichever is larger).

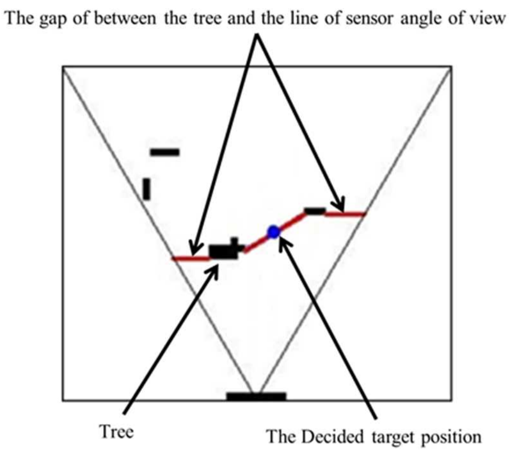

Fig. 4. x–z plane image after deciding the target position

C. Calculation of steering angle and movement distance
After detecting the steering angle and movement distance to the target point, the robot advances toward the target. Here we used an equivalent three-wheeled model with origin O at the center of the front wheels. Points P and W denote the target point and the wheel base of the robot respectively, and the center C of the circular trajectory of the robot is calculated by (1). The steering angle is then calculated by (2) using the length of W and R (the Euclidean distance between C and O). The robot moves through the arc O–P of the circle centered at C. Finally, the chord length D is calculated by (3). From the above, the motion command issued to the robot is

$$u = [\lambda \quad s].$$

$$C = \begin{cases} c_x = \dfrac{p_z}{p_x}\left(W + \dfrac{p_z}{2}\right) + \dfrac{p_x}{2} \\ c_z = -W \end{cases} \qquad (1)$$

$$\lambda = \sin^{-1}\frac{W}{R} \qquad (2)$$

$$s = 2R\sin^{-1}\frac{D}{2R} \qquad (3)$$

D. Controlling each actuator
In the specified order, the system's motors control the steering, accelerator lever and brake levers. The control order is governed by a rotary encoder attached to the rear wheel. Once reach the desired distance, the process returns to Step A.

3. Detection of young plant system

Fig.5. shows the environment in which the robot actually moves. The trees and weeds are densely grown in the forest, and both plant types appear in the x–z plane image. To enable weed avoidance by the robot, the external environment is recognized by combining the depth sensor data and the RGB image acquired by the CCD camera (which is installed next to the depth sensor).

3.1. *Combining Depth data and RGB image*

Combining depth data and RGB image using perspective projection method. The relationship between 2D point position in pixel coordinates ($[x \quad y \quad 1]^T$) and 3D point position in World coordinates ($[X \quad Y \quad Z \quad 1]^T$) is calculated by (4). K is intrinsic parameters of camera and, R, T are the extrinsic parameters.

$$h\begin{bmatrix} x \\ y \\ 1 \end{bmatrix} = K\begin{bmatrix} R & T \end{bmatrix}\begin{bmatrix} X \\ Y \\ Z \\ 1 \end{bmatrix} \qquad (4)$$

3.2. *Extraction of young plants*

The trees are distinguished by the green domains in the RGB image. The pixels of the tree domains in the depth image are identified by the corresponding green pixels in the RGB image. The x–z planar image captures the weed information, as shown in Fig. 6

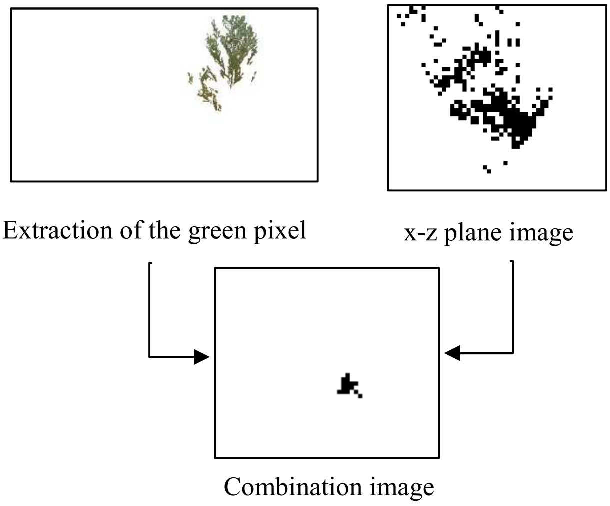

Fig. 6. x–z plane image constructed by combining the depth and RGB image

4. Conclusion

We developed an autonomous self-moving robot. This robot is composed of an "autonomous self-moving system" and a "detection of young plant system". This robot can automatically act by avoiding obstacles in the front. Moreover, it is also possible to judge whether the object in front is young plants or weeds, and to avoid only the young plants.

References

[1] T. Ito, K. Matsumoto, and Y. Banno, "Environment recognition method for mountain forest maintenance robot –Localization and mapping of robot using surrounding trees-," *Proceeding of the 2011 JSME conference on Robotics and Mechatronics*, (2011).

[2] T. Ito, K.Matsumoto, and K. Suganuma, "Improvement of environment recognition performance for mountain forest maintenance robot," *Proceedings of the 2013 JSME conference on Robotics and Mechatronics*,

Development of arm trajectory planning of Seamless Robot

Teedanai Pramanpol, Jiraphan Inthiam, and Eiji Hayashi

Department of Interdisciplinary Informatics,
Graduate School of Computer Science and Systems Engineering, Kyushu institute of technology,
680-4 Kawasu, Iizuka, Fukuoka, 820-5202, Japan
Tel. +819 4829 7500
E-mail: teedanai@mmcs.mse.kyutech.ac.jp, jiraphan@mmcs.mse.kyutech.ac.jp, haya@mse.kyutech.ac.jp

Abstract

This paper presents arm trajectory planning of Seamless Robot. The Seamless Robot is a Human Support Robot (HSR) which is the ongoing developed project at Hayashi Laboratory, this robot is consist of three main parts base, body and arms, this paper will focus on controlling left arm movement. The arm has been designed with four degrees of freedom joints limit are set to values close to a human arm. In order to solve for each joint angle the Levenberg - Marquardt algorithm (LMA) is used for solving the inverse kinematic problem for calculating point to create a trajectory planning of robot`s arms. The result of trajectory planning has been proven in simulation.

Keywords: Trajectory planning, Inverse kinematics, Levenberg-Marquardt Algorithms, Robot manipulator.

1. Introduction

In recent years the market of household or service robot has seen increasing growth in popularity and economically. The Seamless robot is also created to operate as a service robot in an environment close to human. Being a service robot the robot should be able to grasp an object and be able to pass that object to human or deliver the object to other places by using its arm, this is a common task for service robot. Fig. 1. Shows the overall design of the seamless robot, in this paper we will discuss the movement control of the left arm. The left arm of Seamless robot has been designed with four degrees of freedom for a human-like agility, instead of derive for a complete close form solution, the Levenberg-Marquardt algorithm (LMA) is used to solve inverse kinematic problem. The LMA is an iterative algorithm for solving a nonlinear least square problem [3]. As [2] shows that when compare the LMA with other Jacobian-based method, the LMA shows better performance than other method.

Fig. 1. Design of the Seamless robot

This paper presents the implementation of LMA for solving inverse kinematics problem with boundary of each joint was set to the value close to the limit of human arm and also shows the arm trajectory of the robot by selecting point in workspace of the robot

2. Arm structure of Seamless robot

The structure of the arm in Seamless robot was designed to replicate human arm with 3 DOFs shoulder and 1 DOF elbow. Fig. 2. (a) and (b) show the construct of robot arm. The shoulder joint using three MAXON EC motors (two 100 watt 24V combine with 113:1 ratio gearbox and one 30 watt 24V combine with 216:1 ratio gearbox) for the elbow joint we use one MAXON EC motor (one 15 watt 24V combine with 246:1 ratio gearbox) each motor equipped with a 3-phase hall sensor to measure the velocity and direction of rotation. The motor driver ESCON from MAXON was used to control speed for each individual motor, for position control we use microcontroller STM32F4 Discovery to calculate the rotation angle by signal from hall sensors. In Seamless robot we use one microcontroller to control three of shoulder motors and another to control elbow motor. Each microcontroller connects to computer via RS232 connection port. Fig. 3. shows the control system for robot arm.

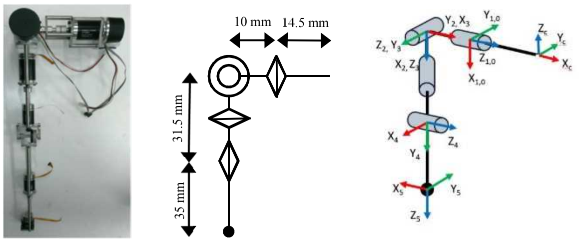

(a) (b) (c)

Fig. 2. Construction of Seamless robot arm (a) actual construct of robot arm, (b) schematic model of robot arm and (c) frame assignment of robot arm

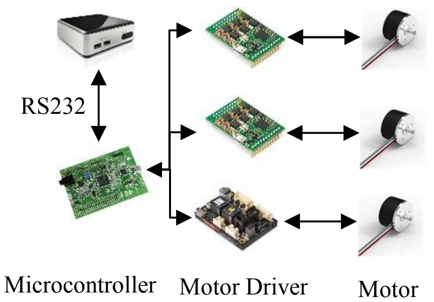

Fig. 3. Diagram of control system in Seamless robot arm

3. Kinematic model

3.1. *Forward kinematic*

The coordinate frame assignment are illustrated in Fig. 2.(c). The Denavit-Hartenberg (DH) parameters are used to derive forward kinematic listed in Table 3.1 except coordinate frame (x_0, y_0, z_0) to (x_c, y_c, z_c) which is the offset from the center of the robot to origin frame that can be transform by using Eq. (1) then from frame (x_1, y_1, z_1) to (x_4, y_4, z_4) represent the frame at each joint respectively, (x_5, y_5, z_5) shows the coordinate frame for end effector.

From the DH parameters, the transformation matrix from joint i to joint i+1 can be derived using Eq. (2) to (5).

Table 3.1. DH Parameters

i	θ_i	d_i	α_i	a_i
1	θ_1	$-LL_1$	90°	0
2	θ_2+90°	0	90°	0
3	θ_3+90°	LL_2	90°	0
4	θ_4	0	-90°	0
5	90°	LL_3	0	0

$$ {}^{center}_{0}\boldsymbol{T} = \begin{bmatrix} \mathbf{0} & \mathbf{0} & \mathbf{1} & \boldsymbol{LL_{center}} \\ \mathbf{0} & \mathbf{1} & \mathbf{0} & \mathbf{0} \\ \mathbf{-1} & \mathbf{0} & \mathbf{0} & \mathbf{0} \\ \mathbf{0} & \mathbf{0} & \mathbf{0} & \mathbf{1} \end{bmatrix} \quad (1) $$

$$ {}^{0}_{1}\boldsymbol{T} = \begin{bmatrix} \boldsymbol{cos(\theta_1)} & \mathbf{0} & \boldsymbol{sin(\theta_1)} & \mathbf{0} \\ \boldsymbol{sin(\theta_1)} & \mathbf{0} & \boldsymbol{-cos(\theta_1)} & \mathbf{0} \\ \mathbf{0} & \mathbf{1} & \mathbf{0} & \boldsymbol{-LL_1} \\ \mathbf{0} & \mathbf{0} & \mathbf{0} & \mathbf{1} \end{bmatrix} \quad (2) $$

$$ {}^{1}_{2}\boldsymbol{T} = \begin{bmatrix} \boldsymbol{cos(\theta_2 + 90^\circ)} & \mathbf{0} & \boldsymbol{sin(\theta_2 + 90^\circ)} & \mathbf{0} \\ \boldsymbol{sin(\theta_2 + 90^\circ)} & \mathbf{0} & \boldsymbol{-cos(\theta_2 + 90^\circ)} & \mathbf{0} \\ \mathbf{0} & \mathbf{1} & \mathbf{0} & \mathbf{0} \\ \mathbf{0} & \mathbf{0} & \mathbf{0} & \mathbf{1} \end{bmatrix} \quad (3) $$

$$ {}^{2}_{3}\boldsymbol{T} = \begin{bmatrix} \boldsymbol{cos(\theta_3 + 90^\circ)} & \mathbf{0} & \boldsymbol{sin(\theta_3 + 90^\circ)} & \mathbf{0} \\ \boldsymbol{sin(\theta_3 + 90^\circ)} & \mathbf{0} & \boldsymbol{-cos(\theta_3 + 90^\circ)} & \mathbf{0} \\ \mathbf{0} & \mathbf{1} & \mathbf{0} & \boldsymbol{LL_2} \\ \mathbf{0} & \mathbf{0} & \mathbf{0} & \mathbf{1} \end{bmatrix} \quad (4) $$

$$ {}^{3}_{4}\boldsymbol{T} = \begin{bmatrix} \boldsymbol{cos(\theta_4)} & \mathbf{0} & \boldsymbol{-sin(\theta_4)} & \mathbf{0} \\ \boldsymbol{sin(\theta_4)} & \mathbf{0} & \boldsymbol{cos(\theta_4)} & \mathbf{0} \\ \mathbf{0} & \mathbf{-1} & \mathbf{0} & \mathbf{0} \\ \mathbf{0} & \mathbf{0} & \mathbf{0} & \mathbf{1} \end{bmatrix} \quad (5) $$

$$ {}^{4}_{5}\boldsymbol{T} = \begin{bmatrix} \mathbf{0} & \mathbf{-1} & \mathbf{0} & \mathbf{0} \\ \mathbf{1} & \mathbf{0} & \mathbf{1} & \mathbf{0} \\ \mathbf{0} & \mathbf{0} & \mathbf{0} & \boldsymbol{LL_3} \\ \mathbf{0} & \mathbf{0} & \mathbf{0} & \mathbf{1} \end{bmatrix} \quad (6) $$

$$ {}^{center}_{5}T = {}^{center}_{0}\mathrm{T}\,{}^{0}_{1}T\,{}^{1}_{2}T\,{}^{2}_{3}T\,{}^{3}_{4}T\,{}^{4}_{5}T \quad (7) $$

$$ {}^{center}_{5}T = \begin{bmatrix} n_x & o_x & a_x & p_x \\ n_y & o_y & a_y & p_y \\ n_z & o_z & a_z & p_z \\ 0 & 0 & 0 & 1 \end{bmatrix} \quad (8) $$

where p_x, p_y, p_z are the global coordinate of end effector shown below:

$$ p_x = -LL_1 - LL_3(c_2c_4 + s_2c_3s_4) - LL_2c_2 - LL_{center} \quad (9) $$
$$ p_y = LL_3[s_4(c_1s_3 - s_1c_2c_3) + s_1s_2c_4] - LL_2s_1s_2 \quad (10) $$
$$ p_z = LL_3[s_4(s_1s_3 - c_1c_2c_3) - c_1s_2c_4] - LL_2c_1s_2 \quad (11) $$

where $c_1 = \cos(\theta_1)$, $s_1 = \sin(\theta_1)$, $c_2 = co\,s(\theta_2 + 90^\circ)$, $s_2 = \sin(\theta_2 + 90^\circ)$, $c_3 = \cos(\theta_3 + 90^\circ)$, $s_3 = \sin(\theta_3 + 90^\circ)$, $c_4 = \cos(\theta_4)$ and $s_4 = \sin(\theta_4)$

3.2. *Inverse kinematic*

The forward kinematics equations are nonlinear. It is clearly that solving for close form solution of inverse kinematic equation is very difficult to derive. In this paper we use LMA to solve for each joint angle. In order to use LMA the Jacobian matrix is necessary, we can obtain Jacobian matrix by using p_x, p_y, p_z as shown in Eq. (12). Eq. (13) is an equation for solving joint angle in each iteration by Q_i is joint angles in current iteration, Q_{i-1} is joint angles in previous iteration, ξ is a given positive coefficient, λ is a non-zero damping coefficient , P_T is target position for end effector, and $\boldsymbol{P_{i-1}}$ is position of end effector from previous iteration.

$$J = \begin{bmatrix} \frac{\partial p_x}{\partial \theta_1} & \frac{\partial p_x}{\partial \theta_2} & \frac{\partial p_x}{\partial \theta_3} & \frac{\partial p_x}{\partial \theta_4} \\ \frac{\partial p_y}{\partial \theta_1} & \frac{\partial p_y}{\partial \theta_2} & \frac{\partial p_y}{\partial \theta_3} & \frac{\partial p_y}{\partial \theta_4} \\ \frac{\partial p_z}{\partial \theta_1} & \frac{\partial p_z}{\partial \theta_2} & \frac{\partial p_z}{\partial \theta_3} & \frac{\partial p_z}{\partial \theta_4} \end{bmatrix} \quad (12)$$

$$Q_i = Q_{i-1} + \xi J^T (diag(M + \lambda I))^{-1} (P_T - P_{i-1}) \quad (13)$$

where $M = JJ^T$

In traditional implementation of LMA [2][3], the limitation of each joint was not consider in the algorithm, in this paper we will also consider about this problem. When the iteration start the algorithm will converge to the region that give the closest result of end effect position, however that region may contents the joint angle that over the limitation of practical joints, so in each iteration variable Q_i need to be check whether the value of each joint is over limit or not, after determine the value if it exceed the joint limit then variable Q_i will be set to a value within the region of joint limit so when the next iteration start it will start by using selected value then continue computing until we get the result for joint angle the implemented algorithm is shown as flowchart in Fig. 4., in this algorithm λ and ξ are set to a constant value, Q_{i-1} is set to the initialize angle of robot arm and ϵ is a accepted error region.

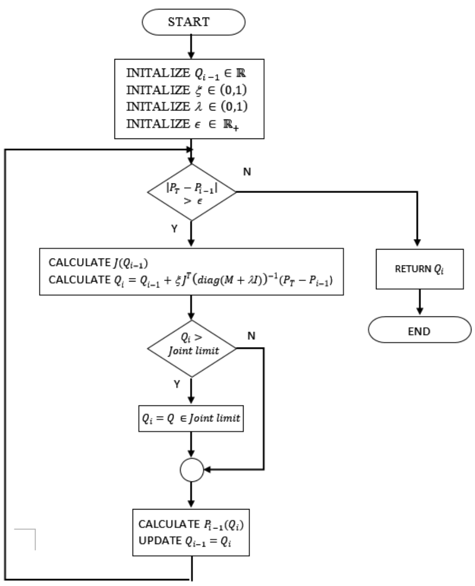

Fig. 4. Flowchart of Levenberg-Marquardt Algorithm

After the angle of each joint is determined if the input position change there are no connection between two set of joint angles therefore a function of time as a polynomial order 3 is used to link each set of joint angle. The equation is shown in Eq. (14)

$$\theta_i(t) = a_0 + a_1 t + a_2 t^2 + a_3 t^3 \quad (14)$$

where
$$a_0 = \theta_0$$
$$a_1 = 0$$
$$a_2 = 0.0012(\theta_f - \theta_0)$$
$$a_3 = -0.000016(\theta_f - \theta_0)$$

4. Simulation and experiment results

The boundary of each parameter need to be set before simulation take place, for the boundary of input coordinates and joints angle are listed below. In experiment we test the system by using two set of input to create two types of movement which are two points path, four points input for each type can be list in as

(i) Boundary of input coordinate
- (a) $x \in [-0.91, 0.1599]\, m$
- (b) $y \in [0, 0.665]\, m$
- (c) $z \in [-0.665, 0.665]\, m$

(ii) Boundary of joint angle
- (a) $\theta_1 \in [-30^\circ, 180^\circ]$
- (b) $\theta_2 \in [-90^\circ, 10^\circ]$
- (c) $\theta_3 \in [-40^\circ, 90^\circ]$
- (d) $\theta_4 \in [0^\circ, 90^\circ]$

(iii) Input for two points path
- (a) $(-0.245, 0, -0.665)$
- (b) $(0, 0.2, 0.4)$

(iv) Input for four points path
- (a) $(-0.4, 0.5, 0)$
- (b) $(-0.1, 0.5, 0)$
- (c) $(-0.1, 0.5, -0.4)$
- (d) $(-0.4, 0.5, -0.4)$

For every experiment value of λ and ξ are set to 0.00755 and 0.005 respectively. The trajectory planning of both two points path and four points path are shown in Fig. 5. and Fig. 6. where Fig. 7. and Fig. 8. show the simulation concept of robot movement. The joint angle of each movement is shown in Fig. 9. and Fig. 10.

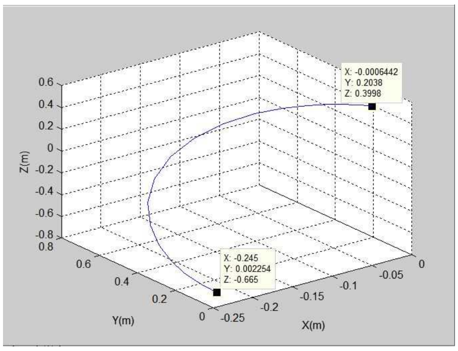

Fig. 5. Trajectory of two points path

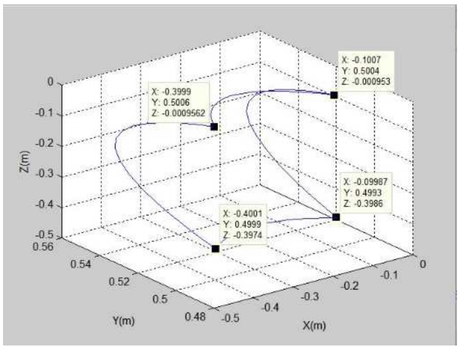

Fig. 6. Trajectory of four points path

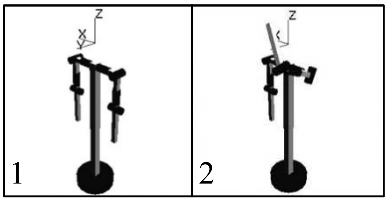

Fig. 7. Simulation concept of two points path

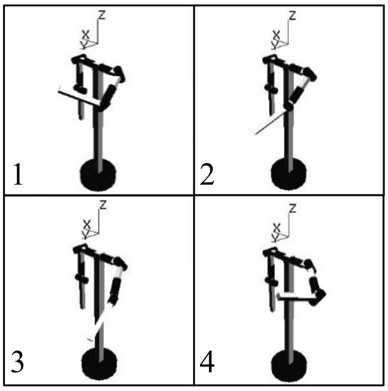

Fig. 8. Simulation concept of four points path

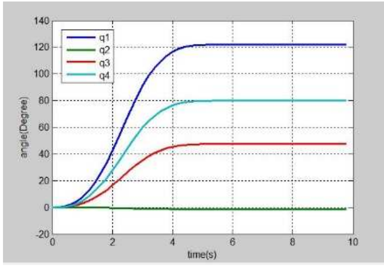

Fig. 9. The joint angle of two points path

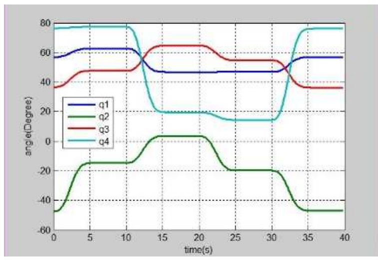

Fig. 10. The joint angle of four points path

5. Conclusion

Using Levenberg-Marquardt algorithm for solving inverse kinematic problem in Seamless robot can give the joint angle that make the end effector close to the target point although some error occur but the calculation can be refine by changing accepted error region, λ and ξ for more accuracy.

References

1. N. Bunathuek, P. Saisutjarit and P. Laksanacharoen, *Design of a Reconfigurable Spherical Robot II* (Hong Kong, China, 2014)
2. I. Duleba and M. Opalka, a Comparison of Jacobian-Based Methods of Inverse Kinematics for Serial Robot Manipulator, *J. Appl. Math. Comput. Sci.,* **23**(2) (2013) 373–382.
3. Samuel R. Buss, *Introduction to Inverse Kinematics with Jacobian Transpose, Pseudoinverse and Damped Least Squares methods*. (Unpublished survey article, 2004.)
4. M. Bun, *Applications of the Levenberg-Marquardt Algorithm to the Inverse Problem* .http://www.math.washington.edu/reu/papers/2009/mark/reu/paper.pdf., (2009).
5. M. W. Spong, S. Hutchinson and M. Vidyasagar, *Introduction Robot Modelling and Control*, John Wiley and Sons, Inc., New Jersey, NJ (2006)

Localization Method of Autonomous Moving Robot for Forest Industry

Ayumu Tominaga
School of Computer Science and Systems Engineering
Kyushu Institute of Technology
680-4, Iizuka City, Fukuoka, Japan, 820-8502
tominaga@mmcs.mse.kyutech.ac.jp

Eeigi Hayashi
Department of Mechanical Information Science and Technology
Kyushu Institute of Technology
680-4, Iizuka City, Fukuoka, Japan, 820-8502
haya@mmcs.mse.kyutech.ac.jp

T. Sasao
Computer Science, Meiji University
214-8571, Kawasaki City, Kanagawa, Japan
sasao@cs.meiji.ac.jp

Abstract

In this study, we are developing an autonomous moving robot for labor-saving in forest industry. Traditional forest management and maintenance consumes excessive labor time. Particularly, the survey and weeding in the forest place large labor burden on the workers. Therefore, the robot which has the weeding mechanism can achieve to reduce the workload. In this paper, we discuss about localize of the robot in the forest. The Monte Carlo is applied for localization, and we are considering basic system.

Keywords: Forest industry, Autonomous moving, Monte Carlo localization, Particle filter

1. Introduction

In this study, we are developing a field robot for labor-saving of forest industry. The robot has a weeding mechanism, and autonomously moves in the forest. The goal is to automate both elimination of the weed plants and observing the growth quality of each tree.

Nowadays, the decrease labor force due to the decline the employment rate and the aging of working population are regarded as problem.[1] In the forestry, between from planting to final cutting takes 50 to 60 years, while this time, the workers must do many tasks. Particularly, the weeding that carries out in summer places large labor burden on the workers. In addition, the survey of the forest on mountain and the observing the growth of each tree are also too. As the background to it, it can be said that planting density is high (3000 trees are planting per a hectare) and work on steep grade is forced. As a result, the survey is not sufficiently carried out, the work is delayed and devastation of the forest is occurring at present.

This study is proposing the autonomous moving robot that automates these tasks. The robot recognizes the external environment and avoid the trees (resources) by a depth sensor and a CCD camera.

In this paper, the method call Monte Carlo Localization (MCL) is used in localization system in forest. It is thought that the localization system is necessary for the following points.

- Ideally, the weeding should be done all over the forest area. In order to move to an unreachable area, it is necessary to track the movement trajectory of the robot.
- When communicate to the user (forestry workers) about the growth of the observed trees, the location information of the tree in the forest is required.

2. System Structure

The robot under development used ATV (All Terrain Vehicle) as a base vehicle in order to cope with rough terrain in the forest. The appearance of the robot is shown in Fig.1. The external environment is recognized by a depth sensor and a CCD camera equipped on the ATV. The brake laver, accelerator laver and steering are controlled by DC motors. The weeding is performed by a multi-blade mechanism attached between the front wheels.

Fig. 1. Appearance of the robot

3. Autonomous Moving System

In this study, the functions required for the robot are to avoid of contact with the trees and to eliminate of weeds. It is important to have ability to keep moving more than anything else in the dynamic environment due to the growth of plants and so on. Therefore, we developed autonomous moving system that searches gap of trees that can pass through moves, mainly using depth sensor for recognition of external situations.

3.1. *Determining of a Trajectory Path Using Depth Sensor*

This subsection describes determining of a movement trajectory path using depth sensor. The depth sensor (InfiniSoleil FX8, Nippon Signal. Inc., Co.) installed on the robot is a product assumed for use outdoor by the TOF (Time Of Flight) measure method. The horizontal and vertical components of the viewing angle are 60 and 50 degree, respectively. The maximum measureable distance of the sensor is 15m. The Fig.2 shown flow chart of determining of the trajectory path.

At first, 3 dimensional point cloud data get from the depth sensor, and an image viewed in a bird's eye view is created. Let this image be an x-z plane image.

Next, the location, number and size of the object in front of the robot are recognized by labeling processing on the x-z image. Thus, the gap of each object that the robot can pass through is searched, the center point of the gap is set as the goal position of the robot should go.

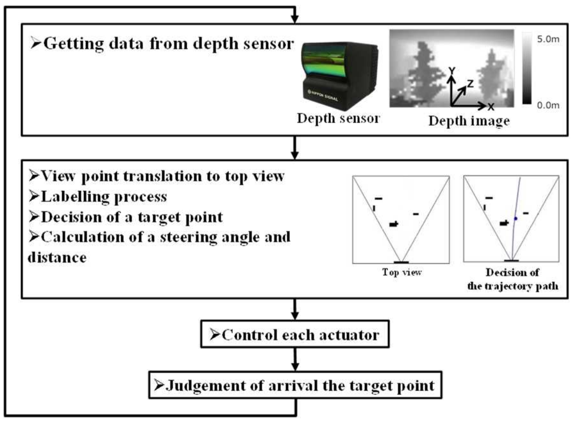

Fig. 2. Flow chart of autonomous moving system

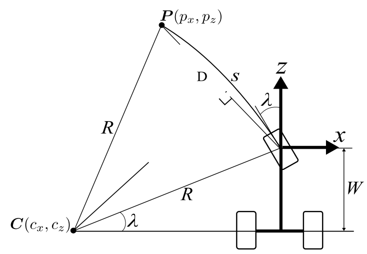

Center of circular trajectory :

$$\begin{cases} C_x = \frac{p_z}{p_x}\left(W + \frac{p_z}{2}\right) + \frac{p_z}{2} \\ C_z = -W \end{cases}$$

Turning radius :

$$R = \sqrt{C_x^2 + C_z^2}$$

Steering angle :

$$\lambda = \sin^{-1} \frac{W}{R}$$

Trajectory path distance :

$$s = 2R \sin^{-1} \frac{D}{2R}$$

P : Target point
C : Center of circular trajectory
W : Wheel base
R : Turning radius
D : Chord length
s : Arc length
λ : Steering angle

Fig. 3 Motion model of the robot

At last, calculate the steering angle and the distance to the target position based on motion model of the robot as shown in Fig.3. The actual movement distance is measured by a rotary encoder equipped to the rear wheel, when reach to the calculated distance, the system will return to the process at the top of flow chart.

3.2. *Mapping for Depth Information and Color Information*

In actual forest, not only the trees, but also weeds are growing. Therefore, the depth sensor will measure the distance of weeds too. As a result, the weeds is treated as an object to avoid target. Therefore, color information obtained from a CCD camera and depth information are integrated to extract three-dimensional distance information of the trees based on image processing.[2]

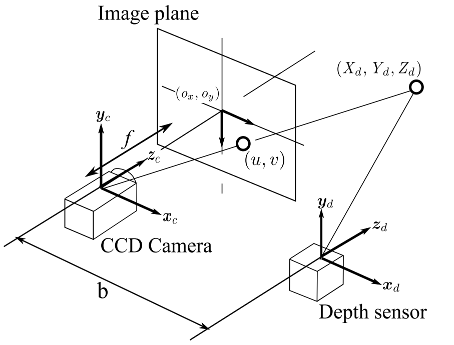

Fig. 4. Relative transform between depth and CCD camera

The coordinate relationship between the depth sensor and the CCD camera is shown by Fig.4. For simplicity, they are arranged in parallel and same height. $[X_d, Y_d, Z_d]^T$ is the point obtained from depth sensor, $[v, u]^T$ is the coordinate in color image, apply the perspective projection transformation matrix $\boldsymbol{K}$, the rotation and translation matrix $[\boldsymbol{R}|\boldsymbol{t}]$ between both sensors. Using the Eq. (1), the pixel coordinates in the color image with respect to the three dimensional coordinates are obtained.

$$w\begin{bmatrix} u \\ v \\ 1 \end{bmatrix} = \boldsymbol{K}[\boldsymbol{R}|\boldsymbol{t}]\begin{bmatrix} X_d \\ Y_d \\ Z_d \end{bmatrix} \qquad \cdots(1)$$

$$\boldsymbol{K} = \begin{bmatrix} f_x & 0 & o_x \\ 0 & f_y & o_y \\ 0 & 0 & 1 \end{bmatrix}, [\boldsymbol{R}|\boldsymbol{t}] = \begin{bmatrix} 1 & 0 & 0 & -b \\ 0 & 0 & 0 & 0 \\ 0 & 0 & 0 & 0 \end{bmatrix}$$

4. Localization method using the trees as landmark

In this robot, it is thought that the localization system is necessary for the following points.

In rough terrain within the actual forest, it is expected that errors will be large with localization using dead reckoning. In addition, the star reckoning by a GPS system will be similar situation because influence of multipass.

We are considering the localization using the tree observed by the robot as landmark, and based on Monte Carlo Localization.

4.1. *Expression of the Trees Map*

In this study, the trees that the robot should be avoid are used a landmark for localization. The global map for global localization is constructed by the information of trees location. In this time, we made the trees map using data of the trees location measured by laser measuring instrument, and used occupancy grids map with 2 dimension expressed. The three map shown Fig. 5. The grids map's range is 35 m square area with 0.5 m square grids. Each grid has occupancy value $m_{x,y}$ as shown Eq. (2).

$$m_{x,y} = \begin{cases} 0.0 & (not\ occupied\ grid) \\ 1.0 & (occupied\ grid) \end{cases} \qquad \cdots(2)$$

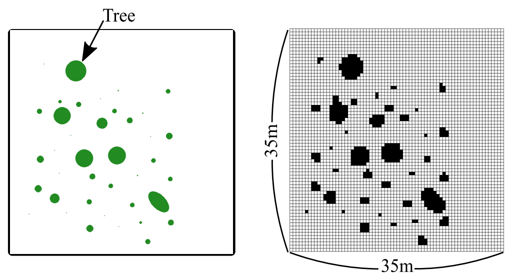

Fig. 5. The tree map and occupancy grid map

4.2. *Monte Carlo Localization*

Monte Carlo Localization (MCL) is a method of estimating the state of robot by assuming the robot's pose with particles, comparing the results observed by each particle with the actually observed results, calculating the likelihood of the particle.[3] It is realize by the following three steps.

- Predict step

$\boldsymbol{x}_t = [x_t \quad y_t \quad \theta_t]^T$ is the state vector of the robot, and prepare a set of N particles with weight ($\boldsymbol{X}_t = \langle \boldsymbol{x}_t^{(i)}, w_t^{(i)} \rangle, i = 1,2,\dots,N$). Each particle is transition according to the motion model f using previous state $\boldsymbol{x}_{t-1}$ and the control input $\mathrm{u} = [s \quad \lambda]^{\mathrm{T}}$. In following equation, $\boldsymbol{e}_t$ is a noise component according to normal disturbing.

$$\boldsymbol{x}_t^i = f(\boldsymbol{x}_{t-1}^i, \widehat{\boldsymbol{u}}_t) \qquad \cdots(3)$$

$$\widehat{\boldsymbol{u}}_t = \boldsymbol{u} + \boldsymbol{e}_t \qquad \cdots(4)$$

- Update step

A likelihood of each particle is calculated by comparing information both of the actual observation data and particle's observation data. First, a local map expressed by an occupied grids map by data that three-dimensional point cloud obtained from depth sensor is created. The coordinate transformation between the local coordinate and the particle $\boldsymbol{x}_t^i$ in the global map gives the grid in the global map $m_{x,y}$ corresponding to the grid in the local map $m_{x,y,local}$. For each grid in the local map, calculate the correlation value with the global map from the Eq. (5) and (6).

$$\rho_{m,m_{local},x_t^{(i)}} = \frac{\sum_{x,y}(m_{x,y}-\bar{m})\cdot(m_{x,y,local}(x_t^{(i)})-\bar{m})}{\sqrt{\sum_{x,y}(m_{x,y}-\bar{m})^2 \sum_{x,y}(m_{x,y,local}(x_t^{(i)})-\bar{m})^2}} \quad \cdots(5)$$

$$\bar{m} = \frac{1}{2M}\sum_{x,y}(m_{x,y} + m_{x,y,local}) \qquad \cdots(6)$$

The M is number of the grids corresponding between the local and global map. The correlation value takes a value ± 1. The likelihood $l_t^{(i)}$ of each particle calculates by Eq. (7). The weight of each particle is Eq. (8) with normalized likelihood.

$$l_t^{(i)}(m_{local}|x_t^{(i)}, m) = max\{\rho_{m,m_{local},x_t^{(i)}}, 0\} \quad \cdots(7)$$

$$w_t^{(i)} = \frac{l_t^{(i)}(m_{local}|x_t^{(i)}, m)}{\sum_i^N l_t^{(i)}(m_{local}|x_t^{(i)}, m)} \qquad \cdots(8)$$

- Resampling step

According to the weight of each particle, resampling the particles. We adopted roulette selection algorism for it.

5. Verification Experiment

We experimented the localization mentioned before in test field. Number of the particles is 1000. Fig. 6 shown the result of update step, and the observations of particles with maximum weight in a t. As the result, small diameter trees observed by the robot are contained large diameter trees observed by the particle. Therefore, it is thought that there is a possibility of adversely affecting the likelihood calculation in the updating step

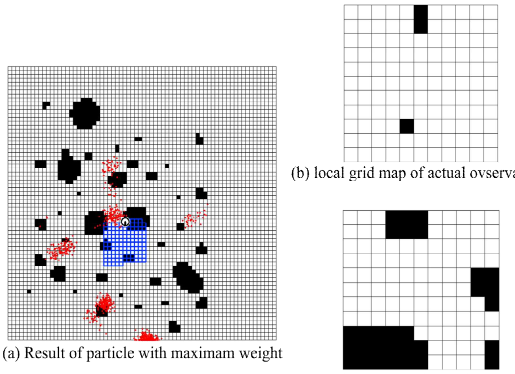

(a) Result of particle with maximam weight

(b) local grid map of actual ovservation

(c) Local grid map of particle's ovservation

Fig. 6. Result of the update step

6. Conclusions

In this paper, we discussed about localization method in the forest. We are constructing the localization system by MCL. In the future, we aim to improve the position estimate accuracy of the robot.

References

1. http://www.rinya.maff.go.jp/j/kikaku/genjo_kadai/, Ministry of Agriculture Forestry and Fisheries, (2016).
2. K. Nakamura, 3-D Object Tracking Based on Integration of 3-D Range and Color Data, No.11-5 *Proceedings of the 2011 JSME Conference on Robotics and Mechatronics*, May 26-28, 2006.
3. S. Thrun, W. Burgard, and D. Fox, *Probabilistic Robotics*, The MIT Press, 2005.

Dynamic Modeling and Motion Control of a Three-Link Robotic Manipulator

Jinho Kim, Andrew S. Lee, Kevin Chang, Brian Schwarz
Department of Mechanical Engineering, University of Maryland, Baltimore County (UMBC), 1000 Hilltop Circle, Baltimore, Maryland, USA, 21250

S. Andrew Gadsden
School of Engineering, University of Guelph, Guelph, Ontario, Canada, N1G 2W1

Mohammad Al-Shabi
Department of Mechanical Engineering, University of Sharjah, University City Rd, Sharjah, United Arab Emirates

E-mail: umbcjhkim@umbc.edu, alee20@umbc.edu, kevicha1@umbc.edu, schwarz4@umbc.edu, gadsden@uoguelph.ca, and malshabi@sharjah.ac.ae

Abstract

This paper presents the dynamic modeling and motion control of a three-link robotic manipulator, also known as the RRR robot. The Kinect motion capture system by Microsoft is used in conjunction with the manipulator. A camera is used to capture the motion of a user's arm and tracks certain angles made by parts of the arm. We consider a pinhole camera model to generate reference angles as per a pinhole camera model in our simulations. These desired angles are fed into the controller and are used by the RRR robot in an effort to copy the movement of the user. A proportional-derivative (PD) controller is developed and applied to the manipulator for improved trajectory tracking. The RRR robot manipulator is dynamically modeled and the results of the proposed control strategy demonstrate good trajectory following.

Keywords: Three-link robotic manipulator, System modeling, Motion capture, PD controller,

1. Introduction

Robotic manipulators have been developed and utilized in all sectors such as industry, medical, and military. Due to its potential to improve precision and enhance robustness, robotic manipulators have been applied to not only military missions but also medical devices in recent years. There are many research topics for medical devices with robotic manipulators such as human-robot collaboration, motion planning, and simultaneous control [1]-[4]. In the military field, we can easily perform robotic manipulator applications as well. For instance, autonomous ground vehicles with robotic manipulators are used in bomb disarming and reconnaissance. To conduct surgery or translate human movement with a robotic manipulator on military missions remotely, it is important to control the robotic manipulator according to operator's movement simultaneously [5]-[11].

In this paper, we consider controlling a system which consists of a camera and robotic manipulator. The pinhole camera model extracts reference angles from simulations in this paper. These desired angles are fed into the controller and are utilized by the robotic manipulator in an effort to mimic the movement of the user. A proportional-derivative (PD) controller is designed and applied to the robotic manipulator for trajectory tracking.

This paper is organized as follows: in Section 2, the pinhole camera model is introduced and the modelling of three-link robotic manipulator is derived using the Euler-Lagrange equation. Based on that, a PD controller is designed in Section 3. Then, the simulation results are presented in Section 4.

2. Pinhole Camera Model

The pinhole camera model is used to obtain reference angles. The camera captures the user's arm motions, then the shoulder, elbow, and wrist angles are extracted through image processing.

The pinhole camera model is shown in Fig. 1. Here, we define $\mathbb{I}$ as the inertial coordinate frame, $\mathbb{C}$ as the camera frame, and $\mathbb{S}$ as the image frame. Then, let $[X_I, Y_I, Z_I]^T$ be the axes of the inertial coordinate frame $\mathbb{I}$, and $[X_{cam}, Y_{cam}, Z_{cam}]^T$ be the position vector in the camera frame $\mathbb{C}$. Let $\left[U_{image}, V_{image}\right]^T$ be the coordinate axes of the image frame $\mathbb{S}$ and O_S represents the principal point where the z-axis of the camera coordinate system intersects the image plane. The focal length of the camera, f, is the distance between O_{cam} and O_S. The mapping from a point $P = [x_c, y_c, z_c]^T \in \mathbb{C}$ onto the image plane can be written as Eq.(1).

$$p = \begin{bmatrix} u \\ v \end{bmatrix} = \frac{f}{z_c}\begin{bmatrix} x_c \\ y_c \end{bmatrix} \tag{1}$$

The user's arm is projected onto the image plane $\mathbb{S}$ through Eq.(1), then the three angles are calculated by extracting three points from the image plane using simple geometry. Let us define two points in $\mathbb{S}$ as $p_1 = (u_1, v_1)$ and $p_2 = (u_2, v_2)$. The angle can be calculated as follows;

$$\theta = \tan^{-1}\left(\frac{v_2 - v_1}{u_2 - u_1}\right) \tag{2}$$

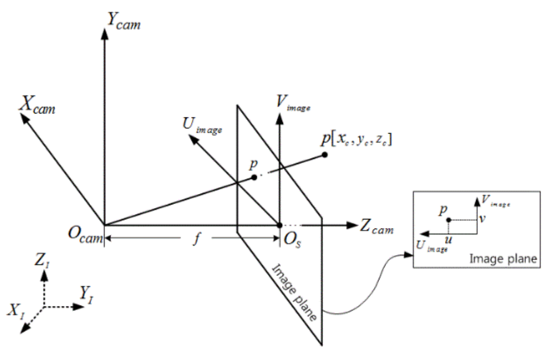

Figure 1. Geometry and coordinate frames for the pinhole camera model

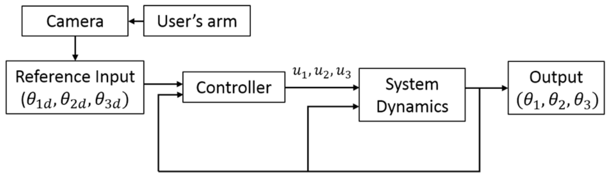

Figure 2. System Diagram

3. Dynamics and PD controller of Robotic Manipulator

In this section, we derive the dynamics of a three-link robotic manipulator and design a PD controller for it. The system diagram is depicted in Fig.2.

3.1. *Dynamics of robotic manipulator*

The configuration of the three-link robotic manipulator is shown in Fig.3. Here, θ_i $(i = 1,2,3)$ denotes the angles between each link, L_i is the length of the link, l_i is the distance from the centroid to corresponding axis, m_i is the mass, and J_i is the moment of inertia. Let τ_i denotes the joint torque and its counterclockwise rotation is assumed to be positive. Then, the Euler-Lagrange equation is applied as shown in Eq.(3)-Eq.(4) where $\mathcal{L}$ is the Lagrangian with kinetic energy $\mathcal{K}$ and potential energy $\mathcal{P}$ of the system [10].

$$\frac{d}{dt}\frac{\partial \mathcal{L}}{\partial \dot{\theta}_i} - \frac{\partial \mathcal{L}}{\partial \theta_i} = \tau_i \tag{3}$$

$$\mathcal{L} = \mathcal{K}_1 + \mathcal{K}_2 + \mathcal{K}_3 - \mathcal{P}_1 - \mathcal{P}_2 - \mathcal{P}_3 \tag{4}$$

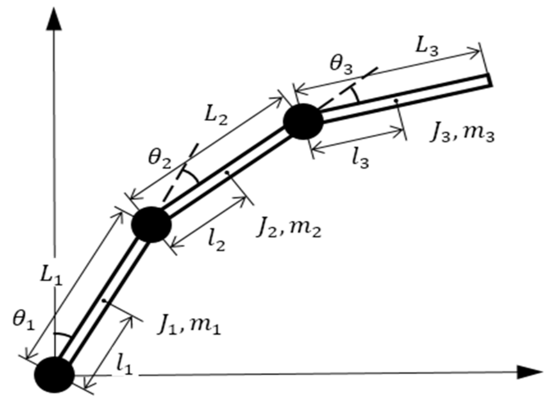

Figure 3. Configuration of the three-link robotic manipulator

In this system, $\mathcal{K}$ and $\mathcal{P}$ of each link can be written as per Eq.(5)-Eq.(6) where $\|v_i\|$ represents the magnitude of the velocity, $l_{i,y}$ is the position of the centroid that is dependent on joint coordinates.

$$\mathcal{K}_i = \frac{1}{2} m_i \|v_i\|^2 + \frac{1}{2} I_i \left(\textstyle\sum_i \dot{\theta}_i\right)^2 \quad (5)$$

$$P_i = m_i g l_{i,y} \quad (6)$$

By these equations, we can obtain the final dynamics of the system in a simple form as the following:

$$u = M(\theta)\ddot{\theta} + C(\theta, \dot{\theta}) + g(\theta) \quad (7)$$

where $M(\theta)$ is the inertia matrix, $C(\theta, \dot{\theta})$ represents the matrix of coriolis and centrifugal elements, $g(\theta)$ is the matrix of gravity elements, and, u is control input. The matrixes and its parameters can be written as follows:

$$M(\theta) = \begin{bmatrix} a_{11} & a_{12} & a_{13} \\ a_{12} & a_{22} & a_{23} \\ a_{13} & a_{23} & a_{33} \end{bmatrix},$$

$$C(\theta, \dot{\theta}) = \begin{bmatrix} b_1 \\ b_2 \\ b_3 \end{bmatrix},$$

$$g(\theta) = \begin{bmatrix} g_1 \\ g_2 \\ g_3 \end{bmatrix},$$

where,

$a_{11} = m_1 a_{c1}^2 + m_2(a_1^2 + a_{c2}^2 + 2a_1 a_{c2} c_2) + m_3(a_1^2 + a_2^2 + a_{c3}^2 + 2a_1 a_2 c_2 + 2a_1 a_{c3} c_{23} + 2a_2 a_{c3} c_3) + I_1 + I_2 + I_3$

$a_{12} = m_2(a_{c2}^2 + a_1 a_{c2} c_2) + m_3(a_2^2 + a_{c3}^2 + a_1 a_2 c_2 + a_1 a_{c3} c_{23} + 2a_2 a_{c3} c_3) + I_2 + I_3$

$a_{13} = m_3(a_{c3}^2 + a_1 a_{c3} c_{23} + a_2 a_{c3} c_3) + I_3$

$a_{22} = m_2 a_{c2}^2 + m_3(a_2^2 + a_{c3}^2 + 2a_2 a_{c3} c_3) + I_2 + I_3$

$a_{23} = m_3(a_{c3}^2 + a_2 a_{c3} c_3) + I_3$

$a_{33} = m_3 a_{c3}^2 + I_3$

$b_1 = -m_2 a_1 a_{c2}(2\dot{\theta}_1 + \dot{\theta}_2) s_2 \dot{\theta}_2 - m_3\big[a_1 a_2(2\dot{\theta}_1 + \dot{\theta}_2) s_2 + a_1 a_{c3}(2\dot{\theta}_1 + \dot{\theta}_2 + \dot{\theta}_3) s_{23} + a_2 a_{c3}(2\dot{\theta}_1 + 2\dot{\theta}_2 + \dot{\theta}_3) s_3\big]$

$b_2 = -m_2\big[a_1 a_{c2}(\dot{\theta}_1^2 + \dot{\theta}_1\dot{\theta}_2) s_2 + a_1 a_{c2}\dot{\theta}_1 s_2 \dot{\theta}_2\big] - m_3\big[a_1 a_2(\dot{\theta}_1^2 + \dot{\theta}_1\dot{\theta}_2) + a_1 a_{c3}(\dot{\theta}_1^2 + \dot{\theta}_1\dot{\theta}_2 + \dot{\theta}_1\dot{\theta}_3) s_{23} + a_2 a_{c3}(\dot{\theta}_1^2 + 2\dot{\theta}_1\dot{\theta}_2 + \dot{\theta}_1\dot{\theta}_3 + \dot{\theta}_2^2 + \dot{\theta}_2\dot{\theta}_3) s_3 + a_1 a_2 \dot{\theta}_1 s_2 \dot{\theta}_2 + a_1 a_{c3}\dot{\theta}_1\dot{\theta}_2 s_{23} + a_2 a_{c3}(2\dot{\theta}_1 + 2\dot{\theta}_2 + \dot{\theta}_3) s_3\big]$

$b_3 = -m_3\big[a_1 a_{c3}(\dot{\theta}_1^2 + \dot{\theta}_1\dot{\theta}_2 + \dot{\theta}_1\dot{\theta}_3) s_{23} + a_2 a_{c3}(\dot{\theta}_1^2 + 2\dot{\theta}_1\dot{\theta}_2 + \dot{\theta}_1\dot{\theta}_3 + \dot{\theta}_2^2 + \dot{\theta}_2\dot{\theta}_3) s_3 + a_1 a_{c3}\dot{\theta}_1\dot{\theta}_3 s_{23} + a_2 a_{c3}(\dot{\theta}_1 + \dot{\theta}_2) s_3 \dot{\theta}_3\big]$

$g_1 = g[c_1(m_1 a_{c1} + m_2 a_1 + m_3 a_1) + c_{12}(m_2 a_{c2} + m_3 a_2) + c_{123}(m_3 a_{c3})]$

$g_2 = g[(m_2 a_{c2} + m_3 a_2) c_{12} + m_3 a_{c3} c_{123}]$

$g_3 = g(m_3 a_{c3} c_{123})$.

3.2. *PD controller*

In this subsection, the PD controller for the three-link manipulator system is presented.

In order to control the system, τ_i can be defined as a control input u_i which controls θ_i with a reference input θ_r. The PD controller of the system are given by

$$u_i = k_{p,i} e_i + k_{d,i} \dot{e}_i \quad (8)$$

where k_p and k_d are proportional and derivative gains, respectively. The angle error, e_i, denotes $\theta_{r,i} - \theta_i$ and the derivative of the angle error, $\dot{e}_i$, denotes $\dot{\theta}_{r,i} - \dot{\theta}_i$.

4. Simulation Results

This section presents simulation results with initial parameters. The simulation used the initial settings which were defined as follows:

$$k_p = [37.5, 24.2, 16.4]$$
$$k_d = [1.34, 0.87, 1.04]$$
$$m_i = [1kg, 1kg, 1kg]$$
$$L_i = [0.2m, 0.2m, 0.2m], l_i = [0.1m, 0.1m, 0.1m]$$
$$J_i = [0.5kg \cdot m^2, 0.5kg \cdot m^2, 0.5kg \cdot m^2].$$

We generated movements of arm and extracted the shoulder, elbow, and wrist angles as reference inputs $\theta_{r,1}, \theta_{r,2}, \theta_{r,3}$. We set these reference inputs as the following:

$$\theta_{r,1} = 3\sin(0.1\pi t)$$
$$\theta_{r,2} = 4\cos(0.1\pi t)$$
$$\theta_{r,3} = 9\sin(0.15\pi t),$$

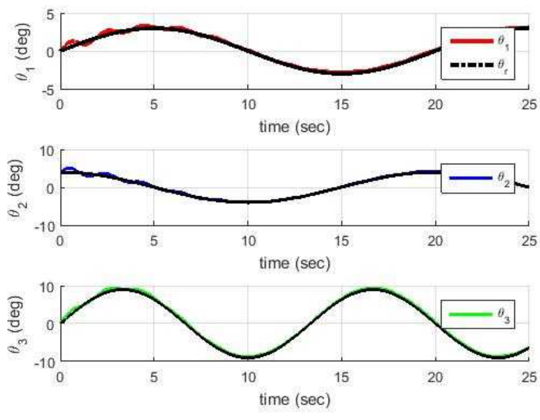

Figure 4. History of each angle. The black dashed lines are reference inputs and colored lines are current angles.

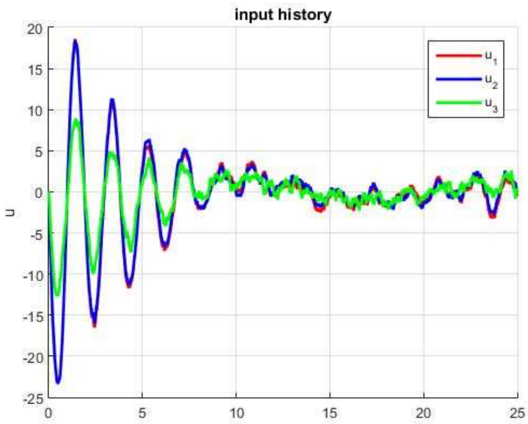

Figure 5. History of three inputs

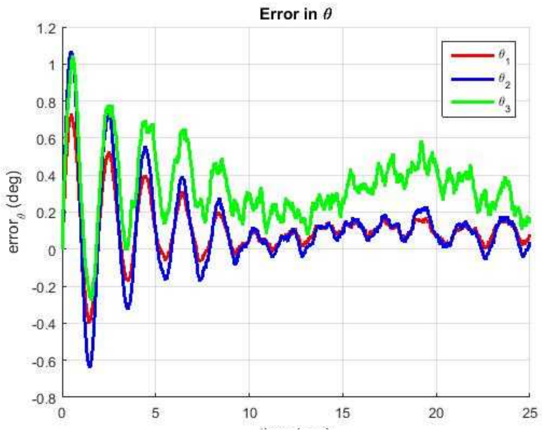

Figure 6. Errors between angles and reference inputs

where, t is time from 0 to 25 seconds in this simulation. The history of each angle is shown in Fig.4 where the black dashed lines are reference inputs $\theta_{r,i}$ and colored lines are current angles. As shown in Fig.4, we can observe that the trajectories of the system angles follow the reference angels with satisfactory results. The initial overshoot in Fig.4 shows acceptable performance of the PD controller for this system.

Histories of the three inputs and errors between angles and reference inputs are shown in Fig.5 and Fig.6, respectively. From Fig.6, we confirm that errors have values less than one degree which is acceptable for a robotic manipulator with linkage dimensions similar to a human arm.

5. Conclusion

This paper presents a three-link robotic manipulator combined with a camera for capturing the user's motion. For the successful control of the system, the pin hole camera model captures the user's arm motion and extracts the shoulder, elbow, and wrist angles through image processing. Then, the dynamics of the system is derived and a PD controller is applied to control the angles of each link. The simulation results verified the efficacy of a PD controller showing satisfying results for tracking movement.

References

1. S. Najarian, M. Fallahnezhad, and E. Afshari, Advances in medical robotic systems with specific applications in surgery—A review, *Journal of medical engineering & technology*, 35(1) (2011) 19-33.
2. H. Jiang, J. P. Wachs, and B. S. Duerstock, Integrated vision-based robotic arm interface for operators with upper limb mobility impairments, *Proc. 2013 IEEE International Conference on Rehabilitation Robotics (ICORR),* (USA, Seattle, Jun. 2013), pp.1-6.
3. T. S. Lendvay, T. C. Brand, L. White, T. Kowalewski, S. Jonnadula, L. D. Mercer, D. Khorsand, J. Andros, B. Hannaford, and R. M. Satava, Virtual reality robotic surgery warm-up improves task performance in a dry laboratory environment: a prospective randomized controlled study, *Journal of the American College of Surgeons*,216(6) (2013): 1181-1192.
4. B. Hannaford, J. Rosen, D. W. Friedman, H. King, P. Roan, L. Cheng, D. Glozman, J. Ma, S. N. Kosari, and L. White. Raven-II: an open platform for surgical robotics research, *IEEE Transactions on Biomedical Engineering,* 60(4) (2013): 954-959.
5. X. Jian and L. Zushu, Dynamic model and motion control analysis of three-link gymnastic robot on horizontal bar, in *Proc. The 2003 IEEE International Conference on Robotics and Intelligent Systems and Signal Processing,* (China, Changsha, Oct. 2003).
6. I. David and G. Robles, PID control dynamics of a Robotic arm manipulator with two degrees of Freedom, *Control de Procesos y Robotica* (2012): 1-7.
7. B. Siciliano, S. Lorenzo, V. Luigi, and O. Giuseppe, *Robotics: modelling, planning and control,* (Springer Science & Business Media, 2010).
8. M.W. Spong, Swing Up Control of the Acrobot, in *Proc. The International Conference on Robotics and Automation,* (USA, San Diego, Oct. 1994), pp.2356-2361.
9. M.W. Spong, The swing up control problem for the acrobot, *IEEE Control System Magazine,* 15(1) (1995): 49-55.
10. M. W. Spong, S. Hutchinson, and M. Vidyasagar, *Robot modeling and control*, (Wiley, New York, 2006).
11. S. A. Gadsden, Smooth Variable Structure Filtering: Theory and Applications, *Ph.D. Thesis, McMaster*, 2011.

Modeling and Simulation for a Quadrotor Vehicle with Adaptive Wing

Qunpo Liu , Fuzhong Wang, Hongqi Wang, Jikai Si

School of Electrical Engineering and Automation, Henan Polytechnic University, 2001 Century Avenue Jiaozuo, 454003, Henan, P.R.China

Hanajima Naohiko

College of Information and Systems, Muroran Institute of Technology, 27-1 Mizumoto-cho,Hokkaido Muroran-shi, Hokkaido (050-8585), Japan

E-mail: lqpny@hpu.edu.cn; wangfzh@hpu.edu.cn, sijikai527@126.com, hana@mondo.mech.muroran-it.ac.jp

www.hpu.edu.cn, www.muroran-it.ac.jp

Abstract

Aiming at developing high power efficiency system for quadrotor vehicle during height keeping and long distance flight, a quadrotor vehicle with adaptive wing is proposed. Angle of the wing respect to flying direction can be adjusted adaptively according to flying speed, to reduce energy expenditure of motor. The dynamic model was built up. Rotor lift were analyzed based on the mechanical structure and its flight principle. The simulation is carried out to verify the effectiveness of high power efficiency.

Keywords: Modeling, Quadrotor vehicle, Simulation, Wing.

1. Introduction

Because of distinct features, such as vertical take-off and landing(VTOL), sharp maneuvering, low cost, simple mechanism, UAVs have attracted more and more interests in a wide range involving rescues, security, inspection, surveillance, aerial photography, mapping, etc. Each individual rotor has a smaller diameter and less kinetic energy than the equivalent single-rotor helicopter. Compared to conventional helicopters, with the large main rotor and tail rotor, the quadrotor is easier to fly, does not have the complex swash plate mechanism and is easier to model and control. The quadrotor has a promising application as commercial, military and academic platforms.

Much research has focused on the Dynamic modeling[1-5], simulation, optimization, controller design[2], and control algorithm[3-5] for quadrotor vehicle. However, there are still some problems in practical use, such as energy expenditure during long distance forward flight. By now, lithium battery is used for power supply for quadrotor vehicle. But the weight of the batteries increases with the capacity. At the same time, the energy expenditure is also increases for increased weight and dimension. Due to the conflict between the weight of the batteries (capacity) and flight distance, flight distance is subject to the restriction. However, there are relatively fewer contributions on the energy expenditure during long distance forward flight for a quadrotor. Therefore, ***T*** how to reduce the energy expenditure during long weight is a problem to solve for the application of quadrotor vehicle.

A quadrotor vehicle with adaptive underbelly wing is proposed. The underbelly wing at certain angles is expected to obtain a horizontal direction of thrust. Advantageously, this may result in a reduction of dip angle for quadrotor body and also can resulting in lower airflow resistance and lower downward force on quadrotor body. And finally, it can eventually reduce energy expenditure during long distance forward flight.

2. Dynamic modeling

This section presents a simple model of the quadrotor dynamics according to Ref. 5-6.

As shown in Fig.1, the quadrotor possesses a simple and symmetrical structure with four rotors and can be controlled by the rotational speed of the four rotors.

For the sake of convenience, T_1 is denoted as the head of the rotorcraft. Meanwhile rotor T_3 is the tail. i.e., $\boldsymbol{T_1}$, $\boldsymbol{T_2}$, $\boldsymbol{T_3}$ and $\boldsymbol{T_4}$ is named front, right, rear, left rotor respectively. Define the following body coordinate system $\boldsymbol{x_b}$, $\boldsymbol{y_b}$, $\boldsymbol{z_b}$: the original point($\boldsymbol{O_b}$) is the center of gravity; $\boldsymbol{x_b}$ is from b $\boldsymbol{O_b}$ the head of the quadrotor; $\boldsymbol{y_b}$ is from $\boldsymbol{O_b}$ to the right side of the quadrotor; and z_b follows the law of right hand.

The notation for the quadrotor model is shown in Fig. 2. Define the following inputs to model the quadrotor: $\boldsymbol{F_{Thrust}}$ is the thrust generated by four motors; F_Z is the the vertical upward thrust force on the quadrotor body; F_{bf} is the air resistance on the body; F_{wa} is the left force on the wing; F_{Wf} is the air resistance on the wing; θ is the pitch of the quadrotor body; $\boldsymbol{\alpha}$ is the angle between the $\boldsymbol{x_b}$ and the wing; $\boldsymbol{\gamma}$ is the angle of between the wing and the horizontal flying direction which marked by a line in green. $\boldsymbol{mg}$ is the weight of the quadrotor. All the analysis is on the assumption of steady volume of air flow situation.

The rotor speed is $\boldsymbol{\omega_i}$ and the thrust force is an upward vector

$$F_{Thrust} = \sum_{i=1}^{4} b\omega_i^2 \tag{1}$$

in the vehicle's negative z-direction, where b > 0 is the lift constant that depends on the air density, the cube of the rotor blade radius, the number of blades, and the chord length of the blade.

When the quadrotor is flying in a certain speed on certain height, the vertical upward thrust force on the quadrotor body should be remained unchanged.

$$F_z = F_{Thrust}\cos\theta + F_{wa} - mg \tag{2}$$

and

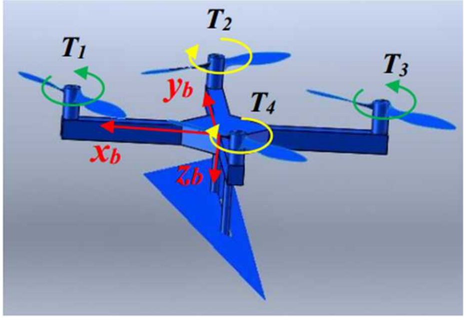

Fig.1 The main structure of a quadrotor

$$F_{wa} = \frac{1}{2}C_y\rho_\infty V_\infty S\cos(\alpha+\theta) \tag{3}$$

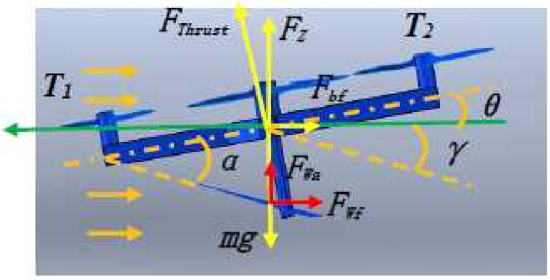

Fig.2 Force modeling of the quadrotor

where, $\boldsymbol{C_y}$ is wing section lift coefficient; $\boldsymbol{S}$ is the area of the wing; $\boldsymbol{\rho_\infty}$ is the air density; $\boldsymbol{V_\infty}$ is the steady speed. F_{wa} is perpendicular to the direction of air flow.

Deviation of the direction of air flow caused by wash velocity can be ignored for low speed.

The force F'_{wf} on the quadrotor body generated by the air resistance on the wing F_{wf} is

$$F'_{wf} = F_{wf} + F_{wf}\cos(-\theta)\times d \tag{3}$$

And it can be counteracted by increasing of $\boldsymbol{\omega_3}$ and reducing of $\boldsymbol{\omega_1}$.

The air resistance F_{Wf} on the wing is

$$F_{wf} = \frac{1}{2}C'_y\rho_\infty V_\infty S\sin(\alpha+\theta) \tag{4}$$

where, $\boldsymbol{C'_y}$ is wing resistance coefficient.

When the quadrotor is fly on same height, the force on the body in vertical direction is

$$F_z = F_{Thrust}\cos\theta + F_{wa} - mg = 0 \tag{5}$$

Therefore, the equation can be obtained using Eq. (3) and (5)

$$mg - F_{Thrust}\cos\theta = \frac{1}{2}C_y\rho_\infty V_\infty S\cos(\alpha+\theta) \quad (6)$$

During the flying, the force on the moving direction is

$$F_x = F_{Thrust}\sin\theta - F_{wf} = ma_x \quad (7)$$

where, a_x is *acceration of quadrotor on* the moving direction.
When the speed is stable, a_x=0,

$$F_{Thrust}\sin\theta = -\frac{1}{2}C'_y\rho_\infty V_\infty S\sin(\alpha+\theta) \quad (8)$$

In the situation without wing of quadrotor,

$$F_{Thrust}\cos\theta = mg \quad (9)$$

In the situation with a wing of quadrotor, the following equation can be deduced from Eq. (6) and (8)

$$\therefore F_{Thrust} = \frac{mgC'_y\sin(\alpha+\theta)}{C'_y\cos\theta\sin(\alpha+\theta) - C_y\sin\theta\cos(\alpha+\theta)} \quad (10)$$

Define that

$$\delta = \frac{C'_y\sin(\alpha+\theta)}{C'_y\cos\theta\sin(\alpha+\theta) - C_y\sin\theta\cos(\alpha+\theta)} \quad (11)$$

Therefore, Eq. (10) can be simplified as

$$F_{Thrust} = \delta mg \quad (12)$$

From Eq.(12), it can be draw that the energy expenditure would be deceased if $0 \le |\delta| < 1$.

3. Simulation results

To verify whether there are same cases meet requirements, analysis is carried out based on MATLAB platform.

In the Eq.(11), there are two parameters C_y and C'_y. Normally, Lift-drag ratio $\boldsymbol{k}$ is used instead. Lift-drag ratio $\boldsymbol{k}$ is relate to wing's angle of attack and can be measured from wind tunnel test:

$$k = \frac{C_y}{C'_y} \quad (13)$$

The lift-drag ratio $\boldsymbol{k}$ is simulated by wind tunnel test data in reference [7], as shown in Fig.3. And it is used in the conclusion of $\boldsymbol{\delta}$.

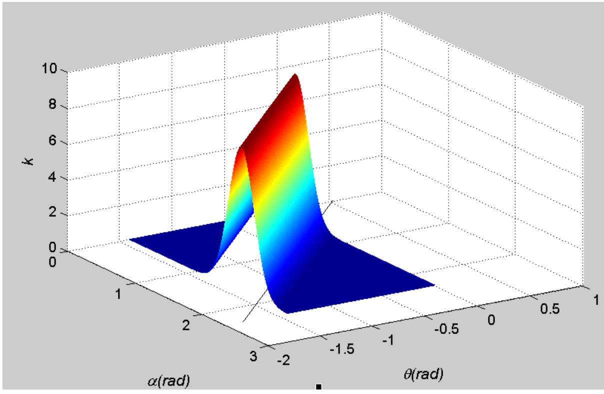

Fig.3 lift-drag ratio $\boldsymbol{k}$

In the area marked A1, the results are not valid because it falls outside the allowable range $(\boldsymbol{\alpha+\theta}) \le \boldsymbol{0}$.

In the area marked A3, the value of $\boldsymbol{\delta}$ is bigger than 1, which is means more energy needed than quadrotor without wing.

As shown in Fig.4 and Fig.5, in the area (A2) with color changing from dark blue to dark violet in middle of the figure, the value of $\boldsymbol{\delta}$ is $0 \le \boldsymbol{\delta} \le 1$. It means the thrust force is smaller than the gravity of guardrotor. Especially in same point, the thrust force is zero in idea situation. And it also can be draw from the simulation results that the thrust force will increase with $(\boldsymbol{\alpha+\theta})$ increasing. Expecially when $\boldsymbol{\alpha+\theta} > \pi/6$ (the line as shown in Fig.5),

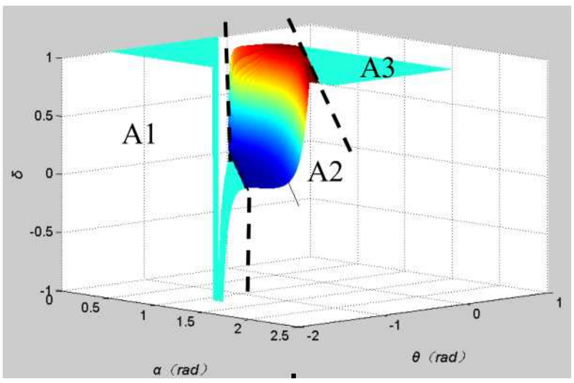

Fig.4 D view of simulation results of $\boldsymbol{\delta}$

value of $\boldsymbol{\delta}$ increase dramatically, which is due to decrease of the lift-drag ratio $\boldsymbol{k}$. In this case however, $\boldsymbol{\delta}$ and the thrust force $\boldsymbol{F_{Thrust}}$ will increase very much even $\boldsymbol{\delta}$ is small in the time.

Therefore, the best to reduce energy expenditure is on situation of $0 < \alpha+\theta < \pi/6$. In this case, the thrust force

$$\left|F_{Thrust}\sin\theta\right| < \left|-\frac{1}{2}C_y'\rho_\infty V_\infty S\sin(\alpha+\theta)\right|$$

Therefore, the flying velocity V should decrease until a new stable equilibrium is reached.

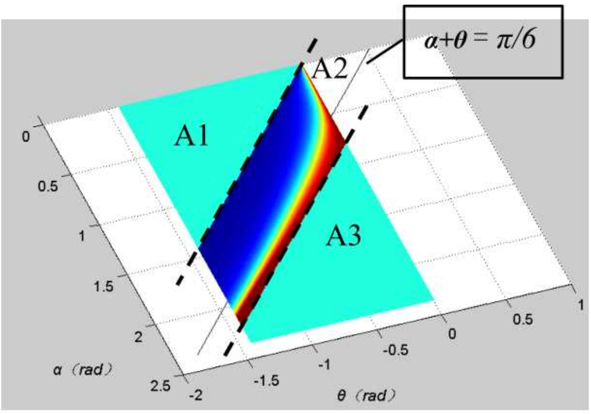

Fig.5 Top view of simulation results of $\boldsymbol{\delta}$

4. Conclusions

In this paper, a quadrotor vehicle with adaptive underbelly wing is introduced. A simplified mathematic model is studied firstly. The force modeling was analyzed. Simulation results show that the proposed quadrotor vehicle with adaptive underbelly wing can reduce energy expenditure by arranging the attitude angle of wing within limited range.

$\boldsymbol{F_{Thrust}}$ will be stable invariable when $(\alpha+\theta)$ does not change. If $\boldsymbol{\theta}$ decreases under influence of air flow, the value of $\boldsymbol{\alpha}$ should increase to keep stable of $\boldsymbol{F_{Thrust}}$. In this case, $\boldsymbol{F_{Thrus*t}\cos\theta}$ will increase according to Eq.(6). The $\boldsymbol{F_{Thrust}}$ will decrease if the flying velocity V remains constant. Considering Eq.(8), the force on x-direction is

References

1. Hai-Nguyen Nguyen,ChangSu Ha,Dongjun Lee, Mechanics, control and internal dynamics of quadrotor tool operation, *Automatica*,61 (2015) 289-301
2. Das A, Lewis F, Subbarao K. Backstepping approach for controlling a quadrotor using lagrange form dynamics[J] *J Intell Robot Syst*, , 56: (2009) 127-151.
3. Wei Dong, et ac. A high-performance flight control approach for quadrotors using a modified active disturbance rejection technique, *Robotics and Autonomous Systems*, 83 (2016) 177-187
4. Juhi Ajmera, V. Sankaranarayanan,point-to-point control of a quadrotor theory and experiment, *IFAC-Papers OnLine*, 49 (1), (2016), 401-406
5. Peter Corke, *Robotics, Vision and Control* (Springer Verlag, Berlin Heidelberg, 2011).
6. WANG Hong-yu, et ac. Modelling and position tracking control for quadrotor vehicle, *Journal of Chinese Inertial Technology*, 20(4) (2012) 455-458
7. WANG Bingliang, et ac. *Vehicle Aerodynamics*(Tsinghua University Press, Beijing, 2013)

Fuzzy Self-tuning PID Control Algorithm for Belt Conveyor Driven by Multi-motor

Caixia Gao, Fuzhong Wang, Ziyi Fu
College of Electrical Engineering and Automation, Henan Polytechnic University, 2001 Century Avenue, Jiaozuo, 454003, P.R.China
E-mail: gcx81@126.com, wangfzh@hpu.edu.cn, fuzy@hpu.edu.cn
www.hpu.edu.cn

Abstract

Aiming at the problems of low efficiency when belt conveyor driven by multi-motor is in light or idle run as well as electrical power unbalance, the speed setting algorithm and fuzzy PID algorithm for speed control and power balance control are introduced. The application shows that, according to the coal flow changes, the speed can be automatically adjusted through this algorithm, making both speed control error and the power control error of which are lower than 2.6%.

Keywords: belt conveyor, power unbalance, fuzzy self-tuning PID

1. Introduction

In order to ensure the safe and stable operation of the transport aircraft, the following problems need to be solved: (1) Mechanical damage of the equipment due to the heavy load and the dynamic tension of the tape during start-up and stopping; (2) Running state power consumption problem; (3) Multi-motor power balance problem. For the above problems, scholars at home and abroad have also carried out researches, but mostly for the smaller angle (35 °and below): Reference 1 uses direct torque control strategy to achieve motor power balance control with fast response and good stability, which is directly affected by the motor parameters. In Reference2, what is proposed is a power balance control strategy for mine belt conveyor motor based on torque compensation. The vector dual closed-loop controller is a conventional PI controller, and its adaptability is not strong. Reference 3 uses the current control method to regulate the power balance of the belt conveyor, when the current of each motor exceeds or falls below 5% of the average current. Because of the characteristics of large inertia and severe hysteresis, the belt conveyor with multi-motor drive is a time-varying and nonlinear control object, it is difficult to adopt conventional fixed-parameter PID control to achieve good control effect; when a single fuzzy controller is used, the response speed is high, but its control accuracy is difficult to meet the requirements. This paper proposes a fuzzy control algorithm based on fuzzy self-tuning PID control algorithm for large-angle mining belt conveyor driven by multi-motor, achieving flexible starting and stopping of belt conveyor, adjusting the speed according to the size of the load automatically, and maintaining multi-motor power balance.

2. The General Control Model of High-inclination Belt Conveyor

Aiming at the problem of mechanical damage to the equipment caused by the falling or rolling of the material (coal) during the heavy load start and stop of the belt conveyor and the dynamic tension, the excessive wear and energy wastage of the mechanical transmission mechanism under light load or no load high speed running condition and dynamic balance of motors, this paper proposes the overall control model of the belt conveyor shown in Fig.1. The control system is mainly composed of speed setting module, speed control module, power balance control module and so on. It adopts double closed-loop structure. The inner loop is composed of the power balance controller. The strategy is using the master-slave control mode, namely, taking the current of the 1# motor as the given value of the current of 2# ~ 4# motor. When the current of 2# ~ 4# motor is not consistent with the No. 1 motor, the power balance fuzzy controller can change the output of the motor by automatically adjusting the opening of the servo proportional valve of the 2# ~ 4# controllable driving device CST, so as to realize the four motor power balance control. The outer ring is composed of a speed control module, and its function is to realize the belt speed control. The basic principle is comparing the tape speed with the given speed. When the belt speed and the given speed is inconsistent, the controller first adjust 1# CST servo proportional valve opening step by step to change the output of 1# motor, then the other three motors automatically tracking the output power of 1#motor , so four CSTs work together to achieve the adjustment of the belt speed. The function of the speed setting module is to determine the speed of the tape during starting, stopping and normal operation according to the coal flow rate in the belt.

Speed control module and power balance control module both use fuzzy self-tuning PID control algorithm, and its structure is shown in Fig.2. It is composed of a fuzzy controller and PID controller. The PID controller mainly realizes the speed and power balance control of the double drum four-drive belt conveyor. The fuzzy controller is mainly used to monitor the control effect and adjust the parameters of the PID controller. By monitoring the tape machine speed and motor power (current) deviation e and the deviation change rate ec continuously, the control effect can be analyzed. Improving the control effect of double-drum four-drive belt conveyor control system is achieved by adjusting the proportion coefficient, integral coefficient and differential coefficient of PID controller using fuzzy reasoning. Speed control fuzzy self-tuning PID input is speed deviation e and speed deviation rate of change ec; three power balance control fuzzy self-tuning PID input are current deviation e and current deviation Rate of change ec of 2# ~ 4# motor and 1# motor. Fuzzy self-tuning PID output are the respective controllable drive CST servo proportional valve opening.

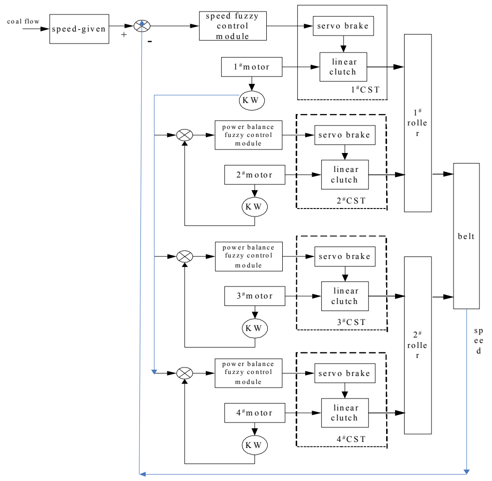

Fig.1 Belt speed and motor power balance control principle

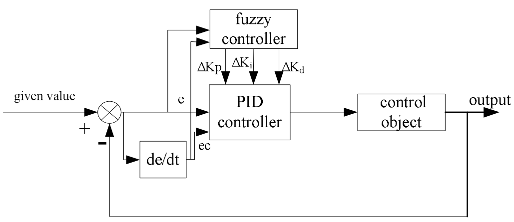

Fig.2 The fuzzy self-tuning PID principle diagram

PID controller uses incremental operation, position output, and the formula is shown in (1), (2), (3).

In the formulas (1) to (3): U (k) is the output of the controller (also called the regulator)

$$\Delta u(k)=u(k)-u(k-1)=K_{p}ec(k)+$$
$$K_{i}e(k)+K_{d}[ec(k)-ec(k-1)] \quad (1)$$

$$u(k)=u(k-1)+\Delta u(k) \quad (2)$$

$$ec(k)=e(k)-e(k-1) \quad (3)$$

First, apply the simulation tools and experimental methods offline. According to the principle of fuzzy control, establish on-line adjust table of PID controller's proportional(fuzzy decision table), including coefficient increment △K_p, integral coefficient △K_i differential coefficient △K_d, and store them in the PLC controller memory for fuzzy on-line reasoning query controller. In the control process, the fuzzy controller applies fuzzy reasoning to find out the corresponding adjustment table (fuzzy decision table) from △K_p, △K_i and △K_d according to the deviation e and deviation change rate ec (de/dt) (4), and get the PID three parameters K_p, K_i and K_d setting value. Finally, adjust the K_p, K_i and K_d to the PID controller.

$$\begin{cases} K_P = K'_P + \{E, E_C\}; & K_P = K'_P + \Delta K_P \\ K_i = K'_i + \{E, E_C\}; & K_i = K'_i + \Delta K_i \\ K_d = K'_d + \{E, E_C\}; & K_d = K'_d + \Delta K_d \end{cases} \quad (4)$$

In the formula (4), K'_p, K'_i and K'_d are the initial pre-setting values of K_p, K_i and K_d obtained through the traditional PID parameter setting method.

3. Speed Setting of Tape Conveyor

In order to reduce the loss of mechanical transmission mechanism and improve the efficiency of the motor, the belt conveyor should operate at the speed in accordance with the speed of its coal flow. At the same time, in order to prevent damage caused by impact on the tape from frequent changes of tape speed, control system set six speed diagrams. When the belt is overhauled (no load), the speed is 0.25m/s; when the coal flow rate is less than or equal to 120t, the speed is 0.65m/s; the coal flow rate is more than 120t and less than or equal to 240t, the speed is 1.35m/s; the coal flow rate is more than 240t and less than or equal to 360t , the speed is 2.00m/s; the coal flow is greater than 360t less than or equal to 480t, the speed is 2.55m/s; the coal flow is greater than 480t less than or equal to 600t , the speed is 3.15m/ s.

In order to reduce the impact on the grid caused by starting current of four drive motors, reduce the mechanical damage to the equipment caused by dynamic tension because of starting and stopping of high-angle tape conveyor, and avoid the material decline or rolling when start, the speed curve of belt starting and stopping should use "S" type speed diagram, as shown in Fig.3.0~t_3 is the starting acceleration phase of the belt conveyor; t_3~t_4 is constant speed running section; t_4~t_7 is the deceleration stage; t_4~t_5 is the early deceleration stage; t_5~t_6 is the constant deceleration stage; t_6~t_7 is the final deceleration stage of the belt conveyor: the acceleration of the tape machine can be set at 0.1 m/s^2 to 0.3 m/s^2 at the time of starting and stopping, and the starting time is controlled in 60s~200s, and both can be set according to site requirements.

$$V_1(t)=\frac{1}{2}k_1t^2 \quad (5)$$

$$V_2(t)=\frac{1}{2}k_1t^2+a_{mq}(t-t_1) \quad (6)$$

$$V_3(t)=\frac{1}{2}k_1t^2+a_{mq}(t_2-t_1)+\frac{1}{2}k_2(t-t_2)^2 \quad (7)$$

In the formulas (5) to (7):k_1 (m/s^3) is the change rate of the acceleration in the stage 0~t_1; k_2(m/s^3) is the change rate of the acceleration in the stage t_2~t_3. a_{mq} (m/s^2) is the maximum acceleration in acceleration section;

$$V_1(t)=V_m \quad t_4<t\le t_5 \quad (8)$$

$$V(t)=V_m-\frac{1}{2}k_3(t-t_4)^2 \quad t_4<t\le t_5 \quad (9)$$

$$S(t)=V_m(t-t_4)-\frac{1}{6}k_3(t-t_4)^3 \quad (10)$$

$$V(t)=(2a_{mz}S+V_6^2)^{\frac{1}{2}} t_5<t\le t_6 \quad (11)$$

$$V(t)=V_6-\frac{1}{2}k_{z4}(t-t_6)^2 \quad t_6<t\le t_7 \quad (12)$$

In the formulas (8) to (12): a_{mz} (m/s^2) is the maximum acceleration in the starting acceleration stage; S(t)is the travel in the constant deceleration stage(m);k_{z4} (m/s^3) is the change rate of acceleration in stage t_6~t_7.

4. Experimental Analysis

Based on the designed speed and power, the belt conveyor control system of balance adaptive fuzzy PID control algorithm has actually operated, with the actual control curve speed and power of the belt conveyor shown in Figure 3. In the figure, the belt start-up time is

180s, the belt speed is fixed at 3.15m/s. Once the belt runs stably, the running speed will change from 3.20m/s to 3.10m/s, and the control error will be less than 2.6%. The operating current fluctuates within the range of 20.5A~21.5A, and the control error is less than 2.6%, which realizes the reliable, safe and energy-saving operation of the main shaft belt transport system.

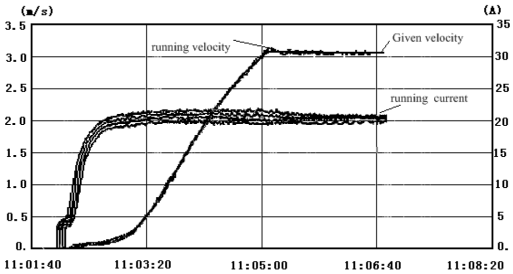

Fig.3 System speed and power curve of actual control

5. Conclusion

(1) "S" speed profile is applied as speed profile in the belt conveyor's starting and stopping, thus preventing the material (coal) from dropping or rolling during the start and stop of the heavy-duty conveyor, and the mechanical damage to equipment caused by the dynamic tension of the tape during start and stop, so as to improve the safety performance of equipment and operators.

(2) According to the size of the coal flow, the speed of the belt conveyor is divided into 6 steps. The fuzzy self-tuning PID algorithm is used to control the speed of the belt conveyor, so the speed control error is less than 2.6%.

(3) Use the master-slave control mode and take the current of the 1# motor as a given value. The fuzzy self-tuning PID control algorithm makes the current of the 2#~4# motor follow the current of the 1# motor, so the control error is less than 2.6%. This realizes high control precision so that the powers of four drive motors are almost balanced or the difference is controlled within an allowable range. By doing so, we prevent the occurrence of motor burnout, improve the safety and reliability of the system, and extend the life of the belt conveyor.

References

1. WANG Zhong-hua, CHEN Xun, YANG Guang-hui. Research of Multi-motor Power Balance Control of Belt System in Coal Mining, *Coal Mine Machinery*, Vol.34 No.8(2013), pp:61-63.
2. XU Lu-hui, LI Fu-dong, ZHANG Chao, ZHANG Xiao-yong, ZONG Cheng-guo. Research of Power Balance of Belt Conveyor Driven by Multi-motor and Its Analysis, *Industry and Mine Automation*, No.5(2011), pp: 63-65.
3. CHEN Yu. Study on Control of Belt Conveyor Based on Intelligent Algorithm Fuzzy Neutral PID Controller, *Coal Mine Machinery*, Vol.35 No.42(2014), pp:39-41.

Continuous Non-singular Fast Terminal Sliding Mode Control for an Active Gravity Field Simulator

Jiao Jia, Yingmin Jia, Shihao Sun
The Seventh Research Division and the Center for Information and Control
School of Automation Science and Electrical Engineering
Beihang University (BUAA), 37 Xueyuan Road, Haidian District
Beijing, 100191, China
E-mail: annebuaa@hotmail.com; ymjia@buaa.edu.cn; jxcrssh@126.com
www.buaa.edu.cn

Abstract

In this study, a global non-singular fast terminal sliding mode controller (FTSMC) is designed for an active gravity field simulator (AGFS). The stability of the control algorithm can be easily verified by using Lyapunov theory. It is shown that the proposed controller can eliminate the chattering effect without losing the robustness property. Simulation results show that faster and high-precision tracking performance can be obtained compared with the conventional continuous sliding mode control method.

Keywords: gravity field simulator, fast terminal sliding mode, robustness, finite-time stability

1. Introduction

Terminal sliding mode (TSM) control[1-4] is a finite time stability control strategy, which can stabilize system states to their equilibrium points or track the desired trajectory in finite time. Due to some superior properties, such as fast convergence, strong robustness, and high precision, TSM has attracted extensive attention in control theory studies and in practical applications. In this paper, a non-singular fast terminal sliding mode controller is applied to an AGFS.

The rest of this paper is organized as follows. The simulation mechanism of the platform is introduced in section 2. In section 3, a NFTSMC is developed and the stability is proved. Simulation examples are given to demonstrate the effectiveness of the proposed control algorithms in section 4. Finally, we end this paper with some conclusions.

2. Simulation Mechanism

The simulation platform[5] is a servo system consisting of an x-axis direction mechanism driven by the x-axis direction motor, a y-axis direction mechanism driven by the y-axis direction motor, a z-axis direction mechanism driven by the z-axis direction motor, a universal joint, a spring buffer, a dual-axis tilt sensor, a tension sensor and an unconstrained suspension section (USS). As described in Fig. 1 the object is connected to the platform through the USS. The USS is linked to the spring buffer. The spring buffer is attached to the universal joint. The universal joint is connected to the z-axis direction mechanism through a tension sensor to detect the force between them. A dual-axis tilt sensor is mounted on the upper end of the spring buffer to determine an angle of the spring buffer with respect to the vertical axis or z-axis (the vertical).

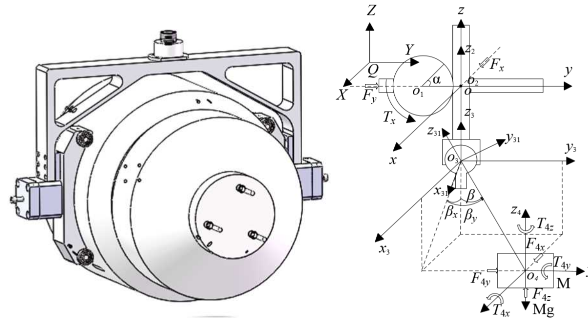

Fig. 1. The USS and coordinate system of the AGFS

3. Continuous FTSMC

The dynamics of the AGFS[5] can be written as

$$\boldsymbol{M}_m\ddot{\boldsymbol{q}}_2 + \boldsymbol{C}\dot{\boldsymbol{q}}_2 + \boldsymbol{G} = \boldsymbol{F}_1 - \boldsymbol{M}_1\boldsymbol{M}_2^{-T}\boldsymbol{F}_2 \tag{1}$$

Define $\boldsymbol{M}(\boldsymbol{q}) = \boldsymbol{M}_m, \boldsymbol{F} = \boldsymbol{F}_1, \boldsymbol{F}_d = -\boldsymbol{M}_1\boldsymbol{M}_2^{-T}\boldsymbol{F}_2$, and we obtain

$$\boldsymbol{M}(\boldsymbol{q})\ddot{\boldsymbol{q}} + \boldsymbol{C}(\boldsymbol{q},\dot{\boldsymbol{q}})\dot{\boldsymbol{q}} + \boldsymbol{G}(\boldsymbol{q}) = \boldsymbol{F} + \boldsymbol{F}_d \tag{2}$$

where $\boldsymbol{q},\dot{\boldsymbol{q}},\ddot{\boldsymbol{q}} \in \boldsymbol{R}^3$ are the vectors of position, velocity and acceleration, respectively , $\boldsymbol{M}(\boldsymbol{q}) = \boldsymbol{M}_0(\boldsymbol{q}) + \boldsymbol{\delta M}(\boldsymbol{q}) \in \boldsymbol{R}^{3\times 3}$, $\boldsymbol{C}(\boldsymbol{q},\dot{\boldsymbol{q}}) = \boldsymbol{C}_0(\boldsymbol{q},\dot{\boldsymbol{q}}) + \boldsymbol{\delta C}(\boldsymbol{q},\dot{\boldsymbol{q}})$, $\boldsymbol{G}(\boldsymbol{q}) = \boldsymbol{G}_0(\boldsymbol{q}) + \boldsymbol{\delta G}(\boldsymbol{q}) \in \boldsymbol{R}^3$, $\boldsymbol{F} \in \boldsymbol{R}^3$ is the vector of applied torque or equivalent force, $\boldsymbol{F}_d \in \boldsymbol{R}^3$ is the vector of driving force operating on the object, $\|\boldsymbol{F}_d\| \le f_d$. Here $\boldsymbol{M}_0(\boldsymbol{q}),\boldsymbol{C}_0(\boldsymbol{q},\dot{\boldsymbol{q}})$ and $\boldsymbol{G}_0(\boldsymbol{q})$ are the nominal parts, whereas $\boldsymbol{\delta M}(\boldsymbol{q}),\boldsymbol{\delta C}(\boldsymbol{q},\dot{\boldsymbol{q}})$ and $\boldsymbol{\delta G}(\boldsymbol{q})$ represent the perturbations in the system matrices. Then, the dynamical model of the AGFS can be rewritten as

$$\boldsymbol{M}_0(\boldsymbol{q})\ddot{\boldsymbol{q}} + \boldsymbol{C}_0(\boldsymbol{q},\dot{\boldsymbol{q}})\dot{\boldsymbol{q}} + \boldsymbol{G}_0(\boldsymbol{q}) = \boldsymbol{F} + \boldsymbol{F}_d + \boldsymbol{T}(\boldsymbol{q},\dot{\boldsymbol{q}},\ddot{\boldsymbol{q}}) \tag{3}$$

where $\boldsymbol{T}(\boldsymbol{q},\dot{\boldsymbol{q}},\ddot{\boldsymbol{q}}) = -\boldsymbol{\delta M}(\boldsymbol{q})\ddot{\boldsymbol{q}} - \boldsymbol{\delta C}(\boldsymbol{q},\dot{\boldsymbol{q}})\dot{\boldsymbol{q}} - \boldsymbol{\delta G}(\boldsymbol{q}) \in \boldsymbol{R}^3$ is the lumped system uncertainty, which is bounded by the following function

$$\|\boldsymbol{T}(\boldsymbol{q},\dot{\boldsymbol{q}},\ddot{\boldsymbol{q}})\| \le b_0 + b_1\|\boldsymbol{q}\| + b_2\|\dot{\boldsymbol{q}}\|^2 \tag{4}$$

Let $\boldsymbol{q}_d \in \boldsymbol{R}^3$ be a twice differentiable desired trajectory, and define the tracking error as $\boldsymbol{e} = \boldsymbol{q} - \boldsymbol{q}_d$. The control objective is to design a feedback control $\boldsymbol{F}$ such that the AGFS output $\boldsymbol{q}$ tracks the desired trajectory $\boldsymbol{q}_d$ in finite time.

Before giving the main results, the following vectors are defined as

$$\boldsymbol{x}^{\gamma} = \left[x_1^{\gamma_1},\ldots,x_n^{\gamma_n}\right]^T, |\boldsymbol{x}|^{\gamma} = \left[|x_1|^{\gamma_1},\ldots,|x_n|^{\gamma_n}\right]^T$$

$$sgn(\boldsymbol{x})^{\gamma} = \left[|x_1|^{\gamma_1} sgn(x_1),\ldots,|x_n|^{\gamma_n} sgn(x_n)\right]^T$$

where $\boldsymbol{x} = [x_1,\ldots,x_n]^T \in \boldsymbol{R}^n$, and $sgn(\cdot)$ is the sign function.

Hence, the TSM can be defined as

$$\boldsymbol{s} = \boldsymbol{\alpha e} + \boldsymbol{\beta} sgn(\dot{\boldsymbol{e}})^{\gamma} = 0 \tag{5}$$

where $\boldsymbol{s} = [s_1,s_2,s_3]^T \in \boldsymbol{R}^3$, $\boldsymbol{\alpha} = diag(\alpha_1,\alpha_2,\alpha_3)$, $\boldsymbol{\beta} = diag(\beta_1,\beta_2,\beta_3)$ and $1 < \gamma_1,\gamma_2,\gamma_3 < 2$. For simplicity, we choose $\gamma = \gamma_1 = \gamma_2 = \gamma_3$. The reaching law is defined as

$$\dot{\boldsymbol{s}} = -\boldsymbol{k}_1\boldsymbol{s} - \boldsymbol{k}_2 sgn(\boldsymbol{s})^{\rho} \tag{6}$$

where $\boldsymbol{k}_1 = diag(k_{11},k_{12},k_{13})$, $\boldsymbol{k}_2 = diag(k_{21},k_{22},k_{23})$, $0 < \rho = \rho_1 = \rho_2 = \rho_3 < 1$.

Design the control input as

$$\begin{aligned}
&\boldsymbol{F} = \boldsymbol{F}_0 + \boldsymbol{F}_1,\\
&\boldsymbol{F}_0 = \boldsymbol{C}_0(\boldsymbol{q},\dot{\boldsymbol{q}})\dot{\boldsymbol{q}} + \boldsymbol{G}_0(\boldsymbol{q}) + \boldsymbol{M}_0(\boldsymbol{q})\ddot{\boldsymbol{q}}_d\\
&\quad -\boldsymbol{\alpha}\boldsymbol{M}_0(\boldsymbol{q})\boldsymbol{\beta}^{-1}\boldsymbol{\gamma}^{-1} sgn(\dot{\boldsymbol{e}})^{2-\gamma}\\
&\boldsymbol{F}_1 = -\boldsymbol{M}_0(\boldsymbol{q})(\boldsymbol{k}_1\boldsymbol{s} + \boldsymbol{k}_2 sgn(\boldsymbol{s})^{\rho})
\end{aligned} \tag{7}$$

where $\boldsymbol{\gamma} = diag(\gamma,\gamma,\gamma)$. Then the system trajectory will converge to the neighborhood of $\boldsymbol{s} = 0$ as

$$\begin{aligned}
&\|\boldsymbol{s}\| \le \Delta = \min\{\Delta_1,\Delta_2\},\\
&\Delta_1 = \|\boldsymbol{M}_0^{-1}(\boldsymbol{q})\|(b_0 + b_1\|\boldsymbol{q}\| + b_2\|\dot{\boldsymbol{q}}\|^2 + f_d)/\underline{k_1}\\
&\Delta_2 = \left(\|\boldsymbol{M}_0^{-1}(\boldsymbol{q})\|(b_0 + b_1\|\boldsymbol{q}\| + b_2\|\dot{\boldsymbol{q}}\|^2 + f_d)/\underline{k_2}\right)^{1/\rho}
\end{aligned} \tag{8}$$

in finite time, where $\underline{k_1} = \min_i\{k_{1i}\} > 0$,and $\underline{k_2} = \min_i\{k_{2i}\} > 0$. Furthermore, the tracking errors $\boldsymbol{e}$ and $\dot{\boldsymbol{e}}$ will converge to the regions

$$\begin{aligned}
&|e_i| \le \Delta_e = 2\Delta/\alpha_i\\
&|\dot{e}_i| \le \Delta_{\dot{e}} = (\Delta/\beta_i)^{1/\gamma_i}
\end{aligned} \tag{9}$$

in finite time.

Consider a Lyapunov candidate function as:

$$V = \frac{1}{2}\boldsymbol{s}^T\boldsymbol{s} \tag{10}$$

By differentiating V with respect to time, substituting (6) and (7) into it, we have

$$\dot{V} = -\boldsymbol{s}^T\boldsymbol{\beta\gamma} diag(|\dot{\boldsymbol{e}}|^{\gamma-1})(\boldsymbol{k}_1\boldsymbol{s} + \boldsymbol{k}_2 sgn(\boldsymbol{s})^{\rho} - \boldsymbol{M}_0^{-1}(\boldsymbol{q})(\boldsymbol{T} + \boldsymbol{F}_d) \tag{11}$$

which can be further changed into the following two forms:

$$\begin{aligned}
\dot{V} = &-\boldsymbol{s}^T\boldsymbol{\beta\gamma} diag(|\dot{\boldsymbol{e}}|^{\gamma-1})((\boldsymbol{k}_1 - diag(\boldsymbol{M}_0^{-1}(\boldsymbol{q})\\
&\times(\boldsymbol{T} + \boldsymbol{F}_d))diag^{-1}(\boldsymbol{s}))\boldsymbol{s} + \boldsymbol{k}_2 sgn(\boldsymbol{s})^{\rho})
\end{aligned} \tag{12}$$

$$\dot{V} = -\boldsymbol{s}^T \boldsymbol{\beta\gamma} diag(|\dot{\boldsymbol{e}}|^{\gamma-1})(\boldsymbol{k}_1\boldsymbol{s} + (\boldsymbol{k}_2 - diag(\boldsymbol{M}_0^{-1}(\boldsymbol{q}) \times(\boldsymbol{T}+\boldsymbol{F}_d))diag^{-1}(sgn(\boldsymbol{s})^{\boldsymbol{\rho}}))sgn(\boldsymbol{s})^{\boldsymbol{\rho}}) \quad (13)$$

For Eq. (11), if we can keep the matrix $\boldsymbol{k}_1 - diag(\boldsymbol{M}_0^{-1}(\boldsymbol{q})(\boldsymbol{T}+\boldsymbol{F}_d))diag^{-1}(\boldsymbol{s})$ positive definite, the structure

$$\dot{V} = -\boldsymbol{s}^T \underline{\boldsymbol{k}}_1 \boldsymbol{s} - \boldsymbol{s}^T \underline{\boldsymbol{k}}_2 sig(\boldsymbol{s})^{\boldsymbol{\rho}} \quad (14)$$

is kept and $\underline{\boldsymbol{k}}_1 = \boldsymbol{\beta\gamma} diag(|\dot{\boldsymbol{e}}|^{\gamma-1})(\boldsymbol{k}_1 - diag(\boldsymbol{M}_0^{-1}(\boldsymbol{q})(\boldsymbol{T}+\boldsymbol{F}_d))diag^{-1}(\boldsymbol{s}))$, $\underline{\boldsymbol{k}}_2 = \boldsymbol{\beta\gamma} diag(|\dot{\boldsymbol{e}}|^{\gamma-1})\boldsymbol{k}_2$. It can be proved that

$$\dot{V} \le -2\underline{k}_1 V - 2^{(\rho+1)/2}\underline{k}_2 V^{(\rho+1)/2} \quad (15)$$

and the settling time is

$$T \le \frac{\ln((\underline{k}_1 V^{(1-\rho)/2} + 2^{(\rho-1)/2}\underline{k}_2)/2^{(\rho-1)/2}\underline{k}_2}{(1-\rho)\underline{k}_2} \quad (16)$$

therefore finite-time stability is guaranteed. Assume $\boldsymbol{M}_0^{-1}(\boldsymbol{q})(\boldsymbol{T}+\boldsymbol{F}_d) = \boldsymbol{Q} = [Q_1, Q_2, Q_3]^T \in \boldsymbol{R}^3$; then if $\underline{k}_1 - |Q_i|/|s_i| > 0$, the region

$$|s_i| \le |Q_i|/\underline{k}_1$$

$$\|\boldsymbol{s}\| \le \|\boldsymbol{M}_0^{-1}(\boldsymbol{q})\|(b_0 + b_1\|\boldsymbol{q}\| + b_2\|\dot{\boldsymbol{q}}\|^2 + f_d)/\underline{k}_1 \quad (17)$$

can be reached infinite time. For Eq. (13), by similar analysis for (12), we can have that the region

$$|s_i|^\rho \le |Q_i|/\underline{k}_2$$

$$\|\boldsymbol{s}\| \le \left(\|\boldsymbol{M}_0^{-1}(\boldsymbol{q})\|(b_0 + b_1\|\boldsymbol{q}\| + b_2\|\dot{\boldsymbol{q}}\|^2 + f_d)/\underline{k}_2\right)^{1/\rho} \quad (18)$$

can be reached infinite time.

Synthesizing inequalities (17) and (18), we have that the region (8) can be reached infinite time. We can explain $\dot{\boldsymbol{e}}_i = 0$ does not hinder the finite-time reachability of the region (17) by substituting the control (7) into (3).

4. Simulation

The nominal values are $\hat{m}_1 = 0.5kg, \hat{m}_2 = 4kg, \hat{m}_{0x} = 16kg$, $\hat{m}_{0y} = 40kg, \hat{M} = 10kg, \hat{k} = 500\,N/m$, $\hat{l}_0 = 1m$, $\hat{g} = 10\,m/s^2$, $\hat{R} = 0.02m$. The parameter values are $m_1 = 0.55kg, m_2 = 4.4kg, m_{0x} = 17.6kg, m_{0y} = 44kg, M = 11kg, k = 550\,N/m, l_0 = 1.1m, g = 9.8\,m/s^2$, $R = 0.022m$. The bound parameters of system uncertainties in (4) are assumed to be $b_0 = 0.8, b_1 = 1, b_2 = 8$.

The reference signals are given by $\boldsymbol{q}_d = [u(t), 0, 0]^T$ according to the simulation mechanism of AGFS and u(t) represent offload quantity of the object gravity. When $u(\mathrm{t}) = 0$ the object's gravity is compensated completely and when $u(t) = 0.2$ the object's gravity is at normal situation. When the value of u(t) is between $(0, 0.2)$, the object's gravity is partly compensated and when u(t) is negative, the object's gravity is greater than earth's gravity.

Firstly, define $\boldsymbol{\alpha} = \mathbf{I}$ corresponding to the controller designed in reference [2].

The object driving input is shown in Fig.2 which is regarded as the system disturbance.

Fig. 3 shows the system output, system output error, the sliding surface function and system control input when $u(t) = \varepsilon(t)$ with TSM controller.

$$\varepsilon(t) = \begin{cases} 0.2\sin(20t) & t \le \pi/40 \\ 0.2 & t > \pi/40 \end{cases}$$

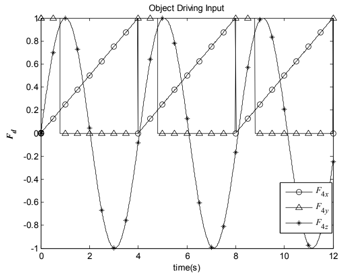

Fig. 2. The object driving input

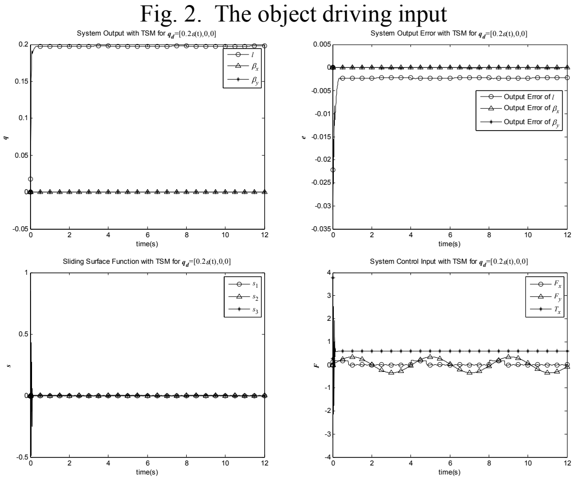

Fig. 3. TSM control of the AGFS when $u(t) = \varepsilon(t)$

Fig. 4 shows the system output, system output error, the sliding surface function and system control input when $u(t) = \varepsilon(t)$ with controller (7).

Fig. 5 shows the system output with FTSMC when the object gravity varies according to the law role of the gravity effect.

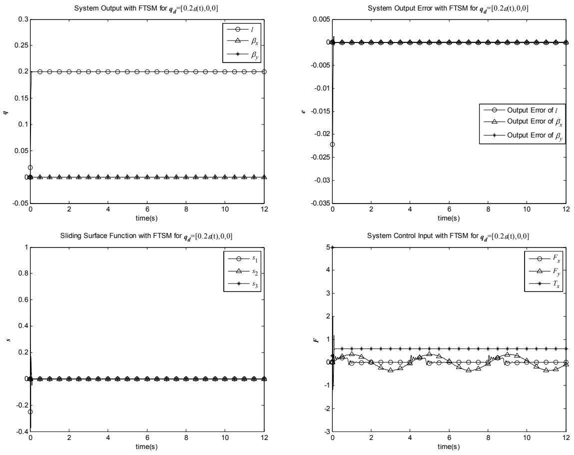

Fig. 4. FTSMC control of the AGFS when $u(t) = \varepsilon(t)$

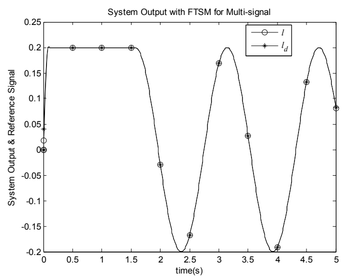

Fig. 5. FTSMC control of the AGFS

For the uncertain system with bounded disturbances and noises, the control parameters of the TSM controller are chosen according to (8) as

$$\boldsymbol{k}_1 = diag(2500, 8000, 8000), \boldsymbol{k}_2 = diag(2000, 2000, 2000),$$
$$\gamma = 1.6, \rho = 1/3, \boldsymbol{\beta} = diag(0.4, 5, 5)$$

for $u(t) = \varepsilon(t)$.

The boundary layer $\|\boldsymbol{s}\| \le 2.2\times10^{-3}$ is firstly reached in the finite time $t = 0.2s$ and $\|\boldsymbol{e}\| \le 2.3\times10^{-3}$ is reached in the finite time $t = 0.5s$ as shown in Fig. 3.

The control parameters of the FTSMC are chosen according to (8) as

$$\boldsymbol{k}_1 = diag(2000, 2000, 2000), \boldsymbol{k}_2 = diag(2000, 2000, 2000),$$
$$\gamma = 1.6, \rho = 1/3, \boldsymbol{\alpha} = diag(12, 10, 10), \boldsymbol{\beta} = diag(0.4, 5, 5)$$

for $u(t) = \varepsilon(t)$.

The simulation results shown in Fig. 4 verify the robustness of the FSTM approach. The boundary layer $\|\boldsymbol{s}\| \le 1.5\times10^{-3}$ is firstly reached in the finite time $t = 0.17s$ and $\|\boldsymbol{e}\| \le 1.5\times10^{-4}$ is reached in the finite time $t = 0.18s$.

With the same control parameters of the FTSMC, Fig. 5 shows the system can track time-varying trajectory with $\|\boldsymbol{e}\| \le 2\times10^{-4}$ when $t \ge 0.13s$.

Therefore the much smaller output error and faster convergence speed are obtained with the FTSMC method.

5. Conclusions

In this paper, a new fast terminal sliding mode controller is developed for the AGFS with the finite-time convergent property. The proposed control algorithms can guarantee the tracking errors converge to arbitrarily small value. And the developed control approach can be used to a more general Lagrange-like second-order nonlinear system.

Acknowledgements

This work was supported by the NSFC (61327807, 61520106010, 61521091, 61134005) and the National Basic Research Program of China (973 Program: 2012CB821200, 2012CB821201)

References

1. Y. Feng, et al., Non-singular terminal sliding mode control of rigid manipulators, *J. Automatica*. **38**(12) (2002) 2159-2167.
2. S. Yu, et al., Continuous finite-time control for robotic manipulators with terminal sliding mode, *J. Automatica*. **41**(11) (2005)1957-1964.
3. M. B. R. Neila and D. Tarak, Adaptive terminal sliding mode control for rigid robotic manipulators, *J. International Journal of Automation and Computing*. **8**(2) (2011) 215-220.
4. D. Zhao, et al., A new terminal sliding mode control for robotic manipulators, *J. International Journal of Control*. **82**(10) (2009) 1804-1813.
5. J. Jia, et al., Modeling and Control of a Suspended Gravity Compensation System with Rigid-Elastic Coupling, *J. Journal of Robotics, Networking and Artificial Life*2016, **3**(2) (2016)79-83.

Weighted Multiple Model Adaptive Control for a Category of Systems with Colored Noise

Yuzhen Zhang, Qing Li, Weicun Zhang
School of Automation and Electrical Engineering, University of Science and Technology Beijing,
30 Xueyuan RoadHaidian District, Beijing, 100083, China
E-mail: zhangyz_ustb@163.com, liqing@ies.ustb.edu.cn, weicunzhang@ustb.edu.cn
www.ustb.edu.cn

Abstract

The multiple model adaptive control (MMAC) of discrete-time stochastic system with colored noise is considered in this paper. Model set contains one adaptive identification and some fixed models. Based on the output errors of the models, a simple weighting algorithm is adopted with guaranteed convergence. The proofs of the stability and convergence of system are presented. Besides, the influence of initial value of adaptive model on system performance is described. Finally, computer simulation results can verify the theoretical results.

Keywords: discrete-time; colored noise; multiple model adaptive control; stability; convergence.

1. Introduction

As the largely change of system parameters makes the dynamical system become complicated. The classical adaptive control can't meet the requirements. Therefore, MMAC developed. The most suitable controller is used to control the system[1].

The weighted multiple model adaptive control (WMMAC) was researched in 1960's[2]. In that system, Kalman filter and posterior possibility evaluator (PPE) algorithm are important[3]. Later, K. S. Narendra put forward the concept of switching multiple model adaptive control[4, 5]. To some extent, WMMAC can be regarded as a kind of slow switching[4, 5]. Therefore, the scheme can alleviate the vibration when switching.

However, the system stability analysis of the WMMAC has been plaguing the researchers all the time. In Refs. 4 and 6, the stability and convergence are proved based on the virtual equivalent system (VES) theory. But, its model set just includes fixed models. If the real model isn't in the model set, the system is not good.

Considering the above problems, in this paper, a finite number of fixed and one adaptive identification models are designed to cover the discrete-time stochastic system with colored noise.

2. Description of WMMAC

For analyzing system clearly, a block diagram of a general discrete-time WMMAC system is shown in Fig.1.

The meanings of symbols are shown: P is the uncertainty plant; C_i is a local controller corresponded to the fixed model; C_θ is the local controller corresponded to the adaptive identification model; $p_i(k)$ is weighted value for its local controller; $p_\theta(k)$ is the weighted value for the adaptive identification controller. Through the algorithm, the weighted values are known. Then, the $u(k)$ can be obtained by weighted sum.

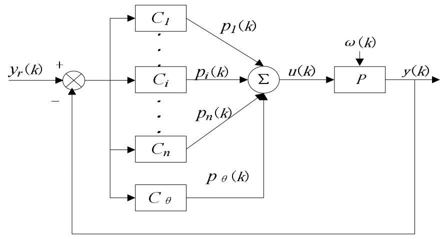

Fig. 1. Concise block diagram of a general WMMAC system

Consider the following discrete-time dynamical plant, the mathematical model is

$$\begin{aligned} A(z^{-1})y(k) &= z^{-d}B(z^{-1})u(k)+C(z^{-1})\omega(k) \\ &= z^{-d}B(z^{-1})u(k)+\upsilon(k) \end{aligned} \tag{1}$$

where

$$\begin{cases} A(z^{-1}) = 1+a_1z^{-1}+a_2z^{-2}+\cdots+a_{n_a}z^{-n_a} \\ B(z^{-1}) = b_0+b_1z^{-1}+b_2z^{-2}+\cdots+b_{n_b}z^{-n_b} \\ C(z^{-1}) = 1+c_1z^{-1}+c_2z^{-2}+\cdots+c_{n_c}z^{-n_c} \\ \upsilon = C(z^{-1})\omega(k) \end{cases} \tag{2}$$

$y(k)$ and $u(k)$ are the output and the input. The $\omega(k)$ is a zero-mean white noise. The $\upsilon(k)$ is colored noise.

The plant also can be written as

$$y(k) = \varphi^T(k-d)\theta + \omega(k) \tag{3}$$

where

$$\begin{aligned} \varphi(k-d) = [&-y(k-1),\cdots,-y(k-n_a),u(k-d),\cdots,u(k-d-n_b), \\ &\omega(k-1),\cdots,\omega(k-n_c)]^{\mathrm{T}} \in R^{(n_a+n_b+1+n_c)\times 1} \end{aligned} \tag{4}$$

$$\theta = [a_1,\cdots,a_{n_a},b_0,\cdots,b_{n_b},c_1,\cdots,c_{n_c}]^{\mathrm{T}} \in R^{(n_a+n_b+1+n_c)\times 1} \tag{5}$$

$\mathrm{M} = \{M_i, M_\theta, i=1,2,\cdots,N\}$ is the model set. For every fixed model, the corresponded controller is designed by pole placement control. At the same time, the one adaptive identification model is designed by indirect pole assignment self-tuning control. The recursive extended least square is used to estimated parameter[7]. That is

$$\begin{cases} \hat\theta(k) = \hat\theta(k-1)+K(k)[y(k)-\hat\varphi^{\mathrm{T}}(k)\hat\theta(k-1)] \\ K(k) = \dfrac{P(k-1)\hat\varphi(k)}{1+\hat\varphi^{\mathrm{T}}(k)P(k-1)\hat\varphi(k)} \\ P(k) = [\mathrm{I}-K(k)\hat\varphi^{\mathrm{T}}(k)]P(k-1) \end{cases} \tag{6}$$

where

$$\begin{cases} \hat\varphi(k) = [-y(k-1),\cdots,-y(k-n_a),u(k-d),\cdots,u(k-d-n_b) \\ \qquad ,\hat\omega(k-1),\cdots,\hat\omega(k-n_c)]^{\mathrm{T}} \\ \hat\theta = [\hat a_1,\cdots,\hat a_{n_a},\hat b_0,\cdots,\hat b_{n_b},\hat c_1,\cdots,\hat c_{n_c}]^{\mathrm{T}} \\ \hat\omega(k) = y(k)-\hat y(k) = y(k)-\hat\varphi(k)^{\mathrm{T}}\hat\theta \end{cases} \tag{7}$$

As initial values will affect the system performance, we will discuss that specifically in simulation studies.

For each local model, its output $y_i(k)$ is used to define the output error $e_i(k)$. As shown in Fig.1, the global control $u(k)$ is obtained by

$$u(k) = \sum_{i=1}^{N+1} p_i(k)u_i(k) \tag{8}$$

In this paper, the algorithm[4] to calculate weight is

$$p_i(0) = l_i(0) = \frac{1}{N+1} \tag{9}$$

$$l_i'(k) = \alpha + \frac{1}{k}\sum_{j=1}^{k} e_i^2(j); e_i(k) = y(k)-y_i(k) \tag{10}$$

where α is 0.001, avoiding $l_i'(k)=0$.

$$l'_{\min}(k) = \min_i\{l_i'(k)\} \tag{11}$$

$$l_i(k) = \frac{l'_{\min}(k)}{l_i'(k)} l_i(k-1) \tag{12}$$

$$p_i(k) = \frac{l_i(k)}{\sum_{j=1}^{N+1} l_j(k)} \tag{13}$$

The convergence character is presented in Ref. 4.

In the computer simulation, in order to prevent the weight converge to zero, we can limit the threshold value.

3. Stability and Convergence of the System

On the basis of VES[4, 6], this section gives the stability proof of the WMMAC system.

3.1. *WMMAC for LTI plant*

Theorem 1. *If a WMMAC system satisfies:*

- *The true model of plant, say M_j, is included in the fixed models of the model set M;*
- *Model M_j generates with probability one the minimum output error in the sense that*
  $$\begin{cases} \sum_{r=1}^{k} e_j^2(r) < \sum_{r=1}^{k} e_i^2(r), \forall k \ge d+1, i \ne j \\ \frac{1}{k}\sum_{r=1}^{k} e_j^2(r) \to R_j; \frac{1}{k}\sum_{r=1}^{k} e_i^2(r) \to R_i \end{cases}$$
  where R_j is a constant, R_i may be constant or infinity, $R_j < R_i, i \ne j$;

- *Each local controller is well defined such that C_i is stabilizing M_i, $i = 1,2,\cdots,N$, and the output of the resulting closed-loop system $\{C_i, M_i\}$, say $y_i(k)$, is tracking the reference signal $y_r(k)$ in the sense that* $\lim_{k\to\infty}\frac{1}{k}\sum_{r=1}^{k}[y_i(r)-y_r(r)]^2 = R', R \le R' < \infty$.

then it is stable.

Proof. First, the weighting algorithm is convergent. So,

$$p_j(k) \to 1;\ p_i(k) \to 0, i = 1,\ldots,N, i \ne j;\ p_\theta(k) \to 0 \quad (14)$$

where $p_j(k)$, $p_\theta(k)$ index weights of the true model and the adaptive identification model.

Then, the VES for WMMAC in this case is similar to the one in Ref. 4. The influence of the adaptive model on the system will be included in $\Delta u(k)$. And,

$$e_i(k) = y(k) - y_i(k) = y(k) - \varphi^{\mathrm{T}}(k-d)\theta_i \quad (15)$$

where $\varphi(k-d) = [-y(k-1),\cdots,u(k-d),\cdots,\hat{\omega}(k-1),\cdots]$.

Follow the proof process in Ref. 4, VES theory can be used to verify the stability. □

Theorem 2. *If a WMMAC system satisfies:*

- *The true model of plant isn't included in the fixed models of the model set* M*;*
- *Model M_θ generates with probability one the minimum output error in the sense that*
$$\begin{cases}\sum_{r=1}^{k} e_\theta^2(r) < \sum_{r=1}^{k} e_i^2(r), \forall k \ge d+1, i = 1,\ldots,N \\ \frac{1}{k}\sum_{r=1}^{k} e_\theta^2(r) \to R_\theta; \frac{1}{k}\sum_{r=1}^{k} e_i^2(r) \to R_i\end{cases}$$
where R_θ is a constant, R_i may be constant or infinity, $R_\theta < R_i$;
- *The adaptive controller C_θ is stabilizing M_θ, and the output of the resulting closed-loop system $\{C_\theta, M_\theta\}$, say $y_\theta(k)$, is tracking the reference signal $y_r(k)$ in the sense that* $\lim_{k\to\infty}\frac{1}{k}\sum_{r=1}^{k}[y_\theta(r)-y_r(r)]^2 = R', R \le R' < \infty$.

then it is stable.

Proof. First, the weighting algorithm is convergent. So,

$$p_\theta(k) \to 1;\ p_i(k) \to 0, i = 1,\ldots,N \quad (16)$$

As the VES for this WMMAC is similar to the one in Ref. 8. The influence of the parameter identification process on the system will be included in $e_i(k)$.

Follow the proof process of Ref. 8, the VES for WMMAC can be decomposed into three subsystems. Then, VES theory can be used to verify the stability. □

3.2. *WMMAC for parameter jump plant*

To consider the parameter jump plant, we assume that the system parameters are piecewise constant function of time, and time interval of parameter jump is long enough.

According to the assumptions, we know that each stage is a WMMAC for LTI plant. The overall system is slow switching between all the stages. Therefore, switching system theory[9] can be utilized to verify the stability of the WMMAC system.

4. Simulation Studies

In this section, the results of computer simulations will be presented. Consider an uncertain discrete-time plant

$$\begin{aligned}(1+a_1z^{-1}+a_2z^{-2})y(k) &= z^{-1}(b_0+b_1z^{-1})u(k) \\ &+(1+c_1z^{-1})\omega(k)\end{aligned} \quad (17)$$

where $\omega(k)$ is obtained by $sqrt(0.01)*randn(1)$ in MATLAB, $c_1 = 0.5$. This discrete-time model can be obtained by the simple continuous-time in (18) with sample time $t_s = 0.5s$ and the zero order hold.

$$G(s) = \frac{h}{s^2 - 3s + 2} \quad (18)$$

For simplicity, four fixed local models are used as the uncertainty of h, that is, $h_1 = 0.7$, $h_2 = 0.8$, $h_3 = 1.2$, $h_4 = 1.3$. The four corresponded controllers are designed by pole placement control.

The expected closed-loop characteristic polynomial is corresponds to the characteristic polynomial of the following continuous-time second-order system

$$\frac{\omega_n^2}{s^2 + 2\xi\omega_n s + \omega_n^2} \quad (19)$$

where ξ is 0.7, ω_n is 1.

Then we can know the four fixed controller easily. At the same time, the adaptive identification model is designed by indirect pole assignment self-tuning control. The recursive extended least square is used to estimated parameter. The initial value is $10^6 * eye(na+nb+1)$. The calculation in detail is shown in formula (6) and (7).

The true model of plant is not included in the four fixed model, which h is 1. The initial value of adaptive model θ will affect the system performance.

The initial value $\theta = (\theta_1+\theta_2+\theta_3+\theta_4)/4$ .The simulation results are shown in Fig.2 and Fig.3.

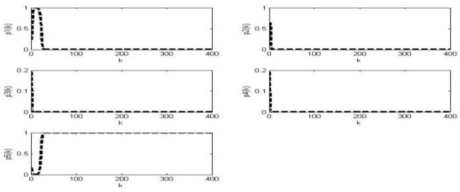

Fig. 2. Controller weight signals of case 1

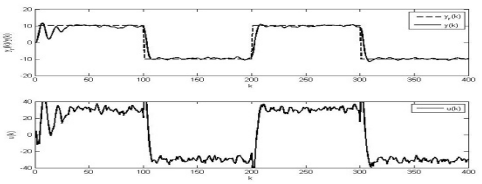

Fig. 3. Output, reference and control signals of case 1

The initial value is the parameter value of the fixed model closest to the real model. The simulation results are shown in Fig.4 and Fig.5.

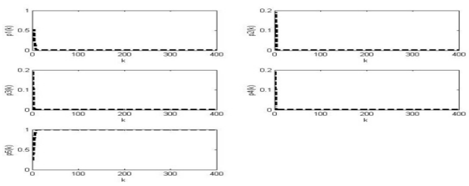

Fig. 4. Controller weight signals of case 2

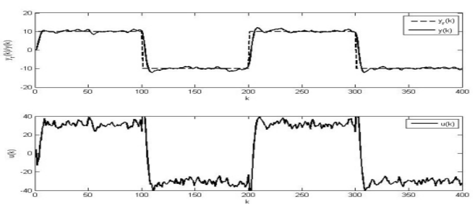

Fig. 5. Output, reference and control signals of case 2

In the two cases, the controller 5 designed according to the adaptive identification model all are chosen rapidly. However, the latter one works better.

5. Conclusions

In this paper, a finite number of fixed and one adaptive identification models are designed for a category of systems with colored noise. This method can effectively deal with issue when the real model isn't in the model set. And, the stability of WMMAC in the case is proven. At the same time, an adaptive model with real-time initial value, the parameter value of the fixed model closest to the real model, can improve the system performance.

Acknowledgements

This work was supported by National Natural Science Foundation of China (61520106010) and National Key Technologies R&D Program (2013BAB02B07).

References

1. K. S. Narendra, X. Cheng. Adaptive control of discrete-time systems using multiple models. *IEEE Transactions on Automatic Control*, 2000, 45(9): 1669-1686.
2. Moose R L, Van Landingham H F, McCabe D H. Modeling and estimation for tracking maneuvering targets. *IEEE Transactions on Aerospace and Electronic Systems*, 1979, AES-27: 448-456.
3. J. Chen, W. Chen, J. Sun. A survey of multiple model adaptive control. *J. Sys. Sci. & Math. Scis*, 2014, 34(12):1421-1437.
4. W. Zhang. Stable weighted multiple model adaptive control: discrete-time stochastic plant. *International Journal of Adaptive Control and Signal Processing*, 2013, 27(7): 562-581.
5. F. Li. Robust multiple model adaptive control base on dynamic optimization model bank. Master Thesis, South China University of Technology, 2004.
6. W. Zhang. Weighted multiple model adaptive control of discrete-time stochastic system with uncertain parameters. *Acta Automatica Sinica*, 2015, 41(3): 541-550.
7. Z. Pang, H. Cui. System identification and adaptive control MATLAB simulation. *Beihang University Press, Beijing, China*, 2009, pp:175-189.
8. W. Zhang. On the stability and convergence of self-tuning control - virtual equivalent system approach. *International Journal of Control*, 2010, 83(5): 879–896.
9. Shorten R, Wirth F, Mason O, Wulff K, King C. Stability Criteria for Switched and Hybrid Systems. *SIAM Review*, 2007, 49(4): 545-592.

Neutral Networks-Based Adaptive Fixed-Time Consensus Tracking Control for Uncertain Multiple AUVs

Lin Zhao
College of Automation and Electrical Engineering, Qingdao University, 308 Ningxia Road, Shinan District Qingdao, 266071, China

Yingmin Jia
The Seventh Research Division and the Center for Information and Control, School of Automation Science and Electrical Engineering, Beihang University (BUAA), 37 Xueyuan Road, Haidian District Beijing, 100191, China

Jinpeng Yu
College of Automation and Electrical Engineering, Qingdao University, 308 Ningxia Road,Shinan District Qingdao, 266071, China
E-mail: zhaolin1585@163.com,ymjia@buaa.edu.cn, yjp1109@hotmail.com
http://www.qdu.edu.cn/

Abstract

This paper is concerned with the fixed-time consensus tracking problem for multi-AUV (autonomous underwater vehicle) systems with uncertain parameters and external disturbances. Firstly, a fixed-time terminal sliding mode is proposed, which can avoid the singularity problem. Then, a continuous distributed consensus tracking control law is designed based on Neutral Network approximation technique, which can guarantee the consensus tracking errors converge to the desired regions in fixed time. A simulation example is given to show the effectiveness of proposed methods.

Keywords: Multi-AUV systems; Terminal sliding mode; fixed-time stability; Neutral Networks.

1. Introduction

Distributed cooperative control of multiple AUVs has been paid to much attention due to its potential applications in oceanographic surveys and deep sea inspections [1]. The distributed cooperative control for multi-AUV systems has been investigated by using the backstepping technique [2] and the adaptive control approach [3]. However, the protocols proposed in them can only guarantee the closed-loop system is asymptotically stable. For the distributed cooperative control, one significant requirement is the fast convergence rate. Compared with the asymptotic control approaches, the finite-time control approaches can not only provide fast convergence rate but also provide higher tracking precision and better disturbance rejection ability [4]. Therefore, many finite-time control laws are proposed for various multi-agent systems in the past few years [5]–[7]. However, the settling time can be estimated dependent on the initial conditions of systems in there. In practical applications, we desire that the settling time is estimated independent on the initial conditions of systems. In this paper, we will further investigate the adaptive finite-time consensus tracking problem for multiple AUVs with uncertain dynamics using fixed-time terminal sliding mode.

2. Systems Description

This paper considers the networked multiple AUV system with *n* following AUVs and one virtual leader, and the communications among them are described by a digraph $\bar{G}$. The definitions and descriptions of graph $\bar{G}$ are given in [7] and [9], which is omitted for brevity. Assume that all the following AUVs have fixed attitudes. The translational dynamics of the *i*-th AUV ($i \in V$) are given as [10]:

$$\begin{aligned} \dot{p}_i &= R_i\left(\Theta_i\right) v_i \\ M_i \dot{v}_i &= -D_i\left(v_i\right) v_i - g_i\left(\Theta_i\right) + \tau_i + w_i \end{aligned} \tag{1}$$

where $p_i = [x_i, y_i, z_i]^T, \Theta_i = [\phi_i, \theta_i, \psi_i]^T$ denote position and attitude vectors in the inertial reference frame, respectively, $R_i(\Theta_i)$ is the kinematic transformation matrix, $v_i = [u_i, v_i, \omega_i]^T$ is translational velocity vector in the body-fixed reference frame, M_i is the inertia matrix, $D_i(v_i)$ is the damping matrix, $g_i(\Theta_i)$ is there storing force vector, $\tau_i \in \Re^3$ is the control force vector, and $w_i \in \Re^3$ is the disturbance force vector. M_i, $R_i(\Theta_i)$, $D_i(v_i)$, $g_i(\Theta_i)$ are defined in [10]. In this paper, we assume that $D_i(v_i)$ and $g_i(\Theta_i)$ have uncertain parameters. Note that $R_i R_i^T = I$. Denote $p_d \in \Re^3$ as the state vector of virtual leader and $\dot{p}_d$, $\ddot{p}_d$ are all assumed to be smooth, bounded and known functions.

Assumption 1. *$\bar{G}$ has a spanning tree, and the leader node is the root node.*

3. Main results

3.1. *Fixed-time terminal sliding mode (FTTSM)*

Denote

$$\begin{aligned} e_{1i} &= \sum_{j=1}^{n} a_{ij}\left(p_i - p_j\right) + b_i\left(p_i - p_d\right) \\ e_{2i} &= \sum_{j=1}^{n} a_{ij}\left(\dot{p}_i - \dot{p}_j\right) + b_i\left(\dot{p}_i - \dot{p}_d\right) \end{aligned} \tag{2}$$

Then, we have $e_1 = \left(H \otimes I\right)\mathrm{E}_1, e_2 = \left(H \otimes I\right)\mathrm{E}_2$, where $e_1 = [e_{11}^T, \ldots, e_{1n}^T]^T$, $e_2 = [e_{21}^T, \ldots, e_{2n}^T]^T$, $\mathrm{E}_1 = [\mathrm{E}_{11}^T, \ldots, \mathrm{E}_{1n}^T]^T$, $\mathrm{E}_2 = [\mathrm{E}_{21}^T, \ldots, \mathrm{E}_{2n}^T]^T$, $\mathrm{E}_{1i} = p_i - p_d$, $\mathrm{E}_{2i} = \dot{p}_i - \dot{p}_d$.

Now, define the FTTSM vector as $s = [s_1^T, \ldots, s_n^T]^T$, where $s_i = [s_{i1}, s_{i2}, s_{i3}]^T \in \Re^3$ is given by

$$s_i = e_{2i} + \alpha_i\left(e_{1i}\right) \tag{3}$$

with $\alpha_i\left(e_{1i}\right) = [\alpha_i\left(e_{1i1}\right), \alpha_i\left(e_{1i2}\right), \alpha_i\left(e_{1i3}\right)]^T$, and

$$\alpha_{i\chi}\left(e_{1i\chi}\right) = \begin{cases} \mathrm{sig}\left(\sigma_{1i}\mathrm{sig}\left(e_{1i\chi}\right)^{m_1} + \sigma_{2i}\mathrm{sig}\left(e_{1i\chi}\right)^{n_1}\right)^{k_1}, \\ \text{if } \bar{\mathrm{s}}_{i\chi} = 0 \text{ or } \bar{\mathrm{s}}_{i\chi} \neq 0, \left|e_{1i\chi}\right| > \phi \\ l_{1i} e_{1i\chi} + l_{2i}\mathrm{sig}\left(e_{1i\chi}\right)^2, \text{if } \bar{\mathrm{s}}_{i\chi} \leq 0, \left|e_{1i\chi}\right| \leq \phi \end{cases} \tag{4}$$

$\chi = 1,2,3, \bar{s}_i = [\bar{s}_{i1}, \bar{s}_{i2}, \bar{s}_{i3}]^T, \bar{s} = \mathrm{sig}(\sigma_{1i}\mathrm{sig}\left(e_{1i\chi}\right)^{m_1} + \sigma_{2i}\mathrm{sig}\left(e_{1i\chi}\right)^{n_1})^{k_1}, m_1, n_1, k_1 \in \Re^+, 0 < m_1 k_1 < 1, n_1 k_1 > 1,$ $l_{1i} = \left(2 - k_1\right)(\sigma_{1i}\phi^{m_1 - \frac{1}{k_1}} + \sigma_{2i}\phi^{n_1 - \frac{1}{k_1}})^{k_1}, l_{2i} = \left(k_1 - 1\right)$ $(\sigma_{1i}\phi^{m_1 - \frac{2}{k_1}} + \sigma_{2i}\phi^{n_1 - \frac{2}{k_1}})^{k_1}, \phi > 0.$

From (3), we can obtain the following equation

$$\dot{s}_i + s_i = \dot{e}_{2i} + \dot{\alpha} + e_{2i} + \alpha_i \tag{5}$$

From the definition of e_{2i}, we further have

$$\dot{e}_{2i} = \left(d_i + b_i\right)\ddot{p}_i - \sum_{j=1}^{n} a_{ij}\ddot{p}_j - b_i\ddot{p}_d \tag{6}$$

and from (1), we can obtain

$$\ddot{p}_i = h_i + R_i\left(\Theta_i\right)M_i^{-1}\tau_i + R_i\left(\Theta_i\right)M_i^{-1}w_i \tag{7}$$

where $h_i = \dot{R}_i v_i - R_i M_i^{-1} D_i v_i - R_i M_i^{-1} g_i$. Assume that $\left\|\left(d_i + b_i\right)R_i\left(\Theta_i\right)M_i^{-1}w_i\right\| \leq \bar{w}_i^*, \bar{w}_i^*$ is an unknown constant. Then, substituting (6) into (5) yields

$$\dot{s}_i + s_i = \left(d_i + b_i\right)R_i\left(\Theta_i\right)M_i^{-1}\tau_i + \left(d_i + b_i\right)R_i\left(\Theta_i\right)M_i^{-1}w_i + \Phi_i \tag{8}$$

where $\Phi_i = -\sum_{j=1}^{n} a_{ij}\ddot{p}_j - b_i\ddot{p}_d + \dot{\alpha} + e_{2i} + \alpha_i + \left(d_i + b_i\right)h_i$.

3.2. *Control law design*

From the approximation property of RBF Neutral Networks (NNs), we have

$$\Phi_i = W_i^T \Gamma_i(Z_i) + \varsigma_i \tag{9}$$

where $Z_i = [p_i^T, \dot{p}_i^T, p_j^T, \dot{p}_j^T, \ddot{p}_j^T, p_d^T, \dot{p}_d^T, \ddot{p}_d^T]^T$ and $\|\xi_i\| \le \xi_i^*$, $\xi_i^* > 0$ is a constant. Denote $\hat{\rho}_i$ as the estimate of $\rho_i = \|W_i\|^2$, then the adaptation law is designed as

$$\dot{\hat{\rho}}_i = -2\kappa_i \iota_i \hat{\rho}_i + \frac{\kappa_i}{2h_i^2} s_i^T s_i \Gamma_i^T \Gamma_i \tag{10}$$

where κ_i, ι_i, h_i are designed positive constants.

Theorem 1. *Suppose that Assumption 1 holds for system (1), then we can choose the control law*

$$\tau_i = -\frac{1}{d_i + b_i} M_i R_i^T \left(\mu_{i1}\mathrm{sig}(s_i)^{m_2} + \mu_{i2}\mathrm{sig}(s_i)^{n_2} + \frac{1}{2h_i^2}\hat{\rho}_i \Gamma_i^T \Gamma_i s_i \right) \tag{11}$$

where $\mu_{i1} > 0, \mu_{i2} > 0, 0 < m_2 < 1, n_2 > 1$ *, such that* s_i *converges into the region*

$$\|s_i\| \le \Delta_s = \min\{2\mu_1^{-\frac{1}{1+m_2}}\left(\frac{\Xi}{1-\Xi_0}\right)^{\frac{1}{1+m_2}}, 2\left(\mu_2\left(\frac{1}{2^{\frac{n_2+1}{2}}-1}\right)^n\right)^{-\frac{1}{1+n_2}}\left(\frac{\Xi}{1-\Xi_0}\right)^{\frac{1}{1+n_2}}\}$$

in fixed time, the local neighborhood state errors $e_{1i\chi}$ *and* $e_{2i\chi}, \chi = 1,2,3$ *converge into the regions* $\Delta_{e_{1i}}$ *and* $\Delta_{e_{2i}}$ *respectively in fixed time, and finally the vectors* E_1 *and* E_2 *converge into regions* Δ_{E_1} *and* Δ_{E_2} *respectively in fixed time, where*

$$\Delta_{e_{1i}} = \max\{\phi, (\frac{(\Delta_s)^{\frac{1}{k_1}}}{\sigma_{1i}})^{\frac{1}{m_1}}, (\frac{(\Delta_s)^{\frac{1}{k_1}}}{\sigma_{2i}})^{\frac{1}{n_1}}\},$$

$$\Delta_{e_{2i}} = \max\{\Delta_s + l_{1i}\Delta_{e_{1i}} + l_{2i}\Delta_{e_{1i}}^2, \Delta_s + (\sigma_{i1}\Delta_{e_{1i}}^{m_1} + \sigma_{2i}\Delta_{e_{1i}}^{n_1})^{k_1}\},$$

$$\mu_1 = \min\{\mu_{1\min} 2^{\frac{m_2+1}{2}}, \varsigma_{\min}^{\frac{m_2+1}{2}} 2^{\frac{m_2+1}{2}}\}, \mu_{1\min} = \min\{\mu_{1i}\},$$

$$\varsigma_{\min} = \min\{\varsigma_i\}, \mu_2 = \min\{\mu_{2\min} 2^{\frac{n_2+1}{2}}, \varsigma_{\min}^{\frac{n_2+1}{2}} 2^{\frac{n_2+1}{2}}\},$$

$$\mu_{2\min} = \min\{\mu_{2i}\}, \varsigma_i = \kappa_i \frac{\rho_i(2o_i - 1)}{2o_i},$$

$$o_i > \frac{1}{2}, 0 < \Xi_0 \le 1, \Delta_{\mathrm{E}_1} = \frac{\sqrt{3\sum_{i=1}^n \Delta_{e_{1i}}^2}}{\sigma_{\min}(H)}, \Delta_{\mathrm{E}_2} = \frac{\sqrt{3\sum_{i=1}^n \Delta_{e_{2i}}^2}}{\sigma_{\min}(H)}.$$

Proof. Denote $\tilde{\rho}_i = \rho_i - \hat{\rho}_i$, and choose the Lyapunov function as

$$V = \frac{1}{2}S^T S + \frac{1}{2}\sum_{i=1}^n \frac{1}{\kappa_i}\tilde{\rho}_i^2 \tag{12}$$

we have

$$\dot{V} \le -\sum_{i=1}^n s_i^T s_i + \sum_{i=1}^n s_i^T (d_i + b_i) R_i M_i^{-1} \tau_i + \sum_{i=1}^n \bar{w}_i^* \|s_i\| + \sum_{i=1}^n s_i^T \Phi_i \tag{13}$$

From

$$s_i^T \Phi_i \le \frac{1}{2h_i^2} s_i^T s_i \|W_i\|^T \Gamma_i^T \Gamma_i + \frac{1}{2}h_i^2 + \frac{1}{2}s_i^T s + \frac{1}{2}\xi_i^{*,2}$$

$$\bar{w}_i^* \|s_i\| \le \frac{1}{2}s_i^T s + \frac{1}{2}\bar{w}_i^{*,2} \tag{14}$$

Substituting (10), (11), (14) into (13) yields

$$\dot{V} \le -\sum_{i=1}^n \sum_{\chi=1}^3 \mu_{i1} |s_{i\chi}|^{m_2+1} - \sum_{i=1}^n \sum_{\chi=1}^3 \mu_{i2} |s_{i\chi}|^{n_2+1} + \sum_{i=1}^n 2\iota_i \tilde{\rho}_i \hat{\rho}_i + \frac{1}{2}\sum_{i=1}^n \left(\bar{w}_i^{*,2} + \xi_i^{*,2}\right) \tag{15}$$

Using the similar proof as in [9], we have

$$\dot{V} \le -\mu_1 V^{\frac{m_2+1}{2}} - \mu_2 \left(\frac{1}{2^{\frac{n_2+1}{2}}-1}\right)^n V^{\frac{n_2+1}{2}} + \sum_{i=1}^n \left(\frac{\varsigma_i}{\kappa_i}\tilde{\rho}_i^2\right)^{\frac{m_2+1}{2}} - \sum_{i=1}^n \frac{\varsigma_i}{\kappa_i}\tilde{\rho}_i^2 + \sum_{i=1}^n \iota_i o_i \rho_i^2 + \frac{1}{2}\sum_{i=1}^n \left(\bar{w}_i^{*,2} + \xi_i^{*,2}\right) \tag{16}$$

Suppose that there exists a compact set Υ such that $\Upsilon = \{\tilde{\rho}_i \mid |\tilde{\rho}_i| \le \Delta\}$, then we have

$$\Xi = \begin{cases} \sum_{i=1}^n \iota_i o_i \rho_i^2 + \frac{1}{2}\sum_{i=1}^n \left(\bar{w}_i^{*,2} + \xi_i^{*,2}\right), \text{if } \Delta < \min\left\{\sqrt{\frac{\kappa_i}{\varsigma_i}}\right\} \\ \sum_{i=1}^n \iota_i o_i \rho_i^2 + \sum_{i=1}^n \left(\frac{\varsigma_i}{\kappa_i}\Delta^2\right)^{\frac{m_2+1}{2}} - \sum_{i=1}^n \frac{\varsigma_i}{\kappa_i}\Delta^2 + \\ \frac{1}{2}\sum_{i=1}^n \left(\bar{w}_i^{*,2} + \xi_i^{*,2}\right), \text{if } \Delta \ge \min\left\{\sqrt{\frac{\kappa_i}{\varsigma_i}}\right\} \end{cases} \tag{17}$$

From (16) and (17), we can further obtain

$$\dot{V} \le -\mu_1 V^{\frac{m_2+1}{2}} - \mu_2 \left(\frac{1}{2^{\frac{n_2+1}{2}} - 1} \right)^n V^{\frac{n_2+1}{2}} + \Xi \qquad (18)$$

It can be seen from Lemma 2 in [8] that the system (12) is practical fixed-time stability. Moreover, s_i will converge into the region $\|s_i\| \le \Delta_s$ in fixed settling time. The next proofs are similar with that of [7] and [9], thus are omitted for brevity.

4. Simulations

We consider a direct network with three AUVs and a virtual leader, the matrices L and B are described as:

$$L = \begin{bmatrix} 0 & 0 & 0 \\ -1 & 1 & 0 \\ -1 & 0 & 1 \end{bmatrix}, B = \begin{bmatrix} 1 & 0 & 0 \\ 0 & 0 & 0 \\ 0 & 0 & 0 \end{bmatrix}$$

We assume that all the AUVs have the same structure and the model parameters are $M_i = \mathrm{diag}\{175.4, 140.8, 140.8\}$, $D_i = \{120 + 90|u_i|$, $90 + 90|v_i|, 150 + 90|\omega_i|\}, \phi_i = \pi/5, \theta_i = -\pi/10, \psi_i = \pi/12$ [10]. The response curves under control law (11) are shown in Fig. 1. Note that the control law (11) can ensure the closed-loop system has desired robustness.

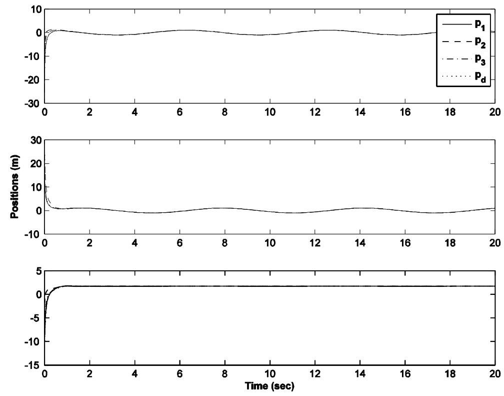

Fig. 1. Response curves of p_d and p_i *(i=1,2,3)* under control law (11).

5. Conclusions

This paper studied the fixed-time consensus tracking control of Multiple AUVs. A FTTSM based adaptive chattering-free control law was designed, which could guarantee the closed-loop system had desired fixed-time tracking performance.

Acknowledgements

This work was supported by the National Natural Science Foundation of China (61603204), Natural Science Foundation of Shandong Province (ZR2016FP03), and Qingdao Application Basic Research Project (16-5-1-22-jch).

References

1. T. I. Fossen, *Marine control systems: guidance, navigation and control of ships rigs and underwater vehicles* (Trondheim: Marine Cybernetics, 2002).
2. R. S. Cui, S.B Ge, V. E. How and Y. S. Choo, Leader–follower formation control of underactuated autonomous underwater vehicles, *Ocean Engineering*,**37**(17–18)(2010) 1491–1502.
3. S. P.Hou and C. C. Cheah, Can a simple control scheme work for a formation control of multiple autonomous underwater vehicles?, *IEEE Trans. Contr. Syst. Tech.*, **19**(5) (2011) 1190–1201.
4. L. Zhao and Y. Jia, Finite-time attitude tracking control for a rigid spacecraft using time-varying terminal sliding mode techniques, *Int. J. Control*, **88**(6) (2015) 1150-1162.
5. S. Li, H. Du and X. Lin, Finite-time consensus algorithm for multi-agent systems with double-integrator dynamics, *Automatica*, **47**(8) (2011) 1706-1712.
6. D. Meng, Y.Jia and J. Du, Nonlinear finite-time bipartite consensus protocol for multi-agent systems associated with signed graphs, *Int. J. Control*,**88**(10) (2015) 2074-2085.
7. L. Zhao and Y. Jia, Decentralized adaptive attitude synchronization control for spacecraft formation using nonsingular fast terminal sliding mode, Nonlinear Dyn., **78**(4) (2014) 2779-2794.
8. B. Jiang, Q. Hu and M. I. Friswell, Fixed-time attitude control for rigid spacecraft with actuator saturation and faults, *IEEE Trans. Contr. Syst. Tech.*, **24**(5) (2016) 1892-1898.
9. L. Zhao, J. P. Yu and C. Lin, Distributed adaptive consensus tracking control for second-order multi-agent systems using fixed-time terminal sliding mode, submitted for publication.
10. S. Li and, X. Y. Wang, Finite-time consensus and collision avoidance control algorithms for multiple AUVs, *Automatica*, **49**(11) (2013) 3359-3367.

Conducted Electromagnetic Interference Prediction of the Buck Converter via Neural Networks

Sumin Han, Fuzhong Wang
School of Electrical Engineering and Automation, Henan Polytechnic University, 2001 Century Avenue
Jiaozuo, 454000, P.R.China
hansumin@hpu.edu.cn; wangfzh@hpu.edu.cn
www.henan polytechnic university.edu

Abstract

This paper proposes an approach using neutral networks to predict conducted electromagnetic interference (EMI) on the power supply line in the buck converter. The experimental scheme is designed to collect the input and output target samples. It establishes a three-layer network including one hidden layer, whose activation function is of the hyperbolic tangent type .By the conducted EMI predicting model trained, interference prediction waveforms is obtained and analyzed . The results demonstrate that the approach is decent.

Keywords: EMI prediction; DM; CM; neural networks; buck converter

1 Introduction

EMI prediction is the key point to realize electromagnetic compatibility (EMC) of the power electronic system. It can also provide a referential opinion for EMC evaluation and design. Because of the existence of nonlinear switching devices in a power electronic system, which frequently switch their working states, producing high di/dt and du/dt signal. Consequently, the dramatic signal can conduct to the sensitive elements by conducted coupled channel, causing interference. Due to the nonlinearity of power electronic elements, and the uncertainty of the interference sources and coupling channels in which parasitic elements may be physically inaccessible inside the module package, EMI prediction problem has been a very complicated and challenging task[1-3]. Prediction accuracy is difficult to improve for many factors of influencing interference.

Deep study of EMI prediction theory has been done throughout the world. Some specialists construct various analysis and prediction models such as: source model, sensitive equipment model, the coupling model and system analysis model and so on. These methods finish prediction through the physical, or equivalent circuit, or the spice model. In general, the model study method is effective to the certain kinds of circuits, whose effectiveness for other circuits is difficult to verify. Furthermore, the modeling process itself is relative complex [4-6].

Some scholars and engineers have proposed many measurement methods to obtain the EMI emission[7-9].These methods of systems generally require relatively large amount of calculation and specialized equipment .Moreover, the different circuit topological structure needs the specific testing scheme. Thus the proposed methods are short of universality to enlarge their usages. Therefore, seeking a more reasonable forecast and analysis method without much measurement has always been a research focus for the scientific research workers in EMC field

The objective of this paper is to employ neural networks to predict the conducted DM EMI on the power line of a buck converter. Section II designs the neural networks of the DM EMI of the buck converter, including the collection of input and output samples and experiment. Section III trains the samples and demonstrates the results and their comparison. Finally, section IV concludes the paper.

2. BP Neural Networks Design

The input signal is passed from the input to output layer through the hidden layer in the typical BP network. Namely, each layer's neurons can only affect the state of the next layer. If the values of the output layer is not expected, the error is propagated backward. According to the prediction error, BP network adjusts the weights and thresholds, so that the predicted values can approximate gradually the expected output[10-11].

The neural network design consists of the following parts: input and output sample collection and preprocessing, BP network training and predicting and the analysis of the results.

2.1. *Input and output samples' acquisition and preprocessing*

The DM and CM interference on the power supply line in the buck converter are identified as the output samples, which produces mainly from the nonlinear switching devices. There are two switching devices in the common buck converter shown in Fig.1, which are MOSFET and diode respectively. Hence, we can preliminarily determine the voltage at the drain and source electrode of the MOSFET, drain current, the diode voltage are most relevant to DM and CM signals. The experimental electric circuit is designed and shown in Fig.2. The values of the electrical components of the buck converter in Fig.1 are

$$R = 100\Omega,\ L = 1\,\text{mH},\ C = 100\mu\text{F}$$

The power supply voltage is set at 5V.

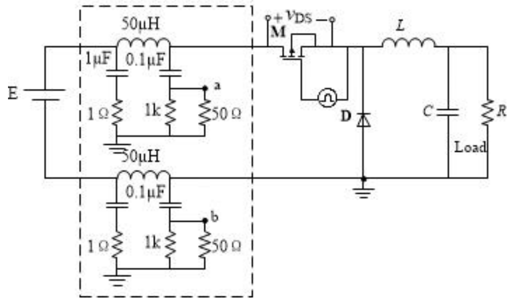

Fig.1 Buck converter and samples collecting scheme

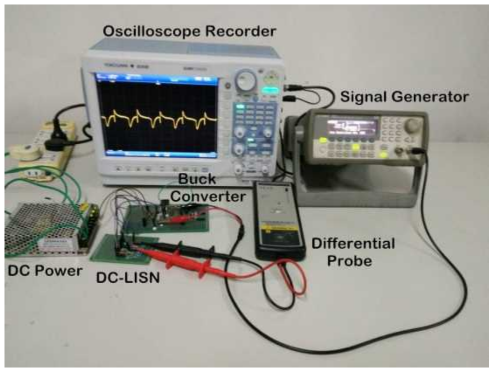

Fig.2 Experiment of the input and output samples collection of the buck converter

As shown in Fig.1, a DC-LISN(Line Impedance Stabilization Network) is connected between the power supply and the converter for acquiring the DM and CM interference signals. The MOSFET of the circuit shown in Fig.2 is driven by a pulse signal working at the basic frequency of 100kHz, which is produced by a function generator.

All the signals are obtained by a scope recorder with a voltage probe ,or a differential voltage probe or a current probe ,as is shown in Fig.2 .Particularly, the DM and CM interference signals still need processing after getting the potential of node a and b,as is expressed

$$v_{\text{dm}} = \frac{v_{\text{a}} - v_{\text{b}}}{2}, \qquad v_{\text{dm}} = \frac{v_{\text{a}} + v_{\text{b}}}{2}$$

where, v_{dm} is the DM signal ,while v_{cm} the CM one. Consequently we get the waveforms of the input and output signals illustrated in Fig.3.There are five kinds of signals, which are the voltage at the drain and source electrode of the MOSFET, expressed $v$ds, drain current ids and the diode voltage vd respectively. Each signal is collected a total of 5001 samples over the five cycles, as is illustrated in Fig.3.

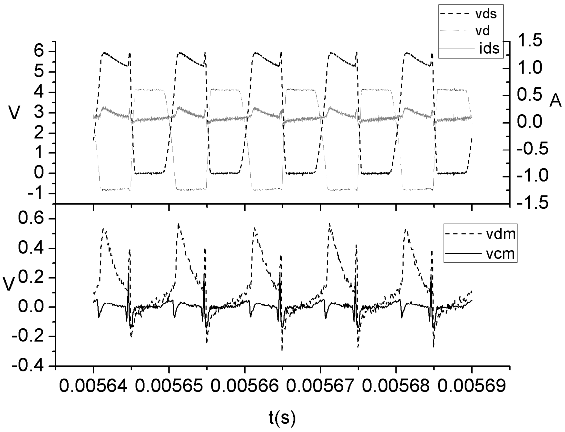

Fig.3 Input and output samples' waveforms

2.2. *Correlation analysis*

The degree of linear correlation between variables can be analyzed by correlation coefficient. The correlation coefficient formula is:

$$\rho_{xy} = \frac{\sum_{i=1}^{n}(x_i - \bar{x})(y_i - \bar{y})}{\sqrt{\sum_{i=1}^{n}(x_i - \bar{x})^2}\sqrt{\sum_{i=1}^{n}(x_i - \bar{x})^2}} \quad (1)$$

where $\bar{x}$ and $\bar{y}$ are the means of each variable. Results are listed in Tab.1,which shows the DM interference v_{dm} is strongly relevant to the drain-source voltage *v*ds and the diode voltage *v*d with the correlation

Tab.1 Correlation coefficient of output and input signals

		input		
		Vds	ids	vd
Output	v_{dm}	0.78356	0.0422	-0.73634
	v_{cm}	-0.00795	0.0007886	0.04268

coefficients of 0.78356 and -0.73634,respectively. While it has hardly relation to the drain current ids with 0.0422.However, the CM interference has a unclear characteristic with the three input signals. Each correlation coefficient is very small, almost approaching to zero. The reason is that there may be other motivators to produce CM interference.

3. BP Neural Networks Training and Forecasting

The BP neural network adopts a three-layer structure, namely input layer, hidden layer and output layer, with three input variables and two output variables, which are represented as x and y respectively. According to the experience and continuous trial and error, we determine that the hidden layer includes seven neurons. The activation function of the output layer is linear identical function, while the hidden layer activation function the hyperbolic tangent. Then, we train the selected samples according to the following algorithm. The hidden layer nodes are represented by h_k ;output layer nodes y_i; thresholds of hidden layer nodes θ_i; thresholds of input layer node θ_k; the connection weights between the input layer and hidden layer nodes v_{ki}; the connection weights between the hidden layer and output layer nodes ω_{jk} ; the desired output t_j, ; the error between the output and expectations Δ_j. Steps are as follows.

(i) Select the initial weights of *v* and *ω*, generally between (1, 1).

(ii) Calculate the information of output layer nodes for all training input sample.

(a) Calculate the output values of the hidden layer nodes.

$$h_k = f_1(\sum_{i=1}^{n} v_{ki}x_i - \theta_i) \quad (2)$$

(b) Calculate the output values of the output layer nodes

$$y_i = f_2(\sum_{k=1}^{q} \omega_{jk}z_k - \theta_k)$$

(c) Sum the errors between the actual output and the expected output of all the samples.

$$e = \frac{1}{2}\sum_{k=1}^{m}\sum_{i=1}^{q}(t_i - y_i)^2 \quad (4)$$

After training the input and output samples, the BP network predicting model is obtained. The model can be applied to predict the DM and CM interference by inputting the tested data. The predicted waveforms and the actual waveforms are as shown in Fig. 4.

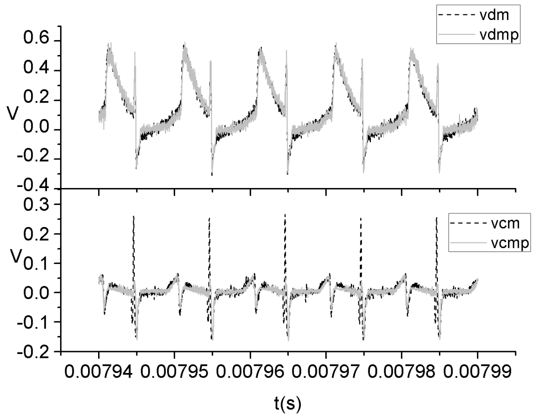

Fig.4. Predicted and actual waveforms of the DM and CM

As can be seen from Fig.4, the predicted DM and CM interference illustrated by vdmp and vcmp are in well accordance with the actual signals illustrated by vdm and vcm. Analysis data show that the relative error of the dependent variable of the scale of DM is 0.045, and CM is 0.582.Namely, the deviation is bigger.

4. Conclusion

This paper proposes the EMI prediction scheme via BP neural network. On the basis of the principle the conducted EMI emission of the buck converter, the structure of the neural network is determined which includes three-layer, three input signals and two signals. The authors adopt BP algorithm to train the network and establish the interference predicting model, by which they obtain the predicted DM and CM waveforms in time domain. Then analysis as well as comparison between the measured and predicted waveforms also demonstrate the predicted results is satisfactory and the validity of the proposed approach. However, the proposed approach still performs effective illustrated in the paper but for a slightly low precision. The predicting approach of this paper can be extended to other topological types of power electronics circuits.

Acknowledgements

This work was supported by the Control engineering open Lab. foundation of Henan Province (KG2011-08). This work was supported by the Science and Technology Research Foundation of Henan Education Department (14A510022). This work was supported by National Key Research and Development Program(2016YFC0600906).

References

1. R. Trinchero, et al.: "EMI Prediction of Switching Converters," *IEEE Transactions on Electromagnetic Compatibility* 57.5(2015):1-4.
2. M. Ferber, et al.: "Conducted EMI of DC–DC Converters With Parametric Uncertainties," *IEEE Transactions on Electromagnetic Compatibility* 55.4(2013):699-706.
3. S. Braun, et al.: "A Real-Time Time-Domain EMI Measurement System for Full-Compliance Measurements According to CISPR 16-1-1," *IEEE Transactions on Electromagnetic Compatibility* 50.2(2008):259-267.
4. G. Frantz, et al.: "EMC models of power electronics converters for network analysis," *European Conference on Power Electronics and Applications*. 2013:1-10.
5. J. Meng, et al.: "Noise Source Lumped Circuit Modeling and Identification for Power Converters," *IEEE Transactions on Industrial Electronics* 53.6(2006):1853-1861.
6. Y. Liu, et al.: "Conducted EMI prediction of the PFC converter including nonlinear behavior of boost inductor," *IEEE Trans. Electromagn. Compat.*, vol. 55, no. 6, pp. 1107–1114, Dec.
7. W.Yan, et al. : " Time domain measurement method for conducted EMI," *Journal of Southeast University* (Natural Science Edition) vol. 39, s2 (2009):31-36.
8. Y. Li, et al.: "Time Domain Measurement System for Conducted EMI and CM/DM Noise Signal Separation," *International Conference on Power Electronics and Drives Systems IEEE*, 2005:1640-1645.
9. Q. Feng et al.: "A novel measurement system for the common-mode- and differential-mode-conducted electromagnetic interference," *Progress in Electromagnetics Research Letters* 48(2014):75-81.
10. T.Yang et al.: "Prediction of electromagnetic interference based on neural network ," *Journal of Beijing University of Aeronautics and Astronautics*, vol. 39, no.5 (2013), pp:697-700.
11. Y.Li et al.: "Artificial neural networks-based prediction of electromagnetic compatibility problems," *Journal of Chongqing University*, vol. 31, no.1 (2008), pp:1313-1316.

Development of a Tomato Harvesting Robot

Shinsuke Yasukawa
Dept. of Human Intelligence Systems, Kyushu Institute of Technology
2-4 Hibikino, Wakamatsu, Kitakyushu, Fukuoka, 808-0196, Japan
E-mail: s-yasukawa@edu.brain.kyutech.ac.jp

Bingh Li
Dept. of Human Intelligence Systems, Kyushu Institute of Technology
2-4 Hibikino, Wakamatsu, Kitakyushu, Fukuoka, 808-0196, Japan
E-mail: li-binghe@edu.brain.kyutech.ac.jp

Takashi Sonoda
Dept. of Human Intelligence Systems, Kyushu Institute of Technology
2-4 Hibikino, Wakamatsu, Kitakyushu, Fukuoka, 808-0196, Japan
E-mail: t-sonoda@edu.brain.kyutech.ac.jp

Kazuo Ishii
Dept. of Intelligence Systems, Kyushu Institute of Technology,
2-4 Hibikino, Wakamatsu-ku, Kitakyushu, Fukuoka, Japan
E-mail: ishii@brain.kyutech.ac.jp

Abstract

Most of commercialized robots are for industry, and the robots for agriculture, forestry and fisheries are under developing and not commercialized yet. The reasons for the difficulty are caused by cost-efficiency of the robotization, safety ensuring of the works using robots, outdoor operations, and knowledge transfer problem from farmers to computer so on. Tomato is one of important fruit vegetables and most tomatoes are produced in the greenhouses, or large-scale farms, where the high temperature and humidity, and long harvest age force the farmers heavy works. With an aim to promote the automation of tomato harvesting, we have organized the tomato harvesting robot competition and developed a tomato harvesting robot. In this paper, we propose the system of tomato harvesting robot.

Keywords: Tomato-Harvesting Robot, Agricultural Robot.

1. Introduction

According to the statistical information of the Ministry of Agriculture, Forestry and Fisheries, Japan's food self-sufficiency rate (calorie base) is about 39%, which is the lowest among major developed countries. In the agricultural field, the aging of the producers and depopulation are progressing, and the labor shortage due to the lack of successors is a big problem. "Smart agriculture" is proposed as a future image that will solve these problems by introduction of robot as the tools to realize the smart agriculture, is expected[1].

Japan is one of the countries where robots are being introduced to production sites, but many of the robots being put into practical use are automation robots for secondary industries, and the ratio of robots in agriculture, forestry and fishery fields is few. If we can disseminate agricultural robots, we can expect labor saving, automation, improvement of productivity, etc. Moreover, it becomes possible to convert information such as management of agricultural crop environment, cultivation, state and quality. From the viewpoint of safety, it is possible to provide accurate information to consumers. There are major challenges to overcome, but there is a possibility that a new robot market will be created in the agricultural field.

Among various fruits and vegetables, tomato is one of the major fruit and vegetables consuming a lot. Many of the shipped tomatoes are cultivated in facilities such as houses, but due to the high temperature and humid work environment and long harvest period, labor load is large and labor saving is desired. In the Netherlands exporting tomato, various techniques are introduced to cultivate tomatoes and realize higher productivity than Japan. In this paper, we describe our tomato-harvesting robot.

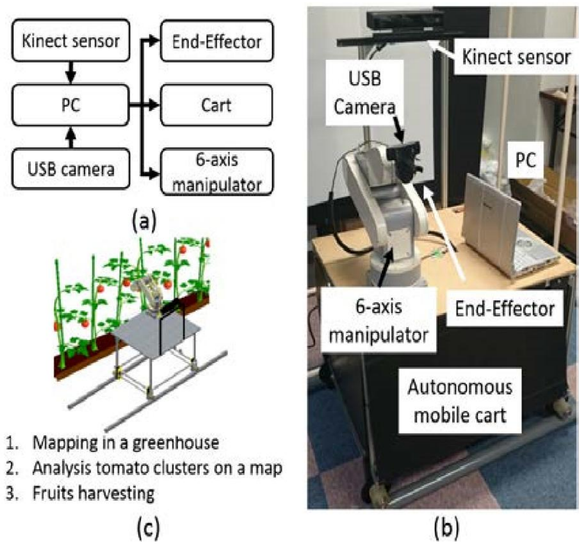

Fig.1 The tomato-harvesting Robot

2. Tomato-Harvesting Robot

The system configuration of the tomato-harvesting robot used in this research is shown in Fig. 1 (a), and its external appearance is shown in (b). The robot assumes the house environment of a large-scale tomato production facility. In the house, there are tomato seedlings with multiple bunches, with shelves aligned in line at a certain interval. And along the shelf rails for the bogies, the workers move and harvest tomatoes. This system consists of a Kinect v.2, a USB camera, a six-axis serial link manipulator, an end effector, a computer, and a moving mechanism that carries them and moves on the rails.

As the strategy,

1) Move to the edge of the shelf with a bogie and generate an environmental map of the entire shelf from the acquired image.

2) By analyzing the environmental map, we extract information such as tomato condition to be harvested, its fruit position and total harvest time.

3) Move the dolly to the front of the harvested bunches and harvest the fruits in order.

3. Tomato Detection Method Using Infrared Image and Specular Reflection

3.1. *IR images of Tomato*

From the spectral reflection characteristics, it is known that tomatoes have high reflectance for both stems and leaves against infrared light, so in this study IR images were taken in order to detect the fruit of tomatoes .

As a previous study, Fujiura and colleagues focused on this characteristic and developed a two-wavelength 3D vision sensor. In this sensor, the distance is measured by placing near-infrared rays and red lasers coaxially and imaging the reflected light on a PSD (Position Sensitive Device) with a lens. Three-dimensional shape is measured by spatially scanning this. When the laser is incident near the fruit center, the sensor captures specularly reflected light and responds strongly. In this system, the pixel whose spatial response is the maximum is detected as the fruit position. Also, the stem and fruit are distinguished by the ratio of response to red light and near infrared light. This sensor blinks the beam and extracts only the component of the blinking frequency at the light receiving portion, thereby removing the sunlight component which is the stationary light.

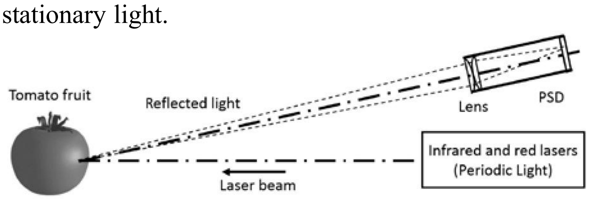

Fig.2 Dichromatic vision sensor as the previous method.

3.2. *Proposed Method*

With reference to the method in Section 3.1, we propose a method for detecting fruits using IR images and specular reflection. In order to acquire IR images and RGB-D images, Kinect v.2 was adopted as a visual sensor. Since Kinect v2 acquires depth data by irradiating with instantaneous infrared light, the IR image can reduce the influence of sunlight.

Fig. 3 shows a flow of three-dimensional position measurement of the fruit. Kinect gets RGB-D image and IR image capturing the stem of tomato at 30 fps (Fig. 3 (a)). Next, the IR image is processed to detect the position of the fruit (Figs. 3 (b) to 3 (d)). From the pixel information of the RGB-D image corresponding to the detection position, the fruit color determination and the three-dimensional position measurement are performed.

In this report, we propose a fruit detection and discrimination method in the room. The fruit on the IR image shows a concentric reaction with a strong center and a weak perimeter. The gradient orientation (8 azimuth angle) of the IR image is calculated not to depend on the absolute value of the response intensity, and the gradient orientation image (Fig. 3 (b), each orientation is represented by eight color) fruit pattern template Match. We extract only the region with high coincidence rate by the binarization process (Fig. 3 (c)) and label it to detect the position of the fruit. Finally, the correspondence between the red region extracted image obtained from the RGB image and the pixel position of the IR image is taken, and the coloring judgment is carried out (Fig. 3 (d)).

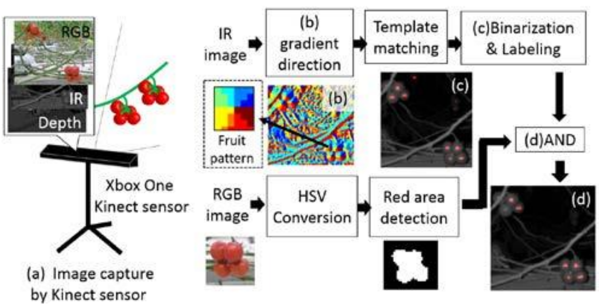

Fig.3 The proposed tomato detection method.

4. Evaluation of proposed method using real environment image

At the house of Hibikinada Saien Co., Ltd., a large-scale production facility, RGB-D images and IR images were acquired using Kinect, and experiments were conducted. 47 pairs of images were used for evaluation of the proposed method. The range that the arm reaches, that is, 260 tufts whose distance to Kinect is within 60 cm to 80 cm was targeted. The number of recognition subjects divided by the number of successful fruit detection and coloring judgment in all the fruits was evaluated as the correct answer rate.

As an example, Fig.4 (a) shows the RGB image in the house and IR image. The box surrounded by the dotted line in the figure is the object to be recognized. Figures 4 (b) and 4 (c) show examples of bunches that succeeded and failed in fruit detection (red in the figure). The correct answer rate of this method was 88.1%. An example of failure was divided into two, fruits (14 cases) shielding the majority of fruits of the main stem and fruits (3 cases) facing the front.

5. Conclusions

In this research, in order to realize a tomato fruit harvesting robot, we proposed an infrared image and fruit harvesting technique using specular reflection. In this method, fruit detection in the chamber is carried out by detecting the center of the fruit which causes specular reflection in the infrared image and strongly responds. As a result of evaluation using the real environment image, the correct answer rate was 88.1%.

The main reason for the failure was shielding of the fruit by the main stem, so we plan to add a detection function for covering objects. In addition, we plan to analyze the information such as generation of environmental map of the entire shelf, selection of the harvesting target bunches and estimation of harvest time as an issue within the action strategy.

References

1. http://www.maff.go.jp/j/tokei/index.html
2. N. Kondo, K. Tanihara, T. Shiigi, H. Shimizu, M. Kurita, M. Tsutsumi, V. K. Chong, S. Taniwaki, Path Planning of Tomato Cluster Harvesting Robot for Realizing Low Vibration and Speedy Transportation, Engineering in Agriculture, Environment and Food,2(3), (2009), 108-115
3. Kondo, N., Yamamoto, K., Shimizu, H., Yata, K., Kurita, M., Shiigi, T., Monta, M., Nishizu, M., A Machine Vision System for Tomato Cluster Harvesting Robot, Engineering in Agriculture, Environment and Food, 2(2), (2009) 60-64
4. Kondo, N., Yata, K., Iida, M., Shiiji, T., Monta, M., Kurita, M., Omori, H., Development of an End-Effector for a Tomato Cluster Harvesting Robot, Engineering in Agriculture, Environment and Food, 3(1), (2010), 20-24

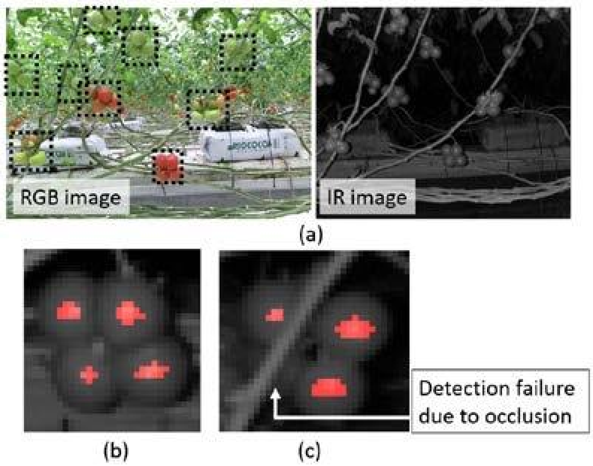

Fig.4 (a) Test images: RGB (left), infrared (right), (b) Successful detection, (c) Unsuccessful detection.

Development of SOM algorithm for Relationship between Roles and Individual’s Role in Rugby
2nd Reports: University Rugby teams analysis using Physical and Psychological data

Yasunori Takemura
Department of Engineering, Nishinippon Insitute of Technology, 1-11 Aratsu Kanda MIyako-gun, Fukuoka 800-0394, Japan

E-mail: takemura@nsihitech.ac.jp

Abstract

Victory or defeat in team sports depends on each player’s technique, physical strength, and psychological condition. It follows that team performance depends on the player’s adaptation to (suitability for) a certain role (position in the team) and the relationships between different roles. We assume that team performance is related to physical and psychological features. Many researchers have proposed that physical features determine a player’s suitability for a position. Psychological features have also been researched as factors of position adaptation. However, each feature has been investigated independently. The present research aims to develop a clustering method that considers both physical and psychological features in judging an individual’s role and adaptation in the game. This paper reports the concept of the algorithm and result of analysis using both physical data and psychological data.

Keywords: clustering, data mining, self-organizing map

1. Introduction

Victory or defeat in team sports depends on each player’s individual technique, physical strength, and psychological condition. Similarly, it can be said that the suitability of an individual to a certain position in the team affects the team’s performance.

In previous research, Barry and Cureton [1], Nicks and Fleishman [2], Larson [3], McCloy and Young [4] and others clustered physical features and conducted factor analysis in investigating sports performance. In Japan, Tokunaga studied the diagnosis criteria for athletic adaptation (i.e., suitability) in sports [5]. These works showed that physical features are one of the strongest factors determining athletic adaptation. However, Matsuda [6] showed that an athlete, no matter how good his/her physical features, is not athletically suited to team sports without having good motivation in terms of setting goals and training. That is to say, for an individual or team to be successful, a player needs to have both good physical features (e.g., techniques, balance, height, and weight) and good psychological features. For example, Saijo [7] presented the psychological features of Japanese and New Zealand rugby players.

In this way, the suitability of a player in a certain position and the relationships between different positions in team sports are related to physical and psychological features. As it stands now, a coach or selector decides the player suitability and relationships between positions him/herself. However, does it follow that good decisions are made? Previous research has not clarified athlete adaptation to positions and relationships between positions considering both physical and psychological features.

In the present study, we develop a clustering algorithm for positioning adaptation and relationships in team sports. This paper reports results of analysis using both physical data analysis and psychological data.

2. Research plan and method

2.1. *Selection about sport and data*

We apply a team-sport clustering algorithm to rugby. Rugby is selected because a rugby team has a large variety of positions and player attributes. A rugby game is called a match. It is a competition between two teams. Each match lasts for 80 minutes plus time added to account for injuries and stoppages during the match. A match consists of two halves of 40 minutes each. The team with the greater number of points at the end of the match wins. Normally, a rugby team has a maximum of 15 players on the field, and seven substitutes. Each player has a specialized position. There are eight forwards, numbered 1 to 8, and seven backs, numbered 9 to 15. Player number 1 is a prop (PR), number 2 is the hooker, number 3 is another prop (PR), numbers 4 and 5 are locks (LOs), number 6 is the blindside flanker (FL), number 7 is the open-side flanker, number 8 is the "number 8" (No. 8), number 9 is the scrum-half (SH), number 10 is the fly-half (or stand-off, SO), number 11 is the left wing (WTB), number 12 is the inside center (CTB), number 13 is the outside center (CTB), number 14 is the right wing (WTB) and number 15 is the fullback (FB).

2.2. *Physical features*

Physical data of members of the N university rugby club were recorded in 2014. The N University rugby club in 2014 comprised 56 students (14 fourth-grade students, 14 third-grade students, 12 second-grade students and 16 first-grade students). There were 32 forwards (FWs) and 24 backs (BKs).

Physical features recorded were height [cm], weight [kg], body fat [%], neck length [cm], brachium length [cm] (R: right and L: left), chest circumstance [cm], waist circumstance [cm], hip circumstance [cm], length of thigh (R, L) [cm], length of calf (R, L) [cm], anteflexion while standing (flexibility) [negative value, cm], number of abdominal crunches completed in 30 s, bench-press weight [kg], number of squats completed in 30 [sec], number of chin-ups completed in one effort, and the distance run in 7 minutes [m]. The data set thus had 19 physical dimensions. Some members played more than one position (Therefore, number of the data is overlapping). There were 12 PRs, 10 LOs, 12 FLs, six No. 8s, six SHs, five SOs, 10 CTBs, seven WTBs and eight FBs.

2.3. *Psychological data*

Psychological data of members of the N rugby club were recorded in 2014. Psychological features measured were those of the Diagnostic Inventory of Psychological Competitive Ability for Athletes (DIPCA.3) [8].

DIPCA.3 measures 12 types of psychological ability in a 48-item questionnaire. DIPCA.3 is often used before mental training, because it reveals athletic strengths and weaknesses. The DIPCA.3 check sheet consists of 48 questions that measure psychological ability and four questions that measure reliability. These questions have already been analyzed by good–poor analysis (G-P analysis), and the answers provide 12 criteria relating to five factors. The factors are motivation in sport, mental stability and concentration, confidence, operation capability and cooperativeness. Additionally, we measure the reliability of the answers by comparing answers to similar questions. To examine these factors in detail, 12 criteria are described. Motivation in sport consists of four criteria: endurance, fighting spirit, self-realization motivation and motivation to win. Mental stability and concentration consist of three criteria: the ability to relax, capacity to concentrate and self-control. Confidence consists of two criteria: determination and confidence. Operation capability consists of two criteria: predictive capability and judgment. Cooperativeness has only one criterion, which is simply described as cooperativeness. DIPCA.3 provides a total score (ability). Each criterion is scored, and the score of each factor is the sum of scores for the related criteria. The total score is calculated by summing the score for each factor.

2.4. *Algorithms of this Clustering system*

This clustering algorithm is reported by 1st reports [9].

3. Experimental Result

The data of the feature map obtained by putting the data group in the SOM is shown in Fig.1. Fig.1 shows the feature map of 10x10. The position and data number of personal data are attached to the best matching unit (BMU) as labels. The color of the feature map indicates the distance from the neighboring unit, which means that the distance between the units is far away from blue to red. As shown in Fig.1, forward (FW) is distributed in the upper part of the feature map, and members in the position of Backs (BK) gather in the lower part. Consider psychological feature quantities input as input

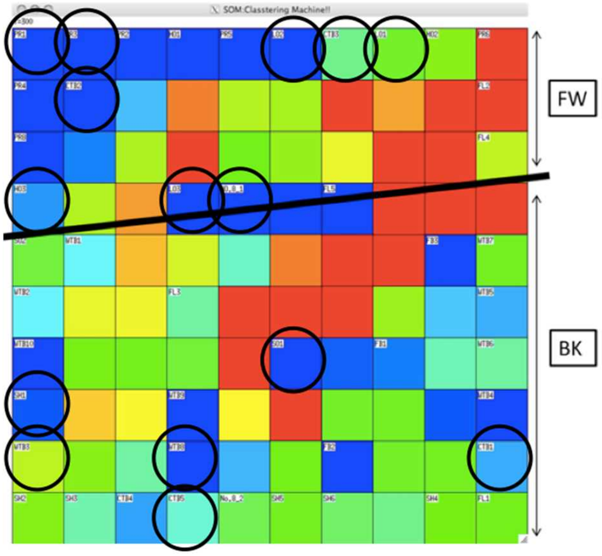

Fig.1 Feature map of experimental result (total score)

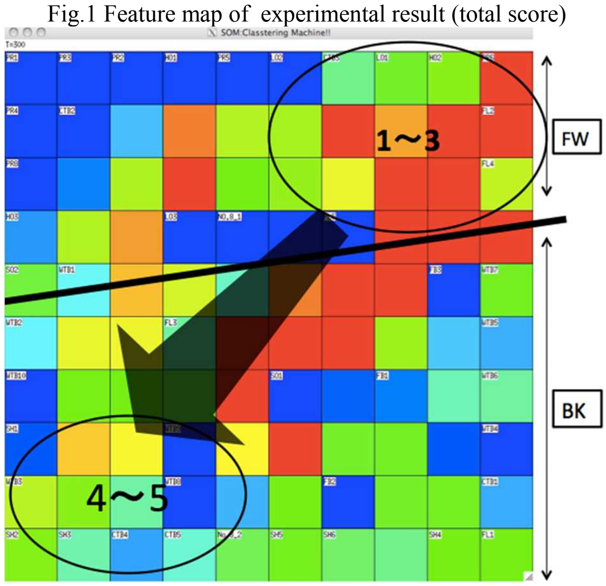

Fig.2 Feature map of experimental result (Cooperativeness)

data. When the overall score of DIPCA.3 (total score is not included in the input data) is examined, the overall score will be higher as it goes to the lower left. Based on the above results, it is considered using using physical characteristics and psychological characteristics that the overall superiority of positioning of this team by the supervisor.

Fig.2 shows the results of evaluation of psychological analysis on cooperativeness. The feature map uses the same map in Fig.1. Therefore, the individual labeling position is the same as Fig.1. For items on cooperativeness, low-level players are gathered in the upper right, and higher-level players are arranged as they go to the lower right. For this reason, in this team, highly level athletes on cooperativeness are often assigned to BK and it is understood that low players are assigned to FW. In other words, coach can analyze the psychological state well and find out that is allocating positions.

As shown in Fig. 3, the unit which is denoted by black circle indicates a regular member. Analysis of this result shows that athletes with high psychological ability values are selected as regular members. In other words, the coach knows that for the selection of regular members in this team, there is a tendency to comprehensively select high level psychological players and high cooperativeness level players as psychological conditions.

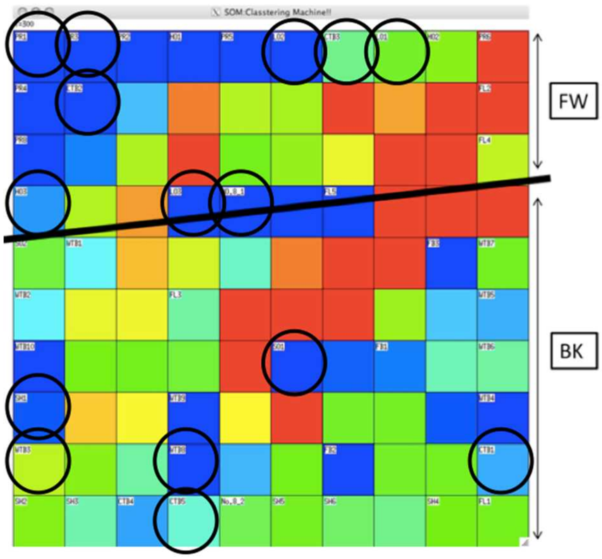

Fig.3 regular position in Feature maps

4. Summary

In this paper, we experimented on clustering machine using SOM with the goal of processing data on individual physical characteristics and psychological features in group sports. In this research, we developed a clustering device that takes physical features and psychological features into 46 input data, and analyzing the results. The feature map is the result of clustering, can be largely categorized into FW and BK, and can clarify psychological features and physical features. And, we can find how coach decide the position and regular members. As a future works, for developing a clustering device, if we can use more detail input data (add the dimensions) can perform more precise diagnosis.

Acknowledgements

This work was supported by a Grant-in-Aid for Young Scientists (B) 15K21570 from JSPS KAKENHI.

References

1. Barry, A.J. and T.K. cureton, "Factor Analysis of Physique and Performance", *Res. Quart.*, 23-3:100 ~ 108, 1961
2. Nick, D.C. and E.A. Fleishman, "What Do Physical Adaptation Test Meassure?,", *A Review of Factor Analysis Studies, Educational and Psycohological Measurement*, 22-1:77-95, 1962
3. Larson, L. A., "A Factor Analysis of Motor Ability Bariables and Tests for College Men, ", *Res. Quart.*, 12: 499-517, 1941
4. Mcloy, C.H. and R.D. Young, *"Test and Meassurement in Health and Physical Education"*, New York, Applenton-Century-Crofts, Inc., pp.51-65, 1954
5. M. Tokunaga, "Factor Analysis about sports adaptation", *Japan Journal of Physical Education, Health and Sport Sciences,* Vol.22-2, pp.71-80,1977
6. I. Matsuda, R.N. Singer, "*Motor learning and human performance*", ISBN978-4-469-26119-6, Taishukan-shoten, 1986, In Japanese
7. O.Saijo, K.Suda, et., al., "On the Psychologicl Aptitude of Rugby Foot Ball Players –From Comarision New Zealand University Selected Team with Nippon College of Physical Education Team –", *Journal of Nippon College of Physical Education*, Vol22-2, pp.135-138, 1993
8. M.Tokunaga, "Evaluation scales for athletes' psychological competitive ability : development and systematization of the scales" *Japan Journal of Physical Education, Health and Sport Sciences*, Vol46-1, pp.1-17, 2001.
9. Y.Takemura, et. al., "Development algorithm for Relationship between Role and Individual Role Adaptation in Rugby", *CD-Proc. of WAC2014*, Hawaii

Ball Dribbling Control for RoboCup Soccer Robot

Shota Chikushi
Graduate School of Life Science and Systems Engineering, Kyushu Institute of Technology
2-4 Hibikino, Wakamatsu, Kitakyushu, 808-0196, Japan
E-mail: chikushi-shota@edu.brain.kyutech.ac.jp

Tharindu Weerakoon
Graduate School of Life Science and Systems Engineering, Kyushu Institute of Technology
2-4 Hibikino, Wakamatsu, Kitakyushu, 808-0196, Japan
E-mail: weerakoontharindu@brain.kyutech.ac.jp

Takashi Sonoda
Graduate School of Life Science and Systems Engineering, Kyushu Institute of Technology
2-4 Hibikino, Wakamatsu, Kitakyushu, 808-0196, Japan
E-mail: t-sonoda@brain.kyutech.ac.jp

Kazuo Ishii
Graduate School of Life Science and Systems Engineering, Kyushu Institute of Technology
2-4 Hibikino, Wakamatsu, Kitakyushu, 808-0196, Japan
E-mail: ishii@brain.kyutech.ac.jp

Abstract

RoboCup is a platform designed to promote the research related to Artificial Intelligence (AI) and robotics. We also organize a RoboCup soccer team "Hibikino-Musashi" and working on co-operated behavior control system using multiple autonomous mobile robots. In order to realize co-operated behavior in the soccer game, the ball handling system is one of the important issues for dribbling and passing the ball to teammate robots. In this paper, a control method of the ball rotation using two active wheels, which are attached in front of the soccer robot and designed to have friction on the upper side of the ball, is proposed. The forward and inverse kinematics between the ball-motion and two active wheels are derived, and the ball handling mechanism is developed and evaluated based on the results of simulations and experiments.

Keywords: RoboCup; ball-wheel kinematics, ball handling mechanism

1. Introduction

The robot competition RoboCup is proposed to be a landmark project whose target is to realize the robot soccer team to defeat the human World Cup champion team until 2050. The project is expected to encourage researchers to develop and promote Artificial Intelligence and robotics from different aspects [1].

The soccer robots should be autonomous and make a goal in the dynamic environment where many robots move around intricately intertwined with other friend and opponent robots. On developing the co-operated behaviors using soccer robots, the invention of new technologies is expected because not only the technical issues of robot development but also human-robot interactions should be considered such as safety regulations not to damage human and robot themselves, reading the situations, ambiguous determinations and so on. The robot technology will be utilized in service markets and human-robot interactive tasks in the future.

We also organize a RoboCup soccer team "Hibikino-Musashi" to join RoboCup Soccer Middle Sized League (MSL) and working on co-operated behavior control system using multiple autonomous mobile robots. To promote intelligence of robots, MSL rules are annually reviewed and updated. In recent years, top teams' robots show collaborated behaviors as a team and different ball passing methods for various situations are developed to achieve high score. In order to realize co-operated behavior in the soccer game, the ball handling system is one of the important issues for dribbling and pass the ball to teammate robots. The quick motion of robots with high ball retention capability has the big influence on planning the action of the robot.

The new soccer robot of "Hibikino-Musashi" is shown in Fig. 1. The robot has omni-directional mobility and an omni-vision camera system on the top, and is controlled by a mounted laptop computer. Comparing with our previous robot [2], the new one can move 1.5 times faster and has the ball handling mechanism in front.

In this paper, a control method of the ball using two active wheels, which are mounted in front of the soccer robot and designed to have friction on the upper side of ball, is proposed. The forward and inverse kinematics between the ball-motion and two active wheels is derived, and the ball handling mechanism is developed and evaluated based on the results of simulations and experiments.

2. Development of Ball Handling Mechanism

Several different ball handling mechanisms for soccer robot have been reported in literature [3], which are mainly classified into two types, one is to control the ball by using two active wheels mounted in the front of the robot and another is by using arms [4]. With the selection of soccer robots going on, the ball handling mechanism by two active wheels has become the mainstream. The advantage of the ball handling mechanism using active wheels is the capability of keeping the ball even in the lateral- and reverse-motion. On the other hand, the disadvantages of the mechanism are the complexity in design and necessity of ball motion control algorithm suitable to the robot motion. The ball should rotate smoothly with respect to the traveling direction of the robot to satisfy the RoboCup regulation and realize smooth robot motion. Moreover, the ball handling mechanism is restricted to cover one-third of the ball [5]. The RoboCup team TechUnited developed the mechanism using two normal wheels and a solenoid kicker which can keep the ball and select loop-pass or grounder-pass [6]-[8]. CAMBADA team developed using two omni-wheels and shows the similar function [9]. However, the forward and inverse kinematics between ball motion and wheels are not well defined and the ball motion is controlled by heuristic methods. We introduce the mathematical model regarding ball motion and active wheels.

The overview of mechanical design of the ball handling mechanism is shown in Fig. 2, and the schematic design is in Fig. 3. In the mechanism, active wheels are attached to the lever tips to rotate the ball. The two levers move upward passively when the active wheels rotate to bring the ball toward its body, and the springs and dumpers are connected between the body and the levers to absorb the collision impact of the ball. The small omni-wheels in the bottom are passive rollers to prevent the ball from contacting to the body. If the robot detects the approaching of the ball, the active wheels on the levers start to rotate to bring the ball inside the robot, the friction between the ball and wheels generated by the spring force get the ball inside the robot.

To recognize the ball situation, the lever shifting angle α_L, which is the angle from the initial position α_{SP} to the maximum angle α_{HP}, is measured by the potentiometer. Then, α_L equals to α_{HP}(Fig.4), the active wheel control starts to synchronize with robot's movements. The ball handling mechanism is designed to hold the ball by four wheels during dribbling.

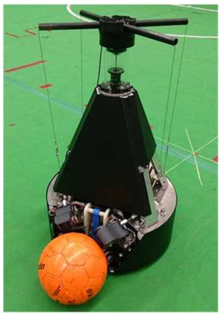

Fig. 1. Soccer robot of "Hibikino-Musashi"

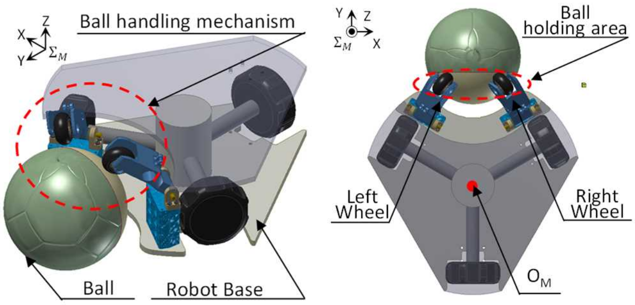

a. Projection view b. Top view

Fig. 2. Overview of the wheel arrangement

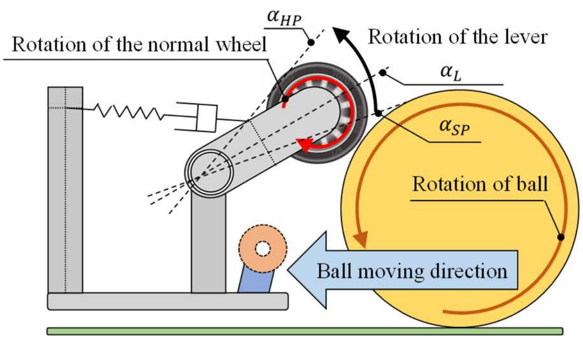

Fig. 3. Overview of ball handlling mechanism

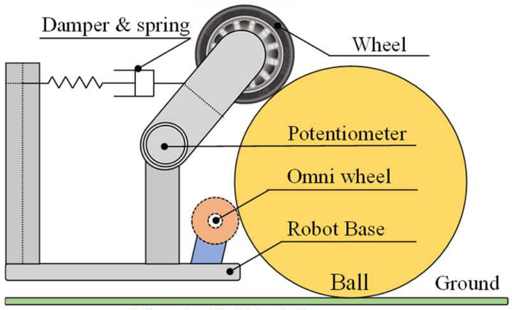

Fig. 4. Ball holding state

3. Kinematics and Experimental Setup

The forward and inverse kinematics between ball motion and active wheels are represented as shown in eq.1, [10].

$$\vec{\omega}_W = (\|\vec{\omega}_B \times \vec{P}\| / r_w) \cdot \vec{\iota_\omega} \qquad (1)$$

Wheel angular velocity vector $\vec{\omega}_W$ can be expressed by velocity vector at contact point and wheel radius r_w. Velocity vector at contact point can be expressed by ball angular velocity vector $\vec{\omega}_B$ and position vector $\vec{P}$ from the ball center to contact point.

To evaluate the kinematics, following experiments are performed to obtain the state variables of ball motion and active wheels. In the experiments, the distance between the wheel and the ball is required to be constant, so that an experimental setup is developed as shown in Fig. 5 and Fig. 6.

The setup is designed to be able to change its wheels around the ball in arbitrary position and angle. Totally, six encoders are attached to the robot as an internal sensor to measure two motions, ball motion and wheels. The four encoders are to determine velocity and orientation of the experimental setup and installed on each omni wheel. The two encoders are attached directly to the active wheel motors.

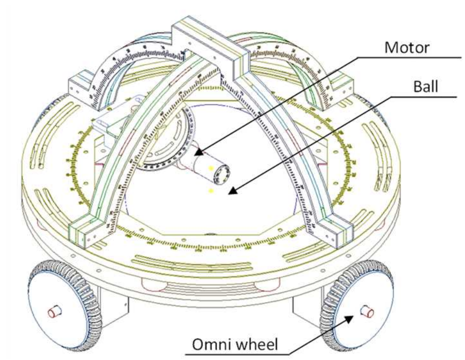

Fig. 5. Experimental device of ball handling mechanism (Projection view)

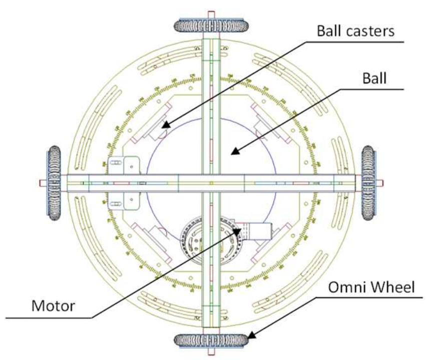

Fig. 6. Experimental device of ball handling mechanism (Top view)

4. Experimental Results

The kinematics between ball motion and wheel is evaluated by translational motions in surge, sway and their combination (see Fig.7-9). The solid and dot lines mean the velocity in x-direction and y-direction, respectively. Black line means the forward kinematics obtained from active wheels' data, and blue are from experimental setup motion.

In the evaluation of surge motion (y-direction in the robot coordinate), the ball is controlled to go backward 270 (deg.) with the velocity of 1.0 m/s. The comparison of the velocities from setup motion and kinematics calculated by active wheel rotation is shown in Fig. 7. The result shows that the experimental setup motion is well controlled to be 1.0 m/s, and velocities from the setup and calculation of kinematics become almost same values.

In the sway motion (see Fig. 8), the velocity of x-direction is controlled to be 1.0 m/s. The experimental data of setup show also good consistent with kinematics calculation. In the experiment of Fig.9, the ball is controlled to go in 225 degree and the velocities in x- and y-direction are equal. As the result, the ball moves in about 240 degree, however, the ball motion data and kinematics calculation show good consistent.

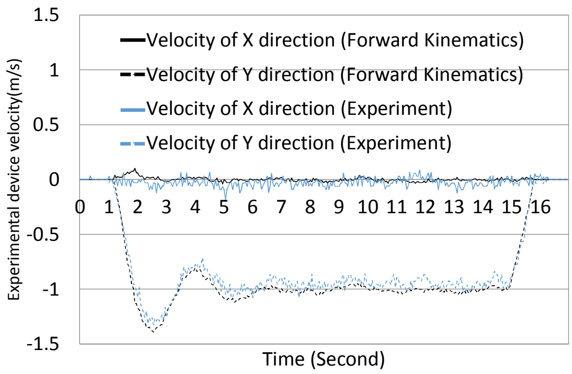

Fig. 7. Experimental results of dribble kinematics (270 °)

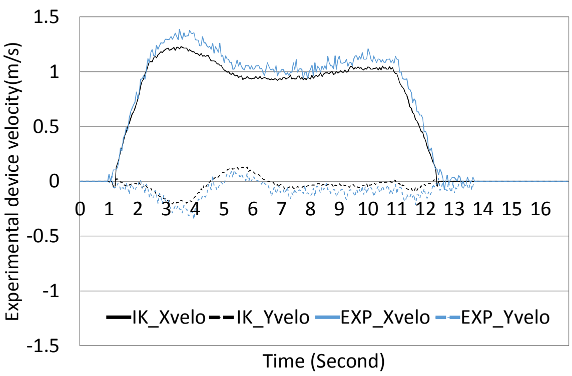

Fig. 8. Experimental results of dribble kinematics (0°)

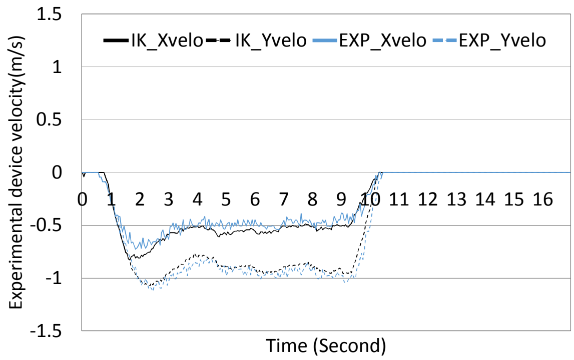

Fig. 9. Experimental results of dribble kinematics (225°)

5. Conclusion

In this paper, the forward and inverse kinematics between the ball-motion and two active wheels are evaluated by surge and sway motions using developed experimental setup. The results show that the ball motion data and kinematics calculation show good consistent. The ball handling mechanism has enough possibility to realize dribbling behavior of the soccer robots.

References

1. R. Soetens, M.J.G. van de Molengraft, B. Cunha, "RoboCup MSL - History, Accomplishments, Current Status and Challenges Ahead" RoboCup 2014: *Robot World Cup XVIII*, 624-635, (2014)
2. S. Chikushi,M. Kuwada, M. Ishikura, T. Nagao, R. Itohara, S. Watanabe,K. Hisano, R. Shimada, K. Matsumoto, M. Tominaga, N. Machida, K. Ishii, H. Miyamoto, T. Sonoda, Y. Takemura "Hibikino-Musashi Team Description Paper 2016" *RoboCup 2016* Leipzig, (2016)
3. S. Stancliff, "*Evolution of Active Dribbling Mechanisms in RoboCup*" 16-471 Project, (2005)
4. K. Fujimoto, K. Ishii, Y. Kitazumi "Development of a ball handling mechanism for a RoboCup Soccer Robot" *Robotics and Mechatronics for Society2011*, (2011)
5. M. Asada, et.al. "Middle Size Robot League Rules and Regulations for 2015" *MSL Technical Committee 1997–2015*, pp. 15, (2015)
6. K.P. Gerrits, M.J.G. van de Molengraft, R. Hoogendijk, M. Steinbuch, "*Ball Handling System for Tech United*

Soccer Robots" Eindhoven University of Technology, (2012)
7. J.J.T.H. de Best, M.J.G. van de Molengraft, M. SteinbuchA "Novel Ball Handling Mechanism for the RoboCup Middle Size League" *Mechatronics* 21(2), 469-478, (2011)
8. C. Lopez, F. Schoenmakers, K. Meessen, Y. Douven, H. van de Loo, D. Bruijnen, W. Aangenent, B. van Ninhuijs, M. Briegel, P. van Brakel, J. Senden, R. Soetens, W. Kuijpers, J. Reijrink, C. Beeren, M. van 't Klooster, L. de Koning, M.J.G. van de Molengraft, "Tech United Eindhoven Team Description 2016" *RoboCup 2016* Leipzig, (2016)
9. B. Cunha, A. J. R. Neves, P. Dias, J. L. Azevedo, N. Lau, R. Dias, F. Amaral, E. Pedrosa, A. Pereira, J. Silva, J. Cunha and A. Trifan "CAMBADA'2015: Team Description Paper" *RoboCup 2015* Hefei, (2015)
10. S. Chikushi, T. Weerakoon, K. Ishii, T. Sonoda "Motion Analysis and Control of the Ball Operation for Dribbling Action in RoboCup Soccer Robot" *SCIS & ISIS* 2016, (2016)

Strategy Analysis of RoboCup Soccer Teams Using Self-Organizing Map

Moeko Tominaga
Graduate School of Life Science Systems Engineering, Kyushu Institute of Technology
2-4 Hibikino, Wakamatsu-ku, Kitakyushu, Fukuoka, 808-0196, Japan
E-mail: tominaga-moeko@edu.brain.kyutech.ac.jp

Yasunori Takemura
Faculty of Engineering, NishiNippon Institute of Technology
1-11, Aratsu, Kanda-town, Miyako-gun, Fukuoka, 800-0397, Japan
E-mail: takemura@nishitech.ac.jp

Kazuo Ishii
Dept. of Human Intelligent Systems, Kyushu Institute of Technology
2-4 Hibikino, Wakamatsu-ku, Kitakyushu, Fukuoka, Japan
E-mail: ishii@brain.kyutech.ac.jp

Abstract

In the soccer games, the player's behavior changes depending on the game situation such as winning or losing, score gap, remaining time. The players act more offensive when their team is losing, or more defensive when their team is winning with minimum score difference. Currently most of robot teams keep the same strategy during the game so that the result of game depends on the ability of each player like speed of robot, quality of localization, obstacle avoidance and ball handling. Next issue for the robot intelligence is collaborated team behavior and strategy. The autonomous soccer robots are required to behave cooperatively and make decision using environment and game situation. In this research, the team strategy is analyzed based on parameters such as the positions of human player, time and actions using Self-Organizing Map (SOM).

Keywords: Strategy, Self-Organizing Map, team behavior, SOM.

1. Introduction

Multi-agent System (MAS) is one of the solutions to the problems that are difficult or impossible for an individual agent or a monolithic system. As human solutions to the applications that require multiple humans to works together, the use of robot teams would be considerable solution for complex tasks. From the point of total cost, the development of multiple simple robots may be possible to reduce the cost rather than a monolithic robot. Asama proposed the robotic systems composed of multiple agent and discussed the importance of "distributed autonomy" in terms of autonomy and cooperativeness[1]. An autonomous and decentralized robot system called ACTRESS is developed and applied into multiple objects pushing problems and showed that the system can solve by parallel and independent action by each robot[2]. Parker proposed a software architecture for MAS called ALLIANCE, which facilitates fault tolerant and robust mobile robot cooperation and demonstrated the feasibility by hazardous waste cleanup using a physical robot team[3].

RoboCup Soccer is a landmark project with the goal of realizing an autonomous robots team that can win the champion of Soccer World Cup until the 2050[4,5]. RoboCup Soccer has been attracting attentions as a standard problem of MAS as it is composed of multiple interacting intelligent agents within an environment. Human teams cannot win soccer games depending on the ability of individual players, and the co-operation with teammates, team behavior, is the important solution. Especially in RoboCup middle size league (MSL), autonomous mobile robots are affected physically by not only teammate and opponent agents but also their environment. It is difficult to describe all behaviors by if-then rules, learning methods such as reinforcement learning[6], Genetic Algorithms[7] have been tried to environmental recognitions. Takahashi and Asada[8] developed a multi-layered learning system using reinforcement learning and applied into RoboCup tasks which are to chase the ball and shoot into the goal with avoiding opponent robot. Suzuki[9] applied Genetic Algorithm into real time localization problem of RoboCup robots.

In this research, we introduce Self-Organizing Map (SOM)[10] into the classification of RoboCup team strategy. SOM is a topologically correct feature map proposed by Kohonen and is well known as an attractive tool for extracting the characteristics of data and map the data into lower-dimensional space through its self-organizing process. We aim at developing a strategy decision system depending on the situation and environment. As the first step, the classification method of each robot using SOM is discussed.

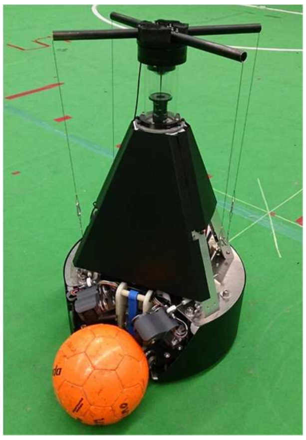

Fig. 1. Soccer robot of "Hibikino-Musashi"

2. Autonomous Mobile Robot Platform for RoboCup

After a decade pass from RoboCup started in 1997, the quality of the game has risen with the development of information and computer technology. We also organize a RoboCup team "Hibikino-Musashi", and have joined to the MSL in the RoboCup Tournament. In recent years, most of robots have the similar shape including the ball handling mechanism, the kick mechanism capable of adjusting the trajectory of the ball, environment recognition system using an omni-directional mirror and omni-wheels that can be moved in the all direction. Our autonomous mobile robot platform is shown in Fig.1.

Currently most of robot teams keep the same strategy during the game so that the result of game depends on the ability of each player like speed of robot, quality of localization, obstacle avoidance and ball handling. Next issue for the robot intelligence is collaborated team behavior and strategy. As the next step, we have been trying to implement a strategy selection algorithm of the team's behavior.

3. SOM for Classify Situation

The learning step of SOM is discussed in the following steps[11], and the conceptual diagram of SOM is shown in Fig. 2. Suffix i denotes the number of input data, and j indicates the number of unit.

Step 1: Assign the weight vectors (w_{ij}) with random values and normalize the input in the range of [0, 1].

Step 2: Compute the Euclidean distance (d_j) between a series of input vectors (x_i) and all the weight vectors at iteration by eq. (1).

$$d_j = \sqrt{\sum_{i=0}^{i=n} \left(x_i - w_{ij}\right)^2} \tag{1}$$

Step 3: Find the winner unit U_c (Best Matching Unit, BMU) which has the minimum Euclidean distance.

$$U_c = \operatorname{argmin}(d_j) \tag{2}$$

Step 4: Calculate the neighborhood radius $\sigma(t)$. σ_0 denotes the initial neighborhood radius, and λ indicates a maximum number of iteration.

$$\sigma(t) = \sigma_0 \exp\left(-{}^{t}/_{\lambda}\right) \tag{3}$$

Step 5: The connecting weight vectors of all neurons are updated by Eq. (4).

$$\overline{w}_j(t+1) = \overline{w}_j(t) + \eta(t) \cdot h_{c,j}(t) \cdot \left[\bar{x}(t) - \overline{w}_j(t)\right] \tag{4}$$

Step 6: The time t increases to t +1. If t < T then go to step 2; otherwise stop the training.
Where t is the training step index, $\eta(t)$is the learning

$$\eta(t) = \eta_0 \cdot \exp(-{}^{t}/_{T}) \tag{5}$$

$$h_{c,j}(t) = \exp\left(-\left\|r_j - r_c\right\|^2 \Big/ 2\sigma(t)^2\right) \tag{6}$$

rate, and $h_{c,j}(t)$ is defined as the neighborhood kernel function, as expressed in Eq. (5) and Eq. (6). r_j and r_c are positions of nodes BMU and j on the SOM grid. Both the learning rate and the neighborhood radius decrease monotonically with time t.

4. Teaching Data Set

As the input vectors (teaching data), we had observed and analyzed the state variables of a human soccer (futsal) game. The human soccer player performed the game 5 to 5 at the futsal court and we observed the positions of all the players and the ball in the field with the coordinates of the grid. (See Fig. 3) Input vectors are not affect behavior selection. That is, the input vector is given by Eq. (7).

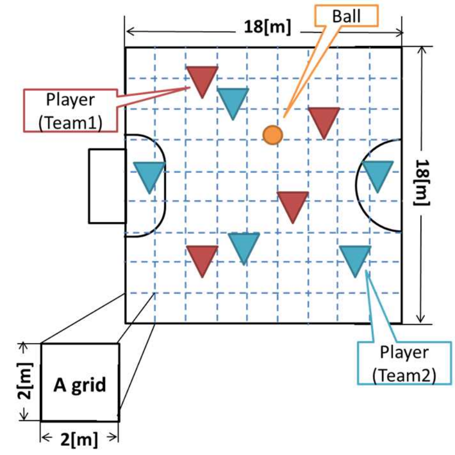

Fig. 3: Observation environment of soccer

$$\bar{x}_i^{(k)} = (P_k, B) \tag{7}$$

$P_k(p_x, p_y)$ is the position of the player k, and $B(b_x, b_y)$ is the position of the ball. Suffix i indicates the *i-th* data set. We set 2 players (k = 2) and the number of input data is 100 sets (maximum i = 100).

5. Classification of Human Behavior

In the method described above, SOM's feature map was made from the position information of the actually observed player and ball. Each parameter of SOM algorithm is shown in Table. 2. In this paper, we focus on 2 players and display the results. One is an experienced futsal player and the other is inexperienced player. Fig. 4-a shows the distance between each player and the ball, Fig. 4-b shows the distance between each player and the goal, and Fig. 4-c shows the distance between the ball and the goal in color.

If the color of the unit is blue, it means that the evaluation factor is far. On the other hand the color of unit becomes near as the color becomes red. As you can see from Fig.4, we can see that they are similar distance relationship in all factors, although there are rotated in map. In other words, the position of the players behavior are almost same.

Table. 2: Parameters setting SOM

Learning frequency	t	3000
The initial learning rate	η_0	10
The initial neighborhood radius	σ_0	0.8
Map size		10×10

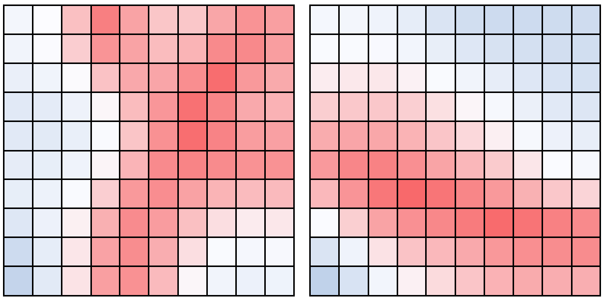

Experienced Player Inexperienced Player

Fig. 4-a: A color-coded SOM of the distance between the ball and each player

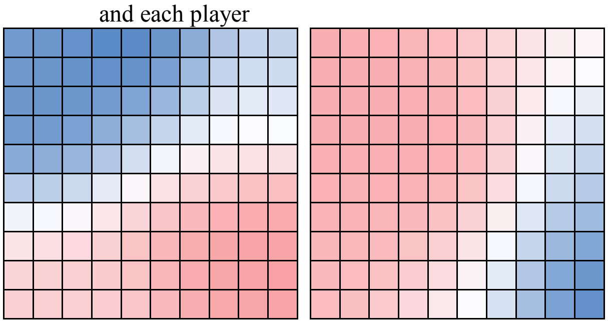

Experienced Player Inexperienced Player

Fig. 4-b: A color-coded SOM of the distance between the goal and each player

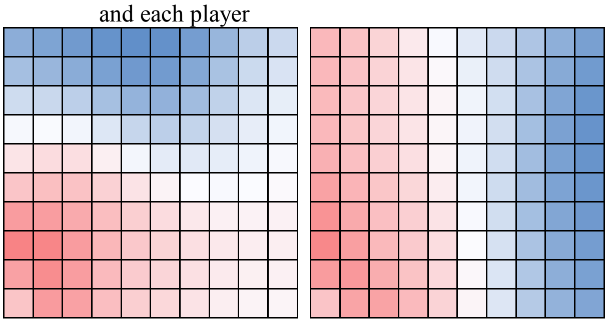

Experienced Player Inexperienced Player

Fig. 4-b: A color-coded SOM of the distance between the ball and the goal

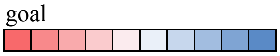

Fig. 4: SOM of soccer game by human

However, the point of the view of inputs, only the position of the ball and their own position are inputted. In fact, it does not include input about the circumstances and environment around the players. Therefore, it is considered that it was not located in feature map considering the relationship with other people and it did not make a difference.

In future works, we will conduct experiments with inputs including relationships with others, situations in games and the surrounded environments factors.

6. Conclusion

In this research, the team strategy is analyzed based on parameters such as the positions of human player, time and actions using Self-Organizing Map (SOM). We developed the SOM map from the position of each player and ball on the field. The colors of SOM map represent the distance relationships of the player, the ball, and the goal, and which kind of differences occurred among players is observed. As a result, there was the difference between experienced and inexperienced people. As a next problem, we aim to analyze the positioning of players including relations with others.

References

1. H. Asama, Distributed Autonomous Robotic System Configurated with Multiple Agents and Its Cooperative Behaviors, *J. Robotics and Mechatronics*, 4(3)(1992), 199-204
2. H. Asama, K. Ozaki, A. Matsumoto, Y. Ishida and I. Endo, Development of Task Assignment System Using Communication for Multiple Autonomous Robots, *J. Robotics and Mechatronics*, 4(2)(1992), 122-127
3. Parker, L. E. , ALLIANCE: An archi- tecture for fault-tolerant multirobot cooperation, *IEEE Transactions on Robotics and Automation* 14(2)(1998) 220-240.
4. http://wiki.robocup.org/Middle_Size_League
5. R. Soetens, M.J.G. van de Molengraft, B. Cunha, “RoboCup MSL - History, Accomplishments, Current Status and Challenges Ahead” RoboCup 2014: *Robot World Cup XVIII*, 624-635, (2014)
6. Richard S. Sutton, Andrew G. Barto, Mikami. M, Minagawa. S, *Reinforcement learning,* Moride Publishing.
7. D. E. Goldberg, *Genetic Algorithms in Search, Optimization, and Machine Learning*, Addison-Wesley Longman Publishing, (1989).
8. Y. Takahashi and M. Asada, Multi-Layered Learning System for Real Robot Behavior Acquisition, *AAAI 2004 Fall Symposium Series, Working Notes: Real-Life Reinforcement Learning*, (2004), 68-75
9. S. Yamada and H. Suzuki, Real-Time Self-Localization Method for Autonomous Mobile Robot, in Proc. of 31st Fuzzy System Symposium, (2015), 149-150 in Japanese
10. Moriyasu. K, Yoshikawa. T and Nonaka. H, Supervised Learning for Agent Cooperative Actions Mechanism by Using Self-Organizing Map, *IPSJ SIG Technical Report*, Vol.2010-MPS-80, 2010
11. Kohonen. T, *Self-Organizing Maps,* Springer Japan
12. Takemura. Y, 2011, *Research of the color constancy using Neural Networks in Robocup MSL*, 27th Fuzzy System Symposium.
13. Wisanu. J, *Application of Self-Organizing Map for analyzing robotic arm’s action with Consciousness-Based Architecture module*.

Feature Extraction for Digging Operation of Excavator

Kazushige Koiwai, Toru Yamamoto
Institute of Engineering, Hiroshima University,
1-4-1, Kagamiyama, Higashihiroshima City, Hiroshima, 739-8527, Japan
E-mail: koiwaik@hiroshima-u.ac.jp, yama@hiroshima-u.ac.jp
http://www.hiroshima-u.ac.jp

Takao Nanjo, Yoichiro Yamazaki
Global Engineering Center, KOBELCO Construction Machinery CO., LTD.,
2-2-1, Itsukaichikou, Saeki-ku, Hiroshima City, Hiroshima, 731-5161, Japan

Abstract

Improvement of the work efficiency is demanded by aging and reducing of the working population in the construction field, so that some automation technologies are applied to construction equipment, such as bulldozers and excavators. However, not only the automation technologies but also expert skills are necessary to improve the work efficiency. In this paper, the human skill evaluation is proposed by the human skill evaluation of the data-driven PID controller. The proposed method is applied to the excavator digging operation. As the result, the difference between the novice operation and the skilled operation is extracted. Moreover, the numerical difference is clarified based on the result.

Keywords: PID Controller, Human Skill Evaluation, Data-Driven

1. Introduction

Japanese Ministry of Land, Infrastructure, Transport and Tourism have started the policy of the integration of construction and ICT (Information and Communication Technology) for public works such as land survey, engineering, construction and maintenance, that is called "i-construction".[1] Aims of this policy are the improvement of the work efficiency and the increasing of productivity. The technologies of IoT (Internet of Things), big data and AI (Artificial Intelligence) will be applied to some construction equipments based on the policy. However, human operations for construction equipments are still required continuously in the field because skilled workers optimize their operations for high productivity in each complicated conditions. Unfortunately, those skilled operators who have the unique technique are reduced in these days because of the aging and reducing of the working population.

As the previous studies, skill based controllers have been proposed.[2,3] These studies considered that the human skill described as a controller with the tuner of PID gains, called the skill-based PID controller. The operation skill have been replicated by the skill-based PID controller experimentally. Moreover, the skill evaluation by using the skill-based PID controller have been performed.[4,5] These research focus on the change of PID gains to extract the feature of the operation skill for the excavator. However, the evaluated operation is applied to the simple lever operation such as the swing operation. In the actual work field, the operation for the excavator is more complicated.

In this study, the data-driven skill-based PID controller is adopted to the actual work operation of the excavator, i.e. the continuous digging operation. The skill feature for the excavator of the continuous digging operation is extracted to compare the novice operation with the

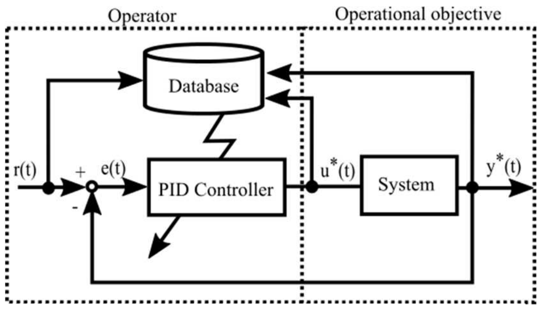

Fig. 1 Scheme of Feature Extraction

professional operation based on the control engineering approach. Moreover, the numerical difference of feature between is verified.

Algorism of Skill Feature Extraction

1.1. *Scheme of skill feature extraction*

The scheme of feature extraction for the human skill is shown in Fig. 1. Based on the engineering approach, the operational objective and the operator are considered as the system and the PID controller with the parameter tuner that is consist of the data driven method. $y^*(t)$ and $u^*(t)$ are denoted as the system output and the system input by the operation.

1.2. *Data-driven PID controller*

The following control law is considered for the skill-based controller:

$$\Delta u(t) = K_I(t)e(t) - K_P(t)\Delta y^*(t) - K_D(t)\Delta^2 y^*(t) \quad (1)$$

where the PID gains, $K_P(t), K_I(t)$ and $K_D(t)$ are tuned by the database. The control error signal $e(t)$ is defined as $e(t) := r(t) - y(t)$ and the difference operator Δ is defined as $\Delta := 1 - z^{-1}$.

The operational objective is considered as the nonlinear system is shown as follows:

$$y^*(t) = h\big(\phi(t-1)\big). \quad (2)$$

Here the $h(\cdot)$ is the nonlinear function using past data and the information vector $\phi(t-1)$ is defined as:

$$\begin{aligned}\phi(t-1) = \ & [y^*(t-1), \cdots y^*(t-n_y), \\ & u^*(t-1), \cdots u^*(t-n_u),] \end{aligned} \quad (3)$$

where n_y and n_u are orders of output and input, respectively. The query $\bar{\phi}(t)$ is defined as:

$$\begin{aligned}\bar{\phi}(t) = \ & [r(t+1), r(t), y^*(t), y^*(t-1), \cdots \\ & y^*(t-n_y), u^*(t-1), \cdots u^*(t-n_u)]. \end{aligned} \quad (4)$$

The dataset of database, $\mathbf{\Phi}(i)$, is constructed as follows:

$$\begin{aligned}\mathbf{\Phi}(i) = \ & [\bar{\phi}(i), K_P(i), K_P(i), K_P(i)], \\ & i = 1,2,\cdots,N \end{aligned} \quad (5)$$

where the index and the total number of datasets is shown as i and N, respectively.

PID gains that is requested by the query are calculated by the following procedure. Distances $d(\cdot)$ between the query $\bar{\phi}(t)$ and $\bar{\phi}(i)$in each datasets are calculated by:

$$d\left(\bar{\phi}(t), \bar{\phi}(i)\right) = \sum_{l=1}^{n_u+n_y+1} \left| \frac{\overline{\phi_l}(t) - \overline{\phi_l}(i)}{\max\overline{\boldsymbol{\phi}_l} - \min\overline{\boldsymbol{\phi}_l}} \right| \quad (6)$$

where the index of an element in a dataset or query is shown as l. $\overline{\boldsymbol{\phi}_l}$ is a set of the element for the index.

Neighbors of data are selected according to their distance from query. The number of neighbor dataset, that is the user specified parameter, is donated as k. The sum of selected PID gains $\boldsymbol{K_{PID}}(m)$ multiplied by a weight is desired PID gains $\boldsymbol{K_{PID}}(t)$ as follows:

$$\boldsymbol{K_{PID}}(t) = \sum_{m=1}^{k} \omega_m \boldsymbol{K_{PID}}\,(m) \quad (7)$$

$$\boldsymbol{K_{PID}}(t) = [K_P(t) \quad K_I(t) \quad K_D(t)] \quad (8)$$

$$\omega_m = \frac{(1+d_m)^{-1}}{\sum_{n=1}^{k}(1+d_n)^{-1}} \ . \quad (9)$$

1.3. *Skill feature extraction*

PID gains are learned by the operational data $u^*(t)$ and $y^*(t)$, which are teacher's signals for the learning scheme in Fig. 2. PID controller, which has the change of PID gains can be expressed as the feature of the human skill.

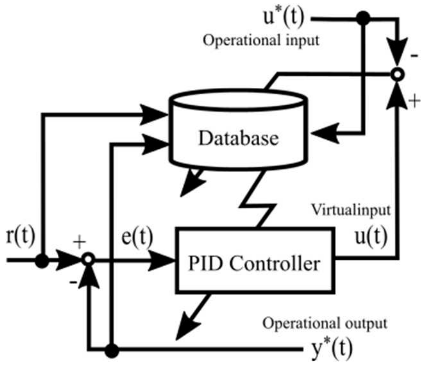

Fig. 2 The Leaning Scheme of Skill Feature Extraction

The following steepest descent method (10) is performed for the learning of PID gains in the database.

$$\boldsymbol{K}_{PID}^{new}(t) = \boldsymbol{K}_{PID}^{old}(t) - g(t)\frac{\partial J(t)}{\partial \boldsymbol{K}_{PID}} \quad (10)$$

where the error criterion $J(t)$,the updating gradient $g(t)$ and the partial differential are expressed as follows:

$$g(t) = (c + a \cdot exp(-b|u^*(t) - u(t)|))^{-1} \quad (11)$$

$$J(t) = \frac{\epsilon(t)^2}{2} \quad (12)$$

$$\epsilon(t) = u^*(t) - u(t) \quad (13)$$

$$\frac{\partial J(t)}{\partial \boldsymbol{K}_{PID}} = \frac{\partial J(t)}{\partial \epsilon(t)}\frac{\partial \epsilon(t)}{\partial u(t)}\frac{\partial u(t)}{\partial \boldsymbol{K}_{PID}} \quad . \quad (14)$$

Coefficients of a, b and c are the appropriate positive constants.

2. Evaluation Result

2.1. *Experimental equipment*

The proposed scheme is applied to the operation of an excavator. The evaluated operation is a continuous digging motion and the excavator, SK200-9 made in Kobelco Construction Machinery, is used for the experiment. The continuous digging motion can be classified into four parts in Fig. 3. First part is called digging that is the operation to scoop the earth and sand with the bucket ①. Then, the load is lifted to the certain height that assumed a carrier of the truck ②. Furthermore, the load is dumped on the ground that assumed the truck bed ③. Finally, teeth of the bucket is repositioned to the starting point of the digging ④.

Fig. 3 Continuous Digging Motion for Excavator

2.2. *Skill evaluation procedure*

The most important operation for actual works is the positioning at the stop motion because the human skill is required by the operation. Therefore, the target for this evaluation is the positioning by the stop operation only. The acceleration should be ignored in this paper. The evaluation procedure is shown as follows.

The proposed method is applied to the specified operation into the continuous digging operation. In this study, the swing operation is selected as the specified operation because the skill is necessary to stop at the proper position and the reference value $r(t)$ of operation is clearer than another operation. The digging operation is performed to record $u^*(t)$ and $y^*(t)$. Here, the pilot pressure and the angle of the swing are set as the input value $u^*(t)$ and the output value $y^*(t)$, respectively. Then, the skill feature is extracted by the comparison of the professional and novice operation. Moreover, the physical quantity that can be measured is evaluated based on the skill feature.

2.3. *Application result of proposed method*

The data of the swing motion in the continuous digging operation is extracted, normalized and resampled by the sampling time of 200ms according to the human quickness of a response. The proposed method is applied to the professional and novice data. The user specific parameter of the proposed method is shown as follows.

The calculation results of PID parameter for the professional operator and the novice operator are shown in Fig. 4 and Fig. 5. As the result, the change of PID gain at the period of deceleration which needs the operation skill has the opposite properties to compare with them. This is the almost same result of the skill evaluation for the single operation. Refer to the reference 4 in the detail

Table 1. User Specified Parameter of database

Item	Symbol	Value
Number of data y	n_y	3
Number of data u	n_u	3
Number of neighbor	k	3
Total number of data set	N	100
Coefficient of updating gradient	a	100
Coefficient of updating gradient	b	1
Coefficient of updating gradient	c	100

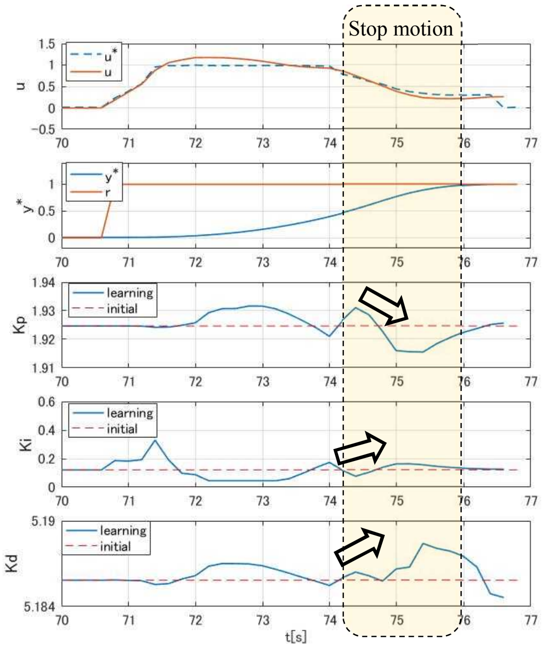

Fig. 5 Professional Skill Feature Extraction

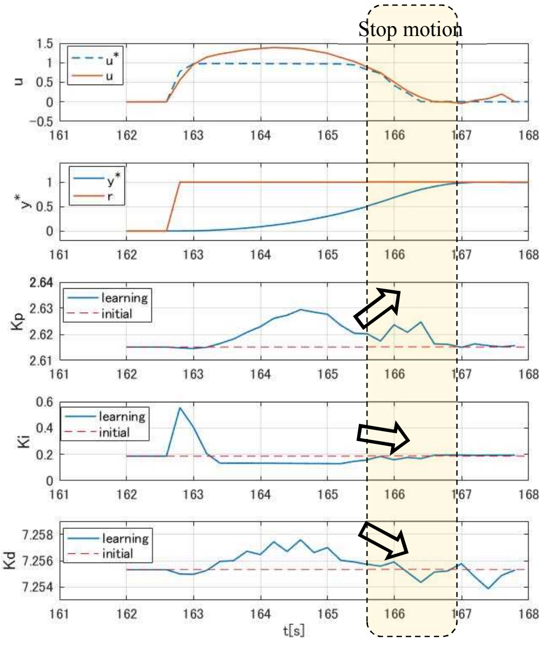

Fig. 4 Novice Skill Feature Extraction

of the single operation. The result shows that the professional operator can be expressed as the proper nonlinear controller and the novice operator can be expressed as the ON/OFF controller.

2.4. *Skill numerical evaluation*

The difference between the ON/OFF controller and the proper nonlinear controller is considered based on the skill feature. Typically, ON/OFF controller has the larger input value compared with the proper controller, that is, the novice operator has the larger operational input. The change of input expresses one of the skill criterion for the excavator operation. The Table 2 shows the change of the input signal for the 10 cycle of the continuous digging operation. As the result, it is verified that the novice has the unnecessary input compared with the professional.

3. Conclusion

The human skill evaluation based on the data-driven PID controller has been performed to the excavator operation of the continuous digging motion. The difference between the novice and professional is verified numerically based on the skill feature. Especially, the skill feature that focuses on the quantity of input signal based on the control engineering approach is extracted numerically. In future work, statistical and stochastic approach will be applied by the increasing of data.

Table 2. User Specified Parameter of database

	Professional	Novice
Maximum of input change	0.54	0.69
Number beyond 0.5 input change	1	4

4. References

1. T.Kakizaki, 'i-Construction (in Japanese)" monthly journal Kensetsu, Vol.60, No.1, (2016), pp. 6-9
2. T.Yamamoto, S.Mori and A.Sakaguchi, Data-Driven Skill-Based PID Control of a Pilot-Scale Helicopter Model. , *Int. J. of Innovative Computing Information and Control*, Vol.4, No.12, (2008), pp.3349-3358
3. Y.Liao and T.Yamamoto, Design and Experimental Evaluation of a Human Skill-Based PID Controller, *J. of Robotics, Networking and Artificial Life*, Vol.2, No.3, (2015), pp.140-143
4. K.Koiwai, T.Yamamoto, T.Nanjo, Y.Yamazaki and Y.Fujimoto, Data-driven human skill evaluation for excavator operation, *Proc. of IEEE Conf. on Advanced Intelligent Mechatronics*, Banff (2016), pp.482-487.
5. K.Koiwai, Y.Liao, T.Yamamoto, T.Nanjo, Y.Yamazaki and Y.Fujimoto, Feature Extraction for Excavator Operation Skill Using CMAC, *J. of Robotics and Mechatronics*, Vol.28, No.5, (2016), pp.715-721.

Design of a Data-Oriented Kansei Feedback System

Takuya Kinoshita
Graduate School of Engineering, Hirosihma University,
1-4-1, Kagamiyama, Higashihiroshima city, Hiroshima, Japan

Toru Yamamoto
Faculty of Engineering Division of Electrical, Systems and Mathematical Engineering, Hirosihma University,
1-4-1, Kagamiyama, Higashihiroshima city, Hiroshima, Japan
E-mail: takuya--kinoshita@hiroshima-u.ac.jp, yama@hiroshima-u.ac.jp
http://www.hiroshima-u.ac.jp

Abstract

In the development of the aging society, it is important for patients with hemiplegia to introduce adaptive welfare equipment. However, it is difficult to determine the suitable reference signal for each person. In this study, the design of a data-oriented cascade control system based on Kansei is proposed. In the proposed control system, there are two controllers which are a data-driven controller and a fixed controller. In particular, a data-driven controller can calculate the suitable reference signal based on Kansei.

Keywords: PID controller, Data-driven controller, Kansei, off-line learning.

1. Introduction

In the development of aging society, it is important for patients with hemiplegia to introduce the adaptive welfare equipment. However, it is difficult to support them by using general welfare equipment because there are a lot of individual disabilities. Therefore, an adaptive welfare equipment is needed in near future. However, it is very difficult to determine the suitable reference signal for each person. In this study, the design of a data-oriented cascade control system based on Kansei is proposed. In the proposed control system, there are two controllers which are a data-driven controller[1] and a fixed controller. In particular, a data-driven controller[1] is for a human and it can calculate the suitable reference signal of a welfare equipment based on Kansei.

2. Schematic figure of proposed control system

The schematic figure of the proposed control system is shown in Fig.1. It is very difficult for patient with hemiplegia to move their foot by only torque τ_B from their brain. Therefore, in the proposed scheme, the Ankle Foot Orthosis[2]: AFO supports them to torque τ_A. In this paper, Kansei signal is defined as walking comfortable $y(t)$ whose maximum value is 1. Therefore, reference comfortable signal $r(t)$ is set as 1. Note that it is important to estimate reference signal of brain $r_{\theta_1}(t)$ because $r_{\theta_1}(t)$ is unknown. Therefore, a data-base controller (primary controller) in outer loop is applied to calculate the estimated reference signalw(t).

3. Controlled object

The schematic figure of tow vertical joint manipulator is shown as leg model in Fig.2. I_1, I_2 are moment of inertia in ankle and knee respectively. m_0, m_1, m_2 are weight of upper body, lower leg and femur. L_1, l_1, L_2, l_2 are whole length and center of gravity distance of lower leg and femur respectively. The torque τ_1 and τ_2 are corresponding to angle of θ_1 and θ_2. The equation of walking motion is expressed as follows:

$$\begin{bmatrix} I_1 + I_2 + m_0 L_1^2 + 2m_{02} + L_1 L_2 C(\theta_2) & I_2 + m_{02} L_1 L_2 C(\theta_2) \\ I_2 + m_{02} L_1 l_2 C(\theta_2) & I_2 \end{bmatrix} \begin{bmatrix} \ddot{\theta_1} \\ \ddot{\theta_2} \end{bmatrix}$$

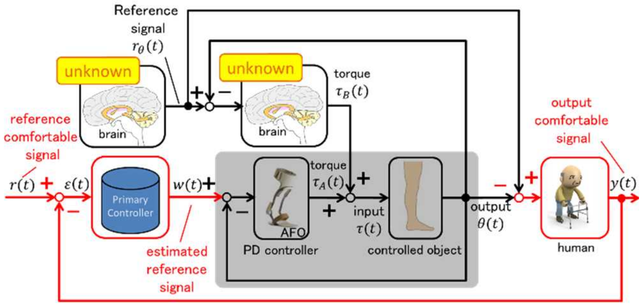

Fig. 1. Schematic figure of the proposed control system.

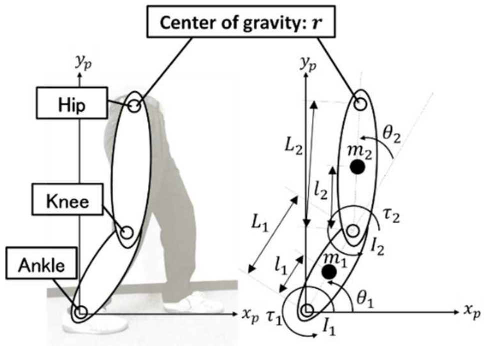

Fig. 2. Leg model: two vertical joint manipulators.

$$+\begin{bmatrix}-m_{02}L_1 l_2 C(\theta_2)\cdot(2\dot{\theta}_1\dot{\theta}_2+\dot{\theta}_2^2)\\ m_{02}L_1 l_2 C(\theta_2)\cdot\dot{\theta}_1^2\end{bmatrix}$$

$$+\begin{bmatrix}(m_1 l_1+m_{02}L_1)C(\theta_1)+m_{02}l_2 C(\theta_1+\theta_2)\\ m_{02}l_2 C(\theta_1+\theta_2)\end{bmatrix}g=\begin{bmatrix}\tau_1\\ \tau_2\end{bmatrix}, \quad (1)$$

where $C(\theta)$ denotes $cos\theta$.

In addition, Kansei signal $y(t)$ in Fig. 1 is expressed as following equation based on Weber-Fechner law[3]:

$$y(t)=\frac{1}{1+\log\left(1+e_\theta(t)\right)} \quad (2)$$

$$e_\theta(t)=r_{\theta_1}(t)-\theta_1(t), \quad (3)$$

where $r_\theta(t)$ is reference signal of $\theta_1(t)$.

4. Design of a data-driven controller in outer loop as primary controller

4.1. *Control law of primary PID controller*

The primary controller in Fig. 2 is designed as a data-driven controller[1] because human characteristic is nonlinear. The primary controller is defined as follows:

$$\Delta w(t)=K_I\varepsilon(t)-K_P\Delta y(t)-K_D\Delta^2 y(t) \quad (4)$$

$$\varepsilon(t):=r(t)-y(t), \quad (5)$$

where K_P, K_I and K_D respectively are proportional gain, integral gain and derivative gain. Δ denotes a difference operator. Note that an inner loop controller of AFO is designed as the following fixed PD controller.

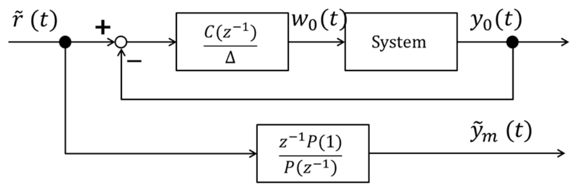

Fig. 3. Block diagram of the FRIT.

$$\Delta\tau_A(t)=K_{P2}\Delta\theta(t)+K_{D2}\Delta^2\theta(t) \quad (4)$$

$$e(t):=w(t)-\theta(t), \quad (5)$$

where K_{P2} and K_{D2} respectively are proportional gain and derivative gain.

4.2. *Design procedure of a data-driven control*

[STEP 1] Create an initial database.

The historical data is needed to use data-driven control scheme. The database is constructed by following information vector:

$$\boldsymbol{\phi}(j):=[\bar{\boldsymbol{\phi}}(j),\boldsymbol{K}(j)] \qquad (j=1,2,,\cdots,N) \quad (6)$$

$$\bar{\boldsymbol{\phi}}(j):=[r(t+1),r(t),y(t),\cdots,y(t-n_y+1), w(t-1),\cdots,w(t-n_u)] \quad (7)$$

$$\boldsymbol{K}(j):=[K_P(t),K_I(t),K_D(t)], \quad (8)$$

where N denotes the number of data.

[STEP 2] Calculate distance and select neighbors' data.

Distance between query $\bar{\boldsymbol{\phi}}(t)$ and $\bar{\boldsymbol{\phi}}(j)$ is calculated by using the following $\mathcal{L}_1$–norm with some weights:

$$d\left(\bar{\boldsymbol{\phi}}(t),\bar{\boldsymbol{\phi}}(j)\right)=\sum_{l=1}^{m_y+n_u+1}\left|\frac{\bar{\boldsymbol{\phi}}_l(t)-\bar{\boldsymbol{\phi}}_l(j)}{\max\bar{\boldsymbol{\phi}}_l(m)-\min\bar{\boldsymbol{\phi}}_l(m)}\right|. \quad (9)$$

$$(j=1,2,,\cdots,N)$$

$\bar{\boldsymbol{\phi}}_l(j)$ denotes the lth element of query $\bar{\boldsymbol{\phi}}(j)$. $\max\bar{\boldsymbol{\phi}}_l(m)$ is a maximum lth element in database. In contrast, $\min\bar{\boldsymbol{\phi}}_l(m)$ is a minimum lth element. In addition, the number of neighbors' data k are selected, which data are based on smallest distance d.

[STEP 3] Calculate control parameters.

Control parameters are calculated by using the following linearly weighted average (LWA):

$$\boldsymbol{K}(t)=\sum_{i=1}^{k}w_i\boldsymbol{K}(i), \quad \sum_{i=1}^{k}w_i=1, \quad (10)$$

where w_i is the weight corresponding to the i th information vector $\bar{\boldsymbol{\phi}}(i)$ in the selected neighbors. It is calculated by following equation:

$$w_i=\frac{1/d_i}{\sum_{i=1}^{k}1/d_i}. \quad (11)$$

In order to calculate effective control parameters, an off-line learning method is described in next section.

4.3. *Fictitious Reference Iterative Tuning: FRIT*

Fig. 3 shows a block diagram of the FRIT[4]. FRIT is a scheme to calculate control parameters directly from closed-loop data which are input $w_0(t)$, output $y_0(t)$ and $e_0(t) = \tilde{r}(t) - y_0(t)$.

$$\Delta w_0(t) = K_I e_0(t) - K_P \Delta y_0(t) - K_D \Delta^2 y_0(t) \quad (12)$$

Therefore, $\tilde{r}(t)$ is derived as follows:

$$\tilde{r}(t) = [\Delta w_0(t) + K_P \Delta y_0(t) + K_I y_0(t) + K_D \Delta^2 y_0(t)]/K_I. \quad (13)$$

In addition, user set a desired reference model expressed by following equation:

$$\tilde{y}_m(t) = \frac{z^{-1}P(1)}{P(z^{-1})}\tilde{r}(t), \quad (14)$$

where $\tilde{y}_m(t)$ is reference model output and $P(z^{-1})$ is user-specified polynomial.

4.4. *Off-line learning method in Data-Driven Control scheme by using FRIT*

In this section, an off-line learning method is described by using FRIT. At first, the number of neighbors' data k is selected and $\boldsymbol{K}^{old}(t)$ is calculated by equation (10) using closed-loop data $w_0(t)$ and $y_0(t)$. Next, the following steepest descent method is utilized to modify the control parameters:

$$\boldsymbol{K}^{new}(t) = \boldsymbol{K}^{old}(t) - \boldsymbol{\eta}\frac{\partial J(t+1)}{\partial \boldsymbol{K}(t)} \quad (15)$$

$$\boldsymbol{\eta} = [\eta_P, \eta_I, \eta_D],$$

where $\boldsymbol{\eta}$ denotes the learning rate and $J(t+1)$ is defined as following error criterion:

$$J(t) := \frac{1}{2}\epsilon(t)^2 \quad (16)$$

$$\epsilon(t) := y_0(t) - \tilde{y}_m(t), \quad (17)$$

The each partial differential of equation (15) are developed as follows:

$$\left.\begin{aligned}
\frac{\partial J(t+1)}{\partial K_P(t)} &= \frac{\partial J(t+1)}{\partial \tilde{y}_m(t+1)}\frac{\partial \tilde{y}_m(t+1)}{\partial \tilde{r}(t)}\frac{\partial \tilde{r}(t)}{\partial K_P(t)} \\
&= \frac{\epsilon(t+1)P(1)\Delta y_0(t)}{K_I^{old}(t)} \\
\frac{\partial J(t+1)}{\partial K_I(t)} &= \frac{\partial J(t+1)}{\partial \tilde{y}_m(t+1)}\frac{\partial \tilde{y}_m(t+1)}{\partial \tilde{r}(t)}\frac{\partial \tilde{r}(t)}{\partial K_I(t)} \\
&= \frac{\epsilon(t+1)P(1)\Gamma(t)}{K_I^{old}(t)^2} \\
\frac{\partial J(t+1)}{\partial K_D(t)} &= \frac{\partial J(t+1)}{\partial \tilde{y}_m(t+1)}\frac{\partial \tilde{y}_m(t+1)}{\partial \tilde{r}(t)}\frac{\partial \tilde{r}(t)}{\partial K_D(t)} \\
&= \frac{\epsilon(t+1)P(1)\Delta^2 y_0(t)}{K_I^{old}(t)}
\end{aligned}\right\}, \quad (18)$$

Where $\Gamma(t)$ is given by following equation:

$$\Gamma(t) = -\Delta w_0(t) - \{K_P(t) + K_D(t)\}y_0(t) + \{K_P(t) + 2K_D(t)\} - y_0(t-1) - K_D(t)y_0(t-2). \quad (19)$$

Therefore, equation (15) and (18) show that control parameters can be learned off-line by using closed-loop data.

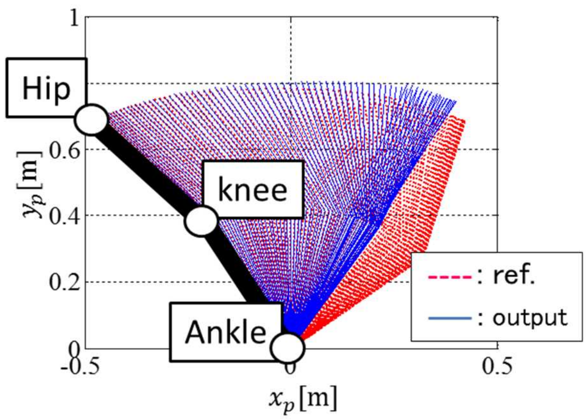

Fig. 4. Walking trajectories by using fixed PID controller as primary controller.

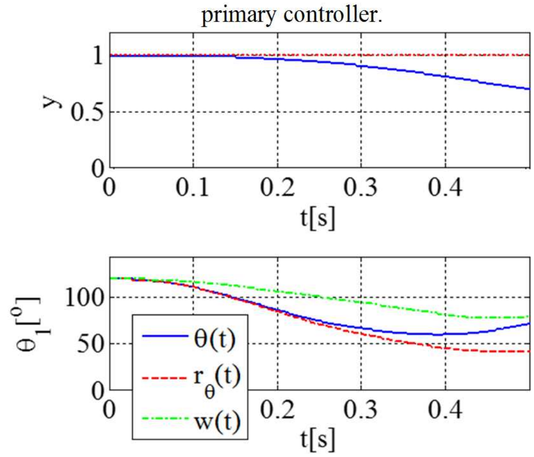

Fig. 5. Trajectories of Kansei signal $y(t)$ and ankle angle $\theta_1(t)$ corresponding to Fig. 4.

5. Numerical Example

In this section, the effectiveness of the proposed scheme is verified. The physical parameters[5,6] in Fig. 2 are set as follows: $I_1 = 0.44[\mathrm{m/s^2}]$, $I_2 = 0.72[\mathrm{m/s^2}]$, $m_1 = 3.26[\mathrm{kg}]$, $m_2 = 7.00[\mathrm{kg}]$, $L_1 = 0.42[\mathrm{m}]$, $L_2 = 0.42[\mathrm{m}]$, $l_1 = 0.24[\mathrm{m}]$, $l_2 = 0.24[\mathrm{m}]$, $g = 0.98[\mathrm{m/s^2}]$, $\boldsymbol{\eta} = [10^4, 10^{-3}, 10^4]$.

Fig. 4 shows the walking trajectories corresponding to Fig. 2 by using fixed PID controller as primary controller.

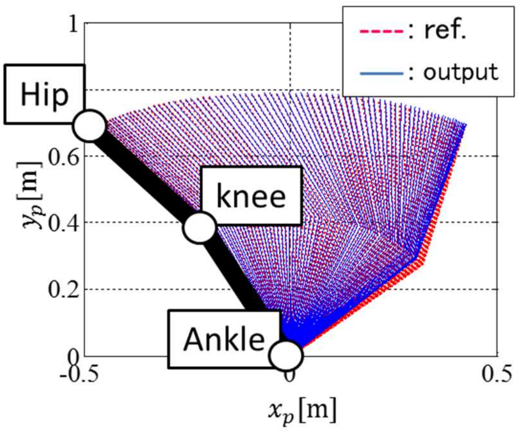

Fig. 6. Walking trajectories by using the proposed scheme.

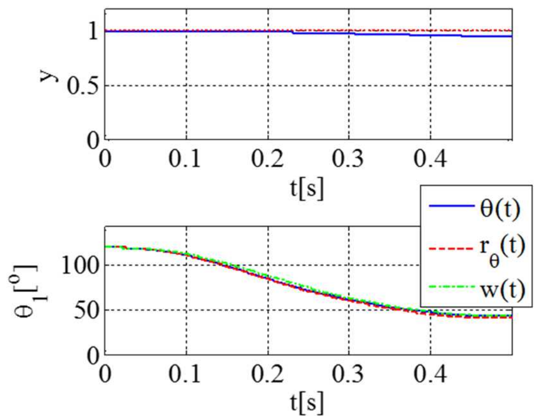

Fig. 7. Trajectories of Kansei signal $y(\mathrm{t})$ and ankle angle $\theta_1(\mathrm{t})$ corresponding to Fig. 6.

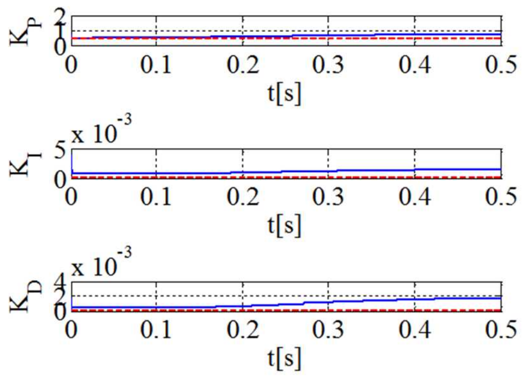

Fig. 8. Trajectories of PID gains corresponding to Fig. 6.

The dotted red line denotes the reference walking trajectory of brain. Walking support is not well in Fig. 4 because the blue solid line does not follow red reference signal. Therefore, the Kansei signal $y(t)$ is not kept around 1 in Fig. 5. Furthermore, fixed PID controller cannot estimate the reference signal well because $w(t)$ does not follow $r_\theta(t)$.

On the other hand, walking trajectories of Fig. 6 by using the proposed scheme is better than Fig. 7. The effectiveness of the proposed scheme is shown by keeping almost $y(t) = 1$ in Fig. 7. The estimated reference signal $w(\mathrm{t})$ is almost same as $r_\theta(\mathrm{t})$ using a data-driven controller and PID gains in Fig. 8 are changed effectively.

6. Conclusion

In this paper, the field of welfare equipment is focused and the scheme based on the data-oriented Kansei feedback has been proposed in order to support each people adaptively. In the proposed scheme, reference signal of a brain can be estimated by using a data-driven controller and it can support walking well. The proposed scheme has been verified by numerical example. In the future, experimental result will be considered.

We are particularly grateful for the assistance given by COI STREAM (Center of Innovation Science and Technology based Radical Innovation and Entrepreneurship Program).

References

1. T. Yamamoto and K. Takao and T. Yamada, “Design of a Data-Driven PID Controller”, *IEEE Trans on control systems Technology*, **17**(1) (2009) 29–39.
2. S. Yamamoto, "Development of Ankle Foot Orthosis for Hemiplegic Patients Based on Gait Analysis (in Japanese)", *The Journal of Japanese Physical Therapy Association,* Vol.39, No.4, pp.240-244 (2012)
3. G. T. Fechner, “Elements of Psychophysics”, New York: holt, Rinehart and Winston (1966)
4. S. Soma, O. Kaneko and T.Fujii, “A New Approach to Parameter Tuning of Controllers by Using One-Shot Experimental Data: A Proposal of Fictitious Reference Iterative Tuning (in Japanese)”, *Trans. of the Institute of systems, Control and Information Engineers*, **17**(2) (2004) 528–536.
5. W. T. Dempster: ``Space Requirements of the Seated Operator", WADC(1955)
6. I. P. Herman: “Physics of the Human Body: Biological and Medical Physics, Biomedical Engineering”, Springer-Verlag GmbH & CO. KG(2007)

Parameter Estimation of a Skill Evaluation Model

Kazuo Kawada
Department of Technology and Information Education, Hiroshima University,
1-1-1 Kagamiyama, Higashi-Hiroshima, Hiroshima 739-8524, Japan
E-mail: kawada@hiroshima-u.ac.jp

Toru Yamamoto
Division of Electrical, System and Mathematical Engineering, Hiroshima University,
1-4-1 Kagamiyama, Higashi-Hiroshima, Hiroshima 739-8527,Japan
E-mail: yama@hiroshima-u.ac.jp

Abstract

In this study, the aim is to construct a "teacher-student model" for optimal skill acquisition. To support the optimal skill acquisition, modeling and estimation of an individual learning process are very important. The first-order system with time delay is introduced as an individual learning process model based the control engineering approach. These system parameters included in the skill evaluation model are estimated by using a real-coded genetic algorithm. In order to evaluate the effectiveness of the proposed scheme, it is employed for the parts classification task.

Keywords: Skill evaluation model, Teacher-student model, Learning process, First-order system, Real-coded genetic algorithm, Parameter estimation.

1. Introduction

In order to effectively promote skill acquisition in the learning and the work, it is necessary to grasp the learning situation of individual learners and workers and to appropriate support based on the learning situation. From the initial learning performance, if the future learning process can be predicted based on individual learning characteristics, the optimum learning support according to individuals can be performed. In response to that problem, the modeling was proposed in which skill evaluation was regarded as "first order + time delay" system in the control engineering[1]. The meaning of each parameters of the time constant T, time delay L and system gain K in the model of skill evaluation model was considered. However, it has not been studied how to estimate parameters of skill evaluation model from initial learning data. In this paper, the estimate method of the skill evaluation model is proposed by using real-coded genetic algorithm[2] (GA) from measured trial data. In addition, the results of estimating the parameters of the skill evaluation model from the initial learning performance data are also discussed.

2. Parameter Estimation of Skill Evaluation Model

2.1. *Fitness value considering characteristics of skill evaluation model*

In order to estimate parameters of the skill evaluation model, it is necessary to eliminate variations in task execution time. Such variations can be divided into two factors: task factors and learner's factors[3,4]. Variations due to task factors are changed due to the order of tasks to be started from among many tasks. On the other hand, the variation due to the learner's factors changes due to accidental delay in execution time or trial and error. Therefore, the estimation of the skill evaluation model excluding learner's factor variations is considered using "part classification task" with small variations due to the task factors.

2.2. *TKL model*

As a requirement of the skill evaluation model, the following is necessary.

1) It is exponential.

2) The parameters can be determined individually.

Generally, the controlled object given in the higher order system is described as the "first-order + time delay" system, and the control system is designed by rough system characteristics. In this paper, it is difficult to make the skill evaluation model strict. However, if the reference is set at the learning start, it can be represented by the model shown in Fig. 1.

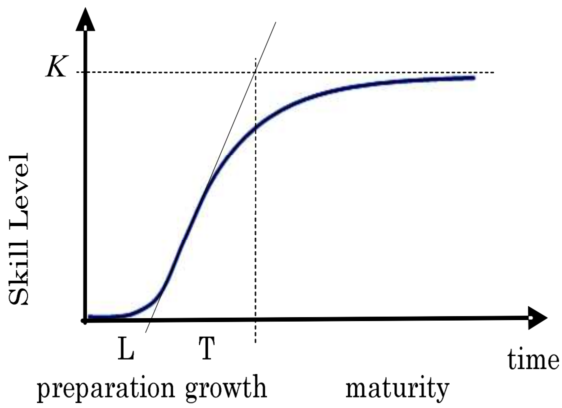

Fig. 1 Skill levels and learning time.

"First order + time delay" system (*TKL* model) is described in the following equation.

$$G(s) = \frac{K}{1+Ts}e^{-Ls} \tag{1}$$

where *T* denotes the time constant, *K* denotes the system gain, and *L* denotes the time delay. The method to calculate these parameters (*T*, *K* and *L*) from measured trial data.

The procedure for obtaining *T*, *K* and *L* from the measured trial data is as follows.

[1] Measure each response time $T_R[1\cdots n]$ from 1 time to *n* times.

[2] a, b and c included in the following Eq.(2) are calculated by the real-coded GA. The estimated response time required for the *n*-th task is as follows:

$$\hat{T}_R[n] = \hat{a} + \hat{b}e^{-ct[n]}. \tag{2}$$

where $t[n]$ represents the real learning time from 1 time to *n* times, and is expressed by the following equation.

$$t[n] = \sum_{i=1}^{n}(T_R[i] - \hat{a}) \tag{3}$$

T_L is the time obtained by subtracting a such as preparation from the Eq.(3), and denotes the response time contributing to the learning effect.

[3] Calculate T, K and L by the following equation, using a, b and c obtained using the real-coded GA.

$$T = \frac{1}{c}, \tag{4}$$

$$K = e^{-ct[1]}, \tag{5}$$

$$L = T_R[1] - a \tag{6}$$

3. Parameter Estimation using Genetic Algorithm

The parameters of skill evaluation model a, b and c are arranged as cells included in a string, whose structure is shown in Fig. 2. These parameters included in the string are given by real values. The real-coded GA is employed, which is explained as follows.

(i) Initialization

The generation number G is set, and the initial individuals are produced with random real-codes within the initial domain which is set in advance. Here, the number of population is set as N.

(ii) Selection

The fitness value $f(l)$ is calculated which is given by

$$f(l) = 1/\{1 + \sum_{t=1}^{t_{end}}\{\hat{T}_R(k) - T_R(k)\}^2. \tag{7}$$

where $\hat{T}_R$ and T_R respectively denote the learning time and the estimated learning time by the parameters of skill evaluation model a, b and c. Each individual P_l is arranged in order, based on the fitness value. Then, α percent individuals with superior fitness values are selected, and saved in the next generation.

(iii) Crossover

The $(100-\alpha)$ percent remaining are generated by the crossover. Two individuals, P_a and P_b are chosen from among the superior α percent, and new individuals P_c and P_d are generated by employing the following procedure:

$$P_c(i) = P_{\text{sup}}(i) - \frac{|P_a(i) - P_b(i)|}{4}, \qquad (8)$$

$$P_d(i) = P_{\text{sup}}(i) + \frac{|P_a(i) - P_b(i)|}{4} \qquad (9)$$

where P_{sup} in Eq.(8) and Eq.(9) refers to the individual with the superior fitness value, *i.e.*, P_a or P_b. Note that this procedure is employed for every cell included in P_a and P_b.

(iv) Mutation

Of all individuals which are randomly selected and given by the crossover, β percent are chosen and replaced with randomly determined values within the initial domain.

(v) Update

The procedure from (i) through (iv) is repeated for generations.

This procedure is summarized in Fig. 3.

4. Experimental Results for Part Classification Task

The parameters T, K and L of the skill evaluation model of the parts classification are calculated and considered. The fourteen kinds of parts shown in Fig. 4 were placed in the mixed state, and tasks for classifying the same parts were prepared. The number of each part is shown in Table 1. The subject was a university student, and he had no experience of executing parts classification task. Subject took 3 minutes break and between each task, and carries out the total of 11 tasks and measured the time required for each task. The execution results in shown in Table 2. It is reduced to the required time 310[s] at the first work and 185[s] at the 11th task. The skill level is the time obtained by subtracting the minimum required time a from the response time in each task in Table 2, and the learning time to each task is the skill level added.

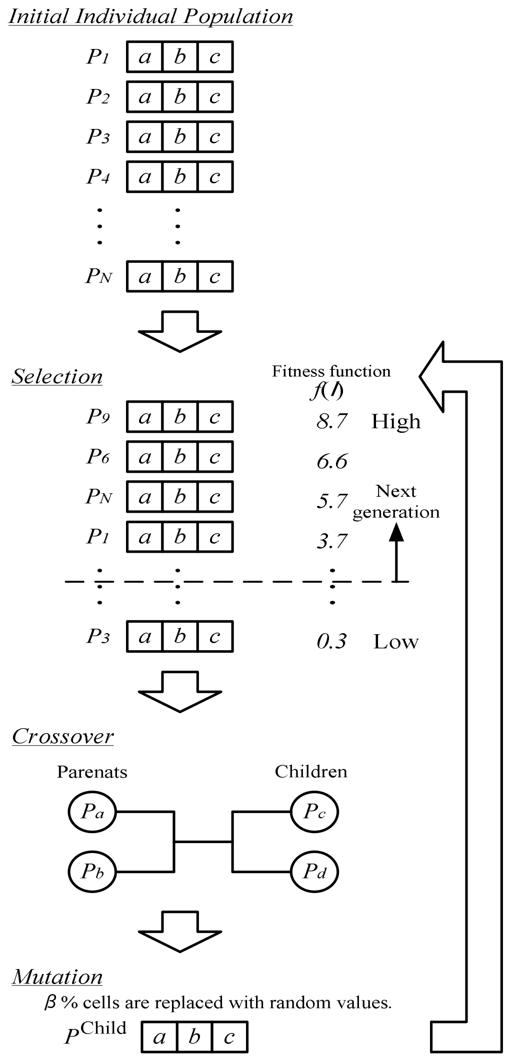

Fig. 3 Calculation flow of the evolutionary computation.

a, b and c were searched by using the real-coded GA, $a = 0.13$, $b = 238$ and $c = 0.0017$ were obtained. T, K and L were obtained from Eq.(4)-Eq.(6), and $T = 588$, $K = 176$ and $L = 178$ were obtained by using these values a, b and c. Fig.5 is shown from these T, K and L.

Next, Fig.6 shows the relationship between the initial learning point and the estimated parameters. From this figure, T, K and L are almost estimated at the initial learning 4 points.

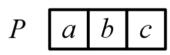

Fig. 2 Structure of the GA string.

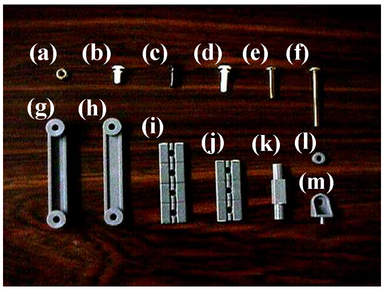

Fig. 4 Parts to be classified.

Table 1 Number of parts.

Fastener Components	Number
(a)	20
(b)	20
(c)	20
(d)	20
(e)	10
(f)	10
(g)	10
(h)	20
(i)	10
(j)	5
(k)	20
(l)	20
(m)	20

Table 2 Number of task and response time.

Number of Task	Response Time[s]
1	310
2	262
3	262
4	224
5	209
6	216
7	188
8	190
9	185
10	181
11	185

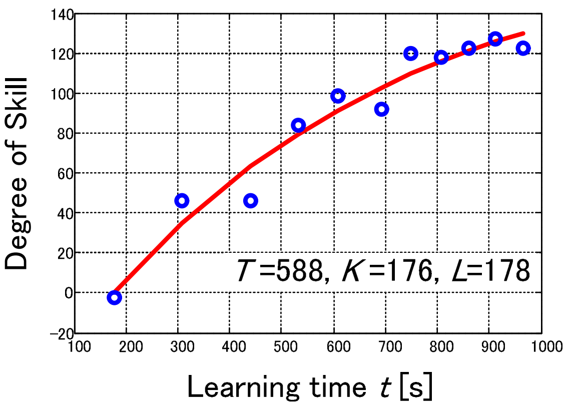

Fig. 5 Estimated skill evaluation model.

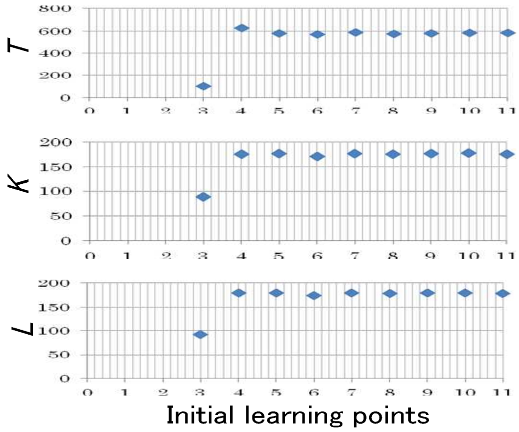

Fig. 6 Relationship between initial learning points and estimated parameters.

5. Conclusion

In order to realize an optimum learning support system by individual skill evaluation in the learning process, the validity of the skill evaluation model based on the control engineering approach was discussed. Next, it applied to the classification task of parts, calculated T , K and L of the parameter of the skill evaluation model, examined it and showed its effectiveness. In the future, it will be applied to the computational learning etc. and plan to develop the learning support system.

This work was supported by JSPS KAKENHI Grant Numbers JP16K12760, JP16H02921.

References

1. M. Nagamatsu, T. Usuzaka, K. Kawada, T. Yamamoto and, Y. Yamane: Consideration on a Model between Teacher and Student Based on Control Engineering Approach, *IEEJ Transactions on Electronics, Information and Systems*, Vol.134, No.10,(2014) pp.1537-1542. (in Japanese)
2. R. Loren and D. B. Benson (eds.), *Introduction to String Field Theory*, 2nd edn. (Springer-Verlag, New York, 1999).
3. M. F. Mason, M.I. Norton, J.D. Van Horn, D.M. Wegner, S.T. Grafton, and C.N. Macrae: Wandering Minds: The Default Network and Stimulus-Independent Thought, *Science*, 315,(2007) pp.393-395.
4. W. Hasenkamp, C.D. Wilson-Mendenhall, E. Duncan, L.W. Barsalou, Mind wandering and attention during focused meditation: A fine-grained temporal analysis of fluctuating cognitive states, *Neuroimage*,59,(2012) pp.750-760.

Human Skill Quantification for Excavator Operation using Random Forest

Hiromu Imaji
Graduate School of Engineering, Hiroshima University,
1-4-1, Kagamiyama, Higashihiroshima City, Hiroshima, 739-8527, Japan
E-mail: imaji-hiromu@hiroshima-u.ac.jp
http://www.hiroshima-u.ac.jp

Kazushige Koiwai, Toru Yamamoto
Institute of Engineering, Hiroshima University,
1-4-1, Kagamiyama, Higashihiroshima City, Hiroshima, 739-8527, Japan
E-mail: koiwaik@hiroshima-u.ac.jp, yama@hiroshima-u.ac.jp
http://www.hiroshima-u.ac.jp

Koji Ueda, Yoichiro Yamazaki
Global Engineering Center, KOBELCO Construction Machinery CO., LTD.,
2-2-1, Itsukaichikou, Saeki-ku, Hiroshima City, Hiroshima, 731-5161, Japan

Abstract

In the construction field, the improvement of the work efficiency is one of important problems. However, the work efficiency using construction equipment is depend on their operation skills. Thus, in order to increase the work efficiency, the operation skill is required to be quantitatively evaluated. In this study, the Random Forest (RF), one of machine learning method, is adopted as the quantitatively evaluation for the operation skill of construction equipment. Evaluated target is the operation on an excavation to load onto a truck for a hydraulic excavator. The RF learns to classify some states by the pilot of skilled worker's operation. States are defined as 'dig', 'lift', 'dump', 'reposition', and 'idle'. The RF with the learning result of skilled worker is applied to other operator's operation. It is revealed that the ratio of 'idle' is related to their skill.

Keywords: human skill, machine learning, random forest, hydraulic excavator

1. Introduction

In the field of construction industry, the application of Information and Communication Technology (ICT) for construction equipment has been proceeded to improve the productivity, which is called 'i-Construction' in Japan.[1] However, work efficiencies of some construction equipment depend on operation skills for each operators. Therefore, it is necessary to establish a method to evaluate the operation skills so that it is possible to improve the productivity in the field of construction industry.

In previous studies, the human skill evaluation based on the engineering approch[2] has been proposed and the evaluation of operation skills based on interviews has been investigated.[3] However, these methods focus on the qualitative evaluation only and it is difficult to utilize them to improve the productivity.

In this paper, a quantification method of operation skills for construction machines based on classifications of operation state using the Random Forest (RF) is proposed. The proposed method is applied to the excavator operation.

RF is a kind of machine learning methods proposed by Leo Breiman in 2001.[4] RF is constructed by some decision tree. Since the decision tree is an aggregate of branching rules, it is widely used to perform data mining for the certain classification problems because the learning result is more readable than other machine learning methods.[5,6] Moreover, RF has the lower computational cost for the classification.

2. Proposed method

2.1. *Classification of decision tree*

The learning data for the decision tree is comprised of a set X and a set Y. The set X consists of feature vectors, $\boldsymbol{x}_i$, which are one-dimensional vectors included the feature of data. The set Y consists of natural number, y_i, which are labels for the classification. Those formula are shown by:

$$X = \{\boldsymbol{x}_i | i = 1,2,\dots,n\}, \quad \boldsymbol{x}_i = \{x_{ij} | j = 1,2,\dots,m\} \quad (1)$$

$$Y = \{y_i | i = 1,2,3,\dots,n\}(y_i = 1,2,3,\dots,K), \quad (2)$$

where n is defined as the number of training data, m is defined as the dimensions of the feature vector and K is defined as the number of labels. A set of training data, T is defined as follows:

$$T = \{t_i | i = 1,2,3,\dots,n\}, \quad t_i = \{\boldsymbol{x}_i, y_i\}. \quad (3)$$

2.1.1. *Training procedure*

The set of initial training data is shown as T_0. The branch part is expressed as a node N_l, and the initial node is N_0. The learning procedure is shown for each step below.

[Step 1-1] Sampling feature vector

The sampled feature vector given as follow:

$$\widehat{\boldsymbol{x}}_i = \{x_{ij} | j \in J\}, \quad (4)$$

where J is a set of $\widehat{m}$, whose components are natural numbers selected randomly without overlap among $1,2,3,\dots,m$.

[Step 1-2] Determination of branching condition

$\bar{J}$ is defined as the selected index of feature vector element. c is defined as the threshold that threshold that divide the training data into two. The selected index, $\bar{J}$, and the threshold, c, have the following conditions:

$$\bar{J} \in J \quad (5)$$

$$\min(x_{i\bar{J}}) < c \le \max(x_{i\bar{J}}) \quad (6)$$

T is divided into a set T_1 with $x_{i\bar{J}} \le c$ and a set T_2 with $x_{i\bar{J}} > c$ .Then, $\bar{J}$ and c which minimize the following $\Phi(T, T_i)$ are obtained.

$$\Phi(T, T_i) = I(T) - \sum_{k=1}^{2} P(T_k|T) I(T_k) \quad (7)$$

$$I(T) = 1 - \sum_{k=1}^{K} P^2(C_k|T) \quad (8)$$

here $P(A|B)$ is the ratio of elements A in B. C_k is a set of t_i with label k. $\hat{J}$, and $\hat{c}$ are obtained with the state of minimized $\Phi(T, T_i)$. Further, nodes N_{l_1} and N_{l_2} are generated for T_1 and T_2.

[Step 1-3] Save training data

$\hat{J}$, $\hat{c}$, l_1, l_2, and T are saved as training data of N_l.

[Step 1-4] End judgment

When T_1 or T_2 do not satisfy the following termination condition shown below, Step 1-1 is repeated with $T_{1,2} \to T$, $l_{1,2} \to l$.

Termination condition:

(i) T_1 or T_2 has a only single label.

(ii) The number of data in the data set is less than or equal to a certain value.

(iii) The certain depth is achieved at a branch.

2.1.2. *Classification procedure*

N_{l_1} or N_{l_2} is called the child node. The feature vector of validation is $\bar{\boldsymbol{x}} = \{\bar{x}_j | j = 1,2,\dots,m\}$. l is initialized with 0.

[Step 2-1] Confirm existence of child nodes

If there is a child node in N_l, step 2-2 is performed. Otherwise step 2-3 is performed.

[Step 2-2] Go to the child node

If $\bar{x}_{\hat{J}} \le \hat{c}$, step 2-1 is performed with N_{l_1} again, otherwise step 1 is performed with N_{l_2} again.

[Step 2-3] Output of results

The label $\hat{y}$ with the largest number of data is the output at T of N_l.

2.2. *Random Forest*

The scheme of random forest is shown in Fig. 1.

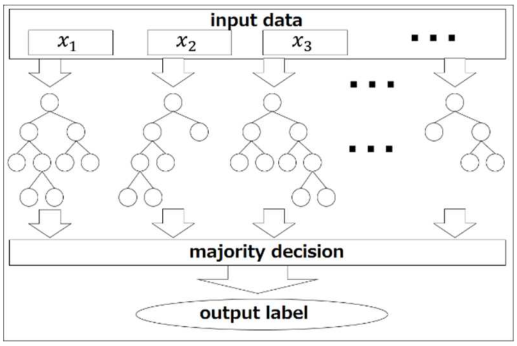

Fig. 1 Scheme of Random Forest

2.2.1. Training of Random Forest

RF is composed of a plurality of decision trees. Therefore, RF needs to generate training data of decision trees. It is assumed that training data is given to RF as Eq. (1) and (2). Thus, a training data of the decision tree in RF is given as follows:

$$\hat{X} = \{\boldsymbol{x}_i | i \in I\}, \hat{Y} = \{\hat{y}_i | i \in I\}, \tag{9}$$

where I is a set of $\hat{n}$, whose components are natural numbers selected randomly without overlap among $1,2,3,\ldots,n$. The data sets expressed by (9) is generated for the number of decision trees and used for training each decision tree. The overlapping between data of decision trees is allowed.

2.2.2. Quantification

N is defined as the total number of decision trees. L is defined as the number of decision trees outputting the specific label. The ratio of L in N is shown as Q, below:

$$Q = \frac{L}{N}, \tag{10}$$

The result of ratio can express the quantification.

3. Experiment Evaluation

3.1. *Experimental device*

The experiment focused on the quantification of the operation skill by the hydraulic excavator. As shown in Fig. 2, it is known that the general work of loading dump of earth and sand with a hydraulic shovel is classified into

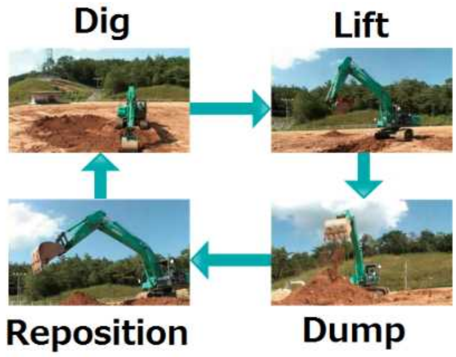

Fig. 2 General hydraulic excavator excavation work

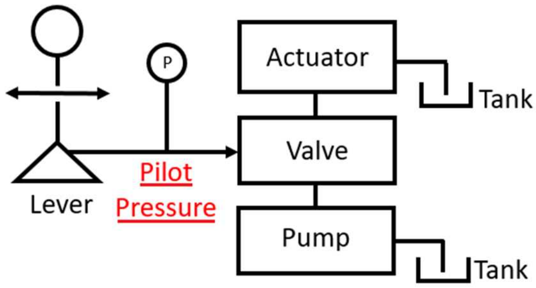

Fig. 3 Pilot Pressure

four states of "dig", "lift", "dump" and "reposition". This study classify the state of work into 5 state, which are above states with “idle”. The “idle” state shows no operation. The operation of the hydraulic excavator is composed of four operations of "bucket", "arm", "boom", and "swing". These input signals of operations were acquired as pilot pressures. The pilot pressure is the input pressure to the valve corresponding to the lever operation amount. A simple configuration diagram of the hydraulic system is shown in Fig. 3. In this paper, eight types of pilot pressures is adopted as the elements of the feature vector to be used for RF, bucket dig / dump, boom up / down, arm pull / push and right turn / left turn.

3.2. *Experimental procedure*

The experimental procedure in this paper is shown below.

[Step 1] RF learn labels of 5 states by pilot pressures of a skilled worker.

[Step 2] Using the Result of Step 1, operation data of unskilled worker, general worker, and skilled worker is classified. At this time, the ratio of the predicted label is evaluated.

Ta ratio of the “idle” state is related to the skill level.

3.3. *Evaluation results*

Table 1 shows parameters of the proposed method. Table 2 shows the result of quantification, that is the ratio of decision trees with the "idle" state. Table 3 shows the result of training with 50 times using the same input / output data. This result shows the the validity of RF. The ratio of decision trees with "idle" is getting bigger from the skilled worker to the unskilled worker in Table 1. The operation that have the larger difference, dump motion, is extracted in Fig. 4-6. The general worker has the single operation with the “idle” state around 1900 step in Fig. 5. The unskilled worker has the shortage of the operation of dump and arm push. The pilot pressure does not reach to 80% or more. Thus, “idle” ratio represents the lack of operation in the work.

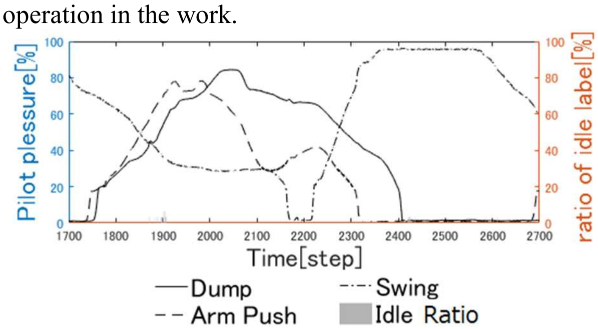

Fig. 4 Part of pilot pressure by skilled worker

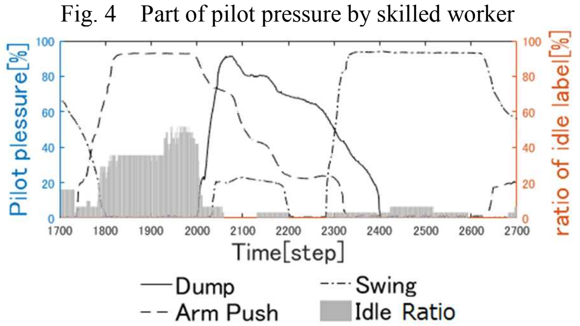

Fig. 5 Part of pilot pressure by general worker

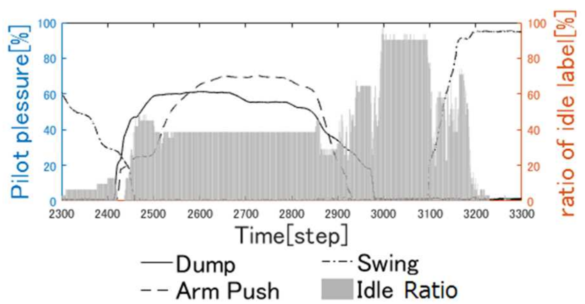

Fig. 6 Part of pilot pressure by unskilled worker

Table 1 parameters of experiment

Step of training data [step]	4309
Step of verification data	4000
Number of decision tree	31
Number of sampling data for decision tree	1436
Number of sampling feature for decision tree	3

Table 2 Ratio of idle

worker	Skilled	General	Unskilled
Area Ratio [%]	0.09	5.32	13.7

Table 3 Verification result of RF significance

worker	Skilled	General	Unskilled
average	0.15	3.45	13.3
Variance	2.92×10^{-5}	1.48×10^{-2}	2.06×10^{-2}
Max	0.26	6.74	15.9
Min	5.00×10^{-2}	1.70	10.5

4. Conclusion

This paper has proposed a quantification method of operation skills in excavation work of a hydraulic excavator based on RF. The paper also clarified the lack of operation by observing the proportion of decision trees in the RF that determined the operation state to be in the "idle" state. As the future work, other state are classified by using internal state and output. Moreover, the proposed method can be utilized to improve the work efficiency.

References

1. T. Kakizaki, i-Construction: On productivity improvement of construction site, *Monthly construction (Japan)*, 60(1) (2016) 6-9.
2. K. Koiwai, Y. Liao, T. Yamamoto, T. Nanjo, Y. Yamazaki, and Y. Fujimoto, Feature extraction for excavator operation skill using CMAC,Journal of *Robotics and Mechatronics*, 28(5) (2016) 715-721.
3. Y. Kawazoe, K. Enomoto, J. Matsumoto, S. Okabe, and S. Handa, Acquisition of Human Operator’s Skills and Dexterity using Neural Network: Automatic Generation of Neural Controller from Chaotic Time Series Data during Stabilizing Control of an Inverted Pendulum, *Proc. of 29th SICE Symposium on Intelligent Systems*, (2002) 217-222.
4. L Breiman, Random Forests, *Machine Learning*, 45(1) (2001) 5-32.
5. J. Kim, J. Lee, and Y. Lee, Data-mining-based coronary heart disease risk prediction model using fuzzy logic and decision tree, *Healthcare Informatics Research*, 21(3) (2015) 167-174.
6. X. Wang, X. Liu, W. Pedryc, and L. Zhang, Fuzzy rule based decision trees, *Pattern Recognition*, 48(1) (2015) 50-59.

Marker Recognition System for Localization of the Rover on the Lunar Space

Na-Hyun Lee
Dep. of Electronic Eng., Pusan National University, Jangjeon-dong, Geumjeong-gu
Busan, 609-735, Republic of Korea

Jang-Myung Lee
Dep. of Electronic Eng., Pusan National University, Jangjeon-dong, Geumjeong-gu
Busan, 609-735, Republic of Korea

E-mail: nahyun7379@pusan.ac.kr, jmlee@pusan.ac.kr
www.pusan.ac.kr

Abstract

This paper proposes a marker realization system for rover localization in the Lunar environment. CPU used in the space environment is not as sensitive to changes of the surrounding environment differently from normal CPU, but it has a lower performance. So it is necessary to use an algorithm reduced amount of computation. In order to reduce the amount of computation on the rover, we propose a rover driving algorithm based on marker recognition. It makes possible to explore the Lunar by using the low- performance CPU. For implementing this algorithm, we performed a marker detection test, and then extracted the center point coordinate of the marker by using Canny Edge Detection and Circular Hough Transform.

Keywords: rover, Lunar space, marker, localization.

1. Introduction

The universe is a vast, still unknown space, and an environment that requires continuous exploration. For stable exploration in specialized environments, many techniques required like a rover localization and obstacle avoidance. So exploration rovers have various sensors, but generally use a vision sensor because it can directly obtain images. Vision sensor usage is various depending on which camera used, how many cameras used, where attached in rover, which algorithm used.

The image processing algorithm for localization in the space environment was mainly used Visual Odometry method using Optical Flow. In this algorithm, feature points are extracted from previous image and matched feature points extracted next image. Matching is the process of searching for the same feature points from two images. The movement amount and direction of rover was measured through position changing of the detected feature points on the image. This method has an advantage that it can localize with only the front images. However, because this algorithm uses difference of previous and current images, if the rover moves too fast or the time interval for taking pictures is too long, the numbers of identical feature points presented in both pictures decrease, so matching accuracy is reduced. For preventing this, it is necessary to take pictures at a short time interval and to process them. It leads increment of computation amount, and as a result, high performance CPU is required.

CPUs used in space have very low performance and capacity compared with general CPUs. Nonetheless, people use CPU for space because it is insensitive to environment changes. General CPUs are extremely sensitive to change of the temperature, and weak to radiation. Lunar and Mars have intensive difference of

temperature more than 100℃. Also, Lunar doesn't have atmosphere, and Mars has very little. So Lunar and Mars will receive the solar radiation much more directly than Earth. In this way, the space has many environmental changes. It is the reason that people use the CPUs for space. But its performance is very poor and expensive. Improving the performance and capacity of CPU for space becomes a costly burden, so an algorithm with a small amount of computation is required.
In this paper, we propose a new rover driving algorithm using a low-performance CPU and marker.

2. Rover driving algorithm based on marker recognition

Rover driving algorithm proposed in this paper is possible to localization and obstacle recognition nevertheless using low-performance CPU. Because of using a low-performance CPU, the vision computation is not processed on the rover itself, but on the earth after transmitting. Then, a rover movement command is transmitted from the earth to the lunar. In this process, a communication delay of about 7 minutes occurs. So it is impossible to perform rover's moving and transmitting at the same time. Also, distance of moving command should not be short. Therefore, the proposed rover driving algorithm needs image processing algorithm that is not affected by previous images.

In this paper, localization algorithm using marker recognition is proposed. It can recognize the marker and get the coordinate of the marker from only current image. By using the position which the marker is attached and depth value obtained by the stereo camera, the horizontal distance between lander and rover can be known. And by using the number of pixels between two points extracted by the marker and the actual distance between two points, it is possible to know the angle between the rover and the marker.

But this method also has a problem. Rover drives in direction far from lander, but rover needs to see the lander for taking pictures of the marker. In other words, the direction of the camera is opposite to the direction of the rover's driving. In this case, it can't confirm whether the obstacles are present forward. In order to solve this problem, we propose a method that the camera shoots 360 degrees at intervals of 15 degrees while rover is stopped. After shooting, pictures are transmitted to the earth and processed on the earth. In order to shoot 360 degrees, it is possible to confirm the presence of obstacles by grasping the situation of the front and the surroundings and to acquire the current position through marker recognition from backward image both.
For implementation this algorithm, first, marker detecting process and extracting process of the coordinates are required. Second, It is required that the process of obtaining the horizontal distance between lander and rover by acquiring the depth value using the stereo camera. Third, it needs to integrate the coordinates of the images and the coordinates of the rover. In the next chapter, we will deal with the image processing algorithm that we used for detecting and recognizing the marker.

3. Image Processing Algorithm

In this paper, edges are detected from the image and the marker is detected by recognizing a circle in the edge image. Marker detecting algorithm used in this paper consists of Canny Edge Detection and Circular Hough Transform.

3.1. *Edge detection*

Canny algorithm used in this paper is widely used for practical edge detection. Canny algorithm process consists of 5 steps.

Step 1: Color conversion
Step 2: Gaussian smoothing
Step 3: Calculation of the image gradient
Step 4: Non-maximum suppression of the grad value
Step 5: Edge determination and connection

In step 1, color of the image was converted to the gray image. In step 2, filtering processing is performed with the converted grayscale image. This filtering is Gaussian smoothing. It is necessary to smooth images for removing the noise before edge detection. In step 3, calculating the gradient is performed. To calculate the image gradient, Canny edge detection algorithm selects a 2×2 neighboring area to get the magnitude and direction the gradient. In step 4, in order to get sharper edges, Non-maximum suppression is performed. Canny method use the 3×3 neighboring area to compare a pixel with its two adjacent pixels along the gradient direction. If a pixel is

bigger than the two adjacent have, the pixel will not change. Otherwise, the pixel will change to 0. In step 5, the edges are finally determined and connected.
Typeset sub-subheadings in medium face italic and capitalize the first letter of the first word only. Section numbers to be in Roman.

3.2. *Circular Hough Transform*

Hough Transform (HT) is usually used for the recognition of contour and shapes from the images.
Circular Hough Transform (CHT) is one of the effective approaches used nowadays for the detection of circles arcs and finding the center of the circles. CHT normally use geometric and Hough region as shown in Fig. 1. Every point in the geometric region of the original circle edges generates a circle in a Hough space region. The circles in the Hough region meet most at a point (x', y') that will correspond to the point (x, y) in the geometric region of the original images. In other words, the point that overlap most in the Hough region is (x', y'), and this point is center point of circle.

The parametric equation for circle in the (x', y') space is shown in Eq. (1).

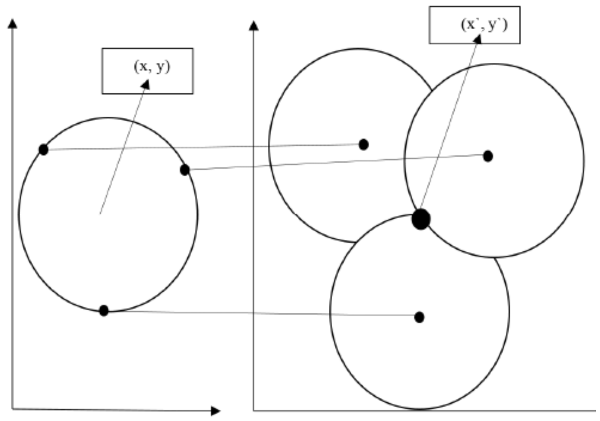

Fig. 1. Geometric region(x, y), Hough Region(x', y')

$$\left(x-x'\right)^2+\left(y-y'\right)^2=r^2 \tag{1}$$

If edge point in the geometric region is (a, b), radius is shown in Eq. (2).

$$\sqrt{\left|x'-\mathrm{a}\right|^2+\left|y'-\mathrm{b}\right|^2}=r \tag{2}$$

4. Marker Detection Experiment

Marker detection experiment executed in this paper was performed to confirm that the marker detection doing well and that coordinates can be acquired from images in normal circumstances. We use the small marker with H written in a circular frame. The thickness of the marker line is 1cm, and the radius of the circle based on outer boundary is 7.5cm (radius of the circle based on inner boundary is 6.5cm). Fig. 2. indicates the shape and size of the marker. Please provide a shortened running head (not more than four words, each starting with a Capital) for the title of your paper. This will appear with page numbers on the top right-hand side of your paper on odd pages.

The image was taken at a distance of 3m in the corridor of the building. And the marker was attached to the wall

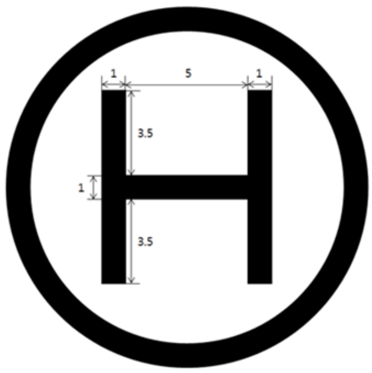

Fig. 2. The shape and size of the marker

surface. Fig. 3. indicates the captured image and the imaging area of camera is 1024×768 pixels. Edge detection was performed from the captured image by using Canny algorithm. Then marker was found from the detected edge image by using Circular Hough Transform and extracted the center coordinate. Fig. 4. indicates result image of Canny Edge Detection. Fig. 5. indicates result image of Circular Hough Transform. Table 1. indicates extracted center coordinate of the marker.

Fig. 3. The captured image

Fig. 4. Result of Canny Edge Detection

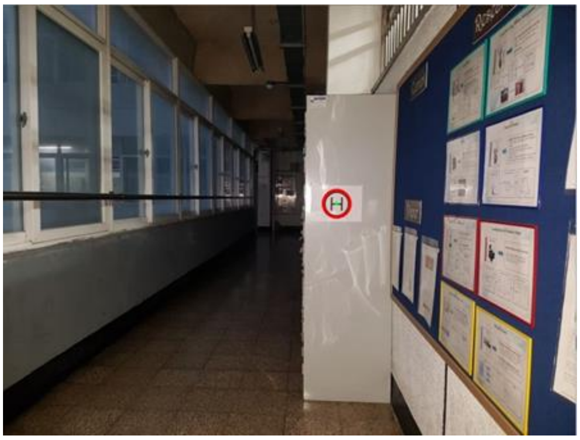

Fig. 5. Result of Circular Hough Transform

Table 1. Extracted center coordinate of the marker

	x	y
extracted center coordinate	596	354

5. Conclusion

In this paper, we propose a driving algorithm of Lunar exploring rover though marker recognition using low-performance CPU. We carried out the marker detecting experiment and extracted center coordinate of the marker. As a result of the experiment, it was confirmed that the marker was well recognized at a distance of 3m even for small size marker. Since it is possible to attach a large marker to the actual lander, it is expected to be able to recognize at far distance.

Acknowledgements

This research was financially supported by the Ministry of trade, Industry and Energy(MOTIE), Korea Institute for Advancement of Technology(KIAT) through the Robot Business Belt Development Project(A012000009), This research is supported by the MOTIE (Ministry of Trade, Industry & Energy).
This research was supported by the Lunar Exploration Program through the KARI grant funded by the MSIP (No. SR16022)

References

1. Hyun-Seop Lim, Dong-Hyuk Lee, and Jang-Myung Lee, *Moving Object Following by a Mobile Robot using a* Single Curvature Trajectory and Kalman Filters, (*Journal of Institute of Control, Robotics and Systems*, 2013)
2. Shi Guiming, Suo Jidong, Remote Sensing Image Edge-Detection Based on Improved Canny Operator (*IEEE International Conference on Communication Software and Networks*, 2016).
3. Miaomiao Zhao, Hongxia Liu and Yi Wan, An Improved Canny Edge Detection Algorithm Based on DCT (*Second International Workshop on Computer Science and Engineering*, 2009).
4. Muhammad Awais, Ibrahima Faye, Nicolas Walter, Mohamad Naufal Saad, Automatic Removal of Auto Fluorescence Device Part Using Circular Hough Transform (*IEEE Student Symposium in Biomedical Engineering & Sciences*, 2015).

Dynamic Model and Finite-Time SMC and Backstepping Control of a Mobile-Manipulator System

Seong-Ik Han
Dep. of Electronic Eng., Pusan National University, Jangjeon-dong, Geumjeong-gu
Busan, 609-735, Korea Republic
Hyun-Uk Ha
Dep. of Electronic Eng., Pusan National University, Jangjeon-dong, Geumjeong-gu
Busan, 609-735, Korea Republic
Jang-Myung Lee
Dep. of Electronic Eng., Pusan National University, Jangjeon-dong, Geumjeong-gu
Busan, 609-735, Korea Republic
E-mail: skhan@pusan.ac.kr, hyunuk.ha@gmail.com, jmlee@pusan.ac.kr
www.pusan.ac.kr

Abstract

A mobile manipulator was designed by combining three-wheeled mobile robot equipped with the DC motor and three-links manipulator equipped with dynamixel motor. The kinematic relation and dynamic model were built via nonholonomic constraint and Euler-Lagrange equation. For the decoupled model of this system, adaptive finite-time controllers sliding mode controller (SMC) and backstepping controller were designed respectively to obtain fast tracking response. Simulation and experimental results show the efficacy of the proposed control scheme.

Keywords: Mobile-manipulator, Finite-time sliding mode control, Finite-time backsteppping control.

1. Introduction

The mobile-manipulator system has more freedom for robot works and then it has drawn more attention recently. However, it's modeling is difficult due to nonholonomic constraint of mobile platform and coupling between mobile platform and manipulator. The kinematic and dynamic coupled model for three-wheeled mobile robot and three-link manipulator system is derived using nonholomonic constraint and Euler-Lagrange equation. SMC [1],[2] and backstepping control [3] are frequently applied to control robot system but these controllers are derived based on the infinite-time stability theorem. Therefore, the convergence time is generally slow and fast response is not guaranteed. Finite-time control term [4],[5] is inserted in both controls to improve convergence time of the mobile robot and manipulator. In addition, the system parameter and uncertainty are obtained by estimation for them via adaptive observers. This leads to complex structure of the whole control system. An assumed parameter feedforward compensator is introduced to compensating unknown parameters and uncertainty.

Simulation for the decoupled mobile platform and manipulator was carried out to show the efficacy of the proposed control scheme.

2.1Description of the Mobile-Manipulator

In this section, the dynamic equations of a three-wheeled mobile manipulator system are derived using the Euler-Lagrange equation. The derived dynamics are modified from the relationship of forces acting on the body and links, and constraints between the wheel and contact surface without considering the Lagrange multiplier method, which is used to solve the nonholonomic constraint problems of mobile robots. The two-wheeled mobile manipulator is shown in Fig. 1,

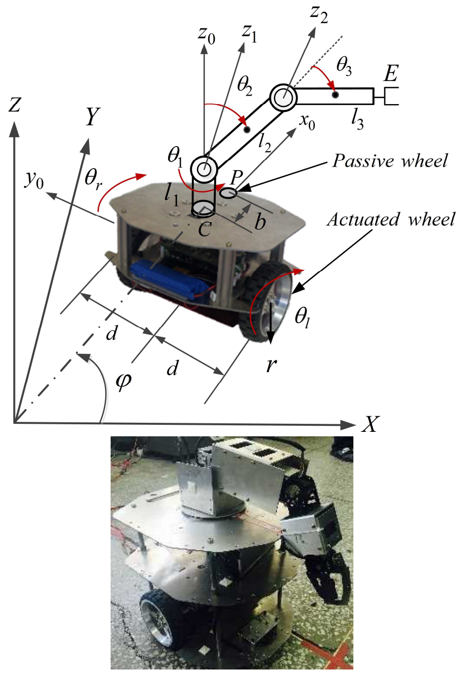

Fig. 1 Schematic diagram and photograph of the three-link and three-wheeled mobile manipulator

where variables are defined as follows: τ_r, τ_l are the torques of two wheels; τ_1, τ_2, τ_3 are the torques of the joint1, 2 and 3; θ_r, θ_l are the rotation angle of the left and right wheel of the mobile platform, respectively; v , φ are the forward velocity and the rotation angle of the mobile platform, respectively; θ_1 is the rotation angle of the link 1 with respect to z_0 axis; θ_2, θ_3 are the rotational angle of the link1 and link 2 with respect to z_1 and z_2 axis, respectively; $m_p = 5kg, m_w = 0.58kg, m_1 = 0.5kg, m_2, m_3$ are the masses of the mobile platform, wheel, link 1, link 2, and link 3, respectively; $I_p, I_{z1}, I_{z2}, I_{z3}$ are the moment of inertia of the mobile platform, link 1, link 2, and link 3, respectively; I_w is the moment of inertia of each wheel; $d = 0.145m$ the distance between the point P and wheels; $R = 0.075m$ is the radius of the wheels; $l_1 = 0.1m, l_2 = 0.2m, l_3 = 0.1m$ are the lengths of the link 1, link 2, and link 3; r_1, r_2, r_3 are the distance between joints and the center of mass of links.

.

For expression simplicity, abbreviations for $s\theta = \sin\theta$, $c\theta = \cos\theta$, and $\theta_{12} = \theta_1 + \theta_2$ are introduced. By selecting the generalized coordinates are selected as $q = [q_v \ q_m]^T = [x \ y \ \varphi \ \theta_1 \ \theta_2 \ \theta_3]^T$, where $q_v = [x \ y \ \varphi]^T$ and $q_m = [\theta_1 \ \theta_2 \ \theta_3]^T$. Total kinematic energy can be expressed as:

$$
\begin{aligned}
T &= \frac{1}{2}(m_0 + m_1)(\dot{x}^2 + \dot{y}^2) + \frac{1}{2} I_o \dot{\varphi}^2 + \frac{1}{2} I_{z1} \left(\dot{\varphi} + \dot{\theta}_1\right)^2 \\
&+ \frac{1}{2} m_2 [\dot{x} - r_2 \dot{\theta}_2 s\theta_2 c_{\varphi\theta_1} - r_2 (\dot{\varphi} + \dot{\theta}_1) c\theta_2 s_{\varphi\theta_1}]^2 \\
&+ \frac{1}{2} m_2 [\dot{y} - r_2 \dot{\theta}_2 s\theta_2 s_{\varphi\theta_1} + r_2 (\dot{\varphi} + \dot{\theta}_1) c\theta_2 c_{\varphi\theta_1}]^2 \\
&+ \frac{1}{2} I_{z2} [(\dot{\varphi} + \dot{\theta}_1)^2 + \dot{\theta}_2^2] + \frac{1}{2} m_3 [\dot{x} - l_2 \dot{\theta}_2 s\theta_2 c_{\varphi\theta_1} \\
&- l_2 (\dot{\varphi} + \dot{\theta}_1) c\theta_2 s_{\varphi\theta_1} - r_3 (\dot{\theta}_2 + \dot{\theta}_3) s\theta_{23} c_{\varphi\theta_1} \\
&- r_3 (\dot{\varphi} + \dot{\theta}_1) c\theta_{23} s_{\varphi\theta_1}]^2 + \frac{1}{2} m_3 [\dot{y} - l_2 \dot{\theta}_2 s\theta_2 s_{\varphi\theta_1} \\
&+ l_2 (\dot{\varphi} + \dot{\theta}_1) c\theta_2 c_{\varphi\theta_1} - r_3 (\dot{\theta}_2 + \dot{\theta}_3) s\theta_{23} s_{\varphi\theta_1} \\
&+ r_3 (\dot{\varphi} + \dot{\theta}_1) c\theta_{23} c_{\varphi\theta_1}]^2 \\
&+ \frac{1}{2} I_{z3} [(\dot{\varphi} + \dot{\theta}_1)^2 + (\dot{\theta}_2 + \dot{\theta}_3)^2]. \qquad (1)
\end{aligned}
$$

The potential energy is obtained as follows:

$$V = m_2 g r_2 \sin\theta_2 + m_3 g \left[l_2 \sin\theta_2 + r_3 \sin(\theta_2 + \theta_3)\right]. \quad (2)$$

Using the Lagrange-Euler equation, the matrix form for the dynamic equations is written as

$$M(q)\ddot{q} + C(q,\dot{q})\dot{q} + G(q) + \tau_d = B\tau - A^T \lambda, \qquad (3)$$

where

$$M(q) = \begin{bmatrix} M_v & M_{vm} \\ M_{mv} & M_m \end{bmatrix}, \quad M_v = \begin{bmatrix} M_{xx} & 0 & M_{x\varphi} \\ 0 & M_{yy} & M_{y\varphi} \\ M_{\varphi x} & M_{\varphi y} & M_{\varphi\varphi} \end{bmatrix},$$

$$M_{vm} = \begin{bmatrix} M_{x\theta_1} & M_{x\theta_2} & M_{x\theta_3} \\ M_{y\theta_1} & M_{y\theta_2} & M_{y\theta_3} \\ M_{\varphi\theta_1} & M_{\varphi\theta_2} & M_{\varphi\theta_3} \end{bmatrix}, \quad M_{mv} = \begin{bmatrix} M_{\theta_1 x} & M_{\theta_1 y} & M_{\theta_1\varphi} \\ M_{\theta_2 x} & M_{\theta_2 y} & M_{\theta_2\varphi} \\ M_{\theta_3 x} & M_{\theta_3 y} & M_{\theta_3\varphi} \end{bmatrix}$$

$$M_m = \begin{bmatrix} M_{\theta_1\theta_1} & 0 & 0 \\ 0 & M_{\theta_2\theta_2} & M_{\theta_2\theta_3} \\ 0 & M_{\theta_3\theta_2} & M_{\theta_3\theta_3} \end{bmatrix}, \quad C(q,\dot{q}) = \begin{bmatrix} C_v & C_{vm} \\ C_{mv} & C_m \end{bmatrix},$$

$$G(q) = [0 \ 0 \ 0 \ 0 \ G_{\theta_2} \ G_{\theta_3}]^T = [G_v \ G_m]^T,$$

$\tau = [\tau_r \ \tau_l \ \tau_1 \ \tau_2 \ \tau_3]^T$, $A^T = \begin{bmatrix} A_v^T & 0 \\ 0 & 0 \end{bmatrix}$, $\lambda = \begin{bmatrix} \lambda_v \\ \lambda_m \end{bmatrix}$, and $B = \begin{bmatrix} B_v & 0_{3\times3} \\ 0_{2\times3} & B_m \end{bmatrix}$. (3) can be rewritten as

$$\begin{bmatrix} M_v & M_{vm} \\ M_{mv} & M_m \end{bmatrix}\begin{bmatrix} \ddot{q}_v \\ \ddot{q}_m \end{bmatrix} + \begin{bmatrix} C_v & C_{vm} \\ C_{mv} & C_m \end{bmatrix}\begin{bmatrix} \dot{q}_v \\ \dot{q}_m \end{bmatrix} + \begin{bmatrix} G_v \\ G_m \end{bmatrix} + \begin{bmatrix} \tau_{dv} \\ \tau_{dm} \end{bmatrix} = \begin{bmatrix} B_v & 0 \\ 0 & B_m \end{bmatrix}\begin{bmatrix} \tau_v \\ \tau_m \end{bmatrix} - \begin{bmatrix} A_v^T & 0 \\ 0 & 0 \end{bmatrix}\begin{bmatrix} \lambda_v \\ \lambda_m \end{bmatrix}, \quad (4)$$

where $M(q)$ is a symmetric and positive definite inertia matrix; $C(q,\dot{q})$ is a matrix of velocity-dependent centripetal and Coriolis forces; $G(q)$ is a gravitational vector; τ_d is a bounded unknown disturbance including unmodelled dynamics and exogenous disturbance; B is the input transformation matrix; and τ is an input torque vector.

Property 1. The inertia matrices M are symmetric, positive definite, and bounded. The norms of C are also bounded.

Property 2. The matrices $\dot{M} - 2C$ are skew-symmetric because of the suitable definition of the corresponding inertia and Coriolis matrix.

Therefore, this modeling method goes through the complex transformation calculation inevitably to remove the Lagrange multiplier. The resulting dynamic equations become complicated as the DOF of the attached manipulator increases.

2.2 *Kinematics of the mobile robot platform*

The nonholonomic constraint for the mobile robot is that the robot can only move in the direction normal to the axis of the driving wheels, i.e., the mobile drives under the condition of pure rolling without slipping. Therefore, the three constraints can be expressed as:

$$\dot{y}\cos\varphi - \dot{x}\sin\varphi = 0, \quad (5)$$

By selecting $q_v = [x \ y \ \varphi]^T$ as the generalized coordinates of the mobile platform, the constraint can be expressed as follows:

$$A_v(q_v)\dot{q}_v = 0, \quad (6)$$

where

$$A_v(q_v) = \begin{bmatrix} -\sin\varphi & \cos\varphi & 0 \end{bmatrix}. \quad (7)$$

The matrix $J(q_v)$ is taken as the basis for the null space of $A(q)$, $J_v^T(q_v)A_v^T(q_v) = 0$, and $J_v(q)$ can be expressed as:

$$J_v(q_v) = \begin{bmatrix} c\varphi & 0 \\ s\varphi & 0 \\ 0 & 1 \end{bmatrix}. \quad (8)$$

A reference to the mobile platform generates a trajectory for the actual platform to follow:

$$\dot{q}_{vr} = J_v(q_v)\chi_{vr}, \quad (9)$$

where $q_{vr} = [x_r \ y_r \ \varphi_r]^T$ denotes the desired time-varying position, orientation trajectory and $\chi_{vr} = [v_r \ \omega_r]^T$ denotes the reference time- varying linear and angular velocity. It is necessary to find the appropriate velocity control law $\xi_{vc} = [v_c \ \ \omega_c]^T$, such that $q_v \to q_{vr}$ as $t \to \infty$. The trajectory tracking problem is to track a reference mobile robot with a posture $q_{vr} = [x_r \ y_r \ \varphi_r]^T$. Therefore, we define the tracking error between the actual and desired posture as:

$$\tilde{q}_v = q_{vr} - q_v = \begin{bmatrix} x_r - x \\ y_r - y \\ \varphi_r - \varphi \end{bmatrix}. \quad (10)$$

The posture tracking error can be expressed as:

$$q_{ve} = \begin{bmatrix} e_x \\ e_x \\ e_\theta \end{bmatrix} = \begin{bmatrix} c\varphi & s\varphi & 0 \\ -s\varphi & c\varphi & 0 \\ 0 & 0 & 1 \end{bmatrix}\tilde{q}_v, \quad (11)$$

where e_x , e_y , and e_φ denote the tangential, normal, and orientation tracking errors of the mobile platform and manipulator, respectively. The error rate can be obtained as:

$$\begin{bmatrix} \dot{e}_x \\ \dot{e}_y \\ \dot{e}_\varphi \end{bmatrix} = \begin{bmatrix} -v + \dot{\varphi} e_y + v_r \cos e_\varphi \\ -\dot{\varphi} e_x + v_r \sin e_\varphi \\ \dot{\varphi}_r - \dot{\varphi} \end{bmatrix}. \tag{12}$$

The target or command velocity is given as:

$$\xi_c = \begin{bmatrix} v_c \\ \dot{\varphi}_c \end{bmatrix} = \begin{bmatrix} v_r \cos e_\varphi + k_x e_x \\ \dot{\varphi}_r + k_y v_r e_y + k_\varphi v_r \sin e_\varphi \end{bmatrix}, \tag{13}$$

where k_x, k_y ,and k_φ are positive constants and $v_r > 0$. This is called the extended kinematic control for mobile platform with link 1. If the perfect velocity tracking is achieved as

$$\xi_{vc} = \begin{bmatrix} v_c \\ \dot{\varphi}_c \end{bmatrix} = \begin{bmatrix} v \\ \dot{\varphi} \end{bmatrix}, \tag{14}$$

the kinematic model is then asymptotically stable with respect to the reference trajectory:

$$q_{ve} = [e_x \quad e_x \quad e_x]^T \to 0 \text{ as } t \to \infty .$$

However, in the proposed model, this kinematic technique is not required and the controller structure is simplified.

3. Design of Finite-Time Controller Design and Stability Analysis

3.1 *Design of a finite-time SMC for a mobile platform*

In (4), the mobile dynamics is separated as follows:

$$M_v \ddot{q}_v + C_v \dot{q}_v + F_v = B_v \tau_v - A_v^T \lambda_v , \tag{15}$$

where $F_v = M_{vm} \ddot{q}_m + C_{vm} \dot{q}_m + \tau_{dv}$. From (28), we have $\ddot{q}_v = J_v \dot{v}_v + \dot{J}_v v_v$. Therefore, (28) can be written as

$$M_v J_v \dot{v}_v + (M_v \dot{J}_v + C_v J_v) v_v + F_v = B_v \tau_v - A^T \lambda . \tag{16}$$

Because of $J_v^T(q_v) A_v^T(q_v) = 0$, multiplying $J_v^T(q_v)$ into the left side of (16) gives

$$M_v' \dot{v}_v + C_v' v_v + F_v' = B_v' \tau_v , \tag{17}$$

where $M_v' = J_v^T M_v J_v$, $C_v' = J_v^T (M_v \dot{J}_v + C_v J_v)$, $F_v' = J_v^T F_v$, and $B_v' = J_v^T B_v$.

Assumption 1. There are constants that satisfy the following boundedness:

$$\|M_v'\| \le \rho_{vm}, \ \|C_v'\| \le \rho_{vc}, \ \|F_v'\| \le \rho_{vf} , \tag{18}$$

where ρ_{vi}, $i = m, c, f$ are positive constants.
Consider the following signal:

$$r_v = v_{vd} - \Lambda_{v1} \int_0^t sig(e_v)^{\gamma_v} d\tau , \tag{19}$$

where $sig(e_v)^{\gamma_v} = [|e_{v1}|^{\gamma_v} sign(e_{v1}), |e_\varphi|^{\gamma_v} sign(e_\varphi)]^T$ and $0 < \gamma_v < 1$ is a constant. We then obtain the following

$$\dot{r}_v = \dot{v}_{vr} - \Lambda_{v1} sig(e_v)^{\gamma_v} . \tag{20}$$

The finite-time sliding mode surface s_v is defined as

$$\begin{aligned} s_v &= v_v - r_v \\ &= v_v - v_{vr} + \Lambda_{v1} \int_0^t sig(e_v)^{\gamma_v} d\tau \\ &= e_v + \Lambda_{v1} \int_0^t sig(e_v)^{\gamma_v} d\tau . \end{aligned} \tag{21}$$

Using (19), (20), and (21), it follows that

$$\begin{aligned} M_v' \dot{s}_v &= M_v' \dot{v}_v - M_v' \dot{r}_v \\ &= -C_v' v_v - F_v' + B_v' \tau_v - M_v' \dot{r}_v \\ &= -C_v' (r_v + s_v) - F_v' + B_v' \tau_v - M_v' \dot{r}_v \\ &= -C_v' s_v - M_v' \dot{r}_v - C_v' r_v - F_v' + B_v' \tau_v . \end{aligned} \tag{22}$$

We define the Lyapunov function as follows:

$$V_v = \frac{1}{2} s_v^T M_v' s_v + \frac{1}{2}(e_x^2 + e_y^2) + \frac{1 - \cos e_\varphi}{k_y} . \tag{23}$$

Considering (24), (39), and property 2, the time derivative of (40) becomes

$$\begin{aligned} \dot{V}_v &= s_v^T M_v' \dot{s}_v + \frac{1}{2} s_v^T \dot{M}_v' s_v + e_x \dot{e}_x + e_y \dot{e}_y + \frac{\dot{e}_\varphi \sin e_\varphi}{k_y} \\ &= s_v^T [-M_v' \dot{r}_v - C_v' r_v - F_v' + B_v' \tau_v] - k_1 e_x^2 \end{aligned}$$

$$-\frac{k_3 v_r \sin^2 e_\varphi}{k_2}$$
$$\leq s_v^T \left(\rho_{vm}\dot{r}_v + \rho_{vc} r_v + \rho_{vf} + B_v' \tau_v\right)$$
$$-k_1 e_x^2 - \frac{k_3 v_r \sin^2 e_\varphi}{k_2}. \quad (24)$$

The control input is specified as

$$\tau_v = \tau_{veq} + \tau_{vr} + \tau_f, \quad (25)$$
$$\tau_{veq} = -B_v'^{-1}\left[-\Lambda_{v2} s_v - \rho_{vm}\|\dot{r}_v\| - \rho_{vc}\|r_v\| - \rho_{vf}\right], \quad (26)$$
$$\tau_{vr} = -\Lambda_{vr} s_v (\|s_v\| + \varepsilon_v)^{-1}, \quad (27)$$
$$\tau_f = -\Lambda_{vf}\, sig(s_v)^{\gamma_v}. \quad (28)$$

where $\Lambda_{vf} = diag(c_{vf}, c_{\varphi f}) > 0$ is a constant matrix.
Substituting (25) into (24), we have

$$\dot{V}_v \leq -\Lambda_{v2} s_v^T s_v - \Lambda_{vr} s_v^T s_v (\|s_v\| + \varepsilon_v)^{-1} - \sum_{i=1}^{2} c_i |s_{vi}|^{\gamma_v + 1}$$
$$-k_1 e_x^2 - \frac{k_3 v_r \sin^2 e_\varphi}{k_2}$$
$$\leq -\Lambda_{v2} s_v^T s_v - \sum_{i=1}^{2} c_i |s_i|^{\gamma_v+1}$$
$$\leq -\lambda_{\min}(\Lambda_{v2}) s_v^T s_v - \lambda_{\min}(c_i)\sum_{i=1}^{2}(|s_{vi}|^2)^{(\gamma_v+1)/2}$$
$$\leq -\frac{2\lambda_{\min}(\Lambda_{v2})}{\lambda_{\max}(\Gamma_v)} V_{v3} - \frac{2^{(\gamma_v+1)/2}\lambda_{\min}(c_i)}{\lambda_{\min}(c_i)} V_{v3}^{\gamma_v}$$
$$\leq -k_{v1} V_{v3} - k_{v2} V_{v3}^{\gamma_v}, \quad (29)$$

where $k_{v1} = \dfrac{2\lambda_{\min}(\Lambda_{v2})}{\lambda_{\max}(\Gamma_v)}$, $k_{v2} = \dfrac{2^{(\gamma_v+1)/2}\lambda_{\min}(c_i)}{\lambda_{\min}(c_i)}$.

Lemma 1: From the definition of finite-time stability [4],[5], the equilibrium point $s = 0$ of is globally finite-time stable; i.e., for any given initial condition $s(0) = s_0$, an extended Lyapunov description of finite-time is given as the following inequality:

$$\dot{V}(s) \leq -\xi_1 V(s) - \xi_2 V^\gamma(s), \quad (30)$$

where $\xi_1 > 0$, $\xi_2 > 0$, and $0 < \gamma < 1$. $V(t)$ converges to an equilibrium point in finite-time t_s given by

$$t_s \leq \frac{1}{\xi_1(1-\gamma)} \ln \frac{\xi_1 V^{1-\gamma}(s_0) + \xi_2}{\xi_2}. \quad (31)$$

Therefore, using Lemma2 and (84), the finite convergence time of the mobile robot is given as

$$t_{vs} \leq \frac{1}{k_{v1}(1-\gamma_v)} \ln \frac{k_{v1} V_v^{1-\gamma_v}(s_{v0}) + k_{v2}}{k_{v2}}. \quad (32)$$

3.2. *Design of a finite-time backstepping controller for a mobile platform*

The state space model of the manipulator from (4) can be expressed as follows:

$$\dot{x}_3 = x_4,$$
$$\dot{x}_4 = M_m^{-1}\left(-C_m \dot{q}_m - G_m - F_{mv} + B_m \tau_m\right),$$
$$y_m = x_3, \quad (33)$$

where $x_3 = [\theta_1, \theta_2, \theta_3]^T$, $x_4 = \dot{x}_3 = [\dot{\theta}_1, \dot{\theta}_2, \dot{\theta}_3]^T$, and $F_{mv} = M_{mv}\ddot{q}_v + C_{mv}\dot{q}_v + \tau_{dm}$.

Assumption 2. There are constants that satisfy the following boundedness:

$$\|M_m\| \leq \rho_{mm}, \ \|C_m\| \leq \rho_{mc}, \ \|G_m\| \leq \rho_{mg}, \ \|F_m\| \leq \rho_{mf}, \quad (34)$$

where ρ_{mi}, $i = m, c, g, f$ are positive constants.
The tracking error and x_4 are written as

$$z_3 = x_3 - y_{mr}, \quad (35)$$
$$z_4 = x_4 - \alpha_3. \quad (36)$$

The following Lyapunov function is defined:

$$V_{m1} = \frac{1}{2} z_3^T z_3. \quad (37)$$

Using (35) and (36), we then have

$$\begin{aligned}\dot{V}_{m1} &= z_3^T \dot{z}_3 \\ &= z_3^T (z_4 + \alpha_3 - \dot{y}_{mr}) .\end{aligned} \tag{38}$$

We specify the finite-time virtual control as follows:

$$\alpha_3 = -c_3 z_3 - \zeta_3 sig(z_3)^{\gamma_3} + \dot{y}_{mr} , \tag{39}$$

where $c_3 = diag(c_{\theta_1}, c_{\theta_2}, c_{\theta_3}) > 0$ is a constant matrix, $\zeta_3 = diag(\zeta_{\theta_1}, \zeta_{\theta_2}, \zeta_{\theta_3}) > 0$ is a constant matrix, $sig(z_3)^{\gamma_3} = \left[|z_{3\theta_1}|^{\gamma_{3\theta_1}} \operatorname{sgn}(z_{3\theta_1}), |z_{3\theta_2}|^{\gamma_{3\theta_2}} \operatorname{sgn}(z_{3\theta_2}), |z_{3\theta_3}|^{\gamma_{3\theta_3}} \operatorname{sgn}(z_{3\theta_3}) \right]$ and $0 < \gamma_3 < 1$ is a constant .

Therefore, we have

$$\dot{V}_{m1} = -c_3 z_3^T z_3 - \zeta_3 |z_3|^{\gamma_3 + 1} + z_3^T z_4 . \tag{40}$$

We redefine the Lyapunov function as follows:

$$V_{m3} = V_{m1} + \frac{1}{2} z_4^T M_m z_4 . \tag{41}$$

We obtain

$$\begin{aligned}\dot{V}_{m3} &= \dot{V}_{m1} + z_4^T M_m \dot{z}_4 + \frac{1}{2} z_4^T \dot{M}_m z_4 \\ &= -c_3 z_3^T z_3 + z_4^T \left(\rho_{mc} \|x_4\| + \rho_{mg} + \rho_{mf} + B_m \tau_m \right. \\ &\quad \left. + \rho_{mm} \|\dot{\alpha}_3\| + z_3 \right) .\end{aligned} \tag{42}$$

Selecting the finite-time control input and adaptive laws as follows:

$$\begin{aligned}\tau_m = B_m^{-1} &\left(-c_3 z_4 - z_3 - \rho_{mm} \|\dot{\alpha}_3\| - \rho_{mc} \|x_4\| - \rho_{mg} \right. \\ &\left. - \rho_{mf} - \zeta_4 sig(z_4)^{\gamma_4} \right) ,\end{aligned} \tag{43}$$

Then, we obtain

$$\begin{aligned}\dot{V}_{m3} &\le -\sum_{i=3}^{4} c_i z_i^T z_i - \sum_{i=3}^{4} \zeta_i |z_i|^{\gamma_i + 1} \\ &\le -k_{m1} V_{m3} - k_{m2} V_{m3}^{\gamma_m} ,\end{aligned} \tag{44}$$

where $k_{m1} = \dfrac{2\lambda_{\min}(c_m)}{\lambda_{\max}(\Gamma_m)}$, $k_{m2} = \dfrac{2^{\gamma_m} \lambda_{\min}(\zeta_i)}{\lambda_{\min}(\zeta_i)}$, and $\gamma_m = \min[(\gamma_i + 1)/2],\ i = 3,4$. Therefore, using Lemma1, the finite convergence time of the manipulator control system is given as

$$t_{ms} \le \frac{1}{k_{m1}(1-\gamma_m)} \ln \frac{k_{m1} V_{m3}^{1-\gamma_m}(z_{m0}) + k_{m2}}{k_{m2}} .$$

4. Simulation Example

To validate the proposed control scheme, the infinite-time backstepping controller (BSC) and finite-time backstepping controller (FBSC) with infinite-time SMC (SMC) and finite-time SMC(FSMC) were designed. Simulation results of each control system for the mobile manipulator system are described in Figs. 2 and 3, where the proposed finite-time control reveals more fast convergence performance than the infinite-time based control sytems.

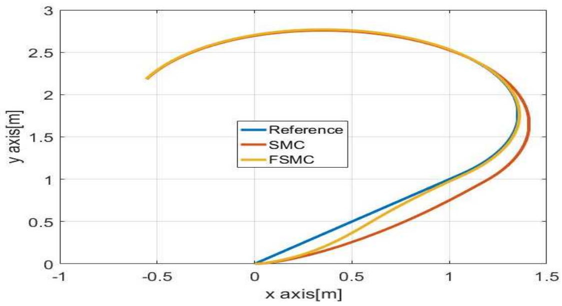

(a)

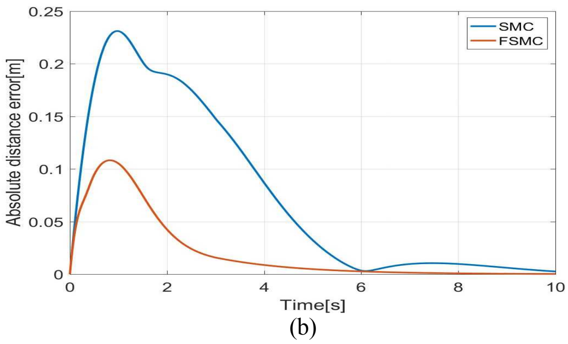

(b)

Fig. 2. Simulation results of the mobile platform. (a) Tracking outputs. (b) Tracking errors.

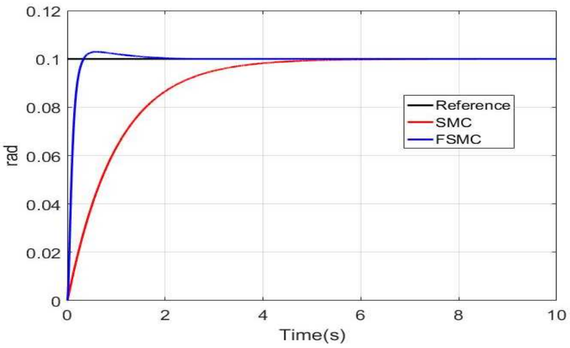

(a)

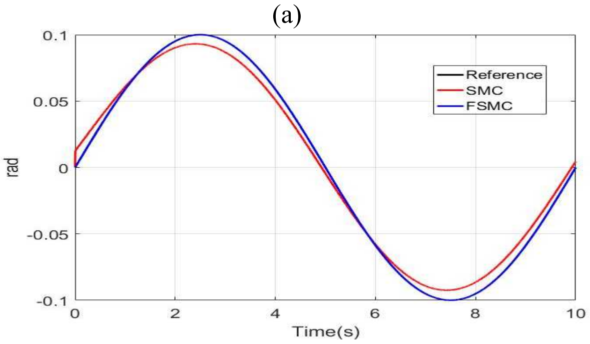

(b)

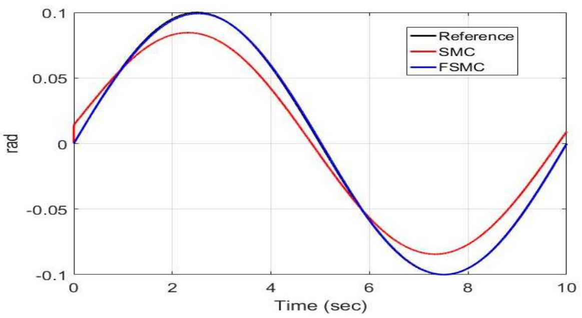

5. Conclusion

Finite-time SMC and backstepping control schemes to guarantee the fast error convergence and small tracking error performance for a mobile-manipulator system are proposed. A finite sliding mode surface and a virtual finite-time error surface are defined to obtain finite-time performance. The finite-time convergence is proved by the finite-time stability analysis of Lyapunov function. Simulation for a mobile manipulator system confirms the theoretical proposal.

Acknowledgements

This work was supported by the National Research Foundation of Korea(NRF) grant funded by the Korea government(MSIP) (NRF-2015R1A2A2A01004457).

References

1. V. I. Utkin, J. Gulder, and J. Shi, Sliding mode control in Electromechanical systems (Taylor & Francis Ltd, 1999).
2. T. Jose, and A. Abraham, Sliding mode control of wheeled mobile robots, *IACSIT Coimbatore Conference*, Singapore, (2012) 17-22.
3. K. Kristic, I. Kanellakopoulos, and P. V. Kokotovic, *Nonlinear and adaptive control design* (Wiley, New York, 1995).
4. S. P. Bhat and D. A, Bernstein, “Finite-time stability of continuous autonomous systems,” *SIAM J. Control Optim.*, **38(3)**, (2000) 751-766.
5. S. Yu, X. Yu, B. Shirinzadeh, and Z. Man, Continuous finite-time control for robotic manipulators with terminal sliding mode, *Automatica*, **41** (2005) 1975–1964.

Bilateral Control of Hydraulic Servo System Based on SMCSPO for 1DOF Master Slave Manipulator

Jie Wang
Department of Mechanical Engineering, Pusan National University, 635-4Jangjeon 2 dong, Geumjeong-gu, Busan, 609-735,South Korea

Karam Dad
Department of Mechanical Engineering, Pusan National University

Min Cheol Lee
School of Mechanical Engineering, Pusan National University
E-mail: wj@pusan.ac.kr, karamdadkallu@gmail.com,mclee@pusan.ac.kr

http://www.pusan.ac.kr

Abstract

In this research reaction force estimation method based on Sliding mode control with sliding perturbation observer (SMCSPO) of a hydraulic servo system for one degree of freedom (DOF) master-slave manipulators is proposed. The reaction force at the end effector of slaver is estimated by sliding perturbation observer (SPO) without using any torque sensor. This research verifies through simulation and experiment that slaver can follow the trajectory of the master device using the proposed bilateral control strategy to give a reference and estimate reaction force from observer.

Keywords: SMCSPO, Bilateral control, Master-Slave, Hydraulic servo system, Nuclear Power Plant.

1. Introduction

There are more than 450 nuclear power plants in the world, 210 in Europe and 24 nuclear power plant in the domestic have been operated. Generally lifetime of a nuclear power plant is 30-60 years, the removal of an aging nuclear power plant is being exaggerated as important problem. 150 nuclear power plant operating had been stopped permanently in 19 countries. 19 nuclear power plants completely dismantled, 100 nuclear power plants are being dismantled and 31 nuclear power plants are due for dismantling in the world [1-2]. Demand for dismantling of nuclear power plant is being continuously increased and the International Atomic Energy Agency (IAEA) predictable the market value of the nuclear facilities dismantling to be about 1 trillion dollar market by 2050 [3].In conventional bilateral control architecture, many studies have used force sensors to detect external force. However, the use of force sensor is the cause of some problems. Robot system with a force sensor is regarded as a two mass resonant system, it is difficult to realize high frequency force sensing [4-5].

Therefore, in this research we use sliding mode control with sliding perturbation observer (SMCSPO) to estimate the reaction force of the slaver and bilateral control of hydraulic servo system for 1DOF master slave manipulators. The reaction force of slaver is estimated by sliding perturbation observer (SPO) without using any sensor.

The remaining part of the paper is organized as follow: Section 2, describe the structure and dynamics of 1DOF hydraulic servo system used in dismantling power plant. In section 3, reaction force estimation method based on sliding mode control with sliding perturbation observer (SMCSPO) is discussed. Section 4, describe the bilateral control between master and slave for 1DOF hydraulic servo system. Section 5, Performance of the estimated reaction force and bilateral control is evaluated by experiments. Section 6, conclude the work.

2. Structure and Dynamics of 1DOF Hydraulic Servo System

Hydraulic servo systems are heavily used in high performance applications such as the machine-tool industry. Examples are material handling, mobile equipment, plastics, steel plants, and automotive testing. In this research the hydraulic actuators of robot for dismantling a nuclear power plant are consist of two hydraulic cylinder and one AC servo motor. Vertical movement required a greater force as compared to horizontal movement in dismantling power plant structure. In this research we use only end effector of 3DOF hydraulic servo system. Size, shape and structure is shown in fig 1 of 1DOF hydraulic servo system used in dismantling nuclear power plant.

Fig. 1 1DOF hydraulic servo system

The dynamics of a robot describe the relationship between forces, torques and motion. The general dynamic equation of a manipulator in free space is described by

$$T = A(\theta)\ddot{\theta} + B(\theta,\dot{\theta}) + g(\theta) \qquad (1)$$

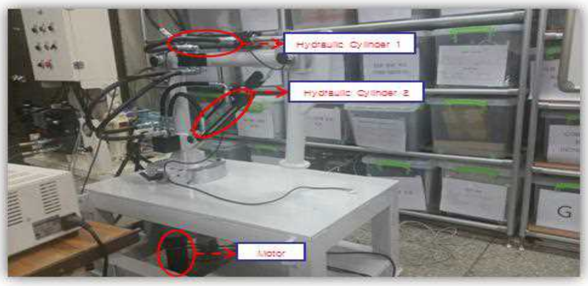

Where θ, $A(\theta)$, $B(\theta,\dot{\theta})$, $g(\theta)$ and T are the vector joint of angles, the mass/inertia matrix, the centrifugal/coriolis torque, the gravity torque in joint space, and the vector of joint torques, respectively. The dynamics equations of each link of hydraulics servo system are as follow

$$(J_{s1}+\Delta J_{s1})\ddot{\theta}_1+(D_{s1}+\Delta D_{s1}+\beta_1)\dot{\theta}_1+0.5M_{s1}L_1 g\sin\theta_1+\tau_{e1}=T_1 \qquad (2)$$

In above equations, J_{s1} is the inertia, D_{s1} is damper, Δ shows the uncertainty of parameters, β_1 is viscosity of cylinder, M_{s1} is mass, L_1 is length, τ_{e1} is reaction torque by contact with environment, T_1 is joint torque of link 1, λ is dynamics effect from link 1, θ_1 is viscosity friction of cylinder 1.

3. Sliding Mode Control with Sliding Perturbation Observer (SMCSPO)

The three links manipulator robot actuator is controlled by sliding mode control (SMC) and reaction force is estimated by sliding perturbation observer (SPO). The governing equation for general second order dynamics with n-degree-of-freedom (dof) is:

$$\ddot{x}_j = f_j(x)+\Delta f_j(x)+\sum_{i=1}^{n}[(b_{ji}(x)+\Delta b_{ji}(x))u_i]+d_j(t)$$

(3)

Where x≜ [X,.. .X_n]^T is the state vector and $Xj \triangleq [xj\ \dot{x}j]^T$. The terms $f_j(x)$ and $\Delta f_j(x)$ correspond to the nonlinear driving terms and their uncertainties. The component b_{ij} and Δb_{ji} represent the elements of the control gain matrix and their uncertainties, while d_j is the external disturbance and u_j is the control input. The terms f_j and b_{ji} are known continuous functions of the state [6]. Estimated perturbation is defined as the combination of all uncertainties.

3.1. *Control Variable Transformation*

Before integrating SO into SMC it is convenient to decouple the control variable using the following transformation [7].

$$f_j(\hat{x})+\sum_{i=1}^{n} b_{ji}(\hat{x})u_i = \alpha_{3j}\bar{u}_j \qquad (4)$$

Where α_{3j} is an arbitrary positive number and $\overline{u}_j$ is the new control variable. The original control vector of general equation is obtained as

$$u = B^{-1}Col[\alpha_{3j}\overline{u}_j - f_j(\hat{x})] \quad (5)$$

Where $u = [u_1 \dots u_n]^T$ and $B = \lfloor b_{ji}(\hat{x}) \rfloor_{n\times n}$. This transformation allows to write the system dynamics as

$$\ddot{x}_j = \alpha_{3j}\overline{u}_j + \psi_j \quad (6)$$

4. Bilateral Control between Master and Slave for 1DOF Hydraulic Servo System

In this research 1DOF hydraulic servo system for master and slave is considered. The dynamics equation of master and slave for hydraulic servo system are described by

$$J_m\ddot{\theta}_m + B_m\dot{\theta}_m = u_m + \tau_h \quad (7)$$

$$J_s\ddot{\theta}_s + B_s\dot{\theta}_s = u_s - \tau_e \quad (8)$$

Where J_m, J_s, u_m and u_s are inertia, position and control input of master and slave of hydraulic servo system, respectively. Action force generated by operator while maneuvering the master device is denoted by τ_h, while reaction force appears when slave device is touching remote environment is defined by τ_e. The structure of bilateral controller is shown in fig. 2.

Fig. 2 Bilateral control structure

Slaver of hydraulic servo system is follow the trajectory of master device when operator operate the master device.

5. Experiments and experimental results

Experiments were performed on 3DOF hydraulic servo system. Master and slave device consist of three links

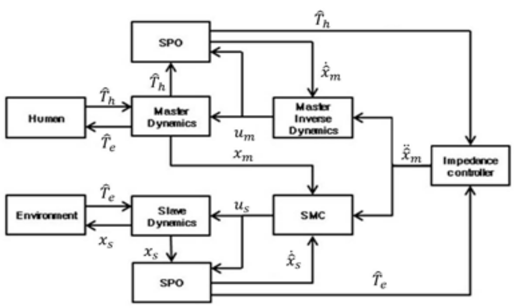

each, in which third link connected with base. We can find the reaction force at the end effector. The whole system for experiment includes master device, slave device and a control system as shown in fig 3.

Fig. 3 System for experiment

5.1. *Experimental results*

The experiment was conducted on a three-link hydraulic servo system. In Fig. 4 shows the experimental result of reference (Master) and end-effector (Salver) trajectories. In Fig. 4 the reference trajectory is shown in blue line and end-effector trajectory shown in red line.

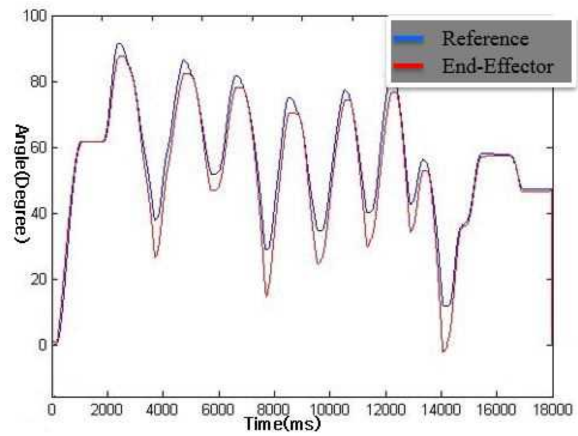

Fig. 4 Experimental result of trajectories

Fig. 5 shows the experimental result of estimated perturbation of end effector.

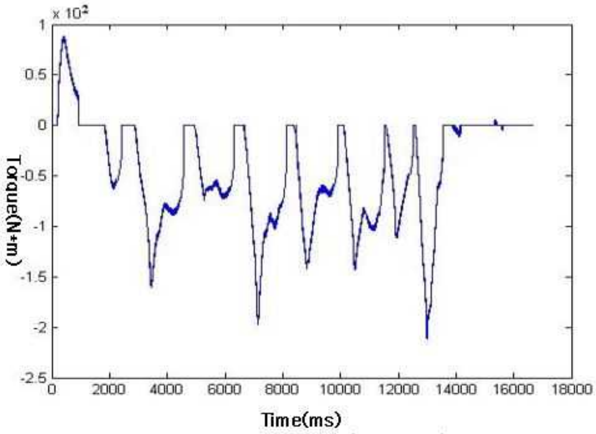

Fig. 5 Estimated perturbation of end-effector

6. Conclusion

This research proposed an estimation method of a reaction force on end effector of one links robot manipulator using SMCSPO without using any sensor. The estimated perturbation showed the uncertainty of dynamics and reaction force. However, it is useful to find the reaction force where the reaction is big enough and not east to use the sensor such as transportation of active uranium in nuclear power plants or disposal of explosive ordnances, remote cutting for nuclear power plant dismantling, debarring, welding and grinding etc. In future research, other factors may also be included to improve the accuracy of force estimation.

Acknowledgements

This section should come before the References. Funding information may also be included here.

References

1. https://www.iaea.org/PRIS/WorldStatistics/OperationalReactorsByCountry.aspx
2. "Development of 21 Core Technologies for Dismantling Nuclear Facilities until 2021," *Korean Prime Minister's Office Press*, 2012.
3. K. M. Kim and J. H. Jang, "Domestic Market Prospect and Core Technology foe Decommissioning of Nuclear Power Plant," *Korean Institute of Construction Engineering and Management Conference Journal*, pp. 37-40, 2013.
4. Y. F. Li and X. B. Chen, "On the Dynamic Behaviour of a Force/Torque Sensor for Robots," *IEEE Transaction Instrumentation and Measurement*, vol. 47, no. 1, pp. 304-308, Feb. 1998.
5. S. Katsura, Y. Matsumoto, and K. Ohnishi, "Analysis and Experimental Validation of Force Bandwidth for Force Control," *IEEE Transaction Ind. Electron.*, vol. 53, no. 3, pp. 922-928, Jun. 2006.
6. H. Elmali and N. Olgac, "Sliding Mode Control with Perturbation Estimation (SMCPE)" *International Journal of Control*, Vol. 56, pp. 923-941,1993
7. M. J. Terra, H. Elmali and N. Olgac, Sliding mode control with perturbation observer, *J. Dyn. Syst. Measurement Control* 119 (1997) 657–665.

Advanced impedance control of haptic joystick for effective mobile robot handling

Gyung-I Choi
Dep. of Electronic Eng., Pusan National University, Jangjeon-dong, Geumjeong-gu
Busan, 609-735, Republic of Korea

Jang-Myung Lee
Dep. of Electronic Eng., Pusan National University, Jangjeon-dong, Geumjeong-gu
Busan, 609-735, Republic of Korea

E-mail: gyungi7379@pusan.ac.kr, jmlee@pusan.ac.kr
www.pusan.ac.kr

Abstract

This paper proposes optimized structure of 6 D.O.F. haptic joystick and tele-operated mobile robot system based on haptic interfaces. Kinematic analysis of specially designed 6 D.O.F. haptic joystick derives the coordinate of end effect. The designed haptic joystick transfers operator's moving command to mobile platform with force controlled coordinate information. Attached ultra-sonic sensors detect nearby obstacles including walls and retransfer the distance between mobile platform and obstacles to the haptic joystick. Attained real-time displacement information controls DC motors between links supporting the handle for effective user handling. Practical simulations and real experiments verified proposed impedance control and its tele-operation system of intelligent haptic joystick.

Keywords: haptic device, tele-operation, mobile platform, impedance control.

1. Introduction

Recently, social needs for the tele-operation have been raised sharply in the field of industry and disaster environment to avoid unexpected blind accident. Tele-operation means communication between master-slave devices from a distance. It is necessary to provide real-time feedback and to develop optimized haptic device for precise tele-operation.

Serial mechanism haptic joystick has universally been used in the industry. Serial mechanism has simple structure and wide workspace, while it has relatively low durability and accuracy. Contrastively, parallel mechanism suits with precise work and force applied to actuator disperse into parallel links. But it is difficult to control in real-time. According to above characteristics, suggested 6 D.O.F haptic joystick designed as combination of serial and parallel mechanisms. The blended mechanism complements each other's defects. Also, end-effect of haptic joystick freely generates movement of 6 D.O.F. for commend parameters.

Ultra-sonic sensors attached to mobile platform detect obstacles and retransfer distance data between the mobile platform and obstacles to haptic joystick. DC motors between links supporting the handle generate virtual impedance, which transfer the distance data to user.

Advanced haptic joystick model is applicable to the industry which requires accurate works in specific environment. In this paper, kinematic of specially designed 6 D.O.F. haptic joystick is analyzed for the coordinate of end effect and simple experiment is preceded using mobile robot as a basic research before it is applied to the industrial robot.

2. Structure Analysis of The 6 D.O.F. Haptic Joystick

The structure of this device is combination of 3 manipulators which has serial joint in parallel as shown in Fig.1 Each of the serial manipulator has 3 D.O.F. that composed of 2 active joints, 1 passive joint and 1 spherical joint. Degree of freedom of 6 D.O.F. serial·parallel mechanism is proved by Gruebler's equation.

3. Kinematic Analysis

The upper platform of hybrid manipulator has been attached between the handle of the joystick and the 3 serial manipulators. When we hold the points generated by the connecting between the upper plate and the serial manipulators as vertices and connect them, we can make the shape of a triangle. The desired end effect is located at the center of this triangle. According to the specially designed manipulator's structural characteristics, kinematic relationship of each parameter can be derived from decoupled analysis of serial manipulator and upper platform.

3.1. *Relative coordinate for kinematic analysis in parallel mechanism*

Fig. 2 - (a) shows the coordinate relationship for the kinematic analysis. Set the reference coordinate system {B} (Base frame) on the center of lower platform and set the coordinate system of end-effector {M} (Moving frame) on the upper platform. When define the position change between these 2 coordinates as vector P_d , it means position of the {M} based on {B}. Define the coordinate of upper platform corner based on {B} as

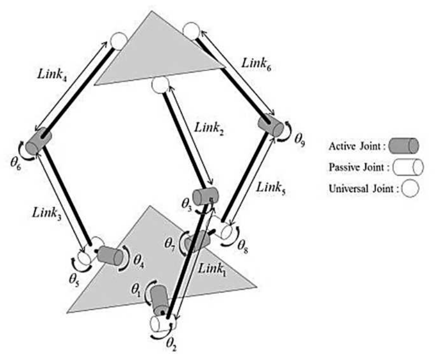

Fig. 1. structure of 6 D.O.F serial· parallel mechanism haptic device.

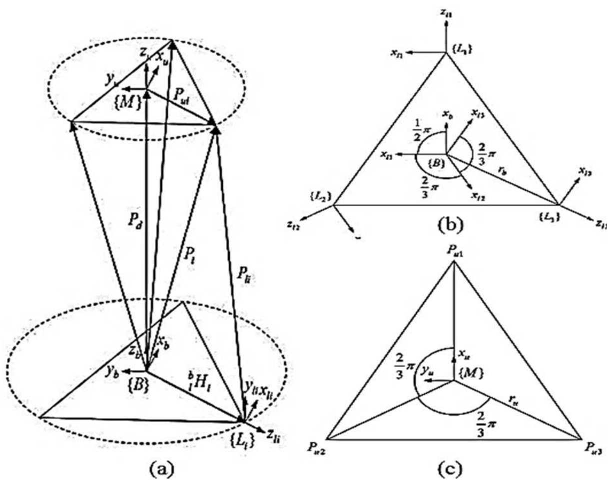

Fig. 2. Coordinate of parallel structure.

vector P_i ($i=1,2,3$) and define the coordinate of upper platform corner based on {M} as vector P_{ui} ($i=1,2,3$). Using relationship between these 2 vectors, define the rotation matrix ${}_b^pR$. Define the reference coordinate system of the serial link as L_i ($i=1,2,3$) , and based on this define the coordinate of upper platform corner as vector P_{li} ($i=1,2,3$). The relationship between {B} and { L_i } is defined as homogeneous transform ${}_l^bH_i$.

Fig. 2-(b) shows the relationship between reference coordinate of lower platform and reference coordinate of each serial link. ${}_l^bH_i$, Conversion relation from reference coordinate of lower platform {B} to serial link coordinate { L_i }, can be expressed as homogenous matrix such as Eq. (1) and its inverse relationship can be expressed as Eq. (2).

$$
\begin{aligned}
{}_b^lH_i &= R(\theta_b, z)R(90, x)T(r_b, z) \\
&= \begin{bmatrix} \cos\theta_{bi} & 0 & \sin\theta_{bi} & r_b\sin\theta_{bi} \\ \sin\theta_{bi} & 0 & -\cos\theta_{bi} & r_b\cos\theta_{bi} \\ 0 & 1 & 0 & 0 \\ 0 & 0 & 0 & 1 \end{bmatrix}
\end{aligned} \tag{1}
$$

$$
{}_l^bH_i = \left({}_b^lH_i\right)^{-1} = \begin{bmatrix} \cos\theta_{bi} & 0 & \sin\theta_{bi} & 0 \\ 0 & 0 & -1 & 0 \\ \sin\theta_{bi} & -\cos\theta_{bi} & 0 & -r_b \\ 0 & 0 & 0 & 1 \end{bmatrix} i \tag{2}
$$

The relationship between P_i and P_{li} obtained using the relative coordinates in Fig. 2 - (c) is shown in Eq. (3) and P_{ui} is derived as Eq. (4).

$$P_i = {}^{0}_{b}H_i P_{li} \quad (3)$$

$$P_{ui} = [r_u \cos\theta_{ui} \quad r_u \sin\theta_{ui} \quad 0]^T \quad (4)$$

3.2. *Kinematic analysis of the haptic joystick*

The coordinate of serial manipulator is as shown in fig. 5 Each of 3 serial manipulators is composed of two links. The position vector P_{li} obtained by Denavit-Hartenberg notation. is shown in Eq. (5).

$$p_{li} = \begin{bmatrix} \cos(\theta_{li})(l_1 \cos(\theta_{2i}) + l_2 \cos(\theta_{2i} + \theta_{3i})) \\ \sin(\theta_{li})(l_1 \cos(\theta_{2i}) + l_2 \cos(\theta_{2i} + \theta_{3i})) \\ l_1 \sin(\theta_{2i}) + l_2 \sin(\theta_{2i} + \theta_{3i}) \end{bmatrix} \quad (5)$$

From given P_{li}, coordinate of upper platform corner P_i is derived as (3) and position of coordinate system of upper platform {M} P_d from coordinate of upper platform corner p_i is derived as (6).

$$P_d = \frac{1}{3}\sum_{i=1}^{3} P_i = \frac{1}{3}\left(P_1 + P_2 + P_3\right) = \begin{bmatrix} x & y & z \end{bmatrix}^T \quad (6)$$

4. Impedance control

Impedance control is the interaction between the manipulator and the environment. Using the analogy to electrical impedance where impedance is the ratio of voltage output to current input, mechanical impedance is the ratio of force output to motion input. In other words, the mechanical impedance is the force resisting to the direction of the applied force. Impedance in a teleoperation system does not appear immediately in the slave device, but through the master device that controls the slave device. The user can acquire the implied information about environment through the master device's impedance information, and instructs the master device to control the slave device based on this information

The lowes-order term in any impedance is the static relation between output force and input displacement, a stiffness. If, in common with much of the current work on robot control, we assume actuators capable of generation commanded forces, T_{act}, sensors capable of observing actuator position, θ, and a purely kinematic relation between actuator position and end-point position, $X = L(\theta)$, it is straightforward to design a feedback control law to implement in actuator coordinates a desired relation between end-point (interface) force, F_{int}, and position, X. Defining the desired equilibrium position for the end-point in the absence of environmental forces (the virtual position) as X_0, a general form for the desired force-position relation is :

$$F_{\text{int}} = K\left[X_0 - X\right] \quad (7)$$

Compute the Jacobian, $J(\theta)$:

$$dX = J(\theta)d\theta \quad (8)$$

From the principal of virtual work :

$$T_{act} = J^t(\theta)F_{\text{int}} \quad (9)$$

The required relation in actuator coordinates is

$$T_{act} = J^t(\theta)K\left[X_0 - L(\theta)\right] \quad (10)$$

5. Simulation

Simulation was performed to verify the workspace of the constructed haptic joystick. Kinematically, both link1 and link2 were chosen equal to 19 cm. Table 1 shows the constraint limits of the angles shown in Fig. 3.

Table 1. Constraint limits of the angles

Angle	Constraint limits
θ_{1i}	$0^\circ \sim 180^\circ$
θ_{2i}	$-60^\circ \sim 160^\circ$
θ_{3i}	$30^\circ \sim 160^\circ$

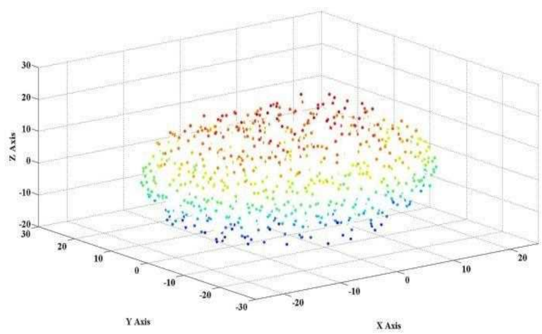

Fig. 3. Workspace of haptic joystick.

6. Experiment

6.1. *Experiment environment*

Fig. 4 is a tele-operation system using a haptic joystick and a mobile robot. The haptic joystick and the mobile robot exchange the data through the bluetooth module. The haptic joystick generates a virtual impedance based on the distance information received through the mobile robot attached ultrasonic sensors and transmits it to the user. The experiment was performed in an environment where obstacles were installed in the traveling path as shown in Fig. 5.

6.2. *Experiment result*

The Fig. 6 is the graph about the relative distance between the mobile robot and the obstacle recognized by the ultrasonic sensor, and the graph in Fig. 5 is the result of the impedance value generated in the joystick. The previous result is the output of the sensor attached to the right side among the three ultrasonic sensors attached the mobile robot, and the other sensors also present the same performance. In graph 6, the ultrasonic sensor outputs a value of 0 if it does not detect any obstacle within 20 cm. Otherwise, the closer to the obstacles, it output the lower value. The impedance value of the graph 7 is maintained at a value of 5 in the normal state, and a higher impedance value is output as the distance from the obstacle becomes closer.

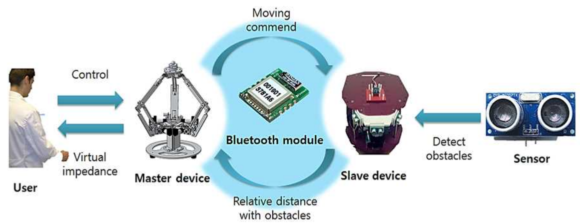

Fig. 4. Tele-operation system using 6D.O.F. haptic joystick.

Fig. 5. Tele-operation system using 6D.O.F. haptic joystick.

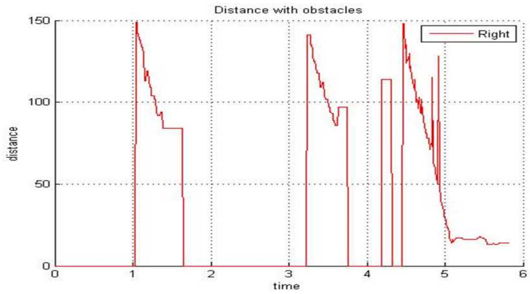

Fig. 6. Obstacle detection distance of right ultrasonic sensor.

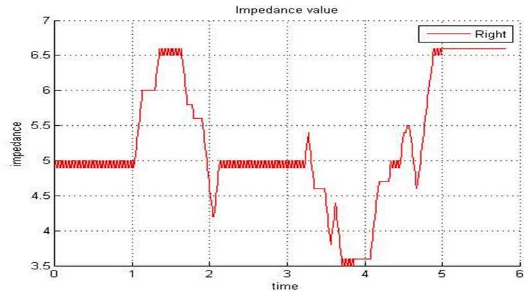

Fig. 7. Impedance value according to distance data.

7. Conclusion

Experimental results show that the impedance value properly changes according to the output value of the sensor, but it is difficult to obtain accurate data due to communication problems such as time delay in data transmission. Therefore, we will focus on this issue in developing a haptic joystick for improved performance.

Acknowledgements

This research was financially supported by the Ministry of trade, Industry and Energy(MOTIE), Korea Institute for Advancement of Technology(KIAT) through the Robot Business Belt Development Project(A012000009)

References

1. Vu, Minh Hung, and Uhn Joo Na. "A new 6-DOF haptic device for teleoperation of 6-DOF serial robots." *IEEE Transactions on Instrumentation and Measurement* 60.11 (2011): 3510-3523.
2. Burns, David T. *Design of a six degree of freedom haptic interface. Diss.* Northwestern University, 1996.
3. Hogan, N., Impedance Control: An Approach to Manipulation, *American Control Conference, 1984* , vol., no., pp.304,313, 6–8 June 1984.

Obstacle Avoidance Method for Electric Wheelchairs Based on a Multi-Layered Non-Contact Impedance Model

Haruna Kokubo, Taro Shibanoki
Ibaraki University, Japan
Takaaki Chin
Hyogo Rehabilitation Center, Japan
Toshio Tsuji
Hiroshima University, Japan

Abstract

This paper proposes an obstacle avoidance method based on a multi-layered non-contact impedance model. The proposed system can calculate a virtual repulsive force before the collision by multi-layered impedance fields covered around the robot. This system therefore regulates desired path to avoid obstacles in a variety of situations. In the experiments, the mobile robot passed through obstacles smoothly, and could stop emergently to avoid the obstacle in front of the robot owing to virtual forces calculated by the proposed model.

Keywords: obstacle avoidance, non-contact impedance, electric wheelchairs, people with disabilities

1. Introduction

According to the World Health Organization (WHO), the population of people with disabilities worldwide accounts for almost 15% and is gradually increasing [1].

Electric wheelchairs and other mobility aids are used to support disabled people in independent living by compensating for lost function. In particular, an electric wheelchair that can be controlled with biosignals such as electroencephalograms (EEGs) and electromyograms (EMGs) has recently attracted attention [2] - [4]. The authors' research group also developed the Cybernetic Human Robot Interface System (CHRIS), which can be used to operate wheelchairs, domestic appliances, video games and other equipment using biosignals [4]. The system has a number of distinctive features, such as adaptability to input signal variations and various input types in line with user requirements. However, these systems can malfunction due to biosignal fluctuations associated with unintended motions. It is also necessary to provide a motion assistance method with these approaches, as obstacle avoidance depends on the operator.

A number of conventional techniques are applied to determine appropriate paths for distinction based on artificial potential fields and fuzzy logic using neural networks and other methods [5], [6]. These systems allow robots to avoid obstacles based on virtual force and so on, but tend to focus only on maintaining the minimum distance necessary for avoidance. The application of such technology to biosignal-controlled electric wheelchairs requires consideration of how to achieve natural movement rather than simple obstacle avoidance.

In this regard, a method known as non-contact impedance control supports natural collision prevention [7] – [9]. The technique can be used to generate virtual external forces that act on the robot based on virtual impedance between the robot and obstacles. (including other robots), which allows the robot to steer away from anything in its path. However, this requires the setting of appropriate parameters for various situations. Additionally, as such approaches are premised on the control of mobile robots, it is necessary to develop a natural obstacle-avoidance method for biosignal-controlled electric wheelchairs.

This paper proposes an obstacle avoidance system for electric wheelchairs based on a non-contact impedance model. The system helps to prevent collisions using mechanical impedance-based covered virtual walls around the robot. It supports smooth avoidance of obstacles and enables collision-preventing emergency stops using virtual walls with different impedance parameters.

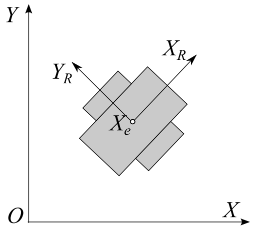

Fig. 1. Kinematics of a mobile robot

2. Control of the mobile robot based on a Multi-Layered Non-Contact Impedance Model

In this study, the mobile robot was compressed into a mass point with two translational degrees of freedom (Fig. 1), and motion planning was performed.

The robot can determine the distance between itself and nearby obstacles using an internal sensor. Multiple virtual walls based on mechanical impedance are used to avoid collision with obstacles via calculation of related virtual external forces.

Figure 2 illustrates the concept of the multi-layered non-contact impedance model. It is considered that P obstacles are present in the direction of movement of the robot, which is surrounded by virtual circles (referred to here as virtual walls) with radii of q_i, $(i = 1, 2, \ldots, I)$ based on a mechanical impedance model.

When the obstacle comes within the ith virtual wall, the norm vector from the wall's surface to the obstacle $d\boldsymbol{X}_o^i \in \Re^2$ is represented as

$$d\boldsymbol{X}_o^i = \boldsymbol{X}_r - q_i \boldsymbol{n}. \tag{1}$$

Here, $\boldsymbol{X}_r$ is the vector of displacement from the center of the sphere (the mobile robot's position) $\boldsymbol{X}_e \in \Re^2$ to the pth obstacle ${}^{(p)}\boldsymbol{X}_o \in \Re^2$ $(p = 1, 2, \ldots, P)$. The direction vector $\boldsymbol{n}$ reflecting the distance between the margin of the virtual wall and the obstacle p is defined as

$$\boldsymbol{X}_r = \boldsymbol{X}_e - {}^{(p)}\boldsymbol{X}_o. \tag{2}$$

$$\boldsymbol{n} = \begin{cases} \frac{\boldsymbol{X}_r}{\|\boldsymbol{X}_r\|}, & \|\boldsymbol{X}_r\| \neq 0 \\ 0, & \|\boldsymbol{X}_r\| = 0 \end{cases}. \tag{3}$$

If the obstacle is inside the virtual wall $(q_{i+1} < \|\boldsymbol{X}_r\| \leq q_i)$, the virtual impedance between the robot and the obstacle causes exertion of a virtual external force on the robot:

$$\boldsymbol{F}_o^i = \begin{cases} \boldsymbol{M}_i d\ddot{\boldsymbol{X}}_o^i + \boldsymbol{B}_i d\dot{\boldsymbol{X}}_o^i + \boldsymbol{K}_i d\boldsymbol{X}_o^i, & q_{i+1} < \|\boldsymbol{X}_r\| \leq q_i \\ 0 & , otherwise \end{cases}. \tag{4}$$

Here, $\boldsymbol{M}_i$, $\boldsymbol{B}_i$ and $\boldsymbol{K}_i$ are the inertia, damping and spring matrices of the non-contact impedance, respectively. It should be noted that if the obstacle is outside the ith virtual wall, the virtual force $\boldsymbol{F}_o^i$ is zero.

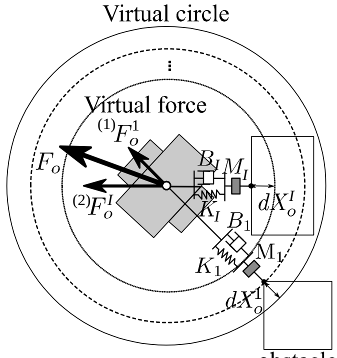

Fig. 2. Structure of the proposed multi-layered non-contact impedance model

The proposed method supports obstacle avoidance with multi-non-contact impedance using various parameters. The virtual extra force from all obstacles in front of the robot is calculated as

$$\boldsymbol{F}_o^i = \sum_{p=1}^{P} {}^{(\boldsymbol{p})}\boldsymbol{F}_o^i. \tag{5}$$

Finally, the resultant force acting on the mobile robot in the non-contact impedance model is defined as

$$\boldsymbol{F}_o = \sum_{i=1}^{I} \boldsymbol{F}_o^i. \tag{6}$$

Additionally, the dynamic equation for the robot regarding non-contact impedance control is expressed as

$$\boldsymbol{M}_e \Delta\ddot{\boldsymbol{X}} + \boldsymbol{B}_e \Delta\dot{\boldsymbol{X}} + \boldsymbol{K}_e \Delta\boldsymbol{X} = \boldsymbol{F}_e + \boldsymbol{F}_o. \tag{7}$$

Here, $\boldsymbol{M}_e$, $\boldsymbol{B}_e$ and $\boldsymbol{K}_e$ are the inertia, damping and spring matrices of the robot, respectively.

A displacement vector $\Delta\boldsymbol{X}$ is given using the reference position $\boldsymbol{X}_t = (x_t, y_t)^{\mathrm{T}}$ and the current position of the robot $\boldsymbol{X}_e = (x_e, y_e)^{\mathrm{T}}$ based on $\Delta\boldsymbol{X} = \boldsymbol{X}_t - \boldsymbol{X}_e$. The limitations of $\Delta\boldsymbol{X}$ and $\Delta\ddot{\boldsymbol{X}}$ [6] and the elements $\boldsymbol{K}_e\Delta\boldsymbol{X}$ and $\boldsymbol{M}_e\Delta\ddot{\boldsymbol{X}}$ in Equation (7) are ignored. Thus, the equation translates to

$$\boldsymbol{B}_e \Delta\dot{\boldsymbol{X}} = \boldsymbol{F}_e + \boldsymbol{F}_o. \tag{8}$$

In Equation (8), the velocity increment $\Delta\dot{\boldsymbol{X}}$ is calculated as

$$\Delta\dot{\boldsymbol{X}} = \frac{1}{\boldsymbol{B}_e}(\boldsymbol{F}_e + \boldsymbol{F}_o). \tag{9}$$

Finally, $\dot{\boldsymbol{X}}_v$ is defined as the velocity of control that allows the robot to avoid an obstacle using

$$\dot{\boldsymbol{X}}_v = \dot{\boldsymbol{X}}_e - \Delta\dot{\boldsymbol{X}}. \quad (10)$$

3. Simulation Experiment

3.1. *Experimental Conditions*

To evaluate the efficacy of the proposed method, two simulation experiments were performed with obstacles located (1) randomly and (2) along the path of movement. The robot had an initial position of $(0.0, 0.0)$ $[m]$ and moved toward a target position $(5.0, 0.0)$ $[m]$ with an initial speed of $(0.6, 0.0)$ $[m/s]$ in experiment (1). In experiment (2), the robot moved in a straight line at a speed of $(0.1, 0.0)$ $[m/s]$. The parameters used in the simulation were $I = 1$, $q_1 = 0.6$ $[m]$, $\boldsymbol{M}_1 = (10.0, 10.0)$ $[kg]$, $\boldsymbol{B}_1 = (5.0, 5.0)$ $[Nm/s]$, $\boldsymbol{K}_1 = (10.0, 10.0)$ $[N/s]$ for experiment (1), and $I = 2$, $q_1 = 0.6$ $[m]$, $\boldsymbol{M}_1 = (0.21,\ 0.21)$ $[kg]$, $\boldsymbol{B}_1 = (0.8, 0.8)$ $[Nm/s]$, $\boldsymbol{K}_1 = (1.0, 1.0)$ $[N/\ m]$, $q_2 = 0.4$ $[m]$, $\boldsymbol{M}_2 = (16.8, 16.8)$ $[kg]$, $\boldsymbol{B}_2 = (12.6, 12.6)$ $[Nm/s]$, $\boldsymbol{K}_2 = (1000.0, 1000.0)$ $[N/s]$ for experiment (2).

3.2. *Results and discussion*

Figures 3 and 4 show the results of the experiments ((a) for (1) and (b) for (2)). Figure 3 shows the paths of the robot in each experiment, and Fig. 4 shows, from top to bottom, velocities (overall and x-/y-axis) and virtual forces in each direction under the proposed method.

It can be seen from Fig. 3 (a) that the robot passed straight by two obstacles and altered its path to avoid another on the right. After the avoidance maneuver, the robot corrected its path toward the target position, avoided obstacles on the left and finally arrived at the target position. Figure 4 (a) shows that the robot slowed down due to virtual forces from the presence of two obstacles under the proposed method at around 1.0 [s] before sensing virtual forces from behind and accelerating to avoid an obstacle at 1.8 [s]. The robot adjusted its velocity as appropriate in response to virtual impedance forces indicating the distance from obstacles on each side.

Figures 3 (b) and 4 (b) show other obstacles in the robot's path after collision avoidance. The robot decelerated gradually, and finally stopped before

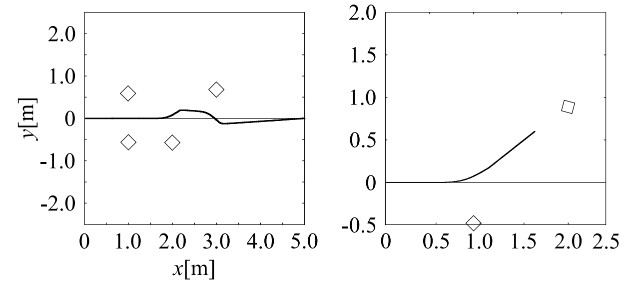

(a) Trajectory in experiment (1) (b) Trajectory in experiment (2)

Fig. 3. Trajectories of each experiment

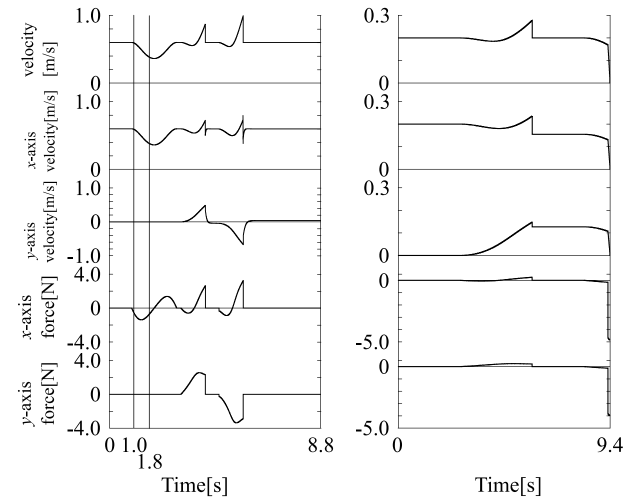

(a) Velocity and virtual force in experiment (1) (b) Velocity and virtual force in experiment (2)

Fig. 4. Velocities and virtual forces of each experiment

collision under the influence of virtual forces from the virtual wall with higher stiffness parameters from the obstacle at around 9.4 [s].

The results indicate that the proposed method supports collision avoidance in various situations.

4. Practical Experiment

A trajectory-tracking control experiment using an actual mobile robot (iRobot Create 2, iRobot Corp.) was performed with the position coordinates detailed in Section 3. The target electric wheelchairs generally have pairs of propulsion and caster wheels, but a control method for a robot with two independently driven wheels was considered here for simplicity. Sufficient friction between the drive wheels and the floor to avoid wheel spin was assumed.

The position coordinates were regarded as target points to be tracked by the robot. Robot position/posture data and target position coordinates were used to determine

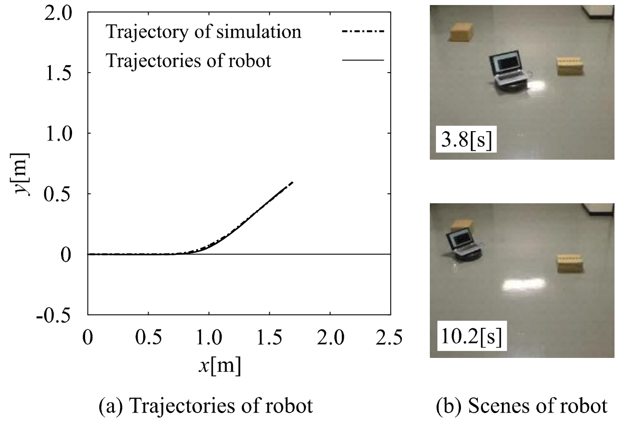

Fig. 5. Experimental results for practical experiment

target velocity, which was defined for each wheel $(v_L, v_R)^{\mathrm{T}}$ using the distance L_T and direction θ_T between the robot and the target position as

$$v_L = K_v \cdot L_T + \Delta v, \quad (11)$$

$$v_R = K_v \cdot L_T - \Delta v, \quad (12)$$

$$\Delta v = K_t \theta_T + K_{tD} \dot{\theta}_T. \quad (13)$$

Here, K_v, K_t and K_{tD} are pre-set constants.

Figure 5 (a) shows the paths observed in the simulation and practical experiments. Solid lines show the results of 10 trials in the practical experiment. Hardly any difference between the results of the two conditions is observed. Figure 5 (b) shows tracking in the sixth trial. As in the simulation experiment, the robot detected the obstacle and decelerated to pass by it with individual wheel velocity regulation in response to virtual reaction forces with the proposed model. The robot subsequently decelerated to avoid collision with other obstacles along its path in response to alternate contact with outer and inner virtual walls.

These results indicate that the proposed multi-layered non-contact impedance model enables obstacle avoidance in various situations. However, the scope of the tracking experiment was limited to the conditions reported here; no experiment using an actual biosignal-controlled electric wheelchair was conducted. The authors plan to verify the efficacy of the proposed method with implementation of the model using range sensors.

5. Conclusion

This paper proposes a multi-layered non-contact impedance model and its application to obstacle avoidance for electric wheelchairs. In this method, multiple virtual walls based on a mechanical impedance model are located around the robot, enabling natural avoidance of obstacles and emergency stops to prevent collisions. In simulation and practical experiments using the method, the robot avoided obstacles in response to virtual forces based on the model.

In future research, the authors plan to implement the method using distance image sensors and apply it in operation of an actual biosignal-controlled wheelchair [4] to evaluate its effectiveness.

Acknowledgements

This work was supported by JSPS KAKENHI Grant Number JP26330226.

References

1. World Health Organization, Disability and health, http://www.who.int/mediacentre/factsheets/fs352/en/, (Accessed November 2016).
2. Y. T. Lin and C. H. Kuo, Development of SSVEP-based Intelligent Wheelchair Brain Computer Interface Assisted by Reactive Obstacle Avoidance, in *Proc. 2016 IEEE International Conference on Industrial Technology*, (Saratov, Russia, 2016), pp. 1572–1577.
3. K.Tanaka, K.Matsunaga and H. O. Wang, Electro-encephalogram-based Control of an Electric Wheelchair, *IEEE Trans. on Robotics* **21**(4) (2005) 762–766.
4. K. Shima, R. Eguchi, K.Shiba and T.Tsuji, CHRIS: Cybernetic Human-Robot Interface Systems, in *Proc. 36th International Symposium on Robotics,* (2005) WE1C3
5. M. Massari, G. Giardini and F. B-Zazzera, Autonomous Navigation System for Planetary Exploration Rover Based on Artificial Potential Fields, in *Proc. Dynamics and Control of Systems and Structures in Space 6th Conference*, (Riomaggiore, Italy, 2004), pp. 153–162.
6. R. M. F. Alves and C. R. Lopes, Obstacle avoidance for mobile robots: a Hybrid Intelligent System Based on Fuzzy Logic and Artificial Neural Network, in *Proc. 2016 IEEE International Conference on Fuzzy Systems*, (Vancouver, Canada2016), pp. 1038–1043.
7. T. Thsuji, M.Hatagi and M. Kaneko, Non-Contact Impedance Control for Manipulators, *J. the Robotics Society of Japan* **15**(4) (1997) 616–623.
8. E. S. Jang, S.Jung and T. C. Hsia, Collision Avoidance of a Mobile Robot for Moving Obstacles Based on Impedance Force Control Algorithm, in *Proc. 2005 IEEE/RSJ International Conference on Intelligent Robots and Systems*, (Edmonton, Canada, 2005), pp.383–387.
9. Z. Li, Z.Wu and Y. Fu, Dynamic Obstacle Avoidance of Mobile Robot Tele-operation Based on Non-contact Impedance Control, in *Proc. 2014 11th World Congress on Intelligent Control and Automation*, (Tianyou, China, 2014), pp. 1421–1426.

A Voice Signal-Based Manipulation Method for the Bio-Remote Environment Control System Based on Candidate Word Discriminations

Taro Shibanoki
Ibaraki University, Japan
Go Nakamura, Takaaki Chin
Hyogo Rehabilitation Center, Japan
Toshio Tsuji
Hiroshima University, Japan

Abstract

This paper proposes a voice signal-based manipulation method for the Bio-Remote environment control system. The proposed system learns relationships between multiple candidate words' phonemes extracted by a large-vocabulary speaker-independent model and control commands based on a self-learning look-up table. This allows the user to control various devices even if false recognition results are extracted. Experimental results showed that the method accurately discriminate slurred words (average discrimination rate: 94.4±2.53 [%]), and that the participant was able to voluntarily control domestic appliances.

Keywords: environment control system (ECS), speech recognition, candidate word, learning-type look-up table

1. Introduction

A variety of environmental control systems (ECSs) for people with disabilities and bedridden elderlies have been developed to be self-sufficient and maintain independent life in recent years.

There are number of studies to develop such systems using biological signals [2] - [5]. As an example, the Bio-Remote – a new ECS developed by our research group [4][5] – has the distinctive features of (1) various input systems such as biological signals, keyboard and mouse input to meet user requirements, (2) flexible adaptation to individual users depending on their capabilities, and (3) learning function to enable adaptation to variations among individuals.

The Bio-Remote has been proven effective in support for the everyday lives of people with spinal injuries through its usefulness in the operation of domestic appliances [5]. However, sensors must be attached to skin surface with paste and medical tapes, it is user's unpleasantness and burden because the procedure to wear electrodes is complicated. Additionally, because of the effectiveness of changes of skin impedance such as perspiration, long-time use of the system is difficult. To overcome these problems, we focus voice signals as an extension input of the Bio-Remote.

A number of speech controlled ECS have been developed, such as Voicecan (Voicecan co., ltd) [6] and Lifetact (Asahi kasei technosystem co., ltd) [7]. These systems discriminate users' intensions from recorded voice signals based on a speaker independent acoustic model and control devices corresponding to discrimination results. It is, therefore, difficult to accurately discriminate speech of patients with dysarthria who speak difficult, since the model used in these systems consider to standard adults' speech. On the other hand, training each user's voice and building a speaker dependent model, it is possible to accurately discriminate speech of patients with dysarthria [8]. However, it takes a lot of time and needs a large amount of data to train a speaker dependent model, it is possible to be a burden to a user.

This paper proposes a novel environment control system for patients with dysarthria using voice signals.

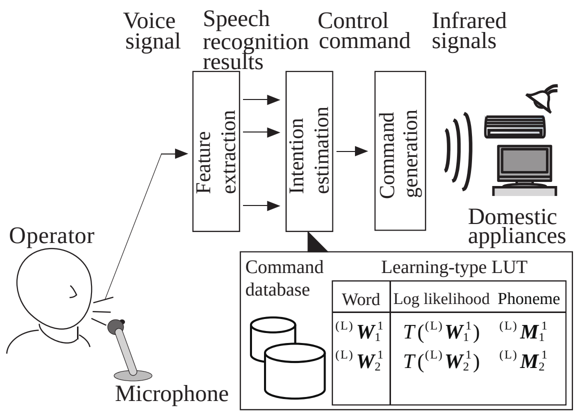

Fig. 1. Overview of the proposed system.

The system trains individual user's features based on the false recognition results using a speaker independent model and can discriminate user's intensions without large amount of training data.

2. Speech controlled Bio-Remote

Figure 1 shows the overview of the proposed system. The proposed system consists of voice signal measurement and feature extraction, operation estimation, and device control stages. The details of each stage are outlined as follows.

2.1. *Voice signal measurement and feature extraction [10]*

Voice signals were recorded using a microphone and digitized using an A/D converter (sampling frequency: f_s [Hz]). Mel-frequency cepstrum coefficients (MFCCs) are then extracted as the inverse cosine transform is applied to the log power spectra of the sampled signals. Feature vector $\boldsymbol{X}$ used for speech recognition is defined as the low-frequency components of each frame of extracted MFCCs [9].

Next, output probabilities $P(\boldsymbol{W})$ of word $\boldsymbol{W} = \{w_1, w_2, \ldots, w_K\}$ (w_k: word, K: number of words) is calculated approximately using N-gram model. Additionally, output probabilities $P(\boldsymbol{X}|\boldsymbol{W})$ of a feature vector $\boldsymbol{X}$ from $\boldsymbol{W}$ is calculated using the acoustic model. A phoneme hidden Markov model (phoneme HMM), which can consider a context and a time variation, is used to calculate $P(\boldsymbol{X}|\boldsymbol{W})$. $P(\boldsymbol{X}|\boldsymbol{W})$ is calculated dividing the words $\boldsymbol{W}$ to phonemes $m = \{m_1, m_2, \ldots, m_J\}$ (m_j: phoneme, J: number of phonemes) and matching phoneme HMM to $\boldsymbol{X}$. Then, the top H words $\boldsymbol{W}_h$ ($h = 1, 2, \ldots, H$) with maximum log-likelihood, their phonemes $\boldsymbol{M}_h$ and log-likelihoods $T(\boldsymbol{W}_h)$ are extracted.

2.2. *Operation discrimination using the learning-type look-up table*

The user's intension is discriminated using the learning-type look-up table (LUT). The user is instructed to speak some words used in device control, and relationships between control commands, and extracted words $\boldsymbol{W}_h$ and phenomes $\boldsymbol{M}_h$, which include false recognition results, and log-likelihoods $T(\boldsymbol{W}_h)$ are learned to the LUT. Then, the control command corresponding to the extracted word can be selected using the trained LUT.

In the learning stage, the user speaks C words, which is used in device control, some times and top V words W^c_v with maximum log-likelihood, and their phonemes M^c_v and log-likelihood $T(W^c_v)$ in H extracted words are corresponded to each discrimination class ($c = 1, 2, \ldots, C$; $v = 1, 2, \ldots, V$; $V < H$). In the discrimination stage, extracted phenomes of top U words with maximum log-likelihood in a new H words are used. First, extracted phoneme ${}^{(D)}M_u$ ($u = 1, 2, \ldots, U$; $U < H$) is compared to phoneme ${}^{(L)}M^c_i$ ($i = 1, 2, \ldots, I_c$; I_c: number of learning data for class c) of each discrimination class memorized in the learning-type LUT. The coincidence between ${}^{(D)}M_u$ and ${}^{(L)}M^c_i$ is then calculated as follows:

$$s^c_{u,i} = \begin{cases} 1 & ({}^{(D)}M_u = {}^{(L)}M^c_i) \\ 0 & (otherwise) \end{cases}. \qquad (1)$$

A class with a maximum value of r^c representing the average of all $s^c_{u,i}$ values is then taken as the discrimination result. When the values for some classes are same, difference between log-likelihoods $T({}^{(D)}W_u)$ and $T({}^{(L)}W^c_i)$ are used to determine the result.

2.3. *Device control*

The domestic appliances are controlled based on discrimination results using the Bio-Remote. The Bio-Remote consists of a sensor unit to measure biological signals and a main unit to control the target device using the measured signals.

The user can directly select appliances and their control commands with the proposed system. As an example, if the user wishes to select the command to switch on the TV, speaks "*TV*" command to select the TV menu. Next, the user speaks "*power*" command so that the operator can finally choose the ultimate target – the "Power" menu option. The control instruction corresponding to the previously learned TV power menu item is then sent from the computer to the main unit, and an infrared signal is transmitted.

3. Speech recognition experiment

3.1. *Method*

In order to verify the efficacy of the proposed method, experiments were performed to demonstrate the accuracy of discrimination. The participants are three healthy males; and assuming slurred speech, they are intended to speak with their tongue touching to maxillary central. A directional microphone (audio-technica corp., AT-9942) and an audio processor (ONKYO copr., SE-U33GXV) are used to record voice signals. A number of discrimination class is seven (C = 7), and participant repeat to speak each word 50 times. 50 sets of each class data are separated into 10 learning data sets and 40 discrimination data sets. The parameters used in the experiment are set as f_s = 16 [kHz], N = 3, H = 10, V = 10 and U = 5. The other parameters, K, J, I_c are adjusted based on durations of input voice signals and results of learning procedure. The Julius [10] is used to record and extract the features of each speech, and recognition results using it are compared to the results using the proposed method.

3.2. *Results and discussion*

Figure 2 shows the discrimination rates for each class using the proposed method and Julius. It plots the average discrimination rates for each class while the set of learning data and discrimination data were changed and discriminated at each data set for 10 times. From this figure, the average discrimination rate for all classes using Julius is 3.52 ± 5.08 [%], and those using the proposed system is 94.4±2.53 [%], respectively. These results indicate that the proposed system can accurately discriminate slurred speech, which is difficult to discriminate a large vocabulary speaker independent model, learning false recognition results in advance. Additionally, when duplicative phenomes are extracted, the system can discriminate user's intensions based on

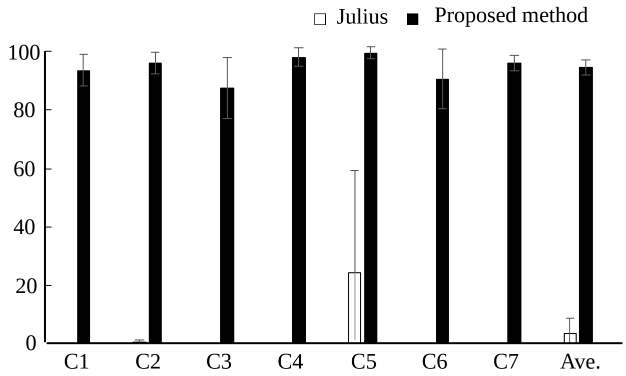

Fig. 2. Comparison of discrimination rates using the proposed method and Julius [10]

the difference of log-likelihood. To realize higher level of discrimination performance, we plan to adjust appropriate discrimination parameters such as number of extracted words U using discrimination.

4. ECS control experiment

Assuming operation in real life, an experiment was performed using the Bio-Remote with the proposed method introduced. In the experiment, the participant A instructed to (1) turn on the light, (2) turn the TV on, (3) play DVD, (4) stop DVD, (5) turn the TV off, (6) play the audio player and (7) turn off the light. The parameters used in the experiment are as same as the Section 3.

An scene showing the operation of the proposed system is given in Fig. 3, and examples of the experimental results are shown in Fig. 4. This shows input signals, extracted phenomes (corresponding to extracted words with the maximum log-likelihood), discrimination resutls, selected devices and control commands in order from the top. From Fig. 4, the subject spoke ``*shoumei* (Light)", thereby moved to the light operation layer. Then, speaking "*onn* (ON)", the light was turned on after approximate 1.6 [s] (see Fig. 4 (1)). The outcomes here also showed that the subject directly move from the light layer to the TV layer as speaking ``*terebi* (TV)", and DVD was played after the TV was turned on around 7.6 [s] (see Fig. 4 (2)). It was therefore indicated that users' intensions were correctly discriminated from slurred speech to learn features of individual speech and devices were controlled based on discrimination result.

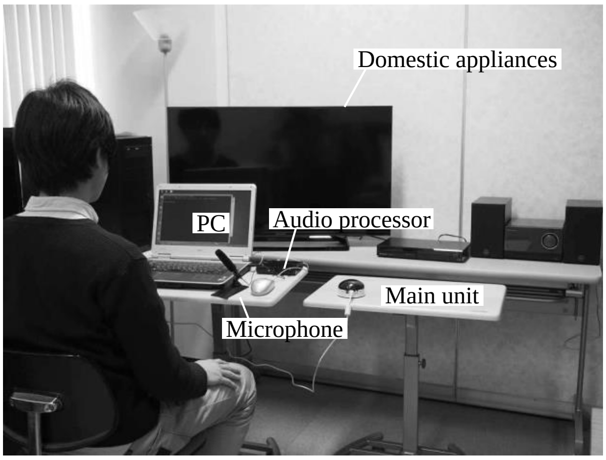

Fig. 3. Operation scene using the proposed system

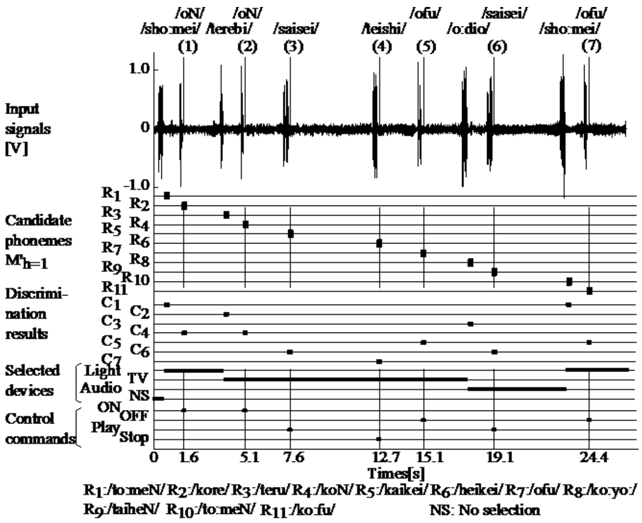

Fig. 4. An example of experimental results

5. Conclusion

This paper proposed a novel speech controlled ECS for patients with dysarthria based on a false recognition results for slurred speech using a large vocabulary speaker independent model. In the experiments performed, the accuracy of speech recognition was evaluated comparing to results using Julius. The results showed that the proposed method was able to discriminate with an accuracy level of 94.4 $\pm$ 2.53 [%] for three healthy males. The method was therefore able to correctly discriminate user intensions. Further, operation experiments using the proposed system showed that the subject can voluntarily control domestic appliances.

In future work, we plan to perform operation experiments for patients with dysarthria and validate the effectiveness of the proposed system. In order to reduce the level of stress involved in Bio-Remote operation, we also plan to discuss the discrimination parameters, and to incorporate an online learning method into it.

Acknowledgements

The authors would like to cordially acknowledge and express appreciation to Mr. K. Harada for his assistance in the implementation of this research. This work was supported by JSPS KAKENHI Grant Number JP26330226.

References

[1] Ministry of Health, Labour and Welfare, "Ministry of Health, Labour and Welfare Fact-Finding Investigation of Fisically Disabled," *http://www8.cao.go.jp/shougai/data/datah23/zuhyo09.html* (accessed December 2016).

[2] A. Craig, P. Moses, Y. Tran, P. McIsaac, L. Kirkup, The Effectiveness of a Hands-Free Environmental Control System for the Profoundly Disabled, *Archives of Physical Medicine and Rehabilitation*, **83** (10) (2002) 1455-1458.

[3] X. Gao, D. Xu, M. Cheng, S. Gao, A BCI-based Environmental Controller for the Motion-disabled, *IEEE Transactions on Neural Systems and Rehabilitation Engineering*, **11** (2) (2003) 137-140.

[4] T. Tsuji, K. Shima, A. Funabiki, S. Shitamori, K. Shiba, O. Fukuda and A. Otsuka, A New Manipulation Method for Environment Control Systems, *The Society of Life Support Technology*, **18** (4) (2006) 5-12 (in Japanese).

[5] T. Shibanoki, G. Nakamura, K. Shima, T. Chin and T. Tsuji, Operation Assistance for the Bio-Remote Environmental Control System Using a Bayesian Network-based Prediction Model, *Proceedings of 37th Annual International Conference of the IEEE Engineering in Medicine and Biology Society* (Milan, Italy, 2015), pp. 1160-1163.

[6] Voicecan Co., Ltd, VOICECAN, *http://www.voicecan.ecweb.jp/* (accessed December 2016).

[7] Asahi Kasei Technosystem, Co., Ltd, LIFETACT, *http://www.asahi-kasei.co.jp/ats/hukushi final.html* (accessed December 2016).

[8] M. S. Hawley, P. Enderby, P. Green, S. Cunningham, S. Brownsell, J. Carmichael, M. Parker, A. Hatzis, P. O. Neill and R. Palmer, A Speech-controlled Environmental Control System for People with Severe Dysarthria, *Medical Engineering & Physics*, **29** (5) (2007) 586-593.

[9] A. Lee and T. Kawahara, Recent Development of Open-Source Speech Recognition Engine Julius, *Asia-Pacific Signal and Information Processing Association Annual Summit and Conference* (Hokkaido, Japan, 2009), pp. 131-137.

Large vocabulary Continuous Speech Recognition Engine, Julius, *http://julius.sourceforge.jp/index.php* (accessed December 2016).

Experiments on classification of electroencephalography (EEG) signals in imagination of direction using Stacked Autoencoder

Kenta Tomonaga, Takuya Hayakawa, Jun Kobayashi
Department of Systems Design and Informatics, Kyushu Institute of Technology,
Kawazu 680-4, Iizuka, 820-8502, Japan

E-mail: jkoba@ces.kyutech.ac.jp
lab.jkoba.net

Abstract

This paper presents classification methods for electroencephalography (EEG) signals in imagination of direction measured by a portable EEG headset. In the authors' previous studies, principal component analysis extracted significant features from EEG signals to construct neural network classifiers. To improve the performance, the authors have implemented a Stacked Autoencoder (SAE) for the classification. The SAE carries out feature extraction and classification in a form of multi-layered neural network. Experimental results showed that the SAE outperformed the previous classifiers.

Keywords: electroencephalography, stacked autoencoder, neural network, portable EEG headset, imagination of direction

1. Introduction

Electroencephalography (EEG) is a non-invasive way for measuring human brain activity. A lot of studies on Brain Machine Interface (BMI) have make use of EEG because of its greater availability than invasive ways. In addition, portable and low-cost EEG devices have been developed and readily accessible nowadays. Having said that, there are unclear points in the accuracy of those portable EEG devices,[1,2] hence the potential of applications using them should be explored.

Seto et al. had studied on classification of EEG signals in imagination of direction measured by a medical EEG device.[3] Following their study, we employed a portable EEG headset to record EEG signals in imagination of direction, and implemented feature extraction with Principal Component Analysis (PCA) and several neural networks for the classification.[4,5] We validated the classification performance and confirmed that the best classification rate of the method using the medical EEG device was still better than those of our methods.

To achieve higher classification rate, we have implemented a Stacked Autoencoder (SAE) for feature extraction and classification of EEG signals in imagination of direction measured by the portable EEG device. G. E. Hinton et al. said that deep autoencoder networks can reduce the dimensionality of data much better than PCA.[6] Therefore, we introduced a SAE to our study. Here we describe the SAE implemented for EEG signal classification and show results of comparative experiments that validate its effectiveness.

2. EEG Data Acquisition and Preprocessing

Fig. 1 shows a wireless portable EEG headset developed by Emotiv Inc., named EPOC.[7] We used the headset for EEG data acquisition in our preceding study.[4,5] EPOC has 14 electrodes and two reference electrodes, recording EEG signals at a sampling rate of 128 Hz. The electrodes are placed on the scalp according to an extended 10-20 system for EEG measurement as shown in Fig. 2.

Fig. 1. Emotiv EPOC (wireless portable EEG headset)

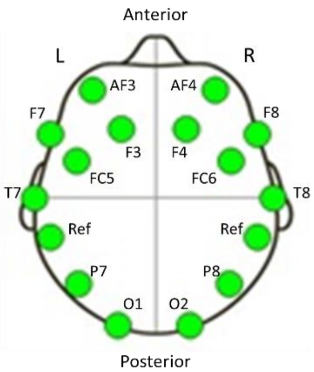

Fig. 2. Electrode placement of EPOC

Nine male university students participated in experiments as subjects for EEG data acquisition. Their average age was 21.9 years. Fig. 3 shows the experimental environment. During the experiments, a subject imagined one figure of arrows shown in Fig. 4. The obtained EEG signals were preprocessed to produce input vectors to a classifier. Fig. 5 is a flowchart of the preprocessing. The input vectors are composed of 23 elements. See Refs. 4 and 5 for more details about the EEG data acquisition and preprocessing.

Fig. 3. Experimental environment

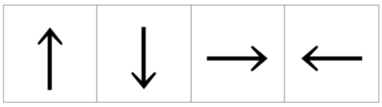

Fig. 4. Arrows indicating directions (up, down, right, and left)

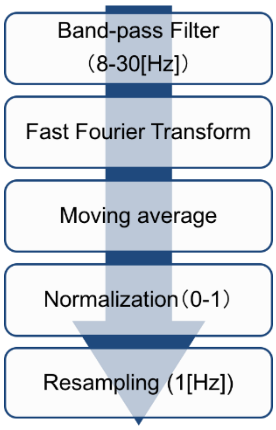

Fig. 5. Flowchart of preprocessing

3. Classification with Stacked Autoencoder

In our previous studies,[4,5] we applied PCA to the preprocessed EEG data for reducing the dimension, and trained three-layered neural networks using the data as feature vectors. This classification method is called "PCA-NN" in this paper.

We introduced deep neural networks in order to achieve better classification performance. Although training a deep neural network was difficult for backpropagation due to vanishing gradient problem, pretraining weights between nodes of a deep neural network can be a solution to the problem.

Stacked Autoencoder (SAE) is a way of constructing a deep neural network, in which deep architectures are initialized by stacking pretrained autoencoders. Fig. 6 illustrates a typical autoencoder that is an hourglass-shaped three-layered neural network. This neural network has the same number of nodes in the input and output layers, and it is trained so that it can yield output values equal to given input ones by backpropagation. As mentioned above, autoencoders can be used for dimensionality reduction. The anterior part between the input and hidden layers of autoencoder works as an encoder, compressing input signals and extracting important information from them. The encoder parts of pretrained autoencoders are stacked for initializing a deep neural network. We trained the autoencoders with the preprocessed EEG data for 1000 epochs.

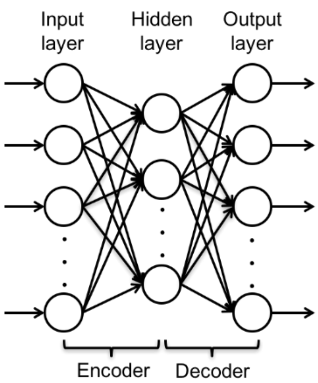

Fig. 6. Autoencoder

We constructed initial SAEs with the pretrained autoencoders and then performed fine-tuning for 1000 or 10000 epochs. Fig. 7 shows the architecture. The SAE has an input layer, two hidden layers, and an output layer. Input vectors to the SAE are composed of 23 elements produced from the EEG signals obtained through the preprocessing shown in Fig. 5. The output layer has four nodes in order to classify given EEG signals into the four directions: up, down, right, and left. The number of nodes of the first and second hidden layers were tentatively set to 20 and 10, respectively. Searching the optimum number of hidden layers and their nodes is a future work.

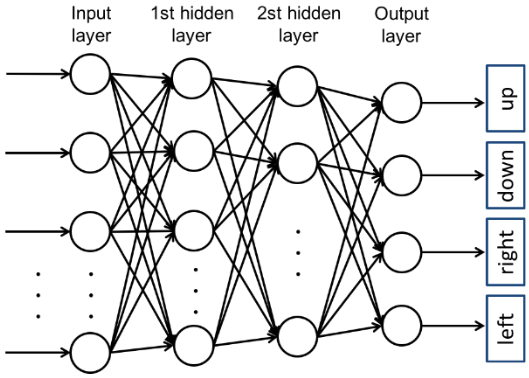

Fig. 7. Stacked Autoencoder with two hidden layers

4. Results and Discussion

The classification rates of the classifiers were evaluated with 5-fold cross validation. Table 1 and Table 2 show the evaluation results for the EEG signals obtained from one of the subjects. In the PCA-NNs, the PCA kept features with a 90% cumulative contribution ratio, and trimmed off the others. In the result, 17-dimensional feature vectors were produced. Therefore, the NNs of the PCA-NN were composed of 17-17-4 nodes in the input, hidden, and output layers. On the other hand, the structure of the SAEs were 23-20-10-4; the number of the input nodes is 23 that is equal to the dimension of the preprocessed input vector.

As shown in Table 1, the maximum classification rate by the PCA-NNs was 35.0% at FC5 electrode. It appears that overfitting caused the poor performance in some of the PCA-NNs trained for 10000 epochs.

Table 2 shows the classification rates of the SAEs. It clarified that the SAEs achieved better classification performance than the PCA-NNs. One of the SAEs realized 61.7% classification rate at FC5 electrode. Nevertheless, the work by Seto et al. using a medical EEG device[3] is still better than the results obtained in this study.

It would be expected for improvement that a deeper SAE could provide superior performance than the SAEs with only two hidden layer used in this study. In addition, we will use denoising autoencoders[8,9] to extract more relevant features for the classification of EEG signals.

Table 1. Classification rate percentages of PCA-NN

Electrode	Epoch 1000	Epoch 10000
AF3	25.8	25.8
F7	29.2	26.7
F3	26.7	29.2
FC5	35.0	25.8
T7	33.3	26.7
P7	31.7	27.5
O1	25.0	25.8
O2	25.0	25.0
P8	34.2	28.3
T8	30.0	25.8
FC6	25.8	26.7
F4	27.5	24.2
F8	24.2	24.2
AF4	26.7	23.3

Table 2. Classification rate percentages of SAE

Electrode	Epoch 1000	Epoch 10000
AF3	35.8	34.2
F7	56.7	49.2
F3	41.7	40.0
FC5	55.8	61.7
T7	40.8	40.8
P7	37.5	41.7
O1	30.0	33.3
O2	28.3	30.8
P8	24.2	29.2
T8	45.0	32.5
FC6	39.2	34.2
F4	34.2	33.3
F8	35.0	32.5
AF4	36.7	35.0

5. Conclusion

We implemented the SAEs for classification of EEG signals in imagination of direction, and compared the performance with those of the NNs trained using the feature vectors extracted by PCA. The results demonstrated that the SAEs achieved the improvement, however the achievement of the preceding study using a medical EEG device is still better than ours using the portable EEG headset. There remains much to explore a way to select the number of layers in the SAEs and to adopt denoising autoencoders as future work.

References

1. M. Duvinage et al., A P300-based quantitative comparison between the Emotiv Epoc headset and a medical EEG device, in *Proc. of the 9th IEEE/IASTED Int. Conf. on Biomedical Engineering* (Innsbruck, Austria, 2012).
2. M. Duvinage et al., Performance of the Emotiv Epoc headset for P300-based applications, *BioMedical Engineering OnLine* **12**(56) (2013).
3. Y. Seto et al., Classification by EEG frequency distribution in imagination of directions, in *Proc. of the 18th Int. Conf. on Knowledge-Based and Intelligent Information & Engineering Systems* (2014), pp. 1300–1306.
4. K. Tomonaga et al., Experiments on classification of electroencephalography (EEG) signals in imagination of direction using a wireless portable EEG headset, in *Proc. of Int. Conf. on Control, Automation and Systems* (Busan, South Korea, 2015), pp. 1805–1810.
5. S. Wakamizu et al., Experiments on Neural Networks with Different Configurations for Electroencephalography (EEG) Signal Pattern Classifications in Imagination of Direction, in *Proc. of IEEE Int. Conf. on Control System, Computing and Engineering* (Penang, Malaysia, 2015), pp. 477–481.
6. G. E. Hinton and R. R. Salakhutdinov, Reducing the Dimensionality of Data with Neural Networks, *Science* **313** (2006), pp. 504–507.
7. Emotiv EPOC, https://emotiv.com/epoc.php.
8. P. Vincent et al., Extracting and Composing Robust Features with Denoising Autoencoders, in *Proc. of the 25th Int. Conf. on Machine Learning* (Helsinki, Finland, 2008), pp. 1096–1103.
9. P. Vincent et al., Stacked Denoising Autoencoders: Learning Useful Representations in a Deep Network with a Local Denoising Criterion, *J. of Machine Learning Research* **11** (2010), pp. 3371–2408.

Influence of Partner Selection on Functional Differentiation: Emergence of Diversity by Isolated Interaction and Preference Change

Saori Iwanga
Department of Maritime Safety Technology, Japan Coast Guard Academy, 5-1 Wakaba
Kure, Hiroshima 7378512, Japan

Akira Namatame
Computer Science Department., National Defense Academy, 1-10-20 Hashirimizu
Yokosuka, Kanagawa 2398686, Japan
E-mail: s-iwanaga@jcga.ac.jp

Abstract

In examining collective behavior, we focus on the interactions of individuals. We also need to describe on two different levels: the microscopic level, where the decisions of the individual agents occur, and the macroscopic level where collective behavior can be observed. What makes collective behavior is interesting and difficult is that the aggregate outcome is what has to be evaluated within the constraints of the environment. The performance of the collective system depends crucially on the type of interaction as well as the heterogeneity in preference of agents.

In this study, for emergence of diversity, we found that it is needed two different speed learning processes. And it is needed isolated interaction for emergence of diversity. But, the utility of less clustered interaction is more than that of isolated interaction if possible. On the whole, we found that isolated interacting is effective for emergence of diversity. Then, once diversity is emerged enough, less clustered interaction is effective to utility of each agent and whole population.

Keywords: collective behavior, diversity, payoff matrix, isolated interaction, preference.

1. Introduction

The studies on multi robots and multi agent simulation began in the late 1980s. Reynolds[1] shows that a collective behavior occurs when three rules are used at the same time by BOIDS and shows the collective behavior is a kind of the complex system. As the example of emerged physical or functional characteristics, there are known study of Sims[2] in the block struggle environment and study of Terzopoulos[3] about artificial fish. Kubo et.al[4] show the emergence of unique individual on competition game for food of ants. However, heterogeneity of individual are often ignored in most of studies[5]. For example, recently a study of shape the formation by multi robots are paid attention. In the multi robots system if there are heterogeneous robots, the robots are removed[6]. There are limits to adaptation performance of multi robots system with heterogeneous robots, and it is hardly not reproduced the emerged diversity in the population on computer simulation.

In examining collective behavior, we focus on the interactions of individuals. We also need to describe on two different levels: the microscopic level, where the decisions of the individual agents occur, and the macroscopic level where collective behavior can be observed[7]. Schweitzer[8] shows that interaction on microscopic level result in the emergence of complex behavior on the macroscopic level. What makes collective behavior is interesting and difficult is that the aggregate outcome is what has to be evaluated within the constraints of the environment. The performance of the collective system depends crucially on the type of interaction as well as the heterogeneity in preference of agents[9].

Axelrod et.al[5, 10]show that agents experience more diverse contacts, the system can become less diverse. As interaction patterns become less clustered, the experience of interacting with more “distant others”, information moves more rapidly throughout. The world becomes so “small” that the sociological “islands” vanish, unable to keep their local ways and remain untouched by events elsewhere. Early innovations spread too fast, and variety that can provide later implements is lost, what they calls as premature convergence. The ideal breeding ground for novel live-forms seems to be an archipelago or a network of mountain valleys.

Sandholm el.al[10] presents a dynamic analysis of the evolution of preferences in a strategic environment. Dynamics run at two speeds at once: while natural selection slowly reshapes the distribution of preferences, players quickly learn to behave as their preferences dictate. They establish the existence and uniqueness of the paired trajectories of society's preferences and aggregate behavior. While aggregate behavior adjusts smoothly in equilibration games, in coordination games aggregate behavior can jump discretely in an instant of evolutionary time.

In this study, we clarify how diversity is emerged in the population.

2. Model

There is a growing literature on the approach of bounded rationality, and the hypotheses employed in these researches reflect the ability of each agent to receive partial information from other agents in the course of their interaction[12]. Our model can be interpreted in like manner; however, we intend to combine the hypotheses of adaptation and local interactions in modeling evolutionary processes. The first hypothesis reflects limited ability to receive, decide, and act upon information they get in the course of interactions for each agent. The second interpretation is that the agents chooses the best action. We formalize these ideas in a model with a finite population of agents in which agents are repeatedly matched within a period to play a game and we consider to describe game. Here are many parameters to be considered such as payoff structure, localization, the shadow of the future, the number of agents and so on. Among these parameters, we examine parameters: payoff structure and localization.

We adopt the payoff matrix given in Table 1, which describes the outcome of the interaction between agents. In this matrix, if both agents chose the same strategy, they can get the positive payoff $1-\theta_i$ or θ_i, otherwise they receive nothing where $0 \le \theta_i \le 1$. The game is coordination game.

There are many situations where interacting agents can benefit from coordinating their actions. Coordination usually implies that increased effort by some agents leads the remaining agents to follow suit, which gives rise multiplier effects. Examples where coordination is important include trade alliance, the choice of compatible technologies or conventions such as the choice of a software or language. These situations can be modeled as coordination games; in which agents are expected to select the strategy the majority does[13, 14]. The traditional game theory, however, is silent on how agents know which equilibrium should be realized if a coordination game has multiple equally plausible equilibria, where these can be Pareto ranked[15,16]. This silence is all the more surprising in games with common interest since one expects that players will coordinate on the Pareto dominant equilibrium[17]. The game theory has been also unsuccessful in explaining how agents should behave in order to improve an equilibrium situation[18].

Considering that payoff parameters θ_i of both agents are 0, it is Nash equilibrium and Pareto optimum that both of them choose S1. Nash equilibrium is the equilibrium state achieved to the most suitable strategy by decisions of all agents. Pareto optimum is the state that there is left no room to raise the benefit of the agent who without getting down the benefit for the other agents.

Table 1. The payoff matrix of agent Ai.

		behavior of other agent	
		S1	S2
behavior of agent Ai	S1	$1-\theta_i$	0
	S2	0	θ_i

2.1. Preference of agent

Payoff parameter θ_i characterizes the preference of the agent. We deal with the expression of heterogeneity of agents. In the population, each agent has different payoff parameter θ_i and $1-\theta_i$ as shown in Table1. If payoff parameter $1-\theta_i$ is greater than θ_i of agent Ai, it means that the agent refers S1. And if parameter $1-\theta_i$ of agent Ai is less than parameter θ_i, the agent prefers S2. For example, if payoff parameter θ_i of agent Ai is less than 0.5, the agent prefers S1. Otherwise, agent Ai prefers S2.

2.2. Social network

In many situations, agents are not assumed to be so knowledgeable as to correctly guess or anticipate the other agent's strategies, or they are less sophisticated in that they do not know how to calculate best replies[12]. The hypotheses we employ in the local interaction model reflect limited ability to receive, decide, and act upon information they get in the course of interactions. Each agent to receive partial information from other agents in the course of their interaction[13]. And each agent chooses an optimal strategy based on information about what other agents have done in its world. The consequences of their behavior take to have an effect on agents with whom they are not directly linked and agents gradually learn the strategy of a population.

Lattice model is used to make clear the ecological characteristic of living beings. Nowak[19] and Axelrod[10] deal with the situation that each one faces the social dilemma and indicate that importance of the structure of space to emerge the corporation in society. We consider the lattice structure as shown in Fig. 1, in which each agent interacts with only neighbors of the agent. In this paper, we deal with von Neumann neighborhood model. In von Neumann neighborhood model, each agent interacts with it's the nearest four agents.

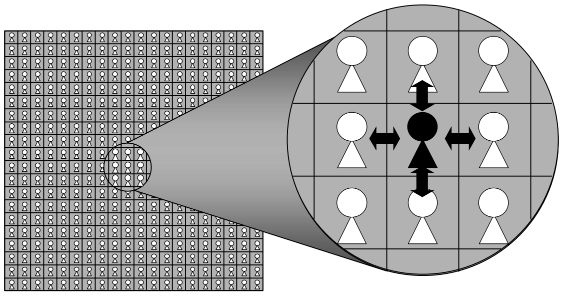

Fig. 1. von Neumann neighborhood model

2.3. Decision of behavior

Agents don't know the behavior the partners will take, but know the behavior the partners took at last. The proportion of agents having chosen S1 at time t is defined by $p_i(t)$ $(0 \leq p_i(t) \leq 1)$ in agent's neighbors. Each agent can take the best response against the behavior the partners took by calculating the expected payoff. Agent Ai compares the average expected utilities by S1 with S2 at time t, which are given as flows.

$$\bar{U}_i(S1,t) = p_i(t)(1-\theta_i),$$
$$\bar{U}_i(S2,t) = p_i(t)\theta_i. \qquad (1)$$

Then, they act so as to maximize their utility. Agent Ai chooses S1 if $\bar{U}_i(S1,t) > \bar{U}_i(S2,t)$, or chooses S2 if$\bar{U}_i(S1,t) < \bar{U}_i(S2,t)$ at next time. The decision rule of agent Ai at time *t*+1 is described as the following two cases depending on its idiosyncratic parameter θ_i .

If $p_i(t) > \theta_i$, agent Ai chooses S1,

otherwise $p_i(t) < \theta_i$, agent Ai chooses S2. (2)

That is best response rule. When $p_i(t) = \theta_i$, we assume that agent chooses the same behavior as last time. We define the right-hand side of (2) as threshold of agent Ai. The crucial point for dealing with diversity in the population is threshold. According to the threshold, agent's behavior is different from each other. Moreover, the proportion of agents having chosen S1 among the partners $p_i(t)$ of the agent is different from each other. So, decision of agent is different from each other. That is, payoff matrix and the world of agent effect on the behavior of agent and form collective behavior in the population. We define the collective behavior $p(t)$ that the proportion of agents having chosen S1 in whole population at time *t*.

2.4. Movable for new neighbors

If an agent wants to get a high payoff, it is effective method to move to another site and change its partners to interact.[14, 20] in their studies, the agent changes partner based on the properties of partners. But, it is often difficult to observe the properties of partner. It is easy to observe the behavior of partners. Often the character of the agent is treated that an internal attribute, such as preference, forms endogenously. But, we cannot observe inside attribute from outside and can observe only an action appeared internal attribute. And we often treat the action of agent given internal attribute beforehand.

However, it is reasonable that action taking by an agent forms the internal attribute. Then, in this study, we set each agent changes partners based on the behavior.

Each agent has parameter μ. If average payoff of agent Ai gotten by interaction with four partners is greater than equal μ, agent Ai stay the site. Otherwise agent Ai move to another site. The rule of change partners is as follows, where *k*=1, 2.

If $\overline{U}_i(Sk,t) \geq \mu$, agent Ai stays the site,
otherwise $\overline{U}_i(Sk,t) < \mu$, agent Ai moves to another site. (3)

There are some agents who want to move another site in the population. The agents make the pairs at random and change the site each other. And all agents who want to change can change the partners at same time. As for the behavior of the agent on the new site, the agent choose the behavior at first which the former agent decided in the site because it is not familiar with the site. After that, the agent decide the behavior by eq. (2).

If agent is movable, agents can contact diverse agents and the interaction is less clustered. On the other hands, the interaction when agents cannot move to another site is clustered and corresponds to isolated interaction.

2.5. Self-reinforcement of preference

In this study, we clarify how diversity is emerged in the population. Each agent can update the payoff parameter by interaction. We define this as "self-reinforcement of preference". If Agent Ai has been chosen S1 for T times in succession, agent Ai increases the payoff $1-\theta_i$ for S1 by delta Δ and decreases the payoff θ_i for S2 by delta Δ. Otherwise, agent Ai has been chosen S2 for T times in succession, agent Ai increases the payoff θ_i for S2 by delta Δ and decreases the payoff $1-\theta_i$ for S1 by delta Δ.

Table 2. Updated payoff matrix of agent Ai after chose S1 for T time steps in succession.

		Behavior of other agent	
		S1	S2
Behavior of agent Ai	S1	$1-\theta_i+\Delta$	0
	S2	0	$\theta_i-\Delta$

The reinforced payoff at next time is given by Table.2 and 3. That corresponds to slow natural selection[11].

Table 2. Updated payoff matrix of agent Ai after chose S2 for T time steps in succession.

		Behavior of other agent	
		S1	S2
Behavior of agent Ai	S1	$1-\theta_i-\Delta$	0
	S2	0	$\theta_i+\Delta$

3. Simulation

3.1. Simulation settings

We arrange agents for an area of 50×50 (2500 agents) with no gap, and four corners and ends of an area connect it with an opposite side. We set payoff parameter θ_i of all agents as 0.5 at first. And we set μ as 0.5 based on preliminary experiment.

At initial time step, we set the initial collective behavior $p(0)$, which is the proportion of agents having chosen S1 in whole population, from 0.0 to 1.0 at intervals of 0.125, where we assume that an agent chooses at random. And each agent makes its decision depend on the best response rule each time step, and then collective behavior $p(t)$ changes. Then, we simulate 100 trials per one initial collective behavior and investigate final collective behavior p^* (at 1000 time step).

We simulated 3 cases as shown in Table.4. M-0.01 is the case with delta Δ of 0.01 and the agent can change its partners. In the case, the interactions of agents are les clustered. S-0.01 is the case with delta Δ of 0.01 and the agent cannot change its partners that is stay the site. In the case, all agents stay the site and always interact with steady four neighbors, which is isolated interaction. M-0.1is the case with delta Δ of 0.1 and the agent can change its partners. Self-reinforcement with delta Δ of 0.1 means faster learning than that with delta Δ of 0.01.

Table 4. Simulation patterns

		Change partners	
		Movable	Stay
delta Δ	0.01	M-0.01	S-0.01
	0.1	M-0.1	---

3.2. Criteria

We evaluate collective behavior with four criteria, stability, arrangement, efficiency and equity. The stability is the path-dependency of collective behavior. We evaluate final collective behavior p^*, which represents the proportion of agents to choose S1 at last, staring from some initial collective behavior $p(0)$. As for arrangement of collective behavior, we investigate the behavior of all agents at last. And we compare that with the arrangement of agents' preferences.

Efficiency is evaluated by the average utility, which also stands for the measure of the desirability of macro level. Here, high Efficiency, that is high average utility, means that agents in the population get high utilities as a whole. We define the proportion of agents $g(u)$ who obtained utility u per one partner at last interaction. Then, Efficiency U is given as follows,

$$U = \int_0^1 ug(u)\,du. \qquad (4)$$

If two populations have the same Efficiency, the utility distributions are different. One population may be equity, another population may be inequity. Then, Equity stands for the measure of the desirability at the micro level. In economics, the inequity is often calculated by the Lorenz curve. The Lorenz curve is represented by the cumulative proportion of the total utility, which is cumulated to the proportion at the level x starting with the poorest agents. Using $g(u)$, the Lorenz curve $L(x)$ is given by $L(x) = \int_0^x \tau g(\tau)\,d\tau / \int_0^1 \tau g(\tau)\,d\tau$. Equity E is obtained by the area under the Lorenz curve and is obtained as follows,

$$E = 2\int_0^1 L(x)\,dx, \qquad (5)$$

where the parameter x satisfying $x = \int_0^w g(\tau)\,d\tau$ and w is the obtained utility.

3.3. Simulation results

The simulation results are shown in Fig.2, 3 and 4 at last. For case M-0.01, the arrangement of agents' behaviors of at last are shown in Fig.2(1) and arrangement of agents' presences at last are shown in Fig.2(2). When initial collective behavior initial collective behavior $p(0)$ is 0.125, all agents comes to choose S1 at last (Fig.2(1)(a)) and final collective behavior p^* becomes 1.0. As for payoff parameters, when initial collective behavior $p(0)$ is 0.125, payoff parameter θ_i of all agents change 1.0 at last (Fig.2(2)(a)). When initial collective behavior initial collective behavior $p(0)$ is 0.875, all agents comes to choose S2 at last (Fig.2(1)(c)) and final collective behavior p^* becomes 0.0. As for payoff parameters, when initial collective behavior $p(0)$ is 0.875, payoff parameter θ_i of all agents change 0.0 at last (Fig.2(2)(c)). Diversity is not emerged in the population.

On the other hand, when initial collective behavior $p(0)$ is 0.5, half of agents choose S1 and the rest agents chooses S1 at last (Fig.2(1)(b)) and final collective behavior p^* becomes 0.5. As for payoff parameters, when initial collective behavior $p(0)$ is 0.5, payoff parameter θ_i of half of agents change to 0.0 and the rest agents change to 1.0 at last (Fig.2(2)(b)). We found that diversity is emerged in the population. Moreover, comparing with Fig.2(1)(b) and Fig.2(2)(b), agents with payoff parameter 0.0 chooses S1, that is, agents who prefer S1 choose S1 according to the preferences. And agents with payoff parameter 1.0 chooses S2, that is, agents who prefer S2 choose S2 according to the preferences. And segregation is formed and agents with the same preference can interact. We define the segregated interaction as selective interaction.

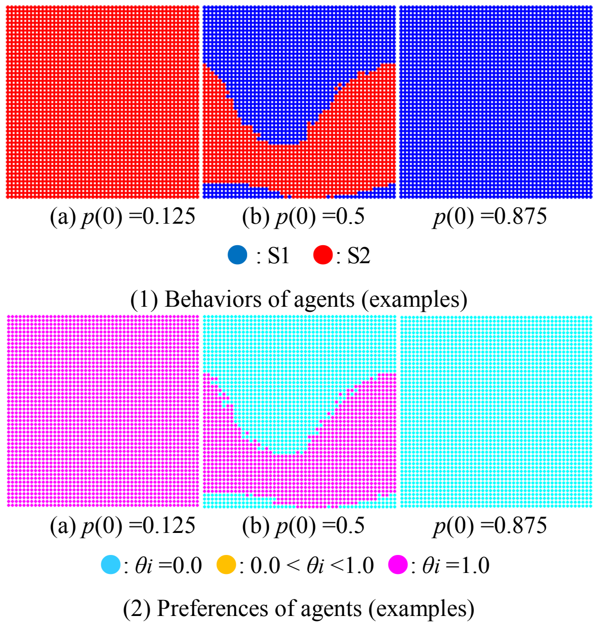

Fig. 2. Assignment of Agents at last: case M-0.01

In case S-0.01 (Fig.3) and M-0.1(Fig.4), the properties of assignment of agents at last are similar to that in case M-0.01. But, in case S-0.01, when initial collective behavior $p(0)$ is 0.125 and 0.875, minority behavior survives (Fig.3(1)(a) and Fig.3(1)(c)). Because the agent cannot change its partners, it is possible to remain the local behavior. As for the preferences, a slight but noticeable diversity is emerged in the population (Fig.3(2)(a) and Fig.3(2)(c)). And in case S-0.01, when initial collective behavior $p(0)$ is 0.5, it is difficult to form selective interaction (Fig.3(1)(b)) unlike case M-0.01.

In case M-0.01 and M-0.1, when initial collective behavior $p(0)$ is 0.5, there are formed selective interaction (Fig.2(1)(b) and Fig.4(1)(b))) .We found that by change partners, there are formed selective interaction of agents with same preference. And when delta Δ is 0.01, segregation is clear and selective interaction are formed than that when delta Δ is 0.1.

The stability of collective behavior shown in Fig.5. In this figure, x-axis represents initial collective behavior $p(0)$ and y-axis represents the average final collective behavior p^*.

In case M-0.01, we found that collective behavior depends on initial collective behavior $p(0)$. If initial collective behavior is more than equal 0.75 collective behavior converges to 1.0 and all agents choose S1 at last in any trials. And otherwise initial collective behavior is less than equal 0.25 collective behavior converges to 0.0 and all agents choose S2 at last in any trials. That is the majority behavior survives and the minority behavior disappears. But, if initial collective behavior is between 0.375 and 0.625, collective behavior becomes intermediate, which means not extreme value like 0.0 or 1.0, depending on the trial and initial collective behavior. If initial collective behavior $p(0)$ is 0.375, final collective behavior p^* becomes 0.05. If initial collective behavior $p(0)$ is 0.5, final collective behavior p^* becomes 0.54. If initial collective behavior $p(0)$ is 0.375, final collective behavior p^* becomes 0.97. Then both behavior S1 and S2 can coexist.

In case S-0.01, collective behavior also depends on initial collective behavior $p(0)$, but the property of final collective behavior p^* is more moderate than case M-0.01, that is, the graph curve of case S-0.01 is gentler than that of case M-0.01.

In case M-0.1, collective behavior depends on initial collective behavior initial collective behavior $p(0)$ and final collective behavior p^* is the most moderate and the graph curve of case M-0.1 is the gentlest in three cases.

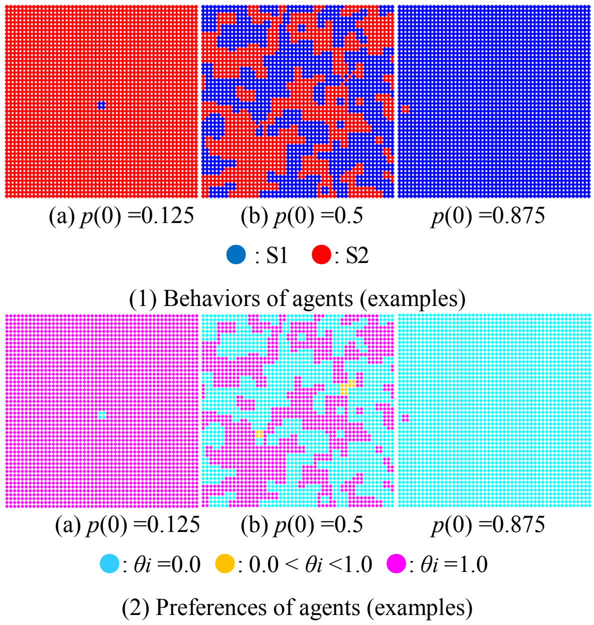

Fig. 3. Assignment of Agents at last: case S-0.01

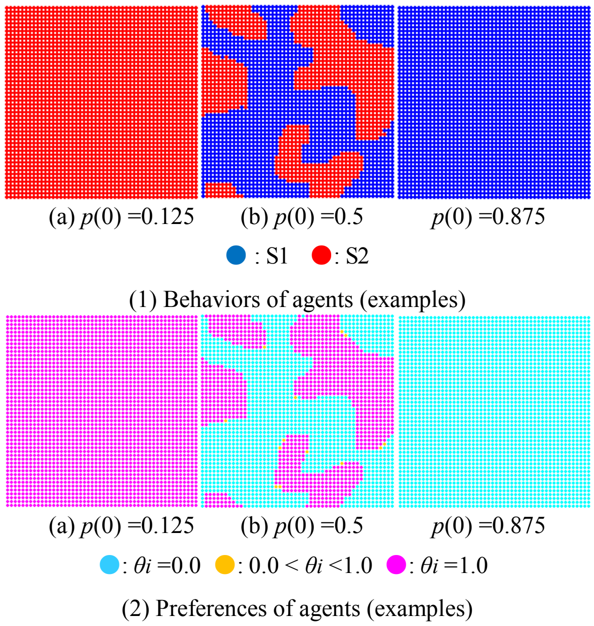

Fig. 4. Assignment of Agents at last: case M-0.1

In Fig.5, for reference, we also show the simulation results of default cases which mean that all agents don't self-reinforce. Default M is the case that the agent can change its partners that is movable. In default M, the agent can change its partners, and there is distinct initial value dependency and become 0.0 or 1.0 depend on initial collective behavior $p(0)$. Default S is the case that the agent cannot change its partners that is stay the site. In default S, the property is similar to case M-0.1 though agents do self-reinforce in the case. And both behavior S1 and S2 can coexist.

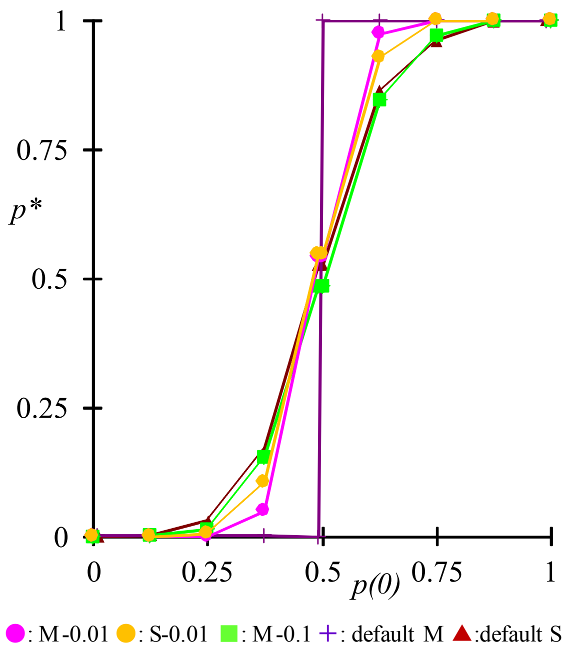

Fig. 5. Stability of Collective behavior

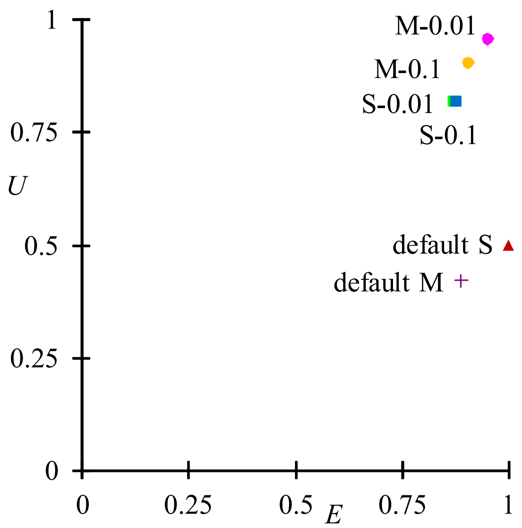

Fig. 6. Efficiency and Equity at last ($p(0) = 0.5$)

The efficiency and the equity at last are shown Fig.6. Because they are lowest when initial collective behavior $p(0) = 0.5$ in all initial collective behavior, we show them as typical efficiency and equity in Fig.6. We found that they are increased in the order of S-0.01, M-0.1 and M-0.01. The efficiency and the equity when the agent can change its partners are higher than that when the agent cannot change its partners. And they when delta Δ is 0.01 are higher than that when delta Δ is 0.1.

4. Discussion

Comparing with M-0.01 and S-0.01, case S-0.01 is effective for emergence of diversity. In case S-0.01, the agent cannot change its partners to interact and stays the site. That is, the interaction of population is isolated. But, the efficiency and equity of S-0.01 are less than that of case M-0.01. We found that less clustered interaction and utility of the population is trade-off. M-0.01 corresponds to less clustered interaction because agents can interact with agents far away. And S-0.01 corresponds to isolated interaction because agents can interact with only neighbor agents. We found what the same as Axelrod et.al[5] shows which the less clustered interaction make world less diverse and suggest isolated area is necessary emergence of diversity. But, if diversity of the population is emerged in less clustered interaction, we found that the utility is more than that of isolated interaction.

Comparing with M-0.01 and M-0.1, the efficiency and equity of M-0.01 are more than that of M-0.1. We found that it is effective to interact with partners of same preferences for utility. In this study, each agent learn on the two phases, best reply and self-reinforcement. The speed of learning of change partner is faster than that of self-reinforcement. As for self-reinforcement, M-0.01 corresponds to slow and M-0.1 corresponds to fast learning. We found what the same as Sandholm[10] shows which the effectiveness of two difference speed learning processes for emergence of diversity. Then, M-0.01 realizes more two difference speed learning process than case S-0.01 because the learning speed of two phases of M-0.01 has more huge differences than that of S-0.01.

Then, for emergence of diversity, it is needed two-speed learning processes. And it is needed isolated interaction for emergence of diversity. But, the utility of less clustered interaction is more than that of isolated interaction. On the whole, isolated interaction is effective for emergence of diversity. Then, once diversity is emerged enough, less clustered interaction is effective to utility of each agent and whole population.

5. Conclusion

The performance of the collective system depends crucially on the type of interaction as well as the heterogeneity in preference of agents. In this study, for emergence of diversity, we found that it is needed two different speed learning processes. And it is needed isolated interaction for emergence of diversity. But, the utility of less clustered interaction is more than that of isolated interaction if possible. On the whole, we found that isolated interacting is effective for emergence of diversity. Then, once diversity is emerged enough, less clustered interaction is effective to utility of each agent and whole population.

6. References

1. C. Reynolds, Flocks, Herds, and Schools: A Distributed Behavioral Model, *Computer Graphics (SIGGRAPH '87 Proceedings of the 14th annual conference on Computer graphics and interactive techniques)* **21**(4) (1987) 25-34.
2. K. Sims, Evolved Virtual Creatures*, Computer Graphics (SIGGRAPH '94 Proceedings of the 21st annual conference on Computer graphics and interactive techniques)* (1994) 15-22.
3. D. Terzopoulos, X. Tu and R. Grzeszczuk, Artificial Fishes: Autonomous Locomotion, Perception, Behavior, and Learning in a Simulated Physical World, *Artificial Life* **1**(4) (1994) 327-351.
4. M. Kubo and Y. Kakazu, Evaluation of Coordinated Motions of Multi - Agent Systems on Competition for Food between Ant Colonies, IPSJ Journal **35**(8) (1994) 1555-1566.
5. R. Axelrod and M.D. Cohen, *Harnessing Complexity* (Basic Books, 2001).
6. M. Rubenstein, A. Cornejo and R. Nagpal, Programmable self-assembly in a thousand-robot swarm, *Science* **345**(Issue 6198) (2041)795-799.
7. M. Sipper, *Evolution of Parallel Cellular Machines: The Cellular Programming Approach* (Springer-Verlag, Heidelberg, 1997).
8. F. Schweitzer (eds.), Interactive Structure Formation with Brownian Particles. *Self-organization of complex structures: from individual to collective dynamics* (Gordon and Breach Science Publishers, 1997) pp. 101-118.
9. W.B. Arthur et.al (eds.), The economy as an interactive system. *The Economy as a Complex Evolving System II* (Addison Wesley, Reading, MA, 1997) pp. 491–533.
10. R. Axelrod, The Evolution of Cooperation (Basic Books, 1985).
11. W.H. Sandholm, Preference Evolution Two-Speed Dynamics and Rapid Social Change, *Review of Economic Dynamics* **4** (2001)637-679.
12. A. Rubinstein, *Modeling Bounded Rationality* (The MIT Press, 1998).
13. B. Huberman and N. Glance, Diversity and collective Action, *Interdisciplinary Approaches to Nonlinear Complex Systems* **62** of the series Springer Series in Synergetics (1993) 44-64.
14. T. Schelling, *Micromotives and Macrobehavior* (Norton, 1978).
15. W.B. Arthur, Inductive Reasoning and Bounded Rationality, *American Economic Review* **84**(2) (1994) 406-411.
16. B. Fogel, K. Chellapia and P.J. Angeline, Inductive Reasoning and Bounded Rationality Reconsidered, *IEEE Trans. or Evolutionary Computation* **3** (2) (1999) 142-146.
17. J. Hansarny and R. Selten, *A Game Theory of Equilibrium Selection in Games* (MIT Press, 1988).
18. D. Fudenberg and D. Levine D. *The Theory of Learning in Games* (The MIT Press, 1998).
19. M.A. Nowak, *Evolutionary Dynamics: Exploring the Equations of Life* (Belknap Press of Harvard University Press (2006).
20. S. Parsons et.al (eds.) Selecting Partners, *Game Theory and Decision Theory in Agent-Based Systems*, Multiagent systems, artificial societies, and simulated organizations: international book series, 5(Kluwer Academic, 2002) pp. 1-29.

Beacon-based tourist information system to identify visiting trends of tourists

Akihiro Yamaguchi[1,*], Masashi Hashimoto[1], Kiyohiro Urata[1], Yu Tanigawa[1], Tetsuya Nagaie[1], Toshitaka Maki[1], Toshihiko Wakahara[1], Akihisa Kodate[2], Toru Kobayashi[3] and Noboru Sonehara[4]

[1]Fukuoka Institute of Technology, Wajiro-Higashi 3-30-1, Higashi-Ku, Fkuoka 811-0295, JAPAN

[2]Tsuda College, Tsuda-Machi 2-1-1, Kodaira, Tokyo 187-8577, JAPAN

[3]Nagasaki University, Bunkyo-Machi 1-14, Nagasaki 852-8521, JAPAN

[4]National Institute of Informatics, 2-1-2 Hitotsubashi, Chiyoda-ku, Tokyo 101-8430, JAPAN

*E-mail: *aki@fit.ac.jp*

Abstract

In this study, we propose a system that provides tourist information and obtains trends of visiting tourists using beacons and cloud service. As part of our research, we are working on the promotion of local area tourism in cooperation with a local community. A low energy Bluetooth device is used as a beacon to transmit a universally unique identifier. In addition, beacons are placed at sightseeing spots and tourist facilities. Our proposed system comprises two application programs; one is a client-side application program that provides area-specific tourist information corresponding to the detected beacon. The other is a server-side application to record time and location information of the detected beacons. In this paper, we describe the scheme of our system, and present the results of experiments conducted using the prototype system in the local tourist area. In addition, we discuss an open platform for information collection services using beacons.

Keywords: Tourism promotion, IoT, Bluetooth beacon, Stamp rally, Cloud service, Local community cooperation

1. Introduction

Tourism promotion is considered to be an important regional activity for revitalizing regional exchange and intergenerational communication.[1)] As part of our research, we cooperate with the local community to promote local tourism in Shingu, Japan.[2)] Although Shingu has many potential tourism resources, for example, a many natural beauty and historic sites, these tourism resources are not well known.

There are two approaches to using information technology in tourism promotion. One is to provide tourist information using the Internet and the other is to collect tourist information, for example, trends in the numbers of tourists and the order in which they visit sightseeing spots. Recently, beacon technology using Bluetooth low energy devices has become very popular and various applications have been studied.[3)] This technology could provide information about places visited by tourists and collect tourist trends.

In this study, we propose a beacon-based system that provides tourist information and obtains visiting trends of tourists using beacons and a cloud service. A prototype of the proposed system was developed for Ainoshima Island in Shingu. We then performed field tests using the developed prototype system. In addition, we discuss an open platform for information collection services using beacons.

2. Beacon-based Tourist Information System

In the following sections, we present an outline of the proposed beacon-based tourist information system and method for identifying sightseeing spots using beacon and Global Positioning System (GPS) information.

2.1. *Outline of the Proposed System*

Our proposed system consists of two parts: a client-side application (the client) and a server-side application (the server). A schematic drawing of the proposed system is shown in Fig. 1. Beacons are placed at the targeted sightseeing spots beforehand.

The server consists of the tourist information database (TIDB) and visiting tourists database (VTDB). Tourist information for the targeted spots and facilities are stored in the TIDB with their corresponding beacon ID. Beacon detection events for each client are stored in the VTDB as a record (user ID, beacon ID, time, and location).

The basic procedure of the proposed system is as follows:

(1) Beacon detection: The client detects the beacon when it enters the range of the target beacon.
(2) Beacon information storage: The client sends the detected beacon ID, client ID, time, and location to the server, where it is stored in the VTDB.
(3) Tourist information retrieval: Visited sightseeing spots are identified using the beacon ID, and the corresponding area-specific tourist information is retrieved from the TIDB on the server.
(4) Identified spot notification: The client is notified when a spot is identified.
(5) Area specific tourist information retrieval: If the client user wants to obtain area-specific tourist information about the identified spots, the client downloads it from the server.

Using this procedure, data about the sightseeing spots visited by each client are accumulated in the VTDB on the server. We can then use these data to identify tourist trends at sightseeing spots and the order in which tourists visit these spots.

2.2. *Identification of Sightseeing Spots Using Beacon and GPS Information*

In this research, a low energy Bluetooth device with iBeacon technology[4)] is used as a beacon. A sightseeing spot where the beacon is installed is identified by the beacon ID and GPS information. In iBeacon technology, a beacon ID consists of a universally unique identifier (UUID: 128 bits), major value (16 bits), and minor value (16 bits). In this research, the UUID is assigned an application-specific number and we use the same UUID through our proposed system. The major value identifies the area in which the beacon is placed. A unique minor value is assigned for each sightseeing spot. We can then identify sightseeing spots by the three values UUID, major value, and minor value. The identification is validated by GPS information.

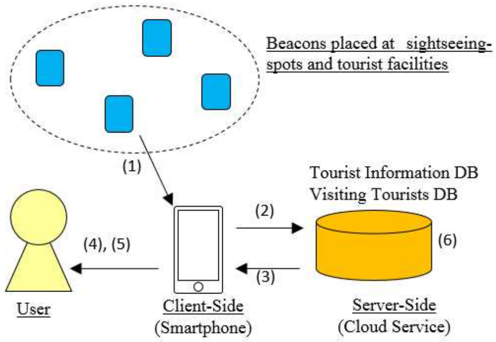

Fig. 1. Schematic drawing of the proposed beacon-based tourist information system: (1) beacon detection, (2) beacon information (user ID, beacon ID, time, and location) storage, (3) retrieval of tourist information corresponding to the beacon ID, (4) identified spot notification, (5) retrieval of area-specific tourist information, and (6) identification of visiting trends from stored data.

To handle sightseeing spots where we cannot put beacons, for example historical monuments in outdoor fields, we introduce a "pseudo beacon" using GPS. The pseudo beacon also has a UUID, major value, and minor value like a normal beacon. When the client's GPS position is near the sightseeing spot where the pseudo beacon is assigned, the client behaves as if it has detected a normal beacon. In order to implement this pseudo beacon, it is necessary to obtain the information about the pseudo beacons in the target area beforehand.

3. Development of the Prototype System

As a prototype of the proposed system, we developed a beacon-based tourist information system for Ainoshima Island in Shingu. The client is implemented as an Android application. The server is implemented using a cloud service. In this prototype system, the TIDB is implemented in the client.

Table 1. Major sightseeing spots in Ainoshima.

Beacon ID (minor)	Sightseeing Spot	Beacon Type
1001	Maruyama restaurant	normal
1002	Waiting place of Ainoshima Port	normal
1003	Ainoshima Tourist Information	normal
1004	Wakamiya-jinjya (Shrine)	normal
1005	Kizuna-Kan (Disaster support facility)	normal
1006	Jingu-ji (Temple)	normal
1007	Waiting place of Shingu Port	normal
1008	Ferry boat "Shingu"	normal
1009	Tsumiishi-duka (Tumulus Cluster)	pseudo

The implemented functions of the prototype system are as follows:

(a) Tourist information function: The sightseeing spots of Ainoshima are listed (Fig. 2(a)) and the user can see tourist information about the selected spot (Fig. 2(b)).

(b) Map function: The user can see the location of sightseeing spots where beacons are installed. Spots identified by beacon detection are highlighted using a colored marker (Fig. 2 (c)).

(c) Stamp rally function: The spots listed in Table 1 are assigned virtual stamps and the user obtains the stamp when the client detects the corresponding beacon. This function is implemented for use in tourism events of the local community. [3,5]

(d) Notification function: When the beacon is detected, the user is notified that the sightseeing spot has been identified (Fig. 2 (d)). After the notification, the user is not notified of identifications of the same spot for an hour to avoid frequent notifications.

(e) Log function: Beacon detection information is stored on the server. New beacon detections of the same beacon are ignored for 10 min after a previous detection to avoid frequent communication with the server.

4. Field Test of the Prototype System

In order to test the developed prototype system and evaluate the performance of the tourist data collection, a field test was performed on Ainoshima. The preparation of the field test (beacon installation) and results are presented below.

4.1. *Installation of Beacons*

For 20 sightseeing spots in Ainoshima and Shingu town, eight beacons were installed in indoor spots and 12 pseudo beacons were assigned to outdoor spots. The major sightseeing spots are listed in Table 1. An Aplix MyBeacon MB004 AC-DR1 was used as the beacon. This beacon is compliant with iBeacon technology. The advertising interval of the beacon was set to 1,285 ms to reduce electric power consumption. The measured power, which is the expected received signal strength indicator (RSSI) at a distance of 1 m from the beacon, was −63 dB.

4.2. *Results of the Field Test*

In the field test, a total of nine users used the prototype system on Ainoshima. They visited the sightseeing spots listed in Table 1 in any order for about 2 h. As a result, all the spots in Table 1 were identified by the detected beacons. In total, 223 beacon detection records were stored on the server. Using these data, we can identify the tourist path of visited sightseeing spots, as shown in Table 2 and Fig. 3.

5. Discussion

In this research, we proposed a beacon-based tourism information system. The prototype system was developed for Ainoshima Island, Shingu, Japan. The developed system worked well in the field test and tourists' paths were identified.

The tourist paths identified by our system are based on beacon detection log data. In comparison to identification using GPS only, our system has two advantages. One is that amount of data for the identification is reduced, as our system uses log data only for sightseeing spots where beacons are installed or pseudo beacons are assigned. The other is that identification is possible for indoor spots where beacons are installed.

To use our system in practice, it would be necessary to increase the participation of local communities and extend the supported area. An open platform for information collection services using beacons is one potential solution for this purpose. If an open Web API to retrieve beacon and tourist information and a management system for registered information are provided, local communities could build their own information collection service by themselves. To construct such an open system is one of our future tasks.

Acknowledgements

The authors would like to thank Shingu Town Office, Shingu Omotenashi Kyokai, and the Consortium of "Fukuoka IT Workouts" for their cooperation. This research was supported by open collaborative research at the National Institute of Informatics (NII) Japan (FY2016).

References

1. Japan Tourism Agency, Case studies of creating tourism destinations 2015, (Retrieved Nov. 20, 2016, from http://www.mlit.go.jp/kankocho/shisaku/kankochi/ikiiki.html).
2. T. Wakahara, T. Maki, K. Yoshii, N. Sato, A. Yamaguchi, Y. Ichifuji and N. Sonehara, The local community support system using linked open data, *IEICE Technical Report*, Vol.115 No.219 (2015), pp. 61-65 (in Japanese).
3. D. Asahi, Y. Yokohata, T. Inoue, H. Maeomichi, and A. Tsutsui, Performance Evaluation of Participatory BLE device Monitoring in a Wide Area Stamp Rally Experiment, *IEICE Technical Report*, Vol.115 No.466 (2016), pp. 33-37 (in Japanese).
4. Apple inc., iBeacon for Developers, (Retrieved Nov. 20, 2016, from https://developer.apple.com/ibeacon/).
5. N. Kichiji, Network analysis of the traffic lines of the tourists visiting Kamiikawa central district in Hokkaido, Japan, in *Econ. J. of Hokkaido Univ.*, Vol. 40 (2011), pp. 89–112.

Table 2. Example of logged data for one test user.

Time	Visited sightseeing spots
11:19	Ferry boat "Shingu"
11:51	Maehato (Ruin of Port)
11:52	Ainoshima Tourist Information
11:53	Waiting place of Ainoshima Port
12:28	Ainoshima elementary school
12:43	Tsurugi-jinjya (Shrine)
12:49	Tsumiishi-duka
13:08	Ainoshima elementary school
13:20	Maruyama restaurant
13:25	Waiting place of Ainoshima Port
13:26	Ainoshima Tourist Information
13:27	Wakamiya-jinjya
13:37	Jingu-ji
13:41	Wakamiya-jinjya
13:42	Kizuna-Kan

Fig. 3. Identified path of visited sightseeing spots from the logged data shown in Table 2. (Map data ©2016 ZENRIN and Google)

Analysis of Survey on Employment Trends

Masao Kubo, Hiroshi Sato
Computer Science, National Defense Academy, Hashirimizu 1-10-20
Yokosuka, Kanagawa 239-8686, Japan

Akihiro Yamaguchi
Fukuoka Institute of Technology, 3-30-1 Wajiro-higashi,
Higashi-ku, Fukuoka, Japan

Yuji Aruka
Faculty of Commerce, Chuo University, Higashinakano
Hachioji-shi, Tokyo, Japan
E-mail: masaok@nda.ac.jp, hsato@nda.ac.jp, aki@fit.ac.jp, aruka@tamacc.chuo-u.ac.jp
www.nda.ac.jp/cs/stuff/masaok.html

Abstract

If there were no changes in the environment surrounding businesses, the numbers of people leaving and entering employment would stay almost the same. Therefore, understanding the numbers allow us to make assumptions about the changes inside and outside companies. However, when categorizing businesses into industry sectors and clusters of business, you will see that the numbers of people leaving and entering employment have been nearly opposed for the last 15 years, and it is difficult to detect changes in the employment environment of Japan's businesses. This study tried to improve the level of detecting changes by applying NMF (non-negative matrix factorization) into the Survey of Employment Trends. While businesses maintain the number of people they employ at a certain level because of severe restrictions, we assumed they respond to the surroundings by changing the composition of employment. Accordingly, we identified the correlation between the numbers of people leaving and entering employment in each sector characterized by employment patterns that we found by applying NMF. As a result we successfully improved the level of detecting changes, which we would like to report in this study.

Key words: resilience, data mining, NMF, machine learning

Introduction

In principle, it is assumed that more employees leave companies when employers believe that the current number of employees is too many; conversely, the number of people entering companies increases when employers believe that the number of employees is too few. Therefore, if these numbers are the same, you can assume that the employer thinks their business environment is stable. While, if the numbers are largely different, you can assume that companies were forced to make corporate changes due to changes in their surrounding environment. Applying this assumption to industry sectors, which are clusters of businesses in the same fields, by studying the numbers of people leaving and entering employment, you must be able to make assumptions about the country-wide changes in the employment environment from the difference between the numbers.

The survey of employment trends is statistical data based on a questionnaire survey of businesses and people leaving and entering employment conducted by the Ministry of Health, Labour and Welfare (MHLW). It has been conducted for several decades, and the results have been published on the internet twice a year since 2000. This survey reported employment information of about 45 types of industries (hereinafter called "sectors") categorized on the basis of the Japan Standard Industrial Classification, excluding agriculture and fisheries.

According to this open data, although a catastrophic incident called the Lehman crisis has occurred, the numbers of people leaving and entering employment in industry sectors in Japan have stayed nearly the same for the last 15 years and it is hard to say that it indicates the changes in employment environment during the period at a glance. One reason is based on the fact that companies have significant restrictions and social responsibilities. Even if companies have deteriorated business performance and more people leave employment, companies are obligated to acquire skills and knowledge provided by new employees to maintain a certain level of business performance and have the social responsibilities to survive the competition and support permanent employees. Therefore, it is assumed that even though the change in the number of employees is small, there should be large changes in the type and characters of human resources they hire.

In this study, we visualize the changes in the environment surrounding employment in Japanese industries, incorporating the changes in human resources they employee from their abilities point of view into the numbers of people leaving and entering employment. Therefore, here we extracted the employment patterns using NMF and defined the characteristics of the numbers of people leaving and entering employment in each sector. It is assumed that the required human resources should be distributed across various sectors in industries, and in certain sectors, employers' employing those human resources must give impact on the number of people leaving and entering employment in the related sectors. Also, these types of human resources probably are likely to be in demand in other sectors. If we can find a set of potential patterns related to the numbers employed, we believe that we can more clearly visualize the changes in the surrounding environment by looking at the changes in the composition of each pattern of the number of people leaving and entering employment.

Non-negative Matrix Factorization (NMF) (Ref.6) is a method to decompose the matrix with elements of either zero or a positive value into the product of two non-negative matrices. Using its feature that subtracting is not allowed, in principle, the method has been widely used in the field of signal separation(Ref.2,5,3). Although there are some application examples of this method to economic activities(Ref.1), there were no examples of this method applied to visualize the employment environment.

1. Survey on Employment Trends

This study examined the MHLW Survey on Employment Trends (Ref.4). The MHLW conducts the questionnaire survey twice a year and publishes the number of employees, those changing careers, and hired employees by industry. This study used 15 years of annual data between 2000 and 2014. The industry classification is based on the Japan Standard Industrial Classification. The following studies use the industrial sector classification called middle classification. It is, roughly speaking, a classification dividing industrial areas, except for agriculture and fisheries into smaller areas. Although the classification has been changing slightly since 2000, this study classification employed a total of 55 types of industries reflecting the changes and including duplication.

2. Recent employment treads in Japan

Using this data, this study provides the data of recent employment trends in Japan. It found that there was no large difference between the numbers of people leaving and entering employment in each industrial sector in the last 15 years. The number of hired employees refers to the number of persons who started working in the sector as of this year, while the number of separated employees refers to the number of persons who left the sector. Figure 1 illustrates the numbers of hired employees and separated employees in each sector included in the survey on employment trends in 2014. Those leaving and entering employment are shown on a bar graph in order of sector. The vertical axis shows the number of people (unit: 1000 people).

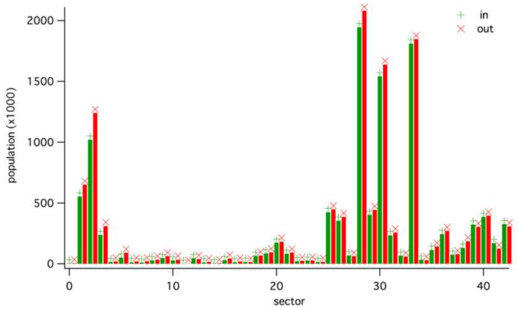

Fig. 1 Results of the Survey on Employment Trends in 2014

Bars with “+” on the top of it represent the number entering employment and bars with “×” represents those leaving employment. You can see that those entering and leaving employment are significantly different across sectors but they are nearly the same if they are in the same sector and same year.

Table 2 Similarities among the numbers of entering and leaving employment between 2000 and 2014

2000	**2001**	**2002**	**2003**	**2004**	**2005**	**2006**	**2007**
0.998	0.993	0.992	0.997	0.996	0.997	0.997	0.999
2008	**2009**	**2010**	**2011**	**2012**	**2013**	**2014**	
0.996	0.936	0.996	0.997	0.996	0.997	0.994	

Table 2 shows the results of these changes in a quantitative manner. When the number of people entering employment in the year y in the sector i is set as $a_{y,j}$, and the number of people leaving employment is $s_{y,i}$, the cosine of the vector of the people entering employment a_y = $(a_{y,0}, \ldots, a_{y,i}, \ldots, a_{y,54})$ and that of the people leaving employment $s_y = (s_{y,0}, \ldots, s_{y,i}, \ldots, s_{y,54})$ is

$$\cos(\angle a_y, s_y) = a_y \cdot s_y / |a_y||s_y| \qquad (1).$$

The value given from this formula in each year is shown in Table 2. The values except 0.936 in 2009, immediately after the Lehman crisis, were over 0.99, which shows that the numbers of people entering and leaving employment are nearly the same across all the sectors at all times except in 2009.

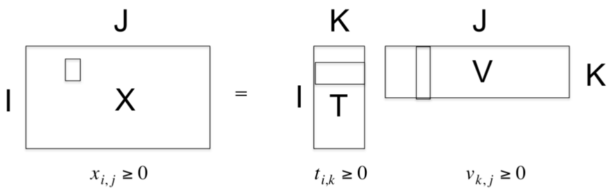

Fig. 2 NMF

3. Non-negative Matrix Factorization (NMF)

The multivariate analysis method to analyze non-negative data into additive components is called non-negative matrix factorization (NMF) and used in various fields(Ref.2,5). Figure 2 shows the schematic diagram of NMF. It decomposes matrix X, where all the factors are non-negative, into matrix T, where all the factors are non-negative, and V. The size K of matrix after the decomposition is given in advance. See Ref.2 for the detailed algorism.

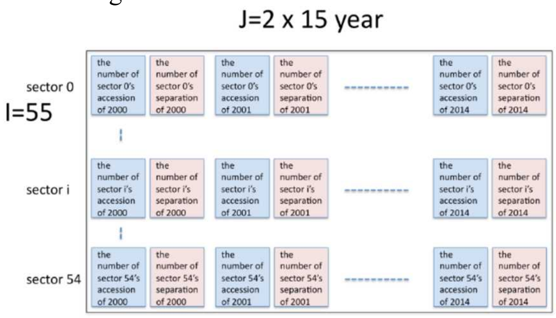

Fig. 3 matrix X in this analysis

3.1. *Structure of matrix X*

This section explains the structure of the decomposed object, matrix X. Figure 3 shows the structure of matrix X. This matrix is structured by listing the numbers of people entering and leaving employment in sector i in row i by year. The data in blue boxes shows factors related to the number of people entering and red shows those related to the number of people leaving employment.

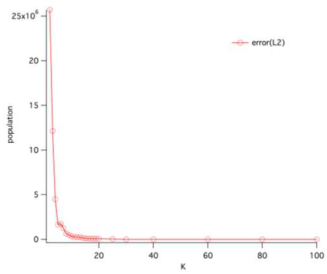

Fig. 4 Decomposition errors

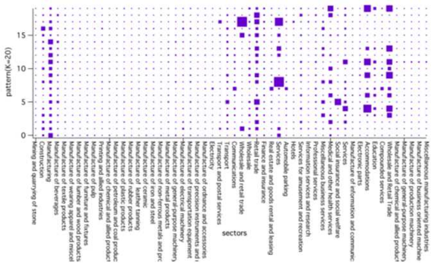

Fig. 5 Patterns obtained

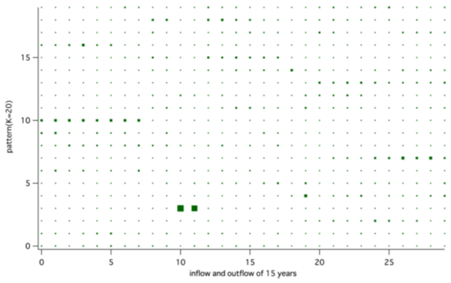

Fig. 6 Pattern's support in each year

3.2. *Analysis results*

Figure 4 shows the relationship between the number of parameters K and the accuracy of NMF decomposition. The vertical axis shows the sum of squares of the difference between the products of T, original matrices listing the numbers of people entering and leaving employment in sectors for 15 years, and V, matrices gained by NMF decomposition. The horizontal axis shows K, the number of patterns, which is equivalent to the horizontal axis of matrix T. It was found that when K is about 20, the error becomes nearly zero. Figures 5 and 6 show the results of decomposition when K=20. Figure 5 shows the patterns where matrix T is transposed. The vertical axis shows pattern numbers and horizontal axis shows sectors. The size of each symbol indicates the importance of the sector included in the pattern. In Figure 5, the combination of sectors where employment increases around the same time and the numbers of the employees are estimated. For example, in manufacturing and retailing industries you can see that growth in employment is expected in any patterns. Also, in the 17th pattern, when the numbers in wholesales and services industries significantly increase, that in manufacturing industry also increases though the number is small. Figure 6 shows matrix V; the vertical axis shows patterns and horizontal axis shows the data of entering and leaving employment. In even rows the breakdown of each pattern of the number of people leaving employment in each year is shown in the size of each symbol. For example the row 10 shows the number of people entering employment in 2005 and row 11 shows that of the people leaving in 2005. You can see that in both rows pattern 4 accounts for a large portion.

Looking at the structure of pattern 4 in Figure 5, employment in accommodation, wholesale and retail industries have large patterns. Also, in some industries the breakdowns of patterns of people entering and leaving employment vary. For example, the 2nd row and 3rd row represents the numbers of people entering and leaving employment in 2001 respectively. The importance of people entering employment is high in pattern 8, while that of those leaving is high in pattern 16. In pattern 8 more employment is seen in service industry, while in pattern 16 more employment is seen in construction industry. As a result of these, when using matrix V, you can see that the breakdowns of the numbers of people entering and leaving employment change.

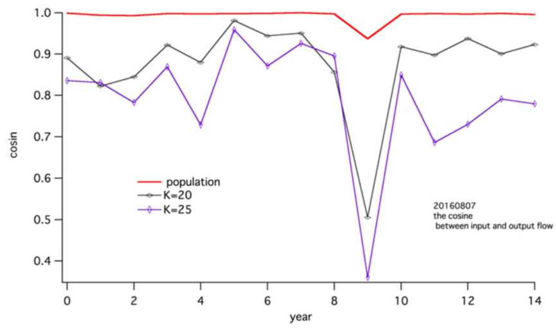

Fig. 7 Differences between the pattern's support of the people entering and leaving employment in each year

Fig. 7 Differences between the pattern's support of the people entering and leaving employment in each year

Now, in order to quantify the difference of breakdowns, the cosines were obtained in accordance with eq.1 and by setting the breakdowns of the numbers of people entering and leaving employment in Figure 6 as the vector, which were then illustrated in Figure 7. The horizontal axis shows years and vertical axis shows cosines. Cosines related to the number of people entering and leaving employment each year described in the Table 2 where K = {20, 25} with different NMFs are shown in thick lines. We found that although simple calculation hardly provides any changes even in the time of Lehman crisis, the suggested method using NMF visualizes detailed changes.

4. Conclusions

This study suggests a method of detecting the changes in the employment environment based on the Survey of Employment Trends. We suggest vectorizing the numbers of people entering and leaving employment based on the industrial sector middle classification of the Survey of Employment Trends by employment patterns found in NMF and using the cosines as the detection index. As a result, we were able to clearly visualize the impact of Lehman crisis, which we assume to have increased the level of detection of the changes in employment environment.

References

1. K. Kajitori, An Attempt to Detect Industry Clusters by Using Non-negative Matrix Factorizations, *Journal of National Fisheries University* 64 (4),pp227-239(2016)
2. H. Kameoka, Non-negative Matrix Factorization. *Journal of the Society of Instrument and Control Engineers* 51,9, pp. 835–844(2012)
3. http://hdl.handle.net/10086/15136.
4. Y. Kubo, M. Kubo, H. Sato, and A. Namatame: Estimation of Locations of Densely Distributed Subjects Using NMF with Nonpixel Information. *Journal of Advanced Computational Intelligence and Intelligent Informatics* Vol. 18 No. 4, 2014
5. Ministry of Health, Labour and Welfare (2016) *Survey on Employment Trends*
6. http://www.mhlw.go.jp/toukei/list/9-23-1.html.
7. H. Sawai: Nonnegative Matrix Factorization and Its Applications to Data/Signal Analysis. *Journal of the Institute of Electronics, Information, and Communication Engineers* 95(9), pp. 829–833 (2012)
8. P. Smaragdis, J.C. Brown: Non-Negative Matrix Factorization for Polyphonic Music Transcription, *2003 IEEE Workshop on Applications of Signal Processing to Audio and Acoustics,* pp.177-180 (2003)

Direction switch behavior to enclose a target

Masao Kubo, Nhuhai Phung, Hiroshi Sato
Dep. of Computer Science, National Defense Academy of Japan, Hashirimizu 1-10-20
Yokosuka, Kanagawa 239-8686, Japan

E-mail: masaok@nda.ac.jp, em54052@nda.ac.jp, hsato@nda.ac.jp
www.nda.ac.jp/cs/stuff/masaok.html

Abstract

This paper discusses a target enclosing behavior when a part of the orbit is blocked. Usually, a orbit to enclose a target supposes to be clear. However this often takes place in realistic environment. For this issue we propose microscopic methods to emerge macroscopic search capability to enclose a target. The group of robots change their direction according to the blocked part.

Keywords: Self organized swarm system, target enclosing, swarm robotics, phase transition.

1. Introduction

Recently, self-organized swarm system[3] which has more sophisticated and intelligent plasticity is required for real world application because it is too complex and dynamic. In this paper, target enclosing behavior of robot collective is discussed from this point of view.

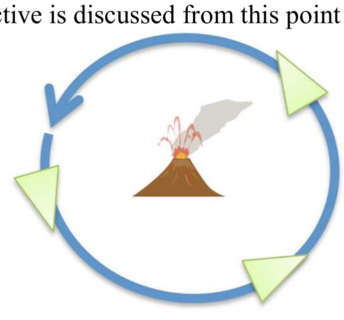

Fig. 1. Target enclosing under an ideal condition

When a part of the orbit to be enclosed with a robot collective is blocked there is no way of producing alternative formations to enclose. For this issue we proposes micro level modifications to emerge intelligent macroscopic dynamics as they find a new better formation by trial and error. In general such a system has to balance exploration and exploitation of collective level adequately. The phase transition property of boids[12] is adopted as this controller.

Fig. 2. Target enclosing under a difficult condition

This paper is composed as follows. Firstly, the proposed scenario that macroscopic states of a collective can be switched between exploration and exploitation is explained. Next a method that the scenario is realized for enclosing task for a robotic swarm. Here 2 microscopic rules, namely, an action selection scheme based on majority decision and a self generating noise rule are proposed. Finally a series of computer simulation shows that the proposed robotic collective can behave flexible under conditions which a simple collective is suspended.

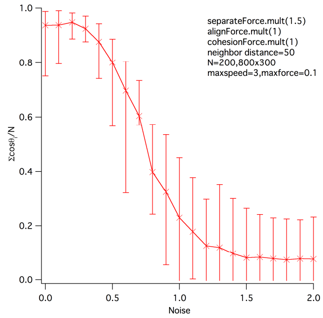

Fig. 3. Phase transition of boids.

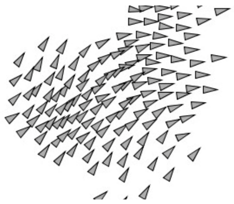

Fig. 4. Example of a synchronized formation.

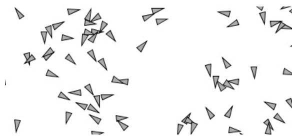

Fig. 5. Example of a disordered formation.

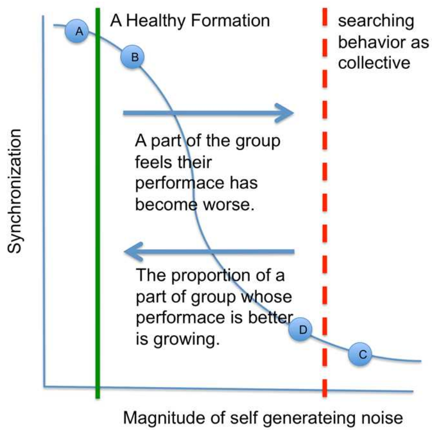

Fig. 6. concept of proposed collective level adaptation by self generating noise.

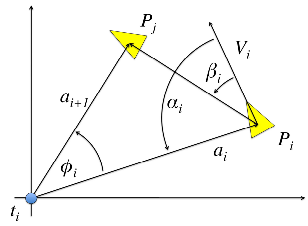

Fig. 7. Model of the enclosing a target algorithm: α, β.

2. The proposed scenario of switch of macroscopic states

Fig.1 shows a typical example of the problem of enclosing a target that a target is surrounded by moving robots. Target enclosing, target capturing and circumnavigation discuss similar topics [13] [5] [4] [9] [2] [11] [6] [7] [14]. This seems to be a fundamental formation of a collective for disaster site because this behavior builds up a dense but ordered robots around a given spot.

Usually, research in these domain suppose that the orbit is clear. However, this is not true in real environment. For example, a cliff around a target in mountain range makes this difficult because of space limitation. Also an invisible unusual strong air current makes robots fly difficult. We aim to build a self organized swarm system to enclose targets which can perform more adaptable.

In this paper, one of the following 2 formations according to their environment arises. The first formation is the ideal one shown in Fig.1. The second formation is shown in Fig.2. The group of the robots stays the part of the orbit to find a path. Once the blocked region is solved, the group can form the first formation immediately.

In order to realize such various group behaviors, if a problem occurs, it is necessary for the group to develop itself that searches for a better formation. Also, if it finds a good formation, the group also needs to converge it that every agent seems to agree with. It is necessary to balance both searching for formation at the collective level and utilizing the search results.

For this issue the phase transition trait of boids based on noise [12] is adopted. It is known that when the noise applied to particles in a particle group simulating boids exceeds a certain strength, the behavior of boids changes from a consistent state to a disordered state.

Fig.3 shows an example of the transition. This indicates the degree of consistency of boid directions when noise is applied to boids whose Separation, Cohesion, and Alignment ratios are 1.3, 1.0, and 1.0 [10]. In the case where a small amount of noise is added (Noise < 0.3), since the deviation of the corresponding boids is corrected by the remaining of the group, the overall behavior does not change. The state of the group at this time is shown in Fig.4. Almost all are moving in the same direction. On the other hand, when the amount of noise exceeds the threshold (Noise > 0.3), it varies sharply. Fig.5 shows the state when Noise = 1. It turns out that individuals are facing different directions.

Here, utilizing this dynamics, realization of collective search activity to recover from a failure and switching of modes of its use are realized. This conceptual diagram is shown in Fig.6. When a group is in an appropriate formation (A), it is assumed that some trouble has occurred. An agent that detects this malfunction selects an action which is different to others. As a result, the whole swarm changes to the state of B. If this detected defect is temporary, this noisy action is corrected and returns to state A. On the other hand, when many similar defects are detected, the macro state shifts to the C state. In the C state, each agent randomly changes their actions, so multiple formations will be tested as future formation candidates. As the number of agents supporting a good formation increases, the swarm shifts to macro state D and eventually reaches A.

In the following, we show how to implement the target enclosing problem as a method to embody the concept of this collective search state and decision making process.

We have already made a similar presentation[7]. However, the verification was not done with a general simulator and there was no way to verify. Therefore, in this paper we adopted a general agent model [10] that the source code is published and a model at the time of collision, and we verify this concept again.

3. Implementation to the target enclosing algorithm

3.1. *The proposed algorithm*

The proposed algorithm is shown as follows[7]. This uses only bearing information about target and its neighbor[9][14]. Additionally this model can change their direction to enclose a target.

Let n be the number of agents. The agents are numbered as $P_1,\ldots,P_n$. Agent P_i determines its action according to its nearest agent P_j and the nearest target t as follows.

$$v_i = f\beta_i \tag{1}$$

$$\omega_i = dir(P_i)\left(\frac{v_i}{\bar{r}} - k\cos\alpha_i\right) \tag{2}$$

where $dir(P_i) \in \{1,-1\}$ represents its direction to enclose the target.

$$dir(P_i) = \begin{cases} 1 & direction(P_i) = CW \\ -1 & direction(P_i) = CCW \end{cases} \tag{3}$$

f, k are positive constants. $direction(P_i) \in \{CW, CCW\}$ means the direction of agent P_i. $direction(P_i)$ is determined basically by majority decision as follows.

$$A_{i,t} = \{P_i \| P_i - P_j | < r_{com}\} \tag{4}$$

$$direction(P_{i,t}) = \begin{cases} CW & \dfrac{1}{|A_{i,t-1}|}\sum_{P_j \in A_{i,t-1}} dir(P_j) + \Delta dir \ge 0 \\ CCW & otherwise \end{cases} \tag{5}$$

Δdir is a random number chosen with a uniform probability from the interval $[-\eta A_{i,t}, \eta A_{i,t}]$.

$$-\eta|A_{i,t}| \le \Delta dir \le \eta|A_{i,t}| \tag{6}$$

where η is a positive constant. As the number of agents in the neighborhood increases, the noise applied becomes stronger, and the agent randomly selects the enclosing direction. Similarly, if there are many agents in the vicinity that select its direction randomly, they become disorderly locally and search for new collective behavior is done. This state is performed until the high density state is eliminated.

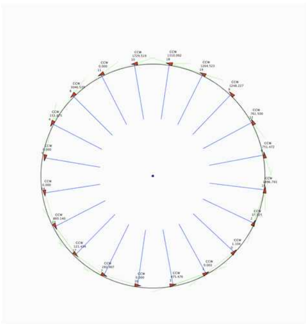

Fig. 8. A snapshot of the formation of the proposed swarm under an ideal condition.

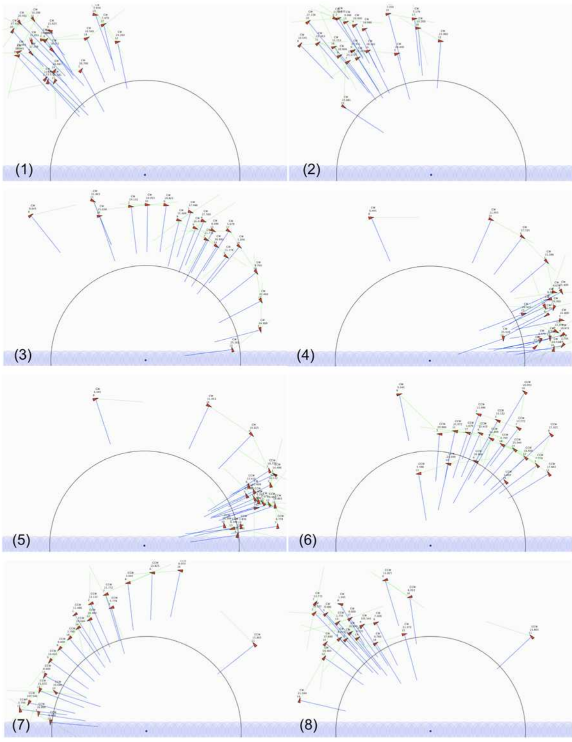

Fig. 9. Snapshots of the formation of the proposed swarm under condition which 2 parts of the orbit are blocked.

3.2. *Collision to wall*

Instead of the past work [7], in case of collision with the wall, according to [10] we changed direction reflectively and the speed was taken as the maximum speed.

4. Experiment

In this section, we show the performance of the proposed model. The parameters are defined as follows: $\bar{r}=300$, $n=20, |T|=1, r_{com}=100, \eta=0.1, f=1, f=1$.

Fig.8 shows the result of enclosing the targets without any blocked area. Each half of agents enclose the target from different direction. The two sub groups collide and consequently the direction of all agents becomes same by the equation 8.

Fig.9(1) - (8) shows the result of the proposed algorithm in case of orbit restricted. The line shown for crossing a circle represents a wall that is difficult to pass. When hitting this wall the robot bounces according to the rule described in subsection 3.2. Here we explain a typical transition. When the agent reaches the obstacle the direction is reflexively changed. As a result, agents gather near the wall as shown in Fig.9(4), (5). As a result, trying to avoid defect by try and error by the equation 6 near here. As the density gets higher, the noise of the equation 5 becomes larger, and the number of agents moving in a direction away from the wall increases. As a result, as shown in Fig.9 (6), it escapes from the vicinity of the obstacle. As they get out, the density decreases, so the direction to enclose the target of the agent is fixed.

From the above, it turns out that the proposed method can generate group behavior suitable for the difference in environment around the target.

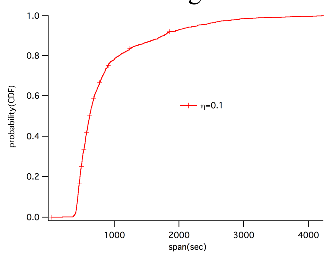

Fig. 10. Interval time span of switch of their direction at obstacles.

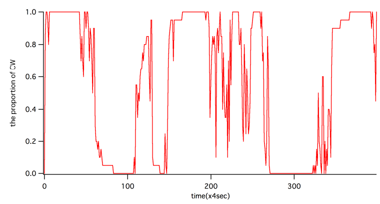

Fig. 11. Transition of the proportion of CW.

4.1. *The trend of changes of their direction*

Next, we investigated the relationship between the time interval at which the enclosure direction changes and η. In the experiment in the previous subsection, we found that the group moves between two obstacles. It is thought that swarms can be reconstructed promptly if the time required for conversion is short. The time required T_c sec is shown in Fig.10 using the cumulative probability density distribution $P[T_c \leq t]$. Although it was found that 60% could change direction quickly, it turned out that it was difficult to change direction even after 12,000 seconds had elapsed. Fig.11 shows the ratio of CW in the direction of direction. 1 or 0 indicates that all correspond to CW or CCW. However, it became 1 at *time* = 200, and since it was 1 many times again before reaching 0, it was confirmed that it took time for trial and error. Improving the time required for this change is a future task.

5. Conclusion

In this paper, we investigated the case where the orbit to enclose a target is physically restricted in the target enclosing problem as a part of the basic technology development for the self - organizing swarm system.

Here we proposed micro level algorithms, namely behavior selection based on majority voting and spontaneous noise generation function in order to realize macroscopic state switching between exploitation and exploration. This is based on the fact that the phase transition phenomenon occurs due to the magnitude of noise in the boids model. As a result of verifying the proposed method by computer experiments, it was found that formation can be switched according to the environment if there is sufficient time.

References

1. E. Castello, T. Yamamoto, Y. Nakamura, H.Ishiguro : Task Allocation for a Robotic Swarm Based on an Adaptive Response Threshold Model, *2013 13th International Conference on Control, Automation and Systems* (ICCAS2013),DOI:10.1109/ICCAS 2013.6703905(2013)
2. Y. Cao, UAV Circumnavigating an Unknown Target using Range Measurement and Estimated Range Rate, *2014 American Control Conference (ACC)* June 4-6, 2014. Portland, Oregon, USA,pp4581-4586.
3. E. Castello, T. Yamamoto, F. Dalla Libera, W. Liu, A. F.T. Winfield, Y. Nakamura, H. Ishiguro: Adaptive Foraging for simulated and Real robotic Swarms: The dynamical response threshold approaches, *swarm intelligence*, vol 10, issue 1,pp1-31(2016)
4. Tae-Hyoung Kim, T. Sugie: Cooperative control for target capturing task based on a cyclic pursuit strategy, *Automatica* 43,1426-1431(2007)
5. Y. Kobayashi, K. Otsubo, S. Hosoe, Autonomous Decentralized Control of Capturing Behavior by Multiple Mobile Robots, *Transactions of the Society of Instrument and Control Engineers*, 43(8), 663-671(2007)
6. M. Kubo, H. Sato, T. Yoshimura, A. Yamaguchi, T. Tanaka, Multiple targets enclosure by robotic swarm, *Robotics and Autonomous Systems* 62, pp1294-1304,2014.
7. M. Kubo, H. Sato, Nhuhai Phung, A. Namatame, Direction switch behavior to enclose a pack of targets based on phase transition, *Proceedings of SWARM 2015,* pp295-298(2015).
8. J. A Marshall, M E.Brouvke and Bruce A Francis: Formations of Vehicles in Cyclic Pursuit; IEEE *Transactions on Automatic Control*, vol49, no11 (2004)
9. Y. Takayama, S. Yamamoto, T. Takimoto, Distributed Formation Control of a Nonholonomic Multi-agent System for Target-enclosing Operations, *Proceedings of 9th SICE System Integration Division Annual Conference* (2008)
10. Daniel Shiffman, *Nature of Code*,(2012)
11. Sarah Tang, Dylan Shinzaki, Christopher G. Lowe, Christopher M. Clark, Multi-Robot Control for Circumnavigation of Particle Distribution, *Distributed Autonomous Robotic Systems Springer Tracts in Advanced Robotics* Volume 104, 2014, pp 149-162
12. Tamás Vicsek, András Czirók, Eshel Ben-Jacob, Inon Cohen, and Ofer Shochet, Novel Type of Phase Transition in a System of Self-Driven Particles, *Phys. Rev. Lett.* 75, 1226.1995
13. Yamaguchi H., A Cooperative Hunting Behavior by Nonholonomic Mobile Robot Troops, *Transactions of the Japan Society of Mechanical Engineers*. C, 69(688), 3285-3292(2003)
14. Ronghao Zhenga, Yunhui Liub, Dong Suna,Enclosing a target by nonholonomic mobile robots with bearing-only measurements, automatica, *Automatica* 53 (2015) 400–407

Force and Motion Analysis of larval zebrafish (*Danio rerio*) using a body dynamics model

Naohisa Mukaidani
Department of System Cybernetics, Graduate School of Engineering, Hiroshima University, 1-4-1 Kagamiyama, Higashi-Hiroshima, Hiroshima, 739-8527, Japan

Zu Soh
Department of System Cybernetics, Institute of Engineering, Hiroshima University, 1-4-1 Kagamiyama, Higashi-Hiroshima, Hiroshima, 739-8527, Japan

Shinichi Higashijima
National Institutes of Natural Sciences, Okazaki Institute for Integrative Bioscience, National Institute for Physiological Sciences, Okazaki, Aichi 444-8787, Japan

Toshio Tsuji
Department of System Cybernetics, Institute of Engineering, Hiroshima University, 1-4-1 Kagamiyama, Higashi-Hiroshima, Hiroshima, 739-8527, Japan
E-mail: mukaidani@bsys.hiroshima-u.ac.jp, sozu@bsys.hiroshima-u.ac.jp, shigashi@nips.ac.jp, tsuji@bsys.hiroshima-u.ac.jp
www.bsys.hiroshima-u.ac.jp

Abstract

This study proposes a method of body dynamics analysis for larval zebrafish incorporating a viscoelastic body model and a fluidic environment model to support the study of development mechanisms in motion generation. The results showed that the estimated fluid drag coefficients enabled the body dynamics model to approximate the paths of actual larvae with an error level of 0.76±0.74 [%] to the total body length.

Keywords: zebrafish, larval zebrafish, dynamics model, drag coefficient

1. Introduction

Zebrafish (Danio rerio), which measure about 3 – 40 [mm] in length, have been widely used in the field of biology to study genetic diseases and the brain structure of vertebrates. Their transparency at the embryonic and larval stages of development facilitates *in vivo* observation of their internal organs and neural circuits, making them highly useful as a model organism for the study of phenomena observed during the stages of growth. For this reason, the behaviors of larval fish have been extensively investigated. For example, changes in swimming distance and velocity during ontogeny were systematically analyzed in the 1980s (Webb, 1984; Webb and Weihs, 1986; Fuiman and Webb, 1988). Subsequent development of computer vision techniques enabled detailed quantification of larval motion, and further analysis helped to elucidate the ontogeny of fin function (Danos and Lauder, 2008), the relationships between drag force and fin/body morphological development from the larval stage to the adult stage (McHenry and Lauder, 2006) and the effects of hydrodynamics on locomotor development (Danos, 2012). Locomotor development was also analyzed in the context of larval body waves (Müller and Leeuwen, 2004), and the function of pectoral fins at the larval stage was investigated by comparing the movements of wild larval fish with those of others lacking pectoral fins as a result of genetic manipulation (Green *et al*., 2011).

Based on the extensive body of behavioral analysis data obtained from such studies, the mechanisms supporting coordination between neural circuits and the body for appropriate motor function have recently attracted attention. For example, Budick and O'Malley classified the behavior of larvae into three repertories (Budick, 2000), and Throsen *et al*. analyzed fin-axis coordination (Throsen *et al*., 2004) to support discussion of neural control. In addition, Higashijima *et al*. succeed in indirect measurement of neural activities in both the motoneurons and spinal interneurons during escape behaviors using a calcium indicator called cameleon (Higashijima, 2003).

The experimental studies described above succeeded in elucidating a number of important mechanisms. The clear-cut experimental results obtained have contributed to enormous efforts regarding the control of complex experimental conditions and static analysis to eliminate the influences of individual differences in body morphology, learning ability and stages of development. However, the effects of individual differences and experimental conditions cannot be completely eliminated in experimental approaches. In addition, it is technically difficult to measure the forces produced by tiny larvae despite the importance of such information in clarifying the neural control of muscles and swimming behavior. In light of such limitations, computer simulation can be seen as a potentially effective approach. For example, Katsumata *et al*. constructed a body dynamics model and carried out fluid simulation for free-swimming larval zebrafish to evaluate the properties of fluid flow around them (Katsumata *et al*., 2009). This zebrafish larva model allowed precise description of fluid behavior.

Considering the needs of biological study, however, both fluid dynamics and local body forces generated by larvae are important in discussing the relationships between ontogeny and nerve control development. In this context, the development of a larva model that can be used to calculate forces generated from the body and those acting on the environment based on motion recorded from actual fish can be seen as effective for analyzing behavioral aspects of fish during ontogeny, such as the relationships between drag force and morphological development as analyzed by McHenry and Lauder (McHenry and Lauder, 2006). Against such a background, this paper proposes a body dynamics model incorporating the considerations of body form and viscoelasticity to support the study of developmental mechanisms in the movement of larval zebrafish. An algorithm for estimation of the external drag forces acting on such fish is also presented. The proposed model enables simulation of target phenomena in uniform virtual environments and with individual conditions, and also allows analysis for the interaction of larval zebrafish morphology and swimming movement.

2. Body dynamics model

As larval zebrafish measure only about 3 [mm] in length, the forces exerted between them and their environments are difficult to measure. In this study, a body dynamics model was constructed based on the sizes and shapes of each part of these fish. A novel method of estimating drag coefficients between larval zebrafish and their environment as well as the driving torque of each joint based on dynamic analysis techniques was also introduced. Fig. 1 shows a zebrafish larva at protruding-mouth stage (72 [h]) and a 3D morphology of the body dynamics model configured from this image. The proposed model is a rigid-link type composed of five parts: a head part consisting of one link, left and right pectoral fin parts with 10 links each, a trunk part with 10 links, and a tail fin part with 10 links. The links are interconnected by joints allowing rotation about the z-axis. The rotational motion of each link and the translational and rotational motion of a representative point $x_{\mathrm{g}} = \left[x_{gx}, \theta_g\right]^T$ of the model can be calculated from the following equation based on the Newton-Euler method:

$$\begin{aligned}\mathrm{I}(\boldsymbol{q})\ddot{\boldsymbol{q}} + \mathrm{h}(\dot{\boldsymbol{q}},\boldsymbol{q}) + \mathrm{g}(\boldsymbol{q}) \\ = \boldsymbol{\tau} - \boldsymbol{k}(\boldsymbol{q} - \boldsymbol{q}_0) - \mathrm{c}\dot{\boldsymbol{q}} + \textstyle\sum_{r,d,j} \boldsymbol{J}_{rdj}^{\mathrm{T}} \boldsymbol{F}_{rdj}\end{aligned} \quad (1)$$

$$\mathrm{I}_g(\boldsymbol{q})(\ddot{\boldsymbol{x}}_g) + \mathrm{h}_g(\dot{\boldsymbol{q}},\boldsymbol{q}) + \mathrm{g}_g(\boldsymbol{q}) = \textstyle\sum_{r,d,j} \boldsymbol{F}_{rdj} \quad (2)$$

where I(q) and $\mathrm{I}_g(\boldsymbol{q})$ represent the inertia matrix, $\mathrm{h}(\dot{\boldsymbol{q}},\boldsymbol{q})$ and $\mathrm{h}_g(\dot{\boldsymbol{q}},\boldsymbol{q})$ are the centrifugal force and the Coriolis force, $\mathrm{g}(\boldsymbol{q})$ and $\mathrm{g}_g(\boldsymbol{q})$ represent the force of gravity, $\boldsymbol{q} = (\boldsymbol{q}_{rj}) \in \mathbf{R}^{30}$ is the rotational angle vector of the joints, $\boldsymbol{q}_0$ is the equilibrium angle of the stiffness component at a joint, $\boldsymbol{\tau} = (\boldsymbol{\tau}_{rj}) \in \mathbf{R}^{30}$ is a vector of rotational driving force, k is the stiffness coefficient (Fig.

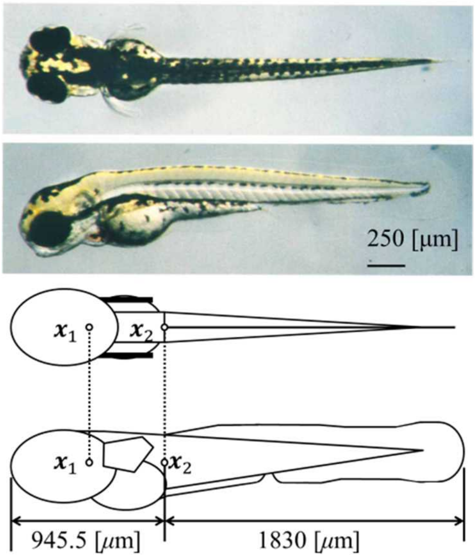

Fig. 1. Shape of a larval zebrafish and the body dynamics model. (a) shows a zebrafish larva at protruding-mouth stage (72 [h]) photographed by Kimmel *et al.* (Kimmel *et al.* 1996). Thin transparent fins surround the dorsal and ventral parts of the trunk. (b) shows the configuration of the body dynamics model approximating the image of the larva. The model's parameters were determined using this approximated shape. Position $\boldsymbol{x}_1$ is the centroid of the head link, and $\boldsymbol{x}_2$ is the joint connecting the head link and the trunk. The time traces of these two points were used to determine the drag coefficients of a fluid environment.

2), c is the viscous damping coefficient (Fig. 2), $\boldsymbol{J}_{rdj}$ is the Jacobian matrix, and $\boldsymbol{F}_{rdj}$ is the friction force exerted between the center of gravity of a link and the external environment. In addition, the subscript $r \in (\mathrm{H, B, C, R, L})$ denotes parts of the model, with H representing the head, B the trunk, C the tail fin, R the right pectoral fin and L the left pectoral fin. The subscript $d \in (\mathrm{A, N})$ denotes direction, with A representing the rostrocaudal direction of the fish and N the normal direction in the rostrocaudal direction. The subscript j denotes links sequentially numbered as $j = 1, 2, \cdots, 10$ from that connecting with the head part. Although the parameters on the left of the motion equation can be determined based on the measured shapes and weights of actual larval zebrafish, drag force is difficult to determine due to the size and complex morphology of the fish. In this study, the drag force $\boldsymbol{F}_{rdj}$ was approximated as a viscous resistance value proportional to the square of the velocity $\boldsymbol{v}_{rdj}$ at

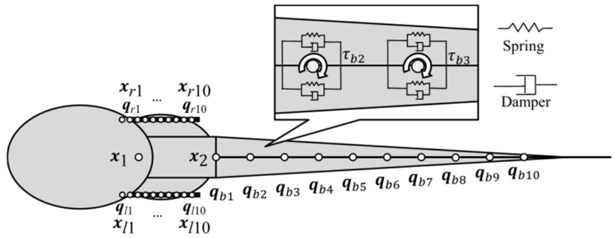

Fig. 2. Viscoelasticity of the body dynamics model. The white circles indicate inter-link joints, and q_{ri} denotes the angle between the links. A pair of damper and spring units is attached to each link in parallel to represent the viscoelastic characteristics of muscles on the left and right sides. As only two-dimensional motion was considered in the model for simplification, the pairs of muscles on the dorsal and ventral parts were combined.

the centroid of a link as shown in the following equation (Mochizuki and Ichikawa, 2010):

$$\boldsymbol{F}_{rdj} = C_{rdj}\rho S_{rdj}\left\|\boldsymbol{v}_{rdj}\right\|\boldsymbol{v}_{rdj} \tag{3}$$

where C_{rdj} is the drag coefficient, ρ is the fluid density and S_{rdj} is the surface area.

As drag force significantly affects the model's motion, C_{rdj} needs to be estimated. However, if different drag coefficients were assigned to each of part *r*, direction *d* and link *j*, the number of coefficients to be estimated would be as many as 82. Accordingly, it was assumed for simplification that the drag coefficients for the rostrocaudal direction of the pectoral fins and the tail fin ($C_{\mathrm{CA}j}, C_{\mathrm{RA}j}, C_{\mathrm{LA}j}$) were 0 because the fins are negligibly thin compared to their total surface area. It was also assumed that the drag coefficients for the same part *r* were identical. As a result, the friction force acting on each link can be determined via estimation of 6 drag coefficients.

3. Drag coefficient estimation algorithm

As Eqs. (1) and (2) describe the relationship between the motion of larval fish and related drag coefficients, these coefficients can be estimated via dynamic analysis by solving Eqs. (1) and (2). However, direct solution of drag coefficients from these equations for each time sample can yield large errors caused by video analysis noise. Accordingly, the coefficients were determined in this study by minimizing the following evaluation function for robustness:

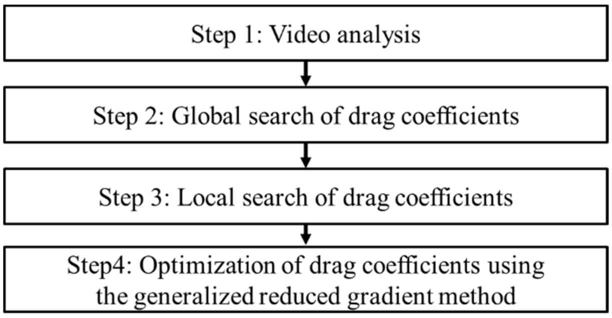

Fig. 3. Four-step flow of the algorithm used to estimate the drag coefficient of the environmental fluid. As drag coefficients are related to the paths of the body dynamics model, the proposed algorithm minimizes the difference between the paths of the actual larva and the body dynamics model. To avoid local minima, the algorithm sequentially performs global search, local search and generalized reduced gradient search where the drag coefficient sets with the smallest errors were chosen at each step.

$$E = \sum_t \frac{1}{P} \sum_{p=1}^{P} \left\| x_p^R(t) - x_p(t) \right\| \tag{4}$$

where P is the number of comparison points, x_p^R represents positions on an actual fish, and x_p represents the corresponding positions on the body dynamics model as shown in Fig. 1. This evaluation function represents the error of paths between an actual fish and the model as simulated using a set of drag coefficients. The proposed algorithm minimizes this evaluation function in M steps as shown in Fig. 3.

In Step 1, the movement of larval zebrafish is recorded using a high-speed camera and video image analysis is conducted (see Fig. 4). First, the tail and pectoral fins are separated as shown in Fig. 4 (a). Image processing steps including binarization, noise reduction and thinning are then performed for each frame of all the separated images to extract the centroid line of the trunk and the pectoral fins. This line is divided by points corresponding to those of the model's joints, and the time-dependent joint angles q_{rj} between the divided points are calculated. As the measurement results obtained from actual fish include noise, the joint angles q_{rj} are filtered using an n-degree low-pass Butterworth filter. Finally, the joint angles are input to the model as shown in Fig. 4 (c).

In Step 2, a global search of the drag coefficients is performed. First, a combination of drag coefficients is selected from a set $(C_{\mathrm{HA1}}^{a1}, C_{\mathrm{HN1}}^{a1}, C_{\mathrm{BA1}}^{a1}, C_{\mathrm{BN1}}^{a1}, C_{\mathrm{RN1}}^{a1}, C_{\mathrm{CN1}}^{a1})$

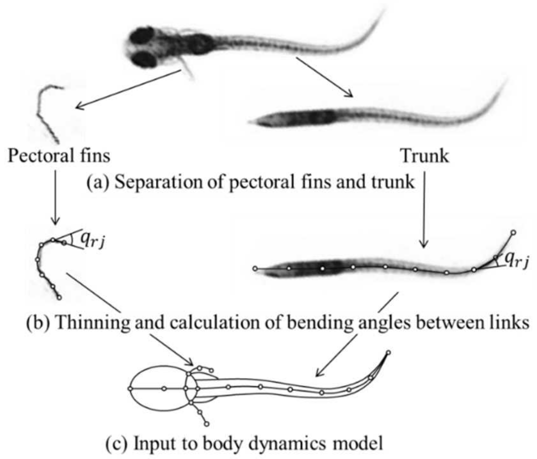

Fig. 4. Video image analysis procedure with recording conducted at 1000 [fps]. (a) As the thinness of pectoral fins makes it difficult to perform image analysis, the trunk and fins are manually separated and lines are drawn on the blurred images of fins for interpolation. (b) Using the processed images, joint bending angles and positions are calculated using Wriggle Tracker software (Library Inc. Tokyo). (c) The outcomes of motion calculation are input to the body dynamics model, and the resulting paths are calculated based on motion equations (Eqs. (1) and (2)) .

defined using the equation below and substituted into Eq. (3).

$$\begin{aligned}(C_{\mathrm{HA1}}^{a_1}, C_{\mathrm{HN1}}^{a_1}, C_{\mathrm{BA1}}^{a_1}, C_{\mathrm{BN1}}^{a_1}, C_{\mathrm{RN1}}^{a_1}, C_{\mathrm{CN1}}^{a_1}) \\ \in \{N_1\Delta C_{\mathrm{HA1}}^{1}, N_2\Delta C_{\mathrm{HN1}}^{1}, N_3\Delta C_{\mathrm{BA1}}^{1}, N_4\Delta C_{\mathrm{BN1}}^{1}, \\ N_5\Delta C_{\mathrm{RN1}}^{1}, N_6\Delta C_{\mathrm{CN1}}^{1} | N_1, N_2, N_3, N_4, N_5, N_6 \\ = 0,1,\cdots,N_{\mathrm{max}}^{1}\}\end{aligned} \tag{5}$$

where ΔC_{rd1}^{1} is the step size for the global search yielding the $a_1 = 1,2,\cdots,(N_{\mathrm{max}}^{1}+1)^6$ variation of drag coefficient sets, and the superscript 1 indicates the step size used in the first optimization step. Data on the motion of actual larvae, including the joint angle and joint angular velocity of each link, are then substituted into Eqs. (1) and (2), and the paths are calculated by repeatedly determining the forward and inverse dynamics for each sample time. This algorithm is described below.

(i) The initial position and initial posture of a representative point on a larval zebrafish $\boldsymbol{x}_g(0)$ are calculated from image analysis results. Other initial values such as translational velocity $\dot{\boldsymbol{x}}_g(0)$, joint angle $\dot{\boldsymbol{q}}(0)$, angular state velocity $\dot{\boldsymbol{q}}_0(0)$ and angular acceleration $\ddot{\boldsymbol{q}}_0(0)$ are also calculated and substituted into Eqs. (1) and (2).

(**ii**) The translational velocity $\boldsymbol{v}_{rdj}(t)$ of each link is derived from the translational velocity $\dot{\boldsymbol{x}}_g(t)$ of a representative point and the angular velocity $\dot{\boldsymbol{q}}(t)$ of each joint. The translational velocity of each link is substituted into Eq. (3) along with the selected combination of drag coefficients to determine the friction force $\boldsymbol{F}_{rdj}(t)$.

(**iii**) The driving torque $\boldsymbol{\tau}(t)$ and the acceleration $\ddot{\boldsymbol{x}}(t)$ are then derived from Eqs. (1) and (2) based on the substitution of $\boldsymbol{F}_{rdj}(t)$, $\boldsymbol{q}(t)$, $\dot{\boldsymbol{q}}(t)$ and $\ddot{\boldsymbol{q}}(t)$.

(**iv**) The position $\boldsymbol{x}(t)$ of the representative point on the model is derived via second-order integration for the acceleration $\ddot{\boldsymbol{x}}(t)$. By repeating steps (**ii**) through (**iv**) for each time step, the path is calculated for the selected drag coefficients. This path is then used to evaluate the coefficients by comparing it to the path of the fish using the evaluation function (Eq. (4)). After evaluation of all combinations of drag coefficients given by Eq. (5), a set of drag coefficients ($C_{\mathrm{HA1}}^{b_1}, C_{\mathrm{HN1}}^{b_1}, C_{\mathrm{BA1}}^{b_1}, C_{\mathrm{BN1}}^{b_1}, C_{\mathrm{RN1}}^{b_1}, C_{\mathrm{CN1}}^{b_1}$) with smaller d_1 [%] values for path error E are selected for a further search procedure in which $b_1 = 1,2,\cdots,(N_{\max}^1+1)^6 d_1/100$.

In Step 3, a local search is performed on the neighbors of the drag coefficient extracted in the previous step. First, a set of combinations of drag coefficients ($C_{\mathrm{HA1}}^{a_m}, C_{\mathrm{HN1}}^{a_m}, C_{\mathrm{BA1}}^{a_m}, C_{\mathrm{BN1}}^{a_m}, C_{\mathrm{RN1}}^{a_m}, C_{\mathrm{CN1}}^{a_m}$) is selected. The search region for these coefficients is defined by the following equation:

$$\begin{aligned}&\left(C_{\mathrm{HA1}}^{a_2}, C_{\mathrm{HN1}}^{a_2}, C_{\mathrm{BA1}}^{a_2}, C_{\mathrm{BN1}}^{a_2}, C_{\mathrm{RN1}}^{a_2}, C_{\mathrm{CN1}}^{a_2}\right)\\ &\quad \in \{C_{HA1}^{b_1}+N_1\Delta C_{HA1}^2, C_{HN1}^{b_1}+N_2\Delta C_{HN1}^2, C_{BA1}^{b_1}\\ &\quad +N_3\Delta C_{BA1}^2, C_{BN1}^{b_1}+N_4\Delta C_{BN1}^2, C_{RN1}^{b_1}\\ &\quad +N_5\Delta C_{RN1}^2, C_{CN1}^{b_1}+N_6\Delta C_{CN1}^2 | N_1, N_2, N_3,\\ &\quad N_4, N_5, N_6 = -N_{\max}^m, \cdots, 0, \cdots, N_{\max}^m\}\end{aligned} \tag{6}$$

where ΔC_{rd1}^2 is the step size of the drag coefficient ($\Delta C_{rd1}^2 > \Delta C_{rd1}^1$) . The selected combination of coefficients is substituted into Eq. (3). Here, a_2 represents the number of drag coefficients in the step 2. Dynamic analysis is performed as described in Step 2, and the simulated path is compared with that of an actual larva using the evaluation function (Eq. (4)). After evaluation of all combinations of the drag coefficients shown in Eq. (5), another set of drag coefficients ($C_{\mathrm{HA1}}^{b_2}, C_{\mathrm{HN1}}^{b_2}, C_{\mathrm{BA1}}^{b_2}, C_{\mathrm{BN1}}^{b_2}, C_{\mathrm{RN1}}^{b_2}, C_{\mathrm{CN1}}^{b_2}$) with smaller d_2[%] values of E is extracted for the end of step 3.

In Step 4, a combination of drag coefficients ($C_{\mathrm{HA1}}^{\min}$, $C_{\mathrm{HN1}}^{\min}, C_{\mathrm{BA1}}^{\min}, C_{\mathrm{BN1}}^{\min}, C_{\mathrm{RN1}}^{\min}, C_{\mathrm{CN1}}^{\min}$) with the smallest evaluation value E is searched using the generalized reduced gradient method (Lasdon, 1974). The initial value for this method is selected from the drag coefficients extracted in step 3, i.e., ($C_{\mathrm{HA1}}^{b_2}, C_{\mathrm{HN1}}^{b_2}, C_{\mathrm{BA1}}^{b_2}$, $C_{BN1}^{b_2}, C_{RN1}^{b_2}, C_{CN1}^{b_2}$).

With appropriate drag coefficients obtained using the method described above, it is possible to determine the local force generated by the fish as the torque $\boldsymbol{\tau}$ in Eq. (1) driving each link.

4. Experiments

To verify the efficacy of the proposed method, drag coefficient estimation was carried out using video images of swimming larvae, and the effect of pectoral fins on their swimming behavior was then explored.

4.1. *Experimental condition*

The experimental conditions configured for the drag coefficient estimation algorithm (Fig. 3) are shown below.

4.1.1. Video image analysis conditions

・Frame rate: $f_s = 1000$ [fps]
・Measurement duration: $\mathrm{t_m} = 0.27$ [s]
・Low-pass filter: $f_{low} = 70$ [Hz], $\mathrm{n} = 2$
・The pectoral fin images used in the experiment were manually interpolated for every frame due to an insufficient level of clarity for analysis. In addition, the pectoral fins and the trunk were separated via manual processing by painting unrelated parts of each frame in white as a background color (see Fig. 4 (b)).
・Software used for video image analysis: Wriggle Tracker (Library Inc., Tokyo)

4.1.2. Configuration for drag coefficient estimation

・Step size: $\Delta C_{\mathrm{HA1}}^1 = 1.3\times10^{-8}$, $\Delta C_{\mathrm{HN1}}^1 = 6.3\times10^{-7}, \Delta C_{\mathrm{BA1}}^1 = 1.3\times10^{-7}$, $\Delta C_{\mathrm{BN1}}^1 = 1.3\times10^{-4}, \Delta C_{\mathrm{RN1}}^1 = 1.3\times10^{-2}$, $\Delta C_{\mathrm{CN1}}^1 = 1.3\times10^{-4}, \Delta C_{\mathrm{HA1}}^2 = 1.3\times10^{-9}$, $\Delta C_{\mathrm{HN1}}^2 = 0.63, \Delta C_{\mathrm{BA1}}^2 = 1.3\times10^{-8}$, $\Delta C_{\mathrm{BN1}}^2 = 1.3\times10^{-5}, \Delta C_{\mathrm{RN1}}^2 = 1.3\times10^{-3}$, $\Delta C_{\mathrm{CN1}}^2 = 1.3\times10^{-5}$
・Number of searches: $N_{\max}^1 = 100, N_{\max}^2 = 4$

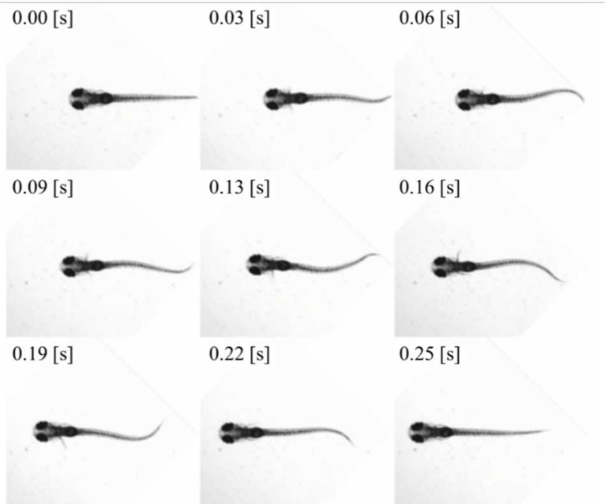

Fig. 5. Video images of wild larval zebrafish motion. The pictures show temporal changes in posture and position for every 0.03 seconds from when the larva started swimming until it stopped.

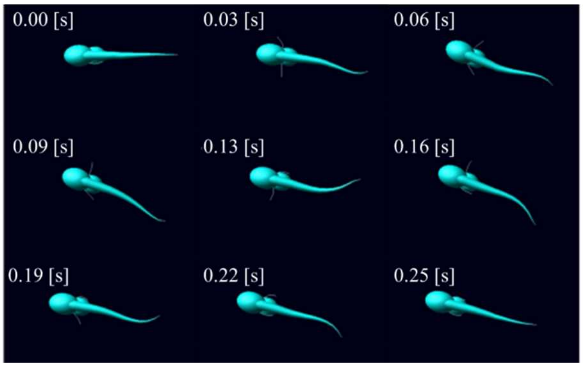

Fig. 6. Video images of the body dynamics model before optimization. The pictures demonstrate a typical example with randomly chosen drag coefficients in which drag force precluded body thrust.

4.1.3. Dynamic analysis conditions

・Equilibrium angle (Eq. 1): $q_0 = 0$
・Density of water (Eq. 3): $\rho = 1.00$ [g/cm^3]
(at a water temperature of 20 [□])
・ Larval model length: $l_b = 2.78$ [mm]
・Mass density of larval model: 3.33 [g/cm^3]
(Calculated based on reference of Avella *et al.* (2012))
・Form of link sets: as shown in Figs. 1 and 4
・Joint stiffness: 15.5 [kNm · rad/m^2] (Long, 1998)
・Joint viscosity: 0.84 [kNms · rad/m^2] (Long, 1998)

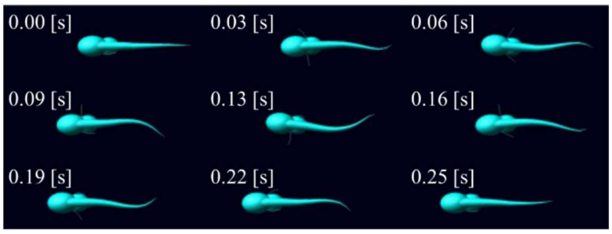

Fig. 7. Video images of the body dynamics model after optimization. When optimal drag coefficients were chosen, the model accurately traced the paths observed from an actual larva.

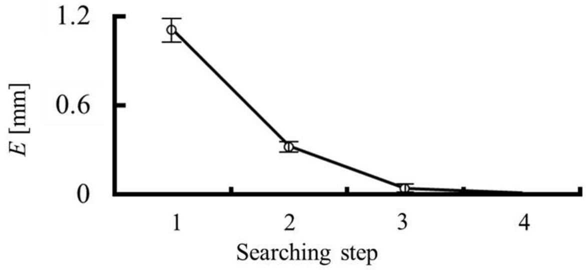

Fig. 8. Video images of the body dynamics model after optimization. When optimal drag coefficients were chosen, the model accurately traced the paths observed from an actual larva

4.1.4. Configuration reading evaluation function

・Number of comparison points in evaluation function (Eq. 4): $N = 2$
・Position of fish for evaluation (Eq. 4):
・Centroid of head $(i = 1)$,
・Point of joint connecting head and trunk $(i = 2)$ (see Fig. 1)

4.2. *Drag coefficient estimation*

Drag coefficients were estimated based on the algorithm presented in Section 2.1. Fig. 5 shows video images of the wild larval zebrafish. Fig. 6 shows the simulated movement of the body dynamics model before optimization, and Fig. 7 shows that after. Fig. 8 shows the average path error between a wild fish and the body dynamics model as given by Eq. (4), and indicates a gradual decrease in each step. After drag coefficient optimization using the generalized reduced gradient method, the path error approached 0 at about 0.76±0.74 [%] compared to the body length. Fig. 9 shows the path of larval movement, with (a) and (b) indicating a position of 70 [%] normalized by body length with the tip of the head as 0 [%] and the end of the tail as 100 [%]. The solid line shows the path of the larval zebrafish, and the dashed

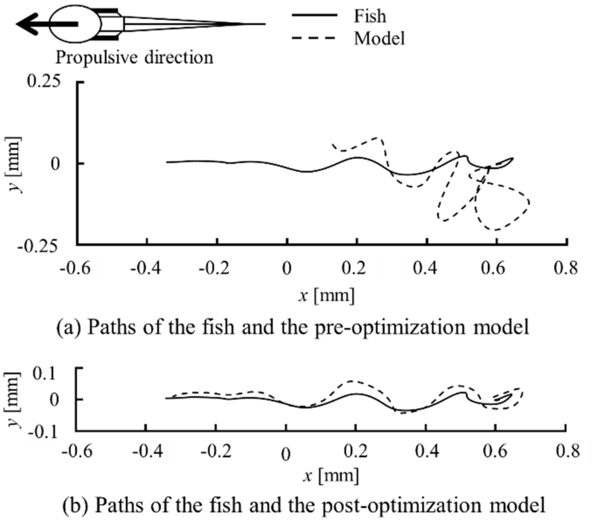

Fig. 9. Comparison of paths obtained before and after optimization. (a) shows a typical path of the body dynamics model when drag coefficients were chosen randomly, and corresponds to the images shown in Fig. 6. (b) demonstrates the path of the body dynamics model given optimal drag coefficients, and corresponds to the images shown in Fig. 7. It is particularly notable that the model successfully traced the backward swimming observed when the actual fish began swimming.

line shows the path of the model before and after drag coefficient optimization. Comparison of the optimized model and the larval zebrafish shows that the former captured the characteristics of fish motion in which both the model and the larval zebrafish started by swimming backward then forward. These results indicate that the body dynamics model with drag coefficients estimated using the proposed algorithm successfully reproduces the movement of wild larval zebrafish.

5. Results and Discussion

Although the pectoral fins of adult zebrafish are known to contribute to thrust (Webb, 1973), their function in developmental-stage larval zebrafish has not been fully elucidated. In this study, the influence of pectoral fins on swimming was examined by comparing the resultant force generated from the pectoral fin part with those of other parts. These resultant forces were calculated by simply adding all force vectors acting on the corresponding links via the following equation:

$$\boldsymbol{F}_r^{\mathrm{res}} = \sum_{dj} \boldsymbol{F}_{rdj} \tag{7}$$

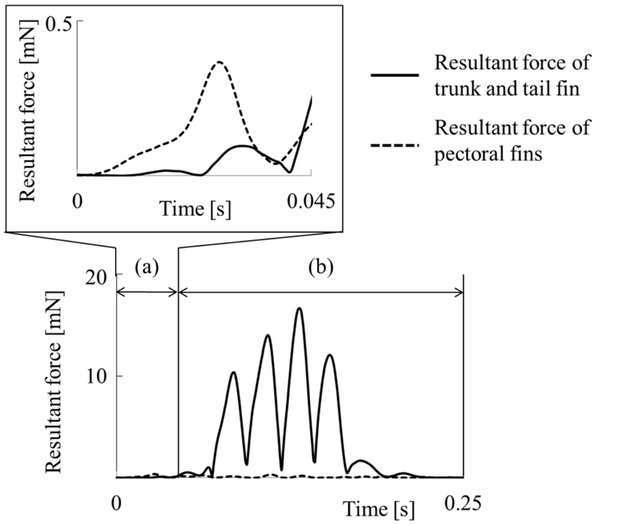

Fig. 10. Resultant force of the trunk and fins. The broken line shows the resultant force of the pectoral fin part, and the solid line shows that of the trunk and tail part. Overall, the force generated from the pectoral fins is negligible compared to that generated from the trunk, which is consistent with biological experiment results [Green *et al.* 2011]. However, in period (a), the larvae initiated swimming and the model predicted that the pectoral fins would generate force to push the fish backward.

The resultant force generated by the trunk and tail fin part ($\boldsymbol{F}_{\mathrm{BC}}^{\mathrm{res}} = \boldsymbol{F}_{\mathrm{B}}^{\mathrm{res}}+\boldsymbol{F}_{\mathrm{C}}^{\mathrm{res}}$) and that of the pectoral fin part ($\boldsymbol{F}_{\mathrm{RL}}^{\mathrm{res}} = \boldsymbol{F}_{\mathrm{R}}^{\mathrm{res}}+\boldsymbol{F}_{\mathrm{L}}^{\mathrm{res}}$) were calculated. In Fig. 10, period (a) shows the time immediately after the larva started swimming (0 – 0.045 [s]) during which it moved backward, and period (b) shows the duration of forward swimming (0.045 – 0.25 [s]). For period (b), the analysis results showed that the average resultant force of the trunk and tail fin part was about $\overline{\boldsymbol{F}}_{\mathrm{RL}}^{\mathrm{res}}$ =78 [μN] and that of the pectoral fin part was about $\overline{\boldsymbol{F}}_{\mathrm{BC}}^{\mathrm{res}}$=4068 [$\mu$N]. As the resultant force of the pectoral fin part accounts for only 2 [%] of the total force generated by the body dynamics model, its influence on swimming can be considered negligible. This result is consistent with those of the experimental studies. Green *et al.* assumed that pectoral fins affected the movement of larval zebrafish and conducted motion analysis on actual fish (Green *et al.*, 2011). The results showed a minimal influence from pectoral fins on swimming in the larval stage; rather, the fins are used to supply oxygen to the gills at this stage of development. This outcome verified the efficacy of the proposed model and drag coefficient estimation algorithm, indicating their suitability for the prediction of unknown dynamic characteristics. In this context, focus was subsequently placed on period (a), for which the average resultant force of the trunk and tail fin part was about $\overline{\boldsymbol{F}}_{\mathrm{BC}}^{\mathrm{res}}$ =39 [μN] and that of the pectoral fin part was about $\overline{\boldsymbol{F}}_{\mathrm{RL}}^{\mathrm{res}} = 121$ [μN]. These results indicate that the trunk and tail fin part have a smaller influence in period (a), allowing pectoral fin movement to contribute more to swimming. Indeed, the fish was observed to maneuver its pectoral fins toward its head, thereby creating force for backward swimming. Such pectoral fin movement may thus be applied to generate force in order to determine the direction of swimming. In this way, the proposed model can provide guidelines for biological experiments.

6. Conclusions and future work

This paper proposed a body dynamics model for larval zebrafish and reported on dynamic analysis of the species. The measured paths of wild larval fish were compared with those obtained from swimming simulation using the proposed model. The results indicated that the model can be used to approximate paths with a high accuracy level of 0.76±0.74 [%] in relation to body length. It was also found to be capable of reproducing paths with characteristics similar to those of wild larval fish as well as supporting estimation of how pectoral fins affect swimming.

In future work, the author plans to elucidate the swimming mechanism of larval fish with focus on the motion generation mechanisms hidden behind the neural circuit. To this end, muscle and neural circuit models will be constructed, and the mechanisms behind the development of swimming behavior in larval zebrafish will be analyzed

7. Reference

1. M. A. Avella, A. Place, S.-J. Du, E. Williams, S. Silvi, Y. Zohar and O. Carnevali, (2012). Lactobacillus rhamnosus accelerates zebrafish backbone calcification and gonadal differentiation through effects on the GnRH and IGF systems, *PLoS* One 7, (2012), e45572
2. S. Budick and D. O'Malley, Locomotor repertoire of the larval zebrafish: swimming, turning, and prey capture, *J. Exp. Biol.* (2000), **203**, 2565-2579.
3. N. Danos and G. V. Lauder, The ontogeny of fin function during routine turns in zebrafish Danio rerio, *J. Exp. Biol.* **210**, (2008), 3374-3386.
4. L. Fuiman and P. W. Webb, Ontogeny of routine swimming activity and performance in zebra *danios* (Teleostei: Cyprinidae), *Anim. Behav.* (1988), **36**, 250-261.
5. M. H. Green, R. K. Ho and M. E. Hale, Movement and function of the pectoral fins of the larval zebrafish (Danio rerio) during slow swimming, *Exp. Bio.* **214**, (2011), 3111-3123.
6. S. Higashijima, Y. Hotta and H. Okamoto, Visualization of cranial motor neurons in live transgenic zebrafish expressing green fluorescent protein under the control of the islet-1 promoter/enhancer, *J. Neurosci,* **20**, (2000), 206–18.
7. Y. Katsumata, U. K. Muller and H. Liu, (2009). Computation of Self-Propelled Swimming in Larva Fishes, *Bio. Sci. and Eng.* 4, **1**, 54-66.
8. C. B. Kimmel, W. W. Ballard, S. R. Kimmel, B. Ullmann and T. F. Schilling, Stages of Embryonic Development of the Zebrafish, *Dev. Dynam*. **203**, (1995), 253-310.
9. L. S. Lasdon, R. L. Fox and M. W. Ranter, Nonlinear optimization using the generalized reduced gradient method, *Revue Francaise d'Automatique. Informatique et Recherche Operationelle*. **3**, (1974), 73-104.
10. J. H. Long Jr. *Muscles,* Elastic Energy, and the Dynamics of Body Stiffness in Swimming Eels, *Amer. Zool.* **38**, (1998), 771-792.
11. M. McHenry and G. Lauder, Ontogeny of form and function: locomotor morphology and drag in zebrafish (Danio rerio), *J. Morphol.* **267**, (2006), 1099-1109.
12. O. Mochizuki and S. Ichikawa, *Hydrodynamics for learning from creatures (in Japanese)*, Yokendo, (2010).
13. U. K. Müller and J. L. van Leeuwen, Swimming of larval zebrafish: ontogeny of body waves and implications for locomotory development, *J. Exp. Biol.* **203**, (2004), 853-868.
14. D. H. Thorsen, J. J. Cassidy and M. E. Hale, Swimming of larval zebrafish: fin-axis coordination and implication for function and neural control, *J. Exp. Biol.* **207**, (2004), 4175-4183.
15. P. W. Webb, Effects of partial caudal-fin amputation on the kinematics and metabolic rate of underyearling sockeye salmon (Oncorhynchus nerka) at steady swimming speeds, *J. exp. Biol.* **59**, (1973), 565-581.
16. P. W. Webb**,** Form and function in fish swimming. *Scient. Am.*, **251**, (1984), 72-82.
17. P. W. Webb and D. Weihs, Functional locomotor morphology of early life history stages of fishes, *Trans. Am. Fish. Soc.* **115**, (1986), 115-127.

Behavior Analysis on Boolean and ODE models for Extension of Genetic Toggle Switch from Bi-stable to Tri-stable

Masashi Kubota[1] Manabu Sugii[2] Hiroshi Matsuno[3]

[1,3]Graduate School of Sciences and Technology for Innovation, Yamaguchi University,1677-1 Yoshida, Yamaguchi-shi, Yamaguchi 753-8512, Japan

[2]Faculty of Global and Science Studies, Yamaguchi University,1677-1 Yoshida, Yamaguchi-shi, Yamaguchi 753-8541, Japan

E-mail:[1]w006vb@yamaguchi-u.ac.jp [2]manabu@yamaguchi-u.ac.jp [3]matsuno@sci.yamaguchi-u.ac.jp

Abstract

The artificial genetic circuit (AGC) is a gene network in which its expression timing, period and function are designed by computational and biological techniques. The AGCs for the functions of electronic circuits like a toggle switch and an oscillation circuit were realized in *E.coli* by Gardner and Elowitz in 2000[1],[2], respectively. We visualized and verified the structure and behavior of Boolean network (BN) and ordinary differential equation (ODE) models for 2-variable genetic toggle switch in the phase plane by using GINsim and Scilab. ODE is the most widely used formalism for biological processes, while BN model allows us to easily understand mathematical expression of biological processes. Then, we extended the models to 3-variable genetic toggle switch from the 2-variable ones demonstrating a mathematical formalization by showing correspondence between state transitions of BN and trajectory paths of ODEs in the phase space.

Keywords: synthetic biology, artificial genetic circuit,

1.Introduction

Currently, artificial genetic circuits can be construct using genetic engineering, which is called synthetic biology. We investigated the behavior and mathematical formalization about genetic toggle switch as artificial genetic circuits. The genetic toggle switch works as an electronic toggle switch so that the state of the gene expression between two genes can be switched by the regulation of related factors. For the bi-stable genetic toggle switch, Gardner et al. showed the constructing method of the bi-stable genetic toggle switch circuit in 2000[1].They specified and confirmed the conditions for the bi-stable behavior, the logical model of mutual suppression and the ordinary differential equations (ODEs).

In this paper, we obtained the state transition graph(STG) from the Boolean Network (BN)model based on the logical model for the bi-stable genetic toggle switch, and associated the STG with the ODE model to investigate the correspondence between the state transitions in STG and trajectories of the ODEs. After that, we extended the bi-stable genetic toggle switch to tri-stable one, and analyzed the dynamic behavior of the ODE model comparing with the state transitions in the STG. In the case of a bi-stable genetic toggle switch, nullcline could be shown in a 2-dimensional diagram. On the other hand, nullcline of the ODEs for the tri-stable genetic toggle switch is drawn as a 3-dimensional graph. A graph of each nullcline can be associated with its STG. The phase plain can be divided into 4 areas centered on the unstable point based on the correspondence between the state transitions in STG and trajectories of the ODEs for the bi-stable genetic toggle switch. The tri-stable genetic toggle switch has 8 state transitions in STG and the phase space can be divided into 8 spaces centered on unstable point. By extending to tri-stable genetic toggle switch, the stable point increased from 2 to 3, nullcline is represented as planes from lines. As a result, the genetic toggle switch has been extended from bi-stable to tri-stable, and we demonstrated a mathematical formalization by the correspondence between state transitions of BN and trajectory paths of ODEs in the phase space.

2.Dynamic behavior, Boolean network and Gene structure of bi-stable genetic toggle switch

The bi-stable genetic toggle switch gets steady state when either repressor 1 gene or repressor 2 gene is expressed in Figure1. Thus, it has 2 stable steady states. Figure 2 shows the logical model and Figure 3 shows the state transition diagram for bi-stable genetic toggle switch. The gene structure of the bi-stable genetic toggle switch produced by Gardner[1] is shown in Figure 1, and ODEs is shown in Figure 4.

When the value of ODEs do not change with time, the set of x and y($\frac{dx}{dt} = 0, \frac{dy}{dt} = 0$) is called nullcline (Figure 4, 5).The intersection of the trajectories of the ODEs is called the stationary point, and the bi-stable genetic toggle switch has 2 stable steady state points (X_A,X_B) and 1unstable point (X_U).The line drawn diagonally from the origin is called separatrix. The convergent stable steady state point is determined depending on the initial value of the ODEs on the phase plane which is divided into the 2 regions (S_A and S_B)by the separatrix (Figure 5-T_1, T_2).

The state transition graph of bi-stable genetic toggle switch shown in Figure 2 has 4 states. In Figure 5, let θ be the value of x and y of the unstable point, and let it be the (x_i = (θ, θ)) threshold. Then the phase space can be divided into 4regions.Each region with each state in the STG are defined in the following conditional formula (Figure 6). R denotes the set of real numbers.

$$P_{00} = \{(x,y) \in R^2 |\ x \leq \theta \ \text{and}\ y \leq \theta\ \},$$
$$P_{01} = \{(x,y) \in R^2 |\ x \leq \theta \ \text{and}\ y > \theta\ \},$$
$$P_{10} = \{(x,y) \in R^2 |\ x > \theta \ \textit{and}\ y \leq \theta\ \},$$
$$P_{11} = \{(x,y) \in R^2 |\ x > \theta \ \textit{and}\ y > \theta\ \},$$

The stable steady state points (X_A,X_B) are in the regions P_{01} and P_{10}, respectively in Figure 6. Because the trajectories never go across the separatrix, the state P_{01} and P_{10} do not transit between the two regions. There is no transition path between [0,1] and [1,0] in the STG. Thus, the four states in the STG of the bi-stable genetic toggle switch can be associated with 4 regions obtained by dividing the phase plane.

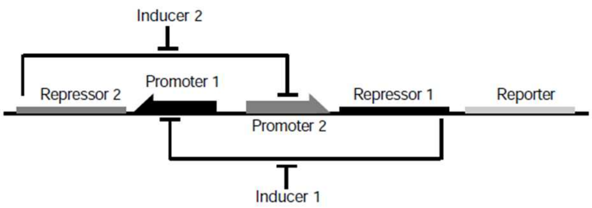

Figure 1 Gene structure

Figure 2 Logical model

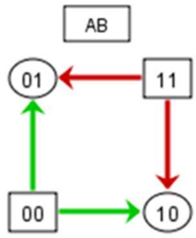

Figure 3 state transition graph

$$\frac{dx}{dt} = \frac{a}{1 + y^m} - x$$
$$\frac{dy}{dt} = \frac{b}{1 + x^n} - y$$

Figure 4 ODEs

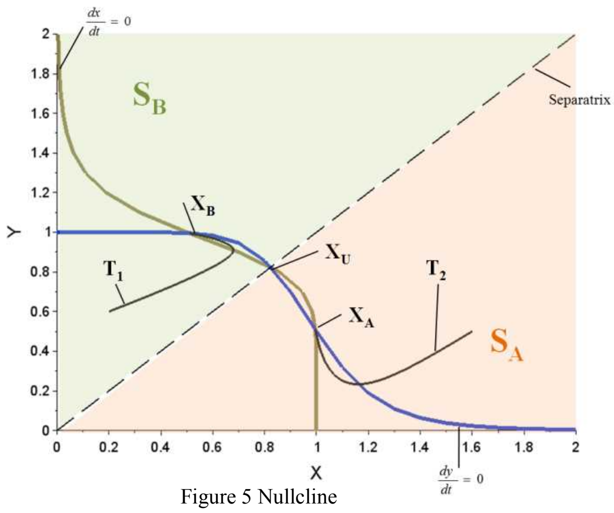

Figure 5 Nullcline

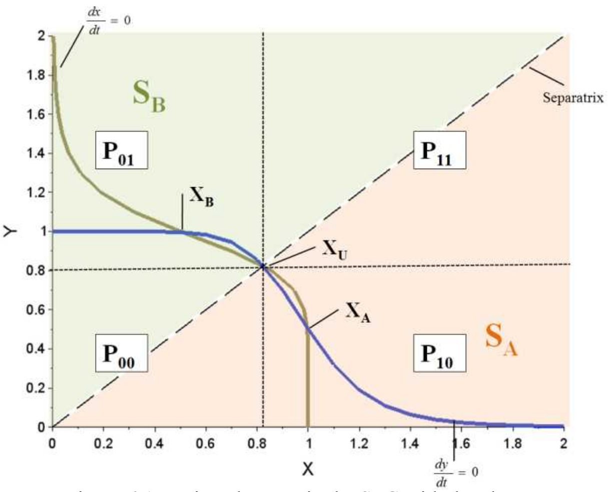

Figure 6 Associate the state in the STG with the phase plane for bi-stable genetic toggle switch

3. **Extension of tri-stable genetic toggle switch**

We extend the STG as a BN model and the correspondence between state transitions of BN and trajectory paths of ODEs in the phase plane representing the bi-stable genetic toggle switch to the tri-stable ones. The tri-stable genetic toggle switch gets stable steady states when one of the repressor genes (A, B and C) is expressing. Thus, it has 3 stable steady states. Figure 7 shows a logical model, and Figure 8 shows a STG of tri-stable genetic toggle switch. Figure 9 shows the ODEs for tri-stable genetic toggle switch obtained by extending the ODEs for the bi-stable ones.

The nullcline of the ODEs for tri-stable genetic toggle switch has 4 intersections, and these intersections are consisted of 3 stable steady state points (X_A,X_B,X_C) and 1unstable point (X_U). In the case of tri-stable genetic toggle switch, it is also possible to control the gene expression by giving various initial value for each parameter (x, y and z)(Figure 10-T_1,T_2,T_3).

In Chapter 2, we distributed the states in the STG and nullcline of the bi-stable genetic toggle switch. There are 8 states in the STG. Let θ be the value of *x, y, z* of the unstable point, and let it be the (X_U = (θ, θ, θ)) threshold. Then the graph of nullcline can be divided into 8 regions. Each region with each state in the STG are defined as shown in the following conditional formula (Figure 11).

$$P_{000} = \{(x,y,z) \in R^3 |\ x \le \theta\ \&\ y \le \theta\ \&\ z \le \theta\ \},$$
$$P_{001} = \{(x,y,z) \in R^3 |\ x \le \theta\ \&\ y \le \theta\ \&\ z > \theta\ \},$$
$$P_{010} = \{(x,y,z) \in R^3 |\ x \le \theta\ \&\ y > \theta\ \&\ z \le \theta\ \},$$
$$P_{011} = \{(x,y,z) \in R^3 |\ x \le \theta\ \&\ y > \theta\ \&\ z > \theta\ \},$$
$$P_{100} = \{(x,y,z) \in R^3 |\ x > \theta\ \&\ y \le \theta\ \&\ z \le \theta\ \},$$
$$P_{101} = \{(x,y,z) \in R^3 |\ x > \theta\ \&\ y \le \theta\ \&\ z > \theta\ \},$$
$$P_{110} = \{(x,y,z) \in R^3 |\ x > \theta\ \&\ y > \theta\ \&\ z \le \theta\ \},$$
$$P_{111} = \{(x,y,z) \in R^3 |\ x > \theta\ \&\ y > \theta\ \&\ z > \theta\ \},$$

The stable steady state points are in the regions [001], [010] and [100] respectively in Figure 11.Trajectories T_1, T_2 and T_3 transit to one of the stable steady state points through the spaces which correspond to the state transition path of STG. In other words, there is no trajectories in the phase space not according to the state transition paths in STG. For example,T_1 is the trajectory of the ODEs for the tri-stable genetic toggle switch when (x, y, z) = (1.8, 1.1, 1.5) is given as an initial state.

Trajectory start from the region [1,1,1] which is associated with the STG. After that, it goes to the region [1,0,1]→[1,0,0] so as to correspond to the state transition path in the STG and reaches to the stable steady state point X_A (Figure 12).Therefore, the state transition in the STG based on the logical model corresponds to the behavior of the ODE model in the phase space for the tri-stable genetic toggle switch after the extension from bi-stable to tri-stable.

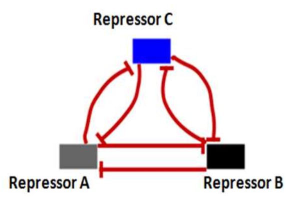

Figure 7 Logical model

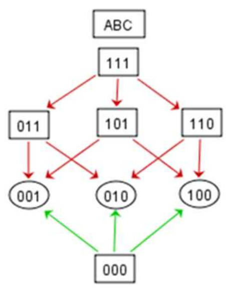

Figure 8 state transition graph

A

$$\frac{dx}{dt} = \frac{a}{1+y^m+z^l} - x$$

B

$$\frac{dy}{dt} = \frac{b}{1+z^l+x^n} - y$$

C

$$\frac{dz}{dt} = \frac{c}{1+x^n+y^m} - z$$

Figure 9 ODEs

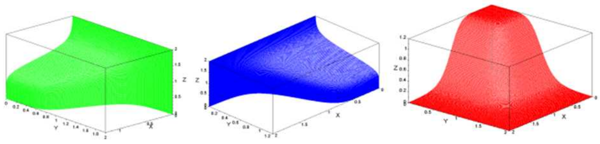

$\frac{dx}{dt} = 0$ $\frac{dy}{dt} = 0$ $\frac{dz}{dt} = 0$

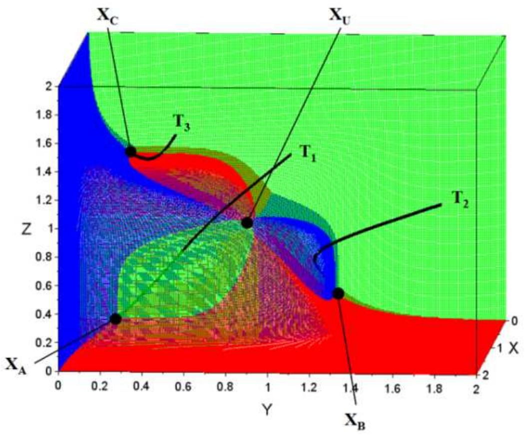

Figure 10 Nullcline

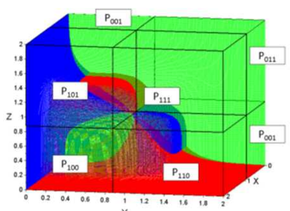

Figure 11 Associate the state in the STG with the phase space for tri-stable genetic toggle switch

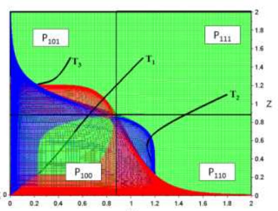

Figure 12 T_1 change regions $P_{111} \rightarrow P_{101} \rightarrow P_{100}$

4. Separatrix of tri-stable genetic toggle switch

The separatrix of the ODE model for the tri-stable genetic toggle switch in the phase space is shown in Figure 16.The trajectories transit to one of the stable steady state points without crossing the separatrix (Figure13,14,15). In other words, there are three regions divided by the separatrix which decide the destination point of the trajectory as a stable steady state point. The separatrix of the ODEs for the bi-stable genetic toggle switch is represented as a line. After the extension from bi-stable to tri-stable, the separatrix is also extended from a line to planes.

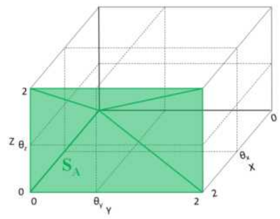

Figure 13 Region S_A

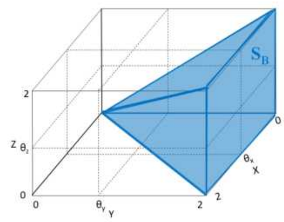

Figure 14 Region S_B

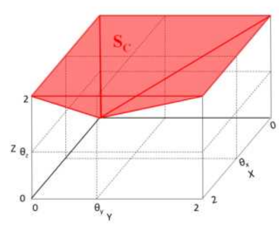

Figure 15 Region S_C

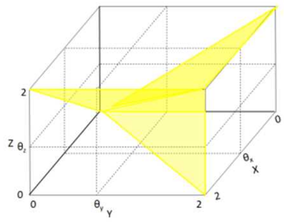

Figure 16 separatrix of the ODEs for tri-stable genetic toggle switch

Movement of Figure 11 from P_{000} to any one of P_{001}, P_{010} and P_{100} is determined by the starting point. Also from P_{111} to P_{001}, P_{010}, P_{100} are similar. We considered how to transit from P_{111} to which regions (P_{001},P_{010},P_{100}) and stabilize. We divided the region P_{111} in detail as in the following formula.(Similarly for P_{000}, P_{001}, P_{010}, P_{100}, P_{011}, P_{101}, P_{110})

$P_{111} = P_{111A} \cup P_{111B} \cup P_{111C}$ where
$P_{111A} = \{(x,y,z) \in P_{111} | \ x > y \ \& \ x > z \ \& \ x > \theta\}$,
$P_{111B} = \{(x,y,z) \in P_{111} | \ y > x \ \& \ y > z \ \& \ y > \theta\}$,
$P_{111C} = \{(x,y,z) \in P_{111} | \ z > x \ \& \ z > y \ \& \ z > \theta\}$,

We divided the areas further on P_{111A} as in the following formula. (Similarly for P_{111B}, P_{111C})

$P_{111A} = P_{111Ay} \cup P_{111Az} \cup P_{111Au}$ where
$P_{111Ay} = \{(x,y,z) \in P_{111} | \ x > y \ \& \ x > z \ \& \ y > z \ \& \ x > \theta\}$,
$P_{111Az} = \{(x,y,z) \in P_{111} | \ x > y \ \& \ x > z \ \& \ y < z \ \& \ x > \theta\}$,
$P_{111Au} = \{(x,y,z) \in P_{111} | \ x > y \ \& \ x > z \ \& \ y = z \ \& \ x > \theta\}$,

We can understand how the trajectory is drawn from the starting point value.

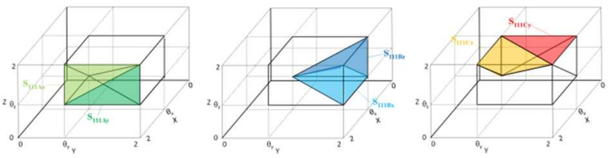

(a)

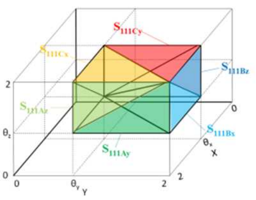

(b)

Figure 18 trajectories started from P_{111Ay} (P_{111Bx},P_{111Cx})and P_{111Az} (P_{111Bz},P_{111Cy}) approach to X_A (X_B,X_C)via different regions, P_{110} and P_{101}, respectively

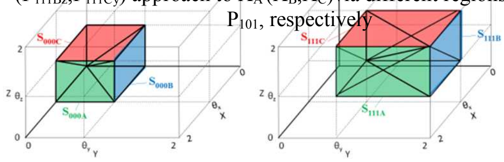

Figure 17 P_{000} and P_{111} are divided into three regions

5. Conclusion

In this paper, we confirmed the state transition of the logical model of the bi-stable genetic toggle switch conducted by Gardner, and found the correspondence between the BN model and the ODE model. By setting the value of the unstable point of the ODEs as θ, the phase plane can be divided into 4regions.We showed the correspondence between the STG and the behavior of the trajectories Then, We extended a genetic toggle switch from bi-stable to tri-stable. The nullcline of the ODEs for bi-stable one isrepresentedas2 dimensional curve in the phase plane but the nullcline of ODEs for tri-stable one is represented as 3 dimensional diagram. The stable steady state point indicated by the intersection of nullcline increased from 2 to 3. Likewise, we distributed the state transitions based on the logical model to the phase space based on the ODE model. We confirmed the correspondence between state transitions of BN and trajectory paths of ODEs in the phase space. Finally we sought the separatrix of the ODEs for the tri-stable genetic toggle switch. The separatrix is also extended from a line to planes after the extension from bi-stable to tri-stable.

By extending from bi-stable to tri-stable, we can generalize the extension to multi-stable genetic toggle switch. The ODEs for multi-stable genetic toggle switch are shown below.

$$\frac{du_i}{dt} = \frac{a_i}{1 + \sum_{j=1} u_j^{n_j}} - u_i \qquad (i \neq j)$$

6. References

[1] Gardner T.S., Cantor C.R., and Collins J.J. Construction of the genetic toggle switch in Escherichia coli. : *Nature*, 403,339-342, (2000)

[2] Elowitz, M.B. & Leibler, S. A synthetic oscillatory network of transcriptional regulators. : *Nature* 403, 335-338, (2000)

Boolean modeling of mammalian cell cycle and cancer pathways

Hideaki Tanaka, Adrien Fauré and Hiroshi Matsuno

Graduate School of Sciences and Technology for Innovation, Yamaguchi University, 1677-1 Yoshida, Yamaguchi-shi, Yamaguchi 753-8512, Japan
e-mail: w015vb@yamaguchi-u.ac.jp, afaure@yamaguchi-u.ac.jp, matsuno@sci.yamaguchi-u.ac.jp

Abstract

The cell division cycle is controlled by a complex molecular network: a recent model of the cell cycle and cancer pathways includes close to a hundred genes [Fumiã and Martins, 2013]. To cope with such complexity, different approaches have been used by modelers. Recently, Deritei et al [2016] have emphasized modularity as a key organizational principle. Their model however, includes only 21 components. This raises the question how the approach would fare on larger models such as the one published by Fumiã and Martins.To explore that question we first convert these two models to a common modeling framework [Naldi et al., 2009]. Preliminary results show that there is only limited overlap between the two models, with shared variables being controlled by different regulators. This suggests that at this stage module definition may still depend on the modeler and thus may not yet reflect actual biological organization.

Keywords: Boolean modeling, Cell cycle, Cancer pathways

1. Introduction

When the same system is modeled by different authors, to the extent that the system is well understood and the modeling approaches are consistent, we should expect converging results. The mammalian cell cycle, due to its fundamental and practical importance in various areas of biology and medicine, is a heavily studied biological system. Yet a single look at two recent logical models [[1] Deriteiet al., [2] Fumiã et al.] reveals important differences in terms of complexity. Our aim is to evaluate the origin, extent and significance of these differences.

In this paper, we first convert the two models to a common modeling framework [[3] GINsim] and check that the transposed models are equivalent to the original models. This preliminary study reveals discrepancies within one of the models, as described in the original paper in terms of logical equations, or in terms of regulatory graph and simulation results [1]. Then we compare the converted models focusing on the common elements. We hoped that the common elements have common logical expression; however, this is not what we found. This suggests that module definition may still depend on the modeler and thus may not yet reflect actual biological organization.

2. Cell cycle

The mammalian cell cycle functions as an excellent case study for coordination between closely connected bistable circuits. It consists in a series of events that take place within the cell, leading to division and duplication of DNA to produce two daughter cells [4]. The cell cycle consists of the following two phases, named inter-phase and M phase (Mitotic phase). Inter-phase consists of the following three phase, named G1 phase (Gap 1 phase), S phase (Synthesis phase), and G2 phase (Gap 2 phase). In G1 phase, the cell gets big for replication and the enzyme required in the next S phase is synthesized. This phase is called preparation phase by researchers.

At the end of G1 phase there is a cell cycle checkpoint. This is a series of safety mechanisms to confirm that the DNA is defect free and that the function of the cell is normal. The G1 checkpoint is known as the restriction point, and requires the presence of growth factors. Cells that proceed through this checkpoint are committed to entering the S phase, during which chromosomal DNA is replicated. When DNA synthesis is completed and all chromosomes have been replicated, S phase is terminated. During the S phase, the amount of intracellular DNA doubles.

The period from the completion of DNA replication to the entry into M phase is called the G2 period. In the G2 phase, active protein synthesis is again performed, and microtubules necessary for mitosis are mainly produced. In the M phase, mitosis and cytokinesis are performed. It is a relatively short period of the cell cycle.

In addition to these four phases, there is a G0 phase which leaves the cell cycle and stops dividing. The cell cycle starts with this phase. Fig.1. shows the cell cycle.

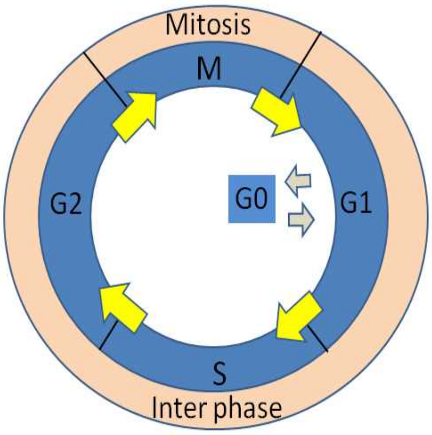

Fig.2.1. Schematic of cell cycle

3. Method

GINsim (Gene Interaction Network simulation) is a computer tool based on a logical formalism for simulation and analysis of regulatory networks [3]. In GINsim, regulatory networks are modeled as logical regulatory graphs (LRG), and state transition graphs represent dynamical behaviors.

Nodes in a logical regulatory graph represent the components system such as protein and mRNA, etc. Arrows connect the nodes, and represent the relationship and effect between the nodes.

To complete the logical regulatory graph, we have to be expressed the relationship between each node using the logical expression. Operator AND, OR and NOT in logical expression are represented by &, | and ! respectively.

Dynamic movement is represented by a State Transition Graph (STG). In this type of graph, node represents the state to give a value of the logical variable for each component. Variables are arranged in the order defined at the modeling stage. The values of 0 represent inactive and 1 represent active state of each components.

We have two types of simulation: asynchronous and synchronous. In asynchronous graph, each value is updated individually. Conversely, in synchronous graph, all values will be updated at the same time. The authors the paper that we use are used synchronous simulation. So in this paper, we use also synchronous simulation to confirm their results.

4. The mammalian cell cycle model

First, we convert the three models proposed by Deritei et al., namely the restriction switch, the phase switch and the full cell cycle model, [3] into GINsim's fromalism.

4.1. The restriction switch

This restriction switch works between G1 phase and S phase in the cell cycle. The restriction point is the point of the G1 phase of the animal cell cycle where the cells are involved in the cell cycle and then extracellular proliferation stimulants are no longer required. This switch model consists of 6 nodes.

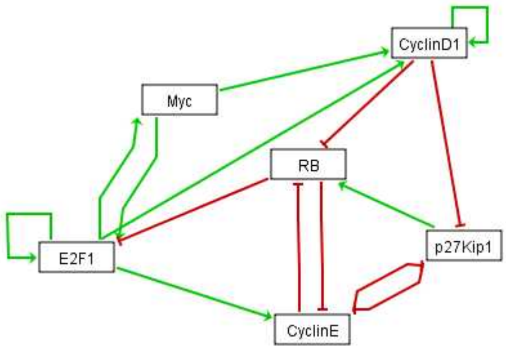

Fig.4.1. The Restriction Switch

When we run simulation, this switch has two stable states, consistent with the original results. This restriction point is a switch-like transition controlled by a bistable molecular control circuit. In the restriction switch, multi stability is essential.

Table 1. Stable state of the restriction switch

Name	CyclinD1	CyclinE	E2F1	Myc	P27Kip1	RB
	1	1	1	1	0	0
	0	0	0	0	1	1

4.2. The phase switch

The phase switch is the network responsible for toggling the cell from G2 into mitosis, then past the spindle assembly checkpoint into cytokinesis. This switch consists of 11 nodes.

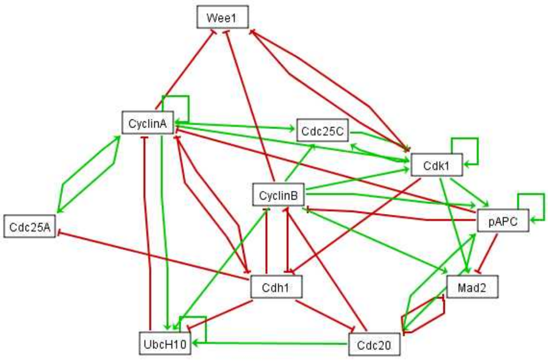

Fig.4.2. The Phase Switch

When we run simulation, this switch has three stable states. This result is also the same result as them. In the phase switch, multi stability is also essential.

Table 2. Stable state of the phase switch

Name			
Cdc20	0	0	0
Cdc25A	0	1	0
Cdc25C	0	1	1
Cdh1	1	0	0
Cdk1	0	0	1
CyclinA	0	1	0
CyclinB	0	1	1
Mad2	0	0	1
pAPC	0	0	1
UbcH10	0	1	1
Wee1	1	1	0

4.3. The full cell cycle model

The cell cycle model is a combination of the restriction switch and the phase switch. These cell cycle switches mutually toggle to generate cyclic dynamics. These two switches within the cell are tightly bound to form a control network of the mammalian cell cycle. This model is formed by four nodes plus two switches. These nodes represent regulatory sub-networks rather than molecular species. The restriction switch has two stable states, and the phase switch has four stable states. These restriction switch and phase switch drive the mammalian cell cycle. So these switches are important for cell cycle. In order to drive the cell cycle of mammals, because the multi-stablility is essential, we can confirm that it meets the conditions.

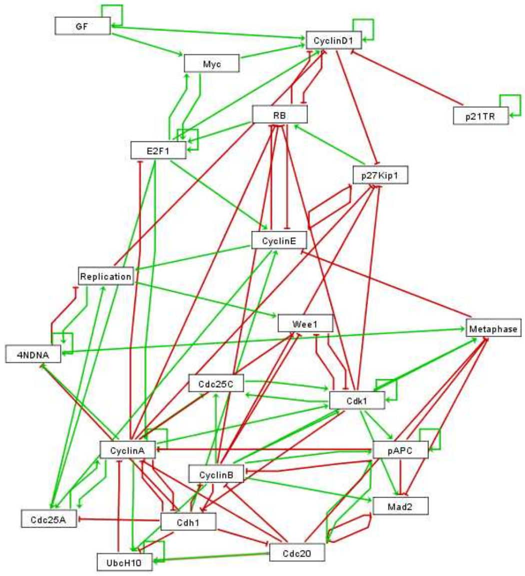

Fig.4.3. The full cell cycle model

5. Boolean network model for cancer pathways

The cancer network proposed, although highly simplified by Fumiã et al [2]. But this model has 96 nodes. So we think this model is complicated and difficult. These equations are update rules of the model.

$$
\begin{gathered}
\sigma_{\mathrm{Mutagen}}(t+1) = \mathrm{input}; \\
\sigma_{\mathrm{GFs}}(t+1) = \mathrm{input}; \\
\sigma_{\mathrm{Nutrients}}(t+1) = \mathrm{input}; \\
\vdots \\
\sigma_{\mathrm{Snail}}(t+1) = \left[+\sigma_{\mathrm{NF-kB}}(t) - \sigma_{\mathrm{GSK-3}}(t) - \sigma_{\mathrm{p53}}(t) + \sigma_{\mathrm{smad}}(t) - 1\right];
\end{gathered} \tag{1}
$$

It includes proteins related to oncogenes, tumor suppressor genes and stability genes, which are the three major classes of mutation targets involved in tumorigenesis. These nodes represent a significant subset of the proteins involved in the cancer and the network edge represents a number of parallel pathways in which the transformed cells maintain an aberrant gene expression pattern and survive and develop further malignancies. The network has input nodes for applying to cells, different environmental stimuli and stresses such as hypoxia, carcinogens, nutrient depletion, proliferation and growth suppression signaling. Here, threshold function is given by these equation.

$$
\begin{gathered}
\mathrm{sgn}(x) = 0 \quad \text{if} \quad x \le 0 \\
\mathrm{sgn}(x) = 0 \quad \text{if} \quad x > 0
\end{gathered} \tag{2}
$$

This kind of expression can also be represented as logical rules in the formalism used by GINsim. Here, when σ=1 the protein is functionally active. On the contrary, when σ=0 the protein is inactive. We calculate the logical expression for each node and input it. As a result, Fig 5.1. was obtained. The topological structure of this cancer network was characterized by Fumiã et al in terms of its shortest path length, clustered coefficient and connectivity.

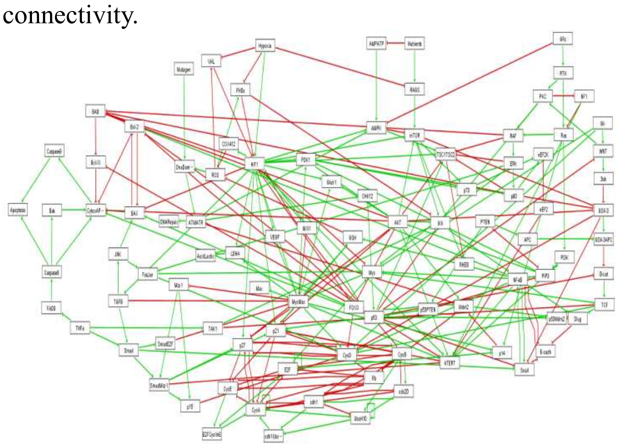

Fig.5.1. The cancer pathways

6. Comparison of the models

A recent model of the cell cycle and cancer pathways includes close to a hundred genes [2]. To cope with such complexity, different approaches have been used by modelers. So we did a comparison of the model of the Cell Cycle model and Boolean Network Model for Cancer Pathways. These models represent the cell cycle. So we examined the same or different parts of these models. First, we have focused on the elements. Looking at these graph, There is a big difference in the number of elements. The cell cycle model has 21 elements and the cancer pathways has 96 elements. In cell cycle model made by Deritei et al [1] have emphasized modularity as a key organizational principle. So there is a big difference.

Next we focused on the common parts of these models. As a result, there were 12 common elements between the cell cycle model and the cancer pathways.

Table 3. Common elements

Name			
GF	p21	CyclinD	CyclinE
E2F	Myc	Rb	Cdc20
Cdh1	CyclinA	CyclinB	UbcH10

Further, all of the elements were also common in the restriction switch. We found that many of these elements has received a lot of influence from the common node. For example, all elements affected by UbcH10 are in common. But this result is not expected. We hoped that all nodes of cell cycle model would be in common with cancer pathways.

From this result, we have to examine the logical expression. But the logical expression was not the same. Because it contains elements that are not in common. All affected elements are the same UbcH10 also the logical expression is different. This suggests that at this stage module definition may still depend on the modeler and thus may not yet reflect actual biological organization.

7. Conclusion

The primary purpose of this study was to create a boolean model based on a recent paper on cell cycle and cancer pathway.

In chapter 3, we describe to convert the models to a common modeling framework . We used GINsim as a common framework. We converted it into a common framework using logical regulatory graph. After that, we use state transition graphs for checking operation etc. Further, GINsim has circuit analyze and expression of stable state that is useful for analysis of biological systems.

In chapter 4, we describe the cell cycle model. Deritei et al [1] have emphasized modularity as a key organizational principle. This cell cycle model is a combination of the restriction switch and the phase switch. Here, we explained the timing of working and the number of nodes in each parts. In the two switches, we confirmed that there are multi stable state. This is a required condition.

In chapter 5, we describe the boolean network model for cancer pathways. First, we show the equations. There are 96 equations. These equations are update rules of the model. We used these equations and thresholds function to decide the logical expressions.

Comparing the cell cycle model and cancer pathways, it appears to differ. However, these models have the same parts. Some elements were common. Further, we found that many of these elements has received a lot of influence from the common elements. From this result, many cell models can be presumed to have common parts.

Finally, future tasks of this study are comparison of behaviors of these models and compare them with other cell cycle models. In this time, we run synchronous simulation only. We have to run asynchronous simulation.

References

[1] D. Deritei, W. Aird, M. Ercsey-Ravasz and E. Regan, Principles of dynamical modularity in biological regulatory networks, *Sci Rep*. 6:21957. doi:10.1038/srep21957, 2016

[2] H. Fumiã and M. Martins, Boolean Network Model for Cancer Pathways: Predicting Carcinogenesis and Targeted Therapy Outcomes, PLoS ONE 8(7):e69008. doi:10.1371/journal.pone.0069008, 2013

[3] C. Chaouiya, E. Remy, B. Mosseand and D. Thie□ry, Qualitative analysis of regulatory graphs: A computational tool based on a discrete formal framework, *Lecture Notes in Control and Information Sciences* 294: 119-126 2004

[4] B. Alberts, A. Johnson, J. Lewis, M. Raff, K. Roberts and P. Walter, *MOLECULAR BIOLOGY OF THE CELL FOURTH EDITION*, 2004

An Estimation Method for Environmental Friction Based on Body Dynamic Model of *Caenorhabditis elegans*

Zu Soh
Department of System Cybernetics, Hiroshima University, 1-4-1 Kagamiyama
Higashi-Hiroshima, Hiroshima 739-8527, Japan

Michiyo Suzuki
Department of Radiation-Applied Biology, National Institutes for Quantum and Radiological Science and Technology,
1233 Watanuki, Takasaki, Gumma 370-1292, Japan

Toshio Tsuji
Department of System Cybernetics, Hiroshima University, 1-4-1 Kagamiyama
Higashi-Hiroshima, Hiroshima 739-8527, Japan

E-mail: sozu@bsys.hiroshima-u.ac.jp

Abstract

Caenorhabditis elegans is a small worm which is approximately 1.3 mm in length. The present study proposes an estimation method for frictional force using locomotion information obtained from video analysis of actual worms. The results indicate that the body model driven by the estimated frictional force can trace the locomotion of the worm within 4% of the body length. The proposed method may be able to be applied to analyze the relationship between friction and gait control.

Keywords: *Caenorhabditis elegans*, frictional force, dynamics model, video analysis, locomotion

1. Introduction

Caenorhabditis elegans is a small soil-dwelling worm with a slender translucent body composed of around 1,000 cells. It is approximately 1.3 mm long and weighs 5.0 µg (Figure 1(a)). Its neural network, which is composed of only 302 neurons, allows the processing of environmental information such as temperature and chemical gradients so that the worm can act in response to its surroundings. Due to the small scale of its neural network, *C. elegans* has become a favored model organism for the analysis of information processing mechanisms hidden inside neural networks, especially since White *et al*. revealed a connective structure between its neurons and muscle cells.[1]

In this context, the mechanism of gait control is an interesting analysis target among various life phenomena because commands generated by neural networks can be easily observed through body locomotion. Accordingly, the worm's information processing mechanism can be investigated by recording its behavior and examining the internal states of its neural network. Recently, dopamine was identified as a key chemical[2] intermediating the distinctive gait changes observed when the worm swims in water and crawls on agar.[3,4] It was also revealed that dopamine-related changes are induced by mechanical stimuli[2]. However, experimental conditions and current technology limit measurement of the amount of force that can be applied to the worm without

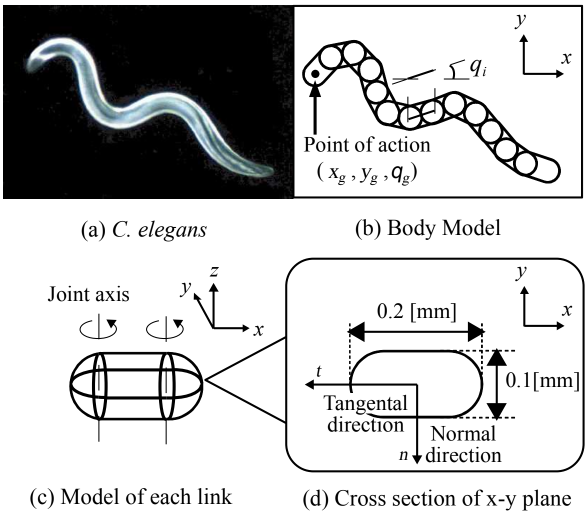

Fig 1. Body dynamics model of *C.elegans*

influencing its behavior. As a result, the input for its neural network system remains unclear.

Computer simulation provides a potential solution to this problem because the worm's thrust is generated by reaction force based on the friction between its body and its environment in the absence of other external forces, and can be calculated using motion equations. The body dynamics model of *C. elegans* first proposed by Niebur and Erdos[5] was able to simulate the worm's undulatory locomotion so that a model worm could travel as fast as a real one. As friction cannot be measured from an actual worm, the friction coefficients included in the model were estimated from the friction measured between glass fiber and agar[6]. Recently, more precise friction coefficients in a gelatin solution and water were calculated by Berri *et al*. and Sznitman *et al*. based on the principles of fluid dynamics.[7~9] However, previous methods have limitations in terms of the range of environments in which they can be applied. An algorithm to determine friction independent of environmental conditions is therefore needed to support estimation of the mechanical stimuli affecting *C. elegans*.

In this paper, the authors propose a body dynamics model incorporating the considerations of dynamic and viscous friction. An estimation method for friction coefficients based on the model is then proposed. As this method requires only locomotion information obtained from video analysis of worms, it enables estimation of friction regardless of the environment and the worm's behavior. Chapter 2 describes the body dynamics model of *C. elegans* and the estimation method for environmental friction. Chapter 3 covers verification of the proposed algorithm and reports on the results of environmental friction estimation. Chapter 4 discusses the relationship between translational force and friction force, and Chapter 5 details the conclusion and outlines future work.

2. Materials and Methods

When *C. elegans* moves on a solid surface such as an agar plate or swims in liquid, it is exposed to different environmental drag forces. As these forces are the basis of propulsion, different drag characteristics or strengths produce different propulsive movements. Drag force can therefore be derived by observing the motion of worms to solve dynamic problems. The following section describes the materials and methods used to record worm motions, and highlights the algorithms used to estimate drag force.

2.1. *Strains and culture*

The *C. elegans* wild-type Bristol N2[10] and the *Escherichia coli* OP50 strain were obtained from the *Caenorhabditis* Genetics Center. Using standard methods[10] worms were grown at 20°C on 6-cm plates containing 10 ml of nematode growth medium (NGM) agar spread with *E. coli* (food). Well-fed worm at the young adult stage were used in all assays.

2.2. *Sample preparation*

6-cm plates containing 4 ml of NGM agar for assay were prepared on the same day of experiments. The plate for the crawling assay (plate A) was uncovered and placed on a clean bench for approximately 1h to dry up excess fluid from the surface. The plate for the swimming assay (plate B) was not dried up and was added 300 μl of S basal buffer[11]. A worm was picked up from a culture plate and washed twice in a few drops of S basal buffer. Immediately after wash, a worm was transferred to an assay plate A or B.

2.3. *Rigid link model*

To estimate the drag forces acting between *C. elegans* and its environment, the worm's body was first approximated using the *N* rigid link model shown in

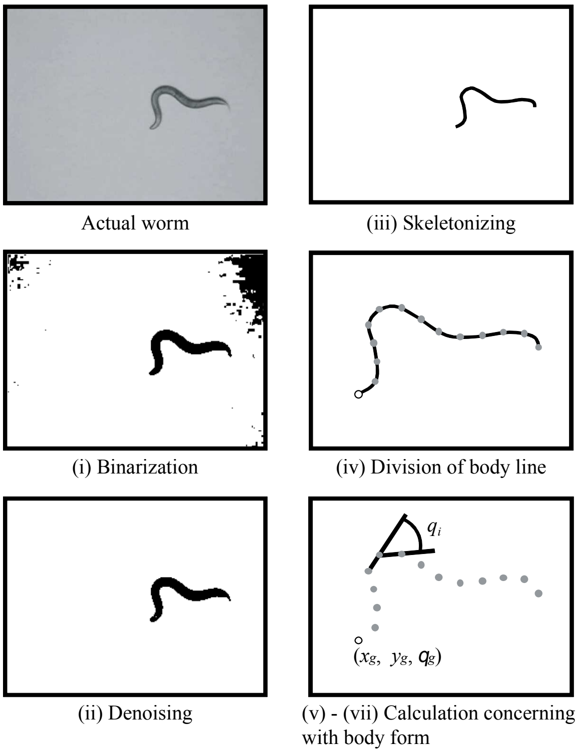

Fig. 2. Image processing

Figure 1 (c), which also illustrates its coordinate configuration. The motion of the model is restricted to the two-dimensional *x-y* plane. The links l_2 - l_{N-1} were connected with adjacent links via rotational joints to allow rotation around the z-axis, and the head link l_1 and tail link l_N had one free end and a joint respectively connected to links l_2 and l_{N-1}. Using this model, the relationship between drag and motion can be derived from Newton-Euler-type motion equations as shown below.

$$I(\boldsymbol{q})\begin{bmatrix}\ddot{q}_0\\ \ddot{\boldsymbol{q}}\end{bmatrix}+h(\boldsymbol{q},\dot{\boldsymbol{q}})+g(\boldsymbol{q})=\begin{bmatrix}0\\ \boldsymbol{\tau}\end{bmatrix}-\sum_j \boldsymbol{J}_j^T\boldsymbol{F}_j, \quad (1)$$

$$I_g(\boldsymbol{q})\ddot{\boldsymbol{r}}_g+h_g(\boldsymbol{q},\dot{\boldsymbol{q}})+g_g(\boldsymbol{q})=\sum_j F_j, \quad (2)$$

where $\boldsymbol{q}=(q_1,q_2,\ldots q_{N-1})^{\mathrm{T}}\in\mathbb{R}^{N-1}$ is a vector of local bending angles, $\boldsymbol{r}=(x,y)^{\mathrm{T}}$ and q_0 denotes the tip position and its posture angle for the head link related to the global coordinate as shown in Figure 1. The terms $I(\boldsymbol{q})$, $I_g(\boldsymbol{q})$ on the left-hand side are inertial forces, $h(\boldsymbol{q},\dot{\boldsymbol{q}})$, $h_g(\boldsymbol{q},\dot{\boldsymbol{q}})$ are Coriolis forces and centrifugal forces, and $g(\boldsymbol{q})$, $g_g(\boldsymbol{q})$ are gravity forces. The first term $\boldsymbol{\tau}\in\mathbb{R}^{N-1}$ on the right-hand side is the torque driving each link, and the second term represents friction, where $\boldsymbol{J}_j^T$ is the Jacobean matrix of the *j*-th joint with a representative point. $\boldsymbol{F}_j=\left(f_{j,t},f_{j,n}\right)^{\mathrm{T}}$ represents the drag force acting on the gravity point of each joint, and can be described in arbitrary form depending on the surrounding environment. In this study, drag force was modeled using the properties of Coulomb friction and viscous drag in a Newtonian fluid as follows:

$$f_{j,d}=-\mu_d\frac{v_{j,d}}{\left|v_{j,d}\right|}-\eta_d v_{j,d}, \quad (3)$$

where $d\in(t,n)$ denotes the tangential and normal directions related to the link, $v_{j,d}$ are the velocities at the gravity point of link j, μ_d is the coefficient of Coulomb friction, and η_d is the viscous drag coefficient.

Equation (2) indicates that the drag coefficients and torque $\boldsymbol{\tau}$ driving each joint can be derived from local bending angles and the related velocities and accelerations $(\boldsymbol{q},\dot{\boldsymbol{q}},\ddot{\boldsymbol{q}})$ and translational acceleration $\ddot{\boldsymbol{r}}_g$, which can be determined from video analysis. Based on this equation, an algorithm for friction coefficient estimation is proposed below.

2.4. *Friction estimation algorithm*

The motion equations (1) and (2) can be solved for drag coefficients given the motion information ($\boldsymbol{q},\dot{\boldsymbol{q}}$, $\ddot{\boldsymbol{q}}$, $\ddot{\boldsymbol{r}}_g$). Among these values, the local bending angle $\boldsymbol{q}$ and the position $\boldsymbol{r}_g$ can be determined by recording the motion of a worm and analyzing the resulting video, and the related time derivations can be used to determine velocity and acceleration. The information obtained can then be used to solve the motion equations for the drag coefficients in relation to each video. However, there are two problems in the implementation of this calculation.

Firstly, it is an ill-posed problem because only *N*+2 coupled equations can be derived from Equations (1) and (2), while there are four unknown drag coefficients plus *N*-1 unknown torque values $\boldsymbol{\tau}\in\mathbb{R}^{N-1}$. To solve this problem, the proposed algorithm involves simultaneous analysis of two different motions of a worm placed in the same environment in which identical drag coefficients are assumed. In this manner, the number of unique coupled equations can be doubled without increasing the number of unknown drag coefficients.

Secondly, the drag coefficients calculated from only one sampling can be significantly affected by video analysis measurement error. To reduce this impact, the proposed algorithm involves the solution of a motion equation for $\ddot{\boldsymbol{r}}_g$ and q_0 for the time duration *T* with different drag coefficients. The coefficients that generate the paths closest to those of the actual worm are then explored by minimizing the following evaluation function:

$$E = \frac{1}{2l(t_{\max}+1)} \sum_{t=0}^{T} \sum_{i=1}^{l} \sum_{j=1}^{2} ||\boldsymbol{x}_i^j(t) - \boldsymbol{r}_i^j(t)||, \qquad (4)$$

Where $\boldsymbol{x}_i^j$ represents the position of the *i*-th evaluation point on the worm, $\boldsymbol{r}_i^j$ represents the corresponding position on the rigid-link body model, and subscript *j* denotes an individual worm.

The proposed algorithm is applied to estimate the drag coefficients for a worm swimming in liquid and crawling on an agar surface. The proposed algorithm consists of four blocks as outlined below.

Block 1: Video analysis

To analyze the body form of *C. elegans* in crawling and swimming, the worm on an assay plate (A for crawling and B for swimming) was video-recorded using a digital camera EXILIM EX-F1 (CASIO COMPUTER CO., LTD., Tokyo) mounted on a stereomicroscope for approximately 10 seconds at 300 frames per second. The resolution of each frame was 512 x 384 pixels. Distinct worms picked up from a culture plate were used for crawling assays and swimming assays. The body form in crawling and swimming of *C. elegans* was analyzed off-line based on the previous method[12] as shown in Figure 2. Briefly, each frame of the video was processed using the following procedures: (i) binarization, (ii) denoising, (iii) skeletonizing, and (iv) division of body line into the 13 parts. After image processing, time-series data concerning with the body form were obtained using the following procedures: (v) length-scale calibration, (vi) acquisition of the *x*- and *y*-coordinates of each point on the body, and (vii) calculation of values concerning with the body form such as the relative angle between adjacent dividing points. Video analyses described above were carried out using the following software: Wriggle Tracker (Library Co. Ltd., Tokyo) for procedures (i)-(iv) and Move-tr/2D (Library Co. Ltd., Tokyo) for procedures (v)-(vii).

Block 2: Selection of drag coefficient

In this block, a set of coefficients is selected in three phases as described below.

[Phase 1]

In Phase 1, drag coefficients are selected from the set $(\mu_n, \mu_t, \eta_n, \eta_t) \in \{(N_1\Delta\mu, N_2\Delta\mu, N_3\eta, N_4\eta) | N_1, N_2, N_3, N_4 = 0, 1, \cdots, N^{\max}\}$ based on iterative alteration of N_1, N_2, N_3, N_4.

After the search for all combinations is complete, d_1 % of the drag coefficients $\left(\mu_n^{E_{1,a}}, \mu_t^{E_{1,a}}, \eta_n^{E_{1,a}}, \eta_t^{E_{1,a}}\right)$ with smaller evaluation values (Equation (4) are selected, and the iteration proceeds to Phase 2, where $a = 1, 2, \ldots, d_1(N^{\max}+1)^4/100$.

[Phase 2]

In Phase 2, better drag coefficients are sought from the set selected in Phase 1. The search is carried out with the set of $(\mu_n^{E_{1,a}} + N_1\left(\frac{\Delta\mu}{2}\right),\ \mu_t^{E_{1,a}} + N_1\left(\frac{\Delta\mu}{2}\right),\ \eta_t^{E_{1,a}} + N_1\left(\frac{\Delta\eta}{2}\right),\ \eta_t^{E_{1,a}} + N_1\left(\frac{\Delta\eta}{2}\right))$ where $N_{1\sim4} = \{-1,0,1\}$. After the search for all combinations is complete, d_2 % of the drag coefficients $\left(\mu_n^{E_{2,b}}, \mu_t^{E_{2,b}}, \eta_n^{E_{2,b}}, \eta_t^{E_{2,b}}\right)$ with smaller evaluation values (Equation (4)) are selected, and the iteration proceeds to Phase 3, where $b = 1, 2, \ldots, 3d_1d_2(N^{\max}+1)^4/10000$.

[Phase 3]

In this phase, the generalized reduced gradient method[13] is applied for the selection of drag coefficients using$\left(\mu_n^{E_{2,b}}, \mu_t^{E_{2,b}}, \eta_n^{E_{2,b}}, \eta_t^{E_{2,b}}\right)$ as initial values so that the friction coefficients with the smallest evaluation values are calculated.

Block 3: Calculation of Motion Equations

In this block, calculation for the path of two rigid-link body models in the time span *T* s is performed with the friction coefficients selected in Block 2. Calculation to solve Equations (1) and (2) for q_0, $\boldsymbol{r}$ is carried out using ADAMS (MSC Software Corporation, Tokyo) multi-body dynamics simulator.

Table 1 Parameters used in simulation

t_{max}	5 s	$\Delta\mu$	1.0×10^{-1}
l	3	$\Delta\eta$	1.0×10^{-3}
m	3.84×10^{-7} g	d_1	1.0 %
N^{max}	10	d_2	0.2 %

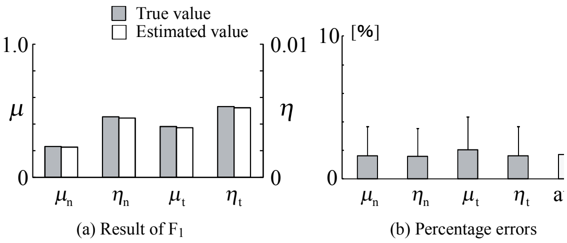

Fig. 3. Estimated results of friction coefficients

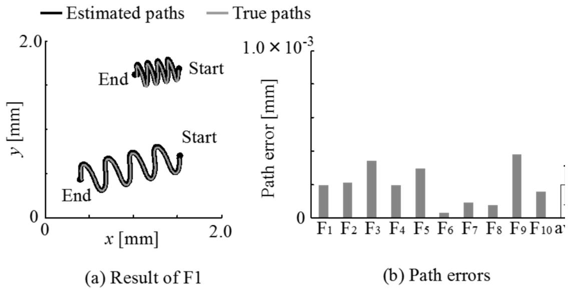

Fig. 4. Estimated paths

Block 4: Evaluation of Drag Coefficients

In Block 4, evaluation is performed for drag coefficients by substituting the paths calculated in Block 3 into an evaluation function (Equation (4)), and the iteration returns to Block 2.

3. Experiments

As a way of verifying the performance of the proposed body dynamics model and the estimation algorithm for friction coefficients, testing was performed to determine whether the algorithm enabled estimation of artificially preset friction coefficients. Such coefficients were then estimated for worms crawling on agar and swimming in a drop of water. Major headings should be typeset in boldface with the first letter of important words capitalized.

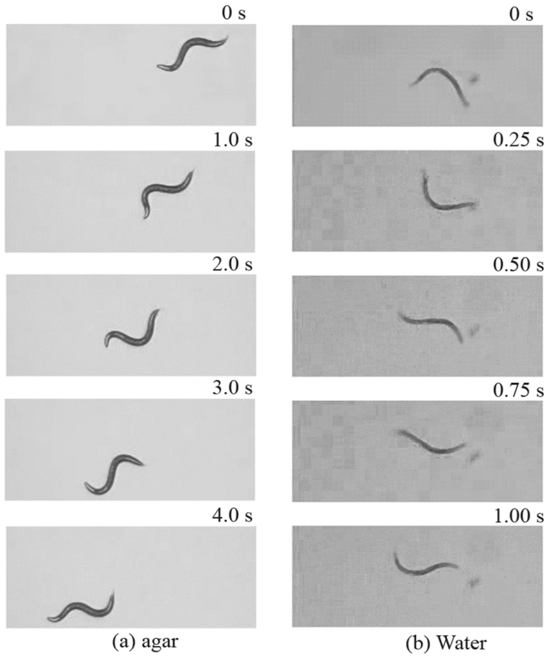

Fig. 5. Locomotion of *C. elegans*

3.1. *Verification*

The locomotion of the body model was simulated using Equations (1) and (2) with artificially preset friction coefficients and time-dependent joint angles. The paths determined from this simulation were then used with the proposed algorithm for friction coefficient estimation. Finally, the errors observed between the preset and estimated friction coefficients were calculated to verify the performance of the algorithm. Here, time-dependent joint angles with the following four patterns were chosen: $q_{i+1} - q_i = 0.4\sin(5t - 0.6i)$, $0.6\sin(5t - 0.6i)$, $0.4\sin(5t - 0.6i) + 0.1$, $0.6\sin(5t - 0.6i) + 0.1$ which are respectively denoted as Locomotion 1~4. In addition, 10 sets of friction coefficients (F_1~F_{10}) were chosen as uniform random numbers in the range of [0,1] for dynamic friction coefficients and [0, 0.01] for viscous friction coefficients. The locomotion pair of 1 and 2 was simulated with the friction coefficients of F_1~F_5 and the other pair (Locomotion 3 and 4) was simulated with the friction coefficients of F_5~F_{10}. The parameters of the body dynamics model and the proposed estimation algorithm are shown in Table 1.

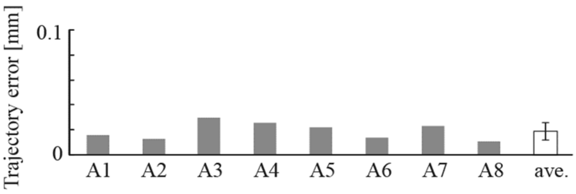

Fig. 6. Resulted value of evaluation function of crawling simulation

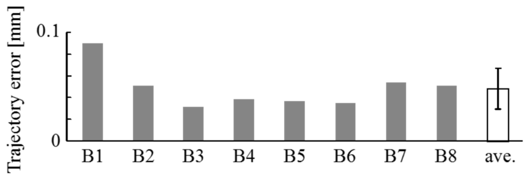

Fig. 7. Resulted value of evaluation function of swimming simulation

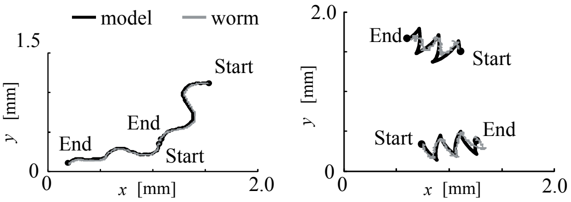

(a) Paths of crawling (b) Paths of swimming

Fig. 8. Paths of joint 7

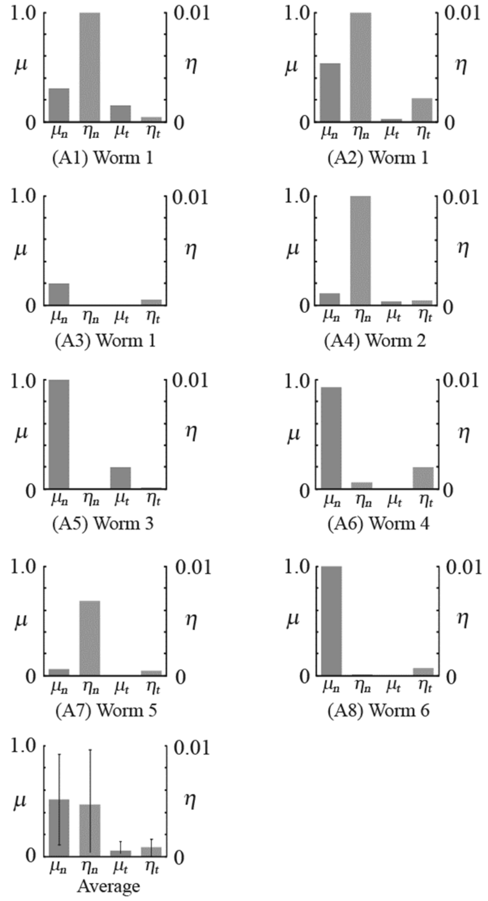

Fig. 9. Estimated friction coefficients (Agar)

Figure 3 shows the friction coefficient estimation results and the related percentage errors against the preset values. Figure 3(b) shows that the average percentage errors were less than 2% with a standard deviation of 2%. Figure 4 shows an example result for the paths of Joint 7 as well as average path errors for all simulations performed. It can be seen that the average error was $1.9\times10^{4} \pm 1.1\times10^{-4}$ mm, which indicates that the proposed algorithm is capable of generating locomotion values with errors smaller than 2.9×10^{-2} % in relation to the worm's length.

3.2. *Estimation of friction coefficients of actual worms*

Friction coefficients for actual worms were estimated using video of their movement on agar and in a drop of water (Figures 5). Each of the time-dependent joint angles determined from image processing was smoothed using a two-order Butterworth low-pass filter (high cutoff frequency: 5 Hz) for denoising. The analysis times for crawling and swimming were respectively set as $t_{\max}$=4 s, 1 s, and the other parameters were the same as those used in the verification simulation.

Figures 6 and 7 show the evaluation function values, which are path errors determined from crawling and swimming simulation for actual worms. The average crawling simulation error was about 0.02 mm (2 % of the worm's length), and the average swimming simulation error was 0.05 mm (4 % of the worm's length). Figure 8 shows the paths of Joint 7 in crawling and swimming simulation. These outcomes indicate that each of the estimation results represented worm paths well. Figures 9 and 10 show friction coefficients estimated from eight video images for crawling and eight for swimming, with the numbers under each picture distinguishing individual worms. It can be seen that the estimated friction coefficients differed greatly even for the same environments. In particular, in Figure 9(A1) and (A3) representing situations in which friction coefficients were estimated from the same worm crawling on the same agar plate, the viscous friction coefficient for the normal

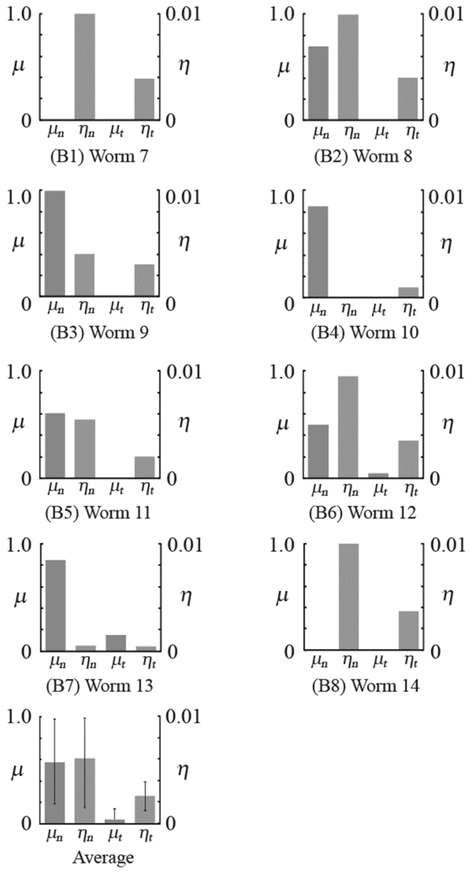

Fig. 10. Estimated friction coefficients (Water)

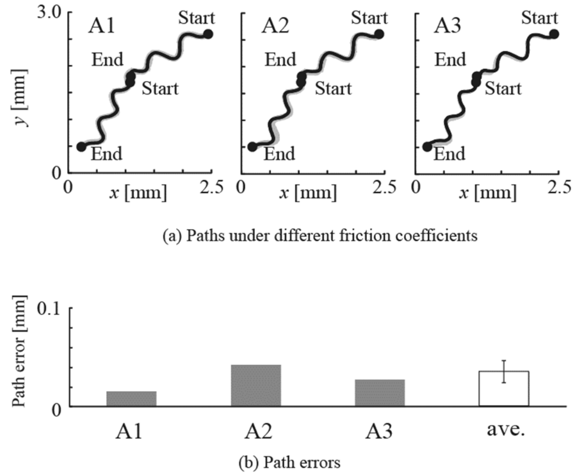

Fig. 11. Comparison of trajectories (Agar)

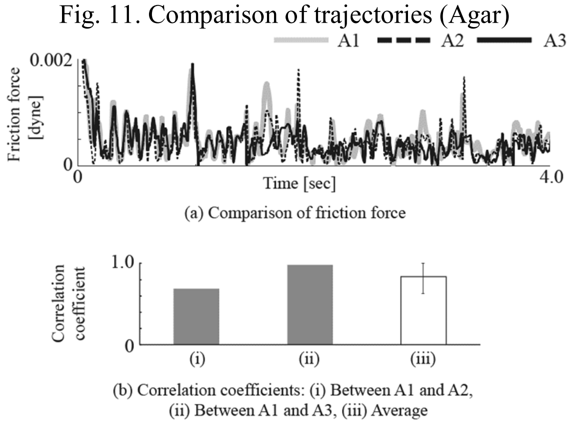

Fig. 12. Comparison of friction force

direction shown in (A1) was much larger than that shown in (A3). The next section discusses this friction coefficient variability.

4. Discussion

This section discusses the cause of variances found in the estimated friction coefficients A1, A2 and A3 (Fig. 10) or the same worm on the same agar plate.

To compare the effects of different friction coefficients adopted for the same joint motion, the time-dependent joint angles $\boldsymbol{q}^{\mathrm{A1}}(t)$ extracted from the locomotion of A1 were substituted into Equations (1) and (2), and paths with the friction coefficients of A2 and A3 were calculated. Figure 11 shows paths resulting from simulation under the time-dependent joint angles $\boldsymbol{q}^{\mathrm{A1}}(t)$ and the friction coefficients A2 and A3. The errors observed between the actual and simulated worm's paths are also shown in Figure 12(b), which indicates that the average path error was about 4% of the worm's length even when different friction coefficients (A1, A2 and A3) were used. Figure 12(a) highlights the friction force at each link accumulated at the point of the head tip. The right-hand side of Equation (2) shows this calculation. From the figure, it can be seen that the total friction generated from friction coefficient A1 showed a strong correlation and similar values to that generated from friction coefficients A2 and A3. As the total friction reactive force is the basis of the propulsion force the worm uses to crawl and swim, this result indicates that the proposed algorithm with path errors as an evaluation function can be used to estimate propulsion force.

In previous studies regarding the dynamic modeling of *C. elegans*, it was reported that a worm's path can be determined from the ratio between the normal and tangential friction coefficient.[5,7] Indeed, the friction coefficient ratio is a dominant factor in determining worm paths. However, according to the simulation performed here, identical locomotion cannot be

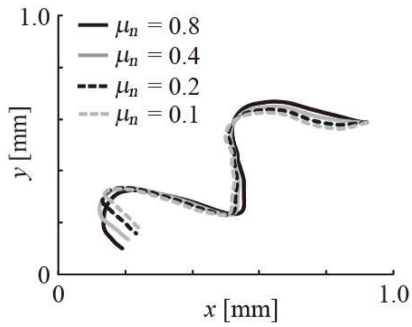

Fig. 13. Paths under the same friction coefficient ratio

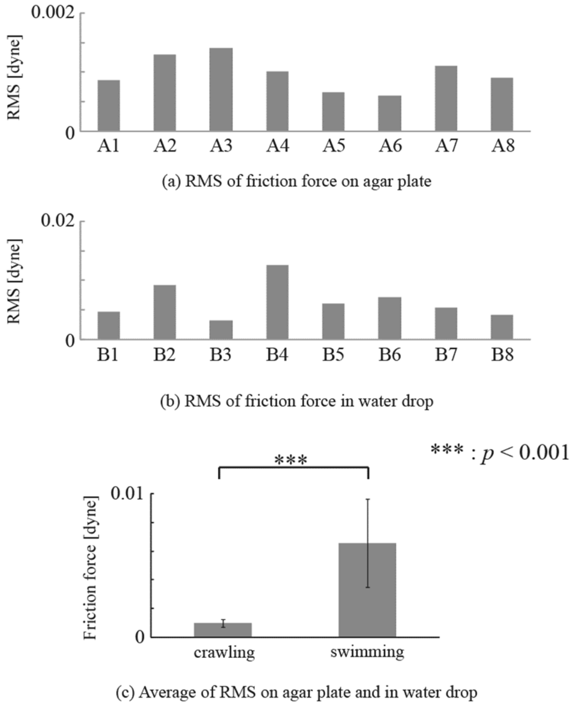

Fig. 14. Average RMS

generated if the same ratio but different friction coefficients are adapted. Figure 13 shows locomotion paths observed when the dynamic friction coefficients were kept at a constant ratio ($2\mu_t = \mu_n$) and the viscous friction coefficient was set to 0 ($\eta_t = \eta_n = 0$). It can be seen that there were path differences depending on the value of μ_n, even though the dynamic friction coefficients were kept at a constant ratio. This suggests that if image processing on actual worms can be carried out with a high degree of accuracy, friction coefficients can be specifically determined because verification simulation under artificially preset configurations (3.1) enabled the estimation of friction coefficients close to actual values with an acceptable level of accuracy.

Finally, the effect of friction in different environments was quantified. Figure 14 shows the average RMS value of the total friction forces as calculated from the crawling and swimming simulation results. The result of a *t*-test to determine the RMS between crawling and swimming showed a significant difference between the two ($p<0.001$). Fig. 15 indicates that worms experience stronger friction forces when swimming than when crawling. Using results obtained from the proposed estimation algorithm allows estimation of the mechanisms behind gait control[8] at the friction level.

5. Conclusion and Future Work

This paper proposed a method for estimating friction coefficients based on a body dynamics model and video images of *C. elegans*. The study verified that the proposed algorithm can be used to estimate friction coefficients under artificially preset configurations, and the results of experiments using actual worms confirmed that it can also be used to generate locomotions with small errors and track worm paths closely. The algorithm can be used to estimate true friction coefficient values under ideal noise-free conditions. Although estimation results were affected by noise contamination from image processing, the propulsion forces affecting locomotion paths could be estimated.

In future works, the authors plan to improve the robustness of the proposed method to support the calculation of time-dependent friction changes acting on worms, and will analyze the mechanisms behind gait control against environmental factors in the context of body dynamics.

Acknowledgements

This work was supported by JSPS KAKENHI Grant Numbers 15H03950 and 20115010.

References

1. J. G. White, E. Southgate, J. N. Thomson and S. Brenner, The Structure of The Nervous System of Nematode *Caenorhabditis elegans*, *Philosophical Transactions of the Royal Society of London*, **314** (1986) 1–340.

2. A. Vidal-Gadea, S. Topper, L. Young, A. Crisp, L. Kressin, E. Elbel, T.,Maples, M. Brauner, K. Erbguth, A. Axelrod, A. Gottschalk, D. Siegel and J. T. Pierce-Shimomura, *Caenorhabditis elegans* selects distinct crawling and swimming gaits via dopamine and serotonin, *Proc. Natl. Acad. Sci. U.S.A.* **108**(42) (2011) 17504-17509.
3. J. Gray and H. W. Lissmann, The Locomotion of Nematodes, *J. Exp. Biol.* **41** (1964) 135-154.
4. J. Korta, D. A. Clark, C. V. Gabel, L. Mahadevan and A. D. T. Samuel, Mechanosensation and mechanical load modulate the locomotory gait of swimming *C.* elegans, *J. Exp. Biol*. **210** (2007) 2383-2389.
5. E. Niebur and P. Erdos, Theory of the locomotion of nematodes, *Biophys. J.* **60** (1991) 1132–1146.
6. H. R. Wallace, Wave formation by infective larvae of the plant parasitic nematode Meloidogyne javanica, *Nematology*. **15** (1969) 65-75.
7. S. Berri, J. H. Boyle, M. Tassieri, I. a Hope and N. Cohen, Forward locomotion of the nematode *C. elegans* is achieved through modulation of a single gait, *HFSP J.* **3**(3) (2009) 186–193.
8. J. T. Pierce-Shimomura, B. L. Chen, J. J. Mun, R. Ho, R. Sarkis and S. L. McIntire, Genetic analysis of crawling and swimming locomotory patterns in *C. elegans*, *Proc. Natl. Acad. Sci. U.S.A.* **105**(52) (2008) 20982–20987.
9. J. Sznitman, X. Shen, P. K. Purohit and P. E. Arratia, The E□ects of Fluid Viscosity on the Kinematics and Material Properties of *C. elegans* Swimming at Low Reynolds Number, *Exp. Mech.* **50**(9) (2010) 1303–1311.
10. S. Brenner, The Genetics of *Caenorhabditis elegans*, *Genetics* **77**(1) (1974) 71-94.
11. E. R. Sawin, R. Ranganathan, and H. R. Horvitz, *C. elegans* Locomotory Rate is Modulated by the Environment through a Dopaminergic Pathway and by Experience through a Serotonergic Pathway, *Neuron*, **26**(3) (2000) 619–631.
12. Y. Hattori, M. Suzuki, Z. Soh, Y. Kobayashi and T. Tsuji, Theoretical and evolutionary parameter tuning of neural oscillators with a double-chain structure for generating rhythmic signals, *Neural Comput.*, **24** (2012) 635-675.
13. G. A. Gabriele and K. M. Ragsdell, The Generalized Reduced Gradient Method: A Reliable Tool for Optimal Design, *J. Eng. Ind.*, **99(**2) (1976) 394–400.

Mouse Cursor-like Control System in Consideration of the DC-EOG Signals using EOG-sEMG Human Interface

Mingmin Yan
Department of Environmental Robotics, Faculty of Engineering, University of Miyazaki
Miyazaki, Japan

Yu Cheng
Department of Electrical and Electronic Engineering, Faculty of Engineering, University of Miyazaki
Miyazaki, Japan

Keiko Sakurai
Interdisciplinary Graduate School of Agriculture and Engineering, University of Miyazaki
Miyazaki, Japan

Hiroki Tamura
Department of Environmental Robotics, Faculty of Engineering, University of Miyazaki
Miyazaki, Japan

Koichi Tanno
Department of Electrical and Systems Engineering, Faculty of Engineering, University of Miyazaki
Miyazaki, Japan
E-mail: yanmm@cc.miyazki-u.ac.jp, hc11047@student.miyazaki-u.ac.jp, z3t1401@student.miyazaki-u.ac.jp, htamura@cc.miyazaki-u.ac.jp, tanno@cc.miyazaki-u.ac.jp
www.miyazaki-u.ac.jp

Abstract

Patients who suffered with the limb disorders cannot take care of themselves by communication barrier. However, it is possible to improve the communication abilities of the patients by using biological signal such as ocular potential and muscle potential which is caused by moving eyes or facial muscle. Therefore, we have developed the human interface using the electrooculogram (EOG) and the facial surface electromyogram (sEMG) signals which can control PC. However, this system could not control the mouse cursor in accordance with the direction and magnitude of the movement of eyes to control PC smoothly and intuitively. Thus, we proposed a new mouse cursor-like control system in consideration of the DC elements of EOG signals using the EOG-sEMG human interface. Our proposed method has both drift and blink countermeasures which had better performance in mouse cursor control, and all subjects could control the mouse cursor for both moving and clicking flexibility.

Keywords: Ocular potential, Facial muscle potential, Biological signal.

1. Introduction

There are a large number of persons with disabilities around the world currently. However, it is possible to improve the communication abilities of patients who suffer from diseases by using a biological signal such as ocular potential and muscle potential caused by movement of the eyes or facial muscle[1].

The aim of this paper is to present a system using biological signals that can efficiently be used as a human computer interface. The authors conducted joint research with multiple companies to develop an interface device called "FARG" that can detect biological signals such as ocular potential and muscle potential on the face as shown in Fig. 1. A conventional method can control a PC as a switch with 7 patterns: 4 patterns of eyes moving in 4 directions (up, down, left, and right), and 3 patterns of facial muscle operation (left blink, right blink, and bite) [2]. However, the purpose of this paper is to control the mouse cursor in accordance with the direction and magnitude of movement of the eyes to control the PC more smoothly and intuitively by using the proposed methods.

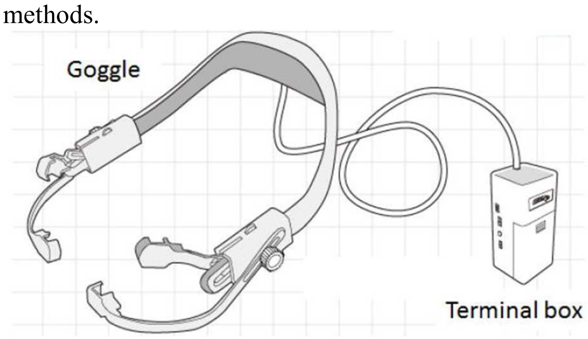

Fig. 1. Appearance of FARG

2. Proposed Method

As we introduced in section 1, our method could recognize 7 patterns of biological signals. However, the patients do not have such great m to operate the PC under their mind except by using support software[3].

In this paper, we propose a modified method to move the mouse cursor to the vertical direction and horizontal direction freely by using the EOG signals and the click by the EMG signals. We set the mouse cursor to click by a right blink and to double-click by biting. The mouse cursor was set to move 50 pixels to the right when the eyes moved to the right direction. In the case of the operation in the sequence of "move to right", "move to right", "bite", the operation performs double-click after the mouse cursor has moved 100 pixels to the right.

In the modified method proposed, we defined the thresholds used in the basic method for recognizing the vertical direction and horizontal direction (up, down, left, and right) as the thresholds that show the EOG signals changes. When the patients gazed on the up, down, left, or right side of the screen. The formula used for computing the pixel of the mouse cursor is shown in Eq. (1), (2) and the update interval is set as 0.1 [sec]. W is the width of the screen; the benchmark is changed into the pixel of the mouse cursor at 0.1 [sec] before (X_{pre}, Y_{pre}). Further, we imported the blink counter-measure.

$$x = \frac{DC1 - DC2}{8 \times T_{LR}} \times \frac{W}{2} + X_{pre} \tag{1}$$

if x<0, x=0, and if x>W, x=W

$$y = \frac{-(DC1 + DC2)}{4 \times T_{LR}} \times \frac{H}{2} + Y_{pre} \tag{2}$$

if y<0, y=0, and if y>H, y=H

3. Experimental Method

In this study, we tried four experiments in order to evaluate the performance of the mouse cursor control system which we built by the methods we proposed. All four experiments are designed step by step in the following sequence: A) horizontal movements only, B) horizontal movements and clicking, C) both horizontal and vertical movements, D) practical application.

3.1. *Experimental Method 1*

In experiment 1, we set the desktop as shown in Fig. 2. We asked the subjects, who are 5 healthy males (subject A, B, C, D, E) in their 20s and 1 female (subject F) in her

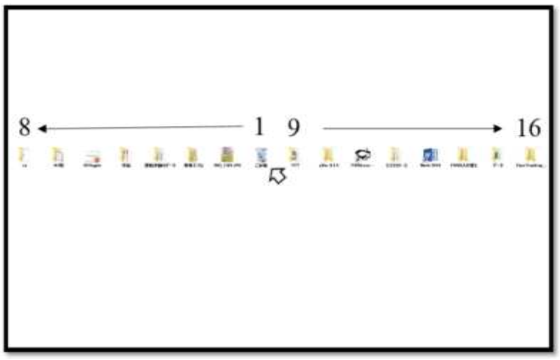

Fig. 2. Desktop for experiments 1 and 2.

20s, to focus on the center of the screen. Next, they moved their sight to the first icon 1, on the left side from the center and stopped on the icon for 1 sec, then moved to the next icon and stopped for 1 sec one by one from icons 1 to 8. After that, they continued moving to the icon on the right side from the center, from icons 9 to 16 on the right edge of the screen. We measured the time from first moving the mouse cursor until moving to the final icon 16. Each subject performed the same experiment 3 times.

3.2. *Experimental Method 2*

In experiment 2, we used the same desktop as in experiment 1. We asked the subjects, who are 2 healthy males (subjects G, H) in their 20s and 1 female (F), to focus on the center of the screen. Then they moved their sight to the next icon on the left side from the center and clicked the icons one by one from 1 to 8. After that, they continued moving to the icon on the right side from the center and clicking the icons from 9 to 16 on the right edge of the screen. We measured the time from starting the moving mouse cursor until clicking the final icon, 16. Each subject performed the same experiment 3 times.

3.3. *Experimental Method 3*

In experiment 3, we set the desktop wallpaper as shown in Fig.3 and cleared all icons. Next, we asked subjects G and H to focus on the 'start' point, then to move their sight to follow the arrows and do their best to finish one circle for 3 tasks at 5 min rest intervals. The EOG signals changed and the times used for one task were recorded as the evaluation standards. The size of the screen was 22 inches with full HD (1920*1080)

3.4. *Experimental Method 4*

In experiment 4, we tried to control Google Earth[4] as verification experiments using the mouse cursor control system that we built. We opened Google Earth and put the map of Japan on the center of the screen. Then we asked the subject to rotate the globe and put the map of Brazil on the center of the screen by the click and drop action of the mouse. Finally, subjects double left clicked the map of Brazil to zoom in the camera. The same subjects were asked to try the operations for 3 times in 5 min intervals. When the mouse cursor moved into the left or right 1/10 area to the sides of the screen, the mouse cursor control function paused until a left blink, right blink or bite were recognized by the EMG signals.

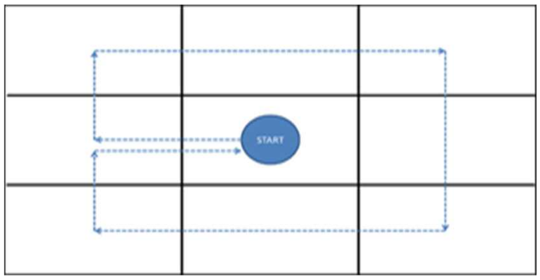

Fig. 3. Desktop wallpaper for experiments 3.

4. Results

4.1. *Results of Experiment 1*

In experiment 1, subjects move their sight to the 16 icons one by one. The time includes 1 [sec] stopped on each icon. Everyone finished the experiments at one time, so it means the correct rate is 100%. The average time of 6 subjects for one task is 87.5 [sec].

4.2. *Results of Experiment 2*

Table 1 shows the time taken by 3 subjects in experiment 2. The average time of 3 subjects for one task is 111 [sec]. As in Experiment 1, the influence of a blink caused the results of subject I to be the worst because the muscle potential caused unstable ocular potential. In addition, we consider one of the reasons is that the threshold is different due to individual differences.

Table 1. Time of 3 Subjects in Experiment 2.

Subject	Task	Time[sec]
F	1	143
	2	168
	3	204
	Ave	172
G	1	62
	2	60
	3	52
	Ave	58
H	1	123
	2	87
	3	100
	Ave	103

4.3. *Results of Experiment 3*

The experiments results of subjects G are shown in Figure 4. The left-top chart shows the ideal value, and the next three ones show the actual data of three tasks. From the results, we can see the influence of a blink was decreased, and with subject G, although there were mistakes that recognized a blink as up in task 3, all of the tasks could finish matching the arrows roughly. Table 2 shows the pixels and time of 2 subjects with the modified method we proposed.

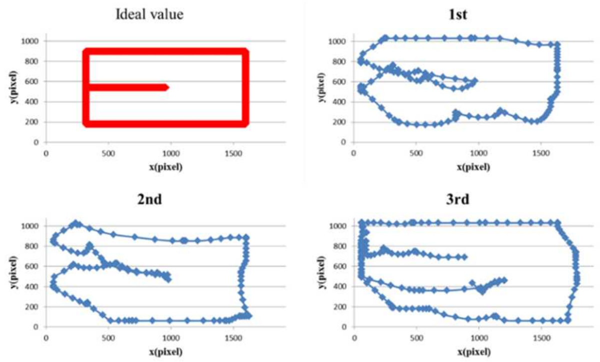

Fig. 4. Experimental results of subject G.

Table 2. Pixels and T of 2 subjects in experiment 3.

Subject	Task	Pixels	Time [sec]
G	1	28874	44.4
	2	24800	41.0
	3	77192	67.1
	Ave	43622	50.8
H	1	84391	60.7
	2	47347	56.2
	3	60780	57.8
	Ave	64172	58.2

4.4. *Results of Experiment 4*

In experiment 4, we asked the subjects to control Google Earth by using the mouse cursor control system and following the steps in the verification experiments. The time that a subject took and the suspend count results are shown in Table 3. With subject G, the experiments could be finished smoothly without any pauses, and with subject H, the experiments were suspended once in the case that the mouse cursor moved from the left 1/10 area to the sides of screen. But in task 3, subject H could finish the experiments in the same time as did subject G.

Table 3. Results of experiment 4.

Subject	Task	Time [sec]	Suspended count
G	1	23.2	0
	2	23.1	0
	3	38.1	0
	Ave	28.1	0
H	1	49.4	1
	2	52.0	0
	3	29.3	0
	Ave	43.6	0.3

5. Conclusion

In this paper, we introduced a PC control method using a biological signal measuring device that could be used for ALS patients. With the proposed method and the experiments results, it is possible to control a mouse cursor by moving the eyes and clicking by moving the facial muscle when using the mouse cursor control system we built. The patients also can control the application as they wish. We validated that the influence of drift and blink cannot be ignored simply, and those influences are also the difficult points in our research. The modified method having both drift and blink countermeasures had better performance of mouse cursor control, and all subjects could control the mouse cursor for horizontal moving and clicking flexibility.

References

1. R. Barae, L. Boquete, and M.Mazo: "System for assisted mobility using eye movements based on electrooculography", *IEEE Transaction on Neural Systems and Rehabilitation Engineering*, vol. 10, no. 4, 2002, pp. 209-218.K. Elissa.
2. H.Tamura, etc.: "Development of the electric wheelchair hands-free semi-automatic control system using the surface-electromyogram of facial muscles", *Artificial Life and Robotics*, Volume 17, Issue 2, pp 300-305, Dec. 2012.
3. M. Yan, H. Tamura, K. Tanno: "A study on gaze estimation system of the horizontal angle using electrooculogram signals" *IEICE Trans on Information and Systems* : E97-D (9), pp 2330 - 2337, 2014.
4. Google Earth, https://www.google.co.jp/intl/ja/earth/, accessed on January 20th, 2016.

A Study on Eyes Tracking Method using Analysis of Electrooculogram Signals

Keiko Sakurai [1], Mingmin Yan, [2], Hiroki Tamura[2] and Koichi Tanno[2]

[1]Interdisciplinary Graduate School of Agriculture and Engineering, University of Miyazaki, Japan

[2] Faculty of Engineering, University of Miyazaki, Japan

[1]z3t1401@student.miyazaki-u.ac.jp

http://www.miyazaki-u.ac.jp/

Abstract

Gaze estimation has been an active research and important technique for seriously physically handicapped person to communicate. In this paper, we proposed eye tracking method using electrooculogram signals which is small-burden. However, there is a problem that the resolution is not so high. Our experiments were conducted to investigate the EOG component strongly correlated with changes in eye movements. The experiment result shows the possibility of eyes tracking method using the analysis of electrooculogram signals.

Keywords: Gaze estimation , Electrooculogram Signal.

1. Introduction

Gaze estimation has been an active research in the past years and gaze estimation is an important technique for seriously physically handicapped person who cannot move their body to communicate. In this paper, we proposed eye tracking method using electrooculogram (EOG) signals which is widely applied in medical field because of the merit that proposed method have low burden of the patients. In eyes movements, a potential across the cornea and retina exists, and it is the source of EOG. The eyeball can be modeled by a dipole. There are several EOG-based Human-Computer Interface [1][2][3] studies in literature. Investigating possibility of usage of the EOG for human-computer interface, a relationship between gaze angle and the EOG is determined. However, in-depth studies evoked that slow changing baseline drift is the difficult point to estimate in continuous EOG signals and this drift only appears in DC signals in the circuit. We have already developed EOG system has the center parameter update technique which reduces baseline drift by segmentation of the signal [2]. Our proposed system [2][3] is possible to improve the communication abilities of those patients who can move their neck or/and eye, though there is the problem not to be so high in resolution.

Table.1 shows the characteristic of the proposed method and conventional method. In previous studies[4][5] the positions of the electrodes were set as plus-channels same with direction of the eye movements. The horizontal channel was in charge of horizontal EOG signals and the vertical channel was in charge of vertical EOG signals. The mainstream of eye movement classification is 4 patterns or 8 patterns using an alternating current (AC) signals conventionally.

We proposed the cross-channel method in order to improve the accuracy of the EOG signals. Our proposed technique classified in 4 patterns using AC and DC signals and this method is able to put the electrodes in place far from the eyeballs (Table.1). The proposed technique can say that wearability is good better than conventional method.

Table.1. Characteristic of the proposed method

	Positions of the Electrodes	Performance	Wearability
Conventional Method	Ch2+ Ch1+ Ch2- Ch1-	○	△
Proposed Cross-channel Method	Ch1+ Ch2+ Ch2- Ch1-	○	○

We had already developed eyes input application for desktop PC with high accuracy gaze estimation[3].

Furthermore, we carried out the large space experiments (the range is -60degrees to 60degrees) and estimate the gaze by the multiple regression analysis using the DC integral value [6]. Although the regression analysis results are good results, the narrower range was better. In this paper, we analyzed DC, AC, DC difference value, DC integral value for regression analysis and we also checked if the accuracy was improved than previous studies [3]. Moreover, we considered the limiting angle of gaze estimation in a wide space ranging from -90 degrees to 90 degrees.

2. Measurement System using EOG Signals

In this section, cross-channel EOG measurement system design is shown [3]. Fig.1 shows the formal scheme for the acquisition and analysis of the EOG signal for the control organization and flow of information through the system. Our proposal system is based on the five features, 1) Amplifier, 2) Low pass filter for channel 1 and 2, 3) High pass filter for channel 3 and 4, 4) A/D-convertor, and 5) PC. Our system consists of five electrodes, an A/D-convertor, a personal computer, and a monitor. In order to effectively filter functions, channel 3 (and channel 4) is used two amplifiers. The horizontal signals and the vertical signals could be recorded by both channels at the same time which is much easier to analyze data using double signals.

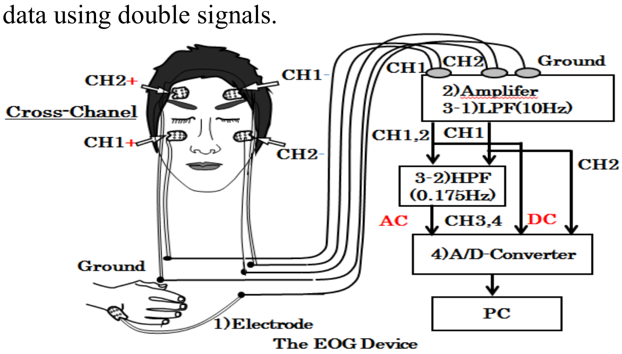

Fig.1 EOG measurement system

3. Method

In this study, we carried out the experiments by our proposal EOG system to make a study the calculation method of the EOG element with strong correlation for the change of the eyeball movements.

3.1. *Experiment environment*

The experiments were designed in order to confirm the effectiveness of the proposal system. Experiment condition is Fig.2 and three healthy subjects participated in this study. We ask the subjects to focus at these targets by moving the eye only as the sequence as 0, -30, 0, -60, 0, -90, 0, 30, 0, 60, 0, 90 degree. Time zoom for watching each target was set as 1 second and repeated 10 times.

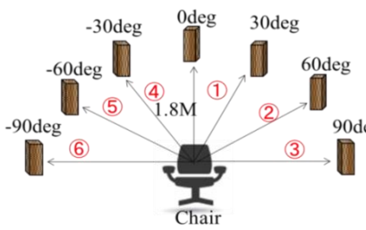

Fig.2 Experiment Environment

3.2. Extraction method of feature value

We carried out the experiments to make a study the calculation method of the EOG element with strong correlation for the change of the eyeball movements. The feature values are (1) AC, (2) DC, (3) DC-Difference value, (4) DC-Integral value.

- Feature value of AC
  The feature value of AC was assumed to be the maximum value when the AC is more than the threshold in the right direction and the minimum value when the less than the threshold in the left direction (Fig.3 (a)).
- Feature value of DC, DC Difference Value
  The feature value of DC is the maximum value and the minimum value (Fig.3(b)), however it is necessary to take the difference with a baseline DC value and the DC value because drift occurs as for the DC signals. The changing baseline drift makes difficult to estimate the EOG signals. The baseline is shown by the dashed line in Fig.3(b). DC difference value$\left(D_{dif}\right)$ is express by Eq.(1) and the maximum value D_{max}^{R}, D_{max}^{L} is as below (Eq.(2), Eq.(3)). When D_{dif} exceeds a certain threshold value, D_{max}^{R} and D_{max}^{L} is taken as the maximum value.

$$D_{dif}(i) = D(i) - D_{base} \quad (1)$$
$$if:\ D_{dif}(i) > Th$$
$$D_{max}^{R} = maxD_{dif}(i)\ :D_{dif}(i) is\ EOG\ active\ on\ Right\ Direction \quad (2)$$
$$D_{max}^{L} = minD_{dif}(i): D_{dif}(i) is\ EOG\ active\ on\ Left\ Direction \quad (3)$$
$$i: the\ number\ of\ raw\ EOG\ data$$

- Feature value of DC Integral Value.

  DC integral value is the linear weighted sum of the DC difference value subtracting baseline and we obtain the value of the eyes position. By taking the maximum value of the DC integral (X^R_{max}, X^L_{max}) is stable when feature can be expressed. The dashed line is the value of DC, and solid line is the sum of the value of DC (Fig.3 (c)). Eq. (4),(5),(6) show DC integral value. The maximum value X^R_{max}, X^L_{max} is as below.

$$X(i) = \sum_{i=1}^{N} D_{dif}(i) : N = 200 \quad (4)$$

$$X^R_{max} = max\, X(i) : X(i)s\ EOG\ active\ of\ Right\ direction \quad (5)$$

$$X^L_{max} = min\, X(i) : X(i) is\ EOG\ active\ of\ Left\ direction \quad (6)$$

$$(i = 0,1,2 \ldots N)$$

$$i: the\ number\ of\ raw\ EOG\ data$$

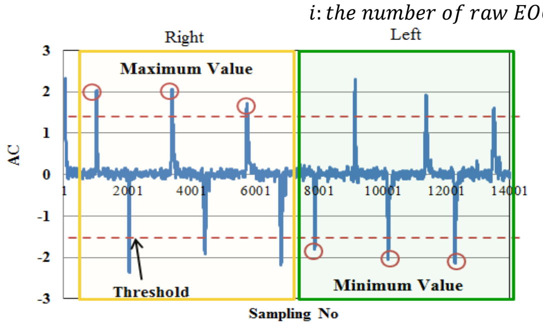

(a) Feature value of AC

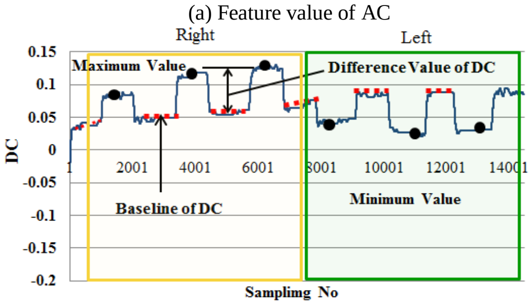

(b) Feature value of DC

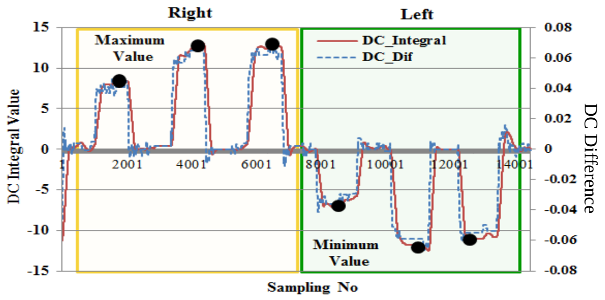

(c) Feature value of DC integral Value

Fig. 3. Feature value of proposed method

3.3. *Data Analysis*

In our previous studies [3][6], we have carried out the gaze estimation in the range from -60 degrees to 60 degrees. Therefore, in this paper we have estimated the gaze from -90 degrees to 90 degrees.

In order to confirm the accuracy of EOG system, we try regression analysis. We tried two types of regression analysis. First is the multiple regression analysis as linear regression analysis, second is the logistic regression analysis as non-linear regression analysis.

DC was known to have a linear relation to the eyeball angle, so we performed a multiple regression analysis with the next explanation variable : AC, DC, DC integral, DC difference. However, most previous works were carried out the experiments in the small space such as desktop PC [3]. We assumed that DC elements might not be linear shape characteristics in the large space such as this experiment and performed a nonlinearity logistic-regression analysis with an explanation variable same as a multiple regression analysis. We computed the predicted gaze degree by two type of regression analysis for each subject. We compared the explanation variables which is the most suitable variable using EOG in large space.

4. Experimental Results

In this section, we describe the gaze estimation results of -30degrees, -60degrees, -90degrees 30degrees, 60degrees and 90degrees. In this experiment, the proposed analysis method is the major analysis items of the angle of the target which subjects look to clarify the correlation between. The result of calculating the respective correlation coefficients R^2 are shown in Table 2. All the result over $R^2 > 0.83$, that shows the correlation of all analyses. In addition, DC integral value is higher in the results.

Table.2. The Correlation Coefficient of the multiple regression

	AC	DC Difference	DC Integral
SubjectA	0.8356	0.7906	**0.9257**
SubjectB	0.8440	0.9080	**0.9222**
SubjectC	0.8452	0.8451	**0.9064**

From the result of the multiple regression analysis, we conducted the logistic-regression analysis about DC integral value. In addition, we calculated the average error between the predicted value and the true value obtained by multiple regression analysis, logistic regression analysis (Fig.4).

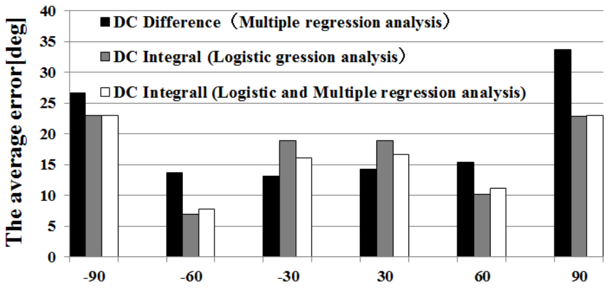

Fig. 4. The average error

Fig.4 shows that 60 degrees and -60 degrees were the small average error among each angle at left and right direction. And the gaze estimation by nonlinear analysis is better for angles bigger than 60degrees or less than -60degrees. The results of all data from -90 degrees to 90 degrees, the multiple regression analysis were 19.5 and logistic regression analysis was 16.2. Fig 4 shows that whether the relation of DC element and eyeball angle is linear or not depends on eyeball angle. Therefore, we established the boundary line (DC Integral Value:±15V) and separated a linear/nonlinearity and combined the results of the logistic-regression analysis and the multiple regression analysis (Fig.4 and Fig.5).

The eyeball angle of the 60degrees and -60 degrees are most easy to judge by EOG and the success rate is 88% without considering the individual difference of 3 subjects. At 90 degrees and -90 degrees, the judgment is difficult because individual is wide and the value of EOG tends to be saturated. About 30 degrees, -30 degrees, two of three people were 60% of success rates. One of the causes having low success rate is the influence of the individual differences. Based on 60 degrees, our analysis method can be classified as pattern 1) center (Fig.5), pattern 2) center to 60 degrees range, pattern 3) 60 degree over, pattern 4) center to -60 degree range and pattern 5) -60 degree less. Our analysis method can be said that 5 patterns are the appropriate number of judgment patterns.

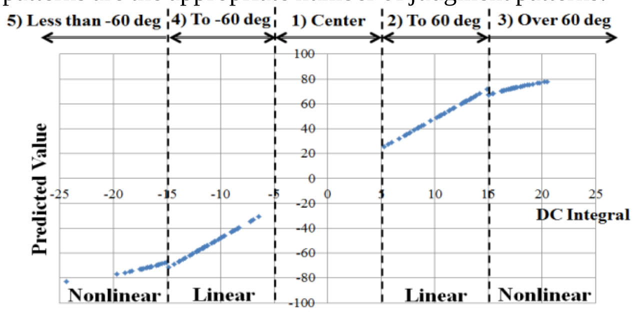

Fig. 5. The relation between the predicted value and the DC Integral value

5. Conclusion

In this paper, we conducted experiments to examine EOG elements that have a strong correlation with eye movement changes and from the experiments, we found that the following three points in this study.

1) From Table 2, DC Integral value is the most effective EOG signals to gaze estimate.
2) In the gaze movement in large space, the right and left 60 degrees is the best success rate.
3) DC integration is possible to classify 5 patterns by combining linear and nonlinear regression analysis results.

When gaze estimation is performed in a large space, we understood that the gaze estimation of 60 degrees on the left and right is the most stable. Therefore, by arranging the object at 60 degrees, our system is possible to perform input of 5 patterns with line of sight. By setting the lower limit of 60 degrees on each side, it is easier to use with success rate of Subject A: 85%, Subject B: 100%, Subject C: 79% without calibration. Therefore, the gaze estimation system of this study is a possibility to use as the application of the communication tool of patients with brain disease.

References

1. S. Venkataramanan, P. Prabhat, S. R. Choudhury, H. B. Nemade, and J. S. Sahambi, Biomedical instrumentation based on Electrooculogram (EOG) signal processing and application to a hospital alarm system, in *Proceedings of the 2nd IEEE International Conference on Intelligent Sensing and Information Processing* (Chennai, India, 2005), pp. 535–540.
2. H. Tamura, M. Yan, M. Miyashita, T. Manabe, K. Tanno, and Y. Fuse, Development of Mouse Cursor Control System using DC and AC Elements of Electrooculogram Signals and its Applications, *International Journal of Intelligent Computing in Medical Sciences & Image Processing*, Vol 5 No1, 2013, pp.3-15.
3. M. Yan, H. Tamura, and K. Tanno, A Study on Gaze Estimation System using Cross-Channels Electrooculogram Signals, in *Proceedings of The IMECS 2014*(Hong Kong,2014), pp112-116.
4. A. B. Usakli, S. Gurkan, F. Aloise, G. Vecchiato, and F. Babiloni, On the Use of Electrooculogram for Efficient Human Computer Interfaces, *Computational Intelligence and Neuroscience* 2010, Article ID 135629.
5. Zhao Lv, Xiao-Pei Wu, Mi Li, Development of a human computer Interface system using EOG, *Health* ,Vol.1 No.1, June 2009, PP. 39-46.
6. Keiko Sakurai , Mingmin Yan, Kazuhiko Inami, et al, A study on human interface system using the direction of eyes and face, *Artificial Life and Robotics*, December 2015, Volume 20, Issue 4, pp 291-298.

Development of Diagnosis Evaluation System of Facial Nerve Paralysis Using sEMG

Shogo Okazaki †, Misaki Syoichizono, Hiroki Tamura ‡
Faculty of Engineering, University of Miyazaki,
1-1,Gakuen-kibanadai-nishi, Miyazaki-shi, Japan

Takahiro Nakashima*, Eiji Kato*, Tetsuya Tono*
**Department of Otolaryngology, Head & Neck surgery, Faculty of Medicine, University of Miyazaki,*
1-1,Gakuen-kibanadai-nishi, Miyazaki-shi, Japan
E-mail: hc10010@student.miyazaki-u.ac.jp †, htamura@cc.miyazaki-u.ac.jp ‡

Abstract

In Japan, diagnostic of facial nerve paralysis is mainly used the electroneuronography (ENoG) method. Previous our research showed the certain correlation between ENoG and surface-electromyogram (s-EMG) data. Therefore, we developed the evaluation system of facial nerve paralysis using s-EMG. We compared with our developed software and manual by experimental person. Form simulation result, our developed software showed the correlation coefficient (R^2) between ENoG is 0.68.

Keywords: Facial Nerve Paralysis, Surface Electromyogram, Electroneuronography, Multiple Regression Analysis

1. Introduction

Although cause of facial nerve paralysis is unclear, the cause is believed that is one of the causes of viral infection. The main treatments are medication and surgical operation when the symptom is serious. Electroneuronography (abbr. ENoG) test is one of facial nerve diagnosis methods currently in using. However, the ENoG test can't carry out within one week after onset. For quantitatively diagnose, we focused on the surface-electromyogram (abbr. s-EMG) [1]. Previous our research, we found that there is a correlation between the ENoG value and features values of the s-EMG. We developed software to extract the features of s-EMG. In this paper, we compared with the results using software and manual results by correlation coefficient R^2 of ENoG value and feature values of s-EMG. In addition, we confirmed how much the manual method can be reproduced in the software method.

2. Previous Research

Previous our research, we investigated the relationship between the ENoG value and the feature values obtained from the s-EMG. Fig.1 shows the attachment position of the electrodes. In the experiment, the following two patterns of facial muscle activity performed five times, and the generated s-EMG measured.

· Motion the mouth horizontally (Motion A)
· Motion closing the eyes strongly (Motion B)

We measured 19 times of facial nerve paralysis: 6 subjects measured twice. Fig.2 shows an example of the s-EMG measured, and sampling frequency is 1000Hz. For these s-EMG, we performed each of frequency analysis by Fast-Fourier-Transform (abbr. FFT) and integrated calculation of s-EMG, and the difference between ch1 and ch2 obtained as the feature values. The reason for taking the difference is that in the Ref.2 a significant difference in the frequency of the s-EMG confirmed on the affected side and the healthy side. As a result, we obtained four kind of feature values. Next, we investigated the relationship between ENoG value and feature values and parameters that strongly influence using Adaptive – Network – Based – Fuzzy – Inference - System (abbr. ANFIS, ANFIS is one of fuzzy inference). Based on the results obtained from ANFIS, we prepared the three rules (shown in Table.1). Here, *freA* is difference between ch1 and ch2 frequency of the motion A, *integA* is difference between ch1 and ch2 integrated value of s-EMG of the motion A, and *integB* is difference between ch1 and ch2 integrated value of s-EMG of the motion B. We prepared three groups that divided the feature values by three rules. For each of the three groups, multiple regression analysis performed with the feature values as the explanatory variables and the ENoG values as the objective variable. The predicted of ENoG value was calculated from the result of multiple regression analysis, and feature values confirmed the correlation with ENoG values. As a result, R^2 was 0.79, and a strong correlation was found. This value set as the result of the manual method, and compare results between software and manual method.

Table 1. Three rules.

	frequency Motion A [Hz]	integrated Motion A [mV]	integrated Motion B [mV]
Rule 1	freA≧14	integA<15 or integA≧42	
Rule 2	freA<15	integA<15 or integ≧42	integB≦34
Rule 3	freA≦30		integB≧30

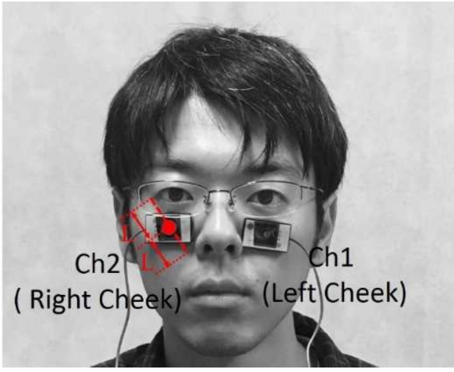

Fig.1. Attachment position of electrodes.

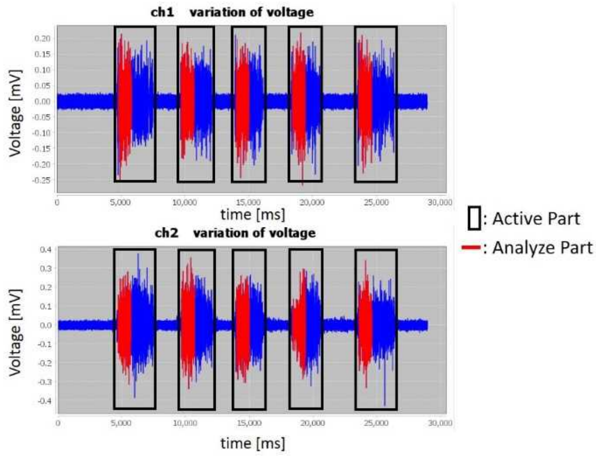

Fig.2. Example of measured s-EMG (Motion B)

3. Algorithm

We developed software that implements the methods for extracting feature values used in previous our research. Fig.3 shows the flow of processing. This section explains the processing of the developed software.

3.1. Search of Activity Start Position

In this subsection explain the method of searching for the position on the active part of N times. *Y(n)* (in Fig.3) is the integrated value of absolute value of *X(t)* for every 100 data. When for 2 seconds from start of s-EMG measurement, motion had set to do nothing. There B (in Fig.3) is threshold, it set a twice of average of integration values for 1 second from measurement start. If *Y(n)* are greater than threshold *B* and more than 7 times for 10 data, activity start position *P(N)* (in Fig.3) is set the position at initially beyond threshold *B*.

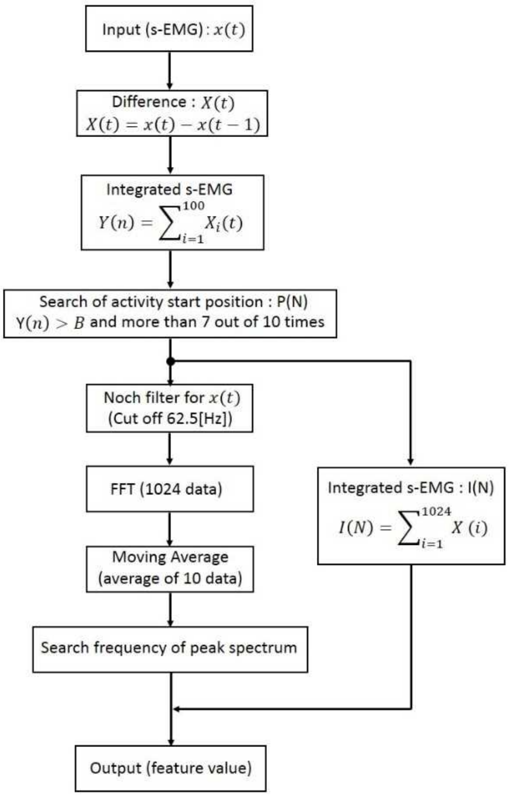

Fig.3. Processing flow of developed software.

3.2 *Frequency Analysis*

In this subsection, frequency analysis by FFT performed on the activity parts of the s-EMG. First, prior to frequency analysis, commercial power supply noise removed by a notch filter, and the frequency band of 62.5Hz cut. After that, FFT performed with 1024 s-EMG data from the starting point *P(N)* of the activity parts. Next, moving average performed on the spectrum obtained by FFT. The moving average performed every 10 spectrum. Then, the peak value of the spectrum after moving average searched, and the frequency at that time extracted. Fig.4 shows an example of the result. The solid line shows the spectrum obtained by FFT and dash line shows the result of moving average on the spectrum.

In this procedure performed on the sEMG data of ch1 and ch2 to extract the frequency. Then, difference in frequency of ch1 and ch2 obtained, and took out as a feature value. Since there are two kinds of motion, the feature value obtained by frequency analysis is two.

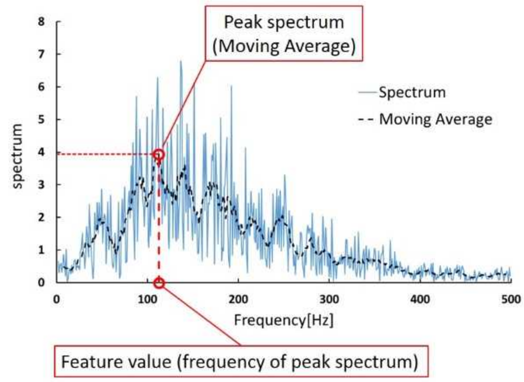

Fig.4. Result of frequency analysis and moving average of spectrum.

3.3. *Integrated s-EMG*

Integrated values calculated using s-EMG data from P*(N)* and the number of FFT data. Then, as the frequency case, the difference between the integrated values of ch1 and ch2 obtained, and two feature values obtained. Finally, a total of four feature values of frequency and integrated value extracted and used as parameters for calculating the predicted value of ENoG value.

3.4. *Execution Screen of Software*

Execution screen of developed out software are show Fig.5, Fig.6, and Fig.7. Fig.5 is reading files of s-EMG measurement. Fig.6 shows the results of position of activity part. These positions can also change by manually. Fig.7 shows the result of ENoG predicted value and condition of facial nerve paralysis diagnosed. Method of diagnosis will described later.

4. Analysis

In the previous section, we presented the method of calculating the feature values. We divided the obtained feature velues according to the rules in Table.1, and multiple regression analysis performed for each divided data groups. After that, we obtain the predicted value of

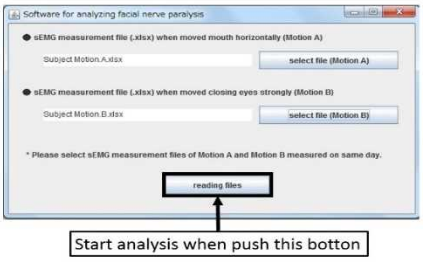

Fig.5. Execution screen for reading files.

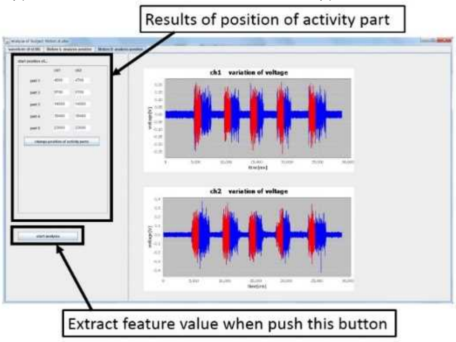

Fig.6. Execution screen to show the results search position of activity parts.

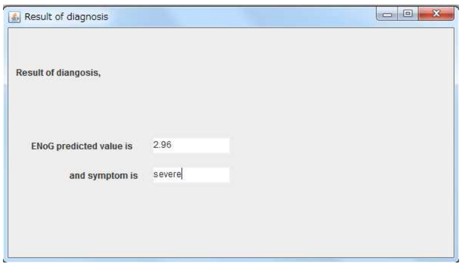

Fig.7. Execution screen to show the results of ENoG predicted value and condition of facial nerve paralysis diagnosed .

EnoG, and we compare the predicted value of EnoG with actual EnoG. Then, medical condition diagnose using predicted value of ENoG. Diagnostic criteria for each symptom are mild if ENoG is 40 or more, moderate if ENoG is greater than 10 and less than 40, and severe if ENoG is 10 or less.

5. Result

Fig.8 shows vertical axis is for the predicted value of ENoG value, and horizontal axis is for the ENoG value.The Area 1, Area 2, and Area 3 are areas of each of states severe, moderate and mild. From the figure, the correlation coefficient R^2 was 0.68. The success rate when diagnosing the condition using the predicted ENoG was 78.95%.

6. Conclusion

Predicted values using software, the result of $R^2 = 0.68$ was obtained. Although the correlation coefficient decreased as compared with $R^2 = 0.78$ when manual analysis performed in the previous research, we confirmed a strong correlation still observed with the ENoG value. However, there were two results that the ENoG predicted value of serious patients were significantly different from the actual ENoG value. From now on, it is necessary to predict the ENoG value for s-EMG data of newly measured facial nerve palsy patients, and investigate whether the correlation between the feature values of s-EMG used this time and the ENoG value is reproducible. Also, as necessary, we intend to update the coefficients of the regression equation and adjust the rules in Table.1.

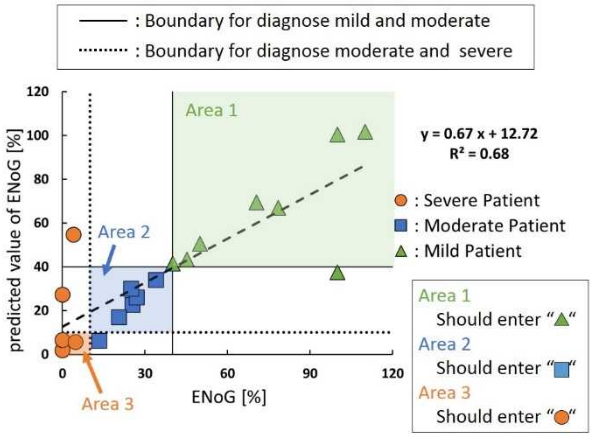

Fig.8. Correlation between the predicted value calculated from the output feature quantities and the ENoG values.

References

1. Kohei Nagatomo, *Analysis of Facial Nerve Paralysis Using s-EMG and Movement of the Facial Muscles During Exercise, FACIAL NERVE RESEARCH JAPAN,* 33, 2013, 95-96p (Japanese)
2. Katsuo Nishimoto, *Deliberation of measure of peripheral facial palsy -Especially using s_EMG-, Japanese Physical Therapy Association,* 19(Supplement), 1992-3, 355p

High CMRR and Wideband Current Feedback Instrumentation Amplifier Using Current Conveyors

Shota Mago, Hiroki Tamura, Koichi Tanno
University of Miyazaki
1-1, Gakuen Kibanadai Nishi, Miyazaki,889-2192, Japan

tanno@cc.miyazaki-u.ac.jp

Abstract

This paper presents a high CMRR and wideband current feedback Instrumentation Amplifier (IA). The proposed IA architecture consists of Fully Balanced Differential Difference Amplifier (FBDDA) and Differential Difference Amplifier (DDA) based on 2nd generation current conveyor (CCII) with a buffer. From the simulation results evaluated by HSPICE, the proposed IA exhibits average CMRR was 109.3 dB higher than the conventional one. Furthermore, the proposed IA has higher closed-loop gain over a larger bandwidth than corresponding voltage feedback.

Keywords: Instrumentation Amplifier, CMRR, Current Conveyor, Differential Difference Amplifier, Current Feedback

1. Introduction

Instrumentation Amplifier (IA) with high CMRR, high input impedance, and configurable differential gain characteristics is used in many application areas, such as medical instrumentation, the read-out circuit of biosensors, signal processing, and data acquisition [1].

Fig.1 shows the conventional IA, which consists of 3 operational amplifiers and 7 resistors. Each resistors require the condition of $R_1 = R_2$, $R_3 = R_4$, $R_5 = R_6$. In this case, the output voltage is described by Eq. (1).

$$V_{out} = \frac{R_5}{R_3}\left(1+\frac{2R_1}{R_G}\right)(V_1 - V_2) \qquad (1)$$

However, CMRR, especially common-mode gain (*Ac*) of this IA is highly dependent on strict resistor matching [2]. For example, if only 0.1% mismatch between R_5 / R_3 and R_6 / R_4, CMRR deteriorates from ideal (infinity) to 66 dB, on condition that differential gain is 0 dB [5]. Thus, resistor mismatches are serious problem for IA.

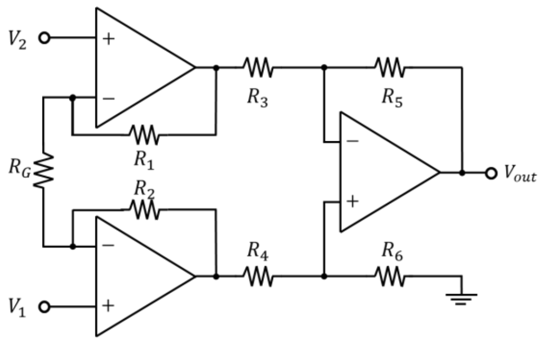

Fig.1. Conventional IA

To overcome this problem, we have proposed an IA architecture which consists of Fully Balanced Differential Difference Amplifier (FBDDA) and Differential Difference Amplifier (DDA) [4]. Its CMRR is extremely higher than that of the conventional IA under the condition of resistor mismatch [3].

On the other hand, in a signal processing system, one of the considerable characteristics is the bandwidth.

Especially, in the biological signal processing, the chopper stabilization technique is often employed for avoiding 1/f noise in MOS devices [4]. In this kind of signal processing, wide bandwidth circuits are required strongly. However, the conventional IA exhibits a narrow bandwidth that is highly dependent on the closed-loop gain, due to the fixed gain bandwidth product.

In this paper, high CMRR and wideband IA, which consists of FBDDA and DDA using current feedback technique, is presented. The proposed IA has advantages that common-mode gain is insensitive to the resistor mismatches and bandwidth is wider than the conventional one and is independent of gain. The proposed IA is evaluated through HSPICE with the set of the parameters of 0.6μm CMOS process. In this paper, we report the detailed simulation results.

2. Voltage Feedback and Current Feedback

Voltage feedback is majority feedback method for the conventional IA. Fig.2 shows the block diagram of voltage feedback. $A_{(s)}$ is the open-loop gain as a function of frequency, β is a feedback factor which is amount of feedback from output. Fig.3. represents frequency response of Fig.2. Fig.3 indicates that if we get higher closed-loop gain reducing β, closed-loop bandwidth will be narrow caused by constant Gain Bandwidth Product (GBP). Therefore, IA with voltage feedback is not suitable for implementation of IA with the chopper stabilization technique and high gain.

Fig. 4 shows the block diagram of current feedback. $Z_{(S)}$ is the open-loop trans-impedance gain as a function of frequency, g_{in} is a trans-conductance which converts input voltage to current, g_f is a trans-conductance which feedback output signal as current. Fig.5 denotes typical frequency response of Fig.4. As long as g_f is fixed, the bandwidth is constant, even if the closed-loop gain is varied by changing g_{in} [6]. Therefore, current feedback has wider bandwidth than voltage feedback, and its bandwidth is independent of the closed-loop gain. Therefore, the current feedback is suitable for high gain IA with the chopper stabilization technique.

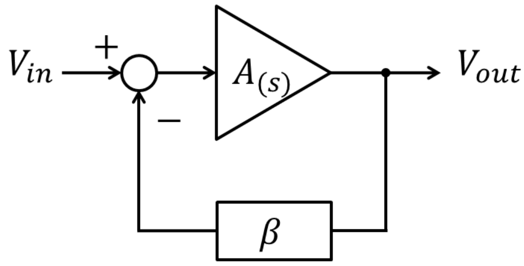

Fig.2. Block Diagram of Voltage Feedback

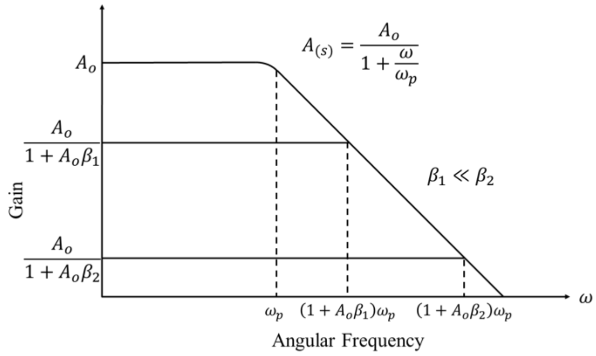

Fig.3. Frequency Response of Voltage Feedback

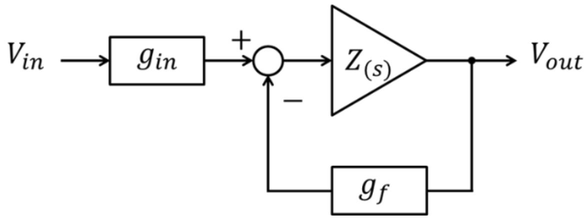

Fig.4. Block Diagram of Current Feedback

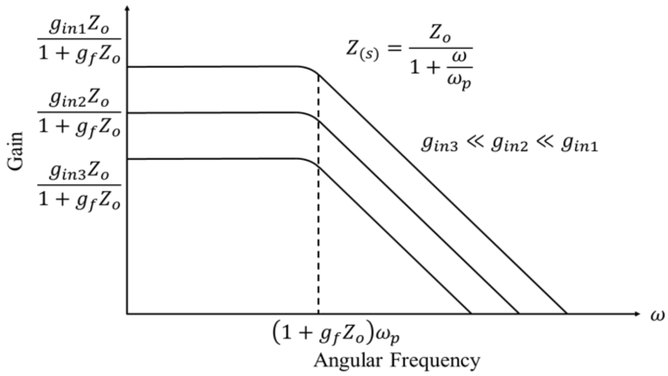

Fig.5. Frequency Response of Current Feedback

3. Proposed Instrumentation Amplifier

Fig. 6 shows the proposed architecture for the high CMRR and wideband IA. The proposed IA consists of 1st stage and 2nd stage shown in Fig.6. 1st and 2nd stages are designed based on FBDDA and DDA respectively, and FBDDA and DDA are realized by using 2nd generation Current Conveyors (CCII) and buffers for implementation of current feedback. As for CCII, terminal Y_i (i=1, 2, 3) exhibits an infinite input impedance in ideal, the voltage at X_i (i=1, 2, 3) follows that applied to Y_i, X exhibits a zero input impedance in ideal. The current supplied to X is conveyed to the high impedance output terminal Z_i [7]. Theoretically, each resistors of the proposed IA no require resistor matches for high CMRR. Furthermore, the proposed IA has higher closed-loop gain over a larger bandwidth than corresponding conventional IA.

The output voltage of 1st stage (V_A and V_B) is given as follows in the case of $R_1 = R_2$.

$$V_A = \frac{1}{2}\left(1 + \frac{2R_1}{R_G}\right)(V_1 - V_2) \qquad (2)$$

$$V_B = -\frac{1}{2}\left(1 + \frac{2R_1}{R_G}\right)(V_1 - V_2) \qquad (3)$$

From Eq. (2) and (3), common-mode signal can be rejected at V_A and V_B before 2nd stage. In addition, output voltage of 2nd stage is given by

$$V_{out} = \left(1 + \frac{R_4}{R_3}\right)(V_A - V_B) \qquad (4)$$

Then, from Eq. (2), (3) and (4), we can derive V_{out} as follows.

$$V_{out} = \left(1 + \frac{R_4}{R_3}\right)\left(1 + \frac{2R_1}{R_G}\right)(V_1 - V_2) \qquad (5)$$

In mismatch condition ($R_1 \neq R_2$), $V_{out,m}$ can be given by

$$V_{out,m} = \left(1 + \frac{R_4}{R_3}\right)\left(1 + \frac{R_1 + R_2}{R_G}\right)(V_1 - V_2) \qquad (6)$$

Eq. (6) represents common mode signal is rejected even if the mismatches in all resistors are occurred. Thus, the proposed IA has much higher CMRR than the conventional one.

4. Simulation Results

In this chapter, simulation results of CMRR and frequency response are shown. The conventional IA and proposed IA were evaluated using HSPICE with 1P 3M 0.6μm CMOS process.

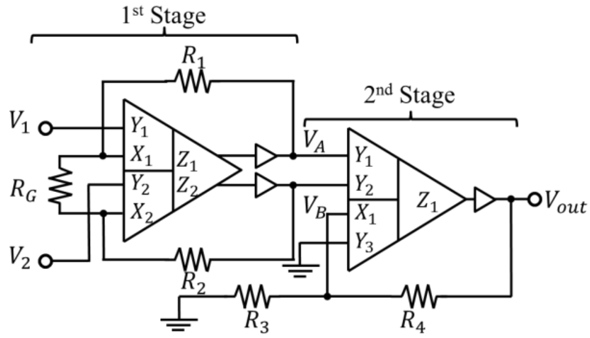

Fig.6. Proposed IA

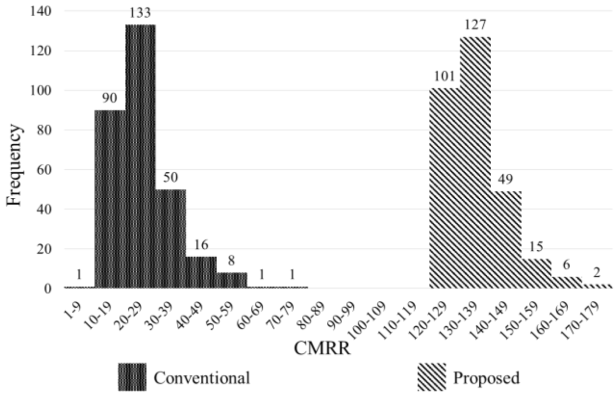

Fig.7. Histogram of CMRR

4.1. *CMRR*

For comparison of conventional and proposed IA, we have simulated 300 times with ±30% all resistor mismatches by Monte Carlo analysis. The simulation result is shown in Fig.7. To evaluate the effect of A_C which is more sensitive to resitor mismatch than differential gain (A_D), A_D of both IAs are set 0 dB for easy estimation.

From Fig. 7, average CMRR of conventional and proposed IA are 24.9 dB and 134.2 dB respectively. The average CMRR of the proposed IA is 109.3 dB higher than conventional one.

4.2. *Frequency Response*

Fig.8 and Fig.9 show the frequency response of the conventional IA and proposed IA, respectively under the condition that the differential gain of both IAs are varied from 12 dB to 20 dB by changing R_G. As closed-loop gain of the conventional IA is getting higher, the cut-off frequency is getting lower. On the other hand, the cut-off frequency of the proposed IA is constant, regardless of change of the closed-loop gain. Therefore, proposed IA is superior to conventional IA in terms of bandwidth.

Lastly, the detailed simulation results are listed in Table 1. From these results, the performance of the proposed IA is much better than that of conventional one.

5. Conclusion

In this paper, high CMRR and wideband current feedback instrumentation amplifier using CCII have been presented. The CMRR and frequency response of conventional and proposed IA were evaluated by HSPICE. As a result, we confirmed the proposed IA has 109.3 dB higher CMRR than the conventional one under the resistor mismatches. Moreover, it was verified proposed IA has higher closed-loop gain over a larger bandwidth than corresponding conventional IA.

The evaluation through the actual fabrication of the LSI is the future work.

Acknowledgements

This work is supported by VLSI Design and Education Center (VDEC), the University of Tokyo in collaboration with Synopsys, Inc. and Cadence Design, Inc.

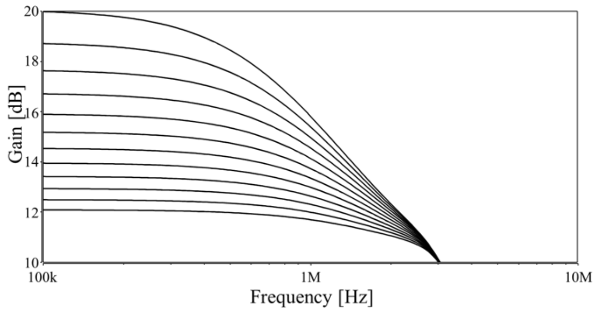

Fig.8. Frequency Response of Convention IA

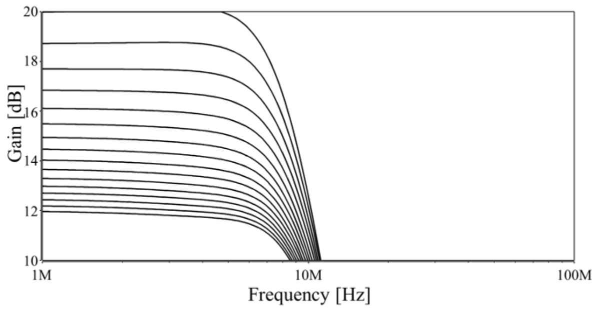

Fig.9. Frequency Response of Proposed IA

Table 1. Summary of the Simulation Results.

Item	Conventional IA	Proposed IA
	AC analysis	
Cut-off Frequency (Differential Gain = 20 dB)	750 kHz	7.8 MHz
Unity Gain Frequency	5 MHz	16.5 MHz
Power Consumption	2.6 mW	1.6 mW
	Monte Carlo analysis	
Average CMRR (Differential Gain = 0dB)	24.9 dB	134.2 dB

References

1. Y. H. Ghallab, W. Badawy, B. J. Maundy, “A Novel Current-Mode Instrumentation Amplifier Based on Operational Floating Current Conveyor,” *IEEE Trans. On Instrumentation and Measurements*, Vol. 54, No. 5, pp. 1941-1948, 2005.
2. J. Szynowski, “CMRR analysis in instrumentation amplifiers,” *Electronics Letters*, vol. 19, no. 14, pp. 547-549, 1983.
3. Z. Abidin, K. Tanno, S. Mago, H. Tamura, “Low Common-Mode Gain Instrumentation Amplifier Architecture Insensitive to Resistor Mismatches,” *Int. Journal of Electrical and Computer Engineering*, pp. 1-7, May 2013.
4. Z. Abidin, K. Tanno, S. Mago, H. Tamura, “Novel Instrumentation Amplifier Architectures Insensitive to Resistor Mismatches and Offset Voltage for Biological Signal Processing,” *proc. of IEEE Int. Symp. on Multiple-Valued Logic*, pp. 194-199, May 2016.
5. B. Baker, “Understanding CMR and instrumentation amplifiers,” *EDN*, pg 14, Nov 26 2014.
6. G. D. Cataldo, A. D. Grasso, S. Pennisi, “Two CMOS Current Feedback Operational Amplifiers,” *IEEE Trans. on Circuits and Systems -2: Express Briefs*, vol. 54, no. 11, pp. 944-948, Nov. 2007.
7. A. S. Sedra, G. W. Roberts, F. Gohh, “The Current Conveyor: History, Progress and New Results,” *IEE Proceedings*, vol. 137, Pt. G, no. 2, Apr, 1990.

Voltage Rectifier Circuit with Voltage Doubler Using New Active Diode

Masayuki Uchihara, Hiroki Tamura, Koichi Tanno †
University of Miyazaki, 1-1 Gakuenkibanadai-Nishi,
Miyazaki City, Miyazaki, Japan

E-mail: tanno@cc.miyazaki-u.ac.jp †

Abstract

In this paper, voltage rectifier circuit with voltage doubler using new Active Diode (AD) is proposed for battery less biological signal measurement system using smartphone. Firstly, we propose the new AD which consists of AD core circuit and Bulk Regulation Transistor (BRT). The advantage of proposed AD (ADB) is insensitive to the threshold voltage of MOSFETs and very useful for low power and low voltage operation. Next, the voltage rectifier circuit with voltage doubler using the ADB is presented. Thanks to the good performance of the ADB, the designed rectifier could operate as theory by only the sin waves from the earphone terminal of smartphone. The ADB were fabricated actually using 1-P 3-M 0.6-μm CMOS process. The detailed simulation and measurement results are reported in this paper.

Keywords: Active diode, Bulk regulation transistor, Voltage rectifier, Voltage doubler

1. Introduction

Recently, healthcare systems using mobile devices receive attention to maintain personal health condition. In the case of realizing this kind of systems, additional sensor to measure biological signals for mobile devices are necessary. However, it is difficult to use just connecting sensor to mobile devices because the electrical characteristics of sensors are different depending on sensors. In order to overcome the problem, we have proposed the sensor conditioner IC (SCIS) for mobile devices such as smartphone. Fig. 1 shows the architecture of the proposed SCIC. In SCIC, we focus on the earphone-mic terminal, which is used for input-output interface and power supply to SCIC. SCIC consists of amplifier which is to amplify the signal from the additional sensor, filter which eliminates noises and AC/DC converter for supplying DC power to the amplifier and filter. In many cases, this kind of circuits, analog-to-digital (A/D) converter is often necessary; however, A/D converter built in mobile devices for analog input from earphone-mic terminal is used in the proposed SCIC.

The battery less SCIC is very important for mobile devices because of light weight and small package. Therefore, in the proposed SCIC, we employed the AC/DC converter as mentioned previously. The AC/DC converter converts from AC signal, which is generated by application program on the mobile devices, to DC voltage. The DC voltage is used for supplying the DC sources for operating the amplifier and filter in SCIC. In the past, some AC/DC converters were proposed. In these circuits, some diodes were used for voltage rectifiers. However, a threshold voltage of the diode cannot be ignored because amplitude of the AC signal is very small. In order to overcome this problem, voltage rectifier using Active Diode (AD), which has ideal diode characteristic, were proposed [1] [2]. The circuit is used a Bulk Regulation Transistor (BRT) for eliminating the dead zone. However, because BRT has a timing at which the back-gate potential becomes indefinite, there is the problem that the AD does not correctly operate at low input voltage.

In this paper, we propose a new AD. The proposed AD is very simple circuit which adds an inverter to conventional AD. Furthermore, we propose new voltage rectifier circuit with voltage doubler using the proposed AD. The proposed AD is evaluated using HSPICE and actual fabrication based on 0.6µm standard CMOS process. We report the detail simulation and experimental results in this paper.

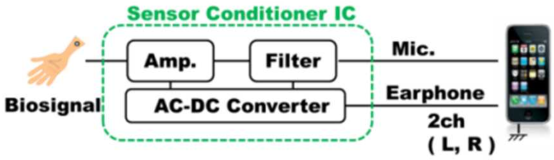

Fig. 1 Architect of sensor conditioner IC(SC-IC)

2. Conventional AD with BRT

A schematic of the conventional AD with BRT is shown in Fig. 2 [3] [4]. The gate, drain and source terminals of the MOSFET in AD (M_1) are connected to the output terminal of the comparator, the positive phase input terminal, and the negative phase input terminal, respectively. Output of comparator in AD makes MOSFET ON or OFF state. At the same time, BRT makes back-gate terminal of M_1 connect source terminal, therefore BRT prevent the back-gate current from flowing. When V_A and V_B are the potential of the terminals A and B, respectively, the operation of the circuit of Fig. 2 is as follows.

(i) In the case of $V_A < V_B$

On condition that $V_A < V_B$, A and B are the drain and source terminals of M_1, respectively. In this case, M_1 turns ON due to the output of the comparator are low. And also, M_2 and M_3 turn OFF and ON, respectively because $V_A < V_B$. As the results, the back-gate terminal of M_1 is connected to the source terminal. In this way, the current from V_{in} flows from the source terminal of M_1 to drain terminal of M_1 without flowing the back-gate current.

(ii) In the case of $V_A \geq V_B$

On condition that $V_A \geq V_B$, A and B are the source and drain terminals M_1, respectively. In this case, M_1 turns OFF because the output of comparator is high. Moreover, M_2 and M_3 turn ON and OFF, respectively because $V_A \geq V_B$. As the results, the back-gate terminal of M_1 is connected to the source terminal. In this case, the current from V_{in} doesn't flow from the source terminal of M_1 to drain terminal of M_1 neither is the back-gate current.

In the above explanation, threshold voltage of MOSFET is ignored. If threshold voltage is considered in the circuit operation, M_2 and M_3 cannot turn ON or OFF immediately because V_{in}, which is a sin wave, gradually increases or decreases. Therefore, M_2 and M_3 turn ON or OFF halfway, as the results, the conventional circuit has a dead band until V_{in} reaches the threshold voltage.

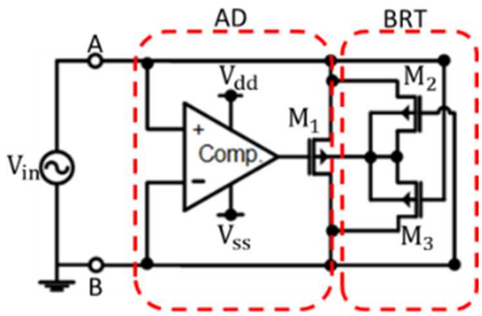

Fig. 2 Conventional ADB

3. Proposed AD with BRT

The schematic of the proposed AD with BRT is shown in Fig. 3. The difference between the proposed ADB and conventional circuit is the control signal for BRT. In the conventional circuit, V_{in}, which is a sine wave and gradually increase or decrease signal, is directly used as the controlling the BRT, therefore, the BRT has dead band. In the proposed ADB, the output signal of the comparator, which is digital signal such as Hi (VDD) or Low (GND), is used as the control signal for BRT. Therefore, the dead band can be omitted, so that we can overcome the problem.

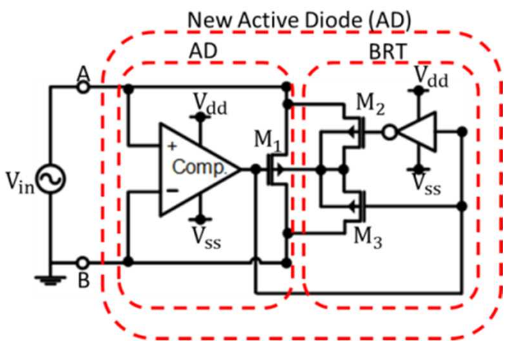

Fig. 3 Proposed ADB

4. Simulation and Experiment Result

The conventional and proposed ADB were fabricated using 0.6 µm standard CMOS process. Fig. 4 shows both the simulation and experimental results of the conventional ADB. From Fig. 4 it can be confirmed that the back-gate voltage of M_1 is an indefinite value.

Fig. 5 shows simulation and experimental results of the proposed ADB. When the change of the back-gate terminal of M_1 was confirmed in the range of V_{in} from -2 [V] to 2 [V], a desired voltage characteristic was obtained. Therefore we could confirm that the proposed ADB operates as the AD without dead band.

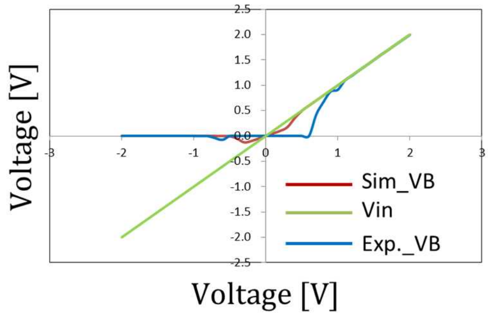

Fig. 4 Simulation and experiment results of the conventional ADB

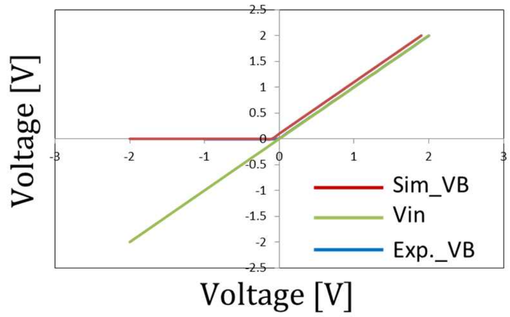

Fig. 5 Simulation and experimental results potential of the proposed ADB

5. Application to AC-DC Converter Using ADB

In this chapter, we explain AC-DC converter using the ADB. Fig. 6 shows the voltage doubler half-wave rectifier circuit, which is widely used. However, this circuits includes diodes, therefore, the problem described in the previous (problem of the threshold voltage and dead band of diode) is remained. Fig. 7 shows the proposed AC-DC converter, which is replaced by the proposed ADB instead of diodes and expanded to bipolar (plus and minus) supply voltage. In order to confirm the usefulness of the proposed AC-DC converter, the circuits were evaluated through HSPICE with 0.6 µm CMOS device parameters.

Fig. 8 shows the output voltage at each output load. From Fig. 8, the desired voltage (2.6V) can be obtained from about 10 kΩ. Fig. 9 shows the power efficiency at each output load. As the output resistance increase, the impedance of the comparator apparently decrease and the total amount of current consumed by the comparator becomes larger than the amount of current consumed by the load. Therefore, the power efficiency decreases from 50 kΩ and the value is approximately 40%. Fig. 10 shows the results of the mask layout of the proposed

AC-DC converter. The estimated chip area is 310 µm × 650 µm.

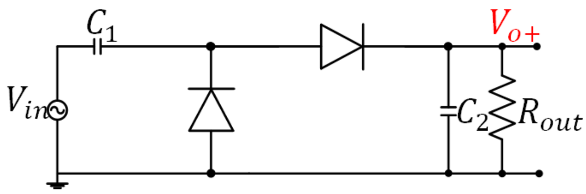

Fig. 6 General Voltage doubler half-wave rectifier

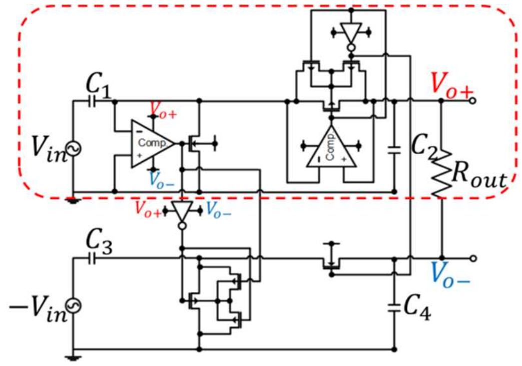

Fig. 7 The proposed AC-DC Converter

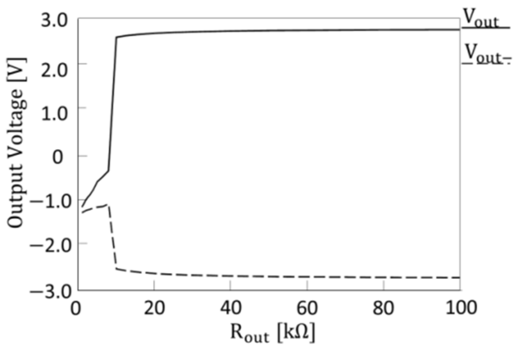

Fig. 8 Output voltage at each output load

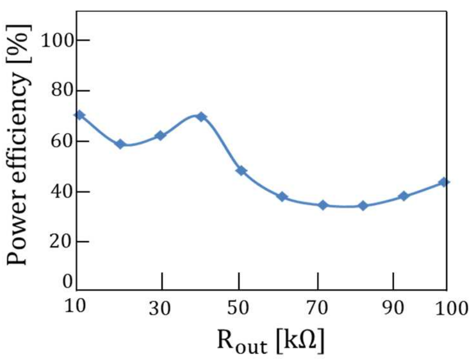

Fig. 9 Power efficiency at each output load

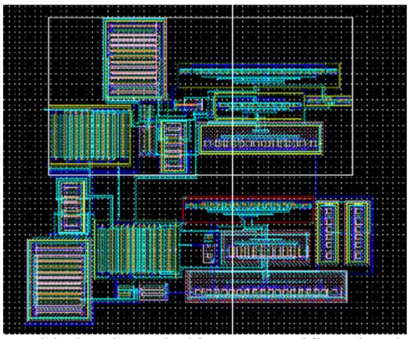

Fig. 10 Doubled voltage half-wave rectifier circuit layout using ADB

6. Conclusion

In this paper, we have proposed a novel active diode (ADB) firstly. As a result of pointing out the problem about the indefinite value of the back-gate potential in the conventional active diode were improved. The improvement was confirmed by HSPICE simulation and experiment using the actual chip fabricated with 0.6um CMOS process. Next, AC-DC converter using the proposed ADB for SCIC using mobile devices has been proposed and designed. The circuits were evaluated through HSPICE. From the simulation results, we could obtain approximately 70% efficiency up to the load of 40 kΩ. For future work, the actual chip fabrication of the sensor conditioner ICs and its evaluation.

References

1. Y. Rao and David P. Arnold, An AC/DC Voltage Doubler with Configurable Power Supply Schemes for Vibrational Energy Harvesting (*IEEE Applied Power Electronics Conference and Exposition*, 2013), pp. 2844-2851
2. E. Dallago et al, Active Autonomous AC-DC Converter for Piezoelectric Energy Scavenging Systems, (*IEEE Custom Integrated Circuit Conference*, 2008) pp.555-558.
3. C. Peters and J. Handwerker, A Sub-500mV Highly Efficient Active Rectifier for Energy Harvesting Applications (*IEEE Trans. Circuits Syst. I*, Reg. papers, vol.58, no.7, 2011), pp.1542-1549
4. D.Maurath, C. Peters, M. Ortmanns, and Y. Manoli, Highly Efficient Integrated Rectifier and Voltage Boosting Circuits for Energy Harvesting Applications, (*Advances in Radio Science*, vol.6, 2008), pp.219-225

Towards Unified Human-Robotic Societies

Peter Sapaty
Institute of Mathematical Machines and Systems,
National Academy of Sciences, Kiev, Ukraine

Masanori Sugisaka
ALife Robotics Corporation Ltd., Oita, Japan

Takao Ito
Department of Engineering, Hiroshima University, Japan
Email: peter.sapaty@gmail.com, icarob@alife-robotics.co.jp, itotakao@hiroshima-u.ac.jp
http://alife-robotics.co.jp/

Abstract

Large numbers of robotic facilities have been accumulated worldwide, but existing robots still remain specialized devices rather than intelligent collaborators for humans. To integrate massive robotics into human societies, more universal approaches are needed. Higher-level, semantic, model supported by special language SGL is described expressing operations and decisions in distributed spaces in a compact form, with traditional system management shifted to automatic language interpretation. Communicating SGL interpreters associated with humans and robots form goal-driven teams under unified control, with corresponding examples presented.

Keywords: world dynamics, human-robotic systems, spatial grasp technology, networked language interpretation, self-evolving patterns

1. Introduction

The world has changed dramatically for the last decade, with numerous conflicts and crises including international terrorism, ethnic, religious and military conflicts, endless floods of refugees, economy collapses too. To withstand this dynamics, new ideologies and system management technologies are desperately needed. Of particular effectiveness may be those allowing for seamless embedment of massive robotics into human societies, with robots taking care of dangerous and critical situations, acting cooperatively with humans and between themselves under unified control.

The paper briefs a high level formalism and supporting technology that can express operations and top decisions in physical, virtual and executive environments regardless of who (humans) or what (robots) should perform them, and in which quantities. This can allow us to make implementation in dynamic environments where manned and/or unmanned resources may not be known a priori but rather defined at runtime, depending on circumstances.

2. Spatial Grasp Technology (SGT)

Key ideas of the developed technology and its possible implementation will be revealed in brief.

2.1. *Self-evolving patterns*

Within SGT, a high-level scenario for any task in a distributed world is represented as *active self-evolving pattern* rather than traditional program, sequential or parallel, inheriting holistic and gestalt [1-2] ideas rather than of communicating agents [3]. This also reflects integral style of human thinking and brain activity [4, 5] when perceiving images as a whole, treating parts and their sense within this whole rather than vice versa.

The self-evolving pattern, expressing top semantics and key decisions of the problem to be solved and starting from any point, spatially *propagates, grows, replicates, modifies, covers, interlinks and matches* the world. It creates distributed operational infrastructures throughout the space covered, with final results retained in the environment or returned as high level knowledge to the starting point, as shown in Fig. 1.

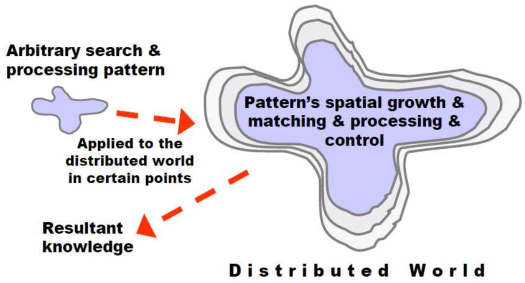

Fig. 1. Spatial pattern growth & coverage & matching.

The spreading & matching patterns can create *knowledge infrastructures* arbitrarily distributed between system components (humans, robots, sensors). Covered by same or other patterns, these can effectively support distributed databases, command and control, situation awareness, and autonomous decisions, also simulate any other models.

2.2. *Spatial Grasp Language, SGL*

SGL [6], the core of the approach, allows us to *directly move through*, observe, and make any actions and decisions in fully distributed environments (whether *physical*, *virtual*, *executive,* or *combined*). It has universal recursive structure, shown in Fig. 2, capable of representing any parallel and distributed algorithms operating over spatially scattered data or other, lower level, distributed systems of arbitrary natures.

2.3. *Networked SGL interpreter*

The interpreter (its architecture stemming from [7]) consists of a number of specialized modules handling and sharing specific data structures. A backbone of the distributed interpreter is its *spatial track system* providing global awareness and automatic C2 over multiple distributed processes, also creating and managing distributed information and control resources. The distributed SGL interpreter may have *any number of nodes*, up to millions even billions, distributed worldwide. It can operate with d*ynamic and changeable topology* with varying number of interacting nodes.

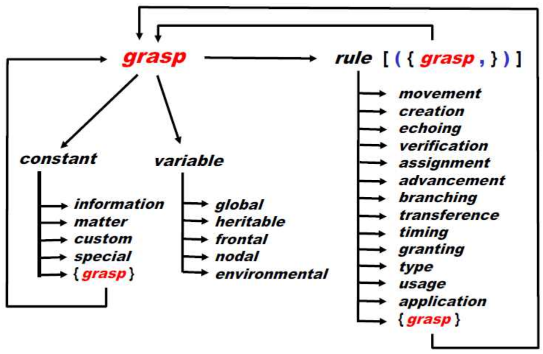

Fig. 2. SGL recursive syntax.

3. Elementary Example

Giving a command to soldier `John` to use robot `Shooter` to fire by coordinates `(x, y)` with confirmation of the robot's success or failure, see Fig. 3.

Fig. 3. Ordering soldier to use robot to shoot by coordinates

```
hop(John);
report_if((hop(Shooter); fire(x, y)),
          success, failure)
```

4. Integral Human-Robotic Teams

In the previous example we showed selective tasking of a human and a robot, whereas will consider here simple scenarios for mixed teams with humans and robots having equal status, as symbolically shown in Fig. 4.

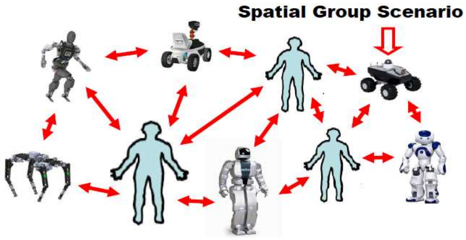

Fig. 4. Mixed team with same status of units.

The highlighted scenario parts may be executed by biological brain & sensors (in a dialog mode, say, via a local screen) if appear in SGL interpreter copies associated with humans, otherwise handled by robots, with overall group control fully automatic too.

- Randomized group movement, starting in any node, with Range distance allowed between units when moving; units reporting individually if "aliens" seen.

```
hop(all);
nodal(Limits = (dx(0,8), dy(-2,5)),
      Range = 200, Shift);
repeat(
 if(seen(unknown), report('alien'));
 Shift = random(Limits);
 if(empty(Shift, Range), WHERE += Shift);
sleep(delay))
```

- Starting from any node, finding topologically central unit of the moving group and hopping into it.

```
frontal(Aver) = average(hop(all); WHERE);
min_destination(
  hop(all); distance(Aver, WHERE));
```

- Creating hierarchical infrastructure from the center found using oriented links infra and *depth* as certain maximum allowed linking distance:

```
repeat_linkup(+infra, firstcome, depth))
```

- Using the created infrastructure, collect at its top and analyze all objects (symbolically: targets) discovered throughout the whole territory covered by the group, issuing OK or alarm if danger.

```
frontal(Seen) = repeat(
  free_detect(targets), hop(+infra));
if(analyze(Seen), out(OK), out(alarm))
```

Integration of the above four cases within a single united scenario allowing the whole group randomly move while keeping threshold distance between units, regularly redefining its changing center and hierarchical infrastructure, and collection and analysis of targets is trivial – can be done starting from any human or robotic unit (a related case in [8]). Any other collective scenarios can be generated too, often on the fly.

5. Fully Semantic Scenario in SGL

At this highest level, it is possible to describe in SGL only what should be done in a distributed space and which top operations and decisions to make, like follows: *Evaluate damage after disaster in points with physical coordinates X1_Y1, X2_Y2, and X3_Y3, and report the maximum one.* The SGL expression will be:

```
report_max_assess(X1_Y1, X2_Y2, X3_Y3)
```

This semantic description is fully formal, and can be automatically implemented in physical space by available manned, unmanned or mixed units. The solution by robotic units R1 and R2 and manned M1, scattered somewhere in the region (all having communicating SGL interpreters installed) is shown in Fig. 5.

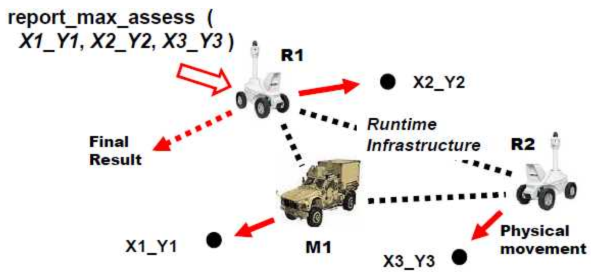

Fig. 5. Automatic solution of semantically defined problem

6. Coastal Waters Cooperative Patrol

This is another scenario example, where manned and unmanned units can work together cooperatively and be substituted by each other at any time, with new ones involved too, as in Fig. 6, following coastline in changing directions and regularly reporting if discover (sensors dependent) "aliens" in key points.

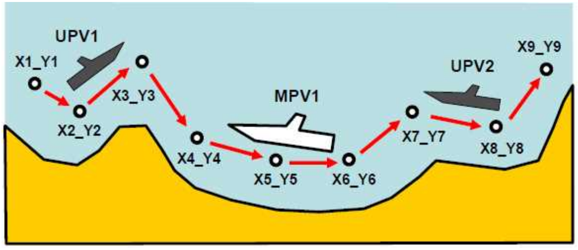

Fig. 6. Simultaneous coastal patrol.

At the beginning we will create a discrete coastal map as a semantic network consisting of coordinates of key points linked with each other by oriented links (all named `r`). Vehicles will follow this chain along or opposite orientation of the links, changing direction at the end or when see a “colleague” ahead, with the scenario oriented on starting simultaneously in points `x1_y1, x5_y5, x9_y9`.

```
stay_create(
  x1_y1; (+r, x2_y2); ...;(+r, x9_y9));
hop(x1_y1, x5_y5, x9_y9);
frontal(R) = random(+r, -r)
WHERE = CONTENT;
repeat(
 repeat(check_report(vision_depth);
        WHERE = hop(R); none(distance));
 invert(R))
```

This semantic level scenario can, for example, be executed by unmanned UPV1 and UPV2 vehicles and manned MPV1, as in Fig. 6. In case of a manned vehicle engaged, the boldfaced operations can be performed manually, whereas in robotic cases -- automatically.

7. Conclusions

The current paper is pioneering on formalization of semantic level operations and top intelligence as regards large distributed systems, which can be implemented by any available resources regardless of being human or robotic, thus paving a real way to integration of multiple robotics into human societies.

Some remotely related works in this direction are conducted in military on formalization of Command and Control (C2) to simplify multilingual international cooperation and also improve chances of formal engagement of robotic facilities in advanced operations. But the developed specialized Battle Management Languages (BML) [9] for unambiguous expression of C2 are not programming languages themselves, therefore needing integration with other linguistic facilities and organizational levels. On the contrary, SGL, being fully formal and universal system language, allows for effective and compact semantic expression of any battlefield scenarios and orders, also directly supporting robotized up to fully robotic systems [8].

SGT, allowing for holistic and intelligent solutions of complex problems in distributed environments, may also be considered as inheriting some ideas (albeit two thousand years old) of Sun Tzu [10] like “win by brain, not by brute force”, which has been confirmed by many presentations at different world events [11-14].

The latest and most advanced version of the technology can be put within a short time on any platform by a small group of system programmers, within existing university environments too. This is currently being discussed with different institutions, Hiroshima University including.

The authors would be glad to communicate with any organizations and individuals who may get interested in this area of research and cooperation.

References

1. M. Wertheimer, *Gestalt theory*, Erlangen, Berlin, 1924.
2. P. Sapaty, “Gestalt-Based Ideology and Technology for Spatial Control of Distributed Dynamic Systems”, International Gestalt Theory Congress, *16th Scientific Convention of the GTA*, University of Osnabrück, Germany, March 26 - 29, 2009.
3. M. Minsky, *The Society of Mind*, Simon & Schuster, New York, 1988.
4. K. Wilber, “Waves, Streams, States, and Self: An Outline of an Integral Psychology”, *The Humanistic Psychologist*, Vol. 31(2-3), 2003.
5. L. Gabriel, “Brain Wave Basics – What You Need to Know about States of Consciousness”, *Thought Medicine. Exploring the Power of Mind from Science to Spirituality*, 2011.
6. P.S. Sapaty, “Spatial Grasp Language (SGL) for Distributed Management and Control”, *Journal of Robotics, Networking and Artificial Life*, Vol.4, Issue 2, 2016.
7. P.S. Sapaty, A Distributed Processing System. European Patent No. 0389655. European Patent Office (1993).
8. P.S. Sapaty, “Military Robotics: Latest Trends and Spatial Grasp Solutions”, *International Journal of Advanced Research in Artificial Intelligence*, Vol. 4, No.4, 2015.
9. Coalition Battle Management Language (C-BML), *RTO Technical Report TR-MSG-048,* February 2012. http://www.dtic.mil/dtic/tr/fulltext/u2/a559456.pdf

10. Sun Tzu (Translated by Thomas Cleary), The Art of War, Shambhala, Boston & London 2005.
11. P. Sapaty, M. Sugisaka, “Optimized Space Search by Distributed Robotic Teams”, *Proc. World Symposium Unmanned Systems 2003*, Jul. 15-17, 2003, Baltimore Convention Center, USA.
12. P. Sapaty, M. Sugisaka, “Countering Asymmetric Situations with Distributed Artificial Life and Robotics Approach”, *Proc. Fifteenth International Symposium on Artificial Life and Robotics* (AROB 15th’10), B-Con Plaza, Beppu, Oita, Japan, Feb. 5-7, 2010.
13. P. Sapaty, M. Sugisaka, “Advanced Networking and Robotics for Societal Engagement and Support of Elders”, *Proc. 16th International Symposium on Artificial Life and Robotics* (AROB 16th ’11), B-Con Plaza, Beppu, Oita, Japan, January 27-29, 2011.
14. P.S. Sapaty, “Advanced Maritime Operations Under Network-Centric Organizations”, *Proceedings of the International Conference Warship 2016: Advanced Technologies In Naval Design, Construction & Operation*, 15-16 June 2016, Guildhall, Bath, UK.

Development of English Text for the engineers to preserve the environment of North-East Asia

Yuji Minami
National Institute of Technology, Ube College
2-14-1 Tokiwadai, Ube, 755-8555, Japan

Fukuchi Kenji, Shinya Tagawa
National Institute of Technology, Ube College
2-14-1 Tokiwadai, Ube, 755-8555, Japan

E-mail : minami@ube-k.ac.jp, fukuchi@ube-k.ac.jp, tagawa@ube-k.ac.jp
www.ube-k.ac.jp

Abstract

Our research began in 2007 as a part of the activities of 'Good Practice' for Education of Engineers in cooperation with the UMICNEA, that is, "Union of Machinery Industrial Cities in North-East Asia". Through our study, we found it necessary to acquire the knowledge of 'Fish Breeding Forest' when developing and preserving the area of North-East Asia, where the river Amur plays an important role for sustaining the environment of this region. We made the research of the origin of the river Amur, named 'the river Onon', located in the area of 'Strictly Protected Area' in Mongolia by the agreement of Mongolia, Russia, and China in 2005. We plan to make it clear that future engineers should find a good way of cooperation through English as a communication tool for the purpose of playing an active part together.

Keywords: North-East Asia, Strictly Protected Area, Amur Green Belt, Fish Breeding Forest

1. Introduction

The purpose of this thesis is to make it clear that the younger generation of engineers who are expected to work especially in the area of North-East Asia should learn the basic concept of safe and sound but dynamic circulation system of environment for the preservation of Amur River Basin.

Before reaching the above-mentioned recognition of the importance of preserving the origin of the River Amur, chronologically speaking, we learned some basic ideas through three major projects in the North-East Asia, such as 'the modern GP at NIT, UC from 2007 to 2009', 'Amur-Okhotsk project from 2005 to 2009', and 'ICAP : International Conference of Aqua-polices' held every 4 years since 1990.

After taking those 3 projects into consideration, we continued to send students to the foreign internship, to exchange students mutually, and planned to make a textbook in English for all those engineers who wish to play active part and to take an important role for developing and preserving the environment of the area of North-East Asia .

2. Projects Taken into Consideration

2.1 Modern GP at NIT, UC from 2007 to 2009

We've learned to continue the mutual exchange program of foreign Internship after 3 years activities of "Education of engineers in cooperation with UMICNEA; the 'Union of Machinery Industrial Cities In North-East Asia'" adopted and supported for contemporary education needs by the Ministry of Education, Culture, Sports, Science & Technology in Japan(2007-2009).

Students of NIT, UC (National Institute of Technology, Ube College, Japan) began their foreign internship activities in 3 universities, such as DIT (DongEui Institute of Technology, South Korea), HIT, WH (Harbin Institute of Technology at Weihai, China), and KnASTU (Komsomolsk-na-Amure State Technical University, Russia). We had one week acceptance program and its PDCA worked well as follows.

Table 1. PDCA Example of Acceptance Program

Period	22-29/April/2013	20-29/April/2014
University	KnASTU, Russia	KnASTU, Russia
1Arrival	*(KHV-NRT-FUK)	*(KHV-NRT-FUK)
2Reception	HAKATA→NIT,UC	HAKATA→NIT,UC
3Day1	President Interview Campus Tour Welcome Party	President Interview Campus Tour Welcome Party
4Day 2	Class Activities Visit Ube City Hall Tokiwa Park Tour Student Academic Conference	Class Activities Visit Ube City Hall Tokiwa Park Tour
5Day 3	Factory Tour UBE Industries	Student Academic Conference
6Day4	Culture Tour 1. Rurikoji Temple 2. Hofu Tenmangu Shrine	Factory Tour 1. UBE Industries 2. UBEKAMA 3. YANAGIYA Machinery
7Day5	NIT,UC→HAKATA	Culture Tour 1. Rurikoji Temple 2. Akiyoshido Cave
8Departure	*(FUK-NRT-KHV)	NIT,UC→HAKATA
		Free
		*(FUK-NRT-KHV)

(* refers to the names of international airport, such as KHV;Khabarovsk, NRT;Narita, FUK;Fukuoka)

In comparison with the present situation of airport convenience, Air Seoul, a South Korean low-cost carrier, launched the new line between Ube and Incheon from 28th of November, 2016. Aiming to continue our foreign internship by using UBE airport, opening of this new line has long been expected among researchers.

Referring to the Incheon international airport, it can deal with 40,000 passengers a day according to our research in 2012 at the meeting of 'Project of the Internationalization of UBE airport' committee. So the new line mentioned above can surely support the sustainability of the activities of NIT,UC foreign internship.

2.2 Amur-Okhotsk project from 2005 to 2009

In the process of continuous activities of foreign internship for 3 years, we happened to find that the big project concerning the river Amur among 3 countries, Russia, China, and Japan had almost done by the end of GP activities mentioned above.

This big project made efforts to prove the essential object, soluble iron, circulating in the Amur River covering the Amur River basin in the North-East Asia including Russia, China, and Mongolia.

This systematic circulation of soluble iron enables the sea of Okhotsk abundant enough to sustain the industry of fisheries in Japan. In brief, as 'Fish-Breeding Forest' directly suggests, soluble iron can breed fish and this object exists abundantly in the area of North-East Asia, that is, the Amur River Basin. Researchers of this field especially call this area '**Giant Fish-Breeding Forest**'.

Moreover, we found out that there existed the agreement of protected area (PA) among 3 countries such as Russia, China, and Mongolia in 2005, which was called "Amur Green Belt" by WWF (World Wide Fund for Nature). "Amur Green Belt" is defined as the network of protected areas (PAs) in the Amur River Basin.

Consequently, we recognized that along with the foreign internship activities as young engineers in the area of North-East Asia, environmental preservation must be taken into consideration.

2.3 ICAP: International Conference of Aqua-polices

According to '**Busan Declaration**' in 2008 at the end of the 5th International Conference of aquapolices (ICAP), all efforts are supposed to be made on the base of '**environment-first principle**'.

In the end of 2.1, Incheon air port is referred to have the capacity of dealing with 40,000 people a day. While this city can be called the biggest hub city of Korea at present, Korea needs the second biggest hub city to become the gateway to Asian Highway covered countries including the area of North-East Asia.

Along with the **environment-first principle**, Busan municipality has shown its future vision in public. First Master plan of **U-City** was established in 2005. Among many projects for developing the **U-City**, there exists **U-Environment** project.

Thanks to this **U-Environment** project, Nakdong-gang River and its riverside trees are monitored, managed and protected well enough to sustain its eco-logical cycle.

3. Strictly Protected Area in Mongolia

As is mentioned in the previous chapter 2, especially in North-East Asia, there exists ‘PA’, the Protected Area with the agreement of 3 countries, Russia, China, and Mongolia. This area holds the Amur River Basin, and this basin is called ‘**Giant Fish-Breeding Forest**’ by ‘Amur Okhotsk Project’ researchers.

Through our activities mentioned above, we recognize the origin of the River Amur must be taken into consideration for the sustainable completion of ecological cycle in the North-East Asia along with the active young engineers playing an important role in this area.

For the sake of learning geographical view of this area in English, the following table is prepared.

Table 2. The Amur River Basic Geographical Data with local city names

City(Local)	City(Global)	lat	long/lon/lng
Николáевск-на-Амýре	**nikol.ru**	**53° 8'32.60"N**	**140°43'53.30"E**
Комсомóльск-на-Амуре	**kmscity.ru**	**50°34'1.33"N**	**137° 0'1.88"E**
Хабаровск	**khabarovskadm.ru**	**48°30'9.83"N**	**135° 3'58.54"E**
Благовещенск	**admblag.ru**	**50°16'21.99"N**	**127°32'25.45"E**
黒竜江省 黒河市	**heihe.gov.cn**	**50°14'42.46"N**	**127°31'41.86"E**
黒竜江省大興安嶺地区漠河県北極村	**Běijí**	**53°28'49.94"N**	**122°21'32.69"E**
Шилка	**Shilka**	**51°50'55.43"N**	**116° 1'58.17"E**
Чиндант	**Chindant**	**50°34'31.71"N**	**115°24'27.24"E**
Улача	**Ulacha**	**50°24'12.99"N**	**113°16'2.22"E**
Онон	**Onon**	**48°37'7.01"N**	**110°36'18.30"E**
Улаанбаатар	**ulaanbaatar.mn**	**47°55'11.44"N**	**106°55'11.81"E**

Table 3. The Amur River Basic Geographical Data with altitude report columns

City(Global)	lat	long/lon/lng	altitude
nikol.ru	**53° 8'32.60"N**	**140°43'53.30"E**	Report1
kmscity.ru	**50°34'1.33"N**	**137° 0'1.88"E**	Report2
khabarovskadm.ru	**48°30'9.83"N**	**135° 3'58.54"E**	Report3
admblag.ru	**50°16'21.99"N**	**127°32'25.45"E**	Report4
heihe.gov.cn	**50°14'42.46"N**	**127°31'41.86"E**	Report5
Běijí	**53°28'49.94"N**	**122°21'32.69"E**	Report6
Shilka	**51°50'55.43"N**	**116° 1'58.17"E**	Report7
Chindant	**50°34'31.71"N**	**115°24'27.24"E**	Report8
Ulacha	**50°24'12.99"N**	**113°16'2.22"E**	Report9
Onon	**48°37'7.01"N**	**110°36'18.30"E**	Report10
ulaanbaatar.mn	**47°55'11.44"N**	**106°55'11.81"E**	Report11

Geographically speaking, two rivers, the Rivers of Silka and Arugun are joined to flow down east into the Amur river making the border of Russia and China.

This Silka River comes from the Onon River which originates at the eastern slope of the Khentii mountains located at the Northeast area of Ulaanbaatar, capital city of Mongolia. This area is administered by the Mongolian government and called 'the **Khan Khentii Strictly Protected Area**'.

In table 2 and 3, Silka and Onon can be found. More city names can be added by young engineers themselves who wish to protect the **Amur River Basin**, in other words, '**Giant Fish-Breeding Forest**'. What should be observed in table 2 is to write each city name in English for the students of different nationalities.

In learning table 3, altitude of each city should be reported by students because the river depends on the upper or lower locations when flowing down to the sea.

This is the first step of learning the Amur River Basin by young active engineers in the North East Asia.

Fortunately, Air Busan, subsidiary of Asiana Airlines, launched the new Busan – Ulaanbaatar line this June.

Moreover, Korean Emart newly opened its store in Ulaanbaatar this July. As we point out in 2.3, Busan is stepping up toward the second biggest hub and gateway city of Korea by launching the new air line and opening the new store. So, we are sure that young engineers in the North East Asia, especially those of Russia, China, Mongolia, Korea, and Japan can cooperate to make efforts to sustain the systematic circulation of 'soluble iron'.

Acknowledgements

This work was supported by JSPS KAKENHI Grant Number 25370686.

References

1. M. Yoshida, K. Fukuchi, S. Tagawa, Y. Park, T. Ito, and Y. Minami, "*Education of engineer in cooperation with the Union of Machinery Industrial Cities in North-East Asia*", Kosen Kyoiku, No34, pp. 865-870, 2011.

2. Y. Minami, M.Yoshida, K. Fukuchi, K. Fujita, S. Tagawa, "*On the Acceptance of Foreign Internship", All Kosen Education Forum, C-1 AP25_3_2*, Kanazawa University, 2014.

3. "Busan Declaration" signed by 41 delegates, *the 5th International Conference of Aquapolices*, Busan Metropolitan City, Korea, May 21-22, 2008.

4. S.Tagawa, K. Fujita, "The Recent Efforts of Global Human Resouces Development", *The 9th International Symposium on Advances in Technology Education (ISATE2015)*, p.125, Nagaoka University of Technology, Nagaoka, Japan, 2015.

5. K. Fukuchi, Y. Minami, "*Development of environmental education concerned water in northeast Asia, Mongolia and far-east Russia along the Amur river*", PCV06, IGNITE-2016, Penang, Malaysia(2016).

Measuring Fragility and its Implications in Network System

Tsutomu Ito*, Katsuhiko Takahashi, Katsumi Morikawa, Takao Ito
Graduate School of Engineering, Hiroshima University,1-4-1 Kagamiyama, Higashi-Hiroshima, 739-8527, Japan
E-mail: fw.eldorado.500cuin@gmail.com

Rajiv Mehta
School of Management, New Jersey Institute of Technology, University Heights, Newark, New Jersey, 07102-1982, U.S.

Seigo Matsuno
Department of Business and Administration, Ube National College of Technology, Tokiwadai 2-14-1 Ube, Yamaguchi, 755-0096, Japan

Makoto Sakamoto
Faculty of Engineering, University of Miyazaki, 1-1 Gakuen Kibanadai-Nishi, Miyazaki, 889-2192, Japan

Abstract

A survey of the relevant literature reveals that a plethora of network analytic facets, such as degree, eigenvalue, density, block, cluster, have been developed and employed to further our understanding of network structures. To extend our understanding of network systems, additional dimensions need to be identified that shed light on the dynamic processes among individual member nodes within network structures. Specific to the context of networked systems, this paper proposes a new concept of fragility. Specifically, it develops and empirically tests a mathematical model of fragility from the standpoint of how ties among network members significantly influence corporate performance, thus uniquely contributing to extant knowledge. Using data drawn from two well-known network organizations, Mazda and Toyota, this research attempts to shed light on the relationship between degree and fragility, to confirm the validity of the new concept as well as enabling a contrast of Mazda and Toyota's network structures. [RM1]Based on the findings, the managerial implications are discussed, the study limitations are identified and directions for further research are suggested.

Keywords: degree, fragility, Keiretsu, relationship, Yokokai.

1. Introduction

As in sociology and psychology, many mathematical models have been developed to increase our understanding of the organizational sciences. As an additional organizational form, within the context of networked structures, dimensions, such as degree, eigenvalue, density, block, and cluster, reveal the static nature of relationships among individual nodes and other members within the whole network. However, dynamic processes are considered to be even more salient in the organizational sciences and allied fields. Accordingly, as newer models and paradigms that illustrate dynamic processes are more desirable, this paper proposes the new concept of fragility that is grounded in the review of the relevant literature as well as rooted in a systematic repeated trial and error assessment. Drawing data from two well-known network organizations, Yokokai in Mazda and Kyohokai in Toyota, from 2004 to 2007, the purpose of this research endeavor is to calculate the relationship between degree and fragility to confirm the validity of new model. Further, the relationship between fragility and corporate performance, is also assessed that forms the basis of the managerial implications discussed in the study. Specifically, this paper makes a unique contribution to extant thought by: 1) Defining the concept of fragility, 2) Discussing the nature of the relationship between fragility and corporate performance, and 3) Empirically testing the dimensional differences between fragility and corporate performance, thus enabling Mazda's networked organization to be contrasted with Toyota.

This paper is structured as follows. Section 2 reviews the literature focusing on network analysis. In section 3, the paper explicates the calculation of degree and fragility. Section 4 discusses our findings based on which the study limitations are identified and directions for further research are proffered in the final section.

2. Background and Literature Review

Indexes, such as degree, eigenvalue, density, block, and cluster have been used widely in empirical research to measure different dimensions of organizational networks. Comprising a most basic facet of centrality, degree was firstly proposed by Nieminen [1] in his research on organizational constellations. Simply put, it is defined as the number of links incident upon a node in a graph. In real society, most of the relationships between members are considered to be mutual. Furthermore, nodes within a network are known to interact with each other. Consequently, direction with weight have been commonly employed to analyze different phenomena within social networks. In this context, Freeman proposed a new index of entire degree, which identifies the centrality of the whole network [2].

More recently, Ito and Sakamoto proposed a new approach to identify the importance of each individual node based on Freeman's model [3], but noted that much more research is necessary to fully understand keiretsu constellations. Although the relationships between network members can be manifest in the form of equity ties, personal ties, transactional ties and work-flow ties, this study examines transactions within a network to reveal the nature of the relationships between business ties and corporate performance. More specifically, owed to the sparsity of knowledge, this investigation contributes to the literature by advancing a new procedure for measuring the interrelationships between members of a keiretsu by suggesting the new concept of fragility to be a determinant of corporate performance.

3. Research Method

Two concepts are applied in this paper: degree and fragility.

3.1. *Degree and Fragility*

Degree, as one of the basic indices of centrality, is considered as the basic index in network analysis. It can be calculated as follows [1].

$$C_D(p_k) = \sum_{i=1}^{n} a(p_i, p_k); \tag{1}$$

where

i≠j;

a (p_i, p_k) = 1 if and only if p_i and p_k are connected by a line

a (p_i, p_k) = 0 otherwise

In an asymmetric network, two indexes of out-degree and in-degree should be calculated

Basically fragility is a physical term, which characterizes how rapidly the dynamics of a material slow down as it is cooled toward the material transition. Accordingly, fragility is defined as the ratio of the entire degree of and the entire degree after moving a specific node. It will be illustrated as follows.

$$F = \frac{C_D(\bar{p})}{C_D} = \frac{\dfrac{\sum_{i=1}^{n-1}[C_D(p^*) - C_D(p_i)]}{(n-1)^2 - 3(n-1) + 2}}{\dfrac{\sum_{i=1}^{n}[C_D(p^*) - C_D(p_i)]}{n^2 - 3n) + 2}} \tag{2}$$

where

C_D: Entire degree of a given network

$C_D(\bar{p})$: Entire degree after removing node p

$C_D(p^*) = \max C_D(p_i)$

Table 2. Results of out-degree and in-degree-sales regression model.

	Models							
	Yokokai				Kyohokai			
Sales	2004	2005	2006	2007	2004	2005	2006	2007
Out-degree								
Partial regression coefficient	5153.172	7124.583	-8079.95	-15695.4	-7537.79	-4448.25	-3779.68	-3619.42
Standard coefficient	0.0645	0.0904	-0.0964	-0.1447	0.1133	-0.0667	-0.0471	-0.0389
t value	0.8611	1.4957	-1.0425	-1.5971	-2.7502	-1.691	-1.2655	-0.9838
Probability	0.3919	0.1384	0.3003	0.1146	0.007	0.0941	0.2087	0.3277
Correlation coefficient	-0.4908	-0.3858	-0.4298	-0.3185	-0.4726	-0.4713	-0.4388	-0.448
Partial correlation coefficient	0.0983	0.1601	-0.1151	-0.8137	-0.2615	-0.1692	-0.1262	-0.1015
In-degree								
Partial regression coefficient	14162.85	7124.583	9322.689	20726.5	6465.408	7605.123	9597.788	11958.24
Standard coefficient	0.8968	0.9221	0.6465	0.6141	0.872	0.906	0.9211	0.922
t value	11.9655	15.2559	6.9917	6.7759	21.1592	22.9715	24.7341	23.3415
Probability	0	0	0	0	0	0	0	0
Correlation coefficient	0.8569	0.8754	0.6962	0.655	0.9187	0.9358	0.9411	0.9393
Partial correlation coefficient	0.8082	0.8559	0.6135	0.6214	0.9016	0.9191	0.9277	0.9242
Coefficient of determination	0.73677	0.77231	0.49155	0.44836	0.85474	0.87921	0.88753	0.88346
Multiple correlation coefficient	0.85835	0.87881	0.70111	0.6696	0.92452	0.93766	0.94209	0.93992
F value	106.362	144.1595	39.1543	29.6667	303.038	353.0187	390.6121	352.4917
Degree of freedom	2, 76	2, 85	2, 81	2, 73	2, 103	2, 97	2, 99	2, 93
AIC	2441.18	2706.92	2678.46	2466.46	3182.65	2989.13	3078.19	2929.59
DW ratio	1.9331	1.6531	2.5664	2.4682	1.5609	1.4931	1.4393	1.3817
Data number	79	88	84	76	106	100	102	96

Table 3. Results of fragility-sales regression model.

	Models							
	Yokokai				Kyohokai			
Sales	2004	2005	2006	2007	2004	2005	2006	2007
Fragility								
Partial regression coefficient	21109945	22124395	1193320	12793233	-19942684.1	-20889146.6	-26007968.4	-29733934.04
Standard coefficient	0.2154	0.1957	0.0177	0.1262	-0.7684	-0.7653	-0.7752	-0.7798
t value	1.9354	1.8511	0.1602	1.0944	12.2438	-11.7689	-12.2705	-12.0763
Probability	0.0566	0.0676	0.8731	0.2773	0	0	0	0
Correlation coefficient	0.2154	0.1957	0.0177	0.1262	-0.7684	-0.7653	-0.7752	-0.7798
Partial correlation coefficient	0.2154	0.1957	0.0177	0.1262	-0.7684	-0.7653	-0.7752	-0.7798
Coefficient of determination	0.04539	0.03832	0.00031	0.01593	0.59041	0.58564	0.6009	0.60807
Multiple correlation coefficient	0.21538	0.19575	0.01769	0.12621	0.76838	0.76527	0.77518	0.77979
F value	3.74558	3.42656	0.02566	0.019779	149.9108	138.50651	150.56441	145.83724
Degree of freedom	1, 77	1, 86	1, 82	1, 74	1, 104	1, 98	1, 100	1, 94
AIC	2540.88	2831.71	2733.25	2508.45	3290.54	3110.40	3205.68	3044.02
DW ratio	1.2302	1.1155	0.9671	1.1641	0.9158	0.9054	0.8992	0.9052
Data number	79	88	84	76	106	100	102	96

3.2. *Data Collection*

Widely considered as successful examples of prominent Japanese networked organizations, data were drawn from Toyota's Kyohokai and Mazda's Yokokai from 2004 to 2007 to establish the status quo of keiretsu as well as longitudinally ascertain changes in their keiretsu structure. Both of these keiretsu organizations include singletons, which refers to a partner firm in the keiretsu that has no relationship with other member firms. However, singletons were removed from the data-set because they have no impact on the calculation of network indexes. Data on Toyota's Kyohokai and Mazda's Yokokai from 2004 to 2007is reported in Table 1.

Table 1. Firms in Yokokai and Kyohokai.

	Firm in Yokokai		Firm in Kyohokai	
	Total	Singleton	Total	Singleton
2004	188	97	215	93
2005	191	89	216	97
2006	190	92	213	93
2007	189	104	213	101

A diagrammatic representation of the inter-firm transactional relationships in 2007 is illustrated in Fig. 1.

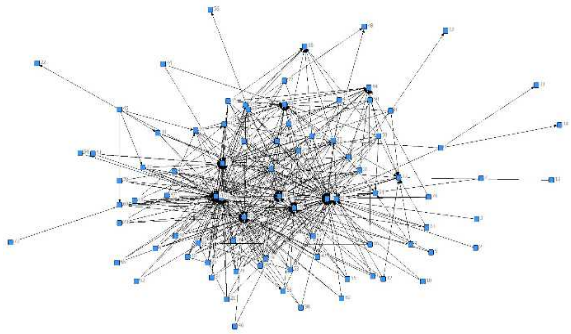

Fig. 1. Transaction network of Yokokai in 2007.

4. Results and Discussion

Using regression analysis, we first tested the relationship between out-degree and in-degree as determinants of sales. The results of out-degree and in-degree-sales regression model is shown in Table 2.

4.1. *Sales and out-degree and in-degree*

All the probabilities of in-degree are significant while out-degree are not significant except for Kyohokai in 2004. Thus, evidently in-degree has a statistically significant impact on sales. In contrasting the results of the Yokokai, the correlation coefficients as well as the coefficients of determination are higher. Thus, it can be inferred that the regression model of Kyohokai has stronger power to explain the relationship between in-degree and corporate performance—as measured by sales. Table 2 indicates that the difference between Yokokai and Kyohokai looks similar, but different in degree.

4.2. *Sales and Fragility*

The results of out-degree and in-degree-sales regression model is shown in Table 3.

Compared with Yokokai, all the probabilities of fragility from 2004 to 2007 are significant, and coefficients of determination are higher. Thus, the model assumptions of Kyohokai hold.

All correlation coefficients are negative. Thus, the assumption of higher fragility having an inverse association with sales is confirmed. Because the meaning of fragility denotes the value of entire degree of a given network after removing a specific node, it is evident that firms in Kyohokai have a higher possibility to improve sales. Conversely, all correlation coefficients are positive means that greater fragility is associated with higher sales—as predicted. However, as the probabilities of each year are larger than 0.05, additional longitudinal data should be collected.

5. Conclusions

Grounded in the review of the relevant literature, this paper proposed a new approach called fragility to shed light on interfirm behaviors within network organizations known as keiretsu. Data were drawn from Yokokai in Mazda and Kyohokai in Toyota to ascertain the relationship between degree and fragility. The results look similar between both the keiretsu when we investigate the relationships between degree and sales. However, different behaviors are manifest when fragility is viewed as a determinant of sales.

6. Directions for Future Research

Based on the results obtained, four fiscal years of data is not sufficient to support contentions of internal validity. In addition to degree, other centrality indexes, such as closeness and betweenness, should be tested as determinants of corporate performance. Furthermore, the original definition of fragility in Physics is a derivative of a mathematical function. Thus, in the future the models tested in this study should be investigated using data drawn from other settings, such as, information technology, the ship-building industry for comparative research as well as replicating the current findings.

Acknowledgements

This work was supported by JSPS KAKENHI Grant Number 16K01243.

References

1. Nieminen J. (1974). On centrality in a graph, Scandinavian *Journal of Psychology* 15, 322-336.
2. Linton C. Freeman (1978/79). Centrality in Social Networks Conceptual Clarification, *Social Networks 1*, 215-239.
3. T. Ito and M. Sakamoto (2005), Importance Analysis of Each Firm in the Keiretsu of Toyota, *Proceedings of the 2005 Information Resources Management Association, International Conference, Managing Modern Organizations with Information Technology*, 930-933, May 15-18, 2005, San Diego, USA.

A Formation of Standard Setter to Transplant Global Standards into Domestic Institution

Kensuke Ogata
Department of Business Administration, University of Nagasaki
123 Kawashimo, Sasebo, Nagasaki, 858-8580, Japan
E-mail: ogata@sun.ac.jp

Abstract

Japanese accounting standard setter, the ASBJ, developed lots of domestic accounting regulations to converge with the global standards in the period of 2005-2008, which substantially differs from the period of 2001-2004. A general organizations theory states that organizations make a change in their strategy and structure in order to change their performance. Based on this theory, we analyzed the change in organizational structure of the ASBJ using social network analysis. According to our result, the ASBJ formed a network in which accounting professions played a central role. The reason could be that the ASBJ made use of knowledge and wisdoms on the global standards Japanese big accounting firms has through their global networks.

Keywords: ASBJ, global convergence, standard setting process, social network analysis

1. Introduction

This paper aims to clarify how an accounting standard setter changes its organizational structure when it changes its standard setting behavior. The theoretical background is Strategy-Structure-Performance paradigm to be extensively studied in organizations theory. The ASBJ developed a lot of standards which mainly aimed at harmonizing with global standards produced by the International Accounting Standards Board (IASB) so as to reform the conventional ones, by means of adopting non-conventional techniques and/or narrowing down the ones to be previously accepted as options for four years after 2005. Under what type of organization did the ASBJ take such a standard setting behavior? To do so, this paper shows the organizational structure of ASBJ at that time using Social Network Analysis (SNA).

This paper is organized as follows. In the second section, we review the previous literature regarding to standard setting processes, and refer to the reason why we focus on the organizational structure of the standard setter and the effectiveness of network theory as an organizational structure analysis. In the third section, we confirm feature of standard setting activities of ASBJ in the period of 2005-2008. The fourth section conducts the organizational structure of ASBJ using SNA. Finally, we mention some reasons why the ASBJ formed that network at that time.

2. Studies on Accounting Standard Setting

2.1. *Previous Literatures*

It is said that accounting standard setting process is a political forum for various stakeholders who can be economically or socially influenced by creations, revisions or removals of specific standards, which can force to alter meanings and amounts of accounting figures (Zeff [1]). Since the early 1970s when researches on the process began in the USA, empirical researches to investigate activities or motivations of lobbyists in a formal process of inviting public comment letters have predominated. Though demonstrating the influence of certain political factors on standard setting process, such researches cannot have a full picture of the process, cannot shed light on behavioral principle of accounting standard setter that has the greatest responsibility for making rules, and cannot explain the dynamics of power, interests and resources in the accounting standard setting process.

In order to illustrate these points, a small number of studies on intra-board political activity and political activity regarding regulatory structures were carried out (Walker and Robinson [2]). Among them, some researches emphasized that the behavior of the setter could be affected by the strategies its chairpersons, its parent organizations, or its regulatory bodies adopted (e.g., Hope and Gray [3]).

In addition, according to traditional organizations theorists, organization could in general change its organizational structure in order to execute a specific strategy. This is called to the strategy-structure-performance paradigm (e.g., Miles and Snow [4]). If we apply this paradigm to the behavior of accounting standard setter, it could (re)organize its own structure to carry a given strategy into effect (Mattli and Büthe [5]).

2.2. *Clarifying Organizational Structure Using SNA*

This paper employs SNA for the purpose of confirming the organizational feature of the standard setter. SNA seeks to model relationships among actors in the network to depict the network structure. The most basic feature of SNA is to quantify the relationships among actors in the network. Another feature of SNA is to describe the network structure using a graph in which the network relationship is drawn with nodes and edges (e.g., Wasserman and Faust [6]). In recent times, some researches which incorporated this analytical method made an appearance for the purpose of defining the organizational feature of standard setters (Perry and Nöelke [7]; Botzem [8]; Richardson [9], and Ogata [10]).

Among a wide variety of analytical methods to capture the network structure in SNA, this paper adopts a continuous coreness analysis. This analytical method is used to identify a set of actors who have a high density of ties among themselves (the core) by having many events in common and another set of actors who have a low density of ties among themselves (the periphery) by having few events (Borgatti and Everett [11]). Here, “common” event refers the organizations, for example, companies, financial institutes, investment institutes, accounting firms, universities, governmental agencies, and other various organizations, which members of the standard setter and/or its related organizations belonged to and/or engaged with as constituencies before they became a member. It rests on an underlying idea that individual preferences and minds on accounting standards and techniques depend on their backgrounds or careers. Analysis based on this kind of data-set can highlight dominant actors in the standard setter in terms of human resources. As a result, we can understand on what value the standard setter has placed or would place much.

3. Standard Settings of the ASBJ

3.1. *Overview of the ASBJ*

In 2001, the ASBJ was created as the first Japanese private accounting standard setter, under mutual cooperation between the ten stock market-related stakeholders, including some industry groups of bank, insurance and investment, business leaders groups and accounting profession community and the regulatory agency, the Ministry of Finance and the subsequent Financial Service Agency of Japan.

The ASBJ is an intra-organization of the Financial Accounting Standards Foundation (FASF). The FASF at the inception was comprised of four internal bodies: Board of Directors, Board of Councilors, ASBJ, and Theme Advisory Council. In 2004, the FASF built a newly organization, Advisors; and furthermore in 2007, the FASF compounded Theme Advisory Council and Advisors into Standards Advisory Council.

3.2. *Standard Settings of the ASBJ from 2005 to 2008*

As shown in Table 1, the ASBJ developed standards at slow pace until 2004. In 2005, it developed seven standards which had not been adopted ever, for example, accounting for business divestitures and share-based payment. Since 2006, it kept issuing standards to the same effect. These standards adopted non-conventional techniques and/or narrowed down the alternatives to be accepted for the global convergence. This triggered a major reform in Japanese financial reporting system.

In the next section, this paper attempt to identify the organizational characteristics of the ASBJ at that time.

Table 1: Transition on Volume of Issued Standards

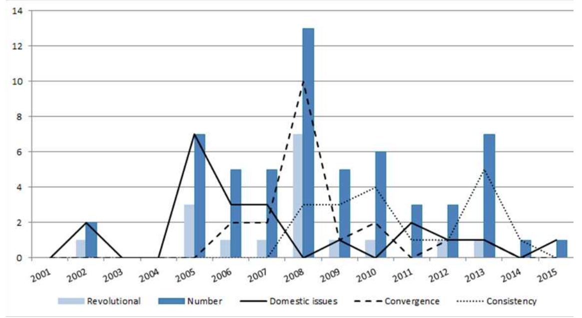

4. The Organizational Structure of the ASBJ

4.1. *Using data*

In conducting organizational structure analysis, this paper uses data based on organizations which provided members to intra-organizations of the FASF. As mentioned before, this assumes that individual preferences and opinions on the accounting standards or techniques should be determined by his/her background or career. Therefore, shedding light on the relations among the organizations in which the members have engaged before taking these seats in the network can give a full account of what actors dominate and what kinds of values are predominant in the standard setter.

This paper prepares a matrix data-set, composed of the organizations which provided human resources to the intra-organizations of the FASF from 2005 to 2008, on the basis of annual reports of the FASF, in rows, and the intra-organizations of the FASF every period in columns. In this case, the larger numbers of members or/and the longer period organizations supply, the higher scores these organizations obtain. This paper as the second step transform this original data-set into the organization-to-organization data-set by means of the affiliation process, contained in social network analysis software, UCINET VI (Borgatti, et al. [12]). We perform a coreness analysis and draw a graph using NetDraw (Borgatti [13]), based on this affiliated data-set.

An original matrix data-set in the period of 2005-2008 comprises 77 organizations. To relativize the standard setting process during this period, we make up another data-set in a period of 2001-2004, which include 69 organizations.

4.2. *Features of Organizational Structure of the ASBJ*

A result of the coreness score in this period is Table 2. This table shows the top four scorers left other organizations far behind. Included were Azusa (coreness score: 0.545, rank: #1), Tohmatsu (0.444, #2), ShinNihon (0.410, #3), and FASF (0.373, #4). The former three organizations are all big accounting firms in Japan that form alliances with the global big accounting firms[1]. In the second group, preparers of financial statements appeared. There were non-financial sectors such as Tokyo Electric Power (0.139, #6), Central JR (0.116, #10), and NEC (0.116, #10) as well as financial sectors such as Nomura Securities (0.127, #7), Mitsui Sumitomo Insurance (0.121, #8), and Meiji Yasuda Life (0.120, #9), on a similar level.

Table 2: Coreness Result of the ASBJ (Top 15 Actors)

#	Organization	Attribute	Coreness
1	Azusa	Pro	0.545
2	Tohmatsu	Pro	0.444
3	ShinNihon	Pro	0.410
4	FASF	Reg	0.373
5	Tokyo Stock Exchange	User	0.155
6	Tokyo Electric Power	NonFin	0.139
7	Nomura Securities	Fin	0.127
8	Mitsui Sumitomo Insurance	Fin	0.121
9	Meiji Yasuda Life	Fin	0.120
10	Central JR	NonFin	0.116
10	Bank of Japan	Reg	0.116
10	NEC	NonFin	0.116
10	ARC	Pro	0.116
14	Bank of Tokyo-Mitsubishi UFJ	Fin	0.085
15	Arata	Pro	0.084

According to Graph 1, which shows a network graph of then-ASBJ, the above actors occupied central positions in this network. Especially, accounting profession actors which are plotted on the right center of this graph constituted the core position of this network. In this paper,

Graph 1: Network Graph of the ASBJ

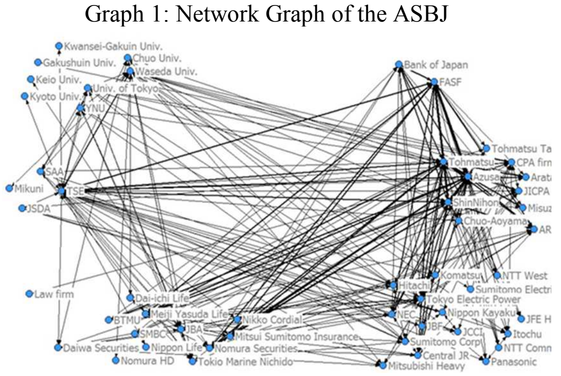

the line gets bigger on the five-scale level on the basis of the strength of relationships.

To emphasize the change of the ASBJ's organization structure, this paper makes a comparison between this period and the previous four years. Table 3 which presents the proportion of the total coreness score acquired by each attribute group to the whole score in the network of the both periods and the difference can show the transition of central actors by attributes[2].

Table 3: Difference of Coreness between Two Periods

	(1) 2001-2004	(2) 2005-2008	Difference (2)-(1)
Aca	21.1%	5.2%	-15.9%
Fin	21.8%	16.2%	-5.6%
Non-Fin	25.5%	18.1%	-7.5%
Pro	20.2%	43.5%	23.3%
Reg	0.4%	11.4%	11.0%
User	9.3%	4.7%	-4.6%
Other	1.7%	0.9%	-0.8%
Total	100.0%	100.0%	0.0%

The results are as follows. The first is that accounting profession group sharply increased the prominence in the network (20.2% to 43.5%). The second is that other groups except for accounting profession and regulator reduced the importance, among them the decline of academic community by 15.9% was the most remarkable. Besides, the third is that financial statements preparers, including financial and non-financial, who might have the strongest influence in the previous four years, also reduced the importance (21.8% to 16.2% in the former case; 25.5% to 18.1% in the latter case). Thus, the ASBJ formed an accounting-profession-centric network.

5. Concluding Remarks

There are three assumed reasons that the ASBJ formed the accounting-profession-centric network in the period of 2005-2008 when conforming Japanese accounting standards to the global standards was needed. First is that, as evidenced by cases of IASB and the US standard setter, accounting standard setters is likely to rest on accounting professions when they should develop the standards being substantially different from the existing ones. Second is that the ASBJ could make use of global networks which some big Japanese accounting firms hold, with an aim to attain the knowledge and wisdoms of global standards. Third is that since the accounting profession organization was the strongest proponent of harmonizing Japanese standards with global standards in Japan, the ASBJ probably made use of its momentum.

Reference

[1] Zeff SA (2002), "Political" Lobbying on Proposed Standards: A Challenge to the IASB. *Accounting Horizons* 16: 43-54

[2] Walker RG and Robinson P (1993), A Critical Assessment of the Literature on Political Activity and Accounting Regulation. *Research in Accounting Regulation* 7: 3-40

[3] Hope T and Gray R (1982), Power and Policy Making: The Development of an R&D Standard. *Journal of Business Finance and Accounting* 9: 531-557

[4] Miles RE and Snow CC (1978), *Organizational Strategy, Structure, and Process*. McGraw-Hill

[5] Mattli W and Büthe T (2005), Accountability in Accounting? The Politics of Private Rule-Making in the Public Interest. *Governance* 18: 399-429

[6] Wasserman S and Faust K (1994), *Social Network Analysis: Methods and Applications*. Cambridge Univ Press

[7] Perry J and Nöelke A (2005), International Accounting Standards Setting: *A Network Approach. Business and Politics* 7(3.5): 1-32

[8] Botzem S (2012), *The Politics of Accounting Regulation, Organizing Transnational Standard Setting in Financial Reporting*. Edward Elgar Publishing

[9] Richardson AJ (2009), Regulatory Networks for Accounting and Auditing Standards: *A Social Network Analysis of Canadian and International Standard-Setting. Accounting, Organizations and Society* 34: 571-588

[10] Ogata K (2010), A Study of Accounting Standard-Setting Using Graph Theory. *Artificial Life and Robotics* 15: 279-283

[11] Borgatti SP and Everett MG (1999), Models of Core/Periphery Structures. *Social Networks* 21: 375-395

[12] Borgatti SP, Everett MG, Freeman LC (2002), UCINET for Windows: *Software for Social Network Analysis. Harvard*, MA: Analytic Technologies

[13] Borgatti SP (2002), NetDraw: Network Visualization. *Harvard*, MA: Analytic Technologies

A Comparison Study on the Vertical Integration and Horizontal Specialization of Chinese ICT Companies

Yunju Chen
Faculty of Economics, Shiga University,
1-1-1, Banba, Hikone City, Shiga Pref.,522-8522, Japan
yun-chen@biwako.shiga-u.ac.jp

Yousin Park
Dept. of Business Administration, Prefectural University of Hiroshima,
1-1-71 Ujina-Higashi, Minami-ku, Hiroshima City, Hiroshima Pref., 734-8558, Japan
ecventure@pu-hiroshima.ac.jp

Iori Nakaoka
Dept. of Business Administration, National Institute of Technology, Ube College,
2-14-1 Tokiwadai, Ube City, Yamaguchi Pref., 755-8555, Japan
nakaoka@ube-k.ac.jp

Abstract

The debate between vertical integration vs. horizontal specialization appears to be reinvigorated. The decision of vertical integration or horizontal specialization affects a firm's profit and competitive advantage, especially in the ICT industry which is difficult to create added value due to the commoditization of digital products. The ongoing commoditization of smartphone brings the rising of Chinese ICT companies but these companies adopt different strategies/operation systems to create their own competitive advantages. In this paper, we focus on top-shared Chinese ICT companies in global smartphone industry, Huawei and Xiaomi, to examine how they design their operation systems in R&D and gain competitive advantages, also to compare their systems with each other. The patent information of these two companies is used to visualize their technical orientations and operation systems in R&D by text mining.

Keywords: patent analysis, social network analysis, Chinese ICT companies, the boundary of the firm, vertical integration, h orizontal specialization

1. Introduction

No doubt smartphone has replaced feature phone to become the core device in electronics industry now. Since iPhone was launched at 2007, the global smartphone market has been changed rapidly. Recently, Chinese ICT companies are on the rise in the global smartphone market and they almost occupy the global top ten besides Samsung and Apple.

Although the open source of Android caused the rising of Chinese ICT companies, they do not simply adopt the cost leadership strategy. For example, Xiaomi is an internet startup with short company history, and its rapid growth tells a story that it may grow up by outsourcing. On the other hand, Huawei has been the giant smartphone firm with long history, and it is also one of the innovative Chinese firms that have top class filings of patents.

However, how Chinese ICT companies adopt different strategies, even the operation systems? It seems that Chinese ICT companies, like Xiaomi and Huawei, develop their operation systems by either make or buy. Actually, the decision of make or buy, in other words, vertical integration or horizontal specialization affects a firm's profit and competitive advantage. The debate between vertical integration vs. horizontal specialization appears to be reinvigorated especially in the ICT industry which is difficult to create added value due to the commoditization of digital products.

In this paper, we focus on top-shared Chinese ICT companies in global smartphone industry, Xiaomi and Huawei, to examine how they design their operation systems in R&D and gain competitive advantages, also to compare their systems with each other. The patent information of these two companies is used to visualize their technical orientations, R&D networks and operation systems in R&D by text mining.

2. Research Background

2.1 *Open innovation and patent analysis*

Companies comprise various activities. In order to carry out their activities, companies inevitably cooperate with other companies to use external resources. At the same time, companies face the issue of what to outsource from other companies and how to manage their own systems while cooperating with other companies. The decision making of what and how to outsource from others refers to the issue of boundary of the firm. The issue of make or buy in the vertical flow of production is the typical issue in the boundary of the firm.

In fact, the boundary of the firm is an important issue in not only production, but also in R&D. Theoretically, much attention has been drawing to using external resource to drive innovation, which is defined as open innovation. Open innovation is the use of purposive inflows and outflows of knowledge to accelerate internal innovation, and expand the markets for external use of innovation, respectively. This paradigm assumes that companies can and should use external ideas as well as internal ideas, and internal and external paths to market, as they look to advance their technology [1]. Horizontal specialization oriented companies tend to outsource and cooperate with other companies, hence benefit from open innovation in R&D.

And the boundary of the firm in R&D also concerns the national innovation system. The national innovation system is the network of institutions in the public and private sectors whose activities and interactions initiate, import, modify and diffuse new technologies [2].

Patent documents are an ample source of technical and commercial knowledge. The patent is one of the indicators of capacity for technological development. There are some researches aimed at visualizing and analyzing patents, or proposing efficient text-mining approaches for creating patent maps. However, there are few researches focusing on R&D management strategies based on text-mining analysis of patents. Therefore, this paper describes the features of Chinese ICT companies' R&D management based on the patent analysis.

2.2 *The overview of Chinese ICT companies*

The global market share of smartphone out of analyst firm IDC shows a major shakeup in the Chinese smartphone market from 2013 Q1 to 2015 Q4. According to Figure 1, 3 Chinese ICT companies of Huawei, Xiaomi and Lenovo occupied the top 3rd-5th share in the global market. Huawei has made a breakthrough in global market share, following Samsung and Apple, but Xiaomi is stalling from the end of 2014.

Xiaomi (Xiaomi Technology Co., Ltd) founded in 2010 by a well-known angel investor Lei Jun, and achieved impressive growth soon after its existence. Xiaomi is a mobile internet company and focuses its businesses on smartphones (Xiaomi Phones), including the OS of MIUI, MiTalk, the e-commerce platform of XIaomi.com, MiBox etc. On the other hand, Huawei (Huawei Technologies Co. Ltd.) was founded in 1987, and started its business by producing private branch exchange switches. Now the company has become one of the top telecommunications equipment suppliers and has active R&D activities since its start. Its businesses comprise mobile and fixed broadband networks, smartphones, tablet computers etc.

Figure 2 shows that while Huawei stably maintains high ROE, Xiaomi explosively expanded ROE in 2013 and 2014, but has declined since then.

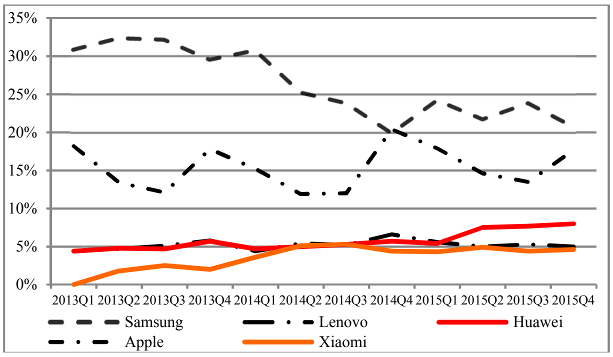

Figure 1 Global market share by vendors

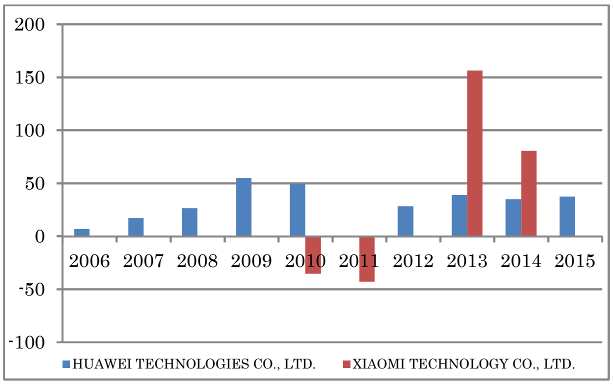

Figure 2 ROE of Huawei and Xiaomi

3. Methodology and data

In the following sections, the R&D strategies/operation systems of Chinese ITC companies are analyzed. In order to examine target companies' R&D strategies and the change of core researchers in their R&D projects, we visualize their patent information in 3 steps: the number calculation of patent publications, text mining, and social network analysis.

We use the IPC (International Patent Classification) code for analyzing the smartphone industry. IPC, established by the Strasbourg Agreement 1971, provides for a hierarchical system of language independent symbols for the classification of patents and utility models according to the different areas of technology to which they pertain.

Table 1 is most frequently used IPC in smartphone industry. Based on these IPC related to smartphone, patents related to smartphone published by each company are extracted and collected from the patent information.

Table1 IPC classes of smartphone

IPC	Description
H01, H02	Electricity: Battery or Capacitor Charging or Discharging
H03, H04	Coded Data Generation or Conversion
G02	Liquid Crystal Cells, Elements and Systems
H02, F21	Electricity: Electrical Systems and Devices
H04,G01, G06, G08	Multiplex Communications
H03, H04	Pulse or Digital Communications
H04	Telephonic Communications
G02, H04	Optical Communications
H04	Telecommunications
G06, G10	Data Processing: Speech Signal Processing, Linguistics, Language Translation, and Audio Compression/Decompression
G06	Data Processing: Artificial Intelligence
G06	Data Processing: Database and File Management or Data Structures
G06	Data Processing: Presentation Processing of Document, Operator Interface Processing, and Screen Saver Display Processing
G06	Interprogram Communication or Interprocess Communication (IPC) (Electrical Computers and Digital Processing Systems)

4. Analysis

4.1 *An approach based on the number of patent publications*

As our first approach, the numbers of patent publications associated with ICT in each of the companies are shown in Figure 3. Every company obtains related patents to a certain extent and the number of patents of all of them kept on increasing during the years except for 2016.

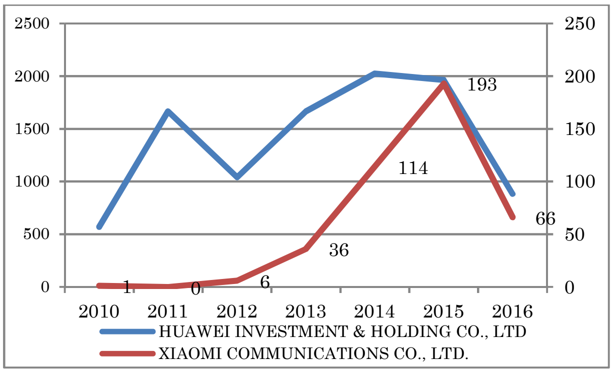

Figure 3 The number of patents of Huawei and Xiaomi

4.2 *An approach by correspondence analysis*

We use the correspondence analysis based on text mining to disclose the technical trends and features by IPC codes associated with smartphone. The reference data in the analysis is the numbers of each their patent document in each year. These figures are based on dates of patent publication, and patents are applied to products in the companies. Figure 4 shows that Xiaomi probably develops different technologies in each year, and Huawei tends to constantly develop technologies that highly related.

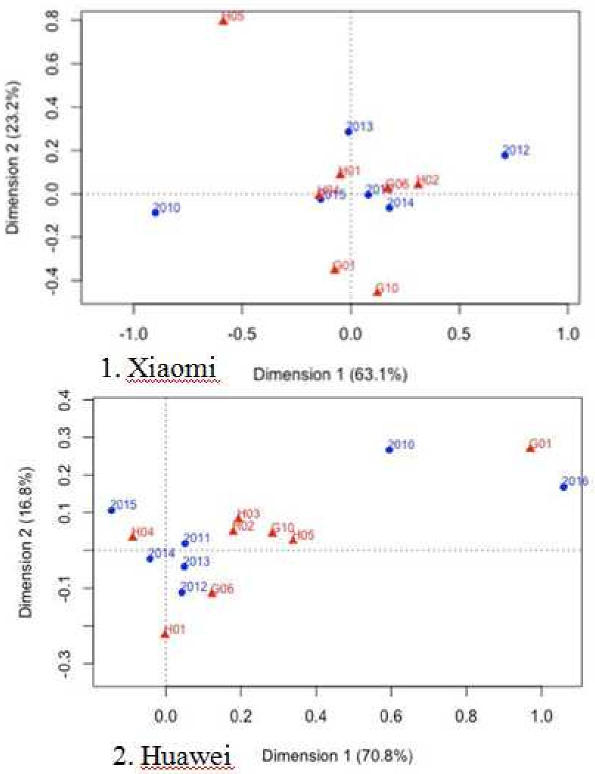

Figure 4 Results of correspondence analysis

4.3 *An approach by the social network analysis*

4.3.1. R&D network Figure 5 is the R&D networks of Xiaomi and Huawei. The results show that Xiaomi and Huawei have different R&D patterns. In Xiaomi's case, several islands that connected only to related patents are observed. It seems there is little relationship between technologies. On the other hand, the technology network of Huawei concentrated on several core patents and technologies are expanded based on these core patents.

Figure 5 R&D Networks of Xiaomi and Huawei

4.3.2. *The evaluation of core rigidity in R&D*

We define that patent applicants are key persons attaining high scores calculated by centrality of social network analysis. Centrality is a well-known index in this field. Freeman proposed three distinct conceptions of centrality: degree, betweenness and closeness [3]. And, it indicates that conditional probability appears where whether or not upper rank *j*% of person at *i* year appears upper rank *j*% of person at *i*+1 year. When such probability scores are high, they have core rigidity [4].

$$\text{Core Rigidity} = \text{Conditional Probability}\left(\frac{\text{upper rank j\% of person at i + 1 year}}{\text{upper rank j\% of person at i year}}\right)$$

We visualize the human resource reallocation of personnel engaged in R&D project by heat-map. Where the color is dark red in heat-map, it indicates an un-executed reallocation of a core engineer; otherwise, the color is light red, it means a radical change of core member in that year. As one of the example, the core rigidity of human resource and the change of R&D area the personnel involved in Xiaomi and Huawei are shown in Figure 6. There is more change in Xiaomi's core rigidity degree than change in Huawei. This is because Xiaomi must obtain to new patent for entering new market such as U.S. and Huawei has been exploiting research and develop for long time.

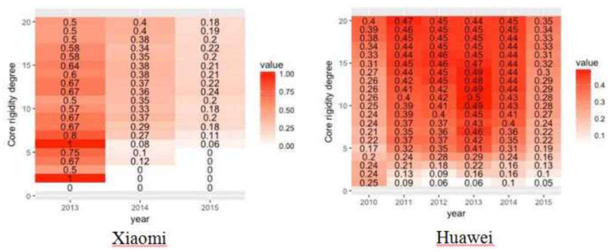

Figure 6 The core rigidity of Xiaomi and Huawei

5. Conclusions

This paper focused on Xiaomi and Huawei, the two major Chinese ICT companies to examine how they design their strategy/operation systems in R&D. Patent data were used to investigate Xiaomi's and Huawei's technology strategies and technical networks. Analysis includes: (1) the number of patent publications, (2) technological orientations, (3) R&D networks, (4) degree of core rigidity of R&D.

From the analysis of R&D network of Xiaomi, we supposed that it probably acquires external related patents rather than develops its own technologies inside the firm. Actually, Xiaomi did buy patents from other companies, for instance, Microsoft. In addition, in the degree of core rigidity of R&D, Xiaomi has rough R&D organization structures and hence has low level of integration. In fact, Xiaomi has few manufacturing facilities of its own, instead it outsource all production to contract manufactures such as Taiwan's Foxconn. And they also have not much invested R&D. Xiaomi's problem for new market entry is a lack of patent holdings and faces intellectual property-related lawsuits. And Xiaomi have tried to apply new patent recently. But Xiaomi's patent portfolio is still thin.

On the other hand, Huawei has high weight on internal R&D, and explores technologies related to core technologies. The heat map of core rigidity of Huawei shows that its R&D structure is more highly integrated than Xiaomi. Huawei is increasing its emphasis on R&D to become more innovative as a foundation for surviving in a highly competitive and rapidly consolidating industry. Being able to continuously and successfully innovate through vertical integration, Huawei is trying to do what can create a competitive advantage.

References

1. H. Chesbrough (2006) *Open Innovation: Researching a New Paradigm*, Oxford University Press
2. L. C. Freeman (1987) Technology and Economic Performance: *Lessons from Japan*, Pinter, London
3. D. A. Levinthal, and J. G. March, The myopia of learning, *Strategic Management Journal*, vol.14 (1993), pp.95–112
4. Leonard-Barton, D. (1992). Core Capabilities and Core rigidities: A Paradox in Managing New Product Development. *Strategic Management Journal*, vol. 13: 111-125.

The Optimized Function Selection Using Wolf Algorithm for Classification

Duangjai Jitkongchuen and Worapat Paireekreng
College of Innovative Technology and Engineering
Dhurakij Pundit University
Bangkok, Thailand
{duangjai.jit,worapat.png}@dpu.ac.th
www.dpu.ac.th

Abstract

Several classification techniques have been widely explored during the past decade. One of the novel approaches in recent years is Nature Based Algorithm. This approach is appropriate to imbalanced dataset. The focus of Nature Based Algorithm mostly is related to selection the optimized functions for self-learning. This is used to solve the NP-hard problems. However, Some Nature Based Algorithms are suitable for general situation; some may be suitable for customized situation. This research proposes the Featured-Wolf (F-Wolf) algorithm to optimize the function selection problem in classification. The proposed algorithm applies the movement of a wolf and characteristics of wolves' leaders which can be more than one leader in a pack. Therefore, the pack can have more than one dominant leader which can help to select the most optimized functions to selection the most relevant features in the dataset. The experiment shows the comparison among other popular Nature Based Algorithms such as Ant Colony Optimization and other classification techniques. The results show that F-Wolf performs better results in terms of accuracy rate.

Keywords: Nature Based Algorithms, Wolf algorithm, Classification

1. Introduction

Data science is now crucial for almost all areas. Data from various sources needs to be analyzed and uses specific analytic tools. One of the most important domain to present the analyzed data is classification. The common techniques used in data mining to solve the classification problem. Some research combined the classification techniques using ensemble technique to improve the classification performance[1].

In addition, the new classification techniques have been investigated to enhance the performance because the characteristics of each dataset have their uniqueness. The adjusted classification model and classifiers needs to be improved. One of the novel approaches in recent years is Nature Based Algorithm (NBA). The approach is related to selection the optimized functions for self-learning. This is the most appropriate technique to solve the NP-hard problems. It also works well with imbalanced dataset. The examples of NBA are such as Grey Wolf Optimizer (GWO)[2] and Ant Colony Optimization [3].

Furthermore, there is an attempt to improve the speed of computational time for classification performance. One of the stage in the pre-processing phase is feature selection. The feature selection has been used for the objective of selecting the most relevant attributes of the data set as input variables. These variables impact on the performance of classification if the relevant variables are chosen to build the classification model. The pre-processing stage eliminates the irrelevant attributes in order to increase the computational time of the model building stage. The example of feature selection can be seen from several data mining, machine learning, and pattern recognition[4]. Moreover, the input variables are the challenge of this area by selecting the appropriate subset of attribute with maintaining of classification performance [5,6].

However, Some Nature Based Algorithms are suitable for general situation; some may be suitable for customized situation. Therefore, some enhancing technique is needed for improving the performance of classification using NBA approach. Feature selection technique can be included in the NBA to perform better in terms of accuracy rate.

This paper proposed the Featured-Wolf (F-Wolf). The main idea of F-Wolf is to imitate the grey wolf behavior including feature selection in the pack. The algorithm uses information exchange within population which leads to generate new candidate individuals for feature selection and perform the better results for classification.

2. Related Works

2.1. *Data Mining and Classification Techniques*

There are many classification techniques that have been used to deal with classification problems and predictions. Examples of these common used classification techniques are Decision Trees (DT), Naïve Bayes (NB), Artificial Neural Networks (ANN) and Support Vector Machines (SVM)[7]. There are different in terms of advantages and disadvantages based on each technique. The factors to decide which technique is suitable for dataset are such as simplicity of the algorithm, up-sampling scale, robustness and outlier handing.

Classification techniques have also been incorporated into the several applications. For example, the mobile services incorporated Artificial Neural Networks (ANN) with feed-forward back-propagation neural network in order to select the different types of particular services[8,9].

The performance of classification model can be assessed by confusion matrix. It is shown in *Table 1*. The confusion matrix presents the results of amount of correct and incorrect instance in each class.

Table 1. Confusion Matrix Terminology.

	Positive Prediction	**Negative Prediction**
Positive class	True Positive (TP)	False Negative (FN)
Negative class	False Positive (FP)	True Negative (TN)

True Positive (TP) and True Negative (TN) are the positive instances and negative instances correctly classified respectively whereas False Positive (FP) and False Negative (FN) are the negative instances and positive instances misclassified respectively.

To measure the performance of the classification, the traditional accuracy rate (1) has been used.

$$ACC = \frac{TP+TN}{TP+FN+FP+TN} \tag{1}$$

2.2. *Soft Computing and Nature Based Algorithm*

The soft computing has been introduced to solve the uncertain problems with intensive computation. The principle of soft computing can implement probabilistic reasoning approach to solve the problems. The examples of techniques used in soft computing are such as evolutionary algorithm. One of the commonly used technique is Ant Colony Optimization (ACO) which can be seen in the recent research[3].

However, to handle different type of data such as categorical and continuous data in the real world, Customized techniques is needed to obtain the better performance in terms of accuracy. Some problems domain such as NP-hard problems also needs the specific techniques and methodology to solve the uncertain variables and alternatives. Therefore, it is also the challenge to implement the adapted Nature Based Algorithm for classification performance.

2.3. *Grey Wolf Optimizer*

The grey wolf optimizer algorithm (GWO) was proposed by Mirjalili et al[10]. It is the recent Nature Based Algorithm which simulate the grey wolf behavior to live in a pack. The social dominant hierarchy of the wolf pack can be defined as leaders, subordinate wolves and members which consist of scouts, sentinels, elders, hunters and caretakers. Each member has a different role in a pack. For example, Sentinels protect and guarantee the safety of the pack. Therefore each level and member is defined as variables called alpha, beta and delta respectively. In addition, the lowest level is omega. The omega wolves have to comply with all the other dominant wolves.

The grey wolves show naturally ability to encircle and identify the position of a prey and other wolves help the hunting for a pack. This behavior can be explained in mathematical model which assumes the leader to be alpha (α). The beta (β) and delta (δ) is similar to the second and the third optimal solutions, respectively. Whereas, the rest of the candidate solutions are assumed to be omega (ω). The hunting is guided by alpha, beta and delta. Besides, the omega wolves would consider the best solutions from three different positions and update the information to the pack.

Nevertheless, the traditional grey wolf algorithm basically simulate with only one pack which leads to encircle on local search. Therefore, splitting the pack of the grey wolf is challenge. The proposed method is included algorithm to reduce the optimum ratio and distribute value to in order to obtain the larger search space. This is also including feature selection.

2.4. *Feature Selection for Classification Problem*

Due to the consuming computational time of building the classification model for training dataset, some methodologies are needed to address to problem. The common methodology used is feature selection. The purpose is to select the subset of input variables which is useful and impact on performance of the classifier. This includes elimination of some irrelevant variables with few contributions towards the prediction results. The use of feature selection can be seen from data mining, machine learning and pattern recognition[4, 11]. The objective of feature selection is to select a subset of useful features from the input variables that impact on accuracy of the classifier and eliminate irrelevant features with little contribution towards the prediction results. Moreover, the challenge is to choose the minimum subset of features with little or no loss of classification accuracy[5,6].

Feature selection can be divided into two categories: model-free method and model-based methods. Model-free methods are based on statistical tests, properties of function and available data such as linear regression, whereas, model-based methods such as neural network develop model to find the significant features and minimize the model output error[12,13]. Therefore, Nature Based Algorithm (NBA) can be also incorporated into classification model in order to select the most suitable variables for classification problem with less impact on performance.

3. Research Methodology

3.1. *Experimental Design*

The data source used for the experiment was obtained from University of California Irvine (UCI) machine learning repository. There are 10 datasets used in this research.

3.2. *The Proposed Featured Wolf (F-Wolf) and Procedure*

The overall and details of F-Wolf procedure are shown below in "Fig. 1.".

Initialize the grey wolf population $X_i (i = 1, 2, ..., n)$
where each wolf consists of choosing attribute with value yes or no.
Initialize parameters (a, A and C)
Calculate the fitness of each search agent based on accuracy rate
X_α = the best search agent
X_β = the second best search agent
X_δ = the third best search agent
while (t < Max number of iterations)
    Update current wolf's position based on top three wolves
    Crossover top three wolves to create new member using choosing attribute
        Uses voting to find the maximum amount of value chosen by leaders
        The values of the attribute is the best entropy is selected
    Sort all wolves based on suitable value
    Insert new member to wolf with least suitable value
    Update a, A and C
    Calculate the fitness of all search agents
    Update X_α, X_β, X_δ
end while

Fig. 1. Procedure of F-Wolf

4. Experimental Results

After the datasets have been prepared, the next step is to build the classification model for prediction. There were 4 different types of algorithms used to compare in the experiment, specifically Featured Wolf (F-Wolf), Ant Colony Optimization (ACO), C4.5 and PART. In this research, the metric to determine the performance of the classification is based on accuracy rate. The preliminary results are shown in *Table 2*.

Table 2. Comparison Results.

Technique	**Accuracy Rate (%)**			
Dataset	**F-Wolf**	**ACO**	**C4.5**	**PART**
Credit-G	***87.96***	79.29	71.70	71.90
Haberman	76.30	79.63	70.59	70.59
Heart-C	***78.00***	69.38	49.17	55.12
Heart-H	70.00	73.47	64.29	62.59
Heart-statlog	***86.67***	77.24	62.22	64.07
Horse	82.50	88.00	82.00	82.33
Iris	***99.09***	98.22	94.67	95.33
Pima diabets	***87.00***	78.89	73.31	73.44
Shuttle	***96.30***	75.60	53.33	53.33
Sonar	***97.59***	87.07	76.92	73.56
Average	86.14	80.68	69.82	70.23

It appeared that the proposed F-Wolf classification model can perform better in terms of accuracy rate compared to other classification techniques. In addition, it performed better than C4.5 and PART. To compare with ACO, the Nature Based Algorithm, the results show that the proposed technique presented the better results with 7 out of 10 datasets. Furthermore, the average accuracy rate for F-Wolf is higher significantly compared to other techniques.

5. Discussion and Conclusions

Classification is an important problem domain for data related area. Several techniques have been proposed to deal with classification. One of the novel approaches in recent years is Nature Based Algorithm (NBA) which appropriate to imbalanced dataset including NP-hard problems. Grey Wolf Optimizer (GWO) is one of the NBA to address the classification problems. However, it may be suitable for one pack situation, therefore, Featured Wolf Algorithm (F-Wolf) is proposed using information exchange within population. This which leads to generate new candidate individuals for feature selection in order to enhance the classification performance.

The results from the experiments based on UCI datasets have shown that the proposed F-Wolf provided the better classification results. The average of accuracy rate for all datasets in the experiment was also higher than other classification techniques. The F-Wolf used crossover to keep the best value in each round but the traditional did not cover.

In the future works, it is important to consider the imbalanced data sets with other Nature Based Algorithm. This includes the investigating the improved performance on prediction results of the classification model. The hybrid Nature Based Algorithm is therefore needed to address the problem. Moreover, the other soft computing techniques such as fuzzy-based techniques or machine learning techniques can be incorporated in the feature selection stage. This is to build the improved classification model.

References

1. W. Paireekreng and T. Prexawanprasut, An Integrated Model for Learning Style Classification in University Students Using Data Mining Techniques, in *Proc. 12th International Conference on Electrical Engineering/Electronics, Computer, Telecommunications and Information Technology (ECTI-CON)*, (Hua Hin, Thailand, 2015).
2. D. Jitkongchuen, P. Phaidang and P. Pongtawevirat, Grey Wolf Optimization Algorithm with Invasion-based Migration Operation, in Proc. *15th IEEE/ACIS International Conference on Computer and Information Science (ICIS 2016),* (Okayama, Japan,2016).
3. W. Paireekreng, D. Jitkongchuen, W. Sukpongthai and R. Suwannakoot, Improving Soft Computing Performance with Ant Colony Optimization for Multiclass Classification: The Application for Learning Style Classification, in *Proc. 7th International Conference on Intelligent Systems, Modelling and Simulation (ISMS2016)*, (Bangkok, Thailand, 2016) pp.101-105.
4. P. Mitra, C. A. Murthy and S. K. Pal, Unsupervised feature selection using feature similarity, *IEEE Transactions on Pattern Analysis and Machine Intelligence*, 24(3) (2002) 301–312.
5. H. Almuallim and T. G. Dietterich, Learning boolean concepts in the presence of many irrelevant features, *Artificial Intelligence*, 69 (1-2) (1994) 279–305.
6. D. Koller and M. Sahami, Toward optimal feature selection, in *Proc. 13th International Conference on Machine Learning*, (1996).
7. X. Wu, et al., Top 10 Algorithms in Data Mining, *Knowledge and Information Systems*, 14 (2008) 1-37.
8. Q. H. Mahmoud, et al., Design and implementation of a smart system for personalization and accurate selection of mobile services, *Requirement Engineering*, 12 (2007) 221-230.
9. A. Cufoglu, et al., A Comparative Study of Selected Classifiers with Classification Accuracy in User Profiling, in *Proc. World Congress on Computer Science and Information Engineering*, (Los Angeles, California, USA, 2009).
10. S. Mirjalili, S. M. Mirjalili and A. Lewis, Grey wolf optimizer, *Advances in Engineering Software*, 69 (2014), 46-61.
11. Miller, Subset Selection in Regression, 2nd edn. (Chapman & Hall/CRC, 2002).
12. S. M. Vieira, J. M. C. Sousa and T. A. Runkler, Two cooperative ant colonies for feature selection using fuzzy models, *Expert Systems with Applications*, 37(4) (2010) 2714-2723.
13. A. E. Isabelle Guyon, An Introduction to Variable and Feature Selection, *Journal of Machine Learning Research*, 3 (2003) 1154-1182.

Tell Agent Where to Go: Human Coaching for Accelerating Reinforcement Learning

Nakarin Suppakun
Institute of Field roBotics, King Mongkut's University of Technology Thonburi
Bangkok, 10140, Thailand

Suriya Natsupakpong
Institute of Field roBotics, King Mongkut's University of Technology Thonburi
Bangkok, 10140, Thailand

Thavida Maneewarn
Institute of Field roBotics, King Mongkut's University of Technology Thonburi
Bangkok, 10140, Thailand
E-mail: nakarin_sup@hotmail.com, suriya@fibo.kmutt.ac.th, praew@fibo.kmutt.ac.th
www.kmutt.ac.th

Abstract

In this work, we proposed a method to accelerate learning by allowing a human to coach a robot behavior by inserting an intermediate target at the early phase of the reinforcement learning. By using an intermediate target, the different pair of policy and reward function was temporarily used to select an action that most likely to drive the robot toward the intermediate location, while the global reward function is still used for updating the state-action value. Q learning algorithm was used to test with the proposed method on three learning tasks: ball following, obstacle avoidance, and mountain car. The proposed technique resulted in better learning performance than the traditional RL.

Keywords: learning from demonstration, reinforcement learning, human assisted learning, semi-supervised learning, robot coaching

1. Introduction

In Reinforcement Learning (RL), long time training is usually required in order to train an agent to perform a given task. A large number of learning episodes is necessary to effectively propagate environmental rewards to each state action pair. However, instead of unnecessarily exploring states and actions freely, if there is a way that a human teacher could guide an agent toward the task completion at an early learning state, the agent could reach the goal state, and get the environmental reward within less learning iteration. In this work, a human coach guides an agent by placing a virtual intermediate target so that the agent would move toward. Another pair of policy and reward function would recognize this virtual target as a new goal state. A greedy policy is used in conjunction with an aggressive reward function until an agent reaches the virtual target. Meanwhile, the agent updates state-action value for every state-action encounter with the global environmental reward. After reaching the virtual target, the agent would be switched back to exploit and explore the states and actions through an e-greedy policy until next human input is provided. In this work, a human only assists an agent in the early phase of learning process.

2. Related Work

Various techniques which using human inputs to assist an agent in learning a given task can be found in many literatures. In the work of A.L. Thomaz, and C. Breazeal[1,2], a human teacher gives a scalar reward after a robot performs a task in a computer simulation. Human teacher was supposed to give the feedback after each action has taken; however, many people misunderstood and give the signal as if guiding what the robot should do next. In work of M. Hirokawa and K. Suzuki[3], a human coach would give a subjective evaluation as a binary feedback signal by modifying the reward function. There is also check for inconsistency of feedback and the signal is discarded if some inconsistency was found. There are also literatures about reward shaping technique[4,5], the concept is that the feedback given by the human was used to modify the reward function by adding the interpreted value to the initial predefined reward (environmental reward). A list of certain feedback words was fixed and each word was predefined their corresponding value based on intensity level of meaning. In the work of S. Griffith et al.[6], the policy shaping technique from an advice feedback was presented. However, they used a simulation feedback instead of an actual human feedback in order to control the consistency and likelihood of the feedback provided. W.B. Knox and P. Stone[7-9] presented the system which allowed human teacher to give a binary feedback on the action taken. Human feedback model was trained by supervising technique and used for action selection as a policy. A variety of combinations on human input and traditional RL were tested[8]; The best combination was to use human input for an action selection only, which convince us to the same idea as well. In the work of W. D. Smart and L. P. Kaelbling[10], they allowed a human to take over the policy for action selection on the early phase of learning, and then let the learning to proceed as usual later on. A human controlled the action directly via a joystick, while an agent updates its state-action value properly. In our work, a human coach assists the learning process by placing an intermediate virtual target to guide the agent toward the desired location. In this proposed method, there is no need for a human coach to manually select an action for each state-action that the agent encounters.

3. Methodology

In the proposed method, an agent performs both exploitation and exploration by ϵ-greedy policy. (greedy with probability $1\text{-}\epsilon$ or random). Whenever a human coach assist an agent by giving an intermediate virtual target, a separated set of aggressive reward function is generated. With this reward function, a separated aggressive policy, which the action with the most reward received would be selected, is used. An agent would move toward the intermediate virtual target until the intermediate target is reached. In the meantime, each state-action encounter along the trajectory path would be updated the state-action value with a corresponding environmental reward (regardless of aggressive reward which was used solely for action selection). After reaching the guided target location, the agent would be switched back to ϵ -greedy policy again until the next guide target is given by a human coach. The process is repeated until the global goal state is reached. In our experiment, the human guidance was only given in the early phase (the first 30 training episodes) and the traditional reinforcement learning was resumed later on.

4. Experimental Setup

All experiments were conducted in a computer simulation program. The first two tasks are in a robot soccer environment as shown in Fig. 1. The first task (ball following) is for the robot to move toward the ball. In the second task (obstacle avoidance), an obstacle (i.e. an opponent robot) was placed between the ball and the robot. From this program, a human coach could assign a virtual intermediate target for the robot by left clicking at the desired coordinate on the screen.

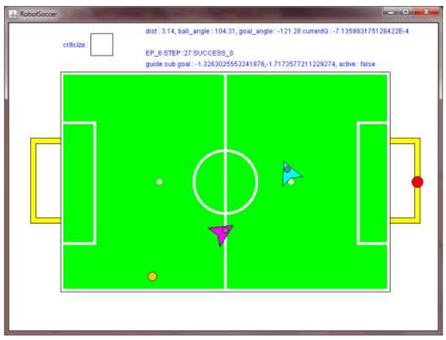

Fig. 1. Simulation program for ball following and obstacle avoidance. Soccer field represents 6 x 4m.

The third task is mountain car problem from Ref. 11. The purpose of this task is to drive a car back and forth in a valley between 2 mountains until the car can reach the top of the mountain on the right. From this program, a human coach give a guided intermediate target for the car by left clicking at the screen. The horizontal position information would be used as a guidance input.

Q reinforcement learning using a radial basis functions (RBFs) network as function approximator was used in our experiment (see Ref. 11). Information for each experimental task was explained as follow.

4.1. *Ball following*

State descriptors consist of the ball linear (Euclidean) distance, the sine and cosine of an angle from the robot heading to the ball, the sine and cosine of an angle to center of the opponent goal, and the linear distance from the opponent goal field line.

List of actions are combination of linear and angular movement. Linear actions consist of *go forward* (0.1 m), *stop*, and *go backward* (-0.1 m). Angular actions consist of *turn left* (15 degrees), *no turn* (0 degree), and *turn right* (-15 degrees). Thus, we have the total of nine actions (3x3). Note that, the completely stop action (stop & no turn) is excluded.

A global reward function *r(s,a)* was defined as follow. If the robot reaches the ball (<= 0.15 m) and the ball is in front of the robot (in between angle -60 and 60 degrees), a positive reward +1.0 is given and the episode is successfully finished. If the ball is not in front of the robot, no score is given and the episode is failed. If the robot moves further away from the ball than the given threshold distance (6 m), a negative penalty score of -0.1 is given and the episode is failed. If the robot goes outside the field on either side, a penalty of -0.1 is given and the episode is failed. Otherwise, no score is given.

An aggressive reward function $\hat{r}(s,a)$ extended the previous conditions by using the intermediate target given by a human coach instead of a global reward. If the current distance to the intermediate target is shorter than previous state's, the positive score of +0.1 is added to the reward. If the current angular distance between the agent heading and the intermediate target is smaller than the previous state's, the positive score of +0.1 is also added. The Greedy approach was used for the aggressive policy that is used in conjunction with the aggressive reward $\hat{r}(s,a)$

4.2. *Obstacle avoidance*

All state descriptors explained in section 4.1 are also used with an addition of the obstacle linear (Euclidean) distance and the sine and cosine angle to the obstacle. The reward *r(s,a)* condition was modified by including that if the robot collides with an obstacle (<= 0.3 m), then the penalty of -0.3 is given, and the episode is failed. List of actions, an aggressive reward function and policy are the same as in section 4.1.

4.3. *Mountain car*

State descriptors consist of the car position (in horizontal axis) and the velocity. List of actions consist of *full throttle reverse, zero throttl*e, and *full throttle forward*. The reward function *r(s,a)* was implemented differently from the original work[11]. A positive reward (+1.0) is only given when the car reaches the target location (top of the right mountain), and no reward for other cases. An aggressive reward function $\hat{r}(s,a)$ was implemented separately as follow. If the current state is closer to the intermediate target than the previous state, a positive reward +0.1 is given. Again, greedy approach was used for an aggressive policy.

5. Results

Figs. 2, 3, and 4 illustrate the learning performance for the three tasks: ball following, obstacle avoidance, and mountain car, respectively. Each method and each task was repeated for 3 trials. In all three tasks, the guidance (coached) approach has higher accumulated rewards than the traditional RL.

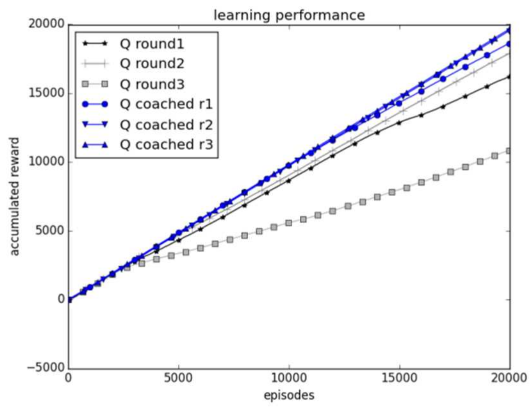

Fig. 2. A comparison learning performance for ball following.

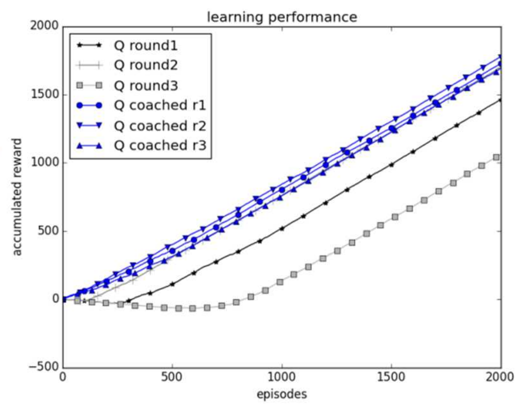

Fig. 3. A comparison learning performance for obstacle avoidance.

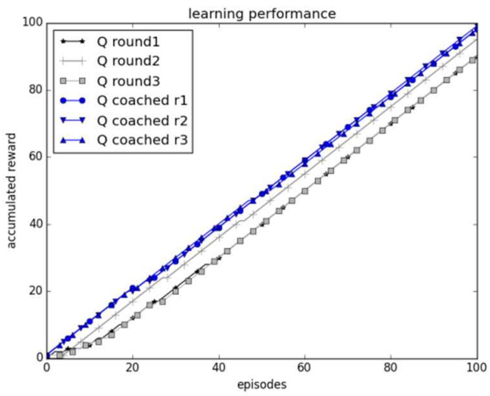

Fig. 4. A comparison learning performance for mountain car.

6. Conclusion

The results showed that with the guided information from a human coach, an agent learn a task more effectively. An agent could use the guided information at the early learning episodes instead of exploring randomly at the beginning phase of the learning. As the agent reached the virtual intermediate target given by the human coach, the agent has performed what the human coach expected and also learned the list of useful actions along the way. The chance for exploration is still available as the policy is switched back to ϵ-greedy after the agent reached the intermediate target and possibly could find the even better solution. The experimental results from three different tasks also show that the proposed method that including an intermediate target from a human coach with reinforcement learning has accelerated the learning performance compared to the traditional RL.

References

1. A.L. Thomaz and C. Breazeal, Reinforcement Learning with Human Teacher: Evidence of Feedback and Guidance with Implications for Learning Performance, in *Proc. 21st Nat. Conf. Artificial Intell.* **1** *(AAAI 2006)* (Massachusetts, Boston, 2006), pp. 1000-1005.
2. A.L. Thomaz and C. Breazeal, Teachable Robots: Understanding Human Teaching Behavior to Build More Effective Robot Learners", *Artificial Intell. J.* **172**(6-7) (2008), pp. 716-737.
3. M. Hirkoawa and K. Suzuki, Coaching Robots: Online Behavior Learning from Human Subjective Feedback, in *Innovations in Intelligent Machines-3, Studies in Computational Intell.* **442** (2013), pp. 37-51.
4. A. C. Tenorio-Gonzalez, E. F. Morales and L. Villaseñor-Pineda, Dynamic Reward Shaping: Training a Robot by Voice, in *Advances in Artificial Intell. (IBERAMIA 2010)* (2010), pp. 483-492.
5. L.A. Leon, A.C. Tenorio and E.F. Morales, Human Interaction for Effective Reinforcement Learning, in *European Conf. Mach. Learning and Principles and Practice of Knowledge Discovery in Databases (ECMLPKDD 2013)* (Prague, 2013).
6. S. Griffith, K Subramanian, J. Scholz, C.L. Isbell and A.L. Thomaz, Policy Shaping: Integrating Human Feedback with Reinforcement Learning, in *Advances in Neural Inform. Process. Syst.* (2013), pp. 2625–2633.
7. W.B. Knox and P. Stone, Interactively Shaping Agents via Human Reinforcement: The TAMER framework, in *Proc. 5th Int. Conf. Knowledge Capture* (2009), pp. 9-16.
8. W.B. Knox and P. Stone, Combining Manual Feedback with Subsequent MDP Reward Signals for Reinforcement Learning, in *Proc. 9th Int. Conf. Autonomous Agents and Multiagent Syst.* **1** *(AAMAS 2010)* (2010), pp. 5-12.
9. W.B. Knox and P. Stone, Reinforcement Learning from Simultaneous Human and MDP Reward, in *Proc. 11th Int. Conf. on Autonomous Agents and Multiagent Syst.* **1** (2012), pp. 475-482.
10. W. D. Smart and L. P. Kaelbling, Effective Reinforcement Learning for Mobile Robots, in *Proc. IEEE Int. Conf. on Robotics and Automation (ICRA'02)* **4** (2002), pp. 3404-3410.
11. R.S. Sutton and A.G. Barto, *Reinforcement Learning: An Introduction* (MIT Press, Cambridge, 1998).

Fall Risk Reduction for the Elderly Using Mobile Robots Based on the Deep Reinforcement Learning

Takaaki Namba
Graduate School of Engineering, Nagoya University,
Furo-cho, Chikusa-ku, Nagoya City, 464-8603, Japan

Yoji Yamada
Graduate School of Engineering, Nagoya University,
Furo-cho, Chikusa-ku, Nagoya City, 464-8603, Japan

E-mail: namba.takaaki@b.mbox.nagoya-u.ac.jp, yamada-yoji@mech.nagoya-u.ac.jp
www.nagoya-u.ac.jp

Abstract

Slip-induced fall is one of the main factors causing serious fracture among the elderly. This paper proposes a deep learning based fall risk reduction measures by mobile assistant robots for the elderly. We use a deep convolutional neural network to analyze fall risks. We apply a deep reinforcement learning to control robots and reduce slip-induced fall risks of the elderly. The results suggest that the applicability of our method to other cases of the fall and other cases of accidents.

Keywords: Safety, Risk Reduction, Mobile Robot, Deep Learning, Reinforcement Learning.

1. Introduction

An increase tendency of the elderly's accidents is showing no signs of stopping in some countries including Japan.[1-2] In order to reduce the increasing fall accidents among the elderly, we take an approach to use mobile assistant robot. We consider safety in the environments where humans and assist robots coexist in the fields of medical welfare and assist living.

This paper proposes a deep learning based fall risk reduction measures by mobile assistant robots for the elderly. First, we collect preparatory data regarding past incidents and accidents data as input data to analyze fall risks and to learn examples of risk reduction measures. Second, we use a deep convolutional neural network[3] to analyze fall risks of the elderly. Third, we apply a deep reinforcement learning[4-5] to control mobile robots and reduce slip-induced fall risks of elderly. Moreover, we evaluate the effect of risk reduction.

2. Risk analysis

The risk analysis is carried out through methods such as FTA (Fault Tree Analysis),[6] HAZOP (Hazard And Operability Study),[7-8] and FMECA (Failure Modes Effects and Criticality Analysis).[9] Conventional risk analyses conducted manually or partially use a probability calculation tool when employed in applications such as system safety requirement analysis or design. This type of analysis has the following limitations:

- Failures to identify hazards may occur depending on the proficiency of the safety management officers, that is, their experience and capability,
- Risk analysis procedures are complex and require a specific number of man-hours depending on the scale of the assessment.

Most analyses and assessments are carried out offline based on prior information and require time to be conducted. The results are not immediately available. Therefore, the measures of risk reduction are often delayed, and it becomes difficult to respond promptly and flexibly in continually changing situations.

In this paper, we use online real-time risk analysis based on the deep convolutional neural network. The input is environmental sensing data aimed at detecting HEs (Hazard Elements), IMs (Initiating Mechanisms, triggers of the accident), and T/T (Target and Threat) in the. Ericson's Hazard Theory.[10] According to the Ericson's Hazard Theory, the accident (mishap) occurs when HE, IMs and T/T are appeared at the same time in specific timing. The sensing data is mainly time-series images of the environment and distance information to the objects and parts of human body.

The main output is the result of risk analysis and the level of risk as quantitative information. The risk is presented with following formula:

$$Risk = S * Ph. \tag{1}$$

$$Ph = F + Ps + A \tag{2}$$

. Eq. (1) shows that the risk is multiplication of the severity of the harm (S) and the probability of the harm (Ph). Eq. (2) displays the probability of the harm (Ph) is the combination of following: frequency of exposure to hazards (F), the probability of occurrence of hazardous event (Ps), the possibility of avoiding or limiting the harm (A). Furthermore, according to the result of risk analysis, we generate a painting of the future by blending a representative hazardous image per each risk category with a current image.

3. Risk reduction

In general, about the safety of machinery, risk reduction carries out through methods such as inherently safe design measures, safe guarding implementation of complementary protective devices and information for use.[11-13] In addition to the above, risk reduction learns from the previous incidents and accidents, [14] which improves the environment, for example, removes hazard elements, supports avoiding hazardous situation and stops the trigger of incidents and accidents.

This paper proposes online real-time risk reduction based on the deep reinforcement learning. Figure 1 illustrates that inputs are following environmental data: the elderly's outer factors and inner factors. Outer factors are some sensing data, for example, images from stereo camera and laser range finder. Inner factors are elderly's physical condition, for example, breathing. The other input is the risk level that is the result of risk analysis as a negative reward.

This deep neural network is trained with the Q-learning algorithm, [4-5] with Adam[15] for optimization of parameters. Moreover, this network uses batch normalization for improving the learning rate and robustness of initial value of weight.[16]

The output is the action as the risk reduction measures.

4. Experiment

We performed an experiment on a simulation. Figure 2 shows a visualization of an environment and an agent. A scenario is that an elderly person who is assisted by mobile robot goes to the toilet at a certain interval in the

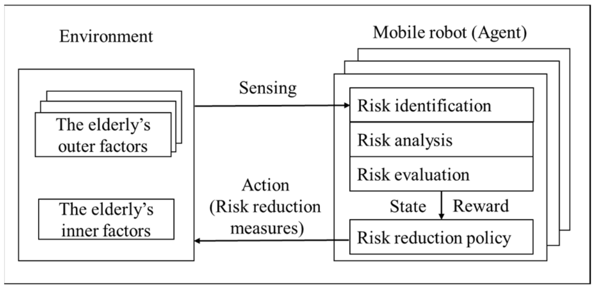

Fig. 1. Reinforcement learning for fall risk reduction of the elderly.

hospital. Sometimes the floor is partially wet. The mobile robot (agent) assists preventing from slip-induced fall for the elderly.

Figure 3 presents a process how the reward changes during training on the simulation. The increase of the reward indicates the reduction of the risk. We evaluate the effects of our approach through these change of graphs. We obtained the result of simulation that the agent is able to act reducing slip-induced fall risks automatically.

Figure 4 depicts an example of the deep neural network model generating risk reduction measures. We apply the combination of 3-streams (the current flow, the chaging

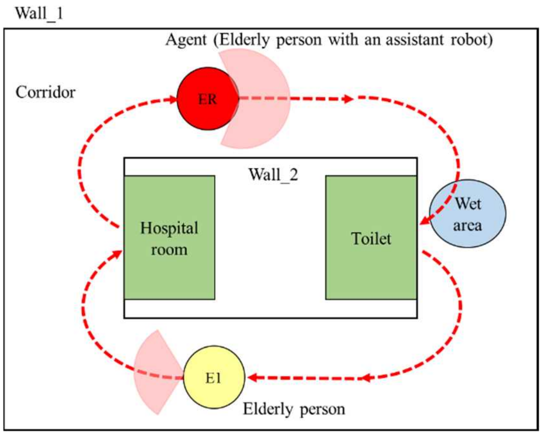

Fig. 2. A simulation environment of experiments. ER is an elderly person assisted by a robot as an agent. E1 is another elderly person. From a hospital room, ER goes to the toilet at a certain interval by walking on the corridor between Wall_1 and Wall_2. E1 also goes to the same toilet. Sometimes it is wet on the floor and ER detects wet area. The fan-shaped area shows the sensing rage of ER and E1.

flow and the changing rate flow) deep convolutional neural network and full connection network to determine the risk reduction measures. The data of input layer composes state and reward vectors.

5. Conclusion

In this paper we proposed a fall risk reduction measures for the elderly using mobile robots based on the deep reinforcement learning, and have presented its usability. The results of experiments suggest that the applicability

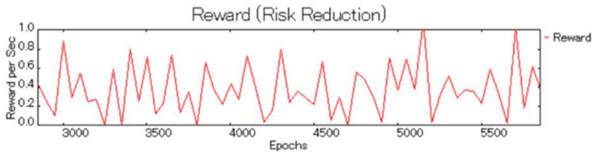

Fig. 3. Change of reward during training on the simulation.

of our method to other cases of the fall and other cases of accidents.

References

1. Takaaki Namba, and Yoji Yamada, A study on an assistance by mobile robots in preventing the elderly from falling, Proceedings of annual meeting of the the Japan Society of Mechanical Engineers 2015, Paper No. J1630205, 2016 (in Japanese).
2. Takaaki Namba, and Yoji Yamada, A study on an assistance by mobile robots in preventing the elderly from falling (Deep Convolutional Neural Network for Fall risk Analysis), *Proceedings of annual meeting of the the Japan Society of Mechanical Engineers 2016*, Paper No. J1640304, 2016 (in Japanese).
3. Alex Krizhevsky, Ilya Sutskever, and Geoff Hinton. Imagenet classification with deep convolutional neural networks, *In Advances in Neural Information Processing Systems 25*, (2012), 1106–1114.
4. Christopher J. C. H. Watkins and Peter Dayan, Q-learning, *In Machine Learning*, vol. 8, (1992), pp. 279-292.
5. Mnih, Volodymyr et al. Playing Atari with Deep Reinforcement Learning". *In:CoRR abs/1312.5602*,(2013).
6. C. Ericson, Fault tree analysis – a history, *In:17th International System Safety Conference. Unionville, VA*, (1999), pp.1-9.

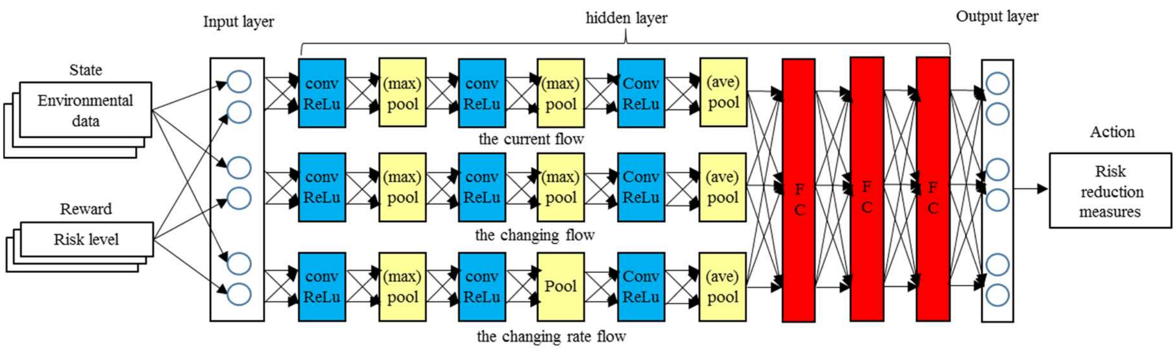

Fig. 4. A deep neural network model generating a risk reduction measures.

7. Faisal I Khan, S.A Abbasi, Techniques and methodologies for risk analysis in chemical process industries, *Journal of Loss Prevention in the Process Industries, Vol.11, Issue 4*, (July 1998), pp.261–277
8. Jordi Dunjóa, Vasilis Fthenakis, Juan A. Vílchez, Josep Arnaldos, Hazard and operability (HAZOP) analysis, *A literature review, Journal of Hazardous Materials, Vol. 173, Issues 1–3*, (15 January 2010), pp.19–32
9. MIL-STD-1629A, *Military Standard, procedures for performing a Failure Mode, Effects and Criticality Analysis*, (Department of Defense, Washington, DC, 1980).
10. Crifton A. Ericson II, *Hazard Analysis Techniques For System Safety, Second Edition*, (John Wiley & Sons, Inc., 2016).
11. ISO12100, Safety of machinery – General principles for design – Risk assessment and risk reduction, 2010.
12. IEC61508-ed2, Functional safety of electrical /electronic / programmable electronic safety-related systems, 2010-04.
13. ISO13482, Robots and robotic devices -- Safety requirements for personal care robots, 2014.
14. David L. Cooke, Learning from Incidents, System Dynamics Society, (2013)
15. Diederik Kingma and Jimmy Ba., Adam: A Method for Stochastic Optimization, *3rd International Conference for Learning Representations (ICLR), San Diego*, (2015)
16. Sergey Ioffe and Cristian Szegedy, Batch Normalization: Accelerating Deep Network Training by Reducing Internal Covariate Shift, *Journal of Machine Learning Research*, (2015)

Histogram Matching Based on Gaussian Distribution Using Regression Analysis Variance Estimation

Yusuke Kawakami
DynaxT Co., Ltd., 2217-6 Hayashi
Takamatsu City, Kagawa 761-0301, Japan

Tetsuo Hattori, Yoshiro Imai, Kazuaki Ando, Yo Horikawa
Graduate School of Kagawa University, 2217-20 Hayashi
Takamatsu City, Kagawa 761-0396, Japan

R. P. C. Janaka Rajapakse
Tainan National University of the Arts, 66 Daci
Guantian District, Tainan 72045, Taiwan
E-mail: riverjp2002@gmail.com, {hattori imai, ando, horikawa}@eng.kagawa-u.ac.jp, janakaraja@gmail.com

Abstract

This paper describes an improvement method for variance estimation which is used in Histogram Matching based on Gaussian Distribution (HMGD). In the previous papers, based on curvature computation, we have described that how to estimate the variance of reference histogram, which is used in HMGD processing. However, we have considered that the histogram of original image is not always ideal shape. And the variance estimation method based on curvature computation might not have high reliability. In this paper, we propose improvement variance estimation method using regression analysis. As for the method, first, we detect the histogram peak of original image by using curvature computation; next, we perform regression analysis using approximation formula of curvature. Then, we illustrate processing results through some experimentation.

Keywords: Image processing, Curvature, Variance estimation, Histogram matching, HMGD

1. Introduction

These days, automated image processing for enhancement of color images has been more familiar to us, for example, Digital Signage, Smart Phone, etc [1-3].

In the previous paper, we have presented that the Histogram Matching based on Gaussian Distribution (HMGD) processing is one of the automated image arrangement method using Elastic Transformation [4-5] based on the brightness axis. And through the comparative investigation, we have illustrated that HMGD processing could improve feeling (or Kansei) impression better than original image[6]. And we have aimed to improve HMGD processing, we have proposed that how to estimate the variance of reference histogram, which is used in HMGD processing based on curvature computation, and also illustrated these results.

However, we have considered that the histogram of original image is not always ideal shape (i.e., Gaussian distribution, etc). And the variance estimation method based on curvature computation might not have high reliability. In this paper, we propose how to perform regression analysis using approximation formula of curvature.

2. Principle

2.1. *Histogram Matching based on Gaussian Distribution (HMGD)*

In the section, we describe the principle of HMGD processing.

Fig. 1 shows the conceptual image of HMGD. Let $f(x)$ and $h(y)$ be two probabilistic density functions (PDF) on real variables x and y, respectively. The PDF is corresponding to histogram of image brightness level which is discretely defined.

In addition, let $y=\phi(x)$ be a continuous and monotonic increase function corresponding to cumulative histogram of image brightness level between variables x and y [7-9]. And let $y=\phi(x)$ be defined by Eq. (1).

$$y=\phi(x)=L\int_0^x f(x)dx. \tag{1}$$

At first, we have to expand brightness level of original image histogram and convert into uniform distribution histogram, because we aim to match Gaussian distribution. From Eq. (1) and Fig. 1, we can derive Eq. (2) and (3).

$$f(x)=h(y)\phi'(x)=h(y)Lf(x). \tag{2}$$

$$h(y)=\frac{1}{L}. \tag{3}$$

We understand the histogram of original image $f(x)$ becomes uniform distribution $h(y)$ by Eq. (3). This means that brightness level of original image $f(x)$ is expanded to $h(y)$.

Then, let $Gauss(z)$ and $\gamma(z)$ be the function that is defined by Eq. (4) and (5), respectively.

$$Gauss(z)=\frac{1}{\sqrt{2\pi\sigma^2}}\exp\left(-\frac{(z-\mu)^2}{2\sigma^2}\right). \tag{4}$$

$$\begin{aligned} y=\gamma(z)&=L\int_0^z Gauss(z)dz \\ &=\frac{1}{\sqrt{2\pi\sigma^2}}\int_0^z \exp\left(-\frac{(z-\mu)^2}{2\sigma^2}\right)dz. \end{aligned} \tag{5}$$

Here, Fig.1 shows the relationship between $y=\phi(x)$ and $y=\gamma(z)$. So we can be obtained following Eq. (6).

$$L\int_0^x f(x)dx=\frac{L}{\sqrt{2\pi\sigma^2}}\int_0^z \exp\left(-\frac{(z-\mu)^2}{2\sigma^2}\right)dz. \tag{6}$$

And we can derive Eq. (7) from differential of Eq. (6).

$$\frac{d}{dx}L\int_0^x f(x)dx=\frac{d}{dz}\frac{L}{\sqrt{2\pi\sigma^2}}\int_0^z \exp\left(-\frac{(z-\mu)^2}{2\sigma^2}\right)dz. \tag{7}$$

If we perform Eq. (7),

$$L\phi'(x)=L\gamma'(z),\quad f(x)=Gauss(z). \tag{8}$$

That is, we understand that $f(x)$ becomes Gaussian distribution $Gauss(z)$ when we take the transform function as (1) and (5). Thus, HMGD processing is the function which defined by cumulative histogram transformation the original histogram into Gaussian histogram[9].

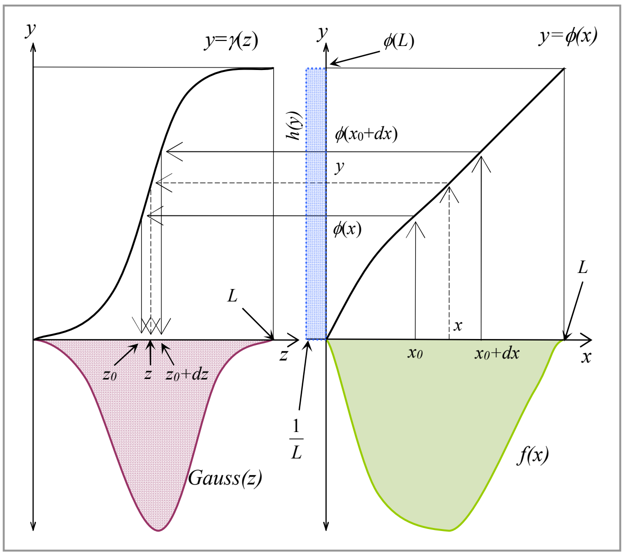

Fig. 1. Conceptual image of HMGD processing[6, 9].

2.2. *Peak Detection of Histogram*

The HMGD processing need to calculate transforms function for brightness peak of histogram. And the solution to detect it is curvature computation of the histogram.

Let y be a function with respect to x, the definition curvature $R(x)$ is given by Eq. (9)[6-9].

$$R(x)=\frac{d^2y}{dx^2}\left(1+\left(\frac{dy}{dx}\right)^2\right)^{-\frac{3}{2}}. \quad (9)$$

Let $g(x)$ and K be Gaussian distribution function and a coefficient which is defined by following equation, respectively.

$$g(x)=\frac{K}{\sqrt{2\pi\sigma^2}}\exp\left(-\frac{(x-a)^2}{2\sigma^2}\right), \quad (10)$$
$$\frac{K}{\sqrt{2\pi\sigma^2}}\int_0^L \exp\left(-\frac{(u-a)^2}{2\sigma^2}\right)du=1.$$

Next, let $y=f(x)$ be a function representing the cumulative histogram which is represented Eq. (11). That is, dy/dx and d^2y/dx^2 be described as Eq. (12) and (13), respectively. From Eq. (12) and (13), we obtain the approximation of curvature $R(x)$ as Eq. (14).

$$f(x)=\int_0^x g(u)du=\frac{K}{\sqrt{2\pi\sigma^2}}\int_0^x \exp\left(-\frac{(u-a)^2}{2\sigma^2}\right)du. \quad (11)$$

$$\frac{dy}{dx}=g(x)\frac{K}{\sqrt{2\pi\sigma^2}}\exp\left(-\frac{(u-a)^2}{2\sigma^2}\right). \quad (12)$$

$$\frac{d^2y}{dx^2}=\frac{dg(x)}{dx}=\frac{(a-x)}{\sigma^2}g(x) \quad (13)$$

$$R(x)=\frac{\frac{(a-x)}{\sigma^2}g(x)}{\left(1+g(x)^2\right)^{\frac{3}{2}}}\approx\frac{(a-x)}{\sigma^2}g(x). \quad (14)$$

From Eq. (14), we understand that the curvature $R(x)$ varies the sign according to the value of x.[9] That is, if $x<a \rightarrow R>0$ (downward convex shape), and if $x<a \rightarrow R<0$ (upward convex shape).

2.3. *Variance Estimation*

In this section, we propose how to estimate the variance of original-image histogram.

Fig. 2 shows the conceptual image of the original image histogram which is variance σ^2 and average a. From Eq. (14), we can describe $R(x)$ following Eq. (15).

$$R(x)\approx\frac{(a-x)}{\sigma^2}g(x)=\frac{1}{\sigma^2}(a-x)g(x). \quad (15)$$

And, let $C=1/\sigma^2$ and $H(x)=(a\text{-}x)g(x)$ respectively, we can derive Eq. (16).

$$R(x)\approx CH(x) \quad (16)$$

Now, we can calculate a constant C by using least-square regression analysis[10] following Eq. (17).

$$R_i=CH_i+\varepsilon_i, \quad \varepsilon_i\sim N(0,\sigma^2) \quad (i=1,\ldots n) \quad (17)$$

That is, we evaluate σ^2 as follows;

$$C=\frac{\sum_{i=1}^{n}(H_iR_i)}{\sum_{i=1}^{n}(H_i)^2}, \quad \sigma^2=\frac{1}{C} \quad (18)$$

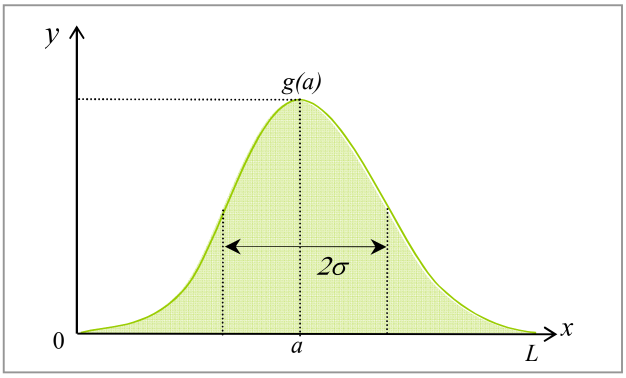

Fig. 2. Conceptual image of the original image histogram.

3. Experimentation

Fig. 3 shows the example of results and the corresponding histogram for original image and HMGD image which applied variance estimation using regression analysis.

In this case, we understand that HMGD image is reducing contrast than original image. And in the HMGD image, the color tones become unnatural.

(a) Image: Original (left) [5], Variance estimated HMGD (right)

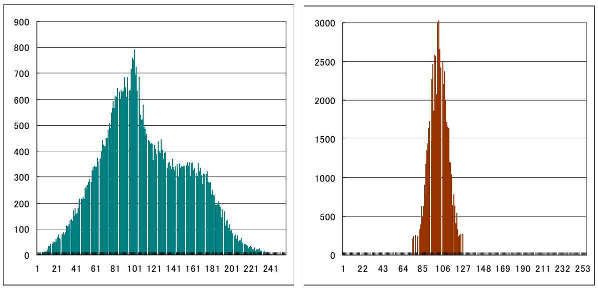

(b) Histogram: Original (left) [5], Variance estimated HMGD (right)

Fig. 3. Example of results and the corresponding histogram.

4. Conclusion

In this paper we proposed we have described that how to estimate the variance of reference histogram, which is used in HMGD processing by using regression analysis. As for the method, first we have detected the brightness peak on the original-image histogram. Then we have performed regression analysis based on the cumulative histogram and its curvature value.

Through the result of experimentation, the variance estimation based on the regression analysis image is reducing contrast than original one, and its color tones become unnatural. That is, we consider that we have to further improvement of this method.

References

1. R. C. Gonzalez and R. E. Woods, *Digital Image Processing* (Addison-Wesley Publishing Company, 1993).
2. B. Jahne, *Digital Image Processing --Concepts, Algorithms, and Scientific Applications-- 4th edition* (Springer, 1995).
3. E. S. Umbaugh, *Computer Vision and Image Processing: A Practical Approach Using CVIP tools* (Prentice Hall PTR, 1998).
4. W. Burger and J. M. Burge, *Principles of Digital Image Processing: Fundamental Techniques* (Springer 2009).
5. T. Izumi, T. Hattori, S. Sugimono, and T. Takashima, Color Image Arrangement Using Elastic Transform on Principal Component Axis (in Japanese), *Journal of Japan Society of Kansei Engineering* **8**(3) (2009) 667-674.
6. Y. Kawakami, T. Hattori, D. Kutsuna, H. Matsushita, Y. Imai, H. Kawano, R.P.C. Janaka Rajapakse, Automated Color Image Arrangement Method Based on Histogram Matching - Investigation of Kansei impression between HE and HMGD -, *International Journal of Affective Engineering* **14**(2) (2015) ISSN 2187-5413, 85-93.
7. Y. Kawakami, T. Hattori, Y. Imai, H. Matsushita, H. Kawano, R. P. C. Janaka Rajapakse, Kansei Impression and Automated Color Image Arrangement Method, *Journal of Robotics, Networking and Artificial Life* **1**(1) (2014) ISSN 2352-6386, 60-67.
8. Y. Kawakami, T. Hattori, Y. Imai, H. Matsushita, H. Kawano, and R. P. C. Janaka Rajapakse, Automated Color Image Arrangement Method Using Curvature Computation in Histogram Matching, in *Proceedings of International Conference on Artificial Life and Robotics* (ICAROB 2015) (Oita, Japan, 2015) ISBN 978-4-9902880-9-9, pp. 272-277.
9. Y. Kawakami, T. Hattori, Y. Imai, Y. Horikawa, H. Matsushita, R. P. C. Janaka Rajapakse, Automated Processing of Multiple-Brightness Peak Histogram Image Using Curvature and Variance Estimation, *Journal of Robotics, Networking and Artificial Life* **3**(1) (2016) ISSN 2352-6386, 55-60.
10. D. G. Kleinbaum, L. L. Kupper, A. Nizam, E. S. Rosenberg, *Applied Regression Analysis and Other Multivariable Methods* (Brooks/Cole Pub Co, 2013).

Histogram Matching Based on Gaussian Distribution Using Variance Estimation
- Comparing between Curvature Computation and Regression Analysis -

Yusuke Kawakami
DynaxT Co., Ltd., 2217-6 Hayashi
Takamatsu City, Kagawa 761-0301, Japan

Tetsuo Hattori, Yoshiro Imai, Kazuaki Ando, Yo Horikawa
Graduate School of Kagawa University, 2217-20 Hayashi
Takamatsu City, Kagawa 761-0396, Japan

R. P. C. Janaka Rajapakse
Tainan National University of the Arts, 66 Daci
Guantian District, Tainan 72045, Taiwan
E-mail: riverjp2002@gmail.com, {hattori imai, ando, horikawa}@eng.kagawa-u.ac.jp, janakaraja@gmail.com

Abstract

This paper describes variance estimation method comparing between regression analysis and curvature computation which is used in Histogram Matching based on Gaussian Distribution (HMGD). In the previous paper, we have described and illustrated that the variance estimation method have been considered of value for HMGD processing results. Though we have considered that histogram of original image is not always ideal. So, in this paper we propose improvement variance estimation method using regression analysis. First of all, we describe the principle of variance estimation methods using curvature computation, and regression analysis. Then, through some HMGD processing experiment, we compare between curvature computation results and regression analysis.

Keywords: Image processing, Curvature, Variance estimation, Histogram matching, HMGD

1. Introduction

These days, automated image processing for enhancement of color images has been more familiar to us, for example, Digital Signage, Smart Phone, etc [1-3].

In the previous paper, we have presented that the Histogram Matching based on Gaussian Distribution (HMGD) processing is one of the automated image arrangement method using Elastic Transformation [4-5] based on the brightness axis. And through the comparative investigation, we have illustrated that HMGD processing could improve feeling (or Kansei) impression better than original image[6]. And we have aimed to improve HMGD processing, we have proposed that how to estimate the variance of reference histogram, which is used in HMGD processing based on curvature computation, and also illustrated these results.

However, we have considered that the histogram of original image is not always ideal shape (i.e., Gaussian distribution, etc). That is, the variance estimation method based on curvature computation might not have high reliability.

In this paper, we describe principle of estimate brightness peak of the original image, and also describe two principle of variance method; (1) curvature computation based, (2) regression analysis based. Then, we illustrate some HMGD processing experiment and compare between curvature computation results and regression analysis results.

2. Principle

2.1. *Brightness Peak Detection of Original Image*

In the section, we describe the principle of brightness peak detection of original image.

The Histogram Matching based on the Gaussian Distribution[4-9] processing need to calculate transforms function for brightness peak of histogram. And the solution to detect it is curvature computation of the histogram.

Let y be a function with respect to x, the definition curvature $R(x)$ is given by Eq. (1)[6-9].

$$R(x)=\frac{d^2y}{dx^2}\left(1+\left(\frac{dy}{dx}\right)^2\right)^{-\frac{3}{2}}. \tag{1}$$

Let $g(x)$ and K be Gaussian distribution function and a coefficient which is defined by following equation, respectively.

$$g(x)=\frac{K}{\sqrt{2\pi\sigma^2}}\exp\left(-\frac{(x-a)^2}{2\sigma^2}\right), \quad \frac{K}{\sqrt{2\pi\sigma^2}}\int_0^L \exp\left(-\frac{(u-a)^2}{2\sigma^2}\right)du=1. \tag{2}$$

Next, let $y=f(x)$ be a function representing the cumulative histogram which is represented Eq. (3). That is, dy/dx and d^2y/dx^2 be described as Eq. (4) and (5), respectively. From Eq. (4) and (5), we obtain the approximation of curvature $R(x)$ as Eq. (6).

$$f(x)=\int_0^x g(u)du=\frac{K}{\sqrt{2\pi\sigma^2}}\int_0^x \exp\left(-\frac{(u-a)^2}{2\sigma^2}\right)du. \tag{3}$$

$$\frac{dy}{dx}=g(x)\frac{K}{\sqrt{2\pi\sigma^2}}\exp\left(-\frac{(u-a)^2}{2\sigma^2}\right). \tag{4}$$

$$\frac{d^2y}{dx^2}=\frac{dg(x)}{dx}=\frac{(a-x)}{\sigma^2}g(x) \tag{5}$$

$$R(x)=\frac{\frac{(a-x)}{\sigma^2}g(x)}{\left(1+g(x)^2\right)^{\frac{3}{2}}}\approx\frac{(a-x)}{\sigma^2}g(x). \tag{6}$$

From Eq. (6), we understand that the curvature $R(x)$ varies the sign according to the value of x [9]. That is, if $x<a \rightarrow R>0$ (downward convex shape), and if $x<a \rightarrow R<0$ (upward convex shape).

2.2. *Variance Estimation*

In this section, we describe how to optimize the shape of the reference histogram, which is used in the HMGD processing[9]. First, we explain the conventional method which is based on the curvature computation, and second, explain the proposed method which is based on the regression analysis.

2.1.1. *Variance Estimation based on the Curvature Computation*

Fig. 1 shows the conceptual image of the original image histogram which is variance σ^2 and average a. And Fig. 2 shows its cumulative histogram. From Eq. (2), we have the following Eq. (7) and Eq. (8).

$$g(a)=\frac{K}{\sqrt{2\pi\sigma^2}}=\frac{K}{\sigma\sqrt{2\pi}}. \tag{7}$$

$$g\left(a\pm\sqrt{2}\sigma\right)=\frac{K}{\sigma\sqrt{2\pi}}\exp\left(-\frac{\left(a\pm\sqrt{2}\sigma-a\right)}{2\sigma^2}\right)=g(a)e^{\mp1} \tag{8}$$

Then, the value of curvature R at $a\pm\sqrt{2}\sigma$ is represented Eq. (9).

$$R\left(a\pm\sqrt{2}\sigma\right)=\frac{\left(a-\left(a\pm\sqrt{2}\sigma\right)\right)}{\sigma^2}\frac{g\left(a\pm\sqrt{2}\sigma\right)}{\left(1+g\left(a\pm\sqrt{2}\sigma\right)^2\right)^{3/2}}=\left(\mp\frac{\sqrt{2}}{\sigma^2}\right)\frac{g(a)e^{-1}}{\left(1+\left(g(a)e^{-1}\right)^2\right)^{3/2}} \tag{9}$$

Let $S=g(a)e^{-1}$, we have Eq. (10).

$$R\left(a \pm \sqrt{2}\sigma\right) = \left(\mp \frac{\sqrt{2}}{\sigma}\right) \frac{S}{\left(1+S^2\right)^{3/2}} \equiv \left(\mp \frac{\sqrt{2}}{\sigma}\right) H. \tag{10}$$
$$H = \frac{S}{\left(1+S^2\right)^{3/2}} = \frac{g(a)e^{-1}}{\left(1+\left(g(a)e^{-1}\right)^2\right)^{3/2}}.$$

That is, we understand that we can obtain reference histogram variance σ^2. For example, let $v = \sqrt{2}\sigma$ be the distance from average a,

$$R(a-v) - R(a+v) = \frac{2\sqrt{2}}{\sigma} H = \frac{4}{v} H, \quad \sigma^2 = \frac{v^2}{2}. \tag{11}$$

2.1.2. *Variance Estimation based on the Regression Analysis*

In the previous subsection, we show the Fig. 1 as the conceptual image of the original image histogram which is variance σ^2 and average a. From Eq. (6), we can describe $R(x)$ following Eq. (12).

$$R(x) \approx \frac{(a-x)}{\sigma^2} g(x) = \frac{1}{\sigma^2}(a-x)g(x). \tag{12}$$

And, let $C=1/\sigma^2$ and $H(x) = (a-x)g(x)$ respectively, we can derive Eq. (13).

$$R(x) \approx CH(x) \tag{13}$$

Now, we can calculate a constant C by using least-square regression analysis[10] following Eq. (14).

$$R_i = CH_i + \varepsilon_i, \quad \varepsilon_i \sim N\left(0, \sigma^2\right) \quad (i = 1, \ldots n) \tag{14}$$

Thus, we can evaluate σ^2 as following Eq. (15).

$$C = \frac{\sum_{i=1}^{n}(H_i R_i)}{\sum_{i=1}^{n}(H_i)^2}, \quad \sigma^2 = \frac{1}{C} \tag{15}$$

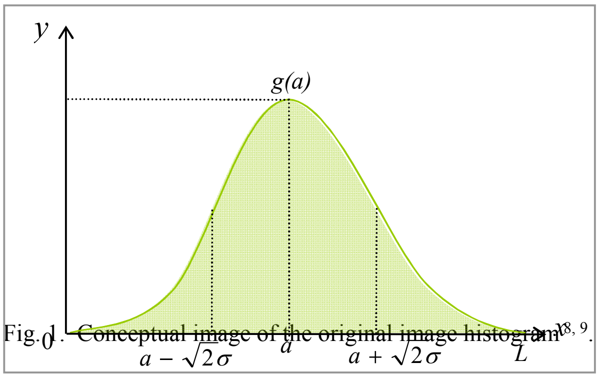

Fig. 1. Conceptual image of the original image histogram[8, 9].

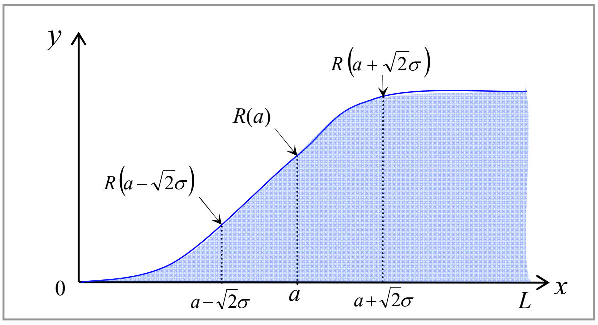

Fig. 2. Conceptual image of the original image cumulative histogram[8, 9].

3. Experimentation

Fig. 3 shows the example of results and the corresponding histogram for original image and for HMGD image which applied variance estimation, respectively.

In this case, we understand that HMGD which applied curvature computation based variance estimation image is softer and more natural contrast and than original image. However, HMGD which applied regression analysis based variance estimation image is reducing contrast than original image, and the color tones become unnatural.

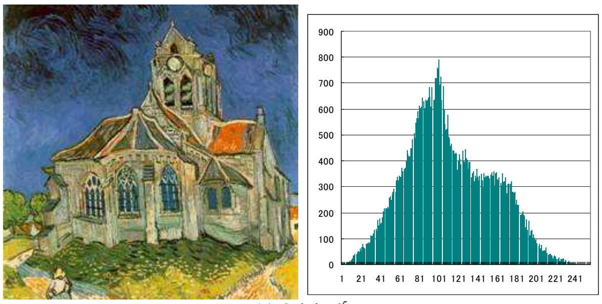

(a) Original[5].

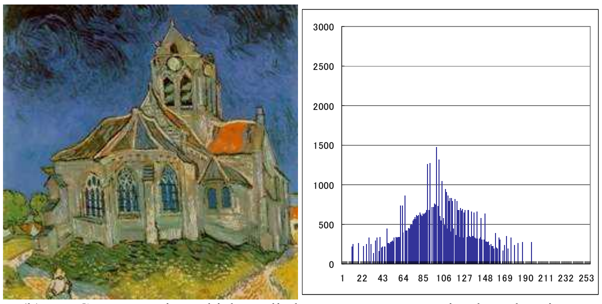

(b) HMGD processing which applied curvature computation based variance estimation[5].

(c) HMGD processing which applied regression analysis based variance estimation.

Fig. 3. Example of results (left) and the correspondence histogram (right).

4. Conclusion

In this paper we described the principle of brightness peak detection, estimate the variance of reference histogram, which is used in HMGD processing by using curvature computation, and we propose variance estimation based on the regression analysis.

Through the comparing experimentation, HMGD processing image which applied variance estimation based on the curvature computation image is becomes soften and natural contrast from original. In contrast, HMGD processing image which applied the variance estimation based on the regression analysis image is reducing contrast than the others, and its color tones become unnatural. That is, we consider that we have to improve algorithm of variance estimation based on the regression analysis.

References

1. R. C. Gonzalez and R. E. Woods, *Digital Image Processing* (Addison-Wesley Publishing Company, 1993).
2. B. Jahne, *Digital Image Processing --Concepts, Algorithms, and Scientific Applications-- 4th edition* (Springer, 1995).
3. E. S. Umbaugh, *Computer Vision and Image Processing: A Practical Approach Using CVIP tools* (Prentice Hall PTR, 1998).
4. W. Burger and J. M. Burge, *Principles of Digital Image Processing: Fundamental Techniques* (Springer 2009).
5. T. Izumi, T. Hattori, S. Sugimono, and T. Takashima, Color Image Arrangement Using Elastic Transform on Principal Component Axis (in Japanese), *Journal of Japan Society of Kansei Engineering* **8**(3) (2009) 667-674.
6. Y. Kawakami, T. Hattori, D. Kutsuna, H. Matsushita, Y. Imai, H. Kawano, R.P.C. Janaka Rajapakse, Automated Color Image Arrangement Method Based on Histogram Matching - Investigation of Kansei impression between HE and HMGD -, *International Journal of Affective Engineering* **14**(2) (2015) ISSN 2187-5413, 85-93.
7. Y. Kawakami, T. Hattori, Y. Imai, H. Matsushita, H. Kawano, R. P. C. Janaka Rajapakse, Kansei Impression and Automated Color Image Arrangement Method, *Journal of Robotics, Networking and Artificial Life* **1**(1) (2014) ISSN 2352-6386, 60-67.
8. Y. Kawakami, T. Hattori, Y. Imai, H. Matsushita, H. Kawano, and R. P. C. Janaka Rajapakse, Automated Color Image Arrangement Method Using Curvature Computation in Histogram Matching, in *Proceedings of International Conference on Artificial Life and Robotics* (ICAROB 2015) (Oita, Japan, 2015) ISBN 978-4-9902880-9-9, pp. 272-277.
9. Y. Kawakami, T. Hattori, Y. Imai, Y. Horikawa, H. Matsushita, R. P. C. Janaka Rajapakse, Automated Processing of Multiple-Brightness Peak Histogram Image Using Curvature and Variance Estimation, *Journal of Robotics, Networking and Artificial Life* **3**(1) (2016) ISSN 2352-6386, 55-60.
10. D. G. Kleinbaum, L. L. Kupper, A. Nizam, E. S. Rosenberg, *Applied Regression Analysis and Other Multivariable Methods* (Brooks/Cole Pub Co, 2013).

An Extended Optimal Stopping Method for Structural Change Point Detection Problem

Yoshihide Koyama
Kagawa University, 2217-20 Hayashi Cho
Takamatsu City, Kagawa 761-0396, Japan

Tetsuo Hattori, Yoshiro Imai, Yo Horikawa, Yusuke Kawakami
Kagawa University, 2217-20 Hayashi Cho
Takamatsu City, Kagawa 761-0396, Japan

Hiromichi Kawano
NTT advanced technology Company Ltd, Mitaka, Tokyo, Japan
E-mail: {hattori, imai, horikawa}@eng.kagawa-u.ac.jp, hiromichi.kawano@ntt-at.co.jp

Abstract

Previously, we have proposed and formulated the SCPD (Structural Change Point Detection) problem in time series data as an Optimal Stopping one using the concept of DP (Dynamic Programming). And also we have shown the solution theorem in the form of inequality. In this paper, based on the relation between the solution of Optimal Stopping and NSPRT (New Sequential Probability Ratio Test), we present the extended Optimal Stopping Method in order to obtain more practical one, considering a loss cost and an action cost involved by failure prediction.

Keywords: Time series data, Structural change point detection, Optimal stopping problem, NSPRT (New Sequential Probability Ratio Test)

1. Introduction

There are three stages to be considered for ongoing time series analysis as follows;

(i) the stage of prediction model construction,

(ii) the stage of structural change detection (and/or disparity detection between the model and observing data),

(iii) the stage of renewal of prediction model.

Above all, it is very important to detect the change point as quickly and correctly as possible in the second stage, in order to renew the accurate prediction model as soon as possible after the change detection.

For the problem of the structural change point detection (SCPD) problem, or change point detection (CPD), some methods have been proposed [1-4]. The standard well known method is Chow Test used in econometrics[2]. Chow Test carries out a statistical test by setting the hypothesis that the change has occurred at time t for all of data obtained so far.

As for the SCPD problem, we have previously formulated the change detection method as a solving method for Optimal Stopping Problem with an action cost, using the concept of DP (Dynamic Programming) [5-6]. Moreover, we have proposed a model-introduced SPRT (Sequential Probability Ratio Test) as a New Sequential Probability Ratio (NSPR) test method[7-8].

In this paper, we extend the Optimal Stopping Problem as a more general problem, and we show the extended solution. Moreover, we present the relation between NSPR and the extended optimal solution theorem for SCPD.

2. Definitions and Equations

2.1. *Structural Change Model* [5-6]

We assume that the structural change is Poisson occurrence of average λ, and that, once the change has occurred during the observing period, the structure does not go back to the previous one. The reason why we set such a model is that we focus on the detection of the first structural change in the sequential processing (or sequential test). The concept of the structural change model is shown in Fig. 1.

Moreover, we introduce a more detailed model. Let R be the probability of the failing when the structure is unchanged. Let Rc be the probability of the failing when the structure change occurred. We consider that Rc is greater than R, i.e., $Rc>R$. The detailed model for the State Ec and E are illustrated as similar probabilistic finite state automatons in Fig.2 and Fig.3, respectively.

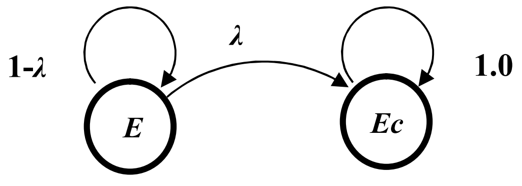

***Ec* :** State that the structural change occurred.
***E* :** State that the structure is unchanged.
λ : Probability of the structural change occurrence. (Poisson Process.)

Fig.1. Structural change model.

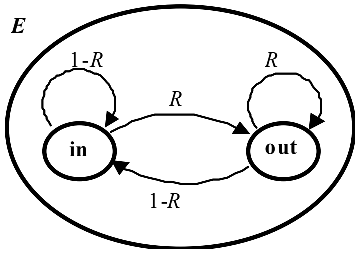

Fig.2. Internal model of the State E.

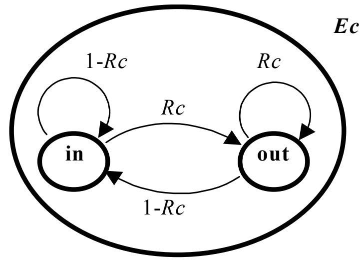

Fig.3. Internal model of the State Ec.

2.2. *Optimal Stopping Formulation and its Slution Theorem* [5-6]

Let the cost(n) be $a \cdot n$ as a linear function for n, where a is the loss caused by the one-time prediction failure. And for simplicity, let T and A denote the Total loss cost and an involved action cost, respectively. Then, the evaluation function is denoted as the following equation (1).

$$T = A + a \cdot n \tag{1}$$

We recursively define a function $ET(n, N)$ to obtain the optimum number of times n that minimizes the expectation value of the evaluation function of Equation (3), using the concept of DP (Dynamic Programming). Let N be the optimum number. Let the function $EC(n, N)$ be the expectation value of the evaluation function at the time when the failing has occurred in continuing n times, where n is less than or equal to N, i.e., $0 \leq n \leq N$.

Thus the function is recursively defined as follows.

$$(\text{if } n = N)\ \ ET(n,N) = A + a \cdot N \tag{2}$$

$$(\text{if } n < N)\ \ ET(n,N) = P(\overline{S}_{n+1} \mid S^n) \cdot a \cdot n + (1 - P(\overline{S}_{n+1} \mid S^n)) ET(n+1,N) \tag{3}$$

where S^n means the state of failing in continuing n times, $\overline{S}_{n+1}$ the state of hitting at the (n+1) th observed data, and $P(\overline{S}_{n+1} \mid S^n)$ means the conditional probability that the state $\overline{S}_{n+1}$ occurs after the state S^n.

The first term in the right-hand side (RHS) of the equation (3) indicates the expectation value of the evaluation function at the time when hitting happens at the (n+1)th data after the continuing n times failing. The second term in the RHS of the equation (3) indicates the expectation value of the evaluation function for the time when failing happens at the (n+1)th data after continuing n times failing.

Then, from the definition of the function $ET(n,N)$, the goal is to find the N that minimizes $ET(0,N)$, because the N is the same as n that minimizes the expectation value of the evaluation function of (1).

[Optimal Solution Theorem (OST)]

The N that minimizes $ET(\underline{0},N)$ is given as the largest number n that satisfies the following Inequality (4).

$$a < (A + a) \cdot P(\overline{S}_n \mid S^{n-1}) \tag{4}$$

where the number N+1 can also be the optimum one that minimizes $ET(0,N)$, i.e., $ET(0,N) = ET(0,N+1)$, only if

$$a = (A + a) \cdot P(\overline{S}_{N+1} \mid S^N)$$

2.3. *Extended Optimal Stopping Formulation*

We extend the meaning of the loss a as the average of loss cost a^* caused by the "so far n-time prediction failure". The "so far n-time prediction failure" does not mean the continuous n-time prediction failure[9]. And A means the loss cost involved by some action, e.g., renewal and/or disposal of some equipments and/or some systems after the structural change point detection.

Then, S^n does not mean "the state of failing in continuing n times", but means "the state of so far n-times prediction failure". Thus we obtain an extended OST as follows.

[Extended Optimal Solution Theorem (EOST)]

The N that minimizes $ET(\underline{0},N)$ is given as the largest number n that satisfies the following Inequality (5).

$$a^* < (A + a^*) \cdot P(\overline{S}_n \mid S^{n-1}) \tag{5}$$

where the number N+1 can also be the optimum one that minimizes $ET(0,N)$, i.e., $ET(0,N) = ET(0,N+1)$, only if

$$a^* = (A + a^*) \cdot P(\overline{S}_{N+1} \mid S^N)$$

2.4. *New Sequential Probability Ratio (NSPR) Based on Structural Change Model* [7-9]

Let $a_1 a_2, \ldots, a_i, \ldots a_n \quad a_i \in \{\text{IN}, \text{OUT}\}$ be a string (or symbol sequence) obtained from the observed data.

Let θ_i and $\tilde{\theta}_i$ be the conditional probability that outputs the observed data (or above symbol sequence, $C_n = a_1 a_2 \ldots a_n$ in the state ***S*0** and ***S*1**, respectively. That is, it means that $\theta_i \in \{R, 1-R\}$ and $\tilde{\theta}_i \in \{R_c, 1-R_c\}$, respectively.

And let $P(a_1 \ldots a_n, \mathrm{H}_0)$ and $P(a_1 \ldots a_n, \mathrm{H}_1)$ be the joint probability of the symbol sequence C_n happens with the event H_0 (the structural change is not occurred) and H_1 (the change is occurred), respectively.

Then, the following New Sequential Probability Ratio (NSPR) Λ_n is represented as the following Eq.(6).

$$NSPR\ \Lambda_n = \frac{P(\mathrm{H}_1 \mid a_1 \ldots a_n)}{P(\mathrm{H}_0 \mid a_1 \ldots a_n)} = \frac{P(\mathrm{H}_1 \mid C_n)}{P(\mathrm{H}_0 \mid C_n)} = \frac{P(C_n, \mathrm{H}_1)}{P(C_n, \mathrm{H}_0)} = \frac{\sum_{k=1}^{n} ((1-\lambda)^{k-1} \cdot \prod_{j=0}^{k-1} \theta_j)(\lambda \prod_{i=k}^{n} \tilde{\theta}_i)}{(1-\lambda)^n \prod_{i=1}^{n} \theta_i} \tag{6}$$

From Eq.(6), we have the following recursive equation (7).

$$\Lambda_n = \frac{1}{1-\gamma} (\Lambda_{n-1} + \gamma)\left(\frac{\tilde{\theta}_n}{\theta_n}\right)$$

$$\text{where} \quad \theta_0 = 1,\ \tilde{\theta}_0 = 1, \Lambda_0 = 0 \tag{7}$$

If the NSPR is greater than 1.0, we can regard that the structural change has been occurred before the present time.

3. Relation between NSPR and EOST

We show the relations using the probability in the Extended Optical Solution Theorem, considering $R_c >> R$.

$$P\left(\overline{S_{n+1}} \mid S^n\right) = (1-R)\left(1 - P\left(E_{cn} \mid S^n\right)\right) + (1-R_c)P\left(E_{cn} \mid S^n\right)$$
$$= (1-R) - P\left(E_{cn} \mid S^n\right)(R_c - R) \qquad (8)$$

Therefore, we have

$$P\left(E_{cn} \mid S^n\right) = \frac{(1-R) - P\left(\overline{S_{n+1}} \middle| S^n\right)}{(R_c - R)},$$
$$P\left(E \mid S^n\right) = \frac{P\left(\overline{S_{n+1}} \mid S^n\right) - (1-R_c)}{(R_c - R)} \qquad (9)$$

Since

$$P\left(E_{cn} \mid S^n\right) = P\left(H_1 \mid S^n\right), \quad P\left(E \mid S^n\right) = P\left(H_0 \mid S^n\right)$$

we have

$$\Lambda_n = \frac{P\left(H_1 \mid S^n\right)}{P\left(H_0 \mid S^n\right)} = \frac{(1-R) - P\left(\overline{S_{n+1}} \mid S^n\right)}{P\left(\overline{S_{n+1}} \mid S^n\right) - (1-R_c)} \qquad (10)$$

If $P\left(\overline{S_{n+1}} \middle| S^n\right)$ is a monotonous decreasing function with respect to n, NSPR becomes an increasing one. From the EOST, the optimal N is the maximum n that satisfies (5), so the N is the the maximum n that satisfies the following Inequality (11).

$$\Lambda_n = \frac{P\left(H_1 \middle| S^n\right)}{P\left(H_0 \middle| S^n\right)} < \Theta \equiv \frac{\left(\frac{A}{A+a^*}\right) - R}{R_c - \left(\frac{A}{A+a^*}\right)} \qquad (11)$$

If $R = 0.05, R_c = 0.9, A = 10, a^* = 1$, then we have the threshold $\Theta = 21.5$.

4. Conclusion

We have proposed the extended Optimal Stopping Formulation for the SCPD problem and its extended solution theorem. Moreover, we have presented the relation between New Sequential Probability Ratio (NSPR) method and the Extended Optimal Solution Theorem. From this relation, we can use the NSPR as an extended optimal stopping method for structural change point detection in ongoing time series data.

References

1. R.Jana and S.Dey, Change detection in Teletraffic Models, *IEEE Trans. Signal Processing*, vol.48, No.3, pp.846-853, 2000.
2. Chow,G.C., Tests of Equality Between Sets of Coefficients in Two Linear Regressions, *Econometrica*, Vol.28, No.3, pp.591-605, 1960.
3. S.MacDougall, A.K. Nandi and R.Chapman, Multisolution and hybrid Bayesian algorithms for automatic detection of change points, *Proc. of IEEE Visual Image Signal Processing*, vol.145, No.4, pp.280-286, 1998.
4. E.S.Page, Continuous inspection schemes, *Biometrika*, Vol.41, pp.100-115, 1954.
5. Tetsuo Hattori, Katsunori Takeda, Izumi Tetsuya, Hiromichi Kawano, "Early Structural Change Detection as an Optimal Stopping Problem (I) --- Formulation Using Dynamic Programming with Action Cost ----", *Proc. of the 15th International Symposium on Artificial Life and Robotics (AROB15th'10)*, ISBN 978-4-9902880-4-4, pp.763-766, 2010.
6. Hiromichi Kawano, Tetsuo Hattori, Katsunori Takeda, Izumi Tetsuya, "Early Structural Change Detection as an Optimal Stopping Problem (II) --- Solution Theorem and its Proof Using Reduction to Absurdity ----", *Proc. of the 15th International Symposium on Artificial Life and Robotics (AROB15th'10)*, ISBN 978-4-9902880-4-4, pp.767-772, 2010.
7. Yoshihide Koyama, Tetsuo Hattori, Hiromichi Kawano, “Model Introduced SPRT for Structural Change Detection of Time Series (I)”, *Journal of Robotics, Networks and Artificial Life* (ISSN: 2352-6386), Vol.1, No.1, pp.55-60 (Atlantis Press, Jun. 2014)
8. Yoshihide Koyama, Tetsuo Hattori, Katsunori Takeda, Hiromichi Kawano, “Model Introduced SPRT for Structural Change Detection of Time Series (II)”, *Journal of Robotics, Networks and Artificial Life* (ISSN: 2352-6386), Vol.1, No.3, pp.237-243 (Atlantis Press, Dec. 2014).
9. Tetsuo Hattori, Yoshihide Koyama, Yusuke Kawakami, Yoshiro Imai, Yo Horikawa, Hiromichi Kawano: "Relation between Optimal Stopping Solution and NSPR for Structural Change Point Detection Problem”, *Proc. of The 2016 International Conference on Artificial Life and Robotics* (*ICAROB 2016*), ISBN 978-4-9908350-1-9, pp.44-47, Jan. 29-31, Okinawa, Japan.

A Study of Sentimental Value Analysis for Tweeting Message

Shunsuke Doi, Shinya Hara, Yoshiro Imai, Tetsuo Hattori
Department of Electronics and Information, Faculty of Engineering, Kagawa University
2217-20 Hayashi-cho Takamatsu City, Kagawa pref 761-0396, Japan

Yusuke Kawakami
DynaxT Co., Ltd.
2271-6 Hayashi-cho Takamatsu City, Kagawa pref. 761-0113, Japan
E-mail: {s13t243, 13t258y}@stmail.eng.kagawa-u.ac.jp, {imai, hattori}@eng.kagawa-u.ac.jp
riverjp2002@gmail.com

Abstract

In the recent years, social media analysis has brought several kinds of effective results to us in the domains of industries, education, social science, economics, and so on. This study focuses on Twitter used by students of universities, analyzes tweeting data (messages) by students from Twitter, and calculates sentimental values from the according data. Our approach includes deciding to select and cheese suitable Twitter accounts who tweet interesting messages and acquire a possible mount of their relevant message, specifying and defining value for word of messages for sentimental dictionary, categorizing and listing such a calculated value for each word or expression as item of the dictionary, using these values as "Sentimental Values" for calculation of tweeting messages, calculating Sentimental Values for tweeting message from students of selected universities, checking statistical relation between the above "Sentimental Values" and published data. It also investigates existence of some relations between calculated sentimental values and practical thought of students. At the same time, it tries to discuss whether the above procedure and analysis can visualize conventionally hidden relationship between contents of tweeting messages and characteristic behavior of students in categorized universities.

Keywords: Twitter, Sentiment analysis, Data mining, Visualization, Hidden relation.

1. Introduction

In recent years, young people use social media such as Twitter. And information processing for social media can bring several kinds of effective results to us in the domains of industries, education, social science, economics, and so on. We can expect that our current environment will bring us useful facilities to analyze messages from Twitter based on data mining[1] and their attractive results to visualize normally hidden relations among several kinds of events and phenomena.

This study is to perform some kind of Big Data Analysis[2] as an example of visualization of sentimental words extracted from messages of Twitter and to analyze hidden or unknown relation between sentimental value and the relevant behavior/phenomena. We have defined translation scheme from words in Twitter's message into sentimental values, applied the scheme into data mining with calculation of sentimental values for tweeting messages acquired from Twitter, and demonstrated relation between sentimental values and categorized human behavior.

This paper includes the following five sections, namely the next section describes our related works, the third section illustrates our approach of sentiment analysis for Twitter, the fourth section discusses our results and their visualization of relation between sentimental values and behavior/phenomena, and finally the last section summarizes our conclusion.

2. Related Work

This section introduces some related works about twitter-based data-mining, knowledge discovery and sentiment analysis.

Ley Zhang of HP Laboratory reported in their article[3] “With the booming of microblogs on the Web, people have begun to express their opinions on a wide variety of topics on Twitter and other similar services. Sentiment analysis on entities (e.g., products, organizations, people, etc.) in tweets (posts on Twitter) thus becomes a rapid and effective way of gauging public opinion for business marketing or social studies. However, Twitter's unique characteristics give rise to new problems for current sentiment analysis methods, which originally focused on large opinionated corpora such as product reviews.”

Mikalai Tsytsarau and Themis Palpanas described in their journal article[4] “In the past years we have witnessed Sentiment Analysis and Opinion Mining becoming increasingly popular topics in Information Retrieval and Web data analysis. With the rapid growth of the user-generated content represented in blogs, wikis and Web forums, such an analysis became a useful tool for mining the Web, since it allowed us to capture sentiments and opinions at a large scale. Opinion retrieval has established itself as an important part of search engines. Ratings, opinion trends and representative opinions enrich the search experience of users when combined with traditional document retrieval, by revealing more insights about a subject. Opinion aggregation over product reviews can be very useful for product marketing and positioning, exposing the customers' attitude towards a product and its features along different dimensions, such as time, geographical location, and experience.”

Alexandra Balahur of European Commission Joint Research Centre pointed out in her international conference paper[5] “This paper presents a method for sentiment analysis specifically designed to work with Twitter data (tweets). The main contributions of this work are: a) the pre-processing of tweets to normalize the language and generalize the vocabulary employed to express sentiment; b) the use minimal linguistic processing, which makes the approach easily portable to other languages; c) the inclusion of higher order n-grams to spot modifications in the polarity of the sentiment expressed; d) the use of simple heuristics to select features to be employed; e) the application of supervised learning using a simple Support Vector Machines linear classifier on a set of realistic data.”

Referring the above works and our previous research, we have tried to apply sentiment analysis and visualize normally hidden relation between sentimental values and behavior/phenomena.

3. Sentimental Analysis as Data Mining

Schematic diagram of our sentimental analysis flow can be illustrated and explained in Fig.1. We have focused on specific data based on speakers' attributes as target users. After connecting Twitter as Web-based Social Media, our system has acquired an amount of data to be analyzed with "twpro API" and "Twitter API". With these data, the main part of our system, which is constructed with multiple numbers (#1-#n) of modules, performs a series of manipulations for information processing from data into generated results which include some temporary files.

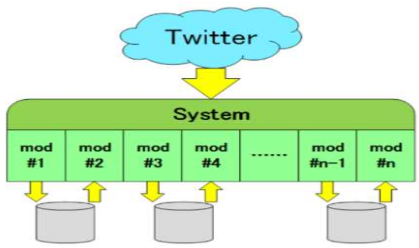

Fig.1. Schematic Diagram for System Configuration of Data Mining of Tweeting Message and Sentimental Analysis.

From top to bottom in Fig.2, our system sequentially defines target users of Twitter, obtains tweeting messages from defined users, prepares Sentimental dictionary based on those messages, computes sentimental values for each users, and then generates sets of such values focused groups (universities in our case). This part is the main body of our system, showing "System Configuration and Processing Flow" and can

accomplish some kind of sentiment analysis and generate our interesting results. We have obtained related relation between the above files based on messages from Twitter.
With the sentimental value for each university, we will compare the published data and try to visualize normally hidden relation between tweeting messages and behavior and/or phenomena in the next section.

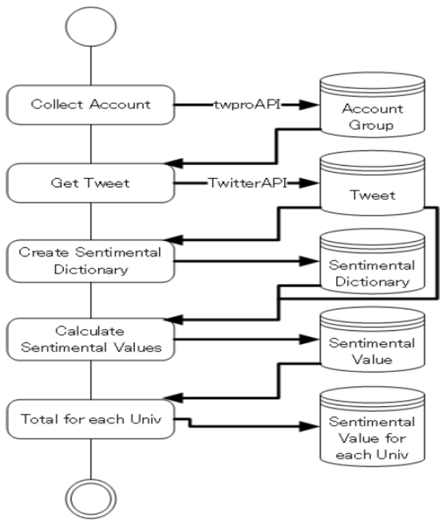

Fig.2. System Flow of Data Mining of Tweeting Message and Sentimental Analysis with Dictionary of Sentiment Value.

4. Results and Discussion

This section compares results in 2014 and 2015 and then discusses comparison of sentimental values in 2014 and 2015.

4.1. *Comparison of analyzed results in 2014 and 2015*

For the cases of 2014 and 2015, we have compared our normalized sentimental values (from 0.0 to 1.0) with the numbers of Starbucks Coffee shop and show the results in Fig.3 and Fig.4 respectively. Our normalized sentimental values have characteristics where the range from 0.0 to 0.5 means negative feelings and the range from 0.5 to 1.0 means positive ones.
Fig.3 may describe that there is negatively-correlated between negative sentimental values and numbers of Starbucks Coffee shops. In 2014, students of university located in the city which has relatively more numbers of Starbucks Coffee shops, urban in other words, used to tweet relatively negative messages.

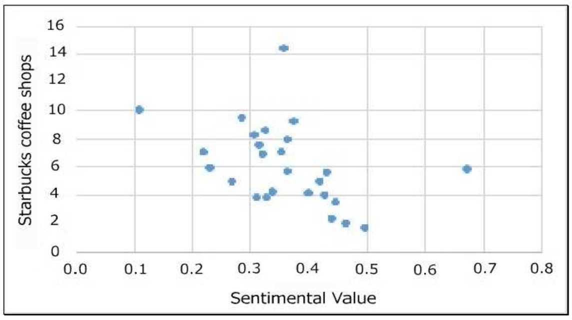

Fig.3. Relation between Sentimental values and numbers of Starbucks Coffee shops.

The next year, 2015, we have faced to the different phenomena. When we dare to ignore narrow range of sentimental values from 0.4 to 0.5 in Fig.4, it may also describe that there seems to be positively-correlated between positive sentimental values and numbers of Starbucks Coffee shops. In 2015, students of university located in the city which has relatively more numbers of Starbucks Coffee shops, namely urban, have changed to tweet relatively positive messages.

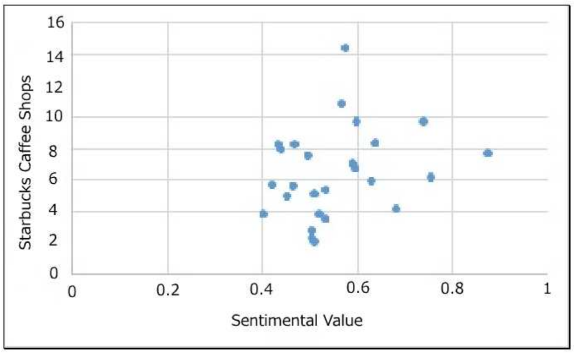

Fig.4. Relation between Sentimental values and numbers of Starbucks Coffee shops.

4.2. *Discussion of Sentimental Values in 2014 and 2015*

By comparison with results in 2014 and 2015, we discuss our approach of sentimental analysis. Table 1 shows our results of sentimental analysis for tweeting messages from students of previously defined universities, whose identifier, IDs are specified from 001 to 026 in Table 1.In 2014, there is only one, ID=018, whose score of sentimental values is more than 0.5, namely others are less than 0.5, so almost in 2014 have tweeted negative messages. In 2015, sentimental values have varied from 0.4 to 0.90 approximately. Fig.5. shows bar chart about normalized sentimental values in 2014 and 2015. Generally speaking, such values in 2014 are relatively lower than ones in 2015.

We can assume that two patterns of relations between 2014 and 2015. One pattern is a group of students who have tweeted negatively in 2014 and 2015. Another includes students who have tweeted negatively in 2014 but done positively in 2015. Fig.6 demonstrates that targets can be divided into two groups described before.

Table 1. Sentimental Values in 2014 and 2015.

ID	2014	2015	ID	2014	2015
001	0.398	0.682	014	0.462	0.509
002	0.362	0.420	015	0.439	0.503
003	0.328	0.402	016	0.352	0.591
004	0.447	0.533	017	0.374	0.739
005	0.109	0.567	018	0.672	0.595
006	0.321	0.875	019	0.431	0.464
007	0.325	0.638	020	0.495	0.504
008	0.418	0.451	021	0.338	0.509
009	0.229	0.628	022	0.311	0.518
010	0.364	0.439	023	0.306	0.434
011	0.428	0.532	024	0.268	0.753
012	0.218	0.467	025	0.284	0.599
013	0.313	0.497	026	0.357	0.574

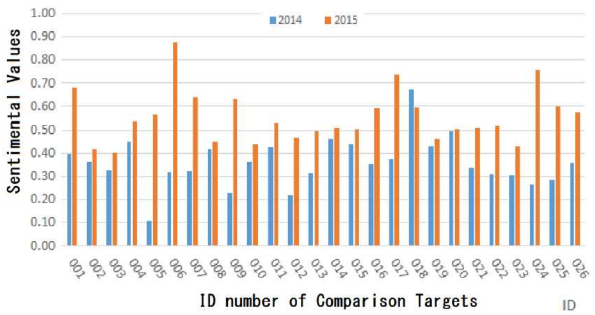

Fig.5. Bar Chart of Sentimental values in 2014 and 2015.

5. Conclusion

We have tried to demonstrate and visualize normally hidden or unknown relations between messages from Twitter and information of published documents by means of sentimental analysis. For example, we have been analyzing relationship between sentimental analyzed results and several information from the above documents, such as population of district, number of governmental universities' students, number of Starbucks coffee shops, and so on.

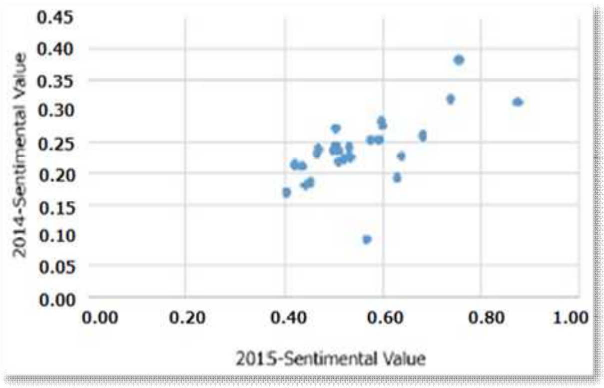

Fig.6. Relation between Sentimental values in 2014 and 2015.

References

1. A. K. Choudhary, J. A. Harding and M. K. Tiwari, Data mining in manufacturing: a review based on the kind of knowledge, *J. Intelligent Manufacturing*, 20(5) (Oct. 2009) pp. 501–521.
2. S. C. Lewis, R. Zamith and A. Hermida, Content Analysis in an Era of Big Data: A Hybrid Approach to Computational and Manual Methods. *J. Broadcasting & Electronic Media*, 57(1) (2013) pp. 34–52.
3. L. Zhang, R. Ghosh, M. Dekhil, M. Hsu and B. Liu, Combining Lexicon-Based and Learning-Based Methods for Twitter Sentiment Analysis, *Technical report*, HP Laboratories, (2011) 7 pages. http://www.hpl.hp.com/techreports/2011/HPL-2011-89.pdf
4. M. Tsytsarau and T. Palpanas, Survey on mining subjective data on the web, *J. Data Mining and Knowledge Discovery* 24(3) (May 2012) pp.478-514.
5. Alexandra Balahur, Sentiment and Social Media Analysis, in *Proc. 4th Workshop on Computational Approaches to Subjectivity* (June 2013) pp. 120-128.

Molecular Artificial Intelligence by using DNA reactions

Yasuhiro Suzuki
Graduate School of Information Science, Nagoya, University, Furocho, Chikusa
Nagoya City, 464-8601, Japan

Rie Taniguchi
Graduate School of Informatin Science, Nagoya University, Furocho Chikusa,
Nagoya City, 464-8601, Japan
E-mail: ysuzuki@nagoya-u.jp, mesomokyuu@gmail.com
http://sci-of-harness.info

Abstract

We have developed molecular Artificial Intelligence system by using DNA molecules, where "intelligence" means that the reaction system can "select" DNA molecules to sustain their reactions. We have bio-chemically implemented the reaction system by using the DNA strand-displacement reaction and have obtained several mutated DNA sequences that can sustain the reactions. We confirmed that when we give non-mutated input and mutated input sequences (the system can also use them as input), the system is able to select higher concentration one, regardless of it having mutation or not. And we confirmed that reaction behaviors in the time series of concentration of non-mutated input and mutated input show oscillations; it would show that the system selects higher concentration one in between non-mutated and mutated one according to its concentration. Since the system exhibits adaptive autonomous behaviors, this DNA reaction networks system realize molecular Artificial Intelligence.

Keywords: Molecular Robotics, Molecular Artificial Intelligence, DNA computing, Seesaw gate

1. Introduction

The aim of this contribution is composing *molecular artificial intelligence, molecular AI* for molecular robots that are made by organic materials such as DNA or proteins.

It has been developed *bio-computers*; various bio-computers with natural media such as DNA, slime molds have been realized; and many kinds of *parts* to synthesize a bio-computer, by using mainly DNA, such as logic gates or circuits have been produced. Based on these progresses, molecular robots have been created.

On the definition of intelligence has been discussed not only in AI but also in philosophy and there have proposed many standpoints and definitions from each of them. We will take the standpoint proposed by *Kazuhisa Todayama* [1] and *Ruth Millican* [2]; in order let *systems* to be *autonomous* likewise a living systems, (there are several requirements that they proposed but) one main requirement is having problems to take care of themselves; such problems are affordable from its environment including us; for example, an electric robot needs electric power supply, in the most of cases, users of the robot (environment) take care of and recharge it or pre-programmed in the robot to go to recharge place themselves, such as a *clean robot* [3].

Their claim is that in order let the robot to be autonomous, we should give only minimal *settings* to adapt its environment; it almost impossible to give such a perfect minimal setting so Millican claims that evolution mechanisms are irreducible to refine the minimal settings by evolutional searching with *mutations* and *natural selections* [2].

On this standpoint, we reconsider *what is intelligence of living systems?*; living systems in wild life must select appropriate food sources from the environment; even if *parents* do not teach appropriate and not *toxic* foods, even if they have *instructors* or not, must select appropriate one and avoid harmful ones, otherwise will go extinct. Hence *select-ability, ability to make appropriate selections* must be one factor of the minimal settings.

We prepare DNA reaction networks that keep on maintaining the start sequence, where the start sequence interacts with an input (*food*) sequence and they transformed into intermediate sequences and from the interactions in the intermediate sequences, start sequence is re-produced. Hence the reaction system can maintain start sequence.

Firstly, we modified a well-known DNA reaction systems, the *seesaw gate* and constructed the self-maintaining reaction system, experimentally and confirmed it works (it is notice that it is not simulation by PC).

Next, we mutated an input sequence randomly and examined if the reaction behaviors were changed. We confirmed that, in 6 cases in 38 trials, even if it has mutation in the input sequences, the system still works correctly and reproduces the start sequences. We examined efficiency of such reactions by comparing reaction speed and quantity changes of input sequences and it has shown that they are not significant different in efficiency between no-mutation and mutated input cases.

Finally, we gave not mutated (normal) input sequences and mutated sequences to the system and observed if the system is able to select *appropriate* one, where *appropriate* means to select the input sequences in the higher concentration regardless of it has mutation or not. We confirmed that the system can select higher concentration irrespective of having mutation or not. And we also confirmed behaviors in the time series of concentration of normal input and mutated input sequences showed oscillations; we conjecture that the because of system select higher concentration one, selected input sequences are switched among non-mutated and mutated input sequences.

These results illustrate that the system made of DNA reaction networks are able to select input sequences in higher concentration so it will able to adapt the environmental change. Therefore, from Biological and philosophical points of views, this system realizes molecular Artificial Intelligence.

2. Methods

Since simple hybridization reactions cannot be cascaded, other reaction mechanism such as strand displacement reactions [4] have been used. Strand displacement is the process which two strands partially or fully hybridize to each other, displacing one or more pre-hybridized strands in the process. Strand displacement can be initiated at complementary single-stranded domains (referred to as toeholds) and progresses through a random walk-like branch migration process. Strand displacement reactions can be cascaded to eliminate this need for external triggers at every step;

this enables the engineering of complex autonomous systems.

Strand displacement releases at least one single stranded nucleic acid product, such as the output. In a DNA strand displacement cascade, this output serves as the input to the downstream reaction. Unlike electric or biological circuits that are powered by a standardized energy source (electrical voltages or ATP concentrations), strand displacement-based circuits cannot be easily recharged because the reactant species for each strand displacement reaction are different.

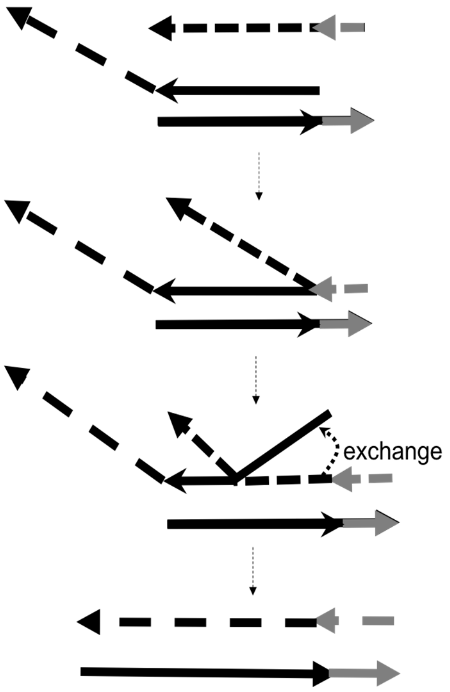

Fig.1. Strand displacement reaction; Strand Displacement Reaction; Dynamic DNA nanotechnology often makes use of toehold-mediated strand displacement reactions. In this example, the short arrow binds to the single stranded toehold region on the strand, and then in a branch migration process across region 2, the strand is displaced and freed from the complex. Reactions like these are used to dynamically reconfigure or assemble nucleic acid nanostructures. In addition, the strands can be used as signals in a molecular logic gate.

We modified the Seesaw gate reaction [4] by composed by the strand displacement reaction (Fig.2.); in order to confirm these reactions (1) and (2) circulate, we add the reaction; fuel + gate:marker → gate:fuel + marker (3);

input + gate:fuel ↔ gete:input + fuel (1),
gate:input + output ↔ gete:output + input (2),
fuel + gate:marker → gate:fuel + marker (3).

The reaction (3) examines the fuel sequence is produced and confirm the reaction (2) regenerate the input sequence. We confirm that the input sequence has been regenerated.

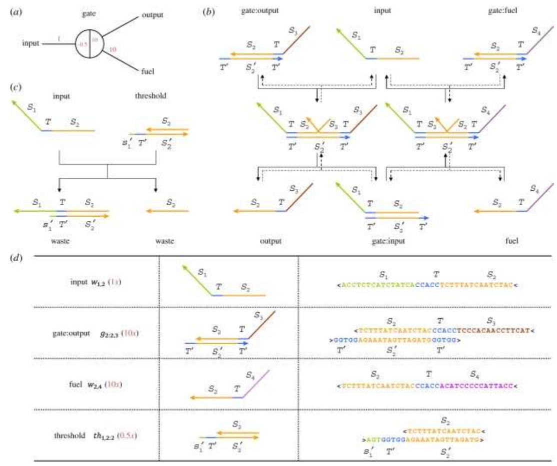

Fig. 2. Fig. 2. Seesaw gate reaction of DNA sequences: (a) Abstract gate diagram. Red numbers indicate initial concentrations. (b) The DNA gate motif and reaction mechanism. S1, S2, S3 and S4 are the recognition domains; T is the toehold domain; T0 is the Watson–Crick complement of T, etc. Arrowheads mark the 30 ends of strands. Signal strands are named by their domains from 30 to 50, All reactions are reversible and unbiased; solid lines indicate the dominant flows for the initial concentrations shown in (a), while the reverse reactions are dotted. (c)

3. Result

From biochemical experiments, we observed that when we added non-mutated input and mutated input, system select higher concentration one (Fig.3). And we also confirmed behaviors in the time series of concentration of normal input and mutated input sequences showed oscillations (Fig.3). And when the concentration decreases, the concentration of another input increases, hence we conjecture that the because of system select higher concentration one, selected input sequences are switched among non-mutated and mutated input sequences. These results illustrate that the system made of DNA reaction networks are able to select input sequences in higher concentration so it will able to adapt the environmental change. Therefore, from Biological and philosophical points of views, thie system realizes molecular Artificial Intelligence (Fig.3).

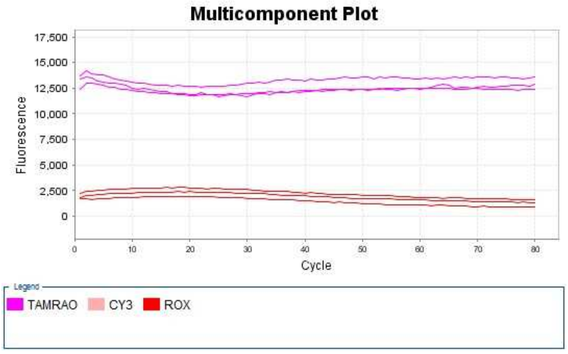

Fig. 3. Time series of concentration of normal input (below) and mutated input (upper); where mutated input was selected and concentration decreases.

Acknowledgements

We thank for thought provoking discussion with prof. Kazuhisa Todayama (Nagoya University). This work supported by Grant in Aid for Scientific Research on Innovative Areas, Molecular Robotics, No: 24104003, (B) No. 16H3093.

References

1. K. Todayama, *Tetsugaku Nyumon* (in Japanese, introduction to philosophy, Chikuma shobo publishing, 2014)
2. R. G. Millican, *Varieties of Meaning,* (MIT press, 2002).
3. D.Y. Zhang, G. Seelig, Dynamic DNA nanotechnology using strand-displacement reactions *Nature Chemistry* 3, 103–113 (2011) doi:10.1038/nchem.957
4. L.Qian and E. Winfree, A simple DNA gate motif for synthesizing large-scale circuits, *J R Soc Interface*. 2011 Sep 7; 8(62): 1281–1297.

Neural Networks by using Self-Reinforcement Reactions

Yasuhiro Suzuki
Graduate School of Information Science, Naogya University, Furocho Chikusa
Naogya City, 464 860, JAPAN

Abstract

We consider a chemical reaction network model in which selections of reaction are stochastic and depend on past history. In this chemical reaction network, we found the emergence of Auto-Catalytic Sets (ACS) and complex dynamics in which ACS are repeatedly created and destroyed; we have called this reaction system as the Self-Reinforcement Reactions, SRR. We developed a neural-networks system by using SRR and confirm the neural network of SRR can solve a linear classification problem.

Keywords: Artificial Chemistries, Chemical Reaction Networks, Perceptron, Linear Classification Problem, Self Reinforcement Reaction, Neural Networks

1. Introduction

We consider an abstract model of chemical reactions, a type of "abstract chemistry". The model assumes that substances can interact with each other according to reaction rules which change the amounts of the substance, and that reaction tendencies change depending on the reaction history. Reaction rules are assumed to be of the form $x \rightarrow y$, meaning that the amount of substance x decreases and the amount of substance *b* increases. Reactions occur at rates which depend on the amount of the first substance *x* and the strength of the reaction x $\rightarrow$ *y*. The strength of each reaction is increased in proportion to how often the reaction has occurred recently.

1.2 An Artificial Chemistry, Abstract Rewriting System On Multisets

We have been proposed an artificial chemistry, based on the Abstract Rewriting System, ARS; the ARS is a theoretical model of computation; we expand ARS on rewriting system on the multiset. A multiset is defined as a simple set and a map, which returns the duplication of element. We denote the duplication (multiplicity) of an element as M (a), for a $\in$ A and in case c /$\in$ A, M (c) = 0; for example M (a) and M (b) of {a, a, b, b} are 2, and M (c) = 0; in the mathematical description, a multiset is described as; < sup, M () >, in which sup is a simple set of elements, in this paper we describe a multiset by denoting the same alphabet in its number of multiplicity such as {a, a, b, b} or a vector w =(M (a1) M (a2) . . . M (an)).

The union of two multisets M1, M2 is the same as the union of simple set and in vector description, the union of multisets is addition of vectors w1 and w2. And inclusion of sets is also the same as the simple set, when M1(a) $\leq$ M2(a) for all a $\in$ A, the multiset M1 is included in M2 and we write M1 $\subseteq$ M2.

A reaction rule is a pair of multiset, we denote A# as a set of all combinations of multisets over A and in the combinations, an empty multiset is included. A reaction rule l $\rightarrow$ r, l, r $\in$ A# is described as a pair of multiset likewise chemical equations or a pair of its vector expression; and in some case, we can describe a reaction rule as a vector r, r = −l + r, it is simple and good for examining the dynamics of an ARMS, but this description cannot illustrate when there are the same species of element in the left-hand side and right-hand side such as a, b → a, c; in this case l = (1, 1, 0) and r = (1, 0, 1) and r = −(1, 1, 0) + (1, 0, 1) = (0, −1, 1).

A reaction is described as the rewriting of a multiset, if the left-hand side of a reaction rule is included in a mul- tiset, these elements in the multiset are excluded and the right-hand side of the rule is merged to the multiset; the case when the multiset is a, a, b, b and the reaction rule is a, b → c, d, the left-hand side of the rule is included in the multiset, {a, b} ⊆ {a, a, b, b} so the {a, b} is excluded from the multiset and it is transformed to {a, b} and the left-hand side of the rule {c, d} is merged to the set and we obtain {a, b, c, d} by this reaction.

We have developed a simple computational model, the Abstract Rewriting System, ARMS based on stoichiometric chemistry and reaction rate model. When we consider fundamental mechanism of living systems. ARMS is a hybrid-model and it is a discrete and continuous model, so if the number of elements (molecules) is small, ARMS is discrete model but when the number of element is large it is equal to Differential equation. AC including ARMS, in the most of models, have been described as an algorithm and implemented in digital media and have not been able to communicate with physical environments.

1.3 Self Reinforcement Reaction on ARMS

Specifically, we considered a form of this model which is implemented according to the following procedure. The state of the system is represented by the amounts [*x*] of the chemical substances, and strengths $w_{y:x}$ of the reaction rules. (For generality, we use “amount” rather than “concentration” or “number of molecules”.) Reactions are executed one at a time. The first substance and the reaction rule are each selected stochastically. The probability of selecting substance x is proportional to the relative amount of the substance [*x*], and the probability of selecting the reaction x → *y* is proportional to the relative strength $w_{y:x}$ of the reaction. When the reaction *x* → *y* occurs, the amount of substance *x* changes from [*x*] to [*x*]-1 and the amount of substance *y* increases from [*y*] to [*y*]+1. The strength of the reaction *x*→*y* is $w = (q*R+1)$ where *q* is the number of times the reaction has occurred in the last *M* reactions of *x* and R is the strength of the reinforcement. If reactions have not been selected recently, or there is no reinforcement, then reactions have minimal strength of $w = 1$ (Fig.1).

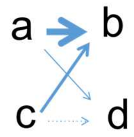

Fig. 1. The schematic example of SRN; in this example, reaction rules are {a → b, a→d, c→b, c→d}; thickness of arrows illustrate speed of reactions (thicker is faster)

The stochastic model we use is based on a well-known model in probabilistic theory, Polya’s Urn (Feller 1957) Selecting a node is equivalent to picking up a ball from an urn, where a node name is painted on each ball. In the urn, there are *N-1* types of balls, excepting itself. Before picking up a ball from the urn, a number *R* balls is added to the urn for each of the *M* most recently selected nodes, in addition to one extra ("permanent memory") ball for each node in the network. Initially, the urn will contain just one ball for each node, and the probability of choosing any node will be the same. The model reaction system can be thought of as a network. Each substance corresponds to

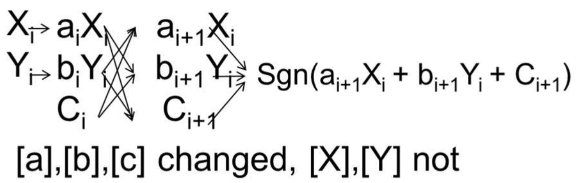

Fig. 2. The schematic example of SRN; in this example, reaction rules are {a → b, a→d, c→b, c→d}; thickness of arrows illustrate speed of reactions (thicker is faster)

a node of the network, and each directed connection between one node to another corresponds to a catalyzed reaction rule. However, since each connection has a probability which depends on recent activity, it is different from other models such as models based on Random Graph (Erdos and Reny 1960). We can think each node has a "memory storage" where it memorizes the names of the *M* most recent outgoing links and uses this memory to determine the probability for selecting an outgoing link. Another way of description is as follows. There are two types of links. Each node has *(N-1) + M* outgoing links. *(N-1)* permanent links and *M* dynamic links. There is one permanent link to every one of the other *(N-1)* nodes. Other dynamic links which are created and destroyed dynamically. Once a link is activated to a node, then an additional replica link is added, and the oldest dynamic links are destroyed. One of the *(N-1) +M* links is chosen randomly with a bias

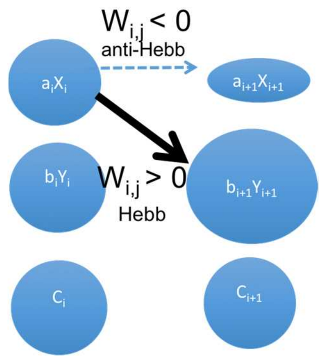

Fig. 3. Schematic image of SRNN; start product is randomly selected in proportion to W^TX, in this example *aX* is selected and a is decreased by LC and the reaction destination is also randomly selected in proportion to W^TX, in this example *by* is selected and is increased by LC; and this interaction is memorized.

weight of *R* for dynamic links compared to permanent links (Fig.1).

1.3 Perceptron

A perceptron is an algorithm for learning a binary classifier: a function that maps its input *x* (a real-valued vector) to an output value

$$f(x) = \begin{cases} 1\, if\ w * x + b > 0 \\ 0 \quad otherwise \end{cases}$$

where *w* is a vector of real-valued weights, *w*x* is the dot product $\sum_{i=1}^{m} w_i\, x_i$, where *m* is the number of inputs to the perceptron and *b* is the bias. The bias shifts the decision boundary away from the origin and does not depend on any input value.

2. Neural Networks implemented by ARMS

From Neural Network viewpoints, strength of weight can be regarded as Hebb rule and change of concentrations as anti-Hebb rule; because the concentration of left hand side of the fired rule is decreased and the firing probability of this rule is decreased. We confirmed that Self Reinforcing Neural Network, SRNN (Fig.2 and 3).

2.1. Linear Classification Problem

A linear classifier achieves is making a classification decision based on the value of a linear combination of the characteristics; in this contribution, the classify sample data $X=(x_n, y_n)$, $n=1,2,3,\ldots,N$ by $ax + by + c=0$, the system decide the weight vector $w = (a, b, c)$ and conjectures the sample data is upper or lower than the classification equation. We set an initial weight vector by random value w = (0.1, -0.3, -0.2) and learning coefficient, LC is 0.5.

In the SRNN, reactions exchange value of element in the weight vector by learning coefficient; select an element in *w* randomly in proportion to $W^T \cdot X$; for example *ax* is selected, *a is decreased by LC*; in the beginning reaction destination is also randomly selected in proportion to $W^T \cdot X$ and the reaction is memorized as in SR and the selected reaction destination is increased by LC (Fig.3).

3. Result

We compare the ability of system of SRNN with the single layer neural network; in order to characterize difficulty of problems, we change the distance between the center of clusters (x_{center}, y_{center}) from -10 to 10, where the negative distance means that the two clusters are overlapped.

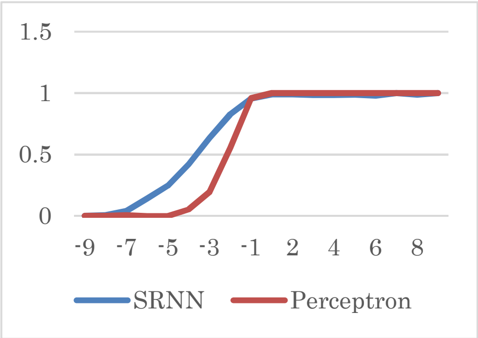

Fig. 4. Compare the SRNN with the single layer Perceptron, the horizontal axis illustrates the distance of the center of clusters, vertical axis illustrates the error rate of clustering.

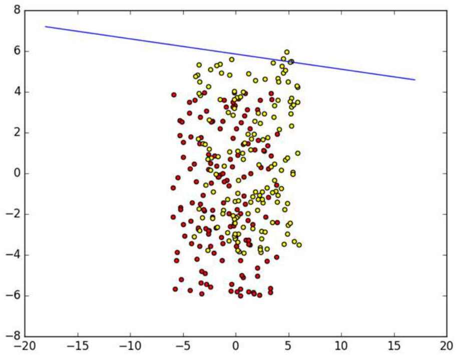

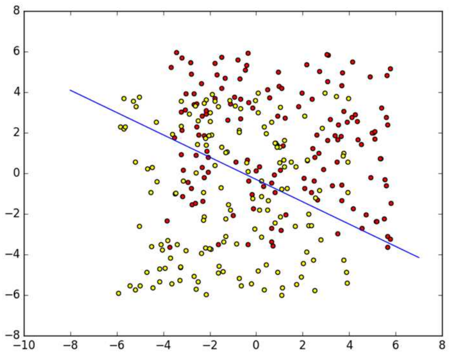

Fig. 4. Fig. 5. The results of sample run of the single layer Perceptron (top) and the SRNN (below) in the same distance of clusters; it shows that SRNN can classify even if the center of clusters are closed.

When the center of clusters are closed, the single layer perceptron cannot classify, while the SRNN can classify the clusters (Fig. 4 and 5).

We compare SRNN with the single layer perceptron by changing the center distance of clusters and examined error rate, where error rate is defined as the ratio of number of correctly classified elements to the total number of data.

Acknowledgements

Grant in Aid for Scientific Research on Innovative Areas, Molecular Robotics, No: 24104003, (B) No. 16H3093.

References

1. Dittrich P., T. Kron, W. Banzhaf (2003) On the scalability of social order: Modeling the problem of double and multi contingency following Luhmann , *Journal of Artificial Societies and Social Simulation,* ***6****(1),* http://jasss.soc.surrey.ac.uk/JASSS.html
2. Erdos P. and A. Reny (1960) On the evolution of random graphs, *Publ. Math. Inst. Hung. Acad. Sci.* **5**, 17-61.
3. Eigen M. and P. Schuster (1979) *The Hypercycle*, Springer Verlag, Berlin.
4. Feller W.(1957) *An Introduction to Probability Theory and Its Applications*, John Wiley & Sons, Inc
5. Ikegami T. (2002) An origin of combinatorial complexity in replicator networks, *Proceedings of the Seventh Intl. Sym. on Artificial Life and Robotics* **1,** 300-301.
6. Jain S. and S. Krishna (2001) A model for the emergence of cooperation, interdependence and structure in evolving networks, *Proc. Nat. Acad. Sci.* **98** (2) 543-547.
7. Suzuki Y., Y. Fujiwara, J. Takabayashi and H. Tanaka (2001) Artificial life applications of a class of P systems: Abstract rewriting systems on multisets in multiset processing. *Lec. Notes in Comp. Sc.,* **2235**, 299-346, Springer Verlag London,
8. Suzuki Y., Q. Zhang. and H. Tanaka (2001) Emergent of networks based on relationship among components, *Proc. Of World Congress on Medical Informatics*, ISO Press, 984-987.
9. Suzuki Y. and H. Tanaka (1997) Symbolic chemical system based on abstract rewriting system and its behavior pattern, *Journal of Artificial Life and Robotics,* **1**, 211-219, Springer Verlag, Tokyo

Artificial Chemistry by Sound Waves

Yasuhiro Suzuki
Graduate School of Information Science, Nagoya University, Furocho, Chikusa
Nagoya City, 464-8601, Japan

Abstract

We consider a chemical reaction network model in which selections of reaction are stochastic and depend on past history. In this chemical reaction network, we found the emergence of Auto-Catalytic Sets (ACS) and complex dynamics in which ACS are repeatedly created and destroyed; we have called this reaction system as the Self-Reinforcement Reactions, SRR. We developed a neural-networks system by using SRR and confirm the neural network of SRR can solve a linear classification problem.

Keywords: Artificial Chemistries, Chemical Reaction Networks, Computer Human Interaction, Fourier Analysis, Sound waves

1. Introduction

Living systems are composed of chemical reactions; almost all interactions in living systems are chemical reactions. However, bio-chemical reactions in living systems are complicated and it is difficult to consider and treat. Hence, abstract model of chemical reactions have been proposed and such Artificial Chemistry, AC has been used as a method of describing interactions for modeling; Multi Agent Systems, Petri Nets, etc. and the AC is one of the methods which based on the Stoichiometric Chemistry. The Stoichiometric Chemistry is a method for describing chemical reactions that treat chemical reactions as changes of quantity of chemical molecular. We have developed a simple computational model, the Abstract Rewriting System, ARMS based on stoichiometric chemistry and reaction rate model. When we consider fundamental mechanism of living systems. ARMS is a hybrid-model and it is a discrete and continuous model, so if the number of elements (molecules) is small, ARMS is discrete model but when the number of element is large it is equal to Differential equation.

Since living systems are composed of bio-chemical reactions, information processing are also chemical reactions. It is well-known that, in a living system such as a cell, the number of molecules is small and fluctuation of reactions also large. Hence, "noise canceling" in information processing would be important.

AC including ARMS, in the most of models, have been described as an algorithm and implemented in digital media and have not been able to communicate with physical environments.

2. An Artificial Chemistry, Abstract Rewriting System On Multisets

We have been proposed an artificial chemistry, based on the Abstract Rewriting System, ARS; the ARS is a theoretical model of computation; we expand ARS on rewriting system on the multiset. A multiset is defined as a simple set and a map, which returns the duplication of element. We denote the duplication (multiplicity) of an element as M (a), for a ∈ A and in case c /∈ A, M (c) = 0; for example M (a) and M (b) of {a, a, b, b} are 2, and M (c) = 0; in the mathematical description, a multiset is described as; < sup, M () >, in which sup is a simple set of elements, in this paper we describe a multiset by denoting the same alphabet in its number of multiplicity such as {a, a, b, b} or a vector w =(M (a1) M (a2) . . . M (an)).

The union of two multisets M1, M2 is the same as the union of simple set and in vector description, the union of multisets is addition of vectors w1 and w2. And inclusion of sets is also the same as the simple set, when M1(a) ≤ M2(a) for all a ∈ A, the multiset M1 is included in M2 and we write M1 ⊆ M2.

A reaction rule is a pair of multiset, we denote A# as a set of all combinations of multisets over A and in the combinations, an empty multiset is included. A reaction rule l → r, l, r ∈ A# is described as a pair of multiset likewise chemical equations or a pair of its vector expression; and in some case, we can describe a reaction rule as a vector r, r = −l + r, it is simple and good for examining the dynamics of an ARMS, but this description can not illustrate when there are the same species of element in the left-hand side and right-hand side such as a, b → a, c; in this case l = (1, 1, 0) and r = (1, 0, 1) and r = −(1, 1, 0) + (1, 0, 1) = (0, −1, 1).

A reaction is described as the rewriting of a multiset, if the left-hand side of a reaction rule is included in a mul- tiset, these elements in the multiset are excluded and the right-hand side of the rule is merged to the multiset; the case when the multiset is a, a, b, b and the reaction rule is a, b → c, d, the left-hand side of the rule is included in the multiset, {a, b} ⊆ {a, a, b, b} so the {a, b} is excluded from the multiset and it is transformed to {a, b} and the left-hand side of the rule {c, d} is merged to the set and we obtain {a, b, c, d} by this reaction.

3. ARMS by Sound Waves

We model the ARMS by using sound waves; where each type of element is characterized as a frequency of sin wave in fixed amplitude, A and n duplication (multiplicity) of an element is differed as nA,; for example, when we define a as *0.1Sin(2)* and b is *0.1Sin(3),* the multiset M_1={a, a, b, b} is denoted as W= $2\times 0.1Sin(2) + 2\times Sin(3)$; we denote a multiset in *Sin* wave form as W and amplitude (duplications) of a in W is denoted as W(a); when M(a)= empty set, $0\times Sin(2)$ .The union of two multisets M1, M2 is the synthesizing W_1 and W_2: and inclusion of W_i is $W_1(a) \leq W_2(a)$ for all a ∈ A, the W_1 is included in W_2 and we write $W_1 \subseteq W_2$. A reaction rule is a pair of *Sin* waves, we denote A# as a set of all combinations of elements over A and in the combinations, an empty multiset is included. A reaction rule $W_l \rightarrow W_r$, l, r ∈ A# is described as a pair of *Sin* waves likewise chemical equations.

A reaction is described as the transforming of a *Sin* wave, if the left-hand side of a reaction rule is included in W, waves represent left-hand side of the rules are filtered and the waves of right-hand side of the rule is synthesized; the case when the multiset is a, a, b, b and the reaction rule is a, b → c, d, the left-hand side of the rule is included in the multiset, {a, b} ⊆ {a, a, b, b} so the {a, b} is excluded from the multiset and it is transformed to {a, b} and the left-hand side of the rule {c, d} is merged to the set and we obtain {a, b, c, d} by this reaction.

4. Neural Networks implemented by ARMS

In the system, which we propose in this paper, Neural Network, NN is implemented by using ARMS; NN in this paper is Self-Reinforcement Neural Network, SRNN, which we have been proposed; in SRNN , we assumes that substances can interact with each other according to reaction rules which change the amounts of the substance, and that reaction tendencies change depending on the reaction history. Reaction rules are assumed to be of the form x → y, meaning that the amount of substance x decreases and the amount of substance b increases. Reactions occur at rates which depend on the amount of the first substance x and the strength of the reaction x → y . The strength of each reaction is increased in proportion to how often the reaction has occurred recently.

Specifically, we considered a form of this model which is implemented according to the following procedure. The state of the system is represented by the amounts [x] of the chemical substances, and strengths w of the reaction rules. (For generality, we use "amount" rather than "concentration" or "number of molecules".) Reactions are executed one at a time. The first substance and the reaction rule are each selected stochastically. The probability of selecting substance x is proportional to the relative amount of the substance [x], and the

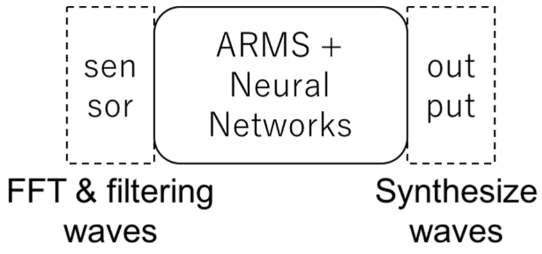

Fig. 1. Neural Networks implemented by ARMS (Self-Reinforcement Neural Networks) and the ARMS communicate with environment via waves; it analyzes input waves by using Fourier Analysis and filtered input waves can be detected by the it (detectable frequencies are given, in this paper but is not mandatory) and transform and synthesize output wave.

probability of selecting the reaction x → y is proportional to the relative strength $w_{x,y}$ of the reaction. When the reaction x → y occurs, the amount of substance x changes from [x] to [x]-1 and the amount of substance y increases from [y] to [y]+1. The strength of the reaction x→ y is $w_{x,y}$ = (q*R+1) where q is the number of times the reaction has occurred in the last M reactions of x and R is the strength of the reinforcement. If reactions have not been selected recently, or there is no reinforcement, then reactions have minimal strength of w = 1.

From Neural Network viewpoints, strength of weight can be regarded as Hebb rule and change of concentrations as anti-Hebb rule; because the concentration of left hand side of the fired rule is decreased and the firing probability of this rule is decreased. We confirmed that SRNN can work as a NN.

5. Communicating with ARMS via waves

In proposed model, input wave is analyzed by Fourier analysis with Fast Fourier Transform, FFT; for the system, detectable frequencies are given, it corresponding to the hearable frequencies (in the case of humankind, it is around 30Hz to 20,000Hz); so even if amplitude is large, if its frequency is out of hearable frequencies, it cannot detect it; practically selecting hearable frequencies is realized by a sensor, which detects frequencies and their amplitudes (Fig. 1). So, in case detectable frequencies are $a_0,\ldots,a_m$ inputted wave *f* is transformed as $W = \sum A_i Sin(a_i)$, (i = 0,…,m), and input to SRNN is $\{A_0, A_1, A_2,\ldots,A_m\}$. The SRNN changes amplitude of inputted wave, in this paper we propose unsurprised learning.

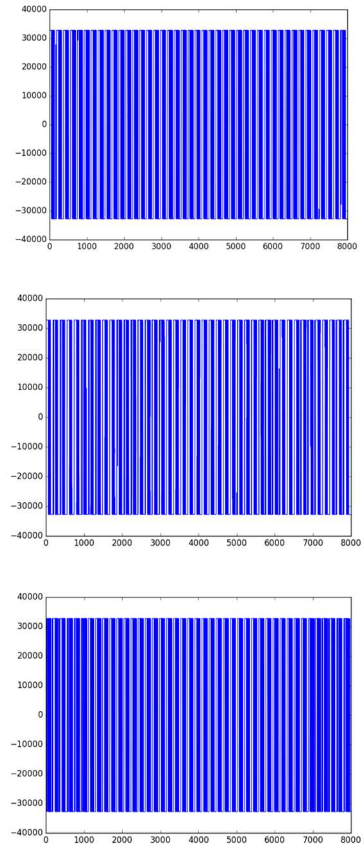

Fig. 2. Sample run of the system with frequency spectrums and time developments is up to bottom; in the sample run, we used the equipped microphone in the PC (MacBook) and record environment sounds for 30 sec; the synthesized wave was outputted through equipped sound speaker.

6. Communicate with SRNN via Sound Waves

As the input device, we used a microphone, which is equipped with the Personal Computer, PC (MacBook); the system record environment sound for 30 seconds then analyzes sound wave by using FFT and filtered detectable frequencies and their amplitude. In the sample runs reported in this paper, we did not define specific reaction rules but the system changes amplitude of frequencies; the system selects a frequency randomly, where the probability of selecting frequency is in proportion to its amplitude; then the amplitude is decreased by A_{df}; then selects a frequency to be added by A_{df}; in the beginning, it is selected randomly according to its amplitude and by the interaction the conditional probability of P(x|y) is changed; which denotes the probability of selecting y when the frequency x is selected and it corresponds to weight of link w_{ij} in SRNN.

In the sample run, environmental sound was created by voice, making noise by hitting desk for 30 sec. then the system analyzes sounds and create sound output; sound spectrums of system illustrate the system changes output sounds through environmental sounds changing (Fig. 2).

7. Future Remarks

We propose a method to communicate with computational models implemented inside a PC from outside via sounds. This framework would be applicable in Artificial Life, Robotics and Human Computer Interactions and Evolutional Language; by using several PCs or robots having this framework can interact with each other by using this sound communications; by integrating computational vision, these agents would be able to create link between sounds and visual information and novel language would emerge among agents / robots; it is important that animals or our human also can participate the process of this emergence of a common language among agents, robots, animals and humankind.

Acknowledgements

Grant in Aid for Scientific Research on Innovative Areas, Molecular Robotics, No: 24104003, (B) No. 16H3093, 15K00268, 24520106

References

1. Dittrich P., T. Kron, W. Banzhaf (2003) On the scalability of social order: Modeling the problem of double and multi contingency following Luhmann, *Journal of Artificial Societies and Social Simulation,* ***6****(1),* http://jasss.soc.surrey.ac.uk/JASSS.html
2. Suzuki Y., Y. Fujiwara, J. Takabayashi and H. Tanaka (2001) Artificial life applications of a class of P systems: Abstract rewriting systems on multisets in multiset processing. *Lec. Notes in Comp. Sc.,* **2235**, 299-346, Springer Verlag London,
3. Suzuki Y., Q. Zhang. and H. Tanaka (2001) Emergent of networks based on relationship among components, *Proc. of World Congress on Medical Informatics*, ISO Press, 984-987.
4. Suzuki Y. and H. Tanaka (1997) Symbolic chemical system based on abstract rewriting system and its behavior pattern, *Journal of Artificial Life and Robotics,* **1**, 211-219, Springer Verlag, Tokyo

Variants of Spiking Neural P Systems with Energy Control

Rudolf Freund
Marion Oswald
Institute of Computer Languages, TU Wien, Favoritenstraße 9-11
Wien, 1040, Austria
E-mail: rudi@emcc.at, marion@logic.at

Abstract

We consider several variants of extended spiking neural P systems (ESNP systems), theoretical frameworks for brain modeling. Special emphasis is laid on ESNPS systems with different colors, and, instead of choosing the rules in the neurons based on the current contents being in a regular set, we also consider the way of choosing the rule to be applied in each neuron consuming the minimal energy. This choice can be accomplished by assigning energy values to each rule or by assigning (different) energy values directly to the colored spikes.

Keywords: colored spikes, computational completeness, energy control, spiking neural P systems

1. Introduction

Spiking neural P systems were introduced in Ref. 1. Energy-controlled P systems have already been considered in Refs. 2 and 3, where energy was assigned to the rules and the multisets of rules consuming the maximal amount of energy and the maximal amount of energy within a specific range were investigated. Computational completeness results for everal variants of P systems – P systems with cooperative rules, catalytic and purely catalytic P systems, P systems with target selection – with different derivation modes and using energy control, i.e., taking only those multisets or sets of rules consuming the minimal amount of energy, have been proved in Ref. 4. Especially for the set derivation modes, introduced in Ref. 5, even deterministic simulations of the computations of register machines could be obtained.

2. Definitions

We assume the reader to be familiar with the underlying notions and concepts from formal language theory, e.g., see Ref. 6.

2.1. *Prerequisites*

We assume the reader to be familiar with the underlying notset of non-negative integers is denoted by **N**, the set of integers by **Z**. Given an alphabet V , a finite non-empty set of abstract symbols, the free monoid generated by V under the operation of concatenation is denoted by V^*. The elements of V^* are called strings, the empty string is denoted by λ, and $V^*\backslash\{\lambda\}$ is denoted by V^+. For an arbitrary alphabet $V=\{a_1,...,a_n\}$, the number of occurrences of a symbol a_i in a string x is denoted by $|x|_{a_i}$. With respect to a specific order on the elements $a_1,...,a_n$ of the alphabet V, the n-tuple

$(|x|_{a_1},...,|x|_{a_n})$ is called the Parikh vector of x. A finite multiset over an alphabet $V=\{a_1,...,a_n\}$ is a mapping $f : V \rightarrow \mathbf{N}$. The set of all multisets over V is denoted by V^o. The families of recursively enumerable string languages is denoted by RE. For any family of languages X, Ps(X) denotes the set of Parikh sets of the languages in X; if we do not distinguish between different symbols and only consider sets of numbers, we write N (X).

2.2. *Register machines*

An d-register machine is a tuple $M = (d,B,l_0,l_h,P)$, where d is the number of registers, B is a set of labels, $l_0 \in B$ is the initial label, $l_h \in B$ is the final label, and P is the set of instructions bijectively labeled by elements of B. The instructions of M can be of the following forms:

- $p:(ADD(r),q,s)$, with $p \in B \backslash \{l_h\}$, $q,s \in B$, $1 \leq j \leq n$. Increases the value of register r by one, followed by a non-deterministic jump to instruction q or s. This instruction is usually called *increment*.
- $p:(SUB(r),q,s)$, with $p \in B \backslash \{l_h\}$, $q,s \in B$, $1 \leq j \leq n$. If the value of register r is zero then jump to instruction s; otherwise, the value of register r is decreased by one, followed by a jump to instruction q. The two cases of this instruction are usually called *zero-test* and *decrement*, respectively.
- l_h: HALT (halt instruction) Stop the machine. The final label l_h is only assigned to this instruction.

The register machines are known to be computationally complete, equal in power to (non-deterministic) Turing machines: they generate or accept exactly the sets of vectors of non-negative integers which can be generated by Turing machines.

3. Extended Spiking Neural P Systems

The reader is supposed to be familiar with basic elements of membrane computing, e.g., see Ref. 7; comprehensive information can be found on the P systems web page, see Ref. 8. For the definition of an extended spiking neural P system we refer to Ref. 9.

An extended spiking neural P system (of degree $m \geq 1$) (an ESNP system for short) is a construct $\Pi = (N,I,R)$ where

- N is the set of cells (or neurons); the neurons may be uniquely identified by a number between 1 and m or by an alphabet of m symbols;
- I describes the initial configuration by assigning an initial value (of spikes);
- R is a finite set of *spiking rules* of the form $i:E/a^k \rightarrow P$ such that $i \in \{1,...,m\}$ (specifying that this rule is assigned to neuron i), E is the *checking set*, a regular set over a (the current number of spikes in the neuron has to be from E if this rule shall be executed), $k \in N$ is the "number of spikes" (the energy) consumed by this rule, and P is a (possibly empty) set of productions of the form (l,w_l) where $l \in \{1,...,m\}$ (thus specifying the target neuron), $w_l \in \{a\}^*$ is the weight of the energy sent along the axon from neuron i to neuron l.

Depending on the purpose of the ESNP system, we may also specify input and output neurons.

Definition 2. A *configuration* of the ESNPS system Π is described by the actual number of spikes in each neuron. A *transition* from one configuration to another one works as follows: for each neuron i, $i \in \{1,...,m\}$, we non-deterministically choose an applicable rule $i:E/a^k \rightarrow P$, i.e., the number of spikes in neuron i is in the regular set E; the application of this rule reduces the number of spikes in neuron i by k and adds w_l spikes to each neuron l specified in P. The computation of Π *halts* if no spiking rule can be applied any more.

3.1. *ESPN systems with colored spikes*

We may extend this model of ESNP systems by allowing more than one variant of spikes, i.e., we may use *colored* spikes a, b, etc.; the set of these colored spikes is denoted by U. In that case, the spiking rules then are of the form $i:E/u \rightarrow P$ where E is a regular multiset over the finite set of colored spikes U, u is a finite multiset over U, and P is a (possibly empty) set of productions of the form (l,w_l) where $l \in \{1,...,m\}$ (thus specifying the target neuron) and w_l is a finite multiset of colored spikes over U sent along the axon from neuron i to neuron l.

A *configuration* of the ESNPS system with colored spikes is described by the actual multiset of colored spikes in each neuron.

The application of a spiking rule $i:E/u \rightarrow P$ reduces the multiset of colored spikes in neuron i by u and adds the multiset w_l to each neuron l specified in P.

4. ESNP Systems with Colored Spikes and Energy Control

We consider two variants: the first variant assigns fixed integer values of energy to each colored spike in the system, i.e., instead of a colored spike $a \in U$ we consider the pair $[a,f(a)]$ with $f(a) \in \mathbf{Z}$. We extend f in the natural way to multisets over U. The energy balance of a spiking rule $i{:}E/u \rightarrow P$ then is $z = f(v) - f(u)$ where v is the sum of all multisets w_l in P. Such variants of P systems will be called *symbol energy-controlled* ESNP systems.
In the second variant, the energy is directly assigned to the rules only, and we write spiking rule $i{:}E/u \rightarrow P <z>$ where z is the assigned integer energy value. Such variants of P systems will be called *rule energy-controlled* ESNP systems.
In the case of *energy-controlled* ESNP systems we now will only cosider spiking rules $i{:}E/u \rightarrow P$ with E being the set of all multisets over U, i.e., we can omit E and simply write spiking rule $i{:}u \rightarrow P$ and $i{:}u \rightarrow P <z>$, respectively. In order to control the application of rules, we will impose the condition that the resulting energy balance of the applied spiking rules must be minimal.

5. Computational Completeness Results

We now investigate the computational power of some of the variants defined above.

5.1. *ESNP systems with colored spikes*

With colored spikes, the simulation of register machines becomes trivial. In contrast to the proof given in Ref. 9, where the contents of the registers had to be encoded by using exponential prime number encoding, we now can directly use the numbers contained in the registers.

Theorem 1. *The computations of any register machine can be simulated by an ESNP system with colored spikes in only one node.*

Proof. Consider an arbitrary d-register machine $M = (d,B,l_0,l_h,P)$. For each register i, $1 \leq i \leq d$, of M, we use a different colored spike a_i. An additional colored spike a_0 is used to encode the label l in $B=\{1,...,m\}$ in B, i.e., l is encoded by a_0^l. We here denote $U:=\{a_i : 1 \leq i \leq d\}$.

The ESNP system with only one neuron $\Pi = (\{1\},I,R)$ now can be constructed as follows:
An increment instruction p:(ADD(r),q,s) then can be simulated by the two spiking rules
$1{:}\ \{a_0^p\}U^o/\ a_0^p \rightarrow (1,a_r\ a_0^q)$ and
$1{:}\ \{a_0^p\}U^o/\ a_0^p \rightarrow (1,a_r\ a_0^s)$.
A zero-test and decrement instruction p:(SUB(r),q,s) then can be simulated by the two spiking rules
$1{:}\ \{a_0^p\}(U\backslash\{a_r\})^o/\ a_0^p \rightarrow (1,a_r\ a_0^s)$ and
$1{:}\ \{a_0^p\ a_r\}U^o/\ a_0^p\ a_r \rightarrow (1,a_0^q)$.
Assuming that the halt instruction has label m, we finally get the simulation of the halt instruction as
$1{:}\ \{a_0^m\}U^o/\ a_0^m \rightarrow \lambda$.
After the application of this rule, no spike a_0 is present any more, hence, no spiking rule can be applied, i.e., the ESNP system Π halts. □

5.2. *ESNP systems with energy control*

We may omit the regular checking sets by replacing them by the condition that the resulting energy balance of the applied spiking rules must be maximal.

Theorem 2. *The computations of any register machine can be simulated by an ESNP system with colored spikes and energy control (symbol or rule energy control) in only one node.*

Proof. Again we consider an arbitrary d-register machine $M = (d,B,l_0,l_h,P)$. For each register i, $1 \leq i \leq d$, of M, we use a different colored spike a_i with 1 being the energy assigned to it. An additional colored spike a_0 with energy 2 is used to encode the label l in $B=\{1,...,m\}$ in B, i.e., l is encoded by a_0^l. Moreover, we use a special energy spike e with energy -1 to balance the spiking rules.
A symbol energy-controlled ESNP system $\Pi = (\{1\},I,R)$ with only one neuron simulating the computations of M now can be constructed as elaborated in the following.

The corresponding rule energy-controlled ESNP system is obtained by omitting the energy assigned to the spikes and just taking the energy listed together with the rules between the brackets < and >; we observe that these energy values exactly coincide with the energy balance of the rule in the case of assigning energy values to each spike. Finally we remark that we can omit the target neuron 1 as we have only one neuron in the whole ESNP ystem:

An increment instruction p:(ADD(r),q,s) then can be simulated by the two spiking rules

$1: [a_0,2]^p \rightarrow [a_r,1]\,[a_0,2]^q\,[e,-1]^{2q+1}\ \langle -2p \rangle$ and

$1: [a_0,2]^p \rightarrow [a_r,1]\,[a_0,2]^s\,[e,-1]^{2s+1}\ \langle -2p \rangle$.

A zero-test and decrement instruction p:(SUB(r),q,s) now can be simulated by the two spiking rules

$1: [a_0,2]^p \rightarrow [a_0,2]^s\,[e,-1]^{2s}\ \langle -2p \rangle$ and

$1: [a_0,2]^p\,[a_r,1] \rightarrow [a_0,2]^q\,[e,-1]^{2s}\ \langle -2p-1 \rangle$.

As the energy balance of the decrement rule has a smaller value, in case it is applicable it has priority over the zero-test rule, which fact, in contrast to the previous construction, makes this one even deterministic.

In all cases it holds that we have to consume all copies of a_0 as otherwise there would exist a rule having smaller energy balance.

Assuming that the halt instruction has label m, the halt instruction can be simulated by the spiking rule

$1: [a_0,2]^m \rightarrow \lambda\ \langle -2m \rangle$

which has the minimal energy balance of all spiking rules in the ESNP system Π.

Yet the ESNP system Π is not going to halt, too, after having applied this rule, as it still has to eliminate the "garbage" of spikes e, which task can be accomplished by the spiking rule

$1: [e,-1] \rightarrow \lambda\ \langle 1 \rangle$.

As this spiking rule has even positive energy balance, it cannot be applied as long as spikes a_0 are present, i.e., as long as the ESNP system Π still simulates the computations of the register machine M.

This observation completes the proof. □

6. Applications

Besides these theoretical computational completeness results as elaborated above ESNP systems with colored spikes allow for using the different colors of the spikes to encode the signal sizes of different sensor inputs as well as of various output effector signals. In contrast to standard spiking neural P systems with only one spike, all these signals can be directly stored in parallel even in one neuron and do not need an exponential prime number encoding, which allows for feasible implementations of control systems.

7. Conclusion

We have considered several variants of extended spiking neural P systems (ESNP systems) with colored spikes. Computational completeness has been shown for the variants using colored spikes, i.e., more than one kind of spikes. Only the simplest ESNP systems with one neuron are needed if we use colored spikes and either regular multisets as checking sets or energy control, i.e., integer energy values assigned to the spikes or the spiking rules themselves. In case of symbol or rule energy-controlled ESNP systems with colored spikes the simulation of deterministic register machines can even be carried out in a deterministic way.

References

1. M. Ionescu, Gh. Păun, T. Yokomori, Spiking neural P systems, *Fundamenta Informaticae* **71**(2–3) (2006) 279–308.
2. Gh. Păun, Y. Suzuki, H. Tanaka, P systems with energy accounting, *Int. J. of Computer Mathematics* **78**(3) (2001) 343–364.
3. R. Freund, Energy-controlled P systems, in *WMC 2002, Lecture Notes in Computer Science*, vol. **2597**, eds. Gh. Păun, G. Rozenberg, A. Salomaa, C. Zandron (Springer, 2003), pp. 247–260.
4. A. Alhazov, R. Freund, and S. Ivanov, Variants of Energy-Controlled P Systems, *NIT 2016* (Valencia, 2016).
5. A. Alhazov, R. Freund, S. Verlan, Computational completeness of P systems using maximal variants of the set derivation mode, in *Proc. 14th Brainstorming Week on Membrane Computing* (Sevilla, February 1–5, 2016).
6. G. Rozenberg, A.Salomaa (eds.), *Handbook of Formal Languages*, vol. 1-3 (Springer, 1997) .
7. Gh. Păun, G. Rozenberg, A. Salomaa (eds.), *The Oxford Handbook of Membrane Computing* (Oxford University Press, 2010).
8. The P Systems Website: http://ppage.psystems.eu
9. A. Alhazov, R. Freund, M. Oswald, M. Slavkovik, Extended spiking neural P systems, in *Workshop on Membrane Computing*, *Lecture Notes in Computer Science* **4361** (Springer, 2006) pp. 123–134.

Motion Improvement of Four-Wheeled Omnidirectional Mobile Robots for Indoor Terrain

Amornphun Phunopas[1]
Department of Production Engineering, King Mongkut's University of Technology North Bangkok, 1518 Pracharat 1 Road Bangsue, Bangkok, 10800, Thailand[1]

Shinichi Inoue[2]
Department of Interdisciplinary Informatics, Kyushu Institute of Technology, Laboratory, 680-4 Kawazu, Iizuka Fukuoka, 820-0067, Japan[2]
E-mail: amornphun.p@eng.kmutnb.ac.th, inoue.shinichi.1800@gmail.com
www.kmutnb.ac.th

Abstract

The four-wheeled omnidirectional platform is great to use for an indoor mobile robot. It can increasingly move and change heading directions. However, the robot is easy to slip when it is moving. One or more wheels are sometimes not touching the ground. This paper approaches to solving these problems by computational simulation in locomotion. The mathematical models simulate the robot movement. The robot struggles to go to the target with randomly simulated slips and untouched ground circumstances. The robot can estimate the positions using the Kalman filter and readjust itself to the planned path. Consequently, this paper demonstrates the motion improvement and compares the results of decreasing errors.

Keywords: Omnidirectional wheel, Indoor mobile robot, Kalman filter, Motion improvement

1. Introduction

It is known that an omnidirectional mobile robot is a holonomic motion. It can travel in multi-directions and change direction rapidly. This platform is famous for use in the automated guided vehicles (AGVs), which use is growing in service robots.[1] The robots can support home care. The robots can flexibly add on many functions for works or for human assistance.

The omnidirectional mobile robot has many wheels that are placed in different directions. It has a complicated mathematical model to control the movement of robots.[2] There is a constraint when moving on a flat, indoor terrain. However, it is difficult to move the robot to the desired position autonomously because the robot's motion is slippery. Therefore, the robot may miss its planned path or, in the worst-case scenario, get lost due to unrecognized circumstances.

The four-wheeled omnidirectional mobile robot has four points to make contact with the floor. Its geometry is a rectangular shape with four connecting points, which are supposed to align all wheels in the same plane. In fact, the floor is not completely flat, and after running the robot many times, each wheel will become eroded unequally. The robot becomes unbalanced or shaky even though all wheels are designed and aligned in the same plane. It is possible that some wheels will not touch the floor when it moves. It is possible that the robot will get stuck and not reach its goal. These problems can be solved by mechanically designing it for rough terrain conditions.[3] For example, the omnidirectional mobile robot employs a suspension system[4] for supporting all wheels to touch the floor in order to cancel out the mechanical noise.

The computational algorithm can reduce error from noises and make the robot move on its planned path. Dead reckoning is the motion estimation of the robot base on speed estimation, direction, and traveling time.[5] The Kalman filter is great to use in noisy systems such as localization and navigation.[6]

This research is about to use the Kalman filter to solve the slip without the wheel touching the ground. The robot will use sensors and computation to resolve the problems. The research is done in simulation by creating the possible conditions of motion randomly using MATLAB. The first section is about the kinematics model; next section is the trajectory to define the state of motion. After that, the simulation section describes the steps of simulation and the conditions of motion, and then the motion improvement section uses the Extended Kalman Filter and shows the simulation results. Finally, conclusion section discusses and concludes the results from the simulation.

2. Kinematics

The omnidirectional mobile robot uses holonomic motion and has four wheels to move in multiple directions. It can be controlled through the planned path in three degrees of freedom. There are two kinematics models: the first is forward kinematics, and the second is inverse kinematics. The robot platform uses the forward kinematics to determine the robot's velocities $(V_x, V_y, \dot{\theta})$ and the inverse kinematics to determine the wheel's angular velocities (w_1, w_2, w_3, w_4). The robot motion is in the XY coordinate as in Fig. 1. The robot's heading angle is determined by θ. The robot can move through the planned paths of motion from the kinematics models. As such, there are eight basic directions for omnidirectional movement in Table 1. Each wheel turns in different directions. CW is clockwise, and CCW is counterclockwise.

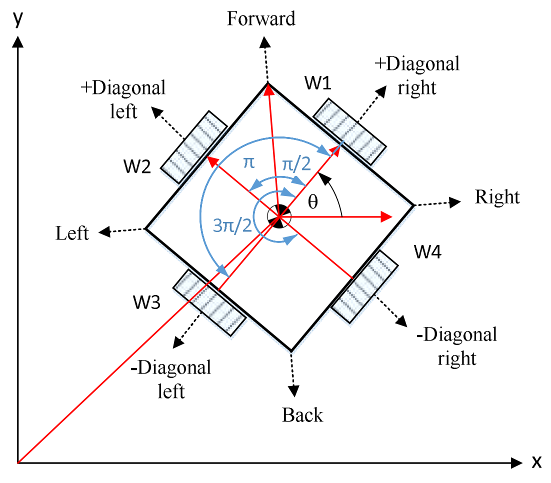

Fig. 1. The robot's configuration and eight directions of motion.

Table 1. Eight directions of the robot's motion relate to the four wheels' rotation direction.

Direction	**W_1**	**W_2**	**W_3**	**W_4**
Forward	CW	CCW	CCW	CW
Left	CW	CW	CCW	CCW
Right	CCW	CCW	CW	CW
Back	CCW	CW	CW	CCW
+Diagonal Right	0	CCW	0	CW
-Diagonal Right	0	CW	0	CCW
+Diagonal Left	CW	0	CCW	0
-Diagonal Left	CCW	0	CW	0

2.1. *Forward Kinematics*

The input of forward kinematics regards the wheels' speed, and the output regards the robot's velocities as in Eq. (1) to simulate the robot's motion. Converting the four wheels' speed into the robot's linear velocity requires the Jacobian matrix as seen in Eq. (2). The parameters R and r are set to 10 cm and 5 cm respectively for the simulation.

$$V_r = \begin{bmatrix} V_x \\ V_y \\ \dot{\theta} \end{bmatrix} = J \begin{bmatrix} w_1 \\ w_2 \\ w_3 \\ w_4 \end{bmatrix} \tag{1}$$

$$J = \frac{r}{2} \begin{bmatrix} -sin\left(\theta + \frac{\pi}{4}\right) & cos\left(\theta + \frac{\pi}{4}\right) & \frac{1}{2R} \\ -sin\left(\theta + \frac{3\pi}{4}\right) & cos\left(\theta + \frac{3\pi}{4}\right) & \frac{1}{2R} \\ -sin\left(\theta + \frac{5\pi}{4}\right) & cos\left(\theta + \frac{5\pi}{4}\right) & \frac{1}{2R} \\ -sin\left(\theta + \frac{7\pi}{4}\right) & cos\left(\theta + \frac{7\pi}{4}\right) & \frac{1}{2R} \end{bmatrix}^T \tag{2}$$

Where W_1 is the angular velocity of wheel 1, W_2 is the angular velocity of wheel 2, W_3 is the angular velocity of wheel 3, and W_4 is the angular velocity of wheel 4. R is the radius of the robot from the center to the wheel, r is the radius of the wheel, V_x is the robot's velocity on the x-axis, V_y is the robot's velocity on the y-axis, and $\dot{\theta}$ is the heading angular velocity of the robot.

2.2. *Inverse Kinematics*

To inverse Eq. (1) will obtain Eq. (3), which provides the robot's velocities.

$$V_w = \begin{bmatrix} w_1 \\ w_2 \\ w_3 \\ w_4 \end{bmatrix} = \frac{1}{r} \begin{bmatrix} -sin\left(\theta + \frac{\pi}{4}\right) & cos\left(\theta + \frac{\pi}{4}\right) & R \\ -sin\left(\theta + \frac{3\pi}{4}\right) & cos\left(\theta + \frac{3\pi}{4}\right) & R \\ -sin\left(\theta + \frac{5\pi}{4}\right) & cos\left(\theta + \frac{5\pi}{4}\right) & R \\ -sin\left(\theta + \frac{7\pi}{4}\right) & cos\left(\theta + \frac{7\pi}{4}\right) & R \end{bmatrix} \begin{bmatrix} V_x \\ V_y \\ \dot{\theta} \end{bmatrix} \tag{3}$$

The planned path of the robot's velocities is assigned as input parameters to obtain the speed of four wheels.

2.3. Trajectory model

The robot can move smoothly. The trajectory is for path planning, which determines speed and acceleration of each wheel. The trajectory advantage is to increase and slow down velocity properly. The robot can rotate to change directions while it is moving. Accordingly, the trajectory of path planning will be applied to the inverse kinematics and then control the speed of four wheels. In reality, the robot has to have odometry sensors for feedback control to control the wheels' speed and the robot's direction. For simulation, the velocity of four wheels can be applied to drive the animated robot. The trajectory uses a polynomial function of time. Polynomials are simple to compute and can provide the required smoothness and boundary conditions using Peter Corke's MATLAB library.[7] A quintic (fifth-order) polynomial is used,

$$S(t) = At^5 + Bt^4 + Ct^3 + Dt^2 + Et + F \quad (4)$$

$$\dot{S}(t) = 5At^4 + 4Bt^3 + 3Ct^2 + 2Dt + E \quad (5)$$

$$\ddot{S}(t) = 20At^3 + 12Bt^2 + 6Ct + 2D \quad (6)$$

where S is function of robot motion (x, y, θ), $\dot{S}$ *is derivative of S as robot velocity* $(V_x, V_y, \dot{\theta})$, $\ddot{S}$ *is derivative of* $\dot{S}$ *as robot acceleration* $(a_x, a_y, \ddot{\theta})$, *t is interval time in step sampling, and (A,B,C,D,E,F) are coefficients.*

3. Simulation

The simulation is implemented by a kinematics model and a trajectory model. The planned path is created for the robot motion, a straight line and a curved line. The trajectory is ready to use to control the robot's position, velocity, and acceleration using Eq. (4-6). Then, the robot converts its body velocity to four wheels' speed using Eq. (3). To display the robot's motion, in animation, see Eq. (1). The Kalman filter is used to improve the robot's motion and simulate every condition of motion as in Fig. 2.

3.1. Conditions of Motion

The robot may not move as the planned path because of friction and external force. However, the robot normally has the feedback control to compensate for the motor's speed to maintain the speed input and direction of the robot. Another problem is the robot possibly getting stuck and being unable to move out from the trap field. However, the wheels still continue as the assigned wheels' speed.

There are two effects from changing the conditions of motion randomly. First, the robot position shifts from the

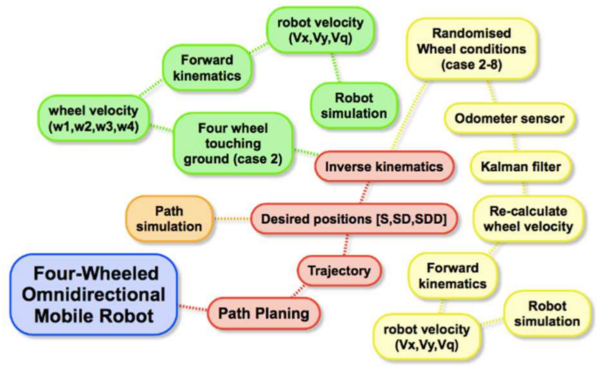

Fig. 2. The simulation procedures.

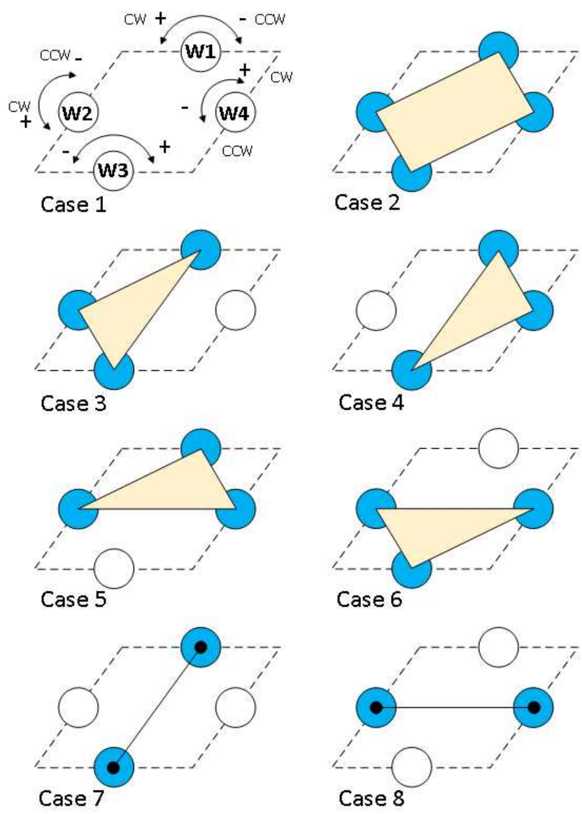

Fig. 3. There are eight possible cases involving the four omnidirectional wheels. This shows the rotation direction of each omnidirectional wheel, clockwise and counterclockwise. In case 1, not all wheels touch the ground. This is not used in the simulation.

planned path, and second, the robot cannot reach the goal's position. There are eight conditions of motion as shown in Fig. 3. The wheels can change the states of motion, as in Table 2, the four wheels drive in Case 2, the three wheels drive in Cases 3 through 6, and the two wheels drive in Cases 7 and 8.

Table 2. The omnidirectional wheels touch and do not touch the floor in the conditions of motion. Eight cases have been determined.

case	W_1	W_2	W_3	W_4
1	0	0	0	0
2	1	1	1	1
3	1	1	1	0
4	1	0	1	1
5	1	1	0	1
6	0	1	1	1
7	1	0	1	0
8	0	1	0	1

Note: 1 is touching and 0 is not touching the ground.

In the example, W_1 and W_3 are stuck, and the robot cannot keep moving in the desired direction in case 8. The robot needs to get out by struggling to the left and right, back and forth, as shown in Fig. 4.

In motion case 2, all wheels are touching the floor while the robot is moving. This is the ideal condition for motion. However, not all wheels can touch the ground all the time in cases 3 through 8.

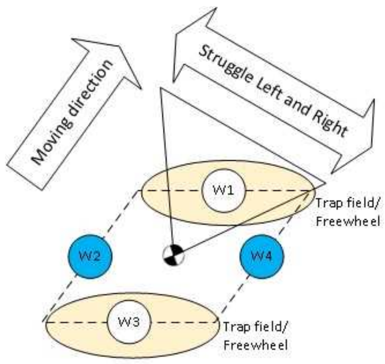

Fig. 4. The omnidirectional mobile robot attempts to move under the conditions of motion case 8. The trap field, or the freewheel, is random in the simulation. This means that the omnidirectional wheel is not touching the floor.

4. Motion Improvement

The planned path trajectory is assigned to the robot's moving path profile. This omnidirectional mobile robot cannot move along to the goal position when it is in motion case condition 3-8. The robot needs to adjust its position to the goal even when the robot goes into a trap field. Motion improvement aims to help the robot approach the goal position using the Kalman filter.

4.1. Kalman Filter

The Kalman filter was invented by Rudolf Kalman. It is a well-known algorithm that is used to estimate the output from a system model and sensor measurements. The Kalman filter was invented for the linear system, but many problems are non-linear. Thus, it needs to linearize the system model. Estimating the measurements of a non-linear system requires a tool known as the extended Kalman filter (EKF). This paper uses the EKF for the four-wheeled omnidirectional mobile robot. The algorithm is iterative to predict, and an update follows Eq. (7-11). However, much research is needed in order to implement the EKF within the omnidirectional mobile robot. Guidelines following the algorithm's steps are described in Ref. 6-8. A difference in this work as compared to other works is the use of random states of motion for the state process.

Predict:

$$\hat{x}_t^- = f(\hat{x}_{t-1}^-, \hat{u}_t^-) + w_t \tag{7}$$

$$P_t^- = F_x P_{t-1} F_x^T + F_v U_t F_v^T + Q_t \tag{8}$$

Update:

$$K_t = P_t^- H_t^T (H_t P_t^- H_t^T + R_t)^{-1} \tag{9}$$

$$\hat{x}_t = \hat{x}_t^- + K_t(z_t - \hat{z}_t) \tag{10}$$

$$P_t = (I - K_t H_t) P_t^- \tag{11}$$

Where $\hat{x}$ is the estimated state. F is the state transition matrix (translation between states). $\hat{u}$ is the control variables. w is the modelled random white noise. P is the state variance matrix (error of estimation). U is the control input error covariance. Q is the process variance matrix (error due to process). z is the measurement variables. H is the measurement matrix (mapping measurements onto state). K is the Kalman gain. R is the measurement variance matrix (error from measurements). Subscripts are as follows: t current time period and t-1 previous time period. Superscript (-) is intermediate steps.

The EKF framework has various sensors for the step update that is referred to as a "sensor fusion.[8]" The values from simulation compared to the original sensors are the heading angle from a compass, the yaw rate from a gyroscope, the wheel's speed from an encoder, the freewheel check from the wheel's rotation and the robot's movement using an encoder and an accelerometer, and target bearing from a camera.

5. Simulation Results

The planned path was a linear path from the start position (x = 20, y = 20) to the goal position (x = 150, y = 150). It started moving to the +diagonal right, as in Table 1, and then attempted to rotate itself because the heading angle was changed. The robot's heading angle started from 0 rad, as in the configuration in Fig. 1. Finally, the robot's heading angle stopped at $\pi/4$ rad. Moving under the conditions of motion randomly, the robot shifted from the

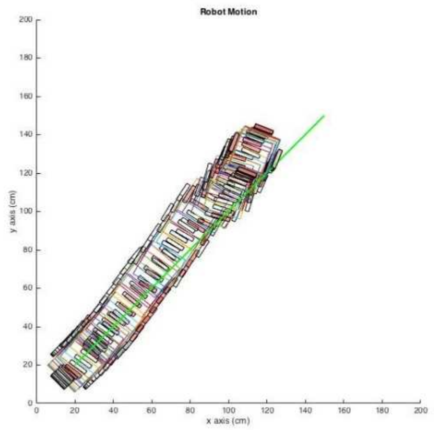

Fig. 5. The robot randomly moved under the eight conditions of motion, following the planned path from the start position to the goal position.

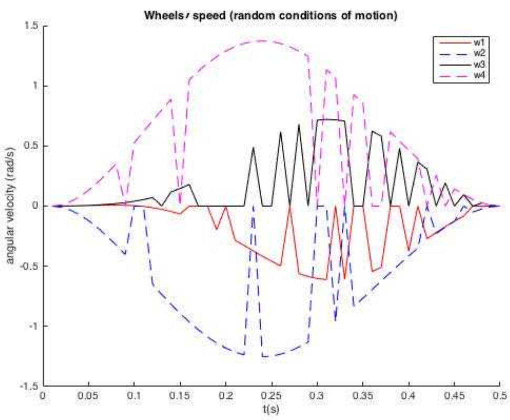

Fig. 6. The four wheels' speed trajectory is related to the planned path. W_1 and W_2 rotated counterclockwise. W_3 and W_4 rotated clockwise.

planned path and had not reached the goal position when the time ended. The robot's actual position is shown in Fig. 5.

Accordingly, each wheel of the robot had the wheel's speed, as shown in Fig. 6. The wheel's speed dropped to zero in the trap field in case of free running, or the wheel did not touch the floor.

The total simulation time was 0.5 seconds, with every 0.01 second per step. After applying the EKF to the robot,

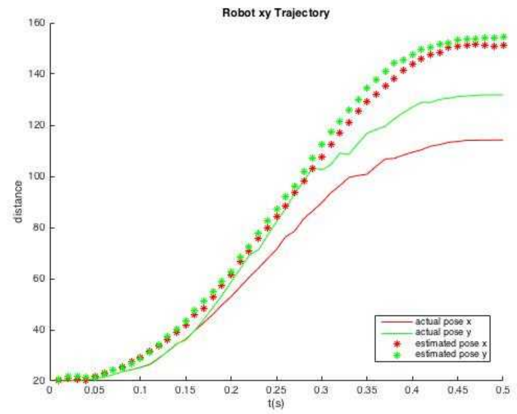

Fig. 7. The robot's actual positions x and y shifted from the planned path. The estimated position x and y from the EKF had a better motion.

the estimated positions x and y were smooth and could reach very close to the goal position as shown in Fig.7.

The robot maintained the position on the planned path. However, the robot's heading angle from

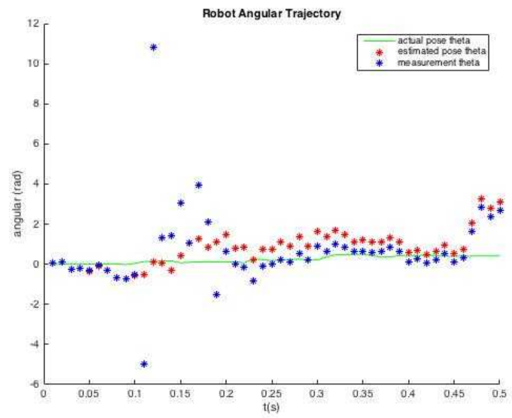

Fig. 8. The robot's heading angle simulated the actual position. The estimated and measured heading angle were the motion improvement from the EKF.

© The 2017 International Conference on Artificial Life and Robotics (ICAROB 2017), Jan. 19-22, Seagaia Convention Center, Miyazaki, Japan

measurement and estimation changed a lot as shown in Fig. 8.

The robot in x and y position could be compared in Fig. 9. The measured position was noisy and affected by the error of the actual position.

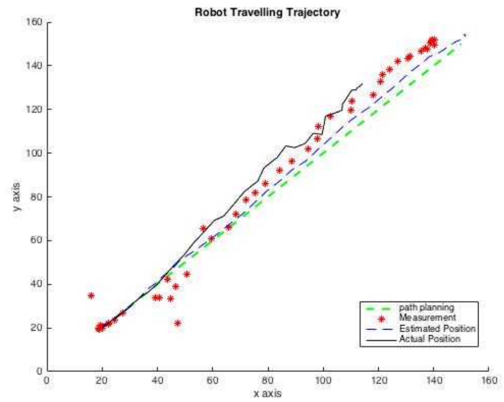

Fig. 9. Comparing the motions of the robot from path planning, measurement, estimation, and actual position.

For the motion improvement, each wheel's speed was generated from the estimated positions. The estimated wheel's speed was very noisy compared to the actual wheel's speed because the robot struggled to the new positions as in Fig. 10.

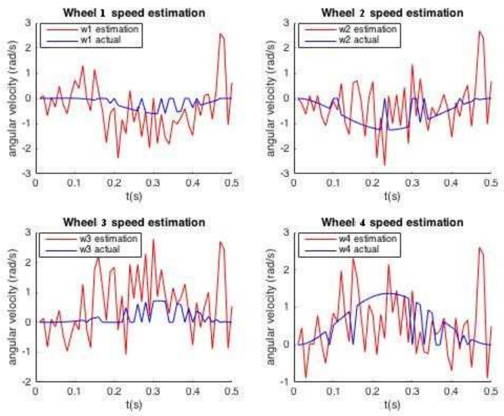

Fig. 10. Comparing the estimated and the actual speed of the four wheels.

6. Conclusion

The robot randomly changed its states of motion in four-wheel, three-wheel, and two-wheel drive. The main error came from the robot motion model, which changed the number of the driving wheel. Generally, the EKF reduces the effects of slip noise and sensor noise in the dead reckoning problem. However, the simulation result shows that the EKF produces better robot motion along the planned path. The robot struggles to traverse its planned path with its assigned trajectory.

The behavior of the robot during the real test may considerably differ from the simulation. Noises from signals are reduced, but the dynamic motion of the robot may not work like the control signals. For real tests in future work, the omnidirectional mobile robot has to have speed control sensors to monitor its wheel speed, and it will be important to check the freewheel and the floor touchless condition when some of the wheels rotate, but the robot does not move, or it moves in the wrong direction.

Acknowledgements

This work was funded by Science and Technology Research Institute, King Mongkut's University of Technology North Bangkok.

References

1. Z. Jie-Tong, *The Development of the Omnidirectional Mobile Home Care Robot*, (Mobile Robots – Current Trends, InTech, 2011) pp.345-362
2. R. Raul and G.F. Alexander, *Holonomic Control of a robot with an omnidirectional drive*, KI Künstliche Intelligenz, BöttcherIT Verlag, 2006.
3. U. Martin and I. Karl, *Analysis Design and Control of an Omnidirectional Mobile Robot on Rough Terrain* (Journal of Mechanical Design, ASME, 2009) vol. 131.
4. S. Jae-Bok and B. Kyung-Seok, *Design and Control of an Omnidirectional Mobile Robot with Steerable Omnidirectional Wheels,* Mobile Robotics, Moving Intelligence, Jonas Buchli (Ed.), InTech.
5. R.C. Dixon, G. Bright and R. Harley, *Robust localisation of automated guided vehicles for computer-integrated manufacturing environments*. S. Afr. J. Ind. Eng. 2013, vol.24, n.1, pp.81-90.
6. S. Caius, C. Cristina and M. Florin, *Mobile Robot Position Estimation Using the Kalman Filter,* Scientific Bulletin of the Petru Maior University of Tirgu Mures, vol. 6, 2009.
7. C. Peter, *Robotics Vision and Control* (Springer Tracts in Advanced Robotics, 2011), pp. 107–128.
8. S. Antonio, N. Urbano and A. Rui, *Fusion of Odometry with Magnetic Sensors Using Kalman Filter and Augmented System Models for Mobile Robot Navigation*, IEEE ISIE 2005, pp. 1551-1556

An Improved Algorithm for Obstacle Avoidance by Follow the Gap Method Combined Potential Field

Chakhrit La-orworrakhun and Suriya Natsupakpong
Institute of Field Robotics, King Mongkut's University Technology Thonburi,
26 Pracha Uthit Rd., Bang Mod, Thung Khru, Bangkok 10140, Thailand
E-mail: chakhrit.yong@mail.kmutt.ac.th, suriya@fibo.kmutt.ac.th
http://www.fibo.kmutt.ac.th/

Abstract

A novel obstacle avoidance algorithm for boat survey, "Follow the Gap Plus", is proposed by combining the "Follow the Gap" method and adapting the "Potential Field" method with an attractive field of obstacles. Then the simulation environment for testing algorithm are generated in various situations with real-world-like environment. The results show that the proposed algorithm can go to the desired destination with better performance than "Follow the Gap" method in the environment with obstacles about 4.47% of total distance, about 7.63% of total time used, and about 54.33% of average change of direction.

Keywords: Survey boat, Obstacle Avoidance, Follow the Gap Method, Potential Field Method, Simulation.

1. Introduction

Currently robot technology have more demand for making life better. Knowledge and techniques applied to robots have more complicated as well. For example, robot movement to the designated destinations need interact with environment in different ways, such as obstacle avoidance, navigation, localization, trajectory planning etc.

In unknown environment, robot must have intelligent navigation system for planning a safety path to the goal. An algorithm for obstacle avoidance should make decision automatically with simple computation. Algorithm must find a safety path, shorter path and smooth change[1]. And when the robot found the obstacles, the algorithm must make quick decision with accuracy. For the objectives mentioned above, a novel obstacle avoidance algorithm for boat survey is proposed by focusing on the development of efficient algorithms used in shorter path and smooth change.

Most survey robots are using on the ground and in the air, whereas no robots for survey is on the water. Survey robots on water is interesting because an environment is different from the ground and have many problems, such as dynamic of the water. Therefore, the simulation of survey robot on the water is selected and developed.

The paper is organized as follows. In section 2, the related algorithms are summarized. In section 3, the proposed algorithm is presented in details. In section 4, the navigation system for testing environment are setup. In section 5, the simulation results are shown with discussion. Finally, section 6 shows the conclusions.

2. Related Works

2.1. *Artificial Potential Field Method*[2-4]

Artificial potential field method is based on the principle of potential field. The robot and obstacle are determined with positive value and the goal is determined with negative value. Therefore, obstacles will be pushed a robot out by created repulsive force. The goal is to attract a robot by created attractive force. So, final force on robot is the summation of all repulsive and attractive force.

This algorithm is popular implemented in mobile robot. Many researchers[3] used [SN1] this algorithm because efficiency and simplicity of mathematical model, however this algorithm has a problem in local minimum and produces a short path.

2.2. *Follow the Gap Method*[5]

Follow the gap method avoids obstacles by finding the gap between obstacles and calculates the gap angle. Afterward, many researchers used this algorithm to implement in autonomous robot, such as autonomous car[6-8] or improve this algorithm by combined with others algorithm[1] for solving local minimum problem and researcher has noticed that this algorithm familiar with avoid obstacles of birds[9]. However, follow the gap method has issues about weight between gap angle and goal to find optimal ratio.

3. Follow the Gap Plus Method

Follow the gap method has problem when user wants the robot to avoid obstacles safely. Users need to set the weight of center gap angle with high value. The result of this makes the distance to the target increases. This proposed algorithm is intended to improve follow the gap method by using the concept of artificial potential field method applied in created repulsive force pushed out from obstacles and turned into attractive force instead. This algorithm is named with “follow the gap plus method”.

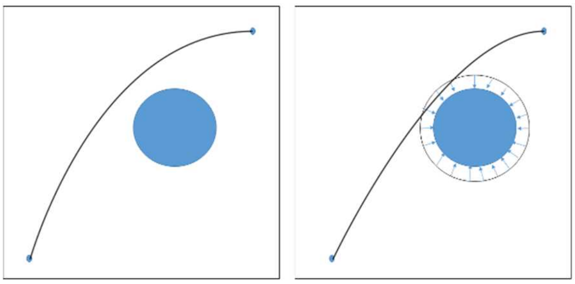

Fig. 1 Concept of follow the gap plus method

Follow the gap plus method has four main step.

Step 1: calculating the gap array and finding the maximum gap.

Step 2: calculating the gap center angle using Eq. (1)

$$\emptyset_{gap_c} = \arccos\left(\frac{d_1 + d_2 \cos(\emptyset_1 + \emptyset_2)}{\sqrt{{d_1}^2 + {d_2}^2 + 2d_1 d_2 \cos(\emptyset_1 + \emptyset_2)}}\right) \quad (1)$$

Where d_1 and d_2 are the distance of obstacles 1 and 2 from robot respectively. $\emptyset_1$ and $\emptyset_2$ are angles of obstacles respectively. $\emptyset_{gap_c}$ is the final calculated gap center angle.

Step 3: combining with attractive field and calculating distance to goal and creating attractive field to obstacle by using inverse repulsive field. Then, finding an angle between robot and obstacle using Eq. (2).

$$\theta = \tan^{-1}\left(\frac{y_O - y}{x_O - x}\right) \quad (2)$$

Determine the position of the robot changes $(\Delta x, \Delta y)$ as follow[2].

$if\ d < r,$
$\Delta x = -sign(\cos\theta)\ and\ \Delta y = -sign(\sin\theta)$

$if\ r \le d \le s + r,$
$\Delta x = \beta(s + r - d)\cos\theta\ and\ \Delta y = \beta(s + r - d)\sin\theta$

$if\ d \ge s + r,$
$\Delta x = \Delta y = 0$[SN2]

If position of robot is outside of the circle of influence, the attractive potential field is zero. Within the circle of influence but outside the radius of the obstacle, the attractive force decreases from maximum value to zero depending on distance to obstacle. The constant $\beta > 0$ is given by allowing the agent to scale in the strength of this field. Then the summation of attractive force from every obstacles is calculated in the result of angle to that position. Then, the summation of gap center angle is calculated using Eq. (3).

$$\emptyset_{new} = \frac{\emptyset_{gap_c} + \emptyset_r}{2} \quad (3)$$

Step 4: calculating the final heading angle. This can be achieved by combining the gap center angle with the goal angle in Eq. (4).

$$\emptyset_{final} = \frac{\frac{\alpha}{d_{min}}\emptyset_{new} + \beta\emptyset_{goal}}{\frac{\alpha}{d_{min}} + \beta} \quad (4)$$

Where d_{min} is minimum distance to obstacle. $\emptyset_{new}$ is calculated gap combined attractive force angle. $\emptyset_{goal}$ is goal angle. α and β are weight coefficients.

4. Navigation System

Autonomous survey boat requires a system for navigating to the goal. This paper proposed a simple navigation system used in survey boat experiment. The survey boat’s navigation system after initial system has three main process.

First, obstacle detection process for detecting obstacle in front of the survey boat is calculated. In this process, laser scanner is used to detect obstacles. Start by checking tilt of boat, if the value is less than the threshold then the environment in front of boat begins to scan and save. Second, avoidance strategy process and a decision making of boat's heading is calculated by an obstacle avoidance algorithm, such as follow the gap method or follow the gap plus method. Third, control steering process for changing boat's heading according to the angle is calculated.

These three processes run respectively and repeat until the goal is reached. If it has other goal, system will update position of new goal and begin the first process. The Flowchart of this system is shown in Fig.2.

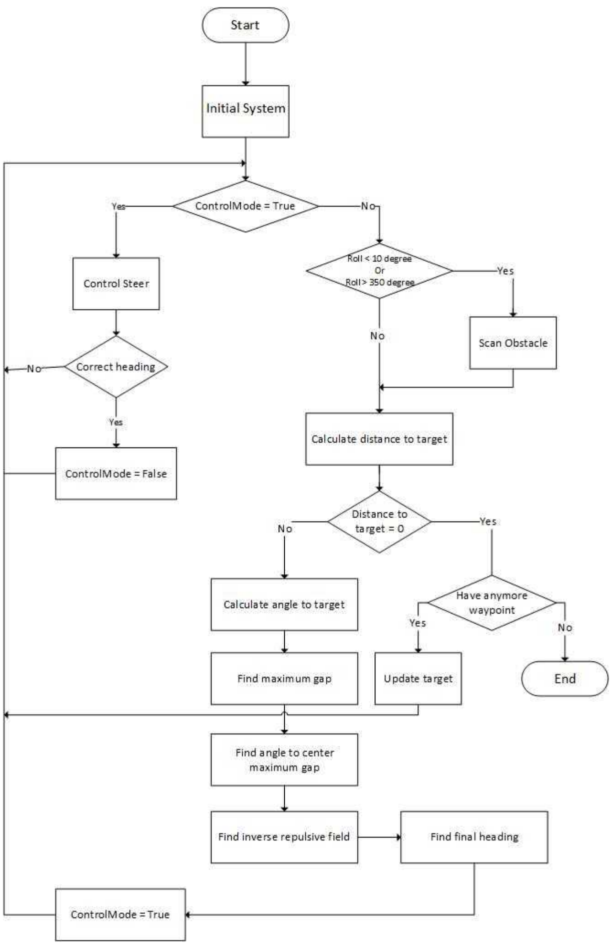

Fig.2. Navigation system flowchart

5. Simulations and Results

The effectiveness of the proposed algorithms has been demonstrated by using the Unity3D software. In the experiments, the environment of canal with dynamic water is simulated. The performance about the shorter path shown in the distance, and about smooth change shown in number of times to change heading direction and change heading angle over 15 degree. [SN3]Two[SN4] interesting scenarios are presented consisting of simple obstacles and similar real-environment[SN5].

5.1. *Scenario 1: Avoiding simple obstacle*

In scenario 1, considers the situation with few and easy shape obstacle. The shortest path is almost a linear path. This situation is suitable for basic testing an algorithm for usability. The results of trajectory path are shown in Fig.3.

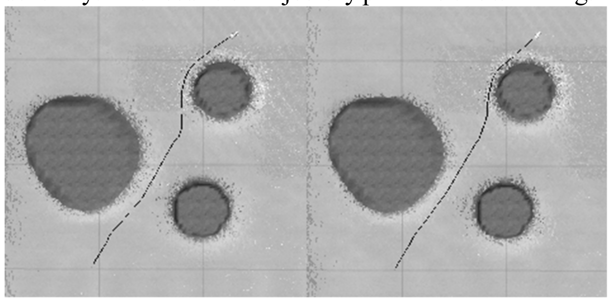

(a) (b)

Fig. 3 Scenario 1 robot trajectory (a) Follow the gap method (b) Follow the gap plus method

Table. 1 The comparison performance of the algorithm in scenario 1.

	Follow the gap method	Follow the gap plus method
Time used (sec)	37.70	36.53
Distance (m)	254.42	251.38
Heading direction change	39	37
Heading change > 15°	0	0

Table. 1 shows that the follow the gap plus method has better performance about 1.19 percentage of total distance, about 3.08 percentage of total time used, less heading direction change 2 times, and both algorithms have no heading change over 15 degrees. Follow the gap plus method has better performance in this scenario because an obstacle closes to the shortest path and attractive force to obstacle makes the path to close obstacle, therefore the path nearby the shortest path. While follow the gap method has only gap angle in calculation, therefore the path is far from the shortest path.

5.2. *Scenario 2: Environment similar real*

In scenario 2, a real-life environment is simulated in straight canal, width about 60 meters with obstructions in the canal. No dynamic obstacle is consider in the experiment. The result of trajectory path is shown in Fig.4.

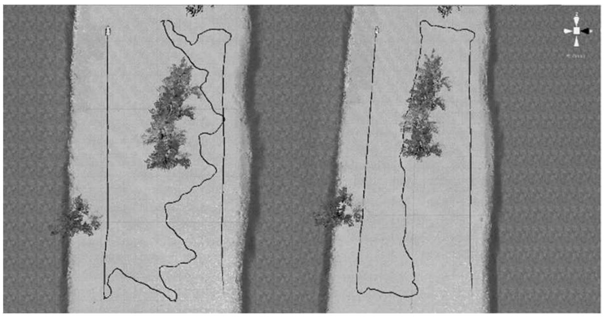

(a) (b)
Fig. 4 scenario 2 robot trajectory (a) Follow the gap method (b) Follow the gap plus method

Table. 2 The comparison performance of the algorithm in scenario 2.

	Follow the gap method	Follow the gap plus method
Time used (sec)	133.06	122.91
Distance (m)	780.15	745.24
Heading direction change	177	168
Heading change > 15°	42	22

Table. 2 shows that follow the gap plus method has better performance about 4.47 percentage of total distance, about 7.63 percentage of total time used, less heading direction change 9 times and less heading change over 15 degrees 20 times. The simulation result shows that the follow the gap plus method uses the different path from the follow the gap method. From waypoint 2 to waypoint 3, the follow the gap method uses path far from obstacle because it uses only center gap degree for decision. Whereas the follow the gap plus method used center gap degree and attractive force to obstacle, in the result the selected path is near obstacle and straight to waypoint 3.

6. Conclusions

The proposed algorithm, follow the gap plus method, is presented for autonomous navigation robot with the shorter and smoother path results and uses less times than follow the gap method. The simulation results show this algorithm can implement to real robot for survey on canal. However, this algorithm emphasized about shorter path, therefore robot approaching near an obstacle. So performance about short and safety path are being turned upside down. So, the future work will focus on improving the performance with safety path, testing with dynamic obstacle and testing with real robot and real environment.

Acknowledgements

Thanks to Hydro and Agro Informatics Institute and Institute of Field Robotics, King Mongkut's University Technology Thonburi for supporting the research funding.

References

1. M. Zohaib, S. M. Pasha, N. Javaid, J. Iqbal, & A. Salaam, An improved algorithm for collision avoidance in environments having U and H shaped obstacles, *Studies in Informatics and Control* 23(1) (2014), pp. 97–106.
2. M. Goodrich, Potential Fields tutorial, 2002.
3. L. Tang, S. Dian, G. Gu, K. Zhou, S. Wang, & X. Feng, A novel potential field method for obstacle avoidance and path planning of mobile robot, *3rd International Conference on Computer Science and Information Technology (2010)*, pp. 633–637.
4. E. N Sabudin, R Omar. and C. K. A. N. H Che Ku Melor, Potential Field Methods and Their Inherent Approaches for Path Planing, *ARPN Journal of Engineering and Applied Sciences (2016)*, pp. 10801-10805
5. V. Sezer, & M. Gokasan, A novel obstacle avoidance algorithm: “Follow the gap method, Robotics and Autonomous Systems, 60(9) (2012), pp. 1123–1134.
6. Design V., Combined fuzzy approach for online speed planning and control with real vehicle implementation 68(4) (2015), pp. 24–27.
7. F. You, R. Zhang, G. Lie, H. Wang, H. Wen, & J. Xu, Trajectory planning and tracking control for autonomous lane change maneuver based on the cooperative vehicle infrastructure system, *Expert Systems with Applications*, 42(14) (2015), pp. 5932–5946.
8. R. Kala, & K. Warwick, Motion Planning of Autonomous Vehicles on a Dual Carriageway without Speed Lanes, *Electronics*, 4(1) (2015), pp. 59–81.
9. H. T. Lin, I. G. Ros, & A. A. Biewener, Through the eyes of a bird: modelling visually guided obstacle flight, Journal of the Royal Society, Interface / the Royal Society (2014), pp. 2-39.

Study on the target positioning for an Omni-directional 3 DOF mobile manipulator based on machine vision

Jiwu Wang[1]
School of Mechanical, Electronic and Control Engineering, Beijing Jiaotong University
Beijing 100044, China[1]

Yao Du[1], **Wensheng Xu**[1]
School of Mechanical, Electronic and Control Engineering, Beijing Jiaotong University
Beijing 100044, China[1]

Masanori Sugisaka[2]
Alife Robotics Corporation Ltd, Japan and Open University, United Kingdom[2]
E-mail: 15121244@bjtu.edu.cn[1]*; ms@alife-robotics.co.jp*[2]
www.bjtu.edu.cn

Abstract

The omni-directional mobile robot with multi DOF, because the operation posture and operation accuracy of the manipulator can be better controlled in a narrow or crowded workplace compared with the general manipulator, is getting more interested in practical applications. The present problem is to improve its flexibility for operating multiple different targets. Target recognition with image processing is an effective solution. Based on the image processing, the position and posture of the target can be determined. Then the signal will be sent to the arm control system. In this paper, the illumination conditions, distortion, etc. are studied in the target recognition. The target position with image processing, is verified with real coordinates. The experiments show target recognition with image processing can effectively improve the flexibility of our robot.

Keywords: mobile robot; machine vision; 3 DOF manipulator; Omni-direction.

1. Introduction

Today, the degree of automation of factories and warehouses becomes increasingly higher and higher. [1] However it is difficult to expand manipulator's functions because its fixed base. This article describes an Omni-directional 3 DOF mobile manipulator, which can increase flexibility of the manipulator and greatly increase its function.

Firstly, through the analysis of the 3 DOF manipulator, established the manipulator kinematics model by the D-[1]H method, and on the basis of this model, derived solving method to the manipulator kinematics equation of the manipulator and the inverse kinematics problem, the analytical solution of problem of manipulator inverse kinematics.

Then the analytical solutions of the forward kinematics equations and inverse solutions are verified and analyzed.

The experimental results prove the effectiveness of the method and the method of the target location.

2. System Overview

In order to realize the automatic control of the robot, the robot control system plays an indispensable role. In this paper, the robot uses four Mecanum wheels to realize the omnidirectional movement of the robot platform. Robot control system is divided into four parts, they are IPC, the main, chassis drives and mechanical arm drive plate, as shown in Figure 1.

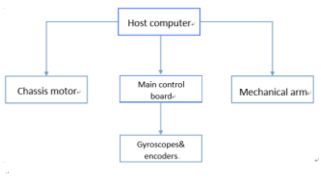

Fig.1. System Overview

IPC runs the Windows operating system, through the serial port and the main control board to achieve communication between the main control board and the two driver boards through the CAN bus communication.

2.1 Design of Omnidirectional Mobile Chassis Based on Mecanum Wheel

In this paper, four Mecanum wheels are installed to realize the omni-directional movement of the platform, as shown in Figure 2. [2]

Fig.2. Mecanum wheel

From Figure 3 you can see the four Mecanum wheels combined installation situation. Each wheel is driven by a DC brush motor alone, with both left-handed and right-handed rotations.

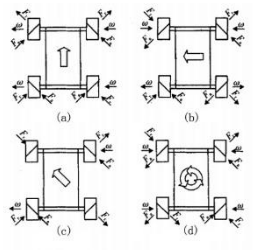

Fig.3.Analysis of chassis movement

Figure 4 shows the Mecanum wheel four-wheel robot chassis model coordinate system. The coordinate system $O_iX_iY_i(i$=1,2,3,4) is established with the center of each wheel position as the origin, and the reference coordinate system OXY is established with the center of the robot as the origin.

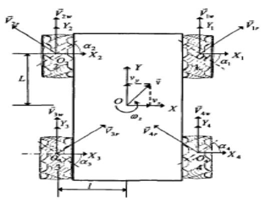

Fig.4. Coordinate modeling of omnidirectional mobile robot

As shown in Figure4, the robot body length is 2L, the body width is 2l, the speed of the robot chassis is = (V_x , V_y), the angular velocity of the robot around the Z-axis is ω_z, the linear velocity of the wheel is $_{iw}$, there$_{iw}$ = $\omega_i R$. (Where ω_i is the angular velocity of each wheel and R is the radius of the wheel). The roller and the ground contact when the line speed $_{ir}$. Suppose that the speed of each wheel is $_i$= (V_{ix}, V_{iy}). Under $O_iX_iY_i(i$=1,2,3,4), can be decomposed along X_i and Y_i, as$_{iw}$ and $_{ir}$, and V_{ix} can be expressed as $-V_{ir}$ sinα_i, V_{iy} is the sum of $_{iw}$ and $_{ir}$ cosα_i. Which satisfy the relation:

$$\begin{aligned} V_{1x} &= -V_{1r}\sin\alpha_1,\quad V_{1y} = -V_{1w}+V_{1r}\cos\alpha_1 \\ V_{2x} &= -V_{2r}\sin\alpha_2,\quad V_{2y} = -V_{2w}+V_{2r}\cos\alpha_2 \\ V_{3x} &= -V_{3r}\sin\alpha_3,\quad V_{3y} = -V_{3w}+V_{3r}\cos\alpha_3 \qquad (1) \\ V_{4x} &= -V_{4r}\sin\alpha_4,\quad V_{4y} = -V_{4w}+V_{4r}\cos\alpha_4 \end{aligned}$$

In the formula αi-i round roller axis and the hub axis angle (i = 1, 2, 3, 4).

Overall, the speed of each wheel i is the speed of the robot and the relative speed of the wheel center O speed vector, that is, $=_i +_z*_l$, consider vector directionality, along the coordinates and X_iY_i Coordinate decomposition formula can be obtained:

$$V_{1x} = V_x - L\omega_z,\ V_{1y} = V_y + l\omega_z$$
$$V_{2x} = V_x - L\omega_z,\ V_{2y} = V_y - l\omega_z$$
$$V_{3x} = -V_x + L\omega_z,\ V_{3y} = V_y - l\omega_z \quad (2)$$
$$V_{4x} = V_x + L\omega_z,\ V4_y = V_y + l\omega_z$$

Taking into account the pipe speed for the non-controlled volume, to eliminate, that is derived omni-directional robot inverse kinematics equation is:

$$W_1 = -V_x \cot\alpha + V_y + (l + L\cot\alpha)\,\omega_z$$
$$W_2 = V_x \cot\alpha + V_y - (l + L\cot\alpha)\,\omega_z$$
$$W_3 = -V_x \cot\alpha + V_y - (l + L\cot\alpha)\,\omega_z \quad (3)$$
$$W_4 = -V_x \cot\alpha + V_y + (l + L\cot\alpha)\,\omega_z$$

From the above equation, the control of the whole robot can be realized.

2.2 Design of Multi - DOF Gripping Manipulator

The design of the robot arm a total of three degrees of freedom, the direction of the X-axis rail, two connecting rods were Y, Z axis.

2.2.1 *Motion Control of Manipulator 's Hand Linear Interpolation*

Calculation shows that the position of the robot joint position and the relationship between the hand space:

(4)

For the robot hand space position, the line is interpolated as it moves from (y_1, z_1) to (y_2, z_2) in a straight line.

Because of simple interpolation from the x-axis or y-axis, there is a great deal of non-uniformity.

Assuming the slope of the line segment is k, when $y_1 \neq y_2$, $k = (z_2 - z_1)/(y_2 - y_1)$, the straight line inclination angle is:

$$\alpha = \arctan k \quad (5)$$

Assuming that d is the distance from any point (y, z) to (y_1, z_1) on this line segment, the point corresponding to d (y, z) is

(6)

Where d is in the range of [0,]. When d is evenly changed in this interval, the movement of the hand (y, z) obtained by the above-described equation is substituted into the joint position expression so as to be able to realize a straight line movement of the hand

2.2.2 *Robot manipulator arm speed control*

It can be seen that the relationship between the spatial position of the robot hand and the joint variable is

(7)

Derivative of the above formula can be obtained

(8)

Written in matrix form

(9)

Is known from the definition of the Jacobian matrix:

(10)

The Jacobian matrix of the manipulator can be obtained

(11)

Jacques array is mainly used to describe the joint displacement and space pose differential relationship, the relationship between the spatial velocity of the robot hand and the angular velocity of the joint is given

$$v=J \quad (12)$$

Conversely, the speed of movement of each joint can be determined from the desired hand speed $=J^{-1} v$.
According to calculations:

$$J^{-1}= \quad (13)$$

2.3 Design of Image Processing.

Template matching is to find the target image in the image. [3] The principle is to measure the similarity between two images by some similarity criteria.

2.3.1 *Template Matching Based on Gray Value*

When the template slides in the image, do similarity matching. The simplest measure of similarity is to calculate the sum of the absolute values of the differences between the template and the image or the sum of squares of all the differences (SAD and SSD).

(14)

$(r+u,c+v)$ denotes the gray value of the row r + u column c + v of the image to be measured, and $t(r,c)$ denotes the gray value of the template image T row r column c. [4] The difference between the values after the change and their mean values will be smaller regardless of whether all the gray values become larger or smaller and then become zero mean and unit variance by dividing the variance so that the image is less sensitive to changes in the brightness level , and has strong robustness.

(15)

m_c is the average gray value of the template, s_t^2 is the variance of all the gray values of the image to be measured, $(r,)$ is the average gray value of the image to be measured.

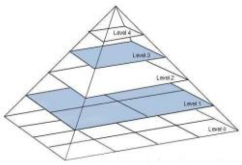

Fig.6.A schematic diagram of the image pyramid

In the pyramid-based search strategy: from the top to the bottom of the search, in the high-level image search to track the template instance to the bottom of the image pyramid, then in a small area to match, in the next search region to locate the results of the matching of a small area the similarity degree is calculated, segmented by the threshold and the local extrema is extracted.

2.3.2 *Realization of crawl*

In order to achieve the robot automatic items crawl, we must get the actual location of items in the world coordinate system.

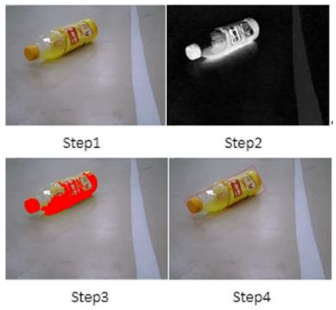

Fig.7. Steps to find items

As shown in figure 7. First, the original image distortion correction and smoothing noise; then extract the image of the saturation S component from the image HSV space, we can clearly see that saturation component of the object we want to crawl is relatively high; The third step is to get the image region with high saturation through the dynamic threshold technique. The final step is to display the obtained area and get the orientation information of the area and the orientation information of the bottle.

3. Conclusion

This paper introduce an Omni-directional 3 DOF mobile manipulator based on machine vision. However, in real-world experiments, the robot was controlled to grasp the bottle. Our experiments have shown that the desired relative position and orientation between the camera and the object have been kept within errors of few centimeters. The next step is to further improve the image processing method to make the image processing faster, so that the robot more accurate understanding of the surrounding environment. Adding some sensors, such as lidar, gives the robot a path planning and obstacle avoidance function. Increase the chassis suspension system to adapt to a richer terrain.

References

1. Wang J, Zhang X and Zhang W, Study on the Improvement of Flexibility for an Industrial Robot based on Machine Vision, *J. Journal of Robotics, Networking & Artificial Life*, 2014, 1(1):45-48.
2. Du B, Zhao J and Song C, Dexterity Analysis for Omni-directional Wheeled Mobile Manipulator Based on

Double Quaternion, *J. Chinese Journal of Mechanical Engineering*,2013,03:585-593.
3. Wang J, Zhang X and Dou H, Study on the Target Recognition and Location Technology of Industrial Sorting Robot based on Machine Vision, *J. Journal of Robotics, Networking & Artificial Life*, 2015, 2(2):108-110.
4. Wang J, Dou H and Zheng S, Study on the Target Recognition based on Machine Vision for Industrial Sorting Robot, *J. Journal of Robotics, Networking & Artificial Life*, 2015, 2(2):100-102.

Informational Narratology and Automated Content Generation

Takashi Ogata
Department of Software Informatics, Iwate Prefectural University
Takizawa, Iwate, 020-0693, Japan

Yoji Kawamura
Kindai University
Higashi-osaka, Osaka, 577-8502, Japan

Akihito Kanai
Hosei University
Machida, Tokyo, 194-0298, Japan

E-mail: t-ogata@iwate-pu.ac.jp, kawamura@bus.kindai.ac.jp, kanai@hosei.ac.jp

Abstract

Several studies have proposed a concept called "informational narratology" or "information narratology." In this paper, we integrate narratological studies, including narratology and various literary theories, into information technologies, such as artificial intelligence and cognitive science, in order to mainly design and develop systems that automatically generate, create, or produce digital narrative contents related to a variety of existing or future narrative genres. Under this framework, we design and develop narrative generation systems, advertise image processing systems, and develop narrative film operation systems. In this paper, we present an overview of the concept of informational narratology, and introduce the above three studies as concrete approaches to its development.

Keywords: Informational narratology, automated content generation, narrative generation, multiple narrative structures, integrated narrative generation system.

1. Introduction

"Narrative" is one of the most important words in the fields of literature and humanities. Furthermore, it is also an academic term that is related to wider areas such as clinical psychology, artificial intelligence (AI), and cognitive science. The concept of the narrative in AI and cognitive science is used particularly as a kind of schemata through which a variety of information in an environment is synthetically recognized and represented. Studies of narrative text analysis have also been attempted using various narrative-relating methods and techniques. Ogata & Kanai[1] and Ogata[2] reviewed narrative studies in diverse academic fields including narratology, literary theories, AI, and cognitive science.

We have performed narrative-related studies from various viewpoints. However, a common outstanding feature is the objective to integrate narratological themes and materials related to literary theories into information science and technologies such as AI and cognitive science. For narrative-related studies from the above perspective, we have proposed a new research framework and concept called "informational narratology" or "information narratology." Informational narratology focuses on the areas of narrative generation and creation, and is different from the previous or traditional narratology, which focuses on the narrative aspects of reading and interpretation. Informational narratology also focuses on automated narrative content generation using computers and AI to utilize the formalized characteristics of narratology.

In this paper, we present an overview of three approaches to the informational narratology, which were developed by the respective authors of this paper, to show the potential and effectiveness of automated narrative generation. We mainly designed and developed systems that automatically generate, create, and produce digital narrative contents for several existing or future genres through narrative communication and simulation. In particular, we designed and developed narrative generation systems (Ogata), advertising image processing systems (Kawamura), and narrative film processing systems (Kanai). In this paper, we propose an overview of the above three systems as mutually related approaches to embody the informational narratology.

2. Theories and Systems of Narrative Generation by Ogata

Although narrative generation systems called Integrated Narrative Generation System (INGS)[2] and Geino Information System (GIS)[3], which are central parts in the current work by Ogata, have been designed and developed, they are based on the following theories for informational narratology.

2.1. *An Overview*

Ogata recognized that there are narratological phenomena through which diverse narratives always emerge and exist. Ogata[4] tentatively showed a hierarchical list that comprehends diverse narrative genres to indicate the large space of the narratological phenomena. Another reason for this attempt is to create new narrative works that absorb and re-construct a variety of elements and characteristics of previous or traditional narratives in the relationships with future digital narratives and narrative generation systems (INGS and GIS) developed by Ogata.

Ogata considered two types of narrative processes: the narrative generation-reception process at the personal narrative level, and the narrative production-consumption process at the social narrative level. As the models and systemization of these processes, INGS and GIS correspond to the former and latter, respectively. In other words, both the narrative generation-reception model and narrative production-consumption model, which are integrated by the next multiple-narrative structure model, are implemented by the INGS corresponding to the narrative generation-reception model and the GIS corresponding to the narrative production-consumption model.

From the perspectives of the mutual relationship or inclusive relationship, as well as a larger narrative model, narrative production, i.e., the consumption process, includes the narrative generation-reception process. Therefore, from a broad perspective, a narrative as a generation-reception process is constructed by a production-consumption process. We use the term “multiplenarrative structure model” to show such multiple narrative phenomena. In addition, at other various levels, the multiple-narrative structures model is a very significant characteristic in narrative phenomena.

According to the above theoretical frameworks, Ogata aims to develop a practical method of narrative generation through the collaboration of narrative-generation systems and humans. At the same time, at a larger social level, he envisions a narrative generation society, where diverse narratives are created and received through the interaction between humans and machines, as mutually equivalent existences, although they have different characteristics and merits, respectively.

2.2. *Phenomenological Multiplicity of Narrative and Expanded Literary Theory*

Ogata’s plan is based primarily on considering a narrative phenomenon that appears with very diverse forms as a single framework. We refer to a personal level’s narrative model as a narrative generation-reception model and a social level’s narrative model as a narrative production-consumption model. These models form an integrated and entire model including multiple narrative structures, where the former model is included in the latter model, and where the repetition of the former constructs the latter.

Further, we refer to previous or traditional narratology and literary theories in order to apply them to the expanded literary theory as a theoretical foundation. Although recent narratology and literary theories have focused on destroying the constructive ideas that rely on the terms of de-construction and others, they have gained an important and novel academic value by considering narratives as objects that can be analyzed technologically depending on structuralism theories. The expanded literary theory[5] returns to this original idea of narratology in an effort to seek to newly create model-oriented narratology and literary theory.

2.3. *Model of Multiple Narrative Structures*

The narrative generation-reception model refers to the narrative generation level by single subjects, namely the level of narrative generation realized by each human as an individual. We refer to this level as a "human system of narratives." On the other hand, the narrative production-consumption model is a social and collective narrative generation level in which many narrative generation-reception systems are included, and this level is considered a "social system of narrative." In the relationship between narrative generation-reception and production-consumption levels, both levels interact with each other to create an entire narrative phenomenon.

The multiple narrative structures model[1] is an idea that focuses on a narrative phenomenon from the viewpoint of the multiplicity of the narrative. In another feature, a single narrative work is structured using such various types of narrative elements as a story or stories, characters, a world or worlds, and so on. These elements are not constructed as a hierarchical structure, and it is difficult to determine the most important element. The narrative elements in a narrative work are composed through appealing each existence and many types of mutual relations among narrative elements. Ogata has surveyed and analyzed kabuki as a narrative genre to show multiple narrative structures from various perspectives.[3]

2.4. *Integrated Narrative Generation System: INGS*

The narratological study by Ogata is not sociology. It does not remain within the range of the model development and the analysis of societies. The study aims to design and construct actual systems that are dependent on the above two levels of narrative generation and the interaction model. Although the analysis and modeling of a phenomenon are objective and static tasks, we insert a subjective and dynamic method into the objective and static model.

The INGS is a mechanism that systematizes the above narrative generation-reception model. The purpose of this mechanism is to simulate narrative generation in a single level. Ogata[1] provided a detailed description.

There are corresponding relationships between the INGS and humans. For example, the conceptual dictionaries in the INGS are equivalent to the conceptual memory of a personal human. The narrative content knowledge bases in the INGS are similar to human episodic memory. Further, narrative generation techniques such as the story-generation techniques in the INGS correspond to the knowledge for making and operating event sequences in the human brain.

2.5. *Geino Information System: GIS*

On the other hand, the GIS is a systematization of the model of the narrative production-consumption process. The GIS is a narrative generation model at the social level, which actualizes both narrative generation-reception and narrative production-consumption processes through collaboration with the INGS.[3] Fig. 1 shows an overview of the GIS architecture, which includes the INGS. Although this system is not actually executed in the current timing different from the INGS, in the near future, we plan to implement it as a system including several INGSs.

The GIS is a social level system considering the following points: First, a society is a space where diverse narratives are continuously generated and received in parallel. However, on the other hand, with respect to a specific narrative production system, it is a subject that continuously repeats narrative production cycles. A society refers to a situation where diverse narrative production-consumption subjects, including individuals, are produced in parallel (namely spatially) and sequentially (namely temporally). According to our theoretical framework, a society refers to a temporal and spatial field where there are many INGS as well as the GIS as a collection of INGSs. Therefore, although a single GIS does not indicate an entire society, the GIS is modeled as a geino production mechanism that is a kind

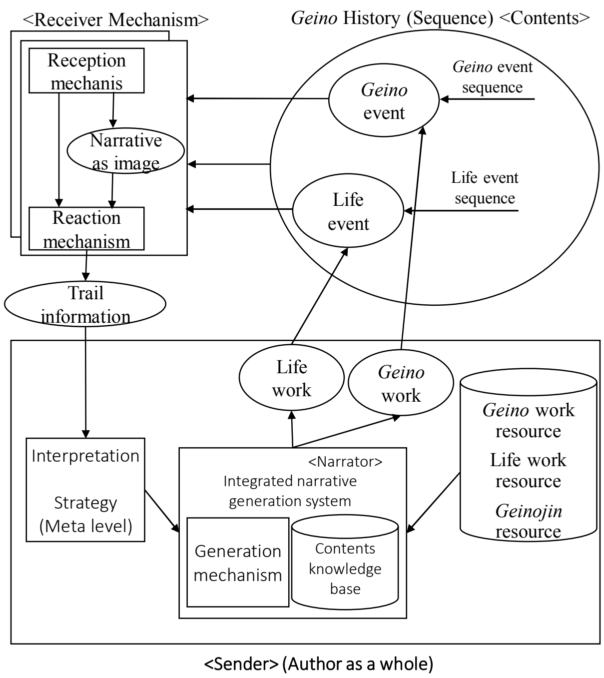

Fig. 1. GIS Architecture

of social-narrative production and a consumption system as a small-scaled social mechanism or system.

2.6. *Vision of Human-Machine Symbiosis System of Narrative*

From the above theories and systems, we seek to approach a situation that we refer to as a "human-society symbiosis system." Alternately, we consider that such a situation will need to be realized in the future society. This is a narrative situation where human authors and machine authors live together with no mutual discrimination in order to continue to collaboratively create narrative works in various genres. This is not necessarily just a wish, but an expectation that the historical progress will take such a route.

In such a social situation, we aim to determine the positioning of narrative-generation systems. There are several phenomenological forms shown below:

With respect to a narrative generation system as a single unit, first, we consider a form where a narrative generation system autonomously exists as itself. Next, there is a form where a human makes narratives using a narrative generation system or a narrative generation system makes narratives using humans. These are variations of a narrative generation case involving the collaboration of both humans and machines. There are many possibilities for collaboration methods. For example, we can consider various possibilities such as methods through which a human completes a narrative, where once a narrative generation system is made, it adds a new part to a narrative that a human made. As these are very practical problems, we will not be able to classify in advance all of the possibilities normatively.

On the other hand, in the case of the narrative generation at a social level, there is a situation where both human-narrative generation and social-narrative generation coexist. If we consider each narrative generation mechanism, such as the GIS, it is related to the problem of the specific gravity of narrative generation.

The most extreme type is a narrative production-consumption mechanism that does not involve humans at all. Then, the most extreme type in the reverse sense is a previous type's narrative generation mechanism, which is formed by only humans or which at least does not include any machines as narrative generation systems. In addition, with respect to concrete usage forms of the GIS, we seek to undertake various narrative generation and representation forms where humans and machines coexist.

As stated above, based on the model of multiple narrative structures, we can envision the phenomenon where both narrative generation mechanisms as humans and narrative generation mechanisms as machines coexist at various levels, and this applies also in the concrete implementation level.

3. An Attempt of the Commercial Film Production Support System (CFPSS) Based on the Image Rhetoric of Commercial Film

There are case studies into effective commercial films with a focus on marketing and advertisement.[6] Some of these studies include elements of advertising expression that have been classified and extracted to enhance advertising effects. Alternatively, other studies classifying advertising expressions according to the nature of the information (comparative, unique selling proposition, preemptive, hyperbole, generic-informatic), and the nature of transformation (user image, brand image, use occasion, generic-transformatic) examine the ideas of advertising expressions.[7] However, these studies provide insight into advertising expressions from a particular vantage point, and are not conducive to developing specific rules for creating images at the microcosm level. Related to print advertisements (text, photo, poster etc.), studies examine an interpretation and analysis of the effect of advertising rhetoric on viewers.[8,9,10] However, these studies do not include analyses related to commercial films. Moreover, as these research approaches aim to interpret and analyze existing advertisements, these studies also exclude information systems to generate specific advertisements according to operating rhetoric. Under such circumstances, Kawamura provided one of the few studies aiming to build an information system that analyzes the advertising image techniques (advertising story, editing). [11,12,13]

Fig. 2 shows the plan of CFPSS.[11] The concept of CFPSS is to generate the various commercial films adapted to the user's keywords and sentences (life scenario) input. CFPSS includes a database of 3643 image shots converted to a commercial film, that searches and classifies image shots based on keywords and sentences. The system includes a function to generate the storyboard based on the selection of advertising story, and playback in the order arranged in the storyboard. The menu of advertising story is as follows;[12]

- Provider story type: The primary structure expresses the provider's story (production and distribution, product function, effect on company). This is the "story of the product" and "story of the company."
- Consumer story type: This primary structure expresses consumers' stories (consumption situation, product acceptance, consumption effect). This is the "story of consumption."
- Overall type: This structure generally expresses both the provider's and consumer's stories. This is represented as provider story type + consumer story type.
- Image type: This structure expresses images related to the consumer situation, though does not express product acceptance and consumption effects in the film. Rather this structure represents a product function. This category also includes structures expressing an image that does not belong to the consumer, provider, or product function.

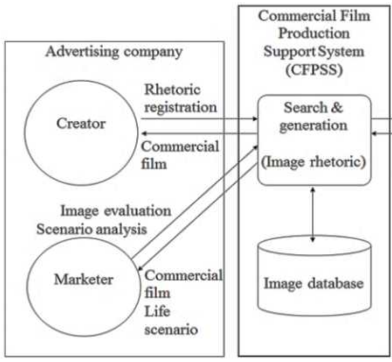

Fig. 2. CFPSS Plan.

Using an advertising story technique, a system was developed to generate commercial films through an interaction between the users and the system, which was tested with an observational experiment. Since the system easily generates commercial films that comply with a variety of requirements, it can be utilized for various experiments in the future. These types of experiments will clarify and enhance the creative know-how (image techniques and rhetoric) to produce individual advertisements.

4. Cutting Techniques and Non-Story Type Rhetoric

For computational and informational narrative film generation, many kinds of cognitive effects can be actualized using a strategy that employs story and non-story rhetorical aspects[17]. Many cognitive effects from narrative films are created through the interaction between cognitive process, story, discourse, and rhetoric. For example, irrational rhetoric cutting techniques for narrative space and time in the film can change the viewer's cognitive transition from story-driven to rhetoric-driven processing. Based on cognitive transition due to narrative processing from story-based to non-story based, cognitive effects such as intensive nostalgia effects can emerge.

The process of the viewer coming to understand the past story may lead to some cognitive effects. Conversely, many films have a primary purpose other than to tell a story. This happens when the purpose of the director is the film rhetoric itself, or the non-story rhetorical aspects rather than the story. When the above issues are considered, a system for computational and informational narrative film generation must include story and non-story rhetorical aspects.

Based on the cutting techniques used to make generate irrational relationships with time or characters in continuous shots, a viewer or a reader can feel less constrained with regard to story comprehension and reset the viewpoint to subtle elements, such as individual shots.

In addition, there are two different cognitive process types for the rhetoric of film. Cognitive effects from certain rhetoric, such as story type rhetoric, are primarily generated by the story or consistent narrative (cognitive process type-1). Conversely, the cognitive effects from the other rhetoric, such as non-story type rhetoric, are caused by the rhetoric of films, in particular the cutting techniques (cognitive process type-2). Many films combine both type of rhetoric. Therefore, the viewers transfer cognitive processes from type-1 to type-2 while viewing the same film.

Cognitive process type-1, the process in which the viewers understand the story, has some cognitive effects. In this process, the “experience” of the film's goal-directed characters and consistent narrative may lead to some affective response. However, the cognitive effects such as nostalgia effects may arise from other sources, as well as cognitive process type-2.

When the constraint is relaxed, an irrational cut of non-story type rhetoric may cause a “resetting of viewpoint” and “affect, which does not arise through comprehending a story, but through the audiovisual situations.” A resetting of viewpoint indicates that the viewer's viewpoint shifts from the need to be told a story to a grasp of the non-story narrative. This reflects the object associations within the moving image and the “mood” or the details of the moving image. “Affect, which does not arise through comprehending a story, but through the audiovisual situation” is caused by the audiovisual situation that emerges from the film's mood and object associations.

In non-story type rhetoric, the editing, recording, and photography are not always subordinate to the overall story. As stated above, the focus is on non-story narrative, the film's mood and object associations or the reality related to the unfamiliar situations rather than on the events in the story. Such associations and situations cause cognitive effects that do not arise in the process of comprehending a story. Kanai[14,15] indicated that when a viewer is able to relax his or her constraint with regard to the need to comprehend a story, this strengthens those cognitive effects including nostalgia effects, which do not arise in the process of comprehending the story. On the contrary, with story type rhetoric, the cognitive effects are those generated by the overall story.

The unfamiliar situations derived from non-story rhetorical elements create new realities. Unfamiliar situations can emerge through the sudden appearance of a section of non-story type rhetoric. In this case, a viewer sometimes cannot understand the consistent story. Therefore, attention to the situation itself is enhanced. The unfamiliar situations generate new cognitive effects related to unknown memories and affects that do not arise through story comprehension.

Non-story type rhetoric is created through cutting techniques used to make irrational relationships between 1) the rhetorical elements of two shots; 2) events and images; or 3) sounds and images[16]. The irrational relationships through the cutting techniques are used in many artistic films and music videos in order to generate situations unfamiliar to the viewers and to create new realities.

5. Conclusions

In this paper, we described the basic ideas of informational narratology as a fusion of narratology, including literary theories and informatics such as AI and cognitive science. In particular, an important direction of informational narratology is the point that it focuses on content generation or production through narrative communication and simulation. Previously, we performed research that focused on each narrative content generation, as discussed above in this paper.

Ogata stated the idea and concept of the model of multiple narrative structures, and presented an overview of two mutually related systems, the Integrated Narrative Generation System (INGS) and Geino Information System (GIS), to show the implementation of the model. Kawamura discussed the Commercial Film Production Support System (CFPSS) based on the Image Rhetoric of Commercial Film. Kawamura’s study mainly focuses on the perspective of the reception in narrative communication. Kanai, who focuses on computational and informational narrative film generation, mainly analyzed the cognitive effects by receivers for movie films, and used a strategy that employs story and non-story rhetorical perspectives.

However, these studies were not integrated in the previous research. If these researches are synthesized, in particular by developing narrative content-generation systems, it will enable the expansion of the constructive feature, namely an academic approach through executing system development, of the informational narratology.

Therefore, one or our future plans is to integrate the above narrative content generation systems proposed by the three authors into a larger system. This will also help to bridge informational narratology studies to the social experimental stage for the distribution of generated or produced narratives.

Acknowledgements

This work is supported by JSPS KAKENHI Grant Number 26330258 and Support Center for Advanced Telecommunications Technologies Research Grant (2015-2017).

References

1. T. Ogata and A. Kanai, A, *An introduction to Informatics of Narratology: Towards the Thoughts and Technologies of Narrative Generation* (Gakubunsha, Tokyo, Japan, 2010).
2. T. Ogata, Computational and cognitive approaches to narratology from the perspective of narrative generation, in *Computational and Cognitive Approaches to Narratology*, eds. T. Ogata and T. Akimoto (IGI Global, Hershey, Pennsylvania, USA, 2016), pp. 1-73.
3. T. Ogata, *Kabuki* as multiple narrative structures, in *Computational and Cognitive Approaches to Narratology,* eds. T. Ogata and T. Akimoto (IGI Global, Hershey, Pennsylvania, 2016), pp. 400-431.
4. T. Ogata, A comprehensive consideration of a narrative genre system, in Literature, in *Proc. of 2nd Annual Conference of Literature, Cognition, and Computer Research Group in Japan Cognitive Science Society* (Tokyo, Japan, 1999), pp.85-91.
5. T. Ogata, Expanded literary theory for automatic narrative generation, in *Proc. of Joint 7th Int. Conf. on Soft Computing and Intelligent Systems and 15th Int. Sympo. on Advanced Intelligent Systems* (Kitakyushu, Japan, 2014), pp. 1558-1563.
6. D. W. Stewart and D. H. Furse, *Effective television advertising: A study of 1000 commercials* (Lexington Books, Lexington, MA, 1986).
7. H. A. Laskey, E. Day and M. R. Crask, Typology of main message strategies for television commercial, *J. Advertising* 18(1) (1989) 36-41.
8. E. F. McQuarrie and D. G. Mick, Figures of rhetoric in advertising language, *J. Consumer Research* 22(4) (1996) 424-438.
9. B. A. Huhmann and P. A. Albinsson, Does rhetoric impact advertising effectiveness with liking controlled?, *European J. Marketing* 46(11/12) (2012) 1476-1500.
10. I. G. Theodorakis, C. Koritos and V. Stathakopoulos, Rhetorical maneuvers in a controversial tide: assessing the boundaries of advertising rhetoric, *J. Advertising* 44(1) (2015) 14-24.
11. Y. Kawamura, An analysis of the rhetoric of commercial film -toward the building of a commercial film production support system based on image rhetoric, in *Proc. 2003 IEEE Int. Conf. Systems, Man and Cybernetics*, (Washington, DC., 2003), 993-1000.
12. Y. Kawamura, An analysis on the story and editing techniques of commercial film -toward the building of a commercial film production support information system, *J. Advertising Science* **50** (2009) 16-32. (In Japanese).
13. Y. Kawamura, An attempt of the commercial film production support system based on the image rhetoric of commercial film (Chapter 4), in T. Ogata and T. Akimoto, *Computational and Cognitive Approaches to Narralotogy,* (IGI Global) (2016) 117-138.
14. A. Kanai, The story as a constraint on film. In *Proceedings of the Third International Conference on Cognitive Science* (Beijing, China, 2001a), pp. 503-506.
15. A. Kanai, Cognitive process model toward the rhetoric of the film, *Cognitive Studies*, **8** (2) (2001b) 139-150.
16. A. Kanai and T. Ogata, Non-story Processing on the film rhetoric composition system. In *Proceedings of 18th Congress of the International Association of Empirical Aesthetics* (Lisbon, Portugal, 2004), pp. 433-406.
17. A. Kanai, Non-Story, Nostalgia, and film cognition: nostalgia-based narrative rhetoric composition. *Computational and Cognitive Approaches to Narratology*, eds. T.Ogata and T. Akimoto (IGI Global, 2016) pp. 376-390.

Analyzing Multiple Narrative Structures of *Kabuki* based on the Frameworks of Narrative Generation Systems

Takashi Ogata
Department of Software Informatics, Iwate Prefectural University
Takizawa, Iwate, 020-0693, Japan

E-mail: t-ogata@iwate-pu.ac.jp

Abstract

Although *kabuki* is a genre of, so to speak, traditional performing arts, it also has many of the characteristics of a contemporary genre, including such various elements as narrative, drama, dance, and music. This analysis and study will contribute to the design and development of studies on digital-narrative generation. The author has previously surveyed and analyzed *kabuki*'s narrative structures from the viewpoint of a multiple narrative structure model, particularly the generation or production processes involved in its creation and its reception and consumption processes. *Kabuki*'s multiple-narrative-structure model means that the entire structure of *kabuki* is constructed through multiple usages of related information. For example, in *kabuki* the element of the "person" is divided into three: a "character" within a narrative work, an actor with a history of performances and who uses a stage name, and a real human with a true name. This multiplicity provides the person with multiple and deep characteristics. In this paper, based on these previous studies, the author discusses a method that bridges this *kabuki* analysis with system design and involves the use of two narrative generation systems: an Integrated Narrative Generation System (INGS) and a Geino Information System (GIS).

Keywords: *Kabuki*, Multiple narrative structures, Integrated narrative generation system, Geino information system.

1. Introduction

Examining its history and characteristics[1], *kabuki*, which originated during the beginning of the Edo era, can be regarded as a synthesized genre of drama that incorporates a variety of geino genres, such as dance, *Noh*, *kyogen*, and ningyo-joururi (puppet drama), into a rich form and also includes various narrative elements. In the West, the basis of drama and other narrative forms originates from Aristotle's opinion[2]: that the story or plot ("mythos") manages the other narrative elements such as characters and thoughts. In contrast, in *kabuki*, the story or plot was originally an element that was added to aid comprehension and to help control a collection of performances by an actor or actors. In *kabuki*, all narrative elements have equal competence. According to Kawatake,[3] Shoyo Tsubouchi (1859–1935), who was a Japanese researcher and author, compared the non-hierarchical and collective characteristics of *kabuki* to a chimera. However, the author of this paper would like to use this analogy to suggest the "multiplicity" of *kabuki*'s characteristics, applying the multiple narrative structure model[4] that forms the theoretical basis of the narrative generation study presented here. In particular, in *kabuki*, a variety of forms ("kata"), which means collections of paternal knowledge relating to various fields, including the dances performed by actors in each *kabuki* scene, frequently use story patterns, etc., to enable the use of free combinations of elements to construct multiple structures in a work.[5,6,7]

The author has been studying *kabuki* in order to introduce the acquired knowledge into two types of mutually related narrative-generation systems, called Integrated Narrative Generation System (INGS)[8] and Geino Information System (GIS).[1] In particular, the author has been studying *kabuki* from the viewpoint of the multiple-narrative-structure model. We generally consider a narrative work, its generation, and its production process from the viewpoint of its construction through multiple structures. For example, a narrative's flow comprises the multiple structures of a story in a semantic flow and a plot in a constructive flow. A *kabuki* narrative is a particularly rich object for the multiple-narrative-structure model. Consequently, we have analyzed the multiplicity of *kabuki* regarding fifteen kinds of elements.[1] For instance, the element of a "person" in *kabuki* can be divided into the following three aspects: the real "person," who lives in the actual world; the "person" as an actor who has a history of performing roles; and the "person" of the *kabuki* character that appears on stage. Each person has their own history or story. In the course of this study, knowledge on the analyzed multiple-narrative structures in *kabuki* will be introduced into the INGS and GIS.

In the author's previous research on *kabuki*, his studies referred to related books and papers [9,10,11]; however, for concrete application and modeling in the INGS and GIS, he must perform a more formal and elaborate analysis of *kabuki*. This paper is the first step towards attempting a more formal analysis of *kabuki*, aiming at the introduction of the performance art into the INGS and GIS.

Before beginning the main discussion on the above theme, the author would like to explain why multiplicity is important, effective, and significant in *kabuki*: (1) First, the multiplicity in *kabuki* enables it to interest a variety of receivers through social-distribution processes. (2) Its narrative values are useful for effecting a diverse and differential interpretation of the world through the power of imaginative- and fictional-narrative production. Multiplicity contributes to this diversity and differentiation of world understanding. (3) Multiplicity can enhance the depth of works.

However, the above characteristics may also be common in other narrative genres. Why then is *kabuki* worthy of being included in a study on multiple-narrative structures? A reason for this is that *kabuki*, which has a long history and exists in the current society, contains multiplicity in very diverse aspects and is part of a genre that combines performing art and drama. *Kabuki* is an embodiment of a very rich multiplicity.

Although, in a previous paper,[1] the author comprehensively researched and analyzed the multiplicity of *kabuki*, in this paper, the author is focusing on the concept of the "person" and is attempting to consider it through concrete modeling by analyzing it using the INGS and GIS.

In addition, the INGS corresponds to the narrative-generation-reception process at the personal narrative level. On the other hand, the GIS corresponds to the narrative-production-consumption process at the social-distribution level. Both of these processes construct an entire narrative process or a mechanism as a whole. The *kabuki* research and analysis discussed in this paper will be extended to an entire narrative mechanism that includes these two processes.

Therefore, we explain the relationships between *kabuki* and the narrative in order to avoid causing misunderstanding and confusion. In *kabuki*, a narrative means the work's story or plot, which is a wider sense of narrative; it can also encompass the narration performed by a character on stage, which is a narrower sense of narrative. In any case, both form partial elements of an entire *kabuki*.

However, the concept of narrative discussed here has wide and comprehensive meanings. It includes a level of representation or expression in addition to levels of story or plot. The media for representation or expression include language, music, image, and further body. From the author's viewpoint, the whole of a *kabuki* stage corresponds to a narrative. In this sense, the narrative generation of *kabuki* naturally has the meaning of generating the whole of a *kabuki* performance.

2. "Person" in *kabuki*: A Basic Consideration

In *kabuki*, there are various kinds of "persons," such as an "actor" and a "character." These are temporally and spatially formed and possess multiple existences and relationships.

First, a person, who is an actor, plays a character on a *kabuki* stage. Concurrently, the actor themselves has a very important and essential value. In *kabuki*, "actor plays" sometimes carry a more important meaning than universal dramas that focus on characters. Originally, especially during the Edo era, *kabuki* scenarios were not written using characters' names, but using actors' names. In other words, many *kabuki* works were written by *kabuki* authors to emphasize and strengthen their personalities and characteristics.

Further, although the person as an actor is a human with a real body, a real person in *kabuki* is divided into two parts: the real actor who is represented by his "stage name," and the real human who is symbolized by his "real name." These correspond to the spatial forms of a person. Concurrently, a unique point is the fact that a stage name, in many cases, has a temporal tradition and history or a kind of story that is inherited over generations. This means that actors who retain the same stage name over multiple performances exist in a current temporal point in continuity with other "real" people. An actor is located in a temporal and historical continuity. Therefore, the existence of various persons and stories can be multiplied in various ways.

On the other hand, a "person" as a character is not limited to the range of a single *kabuki* play. Certain characters, for example, can occasionally appear in other *kabuki* plays, other works in other genres, non-fictional histories, etc. Therefore, a character is an existence that, through its other appearances in the temporal and spatial situations of a *kabuki* play, represents a particular scenario. Concurrently, a character also exists as an overlapped representation of its appearances in other *kabuki* plays and other genres.

Bando Tamasaburo V is an example of an actor who has multiple constructions, as can be seen from the following description:

- He is a man, and his real name is Morita Shinichi.
- He has a history of acting and he inherited the name "Bando Tamasaburo" from his adoptive father and further past persons with the same name.
- He is an actor who has performed many different characters in classical *kabuki*.
- He is something of an innovator who has continued to introduce new dramas in other *kabuki*-related genres, such as "*Tenshu Monogatari*" (Castle Tower Story) (1917) by Izumi Kyoka (1873–1939).
- He is a director of diverse works in the *kabuki* genre.
- He is a performer and an artist who transcends the boundaries of various genres such as dance, classical Chinese opera, and reading aloud.
- He is a movie director, who, among other works, directed "Gekashitsu" (Operating Room) (1992), which is based on "*Tenshu Monogatari*" (Castle Tower Story), an 1895 novel by Izumi Kyoka.
- In recent years, he has fulfilled the role of an educator or trainer and has trained many *kabuki* actors by performing with them.

Discussing "onnagata" is necessary in order to understand the "persons" of *kabuki*. Although *kabuki* originated from *yujo* ("prostitutes") *kabuki*, the transition from *wakashu ("boys") kabuki* to *yaro ("adult men") kabuki* transformed it into a drama genre performed by adult men only[3,9] Real women do not appear on the *kabuki* stage; however, actors, as onnagata, further exhibit the multiplicity of *kabuki* by incorporating real men's sexuality. As onnagata is considered to be one of the most important elements that contribute to the attraction of *kabuki*, it has been the focus of essential discussions.

Additionally, concerning "person," the motif of the "jitsu ha" (actually)[12] transformation also plays an important role. Many characters in *kabuki* are multiplexed and they present complex images through a manipulation of the "actually." In many cases, the transformation of the "actually" is created by transforming the character of an unknown commoner into a famous and historical character, namely a hero. Two contrasting sub-genres in *kabuki*, sewa-mono and jidai-mono, are related to this feature. The sewa-mono is a comparatively real *kabuki* genre where the characters are common people. In contrast, the jidai-mono is a comparatively formal and stylistic *kabuki* genre based on historical worlds and characters. Concurrently, these are also used as concepts to show the performance styles of *kabuki* actors. The style of sewa sometimes infuses with the style of jidai, creating a unique impression on a *kabuki* stage. In jidai-mono, the transformation of a character through the "actually" occasionally creates a trigger for moving from a of sewa-style scene to an original jidai-style scene. Further, these concepts, sewa-mono and jidai-mono or sewa and jidai, occasionally appear in the micro performances of a character. For instance, in a sewa-mono, a character or an actor occasionally acts and speaks in the jidai-mono style. Sewa-mono and jidai-mono or sewa and jidai are concepts that show two types of *kabuki* performance styles, namely realism (sewa) and formalism (jidai). The multiple rhythm through which the formal style is inserted into the realistic style, and the contrary rhythm through which the real style is inserted into the formal style, produces a unique spectacle on the *kabuki* stage.

3. GIS/INGS models

In the author's research framework, *kabuki* narrative generation is implemented using the GIS and INGS. Basically, the GIS is a comprehensive system architecture that contains the INGS as one of its parts. The first two sub-sections in this section describe the GIS and INGS, and their mutual relationship is explained in the last sub-section.

3.1. *GIS: Geino Information System*

Fig. 1 shows an overview of the architecture of the GIS. This architecture corresponds to a narrative production-consumption mechanism that includes the use of many INGSs as a narrative generation-reception mechanism. The GIS is composed of, at its highest level, a sender mechanism, a receiver mechanism, and a geino history.

The first sender mechanism receives external information, which is mainly traces of information outputted by the reception mechanism, through the GIS' mechanism of "interpretation strategy" and selects an interpretation according to an interpretation framework. Lastly, the sender mechanism generates information based on the interpretation. However, this process does not necessarily mean that the GIS simply generates narratives according to the desires and expectations of the receivers. The INGS is placed in the central position of narrative generation by the sender mechanism.

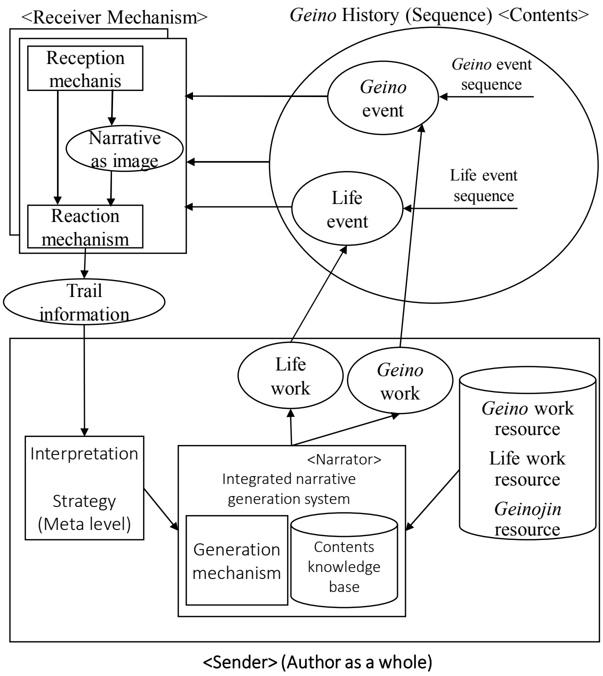

Fig. 1. GIS Architecture

The sequence and repetition by the sender mechanism forms a mechanism for geino histories. In order to continuously generate geino histories, the GIS utilizes special knowledge bases called "work resource," "life resource," and "geino-jin resource," which are not present in the INGS. Although these are similar to the narrative content knowledge bases in the INGS, unique content knowledge is contained in the GIS.

By the geino-jin resource we mean a place in which to store geino-jin information, which includes character information on geino performers and actors as well as their personal information. The life resource corresponds to the part in the geino-jin resource where only the life histories or life courses are extracted. The work resource means that the knowledge relating to geino works is analyzed and processed using various methods. Comparing this to the context knowledge present in the narrative-content-knowledge bases in the INGS, the work resource in the GIS stores more specific narrative information. Analyzing and studying *kabuki* aims at storing the specific narrative content knowledge in the GIS.

In addition to human receivers, the receiver mechanism also includes reception subjects as machinery mechanisms. These receiver mechanisms output, through various methods, information on reactions based on the reception experiences to a work, a sequence of works, the life history of a geino-jin, etc. A geino-history is sequentially formed through circulative and repetitive interaction between both mechanisms of the sender and the receiver. The content of a geino history is classified into geino events and their sequence, and life events and their sequence. The works also include scandals and geino news that focuses on geino-jins' lives themselves.

3.2. *INGS: Integrated Narrative Generation System*

Fig. 2 shows an overview of the INGS architecture. At the macro level, the INGS is divided into the three following generation processes: story, discourse, and representation. Parts corresponding to the mechanisms in this figure concern the "story-generation mechanism," "narrative-discourse mechanism," several "narrative-expression mechanisms," and several "control mechanisms." On the other hand, parts corresponding to the content or knowledge in this figure are part of a "state-event transformation knowledge base," several "conceptual dictionaries," "several language notation dictionaries," and "narrative-content knowledge bases." Ogata[8] presents a detailed list of all of the modules in the current INGS.

3.3. *Relationship between the GIS and INGS*

Simply speaking, specific knowledge in *kabuki* is stored in the GIS and the other general knowledge required for narrative generation is stored in the INGS. Although narrative generation by the INGS concerns narrative generation for each unit of work, narrative generation by the GIS means narrative generation at a more complete

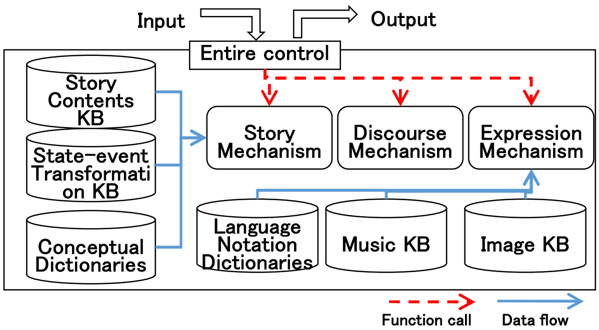

Fig. 2. INGS Architecture

level, where a sequence of narrative works is generated by the INGS. The author's basic idea here is that the latter type of narrative generation is also performed by a kind of narrative technique that transcends a mere accidental sequence.

Ogata[1] has surveyed and analyzed the *kabuki* themes shown below: (1) real incident, (2) work, (3) genre, (4) material or topic, (5) person, (6) story and plot, (7) actor and place, (8) time (era or age), (9) style (form or pattern), (10) theatre (stage and seating), (11) audience, (12) text, (13) production of scenario (*daicho*), (14) direction, and (15) stage performance. In this research plan, these surveys and analyses will be formalized for use in the GIS, including the INGS.

In a generation cycle, the INGS receives the above various knowledge and additional related knowledge from the GIS and then generates narrative conceptual structures for a story as well as a narrative discourse before expressing these structures for narrative representation. This part of narrative expression or representation is conducted by the staging mechanism in the GIS. Furthermore, in the business model, we can consider a variety of possibilities for the actual distribution: expressing or representing on the PC and on the stage, developing and distributing second works through books and other media, etc. However, these matters exceed this paper's range.

4. Toward Designing the "Person" using the GIS and INGS

In this section we show a design plan of the "person" in *kabuki* using the GIS and INGS. The main aspects of a person in *kabuki* are as follows:

(i) A person as an actor, performer, or a player on the *kabuki* stage
(ii) A person as a real human
(iii) A person as a character in a *kabuki* work

The person relating to the above (i) has a stage name. He is defined in the GIS as a part of the geino-jin resource. This geino-jin resource includes several geino-jins who have the same name. These data describe a set of common personalities for actors who have this name in addition to different types of personality each actor possesses.

(ii) concerns a person who has a real name and is living as a real human in the real world. In the geino-jin resource, this type of person is continually represented with the first type of person.

(iii) relates to a person who should be defined in relation with a specific *kabuki* work in order to form an element of the work resource in the GIS. As this person can occasionally be used in many *kabuki* works, it is necessary to store the person as a specific character, not just a character who forms a part of a specific work.

To ensure a concrete execution method during the GIS' narrative-generation cycle, when the INGS generates a narrative it receives various information, including the above three types of person-related information, to create the basic narrative structure. Concurrently, general information except for the basic information on persons is supplied from the INGS side. Although the GIS provides more specific information and knowledge, the INGS prepares more general information.

Further, through the GIS' narrative production-consumption cycle, various sides of the person continue producing or distributing narratives in a wider sense. In particular, the next narrative production in the cycle can be executed by triggering all three of the above types of person. For instance, the *kabuki* narrative production-consumption system can create a series of stages for the actor. It can also produce a series of stages where a kabuki character continuously appears.

A primary effect for narrative generation involving the above method is to employ a concrete method with a person setting to strengthen the impression of the generated narratives and upgrade the quality. Furthermore, this contributes to enlarging the diversity in the narrative distribution in the GIS, namely the deviation and evolution of narratives. In particular, narrative distribution and expansion proceeds from a variety of narrative parts or sides, including the whole of a narrative and narratives. The above method produces diverse possibilities and provides relatively thick profile information on each character that provides concreteness and depth in the development.

5. Conclusions

In this paper, the author focused on the narrative multiplicity in *kabuki* as a means of considering future directions of expansion for narrative-generation research. This examination was based on the system development of two mutually related systems: INGS and GIS. In particular, this paper showed the various types of person involved in *kabuki* towards discussing kabuki's conceptual design using the INGS and GIS. In the future, the author plans to elaborate on designing the person and other elements of *kabuki* in order to approach an experimental implementation using/involving the INGS and GIS.

Acknowledgements

This work is supported by the JSPS KAKENHI Grant Number 26330258 and Support Center for Advanced Telecommunications Technologies Research Grant (2015-2017).

References

1. T. Ogata, *Kabuki* as multiple narrative structures, in *Computational and Cognitive Approaches to Narratology,* eds. T. Ogata and T. Akimoto (IGI Global, Hershey, Pennsylvania, 2016), pp. 400-431.
2. Aristotle, *The Poetics of Aristotle* (trans. S. H. Butcher, Macmillan, London, UK, 1895). Retrieved from https://archive.org/details/poeticstranslate00arisuoft
3. T. Kawatake, *Kabuki: Baroque Fusion of the Arts,* trans. Connel Hoff, F. and J. (The International House of Japan, Tokyo, Japan, 2003).
4. T. Ogata and A. Kanai, *An introduction to Informatics of Narratology: Towards the Thoughts and Technologies of Narrative Generation* (Gakubunsha, Tokyo, Japan, 2010).
5. S. Sugiyama, *Joururi Shiroto Koshaku I, II* [*Joruri Amateur Lecture I, II*] eds. M. Uchiyama and H. Sakurai (Iwanamishoten, Tokyo, Japan, 2004).
6. T. Miki, Kangeki Guhyo [Reviews on Theater Plays] ed. T. Watanabe (Iwanamishoten, Tokyo, Japan, 2004).
7. T. Watanabe, *Kabuki–Kajo naru Kigo no Mori* [*Kabuki: The Forest of Excessive Signs*] (Shinyosha, Tokyo, Japan, 1989).
8. T. Ogata, Computational and cognitive approaches to narratology from the perspective of narrative generation, in *Computational and Cognitive Approaches to Narratology*, eds. T. Ogata and T. Akimoto (IGI Global, Hershey, Pennsylvania, USA, 2016), pp. 1-73.
9. T. Kawatake, *Kabuki: Its Beauty and Tradition,* trans. C. Holmes (Japan Arts Council, Tokyo, Japan, 1992).
10. T. Imao, *Kabuki wo Miru Hito no Tameni* [*For People Viewing Kabuki*] (Tamagawa University Press, Tokyo, Japan, 1979).
11. T. Watanabe, *Kabuki no Mikata* [*Kabuki's Viewpoints*] (Kadokawa Gakugei Shuppan, Tokyo, Japan, 2009).
12. T. Imao, *Henshin no Shiso* [*The Theory of Metamorphosis*] (Hosei University Press, Tokyo, Japan, 1970).

Rhetoric of Commercial Film and the Response of Viewers

Yoji Kawamura
Faculty of Business Administration, Kindai University, 3-4-1 Kowakae
Higashi-osaka, Osaka 577-8502, Japan
E-mail: kawamura@bus.kindai.ac.jp
www.kindai.ac.jp

Abstract

This study first outlines a view of the rhetoric of commercial films as a combination of commercial film techniques. Next, it discusses the relationship between the rhetoric of commercial films and perception/positive factors based on a variety of surveys. It then shows the structure of the relationship between the rhetoric of commercial films and perception/positive factors based on the discussion. Finally, it summarizes the rhetorical patterns in advertisement based on the structure thus identified. This study showed that there is a correlation between the overall rhetorical type and perception/positive factors by introducing the framework of "overall rhetorical types" as a combination of commercial film techniques. Interestingly, the overall rhetorical type, which is an approach to classify commercial films based on commercial film techniques, is found to correlate with the viewer's perception and positive factors. On the basis of the structure identified in the study, expressive characteristics of commercial films can be summarized as 4 expressive characteristics.

Keywords: Commercial Film, Rhetoric, Overall Rhetorical Type, Perception, Positive Factor

1. Introduction

This study first outlines a view of the rhetoric of commercial films as a combination of commercial film techniques. Next, it discusses the relationship between the rhetoric of commercial films and perception/positive factors based on a variety of surveys. It then shows the structure of the relationship between the rhetoric of commercial films and perception/positive factors based on the discussion. Finally, it summarizes the rhetorical patterns in advertisement based on the structure thus identified.

2. Views on Commercial Film Techniques and Rhetoric

Commercial film techniques contained in commercial films are complex with a variety of representation elements, but viewers do not form their perception of the films by comprehending all these techniques or representation elements. In particular, in the case of commercial films with time constraint (between 15 and 30 seconds), it is speculated that viewers use their intuition to capture physiological elements, which cannot be verbalized and form their perception, by focusing on the differences from their own reality.

Commercial films are visual representations that bring certain disturbance to the physical reality in which consumers consume products in the real world. Commercial film techniques and rhetoric are classified in reference to the disturbance (certain manipulation: addition or deletion). In this study, to grasp commercial film techniques and rhetoric systematically, they are defined as "rules that add some manipulation (addition or deletion) to the basic advertisement content, mise-en-scène, editing and sound effects." Here, "the basic advertisement content, mise-en-scène, editing and sound effects" refer to the general consumer's behavior of consuming products in the real world. Advertising story technique expresses "the product function (the product itself or its performance)" and "product reception (the scene in which the consumer receives the product)." Mise-en-scène technique refers to "the real space;" "one consumer;" "the protagonist is not a celebrity with a strong character;" "the protagonist or the product is not in fast movement or in slow motion;" and "the fixed camera shot." Editing technique refers to "a slow tempo (a large number of average number of seconds per shot);" "continuation (movements are usually connected);" and "temporal series (there is no manipulation to chronology)." Sound effect technique refers to "silent (slow tempo music or no music)."

Moreover, advertising story techniques are classified into two categories: "representation of reception (a representation of the scene in which the consumer receives the product)" and "deletion of reception (the scene in which the consumer receives the project is not represented)." Mise-en-scène techniques are classified into two categories: "dynamic (the protagonist or product moves fast, slow or circles; or the camera shot is not fixed)" and "stable (the protagonist or product does not move fast or is not in slow motion; the camera shot is fixed)." Editing techniques are classified into two categories: "dynamic (fast tempo or discontinues movements)" and "stable (slow tempo or no tempo)." Sound effect techniques are classified into two categories: "dynamic (fast tempo)" and "stable (slow tempo or no tempo)." These categories are referred to as technique types. The combination of the technique types constitutes the overall rhetorical types. The number of combination is 16 (2 x 2 x 2 x 2).

Kawamura[1] analyzed the overall rhetorical types of 100 commercial films. 1A and 1B, which are "dynamic" in terms of mise-en-scène, sound effect, and editing techniques, are most frequent and account for 46% of the total films (Fig. 1).

3. Relationship between the Rhetoric of Commercial Films and Perception

Viewers' response is defined as perception and positive factors, and the relationship between the rhetoric of commercial films and perception/positive factors is outlined based on a number of surveys.

3.1. *Rhetoric of Commercial Film and Perception*

Kawamura[2] analyzed the correlation between the rhetoric of commercial films and perception with 16 films of beer and 22 films of personal computers. The relationship (correlation) between the overall rhetorical type (from 1A to 8B) and perception shows that there is a certain structure between the two as seen in 1A being related to "looks delicious," "fresh," and "looks cool;" 1B to "rhythmical," "powerful," and "looks cool;" 2B to

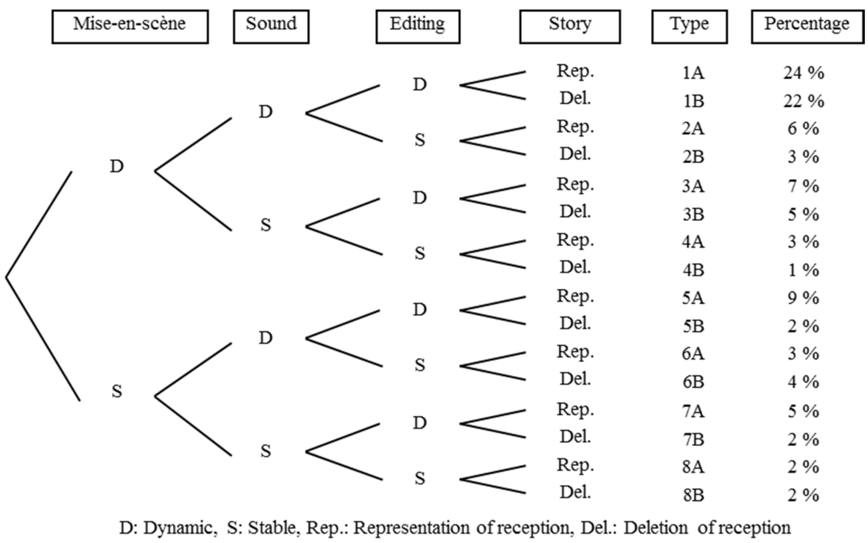

Fig. 1. System and percentage of overall rhetorical types. [1]

"creative" and "vivid;" 3A to "feels clean" and "fashionable;" 7A to "rich nature," "feels cool," and "idyllic;" and 8B to "somehow sad," "simple," and "non-organic." It is shown that out of 106 image words extracted from the data, 80 (76%) correlate with the overall rhetorical type.

3.2. *Rhetoric of Commercial Films and Positive Factors*

Kawamura[1] analyzed the correlation between the rhetoric of commercial films and perception/positive factors with 100 commercial films that were ranked among top ten for the new film category in each month (2004–2005) published by CM Research Institute. The analysis

Table 1. Relationship between the rhetoric of commercial films and perception/positive factors.

Rhetorical Type				Perception[2]	Perception[1]	Positive Factors[1]	Effect Type
Type	Mise-en-scène	Sound	Editing				
1A/B	D	D	D	looks delicious, fresh, looks cool, dazzling, cold, pleasant, lively, congenial, impatient, desperate, sporty, haste, fighting, speedy, light, conspicuous, tense, surprised, rhythmical, thrilling, powerful, fast, futuristic, speed, contemporary	speedy, realistic, eerie, surprise	"because it is sexy" "the firm's attitudes appear to be sincere"	thrilling
2A/B	D	D	S	creative, vivid	fierce, millet, light, gorgeous, colorful		light, vivid
3A/B	D	S	D	speed, stylish, feels clean, fashionable, elegance, simple, refresh	serious, healing, funny, happy, peaceful, sad, pitiful, puzzled, miserable	"it is humorous" "a good story" "cute"	tempo, enjoyable
5A/B	S	D	D		impact, cool, gentle, magnificent	"attracted by the product"	magnificent
4A/B	D	S	S	simple, heartwarming, daily, couple, refresh, relax, tranquil, my pace, fierce, slow, design, transparent, white, chic, mood, change	fashionable		daily
6A/B	S	D	S	tired, a comedy	tranquil, comical, enjoyable, hope	"not fashionable but likeable"	heartwarming enjoyable
7A/B	S	S	D	rich nature, feels cool, idyllic, running feeling, idle feeling, wonder, expectation, doubt, anxiety, indoor, lifestyle feeling	elegance, natural, rich knowledge, wonder	"reassuring" "it is pleasantly persuasive"	nature, reassuring
8A/B	S	S	S	quiet, domestic, pure, warm, somehow sad, drift, simple, non-organic, calm, home, stinking, relaxing, magnificent, Japan, chic, dark	relaxing, calm, gorgeous, heartwarming, fresh, dim, hard, powerful	"it is pleasantly persuasive" "it feels at the cutting-edge of time" "impressive catch phrases" "good visual images/videos"	rest, aesthetic

D: Dynamic S: Stable

showed that there is a structure between the overall rhetorical type (from 1A to 8B) and positive factors as seen in 1A being related to "because it is sexy;" 1B to "the firm's attitudes appear to be sincere;" 3A to "it is humorous" and "a good story;" 3B to "cute;" 5A to "attracted by the product;" 6B to "not fashionable but likeable;" 7A to "reassuring;" 7B to "it is pleasantly persuasive;" 8A to "it is pleasantly persuasive" and "it feels at the cutting-edge of time;" and 8B to "impressive catch phrases" and "good visual images/videos." It is shown that out of 77 image words extracted from the data, 59 (77%) are correlated with the overall rhetorical types, and out of 15 positive factors, 13 (87%) are correlated with the overall rhetorical type.

4. Structure of the Rhetoric of Commercial Films and Perception/Positive Factors

Table 1 shows the relationship between the rhetoric of commercial films and perception/positive factors as examined in 3.1 and 3.2. Kawamura[2] analyzed commercial films of beer (16 films) and personal computers (22 films); Kawamura[1] analyzed commercial films according to product types other than beer and personal computers. (Of the 100 films analyzed, three are films of beer, one of personal computers, and 96 of other products.) The tale shows that there is a close relationship (structure) between the overall rhetorical type and perception regardless of product category.

5. Rhetorical Patterns in Commercial Films

As viewers use diverse knowledge and knowledge processing when perceiving commercial films, it is difficult to structure or verbalize the viewer's perceptions. Consequently, it is not easy to achieve perception that is loyal to the image that the advertiser wants to convey. However, the study showed that there is a correlation between the overall rhetorical type and perception/positive factors by introducing the framework of "overall rhetorical types" as a combination of commercial film techniques. Interestingly, the overall rhetorical type, which is an approach to classify commercial films based on commercial film techniques, is found to correlate with the viewer's perception and positive factors.

On the basis of the structure identified in the study, expressive characteristics of commercial films can be summarized as follows:

- Overall rhetorical type 1 ("dynamic" mise-en-scène, sound effects and editing) overwhelms the viewer and leaves a strong impression of the actors and the company.
- Overall rhetorical types 2, 3, or 5 (one of mise-en-scène, sound effects, and editing is set as "stable") attracts the viewer's attention and interest to the actor's movement, the story, or the product.
- Overall rhetorical types 4, 6, or 7 (two of mise-en-scène, sound effects, and editing are set as "stable") encourages the viewer to relate to/sympathize with the advertisement content or representation.
- Overall rhetorical type 8 ("stable" mise-en-scène, sound effects, and editing) encourages the viewer to evaluate the advertisement concept and representation aesthetically.

Acknowledgements

This work was supported by JSPS KAKENHI Grant Number 22500102.

References

1. Y. Kawamura, A study on the technique-rhetorics and effects of commercial film, *Cognitive Studies* 14(3) (2007) 409-423. (In Japanese).
2. Y. Kawamura, An analysis on rhetoric of the commercial film of beer and personal computer – a symbolic approach on rhetoric of commercial film, *J. Advertising Science* 47 (2006) 33-48. (In Japanese).

Comparison Between Variational Autoencoder and Encoder-Decoder Models for Short Conversation

Shin Asakawa
Center for Information Sciences, Tokyo Women's Christina University, Zempukuji, 2, 6, 1 Nerima, Tokyo 1678585, Japan

Takashi Ogata
Faculty of Software and Information Science, Iwate Prefectural University Takizawa, Iwate, 020-0693, Japan
E-mail: asakawa@ieee.org, t-ogata@iwate-pu.ac.jp

Abstract

We provide a point of view concerning generative models such that they could deal with short conversation. These include the standard recurrent neural network language, sequence to sequence, vector embedding, and variational autoencoder models. These models seem to be possible candidates to describe such conversations, there are several differences among them.

Keywords: neural network language model, recurrent neural networks, vector embedding, variational autoencoder, sequential data processing, variational inference, narrative generation.

1. Introduction

Conversation includes understanding and generation. Therefore, modeling of conversation play an important role in natural language processing (NLP) and machine intelligence. Although previous approaches exist, they are often restricted to specific domains (e.g., booking an airline ticket) and require hand-crafted rules. In this paper, we will provide a brief survey about recent progress concerning sentence generation. First the recurrent neural network language models (RNNLM) will be introduced (section 2). Then we will make brief explanations about recent models: vector embedding models (section 3), variational autoencoder (VAE) models (section 4), and combining models between RNNLM and VAE. In section 6, we will discuss possible contributions of the models cited here to narrative studies.

2. Recurrent Neural Network Models

RNNLMs (RNNLM[7]) represent the state of the art in unsupervised generative modeling for NLP modeling. In supervised settings, RNNLMs decode conditioned on task specific features in machine translation[1,11]. Standard RNNLMs can predict each word of a sentence conditioned on the previous word and an evolving hidden state. RNNLMs can generate sentences word-by-word based on an evolving distributed state representation. RNNLMs can make their internal representation probabilistic models without any significant independent assumptions. However, by breaking the model structure down into a series of next-step predictions, the RNNLM does not expose an interpretable representation of global features like topic or of high-level syntactic properties. Vinyals and Le[12] showed RNNLM (Recurrent Neural Neural Network Language Model) could deal with conversation (Fig. 1).

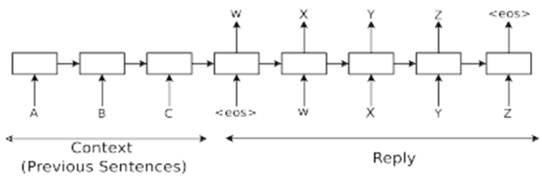

Fig. 1. A schematic diagram of sequence to sequence model, modi ed form Ref. 12

3. Vector embedding models

In order to incorporate a continuous latent sentence representation, we need a method to map between sentences and distributed representations that can be trained in an unsupervised setting. While no strong generative model is available for this problem. In this section we tried to deal with vector embed ding models:

1. skip-thought[4],
2. paragraph vector[5],

Sequence autoencoders have been success in generating complete documents[6]. An autoencoder consists of an encoder function φenc and a probabilistic decoder model p(x|z =φ(x)), and maximizes the likelihood of an example x given z. In the case of a sequence autoencoder, both encoder and decoder are RNNs and examples are token sequences.

The intermediate sentences are generally ungrammatical and do not transition smoothly from one to the other. This suggests that these models do not generally learn a smooth, interpretable feature system for sentence encoding. In addition, since these models do not incorporate a prior over z, they cannot be used to assign probabilities to sentences or to sample novel sentences. It was proposed that unsupervised learning models might take the same model structure as a sequence autoencoder, but generate text conditioned on a neighboring sentence from the target text, instead of on the target sentence itself[4]. Paragraph vector models[5] are non-recurrent sentence representation models. In a paragraph vector model, the encoding of a sentence is obtained by performing gradient-based inference on a prospective encoding vector with the goal of using it to predict the words in the sentence.

4. Variational autoencoder models

The variational autoencoder (VAE[3]) is a generative model that is based on a regularized version of the standard autoencoder. This model imposes a prior distribution on the hidden codes z which enforces a regular geometry over codes and makes it possible to draw proper samples from the model using ancestral sampling. The VAE models the autoencoder architecture by replacing the deterministic function φ(x) with a learned posterior recognition model, q(z|x). This model parametrizes an approximate posterior distribution over z (they employed a diagonal Gaussian) with a neural network conditioned on x. The VAE learns sentences not as single points, but as soft ellipsoidal regions in latent space, forcing the sentences to latent the space rather than memorizing the training data as isolated sentences. If the VAE were trained with a standard autoencoder's reconstruction objective, it would learn to encode its inputs deterministically by making the variances in q(z|x) vanishingly small[9]. Instead, the VAE uses an objective which encourages the model to keep its posterior distributions close to a prior p(z), generally a standard Gaussian (μ = 0; σ2 = 1). Additionally, this objective is a valid lower bound on the true log likelihood of the data, making the VAE a generative model. This objective takes the following form:

$$\begin{aligned} L(\theta; x) &= -\mathrm{KL}(q_\theta(z|x) \| p(z)) \\ &\quad + \mathrm{E}_{q\theta(z|x)}[\log p_\theta(x|z)] \\ &\leq \log p(x). \qquad (1) \end{aligned}$$

This forces the model to be able to decode plausible sentences from every point in the latent space that has a reasonable probability under the prior.

It was used diagonal Gaussians for the prior and posterior distributions p(z) and q(z|x), using the Gaussian reparameterization trick[3]. The model was trained with stochastic gradient descent, and at each gradient step they estimated the reconstruction cost using a single sample from q(z|x), but compute the KL divergence term of the cost function in closed form.

5. Combining model between RNNLM and GAE

A variational autoencoder model was proposed Ref. 2. It was found that on a standard language modeling evaluation where a global variable was not explicitly needed, their model yielded similar performance to existing RNNLMs. The model was also evaluated using a larger corpus on the task of imputing missing words. For this task, it was introduced a novel evaluation strategy using an adversarial classifier, sidestepping the issue of intractable likelihood computations by drawing inspiration from work on non-parametric two-sample tests and adversarial training. In this setting, the model's global latent variable allowed to do well where simpler models fail. In this model several qualitative techniques was introduced for analyzing the ability of their model to learn high level features of sentences. They could produce diverse, coherent sentences through purely deterministic decoding and that they could interpolate smoothly between sentences.

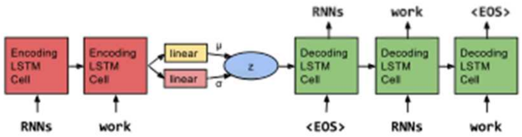

Fig.2. A VAE models from Ref. 2

The model of Ref. 2 allows it to explicitly model holistic properties of sentences such as:

1. style,
2. topic
3. high-level syntactic features

Samples from the prior over these sentence representations remarkably produce diverse and well-formed sentences through simple deterministic decoding. By examining paths through this latent space, we are able to generate coherent novel sentences that interpolate between known sentences. In order to solve the difficult learning problem, the method implemented in this model to demonstrate its effectiveness in imputing missing words, explore many interesting properties of the model's latent sentence space, and present negative results on the use of the model in language modeling.

A class of deep, directed generative models with Gaussian latent variables at each layer[10]. In order to allow for efficient and tractable inference, they introduced an approximate representation of the posterior over the latent variables using a recognition model that acts as a stochastic encoder of the data. For the generative model, they derive the objective function for optimization using variational principles; for the recognition model, they specify its structure and regularization by exploiting recent advances in deep learning. Using this construction, the model could learn the data by the gradient backpropagation that allowed for optimization of the parameters of both the generative and recognition models jointly.

Fig. 4 shows the corresponding computational graph of Fig. 3. Black arrows indicate the forward pass of sampling from the recognition and generative models. Solid lines indicate propagation of deterministic activations, dotted lines indicate propagation of samples. Red arrows indicate the backward pass for gradient computation. Solid lines indicate paths where deterministic backpropagation is used, dashed arrows indicate stochastic backpropagation.

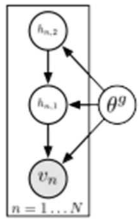

Fig. 3. A plate notation of a variational RNN model

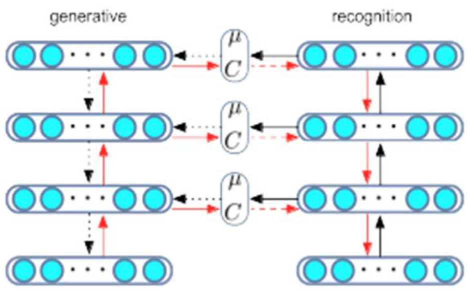

Fig. 4. A computational graph corresponing to Fig. 3

6. Discussion

So far, we tried to compare several methods proposed recently. Studies cited here might suggest a trends toward to generate sentences or topics with computational accountabilities with both RNNLMs and VAEs.

Additionally, the authors also aim at the application to narrative generation[8]. Conversation in narratives, such as folktales and novels, is used for a scene's description where several characters appear in many cases. There are novels that conversation is the central part in narrative progression, such as many novels by F. Dostoyevsky, E. Hemingway, and Y. Kawabata. Main effects of conversation of narratives are, for example, "realistic effect" (Hemingway and Kawabata) and "dramatic effect" (Dostoyevsky). Although the current version of an "Integrated Narrative Generation System (INGS)"[8] that have been developing has not conversational part and the main narratological element is "event", conversation, in addition to description and explanation, is a necessary and important element for completing a narrative's structure and representation. Furthermore, although the INGS is currently an approach to narrative generation based on semiotic processing and knowledge, studying paternal processing approaches by neural networks stated in this paper is an important direction for aiming at the fluency of text generation or representation and the acquisition of diverse narrative knowledge including episodes and scripts.

7. Conclusion

We introduced computational explanations for sentence generations and showed relations between such studies based on neural networks and narrative studies. Despite many studies should be required, it seems to worth trying to go forward along these ways that we employed here. The RNNLMs and VAEs might converge in some ways in the near future, then the results that these method might bring us further steps.

References

1. D. Bahdanau, K. Cho and Y. Bengio, Neural machine translation by jointly learning to align and translate, in *Proceedings in the International Conference on Learning Representations (ICLR)*, eds. Y. Bengio and Y. Le Cun (USA, CA, San Diego, 2015).
2. S. R. Bowman, L. Vilnis, O. Vinyals, A. M. Dai, R. Jozefowicz, and S. Bengio, *Generating sentences from a continuous space*, (2016), arXiv:1511.06349.
3. D. P. Kingma, and M. Welling, *Auto-encoding variational Bayes*, (2014), arXiv:1312.6114v10.
4. R. Kiros, Y. Zhu, R. Salakhutdinov, R. S. Zemel, A. Torralba, R. Urtasun, and S. Fidler, *Skip-thought vectors*, (2015), arXiv:1506.06726.
5. Q. Le, and T. Mikolov, *Distributed representations of sentences and documents*, (2014), arXiv:1405.4053v2.
6. J. Li, T. Luong, and D. Jurafsky, A hierarchical neural autoencoder for paragraphs and documents, in *Proceedings of the 53rd Annual Meeting of the Association for Computational Linguistics and the 7th International Joint Conference on Natural Language Processing (Volume 1: Long Papers)*, (China: Association for Computational Linguistics, Beijing, 2015), pp. 1106-1115.
7. T. Mikolov, S. Kombrink, L. Burget, J. H. Cernocky, and S. Khudanpur, Extensions of recurrent neural network language model, in *IEEE International Conference on Acoustics, Speech and Signal Processing (ICASSP)*, (Czech Republic, Prague, 2011).
8. T. Ogata, Computational and cognitive approaches to narratology from the perspective of narrative generation, in *Computational and Cognitive Approaches to Narratology*, eds. T. Ogata and T. Akimoto (IGI Global, Hershey, Pennsylvania, USA, 2016), pp. 1-73.
9. T. Raiko, and M. Berglund, *Techniques for learning binary stochastic feedforward neural networks*, (2015), arXiv:1406.2989.
10. D. J. Rezende, S. Mohamed, and D. Wierstra, Stochastic backpropagation and approximate inference in deep generative models, in *Proceedings of the 31st International Conference on Machine Learning (Vol. 32)*, (Beijing, China, 2014) pp. 1278-1286.
11. I. Sutskever, O. Vinyals, and Q. V. Le, *Sequence to sequence learning with neural networks, In Z. Ghahramani, M. Welling, C. Cortes, in Advances in Neural Information Processing Systems (NIPS) (Vol. 27)*, eds. N. Lawrence, and K. Weinberger (Canada, Montreal, BC, 2014) pp. 3104-3112.
12. O. Vinyals, and Q. V. Le, *A neural conversational model*, (2015), arXiv:1506.05869.

Changing and Transforming a Story in a Framework of an Automatic Narrative Generation Game

Jumpei Ono
Graduate School of Software Informatics, Iwate Prefectural University
Takizawa, Iwate, 020-0693, Japan

Takashi Ogata
Department of Software Informatics, Iwate Prefectural University
Takizawa, Iwate, 020-0693, Japan

E-mail: g236m001@s.iwate-pu.ac.jp, t-ogata@iwate-pu.ac.jp,

Abstract

We propose the concept of a game system that includes an automatic story-generation function based on a table-top role playing game (TRPG). In this idea, stories are generated or transformed based on communication between a "game manager (GM)," who controls the story generation, and "Players (PLs)," who change and transform the content of a story proposed by a GM. This paper focuses on the mechanism for changing and transforming a story proposed by the GM. In particular, the proposed mechanism has various techniques ranging from macrolevel techniques, which are related to the entire structure of a story, to microlevel techniques, which are related to the partial structures of a story. For instance, when the GM is a real human, these techniques in the PLs, who are computer agents, can produce changed and transformed stories that were not originally conceptualized by the GM.

Keywords: Automatic narrative generation game (ANGG), Integrated narrative generation system (INGS), Table-top role playing game, Story generation, Discourse.

1. Introduction

In this study, we propose a mechanism for a computer game system using an automatic story generation function based on a tabletop-top role playing game (TRPG). Here, stories are generated and transformed via a communication loop between a "game manager (GM)," who generates the first framework of a story and controls or manages the subsequent story generation process, and "Players (PLs)," who modify and transform the story that was first generated by the GM. This paper focuses on the problem associated with the mechanism for changing and transforming a story proposed by the GM. Although this mechanism is currently implemented using a simple method, in this paper, we discuss various techniques that range from macrolevel techniques, which are related to the overall structure of a story, to microlevel techniques that are related to the partial structures of a story. We aim to design and implement the future expansion of the system.

We refer to the game system, including the automatic narrative generation mechanism, as an "automatic narrative generation game (ANGG)." In this system architecture, each GM and PL can be either a computer agent or a human. When the GM is a real human, a variety of narrative techniques employed by PLs who are computer agents enable the production of changed and transformed stories that the GM did not imagine originally. When both the GM and PLs are computer agents, they can use the narrative generation mechanisms in the integrated narrative generation system (INGS) described in the following section to generate a story framework and transform the story framework into the expanded stories. Thus, the ANGG is regarded as a kind of narrative generation system through the corporative relationships between the GM and the PLs.

As Ogata[1] presented a detailed description, Fig. 1 shows an overview of the INGS architecture. From a macro perspective, the INGS is divided into three generation processes or mechanisms, namely a story, discourse, and representation. Ogata[1] presents a detailed list of all of the modules in the current INGS. Generally, the story generation mechanism generates a story structure that contains a sequence of events. Then, the discourse mechanism transforms the story structure generated by the story generation mechanism into a discourse structure that contains edited by the narrative logic, namely the structure of a narrative to be narrated. Further, the representation mechanism transforms the narrative structure into a surface narration using natural language, music, and a picture image.

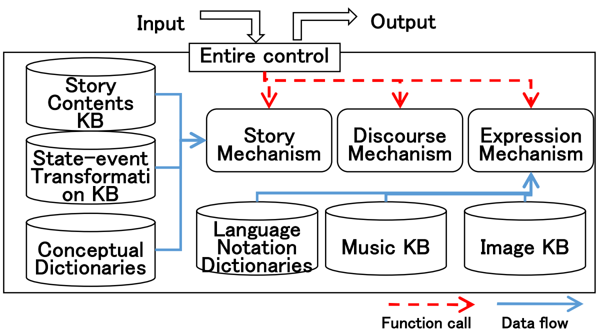

Fig. 1. The INGS Architecture.

The GM and PLs in the ANGG respectively correspond to the story generation mechanism and the discourse mechanism in the INGS. From the perspective of the GM, a story that the GM generated is changed and transformed by the PLs into a more interesting story. In this case, the story is called a discourse in the INGS. The GM also controls and manages the transformation and change process to make an expanded discourse or to indicate the need to make an alternative discourse. On the other hand, the PLs collectively change and transform the story under the control and management of the GM to expand it through the communication cycle between the GM and the PLs.

Ono and Ogata[2-5] presented the architecture of an ANGG system. Ono and Ogata[2] located a mechanism that set a story world in the ANGG, and Ono and Ogata[6] proposed a mechanism for expanding a scene in the framework story generated by the GM in order to make a longer story. In this paper, we focus on the aspect of the story generation and discourse generation techniques with the aim of extending narrative generation techniques in future ANGGs. These correspond to the techniques that are used to arrange the story-generation mechanism and discourse generation mechanism in the INGS, and the many parts can be used in both the ANGG and INGS. However, important differences are that the PLs in the ANGG generate and transform a prepared story framework through the collective and corporative process, and narrative generation is generally conducted considering the interaction and the GM and the PLs.

2. ANGG Overview and Story and Narrative Generation

Fig. 2 shows an overview of the story generation process in the ANGG. From the perspective of story or narrative generation, the ANGG comprises two types of generation mechanisms by the GM and PLs. In particular, in the first step in the communication cycle, the GM generates the framework of a story that is to be incrementally extended into an extended story. Then, the PLs receive the framework story to generate a partial discourse to be inserted or added to the story. Finally, in the PL mechanism, several PLs collectively generate a new partial narrative. Currently, this requires a method that inserts an event between the two events in the framework story until the decided connection condition is satisfied for the next event in the framework story. The framework story refers to a story in the INGS that is generated using the story generation mechanism. On the other hand, the transformed or changed narrative corresponds to a discourse in the INGS that is transformed according to the discourse mechanism. However, in practice, the PLs can also use techniques in the story generation mechanism. In addition, the ANGG uses the "world setting," which means both a set of elements for stories and a set of constraint information that is used to define the range of possibilities.

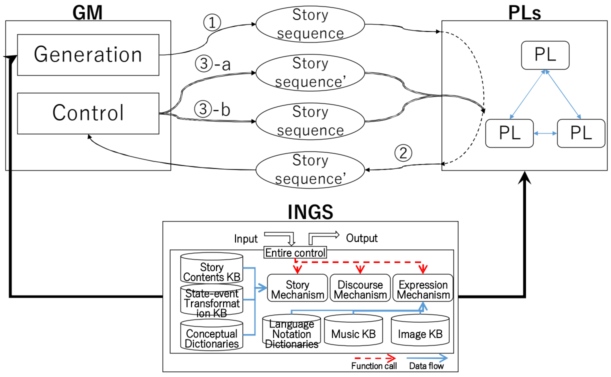

Fig. 2 A story generation process in ANGG.

A variety of collective or corporative narrative generation or transformation methods can be considered in order to extend the ANGG. Based on the current method, all PLs propose candidates for expansions of an original story or discourse, and only one is selected to be given to the GM. Discourses that are made by all PLs can also be combined into the final proposed discourse. In addition, various types of discourses may be proposed to the GM, and include methods that embody or extend a part of the framework story generated by the GM, and that transform the flow of the entire story. Further, each PL plays a character in a story world, and the narrative generation by the PLs is executed based on the characters' perspectives. A function in the communication process among PLs determines which PL is the main character in the story world. Thus, goal-planning story generation is one of the basic narrative-generation methods that are used. We discuss these narrative generation problems faced by PLs in another paper.

After the PLs first propose a discourse that transforms and changes the framework story generated by the GM, the GM evaluates whether to directly adopt the proposition. If the proposed discourse (or the fragmental extension) is adopted, the GM creates a new story that reflects the discourse proposed by the PLs. In contrast, if the proposed discourse or the fragmental extension is not adopted, the GM instructs the PLs to repeat the narrative generation for the framework story until the GM decides to adopt it. After the second process, this cycle, which is referred to as narrative transformation by the PLs and narrative evaluation by the GM, continues until a complete narrative is eventually generated. As stated above, in the ANGG, the GM has roles that include generating the first story framework and controlling the post-game progression. On the other hand, the main role of the PLs is to transform and change the framework story generated by the GM in an attempt to propose partial stories.

In the above system's architecture, the ANGG can use story and discourse generation techniques in the INGS that we have presented. The main types that are relevant to the PLs are described in section 3. The ANGG can also refer to previous research to elaborately design the interactive mechanisms between the GM and the PLs as well as between the PLs. In section 4, we introduce the related previous research.

3. Methods for Story Generation and Transformation

In this section, we introduce various mechanisms that transform a story into various discourse structures.

3.1. *Story and Discourse in a Narrative*

First, the "narrative discourse mechanism" in the INGS architecture shown in Fig. 1 provides the most fundamental narrative mechanism that is used for changing and transforming a story generated by the story generation mechanism. Fig. 3 shows an example where a story structure is transformed into a discourse structure; a relationship specified to discourse, "present-backward" is added to the story structure. The structures for both the story and the discourse have similar tree forms. Each leaf node in a story tree corresponds to an event described with conceptual representation, which is further described by a case structure that consists of one verb concept and eight types of cases, such as "agent" and "object." Each internal node in the tree is equivalent to a "relationship," such as "cause-effect" and "serial," combined with the child nodes. The ANGG can use this type of method as a narrative discourse technique to change and transform the framework of a story that is generated by the GM.

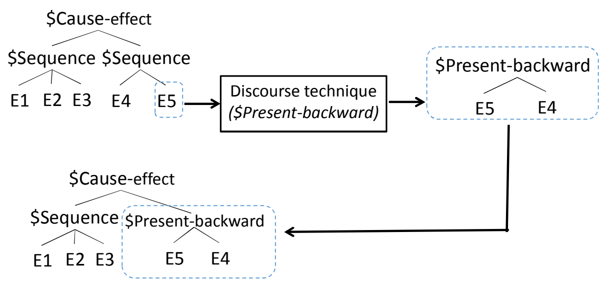

Fig. 3. Transformation from story structure to discourse structure.

We began this study by modifying the theory's context proposed by Genette[7], who is a French narratologist, and we used a computational viewpoint to create a technological method for the design or formalization of the narrative discourse generation mechanism. This allows each of the classified techniques applied by Genette to be used as a rule for associating an input story structure with a transformed output discourse structure. However, the aim of studying the narrative discourse mechanism is not only to apply the narratology proposed by Genette. It is also expanded to other narrative discourse techniques. We designed a more comprehensive narrative discourse system by integrating various narrative discourse types, including the following techniques, into a systematic list.

3.2. *Defamiliarization Techniques*

Zhang, Ono and Ogata[8] classified the methods of the relationships between a product and the story by performing an analysis of over 5000 television commercial films to define its result as "rhetorical techniques of introducing a product into a single event." The previous study classified the rhetorical techniques into either regular rhetoric or standard rhetoric during the of production, distribution, and utilization processes of a product. On the other hand, they defined irregular rhetoric based on "defamiliarization" ("ostranenie" in Russian) or a deviation from the regular rhetoric. Defamiliarization rhetoric indicates techniques that transform the whole of a part or an element included in a story into an extraordinary object that is different from people's ordinary feeling to strengthen the impression of the element itself.

Table 1 shows 12 defined types of rhetoric. A "rhetoric" refers to a technique that is used to introduce a product in an impressive way by employing an advertising scenario, while a "single event" refers to a unit that contains several elements such as a person, object, location, and time, which are associated with a single action in the flow of the story. In the table, rhetorical techniques from R1 to R3 generate scenes of standard or ordinary use methods of products. On the other hand, the rhetorical techniques from R4 to R12 generate defamiliarization scenes by applying the extraordinary rhetoric. The irregular techniques partially use the "changing constraint" method, which changes usable concepts in the conceptual dictionaries in the INGS (Fig. 1) to adjust the semantic range of concepts to enable them to be set into an event.

Table 1. Classification of TV-CF rhetorical techniques.

	Object	Type of Rhetoric
Regular		**R1 original method of manufacturing**: the original way that the product is manufactured.
		R2 original method of purchasing: the original way that the product is purchased.
		R3 core rhetoric: the way that the product is originally used.
Irregular	**Action**	**R4 defamiliarization**: the defamiliarized way that the product is used.
		R5 none use of rhetoric: no deviation, just "hold."
	Person	**R6 character as a narrator**: rather than being involved in the story, the character sends a message to viewers directly.
		R7 state defamiliarization of the character: changing all or part of the character, or the character daily uses the product in an impossible way.
		R8 action defamiliarization of the character: the character does not perform the original action, but performs defamiliarity.
	Things	**R9 state defamiliarization of the product**: changing all or part of the product.
		R10 state defamiliarization of related things of the product: changing all or part of the related things of the product.
		R11 product subjectification: instead of being used by a character, here, it emphasizes that the product exists independently.
	Location	**R12 background defamiliarization**: all or part of the background is changed into something entirely decorative, which is impossible to do daily.

3.3. *Film Rhetoric by Kanai*

Story cutting techniques proposed by Kanai[9] aim to cut a story's consistency in order to strengthen only a specific element in the story. This is done by lacking a temporal sequence and a character's consistency in continuous scenes in a film. For example, in a battle scene in a war film, the use of cutting techniques by inserting a silent scene and a scene where the temporal continuity is ambiguous contribute to strengthening the impression of scenes that are independent of a story's semantic progression.

Kanai and Kodama[9] proposed a high-level classification of cutting techniques that (1) emphasizes editing itself by making a differentiation or discontinuity in the elements among continuous shots, which includes destroying the continuity of events, (2) emphasizes the image itself by irrationalizing or destroying the relationships between an event and the image, which includes repetitive filming of the same object, and (3) emphasizes the sound itself by irrationalizing the relationships between sound and the image, which includes lacking the relationships between speech and the visual image.

Furthermore, considering the above large classification, Kanai[9] presented the following sixteen types of cutting technique. In the description, "dialectic" refers to a unified whole. On the other hand, in "cutting," it appears as itself, and the temporal order cannot be recognized by the user. In "metric," the continuity time of all shots is the same. On the contrary, the continuity time in each shot varies according to the action's time. "Tonal" and "overtonal" do not initially determine the continuity time.

- (1) Dialectic metric, (2) Dialectic rhythmic, (3) Dialectic tonal, and (4) Dialectic overtonal: (1), (2), and (3), respectively have different lengths of shots, and (4) mixes a shot with different sounds into a sequence of shots.
- (5) Temporal sequence cutting metric, (6) Temporal sequence cutting rhythmic, (7) Temporal sequence cutting tonal, and (8) Temporal sequence cutting overtonal: These prevent a receiver from representing the temporal sequence of events in a cognitive manner.
- (9) Characters cutting metric, (10) Characters cutting rhythmic, (11) Characters cutting tonal, and (12) Characters cutting overtonal: These cut the continuity of a character, and there are no shots where the same character continuously appears.
- (13) Temporal sequence/characters cutting metric, (14) Temporal sequence/characters rhythmic, (15) Temporal sequence/characters tonal, and (16) Temporal sequence/characters overtonal: These prevent a receiver from representing the temporal sequence of events in a cognitive manner. In addition, there are no shots where the same character continuously appears.

4. Generation by Narrative Communication

Akimoto and Ogata[10,11] presented a computational narrative model in which literary works are continuously changing owing to the interaction between an author or narrator and a reader or narrator (these are computer agents within the system) for a narrative discourse control mechanism in the INGS. In the system modeling, Jauss' reception theory[12] is simply interpreted as a mechanism to limit the discourse process through the interaction between a narrator mechanism with generative parameters and a narratee mechanism with expectation parameters. In this study, we mixed this Jauss-based mechanism with the Genette-based mechanism mentioned in section 3.1 to form a model and system that control the deviation of a narrative discourse mechanism based on the interaction between a narrator mechanism and a narratee mechanism within a narrative.

This system is a model of Jauss' reception theory, where literary works are repeatedly produced according to a reader's expectations and the corresponding responses from an author; the interaction can continuously or historically change a literary work. In particular, texts of narrative discourses are repeatedly produced through a process according to parameters for a reader (or narratee) as the expectation, and using the same parameters for an author (or narrator) as the generative goals. These parameters are the same as those in the Genette-based mechanism.

The cycle continues according to the interaction between a narrator and narratee. The narrator mechanism has a set of rules for controlling the application of discourse techniques based on the generative parameters to transform a discourse structure. We performed the direct transformation of a discourse structure using techniques defined by Genette's theory. The narratee mechanism evaluates the results by comparing the narratee's expectation parameters with the narrator's generated parameters. In the next cycle, the narrator applies corrections according to the narratee's evaluation in order to achieve reader satisfaction. However, the process eventually reaches a point where the narratee becomes tired or when his/her satisfaction begins to fall. When this happens, "deviation" occurs and the narrator abandons some of the old generative parameters and moves to a new cycle of discourse grounded on the newly found strategy. The narratee's expectations change according to the reconstruction.

Fig. 4 is a detailed process flow of the narrative discourse control based on the interaction between the narrator and narratee mechanisms. As seen in (1), the system selects the corresponding techniques according to the parameter values. In (2), the Genette-based techniques fulfill the functions in the context of the Jauss-based control. In (3), a higher satisfaction can be obtained when a more strongly desired parameter is satisfied. The narratee indicates one parameter with the lowest satisfaction. In (4), the narratee rewrites an expectation parameter using two different procedures. The first rewrites the sufficiency number and degree of desire. The former is increased each time the narratee receives the sufficed discourse. Finally, (5) includes "deviation" from the expectation.

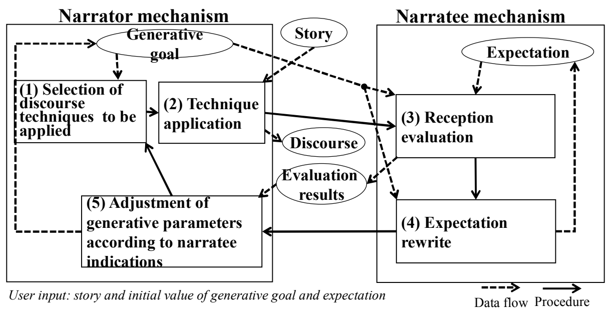

Fig. 4. Interaction between narrator and narratee.

5. Conclusions

In this paper, after we presented an overview of the ANGG system that we developed, we considered story generation and discourse techniques to utilize the GM and PLs used in the ANGG in the future. These techniques are provided by the story-generation mechanism and the discourse mechanism in the INGS. Therefore, although there is common narrative knowledge to be used in both the INGS and the ANGG, an important difference between the two systems is that narrative generation by the ANGG is performed considering the interaction between the GM and the PLs and the collective method among PLs. Table 2 shows a comprehensive list of narrative techniques for the GM and the PLs including the techniques described in this paper.

Table 2. Classification of narrative techniques.

Macro level techniques
• Story-generation techniques • Story grammar techniques • Story-discourse transformation techniques **[Section 3.1]**
Medial level techniques
• Goal-planning techniques
Micro level techniques
• Event transformation techniques • Rhetorical techniques **[section 3.2]** • Cutting techniques **[section 3.3]**

In the future, we plan to extend the design of an integrated mechanism of the ANGG to incorporate various narrative techniques, including those proposed in this paper, interactive processing between the GM and the PLs, and collective processing among the PLs into a system architecture that enables changeable and diverse narrative generation.

Acknowledgements

This work is supported by the JSPS KAKENHI Grant Number 26330258 and the Support Center for Advanced Telecommunications Technologies Research Grant (2015-2017).

References

1. T. Ogata, Computational and Cognitive Approaches to Narratology from the Perspective of Narrative Generation, in Ogata, T. & Akimoto, T. (eds), *Computational and Cognitive Approaches to Narratology* (IGI Global, Pennsylvania, 2016) 1-74.
2. J. Ono and T. Ogata, Architecture of a narrative generation system based on a TRPG model: the use of an integrated narrative generation system for knowledge acquisition (preliminary version), *Bulletin of Netw., Comput., Syst., and Softw.* **5**(1) (2016) 40-48.
3. J. Ono and T. Ogata, A design plan of a game system including an automatic narrative generation mechanism: the entire structure and the world settings, *J. Robotics, Networking and Artificial Life* **2**(4) (2016) 243-246.

4. J. Ono and T. Ogata, Towards a narrative generation system based on a TRPG model: the use of an integrated narrative generation system for an application system, in *Proc. 21nd Int. Symp. on Artificial Life and Robotics* (2016).
5. J. Ono and T. Ogata, Architecture of a narrative generation system based on a TRPG model: the use of an integrated narrative generation system, in *Proc. 4th IIAE Int. Conf. on Industrial Application Engineering 2016* (2016) 138-145.
6. J. Ono and T. Ogata, Implementation of a Scene Expansion Mechanism using an Event sequence: As a Mechanism in an Automatic Narrative Generation Game, *Proc. 3rd Int. Conf. on Knowledge Engineering* (2016). (In printing).
7. G. Genette, *Narrative discourse: An essay in method,* trans. J. E. Lewin (Cornell University Press, New York, 1972).
8. Y. Zhang, J. Ono and T. Ogata, Single Event and Scenario Generation based on Advertising Rhetorical Techniques using the Conceptual Dictionary in Narrative Generation System, *The 4th IEEE Int. Conf. on Digital Game and Intelligent Toy Enhanced Learning* (2012) 162-164.
9. A. Kanai and K. Kodama, Film edit design: Story and irrational cutting, *Cognitive Studies* **17**(3) (2010) 444-458.
10. T. Akimoto and T. Ogata, A narratological approach for narrative discourse: Implementation and evaluation of the system based on Genette and Jauss, in *Proc. of the 34th annual conf. of the Cognitive Science society* (2012) 1272-1277.
11. T. Akimoto and T. Ogata, An information design of narratology: The use of three literary theories in a narrative generation system, *Int. J. Visual Design* **7**(3) (2014) 31-61.
12. H. R. Jauss, *Literaturgeschichte als provokation*, (Suhrkamp Verlag, Frankfurt am Main, 1970).

A Rule-Based Classification System Enhanced by Multi-Objective Genetic Algorithm

Kenzoh Azakami
Graduate School of Science and Engineering, Yamaguchi University, Tokiwadai 2-6-11 Address
Ube, Yamaguchi 755-8611, JAPAN
Shingo Mabu
Graduate School of Sciences and Technology for Innovation, Yamaguchi University, Tokiwadai 2-6-11 Address
Ube, Yamaguchi 755-8611, JAPAN
Masanao Obayashi
Graduate School of Sciences and Technology for Innovation, Yamaguchi University, Tokiwadai 2-6-11 Address
Ube, Yamaguchi 755-8611, JAPAN
Takashi Kuremoto
Graduate School of Sciences and Technology for Innovation, Yamaguchi University, Tokiwadai 2-6-11 Address
Ube, Yamaguchi 755-8611, JAPAN
E-mail: {v001vk, mabu, m.obayas, wu}@yamaguchi-u.ac.jp

Abstract

Recent years, data mining techniques have been developed for extracting rules from big data. However, there are some problems to be considered, for example, it is difficult to judge which rules are important and which are not important; and even in simple classification problems with the small number of classes, a various sub-patterns to be considered potentially exist in each class. To solve the above problems, a rule clustering algorithm using multi-objective genetic algorithm is proposed.

1. Introduction

Data mining is a technique of extracting effective rules from big data. However, data mining has some problems to be considered. That is, a large number of rules are extracted, so it is difficult to judge which are the important rules and which are not important; and even in simple classification problems, e.g., two-class problems, a variety of patterns potentially exist in each class, which makes the problems more difficult. In the conventional method [1], a genetic algorithm (GA)-based clustering was applied to the class association rules extracted by genetic network programming (GNP) [2] to solve the above problems and enhance the classification system. In this paper, a rule clustering algorithm using the multi-objective genetic algorithm (MOGA) is proposed to enhance the conventional classification system. To confirm the effectiveness of the proposed method, the accuracy of the conventional method and proposed method is compared. In addition, the accuracy of the proposed method and other classification methods: Tree-based classifier (J4.8), Multi-Layer Perceptron (MLP), Support Vector Machine (SVM). The data used for the comparisons are Credit approval, Pima Indian, and German, which were downloaded from UCI machine learning repository [3].

2. Association rule extraction by GNP

In the conventional method, a clustering using GA was applied to the rules extracted by GNP. In this section, the method of extracting class association rules is explained.

2.1 Class association rule

As X is the antecedent, and Y is the consequent, an association rule is denoted by X⇒Y. For example, a rule "-people who buy milk and egg also buy bread" , is denoted by {milk, egg}⇒{bread}. A class association rule is denoted by, (A1=1)∧(A2=1)⇒ class1 where the consequent is changed to a class label.

2.2 Rule extraction by GNP

Class association rules are extracted by GNP from a database with attributes of binary values and class labels (Fig. 1). GNP has a structure as shown in Fig. 2. GNP consists of initial nodes and attribute nodes for rule extraction. According to the transition of attribute nodes, many candidate rules are generated. The node transition is repeated by the predefined number of times. The candidate rules that satisfy the evaluation criteria are stored in a rule pool. The evaluation criteria are support, confidence, and χ^2.

2.3 Evolution of GNP

After storing rules, crossover and mutation are performed. In GNP, the crossover is performed by selecting two individuals, and the selected individuals exchange their node connections with each other. The mutation selects one individual, and connections of nodes are randomly changed. Fitness is calculated by Eq. (1). Eq. (1) means individuals that extract important rules are highly evaluated.

$$\text{fitness} = \sum_{r=1}^{R}(\chi^2(r) + 10(n(r)-1)) + \alpha_{new} \quad (1)$$

$\chi^2(r)$: χ^2 value of class association rule r
n(r) : Length of rule r
α_{new} : Reward when a new rule is found
R : Set of extracted rule numbers
The crossover and mutation are repeated by the predefined number of times.

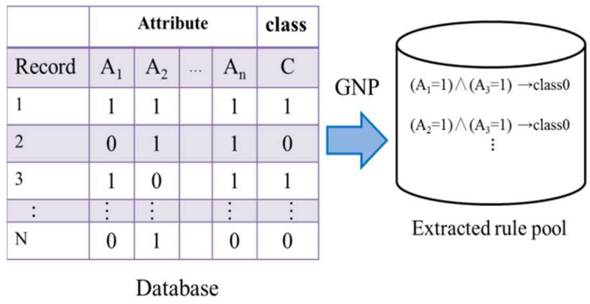

Fig. 1. Flow of rule extraction by GNP

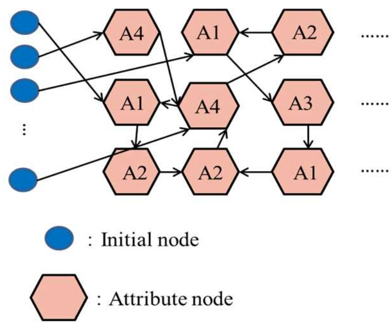

Fig. 2. Structure of GNP in rule extraction

3. Conventional rule clustering by GA

In this section, the conventional GA clustering for the class association rules extracted by GNP is explained.

3.1 Individual initialization

First, several integer arrays are prepared, where the number of arrays is the same as the number of classes, and the length of the arrays are the same as the number of rules in the corresponding classes. All the arrays are initialized by random values ranging from 1 to n, where n means the number of subclasses. The random values in the arrays show the cluster numbers to which each rule is assigned. The flow of GA Clustering is show in Fig. 3.

3.2 Evolution of individuals

The fitness of GA is defined as the classification accuracy for training data, and the individuals for crossover and mutation are selected by tournament selection. Then the crossover exchanges the genes of the selected individuals by crossover, and the mutation changes the genes randomly.

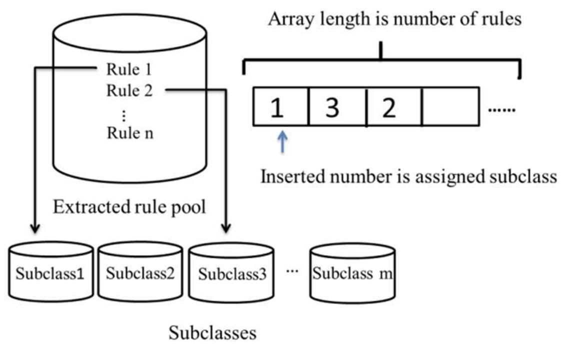

Fig. 3. Extracted rule clustering by GA

4. Proposed rule clustering by Multi-Objective GA (MOGA)

In this section, a class association rule clustering using MOGA is explained. In the conventional method, the fitness is based only on the classification accuracy for the training data. Therefore, the direction of the evolution is biased toward the correct classification for the training data, which loses the generalization performance for new data. The proposed method adds two new criteria, applies MOGA to optimize these three criteria simultaneously, and aims to enhance the clustering accuracy. The two new criteria are inter-cluster variance and intra-cluster variance. Inter-cluster variance ${D_{ij}}^2$ and intra-cluster variation ${S_i}^2$ are calculated as follows:

$$ {D_{ij}}^2 = \sum_{k=1}^{a}(ce_{ik} - ce_{jk})^2 \quad (2) $$

$$ {S_i}^2 = \sum_{r=1}^{n_i}\sqrt{\sum_{k=1}^{a}(ce_{ik} - e_{rik})^2} \quad (3) $$

$$ ce_{ik} = \frac{1}{n_i}\sum_{r=1}^{n_i} e_{rik} \quad (4) $$

e_{rik} : Value of kth attribute of rth rule in cluster i
a : the total number of attributes in a database
n_i : the number of rules in cluster i

Inter-cluster variance, intra-cluster variation and accuracy are used as evaluation functions (f_1 = accuracy, $f_2 = {D_{ij}}^2$, $f_3 = 1 / {S_i}^2$). The evaluation is higher as the values of the evaluation functions are larger.

4.1. Multi-objective algorithm

Considering the trade-off between the evaluation functions, MOGA is applied to the optimization.

4.2.1. Pareto solution

Pareto solutions of the individuals in MOGA are represented as shown in Fig. 4, where each axis corresponds to each evaluation function. The individuals that are not inferior to any other individuals are called Pareto solutions (non-dominated solutions). An example of Pareto solutions is shown in Fig. 5.

4.2.2. Evolution in the proposed method

MOGA obtains the plural number of Pareto solutions (elite individuals), not one elite individual unline standard GA. The evolution of MOGA is performed by crossover and mutation. For selecting crossover and mutation individuals, individuals are ranked, where the individual rank is defined as the number of superior individuals to itself, e.g., the rank of Pareto solutions is 0.

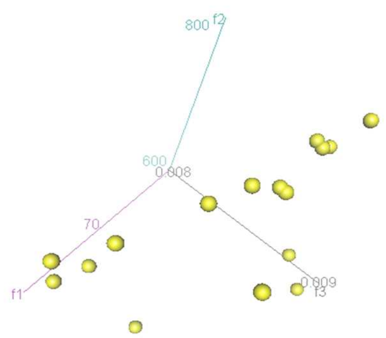

Fig. 4. Pareto solutions on axis

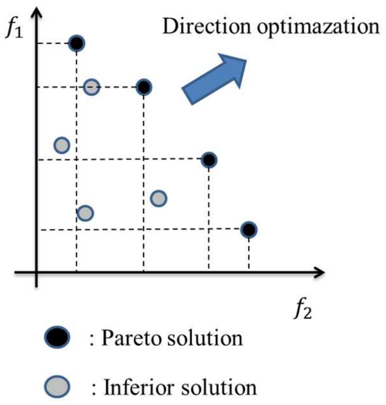

Fig. 3. Pareto solutions example

5. Simulation results

The datasets named German, Pima Indian and Credit approval are used for evaluating the classification accuracy. The results of the accuracy obtained by the proposed method and conventional method are shown in Table 1. The accuracy of the proposed method shown in Table 1 is the best one obtained by Pareto solutions. From Table 1, the proposed method showed higher accuracy than the conventional method. The comparison with J4.8, MLP, and SVM are shown in Table 2. From Table2, the proposed method showed equal to or higher accuracy than J4.8, MLP, and SVM.

Table. 1.Comparison of accuracy between the conventional method and proposed method

German k=20		
	Conventional method	Proposed method
Accuracy [%]	72.5	75.3
Pima Indian k=20		
	Conventional method	Proposed method
Accuracy [%]	77.1	80.4
Credit approval k=20		
	Conventional method	Proposed method
Accuracy [%]	86.6	88.0

k :Number of clusters(Specified value by the designer)

Table. 2. Comparison of accuracy between the proposed method and other classifiers

German				
	Other classifiers			Proposed method
	J4.8	MLP	SVM	
Accuracy[%]	71.5	72.5	76.0	75.3
Pima Indian				
	Other classifiers			Proposed method
	J4.8	MLP	SVM	
Accuracy[%]	75.8	77.1	77.1	80.4
Credit approval				
	Other classifiers			Proposed method
	J4.8	MLP	SVM	
Accuracy[%]	86.4	82.4	85.9	88.0

6. Conclusion

In order to enhance the performance of the classification system using class association rules, MOGA is applied to the rule clustering, and its classification ability was evaluated using three datasets. The results showed that the proposed method with MOGA generated solutions with high accuracy. The future work will be developing a method selecting the best solutions from the generated Pareto solutions. In addition, the Pareto solutions should be analyzed in detail to find the importance of each evaluation function.

References

1. K. Azakami, S. Mabu, M. Obayashi, A. Kuremoto, Performance Enhancement of Classification Systems by Clustering Class Association Rules with Pruning and Its Evaluation, *The Conference Record of 66th Chugoku-branch Joint Convention of Institutes of Electrical and Information Engineers*, (Yamaguchi, 2015)
2. K. Shimada, K. Hirasawa, and J. Hu, Genetic network programming with acquisition mechanisms of association rules, *Journal of Advanced Computational Intelligence and Intelligent Informatic*, Vol. 10(1) (2006) 102-111.
3. UCI Machine Learning Repository, URL:http://archive.ics.uci.edu/ml/datasets.html/ (accessed 2016-5-20)

A Method of Feature Extraction for EEG Signals Recognition Using ROC Curve

Takashi Kuremoto[1], **Yuki Baba**[2], **Masanao Obayashi**[1], **Shingo Mabu**[1], **Kunikazu Kobayashil**[3]

[1]Graduate School of Science and Technology for Innovation, Yamaguchi University, Tokiwadai 2-16-1, Ube, Yamaguchi 755-8611, Japan
[2]Graduate School of Science and Engineering, Yamaguchi University, Tokiwadai 2-16-1, Ube, Yamaguchi 755-8611, Japan

[3]School of Information Science and Technology, Aichi Prefectural University, 1522-3 Ibaragabasama, Nagakute, Aichi 480-1198, Japan
E-mail: {wu, v033vk, m.obayas, mabu}@yamaguchi-u.ac.jp, kobayashi@ist.aichi-pu.ac.jp

Abstract

The feature extraction of Electroencephalograph (EEG) signals plays an important role in mental task recognition of brain-computer interaction (BCI). In this study, a novel method of EEG signal feature extraction is proposed using techniques of fast Fourier transform (FFT) and receiver operating characteristic (ROC) curve. In the proposed method, the raw EEG data was transformed into power spectrum of FFT at first, and then to find frequencies decided by area under curve (AUC) of ROC between the value of spectrums of different classes of metal tasks. Experiment results using benchmark data of EEG signals showed the effectiveness of the proposed feature extraction method when support vector machine (SVM) was used as a classifier.

Keywords: EEG, FFT, ROC, AUC, SVM

1. Introduction

The electronic potential signals of electrodes, which are arrayed on the surface of head, are measured by electroencephalograph and it is called as "Electroencephalogram", i.e., "EEG". When different metal tasks such as motor imagery, calculation, number counting, article considering, and so on, different patterns of EEG signals can be observed. So the analysis and recognition of EEG signal is one of the way to realized brain computer interface (BCI), or brain machine interface (BMI), i.e., people can control the machines or robots by their imaginations [1] [2]. Feature extraction of the EEG signal plays a very important role of mental task recognition to enhance the accuracy and there have been many studies of this theme [3] [4]. In [5], Obayashi et al. proposed to use the nonlinear normalized feature spaces of fast Fourier transformation (FFT) of EEG signals. And the method was improved by selecting the most characterized phases of raw EEG signals in our previous works [6].

In this paper, we propose a novel method using FFT and the value of area under curve (AUC) of receiver operating characteristic (ROC) curves to extract the feature of EEG signal and verified its effectiveness with a powerful classifier: kernel-support vector machine (k-SVM). Benchmark data of EEG classification [7] and BCI competition II data [8] were used in the experiments.

2. Method

To extract the feature vector space of EEG signal for mental task recognition, we propose to use FFT and ROC to find the limited frequencies which AUC values are high when two classes EEG data are compared in the training process, and the power spectrums of these frequencies are used as input vector of classifiers.

2.1. *Fast Fourier Transform (FFT)*

FFT is a kind of discrete Fourier transform (DFT), which is used for frequency analysis of signals in the field of signal processing, invented in 1965 by J. Cooley and J. Tukey at first, and improved continuously. The function of FFT is to show the power spectrum of different frequencies of the time series signals as same as the original Fourier transform but easily to be realized by computers. In this study, we used the FFT function provided by free software package R [9] to process the raw EEG signals.

2.2. Receiver operating characteristic (ROC) curve

Assume that two classes data class A and class B have their probability density functions as shown in Fig. 1. The true positivity of class A will be the shadowed area α in the left and the false positives area 1 – β in more shadowed area. As α and 1 - β are plotted while sliding the threshold along the x axis, a graph as shown in Fig. 2 is obtained. The curve in this graph is called the ROC curve and it shows the divisibility of the two probability density functions. If two distributions completely overlap, the for any position of the threshold we have that α =1 – β.

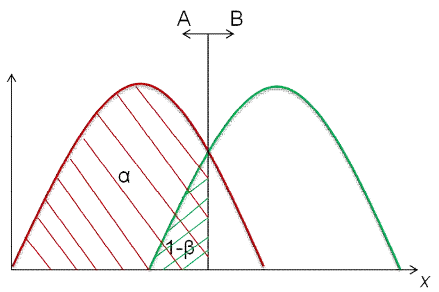

Fig. 1 Overlapping of the probabilities of two classes data.

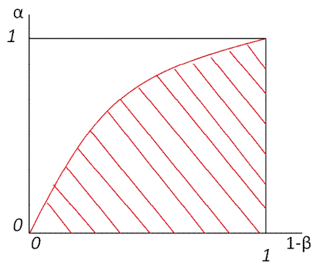

Fig. 2 AUC of a ROC curve

In Fig. 2, the area below the ROC curve is called "area under curve" (AUC). This value takes from 0.0 to 1.0, and it is an indicator of the divisibility of the two distributions. If the value of AUC becomes to 0.5, two distributions completely overlapped. Conversely, when the value of AUC reaches 1.0 (or 0.0), it means that the two distributions are completely separated.

ROC was used to classify cDNA microarray successfully [10] and applied to EEG classification with wavelet transformation (WT) recently [11]. Here, we propose to use the value to AUC of ROC and FFT to distinguish the two classes EEG signals.

3. Feature Extraction

3.1. *Method of using FFT*

Suppose that an EEG signal $x_{m,n}$ (m=1, 2, …, M, n=1, 2, …, N) is given. m indicates the number of channels, and n indicates the number of samples in channel m. The procedure of the conventional method using FFT to extract the feature of EEG [6] is as follows.

Step 1 Divides the EEG signal of all the channels m into multiple windows l (l=1, 2, …, L) along the time domain.

Step 2 Perform FFT on all of the divided windows, and let the result be $F_{m,l}$.

Step 3 Compare the power spectrum of the window l of the channel m to its adjacent window l + 1, and calculate the difference $D_m(l)$ of the frequency spectrum.

$$D_{m,}(l) = \sum_{l=1}^{l=L-1} | F_{m,l+1} - F_{m,l} | \quad (1)$$

Step 4 From Step 3, the maximum $D_m(l)$ in the channel m is determined, and power spectrum in a region of 4 to 45 Hz in the frequency band of the window l is used as a feature space for classifiers such as SVM, multi-layer perceptron (MLP), and so on.

3.2. *Method of using FFT and ROC Curve*

Let the input signals be $x_{k_c,m,n}$ (c=1 or 2, k=1, 2, …, K), where k indicates the kth EEG signal of a set of EEG data, and c indicates the class of mental task. m and n are the same as in section 3.1. The procedure of the novel method is as follows.

Step 1 Perform FFT to all the EEG signals $x_{k_c,m,n}$ and let the result be $F_{k_c,m,p}$ where p indicates the order number of frequencies.

Step 2 Obtain $P_{k_1,m,p}$ and $P_{k_2,m,p}$, which are two probability density functions of $F_{k_c,m,p}$ at p frequency where class c = 1 and 2 of K signals of channel m.

Step 3 Calculate the ROC curve and its AUC $A_{m,p}$ of $P_{k_1,m,p}$ and $P_{k_2,m,p}$.

Step 4 Repeat Step 2 and Step 3 on all channels, a set $A_{m,p}$ of frequency p in channel m is obtained.

Step 5 Find P points of frequencies which $A_{m,p}$ is high.

Step 6 Power spectrum $E_{m,p}$ (p=1, 2, …, P) of the unknown EEG signal are used to as input feature vector of a classifier.

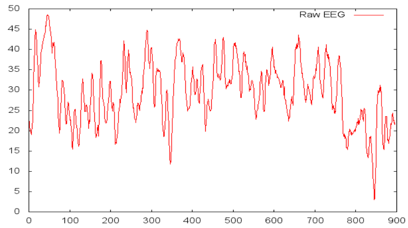

(a) The raw EEG data

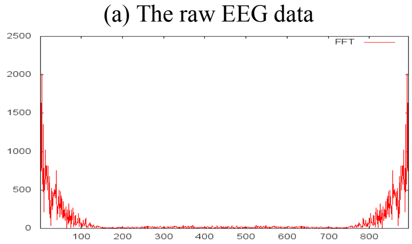

(b) FFT results

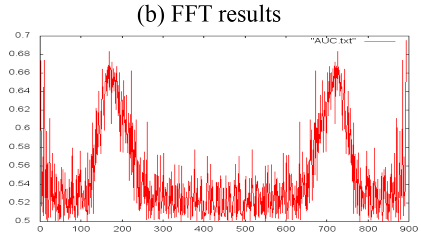

(c) AUC of FFT of 2 kinds of mental tasks

Fig. 3 The procedure to obtain AUC

The procedure of how AUC of FFT of 2 kinds of EEG data patterns is shown in Fig. 3 Frequencies with enough high values of AUC in Fig. 3 (c) are chosen as input features to classifiers.

4. Recognition Experiment

Mental task recognition experiments using EEG data and the methods introduced in Section 3 were performed. Two kinds of EEG data are used: (i) a benchmark data provided by Colorado State University [7] and (ii) BCI Competition II generated by Birbaumer [8]. In the case of (i), there are 5 kinds of mental tasks (see Table 1) were requested to subjects, and their EEG data were obtained 10 trials with 7 channels. Meanwhile in (ii), there are 2 data sets named “Ia” and “Ib” which are EEG data obtained by 2 kinds of tasks: Ia was asked to recognize visual objects displayed on the top or bottom of monitor and move a cursor up or down, and Ib with the same tasks but with not only visually presentation but also auditorily. Details of EEG data used in our experiments are listed in Table 2.

Table 1 Mental tasks in a benchmark database [7].

Mental Task	Contents
Baseline	Relaxing as much as possible
Multiplication	Calculating multiplication mentally.
Letter-composing	Considering the contents of the letter
Rotation	Imagining rotation of a 3-D object
Counting	Imagining writing a number in order

Table 2 EEG data used in the experiments.

Database	Mental Tasks	Data Sets	Chan nels	Samples per Channel	Sampling Freq.
Benchmark [7]	5	10	7	2500	250
Ia [8]	2	135/133	6	896	256
Ib [8]	2	100	7	1152	256

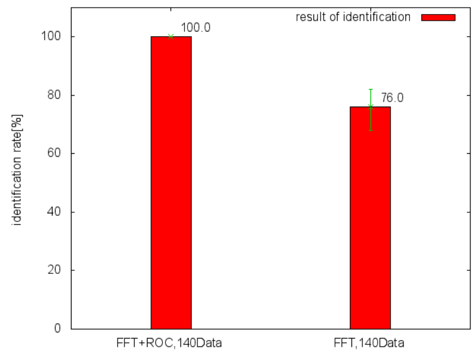

Fig. 4 Results of different feature extraction methods for the benchmark EEG data [7] (5 classes)

Kernel SVM (k-SVM) was used as the classifier, its package and ROC package in R [9] was utilized in our experiments.

As shown in Fig. 4, the average classification rate of the conventional method [6] (FFT, 140 Data) was 76.0%, meanwhile 100.0% of the proposed method (FFT+ROC, 140 Data) for the 5 tasks EEG data. 140 Data indicates that the input dimension to SVM was 140 which came from 20 points of FFT (P in Step 5 of the proposed procedure) signals in 7 channels.

For BCI competition II data Ia and Ib [8] (2 classes), the proposed method also showed its priority to the conventional method as shown in Fig. 5 and Fig. 6 respectively. Additionally, higher dimensionality showed higher recognition rate according to the experiments results. For Ia, 120 Data means 20 points of one channel data, and 6 channel data were used, as well as 216 Data chosen by 36 points per channel. For Ib, 140 Data were obtained by 20x7, and 315 Data from 45 points per channel. The highest recognition rates of our method for Ia and Ib are 91.23% and 77.65%, higher than the best classification rates 90.10% and 56.67% of T. Nguyen et al. [11] respectively.

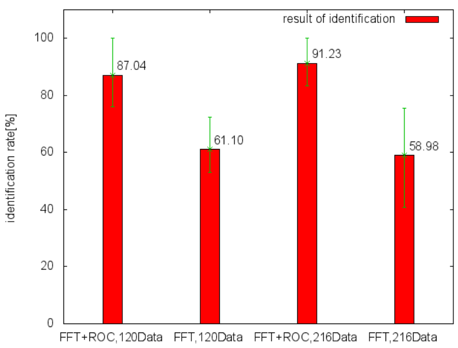

Fig. 5 Results of different feature extraction methods for the BCI competition II data Ia [8] (2 classes)

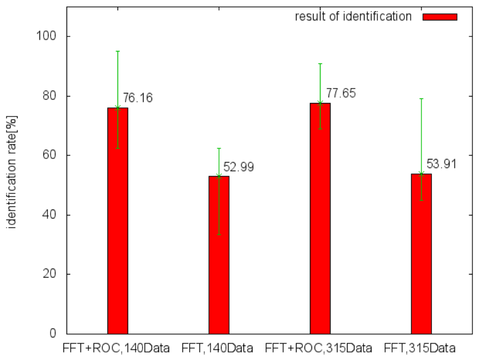

Fig. 6 Results of different feature extraction methods for the BCI competition II data Ib [8] (2 classes)

5. Conclusion

In this paper, we proposed a feature extraction method for EEG pattern recognition. The proposed method uses the AUC value of ROC curves of FFT results for two classes EEG signals to decide the feature vector space for classifiers. Classification experiments were performed using the Gaussian kernel SVM (k-SVM) to confirm the proposed method. As the result of the experiments, the proposed method showed its higher recognition ability than the conventional methods including the conventional FFT feature extraction method and others. We also used ROC of raw EEG data and ROC of wavelet transform (WT) as the input of k-SVM, and experiment results showed that the method described in Section 3, i.e., features extracted by ROC of FFT, was superior to others.

The future work of this study is to confirm the performance of the proposed method by other classifiers such as MLP, K-nearest neighbors (KNN), convolutional neural networks (CNN), and so on.

Acknowledgements

This work was supported by JSPS KAKENHI Grant No. 26330254 and No.25330287.

References

1. N. Birbaumer, L. G. Cohen, Brain-computer interfaces: communication and restoration of movement in paralysis, *Journal of Physiology*, Vol. 579, pp. 621-636, 2006
2. F. Lotte, M. Congedo, A.Lecuyer, F. Lamarche, B. Arnaldi, A review of classification algorithms for EEG-based brain-computer interfaces, *Journal of Neural Engineering*, Vol. 4, pp. 24-48, 2007
3. N. Jrad, M. Conedo, Identification of spatial and temporal features of EEG, *Neurocomputing*, Vol. 90, pp.66-71, 2012
4. A.S. Al-Fahoum, A. A. Al-Fraihat, Methods of EEG signal features extraction using linear analysis in frequency and time frequency domains, ISRN *Neuroscience,* Vol. 2014, 7 pages, 2014
5. M. Obayashi, K. Watanabe, T. Kuremoto, K. Kobayashi, Development of a brain computer interface using inexpensive commercial EEG sensor with one-channel, *Proceedings of the 17th International Symposium on Artificial Life and Robotics* (ISAROB 2012), pp. 714-717, 2012
6. T. Kuremoto, Y. Baba, M. Obayashi, S. Mabu, K. Kobayashi, To extraction the feature of EEG signals for mental task recognition, *Proceedings of 54th Annual Conference of the SICE*, pp. 353-358, 2015
7. Colorado State University, *Brain-Computer Interfaces Laboratory*: http://www.cs.colostate.edu/eeg/
8. BCI competition II: http://www.bbci.de/competition/ii/#datasets
9. The R Project for Statistical Computing: https://www.r-project.org/
10. H. Mamitsuka, Selecting features in microarray classification using ROC curves, *Pattern Recognition*, Vol. 39, Issue 12, pp. 2393-2404, 2006
11. T. Nguyen, A. Khosravi, D. Creighton, S. Nahavandi, EEG signal classification for BCI applications by wavelets and interval type-2 fuzzy logic systems, *Expert Systems with Applications*, Vol. 42, pp. 4370–4380, 2015

Forecasting Real Time Series Data using Deep Belief Net and Reinforcement Learning

Takaomi Hirata[1], Takashi Kuremoto[2], Masanao Obayashi[2], Shingo Mabu[2], Kunikazu Kobayashi[3]

[1]Graduate School of Science and Engineering, Yamaguchi University, Tokiwadai 2-16-1, Ube, Yamaguchi 755-8611, Japan
[2]Graduate School of Science and Technology for Innovation, Yamaguchi University, Tokiwadai 2-16-1, Ube, Yamaguchi 755-8611, Japan

[3]School of Information Science and Technology, Aichi Prefectural University, 1522-3 Ibaragabasama, Nagakute, Aichi 480-1198, Japan
E-mail: {v003we, wu, m.obayas, mabu}@yamaguchi-u.ac.jp, kobayashi@ist.aichi-pu.ac.jp

Abstract

Hinton's deep auto-encoder (DAE) with multiple restricted Boltzmann machines (RBMs) is trained by the unsupervised learning of RBMs and fine-tuned by the supervised learning with error-backpropagation (BP). Kuremoto et al. proposed a deep belief network (DBN) with RBMs as a time series predictor, and used the same training methods as DAE. Recently, Hirata et al. proposed to fine-tune the DBN with a reinforcement learning (RL) algorithm named "Stochastic Gradient Ascent (SGA)" proposed by Kimura & Kobayashi and showed the priority to the conventional training method by a benchmark time series data CATS. In this paper, DBN with SGA is invested its effectiveness for real time series data. Experiments using atmospheric CO2 concentration, sunspot number, and Darwin sea level pressures were reported.

Keywords: deep learning, restricted Boltzmann machine, stochastic gradient ascent, reinforcement learning, error-backpropagation

1. Introduction

Deep learning (DL) is the novel kernel technique of artificial intelligence (AI) developed rapidly in nowadays. As the training method of artificial neural networks (ANNs), in 2006, DL firstly is introduced by Hinton's deep auto-encoder (DAE) [1], which has multiple stacked restricted Boltzmann machines (RBMs). The learning process of DAE is divided into two phases: firstly, pretraining, which is a kind of unsupervised learning using the gradient of network energy of RBMs, and secondly fine-tuning using the supervised learning: error-backpropagation (BP) [2].

To deal with the adaptive behavior acquisition problem in unknown environment, reinforcement learning (RL), which is a kind of machine learning method adjusting is output by the rewards/punishment from the environment when a learner (system) changed its state by the policy of output, has been studied for decades [3] [4]. Recently, RL is also introduced into deep neural networks [5]-[7]. In [5], a deep Q-network (DQN) is proposed and applied to game (named ATARI) control and reached human level. In [6], a computer software named AlphaGo, using a deep neural network and RL, won the world champion of the game Go. In [7], we adopted a policy gradient RL algorithm [8] [9] into a deep belief net (DBN) proposed by Kuremoto et al. [10]-[13] instead of its fine-tuning method BP. And using a benchmark data CATS which is used by time series forecasting competition with ANNs [14] [15], the DBN with RL showed the highest prediction precision comparing to all conventional methods in the competition and the conventional DBN with BP learning [12] [13].

In this paper, we concentrate to investigate the effectiveness of the DBN with RL for real time series forecasting. Three kinds of real time series data which are weekly average of CO2 concentration in atmosphere at Hawaii, monthly average of sea level pressures at Darwin, the number of sunspot monthly provided by

Aalto University [16] were used in the forecasting experiments, and the prediction precision was compared to the conventional BP learning method. And as the results, DBN with RL showed the higher performance than the conventional DBN with BP in the process of fine-tuning of the network.

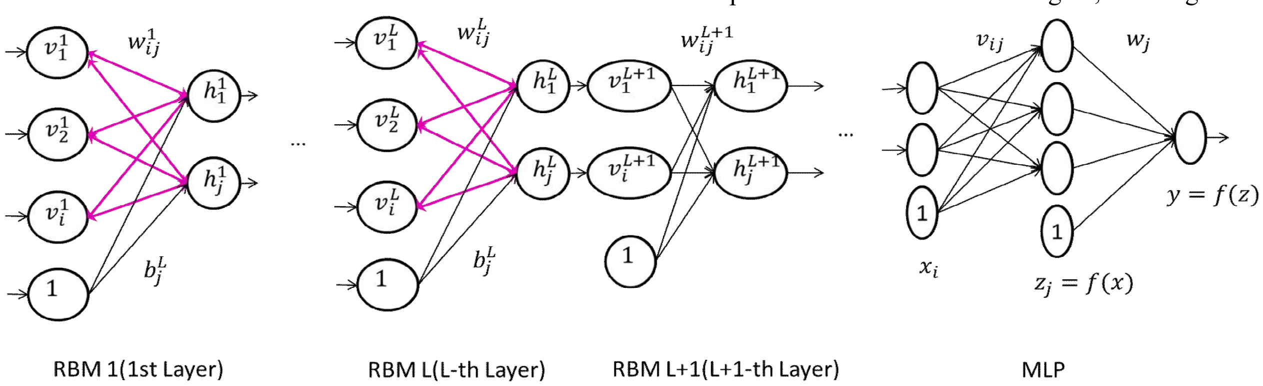

Fig.1. A structure of DBN composed by RBMs and a MLP

2. DBN with BP

In [10] [11], Kuremoto et al. firstly applied Hinton & Slakhutdinov's deep belief net (DBN) with restricted Boltzmann machines (RBMs) to the field of time series forecasting. In [12] and [13], Kuremoto, Hirata, et al. constructed a DBN with RBMs and a multi-layer perceptron (MLP) to improve the previous time series predictor with RBMs. In [7], Hirata et al. adopted a reinforcement learning named "stochastic gradient ascent" (SGA) [8] [9] into DBN instead of the BP learning used in the fine-tuning of the network. In this section, the structure of DBN and learning methods are introduced.

2.1. *DBN with RBMs and MLP*

As a neural predictor model, a DBN composed by multiple RBMs and a MLP is shown in Fig. 1 [7] [12] [13]. The visible layer of RBM 1 (1st Layer) are input with raw data of time series data (omitted in the figure). The hidden layer of RBM L+1 are used as the input layer of the MLP. The output of MLP is with one unit in the case of DBN using BP learning, and it has two units which are parameters of Gaussian distribution function used in the case of SGA learning method [4] [7].

2.2. *BP learning for DBN*

Let E is the mean squared error (MSE) between the output of DBN and the teacher signal, the weight of connections w between layers of RBMs and MLP, and the bias of RBMs b are modified as following.

$$w_{ij}^{L\,new} = w_{ij}^{L\,old} + \alpha \frac{\partial E}{\partial w_{ij}^{L\,old}} = w_{ij}^{L\,old} + \alpha \left(\sum_j \frac{\partial E}{\partial w_{ij}^{L+1\,old}} \cdot w_{ij}^{L+1\,old} \right) \cdot (1 - h_j^L) \cdot v_i^L \quad (1)$$

$$b_j^{L\,new} = b_j^{L\,old} + \alpha \frac{\partial E}{\partial b_j^{L\,old}} = b_j^{L\,old} + \alpha \left(\sum_j \frac{\partial E}{\partial w_{ij}^{L+1\,old}} \cdot w_{ij}^{L+1\,old} \right) \cdot (1 - h_j^L) \quad (2)$$

where a is the learning rate.

2.3. *SGA learning for DBN*

The SGA algorithm and the learning rule for the weight of DBN's layers and parameters of the stochastic policy (Gaussian distribution function) were introduced in [7].

3. Prediction Experiments and Results

We predicted three types of natural phenomenon time series data given by Aalto University [16].

- CO2: Atmospheric CO2 from continuous air samples Weekly averages atmospheric CO2 concentration derived from continuous air samples, Hawaii, 2225 values

- Sea level pressures: Monthly values of the Darwin Sea Level Pressure series, 1882-1998, 1300 values
- Sunspot Number: Monthly averages of sunspot numbers from 1749 through the present, 3078 values

In Fig. 2 to Fig. 4, the one-ahead prediction results of DBN with BP and DBN with SGA were shown. In Table 1, the comparison of forecasting precision (MSE) of these different learning methods for DBN was given. The DBN with SGA showed its priority to the DBN with BP in all cases of real time series data. In Table 2, the number of samples and structures of different DBNs

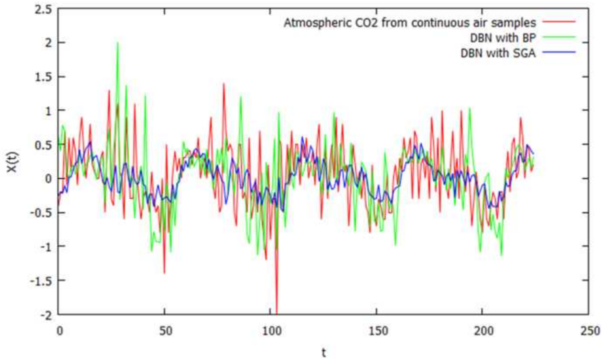

Fig.2. Prediction result of CO2 data

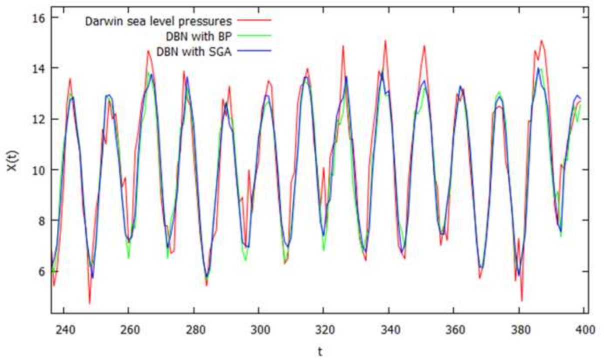

Fig.3. Prediction result of Sea level pressure data

Table.1. Prediction MSE of real time series data [16]

	DBN with BP	**DBN with SGA**
CO2	0.2671	**0.2047**
Sea level pressure	0.9902	**0.9003**
Sun spot number	733.51	**364.05**

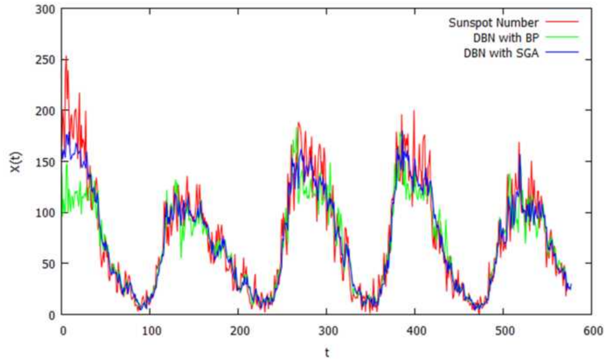

Fig.4. Prediction result of Sun spot number data

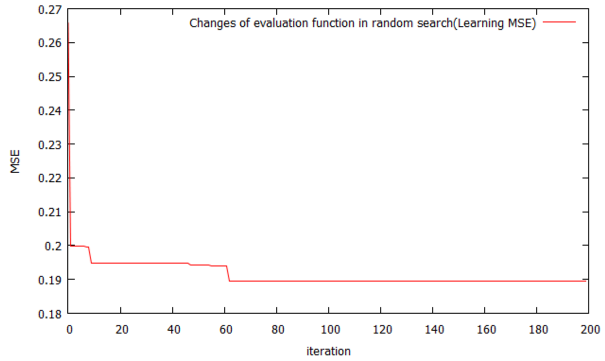

Fig.5. Changes of evaluation function in random search [17] (CO2, DBN with SGA)

were listed. To decide the number of RBMs, and the number of units on different layers of RBMs and MLP, random search (RS) [17] was used in the experiments. As an optimization method, RS used random values of parameter vector spaces to find the lower forecasting error (MSE). The change of evaluation function in the

Table.2. Sizes of time series data and structures of prediction networks

Series	Total size	Testing size	DBN with BP	DBN with SGA
CO2	2225	225	15-17-17-1	20-18-7-2
Sea level pressure	1400	400	16-18-18-1	16-20-8-7-2
Sun spot number	3078	578	20-20-17-18-1	19-19-20-10-2

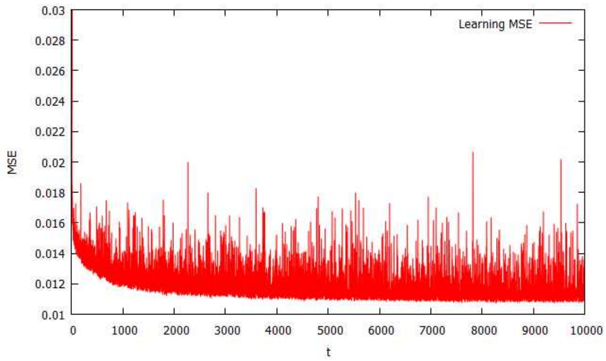

Fig.6. Changes in learning MSE (CO2, DBN with SGA)

case of DBN with SGA for CO2 forecasting is shown in Fig. 5 as a sample. In Fig. 6, the change of MSE in SGA learning process is shown. As a stochastic forecasting method of RL, the vibration of MSE needs to be reduced by tuning learning rates and rewards and we leave it as a future work.

4. Conclusion

In this paper, a reinforcement learning (RL) method "stochastic gradient ascent (SGA)" for fine-tuning of a deep belief net (DBN) with multiple restricted Boltzmann machines (RBMs) and a multi-layer perceptron (MLP) was compared to the conventional method error backpropagation (BP) in the case of real time series forecasting. Different to the supervised learning method which uses learning error exhaustively, RL a reward function which allows a range of errors between the output of the model and the teach signal and it may raise the forecasting precision for the real time series data.

Acknowledgements

This work was supported by JSPS KAKENHI Grant No. 26330254 and No.25330287.

References

1. G.E. Hinton, R.R. Salakhutdinov, Reducing the dimensionality of data with neural networks, Science, Vol.313, 2006, pp. 504-507.
2. D. E. Rumelhart, G. E. Hinton, & R.J. Williams, Learning representation by back-propagating errors, Nature, Vol. 232, No. 9, 1986, pp. 533-536.
3. R.S. Sutton, A.G. Barto: Reinforcement Learning: An Introduction, 1998, The MIT Press
4. T. Kuremoto, M. Obayashi, M. Kobayashi, Neural Forecasting Systems. In Reinforcement Learning, Theory and Applications (ed. C. Weber, M. Elshaw and N. M. Mayer), Chapter 1, pp. 1-20, 2008, INTECH.
5. V. Mnih, *et al.*, Human-level control through deep reinforcement learning, *Nature*, Vol. 518, 2015, pp. 529-533
6. D. Silver, *et al.*, Mastering the game of Go with deep Neural networks and tree search, *Nature*, 529, 2016, pp. 484-489
7. T. Hirata, T. Kuremoto, M. Obayashi, S. Mabu, K. Kobayashi, Deep Belief Network Using Reinforcement Learning and Its Applications to Time Series Forecasting, Neural Information Processing: *23rd International Conference* (ICONIP 2016), Vol.3, Oct. 2016, pp.30-37
8. H. Kimura, S. Kobayashi, Reinforcement learning for continuous action using stochastic gradient ascent, *Proceedings of 5th Intelligent Autonomous Systems*, 1998, pp. 288-295.
9. R.J. Williams: Simple statistical gradient-following for connectionist reinforcement learning, *Machine Learning*, Vol. 8, 1992, pp. 229-256
10. T. Kuremoto, S. Kimura, K. Kobayashi, M. Obayashi, Time series forecasting using restricted Boltzmann machines, *Proc. 8th International Conference on Intelligent Computing* (ICIC 2012), July 2012, pp.17–22.
11. T. Kuremoto, S. Kimura, K. Kobayashi, M. Obayashi, Time series forecasting using a deep belief network with restricted Boltzmann machines, *Neurocomputing*, Vol.137, No.5, Aug. 2014, pp.47–56.
12. T. Kuremoto, T. Hirata, M. Obayashi, S. Mabu, K. Kobayashi, Forecast Chaotic Time Series Data by DBNs, *Proceedings of the 7th International Congress on Image and Signal Processing* (CISP 2014), Oct. 2014, pp. 1304-1309.
13. T. Hirata, T. Kuremoto, M. Obayashi, S. Mabu, Time Series Prediction Using DBN and ARIMA, *International Conference on Computer Application Technologies* (CCATS 2015), Matsue, Japan, Sep. 2015, pp.24-29.
14. A. Lendasse, E. Oja, O. Simula, M. Verleysen, Time Series Prediction Competition: The CATS Benchmark, *Proceedings of International Joint Conference on Neural Networks* (IJCNN'04), 2004, pp1615-1620.
15. A. Lendasse, E. Oja, O. Simula, M. Verleysen, Time Series Prediction Competition: The CATS Benchmark, *Neurocomputing*, Vol. 70, 2007, pp.2325-2329.
16. AML research group, The Aalto University School of Science: http://research.ics.aalto.fi/eiml/datasets.shtml
17. J. Bergstra, Y. Bengio, Random Search for Hyper-Parameter Optimization, *Journal of Machine Learning Research*, Vol. 13, 2012, pp.281-305.

Improvement of Robot's Self-localization by Using Observer View Positional Information

Yo Aizawa, Takuo Suzuki, Kunikazu Kobayashi
Aichi Prefectural University
1522-3 Ibaragasama, Nagakute, Aichi 480-1198, Japan.
Tel::+81-561-64-1111; Fax: +81-561-64-1108
kobayashi@ist.aichi-pu.ac.jp

Abstract

This study aimed to improve the precision of the robot's self-localization in the standard platform league of RoboCup, i.e. a robotic soccer competition. For improving the precision of the self-localization, we suggest a new technique that uses a camera out of the field for assistance. Robots in the field use the unscented particle filter that estimates their position from landmark. When a robot which is equipped with the filter cannot recognize landmarks exactly, particles spread and the precision of the self-localization decreases. Therefore, the overlooking camera out of the field observes each robot's position. When particles spread, the camera out of the field estimates the foot of a robot, and then the robot sprinkles particles on the neighborhood again. In this way, even if a robot cannot recognize landmarks exactly, assists of camera out of the field revise the position of particles and improve the precision.

Keywords: Self-localization, Perspective image, Image processing, Homography, RoboCup

1. Introduction

The RoboCup (Robot Soccer World Cup) project sets a goal that a fully autonomous robot team shall win against the most recent winning team of FIFA World Cup in soccer by 2050.

The RoboCup Soccer Standard Platform League (SPL) is a league that all teams compete with the same standard humanoid robot called NAO developed by Softbank Robotics[1]. The robot operates fully autonomously, that is with no external control, neither by humans nor by computers. In RoboCup Soccer SPL, the robot must process all the calculations on vision processing and decision making using low-end CPU (Intel Atom 1.6GHz). In addition, the robot must devote a lot of computation time to percept a white goal and a mostly white ball in vision processing. Each team has five player robots and one coaching robot that can send instructions at a perspective view from outside the field. An example of the positional relationship between the field and the coaching robot is shown in Fig.1.

Fig. 1. Coaching Robots can observe the almost whole field [1].

In RoboCup Soccer SPL, a self-localization mechanism that estimates its own position and orientation is required. We use an unscented particle filter (UPF)[2] which is currently a mainstream method[3] for self- localization. However, a robot cannot accurately grasp any landmarks, then particles do not converge, so the estimation error of self-localization becomes large.

In addition to the conventional method, by using the coaching robot as the observer, an area where a player is likely to exist is specified. We propose a method to promote convergence of particles by correcting the coordinates of scattering particles based on the information from the coaching robot. From this method, estimation error of the self-location is assumed to be suppressed when the player cannot accurately recognize landmarks.

2. Unscented Particle Filter (UPF)

The UPF is a combination of an unscented Kalman filter (UKF)[4] and a particle filter (PF)[5]. The filter can solve the problem in particle filter which resampling will fail if the new measurements appear in the tail of prior or if the likelihood is too peaked in comparison to the prior[2]. The difference between UPF and PF is whether UPF is used for updating prediction step of PF.

3. Proposed method

When UPF cannot accurately grasp landmarks, particles may not converge. When such a situation occurs, the coaching robot behaves as an observer, assists to estimate the self-localization of the player from the outside, and encourages the convergence of the particles.

3.1. *True perspective image*

At first, the coaching robot gets a perspective image as shown in Fig.2. Then we transform it to a true perspective image using homography transform[6] (see Fig.3). Since the homography transform requires more than four coordinates on an image, the coaching robot will select more than four points out of 17 candidates, i.e. four corners of the field, eight corners of the penalty area, two penalty crosses, two intersections of the center line and the side lines, and a point of the center mark. In Fig.2, we use eight points by indicating red circles.

Fig. 2. A perspective image from a coaching robot.

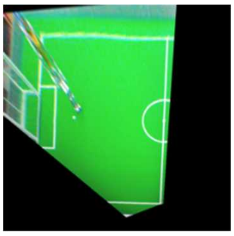

Fig. 3. A true perspective image by homography transform.

3.2. *Estimation of a player's position*

We estimate a straight line with a high possibility that a robot exists. Only the uniform region is extracted from the image after homography transform. Then, the region is denoising by opening processing[7] (see Fig.4). After that, we extract a region of the own team's jersey, it is certain that the player robot will be on the line calculated by simple linear regression analysis (see Fig.5).

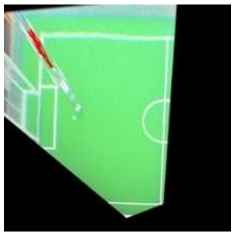

Fig. 4. Extraction of uniform

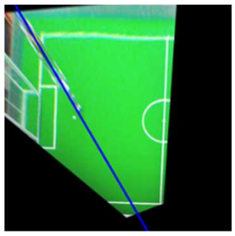

Fig. 5. An estimated line by the simple linear regression analysis.

3.3. *Estimation of a foot position*

Finally, the foot position of the player robot is estimated as the bottom point of non-green regions on the line (Fig.5). We transform the color space of the perspective image into L*a*b* to detect the color of the field. L* stands for lightness and a* and b* are hue and saturation, respectively. The color approaches red as the value of a* becomes high and green as it becomes low, and yellow as the value of b* becomes high and blue as it becomes low. We binarize the image of a* by Otsu's thresholding method. As applying the homography transform to the image, the true perspective image is shown in Fig.6. The estimated foot position is illustrated in Fig.7 as a red dot.

Fig. 6. A binary image of the player robot.

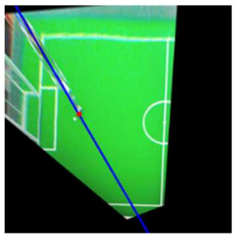

Fig. 7. An estimated foot position (red dot).

3.4. *Determination of resampling position*

Based on the foot position, the locations where particles are scattered are determined. Taking into account the error of the estimated foot position, the positions of particles are determined according to the normal distribution as given by eq. (1).

$$f(x) = \frac{1}{\sqrt{2\pi}\sigma} exp\left(-\frac{(x-\mu)^2}{2\sigma^2}\right), \quad (1)$$

where μ is the mean and σ^2 is the variance. In this paper, the value of μ is defined by the foot position x, and the value of σ is set to 1 / α. The particles are gathered into the foot estimated by increasing the value of α. Based on the above, the positions of particles are indicated by yellow circles in Fig.8.

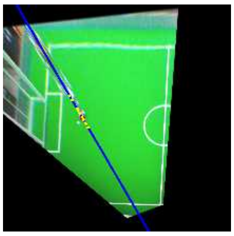

Fig. 8. Resampling Position of Particles

4. Experiment

We verify the accuracy whether the player can assist the self-localization using the image acquired by the coaching robot. Firstly, it is evaluated how the estimated foot position is closer to the true one by comparing the proposed and the conventional methods. Secondly, after correcting the position of the particle by the proposed method, it is verified whether it is close to the true position as compared with the conventional method.
The experiments were conducted using one player under an LED uniform lighting environment using natural light. We use the OpenCV 3.1 library as a tool for image processing. The value of α in the normal distribution in Section 3.4 is empirically set to 6 in order to prevent particles from spreading. The number of particles is 12.

4.1. *Experiment 1 (Verification of the accuracy of the estimated foot position)*

When distributing particles using the proposed method, the accuracy of the estimated foot positionin Section 3.3 is critical the resampling coordinates of the particles is highly baased on the foot position. Therefore, we verify the accuracy of the estimated foot position using the proposed method by measuring the actual foot position. in addition, we compare the estimation error of the self-localization with the conventional method.
In this experiment, we verifies whether an error changes depending on the distance between the coaching and player robots. We then prepared two kinds of routes as shown in Fig.9. The difference of pattern A and B is whether the player robot approaches the coaching robot or not. Experiments were conducted three times each and the errors are averaged.

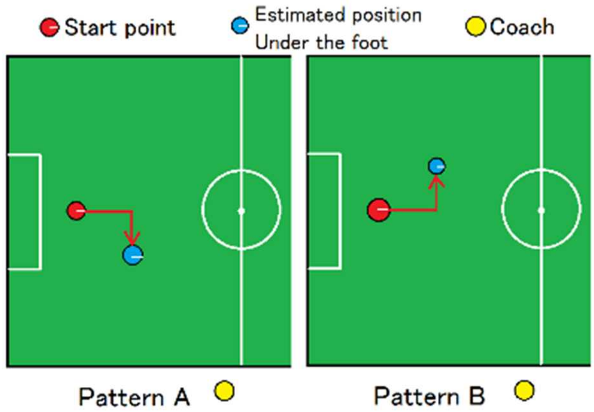

Fig. 9. Two kinds of routes in Experiment 1

4.2. *Result of Experiment 1*

The experimental results in Experiment 1 are shown in Table 1. From Table 1, it is shown that the accuracy of the proposed method is better than that of the conventional method irrespective of pattern A and B. In addition, the improved rate of the accuracy of the estimated foot position is 78%. Therefore, using the estimated foot position, resampling particles is expected to improve the accuracy.

Table 1. Average error of the estimated foot position (Experiment 1)

	Average error [mm] (Improved rate [%])			
Method \ Pattern	Pattern A		Pattern B	
Conventional method	500	(64)	624	(89)
Proposed method	180		71	

4.3. *Experiment 2 (Verification of the accuracy of self-localization after resampling)*

After resampling particles using the proposed method, when the player robot moves again, we verify the accuracy of the self-localization. We also compare the estimation error of the self-localization with the conventional method. As seen in Section 4.1, the player robot moves by two kinds of routes as illustrated in Fig.10. Experiments were carried out three times each and the errors against the true position are averaged to compare the accuracy. When resampling is performed using the proposed method, the direction of the particles is determined according to the normal distribution based on the estimated direction. The normal distribution is

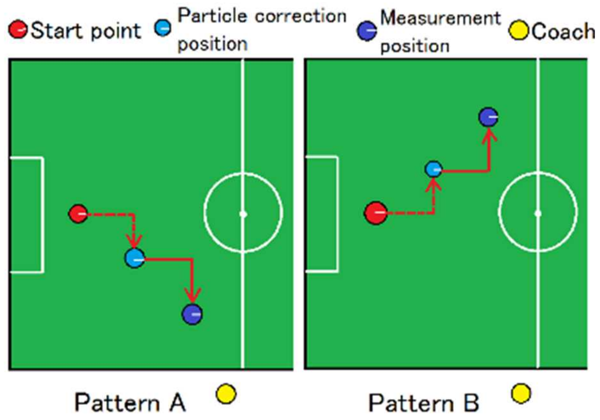

Fig. 10. Two kinds of routes in Experiment 2

given by eq. (1). In self-localization, the direction is corrected by recognizing landmarks. Therefore, the value of μ is set to the previous estimated direction and the value of σ is empirically set to $\pi/8$.

4.4. *Result of Experiment 2*

The results in Experiment 2 are shown in Table 2. From Table 2, it is shown that the proposed method is more accurate than the conventional method irrespective of pattern A and B. In addition, the improved rate of the average accuracy is 64%.

Table 2. Average error of self-localization (Experiment 2)

	Average error [mm] (Improved rate [%])			
Coach \ Pattern	Pattern A		Pattern B	
w/o coach	1,151	(68)	724	(58)
w coach	364		302	

5. Conclusion

In this paper, we have proposed the method for improving the accuracy of the self-localization of UPF used in RoboCup Soccer SPL. In the proposed method, we could correct the position of the particles using the observer (coaching robot) and assist the subject (player robot) who performs self-localization estimation.

As future work, we will assist the estimation of the self-localization for multi-player robots.

Acknowledgements

This work was partly supported by Aichi Prefectural University, Japan.

References

1. RoboCup Technical Committee, *RoboCup Standard Platform League (NAO) Rule Book* (2016).
2. R. van der Merwe, A. Doucet, N. de Freitas, and E. Wan, The Unscented Particle Filter, *Proc. of NIPS* (2000), pp.584-590.
3. T. Röfer, T. Laue, J. Richter-Klug, M. Schünemann, J. Stiensmeier, A. Stolpmann, A. Stöwing, F. Thielke, *B-Human Team Report and Code Release 2015* (2015).
4. S. J. Julier and J. K. Uhlmann, A New Exten- sion of the Kalman Filter to Nonlinear Systems, *Proc. of AeroSense: Proc. of The 11th Int. Symp. On Aerospace/Defence Sensing, Simulation and Controls* (1997), pp.182-193.
5. S. Thrun, W. Burgard, and D. Fox, *Probabilistic Robotics*, The MIT Press (2005).
6. R. Hertley and A. Zisserman, *Multiple View Geometry in computer vision, 2nd Edition,* Cambridge University Press (2003).
7. R. Szeliski, Computer Vision: *Algorithms and Applications*, Springer (2011).

Consideration on the Recognizability of Three-Dimensional Patterns

Chongyang Sun, Makoto Sakamoto, Makoto Nagatomo, Yu-an Zhang, Shinnosuke Yano, Satoshi Ikeda
Faculty of Engineering, University of Miyazaki, 1-1, Gakuen Kibanadai-nishi, Miyazaki-shi, 889-2192
Miyazaki, Japan

Takao Ito, Tsutomu Ito
Institute of Engineering, Hiroshima University, 4-1, Kagamiyama 1-chomeHigashi-Hiroshima, Hiroshima 739-8527
Hiroshima, Japan

Yasuo Uchida
Department of Business Administration, Ube National College of Technology, Tokiwadai Ube, Yamaguchi 755-8555
Yamaguchi, Japan

Tsunehiro Yoshinaga
Department of Computer Science & Electronic Engineering, National Institute of Technology, Tokuyama College
GakuendaiShunan, Yamaguchi 745-8585
Yamaguchi, Japan

Abstract

Due to the advances in computer vision, robotics, and so forth, it has become increasingly apparent that the study of three-dimensional pattern processing should be very important. Thus, the study of three-dimensional automata as the computational model of three-dimensional information processing has been significant. During the past about thirty years, automata on a three-dimensional tape have been obtained. On the other hand, it is well-known that whether or not the pattern on a two- or three-dimensional rectangular tape is connected can be decided by a deterministic one-marker finite automata. As far as we know, however, it is unknown whether a similar result holds for recognition of the connectedness of patterns on three-dimensional arbitrarily shaped tape. In this paper, we deal with the recognizability of three-dimensional patterns, and consider the recognizability of three-dimensional connected tapes by alternating Turing machines and arbitrarily shaped tapes by k marker finite automata.

Keywords: connectedness, finite automaton, marker, pattern, recognizability, three-dimension, Turing machine

1. Introduction

Recently, there have been many interesting investigations on digital geometry [2]. These works form the theoretical foundation of digital image processing. Among them, the problem of connectedness is one of the most interesting topics. For instance, Yamamoto, Morita and Sugata showed that a three-dimensional nondeterministic one-marker automaton can recognize connected tapes. In the case of $L(m)$ space-bounded five-way three-dimensional deterministic Turing machine, they proved that space $m^2\log m$ is necessary and sufficient amount for recognizing connected tapes of size $m \times m \times m$ [3]. Nakamura and Rosenfeld showed that three-dimensional connected tapes are not recognizable by any three-dimensional deterministic or nondeterministic finite automaton. By the way, it is well known that two-dimensional digital pictures have 4- and 8-connectedness, and three-dimensional digital pictures have 6- and 26-connectedness. It is also known that various topological properties can be defined by making use of these connectedness. For example, Nakamura and Aizawa proposed a new topological property of three-dimensional digital pictures — the interlocking component which is a chainlike connectivity. They showed that three-dimensional deterministic one-marker automaton cannot detect interlocking components in a three-dimensional digital picture [3]. Moreover, in [3], Sakamoto, et al. proposed various new three-dimensional automata, and studied several their properties. In general, however, to recognize three-dimensional connectedness seems to be much more difficult than the two-dimensional case, because of intrinsic characteristics of three-dimensional pictures.

In this paper, we consider about recognizability of three-dimensional patterns. First, we deal with the recognizability of three-dimensional connected cubic tapes by three-dimensional alternating automata. Next, we consider whether or not the pattern on a three-dimensional arbitrarily shaped tape is connected can be decided by a deterministic multi-marker finite automaton.

2. Preliminaries

Definition 2.1. Let Σ be a finite set of symbols. A three-dimensional tape over Σ is a three-dimensional rectangular array of elements of Σ. The set of all three-dimensional tapes over Σ is denoted by $\Sigma^{(3)}$. Given a tape $x \in \Sigma^{(3)}$, for each integer j ($1 \le j \le 3$), we let $l_j(x)$ be the length of x along the jth axis. The set of all $x \in \Sigma^{(3)}$ with $l_1(x)=n_1$, $l_2(x)=n_2$, and $l_3(x)=n_3$ is denoted by $\Sigma^{(n_1,n_2,n_3)}$. When $1 \le i_j \le l_j(x)$ for each j ($1 \le j \le 3$), let $x(i_1,i_2,i_3)$ denote the symbol in x with coordinates (i_1,i_2,i_3). Furthermore, we define $x[(i_1,i_2,i_3), (i_1^0,i_2^0,i_3^0)]$, when $1 \le i_j \le i_j^0 \le l_j(x)$ for each integer j ($1 \le j \le 3$), as the three-dimensional input tape y satisfying the following (1) and (2): (1) for each j ($1 \le j \le 3$), $l_j(y) = i_j^0 - i_j + 1$; (2) for each r_1, r_2, r_3 ($1 \le r_1 \le l_1(y)$, $1 \le r_2 \le l_2(y)$, $1 \le r_3 \le l_3(y)$), $y(r_1,r_2,r_3)=x(r_1+i_1-1, r_2+i_2-1, r_3+i_3-1)$. (We call $x[(i_1,i_2,i_3), (i_1^0,i_2^0,i_3^0)]$ the $[(i_1,i_2,i_3), (i_1^0,i_2^0,i_3^0)]$-segment of x.) For each $x \in \Sigma^{(n_1,n_2,n_3)}$ and for each $1 \le i_1 \le n_1$, $1 \le i_2 \le n_2$, $1 \le i_3 \le n_3$, $x[(i_1, 1, 1), (i_1, n_2, n_3)]$, $x[(1, i_2, 1), (n_1, i_2, n_3)]$, $x[(1, 1, i_3), (n_1, n_2, i_3)]$, $x[(i_1, 1, i_3), (i_1, n_2, i_3)]$, and $x[(1, i_2, i_3), (n_1, i_2, i_3)]$ are called the i_1th (2-3) plane of x, the i_2th (1-3) plane of x, the i_3th (1-2) plane of x, the i_1th row on the i_3th (1-2) plane of x, and the i_2th column on the i_3th (1-2) plane of x, are denoted by $x^{(2\text{-}3)}{}_{i_1}$, $x^{(1\text{-}3)}{}_{i_2}$, $x^{(1\text{-}2)}{}_{i_3}$, $x[i_1,*,i_3]$, and $x[*,i_2,i_3]$, respectively[3].

Definition 2.2. A three-dimensional alternating Turing machine (denoted by 3-ATM) is a 10-tuple $M = (Q, q_0, U, E, S, F, \Sigma, \Gamma, \delta)$, where (1) $Q = U \cup E \cup S$ is a finite set of states, (2) $q_0 \in Q$ is the initial state, (3) U is the set of universal states, (4) E is the set of existential states, (5) $F \subseteq Q$ is the set of accepting states, (6) Σ is a finite input alphabet ($\# \notin \Sigma$ is the boundary symbol), (7) Γ is a finite storage tape alphabet containing the special blank symbol B, (8) $\delta \subseteq (Q\times(\Sigma \cup \{\#\})\times\Gamma)\times(Q\times(\Gamma-\{B\})\times\{$east, west, south,north,up,down,no move$\}\times\{$left,right,no move$\})$ is the next move relation. As shown in Fig.2, M has a read-only cubic input tape with boundary symbols #'s ($\# \notin \Sigma$) and one semi-infinite storage tape, initially filled with the blank symbols. M begins in state q_0. A position is assigned to each cell of the input tape and the storage tape, as shown in Fig.1. A step of M consists of reading one symbol from each tape, writing a symbol on the storage tape, moving the input and storage tape heads in specified directions, and entering a new state, according to the next move relation δ [3].

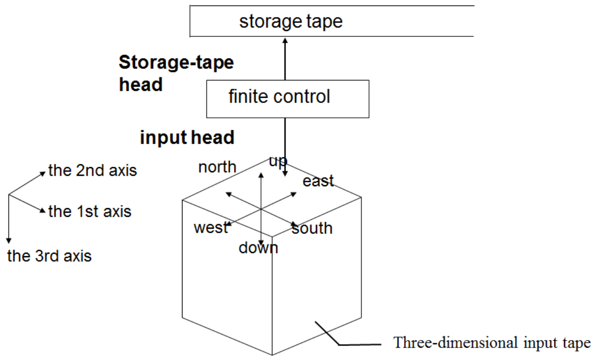

Fig.1:Three-dimensional alternating Turing machine.

Definition 2.3. A three-dimensional k marker finite automaton M(k) is defined by the six-tuple $M = (Q,q_0,F,\Sigma,\{+,-\},\delta)$, where (1) Q is a finite set of states; (2) $q_0 \in Q$ is the initial state; (3) $F \subseteq Q$ is the set of accepting states; (4) Σ is a finite input alphabet ($\# \notin \Sigma$ is the boundary symbol); (5) $\{+,-\}$ is the pair of signs of presence and absence of the marker; and (6) $\delta: (Q\times\{+,-\})\times((\Sigma \cup \{\#\})\times\{+,-\}) \to 2^{(Q\times\{+,-\})\times((\Sigma \cup \{\#\})\times\{+,-\})\times\{\text{east,west,south,north,up,down,no move}\}}$ is the next-movefunction, satisfying the following: For any $q,q_0 \in Q$, any $a,a_0 \in \Sigma$, any $u,u_0,v,v_0 \in \{+,-\}$, and any $d \in \{$east,west,south,north,up,down,no move$\}$, if $((q_0,u_0),(a_0,v_0),d) \in \delta((q,u),(a,v))$ then $a=a_0$, and $(u,v,u_0,v_0) \in \{(+,-,+,-),(+,-,-,+),(-,+,-,+), (-,+,+,-), (-,-,-,-)\}$. We call a pair (q,u) in $Q\times\{+,-\}$ an extended state, representing the situation that M holds or does not hold the marker in the finite control according to the sign $u = +$ or $u = -$, respectively. A pair (a,v) in $\Sigma\times\{+,-\}$ represents an input tape cell on which the marker exists or does not exsit according to the sign $v = +$ or $v = -$, respectively. Therefore, the restrictions on δ above imply the following conditions. (A) When holding the marker, M can put it down or keep on holding. (B) When not holding the marker, and (i) if the marker exists on the current cell, M can pick it up or leave it there, or (ii) if the marker does not exist on the current cell, M cannot create a new marker any more (see Fig.2) [3].

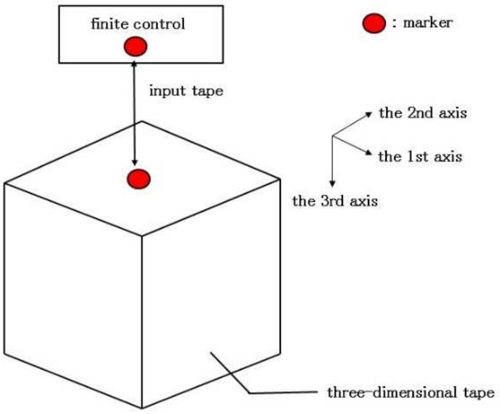

Fig.2:Three-dimensional k marker finite automaton.

3. Recognizability of Connected Tapes by Three-Dimensional Alternating Turing machines

Definition 3.1. Let x be in {0,1}(3). A maximal subset, P of N3 satisfying the following conditions is called a 1-component of x. (1)For any (i1, i2, i3)∈P, we have 1≤i1 ≤l1(x), 1≤i2 ≤l2(x),1≤i3 ≤l3(x), and x(i1,i2,i3)=1. (2)For any (i1, i2, i3), (i0 1, i0 2, i0 3)∈P, there exists a sequence (i1,0, i2,0, i3,0), (i1,1, i2,1, i3,1),···, (i1,n, i2,n, i3,n) of elements in P such that (i1,0, i2,0, i3,0) = (i1, i2, i3), (i1,n, i2,n, i3,n) = (i0 1, i0 2, i0 3), and|i1,j −i1,j−1|+|i2,j −i2,j−1|+|i3,j −i3,j−1|≤1 (1≤j ≤ n). A tape x ∈{0,1}3 is called connected if there exists exactly one 1-compnent of x. We denote the set of all the cubic connected tapes by Tc. It is shown in [3] that a 3-ATM can accept Tc. From this fact and from the fact *L*[FV 3-AFA] ⊇*L*[3-AFA] by using a technique similar to that in [15], the following theorem holds. (3-AFA means 3-ATM without the storage tape and the storage-tape head, FV3-AFA means 3-AFA which cannot move up.)

Theorem 3.1. Tc ∈*L*[FV 3-AFA]. It is shown in [3] that log*m* space is necessary and sufficient for FV 3-ATM's to accept Tc. We below show the necessary and sufficient space for FV 3-SUTM's to accept ¯Tc (=the complement of Tc).

Theorem 3.2. m^2 space is necessary and sufficient for FV 3-ATM's to accept ¯Tc.

Proof: (The proof of sufficiency) It is shown in [3] that Tc is accepted by a deterministic one-way parallel/sequential array acceptor (DOWPS), and it is shown that *L*[DOWPS] = *L*[TR2-DTM(m)] (TR2-DTM(m) means m space-bounded three-way two-dimensional deterministic Turing machine). From these facts and the fact that *L*[TR2-DTM(m)] is closed under complementation, it follows that ¯ Tc is in *L*[TR2DTM(m)], and thus in *L*[TR2-SUTM(m)]. (TR2-SUTM(m) means m space-bounded three-way two-dimensional synchronized alternating Turing machine with only universal states). By applying the same idea of such a two-dimensional case, we can easily get the fact that ¯ Tc is in *L*[FV 3-SUTM(m2)]. (The proof of necessity) Suppose that there is an FV 3-SUTM(*L*(m)) M accepting ¯Tc, where *L*(m) = o(m^2). We assume without loss of generality that M enters an accepting state only on the bottom boundary. Let T0 c ={x ∈ {0,1}(4m+1,4m+1,4m+1) |m≥1 & ∀i1(1≤i1 ≤m + 1)∀ i2(1≤i2 ≤2m + 1) [x [(2i2 −1, 1, 2i1 −1), (2i1 −1, 4m−2i1 + 3, 2i1 −1)], x[(2i2 −1, 1, 4m−2i1 + 3), (2i2 −1, 4m−2i1 + 3, 4m−2i1 + 3)]}, x[(2i1 −1, 4m−2i1 + 3, 2i1 −1), (2i2 −1, 4m−2i1 + 3, 4m−2i1 + 3)]∈{1}(3)] &∀i2(1≤i2 ≤2m) [x [(2i2, 1, 2m + 1), (2i2, 2m + 1, 2m + 1)]∈ {1}(3)] &∀i1(1≤i1 ≤2m)∀i2(1≤i2 ≤2m + 1) [x(2i2 −1, 1, 2i1) = x(2i2 −1,1,4m−2i1 + 2)] & (the other part of x consists of 0's)}, where we define ¯0 = 1 and ¯1 = 0. 4).Clearly T0 c ⊆ Tc. Let s and t be the numbers of states (of the finite control) and storage tape symbols of M, respectively. For each m(m≥1), let V(m) ={x∈T0 c |l1(x) = l2(x) = l3(x) = 4m+1}. For each x in V(m), let S(x) and C(x) be sets of configurations of M defined as follows. S(x) = {((i1, i2, 2m + 1), (q, α, k)) | there exists a computation path IM(x) `* M (x, ((i1, i2, 2m), (q0, α0, k0)))`M (x, ((i1, i2, 2m + 1), (q, α, k))) of M on x (that is, (x, ((i1, i2, 2m+1), (q, α, k))) is an ID of M just after the point where the input head left the (2m+1)th plane of x)}, C(x) ={{ρ1,ρ2}|ρ1 and ρ2 are configurations in S(x) such that (i)in case of ρ1 = ρ2, there exists a sequential computation of M which starts with ID(x,ρ1) and either terminates in a rejecting ID, or enters an infinite loop, and (ii)in case of ρ1 ≠ ρ2, there exist two sequential computations of M which start with ID's(x, ρ1) and (x, ρ2), respectively, and terminate in sync ID's with different sync elements}. (Note that, for each x in V(m), C(x) is not empty, since x is not in ¯ Tc, and so not accepted by M.) Then the following proposition must hold.

Proposition 3.1. For any two different tapes x, y∈V(m), C(x)∩C(y)= ϕ.

[**Proof:** For otherwise, suppose that x6= y(x, y ∈ V(m)), C(x)∩C(y)6= ϕ, and {ρ1, ρ2} ∈C(x)∩ C(y). Let z (with l1(x)=l2(x)=l3(x)=4m + 1) be the tape such that (i)z [(1, 1, 1), (4m + 1, 4m + 1, 2m + 1)] = x[(1,1,1), (4m + 1, 4m + 1, 2m + 1)], and (ii)z [(1, 1, 2m + 2), (4m + 1, 4m + 1, 4m + 1)] = y[(1, 1, 2m + 2), (4m + 1, 4m + 1,4m + 1)]. Since {ρ1,ρ2}∈ C(x), there exist computation paths I_M(z) ⊢* M (z,ρ1) and IM(z) ⊢* M (z,ρ2). Since{ρ1,ρ2}∈C(y), in case of ρ1=ρ2, there exists a sequential computation of M which starts with the ID (z,ρ1) and either terminates in a rejecting ID, or enters an infinite loop, and in case of ρ1 6= ρ2, there exist two sequential computations of M which start with ID's (z, ρ1) and (z, ρ2), respectively, and terminate in sync ID's with different sync elements. This means that z is not accepted by M. This contradicts the fact, that z is in $^{-}$Tc = T(M). □]

Proof of Theorem 3.2(continued): Let p(m) denote the number of pairs of possible configurations of M just after the point where the input head left the (2m+1)th planes of tapes in V(m). Then p(m) $={}_{K}C_{2}$+ K where K = s(4m + 3)^2 L(4m + 1)t$^{L(4m+1)}$. On the other hand, |V(m)| = 2m(2m+1). Since L(m) = o(m), we have|V(m)|≥ p(m) for large m. Therefore, it follows that for large m there must be two different tapes x, y in V(m) such that C(x) ∩ C(y) $\neq \phi$. This contradicts Proposition 6.1 and completes the proof of necessity. □

4. Recognizability of Three-Dimensional Arbitrarily Shaped Tapes by k Marker Finite Automata

Let Σ(3) be a set of points in the three-dimensional Euclidean space with integer coordinates. Each point in Σ(3) is called a vertex, Each unit-length segment connecting two vertices is called an edge. Each region of unit area enclosed by twelve edges is called a voxel. Each voxel can have an input symbol '0' or '1', or a boundary symbol '#'. A voxel is called 0-voxel (1-voxel, or #-voxel) if it has symbol 0 (1, or #). Two-voxels are 6-adjacent (or 27-adjacent) if they share a common edge (or a common vertex) [3]. A 6-adjacent (or 27-adjacent) path is a sequence of voxels c(1),c(2),...,c(i) such that for each 1 ≤ j ≤ i−1, c(j) and c(j + 1) are 6-adjacent (or 27-adjacent). A three-dimensional arbitrarily shaped pathwise-connected tape (p−tape) T is a set of 0, 1-voxels surrounded by #-voxels, where any two 0,1-voxels in T are connected by a 6-adjacent path with only 0,1-voxels in T. (Note that T can contain some 'holes' in its inside.) the pattern P on a p-tape T is the set of all 1voxels that appear there. For the pattern P on a p-tape, a 1-component C is any maximal set of 1-voxels such that any 1-voxels in C are connected by a 6-adjacent path with only 1-voxels in C. A pattern P is connected if and only if any two 1-voxels are connected by a 6-adjacent path with only 1-voxels in P. That is, P is connected if and only if there exists only one 1-component. A k-marker finite automaton M(k) consists of a finite control with a read-only input head and k (labelled) markers operating on a p-tape T. M(k) is started on a 0,1-voxel in its start state with carrying its markers . The markers can be placed on or collected back to the finite control from only the voxel the input head is currently scanning. In each step, M(k) can change its internal state, place a marker 'carried' by the finite control (or collect back a marker (if it exists) to the finite control) on (or from) the voxel the input head is currently scanning, and move the input head to a 6-adjacent cell, according to the current state, the symbol and the presence of marker on the voxel currently scanned by the input head. M(k) is called deterministic if its next-move function is deterministic, otherwise it is called nondeterministic. We assume that M(k) can visit any #-voxel which is 6-adjacent to some 0,1-voxel in T, but can never fall off the tape T beyond these #-cells.

By using the same technique as in the proof of Theorem 3.1 in [1], we get the result.

Theorem 4.1. whether or not the pattern on a p-tape is connected can be decided by a deterministic three marker finite automaton.

It is shown in [1] that there is no deterministic one marker finite automaton which is able to search all mazes (i.e., p-tapes). Moreover, it is shown in [3] that the set of all three-dimensional connected tapes is not recognizable by any three-dimensional nondeterministic multi-inkdot finite automaton (an inkdot machine is a conventional machine capable of dropping an inkdot on a given input tape for a landmark, but unable to further pick it up[3]). This result means that whether or not the pattern on a p-tape is connected cannot be decided by any deterministic one marker finite automaton.

5. Conclusion

In this paper, we considered about recognizability of three-dimensional patterns by some three-dimensional automata. It is an open problem whether the set of all the three-dimensional connected tapes is not accepted by any three-dimensional nondeterministic Turing machine with spaces of size smaller than log*m*, and by any three-dimensional alternating one marker finite automaton with only universal states.

References

[1] M.Blum and C.Hewitt, Automata on a two-dimensional tape, in *IEEE Symposium on Switching and Automata Theory*:155-160 (1967).
[2] A.Rosenfeld, Three-dimensional digital topology, *Information and Control* 50:119-127 (1979).
[3] M.Sakamoto, *Three-Dimensional Alternating Turing Machines*, Ph.D. Thesis, Yamaguchi University (1999).

Four-Dimensional Homogeneous Systolic Pyramid Automata

Makoto Nagatomo, Makoto Sakamoto, Chongyang Sun, Shinnosuke Yano, Satoshi Ikeda
Faculty of Engineering, University of Miyazaki, 1-1, Gakuen Kibanadai-nishi, Miyazaki-shi, 889-2192 Miyazaki, Japan

Takao Ito, Tsutomu Ito
Institute of Engineering, Hiroshima University, 4-1, Kagamiyama 1-chomeHigashi-Hiroshima, Hiroshima 739-8527 Hiroshima, Japan

Yasuo Uchida
Department of Business Administration, Ube National College of Technology, Tokiwadai Ube, Yamaguchi 755-8555 Yamaguchi, Japan

Tsunehiro Yoshinaga
Department of Computer Science & Electronic Engineering, National Institute of Technology, Tokuyama College GakuendaiShunan, Yamaguchi 745-8585 Yamaguchi, Japan

Abstract

Cellular automaton is famous as a kind of the parallel automaton. Cellular automata were investigated not only in the viewpoint of formal language theory, but also in the viewpoint of pattern recognition. Cellular automata can be classified into some types. A systolic pyramid automata is also one parallel model of various cellular automata. A homogeneous systolic pyramid automaton with four-dimensional layers (4-*HSPA*) is a pyramid stack of four-dimensional arrays of cells in which the bottom four-dimensional layer (level 0) has size an ($a \geq 1$), the next lowest 4(a-1), and so forth, the (a-1)st four-dimensional layer (level (a-1)) consisting of a single cell, called the root. Each cell means an identical finite-state machine. The input is accepted if and only if the root cell ever enters an accepting state. A 4-*HSPA* is said to be a real-time 4-*HSPA* if for every four-dimensional tape of size 4a ($a \geq 1$) it accepts the four-dimensional tape in time a-1. Moreover, a 1- way four-dimensional cellular automaton (1-4*CA*) can be considered as a natural extension of the 1-way two- dimensional cellular automaton to four-dimension. The initial configuration is accepted if the last special cell reaches a final state. A 1-4*CA* is said to be a real- time 1-4*CA* if when started with four-dimensional array of cells in nonquiescent state, the special cell reaches a final state. In this paper, we propose a homogeneous systolic automaton with four-dimensional layers (4-*HSPA*), and investigate some properties of real-time 4-*HSPA*. Specifically, we first investigate a relationship between the accepting powers of real-time 4-*HSPA*'s and real-time 1-4*CA*'s. We next show the recognizability of four-dimensional connected tapes by real-time 4-*HSPA*'s

Keywords: cellular automaton, diameter, finite automaton, four-dimension, parallelism, pattern recognition

1. Introduction

In recent years, due to the advances in many application areas such as dynamic image processing, computer animation, VR(virtual reality), AR (augmented reality), and so on, the study of four-dimensional pattern processing has been of crucial importance. And the question of whether processing four-dimensional digital patterns is much more difficult than three-dimensional ones is of great interest from the theoretical and practical standpoints. Thus, the study of four-dimensional automata as a computational model of four-dimensional pattern processing has been meaningful[4-23]. On the other hand, cellular automata were investigated not only in the viewpoint of formal language theory, but also in the viewpoint of pattern recognition. Cellular automata can be classified into some types [2]. A systolic pyramid automaton is also one parallel model of various cellular automata. In this paper, we propose a homogeneous systolic pyramid automaton with four-dimensional layers (4-*HSPA*) as a new four-dimensional parallel computational model, and investigate some properties of real-time 4-*HSPA*.

Let Σ be a finite set of symbols. A four-dimensional tape over Σ is a four-dimensional rectangular array of elements of Σ. The set of all four-dimensional tapes over $\sum$ is denoted by $\Sigma^{(4)}$. Given a tape $x \in \Sigma^{(4)}$, for each integer j ($1 \le j \le 4$), we let $l_j(x)$ be the length of x along the jth axis. The set of all $x \in \Sigma^{(4)}$ with $l_1(x) = n_1$, $l_2(x) = n_2$, $l_3(x) = n_3$, and $l_4(x) = n_4$ is denoted by $\Sigma^{(n_1,n_2,n_3,n_4)}$. When $1 \le i_j \le l_j(x)$ for each $j(1 \le j \le 4)$, let $x(i_1, i_2, i_3, i_4)$ denote the symbol in x with coordinates (i_1, i_2, i_3, i_4). Furthermore, we define

$$x\,[(i_1, i_2, i_3, i_4), (i'_1, i'_2, i'_3, i'_4)],$$

when $1 \le i_j \le i'_j \le l_j(x)$ for each integer $j(1 \le j \le 4)$, as the four-dimensional input tape y satisfying the following conditions :

(i)for each $j(1 \le j \le 4)$, $l_j(y) = i_j - i_j + 1$;

(ii)for each r_1, r_2, r_3, r_4 ($1 \le r_1 \le l_1(y)$, $1 \le r_2 \le l_2(y)$, $1 \le r_3 \le l_3(y)$, $1 \le r_4 \le l_4(y)$), $y(r_1, r_2, r_3, r_4) = x(r_1 + i_1 - 1, r_2 + i_2 - 1, r_3 + i_3 - 1, r_4 + i_4 - 1)$. (We call $x[(i_1, i_2, i_3, i_4), (i'_1, i'_2, i'_3, i'_4)]$ the $[(i_1, i_2, i_3, i_4), (i'_1, i'_2, i'_3, i'_4)]$-segment of x.)

For each $x \in \Sigma^{(n_1,n_2,n_3,n_4)}$ and for each $1 \le i_1 \le n_1$, $1 \le i_2 \le n_2$, $1 \le i_3 \le n_3$, $1 \le i_4 \le n_4$, $x[(i_1, 1, 1, 1), (i_1, n_2, n_3, n_4)]$, $x[(1, i_2, 1, 1), (n_1, n_2, n_3, n_4)]$, and $x[(1, 1, i_3, 1), (n_1, n_2, n_3, n_4)]$ are called the i_1th (2-3) plane, the i_2th (1-3) plane, and the i_3th (1-2) plane of each time of x, and are denoted by $x[i_1, *, *, *]$, $x[*, i_2, *, *]$, and $x[*, *, i_3, *]$, respectively. $x[*, *, *, i_4]$ also has analogous meaning.

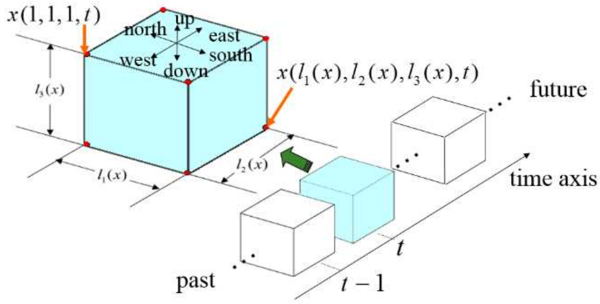

Fig.1 : Four-dimensional input tape.

A four-dimensional homogeneous systolic pyramid automaton (4-*HSPA*) is a pyramidal stack of four-dimensional arrays of cells in which the bottom four-dimensional layer (level 0) has size $4a$ ($a \ge 1$), the next lowest $4(a - 1)$, and so forth, the $(a-1)$st four-dimensional layer (level $(a - 1)$) consisting of a single cell, called the root . Each cell means an identical finite-state machine, $M = (Q, \Sigma, \delta, \#, F)$, where Q is a finite set of states, $\Sigma \subseteq Q$ is a finite set of input states, $\# \in Q-\Sigma$ is the *quiescent state*, $F \subseteq Q$ is the set of *accepting states*, and δ: $Q^{17} \rightarrow Q$ is the *state transition function*, mapping the current states of M and its 16 son cells in a $2 \times 2 \times 2 \times 2$ block on the four-dimensional layer below into M's next state. The input is accepted if and only if the root cell ever enters an accepting state. A 4-*HSPA* is said to be a real-time 4-*HSPA* if for every four-dimensional tape of size $4a$ ($a \ge 1$) it accepts the four-dimensional tape in time $a - 1$. By $\pounds^R$[4-*HSPA*] we denote the class of the sets of all the four-dimensional tapes accepted by a real-time 4-*HSPA*[1].

A 1-way four-dimensional cellular automaton (1-4CA) can be considered as a natural extension of the 1-way two-dimensional cellular automaton to four dimensions [3]. The initial configuration of the cellular automaton is taken to be an $l1(x) \times l2(x) \times l3(x) \times l4(x)$ array of cells in the nonquiescent state. The initial configuration is accepted if the last special cell reaches a final state.

A 1-4CA is said to be a real-time 1-4CA if when started with an $l1(x) \times l2(x) \times l3(x) \times l4(x)$ array of cells in the nonquiescent state, the special cell reaches a final state in time $l1(x) + l2(x) + l3(x) \times l4(x) - 1$. By £R[1-4CA] we denote the class of the sets of all the four-dimensional tapes accepted by a real-time 1-4CA [3].

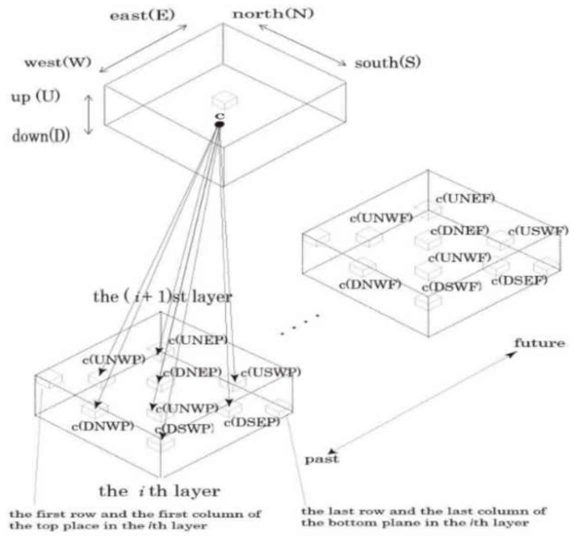

Fig.2 : Four-dimensional homogeneous systolic pyramid automaton.

2. Main Results

We mainly investigate a relationship between the accepting powers of real-time 4-*HSPA*'s and real-time 1-4*CA*'s. The following theorem implies that real-time 4-*HSPA*'s are less powerful than real-time 1-4*CA*'s.

Theorem 2.1. $£^R[4\text{-}HSPA] \subsetneq £^R[1\text{-}4CA]$.

Proof : Let $V = \{ x \in \{0,1\}^{(4)} \mid l_1(x) = l_2(x) = l_3(x)= l_4(x) \& [\forall i_1, \forall i_2, \forall i_3, \forall i_4 \ (1 \le i_1 \le l_1(x), 1 \le i_2 \le l_2(x), 1 \le i_3 \le l_3(x), 1 \le i_4 \le l_4(x))[x(i_1, i_2, i_3, 1) = x(i_1, i_2, i_3, l_{4(x)})]]\}$.

It is easily shown that $V \in £^R[1\text{-}4CA]$. Below, we show that $V \notin £^R[4\text{-}HSPA]$. Suppose that there exists a real-time 4-*HSPA* accepting V. For each $t \ge 4$, let

$W(n) = \{ x \in \{0,1\}^{(4)} \mid l_1(x) = l_2(x) = l_3(x) = l_4(x) \ \& \ x[(1, 1, 1, 2), (t, t, t,t\text{-}1)] \in \{0\}^{(4)}\}$.

Sixteen sons of the root cell $A(t-1,1,1,1,1)$ of M $A_{(t-2,1,1,2,1)}$, $A_{(t-2,1,2,2,1)}$, $A_{(t-2,2,1,2,1)}$, $A_{(t-2,2,2,2,1)}$, $A_{(t-2,1,1,3,1)}$, $A_{(t-2,1,2,3,1)}$, $A_{(t-2,2,1,3,1)}$, $A_{(t-2,2,2,3,1)}$, $A_{(t-2,1,1,2,2)}$, $A_{(t-2,1,2,2,2)}$, $A_{(t-2,2,1,2,2)}$, $A_{(t-2,2,2,2,2)}$, $A_{(t-2,1,1,3,2)}$, $A_{(t-2,1,2,3,2)}$, $A_{(t-2,2,1,3,2)}$, $A_{(t-2,2,2,3,2)}$ are denoted by $C^{(UNWP)}$, $C^{(USWP)}$, $C^{(USEP)}$, $C^{(UNEP)}$, $C^{(DNWP)}$, $C^{(DSWP)}$, $C^{(DSEP)}$, $C^{(DNEP)}$, $C^{(UNWF)}$, $C^{(USWF)}$, $C^{(USEF)}$, $C^{(UNEF)}$, $C^{(DNWF)}$, $C^{(DSWF)}$, $C^{(DSEF)}$, $C^{(DNEF)}$, respectively. For each x in $W(n)$, $x(UNWP)$, $x(USWP)$, $x(USEP)$, $x(UNEP)$, $x(DNWP)$, x(USWP), $x(USEP)$, $x(UNEP)$, $x(UNWF)$, $x(USWF)$, $x(USEF)$, $x(UNEF)$, $x(DNWF)$, x(USWF), $x(USEF)$, $x(UNEF)$ are the states of $C^{(UNWP)}$, $C^{(USWP)}$, $C^{(USEP)}$, $C^{(UNEP)}$, $C^{(DNWP)}$, $C^{(DSWP)}$, $C^{(DSEP)}$, $C^{(DNEP)}$, $C^{(UNWF)}$, $C^{(USWF)}$, $C^{(USEF)}$, $C^{(UNEF)}$, $C^{(DNWF)}$, $C^{(DSWF)}$, $C^{(DSEF)}$, $C^{(DNEF)}$, at time t-2, respectively. Let $\sigma(x) = (x(UNWP), x(USWP), x(USEP), x(UNEP), x(DNWP), x(\text{USWP}), x(USEP), x(UNEP))$, $\gamma(x)=(x(UNWF), x(USWF), x(USEF), x(UNEF), x(DNWF), x(\text{USWF}), x(USEF), x(UNEF))$, and $\rho(x) = (x(UNWP), x(USWP), x(USEP), x(UNEP), x(DNWP), x(\text{USWP}), x(USEP), x(UNEP), x(UNWF), x(USWF), x(USEF), x(UNEF), x(DNWF), x(\text{USWF}), x(USEF), x(UNEF))$. Then, the following two propositions must hold.

Proposition 2.1. (i) *For any two tapes x, y* $\in W(n)$ *whose* 1*st cubes are same*, $\sigma(x) = \sigma(y)$. (ii) *For any two tapes x, y* $\in W(n)$ *whose nth cubes are same*, $\gamma(x) = \gamma(y)$.

[**Proof :** From the mechanism of each cell, it is easily seen that the states of $C^{(UNWP)}$, $C^{(USWP)}$, $C^{(USEP)}$, $C^{(UNEP)}$, $C^{(DNWP)}$, $C^{(DSWP)}$, $C^{(DSEP)}$, $C^{(DNEP)}$ are not influenced by the information of 1st cube. From this fact, we have (i). The proof of (ii) is the same as that of (i). □]

Propositon 2.2. *For any two tapes x, y* $\in W(t)$ *whose* 1*st cube are different*, $\sigma(x) \ne \sigma(y)$.

[**Proof :** Suppose to the contrary that $\sigma(x) = \sigma(y)$. We consider two tapes $x', y' \in W(t)$ satisfying the following :
(i) 1st cube of x and nth cube of x are equal to 1st cube of x', respectively
(ii) 1st cube of y' is equal to 1st cube of y, and nth cube of y' is equal to 1st cube of x.

As is easily seen, $x' \in V$ and so x' is accepted by M. On the other hand, from Proposition 2.1(ii), $\gamma(x') = \gamma(y')$. From Proposition 2.1(i), $\sigma(x) = \sigma(x')$, $\sigma(y) = \sigma(y')$. It follows that y' must be also accepted by M. This contradicts the fact that y' is not in V . □]

Proof of Theorem 2.1 (*continued*) : Let $p(t)$ be the number of tapes in $W(t)$ whose 1st cubes are different, and let $Q(t) = \{ \sigma(x) \mid x \in W(t)\}$, where k is the number of states of each cell of M. Then, $p(t) = 2^{t^2}$, and $Q(t) \le k^4$. It follows that $p(n) > Q(t)$ for large t. Therefore, it follows that for large t, there must be two tapes x,y in $W(t)$ such that their 1st cubes are different and $\sigma(x) = \sigma(y)$. This contradicts Proposition 2.2, so we can conclude that $V \notin £^R[4\text{-}HSPA]$. In the case of four-dimension, we can show that $V \notin £^R[4\text{-}HSPA]$ by using the same technique. This completes the proof of Theorem 2.1. □

We next show the recognizability of four-dimensional connected tapes by real-time 4-*HSPA*'s by using the same technique of Ref.[3]. Let x in $\{0,1\}^{(4)}$. A maximal subset P of $\boldsymbol{N}^4$ satisfying the following conditions is called a 1-*component* of x.

(i)For any $(i_1, i_2, i_3, i_4 \in P$, we have $1 \leq i_1 \leq l_1(x)$, $1 \leq i_2 \leq l_2(x)$, $1 \leq i_3 \leq l_3(x)$, $1 \leq i_4 \leq l_4(x)$, and $x(i_1, i_2, i_3, i_4) = 1$.
(ii) For any (i_1, i_2, i_3, i_4), $(i_1', i_2', i_3', i_4') \in P$, there exists a sequence $(i_{1,0}, i_{2,0}, i_{3,0}, i_{4,0}), (i_{1,1}, i_{2,1}, i_{3,1}, i_{4,1}), \ldots, (i_{1,4}, i_{2,4}, i_{3,4}, i_{4,4})$ of elements in P such that $(i_{1,0}, i_{2,0}, i_{3,0}, i_{4,0}) = (i_1, i_2, i_3, i_4)$, $(i_{1,4}, i_{2,4}, i_{3,4}, i_{4,4}) = (i'_1, i'_2, i'_3, i'_4)$, and $|i_{1,j} - i_{1,j-1}| + |i_{2,j} - i_{2,j-1}| + |i_{3,j} - i_{3,j-1}| + |i_{4,j} - i_{4,j-1}| \leq 1 (1 \leq j \leq 4)$. A tape $x \in \{0, 1\}^{(4)}$ is called *connected* if there exists exactly one 1- component of x.

Let Tc be the set of all the four-dimensional connected tapes. Then, we have

Theorem 2.2. $Tc \notin \pounds^R[4\text{-}HSPA]$.

3. Conclusion

The technique of AR (augmented reality) or VR(virtual reality) progresses like the Pokemon GO and the Virtual Cinema in the world. The virtual technique will spread steadily among our societies in future. Thus, we think that the study of four-dimensional automata is very meaningful as a computational model of four-dimensional pattern processing. In this paper, we proposed a homogeneous systolic pyramid automaton with four-dimensional layers, and investigated a relationship between the accepting powers of homogeneous systolic pyramid automaton with four-dimensional layers(4-*HSPA*) and one-way four-dimensional cellular automata (1-4*CA*) in real time, and showed that real-time 4-*HSPA*'s are less powerful than real time 1-4*CA*'s.

It will be interesting to investigate about an alternating version or synchronized alternating version of homogeneous systolic pyramid automaton with four-dimensional layers. Moreover, we think that there are many interesting open problems for digital geometry. Among them, the problem of connectedness, especially topological component is one of the most interesting topics[17].

Finally, we would like to hope that some unsolved problems concerning this paper will be explicated in the near future.

References

1. K.Culik II, J.Gruska and Salomaa, Sytolic trellis automata, Part I, *International Journal of Computer Mathmatics,* (1991), 55:pp.99-121.
2. C. Iwamoto, K.Inoue, and I.Takanami, Some Properties of Homogeneous Pyramid Automata, *The IEICE Transactions on Information and Systems* (*Japanese Edition*), (1990), J73-D-I(9) : 778-780.
3. C. Iwamoto, K. Inoue, and I. Takanami, Some Properties of Homogeneous Pyramid Automata, *The IEICE Transactions on Information and Systems* (*Japanese Edition*), (1990), J73-D-I(9) : 778- 780.
4. K. Krithivasan and M. Mahajan, Systolic pyramid automata, cellular automata and array languages, *International Journal of Pattern Recognition and Artificial Intelligence*, (1989), 3(3 4):405-433.
5. M.Sakamoto, Three-Dimensional Alternating Turing Machines, Ph.D. *Thesis, Yamaguchi University*, (1999).
6. M.Sakamoto, H.Okabe, and K.Inoue, Some properties of four-dimansional finite automata, *in* 2002 *Chugoku − Section Joint Convention Record of Insistes of Electrical and Information Engineerings, Japan*, (2002), p.351.
7. M.Sakamoto, S.Nagami, K.Kono, A relationship between the accepting powers of three- dimentional layers, *Trans. of SCI*(*Japan*), Vol.17, No.10, (2004), pp.451-458.
8. M.Sakamoto, H.Okabe, S.Nagami, S.Taniguchi, T.Maki, Y.Nakama, M.Saito, M.Kono, and K.Inoue, A note on four-dimensional finite au- tomata, *WSEAS Transactions on Computers*, Issue 5,Vol.3, (2004), pp.1651-1656.
9. M.Sakamoto, T.Ito, N.Tomozoe, and H.Furutani, Asurvey of three-dimensional automata, *The papers of Technical Meeting on Information Systems, IEE, Japan*, IS-07-12, (2007), pp.11-17.
10. M.Sakamoto, T.Ito, H.Furutani, and M.Kono, Some accepting powers of three-dimensional parallel Turning machines, *in 1st European Workshop on Artificial Life and Robotics*, Vienna, Austria, (2007), pp.73-79.
11. M.Sakamoto, N.Tomozoe, H.Furutani, M.Kono, T.Ito, Y.Uchida, and H.Okabe, A survey of automata on three-dimensional input tapes, *WSEAS Transactions on Computers, Issue* 10,Vol.7, (2008), pp.1638-1647.
12. M.Sakamoto, T.Ito, H.Furutani, and M.Kono, Some accepting powers of three-dimensional parallel Turning machines, *International Journal of Artificial Life and Robotics*, *Springer,* Vol.13,No.1, (2008), pp.27-30.
13. M.Sakamoto, M.Fukuda, S.Okatani, T.Ito, H.Furutani, and M.Kono, Path-bouded Three- dimensional finite automata, *International Journal of Artificial life and Robotics, Springer*,Vol.13,No.1, (2008), pp.54-57.
14. M.Sakamoto, S.Okatani, M.Fukuda, T.Ito, and H.Furutani, and M.Kono, A relationship between Turning machines and finite automata on four-dimensional input tapes,

International Journal of Artificial life and Robotics, Springer, Vol.13,No.1, (2008), pp.58-60.
15. M.Sakamoto, S.Okatani, K.Kajisa, M.Fukuda, T.Matsuawa, A.Taniue, T.Ito, H.Furutani, and M.Kono, Hierarchies based on the number of cooperating systems of three-dimensional finite automata, *International Journal of Artificial Life and Robotics*, *Springer*, Vo.4,No.3, (2009), pp.425-428.
16. M.Sakamoto, T.Matsukawa, R.Katamune, H.Furutani, M.Kono, S.Ikeda, T.Ito, Y.Uchida, and T.Yoshinaga, Four-dimensional synchronized alternating Turning machines, *Proceedings of the 10th American Conference on Applied Mathmatics*, Harvard University, Cambridge, USA, (2010), pp.195-200 (CD-ROM).
17. M.Sakamoto, R.Katamune, T.Matsukawa, H.Furutani, M.Kono, S.Ikeda, T.Ito, Y.Uchida, and T.Yoshinaga, Some result about hierarchy and recognizability of four-dimensional sychronized alternating Turning machines, *Proceedings of the 10th American Conference on Applied Mathmatics,* Harvard University, Cambridge, USA, (2010), pp.201-205(CD-ROM).
18. M.Sakamoto, T.Matsukawa, R.Katamune, H.Furutani, M.Kono, S.Ikeda, T.Ito, Y.Uchida, and T.Yoshinaga, Synchronized Alternating Turning Machines on Four-Dimensional In- put Tapes, *WSES TRANSACTIONS on COMPUTERS*,Issue 4,Vol.9, (2010), pp.319-328.
19. M.Sakamoto, R.Katamune, T.Matsukawa, H.Furutani, M.Kono, S.Ikeda, T.Ito, Y.Uchida, and T.Yoshinaga, Hardware Hierarchies and Recognizabilities of Four-Dimensional Synchronized Alternating Turning Machines, *WSEAS TRANSACTIONS on COMPUTERS*, Issue 4, (2010), pp.329-338.
20. M.Sakamoto, T.Ito, X.Qingquan, Y.Uchida, T.Yochinaga, M.Yokomichi, S.Ikeda, and H.Furutani, A Note on Three-dimensional Probabilistic Finite Automata, *The Seventeenth International Symposium on Artificial Life and Robotics* 2012, Oita, Japan, (2012), pp.492- 495 (CD-ROM).
21. M.Sakamoto, Y.Uchida, T.Hamada, T.Ito, T.Yoshinaga, M.Yokomichi, S.Ikeda, and H.Furutani, A Relationship between the Accept- ing Powers of Nondeterministic Finite Automata and Probabilistic Finite Automata on Three-Dimensional Input Tapes, *in the 2012 IEICE General Conference,* Okayama University, (2012), p.4 (CD-ROM).
22. T. Toffoli and N. Margolus, *Cellullar automaton machines − new environment for modeling*, MIT Press, (1987).
23. J. Wiedermann, *Parallel Turing machines, Technical Report RUU-CS-84-11*, Department of Computer Science, University of Utrecht, the Netherlands, (1984).

Reduction of the search space to find perfect play of 6×6 board Othello

Yuki Takeshita
Graduate School of Engineering, Miyazaki University,
Japan, hf11031@student.miyazaki-u.ac.jp

Makoto Sakamoto
Department of Computer Science and System Engineering, Miyazaki University,
Japan, sakamoto@cs.miyazaki-u.ac.jp

Takao Ito
Graduate School of Engineering, Hiroshima University,
Japan, itotakao@hiroshima-u.ac.jp

Tsutomu Ito
Graduate School of Engineering, Hiroshima University,
Japan, 0va71-2538f211n@ezweb.ne.jp

Satoshi Ikeda
Department of Computer Science and System Engineering, Miyazaki University,
Japan, bisu@cs.miyazaki-u.ac.jp

Abstract

In 1993, mathematician Feinstein found out perfect play on 6×6 board Othello gives 16-20 loss for the first player by using computer. He reported on the Web that it took two weeks to search forty billion positions in order to obtain the result. In our previous papers, we confirmed the perfect play he found is correct. And we also found another perfect play different from the one he found to search 884 billion positions. In order to search efficiently, we attempted to reduce the search space to find some perfect play. In this paper, we introduce some techniques to solve 6×6 board Othello by searching about nine billion positions.

Keywords: combinatorial theory, combinatorial optimization, perfect play, miniature Othello

1. Introduction

Othello is a board game derived from Reversi by Goro Hasegawa (JPN) in 1973. Othello rules[1] are completely unified, whereas Reversi has many local rules. According to the Japan Othello Association established by Hasegawa, World Championship has been held every year since 1977, the tournament is held in Japan, the United States and European countries.

Othello is categorized into two-player zero-sum finite deterministic games of perfect information[2]. Games in this class are possible to look ahead in theory, thus if both players choose constantly the best move, these are classified into win, loss or draw game for the first player[3] (the sequence obtained in this way is called perfect play).

6×6 board Othello is solved by mathematician Joel Feinstein in 1993. He reported on the Web that perfect play of 6×6 board Othello gives 16-20 loss for the first player[4]. He also reported, he needed two weeks to obtain his perfect play by searching 40 billion positions. On the other hand, standard 8×8 board Othello is still open in spite of the fact that over twenty years have passed since he solved 6×6 board Othello.

In our previous papers[5, 6], we examined his results and showed that the perfect play he found is correct. In addition, we also found new perfect play. However, we needed five and a half days to find it by searching 884 billion positions.

In the future, in order to solve standard 8×8 board Othello, it is necessary to greatly reduce the search space. Therefore, in this paper, we introduce some techniques to solve 6×6 board Othello by searching about nine billion positions. Moreover, we explain an idea that solves by dividing the problem of large search space into multiple sub-problems using 4×12 board Othello.

2. Othello*

Othello always begins with the setup as shown in Fig. 1. One player uses the black side of the pieces (circular chips), the other the white side. Black always moves first.

Each player puts a piece of own color to an empty square in own turn. A player's move consists of outflanking the pieces of his opponent, he flips outflanked pieces to his color. To outflank means to place the piece on the board so that his opponent's rows of the piece are bordered at each end by the piece of his color. If a player cannot make any move, then he has to pass. If he is able to make a valid move, then passing is not allowed. The game ends when neither player can make any valid move. The winner is the player who has more pieces than his opponent.

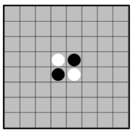

Fig. 1. Othello's setup.

3. Techniques

Perfect analysis of Othello is useful to refer thinking routines of game program. This is because end-game routine of game program is the perfect analysis exactly, and evaluation function in the middle-game routine is available for the ordering of the search in perfect analysis.

3.1. *MiniMax with Alpha-Beta Pruning*

As the technique in computer Othello, regardless of the middle or the end, MiniMax with Alpha-Beta pruning is commonly used. MiniMax algorithm achieves the best moves by both players, Alpha-Beta method cuts unnecessary search in MiniMax. These are commonly used together since MiniMax with Alpha-Beta pruning gives the same results as the simple MiniMax search.

3.2. *Move Ordering*

Appropriate order in search causes pruning by Alpha-Beta method. In our program, all positions progressed one move (from current position) are extracted, and then they are sorted. To realize this, we calculate the evaluation values by machine learning in advance. Therefore, the higher the accuracy of machine learning, the higher the reduction effect of search space.

3.2.1. *Machine Learning*

We adopt reinforcement learning using Monte Carlo method. First, it starts at root node of the tree, several moves of random selection are running. Second, they select optimal child nodes until a leaf node is reached. Third, computer uses the final disc difference as a reward, it updates evaluation value of the position while returning moves. In our program, one cycle including the above three steps is repeated a million times.

3.2.2. *Evaluation function*

The evaluation value is the sum of evaluation values of several patterns. For example, in 6×6 board Othello, it consists of the patterns shown in Fig. 2.

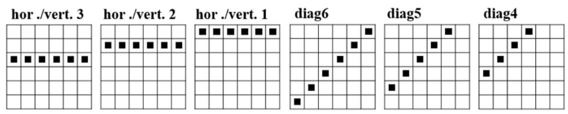

Fig. 2. Evaluate pattern of 6×6 board Othello.

3.3. *Adding Hash Table*

To cut the search of duplication positions, we added a hash table. However, since the same positions hardly occur in rectangular boards, we only implemented on 6×6 board Othello. By this revision, we were able to reduce the search space of 6×6 board Othello by 40 percent.

*Othello is a registered trademark.

4. Experiments

Table 1 shows number of final positions for 6×6 board Othello. From Table 1, comparing the first row with the third row, we can see that our current program has reduced Feinstein's search space by about 78%. Besides, comparing the second row with the third row, we can see that our current program has reduced the search space by about 99%. This is due to the implementation effect of the Move Ordering described Section 3.2.

Table 1. Number of final position for 6×6 board Othello.

Experimenter	Execution time	Final position
Feinstein('93)	2 weeks	40 billion
Takeshita('15)	5.5days	885 billion
Takeshita('16)	2.5hours	9 billion

4.1. *4×12 board Othello*

We found an initial position of 4×12 board Othello as shown in Fig. 3. This position gives win for the first player. The sequence is perfect play which is consistent with 4×8 board and 4×10 board. This is why we choose the position. If the sequence of Fig. 3 is the best moves for both players, 4×12 board Othello gives win for the first player. Therefore, it is necessary to check some positions which branched from white turn.

			❸	②	❶	④	❺				
					○	●					
					●	○					
					⑥						

Fig. 3. A position fixed from move 1 to move 6.

Fig. 4, Fig. 5 and Fig. 6 are three positions that must be checked in order to prove that gives win for the first player on 4×12 board. The Greek alphabets in these figures mean all of places that the second player can put in his turn. 'F' in each figure means 'Finish', this is a place which already finished the search when we check in descending order (Depth 6, Depth 4 and Depth 2).

			●	●	●	●	●				
					○	●	(β)				
				(α)	●	○					
					F						

Fig. 4. Depth 6.

			●	●	●	F					
					○	●	(ε)				
				(γ)	●	○					
					(δ)						

Fig. 5. Depth 4.

				F	●	(η)					
					●	●					
				(ζ)	●	○					

Fig. 6. Depth 2.

Table 2 shows a part of the position fixed from move 1 to move 6 in 4×12 board Othello. These are currently executing sub-problems, however, blacked out cells are already finished. For every element in Table 2, the first Greek alphabets show the places as mentioned above. The following character strings are a sequence to move 6 corresponding to the coordinates in Fig. 7. For further details on the sub-problems, refer to reference 8.

Table 2. Executing sub-problems to prove our perfect play.

Depth 6	Depth 4	Depth 2
(α)	**(γ)f4g1**	**(ζ)f4e1d1g1**
(β)	**(δ)e2g1**	**(ζ)f4e1d1h2**
	(δ)e2h1	**(ζ)f4g1h1h2**
	(ε)h3f4	**(η)h1e1d1e3**
	(ε)h3h4	**(η)h1e1d1f4**
		(η)h1e1d1h2
		(η)h1e3g4h3

a1	b1	c1	d1	e1	f1	g1	h1	i1	j1	k1	l1
a2	b2	c2	d2	e2	○	●	h2	i2	j2	k2	l2
a3	b3	c3	d3	e3	●	○	h3	i3	j3	k3	l3
a4	b4	c4	d4	e4	f4	g4	h4	i4	j4	k4	l4

Fig. 7. Coordinates on 4×12 board.

As we can see (Table 2), eleven problems have already finished, the rest is three problems. If their results are all the black win, it will show that the first player wins in 4×12 board Othello.

5. Consideration

Fig. 8 shows the number of final position for miniature Othello solved by us. The horizontal axis shows each board size and the vertical one represents number of final position by the exponent. The elements in Fig. 8 mean that circles are square boards and the triangles are rectangular boards.

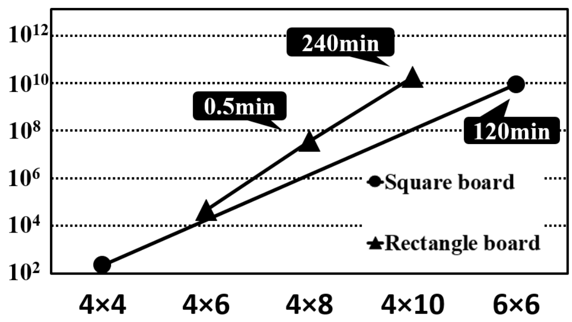

Fig. 8. Number of final position for miniature Othello.

Firstly, in rectangle board, it is reasonable to expect number of final position in 4×12 board is about 10^3 times larger than 4×10 board. Now, given that the execution time in 4×10 board is four hours, the execution time in 4×12 board is considered to be about four thousand hours (when we analyze perfectly from move 1).

Secondly, in square board, number of final position increased about 10^8 times in the transition from 4×4 board to 6×6 board. From this fact, we assume that number of final position in 8×8 board is about 10^{18} at least. Now, given that the execution time in 6×6 board is 2 hours, we know that perfect analysis in 8×8 board is impossible as it stands.

6. Conclusion

In this paper, we attempted to reduce the search space of 6×6 board Othello by implementing Move Ordering (Section 3.2) and Hash Table (Section 3.3). As a result, we succeeded in reducing Feinstein's search space by about 78%. In addition, the technique described in Section 4.1 is available for all boards. Therefore, it could be one key factor for solving even larger boards.

7. Future work

To challenge 6×8 board, 4×14 board and 8×8 board, it is necessary to reduce the search space by exponential order. For that purpose, it is most effective to improve accuracy of Move Ordering. Specifically, we strengthen reinforcement learning and improve search algorithm.

References.

1. Japan Othello Association: *Nihon osero renmei kyougi ru-ru*, [online]www.othello.gr.jp/r_info/rule.html (Retrieved 9 November. 2016)
2. John von Neumann and Oskar Morgenstern: *Theory of Games and Economic Behavior*, Princeton University Press (1944).
3. Jonathan Schaeffer, Neil Burch, Yngvi Björnsson, Akihiro Kishimoto, Martin Müller, Robert Lake, Paul Lu and Steve Sutphen: "Checkers Is Solved," *Science*, Vol. 317, pp. 1518-1522 (2007).
4. British Othello Federation: *Forty Billion Nodes Under The Tree - The Newsletter of the British Othello Federation*, [online]www.britishothello.org.uk/fbnall.pdf (Retrieved 9 November. 2016), pp. 6–8 (1993).
5. Yuki Takeshita, Satoshi Ikeda, Makoto Sakamoto and Takao Ito: "Perfect Analysis in miniature Othello," *Proceedings of the 2015 International Conference on Artificial life and Robotics*, pp.39 (2015).
6. Yuki Takeshita, Makoto Sakamoto, Takao Ito and Satoshi Ikeda: "Perfect Play in Miniature Othello," *Proceedings of the Ninth International Conference on Genetic and Evolutionary Computing*, pp.281-290 (2015).
7. Yuki Takeshita, Makoto Sakamoto, Takao Ito and Satoshi Ikeda: "Analysis for 4×12 board of Othello," *Proceedings of the 2016 International Conference on Artificial life and Robotics*, pp.349-352 (2016).

A Comparative Study On The Delisting Ratings Of Firms From The Un Global Compact In The International Management Environment

Kanako Negishi
Business Administration, National Institute of Technology, Ube College,
Tokiwadai, Ube City, Yamaguchi Pref., 755-8555, Japan
E-mail: negishi @ube-k.ac.jp
www.ube-k.ac.jp/en/

Abstract

This study clarifies unique characteristics of Japanese manufacturing firms in the international management environment using the United Nations Global Compact delisting ratio. Firms have adopted voluntary standards provided by non-governmental organizations and international institutions. Although there are various standards that are not legal binding, there is a recent trend toward integration to achieve comparability for firms' management, which then binds firms' managements as a *de facto* standard. This study examines the firms' delisting ratio by comparing countries.

Keywords: United Nations Global Compact delisting ratio, multi-stakeholder initiative, Japanese manufacturing, international management environment

1. Introduction

The international environment regarding firms' sustainability has changed, and there is also a transition in the firms' international relationship with stakeholders and solutions to sustainability. After the 1990s, many guidelines and principles for firms were developed by public institutions and non-governmental organizations such as the United Nations Global Compact (GC), Global Reporting Initiative (GRI), and Integrated Reporting (IR) to improve international firms' activities. For example, over 9,000 firms participated in GC.

Although there are various guidelines and principles that are not legally binding such as GC, there is a recent trend toward integration to achieve comparability for firms' international management of sustainability. This binds firms' management as a *de facto* standard.[1] GRI does not have legal power to force firms to use the GRI guideline; however, nowadays, this guideline is the most common way to report a firm's sustainability worldwide.[2]

One of the feature of these guidelines and principles is that as the organizations are based on multi-stakeholder initiatives, firms not only adopt the guidelines and/or principles in their management but also participate in the platforms to discuss them with other stakeholders to make decisions and develop a process for the guidelines, principles, and related actions.[3]

Sustainability is a very important agenda for a firm's international management. However, not all firms archive their sustainable management with such international actors; some firms are expelled from GC at fixed intervals. The agenda surrounding firm's environment are complicated recently. It is difficult for firms to solve it solely. However, firms are often expected to approach it by their stakeholders.

Using the GC delisting list, this study clarifies Japanese manufacturing firms' characteristics in the international environment. It contributes to its international strategy on sustainability.

2. Literature Review and Research Object

The recent international environment is a complex web of "soft" low that has constructed new social norms for several important dimensions of business conduct. The part regarding dimensions has been institutionalized in corporate and industry codes, multi-stakeholder initiatives, and private standard-setting bodies.[4]

How do firms develop good relationships with such bodies to archive their sustainable management goals efficiently? Many Japanese firms participate in GC and use the GRI guideline.[5] It is one of the result that firms responded to the pressure from their stakeholders.

GC is one representative initiative, and its participant firms are from both advanced and developing countries. Business associations seem to be most involved in the discussion at the UN level, as reflected in the 'post-2015 business engagement architecture', leading to an issue area priorities framework published by GC.[6]

As noted above, some firms are delisted from GC although the participation norm is only to submit the report to GC. Particularly, the delisting ratio of Japanese Small and Medium Sized Enterprise (SME) is the highest in the GC participants' top-10 ranking by country including all sectors[7], however, ref. 8 shows that domestic governance institutions are crucial in assisting firms fulfill the GC requirement based on the World Bank Governance Indicators which shows high level of the governance in Japan.

The emerging literature lacks information on the practice of Japanese firms. Because, most of guidelines and principles have been developed in advanced Western countries as the concept of sustainability and Corporate Social Responsibility (CSR) also developed mainly in the countries historically. Some of guidelines and principles oriented in Japan adopted by Japanese firms. None of them have not spread globally like GRI whose head office is in Netherlands.

This study focuses on the manufacturing sector, with one of the largest values of foreign direct investment from Japan, to clarify Japanese firms' characteristics in the international environment through a comparative study of Japanese, Chinese, Spanish, and US firms by size, sector, and country.

3. Method and Dataset

This analysis used the data from the GC database of participants. Firms are expelled if they fail to submit their reports to GC at least one year. The first date of delisting in GC is March 27, 2002.Therefore, the data of firms are used from March 27, 2002 to November 11, 2016. The number of delisting firms during this term is shown in Table 1.

According to GC, a company is defined as a firm having over 250 employees, while an SME has under 250 employees except for under 10 employees.

The target countries are Japan, Spain, China, and the U.S. Because Spain ranks at the top of the GC participants by country. I selected the countries based on the ranking in each region.

This study focuses on the manufacturing sector. According to GC, this sector includes automobile and parts, construction and materials, electronic and electrical equipment, healthcare equipment and service, household goods and home construction, industrial engineering, personal goods, and technology hardware and equipment.

Table 1. The number of delisting firms by country and size

Country and size	Number
Spanish company	54
Spanish SME	320
Chinese company	53
Chinese SME	44
Japanese company	0
Japanese SME	64
US company	36
US SME	113

4. Result and Findings

Table 2 shows the delisting ratios of the four countries by size and sectors.

Table 2. Delisting ratio of the Spanish, Chinese, Japanese, and US firms by size and sectors

	Spain		China		Japan		USA	
Sector	Rating of company delisting	Rating of SME delisting	Rating of company delisting	Rating of SME delisting	Rating of company delisting	Rating of SME delisting	Rating of company delisting	Rating of SME delisting
Automobiles and parts	9.09%	58.33%	38.46%	75.00%	0.00%	91.67%	22.22%	50.00%
Construction and materials	34.78%	60.29%	66.67%	46.67%	0.00%	88.57%	27.78%	77.78%
Electronic and electrical equipment	40.00%	41.86%	60.71%	70.83%	0.00%	80.88%	60.00%	61.54%
General industrials	46.15%	55.70%	75.00%	64.71%	0.00%	77.78%	60.87%	70.49%
Healthcare equipment and service	12.50%	30.56%	25.00%	33.33%	0.00%	0.00%	50.00%	72.73%
Household goods and home construction	100.00%	35.71%	50.00%	50.00%	0.00%	81.82%	0.00%	57.14%
Industrial engineering	46.15%	41.10%	75.00%	72.73%	0.00%	100%	50.00%	75.00%
Personal goods	56.25%	60.00%	57.14%	14.29%	0.00%	0.00%	14.29%	46.15%
Technology hardware and equipment	25.00%	50.00%	80.00%	88.89%	0.00%	100%	28.57%	60.00%

4.1. *Size*

Actions undertaken by large firms are more visible, so firm size is an important factor for analysis.[3] It is applicable to Japanese and US firms, but firms in China and Spain are not influenced by size, as shown in Table 1.

Focusing on the manufacturing industry, the features of Japanese firms are shown as the same. In brief, SMEs' delisting ratios are higher than any company in Japan. US firms show the same trend. However, the gap in the ratio between Japanese firms is larger than that in US firms.

On the other hand, Spanish and Chinese firms' delisting ratios are different. They depend on the sector, and gaps between their companies and SMEs are smaller than those of Japanese firms.

4.2. *Sector*

The ratios of SMEs delisting are higher than for companies in the automobiles and parts, electronic and electrical equipment, and technology hardware and equipment sectors in four countries.

In the construction materials, personal goods, and general industrials sectors, only Chinese companies' ratios are higher than those of their SMEs.

Only Japanese SMEs have ratios over 80% in all sectors, and only Japanese companies' have ratios at 0%. There are no gaps among sectors.

5. Considerations and Further Research

From the comparative study in the manufacturing industry, it is clarified that Japanese companies' delisting ratios are the lowest, whereas that of SMEs are the highest, and the trend is similar to the U.S.

Ref.6 noted what multinationals do face, however, especially if they are large, visible and active in countries with different norms and standards than their home country, is the growing pressure to account for social, environmental and ethical problems occurring in various locations of operation. Although not all company in the GC do business globally, companies tend to be pressured stronger than SMEs as the reasons. The result of ratios in Japan and US by size support it.

It is also clarified Japanese companies respond to the expectation by their stakeholders globally. Additionally, there is not large change about the Japanese companies and SMEs delisting ratios between manufacturing sector and all sectors[7].

It is believed that delisting ratios are influenced by the number of firms whether they are supplier or not in the global supply chain. Some firms request their suppliers to behave virtuously. [1] The results indicate a lot of firms in Spain and China participate in GC and use the GRI guideline although Japanese SMEs have better financial conditions. However, western firms provide little to no financial assistance to suppliers to meet their standards.[4] The result of their delisting ratios partly explains it quantitatively.

How can the Japanese SMEs' ratios be explained? It is thought that their main clients are Japanese companies that generally do not request such norms for their suppliers instead of each company's code. In addition, their home country's consumers do not strongly request to be more responsible than in Europe and the U.S.

However, more research is needed to explain the result explicitly to add more data; reason of delisting, the other sectors and countries. It is also needed to explore the relationship between the GC and internal elements such as the governance of management.

References

1. The Global Compact and Global Reporting Initiative, *Making the Connection: Using the GRI G4 Guidelines to Communicate Progress on the UN Global Compact Principles*, https://www.globalreporting.org/resourcelibrary/UNGC-G4-linkage-publication.pdf (25,Nov. 2016 last access)
2. Global Reporting Initiative homepage, https://www.globalreporting.org/information/about-gri/alliances-and-synergies/Pages/UNGC-and-GRI.aspx%20 (25, Nov. 2016 last access)
3. K. Tanimoto, Kigyou to syakai no gabanansukouzou no henka, *in Proc. 90th Annual Meeting of the Japan Academy of Business Administration* (2016).
4. D. Vogel, *The Market for Virtue: The Potential and Limits of Corporate Social Responsibility* (The Brookings Institution, Washington, DC, 2005).
5. KPMG, *The KPMG Survey of Corporate Responsibility Reporting 2013*. https://www.kpmg.com/Global/en/IssuesAndInsights/ArticlesPublications/corporate-responsibility/Documents/corporate-responsibility-reporting-survey-2013-exec-summary.pdf (25 Nov. 2016 last access)
6. A. Kolk, The social responsibility of international business: from ethics and the environment to CSR and sustainable development, *J.World Bus.*, 51(1),(2016) 23-34.
7. K. Negishi, Multinational Enterprises' Global Supply Chain: Study of the Global Reporting Initiative and United Nations Global Compact in Industrial Renaissance: *New Business Ideas for the Japanese Company* (Institute of Business Research, Chuo University, Tokyo, 2017).
8. J. S. Knudsen, Company delisting from the UN Global Compact: Limited business demand or domestic governance failure? *J. Bus. Ethics*, **103** (2011) 331–349.

Application of ViSC to the Natural Grazing in Qinghai Tibet Plateau

Chengshui Niu
Department of Computer Technology and Applications,
Qinghai University, 810016, Xining China
Bingfen Li
School of Mechanical Engineering,
Qinghai University, 810016, Xining China
Yu-an Zhang
Department of Computer Technology and Applications,
Qinghai University, 810016, Xining China
Makoto Sakamoto
Faculty of Engineering, University of Miyazaki,
Miyazaki City 889-2192 Japan

Abstract

"SanjiangyuanRegion" is a complex ecosystem with typical characteristics of alpine grass land, which the livestock production relies mainly on the yak grazing. In recent year, grassland degradation, the reduction of herdsmen income and on-going deterioration of the ecological environment caused by human disturbance are gradually intense, which a scientific and rational grazing mode of combination of ecological animal husbandry and sustainable utilization of grassland should be established urgently. Applying the ViSC combined with the optimization theory, will study establish the optimization of alpine grassland yak grazing system, which provides a theoretical basis for scientific grazing.

Keywords: Sanjiangyuan Region, ViSC, Optimization theory, Grazing systemt

1. Introduction

The Qinghai-Tibet Plateau is a natural laboratory in the fields of earth sciences, life sciences, resources and environmental sciences[1]. Scientific research in this area is relatively scarce at present, so the significance of its research becomes more valuable.

Due to overgrazing, the ecological balance of the Qinghai-Tibet Plateau is seriously imbalanced and desertification is aggravated. The main reason is that the unreasonable herdsmen seasonal grazing methods and population selection is not standardized. In this paper, the grazing intensity of the four seasons is rationally arranged by scientific calculation, and the whole structure of the population tends to be normalized by scientific distribution, which can reduce environmental damage to realize the sustainable grazing.

The unfamiliar with the computer science of Qinghai-Tibetan Plateau area herdsmen leads to them can't directly use the scientific computing for analyzing the data. The scientific visualization of visual information processing possesses prominent merits in terms of high-speed, large capacity, parallel, easy to interact[2]. This article builds an system that displays the scientific analysis of the data by the graphics, which can be a perfect solution to problem of the computer data difficult to understand. So that herdsmen can be clear and intuitive understanding of pastures need to optimize, and make the Qinghai-Tibetan Plateau herdsmen can to carry out scientific wisdom grazing(Wisdom Graze WG).

Corresponding author: Yu-an Zhang, e-mail:2011990029@qhu.edu.cn

2. WG Model Is Established

In the wisdom grazing, how to standardize the flock structure and plan the four seasons grazing, so that to get the maximum profit is the herdsmen most concerned the problems. Limited stocking of yaks within limited meadows is a major constraint for maximum profitability. So Good allocation of grassland and yak is the basis of the herdsmen to get the maximum profit.

Define1 Set there are Task head of yak, Work acres of grass. $Task=F(s)i\ M(s)i\ F(a)i\ M(a)i$, F means the bull，M means the cow，s means the summer，a means the spring and autumn, i=1,2,…8， means ages.

According to the conventional rangeland custom, the flock of yak from summer into autumn will grows one year old, The initial copulation age of the cow is 2 to 3 years old, the bull is 4 to 5 years old, the conception time is about 6 to 9 months per year, the reproduction rate of 68% survival rate is 62%, Adult cattle affected by weather and disease mortality rate of 5%, aging cattle mortality rate of 30%[3]。

Assume the survival rate is SR(i), as follows:

$$SR_{(i)}=\begin{cases} 62\%, & i=0 \\ 95\%, & 0\le i<8 \\ 70\%, & i\ge 8 \end{cases} \quad (1)$$

The variation equation of yak population as follows:

$$F_0^{(a)} = 0.5\sum_{i=3}^{7} 0.68 * M_i^s * SR_{(0)}$$
$$M_0^{(a)} = 0.5\sum_{i=3}^{7} 0.68 * M_i^s * SR_{(0)} \quad (2)$$
$$F_j^{(a)} = F_i^s * SR_{(i)}, i=0,1,2\ldots 6; j=1,2,3,\ldots 7$$
$$M_j^{(a)} = M_i^s * SR_{(i)}, i=0,1,2\ldots 6; j=1,2,3,\ldots 7$$
$$F_8^{(a)} = F_7^s * SR_{(7)} + F_8^s * SR_{(8)}$$
$$M_8^{(a)} = M_7^s * SR_{(7)} + M_8^s * SR_{(8)}$$

During the summer, the grass yield will reach the peak value(*167kg=Ha*)[4]. Assume the maximum value is *MaxGras* and the yield of grass in winter, summer, spring and autumn expresses by *WinterGrass*, *SummerGrass, SpringGrass* and *AutumnGrass* respectively.

A large amount of data from the Zaduo County was collected to demonstrate that the grass production in the spring pasture was growing exponentially. Different rainfall and grassland quality will correspond to different base-a. Spring production of grass can be expressedas:

$$SpringGrass = \sum_{x=1}^{3} (a)^x \quad (3)$$

where$1 < a < \sqrt[4]{summerGrass/3}$, *x=1 ,2 ,3* respectively represents the three month of spring.

In the autumn, pasture harvest and grass dying lead to negative production growth. So the expression of the equation as shown:

$$AutumnGrass = SummerGrass - \sum_{x=1}^{3}(a)^x \quad (4)$$

Where $1/\sqrt[4]{summerGrass/3} < a < 1$, *x=1,2,3* which respectively represents the three month of autumn.

The relationship between summer and winter can be obtained by the actual situation, the formula is as follows:

$$MaxGrass=WinterGrass+ SummerGrass \quad (5)$$

Suppose the total pasture grass production within a year is *SumGrass*. Formula (6) can be obtained by the formula(3),(4),(5), as shown:

$$SumGrass=MaxGrass+AutumnGrass+SpringGrass \quad (6)$$

According to the different food intake, this article divided the yak into four types, calves (newborn yaks), young yak, adult yak and old yak. The amount of eating grass of calves is almost zero in the summe, the amount of eating grass of young yak has a increasing trend from autumn. The amount of eating grass of adult yak almost unchange is *19kg* per day, the old yak's is *15kg* per day[5].

Define 2 Assuming the number of young cattle, adult cattle and old yak are expressed with $TaskT1$, $TaskT2$ and $TaskT3$; the amount of eating grass of them are expressed with $TaskTS1$, $TaskTS2$ and $TaskTS3$ respectively; theyak required grass within a year is *SumWork*.

$$SumWork = \sum_{i=0}^{3} TaskTS(i) \quad (7)$$

where *i = 1,2, 3,* which represents young yak, adult yak, old yak respectively.

Let the alternate date that summer into autumn within one year is a new year, the total amount of grass needed by rangelands according to different yaks age can be expressed as:

$$TaskTS1=\begin{cases} (F_0+M_0)(30*\sum_{x=0}^{11} 0.5X+1), i\epsilon[0,1], \\ (F_1+M_1)(30*\sum_{x=0}^{11} 0.5X+7), i\epsilon[1,2], \\ (F_2+M_2)(30*\sum_{x=0}^{11} 0.5X+14), i\epsilon[2,3], \end{cases} \quad (8)$$

where i is the age of yak and $x\in[0,11]$.

$$TaskTS2 = \sum_{i=3}^{7}(F_i+M_i)19*360 \quad (9)$$

$$TaskTS3=15*360*(F_8+M_8) \quad (10)$$

Define 3 Assume that the supplementary feed amount is *Fodder*. Through the relation between the amount of grass and grass yield, we can get the *fodder*, as shown:

$$Fodder= (SumGrass-SumWork)/15 \quad (11)$$

wher 1 pounds of fodder is equal to 15 pounds of grass

Define 4 Assume the maximum feeding amount of each yak is *TaskI(i)*, *i∈ [1,3],* which represent young yaks, adult yaks and old yaks, respectively. The formula of *TaskI(i)* as follows

$$Task(i) = SumWork/TaskTS(i) \quad (12)$$

Define 5 Assume that the total number of yaks is *TaskSum*. The value of *TaskSum* is:

$$TaskSum = \sum_{i=0}^{3} TaskS(i) + (M_0+F_0) \quad (13)$$

$$TaskS1 = \sum_{i=0}^{2}(M_i+F_i)$$
$$TaskS2 = \sum_{i=3}^{7}(M_i+F_i)$$
$$TaskS3 = (F_8+M_8)$$

Define 6 Suppose that the sum of all the yaks produced profit in a year is *Profit*: Cows lactation is period of *5* months, Total milk production was *350 kg*, The milk fat rate of *5 ~ 7.5*[6] , 2016 annual the milk fat price is *600 ¥/ kg*, Therefore, Assume that pasture yak milk production within a year to get the total income is *Milk*.The value of Milk is:

$$Milk = 0.5 * \sum_{i=3}^{7} 0.68 * M_i^{(s)} * (350 * 0.05) * 600 \quad (14)$$

Yak has a great profit in the field of traffic. Each transportation per yak average can produce 500¥ profit. Assume that the profits that can be generated are *Pack*. The value of *Pack* is:

$$Pack = 500 * \sum_{i=3}^{7} F_i \quad (15)$$

The yak tail cow-hair cut once every two years and one can get *0.25kg*, other coarse cow-hairs cut once a year, each yak can get *0.5-3kg*[6]. Yak hair's the latest price is *72 ¥ / kg* in2016. Assuming that the yak fluff in the whole pasture can make profits is *Fur*. The value of *Fur* is:

$$Fur = 2 * 72 * \sum_{i=3}^{8} (F_i + M_i) \quad (16)$$

The price of a calve is *1700* ¥[7]. Assume a gain from calves in a year as Calf, The value of *Calf* is:

$$Calf = (F_0^{(a)} + M_0^{(a)}) * 1700 \quad (17)$$

By the growth characteristics of yak, "Summer strong, autumn fat, winter thin", we can know the fastest growing in the autumn. According to the literature, we can know that the maximum weight gain of young cattle was *29.41kg.* Winter and spring and summer will be a corresponding reduction. The weight gain was *16.1kg, 18.5kg, 25.2kg*[7]. *I*n the latest market research, we can get that the price of yak is *23 ¥ / Kg,* Assume that a young yak can generate a profit in one year is *Meat*. The value of *Meat* is:

$$Meat = \sum_{i=0}^{2} (29.41 + 16.1 + 18.5 + 25.2) * 46 \quad (18)$$

Through all of the above profits and expenses, we can be obtained the final profit in one year as follows:

$$Profit = Calf + Fur + Pack + Milk - Fodder \quad (19)$$

3. WG Algorithm Analysis

The 0-1 knapsack problem is used in the process of resolving the WG model. The main algorithm as follows:

Algorithm 1: An Algorithm Based on SG Model

Step1 : Define variables: Work, MaxGrass, dFodder, TaskTS1, TaskTS2, TaskTS3, Fodder, Milk, Pack, Fur, Calf, Meat，KeyMap, ValueMap; //ValueMap collection used to store the same age and gender of the yak different profit, KeyMap collection used to store ValueMap basis on different yak number.

Step2：Initialize the variable *Work, MaxGrass, dFodder*

Step3: *HightWork=MaxGrass*Work* // Maximum pasture grazing.

Step4: *TopWork= HightWork+ dFodder*30*15*// Maximum number of farms raised.

Step5: The total number of yaks for each age group is set to be X (i) i∈ [0,8]

Step6: The values plug into the formula(8), formula (9), formula (10). Get TaskTS1, TaskTS2,TaskTS3. put these three values into formula (7) get SumWork.SumWork。

Step7: if $\sum_{i=3}^{7} M_i < (\sum_{i=3}^{7} F_i)*10$ && $\sum_{k=1}^{3}$ TaskTS(i) <TopWork&& while [a….i] conditions are met, Execute Step8.

Step8：Get Pack, Fur profits by the formula (15) and formula(16).

Step9：Get Mi,F0,M0 by formula (2); Get Milk by formula (14); Get the Calf by formula (17).

Step10：Get Meat by the formula (18).

Step11: Get SpringGrass, AutumnGrass, SummerGrass,WinterGrass by formula (3), formula (4), formula (5). Then,Put them into formula (6) to get SumGrass.

Step12：Get Fodder by the formula (11).

Step13：Get profit by the formula (19).

Step14：Placing the values and itself of Fodder, Milk,Pack, Fur, Calf, Meat in Key and V alue of V alueMap. Transform the Xi to a string and put it and its value into theKey and V alue of KeyMap.

Step15： $\sum_{i=0}^{2} X_i > (TopWork/945)$ || $\sum_{i=3}^{7} X_i (TopWork/(19 * 30))$ || $X_8 > TopWork*15$. Judge whether or not the condition is satisfied, if yes, go on, else, goto Step6.

Step16：The V alue of V alueMap is sorted by total profit.Meanwhile the KeyMap is sorted too.

Step17: Return KeyMap.

4. WG Of Visc System

The process of ViSC system is divided into: acquisition layer-integration layer-expression layer[8]. By all levels of rational division of labor and context consistent, the system implements highly available.

The acquisition layer is the key parts of the whole system data. The data collection includes the herdsmen input data and the known data. The collected data is transmitted to the integration layer. Integration layer mainly collecting, selecting and combining the data ,and then returning the required data to the WG system. Eventually, the data are sent to the presentation layer. The presentation layer displays all the databy images to achieve the readability.

The entire process of visualization as the algorithm 2 shown:

Algorithm 2 Based on SG model generation ViSC algorithm

Input: Model related parameters, Pasture grassland area and Maximum grass yield in summer;

Output: Yield of grass, Need grasses, required fodder the relationship between the graphics chart; Dynamic display the data of yak flock chart; Dynamic growth of individual profit in yak chart; Can interactive automatic flock selection chart; The population relationship of yak in pasture chart; Pasture in a variety of profits chart;

Step1: Initialization. //Initialize the existing data.

Step2: The relationship between Yield of grass, Demand of grasses and required fodder. Show the relationship of grass data by the D3 pie chart;

Step3: Dynamic display the data of yak flock. Dynamic display the data of KeyMap and MapValue;

Step4: Dynamic growth of individual profit of yak. Calves profit form the increasing of the weight; Cows profit form the milk production and propagate; Bull profit from consignment; Adult yak profit from

trimming fluff. All of them will expressed by the yak dynamic map;
Step5: Automatic interactive flock selection. Get young yak, adult yak, old yak by the Key of KeyMap. Choose them as X-axis. Find the V alue by Key, all profit is mapped to the Y -axis according to Key;
Step6: The population relationship of yak in pasture: By the numbering all the yaks in the pasture and using weight of it, displaying the relationship by mapping out by point and point. When two adult yaks to crossover, the overlap of each other is greater than 35%. If the relationship between them is a mother-child, then the overlap will be less than 35%, likewise, if the relationship between calves and adult cattle is direct descendant, the relationship between points and points will not be less than twice the diameter of children, if there is a direct relationship, the point between the distance between the point will be no more than three times the diameter of the point;
Step7: Pasture in a variety of profits. Display the V alue of the V alueMap by histogram.

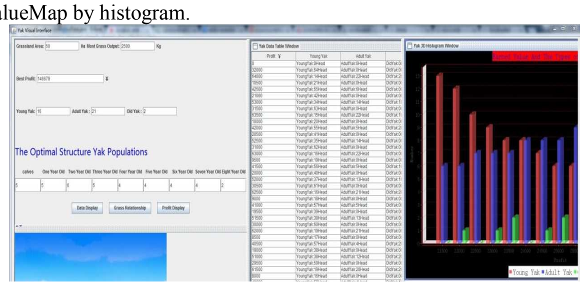

Fig.1. Input data

According to the process in algorithm 2, using scientific computing generated chart carries out wisdom grazing. First, herdsman enter the basic data of grassland area and grassland maximum production value for system. The best pasture profits, the number of three types of yak and the ranch yak age of the number of different age groups in whole year will can be produced. As shown in Fig.1:

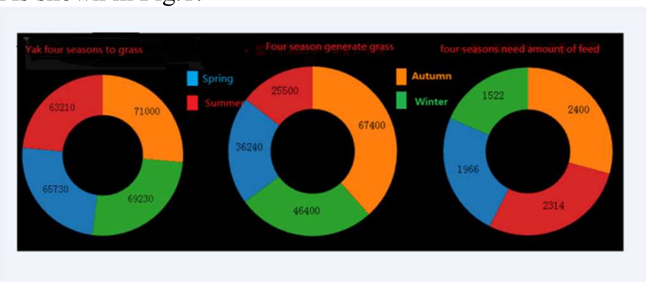

Fig. 2. Yield of grass, Need grasses, required fodder the relationship between the graphics

By entering the basic data, 50 acres of grassland and yield 2500kg, we can gain the grass yield, demanded grass, the maximum of supplementary feeding and the relationship between them of four seasons of the year. As shown in Fig.2: Meantime, All flock structure, profit in the whole ranch can be dynamic displayed. As shown in Fig.3 Herdsmen don't

Yak Data Table Window

Profit ￥	Young Yak	Adult Yak	Old '
0	YoungYak:0Head	AdultYak:0Head	OldYak:0Heac
32000	YoungYak:64Head	AdultYak:0Head	OldYak:0Heac
64000	YoungYak:14Head	AdultYak:22Head	OldYak:2Heac
10500	YoungYak:21Head	AdultYak:0Head	OldYak:0Heac
42500	YoungYak:55Head	AdultYak:6Head	OldYak:0Heac
21000	YoungYak:42Head	AdultYak:0Head	OldYak:0Heac
53000	YoungYak:34Head	AdultYak:14Head	OldYak:1Heac
31500	YoungYak:63Head	AdultYak:0Head	OldYak:0Heac
63500	YoungYak:15Head	AdultYak:22Head	OldYak:1Heac
10000	YoungYak:20Head	AdultYak:0Head	OldYak:0Heac
42000	YoungYak:55Head	AdultYak:5Head	OldYak:2Heac
20500	YoungYak:41Head	AdultYak:0Head	OldYak:0Heac
52500	YoungYak:35Head	AdultYak:14Head	OldYak:0Heac
31000	YoungYak:62Head	AdultYak:0Head	OldYak:0Heac
63000	YoungYak:16Head	AdultYak:22Head	OldYak:0Heac
9500	YoungYak:19Head	AdultYak:0Head	OldYak:0Heac
41500	YoungYak:56Head	AdultYak:5Head	OldYak:1Heac
20000	YoungYak:40Head	AdultYak:0Head	OldYak:0Heac
52000	YoungYak:37Head	AdultYak:13Head	OldYak:1Heac
30500	YoungYak:61Head	AdultYak:0Head	OldYak:0Heac
62500	YoungYak:16Head	AdultYak:21Head	OldYak:2Heac
9000	YoungYak:18Head	AdultYak:0Head	OldYak:0Heac
41000	YoungYak:57Head	AdultYak:5Head	OldYak:0Heac

Figure3. Dynamic display yak population data

know how to produce profits of each yak in the traditional farming process. Fig.4 shows the yak profits growth process of all ages within a year. Using the latest data, the process can be displayed by the form of chart. As shown in Fig.4:

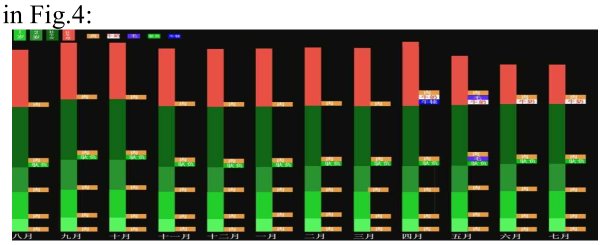

Figure4. Dynamic growth of individual profit in yak

Herdsman have basically know of the situation in the pasture by Fig.2, Fig.4. According to Fig.3, the herdsmen select the yak population and profits, and then producing the profits and flock structure according to the selected order, as shown in Fig.5.

When the herdsmen selecting the flock structure data for their own pastures, choosing its data in Fig.3 and right clicking "yak population diagram", it will generate the yak population diagram as shown in Fig.7. Herdsmen can intuitively analyze whether or not the whole yak population is infected by diseases .

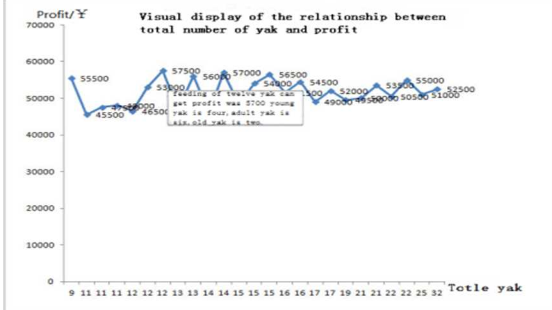

Figure5. Can interactive automatic flock selection

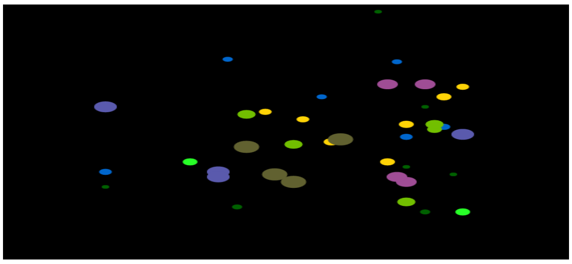

Figure6. The population relationship of yak

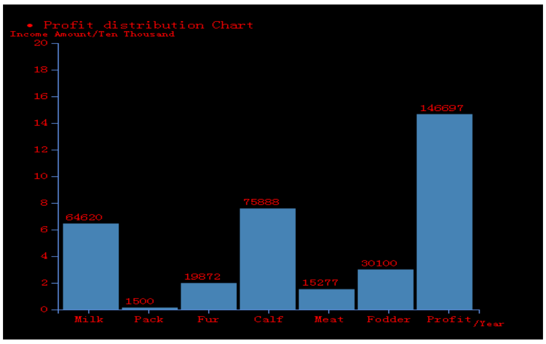

Fig. 7. Pasture in a variety of profits

With the above steps, the herdsmen will be get the data that suits for their pasture situation. Generating the Fig.8 by right clicking the "Pasture in a variety of profits" in Fig.3. After the above steps, the herdsmen can cleanly select the data that can obtain the maximum profits which suit for the reality of pasture. The above steps can clearly reflect the source of profits and costs and can intuitively help the herdsmen to understand how to grazing in each quarter, which makes herdsmen of the whole the nomads of the Qinghai-Tibet plateau graze scientifically and intelligently.

5. Summary

Visualization technology can convert the model data difficult to understand to the graphical form which easy to analyze and view. Showing the data by the five steps of data visualization not only improves the reliability of visual graphics[9], but also demonstrates the dependency between the various data. In the traditional plateau farming, herdsmen can't reasonable use the pastures of grass production, which results in excessive grazing. Visualization can instruct pastoralists in yak breeding, from the experiments in the ZaDuo area, we can conclude that not only the profit of farming is increasing, but also the overall fertility of the pasture is improving. At the same time, the breeding of the whole rangeland can be more standardized, and have a very well influence in genetic diseases, infectious diseases and other diseases prevention.

The herdsmen in Zadou County gives me a lot of experimental opportunities and data and Sanjiang source data center of Qinghai University provides a system service for my system and provides a convenient condition for the smooth promotion of my system. We appreciate your support.

Acknowledgment

This work is supported by Natural Science Foundation of China(No.61363019, No.61640206), Chunhui Research Program from Ministry of Education (Z2015050) and the State Foundation for Studying Abroad to visit the japan .

References

[1] Zhu Liping. "*Development and Prospect of the Qinghai-Tibet Plateau Research[C]*". Academic Exchange Seminar, 2010.

[2] Zhanglv Tan."he theoretical development of information visualization and the construction of the frame system[J]". *Information theory and Practice*, 2013, 36(1):16-19.

[3] Liang YN, et al. "Resource value and conservation strategy of wild yak [J]". *Acta Zoologica Sinica*, 2004, 25 (6): 6-7.

[4] Liu Yuan."National Grassland Monitoring Report, 2014 [J]". *Chinese Journal of Animal Husbandry*, 2015, (8): 18-31.

[5] YE Xue-Bing. "Estimation of Feed Intake and Several Digestive Physiological Indices of Grazing Yaks[J]". *Chinese Herbivorous Animal Science*, 2003, 23 (5): 5-7.

[6] Wenxue Hong, Jinjia Wang. "*Genetic algorithm-based clustering techniqueVisualization and Visualization Analysis Study[J]*". Yanshan University, 2010, 34(2):95-99.

[7] Deng YF, et al. "Studies on the growth performance of yak [C]". *China Cattle Industry Development Conference*.2012.

[8] WANG Qing-hua, LIU Shen-qing. "Study on the Optimum Mathematical Model of Yak Herd Structure and Its Slaughter Scheme [J]". *ChineseYaks*, 1990 (2): 27-36.

[9] Georgin Lau and LeiPan. "*A 5-step guide to data visualization[J]*". Elsever, 28 January 2015, "https://www.elsevier.com/connect/a-5-stepguide-to-data-visualization".

Clinical Evaluation of UR-System-PARKO for Recovery of Motor Function of Severe Plegic Hand after Stroke

Hirofumi Tanabe
Department of Health Sciences, Shonan University of Medical Sciences
16-48 Kamishinano, Totsuka-ku, Yokohama, Kanagawa 244-0806, Japan
E-mail: hirofumi.tanabe@sums.ac.jp

Yoshifumi Morita
Nagoya Institute of Technology
Gokiso-cho, Showa-ku, Nagoya, Aichi 466-8555, Japan

Abstract

The first author has developed TANABE therapy for severe hemiplegic stroke patients. In the therapy, he performed repeated facilitation training using his hands on patients to help them recover their motor function and achieved a good treatment outcome. In this paper we developed a training system (UR-System-PARKO) on the basis of TANABE therapy. The clinical test of the therapeutic effect of the UR-System-PARKO was performed in severe plegic hand. As a result, the active ranges of motion of finger extension were improved, and Electromyogram ignition increased after the training. Moreover, the Modified Ashworth Scale scores of finger extension were increased. These results show the effectiveness of the training by the UR-System-PARKO for recovery of motor function for finger extension of the severe plegic hand.

Keywords: List four to six keywords which characterize the article.

1. Introduction

With Japan's gradual advancement towards a so-called superannuated society, the number of people physically challenged by disease and by aging is increasing.
The corresponding increase in the workload of therapists has become a social issue.

Moreover, according to proposals for health care reform in the rehabilitation field, a system with empiric treatment for evidence-based medicine (EBM) has to be implemented. This change will be accelerated by introducing technology, such as robotics, mechatronics, information processing, and motion control, into the rehabilitation exercises administered by therapists in order to reduce their workload and to improve the therapeutic effects.

Recently, it has been shown that the motor function of stroke patients may be restored even six months or more after the occurrence of the stroke.[1,2] However, the severity of hemiplegia after the stroke was moderate in all patients who recovered motor function in these reports. More than half of the stroke survivors have a severe plegic hand with difficulty in extending the fingers.[3] Therefore, the need for developing a method to treat severe plegic hands is significant.

The first author in an occupational therapist who developed the TANABE therapy for severe hemiplegic stroke patients. With this therapy, he performed repeated facilitation training using his hands on patients to help them recover their motor function, and a good treatment outcome was achieved.[4] In addition to a book on this technique, he has trained many therapists[5] (Fig. 1). As a result, many therapists have successfully restored finger movement in patients with severe plegic hands. This facilitation method increases the output of the extensor digitorum muscle force through extension exercises of the elbow joint while applying resistance to the tips of the fully extended hemiplegic fingers. In this type of training, the therapist has to spend a lot of time with each patient. Therefore, we developed a rehabilitation support system (UR-System-PARKO) designed to reduce the burden on the therapist for resistance training.

The simplified training system previously developed by us for resistance training of hemiplegic upper limbs was applied to a new support system for the hands. This simplified training system provides unidirectional resistance training. We have also developed a brace for securing the plegic hand to the apparatus. The objective of this study was to verify the effect of training on increasing the output of the extensor digitorum muscle force using the UR-System-PARKO on a severe plegic hand.

2. Training System for Recovery of Motor Function

2.1. *The previous training system*

We developed rehabilitation support systems for resistance training of hemiplegic upper limbs, namely UR-System 1[6,7] and UR-System 2[8]. The UR-System 2 is referred to as the previous training system in this paper. The previous training system is a force display system with one degree-of-freedom that has a mechanical system and a controller. The mechanical system consists of a brace, a training arm, and a powder brake (SINFONIA TECHNOLOGY CO., Ltd., PRB-2.5H). The patient moves the training arm by himself/herself. The brace is attached to the tip of the training arm, which is used to secure the patient's forearm to the apparatus. The brace has two degrees-of-freedom, by which the yawing and pitching motions of the forearm are possible. The powder brake generates a brake force that serves as the resistance force during training. Because this system is not equipped with motors, it is extremely safe and low cost. This system is equipped with an encoder and a strain gauge as a force sensor. The angle of the training arm is measured by the encoder and is used in the control program. The resistance force is measured by the strain gauge and is used only for monitoring.

Fig. 1. The author has developed the TANABE therapy for severe hemiplegic stroke patients.

2.2. *Functions of the previous training system*

In the earlier study[7], it was found from an interview that the therapist selectively uses four different resistance patterns during resistance training. These patterns were also detected from the movement analysis performed during the manual training by the therapist using his hands. The four different resistance patterns, namely a step mode, a slope mode, a wall mode, and a constant mode, are installed in the controller. Control programs based on these results are installed in the controller. This system is equipped with the six functions. The Resistance display function enables therapists to perform various types of resistance training by changing the arm length and the resistance level. The maximum resistance was 49 N when the length of the training arm was set to 0.75 m. The touch panel parameter setting function enables therapists to easily set the parameters of the resistance patterns by pushing the buttons on the touch panel display. The parameters consist of the magnitudes and the positions of the resistance patterns. The magnitudes are selected from among nine levels. The positions are determined by moving the training arm and stopping it at the desired position. This function provides good visibility and ease of use for therapists.

2.3. *Modification of the training system to facilitate finger extension*

In order to improve motor function, especially to facilitate finger extension, an additional device was installed in the training apparatus. A thermoplastic splint for fixation was prepared to fix the plegic hand of a hemiplegic patient in complete extension. Rails were laid on the arm-fixing plate to allow sliding the splint on the plate. Rods were set individually to the index, middle, and ring fingers of the plegic hand, and the hand was set on the arm-fixing plate so that the patient could push the arm with her/her fingertips (Fig. 2).

3. Clinical Evaluation of Therapeutic Effect

We conducted clinical tests on patients with severe chronic plegic hands to verify the therapeutic effects of the training with the UR-System-PARKO.

3.1. *Assessment*

The therapeutic effects of the training with the UR-System-PARKO were assessed by using the surface electromyogram (EMG), the modified ashworth scale (MAS), and the active range of motion (A-ROM) test. An EMG electrode pad was applied to the extensor digitorum muscle, and firing of the extensor digitorum muscle during exercise was measured. The MAS is one of the quantitative evaluation methods for spastic paralysis, which is rated in 6 levels. Level 6 indicates no increase in muscle tone.

Level 0 indicates that the affected parts are rigid in either flexion or extension. The A-ROM test is performed to evaluate voluntary motor performance and has been widely used in clinical settings. The A-ROM is measured when a patient moves the joint without any assistance to the muscles surrounding the joint.

3.2. *Patient*

The subject was a hemiplegic patient in his 40s who had suffered a stroke 8 years ago. The MAS score presenting the grade of spasticity was 3. (He had a more marked increase in muscle tone through most of the ROM, but the affected part (s) easily moved). The patient did not experience any pain in the training with UR-System-PARKO. The study content was explained and written consent was obtained from the patient.

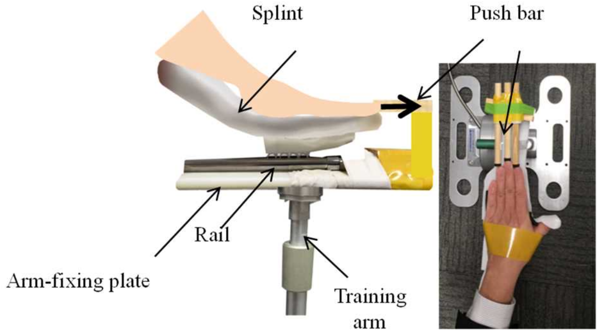

(a) Lateral view (b) View from directly above

(c) Training

Fig. 2. UR-System-PARKO.

3.3. *Methods*

3.3.1. Setting

The fingers of the patient were set on the splint in the fully extended position followed by fixation to the arm of the UR-System-PARKO. First, the therapist tried the technique facilitating the extensor digitorum muscle of the plegic hand to confirm the exercise initiation and completion positions and the grade and timing of resistance loading.

Then, the subject's forearm was set on the splint and fixed to the arm-fixing plate of the UR-System-PARKO. Then, the rods were set to the fingertips of the plegic hand to push the lever. The exercise initiation and completion positions, resistance value, and initiation and completion positions of resistance loading confirmed by the therapist beforehand were entered into the UR-System-PARKO using the operating the panel. The resistance value was set at 15 N.

3.3.2. Comparison of the output of the extensor digitorum muscle force between the positions of applying resistance load

For manual facilitation treatment of the extensor digitorum muscle, the output of the extensor digitorum muscle force can be increased by loading resistance on the fingertips. The position of pushing the UR-System-PARKO lever was set at 2 sites: 1) the fingertips of the plegic hand and 2) the forearm. The subject pushed the UR-System-PARKO lever against the resistance 10 times with each site, and the muscle force output measured using the EMG was compared between the 2 sites.

3.3.3. Comparison of the active range of motion and flexor spasticity of the plegic hand between before and after training with the UR-System-PARKO

Training was set so as to load resistance on the fingertips. The subject moved the hand from the initiation to the completion position and repeated the motion 30 times. A-ROM and MAS were evaluated before initiation and after completion of the exercise training.

3.3.4. Results and considerations

On comparison of the output of the extensor digitorum muscle force between the different resistance loading positions, the muscle force output by pushing the lever with the fingertips of the plegic hand was greater than that by pushing with the forearm on visual observation (Fig. 3). The training with the UR-System-PARKO increased the A-ROM of the finger extension when compared with that before training (Fig. 4). The MAS of the finger extensors was 2 before training, and it increased to 4 after training.

4. Conclusion

A therapeutic effect of the training with the UR-System-PARKO was shown. The UR-System-PARKO can improve the motor function of patients with a severe plegic hand after a stroke. The spasticity of the finger extension is reduced after the training. The A-ROMs of the finger extension are expanded after the training.

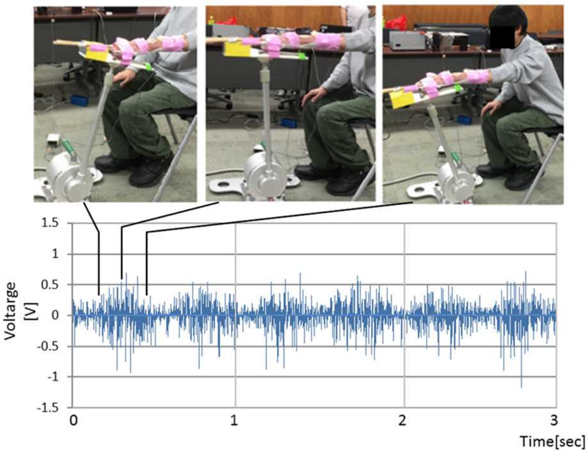

(a) The paralyzed fingers push a lever.

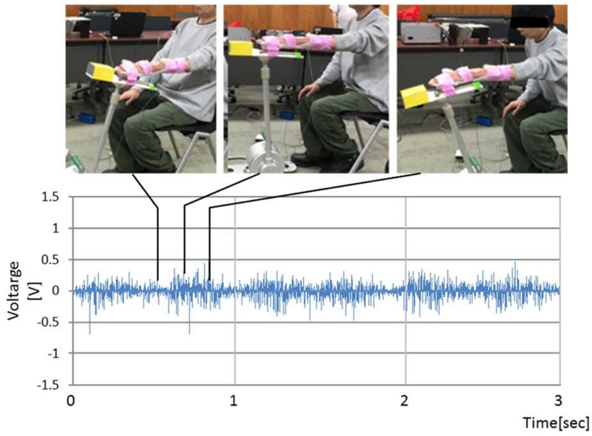

(b) The paralyzed forearm pushes a lever.

Fig. 3. Electromyograms of the extensor digitorum muscle while pushing the lever of the UR-System-PARKO (Firing increased when the subject pushed the lever with the fingertips of the plegic hand compared with that caused by pushing with the forearm.)

References

1. S. L. Wolf, C. J. Winstein, J. P. Miller, P. A. Thompson, E. Taub, G. Uswatte, D. Morris, S. Blanton, D. Nichols-Larsen, P. C. Clark, The EXCITE Trial: Retention of Improved Upper Extremity Function Among Stroke Survivors Receiving CI Movement Therapy, *Lancet Neurol.* **7**(1) (2008) 33–40.

2. J. Whitall, S. M. Waller, K. H. Silver, R. F. Macko, Repetitive bilateral arm training with rhythmic auditory cueing improves motor function in chronic hemiparetic stroke, *Stroke* **31**(10) (2007) 2390-2395.
3. H. Nakayama, H. S. Jørgensen, H. O. Raaschou, T. S. Olsen, Recovery of upper extremity function in stroke patients: the Copenhagen Stroke Study, *Arch. Phys. Med. Rehabil.* **75**(4) (1994) 394-398.
4. H. Tanabe, T. Nagao, R. Tanemura, Application of Constraint-induced Movement Therapy for People with Severe Chronic Plegic Hand, Asian J. Occupational Therapy, **9**(1) (2011) 7-14.
5. H. Tanabe, *The approach that recovers for a central nerve disorder -TANABE Therapy-* (Human Press, Tokyo, 2016).
6. Y. Morita, N. Sato, H. Ukai, H. Tanabe, T. Nagao, R. Tanemura, Y. Takagi and Y. Aoki, Clinical Evaluation of Training System for Recovery of Motor Function after troke in Patients with Hemiplegia, in *Proc. 2nd Int. Conf. on NeuroRehabilitation (ICNR2014 in Aalborg, Denmark)* (2014), pp.83-92.
7. H. Tanabe, M. Mitsukane, N. Toya, R. Takeichi, H. Hattori, Y. Morita, Y. Takagi, N. Hasegawa, Clinical Evaluation of UR-System 2 for Recovery of Motor Function of Plegic Upper Limb after Stroke, *J. Robotics, Networking and Artificial Life*, **3**(1), (2016) 33-36.
8. Y. Morita, N. Toya, R. Takeichi, H. Hattori, H. Tanabe, Y. Takagi, N. Hasegawa, Development of 'UR-System 2': a training system for recovery of motor function of plegic upper limb after stroke, *Advanced Robotics*, **30**(21) (2016)
9. Y. Iida, Y. Hiramatsu, K. Yamazaki, Y. Morita, H. Ukai, H. Tanabe, R. Tanemura, K. Yokoyama, Development of resistance training and evaluation support system for upper limbs - Study on resistance training using robot in CI therapy, in *Proc. 11th SICE System Integration Division Annual Conf.*, (2010), pp.1808–1811. (in Japanese).

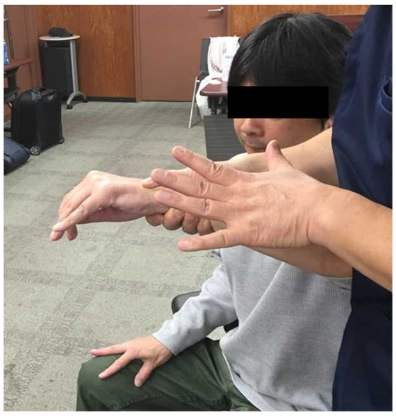

(a) Before training

(b) After training

Fig. 4. Finger extension before and after training.

A Piston Finger Device for Restoring the Motor Function of Chronic Plegic Fingers: Analysis of the Piston Finger Technique

Mengsu Wang*

Department of Electrical and Mechanical Engineering, Nagoya Institute of Technology, Gokiso-cho, Syouwa-ku, Nagoya, Aichi 466-8555, Japan

Hirofumi Tanabe†

Department of Health Sciences, Shonan University of Medical Sciences, 16-48 Kamishinano, Totsuka-ku, Yokohama, Kanagawa 244-0806, Japan

Kenji Ooka*

Department of Electrical and Mechanical Engineering, Nagoya Institute of Technology, Gokiso-cho, Syouwa-ku, Nagoya, Aichi 466-8555, Japan

Yoshifumi Morita*

Department of Electrical and Mechanical Engineering, Nagoya Institute of Technology, Gokiso-cho, Syouwa-ku, Nagoya, Aichi 466-8555, Japan

E-mail: m.wang.188@nitech.jp, hirofumi.tanabe@sums.ac.jp, k.oooka.446@nitech.jp, morita@nitech.ac.jp
http://www.nitech.ac.jp/eng/index.html

Abstract

A piston finger technique (PFT) was developed for restoring the motor function of chronic plegic fingers, with good treatment outcomes, including reduced spasticity and improved muscle shortening. Before developing a piston finger device (PFD) simulating the PFT, we analyzed the PFT by using a motion capture system. The motion of a chronic plegic index finger was investigated after administering two types of PFT-based treatment. The ranges of motion of the proximal interphalangeal and metacarpophalangeal joints of the index finger, and the vibration width and frequency during treatment were measured. These results will be useful for developing a PFD.

Keywords: Piston finger technique, Plegic finger, Spasticity, Motion analysis, Piston finger device

1. Introduction

The number of patients with cerebrovascular disease in Japan in 2014 has reached 1.179 million.[1] The main sequelae of cerebrovascular disease is hemiplegia, and approximately 80% of patients with chronic hemiplegia have chronic finger paralysis. Among the symptoms of hemiplegia, the decreased motor function of the fingers is the most difficult to recover. Owing to hand paralysis, nursing care is needed in many situations in daily life and many patients are forced to give up self-sustaining living.

In hand rehabilitation therapy, the therapist performs treatment by moving the patient’s fingers passively. However, because of the lack of therapists, many patients do not receive adequate treatment. In view of this situation, we aimed to develop a rehabilitation device to support therapists.

(a) Treatment with piston finger technique

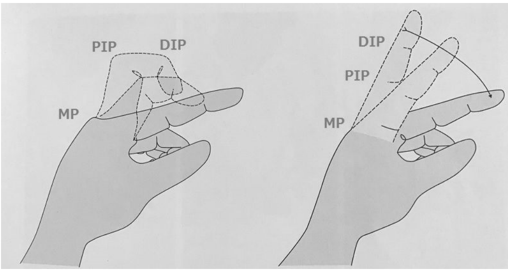

(b) Pattern 1 (c) Pattern 2

Fig. 1. Piston finger technique [6].

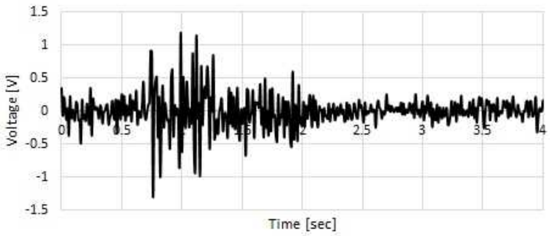

(a) Before PFT treatment.

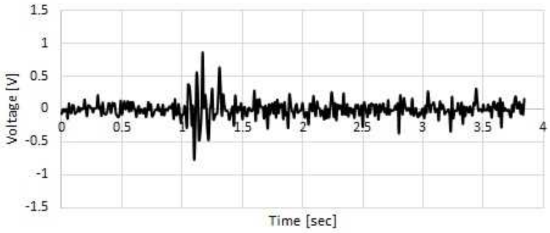

(b) After PFT treatment.

Fig. 2. Electromyograms of the flexor digitorum superficialis muscle of a plegic index finger.

Currently, in Japan, a treatment method has been used for therapeutic stimulation and motion reconstruction of paralyzed limb according to upper motor neuron disorders such as stroke and spinal cord injury by therapeutic electrical stimulation and functional electrical stimulation.[2] In the development of equipment supporting finger rehabilitation, a perception support system has been developed that allows biofeedback transfer from the paralyzed side motion to the non-paralyzed side so that awareness can be directed to the paralyzed side movement sensation through the non-paralyzed side.[3]

In other countries, a robotic interface for training hand and finger functions has been developed. It is a cable-actuated rehabilitation system where each finger is attached to an instrumented cable loop that allows force control and a predominantly linear displacement.[4]

However, only a few studies have been conducted on the validation and motion analysis of manual treatment methods. Moreover, only few research studies have been conducted to develop rehabilitation devices simulating the treatment method.

On the other hand, the second author developed a piston finger technique (PFT) for restoring the motor function of chronic plegic fingers and has achieved good treatment outcomes, including reduced spasticity and improved muscle shortening.[5]

In this study, we performed myoelectric measurement to demonstrate the effectiveness of PFT for a paralyzed index finger. We also analyzed the finger motion with the PFT by using a motion capture system to clarify the finger joint angles and the frequency during the repeated motion by PFT.

2. PFT and Its Treatment Effect

2.1. *What is PFT?*

In general, when stretching treatment is applied to fingers with spasticity, the spastic muscle is temporarily improved. However, the spasticity often occurs again when the patient bends the affected finger. This is one of the troubles of many therapists engaged in the treatment of hemiplegia.

PFT is a technique for improving adhesion of soft tissues and spasticity. In the PFT, the therapist quickly repeats flexion and extension of the patient's finger joints. The PFT can decrease flexor spasticity in a short time and improve muscle contraction. The effect lasts longer than that by stretching treatment. Treatment with the PFT has two patterns as shown in Fig. 1.[5]

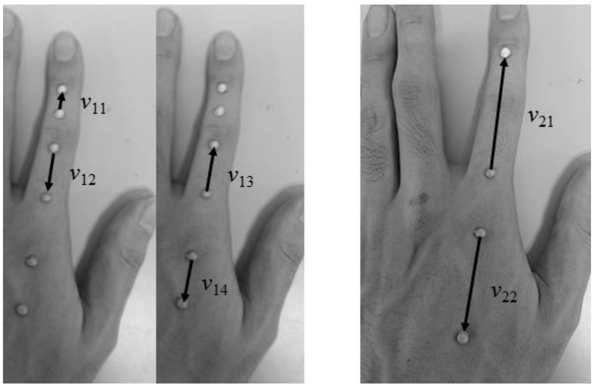

(a) Pattern 1. (b) Pattern 2.

Fig. 3. Marker attachment positions and vectors defined for computation of joint angles.

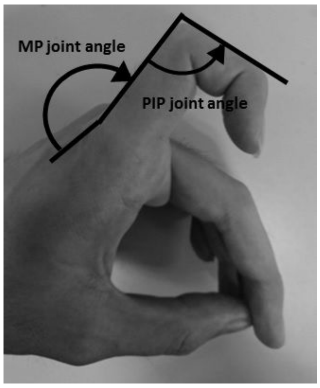

Fig. 4. MP and PIP joint angles.

In Pattern 1, the therapist, with one hand, holds and fixes the patient's plegic thumb with full abduction, and with the other hand, holds and moves the distal phalange of the patient's index finger. From the start positions, the metacarpophalangeal (MP) and proximal interphalangeal (PIP) joints are bended and extended, respectively. Then, the metacarpophalangeal (MP) joint is bended and extended quickly and repeatedly, while the proximal interphalangeal (PIP) joint is extended and bended quickly and repeatedly. PFT treatment is applied to the index, middle, and ring fingers individually or together. After PFT treatment with Pattern 1, the flexor spasticity of the four fingers diminishes.

In Pattern 2, the start positions of the MP, PIP, and distal interphalangeal (DIP) joints are extended fully. Then, the MP joint is bended and extended quickly and repeatedly, while keeping the DIP and PIP joints in the extended position. After PFT treatment with Pattern 2 the MP joints of four fingers can bend to the vicinity of the end feel within the range without feeling pain.

2.2. *Treatment effect of PFT*

To verify the therapeutic effect of the PFT treatment, the therapist applied the PFT treatment to the paralyzed index finger of a male adult in his forties. The paralytic side was the left. Nine years had passed since the onset of stroke.

After treatment, the Modified Ashworth Scale (MAS) scores of the extension of the patient's plegic index finger increased from 1 to 4. This means that spastic paralysis was reduced. Electromyograms of the flexor digitorum superficialis muscle of the patient's plegic index finger before and after treatment are shown in Fig. 2. Figure 2 shows that the abnormal muscle tone of the paralyzed finger during MAS testing by the therapist. The abnormal muscle tone was markedly reduced after PFT treatment. This means that spasticity was reduced by PFT and that the therapeutic effect was confirmed.

3. Analysis of the PFT

We analyzed the patient's finger motion during PFT treatment by using the VICON motion capture system (Vicon Motion Systems Ltd.).

3.1. *Motion measurement*

In Pattern 1, as the DIP joint was kept fully extended, we measured the PIP and MP joint angles of the index finger as shown in Fig. 3(a). Six markers consisting of two markers between the DIP and PIP joints, two markers between the PIP and MP joints, and two markers between the MP joint and the wrist were attached on the center line of the middle phalanges, proximal phalanges, and metacarpals of the index finger, respectively. Vectors $\boldsymbol{v}_{11}$, $\boldsymbol{v}_{12}$, $\boldsymbol{v}_{13}$, and $\boldsymbol{v}_{14}$ were defined as shown in Fig. 3(a).

In Pattern 2, as the DIP and PIP joints were kept fully extended, we measured only the MP joint angle of the index finger as shown in the Fig. 3(b). Four markers consisting of one marker between the DIP and PIP joints, one marker between the PIP and MP joints, and

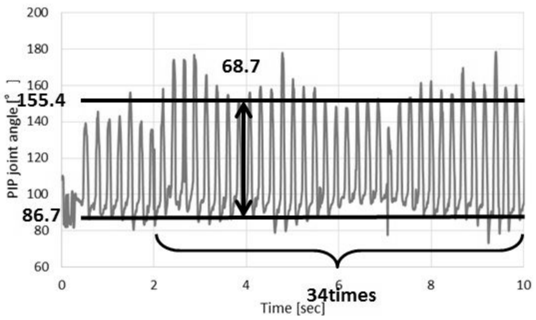

Fig. 5. Time history of PIP joint angle in Pattern 1.

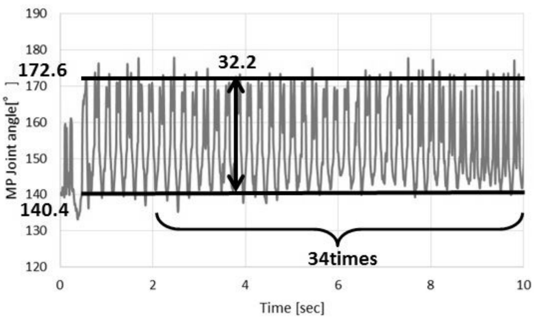

Fig. 6. Time history of MP joint angle in Pattern 1.

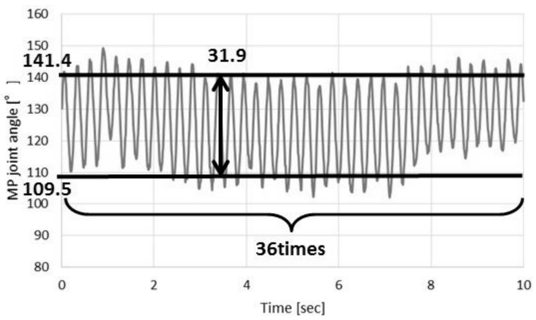

Fig. 7. Time history of MP joint angle in Pattern 2.

Table 1. Summaries of the joint angles in Patterns 1 and 2. (Start and End: start and end positions of the repeated motions, Diff.: difference between Start and End, x ($y - z$), x: mean value, y: maximum value, z: minimum value)

		Pattern 1 (degrees)	Pattern 2 (degrees)
PIP joint angle	Start	155.4 (135–178)	
	End	86.7 (73–96)	
	Diff.	68.7 (39–105)	
MP joint angle	Start	172.6 (168–177)	141.4 (136–148)
	End	140.4 (135–145)	109.5 (102–119)
	Diff.	32.2 (23–42)	31.9 (17–46)

two markers between the MP joint and the wrist were attached on the center line of the middle phalanges, proximal phalanges, and metacarpals of the index finger, respectively. Vectors $\boldsymbol{v}_{22}$ and $\boldsymbol{v}_{23}$ were defined as shown in Fig. 3(b).

3.2. *Computation of joint angles*

We computed the joint angles of the index finger during treatment. For this purpose, we measured the three-dimensional coordinates of the markers with VICON and computed the joint angles from the vectors shown in Fig. 3 (a) and (b). The PIP and MP joint angles were defined as shown in Fig. 4.

In Pattern 1, the PIP and MP joint angles were denoted by θ_{PIP1} and θ_{MP1}, respectively. The angles were computed by applying vectors $\boldsymbol{v}_{11}$, $\boldsymbol{v}_{12}$, $\boldsymbol{v}_{13}$, and $\boldsymbol{v}_{14}$ to the following equations:

$$\theta_{\mathrm{PIP1}} = \cos^{-1}\frac{\boldsymbol{v}_{11}\cdot\boldsymbol{v}_{12}}{|\boldsymbol{v}_{11}||\boldsymbol{v}_{12}|},\ \theta_{\mathrm{MP1}} = \cos^{-1}\frac{\boldsymbol{v}_{13}\cdot\boldsymbol{v}_{14}}{|\boldsymbol{v}_{13}||\boldsymbol{v}_{14}|}. \quad (1)$$

In Pattern 2, the MP joint angle was denoted by θ_{MP2}. The angle was computed by applying vectors $\boldsymbol{v}_{22}$ and $\boldsymbol{v}_{23}$ to the following equation:

$$\theta_{\mathrm{MP2}} = \cos^{-1}\frac{\boldsymbol{v}_{21}\cdot\boldsymbol{v}_{22}}{|\boldsymbol{v}_{21}||\boldsymbol{v}_{22}|}. \quad (2)$$

4. Analysis of the Results of the PFT

We analyzed the patient's finger motion during treatment by the therapist for 10 seconds. The time histories of the PIP and MP joint angles during treatment of Patterns 1 and 2 are shown in Figs. 5 to 7. The summaries of the mean, maximum, and minimum values of the joint angles at the start and end positions of Patterns 1 and 2 are shown in Table 1.

In Pattern 1, we analyzed the joint angles in Figs. 5 and 6 from 2 to 10 sec. We found that the PIP joint angle was moved by the therapist between 86.7° and 155.4°, and the MP joint angle was moved between 140.4° and 172.6°. Moreover, the frequency of the repeated motion was found to be 4.25 Hz.

In Pattern 2, we analyzed the joint angle in Fig. 7 from 0 to 10 sec. We found that the MP joint angle was moved between 109.5° and 141.4°. Moreover, the frequency was found to be 3.6 Hz.

5. Conclusion

The therapeutic effect of PFT was confirmed by the comparison of MAS scores and electromyograms before and after treatment. The motion analysis revealed the joint angles and frequencies of finger motion during PFT treatment. Future studies are needed to develop the specifications of a PFT treatment apparatus.

References

1. Ministry of Health, Labor and Welfare, The overview of the patient survey in 2014. http://www.mhlw.go.jp/toukei/saikin/hw/kanja/14/index.html (in Japanese)
2. T. Matsunaga, The NESS H200 Hand Rehabilitation System for upper extremity paralysis [in Japanese], in *Bull. Jpn. Soc. Prosthet. Orthot. Educ. Res. Dev.,* **29**(2) (2013) 80–82.
3. H. Iwata, K. Enjyoji, R. Komagata, S. Sugano, Somatic sensation-biofeedback system for paralyzed-finger rehabilitation: development of a self-rehabilitation assisting device simultaneously cross-displaying somatic sensation of fingers [in Japanese], in *Proc. the 2008 JSME Conf. on Robotics and Mechatronics*, 2008, 1P1-D14(1)-(2).
4. R. Kato, S. Nakagawa and H. Yokoi, Development of EMG-controlled Powered Exoskeleton for Hand Rehabilitation, in *Precision Engineering Society Academic Lecture Papers Collection*, (2011), pp. 499–500.
5. L. Dovat, O. Lambercy, R. Gassert, T. Maeder, T. Milner, T. C. Leong and E. Burdet, HandCARE a cable-actuated rehabilitation system to train hand function after stroke, *IEEE Trans. Neural. Syst. Rehabil. Eng.* **16**(6) (2008) 582–591.
6. H. Tanabe, Effective approach to reconstruct central nervous system diseases: Tanabe therapy [in Japanese]. (Human Press, Tokyo, 2016).

Verifying the Sleep-Inducing Effect of a Mother's Rocking Motion in Adults

Hiroaki Shibagaki
Department of Computer Science and Engineering, Graduate School of Engineering, Nagoya Institute of Technology
Gokiso-cho, Syouwa-ku, Nagoya, Aichi 466-8555, Japan

Keishi Ashida
Department of Computer Science and Engineering, Graduate School of Engineering, Nagoya Institute of Technology
Gokiso-cho, Syouwa-ku, Nagoya, Aichi 466-8555, Japan

Yoshifumi Morita
Department of Electrical and Mechanical Engineering, Graduate School of Engineering, Nagoya Institute of Technology
Gokiso-cho, Syouwa-ku, Nagoya, Aichi 466-8555, Japan

Ryojun Ikeura
Division of Mechanical Engineering, Graduate School of Engineering, Mie University
1577 Kurimamachiyacho, Tsu, Mie 514-8507, Japan

Kiyoko Yokoyama
Graduate School of Design and Architecture, Nagoya City University
2-1-10 Kitachikusa, Chikusa-ku, Nagoya, Aichi 464-0083, Japan

E-mail: h.shibagaki.502@nitech.jp

Abstract

Previously, we concluded that a mother's rocking motion is the most effective motion for inducing sleep in adults. We call it the candidate rocking motion. In this study, we confirm that the candidate rocking motion is more effective in inducing sleep than using no rocking motion. Moreover, we find that different to aromatherapy, the effectiveness of the candidate rocking motion varies only slightly between individuals. We conclude that the candidate rocking motion is effective for inducing sleep in adults.

Keywords: rocking motion, mother's rocking motion, sleep-inducing effect, electroencephalogram analysis

1. Introduction

Recently, the number of people suffering from high levels of stress has increased. This phenomenon is called a stressful society.[1] Every year, an increasing number of people suffer from stress-related illnesses. Moreover, sleep disorders are becoming more widespread in modern society because stress is one of the causes of insomnia. For the caregivers in nursing homes, it is a large burden to ensure the wellbeing of the patients who suffer from these problems.[2] Many people in modern society would benefit from stress reduction and sleep induction. It is known that when a mother embraces and rocks her baby, the baby feels comfortable and falls asleep quickly. We assume that a rocking motion simulating a mother's embrace would have the same effect on adults. The aim of our project is to develop a relaxation machine that reduces stress and induces sleep using a rocking motion similar to that of a mother. We expect that our research results will be useful for other relaxation systems and robots, such as the Robot for Interactive Body Assistance (RIBA), which assists caregivers in lifting patients in and out of their beds and wheelchairs.[3]

In our previous study, we analyzed a mother's embrace and rocking motion, and we designed and constructed an excitation apparatus that simulates a mother's rocking motion. We found that a mother uses two types of rocking motions and constructed a model .[4] Moreover, we examined ten types of rocking motions and found that the linear motion component of a mother's rocking motion was the most effective rocking motion for inducing sleep in adults. We refer to this motion as the candidate rocking motion.[5] However, we did not compare the sleep-inducing effect of the candidate rocking motion with other sleep-inducing methods, such as aromatherapy or music. [6, 7, 8]

In this paper, we report on our comparison of the sleep-inducing effect on adults of the candidate rocking motion without stimulus and aromatherapy. We evaluated the sleep-inducing effect through an electroencephalogram analysis.

2. Excitation Apparatus Simulating a Mother's Rocking Motion

In our previous work, we analyzed a mother's embrace and rocking motion to identify the motion's features.[4, 5] Based on the analysis results, we created a model of a mother's rocking motion, which is represented by

$$\begin{cases} x^{ref}(t)=A_x \sin(2\pi f_x t), \\ \theta^{ef}(t)=A_\theta \sin(2\pi f_\theta t+\phi)+B_\theta, \end{cases} \qquad (1)$$

where $x^{ref}(t)$ is the position and $\theta^{ef}(t)$ is the angle of the center of gravity of the baby. B_θ was determined from the angle of a comfortable sitting position reported in Ref. 9. We identified the rocking vibrations using the excitation apparatus shown in Fig. 1. The excitation apparatus has two degrees of freedom for linear motion and rotational motion. The parameters of the candidate rocking motion were determined as A_x = 0.098[m], f_x = 2.734[Hz], A_θ = 0[deg], f_θ = 0[Hz], $\phi = \pi/2$ [rad] , and B_θ = 25[rad].[5]

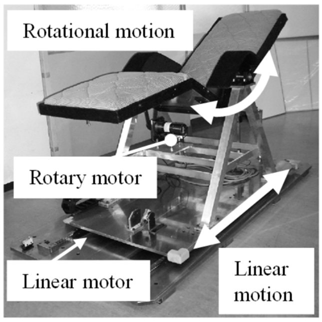

Fig. 1. Photograph of excitation apparatus.

3. Evaluation Method

3.1. *Electroencephalogram analysis and sleep stage*

We computed the sleep stage through an electroencephalogram (EEG) analysis. We used the SYNA ACT MT11 system (NEC Medical Systems Ltd.) to measure the brain waves and the MATLAB computing environment (The MathWorks, Inc.) to conduct a frequency analysis. We placed the EEG electrodes according to the International 10-20 system. To compute the sleep stage, we used the quantitative evaluation method[10] that was developed based on the definition by the Japanese Society of Sleep Research. We differentiate four different sleep stages. Sleep stage W indicates the state when being awake with mental activity, sleep stage 1 indicates the awakening and resting state, sleep stage 2 indicates a light sleeping state, and sleep stage 3 indicates a deep sleeping state.

3.2. *Evaluation index of sleep-inducing effect*

We evaluated the sleep-inducing effect with focus on "sleep latency" and "sleep depth." We define "sleep latency" as the time until the sleep enters stage 2 and denote it as $t_{\min}$. We define "sleep depth" as the total time spent in sleep stage 2 and sleep stage 3, and we denote it as S_{sum}.

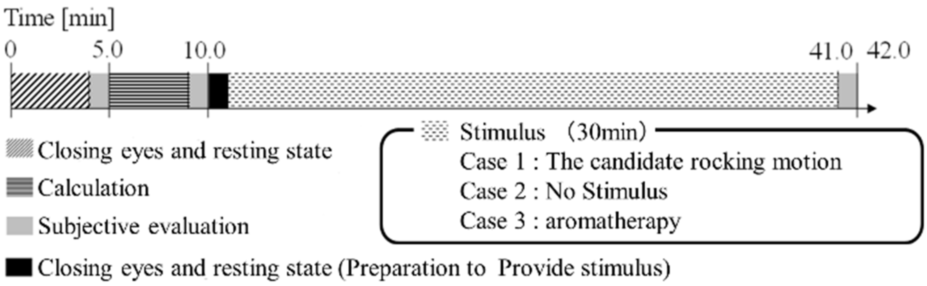

4. Experiment

4.1. *Experimental method*

Fig. 2 shows the experimental protocol. Each experiment took 42 minutes. For each test subject, we conducted three experiments in the morning under different conditions and on different dates. The start times are the same for each test subject. To conduct a comparative study, we prepared three different conditions, namely without rocking motion, with the candidate rocking motion, and with aromatherapy. We refer to them as Case 1, Case 2, and Case 3, respectively. For the aromatherapy, we picked genuine lavender (SANOFLORE) because of its verified relaxing effect.[11]

4.2. *Experimental results and consideration*

The test subjects consisted of ten healthy males. The mean value and standard deviation of their ages were 21.8 ± 0.6. We conducted 30 experiments with a mean room temperature and standard deviation of 23.1 ± 2.3 °C, a mean humidity and standard deviation of 26.8 ± 5.6%, and a mean illuminance and standard deviation of 22.3 ± 14.9 lx.

4.2.1. Sleep stage

We computed the sleep stage from an electroencephalogram (EEG) power spectrum for each interval. Fig. 3 shows the sleep stages of Subject D as an example. Each time interval was 4 minutes. We had nine analysis sections (AS) of sleep stages. AS No. 1 refers to closed eyes and resting state. AS No. 2 refers to calculation. AS No. 3 to AS No. 9 refer to either Case 1, Case 2, or Case 3. We compared Case 2 with Case 1 and Case 3 in AS No. 3 to AS No. 9.

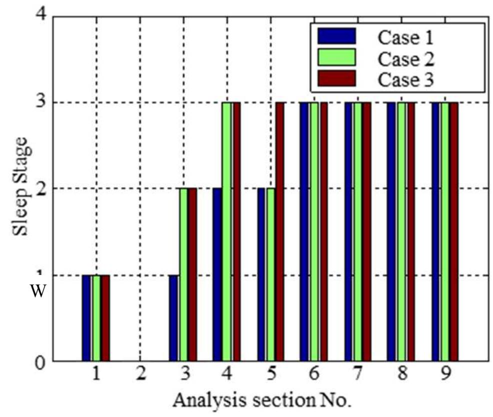

Fig. 3. Sleep stages of Subject D in three cases.

On the other hand, it was reported that there are individual differences in aromatherapy.[12] We had three test subjects for whom t_{min} was larger or S_{sum} was smaller in at least three sections of Case 3 as compared to Case 1. We can conclude that the sleep induction of the three test subjects became worse by applying aromatherapy. Therefore, we prepared two test groups, Group A and Group B. Group A consisted of all ten subjects while Group B did not contain the three test subjects mentioned above and consisted only of the seven remaining subjects. For Group B, we can compare the sleep-inducing effect of the candidate rocking motion with that of aromatherapy under severe conditions.

Figs. 4 and 5 show the mean values and standard deviations of the sleep stages of Group A and Group B, respectively. Most of the mean values of the sleep

Fig. 4. Mean values and standard deviations of sleep stages in Group A.

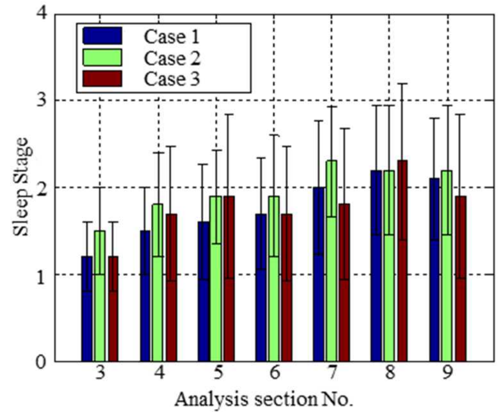

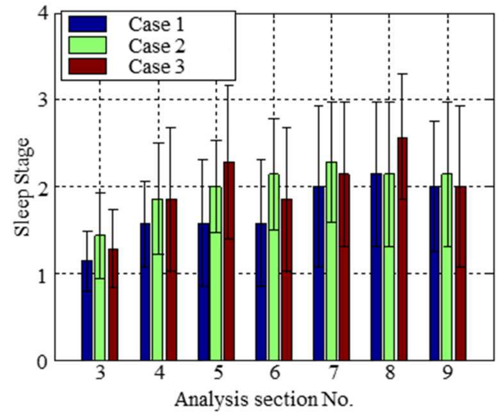

Fig. 5. Mean values and standard deviations of sleep stages in Group B.

stages in Case 2 were larger than the mean values in Case 1. In Fig. 5, most of the mean values of the sleep stages in Case 3 were larger than the mean values in Case 1. In Fig. 4, however, most of the mean values of the sleep stages in Case 3 were equal to or smaller than the mean values in Case 1 from AS No. 6 to AS No. 9.

4.2.2. Evaluation of sleep-inducing effect

We evaluated the sleep-inducing effect using the evaluation indices t_{min} and S_{sum}. The mean values and standard deviations of t_{min} and S_{sum} of Group A and Group B are shown in Figs. 6 and 7, respectively.

Figs. 6 and 7 show that the mean values of t_{min} and S_{sum} in Case 2 were equal to or greater than those in Case 3. We performed a statistical analysis using the IBM SPSS Statistics 22 software package. First, we verified the normal distribution by a Shapiro-Wilk test and the homoscedasticity by a Levene test. The distribution of t_{min} did not exhibit a normal distribution and showed homoscedasticity in both groups. The distribution of S_{sum} exhibited a normal distribution and showed homoscedasticity in both groups. Thus, we

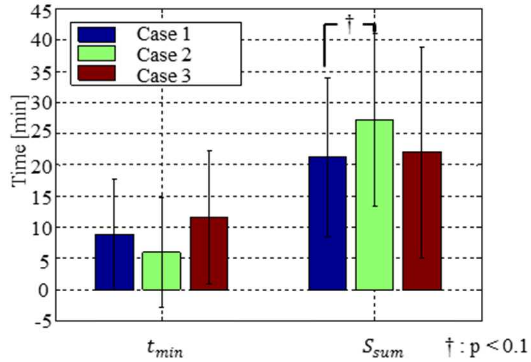

Fig. 6. Mean values and standard deviations of the two performance indices in Group A.

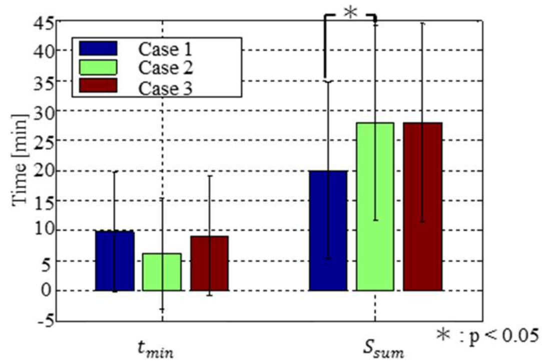

Fig. 7. Mean values and standard deviations of the two performance indices in Group B.

performed a one-way variance analysis and applied the Bonferroni method on S_{sum} of both groups. We also performed the Friedman test and the Wilcoxon signed rank sum test adjusted by the Bonferroni method on t_{min} of both groups.

We observed a significant trend (p=0.055) between the values of the S_{sum} index in Case 1 and Case 2 of Group A and significant differences (p=0.040) between the values in Case 1 and Case 2 of Group B.

4.2.3. Consideration

Fig. 6 shows that in Group A, Case 2 has the smallest mean value of t_{min}. However, there were no significant differences between any two pairs of all the cases. Fig. 7 shows the same results for Group B. However, Fig. 6 and Fig. 7 show that Case 2 has the largest mean value of S_{sum} for both, Group A and Group B. There were no significant differences except between Case 1 and Case 2.

Fig. 7 shows that the mean values of S_{sum} in Case 2 and Case 3 are almost the same and that there is a significant difference between Case 1 and Case 2. However, there is no significant difference between Case 1 and Case 3. Therefore, we assume that, different to the candidate rocking motion, in the case of aromatherapy there are individual differences in the sleep-inducing effect.

5. Conclusion

In this paper, we demonstrated that the candidate rocking motion promotes a deep sleep in adults. We also showed that individual differences in the sleep-inducing effect were smaller in the case of the candidate rocking motion than in the case of aromatherapy.

As future work, we plan to compare the sleep-inducing effect of the rocking motion with sleeping pills.

References

1. Ito, H. and Ishino, Y., Adverse Effects of Sleep Deprivation, Iho Fuji, No.124 (2003) (in Japanese), p.1.
2. Mishima, K., Sleep Problems in Dementia, Proceedings of the Annual Meeting of the Japanese Research Group on Senile Dementia, Vol.17 (2010) (in Japanese), pp.109-113.
3. RIKEN-TRI Collaboration Center for Human-Interactive Robot Research (RTC), World's first robot that can lift up a human in its arms, RIBA, (online), available from <http://rtc.nagoya.riken.jp/RIBA/index-e.html>, (accessed on 28 November, 2016)
4. Morita, Y., Yamaguchi, K., Ashida, K., Ikeura, R., Yokoyama, K., Verification of Sleep-Inducing Effect by Excitation Apparatus Simulating Mother's Embrace and Rocking Motion, Proceedings of the 9th International Workshop on Robot Motion and Control (RoMoCo '13), pp.80-85 (2013)
5. Ashida, K., Morita, Y., Ikeura, R., Yokoyama, K., Ding, M., Mori, Y., Effective rocking motion for inducing sleep in adults - Verification of effect of mother's embrace and rocking motion -, Journal of Robotics, Networks and Artificial Life, Vol. 1, No. 4, pp.285-290 (2015)
6. Yoshida, K., Mizuta, T., Takeshima, Y., Nishida, K., Tsukida K. and Takeda, C., The Effects of Foot Bathing on the Central Nervous System with or without Lavender Oil-An Electroencephalographic Study-, Fukui Medical University research magazine Volume 2, No. 1, No. 2 merger issue (2001) (in Japanese)
7. Momose, K., Fujisawa, Y. and Uchiyama, A., Effects of Music on Physiological Measurements and Mood States, and Their Correlation with Impression of the Music, Journal of International Society of Life Information Science 22(2), 545-551, 2004(in Japanese)
8. Kanazawa, Y., Moritani, K., Momose, I., Furuhashi, S., and Ohtsuka, Y., Examination of Stress relieving Effects of Drinking Chamomile Tea and Peppermint Tea in the Morning, BULLETIN OF TENSHI COLLEGE, vol.10(2010) (in Japanese), pp.23-34
9. Sasaki, Y., Kawamoto, T. and Yamazaki, N., Development of an Experiment Bed for Searching Comfort Semi-Sitting Position, Japanese Journal of Ergonomics, Vol.42, No.6 (2006), pp.373-380.
10. Ashida, K., Yamaguchi, K., Morita, Y., Sato T., Ikeura, R. and Yokoyama, K., Verification of Sleep Inducing Effect by Mother's Embracing and Rocking Motion - Consideration by Sleep Stage Judgment Based on EEG Analysis -, Proceeding of the 2013 JSME Conference on Robotics and Mechatronics, 2A2-G05(1)-(4), 2013(in Japanese)
11. Yurugi Y. and Suzuki T., A review of Lavender Fragrance and Neural Function, The Bulletin of Kansai University of Health Sciences 6(2012) (in Japanese), 109-115
12. Miyajima, M., Moriya, K., and Agishi, Y., The effects of bathing with, lavender oil on relaxation as assessed from changes in skin temperature, JAPANESE JOURNAL OF BIOMETEROLOGY Vol. 34 (1997) (in Japanese) No. 4 P 139-146

Design of Automated Real-Time BCI Application Using EEG Signals

Chong Yeh Sai, Norrima Mokhtar, Hamzah Arof
Department of Electrical Engineering, University of Malaya
Kuala Lumpur, Malaysia

Masahiro Iwahashi
Department of Electrical Engineering, Nagaoka University of Technology
Nagaoka, Niigata, Japan

E-mail: chongyeh.sai@siswa.um.edu.my, norrimamokhtar@um.edu.my, ahamzah@um.edu.my, iwahashi@vos.nagaokaut.ac.jp
www.um.edu.my, www.nagaokaut.ac.jp

Abstract

This study proposed a design of real time BCI application using EEG recording, pre-processing, feature extraction and classification of EEG signals. Recorded EEG signals are highly contaminated by noises and artifacts that originate from outside of cerebral origin. In this study, pre-processing of EEG signals using wavelet multiresolution analysis and independent component analysis is applied to automatically remove the noises and artifacts. Consequently, features of interest are extracted as descriptive properties of the EEG signals. Finally, classification algorithms using artificial neural network is used to distinguish the state of EEG signals for real time BCI application.

Keywords: Electroencephalogram, EEG Pre-processing, Feature Extraction, Supervised Machine Learning, Artificial Neural Network.

1. Introduction

Electroencephalogram (EEG) is the recording of electrical activities of human brain using electrodes attached to the scalp. Conventionally, EEG is used for clinical diagnosis of epilepsy and sleep disorder. In recent decades, EEG have been studied and finding increasing use in Brain Computer Interface (BCI) application. The EEG signals are described in frequency bands of delta (0.5 to 4 Hz), theta (4 to 8 Hz), alpha (8 to 12 Hz) and beta (12 to 32 Hz), each of which is attributed to different aspects of brain activity.

In practical settings, EEG signals are often contaminated by noises and artifacts during the recording. There are two types of artifacts that contaminated the EEG signals, namely, biological and environmental artifacts.[1,2] Biological artifacts are signals arising from non-cerebral origin of the human body, such as cardiac, ocular or muscles activity. On the other hand, environmental artifacts are signals that originate from outside of human body, such as interference from external devices. Artifacts recorded in EEG signals distorted power spectrum and influenced the decision-making process of BCI application. Therefore, a pre-processing step to remove the noises and artifacts of EEG signals is necessary.

Conventional methods using linear filters incurred substantial loss of cerebral activity because of the inherent spectral overlap between neurological activity and signal artifacts.[3,4] Wavelet based multiresolution analysis using Discrete Wavelet Transform (DWT) is more effective in removing the target artifacts, while retaining the cerebral activities of interest in EEG signals.[5,6] Meanwhile, Independent Component Analysis (ICA) algorithm using blind source separation is able to isolate the target artifacts into a separated Independent Component (IC).[2,7] Combinatorial use of Wavelet Multiresolution Analysis (WMA) and ICA are able to isolate and remove noises and artifacts without incurring substantial loss of cerebral activities of interest in EEG signals.[1,8]

In this study, we designed an automated pre-processing step using WMA and ICA to remove noises and artifacts in EEG signals. Then, feature extraction and classification of EEG signals is applied for real time BCI application.

2. Methodology

2.1. *Wavelet Multiresolution Analysis*

WMA incorporates the steps of DWT and inverse DWT.[8] The DWT is an implementation of wavelet transform using discrete set of wavelet scales and transitions.[6,9] DWT consists of sequential application of low- and high-pass filters to decompose a discrete signal into multiple wavelet components, as shown in Figure 1. Here, x[n] represents a channel of EEG signal passed through a low pass filter, g[n] and a high pass filter, h[n] simultaneously. This process is repeated until each channel of the EEG signal is decomposed into n levels of wavelet details, i.e. $D_1(t)$, $D_2(y)$, ..., $D_n(t)$ and a mother wavelet of A_n.

On the other hand, inverse DWT is applied in a similar but reversed sequence by combining wavelet details and mother wavelet into a discrete EEG signal.

2.2. *Independent Component Analysis*

ICA model describes multivariate signals as a mixture of its source components, by assuming that the multivariate signals, x are separable into their statistically independent and non-Gaussian source components, s. The relationship between the signals and its source components is described by the equation

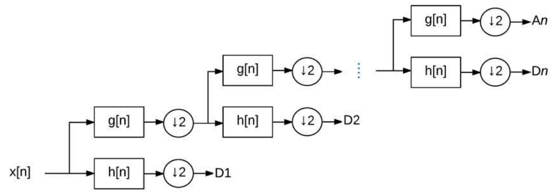

Fig. 1. Block diagram of Discrete Wavelet Transform (DWT) of a discrete signal, x[n]. The annotation ↓2 denotes sampling reduction by a factor of 2, i.e. two-fold down-sampling of the signal.

$$x = As. \tag{1}$$

In equation (1), A is the unknown mixing matrix estimated by using the ICA algorithms.[7,10] The un-mixing matrix, W is then computed as the inverse of estimated mixing matrix. The source components, s are revealed by using the equation

$$s = Wx. \tag{1}$$

On the other hand, inverse ICA is accomplished by multiplying the inverse of estimated mixing matrix, W^{-1} with the source components, s.

2.3. *Artificial Neural Network*

Artificial Neural Network (ANN) is a computational model based on interconnected adaptive neurons that resemble the biological neural network.[11] Each processing neurons operating in parallel receives input from the input layer or its preceding tier and further the processed information to its successive tier or output layer. ANN can be described by the transfer functions of their neurons, the learning rules and the connection formula.[12] ANN are adaptive and able to learn by observing and weighting on the importance of input datasets. In supervised machine learning, ANN model trained with sufficient number of training data can be used to make prediction or classification on test data to determine the dataset in which the test data might belong.

3. Design of System

This study proposed a design of real time BCI application using the following steps: EEG recording, pre-processing, feature extraction and classification. The design of the system is illustrated in Figure 2.

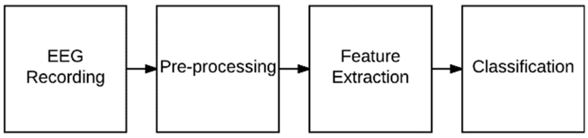

Fig. 2. Block diagram of the design of system for BCI application using EEG signals.

3.1. *EEG Recording*

EEG acquisition equipment g.USBamp (g.tec, Austria) is used to acquire the EEG signals. The electrodes are placed as specified by the 10-20 system. A total of 16 electrodes corresponding to channels FP1, FP2, F3, Fz, F4, T7, C3, Cz, C4, T8, P3, Pz, P4, O1, Oz, and O2 are used in this study. The ground electrode is set at FPz and reference point at the left earlobe (A1). The scalp impedance is kept below 5 kΩ. The recording is conducted with sampling rate of 256 Hz. A notch filter of 50/60 Hz and band pass filter of 0.5 to 100 Hz are applied to remove the electrical noise and frequency bands outside of EEG signals respectively. A sample of five seconds segment of the recorded EEG signals is shown in Figure 3.

3.2. *EEG Pre-processing*

Automated pre-processing step is applied to the recorded EEG signals using the following steps: (1) Wavelet Multiresolution Analysis is applied to decompose each channel by DWT to 8 levels with mother wavelet of db8.[5] Then, only the wavelet components of D3 to D8 corresponding to the frequency range of 0.5 to 32 Hz is retained to remove unwanted noises and artifacts outside the frequency range of interest. (2) Blind source separation using ICA is applied to isolate the artifactual components, in this case, the eye blink artifacts to be removed by wavelet denoise algorithm.[1,13] (3) Separated ICs and wavelet components are recombined using inverse ICA and inverse DWT respectively to reconstruct the clean EEG signals as shown in Figure 4.

3.3. *Feature Extraction*

The pre-processed EEG signals are separated into 1 second epochs and features of interest are extracted by using DWT. Each channel of the EEG signal is decomposed to wavelet details each represent the frequency bands of EEG signals defined as delta (0.5 to 4 Hz), theta (4 to 8 Hz), alpha (8 to 16 Hz) and beta (16 to 32 Hz) bands. The coefficients of the wavelet details are taken as features that characterize the properties of the EEG signals in each corresponding frequency band.

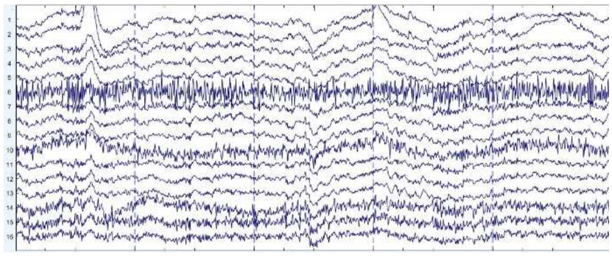

Fig. 3. The recorded 16-channel EEG signals before pre-processing is applied. Eye blinks artifacts is seen on 1s and 3-4s segments of the signals. Also, high frequency noises is seen on channel 6, 10, 14, 15 and 16 (T7, T8, O1, Oz and O2).

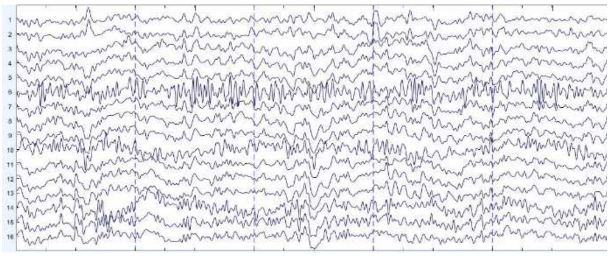

Fig. 4. Similar segment of EEG signals after pre-processing step is applied. Eye blink artifacts and high frequency noises are removed while underlying cerebral activities within frequency range of interest (0.5 to 32 Hz) is retained.

3.4. *Classification*

Classification of EEG signals is conducted using ANN. The ANN model is trained using both target and non-target datasets and applied to classify the test data in real time BCI application. In this study, we applied the system to classify target state of "alert with eyes-open" and non-target state of "relax with eyes-closed".[14] By using 1190 epochs of data and 10 layers of hidden neurons, an overall accuracy of 97.6 % calculated using 10 fold cross validation is achieved as shown in Table 1.

Table 1. Classification result for "alert with eyes-open" and "relax with eyes-closed" EEG signals.

Sensitivity	Specificity	Accuracy
98.0 %	97.2 %	97.6 %

4. Discussion

The proposed system design function to automatically filter and classify target data of EEG signals in real time BCI application. Recorded raw EEG signals are pre-processed using a combination of WMA and ICA to remove noises and artifacts while retaining cerebral activities in frequency bands of interest. The pre-processing steps are important as EEG signals are highly contaminated by noises and artifacts in a practical setting. Wavelet based multiresolution analysis are applied as wavelet decomposition is more effective in preserving the structure of the EEG signals in both time and frequency domains.[5,13] Mother wavelet of db8 is selected due to its balanced performance and computational simplicity for real time application.[5]

After the pre-processing steps, feature extraction using wavelet decomposition is applied to extract the features of interest. The features of interest are the coefficients of wavelet details each corresponding to frequency bands activities of delta, theta, alpha and beta band. The wavelet coefficients are computed due to its better performance in characterizing the structure of EEG signals. Lastly, supervised machine learning using trained ANN model is applied for classification of EEG signals. We are eager to apply the system in BCI applications in real time setting.

5. Conclusion

This study proposed a design of automated real time BCI application using EEG signals. EEG signals are notably noisy and contaminated by artifacts. The proposed pre-processing steps using WMA and ICA effectively removed the noises and artifacts with minimal distortion to the cerebral activities in frequency bands of interest. Then, feature extraction is applied using DWT to extract the coefficient of wavelet details corresponding to each frequency band of interest. Lastly, classification algorithm using ANN are applied to classify the EEG signals in real time BCI application.

Acknowledgements

The authors wish to acknowledge HIR grant (UM.C/HIR/MOHE/ENG/16 Account Code: D000016-16001) and PPP grant (PG260-2015B) for the financial support provided over the course of the study.

References

1. R. Mahajan and B. I. Morshed, Unsupervised Eye Blink Artifact Denoising of EEG Data with Modified Multiscale Sample Entropy, Kurtosis, and Wavelet-ICA, *IEEE Journal of Biomedical and Health Informatics* **19** (2015) 158-165.
2. T. P. Jung, S. Makeig, C. Humphries, T. W. Lee, M. J. McKeown, V. Iragui, *et al.*, Removing electroencephalographic artifacts by blind source separation, *Psychophysiology* **37** (2000) 163-78.
3. N. A. de Beer, M. van de Velde, and P. J. Cluitmans, Clinical evaluation of a method for automatic detection and removal of artifacts in auditory evoked potential monitoring, *J Clin Monit* **11** (1995) 381-91.
4. D. P. Subha, P. Joseph, R. Acharya U, and C. Lim, EEG Signal Analysis: A Survey, *Journal of Medical Systems* **34** (2010) 195-212.
5. M. Mamun, M. Al-Kadi, and M. Marufuzzaman, Effectiveness of Wavelet Denoising on Electroencephalogram Signals, *Journal of Applied Research and Technology* **11** (2013) 156-160.
6. S. Khatun, R. Mahajan, and B. I. Morshed, Comparative Study of Wavelet-Based Unsupervised Ocular Artifact Removal Techniques for Single-Channel EEG Data, *IEEE Journal of Translational Engineering in Health and Medicine* **4** (2016) 1-8.
7. C. Chunqi, D. Zhi, Y. Sze Fong, and F. H. Y. Chan, A matrix-pencil approach to blind separation of colored nonstationary signals, *IEEE Transactions on Signal Processing* **48** (2000) 900-907.
8. N. Mammone, F. L. Foresta, and F. C. Morabito, Automatic Artifact Rejection From Multichannel Scalp EEG by Wavelet ICA, *IEEE Sensors Journal* **12** (2012) 533-542.
9. G. W. Wornell, Emerging applications of multirate signal processing and wavelets in digital communications, *Proceedings of the IEEE* **84** (1996) 586-603.
10. A. Hyvarinen, Fast and robust fixed-point algorithms for independent component analysis, *IEEE Transactions on Neural Networks* **10** (1999) 626-634.
11. I. A. Basheer and M. Hajmeer, Artificial neural networks: fundamentals, computing, design, and application, *Journal of Microbiological Methods* **43** (2000) 3-31.
12. S. Agatonovic-Kustrin and R. Beresford, Basic concepts of artificial neural network (ANN) modeling and its application in pharmaceutical research, *Journal of Pharmaceutical and Biomedical Analysis* **22** (2000) 717-727.
13. J. H. Zhang, K. Janschek, J. F. Bohme, and Y. J. Zeng, Multi-resolution dyadic wavelet denoising approach for extraction of visual evoked potentials in the brain, *IEE Proceedings - Vision, Image and Signal Processing* **151** (2004) 180-186.
14. R. J. Barry, A. R. Clarke, S. J. Johnstone, C. A. Magee, and J. A. Rushby, EEG differences between eyes-closed and eyes-open resting conditions, *Clinical Neurophysiology* **118** (2007) 2765-2773.

A Hybrid Simulated Kalman Filter - Gravitational Search Algorithm (SKF-GSA)

Badaruddin Muhammad, Zuwairie Ibrahim, Mohd Falfazli Mat Jusof
Faculty of Electrical and Electronics Engineering, Universiti Malaysia Pahang,
26600 Pekan, Pahang, Malaysia

Nor Azlina Ab Aziz, Nor Hidayati Abd Aziz
Faculty of Engineering and Technology, Multimedia University,
75450 Melaka, Malaysia

Norrima Mokhtar
Faculty of Engineering, University of Malaya,
50603 Kuala Lumpur, Malaysia

E-mail: badaruddinmuhammad@yahoo.com, zuwairie@ump.edu.my, mfalfazli@ump.edu.my, azlina.aziz@mmu.edu.my, hidayati.aziz@mmu.edu.my, norrimamokhtar@um.edu.my

Abstract

In this paper, simulated Kalman filter (SKF) and gravitational search algorithm (GSA) are hybridized in such a way that GSA is employed as prediction operator in SKF. The performance is compared using CEC2014 benchmark dataset. The proposed hybrid SKF-GSA shown to perform better than individual SKF and GSA algorithm.

Keywords: hybrid, simulated Kalman filter, gravitational search algorithm, CEC2014 benchmark problem.

1. Introduction

The simulated Kalman filter (SKF) and gravitational search algorithm (GSA) are examples of population-based optimization algorithms. GSA has been introduced in 2009 by Rashedi *et al*. [1]. On the other hand, as a new estimation-based metaheuristic [2], the SKF has been introduced by Ibrahim *et al.* [3] in 2015. Even though both algorithms are population-based, however, they are inspired differently. In particular, GSA is inspired by Newtonian law of gravity and law of motion while SKF is inspired by the estimation capability of Kalman filter. In this paper, hybridization between GSA and SKF is proposed. Specifically, GSA is employed during the prediction stage of SKF.

2. Simulated Kalman Filter Algorithm

The SKF algorithm is illustrated in Figure 1. Consider n number of agents, SKF algorithm begins with initialization of n agents, in which the states of each agent are given randomly. The maximum number of iterations, $t_{\max}$, is defined. The initial value of error covariance estimate, $P(0)$, the process noise value, Q, and the measurement noise value, R, which are required in Kalman filtering, are also defined during initialization stage. Then, every agent is subjected to fitness evaluation to produce initial solutions $\{\boldsymbol{X}_1(0), \boldsymbol{X}_2(0), \boldsymbol{X}_3(0), \ldots, \boldsymbol{X}_{n-2}(0), \boldsymbol{X}_{n-1}(0), \boldsymbol{X}_n(0)\}$. The fitness values are compared and the agent having the best fitness value at every iteration, t, is registered as $\boldsymbol{X}_{\text{best}}(t)$. For function minimization problem,

$$\boldsymbol{X}_{\boldsymbol{best}}(t) = \min_{i \in 1,\ldots,n} fit_i(\boldsymbol{X}(t)) \qquad (1)$$

The-best-so-far solution in SKF is named as $\boldsymbol{X}_{\text{true}}$. The $\boldsymbol{X}_{\text{true}}$ is updated only if the $\boldsymbol{X}_{\text{best}}(t)$ is better (($\boldsymbol{X}_{\mathbf{best}}(t) < \boldsymbol{X}_{\mathbf{true}}$ for minimization problem, or $\boldsymbol{X}_{\mathbf{best}}(t) > \boldsymbol{X}_{\mathbf{true}}$ for maximization problem) than the $\boldsymbol{X}_{\text{true}}$.

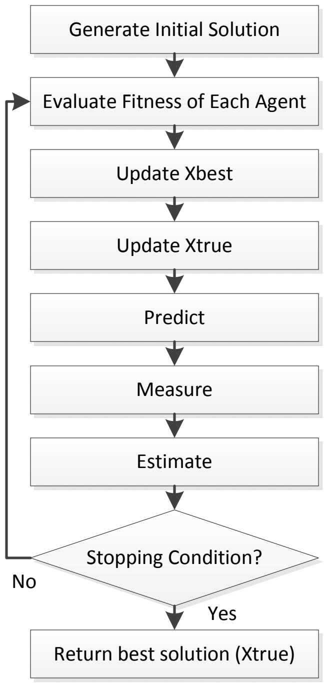

Fig. 1. The SKF algorithm.

The subsequent calculations are largely similar to the predict-measure-estimate steps in Kalman filter. In the prediction step, the following time-update equations are computed as follows:

$$\boldsymbol{X_i}(t|t) = \boldsymbol{X_i}(t) \tag{3}$$

$$P(t|t) = P(t) + Q \tag{4}$$

where $\boldsymbol{X_i}(t)$ and $\boldsymbol{X_i}(t|t)$ are the current state and transition/predicted state, respectively, and $P(t)$ and $P(t|t)$ are previous error covariant estimate and transition error covariant estimate, respectively. Note that the error covariant estimate is influenced by the process noise, Q.

The next step is measurement, which is modelled such that its output may take any value from the predicted state estimate, $\boldsymbol{X}_i(t|t)$, to the true value, $\boldsymbol{X}_{true}$. Measurement, $\boldsymbol{Z}_i(t)$, of each individual agent is simulated based on the following equation:

$$\boldsymbol{Z_i}(t) = \boldsymbol{X_i}(t|t) + \sin(rand\times 2\pi) \times |\boldsymbol{X_i}(t|t) - \boldsymbol{X_{true}}| \tag{5}$$

The $\sin(rand\times 2\pi)$ term provides the stochastic aspect of SKF algorithm and $rand$ is a uniformly distributed random number in the range of [0,1].

The final step is the estimation. During this step, Kalman gain, $K(t)$, is computed as follows:

$$K(t) = \frac{P(t|t)}{P(t|t)+R} \tag{6}$$

Then, the estimation of next state, $\boldsymbol{X}_i(t)$, is computed based on Eqn. (7).

$$\boldsymbol{X}_i(t+1) = \boldsymbol{X}_i(t|t) + K(t) \times (\boldsymbol{Z}_i(t) - \boldsymbol{X}_i(t|t)) \tag{7}$$

and the error covariant is updated based on Eqn. (8).

$$P(t+1) = \big(1 - K(t)\big) \times P(t|t) \tag{8}$$

Finally, the next iteration is executed until the maximum number of iterations, $t_{\max}$, is reached.

3. Gravitational Search Algorithm

In GSA, agents are considered as an object and their performance are expressed by their masses. The position of particle is corresponding to the solution of the problem. $\text{best}(t)$ and $\text{worst}(t)$ denote the best and the worst fitness value of the population t. The *best* and the *worst* for the case of function minimization problem are defined as follows:

$$\begin{aligned} best(t) &= \min_{j\in\{1,\ldots,N\}} fit_j(t) \\ worst(t) &= \max_{j\in\{1,\ldots,N\}} fit_j(t) \end{aligned} \tag{12}$$

while gravitational constant is defined as a decreasing function of time, which is set to G_0 at the beginning and decreases exponentially towards zero with lapse of time.

To give a stochastic characteristic to GSA, the total force acted on agent i in dth dimension is a randomly weighted sum of dth components of the forces exerted from other agents.

According to law of motion, the current velocity of any mass is equal to the sum of the fraction of its previous velocity and the variation in the velocity. Acceleration of any mass is equal to the force acted on the system divided by mass of inertia. Finally, the next iteration is executed until the maximum number of iterations, $t_{\max}$, is reached. In summary, the algorithm of standard GSA is shown in Figure 2.

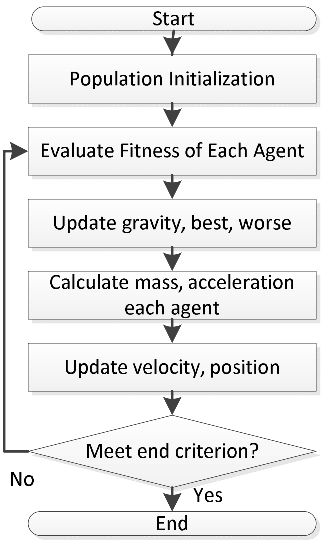

Fig. 2. The GSA algorithm.

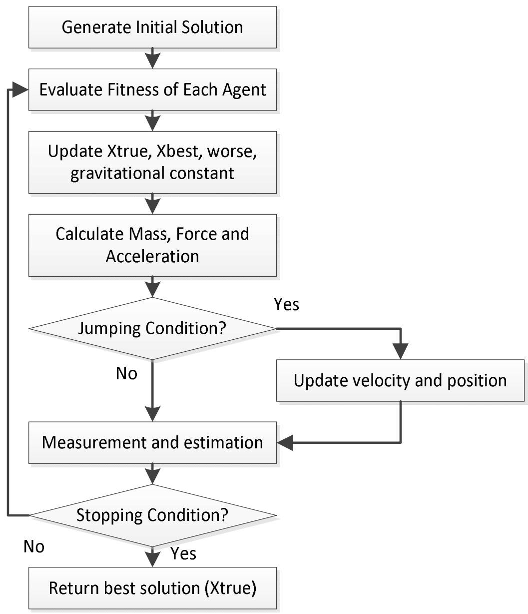

Fig. 3. Hybrid SKF-GSA algorithm.

4. Hybrid SKF-GSA Algorithm

Note that even though the SKF follows predict-measure-estimate steps as in Kalman filter, the states are not updated during the predict step. Hence, in the proposed hybrid SKF-GSA algorithm, GSA is employed as the prediction operator in SKF. An additional variable is introduced in hybrid SKF-GSA, which is the jumping rate, J_r, that is a predefined constant in the range of [0,1]. Prediction based on GSA is performed if jumping rate condition is satisfied. The hybrid SKF-GSA algorithm is shown in Figure 3.

In detail, the hybrid SKF-GSA algorithm begins with initialization of n agents, in which the states of each agent are given randomly. The maximum number of iterations, t_{max}, the initial value of error covariance estimate, $P(0)$, the process noise value, Q, the measurement noise value, R, and jumping rate value, J_r, are also defined during initialization stage. Then, every agent is subjected to fitness evaluation to produce initial solutions. After that, $\boldsymbol{X}_{\mathbf{best}}(t)$ and $\boldsymbol{X}_{\mathbf{true}}$ are updated according to SKF algorithm and *pbest* is updated according to GSA algorithm.

In hybrid SKF-GSA, the purpose of jumping rate, J_r, is to control the occurrence of the prediction. Based on our observation, the performance of SKF cannot be enhanced when GSA is executed at every iteration as the prediction operator of SKF. The following jumping condition is considered:

```
if   rand < Jr
     apply GSA in prediction
else
     proceed to measurement and estimation
end
```

where *rand* is a random number in the range of [0,1]. If *rand* $< J_r$, agents' velocity is updated according to GSA. For the position update, $\boldsymbol{X}_{\mathbf{predict}}$, is required and it is calculated as follows:

$$\boldsymbol{x}_{\boldsymbol{predict}}(t) = x_i(t) + v_i(t+1) \qquad (12)$$

The algorithm continues with measurement and estimation similar to SKF. The next iteration is executed until the maximum number of iterations, t_{max}, is reached.

5. Experiment, Result, and Discussion

The CEC2014 benchmark functions (http://www.ntu.edu.sg/home/EPNSugan/index_files/CEC2014/CEC2014.htm) have been employed for performance evaluation. Table 1 shows the setting parameters used in experiments.

The experimental result for CEC2014 benchmark functions are tabulated in Table 2. Result in bold represents the best performance.

Table 1. Setting Parameters

Experimental Parameters	
Number of agent	100
Number of dimension	50
Number of run	50
Number of iteration	10,000
Search space	[-100.100]
SKF Parameters	
Error covariance estimate, P	1000
Process noise value, Q	0.5
Measurement noise value, R	0.5
GSA Parameters	
α	20
Initial gravitational constant, G_o	100
SKF-GSA Parameters	
Jumping rate, J_r	0.1

Table 2. The Average Fitness Values Obtained by SKF, GSA, and SKF-GSA

Function	SKF	SKF-GSA	GSA
F1	4702013.17	4295218.33	**1400195.11**
F2	24498691.7	8265.524	**7166.7916**
F3	18147.7005	**16725.114**	64249.0520
F4	**532.77148**	538.979	653.4553
F5	520.010016	519.9999	**519.9997**
F6	633.441686	**627.7067**	636.3361
F7	700.246225	700.0133	**700.00014**
F8	**807.981323**	816.2199	1076.43847
F9	1059.13877	**1056.2279**	1217.9866
F10	**1335.18324**	1543.5057	7456.3162
F11	6249.36725	**6178.1897**	8637.6403
F12	1200.23641	1200.0562	**1200.0001**
F13	1300.55973	1300.5183	**1300.3749**
F14	1400.30009	**1400.2931**	1400.3012
F15	1551.6584	1549.9115	**1504.4108**
F16	**1619.12553**	1619.2702	1622.5712
F17	908272.092	880075.612	**161088.839**
F18	6941389.77	**3285.3104**	3731.2078
F19	1950.223	1950.84943	**1923.7518**
F20	34799.058	**25328.3173**	26574.2424
F21	1186640.91	1092401.31	**187636.63**
F22	3429.1058	**3339.9376**	3857.9572
F23	2645.6890	2644.6327	**2500.0000**
F24	2667.2498	2660.3817	**2600.0283**
F25	2730.4018	2731.4575	**2700.0000**
F26	**2766.3853**	2786.2986	2800.0315
F27	3883.3415	**3763.4039**	4577.5301
F28	7223.3697	7757.2433	**6261.3240**
F29	5997.8302	4109.6202	**3100.1482**
F30	19753.2888	18853.2102	**8695.4410**

Based on the averaged performances, Wilcoxon signed rank test is performed and the result is tabulated in Table 3. Based on the level of significant, $\sigma = 0.05$, it is found that statistically, the proposed SKF-GSA is significantly superior to SKF and GSA in solving continuous numerical optimization problems.

Table 3. Wilcoxon Signed-Rank Test Result

Comparison	R^-	R^+
Hybrid SKF-GSA vs GSA	219	246
Hybrid SKF-GSA vs SKF	361	104

6. Conclusion

This paper report an attempt to hybrid SKF algorithm with a well-established GSA algorithm. In this study, GSA is chosen as the prediction mechanism in SKF algorithm. In addition, jumping rate is also incorporated in the proposed SKF-GSA algorithm. During the prediction, GSA is executed not only when the jumping rate condition is satisfied but also if the predicted solution is better. The findings proved that the proposed hybrid SKF-GSA is superior to individual SKF and GSA algorithms

Acknowledgements

This research is supported by a Fundamental Research Grant Scheme (FRGS) awarded to Universiti Malaysia Pahang (RDU160105).

References

1. E. Rashedi, H. Nezamabadi-pour, S. Saryazdi, GSA: a gravitational search algorithm, *Information Sciences.* **179** (13) (2009) 2232-2248.
2. N. H. Abdul Aziz, Z. Ibrahim, S. Razali, N. A. Ab. Aziz, Estimation-based metaheuristics: a new branch of computational intelligence, in *Proc. 3rd National Conf. Postgraduate Research* (Pekan, Malaysia, 2016), pp. 469-476.
3. Z. Ibrahim, N. H. Abdul Aziz, N. A. Ab. Aziz, S. Razali, M. I. Shapiai, S. W. Nawawi, M. S. Mohamad, A Kalman filter approach for solving unimodal optimization problems, *ICIC Express Letters.* **9**(12) (2015) 3415-3422.

Simulated Kalman Filter with Randomized Q and R Parameters

Nor Hidayati Abdul Aziz, Nor Azlina Ab. Aziz
Faculty of Engineering and Technology, Multimedia University
Bukit Beruang, Melaka, Malaysia

Zuwairie Ibrahim, Saifudin Razali, Mohd Falfazli Mat Jusof
Faculty of Electrical and Electronics Engineering, Universiti Malaysia Pahang
Pekan, Pahang, Malaysia

Khairul Hamimah Abas, Mohd Saberi Mohamad
Universiti Teknologi Malaysia
Skudai, Johor, Malaysia

Norrima Mokhtar
Faculty of Engineering, University of Malaya
50603 Kuala Lumpur, Malaysia

E-mail: hidayati.aziz@mmu.edu.my, azlina.aziz@mmu.edu.my, zuwairie@ump.edu.my, saifudin@ump.edu.my, mfalfazli@ump.edu.my, khairulhamimah@utm.my, saberi@utm.my, norrimamokhtar@um.edu.my

Abstract

Inspired by Kalman filtering, simulated Kalman filter (SKF) has been introduced as a new population-based optimization algorithm. The SKF is not a parameter-less algorithm. Three parameter values should be assigned to P, Q, and R, which denotes error covariance, process noise, and measurement noise, respectively. While analysis of P has been studied, this paper emphasizes on Q and R parameters. Instead of using constant values for Q and R, random values are used in this study. Experimental result shows that the use of randomized Q and R values did not degrade the performance of SKF and hence, one step closer to the realization of a parameter-less SKF.

Keywords: Optimization, simulated Kalman filter, random, error covariance, process noise, measurement noise.

1. Introduction

The simulated Kalman filter (SKF) [1] is a relatively new optimization algorithm compared to some well-known optimizer such as genetic algorithm (GA) [2], particle swarm optimization (PSO) [3], and gravitational search algorithm (GSA) [4]. Since the first introduction of SKF, it has been modified and applied extensively. These include fundamental improvements to SKF. For example, to solve combinatorial optimization problems, angle-modulated SKF [5], binary SKF [6], and distance evaluated SKF [7] have been presented to enable the SKF to operate in binary search space. The SKF also has been hybridized with PSO and GSA [8-9]. From the application point of view, airport scheduling has been solved using SKF [10]. Also, recently, the SKF has been employed to select the most significant features for peak detection of EEG signal [11].

2. The Original and Modified SKF Algorithms

The simulated Kalman filter (SKF) algorithm is illustrated in Figure 1. Consider n number of agents, SKF algorithm begins with initialization of n agents, in which the states of each agent are given randomly. The maximum number of iterations, t_{max}, is defined. The initial value of error covariance estimate, $P(0)$, the process noise value, Q, and the measurement noise value, R, are also defined during initialization stage. Then, every agent is subjected to fitness evaluation to produce initial solutions, $\boldsymbol{X}(0) = \{\boldsymbol{X}_1^d(0), \boldsymbol{X}_2^d(0), \ldots, \boldsymbol{X}_{n-1}^d(0), \boldsymbol{X}_n^d(0)\}$ where d refers to the dimensional of the problem. The fitness values are compared and the agent having the best fitness value at every iteration, t, is registered as $\boldsymbol{X}_{\mathbf{best}}(t)$. For function minimization problem,

$$\boldsymbol{X}_{best}(t) = \min_{i\in 1,\ldots,n} fit_i(\boldsymbol{X}(t)) \quad (1)$$

whereas, for function maximization problem,

$$\boldsymbol{X}_{best}(t) = \max_{i\in 1,\ldots,n} fit_i\big(\boldsymbol{X}(t)\big) \quad (2)$$

The-best-so-far solution in SKF is named as $\boldsymbol{X}_{\mathbf{true}}$. The $\boldsymbol{X}_{\mathbf{true}}$ is updated only if the $\boldsymbol{X}_{\mathbf{best}}(t)$ is better (($\boldsymbol{X}_{\mathbf{best}}(t) < \boldsymbol{X}_{\mathbf{true}}$ for minimization problem, or $\boldsymbol{X}_{\mathbf{best}}(t) > \boldsymbol{X}_{\mathbf{true}}$ for maximization problem) than the $\boldsymbol{X}_{\mathbf{true}}$.

The prediction step is subjected to the following time-update equations:

$$\boldsymbol{X}_i^d(t|t) = \boldsymbol{X}_i^d(t) \quad (3)$$

$$P(t|t) = P(t) + Q \quad (4)$$

where $\boldsymbol{X}_i^d(t)$ and $\boldsymbol{X}_i^d(t|t)$ are the current state and transition/predicted state, respectively, and $P(t)$ and $P(t|t)$ are previous error covariant estimate and transition error covariant estimate, respectively.

The next step is measurement. Measurement, $\boldsymbol{Z}_i(t)$, of each individual agent is simulated based on the following equation:

$$\boldsymbol{Z}_i^d(t) = \boldsymbol{X}_i^d(t|t) + \sin(rand \times 2\pi) \times \left|\boldsymbol{X}_i^d(t|t) - \boldsymbol{X}_{true}\right| \quad (5)$$

where $rand$ is a uniformly distributed random number in the range of [0,1].

The final step is the estimation. During this step, Kalman gain, $K(t)$, is computed as follows:

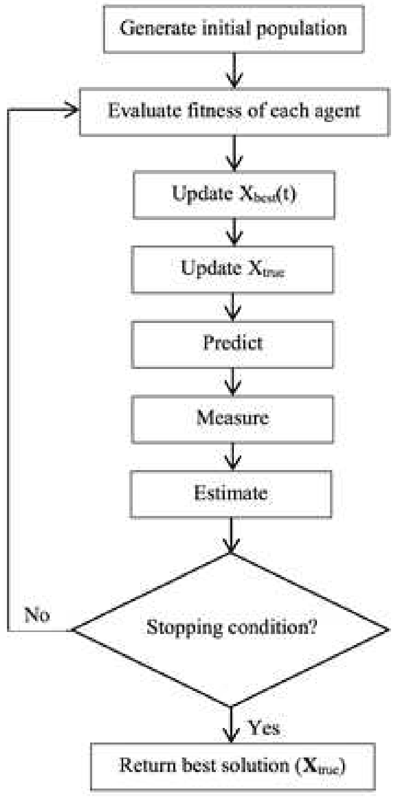

Fig. 1. The SKF algorithm.

$$K(t) = \frac{P(t|t)}{P(t|t)+R} \quad (6)$$

Then, the estimation of next state, $\boldsymbol{X}_i(t)$, is computed based on Eq. (7).

$$\boldsymbol{X}_i^d(t+1) = \boldsymbol{X}_i^d(t|t) + K(t) \times (\boldsymbol{Z}_i^d(t) - \boldsymbol{X}_i^d(t|t)) \quad (7)$$

and the error covariant is updated based on Eq. (8).

$$P(t+1) = \big(1 - K(t)\big) \times P(t|t) \quad (8)$$

Finally, the next iteration is executed until the maximum number of iterations, t_{max}, is reached.

The SKF algorithm requires the determination of P, Q, and R parameters. Earlier, $P = 1000$ and $Q = R = 0.5$ has been suggested [1]. However, based on an analysis on P, it was found that the parameter P alone did not affect the performance of SKF when $Q = R = 0.5$. Hence, Q and R parameters greatly affect the performance of the SKF. Since the determination of Q and R parameters is critical, this study suggests the determination of those parameters

Table 1. Performance comparison between the original SKF with SKF with random Q and R values.

Function No.	Original SKF	Random QR SKF	Sign
1	4.70E+06	4.70E+06	=
2	2.45E+07	3.53E+07	<
3	18148	19599	<
4	532.77	522.09	>
5	520.01	520.01	=
6	633.44	631.86	>
7	700.25	700.31	<
8	807.98	807.73	>
9	1059.1	1064	<
10	1335.2	1366.4	<
11	6249.4	6166.4	>
12	1200.2	1200.2	=
13	1300.6	1300.6	=
14	1400.3	1400.3	=
15	1551.7	1547.8	>
16	1619.1	1619.3	<
17	9.08E+05	8.80E+05	>
18	6.94E+06	3.06E+06	>
19	1950.2	1940.8	>
20	34799	33350	>
21	1.19E+06	1.10E+06	>
22	3429.1	3473.6	<
23	2645.7	2645.5	>
24	2667.2	2664.6	>
25	2730.4	2730.8	<
26	2766.4	2778.4	<
27	3883.3	3876.1	>
28	7223.4	6931.7	>
29	5997.8	9398.7	<
30	19753	19184	>

= similar > Random QR SKF is better < Original SKF is better

could be avoided. Thus, in this work, random numbers, $randn \in [0,1]$, normally distributed at the mean of 0.5, is generated whenever Q and R values are required, at every iteration, every agent, and every dimension.

In the proposed SKF with randomized Q and R values, Eq. (2) is replaced with Eq. (9) as follows:

$$P_i^d(t|t+1) = P_i^d(t) + randn_i^d \tag{9}$$

since the P parameter is dependent on Q. On the other hand, Eq. (6) is replaced with Eq. (10) since the Kalman gain, $K_i(t)$, is dependent on R.

$$K_i^d(t) = [P_i^d(t|t+1)]/[P_i^d(t|t+1) + randn_i^d] \tag{10}$$

Subsequently, Eq. (8) is replaced with Eq. (11).

$$P_i^d(t+1) = (1 - K_i^d(t)) \times P_i^d(t|t+1) \tag{11}$$

3. Experiment, Result, and Discussion

The experiment was conducted based on CEC2014 benchmark dataset for function minimization problems (http://www.ntu.edu.sg/home/EPNSugan/index_files/CEC2014/CEC2014.htm), which includes 30 set of problems. Every run consists of 10,000 function evaluations. After a single run, the same experiment was implemented again until 50 results were recorded and average values were calculated. The average value for every function is depicted in Table 1. Note that for original SKF algorithm, P = 1000 and $Q = R = 0.5$. The sign indicates performance comparison between two algorithms for every problem. Based on the result, however, general conclusion cannot be made. Figure 2 shows an example of convergence curve, which mostly the same.

Table 2 shows further analysis based on Wilcoxon signed-rank test. The R^+ and R^- values were calculated and those values were compared to a threshold value, which is 137. Since both R^+ and R^- values are greater than 137, there is no significant difference between results produced by both algorithms.

Table 2. Wilcoxon Signed-Rank Test

	R^+	R^-
Original SKF vs Random QR SKF	171.0	264

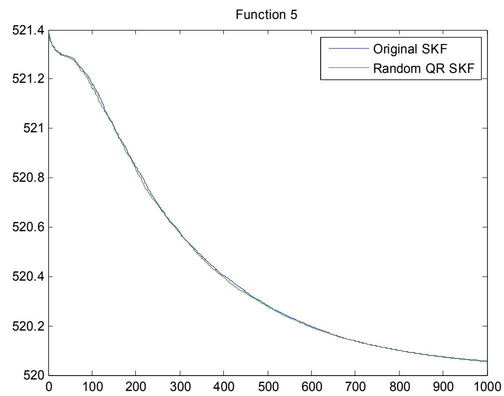

Fig. 1. Convergence curve for function 5.

4. Conclusion

Parameter tuning of an optimization algorithm could be a tedious task, especially, if the algorithm is employed to solve a specific problem. This study proves that Q and R tuning of SKF can be avoided, which is important towards the parameter-less SKF.

Acknowledgements

This research is supported by a Fundamental Research Grant Scheme (FRGS) awarded to Universiti Malaysia Pahang (RDU160105).

References

1. Z. Ibrahim, N. H. Abdul Aziz, N. A. Ab. Aziz, S. Razali, M. I. Shapiai, S. W. Nawawi, M. S. Mohamad, A Kalman filter approach for solving unimodal optimization problems, *ICIC Express Letters.* **9**(12) (2015) 3415-3422.
2. D. Goldberg, *Genetic Algorithms in Search, Optimization, and Machine Learning* (Reading, Addison-Wesley Professional, MA, 1989).
3. J. Kennedy, R. Eberhart, Particle swarm optimization, in *Proc. IEEE Int. Conf. Neural Networks* (1995), pp. 1942–1948.
4. E. Rashedi, H. Nezamabadi-pour, S. Saryazdi, GSA: a gravitational search algorithm, *Information Sciences.* **179** (13) (2009) 2232-2248.
5. Z. Md. Yusof, Z. Ibrahim, I. Ibrahim, K. Z. Mohd Azmi, N. A. Ab. Aziz, N. H. Abd Aziz, M. S. Mohamad, Angle modulated simulated Kalman filter for combinatorial optimization problems, *ARPN Journal of Engineering and Applied Science.* **11**(7) (2016) 4854-4859.
6. Z. Md. Yusof, I Ibrahim, S. N. Satiman, Z. Ibrahim, N. H. Abd Aziz, N. A. Ab. Aziz, BSKF: binary simulated Kalman filter, in *Proc. 3rd Int. Conf. Artificial Intelligence, Modeling and Simulation* (Sabah, Malaysia, 2015), pp. 77–81.
7. Z. Md. Yusof, Z. Ibrahim, I. Ibrahim, K. Z. Mohd Azmi, N. A. Ab. Aziz, N. H. Abd Aziz, M. S. Mohamad, Distance evaluated simulated Kalman filter for combinatorial optimization problems, *ARPN Journal of Engineering and Applied Science.* **11**(7) (2016) 4904-4910.
8. B. Muhammad, Z. Ibrahim, K. H. Ghazali, K. Z. Mohd Azmi, N. A. Ab. Aziz, N. H. Abd Aziz, M. S. Mohamad, A new hybrid simulated Kalman filter and particle swarm optimization for continuous optimization problems, *ARPN Journal of Engineering and Applied Science.* **10**(22) (2015) 17171-17176.
9. B. Muhammad, Z. Ibrahim, K. Z. Mohd Azmi, K. H. Abas, N. A. Ab. Aziz, N. H. Abd Aziz, M. S. Mohamad, Four different methods to hybrid simulated Kalman filter (SKF) with gravitational search algorithm (GSA), in *Proc. 3rd National Conf. Postgraduate Research* (Pekan, Malaysia, 2016), pp. 854–864.
10. K. Z. Mohd Azmi, Z. Md. Yusof, S. N. Satiman, B. Muhammad, S. Razali, Z. Ibrahim, N. A. Ab. Aziz, N. H. Abd Aziz, Solving airport gate allocation problem using angle modulated simulated Kalman filter, in *Proc. 3rd National Conf. Postgraduate Research* (Pekan, Malaysia, 2016), pp. 875–885.
11. A. Adam, Z. Ibrahim, N. Mokhtar, M. I. Shapiai, M. Mubin, I. Saad, Feature selection using angle modulated simulated Kalman filter for peak classification of EEG signals, *SpringerPlus.* **5**(1580) (2016).

Real Detection of 3D Human Hand Orientation Based Morphology

Abadal-Salam T. Hussain
Center of Excellence for Unmanned Aerial Systems (CoEUAS)
Universiti Malaysia Perlis, 01000 Kangar, Perlis, Malaysia

Hazry D.[a], Waleed A. Oraibi[b], M.S Jawad[b], Zuradzman M. Razlan[a], A. Wesam Al-Mufti[b], S. Faiz Ahmed[a], Taha A. Taha[b], Khairunizam WAN[a] & Shahriman A.B[a]
[a]Center of Excellence for Unmanned Aerial Systems (CoEUAS)
[b]School of Electrical System Engineering
Universiti Malaysia Perlis, 01000 Kangar, Perlis, Malaysia
E-mail: abadal@unimap.edu.my, hazry@unimap.edu.my
www.unimap.edu.my

Abstract

This paper describes a new methodology to track a human hand movement in 3D space and estimate its orientation and position in real time. The objective of this algorithm development is to ultimately using it in robotic spherical wrist system application. This method involves image processing and morphology techniques in conjunction with various mathematical formulae to calculate the hand position and orientation. The advantage of this technique is that, there is no need for continuous camera calibration which is required in other conventional methods in similar applications. The result of proposed method shows correctly identifying a large number of hand movements and its orientations. The proposed method could therefore be used with different types of tele operated robotic manipulators or in other human-computer interaction applications. This method is more robust and less computationally expensive, unlike other approaches that use costly leaning functions. The high performance is achieved during experiments testing because of its accurate hand movement identification and the low computational load. *Keywords*: List four to six keywords which characterize the article.

Keywords: 3D human hand, 3D detection, 3D orientation, SCARA robot

1. Introduction

Vision-based tracking of hand motions is one of the hottest area of research, many researchers are working on this area e.g. [1], [2], and [3]. However, the problem of correctly identification of a hand and completely simulating its movement is not yet solve. Several previously proposed algorithms use features extraction from the hand and then classify it using save data or information, and others (e.g. [4] and [5]). Although some of these techniques have reported some levels of success, but suffers from many restrictions such as present gestures and positions which are fed into the system beforehand. Other solution required invasive. In this paper a new method is presented to identify the human hand in real time and analyze the resultant information to obtain the hand's position and orientation in real time without any prior data base information. The plain background is used for hand detection and the results obtained from it shows high consistency with hands of different sizes and colours and the simulated movement and rotation matched that of the subject's hand.

After obtaining and matching the hand's orientation and position in 3D space, these results used as the input to a simulated robotic manipulator and the position and orientation of its end-effector accurately matched the user's hand. Furthermore, additional information from the hand, such as the opening or closing of the end-effector gripper, is obtained and directly sent to the simulated manipulator robot, which emulated the hand action [6].

2. Deduction of 3D Hand Orientation

First the hand position is determined and then, the same set of features can be used to estimates the orientation of the hand in 3D space. The three quantities that would need to be determined are the angles that the hand has rotated with respect to the three principal axes, namely, the x, y and z-axes.

The rotation about the z-axis (depth) can be easily determine, which occurs on the plane parallel to the screen. This angle is measured by using two previously obtained features the reference point (located in the middle of the wrist) and the tip of the hand (farthest point on the hand from the reference point). After obtaining the coordinates for these points on the plane parallel to the screen (the xy plane), a line is drawn between them. Therefore, the angle on which hand is rotated about the z-axis can be computed using atan2 function in MATLAB. In practice, the rotation of a hand lies in the range of 0° - 180°.

Where, the value of b is equal to the difference between the x coordinate of the reference point and the x coordinate of the human hand tip. Similarly, the value of a is equal to the difference between the y coordinate of the reference point and the y coordinate of the hand tip. Using these calculations, the first angle of the orientation of the human hand is obtained.

Besides that, if the hand rotated towards the screen, means the upper half of the hand shape gets larger, refer to Fig. 1. (c) otherwise when the hand rotated backwards, fare from the screen, the hand image become smaller from the upper half refer to Fig. 1. (b) that is recognisable by eye.

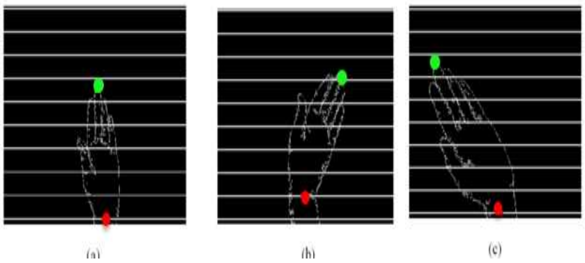

Fig.1. Rotation of the human hand about the z-axis (a) angle of rotation approximately 90°, (b) angle of rotation less that 90°, and (c) angle of rotation greater than 90°.

The calculation of the next two angles required to complete the detection of the orientation of the hand is more difficult. The first of these, the angle about the y-axis (the vertical axis) utilizes the hand width property, which was previously obtained. As noted, the hand width is recorded at the beginning of the algorithm and any subsequent change in this property is noted and compared to the original registered width.

Original registration of the human hand was calculated with a 0° rotation about the y-axis, then the width at this initialization stage is the maximum value. Therefore, each decrease in the hand width reflects a relative rotation about the y-axis. If it is assumed that a full rotation of 90° results in a hand width of 1/2 the maximum hand width, a relationship between the angle and the width can be formed, as shown in (1).

$$\theta_y = \cos^{-1}\left(2\left(\frac{w}{w_o} - \frac{1}{2}\right)\right) \tag{1}$$

This variation, which differs between humans and even between different hands (right or left), can be considered by changing the equation that relates the width to the rotation about the y-axis. Fig. 2. shows an example that demonstrates the algorithm used to determine the rotation about the y-axis.

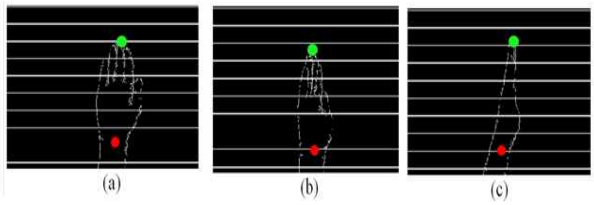

Fig.2. Differing hand widths correspond to rotations about the y-axis (a) no rotation (0°), (b) partial rotation, and (c) full rotation (90°).

3. Robotic Wrist Manipulation

Finally, the accurate hand position and orientation in 3D space obtained from proposed methodology are fed into a robotic manipulator to control the position and orientation of the robotic end-effector such that it mimics the hand movements in real time. The robotic manipulator used in this study is a modified SCARA robot. The proposed design is a SCARA manipulator with a spherical wrist as its end-effector, which gives it complete freedom of movement in 3D space with regards to position and orientation.

Each of the links of the robotic manipulator is assigned to a coordinate frame. The Denavit and Hartenberg (DH) algorithm proposes a matrix method of systematically assigning coordinate systems to each link of an articulated chain. The axis of revolute joint iis aligned with axis zi−1. The xi−1 axis is directed along the normal of axes zi−1 to zifor intersecting axes parallel to zi−1 × zi. The link and joint parameters may be summarized as follows:

(i) Link length aiis the offset distance between axes zi−1 and zialong the xi -axis;

(ii) Link twist αiis the angle from the zi−1-axis to the zi-axis about the xi-axis;

(iii) Link offset diis the distance from the origin of frame i-1 to the xi-axis along the zi−1-axis;

(iv) Joint angle θiis the angle between the xi−1 and xi-axes about the zi−1-axis.

These parameters and conventions are applied with our robotic manipulator. The resultant DH parameters are shown in Table 1.

Table 1. DH parameters for the proposed simulated robotic manipulator link

Link (i)	α_{i-1}	a_{i-1}	d_i	θ_i	q_i **(Variable)**
1	0°	0	L1	θ_1	θ
2	0°	L2	0	θ_2	θ
3	180°	L3	d3	0	d
4	-90°	0	0	θ_4	θ
5	90°	0	0	θ_5	θ
6	**-90°**	**0**	**0**	θ_6	θ

Using these parameters, the inverse kinematics model describing each link angle and link length with respect to the desired position and orientation of the manipulator wrist can be calculated using (2) and (3)

$$d_3 = L_1 - z_{des} \tag{2}$$

$$\theta_2 = \pm\cos^{-1}\left(\frac{p_x^2 + p_y^2 - L_3^2 - L_2^2}{2L_2L_3}\right) \tag{3}$$

Where, *zdes* is the desired orientation and position of the robot arm, which should be identical to the human hand position and orientation. After obtaining, Θ_2 the system for sin Θ_1 and cos Θ_1 shown in (4) can be solved.

$$\begin{bmatrix} -L_3\sin\theta_2 & L_2+L_3\cos\theta_2 \\ L_2+L_3\cos\theta_2 & L_3\sin\theta_2 \end{bmatrix}\begin{bmatrix}\sin\theta_1 \\ \cos\theta_1\end{bmatrix} = \begin{bmatrix} p_x \\ p_y \end{bmatrix} \tag{4}$$

Where, Θ_1 = atan2 (sin Θ_1, cos Θ_1). The desired orientation (rotation) matrix uses the notation shown in (5).

$$R_{des} = \begin{bmatrix} r_{11} & r_{12} & r_{13} \\ r_{21} & r_{22} & r_{23} \\ r_{31} & r_{32} & r_{33} \end{bmatrix} \tag{5}$$

The corresponding rotation matrices for the three rotation angles can then be multiplied, as shown in (6), to obtain R*des*

$$R_{des} = \begin{bmatrix} \cos\theta_z & -\sin\theta_z & 0 \\ \sin\theta_z & \cos\theta_z & 0 \\ 0 & 0 & 1 \end{bmatrix}\begin{bmatrix} 1 & 0 & 0 \\ 0 & \cos\theta_x & -\sin\theta_x \\ 0 & \sin\theta_x & \cos\theta_x \end{bmatrix}\begin{bmatrix} \cos\theta_y & 0 & \sin\theta_y \\ 0 & 1 & 0 \\ -\sin\theta_y & 0 & \cos\theta_y \end{bmatrix} \tag{6}$$

The orientation matrix can then be used to obtain the desired rotation angles, as shown in (7).

$$\theta_5 = \pm\text{atan2}\left(\sqrt{r_{21}^2 + r_{22}^2}, r_{23}\right)$$

$$\theta_4 = \pm\text{atan2}\left(\frac{r_{33}}{\sin\theta_5}, \frac{-r_{13}}{\sin\theta_5}\right) \tag{8}$$

$$\theta_6 = \pm\text{atan2}\left(\frac{-r_{22}}{\sin\theta_5}, \frac{r_{21}}{\sin\theta_5}\right) \tag{7}$$

Consequently, for any desired orientation and position of the robotic manipulator, we can obtain the link angles and lengths required. The matching of the state of the human hand in 3D space to a real robot can be easily accomplished through simple mathematical calculations. An example of this mapping is shown in Fig. 5. and Fig. 6. that the simulated manipulator follows the hand movements.

4. Application and Result

In this manuscript, a new algorithm has been proposed that correctly and accurately extracts the 3D position and orientation of a human hand and then apply this algorithm to a simulated robotic manipulator directly to test its accuracy. In all our experiments, the manipulator was successfully tele operated using a single webcam, the details representation of robot parts in corresponding to human hand parts as shown in Fig. 6.

The extraction of the human hand rotation about the x and z-axes was obtained. In addition, the range of angles for the hand orientation is considered from a realistic point of view but may be deemed insufficient for certain applications in which the exact calibrated angle of the 3D hand orientation is required.

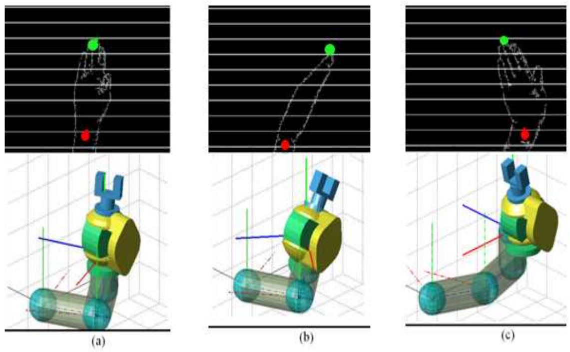

Fig. 5. Simulation of the configuration of a human hand with a robotic manipulator (a) original registered configuration, (b) rotation about two angles, and (c) rotation and translation.

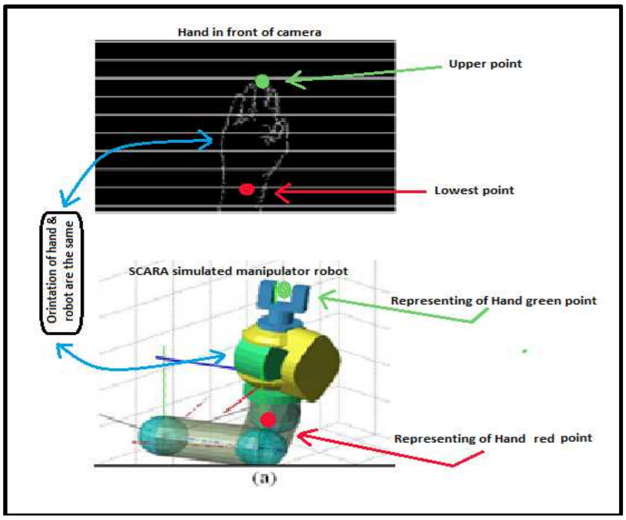

Fig. 6. Show the representation of hand feature points on a SCARA manipulator robot.

References

1. A. T. Hussain, S. Faiz Ahmed & D. Hazry, *Tracking and Replication of Hand Movements by Teleguided Intelligent Manipulator Robot.* (Robotica, Cambridge University Press, Vol. 33, Issue 01, Jan. 2015) pp 141-156. DOI: http://dx.doi.org/10.1017/S0263574714000083 (ISSN: 0263-5747 EISSN: 1469-8668).
2. A. T. Hussain, S. Faiz Ahmed & D. Hazry, *Tracking and Replication of Hand Movements by Teleguided Intelligent Manipulator Robot.* (Robotica, Cambridge University Press, 2014) (ISSN: 0263-5747 EISSN: 1469-8668).
3. M. Kamran Joyo, D. Hazry, S. Faiz Ahmed, M. Hassan Tanveer, Faizan. A. Warsi, A. T. Hussain, *Altitude and Horizontal Motion Control of Quadrotor UAV in the presence of Air Turbulence*. (Systems, Process & Control (ICSPC2), 2013 IEEE International Conference, Published at IEEE Xplore, 2013) PP 16-20. ISBN: 978-1-4799-2208-6, (2013).
4. Hussain, A. T., Said, Z., Ahamed, N., Sundaraj, K., Hazry, D., *Real-time robot-human interaction by tracking hand movement & orientation based on morphology*. (IEEE Xplore, 2012) PP. 283-288. ISBN 978-1-4577-0243-3.
5. Syed Faiz Ahmed, Ch. Fahad Azim, Hazry Desa, Abadal-Salam T. Hussain, *Model Predictive Controller-based, Single Phase Pulse Width Modulation (PWM) Inverter for UPS Systems*, (Acta Polytechnica Hungarica, Journal of applied science Volume 11, Issue Number 6, 2014) pp. 23-38. (ISSN 1785-8860).

Multilevel Non-Inverting Inverter Based Smart Green Charger System

Abadal-Salam T. Hussain [a,b]
[a]*Center of Excellence for Unmanned Aerial Systems (CoEUAS)*
Universiti Malaysia Perlis, 01000 Kangar, Perlis, Malaysia

Waleed A. Oraibi[b], **Hazry D.**[a], **Zuradzman M. Razlan**[a], **S. Faiz Ahmed**[a], **Taha A. Taha**[b] , **Khairunizam WAN**[a] & **Shahriman AB** [a]
[b]*Center of Excellence for Renewable Energy (CERE)*
Universiti Malaysia Perlis, 01000 Kangar, Perlis, Malaysia
E-mail: abadal@unimap.edu.my, hazry@unimap.edu.my
www.unimap.edu.my

Abstract

This paper discusses about the development of low cost efficient battery charging system using PIC Microcontroller. The demand of efficient battery charging system are going increase day by day, because of its usage in various applications such as it use in Hybrid electric cars, PV solar electric generation system, other energy storage systems and many more. In this paper an efficient and cost effective battery charging system is presented that use buck-boost converter topology. First, the software (PIC Programming) simulation is performed using Micro C software and then hardware is developed and tested to check the performance of the developed battery charger system. The efficiency of circuit is 85.66% and it can be use in any battery charging application

Keywords: Battery, Solar Cells, Microcontroller and Battery Charger.

1. Introduction

The Fossil Fuel is the conventional source of energy which is going to be exhausted day by day. According to the energy information administration (EIA) department of energy United States, "the world will face shortage of liquid fossil fuels in the next few years". In the light of forecasting of EIA, in upcoming future fossil fuel may not able to cover the requirement of world. Therefore the alternate energy systems are needed to fill the upcoming shortage (Ahmed K. Abbas, 2014. The buck-boost is used to do both of the operations same like step up and down the output voltage depending on the duty cycle (Abadal-Salam T. Hussain, 2015). The economical battery charger controller for solar panel will be beneficial to optimize the output power as per load requirement. In this paper a PIC Microcontroller based battery charging system is presented that use PIC16F877A microcontroller as the main processor used in the circuit to control on the whole events and to be developed and efficient. As well as the PIC 16F877A is used to control on the input voltage by fixing it to selected level.

2. Related Works

The renewable energy in the resent years is the solution for the problems to produce the clean electrical energy, such as the photovoltaic (PV) technology. The PV technology is based on the conversion of the sunlight into electricity (Abadal-Salam T. Hussain, 2015). Now, the researchers are worked on PV and solar penal systems that trade on this energy (Abadal-Salam T. Hussain, 2015). Lee, Young-Joo Khaligh, one who introduced and do the experimental about the buck-boost non-inverting converter or can called a positive buck-boost converter in 2009 (Syed Faiz Ahmed, 2014). He has done a highly efficient control technique by using pulse width modulation (PWM) controlling dc/dc positive buck–

boost converter. In his proposed control scheme, can control the output voltage for an input voltage, which changes based on the charge status of the power supply. There are many techniques to charge the battery are proposed according to the (Abadal-Salam T. Hussain, 2015).

3. Application and Result

M The microcontroller is main control unit of the circuit which is programmed using Micro C software. First of all, the input voltage coming from solar cell is divided by using voltage divider to decrease the voltage and provide a protection to the PIC. The output voltage from the voltage divider is connected to ADC that including inside the PIC microcontroller. The PWM that producing from the PIC is depended on the input voltage that coming from the voltage dividers . Shown in Fig. 1. simulation circuit at proteus software.

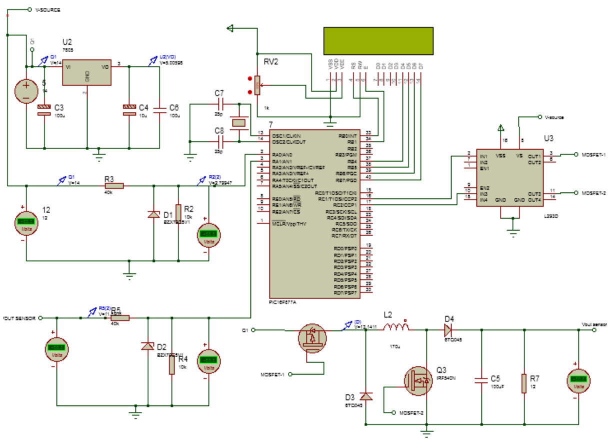

Fig. 1. Buck- Boost Simulation Circuit

The PWM waveform is generated by using PIC microcontroller, depend on the variation of the duty cycle, and input voltage as shown in Fig. 2. The output voltage and current from buck-boost non-inverting converter controlled by using pic microcontroller (PWM) and system loaded with different resistive load are presented in the Table 1 shows the I/O voltages results.

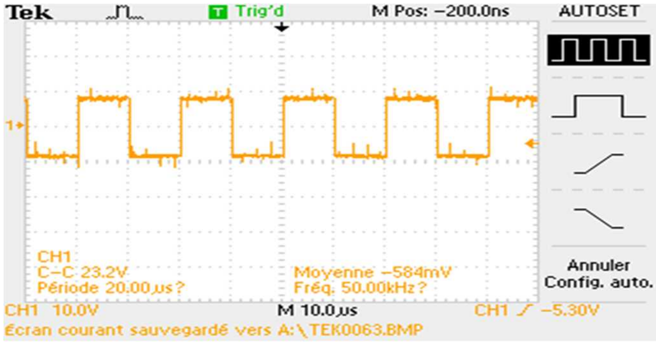

Table 1. Output voltage results for different resistive load

VIN (V)	RESISTIVE LOAD(Ω)	V out (V)	Current (A)
6	8	11.83	1.478
6	12	11.9	0.989
6	18	11.92	0.66
8	8	11.6	1.437
8	12	11.67	0.967
8	18	11.72	0.65
14	8	11.85	1.48
14	12	11.9	0.9911
14	18	11.935	0.6627
16	8	11.86	1.4811
16	12	11.889	0.99
16	18	11.921	0.666

As have seen below at Fig. 3. and Fig. 4.: shown the result of hardware implementation at buck and boost non-inverting converter.

Fig. 3. Shown the result at buck converter.

Fig.2. Wave form of gate driver on 50% of duty cycle.

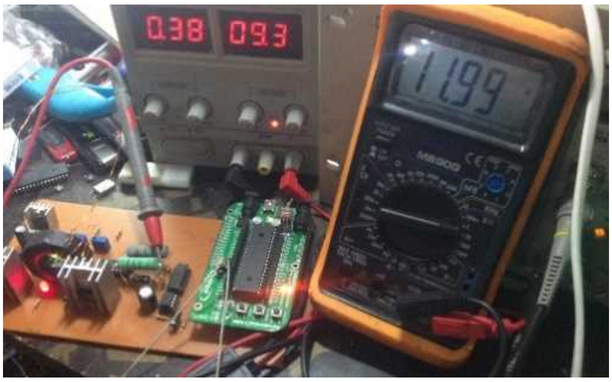

Fig. 4. Shown the result at boost converter.

The current and voltage have followed from the converter to the battery across relay (RL). The yellow and red LED is used to give alarm when the battery is charged fully or when an overload is occurred. The Analog to digital converter ADC had been modeled in the PIC16F877A to convert the analog battery voltage to digital. The battery sense voltage is reduced by using some resistors and sent to the ADC input as show in the Fig. 5. simulation circuit.

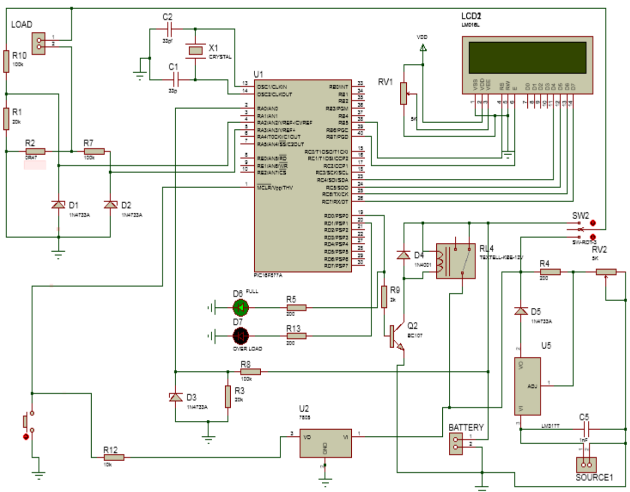

Fig.5. Battery charger circuit simulation

The modeling of ADCs inside the PICs, convert automatically the analog input voltage on the 10 bit digital number. To get higher resolution from ADCs, a smaller step size is provided. The resolution step size is:

Resolution = 5V/1024
= 4.887 mV

Therefore, 4.887mV is the step for each change in input voltage. The programming of ADC's converter is to convert the analog input voltage to digital number.

$$V = \frac{(v \times 4.89)}{20} \times 120 \tag{1}$$

Voltage across 0.8 ohm resistor = V,The load current = Current across 0.8 ohm resistor = V/0.8

Thus,

$$I = \frac{i}{0.8} \tag{2}$$

The reduced voltage from divider is used as a sense voltage from the load to the PIC16F877A to be displayed on the LCD as shown in the FIGURE (4). The one of the main objective was to design an efficient battery charger device based PIC microcontroller that would able to charge the battery with variable dc source as well as to protect the battery from the overcharging by cutting off the supply voltage when the battery is charged fully. The charger circuit was tested by using Proteus simulation software.

The data is collected from the simulation and lap to describe the drawn charging current per the battery voltage until cutoff as show in Fig. 7. and Fig. 8.

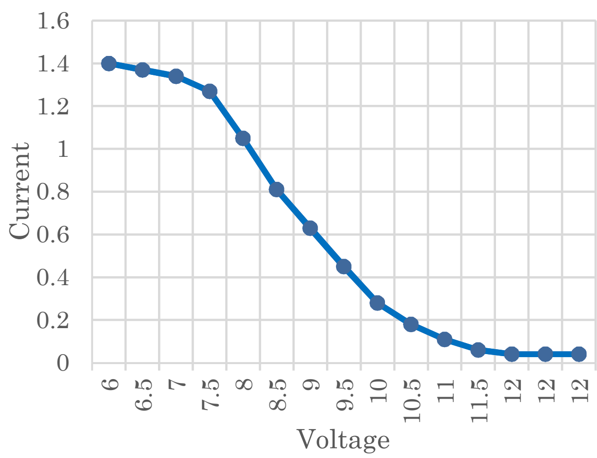

Fig.7. Battery Charging Current

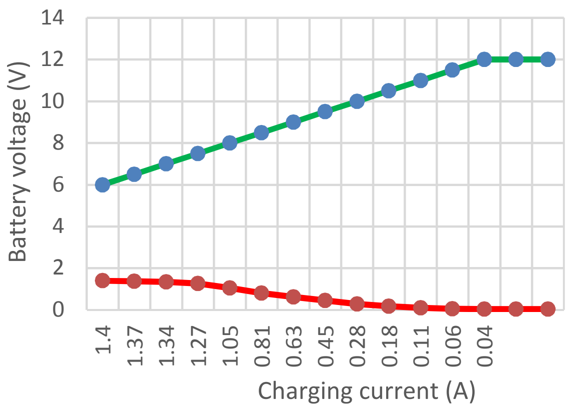

Fig. 8. Charging Current and Battery Voltage

4. Conclusion

In this paper buck-boost inverter based an efficient battery charger system for solar cell application is presented which is based on PIC microcontroller, it is programmed, simulated and design to control on the charging process and to protect the battery against the overvoltage that might occur during the charging process. It automatically cutoff the voltage when the battery is charged fully. When a battery voltage reaches the regulation set point, the charging algorithm slowly reduces the charging current to avoid heating. The circuit is tested and it performed well.

References

1. Ahmed K. Abbas, Abadal-Salam T. Hussain, F. Malek,Waleed A. Oraibi,Qais H. Jeflawi, Israa A. Dahham .” High-Low Voltage Risk Prevention Of UAV Electrical Generation System Based Buck-Boost Inverter” International Journal of Advanced Technology in Engineering and Science (ISSN 2348- 7550), Volume 02, Issue 06, June 2014;
2. Abadal-Salam T. Hussain, Qais H. Jeflawi, F. Malik, Israa A. Dahham, Jailani O. Mahmoud, Mohd Asri Jusoh, Mohd Irwan Yusoff, Muhammad Irwanto Misrun & Gomesh Nair Shasidharan, “Integrated DC-AC Inverter for Hybrid Power System“, Trans Tech Publications, Journal of Applied Mechanics and Materials, Vol. 793 (2015) pp 252-256, ISSN: 1662-7482, doi:10.4028/www.scientific.net/AMM.793.252;
3. Abadal-Salam T. Hussain, F. Malek, Nur Amira Azhar, M. S. Jawad, Syed F. Ahmed, Mohd Asri Jusoh, Mohd Irwan Yusoff, Muhammad Irwanto Misrun, Gomesh Nair Shasidharan, Shouket A. Ahmed & Taha A. Taha, “Efficient Power Generation for Smart Homes Based Titanium Dioxide (TiO2)“, Trans Tech Publications, Journal of Applied Mechanics and Materials, Vol. 793 (2015) pp 430-434, ISSN: 1662-7482, doi:10.4028/www.scientific.net/AMM.793.430;
4. Syed Faiz Ahmed, Ch. Fahad Azim, Hazry Desa, Abadal-Salam T. Hussain, "Model Predictive Controller-based, Single Phase Pulse Width Modulation (PWM) Inverter for UPS Systems", Acta Polytechnica Hungarica, Journal of applied science (ISSN 1785-8860), Volume 11, Issue Number 6, pp. 23-38, (2014);
5. Abadal-Salam T. Hussain, Syed F. Ahmed, F. Malek, M. S. Jawad, Nursabrina Noorpi, Gomesh Nair Shasidharan, Mohd Irwan Yusoff, Muhammad Irwanto Misrun, Taha A. Taha & Shouket A. Ahmed, “Wind Turbine Farm as an Alternate Electric Power Generating System in Perlis - Malaysia”, Trans Tech Publications, Journal of Applied Mechanics and Materials, Vol. 793 (2015) pp 333-337, ISSN:1662-7482, doi:10.4028/www.scientific.net/AMM.793.33.

Design A New Model of Unmanned Aerial Vehicle Quadrotor Using The Variation in The Length of The Arm

Yasameen Kamil
Center of Excellence for Unmanned Aerial Systems (CoEUAS)
Universiti Malaysia Perlis, 01000 Kangar, Perlis, Malaysia

D. Hazry, Khairunizam Wan, Zuradzman M. Razlan, Shahriman AB
Center of Excellence for Unmanned Aerial Systems (CoEUAS)
Universiti Malaysia Perlis, 01000 Kangar, Perlis, Malaysia
E-mail: moonom2002@gmail.com, hazry@unimap.edu.my
www.unimap.edu.my

Abstract

The direction of technological advancement toward autonomous aerial vehicle is increased. As a consequence of this evolution, the quad rotor used to accomplish a complex task in several fields. This paper presents the dynamic model of this miniature aerial vehicle in altitude and new dynamic model for yaw attitude movement, based on varying the arm length of quadrotor instead of varying the speed of motors to obtain a rotation around z-axis. This achieved by fixed a stepper motor in the arm of quadrotor to increase or decrease the length of the arm according to controller command for yawing movement. The controller command achieved by design PID controller with specific parameters to maintain the stability of the quadrotor in the flight path. The equipped energy to the motors during flight and maneuvering is reduced by selecting the motors' speed. The MATLAB software code used to evaluate and presents the comparison between the proposed and conventional quadrotor dynamic model. Simulation results show the robustness performance of the proposed model due to the movement around the z-axis with high system stability

Keywords: *Altitude; Arm's Length; PID; Quadrotor; UAV.*

1. Introduction

The autonomous miniature aerial vehicle has attracted the interest of researchers and represents a challenge in the world of Unmanned Aerial Vehicle (UAV) from few years ago. One of the UAV is the QuadRotor (QR), which has an endless list of applications in civil, military and commercial. The QR is under actuated nonlinear system.

Many methods have been proposed to control the stability of quadrotor. S. Bouabdallah & R. Siegwart, 2007 are focused on the design and the control of quadrotor by using integral backstepping to control position, attitude and altitude. According to the results, the vision sensors and population group must be improved to be dependable. A. Azzam & X. Wang 2010, used PD controller and backstepping based on PID to control the attitude. A.L Salih 2010, used PID controller for developing the stability of pitch, roll, yaw and altitude of the vehicle. Unfortunately, the system contains some transient overshoot because of disturbance and some other reasons like some certain of mechanical parameter and simplification of the controller. M. K. Joyo etc 2013, the position and altitude of quadrotor are controlled by using PID controller in the condition of wind gust and conclude that the controller worked effectively under this condition. H. K. Kim, 2013 proposed PID based on feedback linearization combined with block control technique for controlling the position of QR.

In this paper, a new model for QR yawing attitude is proposed based on varying the length of arms to generate variable torque without altering the motors' speed. This torque can rotate the QR to the desired position and keeping QR balance. Varying the arm's length have been done by using stepper motor in each arm to increase or decrease the length of arm depending on controller command.

2. Architecture and Dynamic Model of Quadrotor

The front motor (m1) and the rear motor (m3) are rotate counter clockwise (C.C.W). The right motor (m2) and the left (m4) are rotate clockwise (C.W). Therefore, the directions of the motors' rotation are maintained a balance torque at the QR frame and try to lift the QR in vertical motion. The lift motion is obtained by increasing the speed of all motors (m1, m2, m3, m4) gradually .

2.1 Dynamic Model of Quadrotor

The motion of any rigid body in space can be represented by rotational and translational motions (L. R. G. Carrillo, 2013). QR is nonlinear system with (6_DOF) and only four inputs which are motor speed and 3-translational and 3-rotational motion.

R represents the rotational matrix from body to earth frame.

$$R = \begin{bmatrix} c\psi\, c\theta & -s\psi\, c\emptyset + c\psi\ s\theta\, s\emptyset & c\emptyset\, c\psi\ s\theta + s\emptyset\, s\psi \\ s\psi\ c\emptyset & c\psi\ c\theta + s\theta\, s\emptyset\, s\psi & c\emptyset\, s\theta\, s\psi - c\psi\, s\theta \\ -s\theta & c\theta\, s\emptyset & c\theta\, c\emptyset \end{bmatrix} \quad (1)$$

Where, c means cos ( ), and s means sin ( ).

The thrust force and control torque which acting on the QR body is generated by the propellers rotation. The thrust vector converts from B frame to E frame by applying Newton-Euler method for the rigid body (L. R. G. Carrillo, 2013) as

$$m\ddot{x} = F.R + [0 \quad 0 \quad -mg]^T - f_a \quad (2)$$
$$I\dot{\omega} = \omega \times I\omega + \tau \quad (3)$$

Where, x¨ is the linear acceleration vector, F is the thrust force generated by motors, fa is the frictional force, τ is the control torque generated by motors, m is the mass of the body, I am the moment of inertia matrix, ω is the angular velocity. Therefore, from (3) and (2), can be write the QR dynamic equation as,

$$\left.\begin{aligned} m\ddot{x} &= u_1(\cos\emptyset \sin\theta \cos\psi + \sin\emptyset \sin\psi) - k_1\dot{x} \\ m\ddot{y} &= u_1(\cos\emptyset \sin\theta \sin\psi - \sin\emptyset \cos\psi) - k_2\,\dot{y} \\ m\ddot{z} &= u_1(\cos\theta\ cos\emptyset) - mg - k_3\,\dot{z} \\ I_y\ddot{\theta} &= (I_z - I_x)\dot{\theta}\dot{\psi} + u_2 - k_4\dot{\theta} \\ I_x\ddot{\emptyset} &= (I_y - I_z)\dot{\emptyset}\dot{\psi} + u_3 - k_5\dot{\emptyset} \\ I_z\ddot{\psi} &= (I_x - I_y)\dot{\theta}\dot{\emptyset} + u_4 - k_6\dot{\psi} \end{aligned}\right\} \quad (4)$$

The thrust induced by variation the speed of the motors is the input vector to the system and defined as

These input vectors are represented a

$$\left.\begin{aligned} u_1 &= b.(\omega_1{}^2 + \omega_2{}^2 + \omega_3{}^2 + \omega_4{}^2) \\ u_2 &= b.l(\omega_3^2 - \omega_1^2) \\ u_3 &= b.l(\omega_4^2 - \omega_2^2) \\ u_4 &= d.(\omega_4{}^2 + \omega_2{}^2 - \omega_3{}^2 - \omega_1{}^2) \end{aligned}\right\} \quad (5)$$

2.2 Proposed Yawing Movement Dynamic Model1

The UAV-QR has a great advantage in variety fields of work. The main challenges in the UAV-QR design are represented by its size and simplicity, robustness control and reducing the consumption energy.

3. Proposed Design Model

The quadrotor faces many problems the main problem is the consumption energy during flight and maneuverability for long time due to the motors' speed, where the two motors' speed must be increased and two other motors must be decreased to produce the yaw movement.

The QR arms are designed to comprise two parts, first part is fixed with the QR frame and the second part is the sliding arm. This design is proposed to varying the arm's length

4. Control Strategy

The QR requires a stable and robust controller during the maneuverability and flight path (A. L. Salih, 2010). In this paper, a PID controller is applied in altitude and yaw attitude movement.

The parameters of PID are adjusted to a specific value to reach steady- state system. The equation of PID defined mathematically (M. K. Joyo) as

$$u(t) = k_p e(t) + k_i \int e(t)dt + k_d \frac{de(t)}{dt} \quad (6)$$

4.1 Altitude Implementation Control Algorithm

The QR must be at desired value from the ground to maintain this distance the altitude controller is used (M. H. Tanveer). Therefore, the QR lift force must be greater than its weight and the earth's gravity to keep the QR at hovering and take-off (M. H. Tanveer, 2013).

$$u(t) = k_p e_z(t) + k_i \int e_z dt + k_d \frac{de_z}{dt} \tag{7}$$

4.2 Yaw Movement Implementation Control Algorithm

QR attitude controlled the angles of orientation pitch, roll, and yaw. In this paper, we present only the yaw angle and only choose yaw angle differential equation. Shown in Fig.1.

$$\ddot{\psi} = \frac{u_4}{I_z} + \frac{k_6}{I_z}\dot{\psi} \tag{8}$$

By solving the differential equation can obtain ψ as the output value, so the control design for the PID controller error signal will be:

$$e_\psi = \psi_{ref} - \psi \tag{9}$$

Where ψref the desired value and ψ is the measured output signal, then, the PID controller become

$$u(t) = k_p e_\psi + k_i \int e_\psi dt + k_d \frac{de_\psi}{dt} \tag{10}$$

5. The Results and Discussion

The physical parameter of simulation as mention is shown in Table I.

Table I. System Parameters

mass	**2kg**
Arm length	0.25 meter
Δl	± 0.05 meter
$l_2 = l_4$	0.3 meter
$l_1 = l_3$	0.2 meter
gravity	9.8m/s2
Ix	1.25Ns2/rad
Iy	1.25Ns2/rad
Iz	2.5Ns2 /rad
b	3.31*10-5
d	7.5*10-6
k1= k2=k3	0.010 Ns/m
k4=k5=k6	0.012 Ns/m

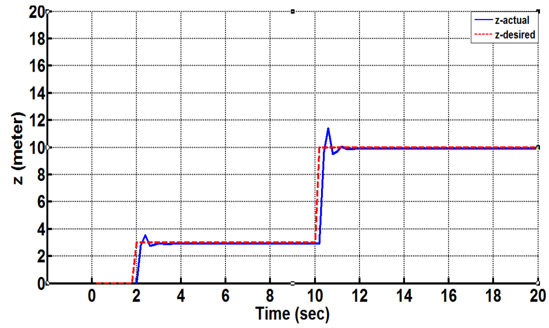

Fig. 1. Altitude and hovering performance

Fig. 1. Shows the yaw movement according the proposed design that based on PID controller and changing the arm's length and shows the ability of the proposed design to orient the QR to the desired angle (0.5 rad) from reference input angle within 3sec.

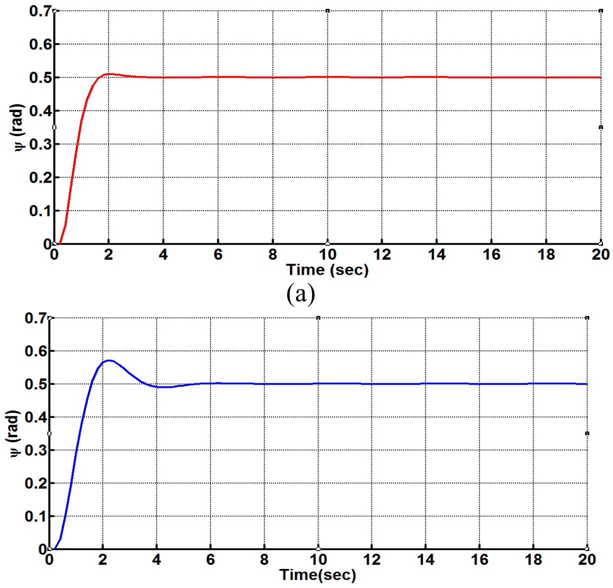

(b)

Fig. 2. The comparison of yaw movement between (a) The Proposed Control Design (b) Conventional Control Design

6. Conclusion

The result shows a good performance in altitude motion by automatically tracking the desired path. A new approach was proposed in yaw attitude based on varying the arms' length to ensure the rotation around the z-axis. The arm length is varying by fixed a stepper motor inside each arm to extend or reduce the length of the arm. In addition, the proposed model in this approach is reduced the energy consumption and extend the motor's lifetime through fixing the motors speed (hovering speed).

References

1. S. Bouabdallah and R. Siegwart, "Full control of a quadrotor," in Intelligent robots and systems, 2007. IROS 2007. IEEE/RSJ international conference on, 2007, pp. 153-158;

2. A. L. Salih, M. Moghavvemi, H. A. Mohamed, and K. S. Gaeid, "Modelling and PID controller design for a quadrotor unmanned air vehicle," in Automation Quality and Testing Robotics (AQTR), 2010 IEEE International Conference on, 2010, pp. 1-5;

3. M. K. Joyo, D. Hazry, S. F. Ahmed, M. H. Tanveer, F. A. Warsi, and A. Hussain, "Altitude and Horizontal Motion Control of Quadrotor UAV in the Presence of Air Turbulence." IEEE Conference on Systems, Process and Control, ICSPC 2013, pp.16-20;

4. H. K. Kim, T. T. Nguyen, S. J. Oh, and S. B. Kim, "Position Control of a Small Scale Quadrotor Using Block Feedback Linearization Control," in AETA 2013: Recent Advances in Electrical Engineering and Related Sciences, ed: Springer, 2014, pp. 525-534;

5. A. Nagaty, S. Saeedi, C. Thibault, M. Seto, and H. Li, "Control and navigation framework for quadrotor helicopters," Journal of Intelligent & Robotic Systems, vol. 70, pp. 1-12, 2013;

6. S.-h. Lee, S. H. Kang, and Y. Kim, "Trajectory tracking control of quadrotor UAV," in Control, Automation and Systems (ICCAS), 2011 11th International Conference on, 2011, pp. 281-285;

7. M. H. Tanveer, S. F. Ahmed, D. Hazry, M. K. Joyo, and F. A. Warsi, "Disturbance and Noise Rejection Controller Design for Smooth Takeoff/Landing and Altitude Stabilization Of Quad-rotor," Journal of Applied Sciences Research, vol. 9, pp. 3316-3327, 2013

Development of Automatic Take Off and Smooth Landing Control System for Quadrotor UAV

Syed. F. Ahmed
Universiti Kuala Lumpur, British Malaysian Institute, Malaysia
Center of Excellence for Unmanned Aerial Systems (CoEUAS)
Universiti Malaysia Perlis, Malaysia

D. Hazry
Center of Excellence for Unmanned Aerial Systems (CoEUAS), Universiti Malaysia Perlis, Malaysia

Kushsairy Kadir
University Kuala Lumpur, British Malaysian Institute, Malaysia

Abadal Salam T. Hussain, Zuradzman M. Razlan, Shahriman AB
Center of Excellence for Unmanned Aerial Systems (CoEUAS), Universiti Malaysia Perlis, Malaysia
E-mail: hazry@unimap.edu.my
www.unimap.edu.my

Abstract

This paper covers the development of automatic takeoff and smooth landing control system for UAV Quadrotor. This paper includes development, simulation, mathematical modeling and experimental results of flight test. Developed UAV model has a system to stabilize the quadrotor. Altitude stabilization in quadrotor make the quadrotor can perform take off and smooth landing perfectly and can avoid crash during landing which was proved during experiment. Yaw, pitch, and roll in quadrotor body is detected by gyro sensor when flying is balanced by gyro sensor. Gyro sensor act as input that detect stabilization problem and input data will be sent to microcontroller to make new output for quadrotor.

Keywords: UAV, Quadrotor

1. Introduction

The Quadrotor is one of the Unmanned Aerial Vehicle (UAV) that use four propeller for flying. They are four unit of brushless DC motor that mount at each of end quadrotor structure (M. Kamran Joyo, 2013). Flying object needs to take off and landing safely. Therefore the development of automatic takeoff and smooth landing system is very crucial for safety system in Quadrotor. The advantages of this system are totally eliminate the use of the pilot to airborne the UAV and it is more secure and reliable for autonomous flight. Quadrotor is very useful in many applications for example in monitoring, surveillance, search & rescue, agriculture and military. Quadrotor also suitable to use at the place that human cannot enter for example danger zone. Uses of quadrotor at this case can save the people life from danger. We can deploy quadrotor for monitoring hazardous zone such as power plant and radioactive leakage area. Installment of automatic takeoff and smooth landing system can make new user easily to handle quadrotor and can avoid air crash (Tanveer, 2013). The knowledge in kinematics and dynamics is very important and useful for understanding the physics and characteristic of quadrotor. Quadrotor attitude and height from bodies to ground can be measured by using two type of sensor. Inertial measurement unit (IMU) is a main part that be used while to predict distance ultrasonic sensor and infrared sensor are used. Micro control unit is a part that handled data processing and control algorithms and generate signal to four brushless DC motor that was mounted at the structure.

2. Objective, Scope and Problem Statement

The flying quadrotor is not easy to take off and landing for new user because quadrotor tends to easily crash when the user controlled it recklessly and strong wind when flying outdoor. The development of automatic takeoff and landing will solve this problem when the system detect emergency or receive the automatic landing command and this will save the quadrotor from crash. When to deploy the quadrotor without automatic command, the user will be difficult to predict the lift force of quadrotor and this will consume more power of battery. The development of automatic takeoff will help new user to solve this problem. Another problem in this project is to make quadrotor maintain its stability in air. The uses of gyroscope in quadrotor will help the quadrotor microcontroller accept four output roll, pitch, yaw and throttle. This input will be process by microcontroller and generate new output for quadrotor to change the speed of quadrotor to make it stable.

3. Literature Review

In 1920 - 1930 quadrotor is already has been design and build at that time but the quadrotor is handle by a man. The quadrotor build at that time is bad performance, lack of stability and very large shape and heavy. People cannot make it unmanned at that time because there a no microcontroller, sensor and electronic control system. Nowadays many of the microcontrollers developed by manufacturer for example: Arduino, PIC18 microchip and basic stamp. All of this microcontroller can be used for making the electronic control system of quadrotor to make it unmanned.

4. Methodology

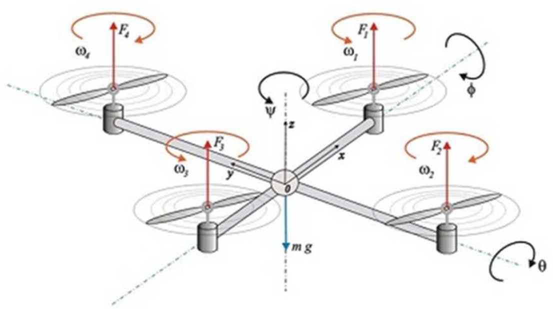

Fig. 1. Direction of propeller and free body diagram

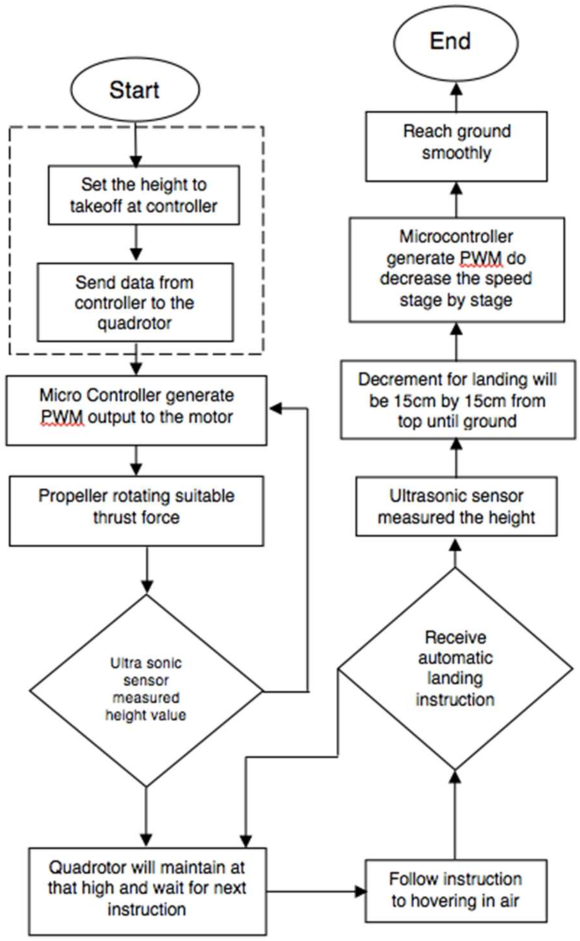

Fig. 2. Flow Chart of the works

In quadrotor front and back propeller must rotate anti-clockwise and right and left propeller must rotate clockwise as shown in Fig. 1. to eliminate torque produced by the motor (Tanveer, 2014). By have a correct orientation of propeller we can hover the quadrotor.

X, Y and Z represent the fixed body frame of quadrotor. The blue arrow is a weight of quadrotor W = mg. The red arrow in Fig. 1. show the angular speed of quadrotor. Ψ is for yaw angle, ϕ is for pitch angle and Θ is for roll angle (Warsi, 2014)(Joyo, 2014).

5. Quadrotor Control System

Closed loop control system is important during takeoff and landing of a quadrotor. Control system is important in the systems that need accuracy. Accurate value of PWM will make quadrotor fly at actual output that already set by the user. This closed loop control system is also can be used to perform smooth landing. When automatic landing button is pressed, the quadrotor will decrease the motor speed due to height level that read by ultrasonic sensor.

6. Results & Analysis

Table 1. Total mass of quadrotor

Part	Quantity	Mass(g)
Propeller	4	40
Receiver	1	12
Brushless DC motor	4	140
Electronic speed controllers	4	80
Quadrotor structure	1	500
Screw, nuts	20	80
Wiring	1.5 meter	38
Arduino board	1	30
	TOTAL	**920**

6.1 *Analysis of Quadrotor Thrust Force*

The average mass of quadrotor is 920 grams. Therefore, we need thrust force equal to quadrotor mass to lift up quadrotor. By using static thrust equation, we can estimate analytical data to make the quadrotor mass equal to thrust force. Firstly we need to find at what rpm the mass of quadrotor is equal to the thrust. Thrust must be multiply by four because quadrotor has four propellers.

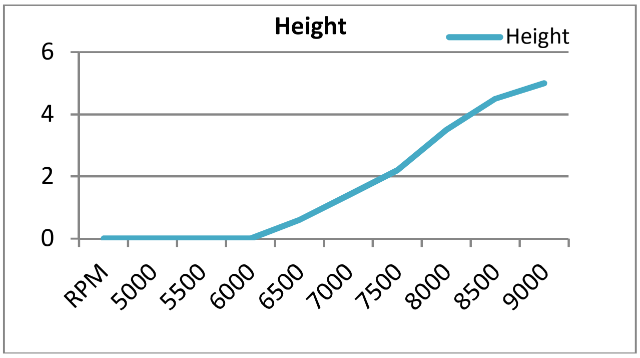

Fig. 3. Automatic takeoff graph

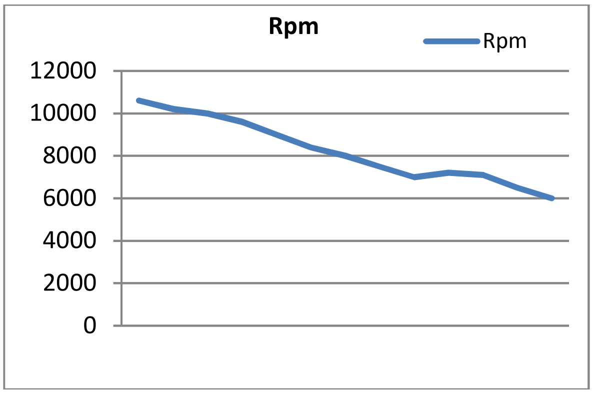

Fig. 4. Automatic smooth landing graph

6.4 *Roll, Pitch and Yaw Error*

Analysis of roll error

Performance of roll stabilization error of roll angle when quadrotor is in static condition is less than one degree. The data taken in this experiment is in 10 second. The red line is in figure below show the good stability without error that we need. The blue wave is the gyro detection in change of roll during static fly and the black wave is error of roll during static fly (M. Kamran Joyo, 2013)

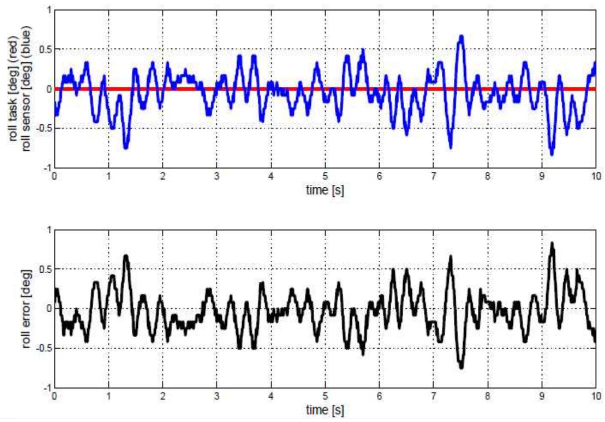

Fig. 5. Error of Roll

Analysis of pitch error

Figure below shows the performance of pitch stabilization pitch angle also less than 1 degree. The data taken in this experiment is in 10 second. The red line is in figure below show the good stability without error that we need. The blue wave is the gyro detection in change of pitch during static fly and the black wave is error of pitch during static fly.

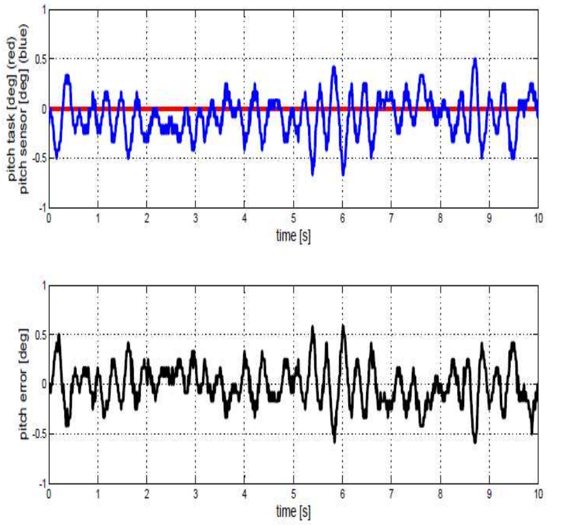

Fig. 7. Error of pitch

Error of pitch and roll must be low to make a good stabilization and the longitudinal acceleration condition. The movement of pitch and roll almost same but the different is in a different axis. Will occur if one of these two angles was different than zero degree during static.

Analysis of yaw error

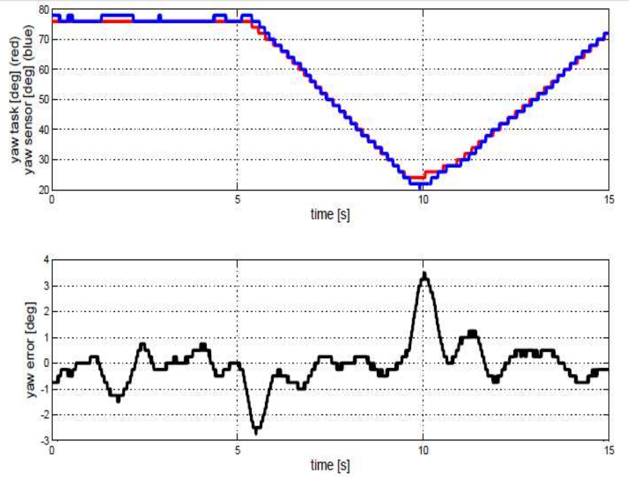

Figure below show the performance of yaw stabilization. Longitudinal acceleration does not effected by error of yaw during static condition. The change of yaw angle of quadrotor can be -90˚, 90˚, -180˚, 180˚ and high than that.

Fig. 8. Error of yaw

Error of yaw in figure above during static is less than 2 degree while when turning to another direction the yaw error become high that 2 degree and less than 4 degree.

7. Conclusion

Development of automatic takeoff and landing that move along Z-axis is look like a simple task but its require many concept such as thrust study, control system, sensor interface, stability study, PWM, and Newton second law of motion. In this paper shows the first step of development quadrotor starting from the body structure.

References

1. M. Kamran Joyo, D. Hazry, S. Faiz Ahmed, M. Hassan, “Position Controller Design for Quad-rotor under Perturbed Condition,” Journal Article, Wulfenia, volume 20, issue 7, pg. 178-179, 2013;
2. Tanveer, M. Hassan, S. Faiz Ahmed, D. Hazry, Faizan A. Warsi, and M. Kamran Joyo. "Stabilized Controller Design For Attitude And Altitude Controlling Of Quad-Rotor Under Disturbance And Noisy Conditions." American Journal of Applied Sciences 10, no. 8 (2013): 819;
3. Tanveer,M.H. Hazry, D. ; Ahmed, S.F. ; Joyo, M.K. ; Warsi, F.A. ; Kamaruddin, H. ; Razlan, Z.M. ; Wan, K. ;Shahriman, A.B. “NMPC-PID based control structure design for avoiding uncertainties in attitude and altitude tracking control of quad-rotor (UAV)” IEEE 10th International Colloquium on ;
4. Warsi, F.A. Hazry, D. ; Ahmed, S.F. ; Joyo, M.K. ; Tanveer, M.H. ; Kamarudin, H. ; Razlan, Z.M., “Yaw, Pitch and Roll controller design for fixed-wing UAV under uncertainty and perturbed condition”, IEEE 10th International Colloquium on Signal Processing & its Applications (CSPA), 2014 (pp. 151-156);
5. Joyo, M.K. Hazry, D. ; Faiz Ahmed, S. ; Tanveer, M.H. ; Warsi, F.A. ; Hussain, A.T., “Altitude and horizontal motion control of quadrotor UAV in the presence of air turbulence”, IEEE 10th International Colloquium on Signal Processing & its Applications (CSPA), 2014 (pp. 16-20);

Auto Pilot Ship Heading Angle Control Using Adaptive Control Algorithm

Abadal-Salam T. Hussain[a,b]
[a]*Center of Excellence for Unmanned Aerial Systems (CoEUAS)*
Universiti Malaysia Perlis, 01000 Kangar, Perlis, Malaysia.

Hazry D.[a]**, S. Faiz Ahmed**[a]**, Wail A. A. Alward**[b]**, Zuradzman M. Razlan**[a] **& Taha A. Taha**[b]
[a]*Centre of Excellence for Unmanned Aerial Systems (CoEUAS)*
[b]*Center of Excellence for Renewable Energy (CERE)*
Universiti Malaysia Perlis, 01000 Kangar, Perlis, Malaysia.
E-mail: abadal@unimap.edu.my, hazry@unimap.edu.my
www.unimap.edu.my

Abstract

In this paper discussed about development of an auto pilot system for ships using adaptive filter. Adaptive filter in the application of auto pilots for ships is presented for controlling the ship such that it follows its predetermined trajectory. Due to random environmental effects such as wind speed or direction and sea current, the path of the ship may alter. The objective of this research is to investigate that whether proposed system will adapts to the random changes and maintain the desired ship trajectory. The proposed auto pilot system is developed using Least Mean Square algorithm (LMS) adaptive filter. The performances of the system are analyzed based on accuracy and computational times. MATLAB Simulink model tool is used for execute the simulations of the auto pilot system for ships.

Keywords: *Autonomous Controls, Ship Heading Angle, Adaptive Controls*

1. Introduction

The history of ships, boats and sailing is spread over centuries. Ship steering control has been an essential topic for researchers for more than 95 years. Early steering control systems were based on an instrument called gyroscope, which was used to determine the direction of travel. In 1911, Elmer Sperry invented an automatic mechanism for ship steering control based on the gyroscope (Sperry, 1992).

In 1922, Minorsky published his work on automatic ship steering, which was an essential breakthrough in the field (Minsky, 1954). Later in the same year, Sperry presented the first automatic ship control system. These early autopilot for ships were entirely mechanical in nature and had a very simple process, wherein the rudder was proportional to the heading error.

Major disadvantage s of traditional controllers such as PID and PD are their inability to adjust with alterations automatically in the environmental and operating conditions. These settings had to be adjusted manually by the user which in many cases may not be completely optimal. Moreover, these obligatory setting which had to be done repeatedly were exhausting and time consuming.

1.1 *Steering Control Overview*

Fig. 1 shows a general block diagram of a ship steering control system made up of reference model, sensor system and feedback control system. The reference model receives the data on the position and speed of the ship from the DGPS (Differential Global Position System) and also receives external data provided by an operator (Deck Officer) and other data concerning the environmental conditions (height and slope of the waves and speed and direction of the wind and currents). The control system also receives information that supplied by the measurement system and determines the forces and moments which are to be supplied to the ship in accordance with the established control objective in most cases together with the reference model system. In this thesis, we will be focusing only on the course keeping characteristics of the auto pilot controller.

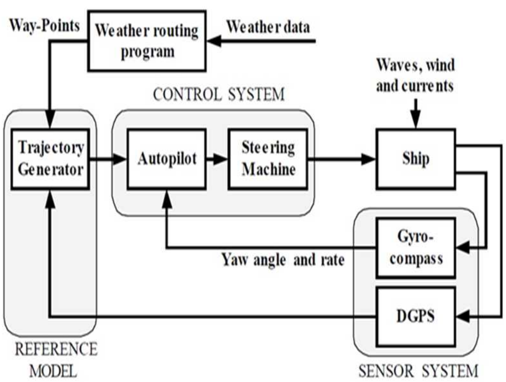

Fig. 1. Steering control

2. Modeling

2.1. *Adaptive Controllers in Auto Pilot Ship System*

Autopilot is one of the most important section used in ships. Autopilots are not just used to lead the ship on a desired trajectory, but also raise the safety level of the journey and control the ship economically. A good autopilot can help to avoid undesired situations on maneuvering and remarkably reduce the numbers of ship operators. In the last few decades, taking the advantage of drastic development of electronics and control theory, several new and effective methods have been proposed and developed for designing ship-autopilots (Barbos, 2008), (M. Kamran Joyo, 2014), (Hussain, 2011).

2.2. *Adaptive Filter*

Fig. 2 represents the general block diagram of any adaptive filter. In this application i.e. the ship steering auto-pilot is designed using an adaptive filter and completely replacing the traditional controllers.

Fig. 2. Adaptive filter

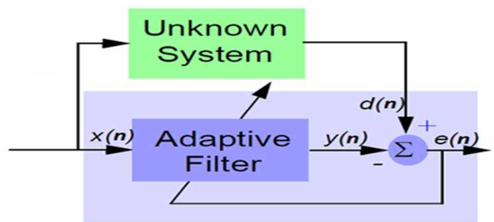

2.3 *Least Mean Square (LMS)*

The LMS algorithm was established by Widrow and Hoff in 1959. Compared to other algorithms, LMS algorithm is relatively simple; it does not require correlation function calculation nor does it require matrix inversions. This algorithm is basically the type of adaptive filter known as stochastic gradient-based algorithms and it consists of two major processes: Filtering process and adaptive process (A.T. Hussain, 2015). LMS algorithm worked on steepest decent method and also took help from the theory of Wiener solution (optimal filter tap weights). This algorithm is basically using the formulas which updates the filter coefficients by using the tap weight vectors w and also update the gradient of the cost function accordingly to the filter tap weight coefficient vector

$\nabla\xi(n)$.

$$w(n+1) = w(n) - \mu\nabla\xi(n)$$

$$w(n+1) = w(n) + \mu E\left\{e(n)x^*(n)\right\} \quad (1)$$

In practice, the value of the expectation E { } is normally unknown, therefore we need to introduces the approximation or estimated as the sample mean.

$$\hat{E}\{e(n)x^*(n)\} = \frac{1}{L}\sum_{l=0}^{L-1} e(n-l)x^*(n-l) \qquad (2)$$

With this estimate we obtain the updating weight vector as,

$$w(n+1) = w(n) + \frac{\mu}{L}\sum_{l=0}^{L-1} e(n-l)x^*(n-l) \qquad (3)$$

And finally, the weight vector update equation become the simple form.

$$w(n+1) = w(n) + \mu e(n)x^*(n) \qquad (4)$$

2.4. *Ship Dynamics & Model*

In this research, Norrbin Model of the ship is considered. This model is extension of the Nomoto's first-order model (Syed Faiz Ahmed, 2014) in an empirical way. To describe large rudder angles as well as course instability, the following model is proposed:

$$T(\ddot{\psi}) + \alpha_1\dot{\psi} + \alpha_3\dot{\psi}^3 = K\delta \qquad (5)$$

Where $\alpha_1 = +1$ for course-stable and $\alpha_1 = -1$ for course-unstable ships. Of course, this model can also be extended with a constant and a quadratic term. This yield, in the steady state, when $\ddot{\psi} = 0$

$$H_N(\dot{\psi}) = \alpha_3\dot{\psi}^3 + \alpha_2\dot{\psi}^2 + \alpha_1\dot{\psi} + \alpha_0 \qquad (6)$$

With Eq. 5 and Eq. 6 can be rewritten as:

$$T(\ddot{\psi}) + H_N(\dot{\psi}) = K\delta \qquad (7)$$

2.5 *Ships Use for Simulation Purposes*

For simulation purpose ROV Zeefakkel ship (ferry) is taken in account which is 45m ferry. The ship model of the ferry can be formed using table 1. The desired heading response is represented by the third order model of Eq 8 with am= 0.9341, bm= 0.2040 and cm= 0.0182. The maximum rudder limit selected is and the maximum rudder rate is.

$$\frac{\psi_d}{\psi_r} = \frac{c_m}{s^3 + a_m s^2 + b_m s + c_m} \qquad (8)$$

Where am, bm and cmare constants.
Van Amerongen demonstrates that the motion of this ship can be described adequately by the Norrbin's nonlinear model with the following parameter values:
When the speed of the ship changes, the values of K and T also vary as found out by Van Amerongen and illustrated in the table below:

3. Results

ROV Zeefakkel performance of LMS Adaptive Controller with Reference heading angle: 20° & 50°, Constant speed: 5m/s, Step Size = Optimal (1x10-5for LMS) and Filter Length : Larger than the optimal value and Smaller than the optimal value.

U(m/s)	*T*	*K*
1	155.0000	0.1
2	077.5000	0.2
3	051.6667	0.3
4	038.7500	0.4
5	031.0000	0.5
6	025.8333	0.6
7	022.1429	0.7
8	019.3750	0.8
9	017.2222	0.9
10	015.5000	1.0

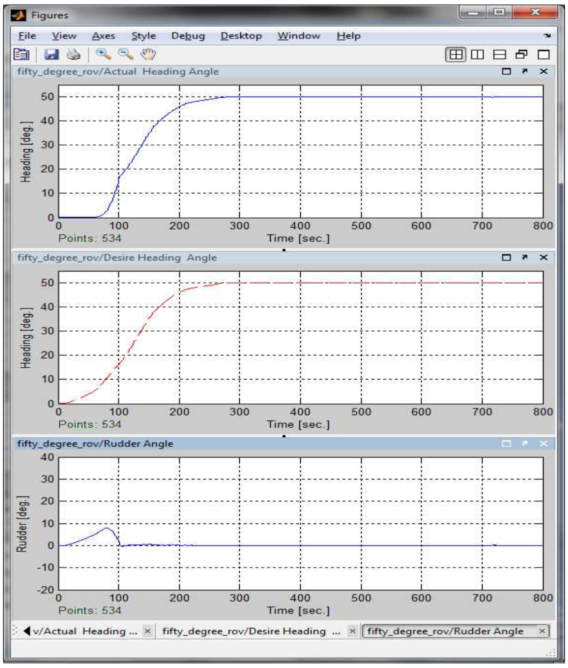

Fig.4. LMS 50° at 5m/s, μ =1x10-6, step size = 40

4. Conclusions

The LMS filter gives very good results in terms of achieving the heading angle that is desired for both 20° and 50°. It is ascertained from the simulation results that the performance of LMS algorithm is better to minimize Mean Square Error (MSE) for different heading degree angles to maintain the desired trajectory using the performance function of the algorithm that minimized the average power in the error signal. As the degree of heading angle was switched from 20° to 50°, we can observe that the filter length and step size μ has to be changed to get an optimum performance from the controller.

References

1. Sperry, E. A. (1922). Automatic steering. *Transactions, Society of Naval, Architects and Marine Engineers*, 61–63;
2. Minsky, M. L., 1954. *Theory of Neural-Analog Reinforcement Systems and Its Application to the Brain Model Problem*, PhD Thesis, Princeton, University, Princeton, NJ;
3. Barbos, M. ; Cristescu, C. , Technical Overview on Designing Wireless Remote Control Steering Mechanisms for Small Ships and Scaled Model Ships, *IEEE International Conference on Automation, Quality and Testing, Robotics*, 2008 Vol. 3, pp. 287 – 291;
4. M. Kamran Joyo, D. Hazry, S. Faiz Ahmed, M. Hassan Tanveer, Faizan. A. Warsi, A. T. Hussain, "Altitude and Horizontal Motion Control of Quadrotor UAV in the presence of Air Turbulence", Systems, Process & Control (ICSPC2), *2013 IEEE International Conference, Published at IEEE Xplore*, PP (16-20), ISBN: 978-1-4799-2208-6, (2013) ;
5. Hussain, A.T., et al.; "Real-Time Robot-Human Interaction by Tracking Hand Movement & Orientation Based on Morphology", *International Conference on Signal and Image Processing Applications (ICSIPA 2011), Published at IEEE Xplore*, PP (283-288), ISBN: 978-1-4577-0243-3, (Feb. 2012) ;
6. A.T. Hussain, S. Faiz Ahmed & D. Hazry; "Tracking and Replication of Hand Movements by Teleguided Intelligent Manipulator Robot", *Robotica*, Cambridge University Press, Vol. 33, Issue 01, Jan. 2015, pp 141-156. DOI: http://dx.doi.org/10.1017/S0263574714000083 (ISSN: 0263-5747 EISSN: 1469-8668) ;
7. Syed Faiz Ahmed, Ch. Fahad Azim, Hazry Desa, Abadal-Salam T. Hussain, "Model Predictive Controller-based, Single Phase Pulse Width Modulation (PWM) Inverter for UPS Systems", Acta Polytechnica Hungarica, *Journal of applied science* (ISSN 1785-8860), Volume 11, Issue Number 6, pp. 23-38, (2014).

Classification of Hippocampal Region using Extreme Learning Machine

Muhammad Hafiz Md Zaini, Mohd Ibrahim Shapiai
Electronic System Engineering, MJIIT, Center of Artificial Intelligence and Robotics (CAIRO), UTM,
54100 Kuala Lumpur, Malaysia

Ahmad Rithauddin Mohamed
Institut Pediatrik, Hospital Kuala Lumpur,
Jalan Pahang Kuala Lumpur, 50586 Kuala Lumpur, Malaysia

Norrima Mokhtar
Faculty of Engineering, University of Malaya,
50603 Kuala Lumpur, Malaysia

Zuwairie Ibrahim
Universiti Malaysia Pahang,
26600 Pekan, Pahang, Malaysia

E-mail: muhdhafizzaini@gmail.com, md_ibrahim83@utm.my*, drahmadrm@gmail.com, norrimamokhtar@um.edu.my, zuwairie@ump.edu.my*

Abstract

Important brain parts like hippocampal usually being manually segmented by doctors. But with the introduction of hybrid between machine learning along with neuroimaging technique, it has proved to shows some promising results regarding on segmenting subcortical structures. However, it is known that Extreme Learning Machine (ELM) is to be superior machine learning technique. This study will investigate on the usage of ELM to segment hippocampal by using various hidden nodes configuration. This study also will address on the usage of full image and region of interest (ROI) using ELM. Bag of features is used as a feature extractor where it will segment the hippocampal of the MRI in order to get its visual words. ELM will used it to learn its feature. Results shows that with suitable hidden nodes, it could achieve up to 100% performance on both cases for full image and ROI in hippocampal segmentation.

Keywords: Extreme learning machine, Hippocampal segmentation, Magnetic resonance imaging, Neuroimaging

1. Introduction

With the introduction of biomedical imaging modality, it has brings great help especially for doctors and medical expert community. Medical imaging can be defined as a modality that deliver information on the subject of the volume underneath the skin [1]. There are other biomedical imaging modalities that has been introduced such as Magnetic Resonance Imaging (MRI), Positron Emission Tomography (PET), radiography and many more to detect stroke, cancer, Alzheimer and epilepsy. However the problem arises when doctors need to make further diagnosis as it only provide raw images for them to diagnose [2]. This can be seen in the cases where doctors usually detect hippocampal manually which can consume a lot of their time and also lead to error at some point [2, 3].

Computer Aided Diagnosis (CAD) is introduced to solve this problem, whereas it can be describe by the means of the usage of machine learning and image processing to process image and interpret it in order to assist doctors and experts [4]. The process to segment subcortical structures is difficult and important task at the same time too especially in brain analysis, this is because, it is where the hippocampal is located [5]. Many research has shown that a patient’s hippocampal who is effected by Epilepsy or Alzheimer tends to become smaller in size compare to a healthy person [6]. The likes of Atlas-based Segmentation, Statistical Model and Machine Learning is the result of a research that has been done in this past years in order to segment hippocampal [6-8]. Machine learning, technique such as Structure Vector Machine (SVM) [5], radial basis [9], Artificial Neural Network (ANN) [10] has been widely used as the learning method in order to learn the structure of the hippocampal. Although it is proven that the aforementioned machine learning could achieve good result, however ELM is known to be superior in machine learning technique point of view as it offer a unified framework where the generalized decision from training data can be used to solve binary classification and predicting a scalar number for regression problem [11]. Therefore, this study will investigate on the usage of ELM to segment hippocampal by using various hidden nodes configuration with normal control from ADNI dataset as its data. Furthermore, this study also will address on the usage of full image and region of interest (ROI) using ELM. Bag of features [12] will be used as a feature extractor where it will segment the hippocampal of the MRI in order to gets its visual words. Thus, it could be feed into ELM to learn its feature.

2. Related Works

Lately, a lot of research has been done particularly in the area of segmenting subcortical structure. Technique such as Atlas selection, Statistical model and Machine learning which can be seen in Figure 1 are some of the result achieved by extensive research that have been done [5-7].

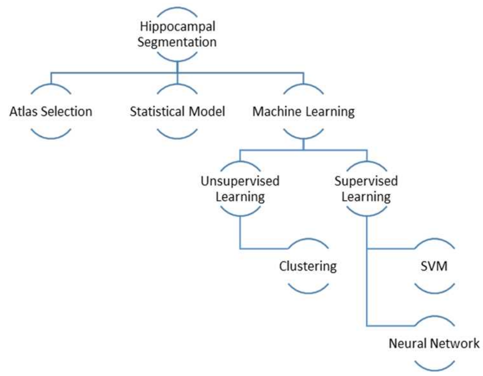

Fig. 1. Hippocampal segmentation technique

2.1. Atlas Selection, Statistical Model and Machine Learning

One of the technique that is popular among researcher is Atlas-based segmentation, where it will register atlas image to the subject image. And the result of the registered atlas will be used to map the coordinates of the structure of interest from the atlas image to the subject image [7]. Since image registration is basically the essence of an extensive variety of medical applications together with visualisation, and image guided surgery and voxel-based morphometry [6, 7]. Hence allowing Atlas-based segmentation to gain benefits from methodological advances driven by a wide range of application areas. However, it has been noted that its performance depends on the image registration accuracy and anatomical differences between the target image [5].

Another technique is statistical models. The idea of statistical model is that a priori shape information will be used as its learning set so that it could learn the variation from it and limit the search space to only acceptable instances defined by the trained model [6]. This technique is widely used among researchers as expert knowledge can be captured in the forms of training examples [13].

Machine learning is one of the method that vastly become favourite among researcher [8, 14, 15], it is used not only to segment subcortical structure but also to detect tumour [6]. Besides, it also can handle large amount of data especially in segmenting or classifying brain anatomical as it needs a lot of raw data in order to get better result [8]. However, machine learning has several limitations that could hinder its accuracy, it needs a lot of data in order to be more accurate [6], and thus a lot of experiments need to be done in order to get its optimal parameter.

2.2. SVM and neural network

The idea of SVM is that it separates the data in the future space by looking for support vectors is one of the reason of the growing interest in applying SVM in neuroimaging as it has good generalization ability [14]. Besides, it also has the capability to classify non-linearly separable data too [6]. Nevertheless, SVM also has several disadvantages that might deter the performance during classification as it is difficult to determine the optimal parameters and to understand its structure algorithm too. Apart from that, SVM also takes a lot of time for training compare to other machine learning approach [6]. Besides that, SVM also is not a sparse model since support vector tends to grows along the size of training samples [9].

Whereas ANN is a data processing technique that can be categorised by the form of architecture between connections of the neurons, its method to determine the weights on the connections which is the training or learning algorithm and its activation function [16]. Its performance depends entirely on the structure of the training set as if it is not well design it might hinder the classification result and might be resulting to overfitting too [6]. But on the hindsight, researcher still opt for ANN as it is capable for classification and regression and it is tolerant towards noise because of the ANN structure which it keeps on improving until it finds the optimal parameter. Plus, ANN can handle and classified more than one output too [6].

3. Employed Techniques

This section will briefly explain the techniques that has been employed in this study.

3.1. Spatial normalization

Spatial normalization is a step where it will transform a brain subject by establish a one-to-one correspondence between the brains by matching it to standard brain form called "template" [12]. This technique is developed mainly to simplify inter-subject comparisons by placing all subjects into a standardized stereotactic template space [17]. Spatial normalization is an important process in this research as it involves large inter-individual variability of human brain, thus with spatial normalization it helps to decrease the number of inter-individual variability and also to ease subject comparison. This permit an exploratory approach looking for group effects across the entire brain, or a hypothesis-driven approach whereby common ROIs may be utilised across all subjects, keeping away from the necessity for ROI tracing for each subjects [18].

3.2. Bag of Feature

Bag of Feature (BoF) is an approach where it represent the whole image or an ROI as a histogram occurrence quantized visual features that also known as "visual signature" of the image [12]. It is also one of the most popular method for content-based visual information retrieval (CBVIR) especially in medical field. One of the advantages of BoF is that it represent a direct identification of the features instead of their quantization, thus this approach is able to classify the intended classification whether the image represent hippocampal or not- hippocampal [12].

3.3. ELM

ELM is a supervised learning technique which is based on single-hidden layer feedforward neural networks (SLFN) [19]. The main idea of ELM is that the hidden node parameters don't need to adjust as they can be assigned with random values. Unlike conventional neural network, ELM also does not need much parameter selection which make it appropriate to be applied in neuroimaging, and ELM also fast in training with good generalisation performance too [20].

ELM can be formulated by:

$$f(x) = \sum_{i=1}^{L} \beta_i G(a_i, b_i, x) \quad (1)$$

From the formula above, a_i are the input nodes and b_i is the bias of the i^{th} , which they are defined as the learning parameters of the i^{th} hidden nodes. Whereas x is defined as the input vector with d dimensions and β_i is the output weight from the i^{th} hidden node. As for $G(a_i, b_i, x)$ is the output of i^{th} hidden node with respect to input x and G activation function. The activation function can be nonlinear continuous functions such as sigmoid, Gaussian and many more.

During training phase, hidden nodes and output nodes parameter must be determined. According to ELM theory, the hidden node parameters a_i and b_i are assigned with values randomly regardless of its nature and will remained fixed after that. But in this scenario, β_i is the only parameter that needs to be determined based on training data. In ELM, given a training data $(x_i, t_i), i = 1, \ldots, N$ where $x_i \in R^d$ and $t_i \in \{-1, +1\}$, thus in order to minimize the training error in the cost function that is formed in least square sense and given can be seen in equation (2).

$$E = \min \sum_{j=1}^{N} \left(\sum_{i=1}^{L} \beta_i G(a_i . x_j + b_i) - t_j \right)^2 \quad (2)$$

Equation 2 can be further simplified as shown in formula (3).

$$H\beta = T \quad (3)$$

$$H = \begin{bmatrix} h(x_1) \\ \vdots \\ h(x_N) \end{bmatrix},$$

$$H = \begin{bmatrix} G(a_1, b_1, x_1) & \cdots & G(a_L, b_L, x_1) \\ \vdots & \cdots & \vdots \\ G(a_1, b_1, x_N) & \cdots & G(a_L, b_L, x_N) \end{bmatrix}_{N \times L}$$

$$\beta = \begin{bmatrix} \beta_1 \\ \vdots \\ \beta_L \end{bmatrix}_{L \times 1} \text{ and } T = \begin{bmatrix} t_1 \\ \vdots \\ t_N \end{bmatrix}_{N \times 1}$$

Where H is the hidden layer output matrix of SLFN. While the i^{th} column of is the i^{th} hidden node output with respect to input $x_1, x_2, \ldots, x_N$. $h(x)$ is defined as $h(x) = [G(a, b, x), \ldots, G(a_L, b_L, x)]$ and called the hidden layer feature mapping. The i^{th} row H is the hidden layer feature mapping with i^{th} input x_i. In this case, solving the linear system in equation for β is equivalent to training the network. If the number of training samples equal to the number of hidden nodes, $L = N$ then H is a square matrix and β can be found by calculating the inverse of H where a zero training error is obtained. Thus, if L < N then it is not a square matrix and a solution can be found using Moore–Penrose generalized inverse of matrix H as given in Equation (4)

$$\beta = H^{\dagger} T \quad (4)$$

In binary classification problems, the decision function for ELM with one output node can be written in a vector form from Equation (1) and is given in Equation (5).

$$f(x) = sign\left(\sum_{i-1}^{L} \beta_i G(a_i, b_i, x) \right) = sign(\beta . h(x)) \quad (5)$$

where, β is the estimated output weight vector in equation (4) and $h(x)$ is a vector that maps the d-dimensional input space to L-dimensional hidden layer feature space.

4. Proposed Methodology

Since the objective of this study is to investigate on the usage of ELM to segment hippocampal by using various hidden nodes configuration. And also, to investigate on the usage of full image and region of interest (ROI), the overall process is being highlighted on flowchart in Figure 2.

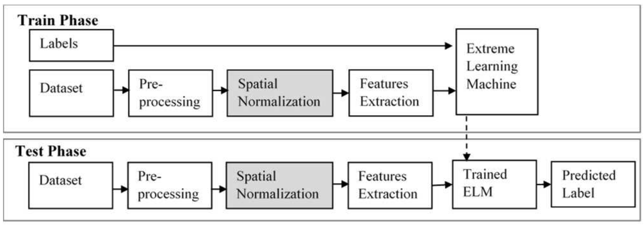

Fig. 2. Experiment methodology

The process first started with acquiring dataset from ADNI database, it can be downloaded directly from adni.loni.usc.edu website. A total of 68 MRI from Normal Control (NC) data from the ADNI1: Annual 2 Year 1.5T dataset has been downloaded from http://ida.loni.usc.edu details can be seen in table 1. Next, is the pre-process step, all of them has undergoes through spatial normalisation process that will register the MRI image into template's image. Then, the normalised image will be fed into BoF in order to get its visual words where it will be later on used as the training and testing feature for the ELM.

Table 1. Dataset descriptions

Specification	Description
Age	61 – 91 years' old
Gender	Male (11), Female (9)

4.1. Spatial Normalisation

The first step is to correct the origin of the raw MRI data, the main purpose is to reposition the crosshair position so that it would provide better normalisation result of the subject's structural MRI to the template's structural MRI which in this case, it is the MNI152 space.

Next, is to realign and reslice. Fundamentally, the function of realign and reslice is to registers all images of a subject to generate parameter files so that it can be used later on to correct for head motion. By realigning the images of the subject, it will match the image by transforming it to manipulate the scan. The realign function only allows translations by moving the image in X, Y and Z direction and rotation. After the realignment process the next step will be reslice. Reslice is a function where it will refine which images are needed as sometimes the MRI might not have the same thickness as others thus corrects its motion.

The last step of spatial normalisation is to normalise the subject's MRI to the template's MRI, so that it could put the subject's MRI into standardised MNI space. The function of this step is mainly to determine the transformation that minimises the differences between two scans by minimising the sum of squares of intensity differences. The result of the normalised MRI can be seen in Figure 3

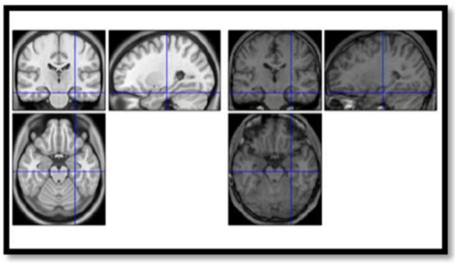

Fig. 3. Spatial normalisation result

4.2. Feature extraction using BoF

The next step is to segment hippocampal and non-hippocampal so that the segmented image can be feed into BoF to get its Visual Words. There are several steps involved in order to extract the Visual Words which are to extract its features, learn "Visual Vocabulary" and quantize features using Visual Vocabulary and lastly to represent each image by frequencies of Visual Words which can be seen in Figure 4.

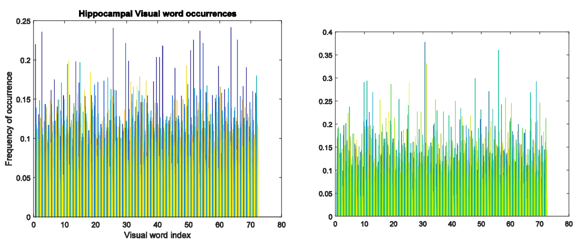

Fig. 4. Hippocampal and non-hippocampal visual word

5. Experiment, Result, and Discussion

This part will discuss on the result of the experiment that have been conducted for hippocampal classification in two experiments 1) full MRI image and 2) ROI of MRI image. 68 MRI from NC has been pre-processed using spatial normalisation technique. From the pre-processed MRI, 2-4 hippocampal from sagittal, axial and coronal has been extracted resulting to 140 extracted images of hippocampal and non-hippocampal. All of them has been fed into bag of feature in order to extract its feature vector. Both of the experiment will used 60% from the extracted images as the training sample and another 40% as testing set. Table 2 below shows the clarification on how the experiment has been setup. Whereas the parameter for both of the experiment can be seen on table 3

Table 2. Distribution dataset for training and testing

Model	Training Set	Testing Set
Full image	Training 60%: 84 feature vector	
ROI	Test 40%: 56 feature vector	

Table 3. Experiment's parameter setup

Parameter	Experiment 1	Experiment 2
Hidden Nodes	10, 30, 50, 100, 300, 500, 800, 1000, 1200, 1500	
Activation Function	Sigmoid function	
Experiment Runs	30	

As mentioned previously, two set of experiment have been conducted where the first experiment is to test on different configuration of hidden neurons for full image of MRI. The investigated hidden nodes are 10, 30, 50, 100, 300, 500, 800, 1000, 1200 and 1500 with 30 set of experiment where all of the image will be sorted by using pseudorandom method. The results for the first experiments are tabulated in Table 4.

Table 4. Experiment 1 result

Hidden	Training			
	AVG	**MIN**	**MAX**	**STD**
10	0.684325	0.619048	0.755952	0.028971
30	0.905357	0.863095	0.940476	0.022126
50	0.969048	0.952381	0.982143	0.009431
100	0.999405	0.994048	1	0.001816
300	1	1	1	0
500	1	1	1	0
800	1	1	1	0
1000	1	1	1	0
1200	1	1	1	0
1500	1	1	1	0
Hidden	**Testing**			
	AVG	**MIN**	**MAX**	**STD**
10	0.63869	0.544643	0.75	0.044719
30	0.82381	0.741071	0.883929	0.03632
50	0.892262	0.839286	0.946429	0.025463
100	0.88244	0.803571	0.928571	0.029106
300	0.971131	0.919643	0.991071	0.01718
500	0.982143	0.955357	1	0.013055
800	0.98869	0.964286	1	0.010469
1000	**0.993452**	**0.964286**	**1**	**0.008432**
1200	0.988393	0.955357	1	0.011523
1500	0.996131	0.991071	1	0.0045

From the table result above, it shows that ELM could clearly distinguish between hippocampal and non-hippocampal image where both training and testing result could achieve as high as 100%. This could be seen in bar chart below that shows the average of training and testing accuracy. When the more the number of hidden neuron is applied, the higher the accuracy will be. In this experiment 1000 hidden neurons are the optimum hidden neuron parameter for this experiment set, because the average of the testing accuracy will start to decrease a little bit when the number of hidden neuron applied is increased to 1200 but when 1500 hidden neuron is applied it started to increased back.

As for the second experiment, all of the segmented image of both hippocampal and Non-hippocampal will be classified using ROI of MRI image using similar parameters setup as given in Table 3. The results for the second experiments are tabulated in Table 5. Experiment will be setup with the same configuration as experiment 1 which can be seen in table 1 and table 2. The result can be seen on table below.

Table 5. Experiment 2 result

Hidden	Training ROI			
	AVG	**MIN**	**MAX**	**STD**
10	0.803968	0.744048	0.845238	0.026247
30	0.940476	0.89881	0.964286	0.014327
50	0.984325	0.952381	1	0.011107
100	1	1	1	0
300	1	1	1	0
500	1	1	1	0
800	1	1	1	0
1000	1	1	1	0
1200	1	1	1	0
1500	1	1	1	0
Hidden	**Test ROI**			
	AVG	**MIN**	**MAX**	**STD**
10	0.763988	0.696429	0.839286	0.034911
30	0.891071	0.848214	0.9375	0.024072
50	0.905952	0.821429	0.955357	0.035462
100	0.88006	0.794643	0.9375	0.036976
300	0.982738	0.964286	1	0.009649
500	**0.993155**	**0.973214**	**1**	**0.006062**
800	0.998214	0.991071	1	0.003632
1000	0.999405	0.991071	1	0.002265
1200	0.999702	0.991071	1	0.00163
1500	0.999702	0.991071	1	0.00163

The results of the second experiment show that it could offer a better result compare to experiment 1. This is because, the average testing accuracy in experiment 2 is higher than experiment as tabulated in Table 5. The comparison performance between experiment 1 and experiment 2 are shown in figure 5

The optimum hidden neurons for experiment 2 is 500 because after that, the testing accuracy remains the same when the number of hidden neurons applied is increased.

However, some things worth to be mention, where ELM could not give a good classification result when the parameter between hippocampal and non-hippocampal is almost the same. This could be seen in the result of Experiment 2 on hidden neurons 500 to 1500. Which in this case the testing result shows 1 of the testing is classified wrong. One of the reason that could be deducted is its visual word's is almost the same with the non-hippocampal's visual words, figure 6 shows the comparison between the classified wrong image's visual words and non-hippocampal's visual words. Aside from that, this study proves that ELM could be applied in Neuroimaging problems especially on segmenting brain subcortical problem.

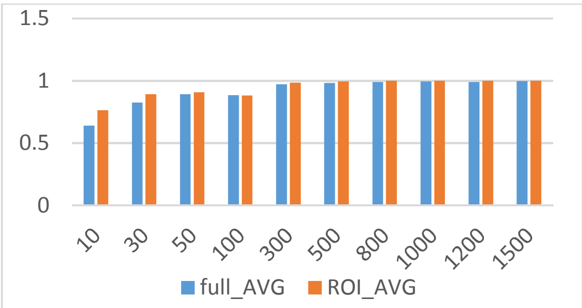

Fig. 5. Comparison test average between full image and ROI

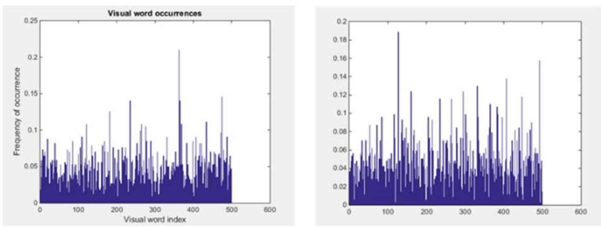

Fig. 6. Visual word occurrences between wrongly segment hippocampal and non-hippocampal

6. Conclusion

In general, ELM has been tested to two different type of hippocampal segmentation which are full image and ROI. Besides that, several hidden nodes configuration for ELM has been investigated too. From the result of experiment 1 and 2, this study could deduct that ELM could easily classify between hippocampal and non-hippocampal image this is because the result for both experiment 1 and 2 could achieve as high as 100%! Besides that, from the experiment conducted also, a hypothesis could be made, where the accuracy result is influenced by the number of hidden neurons applied. This clearly shows the ability of ELM's where it has good generalisation performance, as its only need to adjust the hidden neuron's parameter in order to increase its accuracy. For future works, ELM could be further improved into structured-ELM so that it could be experimented in more complicated problem especially regarding hippocampal segmentation problems.

Acknowledgements

The author would like to thank to Universiti Teknlogi Malaysia for financially supporting this research work through University Matching Grant, vote R.K130000.7343.4B188.

References

1. I. Bankman, *Handbook of medical image processing and analysis*: academic press, 2008.
2. M. Mizotin, J. Benois-Pineau, M. Allard, and G. Catheline, "Feature-based brain MRI retrieval for Alzheimer disease diagnosis," in *2012 19th IEEE International Conference on Image Processing*, 2012, pp. 1241-1244.
3. P. Suppa, H. Hampel, L. Spies, J. B. Fiebach, B. Dubois, and R. Buchert, "Fully automated atlas-based hippocampus volumetry for clinical routine: Validation in subjects with mild cognitive impairment from the ADNI cohort," *Journal of Alzheimer's Disease,* vol. 46, pp. 199-209, 2015.
4. C. L. Leggett and K. K. Wang, "Computer-aided diagnosis in GI endoscopy: looking into the future," *Gastrointestinal Endoscopy,* vol. 84, pp. 842-844, 2016.
5. Y. Hao, T. Wang, X. Zhang, Y. Duan, C. Yu, T. Jiang, *et al.*, "Local label learning (LLL) for subcortical structure segmentation: application to hippocampus segmentation," *Human brain mapping,* vol. 35, pp. 2674-2697, 2014.
6. J. Dolz, L. Massoptier, and M. Vermandel, "Segmentation algorithms of subcortical brain structures on MRI for radiotherapy and radiosurgery: a survey," *IRBM,* vol. 36, pp. 200-212, 2015.
7. O. T. Carmichael, H. A. Aizenstein, S. W. Davis, J. T. Becker, P. M. Thompson, C. C. Meltzer, *et al.*, "Atlas-based hippocampus segmentation in Alzheimer's disease and mild cognitive impairment," *Neuroimage,* vol. 27, pp. 979-990, 2005.
8. N. Oktar and Y. Oktar, "Machine Learning and Neuroimaging," *Journal of Neurological Sciences (Turkish),* vol. 32, pp. 001-004, 2015.
9. Y. Wang, Y. Fan, P. Bhatt, and C. Davatzikos, "High-dimensional pattern regression using machine

learning: from medical images to continuous clinical variables," *Neuroimage,* vol. 50, pp. 1519-1535, 2010.

10. M. Lai, "Deep learning for medical image segmentation," *arXiv preprint arXiv:1505.02000,* 2015.
11. Z. Bai, G.-B. Huang, D. Wang, H. Wang, and M. B. Westover, "Sparse extreme learning machine for classification," *IEEE transactions on cybernetics,* vol. 44, pp. 1858-1870, 2014.
12. O. B. Ahmed, J. Benois-Pineau, C. B. Amar, M. Allard, and G. Catheline, "Early Alzheimer disease detection with bag-of-visual-words and hybrid fusion on structural MRI," in *Content-Based Multimedia Indexing (CBMI), 2013 11th International Workshop on*, 2013, pp. 79-83.
13. T. F. Cootes and C. J. Taylor, "Statistical models of appearance for computer vision," ed: Technical report, University of Manchester, 2004.
14. J. Morra, Z. Tu, A. Toga, and P. Thompson, "Machine learning for brain image segmentation," *Biomedical Image Analysis and Machine Learning Technologies: Applications and Techniques: Applications and Techniques,* p. 102, 2009.
15. J. H. Morra, Z. Tu, L. G. Apostolova, A. E. Green, A. W. Toga, and P. M. Thompson, "Comparison of AdaBoost and support vector machines for detecting Alzheimer's disease through automated hippocampal segmentation," *IEEE transactions on medical imaging,* vol. 29, p. 30, 2010.
16. L. Fausett, *Fundamentals of neural networks: architectures, algorithms, and applications*: Prentice-Hall, Inc., 1994.
17. P. T. Fox, "Spatial normalization origins: Objectives, applications, and alternatives," *Human brain mapping,* vol. 3, pp. 161-164, 1995.
18. S. Krishnan, M. J. Slavin, T.-T. T. Tran, P. M. Doraiswamy, and J. R. Petrella, "Accuracy of spatial normalization of the hippocampus: implications for fMRI research in memory disorders," *Neuroimage,* vol. 31, pp. 560-571, 2006.
19. A. Annema, K. Hoen, and H. Wallinga, "Precision requirements for single-layer feedforward neural networks," 1994.
20. N.-Y. Liang, G.-B. Huang, P. Saratchandran, and N. Sundararajan, "A fast and accurate online sequential learning algorithm for feedforward networks," *IEEE Transactions on Neural networks,* vol. 17, pp. 1411-1423, 2006.